NATURE ENVIRONMENT & POLLUTION TECHNOLOGY

*A Multidisciplinary, International Journal
on Diverse Aspects of Environment*

Technoscience Publications
website: www.neptjournal.com

INSTRUCTIONS TO AUTHORS

Scope of the Journal

The Journal publishes original research/review papers covering almost all aspects of environment like monitoring, control and management of air, water, soil and noise pollution; solid waste management; industrial hygiene and occupational health hazards; biomedical aspects of pollution; conservation and management of resources; environmental laws and legal aspects of pollution; toxicology; radiation and recycling etc. Reports of important events, environmental news, environmental highlights and book reviews are also published in the journal.

Format of Manuscript

- The manuscript (*mss*) should be typed in double space leaving wide margins on both the sides.
- First page of mss should contain only the title of the paper, name(s) of author(s) and name and address of Organization(s) where the work has been carried out along with the affiliation of the authors.

Nature Environment and Pollution Technology
Vol. 21, No. (2), June 2022

CONTENTS

The Journal is Currently **Abstracted** and **Indexed** in:

CNKI Scholar (China National Knowledge Infrastructure)

Scopus CiteScore (2020) 0.60

Scopus®, SJR (0.154) 2020	Index Copernicus (2020) = 119.70
Chemical Abstracts, U.S.A.	Indian Science Abstracts, New Delhi, India
Pollution Abstracts, U.S.A.	Elsevier Bibliographic Databases
Paryavaran Abstract, New Delhi, India	Zoological Records
Electronic Social and Science Citation Index (ESSCI)	Indian Citation Index (ICI)
CrossRef (DOI)	EBSCO: Environment Index™
Google Scholar	DOAJ
Environment Abstract, U.S.A.	ProQuest, U.K.
WorldCat (OCLC)	British Library
Indian Science	JournalSeek
SHERPA/RoMEO	Directory of Science

CAB Abstracts, U.K.

Ulrich's (Refereed) database

Zetoc

J-Gate

Centre for Research Libraries

Connect Journals (India)

Research Bible (Japan)

Elektronische Zeitschriftenbibliothek (EZB)

CNKI Scholar (China National Knowledge Infrastructure)

AGRIS (UN-FAO)

CSA: Environmental Sciences and Pollution Management

Access to Global Online Research in Agriculture (AGORA)

Present in UGC-CARE List (Group II)

UDL-EDGE (Malaysia) Products like *i*-Journals, *i*-Focus and *i*-Future

www.neptjournal.com

Nature Environment and Pollution Technology

Geochemical Characteristics and Geological Significance of Cassiterite in the Dalong Tin Deposit, Baoshan Block, SW China

Chuanyu Zhang*(**), Wanting Li*, Haijun Yu**†, Yingxiang Lu**, Jianze Sha** and Shusheng Yang****

*Faculty of Land Resource Engineering, Kunming University of Science and Technology, Kunming, 650093, China
**MLR Key Laboratory of Sanjiang Metallogeny and Resources Exploration and Utilization, Yunnan Geological Survey, Kunming, 650051, China
***School of Earth Science, Yunnan University, Kunming, 650500, China
†Corresponding author: Haijun Yu; yhj307@163.com

ABSTRACT

The Dalong tin deposit, located in the Luziyuan polymetallic ore field of the southern Baoshan block, Southwest China, is composed of lenticular and bedded orebodies hosted in a Cambrian slate-marble sequence. As the only tin deposit in the orefield, the genesis of the Dalong deposit is of great significance to the understanding of regional metallogenic regularity. Based on a systematic field survey and petrographic observation, EPMA and LA-ICP-MS major/trace element analyses of cassiterite were carried out in this study. The enrichment of Fe, W, and Ti in cassiterite, as well as the depletion of Nb, Ta, and Mn, reveal cassiterite's features in granitic magmatic-hydrothermal deposits. The Dalong deposit can be categorized as a magmatic-hydrothermal vein-type deposit because of its sulfur isotopic properties, and the main sources of ore-forming fluid and minerals are thought to be buried intermediate-acid intrusions in the mining area's depths.

INTRODUCTION

The Baoshan block is located in the southern section of Sanjiang Tethys, where several large-giant lead-zinc polymetallic deposits (such as the Luziyuan, Hetaoping, Jinchanghe, Xiyi, Meng xing deposits) with total resources of more than 8 Mt Zn + Pb (Gao et al. 2016), as well as dozens of small- to medium-sized deposits have been discovered in recent years, making it one of the most important polymetallic mineralization areas in Southwest China (Fig. 1). The Dalong tin deposit is located in the Luziyuan ore field at the southern end of the Baoshan block, followed by Luziyuan iron-lead-zinc polymetallic deposit, Shuitoushan lead-zinc deposit, Fangyangshan copper-lead-zinc deposit, and Xiaogangou gold deposit, from the center to the periphery, showing good mineralization temperature zoning and great prospecting potential. However, as an important deposit in the orefield, research on the Dalong tin deposit is currently mainly concentrated on the geological characteristics of the deposit (Cheng et al. 2006, Xie & Liang 2018), instead of the trace elements of cassiterite & the genesis of the deposit. This has greatly restricted the understanding of metallogenetic regularity of the Luziyuan ore field and even the Baoshan block.

Cassiterite (SnO_2), the most important tin ore mineral, can form both in magmatic and hydrothermal systems over broad P-T conditions. Due to its refractory properties, cassiterite is resistant to post hydrothermal disturbances (Plimer et al. 1991, Jiang et al. 2004). Therefore, trace elements in cassiterite are taken as an indicator to fingerprint the source of ore-forming fluids and physico-chemical conditions of mineralization processes (Schneider et al. 1978, Murciego et al. 1997, Hennigh & Hutchinson 1999). In recent years, with the development of modern microanalytical techniques, the in-situ laser-ablation inductively coupled mass spectroscopy (LA-ICP-MS) has been successfully applied to determining trace element content in cassiterite (Wang et al. 2014a, Guo et al. 2018a, 2018b, Chen et al. 2019, Cheng et al. 2019, Fei et al. 2020, Liu et al. 2021, Gemmrich et al. 2021), which greatly improves the efficiency and precision of this test. In this paper, based on previous studies and combined with field geological survey and geological characteristics observation of the deposit, we carried out EPMA and LA-ICP-MS analyses on major and minor/trace elements of cassiterite in the Dalong deposit, and also make a comparison of reported sulfur isotope characteristics between Dalong deposit and other typical deposits in the Baoshan block. After these, we discussed (1) the trace elements substitution mechanism in

cassiterite; (2) the genesis of cassiterite; (3) the source of sulfur in the Dalong deposit. These results are helpful to better understand the origin of the Dalong deposit and the metallogenic mechanism of the Luziyuan orefield.

GEOLOGICAL SETTING

On the east side of the India-Eurasia collision zone is the Baoshan block (Fig. 1a). It is a distinct terrane from the Gondwana continent that formed part of the Sibumasuterrane in the Late Paleozoic (Metcalfe 2011). The Nujiang fault and the Lancangjiang fault define the western and eastern

boundaries of the Baoshan block, respectively, but the north section of it is lost in the Bijiang area due to the convergence of the two faults (Tao et al. 2010). The Gongyanghe Group formed from Neoproterozoic to Middle Cambrian constitutes the metamorphic basement of the Baoshan block, which is covered by a set of shallow to semi-deep marine clastic rocks and carbonate rocks and siliceous rocks formed from Late Cambrian to Mesozoic. The structural deformation in the region is characterized by the development of densely arranged faults and folds. The structural lines are mainly distributed in the SN, NW, and NE directions, and are generally curved toward the east. Frequent magmatic activities are dominated
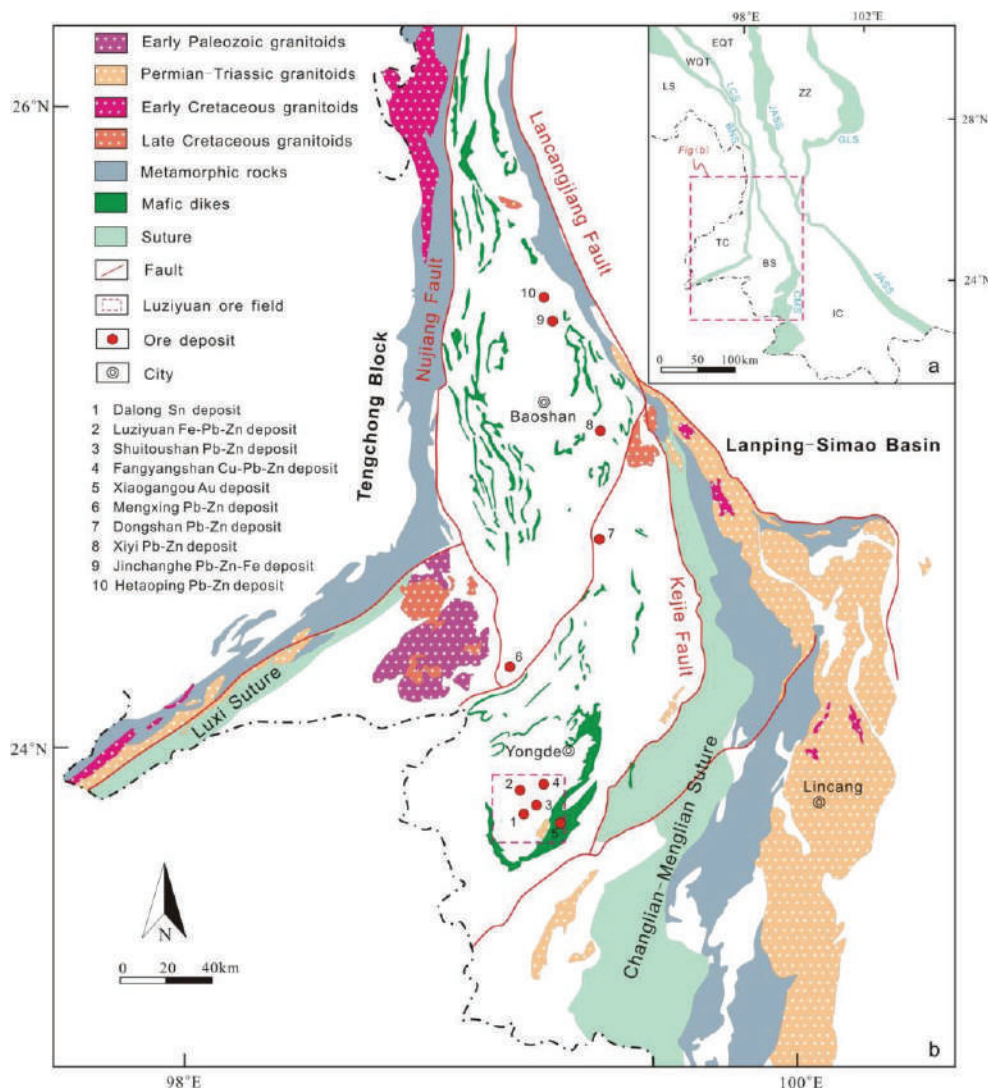
Fig. 1: **a** Tectonic setting of Baoshan block (after Deng et al. 2014, Wang et al. 2014b); **b** Geological sketch map showing the regional tectonic framework of the Baoshan block and the distribution of sedimentary and igneous units (after Deng et al. 2014, Liao et al. 2015, Li et al. 2015). BNS = Bangong - Nujiang suture, BS = Baoshan block, CMS = Changning - Menglian suture, EQT = East Qiangtang terrane, GLS = Garze - Litang suture, IC = Indochina block, LCS = Lancang suture, LS = Lhasa terrane, SC = South China block, TC = Tengchong block, WQT = West Qiangtang terrane, ZZ = Zhongza block.

by intermediate-acid intrusive rocks and are mainly concentrated in the Early Paleozoic and Mesozoic in the Baoshan block (Fig. 1b). Among them, the Early Paleozoic granites are mainly distributed in the central and southern Baoshan block, with an age range roughly between 502Ma and 448 Ma, during the unification Gondwanaland period (Chen et al. 2007, Liu et al. 2009, Dong et al. 2013), while outcrops of Mesozoic granites are mainly exposed on the edge of the Baoshan block (Muchang alkali granite: 266 ± 5.4 Ma (Ye et al. 2010); Gengma monzogranite: 232-221Ma (Nie et al. 2012); Zhibenshan granite: 127 ± 1.6Ma (Tao et al. 2010); Kejie granite: 93 ± 13Ma (Tao et al. 2010); Bangmiao granite: 83-85Ma (Dong et al. 2013).

The first, second, third, and fourth members of the Upper Cambrian Baoshan Formation, all striking NE and dipping NW are exposed strata in the Dalong mining district. The Sn orebodies are mostly found in the limestone or slate of the Baoshan Formation's later three members (Fig. 2a).

The principal fold structure in this area is the Wumulan anticline, which runs in an NNE direction and has the Dalong

deposit on its NW limb. The fault structures primarily trend NE, NW, and nearly SN. The main storage of tin ore bodies is on the NE and NW-trending faults, as well as their subsidiary EW-trending interlayer fracture zone, whereas the approximately SN-trending faults crosscut both the earlier faults and orebodies. Magmatic rocks can be scarcely found in the Dalong ore district, nevertheless, both regional gravity anomalies and airborne magnetic surveys have inferred a concealed intermediate-acid intrusion distributed within about 300km^2 in the deep of the Dalong ore district. (Jiang et al. 2013, Liang et al. 2015).

The Dalong deposit is composed of 11 tin orebodies, which are mainly struck between 240° and 290° with dip angles of 35-60º. The orebodies are generally 40 to 500m long and 0.65 to 2.65m thick (Fig. 2b). Furthermore, the orebodies are mostly stratified and locally lenticular in shape, with the characteristics of expansion, contraction, and pinching out along the strike and tendency, which are controlled by faults. The ores are mainly hosted in quartz veins, the tin grade ranges from 0.11% to 4.97%, with an average of 0.63%. Mineral assemblages are relatively simple in the
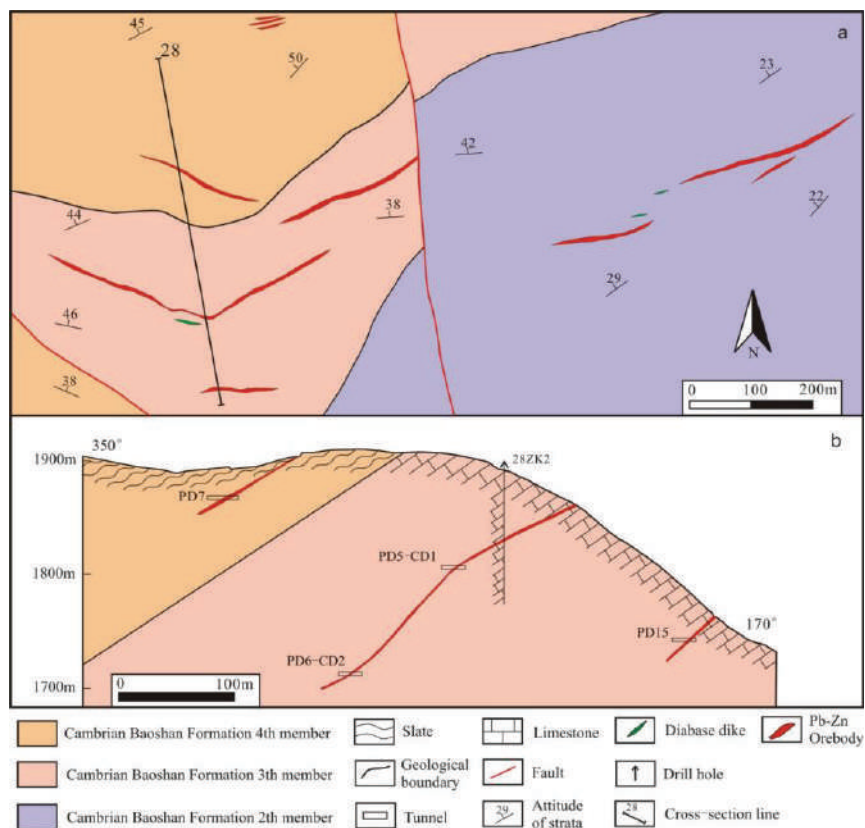
Fig. 2: **a** Geological sketch map of the Dalong deposit (modified after Cheng et al. 2006); **b** Geological section along the Number 28 exploration line in the Dalong deposit

deposit. The metallic minerals are mainly cassiterite, pyrite, chalcopyrite, arsenopyrite, limonite, with minor pyrite, tetrahedrite, sphalerite (Fig 3(a-d)), the nonmetallic minerals mainly include quartz, sericite, and calcite. The ores appear as disseminated, vein, veinlet, stockwork, or honeycomb (Fig 3b), and geodes are commonly observed (Fig 3a). The main textures of the ore include euhedral-subhedral (Fig. 3a-b), cataclastic and metasomatic residual textures. Alteration types- include silicification, pyritization, monetization, and weak sericitization.

Cassiterite in the Dalong deposit is mostly brown to dark brown and occurs in euhedral-subhedral granular aggregates coexisting with quartz (Fig 3(a-b), e). The cassiterite crystals are mainly short columnar shaped, with variable grain sizes (1-15mm in diameter), except that some grains have obvious cracks and broke into irregular shapes (Fig. 3c). Dissolution occurs on the edge of some cassiterite, mostly in a zigzag or harbor shape, and a typical zonal structure is occasionally developed in some cassiterite, suggested by alternating bright and dark rings in the cathodoluminescence (CL) images (Fig. 3f).

MATERIALS AND METHODS

Samples for this study were collected from adits in the Dalong deposit. After being separated from ore samples, large cassiterite grains with the least cracks and inclusions were chosen by hand under a binocular microscope, mounted in epoxy resin, and polished to expose the interior surface. Major compositions of cassiterite were determined by EPMA (JEOL JXA-8230) at Wuhan Sample Solution Analytical Technology Co. Ltd. The accelerating voltage was 15 kV, and the sample current was 5×10^{-8}A with a 1 μm probe diameter. In situ trace, elemental analyses were performed using an iCAPRQ ICP-MS coupled with an NWR 193nm laser, in the Guangzhou Tuoyan Testing Technology Co. Ltd. Cassiterite grains were analyzed using a laser energy density of 5J.cm^{-2}, a spot size of 50μm, and a laser pulse rate of 6Hz. Helium was used as a carrier gas and was mixed with argon via a Y-connector before entering the ICP-MS. Each spot analysis incorporated a background acquisition of approximately 50s followed by 45s of sample data acquisition. The contents of trace elements for unknown samples were corrected based on the external calibration material NISTSRM 610.
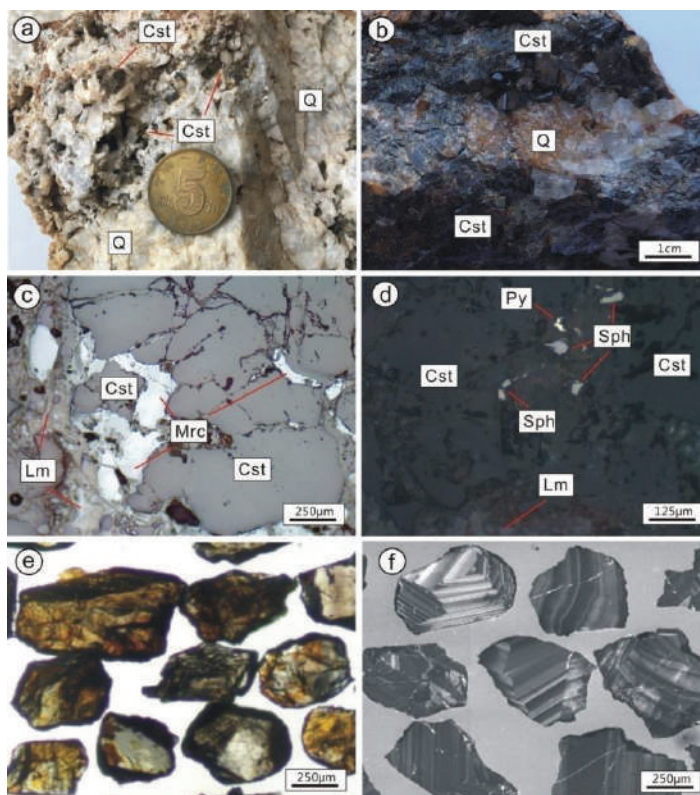
Fig. 3: The micrograph and CL image in the Dalong deposit. **a** Brown cassiterite-quartz geode in quartz vein; **b** Massive cassiterite ore. The cassiterite is dark brown, coarse-grained, euhedral, and associated with quartz; **c** Cassiterite is metasomatized by marcasite and limonite along with fractures and grain boundaries; **d** Cassiteriteis associated with pyrite and sphalerite; **e** Cassiterite grains under transmitted light; **f** The clear zonal structure in cassiterite under cathodoluminescence (CL). Cst-cassiterite; Lm-limonite; Mrc-marcasite; Py-pyrite; Sp-sphalerite; Q-quartz

RESULTS

Results of EPMA analysis of major elements in cassiterite from Dalong deposit are shown in Table 1. The content of SnO_2, FeO and TiO_2 in cassiterite is 98.32 - 100.11wt%, 0.01 - 0.08 wt %, and 0.02- 0.57 wt %, respectively, with a negative correlation between TiO_2 and SnO_2(Fig. 4a). It is suggested that Ti can enter the cassiterite crystal lattice via a simple bivalent cation substitution of $Ti^{4+} \leftrightarrow Zn^{2+}$, which

is also confirmed by the time-resolved LA-ICP-MS depth profiles observed in this study (Fig. 5). Cassiterite grains are relatively depleted in Nb (0.73-67 ppm), Ta (0-1.11ppm), Mn (0.11-8ppm), Sc (2-23 ppm), Zr (0.05-61 ppm), and Hf (0.01-5ppm), and rich in Ti (480-4299ppm), Fe (69-899 ppm) and W (640-3414ppm), revealed by in-situ LA-ICP-MS analyses (Table 2). There are clear positive correlations between Zr and Hf, Nb and Ta, V and Sc, as shown in Figure 6. The Co and Ni concentrations are usually steady in the
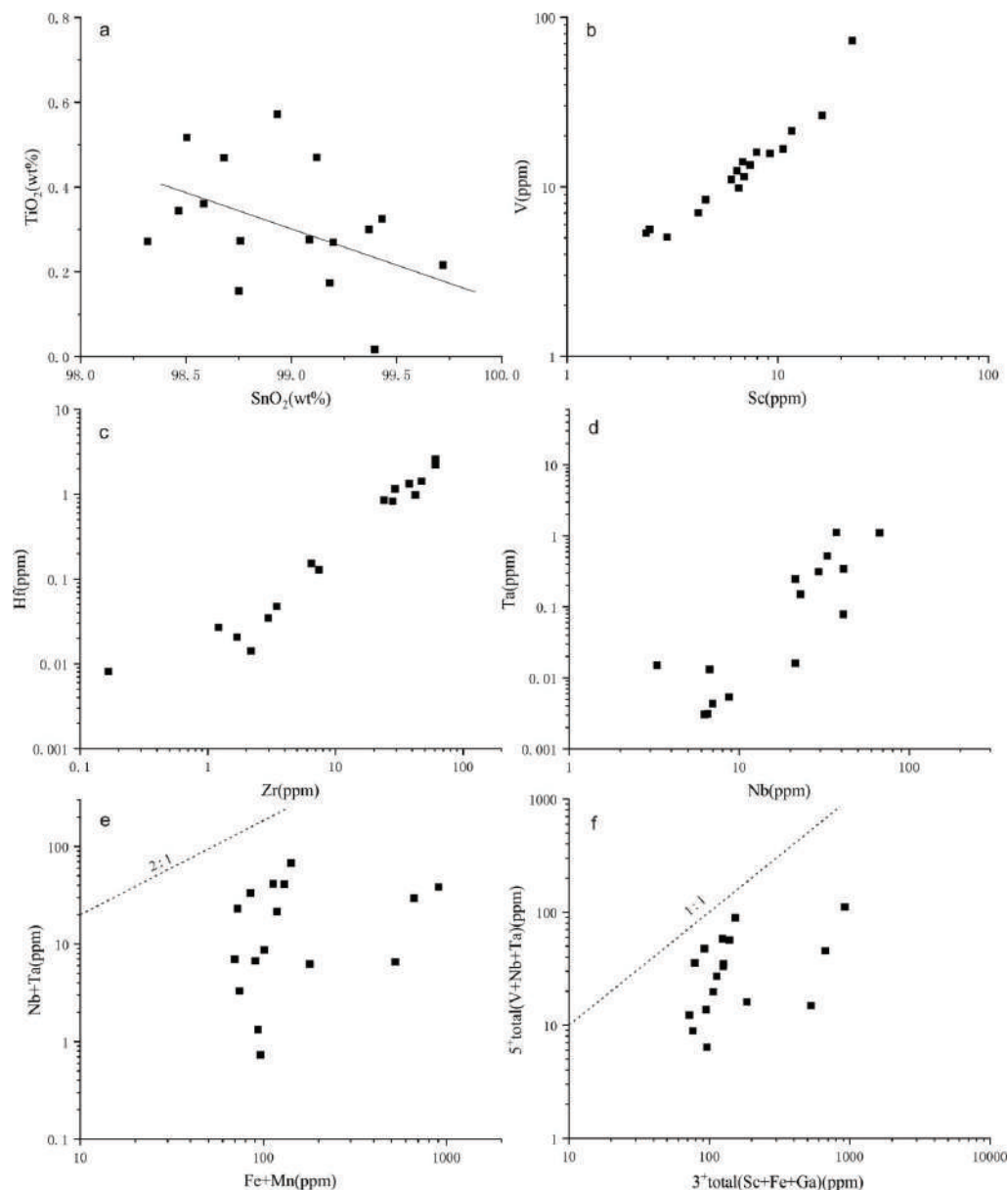
Fig. 4: Binary plots of (a) TiO_2 vs. SnO_2, (b) V vs. Sc, (c) Hf vs. Zr, (d) Ta vs. Nb, (e) Nb+Ta vs. Fe+Mn, (f) V+ Nb+Ta vs. Sc+Fe+Ga in cassiterites from the Dalong deposit.

Table 1: Major element compositions (wt.%) of cassiterite by EPMA from the Dalong deposit.

Spots	DL7-1	DL7-2	DL7-3	DL7-4	DL7-5	DL7-6	DL7-7	DL7-8	DL7-9	DL7-10	DL7-11	DL7-12	DL7-13	DL7-14	DL7-15	DL7-16	DL7-17
TiO_2	0.22	0.52	0.57	0.34	0.33	0.36	0.30	0.47	0.27	0.47	0.27	0.27	0.17	0.28	0.09	0.16	0.02
SnO_2	99.72	98.50	98.93	98.47	99.43	98.58	99.37	99.12	99.20	98.68	98.32	98.76	99.18	99.09	100.11	98.75	99.40
Nb_2O_5	0.00	0.00	0.01	0.00	0.01	0.00	0.00	0.00	0.04	0.00	0.00	0.01	0.02	0.03	0.01	0.02	0.01
ZrO_2	0.01	0.00	0.09	0.01	0.10	0.00	0.00	0.00	0.05	0.00	0.00	0.02	0.02	0.02	0.00	0.06	0.00
Al_2O_3	0.00	0.00	0.00	0.01	0.00	0.00	0.00	0.00	0.01	0.00	0.00	0.00	0.00	0.00	0.01	0.00	0.00
Cr_2O_3	0.00	0.00	0.00	0.03	0.03	0.00	0.01	0.01	0.03	0.00	0.01	0.02	0.00	0.00	0.00	0.00	0.01
MnO	0.00	0.01	0.04	0.01	0.00	0.00	0.00	0.02	0.02	0.00	0.00	0.00	0.00	0.00	0.00	0.00	0.01
FeO	0.00	0.02	0.00	0.03	0.02	0.08	0.00	0.07	0.04	0.05	0.06	0.05	0.00	0.04	0.01	0.02	0.03
HfO_2	0.00	0.00	0.10	0.04	0.00	0.00	0.03	0.00	0.06	0.01	0.00	0.00	0.00	0.05	0.00	0.04	0.00
MgO	0.01	0.01	0.01	0.01	0.01	0.00	0.01	0.00	0.01	0.00	0.04	0.00	0.02	0.00	0.00	0.00	0.02
Ta_2O_5	0.04	0.03	0.18	0.05	0.05	0.00	0.08	0.07	0.04	0.08	0.10	0.03	0.09	0.05	0.01	0.04	0.05
WO3	0.00	0.10	0.12	0.00	0.00	0.00	0.00	0.00	0.00	0.00	0.00	0.00	0.01	0.00	0.00	0.00	0.00
Total	99.99	99.20	100.06	99.01	99.98	99.02	99.81	99.76	99.77	99.28	98.79	99.15	99.52	99.55	100.24	99.09	99.55
base on 4 oxygen																	
Ti	0.008	0.020	0.021	0.013	0.012	0.014	0.011	0.018	0.010	0.018	0.010	0.010	0.007	0.010	0.003	0.006	0.001
Sn	1.991	1.977	1.968	1.982	1.982	1.985	1.986	1.979	1.983	1.980	1.985	1.987	1.990	1.986	1.995	1.990	1.996
Nb	0.000	0.000	0.000	0.000	0.000	0.000	0.000	0.000	0.001	0.000	0.000	0.000	0.001	0.001	0.000	0.001	0.000
Zr	0.000	0.000	0.002	0.000	0.002	0.000	0.000	0.000	0.001	0.000	0.000	0.000	0.000	0.000	0.000	0.002	0.000
Al	0.000	0.000	0.000	0.001	0.000	0.000	0.000	0.000	0.001	0.000	0.000	0.000	0.000	0.000	0.001	0.000	0.000
Cr	0.000	0.000	0.000	0.001	0.001	0.000	0.000	0.000	0.001	0.000	0.000	0.001	0.000	0.000	0.000	0.000	0.000
Mn	0.000	0.000	0.002	0.001	0.000	0.000	0.000	0.001	0.001	0.000	0.000	0.000	0.000	0.000	0.000	0.000	0.001
Fe	0.000	0.001	0.000	0.001	0.001	0.003	0.000	0.003	0.002	0.002	0.003	0.002	0.000	0.002	0.000	0.001	0.001
Hf	0.000	0.000	0.001	0.001	0.000	0.000	0.000	0.000	0.001	0.000	0.000	0.000	0.000	0.001	0.000	0.001	0.000
Mg	0.001	0.001	0.001	0.001	0.000	0.000	0.001	0.000	0.001	0.000	0.003	0.000	0.001	0.000	0.000	0.000	0.001
Ta	0.001	0.000	0.002	0.001	0.001	0.000	0.001	0.001	0.001	0.001	0.001	0.000	0.001	0.001	0.000	0.001	0.001
W	0.000	0.001	0.002	0.000	0.000	0.000	0.000	0.000	0.000	0.000	0.000	0.000	0.000	0.000	0.000	0.000	0.000
total	2.000	1.999	1.998	2.002	2.001	2.002	2.000	2.002	2.002	2.001	2.002	2.001	2.000	2.000	2.000	2.000	2.001
Nb+Ta	0.001	0.000	0.003	0.001	0.001	0.000	0.001	0.001	0.001	0.001	0.001	0.001	0.002	0.001	0.001	0.001	0.001
Fe+Mn	0.000	0.001	0.002	0.002	0.001	0.003	0.000	0.004	0.003	0.002	0.003	0.002	0.000	0.002	0.000	0.001	0.002

Table 2: Trace element compositions (ppm) of cassiterite by LA-ICP-MS from the Dalong deposit.

Spots	DL7-1	DL7-2	DL7-3	DL7-4	DL7-5	DL7-7	DL7-8	DL7-9	DL7-11	DL7-12	DL7-13	DL7-14	DL7-16	DL7-17	DL7-18	DL7-19	DL7-20
Sc	2.37	2.47	6.53	6.40	16.24	7.94	2.98	6.01	6.92	11.65	22.60	6.83	4.55	10.61	4.20	7.39	9.21
Ti	631	708	1853	2932	888	3263	481	1822	2436	4299	3335	3186	1268	3606	1134	2044	3456
V	5.32	5.61	9.82	12.44	26.32	16.02	5.06	11.05	11.49	21.39	72.74	14.04	8.40	16.73	7.02	13.44	15.72
Cr	0.118	0.930	0.249	0.000	0.011	0.591	0.171	0.000	0.548	1.419	5.133	0.000	0.488	0.750	0.371	0.180	0.272
Mn	0.257	0.108	0.867	0.035	0.308	2.886	0.555	0.428	0.125	0.407	8.401	0.124	0.695	0.163	0.149	0.127	0.315
Fe	69.4	73.8	178.0	72.2	96.3	662.2	92.9	100.5	118.7	141.0	898.7	85.0	523.9	113.0	90.2	118.2	129.6
Co	5.77	5.884	5.65	5.48	5.74	5.86	5.66	5.44	5.36	5.65	5.62	5.42	5.46	5.36	5.27	5.24	5.060
Ni	42.22	42.05	42.15	42.29	41.95	41.23	42.48	41.03	40.60	39.78	40.19	40.62	40.27	40.42	39.55	39.35	38.06
Cu	0.315	0.612	0.527	0.627	0.128	3.055	0.264	0.649	0.519	0.387	3.679	5.612	4.130	0.047	0.379	0.012	0.454
Zn	0.552	0.023	1.195	0.098	0.049	9.036	0.998	0.212	0.979	0.305	11.197	0.085	5.434	0.132	0.445	0.039	0.584
Ga	0.081	0.177	0.169	0.145	0.211	0.254	0.141	0.178	0.114	0.179	0.420	0.169	0.201	0.217	0.209	0.306	0.160
Rb	0.000	0.016	0.000	0.014	0.000	0.000	0.019	0.001	0.000	0.005	0.094	0.014	0.000	0.009	0.000	0.029	0.008
Sr	0.015	0.004	0.009	0.008	0.053	0.098	0.021	0.050	0.045	0.024	1.330	0.000	0.127	0.009	0.003	0.011	0.028
Zr	1.21	6.47	2.18	28.12	0.04	37.80	0.17	2.98	24.03	60.80	29.31	60.84	1.69	47.21	3.45	7.43	42.18
Hf	0.027	0.153	0.014	0.830	0.000	1.331	0.008	0.035	0.851	2.573	1.155	2.233	0.021	1.421	0.048	0.128	0.976
Ta	0.004	0.015	0.003	0.151	0.000	0.312	0.000	0.005	0.247	1.099	1.113	0.521	0.003	0.343	0.013	0.016	0.079
W	789	1795	2357	2113	2298	2591	1414	2435	1482	2793	3361	3004	2844	2636	2765	3414	2631
Nb	6.99	3.29	6.24	22.98	0.73	29.31	1.32	8.72	21.38	66.80	37.28	32.93	6.55	41.11	6.71	21.38	40.95
Mo	0.023	0.000	0.008	0.000	0.028	0.024	0.000	0.008	0.000	0.000	0.068	0.023	0.051	0.545	0.017	0.009	0.017
Cs	0.057	0.056	0.042	0.052	0.057	0.050	0.051	0.081	0.040	0.050	0.140	0.036	0.047	0.051	0.045	0.051	0.071
Ba	1.105	1.083	1.169	1.080	1.020	1.114	1.065	1.179	0.982	1.085	1.095	1.092	1.207	1.225	1.210	1.107	1.121

cassiterite samples (5-6 ppm Co, 38-42 ppm Ni), while the concentrations of other trace elements are very low (e.g., 5.61 ppm Cu, 0.42 ppm Ga, 1.33 ppm Sr, 0.55 ppm Mo, and 1.23 ppm Ba).

DISCUSSION

Distribution of Trace Elements in Cassiterite

Cassiterite has a tetragonal lattice structure similar to that of rutile, with Sn^{4+} ions in six-fold coordination with oxygen, thus can incorporate a wide range of trace elements, such as Ti, W, Fe, Ta, Nb, U, Mn, V, and Sc (Plimer et al. 1991, Murciego et al. 1997). These elements either displace Sn^{4+} in cassiterite lattice or exist as mineral inclusions (Taylor 1979). In this study, representative time-resolved LA-ICP-MS depth profiles for cassiterite are given in Fig. 5. Most of the measured elements are characterized by a smooth profile, indicating that the samples analyzed are homogeneous and absent of mineral inclusions.

Quadrivalent elements such as Zr, Hf, and Ti can substitute directly for Sn^{4+} in cassiterite without any additional charge balance considerations (Cheng et al. 2019). Nb and Ta in cassiterite exist in the form of 5^+ ions and enter into the cassiterite lattice by the reactions: $2(Ta, Nb)^{5+}+(Fe, Mn)^{2+}=3Sn^{4+}$ (1) (Möller et al. 1988). Under geological conditions, Sc only occurs in Sc^{3+} valence state, therefore, the positive correlation between V and Sc in cassiterite of the Dalong deposit (Figs. 5b) indicate that V exist as V^{5+} for a charge-balanced coupled substitution of $Sc^{3+} + V^{5+} = 2Sn^{4+}$, and this substitution ($X^{3+} + Y^{5+} = 2Sn^{4+}$ (2)) may occur in cassiterite for many elements (Cheng et al. 2019). If reactions (1) and (2) are the dominant substitution mechanisms for cassiterite, there should be a 2:1 balance between total pentavalent (Nb, Ta) and total divalent (Fe, Mn) cations, and a 1:1 balance between total trivalent (Sc, Fe, Ga) and total pentavalent (V, Nb, Ta) cations. However, in almost all cases,

there is a significant excess of trivalent cations (Fig. 4e, f), which means that an additional mechanism is required to incorporate these trivalent cations (mostly Fe^{3+}), for example, the coupled substitution: $Fe^{3+}+OH^-=Sn^{4+}+O^{2-}$, as previously proposed (Möller et al. 1988, Tindle & Breaks 1998, Pieczka et al. 2007). Zr-Hf and Nb-Ta have similar ionic radii and ionic charge, thus display similar geochemical behavior and maintain a relatively constant Zr/Hf value of 35 to 40 and an Nb/Ta value of 10 to 20 in most geological systems (Hoskin & Schaltegger 2003, Münker et al. 2003). This may be the main reason for the positive correlation between Zr and Hf as well as Nb and Ta in the Dalong cassiterite samples (Fig. 4c & 4d).

Cathodoluminescence (CL) is an effective means for revealing the complicated microtextures of minerals (Rusk a& Reed 2002). The cathodoluminescence properties of cassiterite largely depend on trace elements' content (Hall & Ribbe 1971, Farmer et al. 1991). Previous research has revealed that Ti and W work as activators, while Fe acts as a quenchant of cassiterite luminescence intensity (Farmer et al. 1991, Wille et al. 2018). Some cassiterite grains in the Dalong tin deposit have clear zonal structures of alternating bright and dark in cathodoluminescence images (Fig. 3f, Fig. 6). The TiO_2 concentration of the annulus is high in the bright band and low in the dark band, and gradually decreases from core to edge, according to electron probe microanalysis (EPMA) (except for slight fluctuations in the bright band) (Fig. 6). The substitution of Sn by Ti is easier to occur at high temperatures (Hu 1988), thus the regular variation characteristics of Ti content may reflect the gradual decrease of ore-forming temperature, and the ore-forming environment is generally relatively stable, but slightly turbulent.

Genesis of Cassiterite

Previous studies have pointed out that elements in cassiterite can be used as indicators of the formation environment
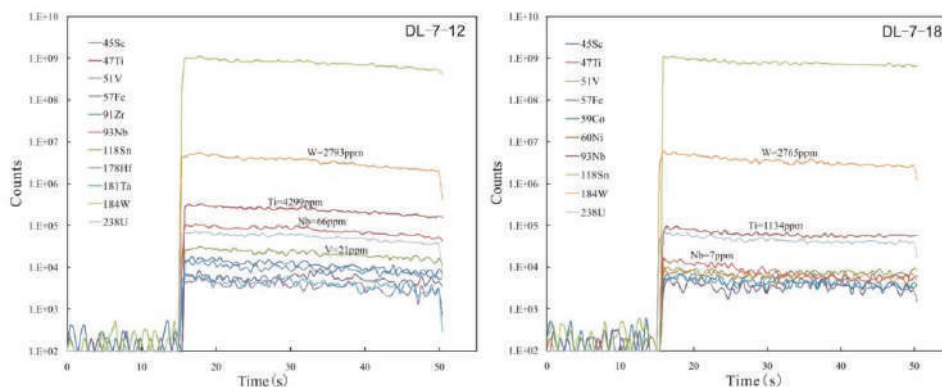
Fig. 5: Representative time-resolved LA-ICP-MS depth profiles for cassiterite from the Dalong deposit.

and ore-forming fluid composition (Schneider et al. 1978, Murciego et al. 1997, Hennigh & Hutchinson 1999). Most of the primary Tin-bearing deposits in the world are magmatic-hydrothermal origin, spatially and genetically related to highly differentiated granite (Taylor 1979, Heinrich & Eadington 1986, Hosking, 1988), and only a few occur as volcanogenic massive sulfide (VMS) deposits or sedimentary-exhalative (SEDEX) deposits, eg., Neves Corvo Cu-Sn VMS deposit (Oliveira et al. 1997), Kidd Creek Cu-Zn-Ag-(Sn) VMS deposit (Hennigh & Hutchinson 1999), and Sullivan Fe-Pb-Zn-(Sn) SEDEX deposit (Hamilton et al. 1982). Cassiterites from granite-related tin deposits display variable colors, while those from SEDEX or VMS deposits are generally colorless (Guo et al. 2018a). In a magmatic-hydrothermal system, the crystallization differentiation of magma will enrich the incompatible elements such as W and Zr in the residual melt, and W can be incorporated into cassiterite by isomorphism or as mineral inclusions, resulting in an increase in the W content of cassiterite in granite-related deposits (Guo et al. 2018b). As for the process of submarine exhalation sedimentation is characterized by low temperature and reduction environment. Under such conditions, the Fe^{2+} is easy to combine with S to form sulfides instead of oxides, leading to low Fe content of cassiterite in the submarine hydrothermal system (Pavlovaer al. 2015). Therefore, cassiterite from granite-related deposits generally contains a larger amount of Fe and W, compared to those from SEDEX/VMS deposits, which provides a method to effectively distinguish the genesis of tin mineralization of these two types. Cassiterites from the Dalong deposit have considerable W contents and relatively high Fe contents and

are all plotted in the granite-related tin deposits area in the Fe-W discriminant diagram (Fig. 7a). Cassiterite created in high-temperature systems, such as granites and rare-element pegmatites, is thought to have low Fe and Mn contents and high Nb and Ta contents, as opposed to cassiterite formed in low-temperature hydrothermal environments (Taylor 1979, Tindle & Breaks 1998). Based on this, an Nb-Ta vs Fe-Mn diagram (Fig. 7b) is proposed to trace the genesis of cassiterite (Tindle & Breaks 1998). In this diagram, our data of cassiterite are distributed in the area of the epithermal and hydrothermal deposits, suggesting a magmatic-hydrothermal origin. Furthermore, Chen et al. (2000) put forward that the Mn content of cassiterite decreases significantly with the addition of external hydrothermal fluid, thus, the depletion of Mn in cassiterite from the Dalong deposit may imply the addition of low-temperature fluids during mineralization.

Sources of Sulfur

Sulfur isotopic characteristics can define the formation environment of sulfide and the source of sulfur, which play an important role in inferring the source and forming process of ore deposits (Hoefs 1987, Ohmoto 1997). The $\delta^{34}S$ values of sulfides in the Dalong deposit ($\delta^{34}S$ = 6.88 -10.04) (Xie & Liang 2018), similar to those in Luziyuan deposit ($\delta^{34}S$ = 8.9 - 14.2 ‰) (Xu et al. 2019, Yang et al. 2019), Shuitoushan deposit ($\delta^{34}S$ = 4.1 - 12.2 ‰) (Deng et al. 2017, Zhang et al. 2021), Fangyangshan deposit ($\delta^{34}S$ = 8.24 -14.91) (Xu et al. 2021), Jinchanghe deposit ($\delta^{34}S$ = 2.5 - 11.1‰ (Huang 2014, Li et al. 2019), and Hetaoping deposit ($\delta^{34}S$ = 3.7 - 7.1‰, Chen et al. 2017) in the Baoshan block, range between those of the granite-derived sulfur ($\delta^{34}S$ = −4.0 ~ 9.0‰) (Hoefs
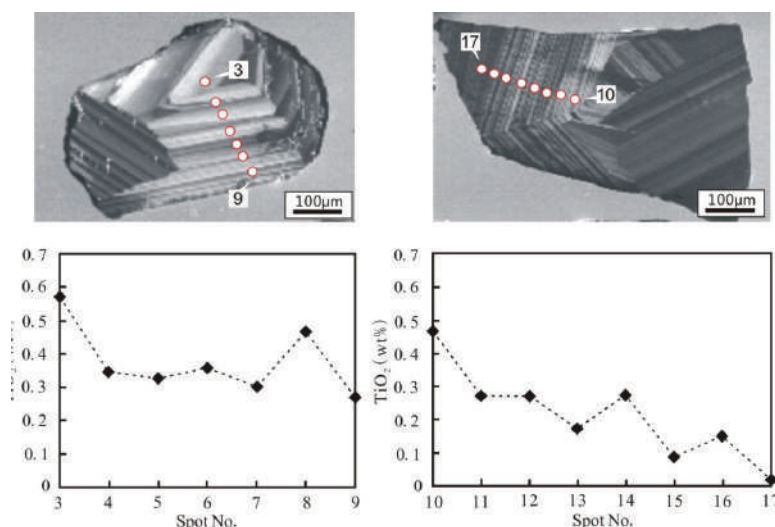
Fig. 6: The zonal structure in the CL image and the compositional variation of cassiterites from the Dalong deposit.
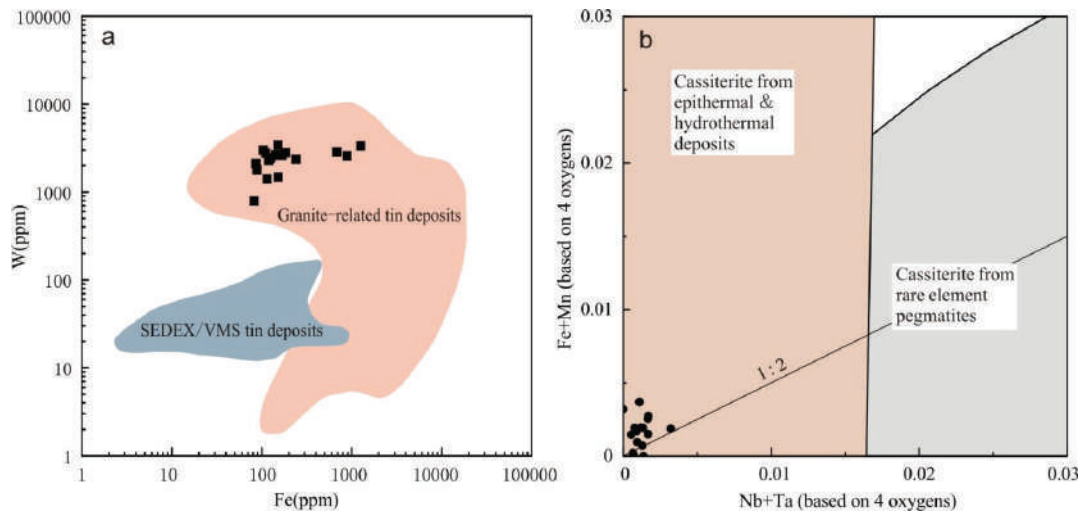
Fig. 7: a. Binary plot of Fe versus W contents in cassiterite from the Dalong deposit (modified from Hennigh & Hutchinson, 1999, Guo et al. 2018a);
b. Covariation plot of Nb+Ta with Fe+Mn in cassiterite grains from the Dalong deposit (EPMA data) (modified from Tindle & Breaks 1998,
Tan et al. 2018).

1987) and the Cambrian-Triassic seawater sulfate (δ^{34}S =15.0 ~ 35.0‰) (Claypool et al. 1980) (Fig. 8), suggesting a mixture source of sulfur (Ohmoto 1997). As it is reported that regional concealed intermediate-acid intrusions have been detected at depth under these deposits (reported by Chen et al. 2017, Huang 2014, Liang et al. 2015), a mixed source of sulfur for the Dalong deposit is proposed in this paper, which is initially derived from granite and gradually interfused by seawater during mineralization.

Deposit Type

The orebodies of the Dalong deposit are hosted in calcareous slate, banded micrite limestone, and structural breccia of Upper Cambrian Baoshan formation in vein and lenticular shape, and are strictly controlled by structures. The formation of the deposit is later than the host rock, and the boundary of them is clear, showing typical epigenetic metallogenic characteristics. The mineral composition is simple, mainly composed of cassiterite, pyrite, chalcopyrite, arsenopyrite, quartz, and calcite, associated with correspondingly weak mid-low temperature hydrothermal alterations, such as silicification, pyritization, and sericitization. These geological features are similar to those of typical hydrothermal vein-type tin deposits (Taylor 1979, Hosking 1988, Jiang et al. 2020), suggesting a hydrothermal genesis of the Dalong tin deposit. As discussed above, the trace element composition of cassiterite in Dadong deposits is consistent with that in magmatic-hydrothermal deposits, instead of SEDEX/VMS deposits. The low Mn content of cassiterite and relatively high δ^{34}S of sulfides indicate that the ore-forming materials originated from deep intermediate-acid intrusions, and maybe

gradually interfused by seawater during mineralization. In summary, combined with the geological characteristics of the deposit, the trace element composition of cassiterite, and the sulfur isotope geochemistry of sulfides, the Dagong deposit is supposed to be a magmatic-hydrothermal vein-type tin deposit.

CONCLUSION

(1) The cassiterite is enriched in Fe, W, and Ti, and deplet-
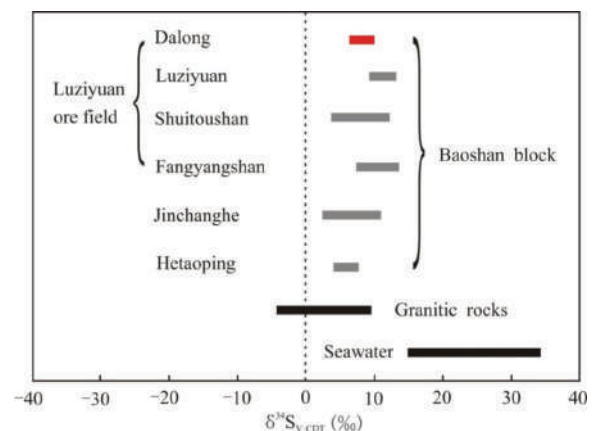
Fig. 8: The sulfur δ^{34}S values of ore deposits in the Baoshan Block. Data for Dalong deposit are from (Xie & Liang 2018); data for Luziyuan deposit are from (Xu et al. 2019, Yang et al. 2019); data for Shuitoushan deposit are from (Deng et al. 2017, Zhang et al. 2021); data for Fangyangshan deposit are from (Chen 2019); data for Jingchanghe deposit are from (Huang 2014, Li et al. 2019); data for Hetaoping deposit are from (Chen et al. 2017); data for granitic rocks are from (Hoefs 1987); data for seawater are from (Claypool et al. 1980).

ed in Nb, Ta, and Mn, which indicate that the Dalong deposit was formed in a granite-related magmatic-hydrothermal system.

(2) The similar sulfur isotopic characteristics of the Dalong tin deposit and the Luziyuan, Shuitoushan, and Fangyangshan deposits in the Luziyuan ore field indicate that they have similar sources of sulfur, which is originally derived from the concealed intermediate-acid intrusions in deep and then mixed by seawater during mineralization.

(3) The Dalong tin deposit belongs to a magmatic-hydrothermal vein-type deposit in genesis. The concealed intermediate-acid intrusions provide the most important ore-forming fluid and metallogenic materials for mineralization.

REFERENCES

Chen, F., Deng, J., Shu, Q., Li, G., Cui, X., Zhao, F. and Wang, Q. 2017. Geology, fluid inclusion, and stable isotopes (O, S) of the Hetaoping distal skarn Zn-Pb deposit, northern Baoshan block, SW China. Ore Geol. Rev., 90: 913-927.

Chen, F., Li, X., Wang, X., Li, Q. and Siebel W. 2007. Zircon age and Nd – Hf isotopic composition of the Yunnan Tethyan belt, Southwestern China. Int. J. Earth Sci., 96(6): 1179-1194.

Chen, J., Wang, R.C., Zhou, J.P. and Ji, J.F. 2000. The geochemistry of Tin. Nanjing University Press, Nanjing, pp 1-320 (in Chinese with English abstract)

Chen, L., Ni, P., Dai, B., Li, W., Chi, Z. and Pan J. 2019. The genetic association between Quartz Vein- and Greisen-Type mineralization at the Mapping W – Sn deposit, Southern Jiangxi, China: Insights from zircon and cassiterite U – Pb ages and cassiterite trace element composition. Minerals, 9(7): 411.

Cheng, H.L., Xiang, H.L. and Yang, S. 2006. Geological characteristics of Dalong tin polymetallic deposit in Yunnan and its exploration prospective. Mineral Resour. Geol., 03: 255-259 (in Chinese with English abstract)

Cheng, Y., Spandler, C., Kemp, A., Jingwen, M.J., Rusk, B., Hu, Y. and Blake, K. 2019. Controls on cassiterite (SnO2) crystallization; evidence from cathodoluminescence, trace-element chemistry, and geochronology at the Gejiu tin district. Am. Mineral., 104(1): 118-129

Claypool, G.E., Holser, W.T., Kaplan, I.R., Sakai, H. and Zak, I. 1980. The age curves of sulfur and oxygen isotopes in marine sulfate and their mutual interpretation. Chem. Geol., 28: 199-260.

Deng, J., Wang, Q., Li, G. and Santosh, M. 2014. Cenozoic tectonic-magmatic and metallogenic processes in the Sanjiang region, Southwestern China. Earth Sci. Rev., 138: 268-299.

Deng, M.G, Zhao, J.X., Liu, F.X., Yu, H.J. and Sun, B.D. 2017. Discussion on sources of metallogenic fluids and materials of the Shuitoushan Pb-Zn deposit in Zhenkang, western Yunnan: Evidence from H, O, S and Pb isotopes. Acta Petrol. Sin., 33: 2001-2017. (in Chinese with English abstract)

Dong, M., Dong, G., Mo, X., Santosh, M., Zhu, D., Yu, J., Nie, F. and Hu, Z. 2013. Geochemistry, zircon U – Pb geochronology and Hf isotopes of granites in the Baoshan Block, western Yunnan: Implications for early paleozoic evolution along the Gondwana margin. Lithos, 179: 36-47.

Farmer, C.B., Searl, A. and Halls, C. 1991. Cathodoluminescence and growth of cassiterite in the composite lodes at South Crofty Mine, Cornwall, England. Mineral. Mag., 55(380): 447-458.

Fei, G.C., Menuge, J., Li, Y.Q., Yang, J.Y., Deng Y., Chen, C.S., Yang, Y.F., Yang, Z., Qin, L.Y., Zheng, L. and Tang, W.C. 2020. Petrogenesis of the Lijiagou spodumene pegmatites in Songpan-Garze Fold Belt, West Sichuan, China: Evidence from geochemistry, zircon, cassiterite, and coltan U-Pb geochronology and Hf isotopic compositions. Lithos, 364-365.

Gemmrich, L., Torró L., Melgarejo, J.C., Laurent, O., Vallance, J., Chelle-Michou, C. and Sempere, T.P.A. 2021. Trace element composition and U-Pb ages of cassiterite from the Bolivian tin belt, Mineralium Deposita. HAL Open Sci., 36: 1-64.

Guo, J., Zhang, R., Li, C., Sun, W., Hu, Y., Kang, D. and Wu, J. 2018a. The genesis of the Gaosong Sn–Cu deposit, Gejiu district, SW China: Constraints from in situ LA-ICP-MS cassiterite U – Pb dating and trace element fingerprinting, Ore Geol. Rev., 92: 627-642.

Guo, J., Zhang, R., Sun, W., Ling, M., Hu, Y., Wu, K., Luo, M. and Zhang, L. 2018b, Genesis of tin-dominant polymetallic deposits in the Dachang district, South China: Insights from cassiterite U – Pb ages and trace element compositions. Ore Geol. Rev., 95: 863-879.

Hall, M.R. and Ribbe, P.H. 1971. An electron microprobe study of luminescence centers in cassiterite. Am. Mineral., 56: 31-45.

Hamilton, J.M., Bishop, D.T., Morris, H.C. and Owens, O.E. 1982. Geology of the Sullivan Orebody, Kimberley, B.C., Canada,

Hennigh, Q. and Hutchinson R. 1999. Cassiterite at Kidd Creek: An example of volcanogenic massive sulfide-hosted tin mineralization. Econ. Geol., 61: 431-440.

Hoefs, J.S. (ed). 1987. Stable isotope geochemistry. 3rd edition. Spring Verlag, Berlin, Germany, pp.1-250.

Hoskin, P.W.O. and Schaltegger, U. 2003, The composition of zircon and igneous and metamorphic petrogenesis. Rev. Mineral. Geochem., 53(1): 27-62.

Hosking, K. (ed). 1988. The World's Major Types of Tin Deposit: Geology of Tin Deposits in Asia and the Pacific,

Hu, Z.N. 1988. Typomorphic characteristics of cassiterite in the Yunlong Tin Deposit, Yunnan Province. Acta Mineral. Sin., (04): 381-384 (in Chinese with English abstract)

Huang, H. 2014. The Research on Geological Characteristics and Metallogenesis of the Jinchanghe Fe-Cu-Pb-Zn Polymetallic Deposit, Yunnan Province. China University of Geosciences, Beijing, pp.1-95 (in Chinese with English abstract)

Jiang, C.X., Lu, Y.X., Chen, Y.Q., Yang, S.S., Zhou, D. and Yu, H.J. 2013. Metallogenic model and integrated prospecting pattern of the Luziyuan Pb-Zn polymetallic deposit, southwestern Yunnan Province. Geol. Bull. China, 32(11): 1832–1844.

Jiang, S., Yu, J. and Lu, J. 2004. Trace and rare-earth element geochemistry in tourmaline and cassiterite from the Yunlong tin deposit, Yunnan, China: implication for migmatitic–hydrothermal fluid evolution and ore genesis. Chem. Geol., 209(3-4): 193-213.

Jiang, S.Y., Zhao, K.D., Jiang, H., Su H.M., Xiong S.F. 2020, Spatiotemporal distribution, geological characteristics and metallogenic mechanism of tungsten and tin deposits in China: An overview, Chin Sci Bull, 65(33): 3730-3745 (in Chinese with English abstract)

Li, G., Wang, Q., Huang, Y., Chen, F. and Dong P. 2015. Discovery of Hadean–Mesoarchean crustal materials in the northern Sibumasu block and its significance for Gondwana reconstruction. Precamb. Res., 271: 118-137.

Li, Z.H., Liu, X.L., Chen, J.H., Luo, Y., Zhang, C.Z. and Wang, S.S. 2019. S-Pb isotopic characteristics of Jinchanghe iron-copper-lead-zinc polymetallic deposit in Baoshan City, Yunnan province. J. Geomech., 25(S1): 115-118 (in Chinese with English abstract)

Liang, S., Jiao, Y. and Guo J. 2015. Prediction of hidden granites in the Luziyuan Area of Yunnan Province and the prospecting direction. Acta Geol. Sin., 89(5): 1781-1782.

Liao, S.Y., Wang, D., Tang Y., Yin F., Cao, S., Wang, L., Wang, B. and Sun, Z. 2015. Late Paleozoic Woniusi basaltic province from Sibumasu terrane: Implications for the breakup of eastern Gondwana's northern margin.. Geol. Soc. Am. Bull., 127(9-10): 1313-1330.

Liu, S., Hu, R., Gao, S., Feng, C., Huang, Z., Lai, S., Yuan, H., Liu, X., Coulson, I.M., Feng, G., Wang, T. and Qi, Y. 2009. U–Pb zircon, geochemical and Sr–Nd–Hf isotopic constraints on the age and origin of early Palaeozoic I-type granite from the Tengchong–Baoshan Block, Western Yunnan Province, SW China. J. Asian Earth Sci., 36(2): 168-182.

Liu, S., Liu, Y., Ye, L., Wei, C., Cai, Y. and Chen, W. 2021. The genesis of Dulong Sn-Zn-in polymetallic deposit in Yunnan Province, South China: Insights from cassiterite U-Pb ages and trace element compositions. Minerals, 11(2): 199.

Metcalfe, I. 2011. Gondwana dispersion and Asian accretion: Tectonic and palaeogeographic evolution of eastern Tethys. J. Asian Earth Sci., 66: 1-33.

Möller, P., Dulski, P., Szacki, W., Malow, G. and Riedel, E. 1988. Substitution of tin in cassiterite by tantalum, niobium, tungsten, iron and manganese. Geochim. Et Cosmoch. Acta, 52(6): 1497-1503.

Münker, C., Pfänder, J.A., Weyer, S., Büchl, A., Kleine, T. and Mezger, K. 2003. Evolution of planetary cores and the earth-moon system from Nb/Ta systematics. Sci. Am. Assoc. Adv. Sci., 301(5629): 84-87.

Murciego, A., Garcla Sanchez, A., Dusausoy, Y., Martin Pozas, J.M. and Ruck R. 1997. Geochemistry and EPR of cassiterites from the Iberian Hercynian Massif. Mineral. Mag., 61(406): 357-365.

Nie, F., Dong, G.C., Mo, X.X., Zhu, D.C., Dong, M.L. and Wang, X. 2012. Geochemistry, zircon U-Pb chronology of the Triassic granites in the Changning-Menglian suture zone and their implications. Acta Petrol. Sin., 28: 1465-1476 (in Chinese with English abstract)

Ohmoto, H.G.M.B.. 1997. Sulfur and Carbon Isotopes[A]. In: Barnes, H. L. (ed.), Geochemistry of Hydrothermal Ore Deposits[C]. 3rd Edition. John Wiley and Sons., New York, pp. 65-112.

Oliveira, J.T., Pacheco, N., Carvalho, P. and Ferreira A. (eds.). 1997. The Neves Corvo Mine and the Paleozoic Geology of Southwest Portugal: In Barriga, F.J.A.S. and Carvalho, D. (eds.), Geology and VMS Deposits on the Iberian Pyrite Belt. Society of Economics Geologists, Lisbon, pp. 422-436.

Pavlova, G.G., Palessky, S.V., Borisenko, A.S., Vladimirov, A.G., Seifert, T. and Phan, L.A. 2015. Indium in cassiterite and ores of tin deposits. Ore Geol. Rev., 66: 99-113.

Pieczka, A., Gołębiowska B. and Parafiniuk, J. 2007. Geochemistry and origin of the cassiterite from Rędziny, Lower Silesia, Poland. Mineralogia, 38(2): 219-230.

Plimer, I.R., Lu, J. and Kleeman, J.D. 1991. Trace and rare earth elements in cassiterite sources of components for the tin deposits of the Mole Granite, Australia. Mineral. Dep., 26(4): 73.

Rusk, B. and Reed, M. 2002. Scanning electron microscope-cathodoluminescence analysis of quartz reveals complex growth histories in veins from the Butte porphyry copper deposit, Montana. Geology, 30(8): 727-730.

Schneider, H.J., Dulski, P., Luck, J.M., Ller, P. and Villalpando, A. 1978. Correlation of trace element distribution in cassiterites and geotectonic position of their deposits in Bolivia. Mineral. Dep. 13(1): 54-65.

Tan, S.C., Guo, X.Y., He, X.H. and Xie, Z.P. 2018. Mineral chemical characteristics and genesis of cassiterite in Gejiu Tin-Polymetallic deposit, Yunnan Province. J. Jilin Univ. Earth Sci. Edn., 48(03): 736-753 (in Chinese with English abstract)

Tao, Y., Hu, R.Z., Zhu, F. L., Ma, Y. S., Ye, L. and Cheng, Z.T. (2010). Ore-forming age and the geodynamic background of the Hetaoping lead-zinc deposit in Baoshan, Yunnan. Acta Petrol. Sin., 26: 1760-1772 (in Chinese with English abstract)

Taylor, R.G. (ed.). 1979. Geology of Tin Deposits. Elsevier Scientific Pub. Co, New York.

Tindle A.G. and Breaks, F.W. 1998. Oxide minerals from the Separation Rapids rare-element granitic pegmatite group, Northwestern Ontario. Canad. Mineral., 36(2): 609-635.

Wang, Q., Deng, J., Li, C., Li, G., Yu, L. and Qiao, L. 2014a. The boundary between the Simao and Yangtze blocks and their locations in Gondwana and Rodinia: Constraints from detrital and inherited zircons. Gondwana Res., 26(2): 438-448.

Wang, Z.Q., Chen, B. and Ma, X. H. 2014b. In situ LA-ICP-MS U-Pb age and geochemical data of cassiterite of the Furong tin deposit, the Nanling Range: Implications for the origin and evolution of the ore-forming fluid, China Sci. Bull., 59(25): 2505-2519 (in Chinese with English abstract)

Xie, J.M. and Liang, Q. L. 2018. Study on geological characteristics and prospecting indicator of Dalong Sn mining area in Yunnan Province. China Metal Bull., (09): 34-35. (in Chinese)

Xu, R., Chen, W., Deng, M., Li, W., Chen, F., Lai, C., Sha, J., Jia, Z. and Liu, W. 2021. Geology and C-O-S-Pb isotopes of the Fangyangshan Cu-Pb-Zn deposit in the Baoshan block (SW China): Implications for metal source and ore genesis. Ore Geol. Rev., 132: 103992.

Xu R., Li, W., Deng, M., Zhou, J., Ren, T. and Yu, H. 2019. The genesis of the superlargeLuziyuan Zn-Pb-Fe(-Cu) distal skarn deposit in western Yunnan (SW China): Insights from ore geology and C-H-O-S isotopes. Ore Geol. Rev., 107: 944-959.

Yang, Y., Ye, L., Bao, T., Gao, W. and Li, Z. 2019. Mineralization of Luziyuan Pb–Zn skarn deposit, Baoshan, Yunnan Province, SW China: evidence from petrography, fluid inclusions, and stable isotopes. Geol. Mag., 156(4): 639-658.

Ye, L., Gao, W., Cheng, Z., Yang, Y. and Tao Y. 2010. LA-ICP-MS Zircon U-Pb geochronology and petrology of the Muchang Alkali Granite, Zhenkang County, Western Yunnan Province, China. Acta Geol. Sin., 84(6): 1488-1499.

Zhang, C.Y., Li, W.C., Yu, H.J. and Li, W.T. 2021. The genesis of the Shuitoushan Pb–Zn deposit, Baoshan Block, Sanjiang region: Constraints from fluid inclusions and O, S, Pb isotopes. Geol. J., 65: 111-121.

Original Research Paper

https://doi.org/10.46488/NEPT.2022.v21i02.002

Open Access Journal

Estimating the Water Quality Class of a Major Irrigation Canal in Odisha, India: A Supervised Machine Learning Approach

S. K. Bhoi*, C. Mallick** and C. R. Mohanty***†

*Department of Computer Science and Engineering, Parala Maharaja Engineering College, Berhampur-761003, Odisha, India

**Department of Basic Science, Parala Maharaja Engineering College, Berhampur-761003, Odisha, India

***Department of Civil Engineering, Parala Maharaja Engineering College, Berhampur-761003, Odisha, India

†Corresponding author: C. R. Mohanty: chitta123@yahoo.com

ABSTRACT

Contamination of surface water by rapid industrialization, natural and anthropogenic activities is of great concern over the last few decades. Nowadays, canal water systems are no exception to this form of contamination, which results in water quality degradation. To classify the canal water based on the Bureau of Indian Standards (BIS), it was thought to develop a quick and inexpensive approach as an alternative to the time-consuming analysis approach. With this motivation, the present study explores building a machine learning model for water quality classification of a major canal namely the Talaldanda canal operating in the state of Odisha, India. The water quality class is predicted using supervised machine learning (ML) prediction models for the new canal water input parameters. The water quality parameters such as pH, dissolved oxygen (DO), biochemical oxygen demand (BOD), and total coliform (TC) at six strategic locations of the canal from the year 2013-2020 were collected from Odisha State Pollution Control Board for the training phase. The supervised ML models used in the study are Decision Tree (DT), Neural Network (NN), k-NN (k-Nearest Neighbor), Naïve Bayes (NV), Support Vector Machine (SVM), and Random Forest (RF). The predictions of the models are evaluated using the Orange-3.29.3 data analytics tool. When analyzing the performance parameters by sampling the training data into training and testing using cross-validation, the results show that DT has a higher classification accuracy (CA) of 96.6 percent than other ML models. In addition, the likelihood of DT correctly predicting water quality class for the testing dataset is higher than that of other prediction models.

INTRODUCTION

Water is one of the most important renewables and finite natural resources on earth. Over the years, demand for freshwater for households, agriculture, and industrial use has led to the degradation of water quantity and quality of water bodies. Water pollution has, therefore, emerged as an important issue in India. The quality of water in the canals has also deteriorated drastically over the years due to the letting of sewage/sullage effluents, agricultural runoff carrying toxic chemicals, dumping of garbage and dead animals, and human defecation along the canal banks, etc. (Solanki et al. 2007, Shankar &Balasubramanya 2008, Rincy &Tessy 2010, Guru Prasad 2003). Many studies have found that natural and anthropogenic activities, as well as their physicochemical properties, are causing canal water quality to deteriorate.

Water quality parameters are classified into five categories based on their permissible limits and purposes - Class A, Class B, Class C, Class D, and Class E (BIS 1982). Due

to imbalance in these parameters the water quality reduces and also the class level changes. This seriously affects human life. Therefore, regular monitoring of water quality is needed as it's a basic need of consumption (Prati 1971, Schaeffer &Konnanur 1977). Regular monitoring increases the size of data as the parameter size also increases. Therefore, some prediction models need to be implemented in this monitoring so that the time for manual evaluation is saved (Prati1971, Schaeffer &Konnanur 1977).

The delta area of the Mahanadi river basin in India primarily depends on Taladanda canal water as a source of drinking water for livestock, intensive agriculture, intensive aquaculture, poultry farms, and other purposes, with irrigation by far the largest user. Taladanda canal was dug in 1862 by the East India Company for irrigation purposes as well as to serve as a waterway in the coastal part of Odisha, India, and completed by the British government in 1869. This canal scheme is situated in the Mahanadi river basin having a command area in the two coastal districts of Odisha. The

canal is nearly 85 km long starting from Cuttack in Odisha, India, and ending at Athrabanki, Paradeep of India. The details of sampling locations and study maps are illustrated in Fig. 1.

Previous studies have revealed that DO concentrations in the Taladanda canal are influenced by environmental conditions upstream points and along the sections of the canal (Prusty& Biswal 2017, Das & Acharya 2003). The poor water quality in respect of pH, DO, BOD, and FC (Fecal Coliforms) in Taladanda Canal at Paradeep area is due to human activities and industrialization (Samantray et al. 2009, Prusty& Biswal 2020a, 2020b, Das &Panda 2010, Mishra 2012).

Several studies have been conducted to develop an effective machine learning-based model for water sample prediction and quality analysis. ML is a branch of Artificial Intelligence (AI) (Patro et al. 2020, Panda et al. 2020, Nayak et al. 2018) that deals with the problems of automation, optimization, etc. ML is divided into four types, 1. Supervised Learning, 2. Unsupervised Learning, 3. Semi-Supervised Learning, 4. Reinforcement Learning. A deep learning (DL) model with random forest, XGBoost, and ANN (artificial neural network)was used for the prediction of groundwater at Arang of Raipur district, India with an observation that DL was found to be better with higher classification accuracy (Singha et al. 2021). Bisht et al. (2019) employed prediction intelligence to predict water quality in the Ganga River in India using SVM, with a prediction accuracy of 96.66%. Other researchers such as Ahmed et al. (2019) predicted the water quality of different River Basins in India using Adaptive Neuro-Fuzzy Inference System (ANFIS), RBF-ANN (Radial Basis Function), and MLPNN (Multilayer Perceptron) (Ahmed et al. 2019, Aldhyani et al. 2020)

From the previous studies, it is observed that no studies are available to classify the Taladanda canal water quality by developing a quick and inexpensive technique as an alternative to the time-consuming analysis approach (Ross 1977). Therefore, these facts have motivated the investigators to conduct the study to classify the canal water using a supervised ML model.

MATERIALS AND METHODS

Study Area Description

The canal has many stations with the starting point as Jobra, then Ranihat, Chatrabazaar, Nuabazaar, Biribati, and Atharabanki as shown in Fig. 2. It is a nearly 150 years old canal built for irrigation, navigation, drinking, bathing, industrial water supply, municipality water supply, etc. However, the canal is contaminated and the water quality has degraded in recent years.

The main cause of this is the pollution of water, air, and soil. Industry wastes, medical wastes, plastics, carbon emis-
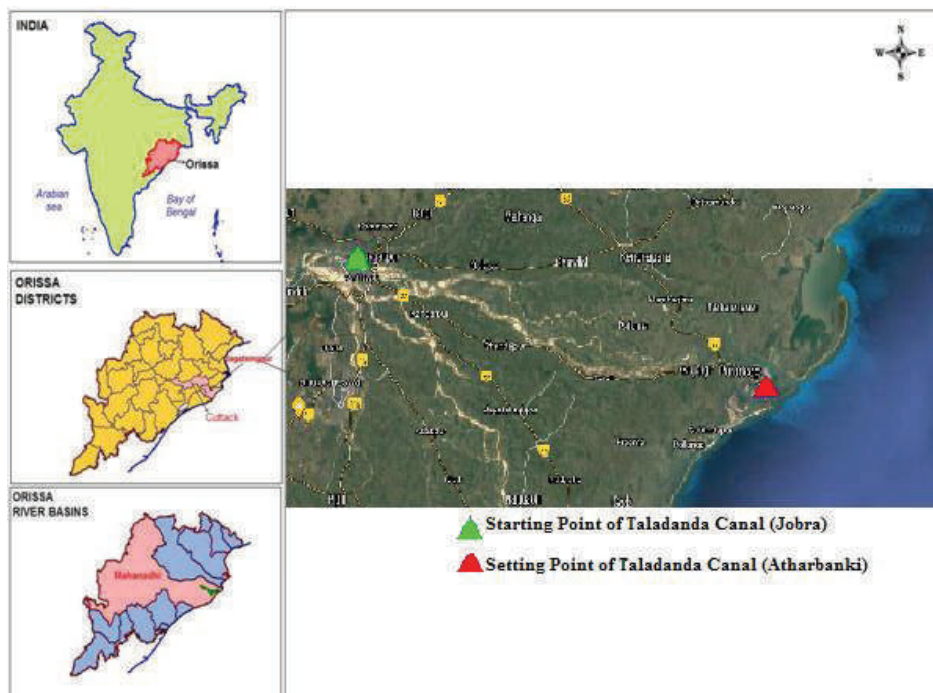
Fig. 1: Study area showing Taladanda Canal with starting and ending point.
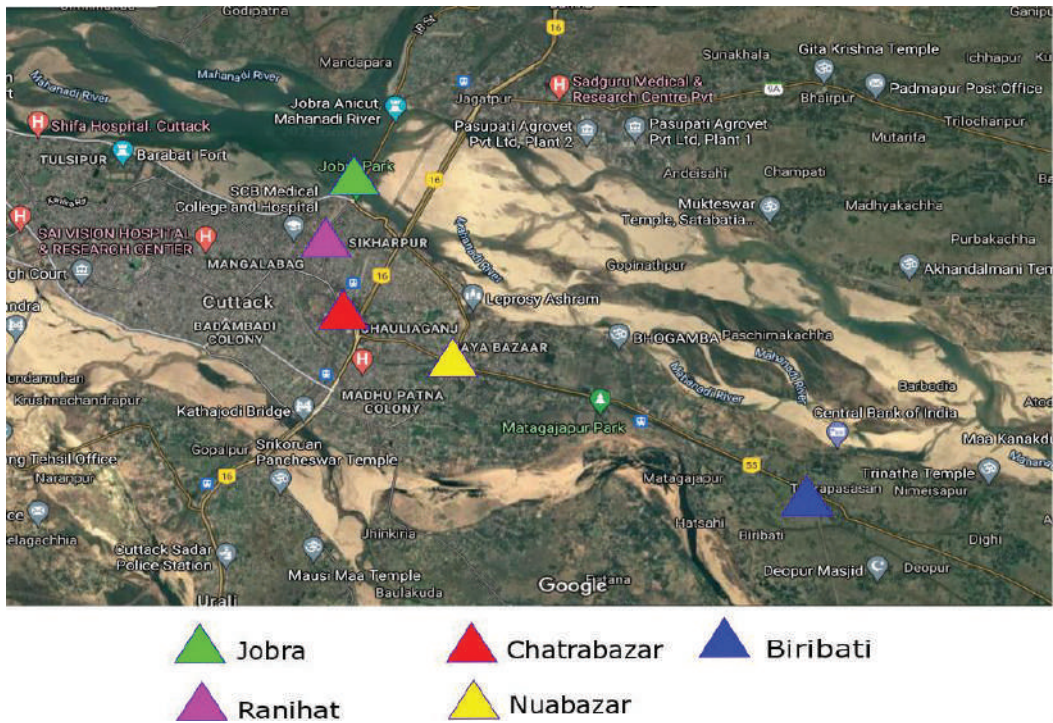
Fig. 2: Location of sample collection stations in the canal.

sions from industries, human wastes, hazardous chemicals waste from industries, are some of the main pollutants that reduce the water quality.

Methodology

In this section, methodologies adopted to classify the water quality of Indian rivers have been discussed.

Data collection: The data collected for the training phase is taken from State Pollution Control Board, Odisha, India from the year 2013 to 2020 (OPCB 2020). This data was collected year wise and it is the average of the observations taken per year. The data consists of 6 stations data of the canal. Due to the smaller dataset for training, we have also generated a synthetic dataset as per the permissible limits for Class A, Class B, and Class C only (Jayalakhmidevi & Belagadi 2005, Meenakumari & Hosmati 2003).

Data pre-processing: Raw data are always noisy and inconsistent. Data pre-processing helps in enhancing the quality of the model. As this data contains various missing values, the mean imputation technique is used to fill these missing values.

Training dataset: The training dataset from the year 2013 to 2020 was collected from Odisha State Pollution Control Board, India (OPCB 2020). The water quality parameters were pH, DO (mg.L^{-1}), BOD (mg.L^{-1}), TC (MPN.100mL^{-1}) and Existing Water Class (target class). Table 1 shows the water quality class and its intended use, whereas Table 2 shows the parameter value for pH, DO, BOD, and TC tolerance level for classes A to E.

Table 1: Water quality class.

Water Class	Purpose
A	Drinking after proper disinfection without conventional treatment
B	Outdoor Bathing
C	Drinking after proper disinfection with conventional treatment
D	Fishing and other animal activities
E	Irrigation and Industry cooling, etc.

Table 2: Water quality parameters of the classes.

Class	pH	DO	BOD	TC
A	6.5-8.5	6 and above	2 or less	50 or less
B	6.5-8.5	5 and above	3 or less	500 or less
C	6.5-8.5	4 and above	3 or less	5000 or less
D	6.5-8.5	4 and above		
E	6.5-8.5			

A sample of training data for the year 2013 is shown as follows for 6 stations of Taladanda Canal in Table 3: Sample average data of the year 2013.

For training, we have considered 2013-2020 water quality data. So, the number of instances is 6×8 = 48 instances (rows), where 6 is the number of stations per year and 8 is the number of years (2013-2020). So, it is a smaller dataset for training, therefore, we have generated data or instances for increasing the input size. For that, we have considered Table 2 tolerance levels and used pseudorandom number distribution to generate 100 instances for each Class A, Class B, and Class C except Classes D and E because they have other parameters for validation(BIS1982). So, the total numbers of instances generated are 48+100+100+100= 348 instances. These 348 instances are now used as input for training in a prediction model.

Testing dataset: For testing, we have collected data with 4 observations at each station in a year-wise manner from the year 2014 to 2018. The average of the observations is taken for each parameter. The data contains the same set of parameters for each year. So, the total instances used for testing are 6×5=30 instances, where six is the number of stations and five is the number of years for which the data is recorded.

Machine Learning and Prediction of Water Quality Class

In this work, we have considered six supervised machine learning prediction models for predicting the output or target class (water quality class) for the testing dataset. The models considered are discussed as follows (Aldhyani et al. 2020):

Neural network: NN solves the multiclass classification problem which will best suit for our work to predict the class as per the water quality parameters. It has more than one neuron or N neurons in the output layer which facilitates it to solve the multiclass classification problem. Mostly the last layer of the network is the softmax function that is an algebraic simplification of N number of logistic classification.

k-NN: It also solves the multiclass classification problem. It can use classification on regression. In this method, the target or output is a membership class. A member is classified based on the votes of its neighbors, with the member assigned to that class which is the most common from its k nearest neighbors.In this classification, the function is approximated in a local maximum, and all other computations are ignored until the function is evaluated. If k=1, that unknown member will be allocated to that one class.

Naïve bayes: It also solves the multiclass classification problem. It is mainly used for the construction of classifiers: by modeling, class labels for assignment of class labels to problems represented as vectors, where class labels are taken from sets with finite data. It assumes the value of a selected feature as independent of other features. The parameter estimation mainly uses the maximum likelihood method.

Decision tree: It also solves the multiclass classification problem. In this method, the non-leaf nodes are labeled with input features. The values of target characteristics are labeled on the arc from the indicated nodes. A class or probability distribution is assigned to a leaf node. The tree is built by separating the source set into root nodes and subsets like successors children. The categorization features are used to separate the data.This process is repeated recursively and called recursive partitioning. This process stops when the subset at a root node has the same values of target output or when no values are added to the prediction after splitting.

SVM: It also solves the multiclass classification problem. It mainly aims to maximize the margin by maximizing the minimum distance from the hyperplane to the nearest example. In this method, for the multiclass problem, additional parameters and constraints are implemented to efficiently classify or predict the classes.

Random forest: It also solves the multiclass classification problem. In this method, several decision trees are ensembled for classification purposes. Each tree in this forest outputs a prediction and the majority of votes for the class is called the output class. It is a faster and a flexible method to implement with some constraints.

Steps for Prediction of Water Class

The steps for predicting the water class are shown in Fig. 3 and discussed as follows:

Step 1: In the first step, the input is taken as the training dataset and fed into the ML model.

Table 3. It is the average data of the number of observations taken.

Taladanda Canal water monitoring station	pH	DO	BOD	TC	Existing water class
Jobra	7.9	7.6	3.7	58475	Other class (E)
Ranihat	7.7	8.3	8.9	106750	Other class (E)
Chatrabazar	7.6	5.3	7.8	116250	Other class (E)
Nuabazar	7.6	5.5	5.0	99000	Other class (E)
Biribati	7.8	7.4	4.8	66250	Other class (E)
Atharabanki	7.8	5.4	4.9	113317	Other class (E)
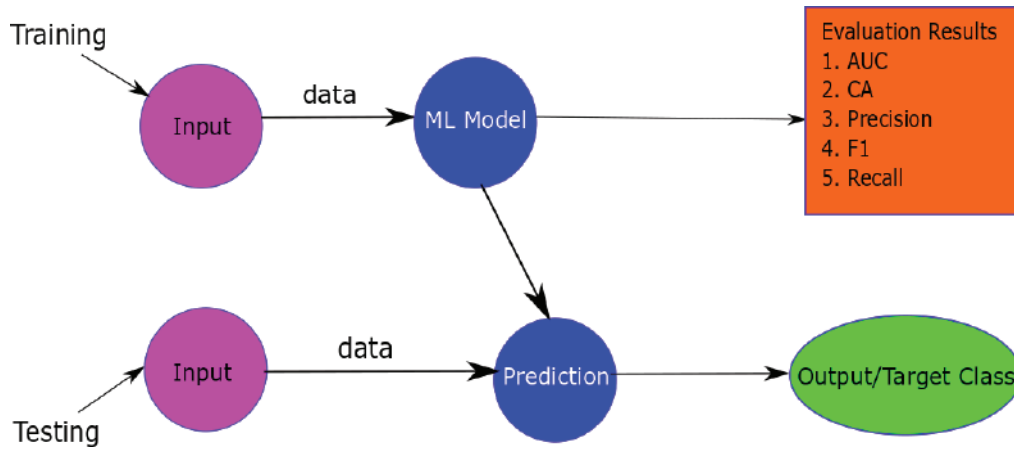
Fig. 3: Flowchart of a prediction model to estimate the water class.

Step 2: The ML model uses cross-validation as the sampling technique for training and testing.

Step 3: The evaluation results are then analyzed to know the model which has a higher classification accuracy (CA).

Step 4: That ML model with higher CA is selected for predicting the water class. However, we can take all ML models for testing.

Step 5: The testing is done by taking the testing dataset as input and fed into the prediction module to get the target class with a higher probability.

Step 6: The prediction model which shows a higher probability of estimation of water class for the input parameters is considered for taking the class data.

RESULTS AND DISCUSSION

The performance of the methodology is evaluated using Orange-3.29.3 data analytics tool installed in a Core-i3 machine with 8 Gb RAM, 2.4 GHz processor, and 64-bit Windows 10 OS platform.

From Fig. 4, it is observed that the input file of training
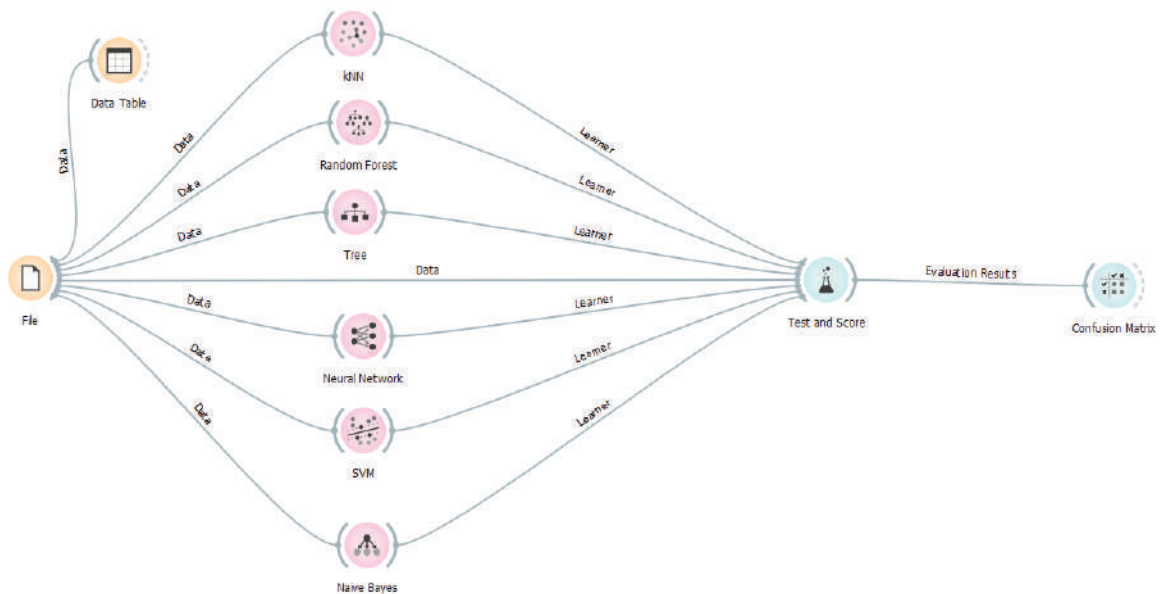
Fig.4: Orange workflow for evaluating the results of different ML algorithms.

is fed into the ML models for training using the cross-validation sampling technique with 10 folds. The test and score module shows the different performance parameters of the ML models and the confusion matrix shows how accurately the instances are predicted from the actual. The performance parameters taken are:

1. AUC (area under the curve): It describes how much the ML model classifies the classes well. The model with 100% accuracy of prediction has an AUC of 1.0.

2. CA (classification accuracy): The number of predictions made correct from the observed values is called CA. Eq. (1) shows the formula for CA:

$$CA = (TP+TN)/(TP+FP+TN+FN) \qquad …(1)$$

Where TP is the true positive, TN is the true negative, FP is the false positive, and FN is the false negative.

3. F1: The F1 score shows the harmonic mean of precision and recall to better understand accuracy. It is shown as follows in Eq. (2).

$$F1= (2*Precision*Recall)/(Precision+Recall) \qquad …(2)$$

4. Precision: It shows how many examples of a positive class are correctly classified out of the entire number of instances classified in that class? Eq. (3) shows the formula for precision:

$$Precision = TP/(TP+FP) \qquad …(3)$$

5. Recall: Recall means the proportion of instances correctly classified for a particular class. Eq. (4) shows the formula for Recall:

$$Recall = TP/(TP+FN) \qquad …(4)$$

From Table 4, it is observed that the CA of DT is greater than other ML models. So, we can conclude that this model will be better for prediction. It is also seen that the AUC of RF is better, F1 is better in DT, Precision is better in RF, and Recall is better in DT. Those results can be visualized from Fig. 5 to 9 respectively. However, we have taken the main parameter as CA for prediction.

The confusion matrix (CM) mainly shows the actual number of instances predicted accurately. As we know, we have taken 348 instances in the training set. The diagonal

Table 4: Performance parameters generated from Orange tool for evaluation.

Model	AUC	CA	F1	Precision	Recall
kNN	0.988	0.951	0.951	0.954	0.951
Tree	0.979	0.966	0.966	0.966	0.966
SVM	0.859	0.477	0.430	0.438	0.477
RF	0.996	0.966	0.965	0.967	0.966
NN	0.846	0.598	0.571	0.566	0.598
Naïve Bayes	0.929	0.799	0.796	0.804	0.799
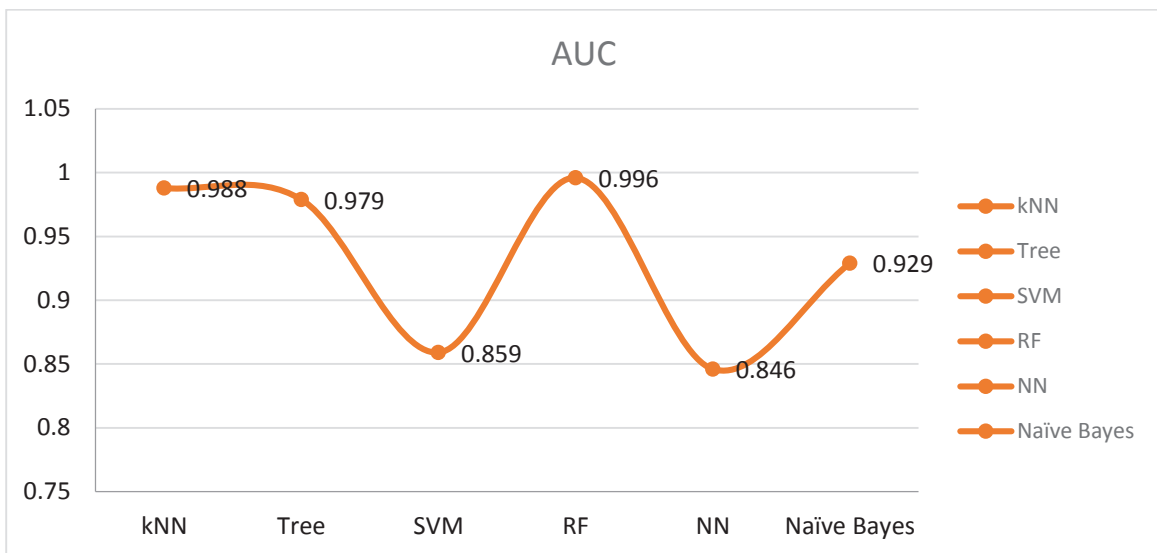
Fig. 5: Performance of AUC of all ML models.

matrix of a CM shows the number of instances accurately predicted for a particular class. Therefore, Fig. 10 (a-e) shows the confusion matrix of different ML models. The left part is marked with "Actual" which means the actual instances and the top part is marked with "Predicted" which shows the actual instances to be predicted accurately.
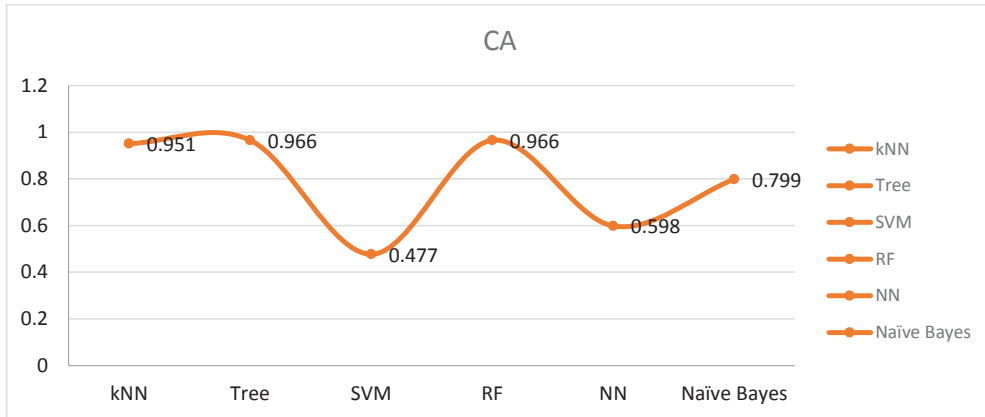
Fig. 6: Performance of CA of all ML models.
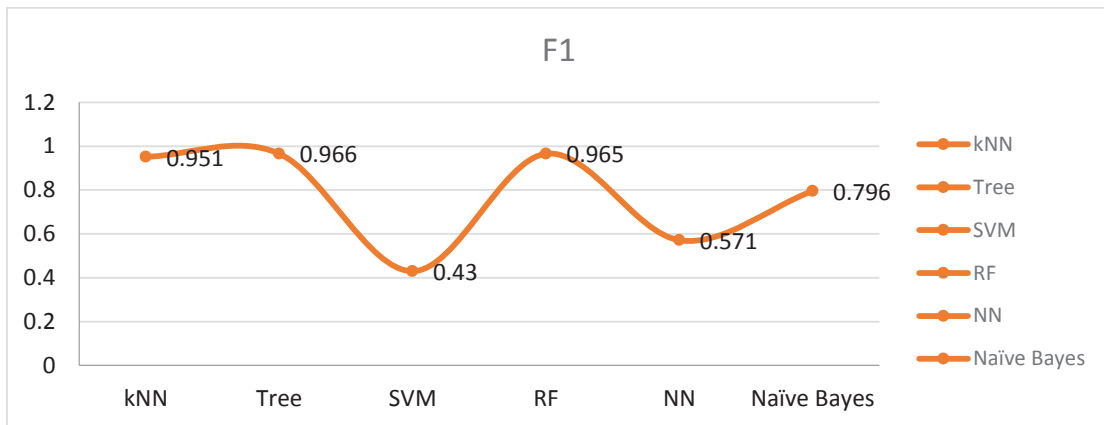
Fig. 7: Performance of F1 of all ML models.
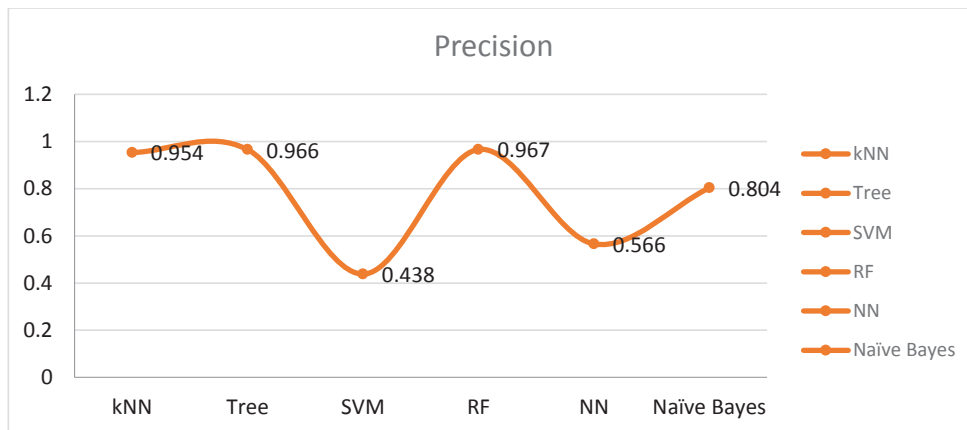
Fig. 8: Performance of precision of all ML models.
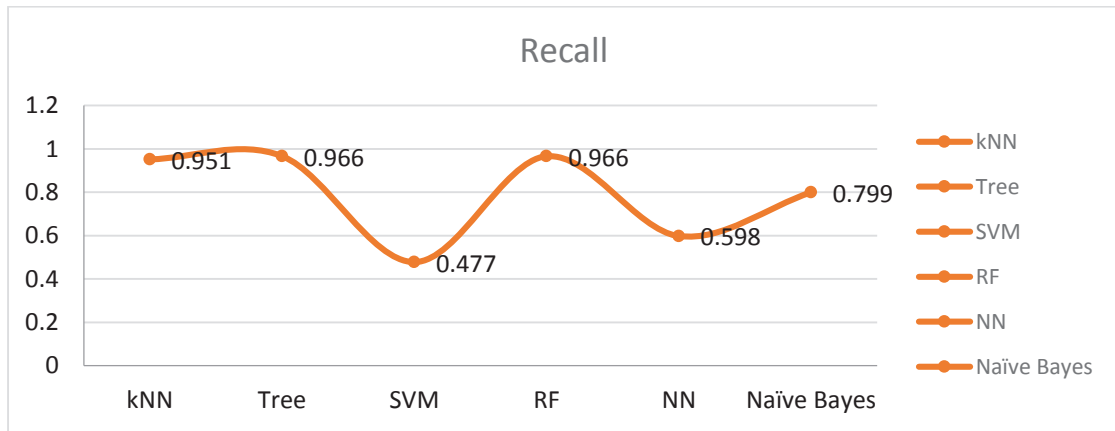
Fig. 9: Performance of Recall of all ML models.
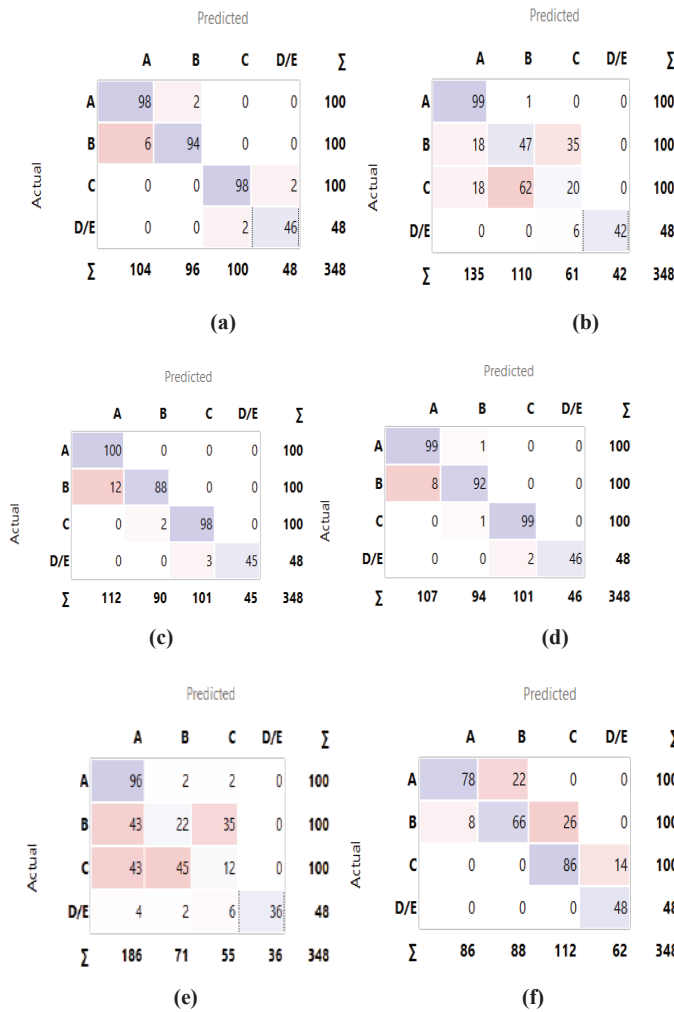
Fig. 10: Confusion matrix for 348 instances (a) Tree (b) NN (c) k-NN (d) RF (e) SVM (f) NB

Fig. 11 shows the prediction model design using the Orange workflow. The prediction module for each ML model is forecasted with a probability value for a certain class for each case (testing set) (0.00 to 1.00). Therefore, our main goal is to find that water class that has a higher probability of prediction for the ML model. From the results shown in Fig. 11 to 14, it is observed that for water class D/E the probability is higher using the DT ML model. So, we can use that data as the prediction data (water class) for each instance (input testing set with four parameters). Fig. 12 shows that for class A, the probabilities of prediction are very low for each ML model. Fig. 13 shows the probabilities of prediction for each ML model for class B. Fig. 14 shows the probabilities of prediction for each ML model for class C. Fig. 15 shows the probabilities of prediction for each ML model for class D/E.From this figure, it is observed that DT predicts the classes with a probability of 1.00 for every 30 instances, and the average probability is 1.0. For other ML models, the average of these probabilities of 30 instances is smaller than DTs average probability. Therefore, we consider the DT column of Fig. 15 as the classes predicted with a high probability for each instance (input).

CONCLUSION

Using supervised machine learning (ML) prediction models, the water quality class is predicted for the new input parameters of the water samples taken in this study. The input parameters considered for the study are pH, dissolved oxygen (DO), biochemical oxygen demand (BOD), total coliform (TC), and target water class. The predictions of the models are evaluated using the Orange-3.29.3 data analytics tool. From the results, it was found that DT shows a higher classification accuracy (CA) of 0.966 than other ML models. Also, for the testing dataset, the average probability of prediction of water quality class D/E for the DT ML model is 1.00, which is greater than other prediction models. So, for these types of datasets, DT will be a better prediction model to categorize the water class well. In the future, the model may be implemented in predicting the water quality for other sources of water like rivers, ponds, groundwater in different locations. The main research challenge is the improvement of prediction accuracy of water pollution levels in larger or smaller datasets in different water sources. These research areas need to be explored.
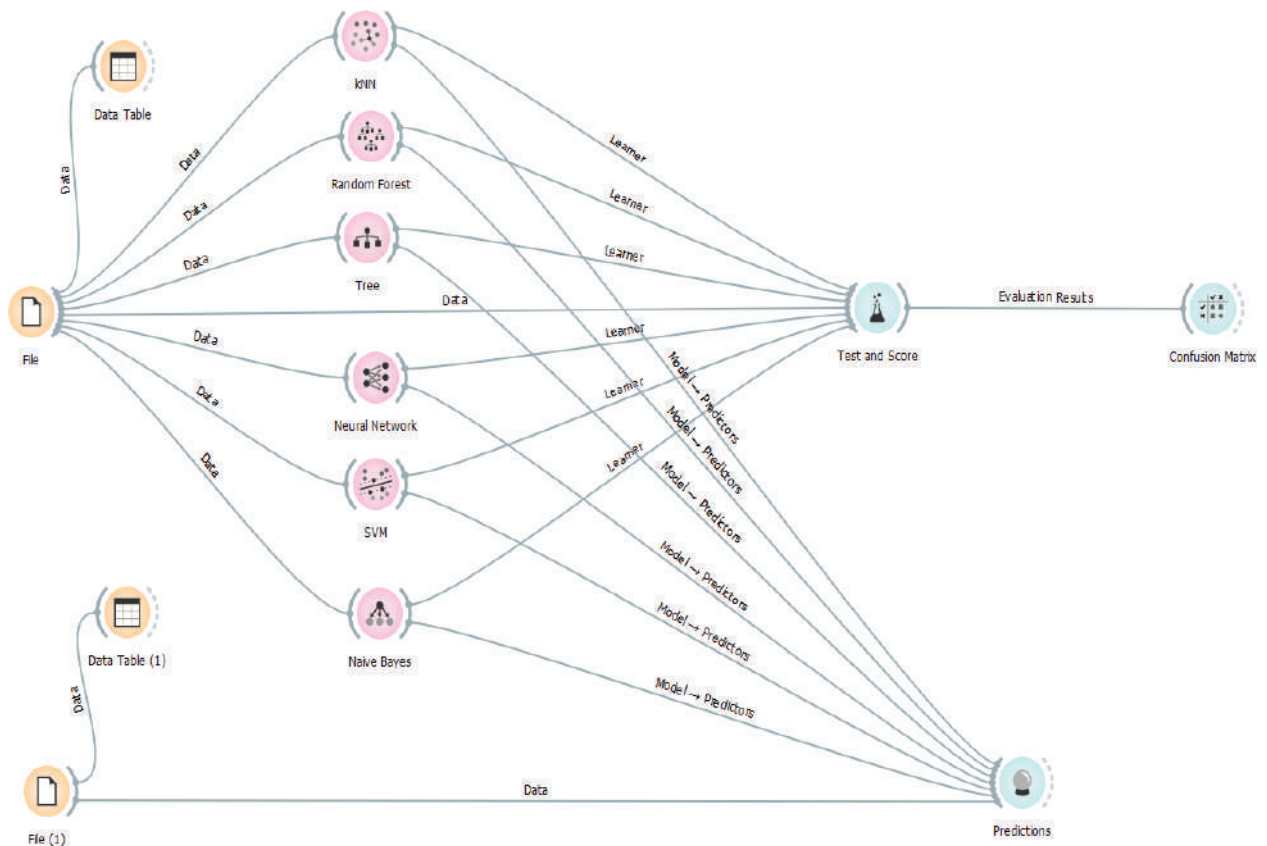
Fig. 11: Orange workflow for prediction of water class for the testing input.

	kNN	Random Forest	Tree	Neural Network	SVM	Naive Bayes
1	0.00 → D/E	0.00 → C	0.00 → D/E	0.00 → D/E	0.00 → D/E	0.01 → C
2	0.00 → D/E	0.00 → C	0.00 → D/E	0.00 → D/E	0.00 → D/E	0.01 → C
3	0.00 → D/E	0.00 → C	0.00 → D/E	0.00 → D/E	0.00 → D/E	0.01 → C
4	0.00 → D/E	0.00 → C	0.00 → D/E	0.00 → D/E	0.00 → D/E	0.01 → C
5	0.00 → D/E	0.00 → C	0.00 → D/E	0.00 → D/E	0.00 → D/E	0.01 → C
6	0.00 → D/E	0.00 → C	0.00 → D/E	0.06 → C	0.06 → C	0.01 → C
7	0.00 → D/E	0.00 → D/E	0.00 → D/E	0.00 → D/E	0.00 → D/E	0.01 → C
8	0.00 → D/E	0.00 → C	0.00 → D/E	0.00 → D/E	0.00 → D/E	0.01 → C
9	0.00 → D/E	0.00 → C	0.00 → D/E	0.00 → D/E	0.00 → D/E	0.01 → C
10	0.00 → D/E	0.00 → C	0.00 → D/E	0.00 → D/E	0.00 → D/E	0.01 → C
11	0.00 → D/E	0.00 → D/E	0.00 → D/E	0.00 → D/E	0.00 → D/E	0.01 → C
12	0.00 → D/E	0.00 → C	0.00 → D/E	0.00 → D/E	0.00 → D/E	0.01 → C
13	0.00 → D/E	0.00 → D/E	0.00 → D/E	0.04 → C	0.04 → C	0.01 → C
14	0.00 → D/E	0.00 → C	0.00 → D/E	0.00 → D/E	0.00 → D/E	0.01 → C
15	0.00 → D/E	0.00 → C	0.00 → D/E	0.00 → D/E	0.00 → D/E	0.01 → C
16	0.00 → D/E	0.00 → C	0.00 → D/E	0.00 → D/E	0.00 → D/E	0.01 → C
17	0.00 → D/E	0.00 → C	0.00 → D/E	0.00 → D/E	0.00 → D/E	0.01 → C
18	0.00 → D/E	0.00 → D/E	0.00 → D/E	0.00 → D/E	0.00 → D/E	0.01 → C
19	0.00 → D/E	0.00 → D/E	0.00 → D/E	0.04 → C	0.05 → C	0.01 → C
20	0.00 → D/E	0.00 → D/E	0.00 → D/E	0.00 → D/E	0.00 → D/E	0.01 → C
21	0.00 → D/E	0.00 → D/E	0.00 → D/E	0.00 → D/E	0.00 → D/E	0.01 → C
22	0.00 → D/E	0.00 → D/E	0.00 → D/E	0.00 → D/E	0.00 → D/E	0.01 → C
23	0.00 → D/E	0.00 → D/E	0.00 → D/E	0.01 → D/E	0.00 → D/E	0.01 → C
24	0.00 → D/E	0.00 → C	0.00 → D/E	0.00 → D/E	0.00 → D/E	0.01 → C
25	0.00 → D/E	0.00 → C	0.00 → D/E	0.07 → C	0.03 → C	0.01 → C
26	0.00 → D/E	0.00 → C	0.00 → D/E	0.00 → D/E	0.00 → D/E	0.01 → C
27	0.00 → D/E	0.00 → C	0.00 → D/E	0.00 → D/E	0.00 → D/E	0.01 → C
28	0.00 → D/E	0.00 → C	0.00 → D/E	0.00 → D/E	0.00 → D/E	0.01 → C
29	0.00 → D/E	0.00 → C	0.00 → D/E	0.00 → D/E	0.00 → D/E	0.01 → C
30	0.00 → D/E	0.00 → C	0.00 → D/E	0.05 → C	0.01 → C	0.01 → C

Fig. 12: Prediction of class A using different ML models for the input instances with probability values (0.00-1.00).

	kNN	Random Forest	Tree	Neural Network	SVM	Naive Bayes
1	0.00 → D/E	0.00 → C	0.00 → D/E	0.01 → D/E	0.00 → D/E	0.02 → C
2	0.00 → D/E	0.00 → C	0.00 → D/E	0.00 → D/E	0.00 → D/E	0.02 → C
3	0.00 → D/E	0.00 → C	0.00 → D/E	0.00 → D/E	0.00 → D/E	0.02 → C
4	0.00 → D/E	0.00 → C	0.00 → D/E	0.00 → D/E	0.00 → D/E	0.02 → C
5	0.00 → D/E	0.00 → C	0.00 → D/E	0.01 → D/E	0.00 → D/E	0.02 → C
6	0.00 → D/E	0.00 → C	0.00 → D/E	0.32 → C	0.24 → C	0.02 → C
7	0.00 → D/E	0.00 → D/E	0.00 → D/E	0.02 → D/E	0.00 → D/E	0.02 → C
8	0.00 → D/E	0.00 → C	0.00 → D/E	0.00 → D/E	0.00 → D/E	0.02 → C
9	0.00 → D/E	0.00 → C	0.00 → D/E	0.00 → D/E	0.00 → D/E	0.02 → C
10	0.00 → D/E	0.00 → C	0.00 → D/E	0.00 → D/E	0.00 → D/E	0.02 → C
11	0.00 → D/E	0.00 → D/E	0.00 → D/E	0.00 → D/E	0.00 → D/E	0.02 → C
12	0.00 → D/E	0.00 → C	0.00 → D/E	0.00 → D/E	0.00 → D/E	0.02 → C
13	0.00 → D/E	0.00 → D/E	0.00 → D/E	0.36 → C	0.34 → C	0.02 → C
14	0.00 → D/E	0.00 → C	0.00 → D/E	0.00 → D/E	0.00 → D/E	0.02 → C
15	0.00 → D/E	0.00 → C	0.00 → D/E	0.00 → D/E	0.00 → D/E	0.02 → C
16	0.00 → D/E	0.00 → C	0.00 → D/E	0.00 → D/E	0.00 → D/E	0.02 → C
17	0.00 → D/E	0.00 → C	0.00 → D/E	0.00 → D/E	0.00 → D/E	0.02 → C
18	0.00 → D/E	0.00 → D/E	0.00 → D/E	0.00 → D/E	0.00 → D/E	0.02 → C
19	0.00 → D/E	0.00 → D/E	0.00 → D/E	0.37 → C	0.35 → C	0.02 → C
20	0.00 → D/E	0.00 → D/E	0.00 → D/E	0.00 → D/E	0.00 → D/E	0.02 → C
21	0.00 → D/E	0.00 → D/E	0.00 → D/E	0.00 → D/E	0.00 → D/E	0.02 → C
22	0.00 → D/E	0.00 → D/E	0.00 → D/E	0.00 → D/E	0.00 → D/E	0.02 → C
23	0.00 → D/E	0.00 → D/E	0.00 → D/E	0.05 → D/E	0.00 → D/E	0.02 → C
24	0.00 → D/E	0.00 → C	0.00 → D/E	0.01 → D/E	0.00 → D/E	0.02 → C
25	0.00 → D/E	0.00 → C	0.00 → D/E	0.24 → C	0.09 → C	0.02 → C
26	0.00 → D/E	0.00 → C	0.00 → D/E	0.00 → D/E	0.00 → D/E	0.02 → C
27	0.00 → D/E	0.00 → C	0.00 → D/E	0.00 → D/E	0.00 → D/E	0.02 → C
28	0.00 → D/E	0.00 → C	0.00 → D/E	0.00 → D/E	0.00 → D/E	0.02 → C
29	0.00 → D/E	0.00 → C	0.00 → D/E	0.00 → D/E	0.00 → D/E	0.02 → C
30	0.00 → D/E	0.00 → C	0.00 → D/E	0.22 → C	0.05 → C	0.02 → C

Fig. 13: Prediction of class B using different ML models for the input instances with probability values (0.00-1.00).

	kNN	Random Forest	Tree	Neural Network	SVM	Naive Bayes
1	0.00 → D/E	0.50 → C	0.00 → D/E	0.05 → D/E	0.00 → D/E	0.66 → C
2	0.00 → D/E	0.50 → C	0.00 → D/E	0.01 → D/E	0.00 → D/E	0.66 → C
3	0.00 → D/E	0.50 → C	0.00 → D/E	0.00 → D/E	0.00 → D/E	0.66 → C
4	0.00 → D/E	0.50 → C	0.00 → D/E	0.01 → D/E	0.00 → D/E	0.66 → C
5	0.00 → D/E	0.50 → C	0.00 → D/E	0.03 → D/E	0.00 → D/E	0.66 → C
6	0.00 → D/E	0.50 → C	0.00 → D/E	0.45 → C	0.27 → C	0.66 → C
7	0.00 → D/E	0.40 → D/E	0.00 → D/E	0.09 → D/E	0.00 → D/E	0.85 → C
8	0.00 → D/E	0.50 → C	0.00 → D/E	0.00 → D/E	0.00 → D/E	0.66 → C
9	0.00 → D/E	0.50 → C	0.00 → D/E	0.00 → D/E	0.00 → D/E	0.66 → C
10	0.00 → D/E	0.50 → C	0.00 → D/E	0.00 → D/E	0.00 → D/E	0.66 → C
11	0.00 → D/E	0.40 → D/E	0.00 → D/E	0.02 → D/E	0.00 → D/E	0.85 → C
12	0.00 → D/E	0.50 → C	0.00 → D/E	0.01 → D/E	0.00 → D/E	0.66 → C
13	0.20 → D/E	0.40 → D/E	0.00 → D/E	0.48 → C	0.34 → C	0.85 → C
14	0.00 → D/E	0.50 → C	0.00 → D/E	0.00 → D/E	0.00 → D/E	0.66 → C
15	0.00 → D/E	0.50 → C	0.00 → D/E	0.00 → D/E	0.00 → D/E	0.66 → C
16	0.00 → D/E	0.50 → C	0.00 → D/E	0.00 → D/E	0.00 → D/E	0.66 → C
17	0.00 → D/E	0.50 → C	0.00 → D/E	0.00 → D/E	0.00 → D/E	0.66 → C
18	0.00 → D/E	0.40 → D/E	0.00 → D/E	0.01 → D/E	0.00 → D/E	0.85 → C
19	0.20 → D/E	0.40 → D/E	0.00 → D/E	0.48 → C	0.34 → C	0.85 → C
20	0.00 → D/E	0.40 → D/E	0.00 → D/E	0.00 → D/E	0.00 → D/E	0.85 → C
21	0.00 → D/E	0.40 → D/E	0.00 → D/E	0.00 → D/E	0.00 → D/E	0.85 → C
22	0.00 → D/E	0.40 → D/E	0.00 → D/E	0.02 → D/E	0.00 → D/E	0.85 → C
23	0.00 → D/E	0.40 → D/E	0.00 → D/E	0.19 → D/E	0.00 → D/E	0.85 → C
24	0.00 → D/E	0.50 → C	0.00 → D/E	0.04 → D/E	0.00 → D/E	0.66 → C
25	0.00 → D/E	0.50 → C	0.00 → D/E	0.43 → C	0.12 → C	0.66 → C
26	0.00 → D/E	0.50 → C	0.00 → D/E	0.00 → D/E	0.00 → D/E	0.66 → C
27	0.00 → D/E	0.50 → C	0.00 → D/E	0.00 → D/E	0.00 → D/E	0.66 → C
28	0.00 → D/E	0.50 → C	0.00 → D/E	0.01 → D/E	0.00 → D/E	0.88 → C
29	0.00 → D/E	0.50 → C	0.00 → D/E	0.01 → D/E	0.00 → D/E	0.66 → C
30	0.00 → D/E	0.50 → C	0.00 → D/E	0.41 → C	0.06 → C	0.66 → C

Fig. 14: Prediction of class C using different ML models for the input instances with probability values (0.00-1.00).

	kNN	Random Forest	Tree	Neural Network	SVM	Naive Bayes
1	1.00 → D/E	0.50 → C	1.00 → D/E	0.93 → D/E	1.00 → D/E	0.31 → C
2	1.00 → D/E	0.50 → C	1.00 → D/E	0.99 → D/E	1.00 → D/E	0.31 → C
3	1.00 → D/E	0.50 → C	1.00 → D/E	1.00 → D/E	1.00 → D/E	0.31 → C
4	1.00 → D/E	0.50 → C	1.00 → D/E	0.99 → D/E	1.00 → D/E	0.31 → C
5	1.00 → D/E	0.50 → C	1.00 → D/E	0.96 → D/E	1.00 → D/E	0.31 → C
6	1.00 → D/E	0.50 → C	1.00 → D/E	0.17 → C	0.43 → C	0.31 → C
7	1.00 → D/E	0.60 → D/E	1.00 → D/E	0.88 → D/E	1.00 → D/E	0.12 → C
8	1.00 → D/E	0.50 → C	1.00 → D/E	1.00 → D/E	1.00 → D/E	0.31 → C
9	1.00 → D/E	0.50 → C	1.00 → D/E	1.00 → D/E	1.00 → D/E	0.31 → C
10	1.00 → D/E	0.50 → C	1.00 → D/E	1.00 → D/E	1.00 → D/E	0.31 → C
11	1.00 → D/E	0.60 → D/E	1.00 → D/E	0.97 → D/E	1.00 → D/E	0.12 → C
12	1.00 → D/E	0.50 → C	1.00 → D/E	0.99 → D/E	1.00 → D/E	0.31 → C
13	0.80 → D/E	0.60 → D/E	1.00 → D/E	0.12 → C	0.27 → C	0.12 → C
14	1.00 → D/E	0.50 → C	1.00 → D/E	1.00 → D/E	1.00 → D/E	0.31 → C
15	1.00 → D/E	0.50 → C	1.00 → D/E	1.00 → D/E	1.00 → D/E	0.31 → C
16	1.00 → D/E	0.50 → C	1.00 → D/E	1.00 → D/E	1.00 → D/E	0.31 → C
17	1.00 → D/E	0.50 → C	1.00 → D/E	1.00 → D/E	1.00 → D/E	0.31 → C
18	1.00 → D/E	0.60 → D/E	1.00 → D/E	0.99 → D/E	1.00 → D/E	0.12 → C
19	0.80 → D/E	0.60 → D/E	1.00 → D/E	0.12 → C	0.26 → C	0.12 → C
20	1.00 → D/E	0.60 → D/E	1.00 → D/E	1.00 → D/E	1.00 → D/E	0.12 → C
21	1.00 → D/E	0.60 → D/E	1.00 → D/E	1.00 → D/E	1.00 → D/E	0.12 → C
22	1.00 → D/E	0.60 → D/E	1.00 → D/E	0.97 → D/E	1.00 → D/E	0.12 → C
23	1.00 → D/E	0.60 → D/E	1.00 → D/E	0.75 → D/E	1.00 → D/E	0.12 → C
24	1.00 → D/E	0.50 → C	1.00 → D/E	0.96 → D/E	1.00 → D/E	0.31 → C
25	1.00 → D/E	0.50 → C	1.00 → D/E	0.26 → C	0.76 → C	0.31 → C
26	1.00 → D/E	0.50 → C	1.00 → D/E	1.00 → D/E	1.00 → D/E	0.31 → C
27	1.00 → D/E	0.50 → C	1.00 → D/E	1.00 → D/E	1.00 → D/E	0.31 → C
28	1.00 → D/E	0.50 → C	1.00 → D/E	0.99 → D/E	1.00 → D/E	0.09 → C
29	1.00 → D/E	0.50 → C	1.00 → D/E	0.99 → D/E	1.00 → D/E	0.31 → C
30	1.00 → D/E	0.50 → C	1.00 → D/E	0.32 → C	0.88 → C	0.31 → C

Fig. 15: Prediction of class D/E using different ML models for the input instances with probability values (0.00-1.00).

REFERENCES

Ahmed, A.N., Faridah B.O., Haitham, A.A., Rusul, K.I., Chow, M.F., Md Shabbir, H., Mohammad, E. and Ahmed, E. 2019. Machine learning methods for better water quality prediction. J. Hydrol., 578: 124084.

Aldhyani, T.H., Al-Yaari, M., Alkahtani, H. and Maashi, M. 2020. Water quality prediction using artificial intelligence algorithms. Appl. Bion. Biomech., 5: 1-12.

Bisht, A.K., Singh, R., Bhutiani, R. and Bhatt, A. 2019. Application of Predictive Intelligence in Water Quality Forecasting of the River Ganga Using Support Vector Machines. In Predictive Intelligence Using Big Data and the Internet of Things, IGI Global, Pennsylvania, USA, pp. 206-218.

Bureau of Indian Standards (BIS). 1982. Tolerance Limits of Parameters for Use. https://www.indiawaterportal.org/articles/indian-standard-drink-ing-water-bis-specifications-10500-1991

Das, J. and Acharya, B.C. 2003. Hydrology and assessment of lotic water quality in Cuttack City, India. Water, Air Soil Pollut., 150(1): 163-175.

Das, M. and Panda, T. 2010. Water quality and phytoplankton population in sewage fed river of Mahanadi, Orissa, India. J. Life Sci., 2(2): 81-85.

Guru Prasad, B. 2003. Evaluation of water quality in Tadepallimandal of Guntur district, AP. Nat. Environ. Pollut. Technol., 2(3): 273-276

Jayalakhmidevi, O. and Belagadi, S.L. 2005. Water quality assessment from different districts of southern Karnataka. Nat. Environ. Pollut. Technol., 4: 589-596

Meenakumari, H.R. and Hosmati, S.P. 2003. Bacteriological examination of groundwater samples in and around Mysore city, Karnataka, India. Nat. Environ. Pollut. Technol., 2(2): 213-215

Mishra, L. 2012. Water quality assessment and modeling of Cuttack city. Doctoral Thesis, National Institute of Technology, Rourkela, Odisha, pp. 1-42.

Nayak, S.K. and Panda, S.K. 2018. A user-oriented collaborative filtering algorithm for recommender systems. In 2018 Fifth International Conference on Parallel, Distributed and Grid Computing (PDGC), 20-22 December 2018, Jaypee University of Information Technology, India, IEEE, India, pp. 374-380.

Odisha Pollution Control Board (OPCB). 2019. Annual Report. http://ospcboard.org/publications-reports/

Panda, S.K., Bhoi, S.K. and Singh, M. 2020. A collaborative filtering rec-ommendation algorithm based on a normalization approach. J.Amb. Intell. Hum. Comput., 11: 1-23.

Patro, S.G.K., Mishra, B.K., Panda, S.K., Kumar, R. and Apoorva, A. 2020. Hybrid Social Recommender Systems for Electronic Commerce: A Review. In 2020 International Conference on Computer Science, Engineering and Applications (ICCSEA), 13-14 March 2020, Gunupur, Indian, IEEE, India, pp. 1-6.

Patro, S.G.K., Mishra, B.K., Panda, S.K., Kumar, R., Long, H.V., Taniar, D. and Priyadarshini, I., 2020. A hybrid action-related K-nearest neighbor (HAR-KNN) approach for recommendation systems. IEEE Access, 8: 90978-90991.

Prati, L. 1971. Assessment of water quality by a single index of pollution. Water Res., 5: 741-751

Prusty, R. and Biswal, T. 2017. Water quality assessment of Taladanda Canal in the command area of Cuttack city. Int. J. Adv. Agric. Sci. Technol., 4: 40-48.

Prusty, R. and Biswal, T. 2020a. Assessment of Pollution Load in Terms of Water Quality Index and Modelling of Taladanda Canal and Mahanadi River in Paradip Area, Odisha, India. Asian J. Water, Environ. Pollut., 17(4), 59-72.

Prusty, R. and Biswal, T. 2020b. Physico-chemical, bacteriological, and health hazard effect analysis of the water in Taladanda Canal, Paradip area, Odisha, India. J. Groundw. Sci. Eng., 8(4): 338-348.

Rincy, J. and Tessy, P.P. 2010. Water quality and pollution status of Cha-lakudy river at KathiKudam, Thrissur District, Kerala, India. Nat. Environ. Pollut. Technol., 9(1): 113-118.

Ross, S.L. 1977. An index system for classifying river water quality. Water Pollut. Control, 76(1): 113-122

Samantray, P., Mishra, B.K., Panda, C.R. and Rout, S.P. 2009. Assessment of water quality index in Mahanadi and Atharabanki Rivers and Taldanda Canal in Paradip area, India. J.Hum. Ecol., 26(3): 153-161.

Schaeffer, D.J. and Konnanur, G.J. 1977. Communicating environmental in-formation to the public: A water quality index. J. Environ. Edu., 8: 16-26

Shankar, B.S. and Balasubramanya, N. 2008. Evaluation of quality indices for the groundwaters of an industrial area in Bangalore, India. Nat. Environ. Pollut. Technol., 7(4): 663-666

Singha, S., Pasupuleti, S., Singha, S.S., Singh, R. and Kumar, S. 2021. Prediction of groundwater quality using efficient machine learning technique. Chemosphere, 276: 130265.

Solanki, V.R., Murthy, S.S., Kour, A. and Sabita Raja, S. 2007. Variation in dissolved oxygen and biochemical oxygen demand in two freshwater lakes of Bodhan, Andhra Pradesh, India. Nat. Environ. Pollut. Technol., 6(4): 623-628.

Analysis of Carbon Emission and Its Temporal and Spatial Distribution in County-Level: A Case Study of Henan Province, China

Sen Li, Yanwen Lan† and Lijun Guo

Zhumadian Municipal Ecology and Environment Bureau, Guangtai Building, Zhumadian, 463000, R. P. China

†Corresponding author: Yanwen Lan; yanwen@bupt.cn

ABSTRACT

Estimating carbon emissions and assessing their contribution are critical steps toward China's objective of reaching a "carbon peak" in 2030 and "carbon neutrality" in 2060. This paper selects relevant statistical data on carbon emissions from 2000 to 2018, combines the emission coefficient method and the Logarithmic Mean Divisia Index model (LMDI) to calculate carbon emissions, and analyses the driving force of carbon emission growth using Henan Province as a case study. Based on the partial least squares regression analysis model (PLS), the contributions of inter-provincial factors of carbon emission are analyzed. Finally, a county-level downscaling estimation model of carbon emission is further formulated to analyze the temporal and spatial distribution of carbon emissions and their evolution. The research results show that: 1) The effect of energy intensity is responsible for 82 percent of the increase in carbon emissions, whereas the effect of industrial structure is responsible for -8 percent of the increase in carbon emissions. 2) The proportion of secondary industry and energy intensity, which are 1.64 and 0.82, respectively, have the most evident explanatory effect on total carbon emissions; 3). Carbon emissions vary widely among counties, with high emissions in the central and northern regions and low emissions in the southern. However, their carbon emissions have constantly decreased over time. 4) The number of high-emission counties, their carbon emissions, and the degree of their discrepancies are gradually reduced. The findings serve as a foundation for relevant agencies to gain a macro-level understanding of the industrial landscape and to investigate the feasibility of carbon emission reduction programs.

INTRODUCTION

The issue of climate change is one of the most severe challenges in the world today, which has attracted much attention from the international community. With the development of China's industry, greenhouse gas emissions, mainly CO_2, are gradually increasing, it is urgent to realize a low-carbon economy as soon as possible (Shu et al. 2018). According to the Intergovernmental Panel on Climate Change (IPCC fifth)'s study report, only severe emission controls can reduce the global warming trend (Stocker et al. 2013). The Chinese government, as the world's largest energy consumer and CO_2 emitter, places a high priority on climate change, publicly declaring in 2015 that China's carbon emissions will peak by 2030 and that "carbon neutrality" will be achieved by 2060 (Song et al. 2020). As China's largest carbon-consuming province, Henan, the CO_2 emission reduction and peaking plan directly affect the national peaking progress. To further respond to climate change, promote sustainable economic and social development in China, how to reduce carbon emissions in the field of final consumption has gradually become an urgent question that should be answered. Effectively assessing the contribution of carbon emissions

according to the emission inventory and predicting the carbon emissions are crucial.

Henan is in the center of China, with a wide area of jurisdiction, a large population, a complex industrial structure, strong dependence on fossil energy, large differences between economic and industrial, and a typical carbon emission situation. Currently, there are 18 cities and 158 counties under the jurisdiction of Henan Province. As China's administrative regions are divided into three government levels, which are provincial administrative districts, city administrative districts, and county administrative districts, the different scale analysis and evaluation of carbon emissions, along with spatial and temporal distribution of carbon emissions and their drivers can provide a data basis for emission reduction, which has a great significance.

Past Studies

As an important strategy for economic and social development, the field of the low-carbon economy has become a topic in recent years.

The emission coefficient approach (Abdul-Wahab 2015), life cycle assessment method (Dascalaki et al. 2020), economic input-output analysis (Qi & Zhang 2013), and other

methods are currently used to estimate carbon emissions. It has now been established that there is a link between carbon emissions and economic growth. Grossman & Krueger (1992) investigated the link between pollution and economic growth. They discovered an inverted U-shaped association between these two factors.

In terms of the calculation scope, Zhu et al. (2018) analyzed China's carbon emissions, predicted that China's emissions could rise by more than 50 % in the next 15 years. Guo et al. (2011) adopted the data envelopment analysis method (DEA) to evaluate the carbon emission performance of 29 Chinese provincial administrative regions by computing the potential of carbon emission reductions and the energy structural adjustment (ESA) with the energy conservation technology (ECT). Their study shows that ECT promotion and reductions in inter-regional technological disparity would be effective in reducing carbon emissions in technically inefficient regions. Martinez-Botas (2013) described a model that analyzed the cost and impact of alternating current CO_2 emission transmission types from 2010 to 2050. In the semi-prefabricated construction process, Mao et al. (2013) constructed a quantitative model by defining a calculation boundary with five emission sources. Nässen et al. (2007) evaluated overall energy usage using the input-output approach, comparing the performance of top-down and bottom-up methods of a particular energy. Frankignoulle (1998), Mao et al. (2013), and Mi et al. (2017) are among the studies that address this topic.

Many academics are interested in determining the elements that influence carbon emissions. Ehrlich and Holdren (1971 & 1972) used the IPAT model (I=Human Impact, P=Population, A=Affluence, T=Technology) to examine the effects of population size, affluence, and technology on the environment, dubbed the environmental pressure control model. The carbon emission intensity of several African countries was decomposed by Ebohon & Ikeme (2006) using the structural decomposition method. They discovered that the primary elements impacting carbon emission intensity are energy intensity, energy type, and economic structure.

Lin (2016) studied the influencing elements of carbon dioxide emissions in China's food industry from 1999 to 2012 using an input-output technique. Emission factors, energy structure, energy intensity, and overall output are the key driving forces. From the perspectives of population, carbon emissions per capita, energy intensity, and carbon emissions per unit of energy, Tavakoli (2017) employed the Kaya model to examine the carbon emission driving forces and their evolving features of the European Union. Between 1970 and 2000, Lantz & Feng (2006) used an econometric model to do regression analysis of Canada's per capita GDP, population, technology, and carbon emissions. In recent years, the

Logarithmic Mean Divisia Index Model (LMDI) in Di's index decomposition method has been frequently employed in assessing the components that influence CO2 emissions. The LMDI model was developed by Lin & Ahmad (2017) for the period 1990-2014. In 2009, Pakistan carried out a comprehensive factor analysis based on carbon emissions from energy usage. (Market Allocation Model) MARKAL (Chi et al. 2021), Long-range Energy Alternatives Planning System Model (Leap) (Jaskolski 2016), and Environmental Kuznets Curve) EKC (Chi et al. 2021), among others, are similar methodologies for this topic.

Although lots of work have been done on carbon emission and its driving factors, previous studies always adopted a unitary method. What's more, most of the works away considered few types of energy, which lacked detailed investigations of carbon emissions. Furthermore, the research mostly focuses on large-scale carbon emissions, leaving small-scale carbon emissions, particularly in counties, largely unexplored. As a result, this paper integrates the carbon emission factor technique with the LMDI decomposition model, taking into account 17 different energy sources, including power for the consumer terminal (McPherson & Karne 2014, Mishra & Smyth 2017). The terminal consumer industry in Henan Province was studied in terms of energy consumption intensity, GDP growth, population growth, and industrial structure from 2000 to 2018. Then carbon emission driving forces in the five aspects of the energy structure are analyzed; Then the partial least square regression analysis method is also adopted to analyze the contribution of inter-provincial carbon emission factors, which complements the analysis results of carbon emission driving factors. Furthermore, by analyzing the carbon emission relationship between provinces and counties, a county-level downscaling carbon emission estimation model is formulated, and the temporal-spatial distribution and evolution of carbon emissions in county-level are analyzed. Finally, carbon emission driving forces and carbon emission estimates are integrated to systematically examine Henan Province's future carbon reduction potential and make some plausible recommendations.

MATERIALS AND METHODS

LMDI-Based Driving Factors Decomposition

It should be mentioned that "carbon emission" and "carbon dioxide emission" are two different concepts, and carbon dioxide emissions are a part of carbon emissions. In this paper, we use the definition of carbon emissions to replace the "carbon dioxide emissions".

According to the method provided by IPCC, the emission of CO_2 of the final consumption can be calculated as follows:

$$C = \frac{44}{12} \times \sum_i B_i P_i E_i \qquad \ldots(1)$$

In which, C *(100 mt)* represents the total carbon emissions, I identifies the type of energy, B_i is the standard coal conversion coefficient of the *i-th* energy, P_i is the carbon emission coefficient of the *i-th* energy, and E_i indicates the total consumption of the *i-th* energy. The factors of energy conversion for standard coal and carbon emission coefficients are shown in Table1.

By formula 1, we can get the total carbon emissions of the final consumption. Table 1 list the factor of energy conversion for standard coal and carbon emission coefficients.

This paper adopts the Kaya inequality model and analyzes the affecting factors of carbon emissions in Henan Province into six aspects: population scale, economic scale, industrial structure, energy structure, energy intensity, and carbon emission factors. The formula can be expressed as:

$$C = \sum_i^7 \sum_j^{17} \frac{C_{i,j}}{E_{i,j}} \times \frac{E_{i,j}}{E_i} \times \frac{E_i}{GDP_i} \times \frac{GDP_i}{GDP} \times \frac{GDP}{POP} \times POP \qquad \ldots(2)$$

$$= \sum_i^7 \sum_j^{17} B_{i,j} * e_{i,j} * q_i * g_i * pa * P$$

In formula (2), $C_{i,j}$ is the amount of carbon dioxide emitted by *j-th* energy in the *i-th* industry; $E_{i,j}$ is the total amount of energy consumed by the *j-th* energy in the *i-th* industry;

Table 1: The factors of energy conversion for standard coal and carbon emission coefficient.

Energy type	Converted coefficient	Emission factor
raw coal	0.7143	0.7559
Washed coal	0.9	0.7559
Other coal washing	0.2857	0.7559
Briquette	0.6	0.7559
Coke	0.9714	0.855
Coke oven gas	0.5714	0.3548
Blast furnace gas	0.6	0.3548
Other gas	1.1	0.6449
Other coking products	0.7143	0.7559
Crude	1.4286	0.5857
Gasoline	1.4714	0.5538
Kerosene	1.4714	0.5714
Diesel oil	1.4571	0.5912
Fuel oil	1.4286	0.6185
Other petroleum products	1	0.5857
Liquefied petroleum gas	1.7143	0.5042
Natural gas	1.33	0.4483
Hydropower, nuclear power	0.1229	0

E_i is the total energy consumption in the *i-th* industry; GDP_i is the gross national product of the *i-th* industry; GDP is the gross national product of all industries in the certain year; POP is the total population; $B_{i,j}$ is the emission factor of the *j-th* energy in the *i-th* industry; $e_{i,j}$ is the energy structure of the *i-th* industry; q_i is the energy intensity of the *i-th* industry; g_i is the industrial structure of the *i-th* industry; pa is the GDP per capita and p is the total population.

In this part, we take 2000 as base year 0, set the carbon emissions in 2000 as the base amount of carbon emission, and let t denote the target year. The total carbon emissions of Henan Province will be decomposed into population-scale effect, economic scale effect, industrial structure effect, energy structure effect, and energy intensity effect, which can be expressed as:

$$\delta C = \delta C_e^{0,t} + \delta C_q^{0,t} + \delta C_g^{0,t} + \delta C_{pa}^{0,t} + \delta C_p^{0,t} \quad \ldots(3)$$

In which, $\delta C_e^{0,t}, \delta C_q^{0,t}, \delta C_g^{0,t}, \delta C_{pa}^{0,t}, \delta C_p^{0,t}$ represent the effects, in other words, the increment in CO_2 emissions caused by changes in energy structure, energy intensity, industrial structure, economic scale, and population-scale respectively.

According to the LMDI additive decomposition method, the influence of each factor on the carbon emissions of *0 - t* years can be further obtained. Which can be expressed as:

$$\begin{cases} \delta C_e^{0t} = \frac{C_e^t - C_e^0}{\ln C_e^t - \ln C_e^0} \times \ln\left(\frac{e_{i,j}^t}{e_{i,j}^0}\right) \\[2ex] \delta C_q^{0t} = \frac{C_q^t - C_e^0}{\ln C_q^t - \ln C_q^0} \times \ln\left(\frac{q_{i,j}^t}{q_{i,j}^0}\right) \\[2ex] \delta C_g^{0t} = \frac{C_g^t - C_g^0}{\ln C_g^t - \ln C_g^0} \times \ln\left(\frac{g_{i,j}^t}{g_{i,j}^0}\right) \\[2ex] \delta C_P^{0t} = \frac{C_P^t - C_P^0}{\ln C_P^t - \ln C_P^0} \times \ln\left(\frac{P_i^t}{P_i^0}\right) \\[2ex] \delta C_e^{0t} = \frac{C_{pa}^t - C_e^0}{\ln C_{pa}^t - \ln C_{pa}^0} \times \ln\left(\frac{pa_i^t}{pa_i^0}\right) \end{cases} \ldots(4)$$

The above formula can be used to obtain the driving effects of the five factors on the increment of emissions from the base year 0 to the target year *t*.

PLS Modeling and Analysis

In this section, the PLS model is adopted to evaluate the impact of the factors on carbon emissions.

Partial least squares regression can simultaneously integrate multiple linear regression, principal component analysis, and canonical correlation analysis between variables. It can organically combine the modeling and forecasting data analysis approach with the non-model data cognitive analysis method, in which the information is successfully recombined to reduce the interference caused by information overlap and redundant data. There are two types of PLS: single dependent variable PLS and multiple dependent variables PLS. Because carbon emission is the only dependent variable considered in this paper, so single dependent variable PLS regression is involved in analysis.

Consider a PLS regression progress with P independent variables and one dependent variable, and further assume that each variable has N observation samples for regression analysis. Therefore, the set of the independent variables and the dependent variables are expressed as $X = [x_1, x_2, ..., x_N]_P?_N$ and $Y = [y]$, respectively. According to the PLS model, it is necessary to extract m principal component variables from the independent variables. The purpose of the PLS model is to explain the independent variables as much as possible while ensuring the greatest correlation between the dependent variables, which is a linear combination of all independent variables. The detailed process of modeling is as follows.

1. Data standardization

The main function of data standardization is to eliminate the dimensional relationship between variables, to make the data comparable. The standardized process can be expressed as:

$$\begin{cases} x_{i,j}^* = \dfrac{x_{i,j} - \overline{x_{i,j}}}{s_j}, j \in [1, P] \\ y_j^* = \dfrac{y_j - \overline{y_j}}{s_j}, j \in [1, P] \end{cases}$$

...(5)

The set of processed independent variables is expressed as $X^* = [x_{i,j}^*]_{N?P} = [x_1^*, x_2^*, ..., x_P^*]$. $\overline{x}_{i,j}$ and $\overline{y}_j$ represents the mean value of $x_{i,j}$ and y_j respectively.

2. Variable composition analysis

According to the model of PLS, the component $t_1 = x_i^* w_1$ is extracted first, in which w_1 is the first axis of x^*, and $\|w_1\| = 1$. According to the idea of the principal component analysis method, the maximum covariance between t_1 and x^* should be satisfied, that is $\max_{\|w_1\|} J = Cov(t, y)$. The aforementioned problem can be solved using the Lagrangian algorithm. The procedure would finish if the set accuracy value was reached; otherwise, the regression residual would be utilized to supplement the regression process for the selection of the second component, and iteration would continue. Finally, the regression result would be determined.

3. Cross-validation analysis

Partial least squares regression equation can select some components to get a model with better prediction performance. The cross-validity coefficients for principal components t_h can be defined as:

$$Q_h^2 = \frac{\sum_{k=1}^{P} y_k - y_{k,h-1}^*}{\sum_{k=1}^{P} y_k - y_{-k,h}^*}$$

...(6)

The formula $y_{k,h-1}^*$ represents the predicted value corresponding to the i-th sample point when the first $h - 1$ component regression is selected. Moreover, $y_{-k,h}^*$ is the predicted value obtained by the first h component regression after removing the i-th sample point.

Choosing the component t_g can significantly improve the prediction model when $Q_h^2 \geq 0.0957$. Otherwise, the component would be discarded.

This paper combines the five factors mentioned above in the decomposition of LMDI. The provincial and municipal-level checkable items in the Henan provincial statistical yearbook are adopted. The total GDP, the total population, the urbanization rate, the proportion of secondary industries in Henan Province from 2000 to 2018 are selected and set as independent variables, and the carbon emissions are selected as the dependent variables.

The final regression model can be obtained through PLS regression, which is expressed as follows:

$$Y^{predict} = \sum_{i=1}^{6} a_i x_i + c + e$$

...(7)

In which, e is the error value, a_i is the regression coefficient of x_i, and c is a constant value.

Construction of the Estimation Model at the County Level

The regression model generated using the partial least squares method is only suited for inter-provincial carbon emission prediction due to inadequate data, and it must be downscaled to be corrected at the county-level carbon emission forecast. Considering that the calculation of provincial carbon emissions is derived by summing the carbon emissions in all counties, the two carbon emission regression models in different levels correspond to the six independent variables that are consistent and should have the same slope. So, the corresponding regression coefficients in the carbon emission

regression equations are the same, and only the constant term and the error term caused by carbon emissions downscaling need to be adjusted.

Let B denotes the set of the county in Henan Province, and let $X^t_j = [x_1^t, x_2^t, ..., x_6^t]_{|B| \times 6}$, $j \in B$ denotes the set of the independent variables in year t. The dependent variable in a year t is denoted by $y^t_j, j \in B$.

For the county data in each year, their carbon emissions can be represented by a linear combination of the six statistical elements of the county, which can be expressed as:

$$y^t_j = \sum_{i=1}^{i=6} a_i x^t_{j,i} + cl^t + \rho^t_j + \beta^t_j, \forall j \in B \qquad \text{...(8)}$$

Where a_i is the regression coefficient of the independent variable $x_{i,j}$, cl^t is the constant value in a year t, b^t_j and r^t_j are the downscaling error item and prediction error item respectively.

To obtain the value of the constant, we sum forecast formulas for all counties in the same certain year. Then the final forecast equations for all counties in that year can be obtained, which can be expressed as:

$$y^t = a_i \sum_{j \in B} x^t_{j,i} + |B|(cl^t) + \sum_{j \in B}(\rho^t_j + \beta^t_j)$$
$$= a_i x_i + |B|(cl^t) + \sum_{j \in B}(\rho^t_j + \beta^t_j) \qquad \text{...(9)}$$

According to the proportional relationship of the constant term, we have:

$$|B|\, cl^t = C \qquad \text{...(10)}$$

The error term is the result of a correlation between the six key components and the constant term, which cannot be calculated directly. As a result, it can be allocated based on the fraction of expected carbon emissions without taking the error term into account. Let $y_i^{t*} = a_i x_{j,i}^t + cl^t$, the calculation progress is as follows:

$$\rho^t_j + \beta^t_j = (y^t - y^{t*}) \times \frac{y_j^{t*}}{y^t} \qquad \text{...(11)}$$

Finally, the value calculated can be brought into the formula (8) to get the annual carbon dioxide emissions of each county.

RESULTS AND DISCUSSION

The carbon emission coefficient is used in this section to determine Henan Province's carbon emissions from 2000 to 2018. The LMDI decomposition model analyses five components that are regarded to be the key driving forces of carbon emissions: GDP, population, industrial structure, energy structure, and energy intensity. The PLS regression model is formulated to calculate the six indicators including

Table 2: Decomposition results of carbon emission drivers.

Year	ESE	EIE	ISE	EGE	PGE
2001	-68.3	-696.9	330.6	758.7	269.5
2002	-81.3	-882.3	186.9	805.2	378.9
2003	-86.6	-575.2	-124.6	1244.6	381.6
2004	169.4	4320.1	353.3	1481.4	538.9
2005	614.0	5653.7	400.2	1934.0	927.3
2006	210.1	10520.8	149.5	1840.1	870.2
2007	226.2	11419.5	205.2	2264.3	1149.9
2008	173.7	11738.5	-90.2	2310.1	575.3
2009	168.9	14972.3	-8.0	133.8	735.7
2010	1211.1	14996.9	-7.2	1950.2	448.4
2011	675.6	16721.3	-201.5	1617.1	494.0
2012	454.4	14581.7	-179.2	827.6	317.9
2013	820.2	12248.0	-98.1	402.1	473.0
2014	2037.1	14472.4	-132.6	1199.0	-338.3
2015	1966.5	14444.1	-151.7	409.7	198.5
2016	1699.9	13063.6	-69.6	750.6	-15.6
2017	782.4	11134.0	-454.5	1081.7	253.2
2018	914.7	6299.4	-450.4	973.2	-68.0

the population, the urbanization rate, the proportion of the secondary industry, the energy intensity, and household consumption level to evaluate the contribution of carbon emissions. Finally, the corresponding downscaling county carbon emissions model is given, and the temporal and spatial distribution of the carbon emissions is analyzed.

Driving Force Analysis in Henan Province

In Table 2, ESE, EIE, ISE, EGE, PGE denote the effect of energy structure, the effect of energy intensity, the effect of industrial structure, the effect of economic growth, and the effect of population growth.

Table 2 lists the results of the driving forces of the five major factors for the carbon emissions in Henan Province from 2000 to 2018. In Fig. 1, the corresponding cumulative contribution to carbon emissions is visually displayed. It can be seen from Table 2 and Fig. 1, from 2000 to 2018, energy intensity has accounted for 80% of the carbon dioxide increment in Henan Province, followed by economic growth effects and energy structure effects, which are 12% and 11%, respectively. The contribution of energy intensity first grew, then fell, contributing little to the increase in carbon emissions. The impact of the industrial structure was shown to be negatively connected with the increase in carbon emissions, which accounted for -8% of total emissions.

Fig. 2 shows the carbon emissions of the three major industries of terminal consumption in Henan Province. The secondary industry is responsible for the majority of the province's carbon emissions, with the tertiary industry coming in second. Both industries increased and then dropped, with the latter reaching its highest point in nearly two decades in 2011. The change in carbon emissions in the tertiary sector is not immediately apparent. We may deduce that the secondary industry is the biggest source of carbon dioxide emissions in Henan Province based on the pattern of carbon emissions of the three industries.
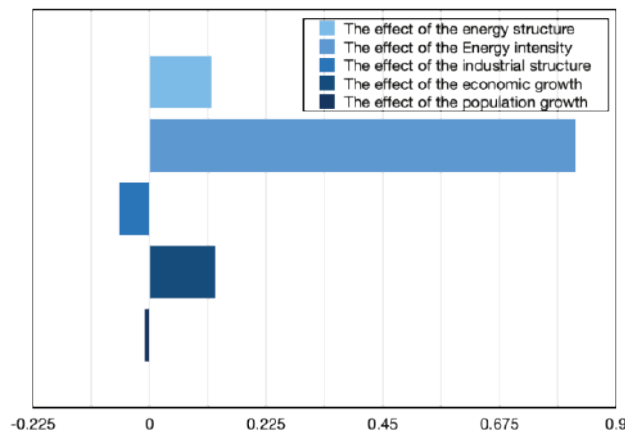
PLS-Based Carbon Emission Regression Analysis

In this section, the statistical data and the results of the carbon emissions are used to perform regression through the SIMCA-P software. The historical GDP, the population, the urbanization rate, the proportion of the secondary industry, the energy intensity, and the household consumption level are selected as independent variables, which denotes by X_1, X_2, ..., X_6, respectively. Moreover, the indicator of carbon dioxide emissions is considered as the dependent variable.

Through the SIMCA-P, we can get the calculation value of the cross-validity. In the regression process of the carbon emissions prediction of Henan Province between 2000 and 2018, the optimal number of principal components is 2, and the value of the cross-validity, $Q_2^2 = 0.79848 > 0.0975$, satisfies the corresponding principal component extraction criteria. The index $R2VY(cum)$ is 0.933055, which indicates that the two components can explain 93.3055% of the dependent variable variation information, which contains sufficient information of independent variables and have good applicability to the model.

Fig. 3 shows the comparison between the regressed value of the carbon emissions and the actual value of carbon emissions from 2000 to 2018. From Fig. 3 we can see that there is a small gap between the two curves. Through the calculation of relative error between the two values in the considered time domain, the average relative error between the predicted value and the actual value is -0.33185801 between 2000 and 2018, which has a good performance of prediction.

Fig. 1: The contribution of the factors to carbon emissions.
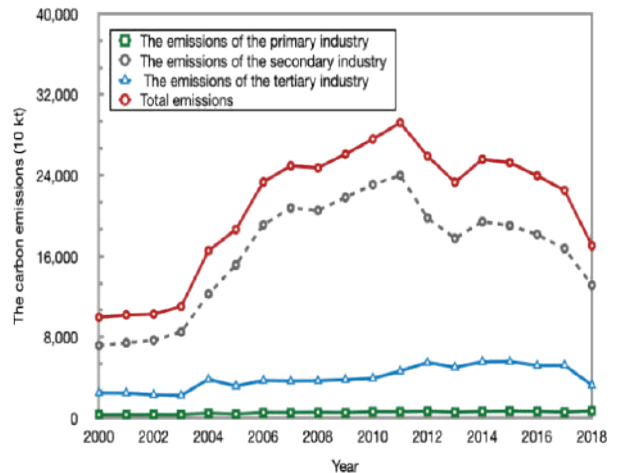
Fig. 2: The carbon emissions in the three industries.

As the fitting degree and accuracy of the model are easily affected by the specific points, in Fig. 4, a photo of T^2 an ellipse is constructed to test whether the specific points exist. As Fig. 4 shows, all the sample points are within the specified range and there are no specific points. We can conclude that the model has good adaptability to sampled data.

Fig. 5 shows the importance of selected six independent variables (Variable Importance in Projection, VIP), which are used to express the explanatory power of the independent variables on the dependent variable. The six factors sorted by importance are the proportion of the secondary industry, energy intensity, urbanization rate, population, GDP, and household consumption level. Among them, the VIP of the secondary industry is 1.64, which contributes most to carbon emissions, while the VIP of carbon emissions intensity is 0.82. So to decrease carbon emissions, the changing of industry structure is the primary policy that should be considered in addition to energy intensity.

Temporal and Spatial Distribution of Carbon Dioxide Emissions in Counties of Henan Province

In this part, we give the CO_2 emissions, the numbers of countries with different emission levels, and associate with geographic information to analyze the temporal and spatial distribution of carbon dioxide emissions in counties of Henan Province.

Due to the changes in the statistical method of the Henan statistical yearbook in the year 2010, there exists a big difference between the dada 2000-2009 and 2010-2018. Considering the unity and adequacy of the data, we summarize the carbon dioxide emissions of counties in Henan Province in the years 2010, 2014, and 2018, which are listed in Table 2. In the table, AE, AEI, VE, VEI denote carbon emissions, carbon emission intensity, carbon emission variance, and carbon emission intensity variance respectively. It can be observed in the table that the average emission, emission intensity, emission variance, and emission intensity variance of counties have decreased year by year. The results indicate that the economy between counties is developing towards a green economy. Moreover, the difference in emissions and emissions levels is gradually shrinking.

Let *DED* and *DEI* denote the numbers of counties counted according to their carbon emissions and their intensity. We count the number of counties according to different intervals. For the carbon emissions, we set the split points as A:26.8, B:53.5, C:80.3, D:133.8, E:187.3, F:500 (10 kt).

Fig. 3: The comparison of regressed carbon emissions and the actual carbon emissions.

Table 3: CO_2 emissions at county-level in Henan Province

Year	AE (10 kt)	VE	AEI	VEI
2010	176	1.48	9240	1.6
2014	163	0.725	6110	0.725
2018	108	0.482	2710	0.237

Fig. 4: The T^2 ellipse of sample points.
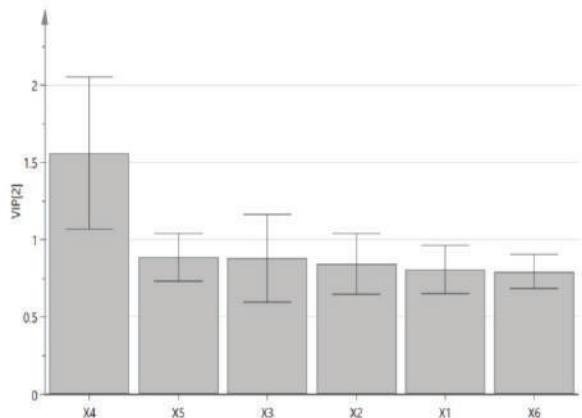
Fig. 5: The VIP indicators of the variables.

For the carbon emissions intensity, we set the split points as A:0.22, B:0.43, C:0.87, D:1.30, E:2.16, F:11.

Table 4 shows the distribution of carbon dioxide emissions of counties in Henan Province. We compared the number of counties in Henan Province by carbon emissions and carbon emission intensity in different intervals in 2010, 2014, and 2018. We used intervals to compare the number of counties in Henan Province by carbon emissions and carbon emission intensity in different intervals in 2010, 2014, and 2018. The right border of the interval is defined as the highest value of carbon emissions and carbon emissions intensity in counties in any given year between 2010 and 2018, while the left boundary is defined as zero. The emission volume in any year is divided into 6 intervals according to the 10%, 20%, 30%, 50%, 70% of the maximum value. Similarly, for the measurement of carbon emissions, set the split point according to 5%, 10%, 20%, 30%, and 50% of the maximum value. The fifth interval and the sixth interval are regarded as the ultra-high emission interval and the high emission interval respectively. The third and fourth intervals are regarded as the medium emission intervals. And the first

interval and the second interval are regarded as low emission intervals. It can be seen from Table 3 that the number of counties with high carbon emission intensity and carbon emissions gradually decreases in the time domain, and the number of counties with low carbon emissions and carbon emission intensity gradually increases. It can be concluded that the status of carbon emissions of all counties in Henan Province is gradually improving.

Fig. 6 and Fig. 7 use ArcGIS tools to show the spatial distribution of carbon emissions and emission intensity in Henan Province. The results show that areas with high carbon emissions are mainly concentrated in most areas of northern Henan and a small part of central Henan, such as Zhengzhou, Luoyang, and their surrounding counties, while the carbon emissions in southern Henan are at a relatively low level. The higher carbon emission intensity is mostly concentrated in the central and a small number of northern regions, such as Pingdingshan, Sanmenxia, Jiaozuo, Anyang, etc. The obvious feature of such regions is that the coal-related industries in such regions are relatively thriving. According to the data in Table 3, the number of high carbon emission counties ac-
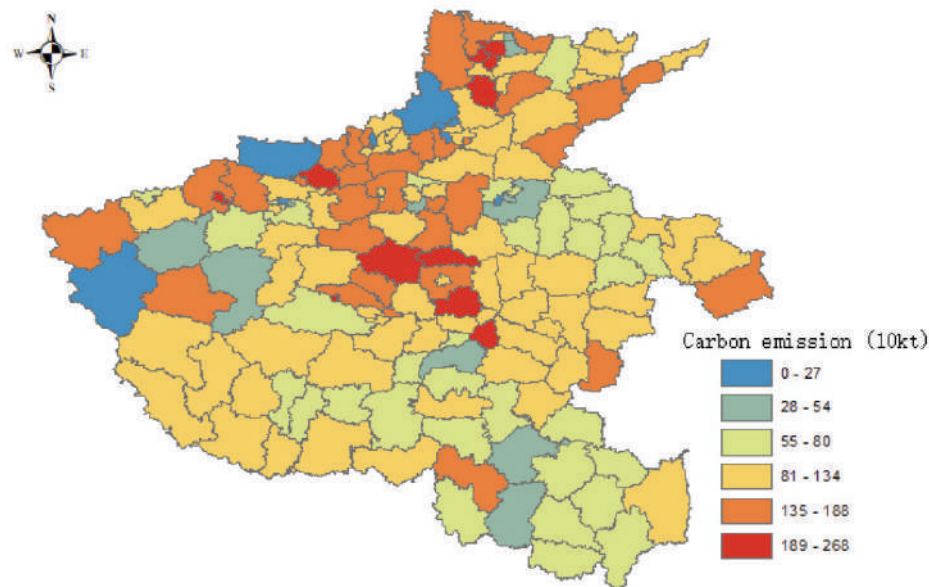
Fig. 6: The distribution of county emissions in Henan Province in 2018.

Table 4: Distribution of CO_2 emissions in counties of Henan Province.

YEAR	DEA (10kt)						DEI					
	0-A	A-B	B-C	C-D	D-E	E-F	0-A	A-B	B-C	C-D	D-E	E-F
2000	4	2	18	42	28	63	11	40	74	12	12	8
2014	6	3	9	36	53	50	11	40	74	18	8	6
2018	7	11	34	62	32	11	29	73	41	6	5	3
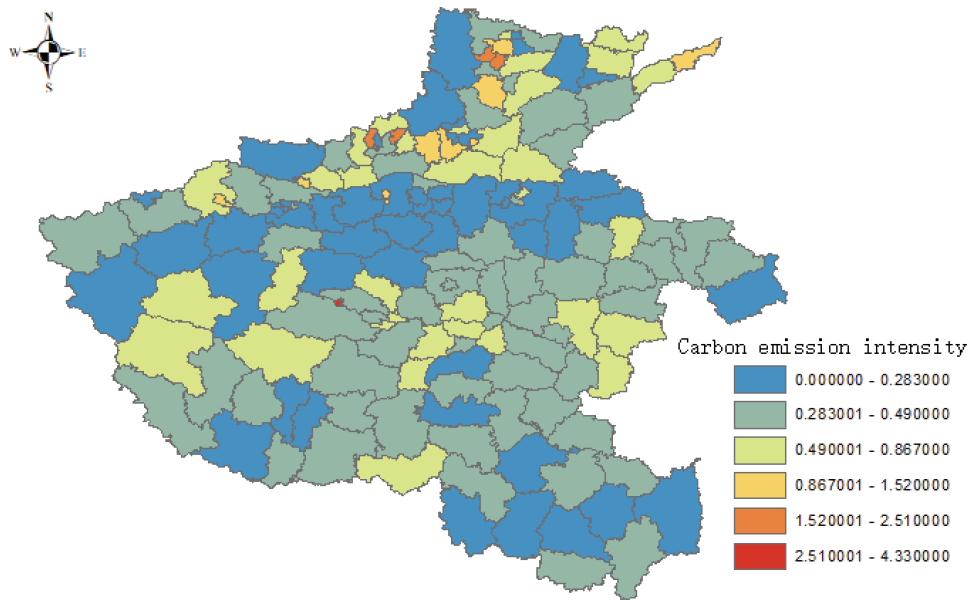
Fig. 7: The distribution of county-level carbon emission Intensity in 2018.

counted for 32.4% in 2010, and the number of high emission intensity counties accounted for 3.8%, which dropped to 7% and 1.9% n 2018. The proportion of counties with ultra-low carbon emissions and emission intensity increased from 2.5% and decreased to 7% in 2010 to 4.6% and 18.5% in 2018, indicating the large reduction efforts of carbon emissions have been done in Henan Province.

CONCLUSION

This article examines the driving forces of carbon growth using Henan Province's terminal consumption, pertinent statistical data on carbon emissions from 2000 to 2018, and a combination of the carbon emission factor method and the LMDI factor decomposition method to calculate carbon emissions. The contribution of provincial carbon emission factors is analyzed using partial least squares regression analysis, which complements the analysis of driving forces, and a county downscaling carbon emission estimation model is built to analyze the temporal and spatial distribution of carbon emissions in the province. The research presented in this article can serve as a foundation for relevant departments to develop policies for reaching carbon emission peaks.

REFERENCES

Abdul-Wahab, S.A. 2015. CO_2 greenhouse emissions in Oman over the last forty-two years: Review. Renew. Sustain. Energy Rev., 52: 1702-1712.

Chi, M., Liu, Z. and Wang, X. 2021. Provincial CO_2 emission measurement and analysis of the construction industry under China's carbon neutrality target. Sustainability, 13(4): 1876.

Dascalaki, E.G., Argiropoulou, P. and Balaras, C.A. 2020. Analysis of the embodied energy of construction materials in the life cycle assessment of Hellenic residential buildings. Energy Build., 232: 110651.

Ebohon, O.J. and Ikeme, A.J. 2006. Decomposition analysis of CO_2 emission intensity between oil-producing and non-oil-producing sub-Saharan African countries. Energy Policy, 34(18): 3599-3611.

Ehrlich, P.R. and Holdren, J.P. 1971. Impact of population growth. Science, 171(3977): 1212-1217.

Ehrlich, P.R. and Holdren, J.P. 1972. Impact of Population Growth in Population, Resources and The Environment. US Government Printing Office, Washington DC.

Frankignoulle, M.A. 1998. Carbon dioxide emission from European estuaries. Science, 282(5388): 434-436.

Grossman, G.M. and Krueger, A.B.1992. Environmental impacts of a North American free-trade agreement. CEPR Discuss. Papers, 8(2): 223-250.

Guo, X.D., Zhu, L. and Fan, Y. 2011 Evaluation of potential reductions in carbon emissions in Chinese provinces based on environmental DEA. Energy Policy, 39(5): 2352-2360

Jaskolski, M. 2016. Modeling long-term technological transition of Polish power system using MARKAL: Emission trade impact. Energy Policy, 97: 365-377.

Lantz, V. and Feng, Q. 2006. Assessing income, population and technology impacts on CO2 emissions in Canada: Where is the EKC? Ecol. Econ., 57(2): 229-238.

Lin, B. 2016. CO_2 emissions of China's food industry: An input-output approach. J. Cleaner Prod., 112: 1410-1421.

Lin, B. and Ahmad, I. 2017. Analysis of energy related carbon dioxide emission and reduction potential in Pakistan. J. Cleaner Prod., 143: 278-287.

Mao, C., Shen, Q., Shen, L. and Tang, L. 2013. Comparative study of greenhouse gas emissions between off-site prefabrication and conventional construction methods: Two case studies of residential projects. Energy Build., 66(5): 165-176.

Martinez-Botas, R.T. 2015. Reducing China's road transport sector CO_2 emissions to 2050: Technologies, costs, and decomposition analysis. Appl. Energy, 157: 905-917.

McPherson, M. and Karney, B. 2014. Long-term scenario alternatives and

their implications: Leap model application of Panama's electricity sector. Energy Policy, 68: 146-157.

Mi, Z., Jing, M. and Guan, D. 2017. Chinese CO_2 emission flows have reversed since the global financial crisis. Nature Commun., 8(1): 1712.

Mishra, V. and Smyth, R. 2017. Conditional convergence in Australia's energy consumption at the sector level. Energy Econ. 62: 396-403.

Nässen, J., Holmberg, A., Wadeskog, M. and Nyman, D. 2007. Direct and indirect energy use and carbon emissions in the production phase of buildings: An input-output analysis. Energy, 32(9): 1593-1602.

Qi, S. and Zhang, Y. 2013. Research on the influencing factors and reduction strategies of carbon emission of the construction industry in China. Soft Sci., 27: 39-43.

Shu, C., Xie, H.L. and Jiang, J.F. 2018. Is urban land development driven by economic development or fiscal revenue stimuli in China? Land Use Policy, 77: 107-115.

Song, Y., Sun, J. and Zhang, M. 2020. Using the Tapio-Z decoupling model to evaluate the decoupling status of China's CO2 emissions at the provincial level and its dynamic trend. Struct. Change Econ. Dynamics, 52: 120-129.

Stocker, T.F., Qin, D. and Plattner, G.K. 2013. Climate Change 2013: The Physical Science Basis. Contribution of Working Group I to the 5th Assessment Report of the IPCC, Cambridge University Press, Cambridge, pp. 659-740.

Tavakoli, A. 2017. A journey among top ten emitter countries, decomposition of Kaya identity. Sustain. Cities Soc., 38: 254-264.

Zhu, C.G., Gu, C.L. and Ma, R.H. 2018. The influential factors and spatial distribution of floating population in China. Acta Geogr. Sin., 56(5): 549-560.

Traffic Noise Pollution Assessment in Major Road Junctions of Imphal City, Manipur (India)

Ramtharmawi Nungate and Wazir Alam†

Department of Forestry and Environmental Science, Manipur University (A Central University), Canchipur, Imphal-795003, Manipur, India
†Corresponding author: Wazir Alam; wazir@manipuruniv.ac.in

ABSTRACT

Noise pollution assessment was carried out in selected traffic junctions of Imphal city of Manipur, India, using noise parameters and indices such as L_{10}, L_{50}, L_{90}, L_{eq} for the different periods of the day, i.e., morning, noon, and evening hours. The study of equivalent noise level (L_{eq}), noise parameters, and various noise indices have enabled the evaluation of the overall traffic noise environment of the city. The noise indices such as traffic noise index (TNI), noise climate (NC), traffic noise pollution level (L_{NP}), noise exposure index (NEI) along with day time (L_D), night time (L_N) average, and day-night (L_{dn}) noise levels were assessed for the selected traffic junctions. Moreover, spatial noise mapping was carried out using the geostatistical interpolation technique to evaluate the changes of traffic noise scenarios during the different time zones of the day. The L_{eq} values in a few traffic junctions exceeded the required noise standards. The study shows equivalent noise levels ranging between 52.2-69.9 dB(A) during the morning (7-10 am), 52.4 -69.3 dB(A) during noon (12 noon-2 pm), and 54.6-71.1 dB(A) during the evening (4-7 pm) hours, respectively.

INTRODUCTION

A sound is a form of mechanical energy generated from a vibrating body and transmitted through a medium in a series of cyclic compressions and rarefactions (Chanlett et al. 1973). Generally, the high-intensity sound causes noise pollution, which is considered to be an emerging urban environmental problem. High-intensity sound levels produced by increasing traffic volume result in chaotic and disturbed urban environments leading to various health issues (Al-Omari & Sharabi 2006). However, due to indirect and passive impacts, noise pollution studies received less priority than the other forms of urban environmental pollution. Selected studies across the world have revealed the effects of noise pollution on human health and urban biodiversity resulting from exposure to high noise levels (Sharma et al. 2014, Tyagi et al. 2014, Marathe 2012, Chauhan et al. 2010, Ogunsote 2010, Vera & Vila Goday 1992). Continual exposure to high-intensity noise can cause direct, indirect, and cumulative health impacts depending upon the noise sources, intensity, power, exposure time, and duration (Getzner & Zak 2012). Pervasive traffic noise pollution can cause various health impacts such as physical, physiological, psychological, heart problem, nervous system disorder, deafness, mental breakdown in individuals (Aluko & Nna 2015, Welch et al. 2013, Adedeji & Folurunso 2010, Banerjee et al. 2009, Singh & Davar 2004, Li et al. 2002). It can also cause indirect impacts on the economy, as high

noise levels can deteriorate the working environment, efficiency, and performances of workers leading to a reduction in workforce and productivity (Pignier 2015, Al Refaee et al. 2013). Higher noise levels can impact wildlife and urban biodiversity by disturbing their habitats, ecological niches, disrupting breeding grounds, matting, and reproductive patterns in animals (Ortega 2012, Parris & Schneider 2009, Popper & Hastings 2009). As the impacts of noise pollution are indirect and passive, people are the least concerned about the impacts of noise pollution (Alam 2011). So for sustainable urban planning and management, regular monitoring and assessment of the noise environment are essential to curb the escalating noise pollution emerging from rapid urbanization and various developmental activities. In this regard various noise pollution abatement measures can be adopted such as design and fabrication of silencing devices, proper traffic management, banning on electronic horns, creating noise zones/noise barriers, development of open and green spaces, planting of green zones and trees to curb the escalating noise levels (Garg et al. 2017, Onder & Akay 2015, Onder & Kocbeker 2012, Mihaiescu & Mihaiescu 2009).

STUDY AREA

Imphal is capital city of the state of Manipur in India. It is one of the significantly growing cities in the north-eastern Indian region due to its strategic location and excellent prospects for

various developmental initiatives for the south-east Asian region. Geographically the city extends between 24.48°-24.82° N latitude and 93.56°-93.95° E longitudes and covers 29.57 sq. km. (Fig. 1), with a population size of 9,74,105 (Census 2011). There are three major national highways, NH-53, NH-150, and NH-39, connecting Imphal to other Indian states and the international border town, Moreh, near Myanmar (Table 1). Imphal city is the fastest-growing urban center in the state due to developed basic civic facilities and services that have resulted in a sharp increase in the urban population in recent years. Moreover, the increasing population and number of vehicles have changed the overall traffic scenario of the city in the last few decades.

MATERIALS AND METHODS

Collections of Noise Levels

Noise levels were recorded during the morning, noon, and evening hours for selected traffic junctions of Imphal city using the sound level meter (SLM, Model: Lutron, SL-4001) in A-weighted decibels scale [dB (A)]. This scale represents and resembles human hearing range between 50-100 dB. The measurements were made at 1.5 m above the ground parallelly facing the source The coordinates of 30 spatially distributed traffic junctions used for noise mapping and delineation of vulnerable noise zone were collected using GPS (Garmin, etrex 20), respectively.

Assessment of Equivalent Noise Level (L_{eq})

Energy equivalent continuous sound level (L_{eq}) can be

defined as the steady sound pressure level over a given period with the same amount of total energy as the actual fluctuating noise over that period. L_{eq} is the rms sound level for measuring duration for an averaging time (Canter 1996)

$$L_{eq} = 10 \log \left(\frac{1}{t} \int_0^T \frac{P^2(t)}{P_0} dt \cdot dt \right) = L_{eq} = 10 \log \frac{1}{T}$$
$$\sum_{i=1}^N T_i ((10)^{L_i/10}) \qquad \ldots(1)$$

where T= total time of operation; T_i= total time duration of the ith phase, $L_i = L_{eq}$ value of ith phase and N= No. of phases; P(t) = sound pressure, P0 = reference sound pressure of 20 μPa. The L_{eq} is the energy equivalent sound level in dB (A) for any time under consideration. The daytime average sound pollution level (L_D), night-time average sound pollution level (L_N), and Day-night average (L_{dn}) is calculated as per the given equations.

$$L_D = 10 log_{10} \times \frac{1}{2} \left[Antilog \left(\frac{L_{eq}(M)}{10} \right) + Antilog \left(\frac{L_{eq}(A)}{10} \right) \right]$$
$$\ldots(2)$$

$$L_N = 10 log_{10} \times \frac{1}{2} \left[Antilog \left(\frac{L_{eq}(A)}{10} \right) + Antilog \left(\frac{L_{eq}(E)}{10} \right) \right]$$
$$\ldots(3)$$

$$L_{dn} = 10 log_{10} \times \frac{1}{24} \left[15.(10)^{(L_D/10)} + 15.(10)^{(L_N+10)/10} \right]$$
$$\ldots(4)$$

Assessment of L_{10}, L_{50}, L_{90}

L_{10} is defined as the sound pressure level (SPL) that does not
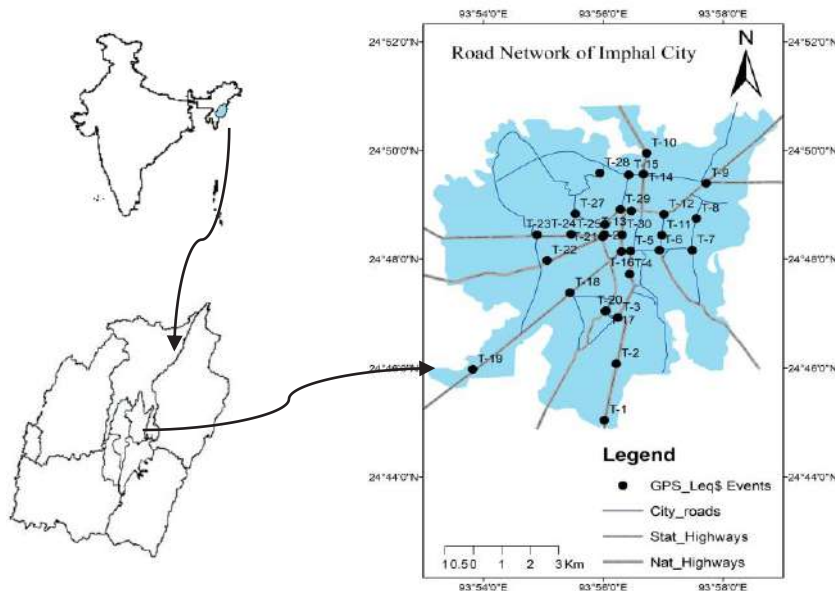
Fig.1: The study area and noise assessment locations.

Table 1: Table showing selected traffic-junctions of Imphal city.

Sl. No.	Name of Locations	Coordinates		Elevation [m]
		Lat [N]	Lon [E]	
T-1	Manipur University Gate	24.7507	93.9336	779
T-2	Kakwa Traffic point	24.7681	93.9370	780
T-3	Singjamei Traffic point	24.7822	93.9373	785
T-4	Keishamthong-Hijam Irabot Point	24.7954	93.9407	783
T-5	Kangla- Babupara Road	24.8025	93.9410	784
T-6	Konung- Mamang Road	24.8028	93.9490	784
T-7	Soibam leikai-Junction Road	24.8028	93.9581	785
T-8	JN Institute of Medical Science (JNIMS) Gate	24.8125	93.9592	783
T-9	Khurai Thoudam Leikai, Ayangpalli	24.8233	93.9620	782
T-10	Chingmeirong-Sangakpham	24.8325	93.9454	787
T-11	Checkon Traffic point	24.8074	93.9497	783
T-12	Hatta-Checkon Road	24.8138	93.9503	784
T-13	Kangla-BOC Road	24.8148	93.9412	784
T-14	Chingmeirong-Dewhlaland	24.8261	93.9445	786
T-15	Assembly House Gate	24.8259	93.9405	787
T-16	Kangla-GP Womens College Road	24.8023	93.9384	782
T-17	Keishampat Traffic point	24.7842	93.9339	783
T-18	Kwakeithel Traffic point	24.7898	93.9241	782
T-19	Imphal International Airport	24.7664	93.8970	780
T-20	Mayailambi-Ningom Leirak Road	24.7843	93.9341	783
T-21	Waheng leikai-Humped bridge Road	24.8069	93.9332	782
T-22	Sagolband-Khamnam Leikai Road	24.7996	93.9177	785
T-23	Naoremthong Bridge-Uripok Road	24.8075	93.9148	783
T-24	Uripok-Bachaspati Leikai Road	24.8077	93.9243	783
T-25	Flyover-samumakhong Road	24.8076	93.9336	784
T-26	Nagamapal Traffic point	24.8106	93.9338	783
T-27	Rims-Uripok-Nagamapal Road	24.8140	93.9255	783
T-28	Lamphel-Sanakeithel-Thangmeiband	24.8264	93.9324	781
T-29	Khoyathong Traffic point Road	24.8153	93.9381	782
T-30	Kangla Gate-Biotech Park Road	24.8075	93.9385	784

exceed 10% of the total time under consideration. It is also called impulse noise or instantaneous noise. L_{10} is a valid descriptor of road traffic noise as it takes account of any annoying peaks of noise or upper limit of fluctuating noise such as that from road traffic. L_{50} is the statistical average that considers 50% of the time under consideration and L_{90} is the 90% of the time under consideration. L_{90} is also called the ambient background noise level in the absence of any vehicular motor traffic.

Assessment of TNI, NC, LNP and NEI

Traffic noise index (TNI) indicates the degree of variation in traffic noise levels and give the measure of annoyance behavior of human. It indicates the overall fluctuations of noise over time and disorderliness of traffic noise levels. Traffic noise index (TNI) or traffic noise pressure levels are estimated by the following equation (Banerjee et al. 2009) given below.

$$TNI = 4 \times (L_{10}-L_{90}) + (L_{90} -30) \text{ dB (A)} \qquad …(5)$$

Noise climate (NC) indicates traffic noise annoyance. More the value of noise climate (NC), more is the difference between the peak noise and the background noise level in the absence of any motor vehicular traffic. Noise Climate is the range over which sound levels fluctuate in an interval of time and is estimated by the relation given below (Prachiti et al. 2014)

$$NC= (L_{10} - L_{90}) \text{ dB (A)} \qquad …(6)$$

Noise pollution level (L_{NP}) is also used to express the varying levels of noise that can cause physiological and psychological disturbances. It is expressed as shown below.

$$L_{NP} =L_{50}+ (L_{10}-L_{90}) + (L_{10}-L_{90})^2/60 \qquad …(7)$$

The noise exposure index (NEI) is the measurement to assess noise-induced hearing loss and is determined by the given equation (Oyedepo et al. 2019)

$$NEI = [{}^{t1}/_{T1} + {}^{t1}/_{T1} + {}^{t1}/_{T1} + \cdots \ldots \ldots \ldots \ldots + {}^{tn}/_{Tn}]$$
$$…(8)$$

where, t_1, t_2, $t_3...t_n$ are the actual limit of exposure and T_1, T_2, $T_3...T_n$ represents the permissible limits of exposure at the corresponding noise levels, respectively. The higher value of NEI (>1) is considered as exposure to excessive noise according to American National Standards (ANS) (NIOSH 1998).

Statistical Analysis and Cluster Analysis

The statistical correlation analysis was carried out to assess the co-variability between traffic noise descriptors and noise indices. The correlation (*r*) value in the range of $0.7 \leq r \leq \pm 1.0$, indicates strong co-variability/correlation between the parameters. Similarly, the correlation is considered to be moderate and weak if correlation lies between the value ±0.5 to ±0.7 and 0 to ±0.5, respectively. To identify the traffic junctions with similar noise characteristics, a hierarchical cluster analysis (CA) and dendrogram were plotted for the grouping of the traffic junctions.

Spatial Mapping

Spatial noise mapping is a statistical interpolation method used to better visualize and delineate vulnerable noise zones for the study area. Noise zone maps were prepared using ArcGIS software, using a geostatistical interpolation "kriging" technique which is an effective interpolation method to predict the unknown values using the coordinated spatial noise data (Alam 2011).

RESULTS AND DISCUSSION

Traffic Noise Descriptors and Noise Indices

Traffic noise descriptors such as annoying peak noise level (L_{10}), statistical average or 50th percentile (L_{50}), background noise level (L_{90}), and energy equivalent continuous noise levels (L_{eq}) and noise indices are presented in Table 2. It was observed that traffic noise levels exceed during evening hours than morning and noon hours due to high traffic congestions. The energy equivalent noise (L_{eq}) and background noise (L_{90}) levels exceed the noise standards of 65 dB(A) (CPCB 2000) in some of the traffic junctions of the city (Fig. 2).

Maximum noise level was recorded at traffic junction T-5 (83.2 dB(A)) followed by T-30 (82.8 dB(A)), T-9 (82.6 dB(A)), T-5 (80.9 dB(A)), T-7 (80.8 dB(A)), T-26 (80.6 dB(A)), T-4 (80.5 dB(A)) respectively, during evening hours. A similar trend was observed for L_{10}, L_{50}, and L_{90}. The annoying peaks of noise (L_{10}) were found higher than the noise standards of 65 dB(A) for the traffic flow scenario (Table 3).
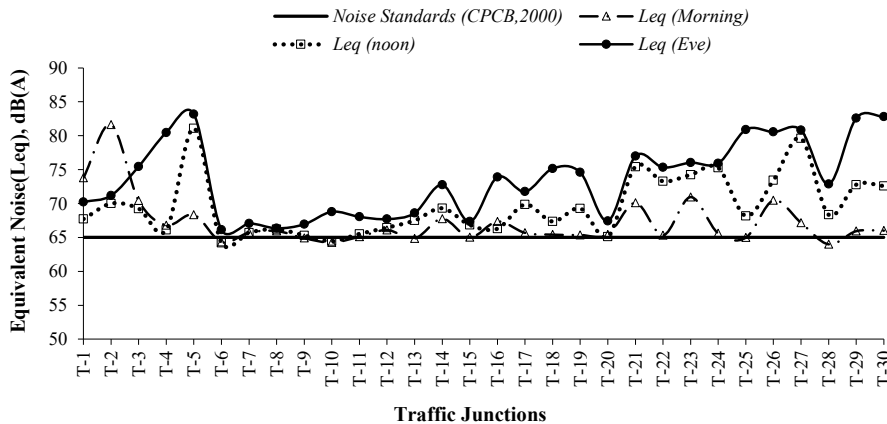
Fig. 2: Comparison of equise level (L_{eq}) with noise standards (CPCB 2000) for the traffic junctions during the morning, noon and evening hours.

Table 2: Traffic noise descriptors during morning (M), noon (N) and evening (E) hours.

Sl. No.	L_{10} dB(A)			L_{50} dB(A)			L_{90} dB(A)			L_{eq} dB(A)		
	M	N	E	M	N	E	M	N	E	M	N	E
T-1	51.0	53.1	56.4	64.9	59.1	62.4	73.3	65.1	69.0	73.8	67.7	70.2
T-2	54.3	56.7	58.4	64.1	62.8	66.4	72.1	67.7	71.0	81.6	70.0	71.2
T-3	52.7	51.1	61.3	60.1	58.6	68.7	69.2	65.9	73.9	70.4	69.2	75.5
T-4	54.6	49.4	61.6	61.5	59.3	74.0	63.5	65.1	78.5	66.8	66.1	80.5
T-5	51.1	55.9	66.8	63.0	62.5	77.6	67.1	64.5	81.9	68.4	81.1	83.2
T-6	48.6	50.4	54.6	57.6	57.3	60.5	62.2	62.9	64.8	64.3	64.2	66.1
T-7	49.7	49.7	53.3	57.5	57.5	61.9	63.6	63.6	65.2	65.7	65.7	67.1
T-8	50.2	50.2	53.4	59.4	59.4	61.1	64.7	64.7	65.2	66.0	66.2	66.4
T-9	46.3	48.1	50.2	56.8	58.7	59.7	62.9	63.1	64.5	64.9	65.3	66.9
T-10	53.2	51.3	58.0	58.7	57.1	65.2	62.8	62.9	67.6	64.3	64.4	68.8
T-11	51.3	48.3	58.3	60.2	58.7	61.4	64.1	64.5	65.8	65.1	65.5	68.0
T-12	50.1	46.7	52.6	56.9	63.7	60.5	63.6	65.7	64.3	66.1	66.4	67.7
T-13	48.6	51.0	58.2	56.2	63.5	63.1	62.6	66.6	66.6	64.9	67.5	68.6
T-14	52.0	50.3	58.2	65.2	60.1	68.9	67.1	68.7	72.5	67.8	69.3	72.7
T-15	48.2	49.3	51.3	57.3	57.9	62.6	62.5	64.5	66.0	65.0	66.8	67.3
T-16	51.3	52.6	58.0	60.5	62.3	66.8	66.4	65.1	72.3	67.4	66.3	73.9
T-17	52.3	53.3	62.1	60.3	66.3	68.0	64.0	69.5	69.4	65.7	69.8	71.8
T-18	52.1	50.0	58.6	59.6	63.3	67.4	63.4	66.0	73.1	65.4	67.3	75.2
T-19	50.3	58.6	60.1	58.0	62.7	68.3	64.0	67.7	71.1	65.4	69.3	74.6
T-20	51.3	50.6	51.8	58.0	60.6	61.4	63.1	63.7	64.9	65.4	65.1	67.4
T-21	50.8	58.3	62.6	61.3	69.7	69.6	69.1	74.1	74.1	70.1	75.4	77.0
T-22	50.1	58.3	60.6	57.9	65.4	67.9	62.7	71.8	73.9	65.3	73.3	75.3
T-23	61.4	51.8	61.7	68.3	68.5	70.8	70.5	72.3	74.7	71.0	74.2	76.0
T-24	51.2	59.2	63.6	58.0	69.0	69.7	64.3	73.3	74.9	65.6	75.3	75.9
T-25	48.6	51.8	62.3	58.6	62.5	72.1	62.8	67.3	76.5	65.0	68.2	80.9
T-26	58.4	57.3	68.3	66.0	64.4	76.5	68.1	71.9	78.4	70.5	73.4	80.6
T-27	52.1	61.4	60.6	60.9	73.3	73.0	66.1	78.7	79.6	67.2	79.6	80.8
T-28	48.1	50.3	57.3	58.2	61.0	65.8	62.0	67.7	69.6	64.0	68.4	72.9
T-29	58.3	58.3	66.8	61.4	64.3	76.7	64.6	71.3	82.0	65.9	72.8	82.6
T-30	50.3	52.3	66.4	59.0	65.3	78.0	63.9	70.6	80.9	66.0	72.6	82.8

The higher value of TNI indicates more disturbances due to fluctuating noise concerning L_{10}. More annoyance *w.r.t.* TNI was observed in the evening hours as compared to morning and noon hours.

Similarly, L_{NP} is a better indicator that accounts for variations in the sound signal and serves as a measure for noise pollution descriptor for physiological and psychological disturbance for the human. The highest TNI of 106.4 dB(A) is recorded at T-27 during noon and evening hours, followed by T-4, T-5, T-29, and T-30 (Table 3). NC also in-

dicates traffic noise annoyance occurred due to sound level fluctuations in an interval of time. More NC represents more differences between the L_{10} and L_{90}. It is found that fluctuations between annoying peaks noise were higher during the morning hours than noon and evening hours, indicating more noise contribution from road traffic during morning hours. This also suggests that the background noise levels during morning hours are less due to fewer heavy motor vehicles.

NEI represents the noise exposure level *w.r.t.* the reference duration (*t*) to the permissible limit of noise exposure

duration (T) at the corresponding noise level. The NEI values (Table 4 & Fig. 3) of morning hours show higher NEI followed by the noon and evening hours. Some of the traffic junctions (T-6, T-9, T-11, T-12, T-20) show higher NEI values (NEI>1) throughout the assessment period (morning, noon, evening), indicating a high level of noise exposure due to excessive traffic congestion and noise levels. The higher value also suggests the possibility of annoyance among the exposed population due to elevated noise levels throughout the exposed time. During morning hours 67.7%, noon hours 48.4%, and evening hours 26.1% of locations exhibit higher NEI (NEI>1) values which are considered undesirable. Similarly, day time (L_D), night time (L_N), and day-night (L_{dn}) average noise level exceeding 80 dB(A) is not acceptable as they may have undesirable impacts on human health.

Moreover, the higher L_{dn} values also indicate that people in the vicinity of the traffic junctions are more vulnerable and exposed to noise pollution.

Statistical Assessment

The correlation between the noise descriptors and noise indices (Table 5), shows the co-variability between the parameters. Higher correlation (r) (> ±0.7) indicates a significant strong co-variability between the noise descriptors and noise indices (at $p < 0.05$). TNI, NC, and L_{NP} show a strong correlation with each other. Similarly, the noise descriptor, $L_{eq,}$ and L_{50} show a high to moderate correlation with the TNI and NC. The CA shows the traffic junctions with similar noise descriptors or equivalent noise levels during the morning (Fig. 4), noon (Fig. 5), and evening (Fig. 6) hours, respec-
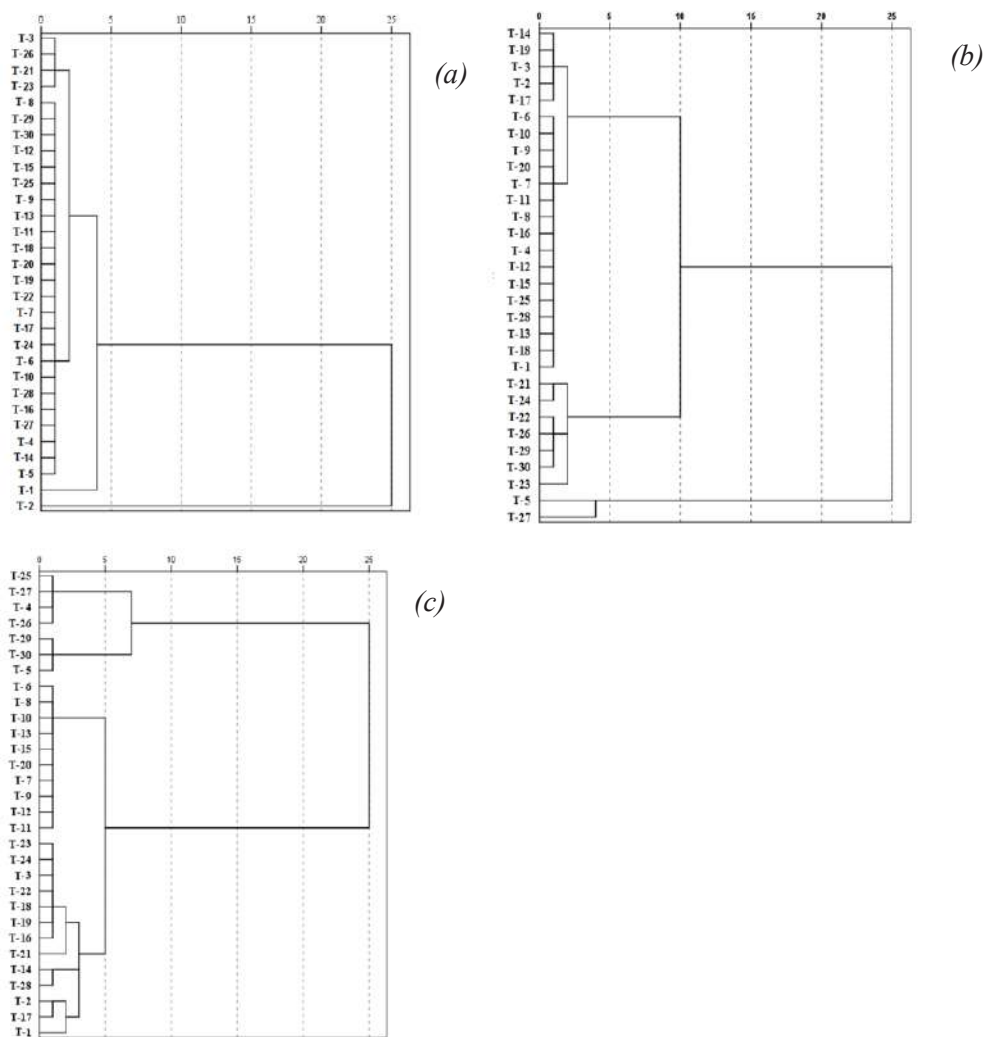
Fig. 3: Dendogram showing the cluster of traffic junctions with similar trend of noise levels during (a) morning (b) Noon and (c) evening hours

Table 3: Traffic Noise Index (TNI), Noise Pollution Level (L_{NP}) and Noise Climate (NC) for the selected traffic junctions.

Sl No.	TNI dB(A)			L_{NP} dB(A)			NCdB(A)		
	M	N	E	M	N	E	M	N	E
T-1	110.0	71.0	76.7	95.4	73.5	77.6	22.3	12.0	12.6
T-2	95.5	70.7	78.9	87.2	75.8	81.7	17.8	11.0	12.6
T-3	88.9	80.4	81.8	81.2	77.0	84.0	16.5	14.8	12.6
T-4	60.1	82.0	99.3	71.6	79.0	95.7	8.9	15.7	16.9
T-5	85.0	60.4	97.1	83.2	72.4	96.5	16.0	8.6	15.1
T-6	73.1	70.3	65.5	74.4	72.4	72.4	13.6	12.5	10.2
T-7	75.2	75.2	70.9	74.6	74.6	76.1	13.9	13.9	11.9
T-8	78.0	78.0	70.7	77.4	77.4	75.2	14.5	14.5	11.8
T-9	82.7	78.1	77.3	77.9	77.4	77.4	16.6	15.0	14.3
T-10	61.7	67.9	66.4	69.9	71.0	76.3	9.6	11.6	9.6
T-11	72.6	83.2	85.3	75.8	79.3	69.8	12.8	16.2	7.5
T-12	74.2	92.6	69.2	73.4	88.7	74.4	13.5	19.0	11.7
T-13	74.4	83.4	62.0	73.4	83.2	72.8	14.0	15.6	8.4
T-14	82.6	94.0	85.4	84.2	84.2	86.7	15.1	18.4	14.3
T-15	75.6	80.1	80.1	75.0	77.0	80.8	14.3	15.2	14.7
T-16	81.6	72.7	85.2	79.3	77.5	84.5	15.1	12.5	14.3
T-17	69.0	88.0	61.2	74.2	86.9	76.2	11.7	16.2	7.3
T-18	67.1	84.0	86.4	73.0	83.6	85.3	11.3	16.0	14.5
T-19	75.2	65.0	74.1	74.9	73.2	81.4	13.7	9.1	11.0
T-20	68.6	72.9	74.2	72.1	76.5	77.3	11.8	13.1	13.1
T-21	93.9	91.5	78.8	85.1	89.7	83.4	18.3	15.8	11.5
T-22	70.5	82.1	83.7	73.2	81.9	84.1	12.6	13.5	13.3
T-23	67.9	103.8	83.8	78.8	96.0	86.6	9.1	20.5	13.0
T-24	73.5	85.5	78.6	73.9	86.4	83.1	13.1	14.1	11.3
T-25	75.3	83.9	89.3	76.1	82.1	89.7	14.2	15.5	14.2
T-26	67.2	85.8	78.9	77.3	82.6	88.4	9.7	14.6	10.1
T-27	78.1	100.5	106.4	78.2	95.5	97.9	14.0	17.3	19.0
T-28	73.9	89.9	76.4	75.3	83.4	80.6	13.9	17.4	12.3
T-29	53.3	80.2	97.8	68.3	80.1	95.8	6.3	13.0	15.2
T-30	74.9	95.4	94.3	75.7	89.2	95.9	13.6	18.3	14.5

tively. The CA categorizes the traffic junctions with similar equivalent noise levels and locations with possible potential impacts due to higher values of noise indices (Table 6).

Noise Mapping

Spatial noise mapping shows the interpolated vulnerable noise maps prepared using the existing data concerning their geographical coordinates. The noise mapping delineates the noise zones and shows the variations of noise levels at various locations during the morning, noon, and evening hours. The noise map during the morning hours shows a greater extent of the noise environment of Imphal city because of more traffic congestions occurring during these hours due to plying of more vehicles for offices and schools. The higher extended noise zones during the morning hours spread towards the south-eastern region of the city in the state and national highways. Similarly, recorded high noise levels in the central commercial zone of the city due to more traffic congestion and gathering of people in the central zone of the city markets during the noon hours. In the evening hours, high noise levels
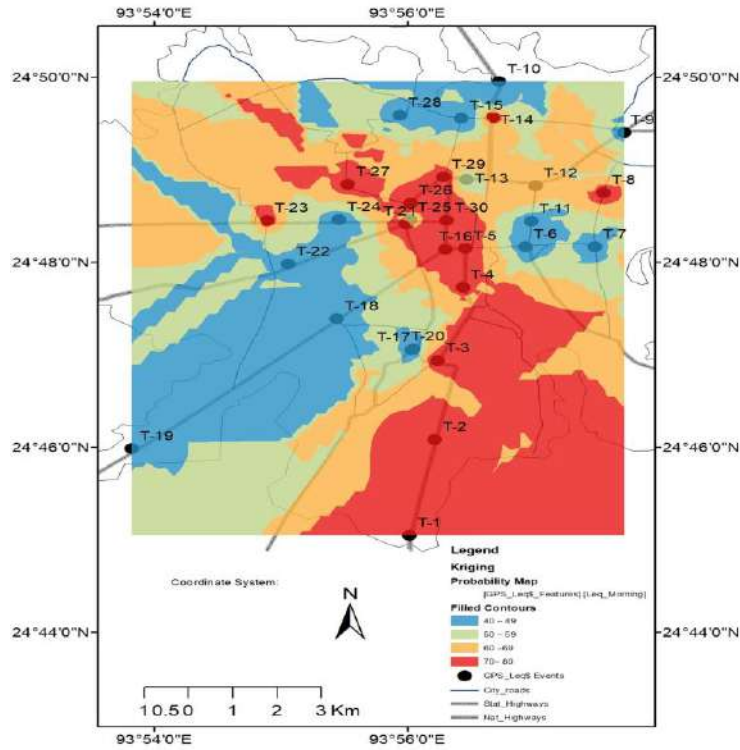
Fig. 4: Spatial variation mapping of noise levels in Traffic Junctions of Imphal city during morning (7-10 am) hours.
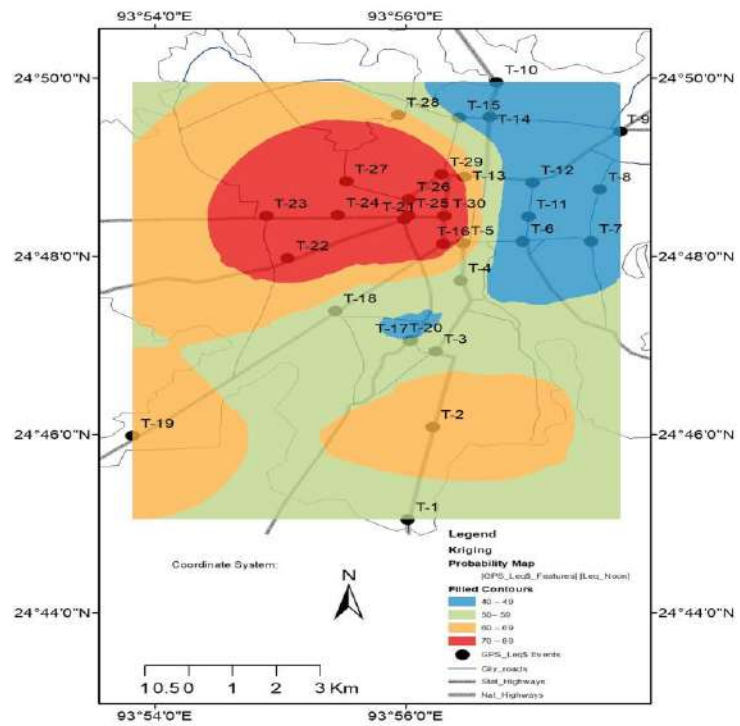
Fig. 5: Spatial variation mapping of noise levels in Traffic Junctions of Imphal city during noon (12-2 pm) hours.

Table 4: Noise Exposure Index (NEI) and Day time (L_D) and Night time (L_N) average.

Sl No.	NEI			$L_{day}(L_D)$ dB(A)	$L_{night}(L_N)$ dB(A)	$L_{daynight}(L_{DN})$ dB(A)
	M	N	E			
T-1	0.76	1.11	0.68	73.0	69.2	76.4
T-2	0.53	0.73	0.45	79.2	70.6	79.8
T-3	0.82	1.09	0.31	74.4	73.4	79.9
T-4	1.35	1.17	0.19	77.8	77.6	84.0
T-5	0.87	1.08	0.10	82.3	82.3	88.7
T-6	1.52	1.54	1.07	66.7	65.3	71.9
T-7	1.35	1.35	0.97	68.0	66.4	73.1
T-8	1.14	1.14	0.98	67.9	66.3	73.0
T-9	1.62	1.39	1.22	67.6	66.2	72.8
T-10	1.43	1.50	0.76	68.1	67.1	73.7
T-11	1.17	1.25	1.01	68.2	67.0	73.6
T-12	1.42	1.33	1.12	68.6	67.1	73.8
T-13	1.61	0.88	0.82	69.0	68.1	74.6
T-14	1.01	0.88	0.37	72.2	71.4	77.9
T-15	1.54	1.26	0.94	68.3	67.1	73.7
T-16	0.98	1.04	0.43	72.3	71.6	78.1
T-17	1.17	0.70	0.59	71.5	70.9	77.4
T-18	1.24	1.02	0.38	73.2	72.8	79.3
T-19	1.26	0.82	0.51	73.1	72.7	79.2
T-20	1.34	1.24	1.04	67.9	66.4	73.1
T-21	0.90	0.32	0.29	76.8	76.3	82.8
T-22	1.48	0.45	0.33	74.7	74.4	80.9
T-23	0.61	0.49	0.27	76.0	75.2	81.8
T-24	1.24	0.33	0.26	75.8	75.6	82.0
T-25	1.42	0.81	0.45	78.2	78.1	84.5
T-26	0.85	0.49	0.24	78.7	78.3	84.8
T-27	0.96	0.22	0.23	80.4	80.2	86.7
T-28	1.55	0.99	0.70	71.6	71.2	77.6
T-29	1.13	0.50	0.11	80.1	80.0	86.4
T-30	1.28	0.64	0.12	80.3	80.2	86.6

were witnessed in the core city zone and the north-western and south-eastern extent of the city, comprising significant state and national highways.

CONCLUSION

The traffic noise assessment for selected traffic junctions of the Imphal city was an attempt to appraise the traffic noise scenario considering noise descriptors, indices, and vulnerable noise zone mapping. Noise descriptors were found beyond the noise standards in many traffic junctions due to the increasing number of vehicles, high traffic congestions,

poor road conditions, lack of diversion roads/flyovers, and poor traffic management system. Similarly, traffic noise indices such as L_{NP}, NC, NEI represent the higher traffic noise scenario, abrupt noise fluctuations, and noise exposure levels. Spatial noise mapping and cluster analysis indicate the vulnerable traffic junctions of the city based on their elevated noise levels. The study highlights the requirement of direct or indirect noise pollution control management and mitigation initiatives such as the development of pedestrian and cycling lanes, increasing more greenery along the road-side, restricting the use of pressure and multi-tone horns, checking the vehicle's condition, constructing road medians,

Table 5: The correlation of noise descriptors, indices during morning, noon and evening hours.

	L_{10}	L_{50}	L_{90}	L_{eq}	TNI	NC	L_{NP}	NEI
L_{10}	1.00							
L_{50}	0.76*	1.00				Morning hours		
L_{90}	0.50	0.81*	1.00					
L_{eq}	0.43	0.68	0.90*	1.00				
TNI	-0.32	0.22	0.66	0.60	1.00			
NC	-0.54	0.00	0.46	0.42	0.97*	1.00		
L_{NP}	-0.01	0.57	0.84*	0.74*	0.92*	0.82*	1.00	
NEI	0.65	0.86*	0.93*	0.83*	0.45	0.23	0.68	1.00

	L_{10}	L_{50}	L_{90}	L_{eq}	TNI	NC	L_{NP}	NEI
L_{10}	1.00							
L_{50}	0.69	1.00				(b) Noon hours		
L_{90}	0.75*	0.91*	1.00					
L_{eq}	0.77*	0.77*	0.78*	1.00				
TNI	0.10	0.60	0.66	0.30	1.00			
NC	-0.35	0.31	0.35	0.01	0.93*	1.00		
L_{NP}	0.21	0.81*	0.78*	0.49	0.94*	0.81*	1.00	
NEI	0.80*	0.89*	0.95*	0.78*	0.53	0.21	0.68	1.00

	L_{10}	L_{50}	L_{90}	L_{eq}	TNI	NC	L_{NP}	NEI
L_{10}	1.00							
L_{50}	0.92*	1.00				(c) Evening hours		
L_{90}	0.89*	0.97*	1.00					
L_{eq}	0.88*	0.97*	0.99*	1.00				
TNI	0.48	0.74*	0.83*	0.80*	1.00			
NC	0.08	0.42	0.53	0.50	0.91*	1.00		
L_{NP}	0.69	0.90*	0.94*	0.92*	0.95*	0.76*	1.00	
NEI	0.88*	0.92*	0.95*	0.92*	0.73*	0.42	0.85*	1.00

*Indicates significant r at $p < 0.05$ (2-tailed)

Table 6: Clusters Analysis (CA) representing the Traffic Junctions with showing similar noise levels.

Group	Noise Range, dB(A)	Sampling Stations		
		Morning	Noon	Evening
Group A	Above 75	T-1, T-2	T-5, T-21, T-24, T-27	T-4, T-5, T-25, T-26, T-27, T-29, T-30
Group B	70-75	T-3, T-21, T-23, T-26	T-22, T-23, T-26, T-29, T-30	T-1, T-2, T-17, T-28, T-14, T-21, T-16, T-19, T-18, T-22, T-3, T-24, T-23
Group C	60-70	T-4, T-5, T-6, T-7, T-8, T-9, T-10, T-11, T-12, T-13, T-14, T-15, T-16, T-17, T-18, T-19, T-20, T-22, T-24, T-25, T-27, T-28, T-29, T-30	T-1, T-2, T-3, T-4, T-6, T-7, T-8, T-9, T-10, T-11, T-12, T-13, T-14, T-15, T-16, T-17, T-18, T-19, T-20, T-25, T-28,	T-6, T-7, T-8, T-9, T-10, T-11, T-12, T-13, T-15, T-20
Group D	50-60	Nil	Nil	Nil
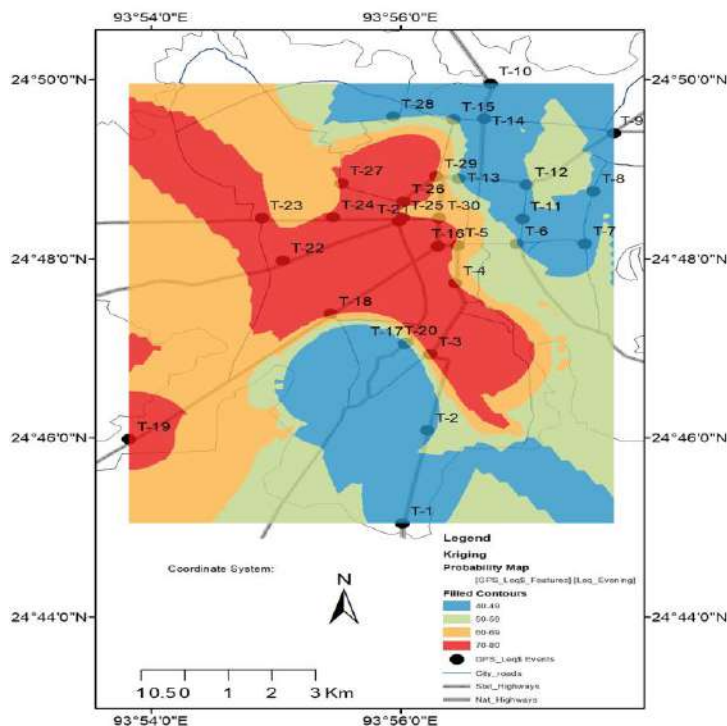
Fig. 6: Spatial variation mapping of noise levels in Traffic Junctions of Imphal city during evening (4-7 pm) hours.

etc. along with strict enforcement of noise pollution control regulations and traffic rules.

REFERENCES

Adedeji, Y.M.D. and Folurunso, C.O. 2010. Pollution management in housing environment and health of urban dwellers. International Conference Organized by School of Environment Technology, Federal University of Technology, Akure.

Al Refaee, K., Alaboud, E., Alramahi, N. and Weshah, S. 2013. Noise pollution and its effect on the profitability of industrial companies: A study from cement factories in Jordan. Glo. J. Manag. Bus. Res., 13(5): 26-34.

Alam, W. 2011. GIS-based assessment of noise pollution in Guwahati city of Assam, India. Int. J. Environ. Sci., 2(2): 743-751.

Al-Omari, J.A. and Sharabi, R., 2006. Evaluation of traffic noise pollution in the city of Amman, Jordan. Environ. Monit. Asses., 120(1-3): 499-525.

Aluko, E. and Nna, V. 2015. Impact of noise pollution on the human cardiovascular system. Int. J. Trop. Diseas. Health, 6: 35-43.

Banerjee, D., Chakraborty, S.K., Bhattacharyya, S. and Gangopadhyay, A. 2009. Appraisal and mapping the spatial-temporal distribution of urban road traffic noise. Int. J. Environ. Sci. Technol. 16(2): 325-335.

Canter, L.W. 1996. Environmental impact assessment. Mc-Graw-Hills Inc., New York, pp. 304-340.

Census. 2011. District Census Handbook, Bishnupur, Census of India, Series 15, Part XII-B. Directorate of Census Operation, Government of Manipur.

Chanlett, E.T. 1973. Environmental Protection. Mc-Graw Hills Inc., New York, pp.140-142.

Chauhan, A., Pawar, M., Kumar, D., Kumar, N. and Kumar, R. 2010. Assessment of noise level status in different areas of Moradabad City. Reprod. Opi., 2(5): 59-61.

CPCB, 2000. The Noise Pollution (Regulation and Control) Rules. Central Pollution Control Board, New Delhi.

Garg, N., Sinha, K., Dahaiya, M., Gandhi, V.M., Bhardwaj, R.B. and Akolkar, A. 2017. Evaluation and analysis of environmental noise pollution in seven major cities of noise. Arch. Acous., 42(2): 175-188.

Getzner, M. and Zak, D. 2012. Health impacts of noise pollution around airports: Economic valuation and transferability. Environmental health-merging issues and practice, Jacq. Oosth. Intech., 79: 247-272.

Li, B., Tao, S. and Dawson, R.W. 2002. Evaluation and analysis of traffic noise from the urban main roads in Beijing. Appl. Acous., 63: 1137-1142.

Marathe, P.D. 2012. Traffic noise pollution. Int. J. Edu. Develop., 9(5): 63-68.

Mihaiescu, T. and Mihaiescu, R. 2009. Traffic noise pollution in urban areas: Case study-Bistritatown. Pro-Environment, 2: 222-225.

NIOSH. 1998. Criteria for a Recommended Standard, Occupational Noise Exposure. National Institute for Occupational Safety and Health Department of Health and Human Services, Public Health Service Centers for Disease Control and Prevention, Cincinnati, Ohio.

Ogunsote, O.O. 2010. Environmental Control-Acoustics and Noise Control. Unpublished Lecture Notes. Department of Agriculture, Federal University of Technology, Akure.

Onder, S. and Akay, A. 2015. Reduction of traffic noise pollution effects by using vegetation, Turkey. J. Eng. Ecosys. Develop., 2(2): 23-35.

Onder, S. and Kocbeker, Z. 2012. Importance of the green belts to reduce noise pollution and determination of roadside noise reduction effectiveness of bushes in Konya, Turk. Int. J. Agri. Biosys. Eng., 6(6): 373-376.

Ortega, C. 2012. Effects of noise pollution on birds: A brief review of our knowledge. Ornithol. Mono., 74(1): 6-22.

Oyedepo, S.O., Adeyemi, G.A., Olawole, O.C., Ohijeagbon, O.I., Fagbemi, O.K., Solomon, R., Ongbali, S.O., Babalola, O.P., Dirisu, J.O., Efemwenkiekie, U.K., Adekeye, T. and Nwaokocha, C.N. 2019. A GIS-based method for assessment and mapping of noise pollution in Ota metropolis, Nigeria. Methods, 6: 447- 457.

Parris, K. and Schneider, A. 2009. Impacts of traffic noise and traffic volume on birds of roadside habitats. Ecol. Soc., 14(1): 29.

Pignier, N. 2015. The Impact of Traffic Noise on Economy and Environment: A Short Literature Study: Performed within the Scope of the ECO2 Project 'Noise Propagation from Sustainable Ground Vehicles'. Technical Report, TRITA-AVE, 29, pp.1-16.

Popper, A. and Hastings, M. 2009. The effect of human-generated sound on fish. Int. Zool., 4(1): 43-52.

Prachiti, M., Joshi, N., Ambika J. and Bist, B. 2014. Study of fluctuating noise levels in Palghar, Mumbai, India. Pollut. Res., 33(2): 1-6.

Sharma, R., Myrthong, I. and Lal, B. 2014. Noise-induced health impacts in urban areas: A case study in Allahabad. Int. J. Sci. Res. Pub., 4(12): 1-6.

Singh, N. and Davar, S.C. 2004. Noise pollution-source, effects, and control. J. Hum. Ecol. 16(3): 181-187.

Tyagi, V., Kumar, K. and Jain, V.K. 2013. Road traffic noise attenuation by vegetation belts at some sites in the Tarai region of India. Arch. Acous., 38(3): 389-395.

Vera, M.N. and Vila Goday, J.F. 1992. Physiological and subjective effects of traffic noise: The role of negative statements. Int. J. Psych., 12: 267-279.

Welch, D., Shepherd, D., Kim, N., Samantha, M. and Dirks McBride, D. 2013. Road traffic and health-related quality of life: A cross-sectional study. Noise Health, 15(65): 224-230.

Tuning of Carbon Microspheres and Graphene Structures with Hetero Atoms for Organic Dye Degradation and Heavy Metal Remediation - Influence of Fructose as a Precursor

S. Sudhaparimala† and R. Usha

Department of Chemistry, Ethiraj College for Women, University of Madras, Chennai-600008, Tamil Nadu, India
†Corresponding author: S. Sudhaparimala; sudha92@gmail.com

ABSTRACT

In today's context, there is a tremendous potential for the design of smart nanomaterials of carbon origin for multi-dimensional applications. The role-play of precursor is significant in the design of nanometric carbon materials apart from other experimental parameters. Correlation of the synthetic methodology, the microstructure of the product helps to tune and widen the applications aspect. The present study aimed to tune the simple ketose (reducing monosaccharide) of fructose to functionalize (with O, N, and S atoms) carbon layers, microspheres of carbon, to optimize the experimental conditions, and to establish the mechanism involved in the process. The study further explored the catalytic ability of the carbon samples in the degradation of thiazine and xanthene-based textile dyes and the sensing of heavy metal ions of chromium and copper. A simple hydrothermal process, fructose as a precursor, alkaline pH, and appropriate calcination temperature provided micro and nanostructures of carbon viz. carbon microspheres (CMs), graphene oxide (GO), sulfur doped graphene oxide (S-GO), and nitrogen-doped reduced graphene oxide (N-rGO). In this study a simple mechanism for the conversion process is suggested. Further, the results of the preliminary screening study on the catalytic ability of the sulfur and nitrogen-doped graphene samples in the presence of UV and Visible light upon the degradation of methylene blue (MB), methyl orange (MO), Rhodamine-B (Rh-B) dyes were satisfactory. The adsorbent and the ion exchange capacity of the carbon microspheres were found to be excellent. The results of the study will contribute positively to the treatment and management of industrial wastewater.

INTRODUCTION

In recent years, among the carbon-based nanomaterials, two-dimensional graphene has received significant attention due to its unique optical, electronic, mechanical, and thermal properties used in many fields such as catalysis, nanoelectronics, sensors, capacitors, and nanocomposites. There are only a few recent research reports available on the use of synthetic carbohydrates (aldose and ketose) as a precursor for the synthesis of carbon-based nanomaterials, graphene in particular. Sunil et al. (2020) reported the synthesis of reduced graphene oxide from glucose as a precursor by the hydrothermal method and suggested a reaction mechanism. Mingfei et al. (2020) reported that the green precursor of fructose was used for the synthesis of carbon quantum dots by the hydrothermal method. There are no reports available to date on synthetic fructose as a precursor for the synthesis of 2D carbon nanomaterial (graphene-based nanomaterials) by hydrothermal method. Sudhaparimala and Usha (2021) reported a facile synthetic approach to the functionalization of graphene with the atoms of Oxygen and sulfur from the

reducing monosaccharide of glucose as a precursor for the catalytic removal of Chlorophenols and textile dyes.

There is also a broader scope for reducing monosaccharides of fructose as the resource for the design of graphene-based materials. In this context, there is a need to understand the first principles in building graphene structures with non-metal atoms of O, S, and N for tailoring their applications. Such a study will enhance the scope of biomass conversion to bio graphene-based materials since the glucosidal or fructosidal monosaccharides with active functional groups are the basic units of biomass.

Taking into consideration the above factors, the present research study provides a simple approach for the building of graphene layers with non-metal atoms of O, S, and N doped and spherical carbon microspheres from the precursor of fructose. Based on the analytical scrutiny of the microstructures a mechanistic pathway has been suggested. A correlative study between these structural aspects and their application as an adsorbent and photocatalyst in the degradation of toxic dyes and the ability to sense the presence of heavy metal ions has been successfully carried out.

Wastewater from the textile industry contains dyes mixed with various contaminants at a variety of ranges while paper and textile industries contribute dyestuffs of thiazine, azo and xanthene origin and their complete degradation is challenging globally. Degradation of simple representative examples of such dyes being Methylene blue, Methyl orange, and Rhodamine-B have been reported respectively (Bharatia et al. 2017).

Among all the pollutants, heavy metals have also received paramount attention from environmental chemists due to their toxic nature. Metals such as arsenic (As), lead (Pb), cadmium (Cd), nickel (Ni), mercury (Hg), chromium (Cr), cobalt (Co), zinc (Zn), and selenium (Se) become toxic when they are not metabolized by the body and accumulate in the soft tissues. They may enter the human body through food, water, air, or absorption through the skin when they come in contact with humans in agriculture, manufacturing, pharmaceutical, industrial or residential settings (Van Ael et al. 2012) Fabrication of the 2D carbon materials for sensing and ion exchange medium will open up another dimension to their applications. Existing reports on such applications are limited.

Considering these factors, there is a need to develop a new, efficient economic, and green catalyst. A new approach to the synthesis of functionalized graphene from a much-unexplored precursor of fructose and their ability to function as efficient adsorption and photocatalyst in the dye degradation is considered. In this current study, the simple monosaccharide of fructose (ketose) was used as a precursor for the synthesis of 2D carbon-based nanomaterials (CBNs) doped with non-metal atoms of O, N, S, and carbon microspheres by a simple hydrothermal method. The study was also undertaken to suggest a reaction pathway, screen them for the degradation of organic dyes, sensing of heavy metal ions by simple experimental methods. The results of the study will enhance the understanding of biomass conversion to smart materials and tailoring them for industrial wastewater management.

MATERIALS AND METHODS

Materials

Chemicals used for the synthesis of carbon microspheres and graphene-based nanomaterials (GBNs) are fructose (Merck chemicals), sulfuric acid (H_2SO_4), sodium hydroxide (NaOH) (Nice chemicals), glacial acetic acid (Nice chemicals), 99.9% ethanol (Analytical CS reagent), ammonia (NH_3), methylene blue (MB) stain (Merck chemicals), methyl orange (Nice Chemicals), Rhodamine Black (Merck Chemicals), calcium carbonate (Spectrum), magnesium sulfate (Nice chemicals), copper sulfate (Nice chemicals), zinc sulfate (Nice chemicals), buffer solution (pH=10) potassium dichromate (Nice chemicals), ethylene diamine tetraacetic acid (EDTA) (Nice chemicals), Eriochrome black-T (EBT) (Nice chemicals).

Method of Synthesis

Preparation of functionalized carbon microspheres (CMs) and functionalized graphene-based nanomaterials (GO, S-GO, N-rGO) by hydrothermal method

The experimental conditions were optimized for the synthesis of carbon-based nanomaterials using fructose by changing the reaction parameters like pH and temperature by hydrothermal method. Two samples were collected at the end of the process based on the decomposition temperature of the fructose at 180°C (GO) and 220°C (CMs) respectively at pH at 9 (adjusted by adding sodium hydroxide) for 5 h. The black solid sample (carbon microspheres (CMs) was obtained at 220°C (Sudhaparimala & Usha 2020).

For doping with sulfur, the graphene oxide (GO) (brown gel) sample obtained from hydrothermal treatment was treated with sulfuric acid in the ratio of 1:5 and heated at 80°C. The black solid residue obtained upon doping (GO-180°C) was further dried at room temperature. For the introduction of nitrogen, about 0.5 M fructose solution was hydrothermally heated after adding liquid ammonia in the ratio of 1:10, at 220°C for 5 h at pH=9 resulting in a resultant brown solid sample.

All the four product samples namely brown gel graphene oxide (GO) sample and brownish-black solid samples of sulfur-doped graphene oxide (S-GO), nitrogen-doped reduced graphene oxide (N-rGO) and carbon microspheres (CMs) were treated with ethanol for the removal of organic impurity. The samples were then refrigerated and stored for further characterization.

Material Characterization

The functional groups, bonding characteristics, and structural defects in the as-synthesized functionalized GBNs (GO, S-GO, and N-rGO) and carbon microspheres (CMs) were analyzed using the FT-IR (IR Affinity-1, Shimadzu) and Micro-Raman spectrometer (Bruker, RFS). The Avance III 500 NMR spectrometer was used for structural analysis. The microstructural analysis was carried out using powder X-ray diffractogram (PXRD) using a Cu-K radiation (PAN analytical model Xpert pro), surface morphology using a Field Emission Scanning Electron Microscopic (SEM) (Fei Quanta), and transmission electron microscopic (TEM) (Joel) image. The surface elemental composition and chemical state of the elements were identified using X-ray photoelectron

spectroscopy (XPS) (Ulvac-Phi, Inc.; Model: PHI5000 Version Probe III). The decolorization efficiency of the synthesized samples upon organic dyes under dark and light (UV and Sunlight) were screened with respect to time and also screened for the sensing capability of metal ions using colorimetry (Photometer μM).

Screening the photocatalytic efficiency of the carbon microspheres, oxygen and sulfur, nitrogen-doped graphene (GO, S-GO And N-rGO) as a catalyst on the decolorization of textile dyes

The as-synthesized samples of carbon microspheres and functionalized GBNs (S-GO, N-rGO) were screened individually for their catalytic activity in the discoloration of methylene blue (MB), methyl orange (MO), Rhodamine-Black (Rh-B) solution (2 ppm). The catalyst and the dye solution were taken in the ratio of 2mg/10mL (w/v) and the reaction mixtures were incubated in dark, UV, and sunlight medium at a pH of 3. The discoloration efficiency was measured in terms of optical density units for every half an hour for a total duration of two hours.

Detection of toxic metal ions (copper and chromium) by colorimetric method

The sensing efficiency of the samples for the metal ions of copper (Cu^{2+}) and chromium (Cr^{6+}) ion was screened by colorimetric method using different concentrations of copper sulfate (300 mM, 100 mM, and 50 mM) and potassium dichromate (50 mM, 10 mM, 0.1 mM, 0.01 mM) solution respectively. The optical density values were measured and compared with and without using as-synthesized samples (CMs, S-GO, N-rGO) as a catalyst in the concentration of 100 ppm (w/v).

Estimation of calcium and magnesium ion using assynthesized samples as a catalyst

The ions of Calcium and Magnesium were estimated by the usual EDTA titration using EBT indicator with and without the presence of synthesized samples (CMs, S-GO, N-rGO) at different concentrations (100 ppm, 200 ppm, 300 ppm, 400 ppm, 500 ppm). The role-play of the CBNs was studied using FT-IR spectra of the recovered samples after the estimation of metal ions.

RESULTS AND DISCUSSION

The basic structural aspects, microstructural and morphology of the as-synthesized samples of graphene oxide at 180°C (GO), carbon microspheres at 220°C (CMs), sulfur-doped graphene oxide at 180°C (S-GO), and nitrogen-doped reduced graphene oxide at 220°C (N-rGO) were analyzed.

FT-IR spectra of the precursor (fructose), assynthesized carbon microspheres and functionalized GBNs (GO, S-GO and N-rGO)

The functional groups corresponding to C-O, C=O, C=C, O-H, C-H in as-synthesized samples were identified and represented in Fig. 1(a). The intensity of the bands corresponding to C-O, C=O, O-H has decreased with respect to the precursor which signifies a decrease in oxygen functionality in all the as-synthesized samples (Mohammed 2014, Hassan et al. 2014, Sudhaparimala & Usha 2020). The band at 796cm^{-1} due to C=S group (Rao et al. 1963) and 2225cm^{-1}, 1395cm^{-1} due to stretching vibrations of graphitic carbon nitride and C=N functional groups were identified in S-GO and N-rGO respectively. In N-rGO, the band corresponding to C=C has increased when compared with S-GO indicating the decrease in the number of sp^2 carbon upon doping with sulfur. (Vasilios et al. 2015)

Micro-Raman spectra of as-synthesized Carbon Microspheres and functionalized GBNs (S-GO and N-rGO)

Micro-Raman spectrum is used as a characterization tool for analyzing the nature, amount, and types of structural defects present in graphene-based nanomaterials. In Fig. 1(b) the G-band of the micro-Raman spectra represents allowed high-frequency E_{2g} phonon of sp^2 carbon and D-band represents A_{1g} phonons around the Brillouin zone corner K and is activated by an intravalley double resonant process of sp^3 carbon, the 2D band represents overtone of D band, D' band coming from the intravalley double resonant process of E_{2g} phonon (Mark et al. 2011).

The I_D/I_G ratio indicates that the amount of defects has increased on doping with sulfur and decreased on doping with nitrogen. It may be due to the higher electronegativity of nitrogen compared to a sulfur atom which was well correlated with FT-IR analysis also. From the I_{2D}/I_G ratio, the numbers of layers in as-synthesized graphene nanomaterial were analyzed which increased functionalization with sulfur. It further indicates the decrease in the number of layers and the presence of sulfur-based functional groups at the edges of the plane of graphene (Erick et al. 2020, Isaac et al. 2013, Zhangting & Zhenhua 2017). The ratios of I_D/I_G, $I_D/I_{D'}$ and I_{2D}/I_G of synthesized carbon microspheres and functionalized GBNs are presented in Table 1.

From the results, the I_D/I_D ratio was found to be less than 3.5(< 3.5) for all the GBNs. The samples have a one-dimensional defects as observed in the grain boundaries of the synthesized graphene nanomaterials. The average defect distance has increased on functionalization which confirmed

Table 1: Comparison of the Intensity ratio of I_D/I_G, I_{2D}/I_G, and $I_D/I_{D'}$ of the as-synthesized samples.

Name of the sample	I_D/I_G ratio	I_{2D}/I_G ratio	$I_D/I_{D'}$ ratio	Average defect distance (L_D in nm)
CMs	0.3424	0.9498	0.6903	23.6952
GO	1.2714	0.9614	2.9820	12.2965
S-GO	0.9796	0.9796	1.3373	13.7713
N-rGO	0.4166	0.6736	0.5814	21.4800

the defects in the edges of the graphene plane and not in the basal plane (Isaac et al. 2013, Zhangting & Zhenhua 2017).

Carbon-13 Nuclear Magnetic Resonance (C-13 NMR) spectrum of graphene oxide

The C-13 NMR spectrum of the as-synthesized of graphene oxide is presented in Fig. 1(c). The NMR of the gel obtained at 180°C showed chemical shift value due to cyclodextrin with more number of layers and the results well correlated with the report (Anton et al. 2019).

The presence of sp^2 carbon was indicated by the peak in the range of 100-150 ppm The Oxygen functionality in the graphitic structure was identified in the range of 60-90ppm with 37 NMR peaks due to GO (Tapas et al. 2016, Guangxu et al. 2018). From the NMR result, it is established that the gel form of oxygen functionalized graphene obtained at 180°C is an intermediate in the formation of the final product of solid graphene oxide. The result correlated well with FT-IR and micro-Raman analysis. The confirmation from the NMR study is the first report of its kind in the synthesis of GO samples from fructose as a precursor by the hydrothermal method. It aids in the suggestion of a mechanistic pathway for the functionalization of graphene layers using non reducing monosaccharides.

Powder X-ray Diffraction (PXRD) spectra of synthesized GBNs and Carbon Microspheres Samples

The PXRD spectrum of the as-synthesized samples was given in Fig. 1(d). It can be seen that the 2θ values increased upon functionalization with sulfur or nitrogen on graphene. The d-spacing value has decreased on doping with sulfur and nitrogen which indicates that the functional groups are present at the edges and not in the basal plane of graphene. As the size of the doping element increased, the d–spacing value decreased thus increasing structural defect which was well correlated with the Micro-Raman analysis of graphene-based nanomaterial (Guangxu et al. 2018, Agata et al. 2017). The broadness of the peak has increased in the functionalized carbon nanomaterials (S-GO and N-rGO) than carbon microspheres (Mohammed 2014, Hassan et al. 2014, Erick et al. 2020). The 2θ values, d-spacing value, and miller indices of the as-synthesized samples are presented in Table 2.

High-Resolution Scanning Electron Microscopic (HR-TEM) and Field Emission Scanning Electron Microscopic (FE-SEM) images of the as-synthesized samples

The surface morphology of the as-synthesized samples as presented in Fig. 2 indicated a perfect, uniform spherical well-dispersed morphology of the carbon microspheres (CMs) (Fig. 2b) which correlates with the report (Shunji-an et al. 2015, Sanja et al. 2015). The layer structures of graphene oxide were observed in Fig. 2a and correlate with a report (Tapas et al. 2016). The layer structure with spherical aggregates were observed in S-GO (Fig.2c) (Qinghong et al. 2018, Sudhaparimala & Usha 2020). In the case of N-rGO, layer structure with spherical dots (Fig.2d) were observed indicating more surface defects with less microstructural defects as indicated by micro raman analysis (Fig.1(b)) (Guangxu et al. 2018).

Wide scan X-ray Photoelectron spectroscopic (XPS) images of Carbon Microspheres, Sulfur-doped graphene Oxide, and Nitrogen-doped reduced graphene Oxide

Wide scan X-ray photoelectron spectroscopic images of carbon microspheres (CMs), sulfur-doped graphene oxide (S-GO), and nitrogen-doped reduced graphene oxide (N- rGO) are given in Fig. 3. The binding energy value corresponding to C (1s) was identified due to alkane (284.6 eV), alkene (285.9 eV) was hydroxyl (285.6 eV), epoxy (286.3eV), carbonyl (287.3eV), Carboxyl (289.1eV) indicating the presence of functional groups on the surface of assynthesized samples. The additional binding energy peak corresponding to C-S was identified at 285.4eV in S-GO and C-N peak was identified at 287.7eV in N-rGO confirming the doping of the heteroatoms of sulfur, and nitrogen respectively and it correlates with the reports (Agata et al. 2017, Qinghong et al. 2018, Ho et al. 2011).

Table 2: Comparison of d-spacing, 2θ value, and miller indices of the as-synthesized samples.

Name of the sample	2θ	d-spacing	Miller indices
CMs	19.6567°	0.3963	001
S-GO	20.3087°	0.3932	001
N-rGO	20.1325°	0.3916	001

The defect on the surface of the as-synthesized samples was confirmed using the intensity ratio of sp^3/sp^2 carbon using C (1s) XPS spectrum (Agata et al. 2017). It can be seen that the one-dimensional grain boundaries defect in graphene structure increased on doping upon more with sulfur than nitrogen due to the electronegativity difference between the atoms which is well correlated with Micro-Raman analysis. The presence of carboxyl and carbonyl functional groups was profound in S-GO while hydroxyl, epoxy groups are prominent in N-rGO as confirmed by broad scan X-ray photoelectron spectroscopic image of O(1s). The layer with more spherical aggregates was introduced upon functionalization with sulfur than nitrogen. The intensity ratio of sp^3/sp^2 carbon from XPS was compared with the I_D/I_G ratio obtained from Micro-Raman analysis and carbon to oxygen ratio on the surface of the synthesized samples from XPS and EDX analysis as presented in Table 3.

The carboxy and carbonyl functional groups were present at higher concentrations on the surface of CMs and S-GO. The hydroxyl and epoxy groups were found to be high in the case of N-rGO, which indicates that the functional groups present at the edges are not in the basal plane which correlates with PXRD reports. The C/O ratio was comparatively less on doping with sulfur than nitrogen which correlates well with EDX analysis it is clear that the increased C/O ratio of nitrogen-doped reduced graphene oxide indicates the more reduction of oxygen functionality by the introduction of nitrogen than sulfur due to the greater size and electronegativity of the elemental nitrogen. (Agata et al. 2017)
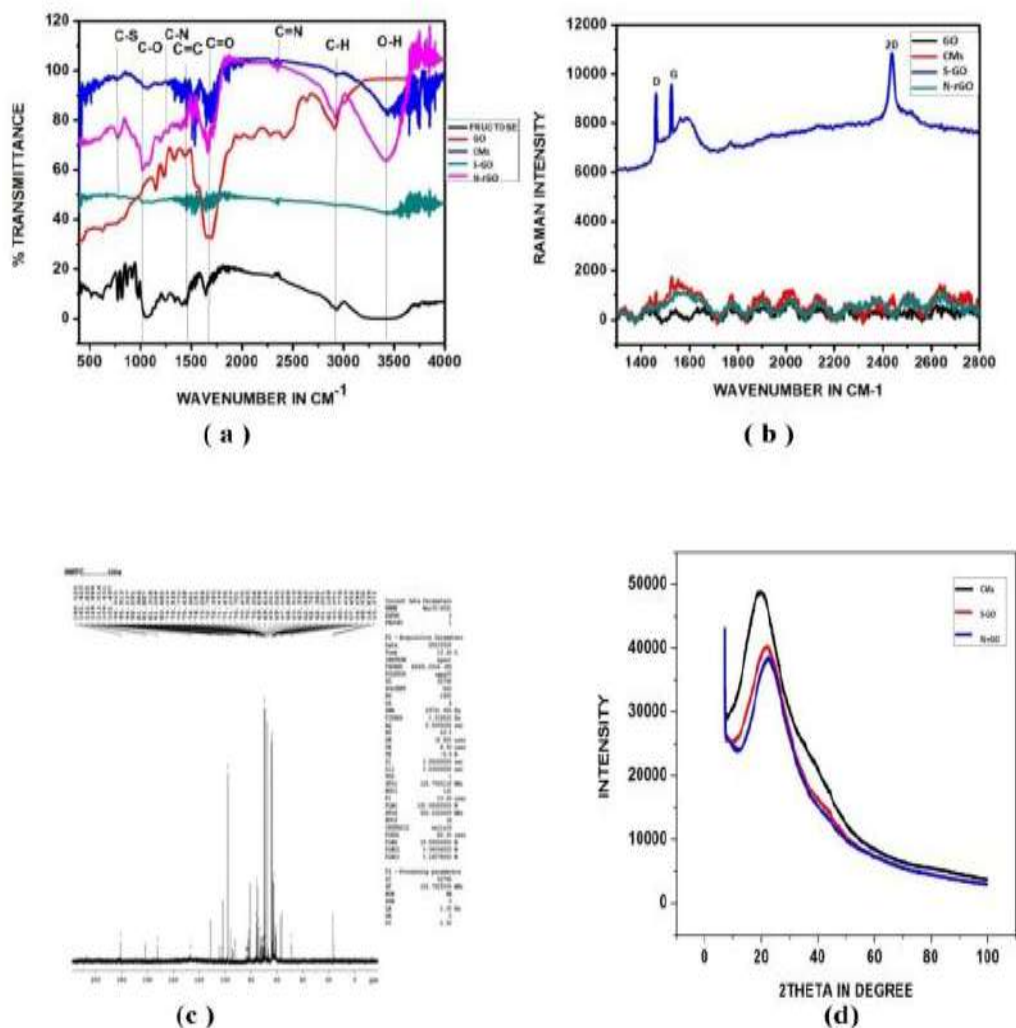
Fig. 1: (a) FT-IR- spectrum of fructose, CMs, GO, S-GO, N-rGO, (b) micro-Raman spectrum of CMs, GO, S-GO, N-rGO, (c) carbon-13 NMR spectrum of graphene oxide, (d) PXRD spectrum of CMs, S-GO, N-rGO.

Table 3: Comparison of carbon to oxygen ratio from EDX and XPS analysis and compared the intensity ratio of sp^3/sp^2 carbon from XPS analysis and I_D/I_G ratio from Micro-Raman analysis of the as-synthesized samples.

Name of the sample	Name of the element	Percentage of elements from wide scan spectrum of XPS analysis	Percentage of elements from EDX analysis	C/O ratio from wide scan spectra of XPS analysis	C/O ratio from EDX analysis	sp^3/sp^2 ratio from XPS analysis	I_D/I_G ratio from micro-Raman analysis
CMs	Carbon	68.83	79.16	2.1922	3.7985	1.5113	1.2714
	Oxygen	31.17	20.84				
S-GO	Carbon	49.88	59.55	1.2121	1.7351		
	Oxygen	41.15	34.32			1.6484	0.9796
	Sulfur	8.9637	6.13				
N-rGO	Carbon	47.77	78.37	1.2143	3.9521		
	Oxygen	39.34	19.83			1.5015	0.4166
	Nitrogen	12.88	1.8				

The above characterization reports confirm the micro-structure of graphene oxide (GO), sulfur-doped graphene oxide (S-GO), nitrogen-doped reduced graphene oxide (N-rGO), and carbon microspheres (CMs) were synthesized by hydrothermal method. Based on the properties, the as-synthesized solid samples of CMs, S-GO, N-rGO were screened as adsorption and photocatalyst for the decoloration of dyes and used as adsorption catalysts for the detection of heavy metal ions.

From the above results, the following reaction mechanism is suggested for the synthesis of graphene oxide, sulfur-doped graphene oxide, and nitrogen-doped reduced graphene oxide using fructose as precursor represented in Fig. 4. The mechanistic pathway suggested is based on the correlative
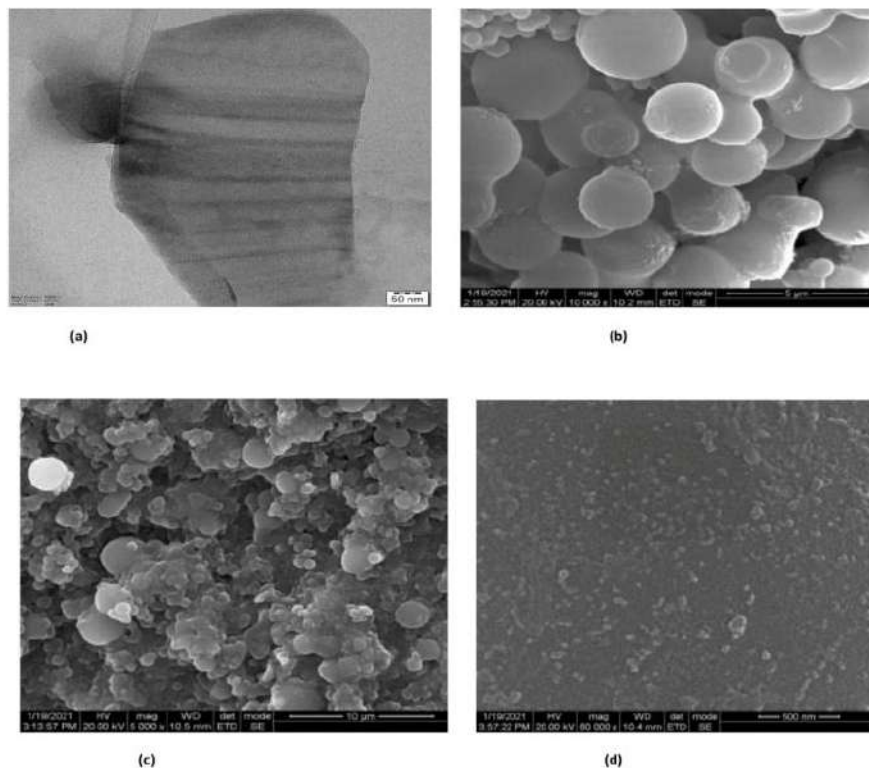
Fig. 2: a). HR-TEM image of graphene oxide and FE-SEM images of b) CMs, c) S-GO, d). N-rGO.
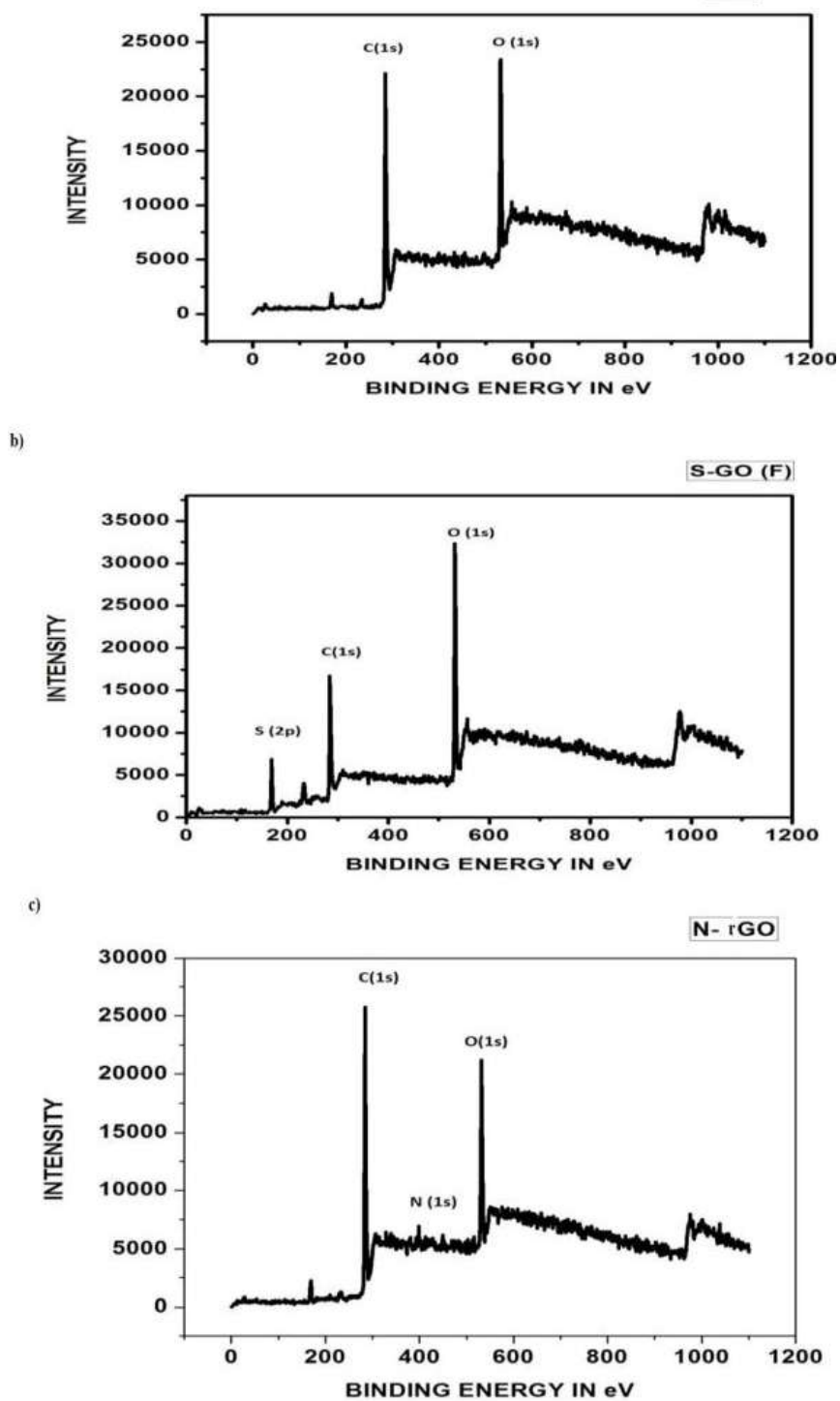
Fig. 3: Wide scan X-ray photoelectron spectroscopy (XPS) images of a). Carbon microspheres b). Sulfur-doped graphene oxide and c). nitrogen-doped reduced graphene oxide.
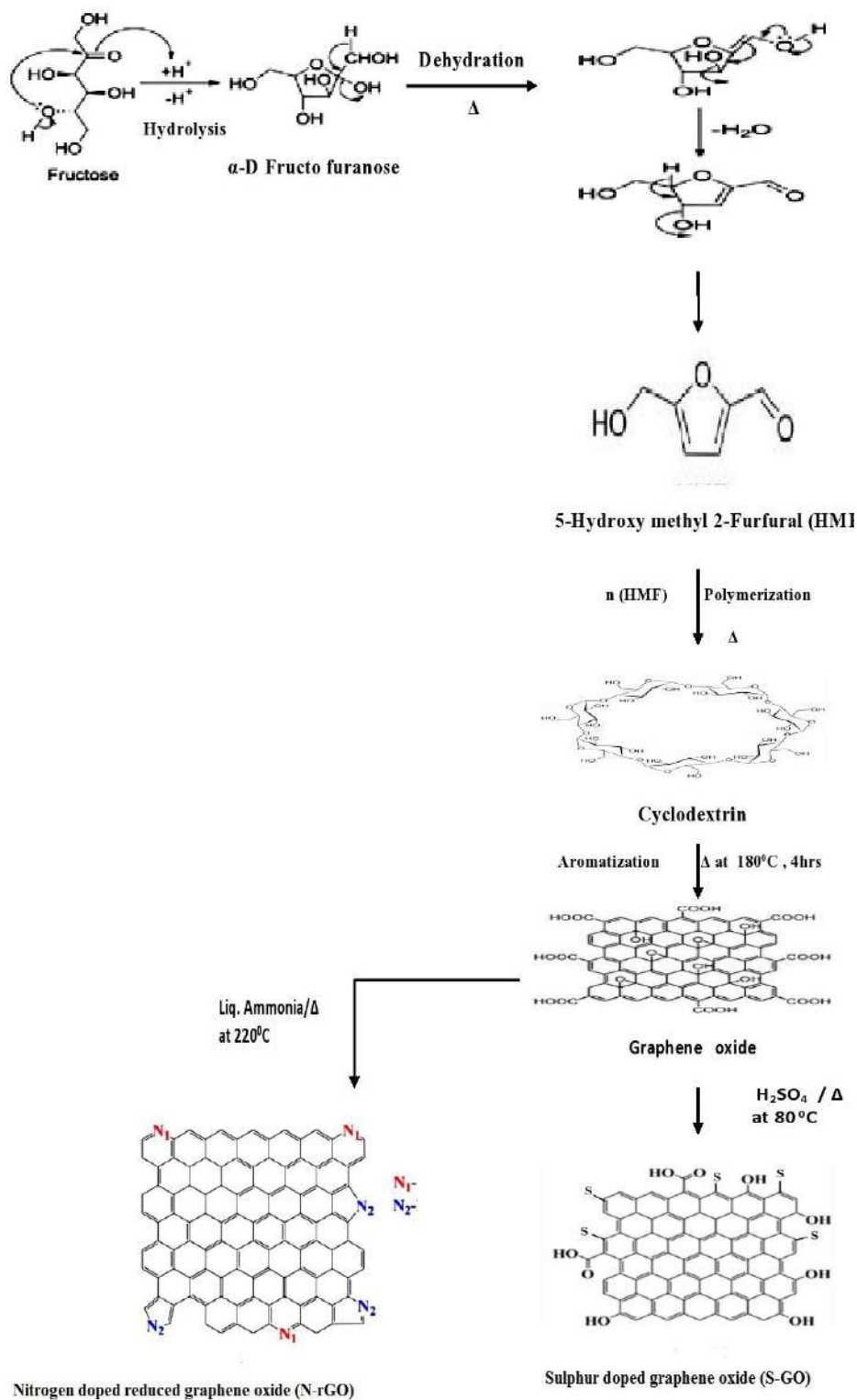
Fig. 4: A suggested reaction mechanism for the preparation of graphene oxide, sulfur-doped graphene oxide, and nitrogen-doped reduced graphene oxide from fructose as a precursor.

analytical results of the present study and not found in the literature.

Catalytic Application Study

Adsorption and photocatalytic decoloration of organic dyes (Methylene blue (MB), Methyl orange (MO), Rhodamine-Black (Rh. B) using as-synthesized samples as a catalyst: The experimental conditions were optimized for the decoloration of dyes using different (acidic, basic, and neutral) mediums under dark and UV light. The decoloration of dyes was found to be better under acidic conditions. Based on the optimization, the preliminary screening of the Catalytic decoloration of Methylene blue (MB), Methyl Orange (MO), Rhodamine-B (Rh-B) was carried out with the concentration of 2 ppm, (2mg.10mL^{-1}), pH=3 for 2 h in the dark, UV-light and Sunlight represented in Fig. 5.

The results indicate that all the sample shows adsorption property for the decoloration of organic dyes. Among the samples, the carbon microsphere has a good adsorbent feature due to the presence of uniform spherical-like morphology and the carboxyl functional group on the surface. Nurettin et al. (2017), reported that the maximum adsorption capacity of 67% for 0.1-g carbon microsphere for 50-ppm dye solu-

tions in DI water correlated with our report. The presence of oxygen-containing acidic functional groups in S-GO was effective in the photocatalytic activity for the removal of anionic dyes (methyl orange) and less acidic functional group on the surface in N-rGO was effective for the removal of cationic dyes (methylene blue and Rhodamine-B). This is due to the electronegative difference between the adsorbate and functional group existing on the surface of the adsorbent which enhanced surface defects in grain boundaries that are involved in the oxidation reaction for the decoloration of dyes under UV light and Sunlight.

From our results, S-GO was a more effective photocatalyst for the decoloration of dyes than N-rGO. The photocatalytic activity of S-GO was found to be more by using aldose as a precursor than ketose. It is attributed to the introduction of more heteroatoms, functional groups, elemental compositions existing on the surface with fewer structural defects as reported by Sudhaparimala et al. (2021).

Remediation of Toxic Heavy Metal Ions in Industrial Pollutants

Detection of copper and chromium ion using as-synthesized samples as adsorption catalyst by the colorimetric
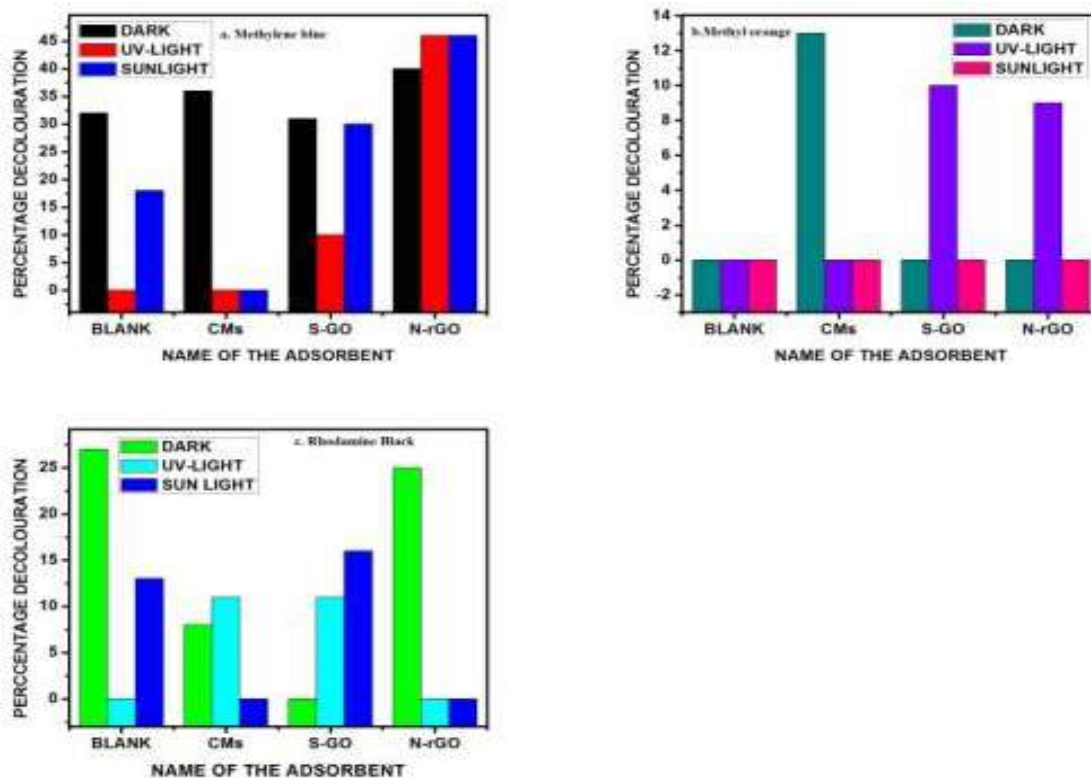
Fig. 5: Adsorption and photocatalytic decoloration of organic dyes a). Methylene blue (MB), b). Methyl orange (MO), c). Rhodamine-Black (Rh. B) using as-synthesized samples as a catalyst.

S. Sudhaparimala and R. Usha
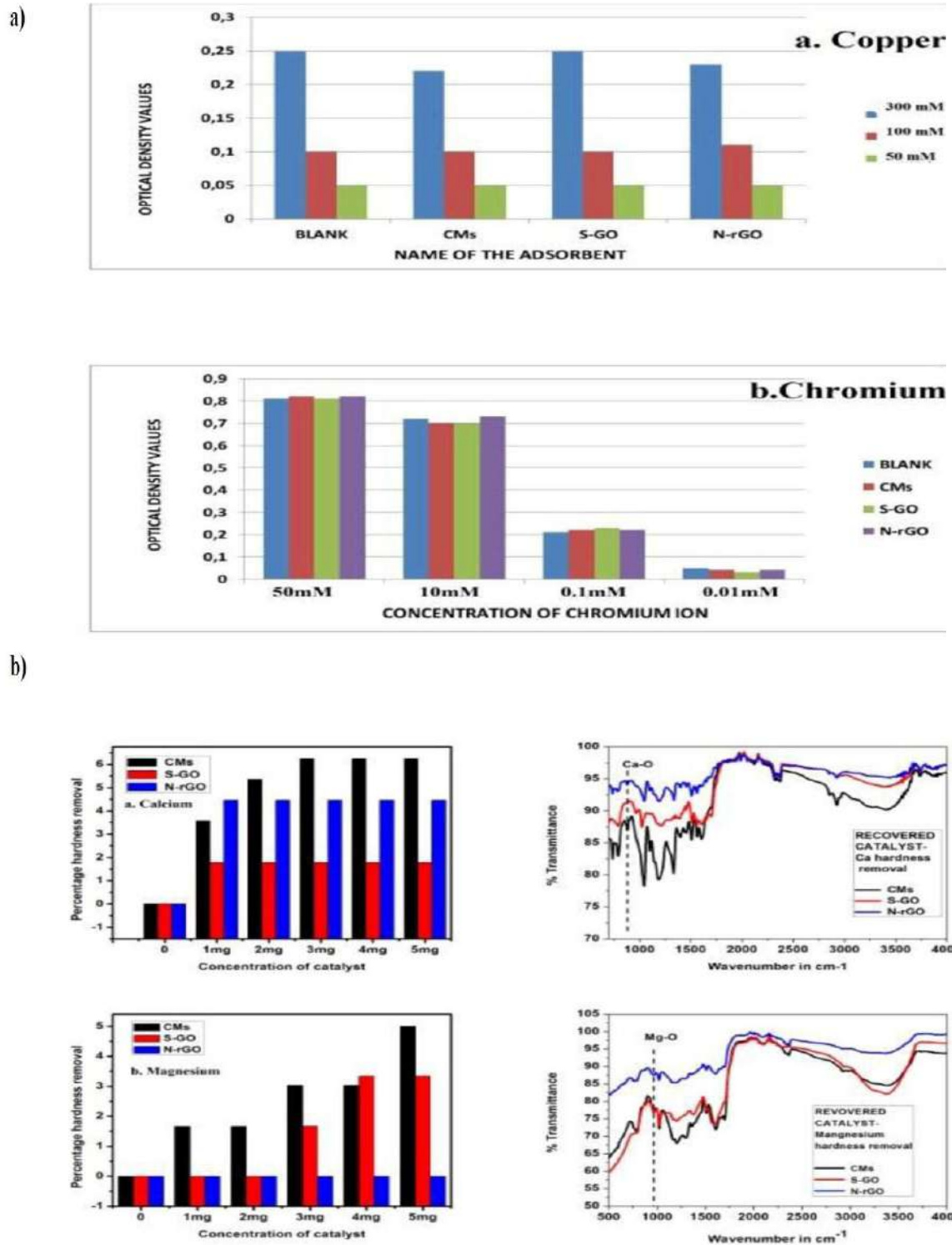
Fig. 6: 6(a) Detection of copper and chromium ion using as-synthesized samples as an adsorbent by colorimetric method, 6(b) estimation of a). Calcium ion b). Magnesium ion by using as-synthesized sample as an adsorbent by EDTA titration along with FTIR analysis of the recovered catalyst.

method: The preliminary screening of metal ions (Cu^{2+} and Cr^{6+}) detection was carried out individually using optical density values of different millimolar concentrations (300 mM, 100 mM, 50 mM) of copper sulfate and (50 mM, 10 mM, 0.1 mM, 0.01 mM) of metal ions and using a catalyst with the concentration of 100 ppm (w/v) and the results are represented in Fig. 6(a).

The effective adsorption of copper and chromium ions was detected at 300 mM and 0.01 mM concentrations respectively. The sample of CMs and N-rGO show a positive result for the detection of copper and chromium ion and S-GO shows a positive result for the detection of chromium ion. It may be due to the electronegativity difference between the adsorbate and adsorbent, morphology, and the functional groups existing on the surface as observed and correlated with SEM and XPS analysis. (Siti et al. 2020) reported that the interactions between graphene nanomaterial as adsorbents and heavy metals correlated with our report.

Estimation of calcium and magnesium ion in water using as-synthesized samples as adsorption catalyst by EDTA titration method

Limei et al. (2015) reported that EDTA functionalized magnetic graphene oxide (EDTA-mGO), a good adsorbent for Pb(II), Hg(II), and Cu(II). In this current study, the hardness of water (Ca^{2+} and Mg^{2+} ion) was detected by the EDTA titration method. In this study, the percentage hardness of water for the removal of heavy metal ions (Ca^{2+} and Mg^{2+}) was calculated by comparing with and without using a catalyst as represented in Fig. 6(b). All the synthesized samples showed activity in the removal hardness of Ca^{2+} or Mg^{2+} ion with increasing concentration of the catalyst. Among the three samples, the carbon microsphere showed better adsorption for (Ca^{2+} or Mg^{2+}) than S-GO and N-rGO due to the surface morphology and more carboxyl functional groups existing on the surface of CMs. The catalyst samples were recovered after the titration and the metal oxide stretching (Ca-O and Mg-O) was identified in the range of 900-1000cm^{-1} from FT-IR analysis

CONCLUSION

The study provided a simpler approach to the synthesis with the underlying principle in the conversion of ketose units to functionalized graphene structures and microspheres of carbon. The correlation of experimental parameters with the resulting structures provided the mechanistic pathway. The structure-activity relationship enabled the screening of their capacity to catalyze the degradation of amino dyes by adsorption and photocatalytic mode and exchange of heavy metal ions. The study of the influence of electronegativity of

the doped atoms (O, N and S), defects in the structure, and morphology upon their catalytic and ion exchange capacity adds more value. The results of the study will contribute much towards biomass conversion to smart nanomaterials, safe and efficient treatment of industrial (textile) wastewater. Finally, the study involving a simple precursor, lab set up, energy, and cost-saving approach provided important cues in the management of water pollution.

REFERENCES

Agata, Ś., Bartosz, G., Noel, D. and Grażyna, G. 2017. Nitrogen-doped reduced graphene oxide as electrode material for high rate supercapacitors. Appl. Surf. Sci., 399: 265-271.

Anton, S.M., Mikhail, A.V. and Peter, M.T. 2019. Solid-state 13C NMR of carbon nanostructures (milled graphite, graphene, carbon nanotubes, nanodiamonds, fullerenes) in 2000–2019: Fuller. Nanotubes Carbon Nanostr., 8: 1-14.

Bharatia, B., Sonkara, A.K., Singh, N., Dash, D. and Chandana, R. 2017. Enhanced photocatalytic degradation of dyes under sunlight using biocompatible TiO2 nanoparticles. Mater. Res. Express, 4: 085503.

Erick, S., Lim, H., Nicole, K.A., Sara, P., Nahrizul, A.K., Ehsan, Z., Nasrul, A.B.A.R., Bahman, A.H. and Babak, S. 2020. Hydrothermal synthesis of carbon microspheres from sucrose with citric acid as a catalyst: Physicochemical and structural properties. J. Taibah Univ. Sci., 14(1): 1042-1050.

Guangxu, H., Weiwei, K., Qianhao, G., Baolin, X., Quanrun, L., Jianbo, J. and Chuanxiang, Z. 2018. One-step green hydrothermal synthesis of few-layer graphene oxide from humic acid. Nanomaterials, 8(215): 1-9.

Hassan, A.F., Abdel-Mohsen, A.M. and Fouda, M.M.G. 2014. Comparative study of calcium alginate, activated carbon, and their composite beads on methylene blue adsorption. Carbohyd. Polym., 102: 192-198.

Ho, K., Maria, E., Fortunato, H.X., Jin, H.B. and Kenneth, S.S. 2011. Carbon microspheres as supercapacitors. J. Phys. Chem., 10: 1-6.

Isaac, C., Luis, J., Wonjun, P., Helin, C. and Yong, P.C. 2013. Raman spectroscopy of graphene and related materials. New Develop. Photon Mater. Res., 19: 1-20.

Limei, C., Yaoguang, W., Liang, G., Lihua, H., Liangguo, Y., Qin, W. and Bin, D. 2015. EDTA functionalized magnetic graphene oxide for removal of Pb(II), Hg(II), and Cu(II) in water treatment: Adsorption mechanism and separation property. Chem. Eng. J., 281: 1-10.

Mark, W., Joe, H. and Madison, W.I. 2011. The Raman spectroscopy of graphene and the determination of layer thickness. Thermo Fisher Sci., 6: 1-6.

Mingfei, P., Xiaoqian, X., Kaixin, L., Jingying, Y., Liping, Hong. and Shuo, Wang. 2020. Fluorescent carbon quantum dots-synthesis, functionalization, and sensing application in food analysis. Nanomaterials, 930(10): 1-25.

Mohammed, B.A. 2014. Removal of textile dyes (maxilon blue, and methyl orange) by date stones activated carbon. Int. J. Adv. Res. Chem. Sci., 1(1): 48-59.

Nurettin, S., Muhammad, F., Saif, U.R., Selin, S.M., Sahiner, M.S. and Nahit, A. 2017. Synthesis, characterization, and use of carbon microspheres for removal of different dyes from aqueous environments. Water Air Soil Pollut., 228(10): 1-10.

Qinghong, W., Can, G., Yuxuan, Z., Jiapeng, H. and Hongqiang, W. 2018. Reduced graphene oxide-wrapped fes2 composite as anode for high-performance sodium-ion batteries. Nanomicro Lett., 10(30): 1-9.

Rao, C.N.R., Venkataraghvan, R. and Kasturi, T.R. 1963. Contribution of the infrared spectra of organao sulfur compound. Canad. J. Chem., 6: 636-42.

Sanja, K., Branka, K., Vladimir, D., Andjelka, Z. and Bjelajac, R. 2015. Structural properties of carbon microspheres obtained by hydrothermal treatment of fructose. Sci. Paper, 56: 155-158.

Shunjian, X., Yufeng, L., Wei, Z., Zonghu, X., Yongping, L., Hui, O., Huanwen, W. and Feng, Y. 2015. Synthesis of carbon microspheres from saccharides based on the hydrothermal process. Int. Conf. Mater. Chem. Environ. Protect., 5: 1-15.

Siti, Z.N.A., Wan, N.S., Ahmed, F.S., Norhariza, Y., Mohd, Z.M., Mohd, Y. and Farhana, A. 2020.Adsorptive removal of heavy metal ions using graphene-based nanomaterials: Toxicity, roles of functional groups and mechanisms. Chemosphere, 248: 1-15.

Sudhaparimala, S. and Usha, R. 2021. Functionalization of graphene with O and S for catalytic degradation of chlorophenols and dyes. Mater. Sci. Forum, 1019: 194-204.

Sudhaparimala,S. and Usha, R. 2020. Energy-efficient functionalization of graphene for tunable fluorescence. IOP Sci. – J. Phys. Conf. Ser., 1706: 1-12.

Sunil, K.C., Saritha, S., Rajesh, K.N., Chethan, G., Mustak, M.S. and Narayana, Y. 2020. Facile, cost-effective, and eco-friendly synthesis of carbonyl-rich partially reduced graphene oxide using glucose as a sole precursor. SN Appl. Sci., 2(1323): 1-8.

Tapas, K.D., Seemita, B., Pandey, M., Vishwanath, B., Kshirsagar, R.J. and Sudarsan, V. 2016. Effect of surface functional groups on hydrogen adsorption properties of Pd dispersed reduced graphene oxide. Int. J. hydro.Energy, 6: 1-10.

Van Ael, E. Covaci, A., Blust, R. and Bervoets, L. 2012. Persistent organic pollutants in the Scheldt estuary: Environmental distribution and bio-accumulation. Environ. Int., 48: 17-27.

Vasilios, G., Jason, A., Perman, M., Jiri, T. and Radek, Z. 2015. A broad family of carbon nanoallotropes: Classification, chemistry and applications of fullerenes, carbon dots, nanotubes, graphene, nanodiamonds, and combined superstructures. Chem. Rev., 115: 4744-4822.

Zhangting, W. and Zhenhua, N. 2017. Spectroscopic investigation of defects in two-dimensional materials. Nanophotonics, 6(6): 1219-1237.

Study on the Construction of Residual Plaque Landscape Ecological Restoration Model in the Process of Rapid Urbanization

Huang Leichang*†, Yang Li**, Bi Shanhua*, Gong Yilu*, Zhang Yu*, Jia Xiaoyu* and Feng Xu*
*School of Art & Design, Dalian Polytechnic University, Dalian, China
**School of Art & Design, Liaoning Vocational College of Light Industry, Dalian, China
†Corresponding author: Huang Leichang; baomason@163.com

ABSTRACT

The current rapid urbanization, industrialization, and expansion of urban construction patterns have resulted in a large number of residual plaques in the urban area, including both the original plaques that are extremely fragmented and the new plaques that are metabolized by urban production, especially natural habitat patches are more pronounced. Ecological restoration of residual plaques plays an important role in maintaining biodiversity, protecting native species, providing ecological services, revitalizing land resources, inheriting regional characteristics, shaping urban image, and improving the ecological environment. Therefore, research on the subject is necessary and urgent. The topic is based on the ecological survey of urban residual patches and the study of the characteristic attributes of current urbanization, defining the connotation, extension, type, characteristics, and influencing factors of urban residual patches, and analyzing the process of fragmentation of residual plaques in cities and their artificial interference relationship. From the macro, meso, and micro scales, from the top level of ecological planning, the whole process of life cycle management, and the moderately disturbed bottom layer of ecological engineering nodes, three levels are restored, theoretical integration guidance and technical restoration. Based on the three dimensions of the continuous symbiosis of nature, cost control of the economy, and public participation of the society, repair and activate the remaining plaques of the city to provide technical support for the construction and sustainable development of urban ecological civilization.

INTRODUCTION

Foreign Research Progress

Foreign studies on urban residual plaques have focused on the overall protection and sustainable use of natural plaques leftover from industrial wasteland and urbanization and industrialization from the 1970s to the end of the 20th century. Foreign studies on residual plaques are mainly manifested in several aspects: the ecological value of urban residual plaques, the fragmentation and artificial interference analysis of urban residual plaques, the investigation of species and the analysis of integrated ecological services, and the investigation of urban residual plaques, ecological evaluation, and management, sociology of urban residual plaques - public participation and other research, the main countries are Germany, France, Japan, Singapore, London, Australia; research perspectives include sociology, cultural landscape, habitat, community in terms of interference factors, the focus is on the study of natural plaque habitats, especially biodiversity, plant communities, and post-regeneration habitats. The focus of industrial waste plaques is on the reuse of industrial wasteland based on the needs of public space construction (Gemmell 1982).

Domestic Research Progress

Domestic research is first of all a high priority and a latecomer advantage at the national level, mainly in the 18th Party Congress in 2013, which clearly states that urban ecological civilization construction is the level of national strategy. In 2016, the urban double repair of the ministry of housing and urban-rural development, the proposal of ecological restoration and urban repair, the introduction of the National No. 1 document on the happy farms, family farms, and other related policies 2016 greatly promoted the study of urban residual plaques. Secondly, China's research on urban residual plaques mainly focuses on urban wildlife habitat survey and biodiversity conservation, protection and construction of local habitats, and basic theoretical research on sustainable and ecological design standards. Finally, in general, China's research on residual plaques started relatively late, and the systematic basic theories, norms, and standards are lacking. Especially from the perspective of ecological engineering, it has only gradually started in recent years but is mainly distributed in agriculture.

There have been some studies on the residual plaque at home and abroad, but there are still some shortcomings. Most

of the research is mainly based on analysis, research and suggestions. The research objects are mainly for the study of individual residual plaques, such as industrial wasteland, damaged natural environment, and biological environment. The research and application of the case are also partial individuals, and there is no systematic system of ecological restoration and the supporting ecological engineering (Xili & Dihua 2009). At present, China is facing a critical period of urbanization, urbanization is accelerating, the landscape matrix is severely fragmented and reduced, and rational planning and restoration of the ecological environment of urban residual plaques are of great practical significance for revitalizing urban land and activating urban vitality. Comprehensive systematic research on the ecological restoration of plaque landscape is essential (Goode 1990).

MATERIALS AND METHODS

In the process of urban renewal, the urban matrix that cannot quickly adapt to the development of the big environment is gradually increasing. Plaque is a block-like region with different properties or appearances from surrounding units. It is an inevitable product leftover from urban renewal and renewal, and it is also additional energy from urban production metabolism. According to the origin and type, plaques can be divided into interfering plaques, residual plaques, environmental resource plaques, and introduced plaques (Fig. 1). Under the strong impact of the rapid development of the city, the extremely broken original plaques and the landscape ecological restoration of the new plaques produced by the city can maintain the natural ecosystem, improve the urban ecological resources, strengthen the urban regional characteristics, and protect the ecology, The potential functionality of species and ecological services. Factors affecting the formation of residual plaques are multi-dimensional, multi-faceted, and complex. Remnant plaques in cities have enormous value. They urgently need people to understand their formation factors, specifically explore their potential effects, carry out the ecological restoration of fragmented residual plaques, restore their ecological functions, and improve the urban landscape ecosystem. To achieve the sustainable development of residual plaque landscape ecology in the process of urbanization (Hua 2015).

Behavioral Interference in the Process of Urbanization

The continuous advancement of urbanization, the rapid development of industrialization, and the contagious urban construction model have directly or indirectly led to the destruction and disappearance of the internal and external ecological landscapes of the city, and the construction of high-intensity, high-density, and disordered landscapes. The

ecological environment has brought many negative effects (Xiaohu 2010). Rapid urbanization occupies a large amount of land in the city, seriously disturbing the landscape habitats in the area, and the fragmentation of the landscape matrix is shrinking at the same time, which affects the generation of spotted plaques in a large area (Minghui 2005). The acceleration of urbanization has broken the balance of the urban ecological environment and interfered with the healthy and sustainable development of natural habitats. After the large-scale expansion of the city, the ecological environment is disturbed by various behaviors such as encroachment, division, destruction, transformation, etc., so the landscape matrix gradually degenerates, splits, and breaks.

Social Interference Under the Advancement of Science and Technology

The advancement of science and technology has changed the mode of production and life of human beings. Some functional sites have been eliminated in the trend of rapid construction of cities, and these functional sites have gradually turned into scattered unused land. Such as industrial wasteland, village sites, wetlands, parks, etc. Long-term technological development has seriously damaged the city's landscape ecosystem. Factors such as city size, urban nature, urban resources and geographic location (climate), and degree of economic development are all factors affecting residual plaques in cities. They act on the formation of residual plaques from different perspectives of the city, and any changes in one factor will affect the change and formation of residual plaques. The impact of advances in science and technology on residual plaques is a combination of multiple factors and multiple conditions.

Human and Natural Interference Under the Influence of Unexpected Events

Residual plaques are affected by emergencies including human interference and natural disturbances during long-
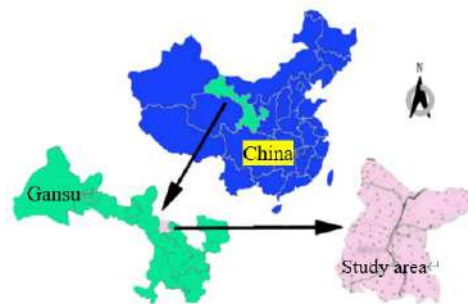
Fig.1: Types of plaques.

term evolution. The survival activities of human beings are accompanied by the destruction of natural habitats. The various interference activities of human beings are the main reason for the frequent fragmentation of urban patches (Renae 2004). Deliberate or unintentional interference behaviors such as uncontrolled mining resources, over-exploitation and construction, and polluting urban environments have become important factors affecting residual plaques (Jun 2016). The population, density, intensity, type, time, and space characteristics of human disturbance also directly lead to an increase in the number of residual plaques. The human disturbance is more and more
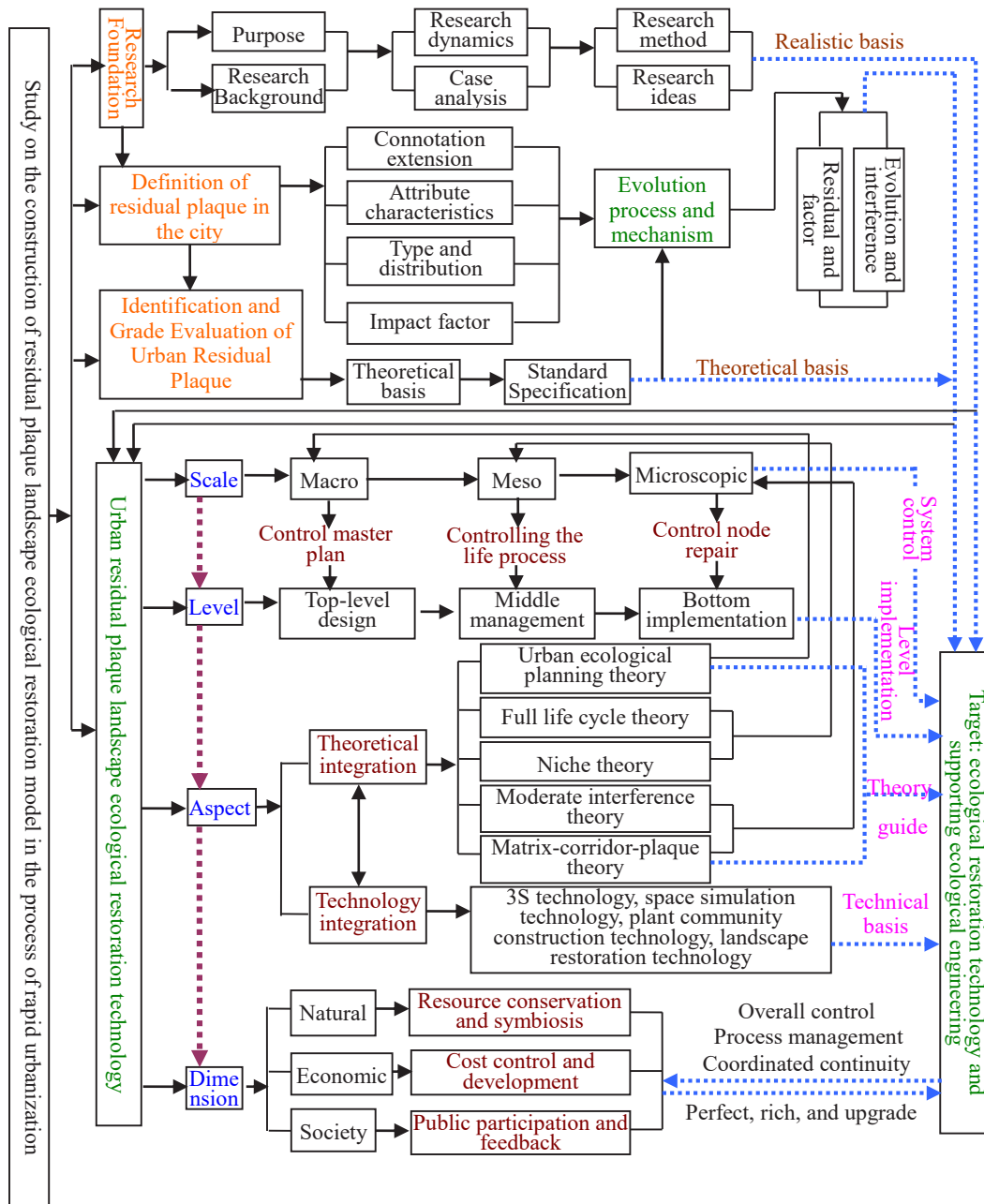
Fig.2: Residual plaque ecological restoration model.

intense in the process of human life structure and lifestyle change.

Natural disasters are irresistible disturbances caused by natural variability on the earth. Natural disturbances bring about many negative phenomena such as earthquakes, tsunamis, volcanic eruptions, landslides, mudslides, sandstorms, droughts, floods, fires, typhoons, insect pests, and so on. Natural habitats are affected by sudden disasters, breaking the balance of the original natural ecosystems, causing natural phenomena such as reduced biomes, harsh soil conditions, and air pollution, making the regional ecosystems unable to self-regulate for a period of time. , induce the formation of residual plaque. After the landscape substrate is seriously disturbed, the species will migrate to the remaining plaques, thereby changing the original species composition in the region, affecting the species changes in the remaining plaques, and succeeding into new residual plaques (Shiyomi et al. 2001).

Connotation Extension of Residual Plaques in the Process of Urbanization

Residual plaques are special plaques formed by economic, social, demographic, geographical space, and other aspects. They are plaques left by the flora and fauna in the background under the influence of large-scale disturbances. The connotation can be summarized as follows: (1) It is an incomplete partial or broken plaque after being strongly disturbed by human activities. (2) Small-area areas that have not been invaded and left behind during the development and construction of large-scale urban areas; (3) Natural landscape mosaics existing in artificially constructed areas after extensive disturbance of natural matrices; (4) For a long period of time, it has not been subjected to strong artificial disturbance, and it is reserved for planning and control land for future development or construction prohibition; (5) idle and legacy land with special natural resources and ecological value in the process of urbanization(Bin & Shengquan 2007). The characteristics of residual plaques in the process of urbanization are mainly fragmentation, residue, localization, strong interference, the humanity of development, subordinate weakness, and residual plaques reduce the connectivity of the city, showing an island shape as natural habitat (Zhu & Weiliang 2011).

Attribute Types of Residual Plaques in the Process of Urbanization

(1) Residential plaques mainly refer to urban residential plaques with the original indigenous settlements such as the village of the city as the main body. In the process of urbanization, the expropriation of rural cultivated land and residential land has increased, and some farmers still live in the original rural settlements after losing the cultivated land. However, the development of the village lags behind the development of the city, which makes the original and continuous rural villages become external and powerful and become scattered and broken individuals embedded in the high-rise buildings of the city, forming a residential plaque that affects the overall style of the city.

(2) Natural plaques mainly refer to typical natural fragmentation ecological patches with natural resources as the main body. These plaques often retain high regional characteristics and have important restoration value. Global climate change, rapid population growth, industrialized economic production, over-exploitation of natural resources, and deforestation and excessive colonization caused by rapid urban development have severely damaged the original natural resource structure and the degradation of natural matrices. The reduction of biological species of natural matrices, the destruction of plant diversity, and the reduction of soil functionality have led to the formation and retention of residual plaques (Weiguo et al. 1998).

(3) Industrial waste patch mainly refers to the abandoned plaques left after industrial activities such as quarrying, sand mining, metal mining, coal mining, smelting, and other productive factories, including heavy industry and light industry, Class factory land, warehouse land, external transportation, and public land. Due to the stagnation of some industrial production activities, the factory is abandoned, and the crude pollution of industrial production, the dumping of industrial waste, the storage of industrial facilities, and the ecological and environmental hazards are multifaceted and difficult to recover, thus forming a declining industrial waste patch of extreme degradation.

(4) Various cultural patches, such as cultural palaces with cultural activities as the main function, old cinemas, cultural exchange centers, etc. In the process of continuous openness and development of the city, the cultural life of human beings is also constantly improving. People are simply pursuing material life and pursuing a deeper spiritual life. The development of science and technology has led to the development of the social economy, and the human way of life is constantly improving and changing. People's outdoor activities mostly choose large shopping malls, characteristic towns, agricultural sightseeing parks, scenic tourist areas, and other fresh, exciting, individual, and attractive places. Therefore, all kinds of historical and cultural sites have declined, and they were isolated by new urban buildings to form fragmented cultural patches.

RESULTS AND DISCUSSIONS

Structural Design of "The model-3323"

The "3323" structure design is 3 scales, 3 levels, 2 aspects, 3 dimensions:

(1) Three scales of restoration: It is the overall control from macroscopic planning to macroscopic management to microscopic design;

(2) Three levels of restoration: It includes the overall restoration of the top level of the ecological planning, the process restoration of the whole life cycle management, and the restoration of the underlying ecological engineering nodes with moderate interference, which is the implementation guarantee;

(3) Two aspects of repair: It refers to the theoretical integration guidance and technical integration repair guarantee; it is system integrity;

(4) The repair of three dimensions: Including the three dimensions of continuous symbiosis based on nature, cost control of the economy, and public participation (feedback) of the society, it is relationship coordination.

The scale focuses on the overall local system control to promote positive repair; the level of attention to the top layer, the process, and the control of different niches of the bottom layer, to ensure the operability of repair (Zhang 2006); the level emphasizes the integrity and sustainability of the repair, From theoretical guidance to technical support, the repair is an open system that can be adjusted according to development; the dimension is highlighted by the symbiosis and constraints of restoration, and costs, resources, and humans mutually promote each other's constraints and are the guarantee of benign operation after repair (Fig. 2).

Theoretical Integration of Residual Plaque Ecological Restoration Model

Based on the "3233" structure, from the macro-master planning theory and other existing theories and the integration of related theories, the whole life cycle theory of the process management, the integration of niche and related theories, the microscopic moderate interference, the matrix-plaque Block-corridor, and related theoretical integration is the basis of research to analyze the urban green space landscape, and the resulting theory will guide the ecological restoration technology and control it as a whole. The urban ecosystem is the "matrix", in which the broken and scattered point-like areas are "plaques", the strip-shaped areas connecting various point-like plaques, protecting ecological diversity, and promoting landscape ecological restoration are " Corridor" (Gongqiao 2007).

Technical System Study of Residual Plaque Ecological Restoration Model

From the three sub-system dimensions of nature, economy, and society, from the top-level design, middle-level management, and the implementation of the underlying nodes, the research on ecological restoration technology ensures the coordinated development of various elements of the city and the implementation of ecological restoration at the level. The social subsystem allows the city's main body to actively participate and repair feedback to form a virtuous circle. The economic subsystem selects the technology from cost control and repair, and based on the repair of the natural subsystem, it optimizes the technology integration from the aspects of moderate interference.

CONCLUSION

(1) Residual plaques are formed by natural or artificial disturbances of the surrounding land. The landscape background becomes a discontinuous plaque mosaic or block that is isolated from each other by an external force. Its turnover rate is faster and the stay time is shorter(Wilcover et al. 1986, Lovejoy 1986). From the identification, evaluation, and mechanism evolution to the restoration of residual plaques, urban ecosystems are constantly updated and constantly changing, and new problems will continue to arise.

(2) The opening of the landscape ecological restoration technology system of residual plaques, the integration of new technologies and new materials, the renewal of old technologies and old materials, and the integration and upgrading of various technologies, have led to the sublimation of research theories and the ultimate realization of residual plaques. The ecological restoration technology system is of openness and sustainable development.

(3) In the study of the construction of further residual plaque landscape ecological restoration model, it is necessary to carry out more in-depth theoretical research and technical system on the scale, level, aspect, and dimension design of different residual plaques. The practical exploration finally realizes the sustainable relationship between residual plaque and landscape ecological design.

ACKNOWLEDGMENT

REFERENCES

Bin, G. and Shengquan, C. 2007. Preliminary study on the concept and classification of urban natural remains. J. Shanghai Jiaotong Univ. Agric. Sci., 25(3): 223-227.

Gemmell, R.P. 1982. The Origin and Botanical Importance of Industrial Habitats Urban Ecology M. Oxford Blackwell Scientific Publications, Oxford, pp. 33-39.

Gongqiao, X. 2007. Using the basic principles of landscape ecology to planning urban green space system patches and corridors J. Zhejiang Agric. Forest. Univ., 24(5): 599-603.

Goode, D.A. 1990. Natural conservation in English cities. Acta Ecol. Sin., 10(1): 96-105.

Hua, H. 2015. The significance of ecological restoration design in contemporary urban green space landscape planning. J. Art. Sci. Technol.,(2): 7-8.

Jun, P. 2016. Study on the Diversity of Residual Plaque Plants in Desert Steppe D. Ningxia University, Yinchuan.

Lovejoy, J.E.1986. Edge and Other Effects of Isolation on Amazon Forest Fragmentation C. Soulem E. Conservation Biology: The Science of Scarcity and Diversity. Sinauer Associates, Sunderland, MA, pp. 257-285.

Minghui, L. 2005. Ecological degradation and restoration of urban Greenland soil. J. Guangdong Garden, (6): 19-21.

Renae, N.S. 2004. Fragmentation and internal disturbance of natural vegetation reserves in the Perth metropolitan area, Western Australia. J. Landsc. Urban Plan., 68(4): 389-401.

Shiyomi, M., Takahashi, S. and Yoshimura, J. 2001. Spatial heterogeneity in a grassland community: Use of power-law. J. Ecol. Res., 16: 487-495.

Weiguo, S., Ping, M. and Yu, Z. 1998. Characteristics of Fragmented Habitats and Their Impact on Ecosystem Processes. Biodiversity and Human Future. China Forestry Publishing House, Beijing, pp. 309-315.

Wilcover, D.S., Mclellan, C.H. and Dobson, A P. 1986. Habitat Fragmentation In the Temperate Zone C. Soulem E. Conservation Biology: The Science Of Scarcity and Diversity. Sinauer Associates, Sunderland, MA, pp. 237-256.

Xiaohu, W. 2010. Natural patches of remnants in urban central areas. J. Shanxi Architect., 36(21): 4-5.

Xili, H. and Dihua, L. 2009. Advances in the study of urban survival near-natural habitats. J. Nat. Resour., 24(4): 561-566.

Zhang, N. 2006. Scale issues in ecology: connotation and analysis methods. Acta Ecol. Sin., 26(7): 2340-2355.

Zhu, Y. and Weiliang, C. 2011. Landscape restoration of beach wetland after Shanghai World Expo. J. Chin. Garden, (3): 19-23.

Hydraulic Performance and Energy Loss Effect of Pit Structure Optimized Drip Irrigation Emitter

Tianyu Xu*, Shuteng Zhi*, Qiuyue Yu** and Ennan Zheng*†

*School of Hydraulic and Electric Power, Heilongjiang University, Harbin, 150080, China

**Rural Energy and Environmental Protection Institute, Heilongjiang Academy of Agricultural Sciences, Harbin 150086, China

†Corresponding author: Ennan Zheng ; 1115291208@qq.com

ABSTRACT

The pit structure optimized drip irrigation emitter (PODE) is a novel type of irrigation emitter that may provide shunts, quick diversion, and mixed flow to maximize energy loss. To study the influence of the geometric parameters of the flow channel on the hydraulic characteristics and energy loss effect, twenty-five sets of orthogonal test schemes were established. Using numerical simulation and verification tests, the flow index and energy loss coefficient were obtained. The results showed that the flow index of the PODE was 0.4632-0.5265, and its hydraulic performance was good. The energy loss coefficient under the pressure head of 5-15 m was 510-2221, which showed that the energy loss effect was obvious. The influence order of the geometric parameters on the flow index was B>P>C>D>A, the optimal solution was $P_{0.6}D_{1.4}A_{85}B_{0.25}C_{0.12}$. The determination coefficient of the regression model based on geometric parameters and flow index was 0.85. In addition, the verification test showed that the relative error among the test value, simulated value, and estimated value were less than 5%, and the flow index can be estimated reliably. The research can provide a reference for the pre-research and evaluation of the hydraulic performance and energy loss effect of the PODE.

INTRODUCTION

Bionics is a scientific method of engineering structural innovation that imitate the structure and function of biological systems in some aspect (Koch et al. 2009, Xing et al. 2012). Plants are an indispensable and important part of the biological cycle system. Many inventions and creations are derived from the bionics of plant structure or morphology. Plant bionics has a very wide range of applications (Luo et al. 2016, Barthlott et al. 2017). Drip irrigation technology is one of the high efficient water-saving irrigation technologies in agriculture. Its main advantages are good water-saving effect, no damage to soil structure, and high irrigation uniformity (Sun & Kang 2000, Lu et al. 2018). The core component of drip irrigation technology is the drip irrigation emitter, which can effectively eliminate the excess energy at the inlet and ensure uniform flow (Li et al. 2020, Mohamed & Ahmed 2017, Wei et al. 2014).

The flow index, energy dissipation effect, and anti-clogging ability are all important factors in the drip irrigation emitter's performance. The geometry of the emitter channel structure determines the three factors of performance (Li et al. 2009, Yuan et al. 2014). Many experts have proposed novel design concepts and structural types of emitters to improve

hydraulic performance (Feng et al. 2017, Guo et al. 2014, Zhang et al. 2014, Yu et al. 2018). The flow index of the fractal flow channel emitter, which was constructed using fractal theory, was between 0.49 and 0.53, significantly improving the turbulence degree of the fluid in the flow channel (Li et al. 2007). The two-way opposing channel improved energy dissipation efficiency by allowing the fluid in the channel to hedge and mix (Guo et al. 2016). The hydraulic performance of the perforated drip irrigation emitter based on a perforated plate construction was good, with a flow index of 0.47-0.51 (Xing et al. 2021). The development and use of drip irrigation emitters benefited greatly from the design of a novel emitter channel.

Based on the similarity between the drip irrigation emitter and the pit structure of the plant xylem, the optimized structure of the pit drip irrigation emitter was designed (Xu & Zhang 2019, 2020). The pit structure optimized drip irrigation emitter (PODE) was used as the research object in this article, and the numerical simulation and test were used to obtain pressure and flow rate in the flow channel, and the hydraulic performance was used to analyze the drip irrigation emitter's flow mechanism. It can: (1) obtain the flow index and the energy loss coefficient of the PODE, (2) analyze the influence of geometric parameter changes on the

performance of the PODE, and (3) evaluate the prediction model and flow characteristics of the PODE. The results provide a reference for the new bionic drip irrigation emitters and offer a deeper understanding of channel design in the drip irrigation technology.

MATERIALS AND METHODS

Flow Channel Structure Design

The PODE was designed according to the torus-margo bordered pit structure in plant xylem tracheids (Fig. 1a). Preliminary work (Xu & Zhang. 2020) found that the PODE had better working performance than the pit drip irrigation emitter (PDIE). The structure of PDIE and PODE are shown in Fig. 1b & 1c.

Numerical Simulation Model

Control Equation

The non-direct numerical simulation method was chosen to be investigated in this research. The standard k–model was found to have a lot of application in the PODE model's turbulent flow. The control equations are as follows:

$$\frac{\partial(\rho k)}{\partial t} + \frac{\partial(\rho k u_i)}{\partial x_i} = \frac{\partial}{\partial x_j}\left[\left(\mu + \frac{\mu_t}{\sigma_k}\right)\frac{\partial k}{\partial x_j}\right] + G_k + G_b - \rho\varepsilon - Y_M + S_k$$

$$\frac{\partial(\rho\varepsilon)}{\partial t} + \frac{\partial(\rho\varepsilon u_i)}{\partial x_i} = \frac{\partial}{\partial x_j}\left[\left(\mu + \frac{\mu_t}{\sigma_\varepsilon}\right)\frac{\partial\varepsilon}{\partial x_j}\right] + C_{1\varepsilon}\frac{\varepsilon}{k}(G_k + C_{3\varepsilon}G_h) - C_{2\varepsilon}\rho\frac{\varepsilon^2}{k} + S_\varepsilon$$

$$\dots(1)$$

In the model, the turbulent dissipation rate ε is defined as:

$$\varepsilon = \frac{\mu}{\rho}\overline{\left(\frac{\partial u_i'}{\partial x_k}\right)\left(\frac{\partial u_j'}{\partial x_k}\right)} \qquad \dots(2)$$

Turbulent viscosity μ_t can be expressed as a function of k and ε as follows:

$$\mu_t = \rho C_\mu \frac{k^2}{\varepsilon} \qquad \dots(3)$$

Where G_k is the generation term of the turbulent energy k due to the average velocity gradient, G_b is the generation term of the kinetic energy k caused by buoyancy, Y_M represents the contribution of pulsation expansion in compressible turbulence, $C_{1\varepsilon}$, $C_{2\varepsilon}$, and $C_{3\varepsilon}$ are the empirical constant, σ_k and σ_ε are the Prandtl numbers corresponding to the kinetic energy k and the turbulent dissipation rate ε, respectively. S_k and S_ε are user-defined source items.

Structure and Geometric Parameters

The PODE model was composed of an inlet, flow channel, and outlet (Fig. 2). The flow channel included pit aperture P(mm), pit depth D(mm), arc angle A(°), bottom height B(mm), and right width C(mm) (Fig. 3a).

The value range of geometric structural parameters of the flow channel was as follows: P was 0.6 mm-1.0 mm, D was 1.0 mm-1.4 mm, A was 85°-95°, B was 0.25 mm-0.45 mm,

(a) pit structure   (b) PDIE   (c) PODE
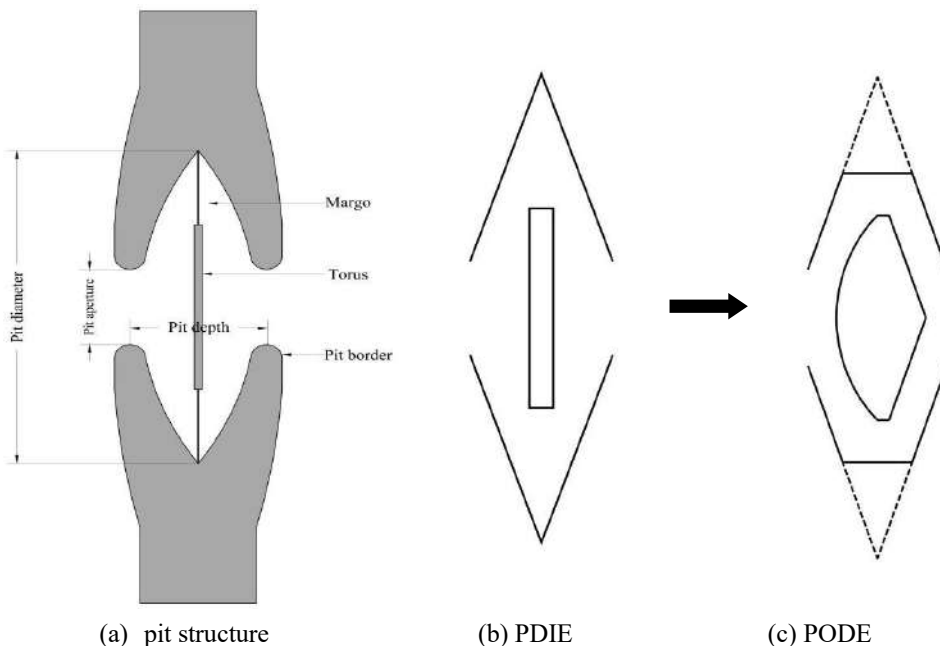
Fig. 1: Schematic diagram of torus-margo bordered pit structure and optimization model.

C was 0.12 mm-0.24 mm. The depth of the PODE model depth was 0.8 mm and the number of channel units was 10.

Meshing and Boundary Conditions

The PODE model was built using SolidWorks software. AN-SYS MESH software was used to partition the model fluid domain grid. The unstructured tetrahedron and hexahedron meshes were utilized to mesh the whole channel due to the irregularity of the flow channel. The anticipated pressure drop difference was less than 0.5 percent, and the number of grids had no effect on the calculation findings, according to the prediction accuracy of the input and exit pressure drop. The maximum element size was 0.03 mm, the minimum element size 0.009 mm, and the total mesh number of the flow channel was about 0.38 million. The fluid domain grid is shown in Fig. 3b.

The pressure values for the entrance of the flow channel were set to 50, 75, 100, 125, 150, 175, 200, 225, and 250 kPa, respectively, while the outflow border was set to the outflow boundary. The no-slip condition was applied to the whole channel's wall faces. The computing hardware platform was the five PowerCube-S01 cloud cubes high-performance parallel computers, and the calculation software was ANSYS FLUENT 17.1.

Experimental Model and Scheme

Construction of the Experimental Model

The test rigs were 5 sets of test models. The test PODE structure was connected with the inner wall of the pipe (the contact surface was the front of the PODE). A pressure level set of tests was designed for each time 25 kPa increased within the

Fig. 2: Schematic diagram of the PODE model.

(a) Geometric parameters   (b) Fluid domain meshing
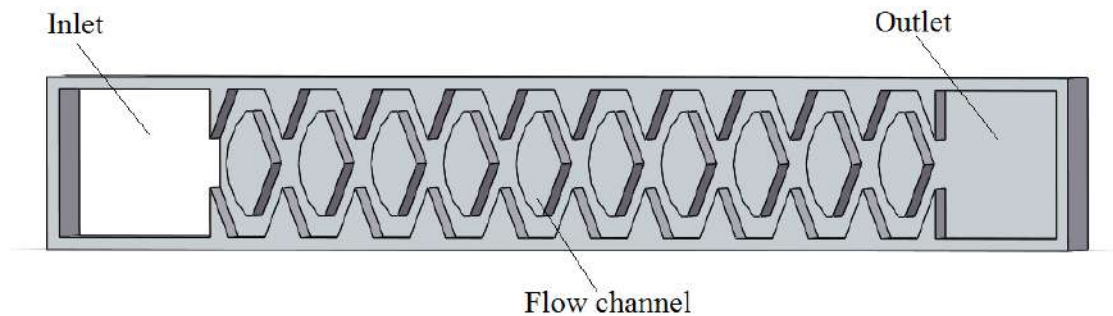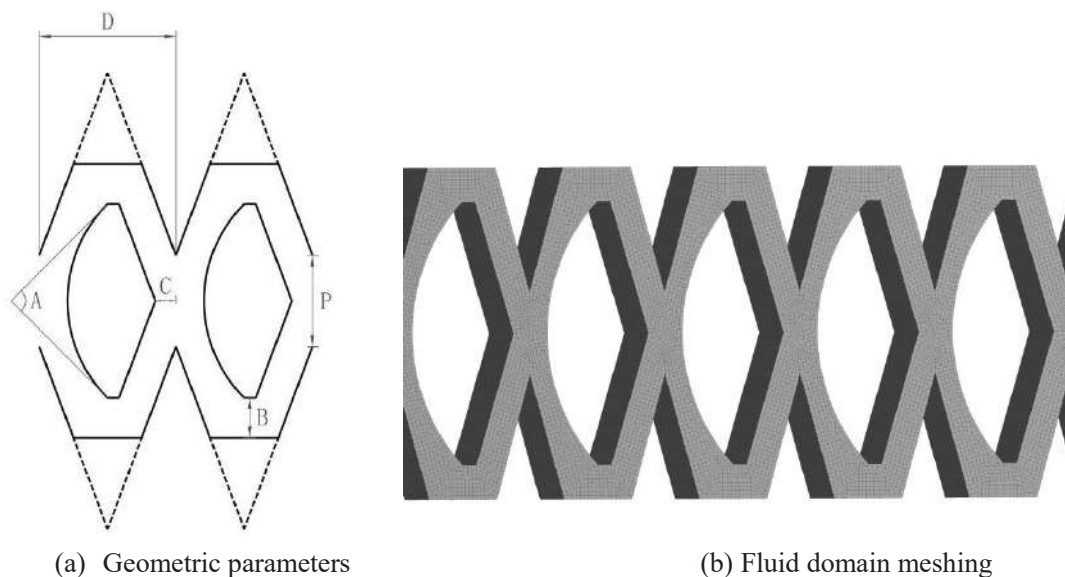
Fig. 3: Schematic diagram of the PODE model.

pressure scope range of 50-250 kPa. Each test lasts 15 min, and each pressure level did 3 times of test measurements to take the average values. The flow channel of the PODE was made of plexiglass. A high-precision engraving machine, the EM-G32S-X32, was employed, with a manufacturing precision of 0.01mm and a repeatable positioning accuracy of 0.005 mm. The physical picture of the plexiglass test model is shown in Fig. 4.

Orthogonal Experiment Scheme

The geometry structure parameters of PODE were five factors and five levels (Table 1). The structural schemes of PODE were designed according to the orthogonal experimental design table L25(56). The structural parameter scheme is shown in Table 2.

Calculation Method of Energy Loss Coefficient and Flow Index

The model can be used to examine the fluid flow in a pit structure optimized drip irrigation emitter using the energy conservation law (Bernoulli equation) (Fig. 5). Assuming that the flow between arbitrary sections satisfies the Bernoulli equation, which was written in sections from the inlet to the exit sections Z_1, Z_2, Z_n as :

$$\frac{P_1}{\rho g} + \frac{V_1^2}{2g} + z_1 = \frac{P_2}{\rho g} + \frac{V_2^2}{2g} + z_2 + \xi_1 \frac{V_2^2}{2g} + \lambda \frac{l_1 V_2^2}{2Dg}$$

$$\frac{P_2}{\rho g} + \frac{V_2^2}{2g} + z_1 = \frac{P_3}{\rho g} + \frac{V_3^2}{2g} + z_3 + \xi_2 \frac{v_3^2}{2g} + \lambda \frac{l_2 V_3^2}{2Dg}$$

$$\cdots\cdots$$

$$\cdots\cdots$$

$$\frac{P_{n-1}}{\rho g} + \frac{V_{n-1}^2}{2g} + z_{n-1} = \frac{P_n}{\rho g} + \frac{V_n^2}{2g} + z_n + \xi_{n-1} \frac{V_n^2}{2g} + \lambda \frac{l_{n-1} V_n^2}{2Dg}$$

$$\dots(4)$$

Where P_n and V_n are the average pressure and flow velocity at section n, ρ is the fluid density, g is the acceleration of gravity, z_n is the position head of water at the section, ξ_{n-1} is the local loss coefficient of section *n-1* to section *n*, λ is the friction factor of head loss, l_{n-1} is the length between two adjacent sections, D is the hydraulic radius of the rectangular section flow channel, a and b are the width and depth of the flow channel section, the expression of D is:

$$D = \frac{A}{\chi} = \frac{ab}{2(a+b)} \qquad \dots(5)$$

Table 1: Geometry parameters values of the flow channel.

Level	Geometry parameters values				
	P.mm⁻¹	D.mm⁻¹	A.°⁻¹	B.mm⁻¹	C.mm⁻¹
1	0.6	1.0	85	0.25	0.12
2	0.7	1.1	87.5	0.30	0.15
3	0.8	1.2	90	0.35	0.18
4	0.9	1.3	92.5	0.40	0.21
5	1.0	1.4	95	0.45	0.24

Note: P is the distance of pit aperture (mm); D is the distance of pit depth (mm); A is the arc angle of the torus (°); B is the distance of bottom height (mm); C is the distance of right width (mm).
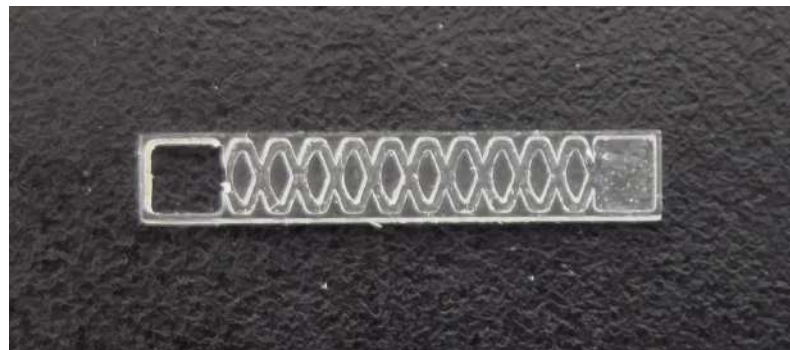
Fig. 4: Prototype of PODE models.

Add the two sides of the equations of Eq. (4) so that:

$$\frac{P_1 - P_n}{\rho g} = z_n - z_1 + \xi_1 \frac{V_2^2}{2g} + \xi_2 \frac{V_3^2}{2g} + \cdots + \xi_{n-1} \frac{V_n^2}{2g} + \lambda \frac{L V_n^2}{2Dg}$$

...(6)

Where $l_1 + l_2 + l_3 + \cdots + l_{n-1} = L$, L is the total length of the flow channel. Positioning head due to the horizontal flow path, so $Z_1 = Z_2 = Z_3 = \cdots = Z_n$.

Known by the continuity equation:

$$V_1 A_1 = V_2 A_2 = V_3 A_3 = \cdots = V_n A_n \qquad \text{...(7)}$$

In Eq. (7), $A_i (i=1,2...,n)$ is the flow area at the corresponding section, substituting Eq. (7) into Eq. (6) we get:

$$\frac{\Delta P}{\rho g} = \left[\lambda \left(\frac{A_1}{A_n} \right)^2 \frac{L}{D} + \sum_{i=1}^{n-1} \xi_i \left(\frac{A_1}{A_{i+1}} \right)^2 \right] \frac{V_1^2}{2g}$$

...(8)

Table 2: Orthogonal experiment scheme of the flow channel.

Level	Geometry parameters values				
	P.mm^{-1}	D.mm^{-1}	A.$^{\circ -1}$	B.mm^{-1}	C.mm^{-1}
1	0.6	1.0	85	0.25	0.12
2	0.6	1.1	87.5	0.30	0.15
3	0.6	1.2	90	0.35	0.18
4	0.6	1.3	92.5	0.40	0.21
5	0.6	1.4	95	0.45	0.24
6	0.7	1.0	87.5	0.35	0.21
7	0.7	1.1	90	0.40	0.24
8	0.7	1.2	92.5	0.45	0.12
9	0.7	1.3	95	0.25	0.15
10	0.7	1.4	85	0.30	0.18
11	0.8	1.0	90	0.45	0.15
12	0.8	1.1	92.5	0.25	0.18
13	0.8	1.2	95	0.30	0.21
14	0.8	1.3	85	0.35	0.24
15	0.8	1.4	87.5	0.40	0.12
16	0.9	1.0	92.5	0.30	0.24
17	0.9	1.1	95	0.35	0.12
18	0.9	1.2	85	0.40	0.15
19	0.9	1.3	87.5	0.45	0.18
20	0.9	1.4	90	0.25	0.21
21	1.0	1.0	95	0.40	0.18
22	1.0	1.1	85	0.45	0.21
23	1.0	1.2	87.5	0.25	0.24
24	1.0	1.3	90	0.30	0.12
25	1.0	1.4	92.5	0.35	0.15

Where,

$$\xi = \left[\lambda \left(\frac{A_1}{A_n} \right)^2 \frac{L}{D} + \sum_{i=1}^{n-1} \left(\frac{A_1}{A_{i+1}} \right)^2 \xi_i \right]$$

...(9)

Eq. (8) is simplified to:

$$\frac{\Delta P}{\rho g} = \xi \frac{V_1^2}{2g}$$

...(10)

Expressed as:

$$\xi = \frac{2}{V_1^2} \cdot \frac{\Delta P}{\rho}$$

...(11a)

Expressed by flow rate:

$$\xi = \frac{2a^2 b^2}{q^2} \cdot \frac{\Delta P}{\rho}$$

...(11b)

In Eq. (11a, b), ξ is the flow channel energy loss coefficient (frictional head loss and local head loss), q is the average flow rate of the flow channel. Obviously, ξ reflects the energy dissipation capacity of pit structure optimized drip irrigation emitter flow channel. The expression of q is:

$$q = kH^x$$

...(12)

Where k is the flow coefficient; H is the inlet pressure, kPa; x is the flow index.

RESULTS AND DISCUSSION

Flow-Pressure Relationship and Flow Index of Flow Channel

The numerical simulation results of the orthogonal experiment are shown in Table 3. Formula (12) is used to fit the relationship between flow and pressure. The coefficient of determination was 0.996-0.999, and the regression equation had a good correlation. The flow index of different geometric parameters ranged from 0.4632 to 0.5265. Taking experiment schemes 21 and 22 as the example (Fig. 6), the root mean square error between the fitted value and the experimental value is 0.005 and 0.008 L.h^{-1}, which more accurately reflects the relationship between the pressure and flow of the PODE.

Energy Loss Mechanism and Velocity Distribution

The energy loss effect of the flow channel was solved by the Bernoulli equation (11b). The results showed that the energy loss coefficient of the channel structure was 510-2221 at 5-15 m in the 25 experiment schemes (Table 4), which showed that the energy loss effect was obvious.

Take scheme 1 (maximum energy loss coefficient) and scheme 15 (minimum energy loss coefficient) under 50kpa pressure as an example. The fluid velocity at all points in
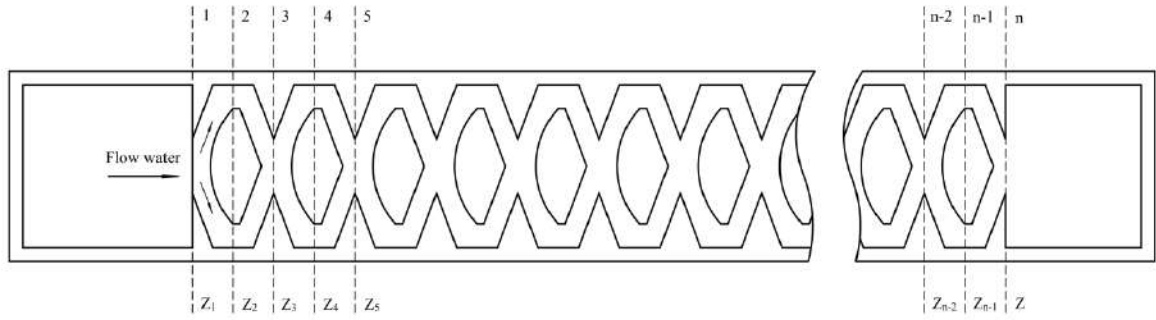
Fig. 5: Schematic diagram of water flow in PODE flow channel.

the flow channel was not the absolute flow velocities in the PODE (Fig. 7). The comparing velocities within different sites in the flow channel, on the other hand, were accurate. The arc structure on the left side of the torus caused the fluid

Table 3: Orthogonal experiment numerical simulation results.

Level	Flow rate q. L·h⁻¹	Flow coefficient	Flow index	Level	Flow rate q. L·h⁻¹	Flow coefficient	Flow index
1	1.467	0.1863	0.5265	14	2.685	0.3937	0.4914
2	1.890	0.2573	0.5112	15	3.049	0.4416	0.4942
3	2.269	0.3330	0.4925	16	1.611	0.2531	0.4735
4	2.542	0.3748	0.4899	17	1.987	0.2909	0.4918
5	2.77	0.4073	0.4904	18	2.519	0.3880	0.4778
6	1.694	0.2403	0.4989	19	2.818	0.4279	0.4813
7	2.017	0.3160	0.4735	20	2.596	0.3729	0.4964
8	2.396	0.3499	0.4919	21	1.798	0.2929	0.4632
9	2.280	0.3120	0.5102	22	2.206	0.3494	0.4705
10	2.796	0.3931	0.5028	23	2.163	0.3292	0.4814
11	1.840	0.2886	0.4734	24	2.631	0.3927	0.4870
12	1.760	0.2435	0.5056	25	2.998	0.4350	0.4933
13	2.152	0.3236	0.4854				

Note: q, flow rate value under inlet pressure 50 kPa; Flow index is estimated by the regression model.

(a) experiment scheme 21

$q = 0.2929H^{0.4632}$
$R^2 = 0.9999$
$P < 0.05$

(b) experiment scheme 22

$q = 0.3494H^{0.4705}$
$R^2 = 0.9999$
$P < 0.05$
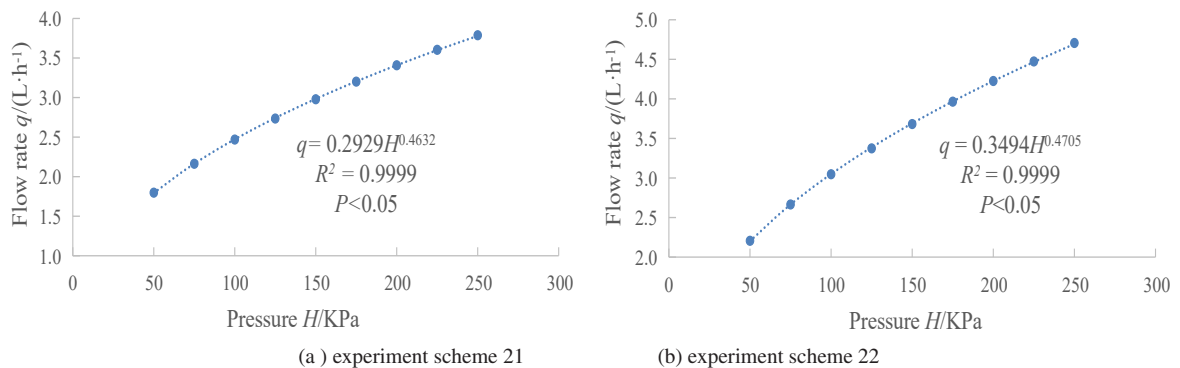
Fig. 6: Relationship between flow rate and pressure for test schemes 21 and 22.

(a) Experimental scheme 1

(b) Experimental scheme 15
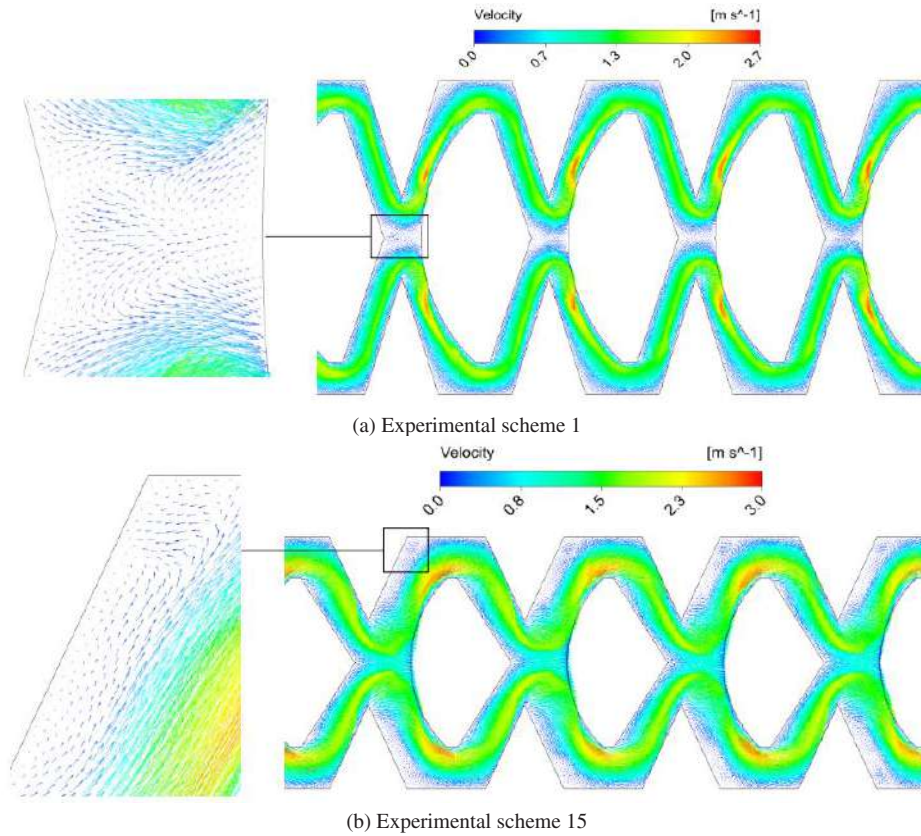
Fig. 7: Relationship between flow rate and pressure for experimental schemes 1 and 15.

Table 5: Range analysis results for orthogonal experiment.

Scheme		Flow index				
	Level	P.mm^{-1}	D.mm^{-1}	A.$^{\circ-1}$	B.mm^{-1}	C.mm^{-1}
Ki value	1	2.5105	2.4355	2.4690	2.5201	2.4914
	2	2.4773	2.4526	2.4526	2.4599	2.4659
	3	2.4500	2.4290	2.4290	2.4679	2.4454
	4	2.4208	2.4598	2.4542	2.3986	2.4411
	5	2.3954	2.4771	2.4410	2.4075	2.4102
Ki avg value	1	0.5021	0.4871	0.4938	0.50402	0.49828
	2	0.49546	0.49052	0.49052	0.49198	0.49318
	3	0.49000	0.48580	0.48580	0.49358	0.48908
	4	0.48416	0.49196	0.49084	0.47972	0.48822
	5	0.47908	0.49542	0.48820	0.48150	0.48204
Best level		1	5	1	1	1
R		0.0230	0.0096	0.0080	0.0243	0.0162
Number of levels		5	5	5	5	5
Number of repeats per level r		5	5	5	5	5

Note: Ki is the sum of the flow index for level i; Ki avg is the arithmetic mean of Ki

coming into the pit aperture to flow up and down at both ends, resulting in two high-speed areas at the arc boundary. The complete low-speed vortex is not observed in Fig. 7. The junction of the two units in scheme 1 and the upper and lower boundaries on the left side of the unit in scheme 2 produced low-speed mixing. It was discovered that the energy loss impact of the PODE model was related to the flow rate and velocity distribution by combining the flow velocity distribution and geometric structural factors. The low-flow PODE model in the mixing area at the unit connection had a better energy loss effect.

Influencing Factors of Flow Index

Based on the range analysis of the flow index simulation values (Table 3), the results are shown in Table 5. The range value showed that the order of the influence of each geometric parameter on the flow index was B>P>C>D>A. The optimal solution was $P_{0.6}D_{1.4}A_{85}B_{0.25}C_{0.12}$.

Further analysis of the trend of the relationship between each parameter and the flow index (Fig. 8), it can be seen that the flow index decreases with the increase of P, A, B, and C, and increases with the increase of D.

The analysis of variance (Table 6) showed that the corresponding P-value of factor B is less than 0.05, which had a significant influence on the flow index, while the factors P, D, A, and C have no significant influence on the flow index.

Establishment and Verification of Flow Index Prediction Model

Based on the results of the orthogonal experiment, SPSS software was used to perform a multiple linear regression with a confidence level of 95%, and the regression model between the flow index and each parameter was calculated as

$$x = 0.6265 - 0.0573P + 0.0181D - 0.0006A - 0.1146B - 0.1248C$$

$$\dots(13)$$

The regression coefficient significance test F statistic value of this model was 21.144, the coefficient of determination R^2 was 0.85, the significance level Sig.=0.000, the regression effect was significant, and the established regression equation was valid.

To further verify the reliability of the regression model, three groups of different sizes were selected within the range of geometric parameters (Table 7), and the model samples were processed for testing, the simulation values and test values of the flow index, and the estimated values of the regression model were showed in Table 7. The calculation showed that the relative error of the flow index was -1.80% to 1.29%, which was less than 5%, indicating that the regression model of formula (13) can accurately reflect the quantitative relationship between the flow index and the geometric parameters of the flow channel. The formula (13) can be used to pre-research and evaluate the flow index of this type of drip irrigation emitter, which improved the effectiveness of the drip irrigation emitter test arrangement to a certain extent.

CONCLUSION

(1) The geometric parameter design of the OSPE was carried out. The flow index obtained by the orthogonal experiment was 0.4632-0.5265, indicating that

Table 6: Variance analysis of the effect of geometric parameters on flow index.

Variance source	Sum of square	Degree of freedom	Mean sum of square	F Value	P-Value
P	0.0016	4	0.0004	2.4511	0.0794
D	0.0003	4	0.0001	0.3153	0.8643
A	0.0003	4	0.0001	0.3153	0.8643
B	0.0020	4	0.0005	3.2037	0.0347
C	0.0007	4	0.0002	0.8528	0.5087

Table 7: Verification scheme and results.

Level	Geometry parameters values					Flow index			Error/%	
	$P.mm^{-1}$	$D.mm^{-1}$	$A.°^{-1}$	$B.mm^{-1}$	$C.mm^{-1}$	Simulation value	Test value	Estimated value	S/E	T/E
1	0.6	1.0	90	0.40	0.21	0.4905	0.4898	0.4842	1.29%	1.14%
2	0.8	1.2	92.5	0.30	0.15	0.4965	0.4905	0.4938	0.55%	-0.67%
3	0.9	1.4	87.5	0.25	0.12	0.4988	0.4953	0.5042	-1.07%	-1.80%
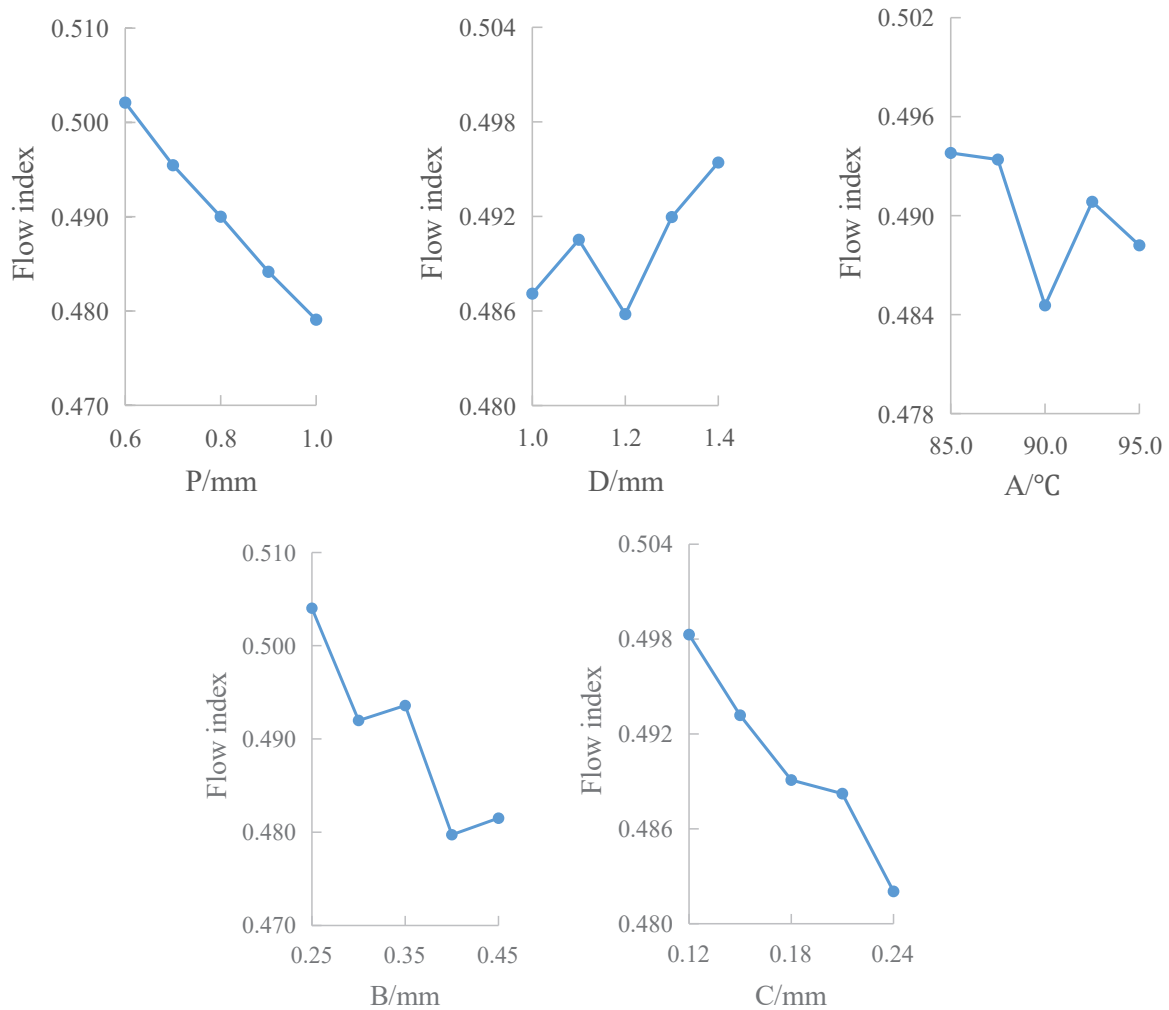
Fig. 8: Effect of geometric parameter on flow index.

its hydraulic performance was good. The energy loss coefficient under the pressure head of 5-15 m was 510-2221. Compared with the traditional unit flow channel structure, the energy loss effect was significantly improved, indicating that the structure of this type of drip irrigation emitter was reasonable and has application prospects.

(2) There was no low-speed vortex zone in the model flow channel, and the anti-clogging performance was good. The results showed that the flow index decreased with the increase of P, A, B, and C, and increased with the increase of D. B had a significant effect on the flow index, while the other parameters had no significant effect on the flow index. The influence order of the geometric parameters on the flow index was B>P>C>D>A, The optimal solution was $P_{0.6}D_{1.4}A_{85}B_{0.25}C_{0.12}$.

(3) The flow index prediction model was established, and the relative error among the test value, simulated value, and estimated value was less than 5%, which proved the accuracy and reliability of the regression model.

ACKNOWLEDGEMENT

REFERENCES

Barthlott, W., Mail, M., Bhushan, B. and Koch, K. 2017. Plant surfaces: structures and functions for biomimetic innovations. Nano-Micro Lett., 9(23): 1-40.

Feng, J., Li, Y., Wang, W. and Xue, S. 2018. Effect of optimization forms of flow path on emitter hydraulic and anti-clogging performance in the drip irrigation system. Irrig. Sci., 36: 37-47.

Koch, K., Bhushan, B. and Barthlott, W. 2009. Multifunctional surface structures of plants: an inspiration for biomimetics. Prog. Mater. Sci., 54(2): 137-178.

Guo, L., Bai, D., Wang, X. and He, J. 2016 Analysis of working mechanism and hydraulic performance of two-way flow channel stabilizer in bubbler irrigation emitter. J. Drain. Irrig. Mach. Eng., 34(3): 270-276.

Luo, Y., Liu, W., Li, W. and Xie, W. 2016. Heat and mass transfer characteristics of leaf-vein-inspired microchannels with wall thickening patterns. Int. J. Heat Mass Transf., 101: 1273-1282.

Lu, H., Kang, S., Du, T., Ling, T., Ding, R. and Li, S. 2018. Current status and future research trends on water-saving high-efficiency and eco-friendly agriculture. J. Agric., 8(1): 155-162.

Li, J., Bai, D., Wang, X. and Guo, L. 2020. Geometric parameters design and experimental study on new type drip emitter. J. Drain. Irrig. Mach. Eng., 38(1): 95-101.

Li, Y., Yang, P. and Ren, S. 2007. Effects of fractal flow part designing and its parameters on emitter hydraulic performance. Chin. J. Mech. Eng., 43(7): 109-114.

Li, Y., Yang, P., Xu, T., Liu, H., Liu, H. and Xu, F. 2009. Hydraulic property and flow characteristics of three labyrinth flow paths of drip irrigation emitters under micro-pressure. Trans. ASABE, 52(4): 1129-1138.

Mohamed, A.M. and Ahmed, I.A. 2017. Gene expression programming approach for modeling the hydraulic performance of labyrinth-channel emitters. Comp. Electr. Agric., 142: 450-460.

Sun, J.S. and Kang, S.Z. 2000. The present situation of water resources usage and developing countermeasures of water-saving irrigation in China. Trans. Chin. Soc. Agric. Eng., 16(2): 1-5.

Tian, J., Bai, D., Yu, F. and Guo, L. 2014. Numerical simulation of hydraulic performance on bidirectional flow channel of drip irrigation emitter using Fluent. Trans. Chin. Soc. Agric. Eng., 30(20): 65-71.

Wei, Z., Yuan, W., Zhou, X. and Zhao, G. 2014. Research progress of pressure compensating emitters in micro-irrigation systems in China. Trans. Chin. Soc. Agric. Mach., 45(1): 94-101.

Xing, D., Chen, W., Zhao, L. and Ma, J. 2012. Structural bionic design for high-speed machine tool working table based on distribution rules of leaf veins. Sci. China Technol. Sci., 55(8): 2091-2098.

Xing, S., Wang, Z., Zhang, J., Liu, N. and Zhou, B. 2021. Simulation and verification of hydraulic performance and energy dissipation mechanism of perforated drip irrigation emitters. Water, 13(2): 171.

Xu, T. and Zhang, L. 2019 Hydraulic performance and energy dissipation effect of pit structure flow channel emitter, IFAC. Papers Online, 52(30): 143-148.

Xu, T. and Zhang, L. 2020 Influence and analysis of structure design and optimization of a pit drip irrigation emitter on the performance. Irrig. Drain., 69(4): 633-645.

Yuan, W., Wei, Z., Chu, H. and Ma, S. 2014 Optimal design and experiment for divided-flow emitter in drip irrigation. Trans. Chin. Soc. Agric. Eng., 30(17): 117-124.

Yu, L., Li, N., Liu, X., Yang, Q., Li, Z. and Long, J. 2018. Influence of dentation angle of labyrinth channel of drip emitters on hydraulic and anti-clogging performance. Irrig. Drain., 68: 256-267.

Zhang, S., Zhou, T., Ran, W. and Li, X. 2014 Exploration on internal in-laying drip irrigation pipe and standards. Agric. Sci. Technol., 15(5): 866-869.

Original Research Paper https://doi.org/10.46488/NEPT.2022.v21i02.008 **Open Access Journal**

Use of Gram-Positive Grass *Bacillus* as Autonomous Repair Agent in Concrete

Nishant Kumar*† and Sunil Saharan*
*Department of Civil Engineering, Sharda University, Greater Noida, India
†Corresponding author: Nishant Kumar; nishant.kumar4@sharda.ac.in

ABSTRACT

Due to various reasons, crack formation may occur in the concrete structure. Crack formation increases the permeability of concrete to detrimental substances including different types of chemicals, glasses, and water, which upon contact with concrete leads to significant impairment in various properties of concrete including strength, durability, etc. In the present investigation, special microbiological growth having the ability to precipitate calcite through the process of biomineralization is induced in the concrete to evaluate the performance of the concrete. The bacteria were directly added to the concrete mix instead of encapsulating them into clay pellets. Bacteria were classified into two groups i.e. A & B. i. e. 50 & 100 g of bacteria powder were added into 1 L of water respectively. Out of the two groups A and B, 4 samples each were taken of 10 mL, 20 mL, 30 mL and 40 mL, and mixed in the concrete. The results showed that compressive strength and flexural strength increased up to 23.57% and 35% respectively more than the control specimen and the optimum capacity achieved at 30 mL bacterial concentration.

INTRODUCTION

"Concretus", which originates from the Latin language means condensed and hardened, is a versatile construction component. The first known use of cement was twelve million years ago whereas concrete-like building materials were used back in 6500 BC (Alhalabi & Dupodia 2017, Ahn 2008). However, during the Roman Empire, concrete was formed. Concrete is a globally used construction material that is diverse and so versatile that it can be used in all construction types or can be modified to be applied in specialized construction fields (Irwan et al. 2016).

Concrete is an amalgamation of water, aggregates, and cement. Cement is the most important component of concrete. Cement's job is to hold the aggregates together while also filling up the gaps between coarse and fine particles (Ahn & Kishi 2008, Binici et al. 2008). Concrete is favored as a construction material due to its high compressive strength, durability, low cost, and ability to be molded into any desired shape (Seifan et al. 2016). Concrete is the most commonly used building material across the world constitutes cement, fine aggregate, coarse aggregate, and water mixed in proper proportions. The strength and durability of concrete depend upon various factors like proportioning, mixing, and compacting of the ingredients (Topcu & Canbaz 2004, Kishi et al. 2007, Demirboga & Guil 2006).

Despite its huge popularity, the life span of concrete is reduced by the formation of cracks which also shortens the

structure's life. There have been numerous studies on concrete to improve the concrete for better long life (Luhar & Gourav 2015, Isa & Turhan 2007). Self-healing of concrete is one of the outcomes of many such studies. The two main areas of research in self-healing concrete are the natural way of hydrates to seal cracks over time and the artificial way to seal cracks manually (Alhalabi & Dupodia 2017). During the studies, it has been known that some methods including the application of chemicals and polymers lead to health and environmental risks and are effective only for a short period of time. Thus, there is a huge demand for methods that are environmentally suitable and efficient (Seifan et al. 2016).

The term Self-Healing means the properties to heal itself without any external help. It means that the cracks that occur in concrete mend on their own, without the need for external assistance. When air moisture combines with the non-hydrated concrete clinker existing in the fracture, the goal of self-healing is for the fissures to fill themselves (Bang et al. 2001, Homma et al. 2009). The durability of concrete is measured in terms of resistance to wear and tear. The most common test to measure the durability of concrete is to measure its permeability by Rapid Chloride Penetration test. The addition of any mineral admixture, especially a pozzolanic mineral admixture may lead to improvement of durability and quality of concrete (Binici et al. 2009, Chindaprasirt et al. 2007). Due to the autogenous crack repair, the durability of the concrete is also enhanced. Also, the reduction in corrosion to steel reinforcement is achieved as the cracks

repair themselves thereby reducing the ingress of water in concrete (Alhalabi & Dupodia 2017, Quayum et al. 2015). With respect to the autogenous method to repair cracks in concrete, the idea behind creating self-healing concrete was first created in 1994. The first technique that was adopted in creating self-healing concrete was introducing small pellets (clay encasing) in the concrete mix. This clay casing consists of bacteria that gets activated when a crack is generated in the structure and repairs the crack. This technique of producing self-healing concrete with bacteria is comparatively new and has its challenges also. The cost of production of concrete with self-healing properties is comparatively higher than conventional concrete as it requires the production of bacteria. The type of bacteria also is to be chosen carefully. There is a possibility of bacteria being dormant and dying in the concrete also due to the alkalinity of concrete (Irwan et al. 2016).

A different way of evaluating the effective properties of self-healing concrete is done using the Computational hominization tool. With this method, macro and micro scales are linked together from which multi-scale modeling can be done (Quayum et al. 2015). Bio- Concrete or self-healing concrete consists of calcium lactate $(Ca(C_3H_5O_2)_2)$ and certain microbes which are planted or encased in pellets or cases that get activated or break when a crack is formed and water reaches the crack These microorganisms make limestone $(CaCO_3)$ as a result of their reaction with water, which eventually fills the fissure. The rate of crack filling is determined by the percentage of microorganisms introduced to the mix as well as the amount of water in the crack (Seifan et al. 2016, Ahn & Kishi 2009).

MATERIALS AND METHODS

Review Stage

The properties of the material used and the various test conducted are described below:

Cement: OPC 43 Grade cement of Birla Ultratech Cement make was used. The experimentation is done as per the Indian Standards (IS 8112 1989, IS 4031 1996). The weight of the sample taken was 300 g. The properties are discussed in Table 1.

Fine aggregates: Fine aggregates are collected from a river that lies in grading zone III. As per IS 383 (1970), the sieve analysis was done. The results of specific gravity, fineness modulus, and water absorption of fine aggregates are discussed in Table 2.

Coarse aggregates: Locally crushed aggregate of size 20 mm were used. The tests were performed according to Indian Standards (IS 383 1970, IS 2386 1963). The results

of specific gravity, water absorption, and fineness modulus are shown in Table 3.

Mix Design

After performing all the tests, a mix design as per IS 10262 (2019) was prepared. W/C ratio of 0.43 was used. Bacillus subtilis (in powder form) was mixed with water to form the bacterial solution. The solution was made with different concentrations of cells. The bacteria solution was classified into two groups as shown in the table. A varying percentage of calcium lactate was used for different bacterial concentrations. The maximum percentage used was 4% by weight of cement. An increase in the percentage of calcium lactate results in increased setting time and decreased hydration of cement which in turn results in a decrease in the strength of concrete. Calcium lactate on reacting with water forms many hydrates, among which the most common is pentahydrate when Calcium Lactate is added to the concrete mix. It combines with the water in the mix to create hydrate, resulting in a decrease in the water content of concrete. The concrete dehydrates as a result of the lower water concentration, and its strength suffers as a result. Table 4 shows the mix design proportions, whereas Fig. 1 shows the different percentages of bacteria content as well as different calcium lactate percentages.

Table 1: OPC properties.

S.No.	Properties	Values	Standard Values
1	Consistency	30%	-
2	Initial Setting Time	43 min	Not less than 30 min
3	Final Setting Time	360 min	Not greater than 600 min
4	Specific Gravity	3.12	-
5	Fineness	5%	Less than 10%

Table 2: Fine aggregate properties.

S.No.	Properties	Values Obtained
1	Specific Gravity	2.6
2	Water Absorption	1%
3	Fineness Modulus	2.3
4	Grading Zone	III

Table 3: Coarse aggregate properties.

S.No.	Properties	Values Obtained
1	Aggregate Type	Crushed
2	Specific Gravity	2.63
3	Water Absorption	0.70%
4	Fineness Modulus	6.23
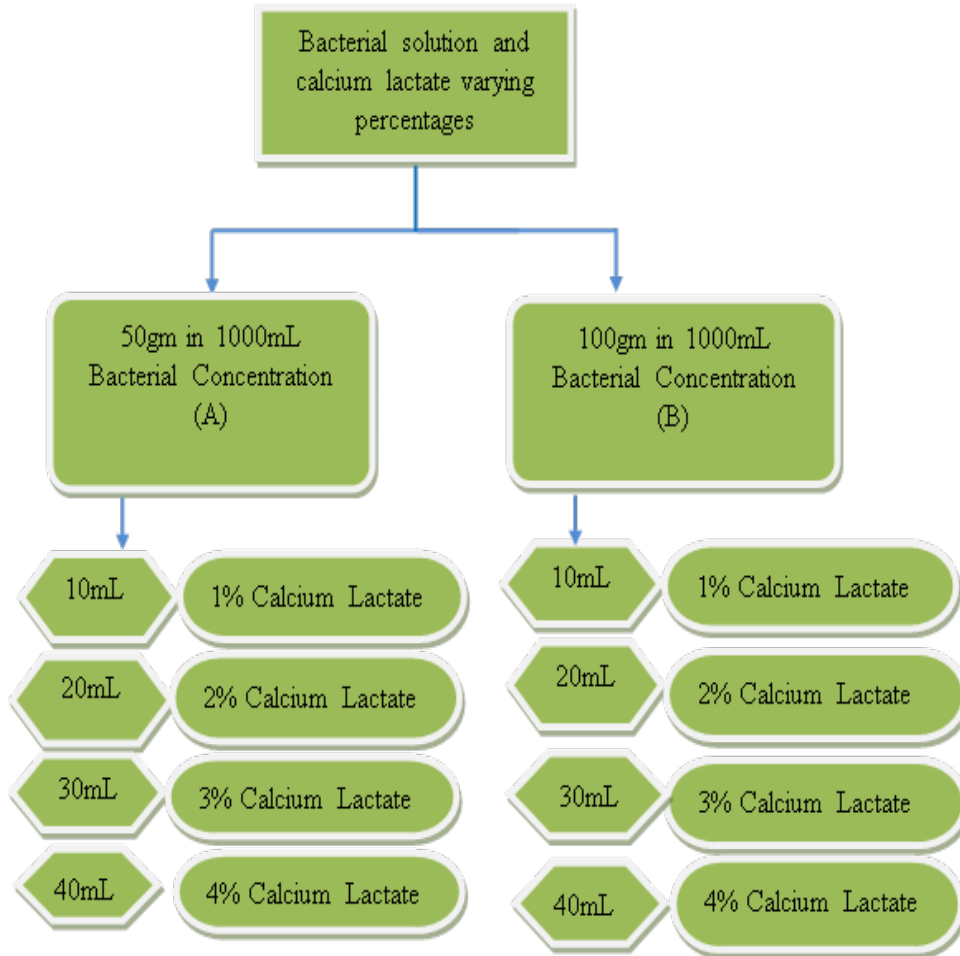
Fig. 1: Bacteria and calcium lactate dosage.

Workability Tests

The workability tests of fresh concrete were carried out to determine whether the concrete is workable or not. The tests which had been carried out to assess the workability of fresh concrete are:

Slump cone test: The slump test gives us an idea of the w/c

Table 4: Mix proportions.

Material	Quantity/Value
Grade	M30
Cement	458 kg
Fine Aggregate	591 kg
Coarse Aggregate	1130 kg
Water	197 kg
Water/Cement Ratio	0.43
Mix Proportion	1:1.29:2.46

ratio needed for concrete which is used for different works. Although it is depicted as a measure of consistency, the slump test does not assess the workability of concrete; rather, it is extremely useful in distinguishing the variations within the consistency of a given nominal percentage. The test was carried out using the IS code for Slump, which is IS 1199 (1959). The slump test apparatus consists of a mold in the shape of a frustum of a cone (Slump cone) with a height of 300 mm, bottom and top diameters of 200 mm and 100 mm, respectively, and a steel rod (tamping rod) with a diameter of 16 mm, a length of 600 mm, and one end rounded.

Compaction factor test: Workability is that property of the concrete which decides the sum of work required to create full compaction. This test indicates the method for deciding the workability of concrete when the nominal maximum size of the total does not surpass 38 mm. As compared to the slump test, the compaction factor is more precise and sensitive and is specifically used in case of low workability

concrete mixes. The concrete which is to be compacted by vibration may fail to slump, therefore this test is used in such concrete structures. The IS code for the compaction factor test is IS 1199 (1959) was followed to carry out the test.

Flow table test: This method entails establishing a procedure for assessing the fluidity of concrete using a flow table. This approach determines the spread of a jolted concrete pile and acts as an indicator of concrete consistency and tendency to separate. In terms of segregation, the flow table test is really useful. It can also be used to evaluate the consistency of stiff, rich, rather than cohesive combinations. This test cannot be used to determine workability since concrete with the same flow can have a wide range of workability. The IS code for flow test is IS 1199 (1959) was followed to carry out the test.

Vee-bee consistometer test: Vee-Bee Consistometer measures the workability of the mix as specified in IS 1199 (1959). The amount of time it takes to vibrate a concrete specimen into a barrel in the shape of a funnel-shaped frustum is a measure of the blend's consistency or workability.

pH Test of Water

pH is the amount of hydrogen ion concentration in solution and defined as the negative log of H+ ions concentration materials. Litmus paper was used to determine the pH value of the concrete.

Casting of Specimen

After the completion of the workability tests casting of specimens was done. The total number of specimens cast was 135 which included 81 cubes and 54 beams. 8 bacterial solution concentrations and 1 control concentration were taken into account while casting the specimens. For each given concentration 9 cubes and 6 beams were cast. The size of each cube and beam was 150*150*150 mm and 100*100*500 mm respectively. Proper lubrication of each mold was done. The molds were filled in 3 layers with subsequent tamping (25 blows) at each layer. After 24 h of casting both cubes and beams were demolded.

Curing

Effective curing maintains the hydration of concrete by preventing evaporation of water from the concrete surface. In current research work after properly demolding all the specimens, they were put in the curing tank. The pH of water used for curing was 7.3. All the specimens were distributed based on a specific curing period which includes 7, 14, 28, and 60 days.

Crack Initiation

Cracks, with the crack width in the range of 0.1 mm to 1 mm, were initiated in the specimens after 7 days of casting as shown in Fig. 2 and Fig. 3. Crack initiation was done by two methods:

By using CTM: The specimen was placed in the CTM and load was applied. The load applied was gradually increased at the rate of $0.5\ KN.s^{-1}$. The increase in load was continued until the specimen developed the crack. The maximum load applied when the specimen developed the crack was recorded. Once the crack was initiated in a specimen, it was taken out of the CTM and put in a curing tank for self-healing.

By using nails: In this method, the cracks are induced manually by the use of nails. The specimen was first wrapped in adhesive followed by manual embedding of nails of different sizes viz 3, 4, and 5 inches (to initiate cracks of different widths) into the specimen. Succeeding this, the nails were withdrawn and adhesive was removed. Then the specimens with cracks in them were put in a curing tank for self-healing.

RESULTS AND DISCUSSION

Tests were done on materials, fresh concrete, and hardened concrete.

Tests on Fresh Concrete

Slump test: Slump cone test was done. The values obtained

Fig. 2: Initiation of cracks on concrete.

Fig. 3: Initiation of cracks on concrete.

from the slump test of all the mixtures are formulated in Table 5.

As provided in Table 5, the slump values increased with an increase in bacteria content. Fig. 4 and Fig. 5 show the variation in slump values.

Compaction factor test: The result shows that the compaction factor of the control specimen was 0.79 and that of the bacterial specimen was 0.85 as shown in Table 6.

Vee-bee consistometer test: The result shows that time taken by control concrete was 10 seconds whereas by bacterial concrete was 7 seconds which is also shown in Table 7.

Test on Hardened Concrete

Compressive strength: The strength was obtained after 7, 14, and 28 days of normal water curing period. The results are tabulated in Table 8 and variations of strength are represented by Fig. 5-11.

As per the experimentation done, it is shown that if the percentage of the bacterial content is increased, it will result in an increase in the compressive strength. After 28 days of normal water curing, the strength of bacterial concrete was assessed and found to be 23.57% more when compared to the control specimen.

After 7 days of the normal water curing period, the compressive strength of Group A bacterial concrete was assessed and was found 22.09% more when compared to the control specimen.

After 14 days of the curing period, the compressive strength of Group A bacterial concrete was assessed and was found 14.89% more when compared to the control specimen.

After curing the sample for 28 days and testing in a Compressive Testing Machine for calculating the compressive strength, it was observed that the compressive strength of Group B bacterial concrete was assessed and was found 26.57% more as compared to the control specimen.

Flexural strength: The flexure (bending) strength of beam samples is obtained after 7 and 28 days of curing of samples. The results are formulated in Table 9 and varieties of strength are represented by Figs. 12-15. After 28 days of normal curing, the strength of bio concrete was evaluated and found to be 48.34% more in comparison to the control concrete specimen.

Table 5: Slump Test Results.

Mix	Bacterial Content	Slump Value
Control	0 mL	58 mm
Bacterial concrete	A-10 mL	61 mm
Bacterial concrete	A-20 mL	63 mm
Bacterial concrete	A-30 mL	66 mm
Bacterial concrete	A-40 mL	67 mm
Bacterial concrete	B-10 mL	62 mm
Bacterial concrete	B-20 mL	65 mm
Bacterial concrete	B-30 mL	68 mm
Bacterial concrete	B-40 mL	69 mm

Table 6: Compaction factor.

Mix	Compaction Factor
Control Specimen	0.79
Bacterial Specimen	0.85

Table 7: Vee bee consistometer.

Mix	Time in Seconds
Control concrete	10
Bacterial concrete	7
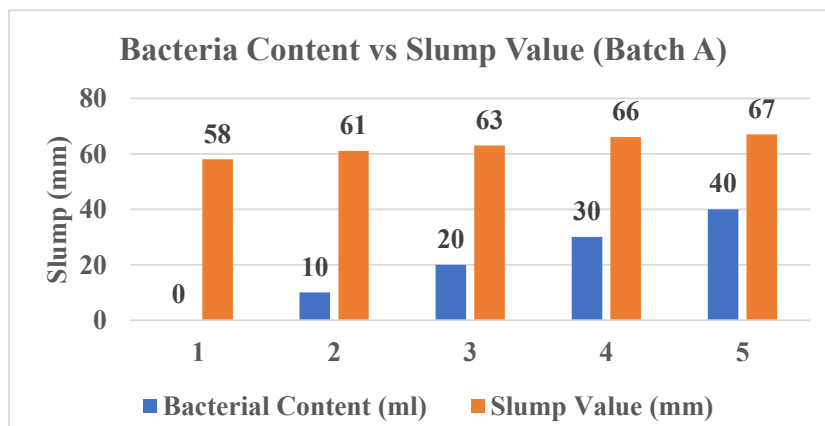
Fig. 4: Slump Values (Batch A).
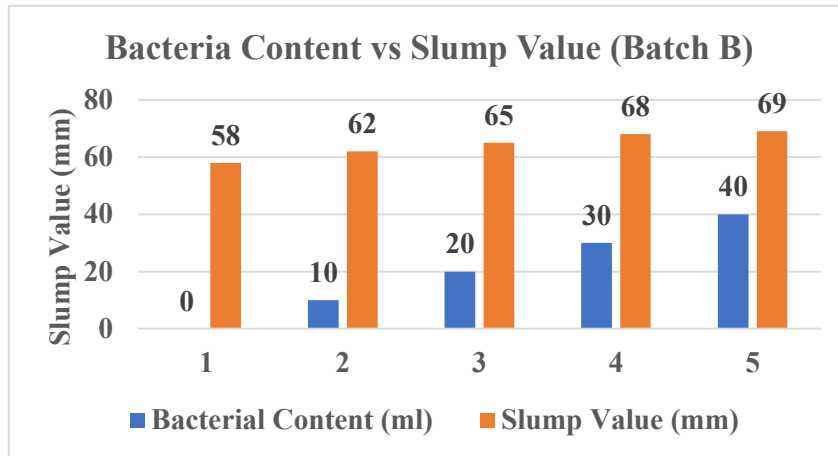
Fig. 5: Slump Values (Batch B).
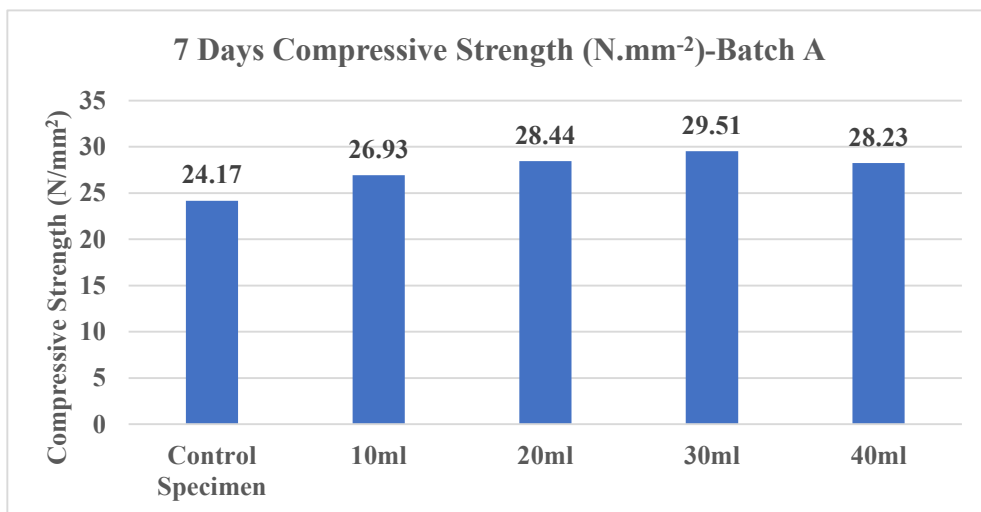
Fig. 6: 7 days compressive strength variation-Batch A.

Fig. 7: 14 days compressive strength variation-Batch A.
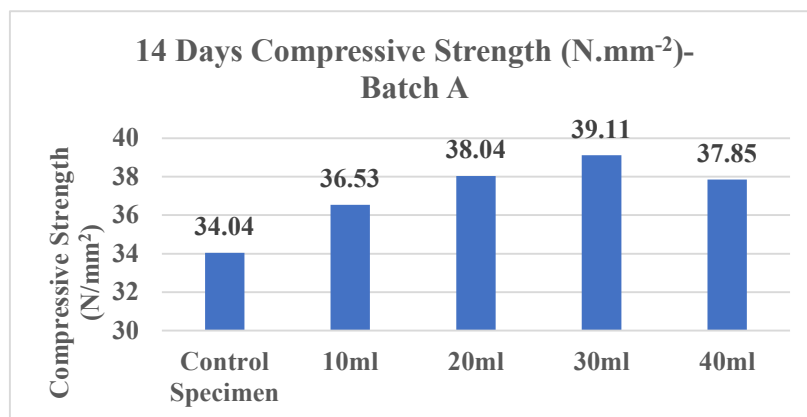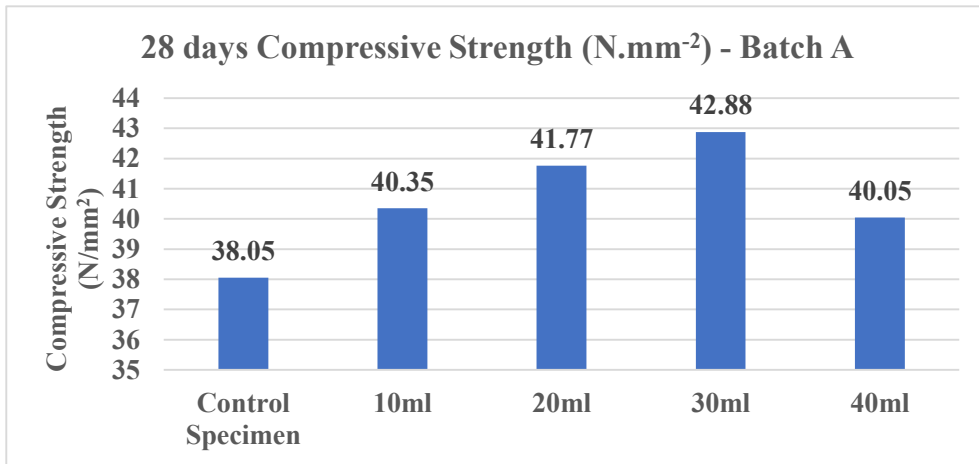
28 days Compressive Strength (N.mm^{-2}) - Batch A

Fig. 8: 28 days compressive strength variation-Batch A.

7 days compressive strength (N.mm^{-2}) - Batch B

Fig. 9: 7 days compressive strength variation-Batch B.
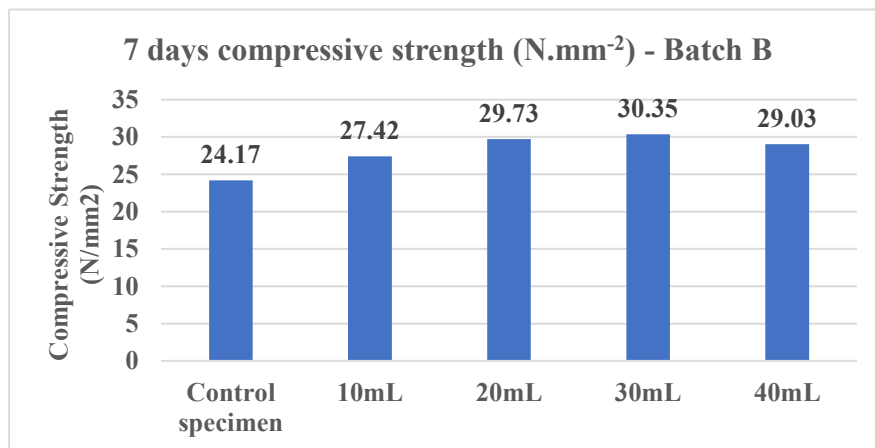
14 days Compressive Strength (N.mm^{-2}) - Batch B
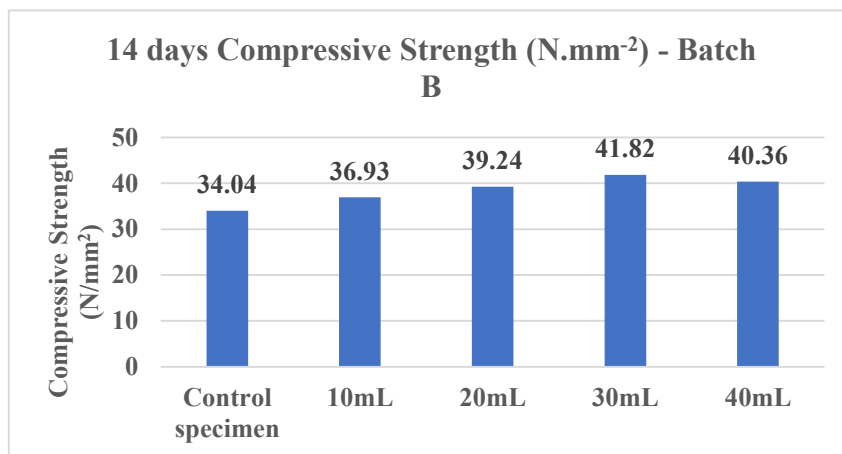
Fig. 10: 14 days compressive strength variation-Batch B.
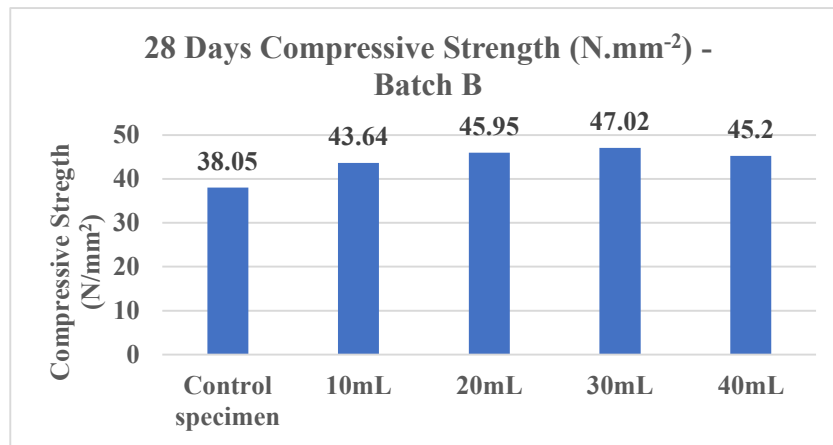
Fig. 11: 28 days compressive strength variation-Batch B.

After 7 days of the curing period, the flexural strength of Group A bacterial concrete was assessed and was found 50% more as compared to control concrete.

After 28 days of the normal curing period, the flexural (bending) strength of Group A bacterial concrete was assessed and was found 34.21% more as compared to the control concrete specimen.

After 7 days of the curing period, the flexural strength of Group B bacterial concrete was assessed and was found 95% more as compared to the control concrete specimen.

After 28 days of the curing period, the flexural strength of Group B bacterial concrete was assessed and was found 68.42% more as compared to the control concrete specimen.

Crack formation occurs frequently in concrete and results in decreased strength and hence durability of concrete. To attain and maintain the optimum durability of concrete, repair of these cracks is vital, but the costs involved in this repair are usually high. The current research focuses on the development of self-healing concrete by the use of bacteria having healing properties. The use of bacteria in concrete contributes to an increase in compressive strength, flexure strength, and hence durability of concrete. Moreover, this technology is cost-effective and eco-friendly. In the current research, Bacillus subtilis was used to heal the cracks in concrete. The bacteria were blended in different concentrations with the concrete mix while casting the specimens. Along with bacteria, calcium lactate was added to the mix which acts as a nutrient for the bacteria. Following the setting of concrete specimens, cracks were induced by two methods viz (a) By using CTM (b) By using Nails Then the specimens were put in a curing tank, and healing was assessed every 20 days up to 60 days. The specimens of group A contained 50 mg of bacteria in 1000 mL and the specimens of group B contained 100 mg of bacteria in 1000 mL. The sub concentrations for either of the groups were 10 mL, 20 mL, 30 mL, and 40 mL. After 60 days of curing, healing capacity was appraised for each concentration as shown in Fig. 16 and the following results were obtained:

- At 10 mL concentration, partial healing was acquired for both groups.

- At 20 mL concentration, specimens of group A acquired approximately 60% healing while it was approx.70% for group B specimens at the same concentration.

- At 30 mL concentration, group A specimens achieved

Table 8: Compressive strength (N.mm^{-2}).

No. of Days	Strength C.S	Group A				Group B			
		10 mL	20 mL	30 mL	40 mL	10 mL	20 mL	30 mL	40 mL
7	24.17	26.93	28.44	29.51	28.23	27.42	29.73	30.35	29.03
14	34.04	36.53	38.04	39.11	37.85	36.93	39.24	41.82	40.36
28	38.05	40.35	41.77	42.88	40.05	43.64	45.95	47.02	45.20
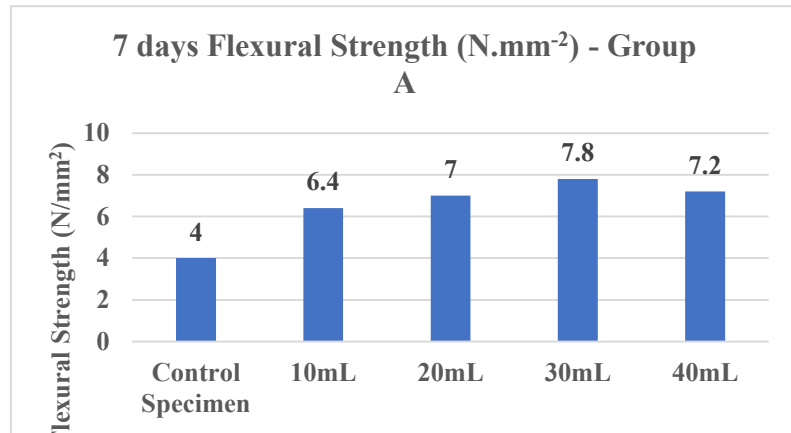
Fig. 12: 7 days flexural strength-Group A.
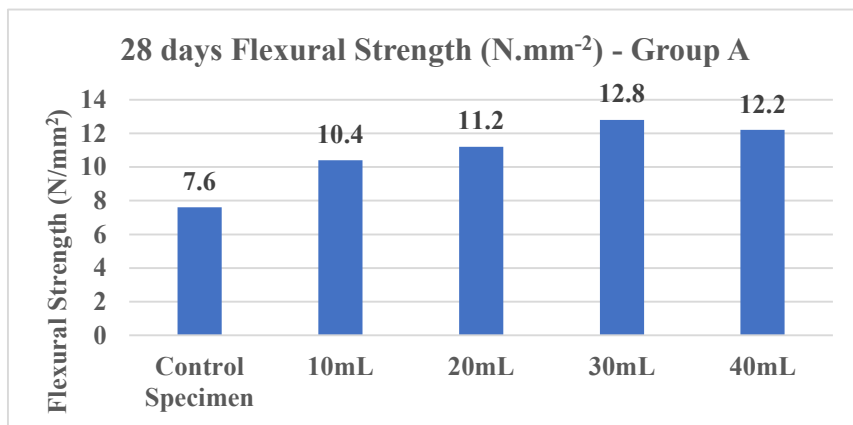
Fig. 13: 28 days flexural strength-Group A.
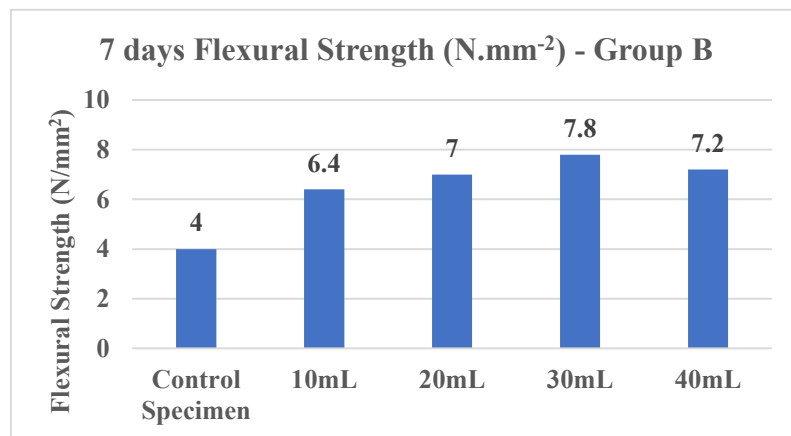
Fig. 14: 7 days flexural strength-Group B.

Table 9: Flexural strength (N.mm^{-2}).

No. of Days	Strength							
	C.S	Group A				Group B		
		10 mL	20 mL	30 mL	40 mL	10 mL	20 mL	30 mL	40 mL
7	4	5	5.4	6	5.6	6.4	7	7.8	7.2
28	7.6	8.8	9.6	10.2	9.7	10.4	11.2	12.8	12.2

28 days Flexural Strength (N.mm^{-2}) - Group A
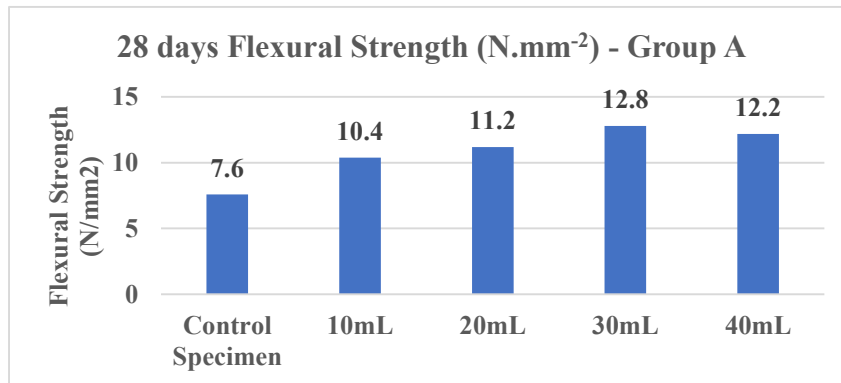
Fig. 15: 28 days flexural strength-Group B.
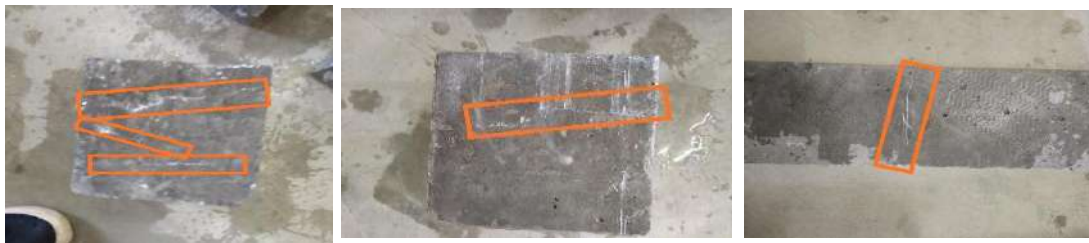
Fig. 16: Healing of cracks in cube and beam samples.

around 85% healing whereas specimens of group B were completely healed at the same concentration.

- At 40 mL concentration, both group A and group B specimens were completely healed.

CONCLUSION

Crack formation occurs frequently in concrete and results in decreased strength and hence durability of concrete. To attain and maintain the optimum durability of concrete, repair of these cracks is vital, but the costs involved in this repair are usually high. The current research focuses on the development of self-healing concrete by the use of bacteria having healing properties. The bacteria in concrete contribute to an increase in compressive strength, flexure strength, and hence durability of concrete.

The conclusion drawn based on current experimental investigations are as follows:

1. The alkaliphilic aerobic microorganism Bacillus subtilis can be cultured in the laboratory and is proved to be safe, non-pathogenic, and cost-effective.

2. The bacteria have the potential of healing the cracks in the concrete. It has been proved that 40 mL, as well as 30 mL bacterial concentrations significantly fill the cracks, developed, and result in an increase in the strength of concrete.

3. The compressive and flexural strength was increased till 30 mL bacterial content followed by a decrease in the respective strengths up to 40 mL bacterial content.

4. The compressive strength of bacterial concrete was increased by 25.79% as compared to control specimens at 28 days.

5. The flexural strength of bacterial concrete was increased by 68.42% as compared to control specimens at 28 days.

6. Bacterial spores are resistant to harsh environmental conditions and when the environmental conditions are favorable, they become metabolically active and utilize calcium lactate in concrete and cause hydrolysis of urea to produce ammonia and carbon dioxide resulting in the formation of calcium carbonate precipitate which fills the cracks in concrete.

7. This technology works by the process of biomineralization which results in improved strength of the concrete.

8. The most expensive ingredient in the development of self-healing concrete is nutrient i.e. calcium lactate.

9. The concentration of calcium lactate influences the setting time of concrete; therefore, it is necessary to regulate the concentration of nutrients used in concrete.

10. After exceeding the calcium lactate by 3% the initial setting time was varied by 65 min.

11. The use of bacteria in bacterial concrete is convenient and eco-friendly. Moreover, this innovative technology is cost-effective.

ACKNOWLEDGMENT

REFERENCES

Ahn, T.H. 2008. Development of Self-Healing Concrete Incorporating Geo-Materials: A Study on Its Mechanism and Behavior in Cracked Concrete. Ph.D. dissertation, Department of Civil Engineering, The University of Tokyo, Japan.

Ahn, T.H. and Kishi, T. 2008. The Effect of Geomaterials on the Autogenous Healing Behavior of Cracked Concrete. Proceeding of 2nd ICCRRR2008, November 2008, Cape Town, South Africa, CRC Press, Boca Raton, Florida, pp. 235-240.

Ahn, T.H. and Kishi, T. 2009. A New Method as the Self-Healing Design to Repair Cracks in Cracked Concrete. 4th International Conference on Construction Materials: Performance, Innovations and Structural Implications, 24-26 August 2009, Nagoya, Japan, Japan Concrete Institute, Tokyo, Japan, pp. 1339 -1346.

Alhalabi, Z.S. and Dopudja, D. 2017. Self-healing concrete: Definition, mechanism, and application in different types of structures. Int. Res. J., 5: 55.

Bang, S.S., Galinat, J.K. and Ramakrishnan, V. 2001. Calcite precipitation induced by polyurethane-immobilized Bacillus pasteurii. Enzyme Microb. Technol., 28: 404-409.

Binici, H., Aksogan, O., Kaplan, H., Gorur, E.B. and Bodur, M.N. 2008. Performance of ground blast furnace slag and ground basaltic pumice concrete against seawater attack. Constr. Build. Mater., 22: 1515.

Binici, H., Aksogan, O, Kaplan, H., Gorur, E.B. and Bodur M.N. 2009. Hydro-abrasive erosion of concrete incorporating ground blast-furnace slag and ground basaltic pumice. Constr. Build. Mater., 23: 804.

Chindaprasirt, P., Homwuttiwong, S. and Jaturapitakkul, C. 2007. Strength and water permeability of concrete containing palm oil fuel ash and rice husk–bark ash. Constr. Build. Mater., 21: 1492.

Demirboga, R. and Gul, R. 2006. Production of high-strength concrete by use of industrial by-products. Build. Environ., 41: 1124.

Homma, D., Mihashi, H. and Nishiwaki, T. 2009. Self-healing capability of fiber-reinforced cementitious composites. J. Adv. Concr. Technol., 7(2): 217-228.

Irwan, J.M., Anneza, L.H., Othman, N., Faisal, A., Zamer, M.M. and Teddy, T. 2017. Mechanical properties of concrete with Enterococcus faecalis and calcium lactate. Proc. Eng., 71: 592.

Isa, Y. and Turhan, B. 2007. Usage of industrial by-products to produce plain concrete elements. Constr. Build. Mater., 21: 686.

IS 10262. 2019. Code of Practice for IS Method of Mix Design. Bureau of Indian Standards, New Delhi.

IS 8112. 1989. Ordinary Portland Cement – 43 Grade Specification. Bureau of Indian Standards, New Delhi.

IS 4031. 1996. Method of Physical Test for Hydraulic Cement. Bureau of Indian Standards, New Delhi.

IS 2386. 1963. Method of Test for Aggregates for Concrete. Bureau of Indian Standards, New Delhi.

IS 1199. 1959. Method of Sampling and Analysis of Concrete. Bureau of Indian Standards, New Delhi.

IS 383. 1970. Specification for Coarse and Fine Aggregates from Natural Sources for Concrete. Bureau of Indian Standards, New Delhi.

IS 456-2000. Code of Practice for Plain and Reinforced Concrete. Bureau of Indian Standards, New Delhi.

Kishi, T., Ahn, T.H., Hosoda, A. and Takaoka, H. 2007. Self-healing behavior by cementitious recrystallization of cracked concrete incorporating expansive agent. Proceedings of the 1st International Conference on Self-Healing Materials, 18-20 April 2007, Delft, Netherlands, Springer, Dordrecht, pp. 171-186.

Luhar, S. and Gourav, S. 2015. A review paper on self-healing concrete. J. Civil Eng. Res., 5: 53.

Quayum, M.S., Zhuang, X. and Rabczuk, T. 2015. Computational model generation and RVE design of self-healing concrete. Front. Struct. Civ. Eng., 9: 383.

Seifan, M., Samani, A.K. and Berenjian, A. 2016. Bio concrete: Next generation of self-healing concrete. Appl. Microbiol. Biotechnol., 100: 2591.

Topcu, I.B. and Canbaz, M. 2004. Properties of concrete containing waste glass. Cem. Concr. Res., 42: 267.

Original Research Paper

Open Access Journal

Effective Utilization of Stabilized Spent Wash Bio-Compost for Tomato Crop and Comparison of its Yield with Commercial Composts

A. S. Byakodi*† and B. T. Suresh Babu**

*Research Centre, Department of Civil Engineering, Angadi Institute of Technology & Management, Belagavi, Karnataka, India
**Department of Civil Engineering, Angadi Institute of Technology & Management, Belagavi, Karnataka, India
†Corresponding author; A. S. Byakodi; amarsbenv@gmail.com

ABSTRACT

India is an agro-based country and in the year 2020, about 1082 lakh hectares of agricultural land have been planted, in turn, consuming 3161 lakh tonnes of fertilizer annually. However, excessive fertilizer usage has a negative impact on the soil quality and is evident by the fact that the crop response ratio has decreased from 12.1 in the 1960s to 5.0 in the 2010s. Hence, organic compost can be used as an alternative to fertilizer, reducing its negative impact on soil quality. The present study is a part of a larger investigation and its scope is confined to the utilization of bio-composts for the growth of tomato crops. Additionally, a comparison of these bio-composts was carried out with commercial composts through assessment of yield and number of fruits. Seeds were sown on prepared land, germination was observed on the 7th day, and saplings were produced on the 30th day. The dosage of each compost was fixed at 60ml per plant and was applied on the 31st and 51st days of the study period. Commercial composts produced yields of 673 ± 32.01, 830 ± 32.19 and 1560 ± 77.62 g respectively, with 54 ± 4.16, 81 ± 11.50, and 104 ± 13.50 fruits. All the bio-composts outperformed control and commercial composts in terms of yield. With 140 ± 11.50 fruits, BC5 produced a maximum yield of 2938 ± 93.72 g, which is 723 % higher than the control. Hence, it is concluded that the use of bio-compost is more effective than commercial composts and provides a much higher yield. Further studies need to be conducted to evaluate the quality of yield obtained by various bioassay tests.

INTRODUCTION

India is a developing country with a large proportion of its population depending on agriculture. The use of fertilizer is an important component of providing nutrients to the soil and increasing crop yield. In 1906, Tamil Nadu witnessed the establishment of India's first fertilizer industry. Since then, there have been significant advances in the types and quantities of fertilizers produced. The Fertilizer Association of India (FAIb 2020) was founded in 1955 and is responsible for overseeing all aspects of fertilizers regulation in India. In 1951-1952, India produced a total of 20.16 lakh tonnes of fertilizers, comprising nitrogen and phosphorus nutrients (FAId 2020). Out of which only 6.38 lakh tonnes were utilized (FAIa 2020) and additional 6000 tonnes of potassium fertilizer was imported due to the unavailability of resources in India. Furthermore, 4275.22 lakh tonnes of fertilizers, comprising straight and complex fertilizers, were produced in 2019-20. Out of which 2896.96 lakh tonne was utilized and additional 264.09 lakh tonnes of potassium fertilizer are met through imports (FAIc 2020).

According to current data, India's agricultural sector has planted 1082 lakh hectares, which is the most in recent years.

Chemical fertilizers are often utilized at a rate of 150kg per hectare of land for important crops such as maize, ragi, toor, and wheat (Purashekhara 2020). Demand for food grains has risen manifold as a result of the growing population. Farmers are increasingly opting for intensive farming, in which soil resources are exploited to a greater extent to increase yield, resulting in an imbalance of available nutrients in the soil and a decrease in its fertility. While chemical fertilizers may increase production initially, they degrade the soil's quality over time. This is demonstrated by the crop response ratio shown in Fig. 1. The crop response ratio refers to the amount of grain produced in relation to the number of fertilizers applied. This has decreased significantly throughout the decades, from 12.1 in 1960 to 5.0 in 2017 (Katyal 2019). Additionally, the usage of chemical fertilizers can result in the leaching of surplus nutrients, resulting in the eutrophication of stagnant water bodies and negatively impacting the ecosystem as well as the surrounding environment.

The unavailability of organic manure and increased chemical fertilizer cost have necessitated the development of eco-technology for organic waste recycling in the agri-

culture system. Due to the increased need for agricultural yields, it is necessary to maintain a healthy balance of soil health and nutrients. Thus, recycling and reusing renewable organic waste to meet the challenges of the present scenario is of the utmost importance. There are several sources of organic manure, including significant contributions from municipal waste, animal excreta, and industrial waste. Solid waste from agro-industries is one of the finest sources for organic compost generation. This enables the recycling of plant nutrients contained in industrial waste, as well as a disposal method that has a lower impact on the surrounding environment. The sugar industry and distilleries are two of India's primary agro-based industries.

India is the world's largest producer of sugar, with a capacity of 290 lakh tonnes. One significant by-product of these industries is pressmud, which is organically rich and accounts for around 3.5–4.0% of the cane crushed (Lokhande 2005). India produces around one lakh tonne of pressmud daily during the sugarcane crushing season. Due to the enormous amount generated and its intrinsic properties, any industry faces significant challenges in safely disposing of the waste. Distilleries, meanwhile are secondary agro-based industries that generate around 22 lakh liters of industrial alcohol daily (Chinimandi.com 2019). Manufacture of industrial alcohol or ethanol, intern generates one of the more complicated liquid wastes known as spent wash. This spent wash is generated at a rate of 10 to 12 liters per liter of ethanol produced, resulting in lakhs of liters of spent wash being generated every day. The distilleries have significant challenges in safely disposing of this massive amount of liquid waste. Hence, the use of these abundantly available waste by-products for the production of organic compost will reduce the dependency on chemical fertilizers and make way for a sustainable agricultural practice.

Numerous researchers have investigated the composition of organic compost prepared from pressmud and its influence on crop yields. As Solaimalai et al. (2015) mentioned,

pressmud is a good source of plant nutrients and should be composted before being used as manure. Composted pressmud applied at a rate of 25 tonnes per hectare improved sugarcane production by 7.50 tonnes. Similarly, its application at a rate of 20 tonnes per hectare enhanced maize and wheat crop yields by 129.4 and 65.2 % respectively, illustrating its potential. (Sarangi et al. 2008) have investigated compost made from pressmud and found that when applied at a rate of 25 tonnes/ha, it increased sugarcane production by 6.11%. (Diaz 2016) has proposed that using compost made from pressmud can also be used to manage weeds and insects in the field. This is due to its intrinsic characteristics and chemical composition. (Kumar et al. 2017) advised adding 20 tonnes/ha of composted pressmud, which saved 25% of the necessary fertilizers and showed a substantial increase in the soil's residual nutrient content. Pressmud compost has also shown an increase in soil texture, water holding capacity, and other physic-chemical properties, enhancing soil quality internally. According to the literature studied thus far, composted pressmud has shown promising results for enhancing crop production. Hence, there is significant scope for production and utilization of organic compost prepared from pressmud and stabilized spent wash.

The current article is part of a broader study, examining the treatment and disposal of two complicated waste by-products by aerobic composting. Previous investigations have utilized pressmud as the base material in aerobic composting with treated spent wash, termed as stabilized spent wash. This stabilized spent wash was applied to composting heaps in various proportions of 0, 25, 50, 100, 150, and 200% (v/w). The entire composting process was carried out over 50 days under predefined operating conditions. These bio-composts were compared to the Fertilizer Control Order (FCO) (Ministry of Agriculture 1985) issued by the Ministry of Agriculture, Government of India. The FCO establishes guidelines for the concentration of nutrients in compost materials. Our
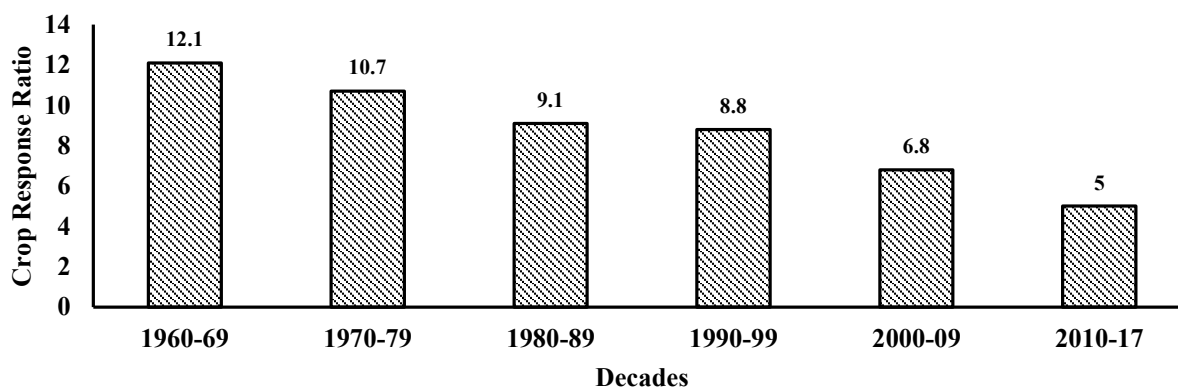
Fig. 1: Trend in crop response ratio for previous decades (Katyal 2019).

investigations have revealed that all bio-composts had greater nutrient concentration than the specified criteria. The present article is a continuation of the previous investigation carried out. Hence, the scope of this article is confined to the use of BIO-COMPOST on a selected crop and a comparison of yield to commercial composts.

MATERIALS AND METHODS

The Ministry of Agriculture's Fertilizer Control Order (FCO) regulates the nutritional requirements for organic composts. The FCO recommends a TOC of at least 12.5%, a TKN of at least 0.80%, a Phosphorus and Potassium content of at least 0.40%, and a C/N ratio of less than 20. Previous investigation has revealed that all of the bio-composts had higher nutrient concentrations than the prescribed standards. Representative samples of the bio-compost were collected and analyzed for physic-chemical properties to determine the nutrient concentration. table 1 indicates the nutrient concentration of various bio-composts prepared.

Additionally, as mentioned previously, the goal of this study is to compare the yield of bio-composts to that of commercial composts. the yield performance of bio-composts was compared using cow dung compost, municipal compost, and vermicompost in this study. Table 2 summarizes the nutrient content of these commercial composts.

The entire research was conducted at the Research Centre, Department of Civil Engineering, Angadi Institute of Technology & Management in Belagavi, Karnataka. A suitable location for the cultivation of a tomato crop has been identified near Itagi village in the Belagavi district of Karnataka. Black cotton soil was present at the selected site. Before seed sowing, the land was cleaned and prepared, as shown in Fig. 3. Tomato

Table 1: Physic-chemical characteristics of bio-composts.

Characteristics	Stabilized spent wash addition						FCO Standards
	0% BC1	25% BC2	50% BC3	100% BC4	150% BC5	200% BC6	
pH	7.59	7.72	7.67	7.68	7.64	7.81	6.5-7.5
EC [mS.cm^{-1}]	3.53	5.58	7.96	8.32	8.87	8.32	< 4dS.m^{-1}
Moisture Content [%]	49.26	55.34	54.16	52.25	49.52	53.18	25% max
Bulk Density [g.cm^{-3}]	0.550	0.540	0.545	0.530	0.515	0.575	< 1 gm.cm^{-3}
TOC [%]	25.33	23.58	24.84	23.53	25.92	23.73	12% Min
TKN [%]	1.13	1.88	1.62	1.49	2.16	1.16	0.8% Min
C/N Ratio	29.60	12.70	15.35	16.07	12.28	21.73	< 20
Potassium [%]	7.29	7.47	10.86	12.18	15.90	15.12	0.4% Min
Phosphorous [%]	8.56	5.85	6.85	6.93	6.55	5.86	0.4% Min

Table 2: Physic-chemical characteristics of commercial composts.

Characteristics	Commercial Compost			FCO Standards
	Cow dung Compost[*] CC	Municipal Compost[*] MC	Vermicompost[*] VC	
pH	7.68	7.64	7.81	6.5-7.5
EC [mS.cm$^-$]	8.32	8.87	8.32	< 4dS.m^{-1}
Moisture Content (%)	52.25	49.52	53.18	25% max
Bulk Density (gm/BC-3)	0.530	0.515	0.575	< 1 gm.cm^{-3}
TOC [%]	23.53	25.92	23.73	12% Min
TKN [%]	1.49	2.16	1.16	0.8% Min
C/N Ratio	16.07	12.28	21.73	< 20
Potassium [%]	12.18	15.90	15.12	0.4% Min
Phosphorous [%]	6.93	6.55	5.86	0.4% Min

* Physic-chemical characteristics received from respective commercial compost vendors.

seeds were obtained commercially from Unisem Agritech Private Limited. The variety of seeds chosen was USM-KA-REENA, which had a minimum genetic purity of 90%.

Commercial composts (cow dung compost, municipal compost, and vermicompost) were obtained from local vendors in Belagavi. At the Research Centre, aerobic composting of pressmud and stabilized spent wash resulted in bio-composts. Before application on the field, all of these composts were sieved through a 4mm sieve (Fig. 2) to ensure uniformity in particle size. The present study was carried out in three plots parallelly and continued for a total of 76 days. Throughout the study period, the temperature of the atmosphere varied between 19°C and 38°C.

Initially selected species of tomato seeds were sown in prepared land and covered with soil to produce saplings (Fig. 3). In addition, water was immediately added to the seeds for optimal development. The seed germinated for the first time on the 7th day after sowing and the bulk of seeds germinated until the 11th day (Fig. 4). Watering was done at 6-day intervals during this period. Thirty days were required

to produce tomato saplings, which were then placed in an open field to continue growing.

As shown in Table 1, bio-composts containing 0% (BC1), 25% (BC2), 50% (BC3), 100% (BC4), 150 % (BC5) and 200 % (BC6) stabilized spent wash were used. Additionally, commercial composts were utilized to compare yields, including cow dung compost, municipal compost, and vermicompost. Also, the control group of the study was maintained without the addition of any nutrients. Ten rows were made in each plot to investigate the effect of the aforementioned composts, as shown in Fig. 5.

Each row was planted with fifteen saplings and the composts were applied at a rate of 60mL per plant. The first application of these composts was done one day after the saplings were planted, followed by water to facilitate nutrient absorption by the plants. Similarly, the second application was made after twenty days after the first application. Watering was carried out at a 10-day interval during this period.

As the tomato crop continued to grow, flowering was noticed on the 17th day following the initial application of

Fig. 2: Bio-compost passing through 4mm sieve for uniform particle size.

(a)   (b)

Fig. 3: Preparation of land for sowing of tomato seeds.
(a) Leveling and cleaning of land (b) Sowing of seeds (c) Watering of sown seeds

compost. Similarly, the tomato's initial glimpse was observed after seven days of flowering. The tomato crop was allowed to grow for a total of 76 days from the time of seeding until it was harvested. The harvested crops were collected row-wise and weighed accurately along with the number of tomato fruits. Furthermore, a comparison of these yields was carried out to determine the effectiveness of these composts. The entire methodology of the study is detailed in Fig. 6 for ease of understanding.

RESULTS AND DISCUSSION

The addition of nutrients is an important aspect of farming to gain more yield to meet the increasing demand for food grains. The purpose of this study is to determine the efficacy of bio-composts on a selected tomato crop. the ground preparation for seed sowing and the planting of saplings on an open field were carried out according to the established methodology. the performance of each of the bio-composts, commercial composts, and control was assessed at the end of

Fig. 4: Germination of tomato seeds.

(a)

(b)

(c)

(d)

Fig. 5: Tomato crop growth phases. (a) Application of saplings onto the open field (b) Application of compost to each row of crops (c) Intermediate growth phase of tomato crop (d) Final yield of tomato crop
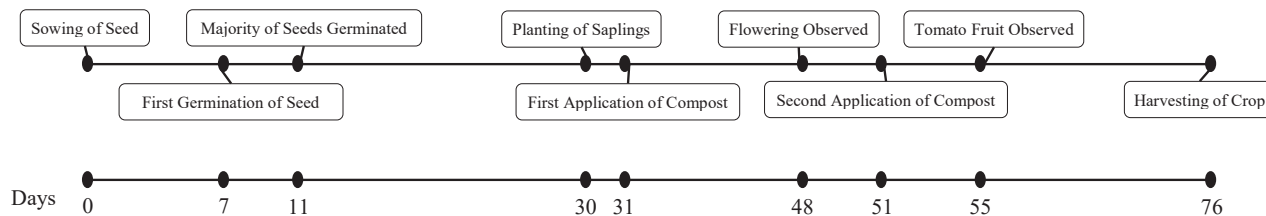
Fig. 6: Flowchart of the methodology used for the study.

harvesting of tomato crop. These assessments were mainly based on the yield of the tomato crop, additionally, several tomato fruits were also analyzed. At the end of the harvesting period, the produce from each row of the plots was gathered and weighed accurately. Table 3 illustrates the yield of tomato crops for the application of various composts.

Control for the study was applied with only water from sowing to harvesting at the predetermined frequency. Control has shown a yield of 356.7 ± 38.28 g which is the least among the study conducted. Municipal compost, cow dung compost, and vermicompost applications have yielded 673 ± 32.01 g, 830 ± 32.19 g, and 1560 ± 77.62 g of tomato crop. This corresponds to an increase in yield of 88%, 132%, and 337% respectively, over control.

Furthermore, the application of bio-composts obtained by aerobic composting of pressmud and stabilized spent wash produced significantly superior results than the control and commercial composts. As previously mentioned, BC1 to BC6 contain a stabilized spent wash addition of 0, 25, 50, 100, 150, and 200% respectively. the yield from these bio-compost applications has shown an increasing trend similar to the addition of stabilized spent wash, with a maximum yield produced of 150% (BC5). Following that, the yield decreased

slightly in BC6. Yields of 419 ± 45.51, 2243 ± 120.09, 2476 ± 51.73, 2483 ± 102.02, 2938 ± 93.72 and 2535 ± 86.26 g were observed in BC-1, BC-2, BC-3, BC-4, BC-5 and BC-6 respectively. Fig. 7 indicates the variation of tomato crop yield with pooled standard deviation.

These findings followed a pattern consistent with the nutritional content of the bio-composts utilized in the study. in the majority of the parameters analyzed, BC5 had shown maximum nutrient concentration as indicated in Table 1. The highest production of tomato crop was recorded in BC5 with 2938 ± 93.72 g of yield, indicating a 723 % increase compared to control. Also, BC5 has shown an increase of 336%, 253%, and 88% compared to municipal compost, cow dung compost, and vermicompost respectively, for the same dosage applied. This is a significant increase in tomato crop production over commercial composts. Furthermore, it suggests that aerobic composting of pressmud and stabilized spent wash is an optimal approach for recycling plant nutrients from waste by-products and provides an option for their safe disposal.

Table 4 indicates the Pearson correlation matrix between the yields of tomato crop for various composts applied. The data in the correlation matrix indicates a positive correlation

Table 3: Comparison of tomato yield for various compost applications.

Sl. No.	Composts	Range*	Mean ± SD
1.	Control	316 – 392	356.7 ±38.28
2.	BC1 (0%)	374 – 465	419 ±45.51
3.	BC2 (25%)	2120 – 2360	2243 ± 120.09
4.	BC3 (50%)	2422 – 2525	2476 ±51.73
5.	BC4 (100%)	2395 – 2595	2483 ± 102.02
6.	BC5 (150%)	2856 – 3040	2938 ±93.72
7.	BC6 (200%)	2464 – 2631	2535 ±86.26
8.	Municipal Compost (MC)	641 – 705	673 ± 32.01
9.	Cow dung Compost (CC)	796 – 860	830 ±32.19
10.	Vermicompost (VC)	1480 – 1635	1560 ± 77.62

* All units are in grams
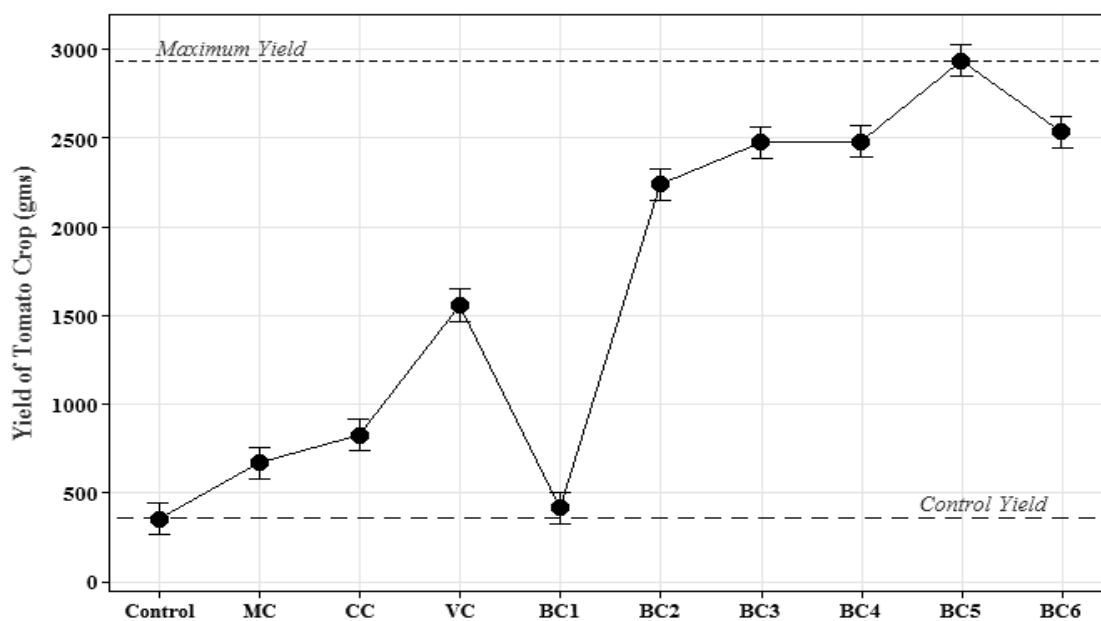
Fig. 7: Mean variations of tomato crop yield for compost applied.

Table 4: Pearson correlation matrix for yields of various composts applied.

Correlation Table	Control	MC	CC	VC	BC1 (0%)	BC2 (25%)	BC3 (50%)	BC4 (100%)	BC5 (150%)	BC6 (200%)
Control	1^f									
MC	0.9947	1^e								
CC	0.9999	0.9960	1^e							
VC	0.9979	0.9993	0.9986	1^d						
BC1 (0%)	0.9902	0.9993	0.9920	0.9972	1^f					
BC2 (25%)	0.9966	0.9998	0.9976	0.9998	0.9983	1^c				
BC3 (50%)	0.3028	0.3991	0.3153	0.3642	0.4328	0.3803	1^b			
BC4 (100%)	0.9491	0.9765	0.9532	0.9676	0.9838	0.9718	0.5875	1^b		
BC5 (150%)	0.9514	0.9780	0.9553	0.9694	0.9851	0.9735	0.5816	0.9999	1^a	
BC6 (200%)	-0.7822	-0.7141	-0.7740	-0.7400	-0.6877	-0.7283	0.3569	-0.5463	-0.5523	1^b

Each cell indicates the Pearson correlation coefficient.
Grouping information is based on one-way ANOVA with post hoc Tukey test at $p \leq 0.05$

between all the yields for various composts applied with an exception of BC6. It is indicated by the negative sign, intern interpreting a reduction in yield of the crop compared to other variations. Further, one-way ANOVA analysis was carried out to assess the variance between groups and results indicate there is a significant difference between the yields of various composts applied. As a result, post hoc Tukey tests were used to determine the yield groups that differed significantly, as shown in Table 5 with different alphabets.

In addition, as shown in Table 5, observations were made on several tomato fruits generated for all the study's variations. The control group for the study had the least tomato fruits of 35 ± 6.11. Municipal compost, cow dung compost, and vermicompost yielded 54 ± 4.16, 81 ± 11.50, and 104 ± 13.50 fruits respectively, which is consistent with crop yield. BC1 of the prepared compost produced 37 ± 8.02 tomato fruits, which is the lowest number for BIO-COMPOSTs. Whereas BC2, BC3, BC4, BC5 and BC6 each had 137 ± 10.97, 141 ± 6.66, 126 ± 7.55, 140 ± 11.50 and 148 ± 17.50 fruits respectively. When compared to the control, this shows that adding compost increases fruit yield. Furthermore, bio-composts have outperformed

Table 5: Comparison of the number of tomato fruits for various compost applications.

Sl. No.	Composts	Range*	Mean ± SD
1.	Control	30-42	35 ± 6.11
2.	BC1 (0%)	29-45	37 ± 8.02
3.	BC2 (25%)	128-149	137 ± 10.97
4.	BC3 (50%)	135-148	141 ± 6.66
5.	BC4 (100%)	118-133	126 ± 7.55
6.	BC5 (150%)	129-152	140 ± 11.50
7.	BC6 (200%)	130-165	148 ± 17.50
8.	Municipal Compost (MC)	49-57	54 ± 4.16
9.	Cow dung Compost (CC)	70-93	81 ± 11.50
10.	Vermicompost (VC)	91-118	104 ± 13.50

* All units are in Nos.

commercial composts in a number of ways, indicating their efficacy.

CONCLUSION

India is a predominantly agricultural country, with the bulk of its population dependent on agriculture. Nutrient addition via fertilizers enables agricultural production enhancement. However, frequent use of fertilizers has harmed soil quality, as seen by the decline in crop response ratios. Thus, an alternative to fertilizers may be used in the form of organic compost, which enhances the soil quality and nutrient concentration over time. The present study is a part of a larger investigation and its scope is confined to the utilization of the bio-composts from previous investigations to assess its effect on the tomato crop. Additionally, commercial composts (Municipal compost, Cow dung compost, and Vermicompost) were also utilized, to compare the yield of tomato crop with the bio composts. The performance of each compost was primarily determined by crop yield, as well as the number of tomato fruits. The entire study lasted 76 days from seeding to harvesting. The dosage of each compost was fixed at 60 ml per plant and was applied on the 31st and 51st days of the study. Crop harvesting revealed a minimum yield of 356.7 ±38.28 g with 35 ± 6.11 fruits for control. Commercial composts produced yields of 673 ± 32.01, 830 ±32.19, and 1560 ± 77.62 g respectively, suggesting an increase in yield of 88%, 132%, and 337% over control. Similarly, bio-composts yielded significantly more than commercial composts and control. A maximum yield of 2938 ±93.72 g with 140 ± 11.50 fruits was recorded in BC-5, indicating a 723% increase in yield over control. Additionally, as compared to municipal compost, cow dung compost, and vermicompost, BC-5 yields increased by 336%, 253%, and 88% respectively. The results indicate that bio-composts have a greater concentration of nutrients than commercial composts

and produce a much higher yield. Hence, it can be concluded that the use of these bio-composts from pressmud and stabilized spent wash is suitable for the growth of a selected crop. Further studies are to be conducted for assessing the quality of yield produced through various bioassay tests.

REFERENCES

Chinimandi.com 2019. State Wise Molasses Production in India. https://www.chinimandi.com/state-wise-molasses-production/

Diaz, P. 2016. Consequences of compost press mud as fertilizers. DJ Int. J. Adv. Microbiol. Microbiol. Res., 1(1): 28-32. https://doi.org/10.18831/djmicro.org/2016011005

Fertilizer Association of India (FAI$_a$). 2020. Consumption of Fertilizers. https://www.faidelhi.org/general/con-npk.pdf

Fertilizer Association of India (FAI$_b$). 2020. Establishment of FAI. https://www.faidelhi.org/

Fertilizer Association of India (FAI$_c$). 2020. Production, Consumption, and Import of Fertilizers. https://www.faidelhi.org/general/Prodn-imp-cons-fert.pdf

Fertilizer Association of India (FAI$_d$). 2020. Production Capacity of Fertilizers. https://www.faidelhi.org/general/prodn-np.pdf

Katyal, J.C. 2019. Fertilizers use efficiency research: looking back to move forward. Indian J. Fertilizers, 15(12): 1384-1401.

Kumar, S., Meena, R., Singh Jatav, H., Banjara, T. and Jinger, D. 2017. Use of pressmud compost for improving crop productivity and soil health. Int. J. Chem. Stud., 5(2): 384-389.

Lokhande, M.A. 2005. A study of the Indian sugar industry in the post reforms era. J. Coop. Manag., 40(1): 7-12.

Ministry of Agriculture. 1985. Biofertilizers and Organic Fertilizers in Fertilizer (Control) Order. , Government of India, National Centre of Organic Farming. Government of India Press, New Delhi. pp 1-68.

Purashekhara, S.V. 2020. Could organic city compost reduce production costs in agriculture? Science the Wire. https://science.thewire.in/environment/agriculture-costs-chemical-fertilisers-organic-city-compost-soil-fertility/

Sarangi, B.K., Mudliar, S.N., Bhatt, P., Kalve, S., Chakrabarti, T. and Pandey, R.A. 2008. Compost from sugarmill pressmud and distillery spent wash for sustainable agriculture. Dyna. Soil Dyna. Plant, 2(1): 35-49.

Solaimalai, A., Bhaskar, M., Ramesh, P.T. and Ravishankar N. 2001. The utilization of press mud as a soil amendment and organic manure: A review. Agric. Rev., 22(1): 25-32.

Study on the Effect of Shrubs on Wind Erosion Control in Desert Regions

Naqi Lessani*, Hanfeng Wang*† and Ahmad Hamed Nikmal**

*School of Civil Engineering, Central South University, Changsha, P. R. China
**School of Civil Engineering and Environment, University of Science and Technology, Beijing, P. R. China
†Corresponding author: Hanfeng Wang; wanghf@csu.edu.cn

ABSTRACT

The wind velocity reduces by encountering vegetation; thus, a shelter zone is generated at downstream of vegetation. Hence, planting vegetation, mainly shrubs, has widely been used to control sand transportation. However, plant shrubs in a large area of the desert are practically unsustainable and uneconomical. In this study, Computational Fluid Dynamic (CFD) and wind tunnel experiments were carried out to optimize the planting method of shrubs that could decrease the number of shrubs and increase wind erosion controlling efficiency in desert regions. The effects of shrub height, porosity, the number of shrub rows, and space between shrub rows on wind erosion control were studied. Based on the present study results, the downstream of shrubs was divided into three different zones: first erosion zone, sedimentation zone, and second erosion zone. Moreover, with the increase of shrub porosity, the first erosion zone's length increased. In contrast, the sedimentation zone's length decreased, whereas the length of the first erosion and sedimentation zones increased with shrub height. Hence, to make a better shelter zone, it is recommended to plant denser shrubs rows at the upstream and sparsely shrub rows at the far downstream.

INTRODUCTION

Vegetations have over time been used to control wind erosion in desert regions near infrastructures, particularly railway lines located in desert regions. Human activities and climate change have intensified the rate of desertification surges (Qu et al. 2007). Wind erosion occurs in arid and semi-arid regions, negatively affecting the environment and the infrastructures (Prospero 1999, Griffin et al. 2001, Lv & Dong 2012, Cheng et al. 2017). Sandstorms cause huge damage to infrastructures (Yao et al. 2012, Sarkar et al. 2019).

Vegetations have been considered to be effective in controlling wind erosion (Hong et al. 2020). Trees and shrubs have widely been used to create shelterbelts. However, in desert regions, shrubs have proven to be more likely employed than trees, and shrubs can survive in conditions with limited moisture and nutrients (Zhang 1994, Xu 1996, Lv & Dong 2012).

The morphology of shrubs and the arrangement are significant features that govern wind velocity reduction effectiveness: Porosity, shape, height, configuration, thickness, spacing, shrub coverage are factors that determine the efficiency of vegetations shelterbelt in wind erosion control (Cornelis & Gabriels 2005, Lv & Dong 2012, Jian et al. 2018, Liu et al. 2018).

An additional row of the tree has a significant effect on wind velocity reduction, which is almost twice (Rosenfeld et al. 2010). Wind mitigation zones are better provided by trees with large bottoms and narrow tops. In actuality, most trees have a narrow bottom and a wide top, resulting in a considerable rise in the total shelterbelt effect coverage percentage. Single plants, on the other hand, have a lower efficiency (Liu et al. 2018). Sand transportation is reduced by 92 percent when grasses grow to cover 28 percent of the ground surface (Ash & Wasson 1983).

In straw checkboard systems, vegetation such as reeds, wheat, saxual tree, and other plants are planted. A square-shaped straw checkboard measuring 1 m by 1 m reduces wind velocity and stabilizes sand delivery (Station 1986). The best wind reduction efficiency and dune fixing were observed with a 10 cm to 20 cm height with a 1 m by 1 m square straw checkboard (Qiu et al. 2004). In a small-sized straw checkboard, sand transportation rate varies logarithmically, and in the large-sized straw checkboard, sand transportation rate and wind velocity vary exponentially (Gao et al. 2004). The height and density, which are split into three zones, have a major impact on the variation of wind field characteristics at the leeward of the straw checkboard barrier belt (Qu et al. 2007). The wind velocity on both sides of the straw checkboard barrier decreased and a formula was developed to estimate the straw checkboard barrier's lifetime (Bo et al. 2015).

The technology of computational fluid dynamics (CFD) has been widely employed to study the aerodynamics and

characteristics of porous media (Bitog et al. 2009, Jian et al. 2018). To simulate porous material in the CFD approach, an additional term is introduced to the momentum equation (Li et al. 2006, Yoshida 2006, Mochida et al. 2008). The result of an experiment and a CFD simulation of a porous fence with a well-fitting k-turbulence model (Santiago et al. 2007). Previous research has shown that CFD simulation can accurately predict flow characteristics near vegetation (Guo & Maghirang 2012).

The majority of previous researches focused on vegetation coverage and wind erosion control. However, few studies focused on recommending the plantation design of shrubs as a function of height, porosity, row spacing and a number of rows on wind erosion control. In this study, based on the threshold friction velocity, the shrub's downstream is divided into the first erosion zone, sedimentation zone and second erosion zone. The effect of shrub height, porosity, the number of rows and the shrub rows space on each zone were studied in details. The specific objective of this study is to determine the length of each zones as function of shrubs height, porosity. Thus, the best space between each rows of shrubs can be recommended for planting, which decrease the total number of shrubs, but at the same time increase sand controlling efficiency in desert regions.

Threshold Friction Velocity

Threshold friction velocity is the minimum friction velocity that lifts off the sand particles from the ground surface. It depends on soil properties such as soil texture, salt content, moisture content, and surface characteristics (Shao & Lu 2000). An empirical formula that describes a relationship between threshold friction velocity, friction velocity, and particles diameter was developed the formula is presented in equation (1) (Tsoar 1994).

$$u_{*_t} = A\sqrt{\frac{\rho_p - \rho}{\rho} gd} \qquad \dots (1)$$

Where u_{*_t} is the threshold friction velocity, A is a constant which is equal to 0.01, ρ_p is the density of sand, ρ is the density of air, and g is the gravitational acceleration.

The Bagnold formula is another name for the formula. It accurately predicts the friction velocity of particles larger than 0.1 mm. It is, however, unable of predicting the size of particles smaller than 0.075 mm. To address this deficiency, a formula was devised that took into account both cohesive force and aerodynamic lift, as shown in equation (2) (Thomas 1988).

$$u_{*_t} = A\sqrt{\sigma_p gd} F(R_{e_{*_t}}) G(D)\sqrt{b^2 - 4ac} \qquad \dots (2)$$

A, F and G are coefficients obtained from the wind tunnel; F is a function of the particles Reynold number at threshold friction velocity; whereas σ_p is the ratio of the densities of particles to the air.

As shown in Equation (3), a formula was developed that follows Bagnold's formula with an additional coefficient that incorporates sediment moisture in terms of cohesive force (Dong et al. 2007). It was estimated that the wind velocity for sand transportation in the desert region is 12 m.s⁻¹ (Wu & Zhang 2012).

$$u_{*_t} = 0.16\sqrt{\frac{\rho_p - \rho_a}{\rho_a} gd} (1 + 478.20w^{1.52}) \quad \dots (3)$$

Where, w is the moisture content.

MATERIALS AND METHODS

Numerical Simulation

Governing equation: The two-dimensional turbulent incompressible transient flow was modeled around the shrub. The mass and momentum equations are solved in form of the Reynolds Averaged Navier Stokes (RANS) equations which is given as:

$$\frac{\partial u_i}{\partial x_i} = 0 \qquad \dots (4)$$

$$\rho u_j \frac{\partial u_i}{\partial x_j} = -\frac{\partial p}{\partial x_i} + \frac{\partial}{\partial x_j}(\mu \frac{\partial u_i}{\partial x_j}) + S \qquad \dots (5)$$

An additional source term is added in the momentum equation to represent the porous medium's momentum sink. The additional source term (S_i) in the whole flow domain is set to zero, except inside the shrubs. The additional source term could be written as follows:

$$S_i = (\frac{\mu}{a}\upsilon + c_2 \frac{1}{2}\rho\upsilon^2) \qquad \dots (6)$$

Where C_2 is the inertial resistance; v is the magnitude of wind velocity; ρ is the density of air and α is the aerodynamic porosity. The first term in equation (6) can be ignored (Bitog et al. 2011). The second term is the inertial resistance for a porous media which can be defined as (Guo & Maghirang 2012):

$$c_2 = \frac{k_r}{w} \qquad \dots (7)$$

Where k_r is the drag coefficient and w is the width of shrubs.

Simulation Setup

The shrub's height ranges from 0.2 to 2 meters. The size of the computational domain was set to be 120H in length and 20H in height, where H is the shrub's height. The typical K-epsilon turbulence model was used, along with a wall function. The entrance velocity profile, which is the logarithmic profile specified in Equation, was used (8).

$$u_{in} = \frac{u_*}{k} \ln\left(\frac{z}{z_0}\right) \qquad \ldots (8)$$

Where u_{in} is the incoming flow velocity at height z (m.s^{-1}), where z is the height from the ground (m), K is the von Karman constant, and is friction velocity far upstream, which in this simulation 7 m.s^{-1} and 20 m.s^{-1} were applied.

Equations (9) and (10) were used to obtain the inlet's turbulent kinetic energy and turbulent dissipation rate.

$$\varepsilon_{in} = \frac{u_*^2}{kz} \qquad \ldots (9)$$

$$k_{in} = \frac{u_*^2}{\sqrt{c_u}} \qquad \ldots (10)$$

Where u_* is friction velocity far upstream.

Wind Tunnel Setup

The wind tunnel test was conducted to measure wind velocity at the downstream of Cedar shrub for obtaining its aerodynamic porosity, and at the same time validate the results of the CFD simulation. The experiment was carried out in Central South University's School of Civil Engineering's open circuit small wind tunnel laboratory.

Three Cedar shrubs with an average height of 20 cm, widths of 15 cm, 20 cm, and 15 cm from up to the downside of the shrub respectively, were distributed linearly in the wind tunnel.

A 2 cm thick Tongger desert sand was laid around the Cedar shrub in the test section of the wind tunnel. The sand bed surface was flattened using a steel ruler to make sure uneven surfaces were removed. The sand diameter used in this experiment varied from 0.5 mm to 1 mm. To evaluate the effect of different wind velocities on sand transportation, three different wind velocities 7 m.s^{-1}, 11.0 m.s^{-1}, and 20 m.s^{-1}, were applied. Then, sand transportation was observed around the single row of the shrubs. Fig. 1 shows the sand bed before the wind was blown.

RESULTS AND DISCUSSION

Wind Tunnel Measurement and Observation

The wind velocity at the downstream was measured using a hotwire anemometer. Cedar shrub's aerodynamic porosity; which is downstream over the upstream wind velocity, is calculated as shown in Fig. 3(a). Due to the acceleration of wind velocity between two columns of Cedar shrub, sand particles are transported through the gap between two-column of Cedar shrub downstream as shown in Fig. 2 (b). In this case, the incoming wind velocity was set to 11 m/s, which is below the threshold friction velocity for sand transportation.

Due to the Cedar shrub's presence, when sand particles collide with the shrubs, part of the sand particles rebound, and are deposited at the windward of the Cedar shrub, while the majority of particles pass over or through the shrubs. Fig. 2 (c) and (d) show the sand transportation at the windward, and leeward sides of the Cedar shrubs under 20 m.s^{-1} wind velocity. As shown in Fig. 2(c), sand particles were deposited on the windward side. However, sand particles at the leeward side were swept away to about a distance of 1.4 m. Also, from Fig. 2(d) it can be observed that sand particles at the leeward, 1.4 m away from the Cedar shrubs, began sedimentation. This can be attributed to the change of wind velocity at the leeward side of a porous shelterbelt.

Numerical Analysis

In this section, the results obtained from the CFD simulations in the previous section are discussed.

Shrub porosity: 7 m.s^{-1} wind velocity was employed to obtain the leeward wind velocity of Cedar shrub and compare it against the wind tunnel test data. For the rest of the simulation, 20 m.s^{-1} wind velocity was used.

Fig. 1: Sandbed in the wind tunnel test section.
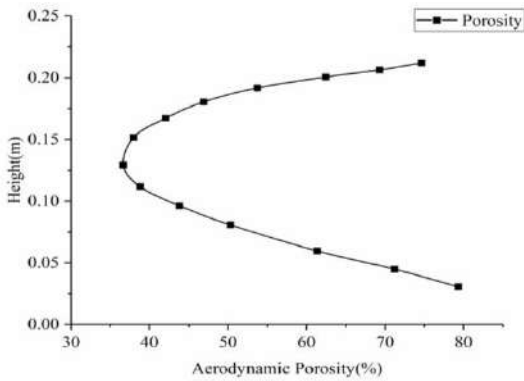
(a)

(b)

(c)

(d)

Fig. 2: (a) Aerodynamic porosity of Cedar shrub obtained in a wind tunnel (b) Sand transportation at leeward of Cedar shrub under 11 m.s⁻¹ (c) And (d) Show the sand transportation at the upstream, and downstream side of the Cedar shrub under 20 m/s wind velocity respectively.

The wind velocity at the leeward the surface is high as shown in Fig. 3(a), due to the high porosity at the bottom of Cedar shrub and low porosity at its middle. Also, the results obtained by CFD simulation, and wind tunnel measurement are virtually in good agreement. Fig. 3(b) shows that the wind velocity at a relative distance of 1.4 m, the wind velocity dropped to under 12 m.s⁻¹, which is the threshold friction velocity.

The wind velocity at the leeward gradually decreases, which reached its lowest value at a relative distance of 2 m. From a relative distance of 2 m to 3 m, the wind velocity is constant, and from a relative distance of 3 m above, the wind velocity began the recovery stage. Wind velocity at heights of 10 cm, and 18 cm share the same characteristics, which make a parabolic-shaped curve.

Fig. 3(b), Fig. 2(c), and (d) illustrate an appropriate correlation between near-surface wind velocity and
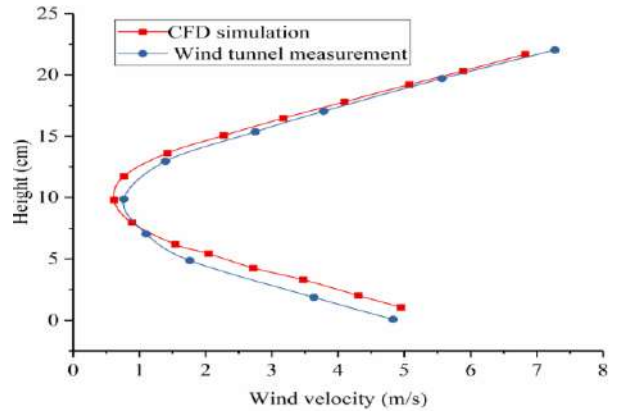
(a)
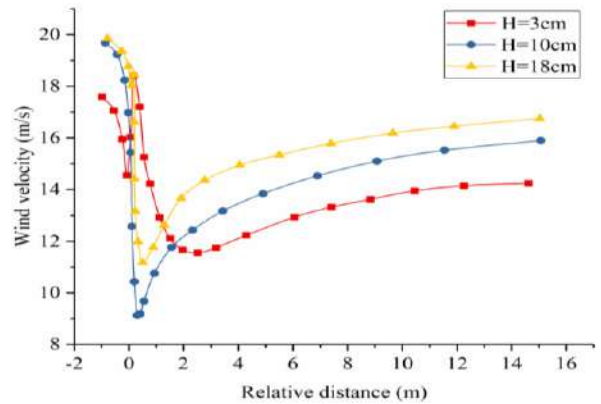
(b)

Fig. 3: (a) The vertical leeward wind velocity of Cedar shrub, x/h=0.5 (b) Horizontal wind velocity at three different heights from the ground surface.

Table 1: Erosion and sedimentation zones length for a 0.2 m high shrub.

Zone (m) Porosity (%)	L_e	L_a
60.0	Complete erosion zone	No sedimentation zone
50.0	Complete erosion zone	No sedimentation zone
40.0	1.4	2.7
30.0	0.8	5.0
15.0	0.6	6.0

sedimentation (Gao et al. 2004). Between relative distances 0 m and 1.4 m, the wind velocity exceeded the threshold friction velocity. Therefore, compared to Fig. 2(d), it can be seen that no sedimentation occurs at this distance. Consequently, using the characteristics of wind velocity is a proper method of evaluating sand transportation. Fig. 3(b) shows that the near-surface wind velocity at the downstream side can be divided into three zones: the first erosion zone L_e, sedimentation zone, and second erosion zone L_a. The length of these three zones depends on many factors such as incoming wind velocity, porosity, and height of the shrub. The three zones are illustrated in Fig. 4.

The first erosion zone is the distance where the wind velocity exceeds the threshold friction velocity. The sedimentation zone is the distance where the wind velocity is below threshold friction velocity.

It is essential to determine the length of the first erosion zone, and sedimentation zone as a function of shrub porosity. In Fig. 5, the grey color shows the sedimentation zone. As can be seen that the length of the first erosion zone increases with the decrease in porosity. When the porosity is beyond 40%, no sedimentation zone is generated.

The length of the first erosion zones for a shrub with 40%, 30%, and 15% porosity is 1.4 m, 0.8 m, and 0.6 m respectively. While the length of the sedimentation zones is 2.7 m, 5 m, and 6 m, respectively. Increasing the porosity decreases the length of the sedimentation zone.

Fig. 6(a) shows that shrub with low porosity has better wind velocity reduction where the first erosion zone is short, whereas the sedimentation zone is large.

Shrubs with porosity higher than 40% have wind velocity reduction; however, the wind velocity exceeds the threshold friction velocity. From Fig. 6(b) can be seen that the wind velocity at downstream near the surface is high. This is due to the high porosity of the shrub at the bottom and low porosity in the middle. Therefore, generally, because of this phenomenon, the first erosion zone occurs downstream. For cases in which the porosity of the shrub is less than 40 %, thus the sedimentation zone is generated.

Fig. 7(a), and (b) show shrub with 0.4 m height, 15%, 30%, and 40% porosity have 0.7 m, 0.9 m, 2 m first erosion zone length, while it has 14 m, 10 m, and 5 m sedimentation zone respectively. For this case, when the shrub porosity is beyond 40%, no sedimentation zone is generated, rather a

Fig. 4: Erosion zones and sedimentation zone.

complete erosion zone was observed. For the shrub with 0.6 m height and 15%, 30%, 40%, and 50% porosity, the length of the first erosion zones are 0.8 m, 1.4 m, 2.5 m, and 4 m, respectively whereas, the length of sedimentation zones is 25 m, 18.5 m, 11.5 m and 6 m. Also, in this case for a shrub with porosity greater than 50 %, no sedimentation zone exists and likewise, for the 2 m height shrub with porosity greater than 60 %, no sedimentation zone is generated.

There is no sedimentation zone when the porosity of the shrub is greater than 40% for shrubs of 0.2 m and 0.4 m in height. No sedimentation zone is created if the porosity of a shrub with a height of 0.6 m, 0.8 m, or 1.2 m exceeds 50%, and if the porosity of a shrub with a height of 2 m surpasses 60%. As a result of the increased porosity and height, the length of the initial erosion zone increases. The length of the sedimentation zone, on the other hand, increases as the height and porosity decrease.

Fig. 5: Erosion zone and sedimentation zones of a 20 cm height shrub:
(a) φ=15 %. (b) φ=30 %. (c) φ=40 %. (d) φ=50 %. (e) φ=60 %.
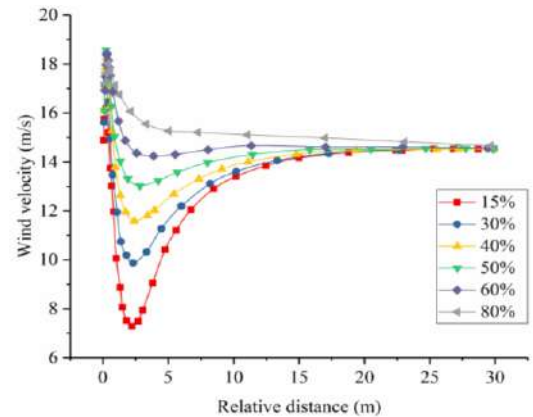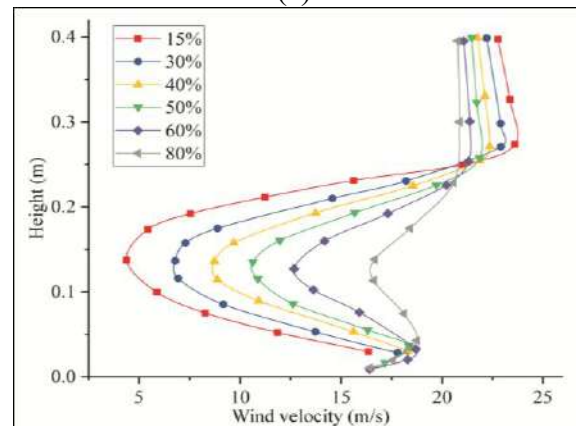
Fig. 6: (a) Horizontal wind velocity at height $y = 0.03$ m and (b) Vertical wind velocity at relative distance $x = 0.1$ m.

Shrub height: The shrub's height is one of the most critical factors that affect the characteristics of wind patterns at the leeward. The model with geodesic dome-shaped, and six different heights was simulated. Fig. 9 and 10 show plots of leeward vertical and horizontal wind velocity at x = 0.1 m, and y = 0.03 m, respectively. The wind velocity at the near ground surface decreases less, which is due to the high porosity of the shrub at the bottom. The biggest reduction in wind velocity happens near the middle of the shrub, though. As shown in Fig. 10, the highest horizontal wind velocity reduction for all porosity situations near the surface occurs at roughly 10h.

From Table 4, can be observed that by increasing shrub height, the length of the first erosion zone enlarges, and the

length of the sedimentation zone also significantly enlarges. As the shrub porosity exceeds 50 % for a shrub with 0.2 m and 0.4 m height, a full erosion phenomenon occurs with no sedimentation zone. If the porosity exceeds 60% for shrubs shorter than 2 m, no sedimentation zone is generated. A shrub with 60% porosity and 2 m height has an 18 m sedimentation zone, while for a shorter shrub for the mentioned porosity, no sedimentation zone is generated (Fig.8).

Effect of rows number and space: Generally, shrubs with high porosity have a lesser effect on wind velocity reduction. 0.4 m high shrub with 70 %, and 80 % porosity with the different number of rows and rows spacing were simulated. First, the distance between single, double, triple, and four rows was set at 0.4 m. After evaluating wind velocity
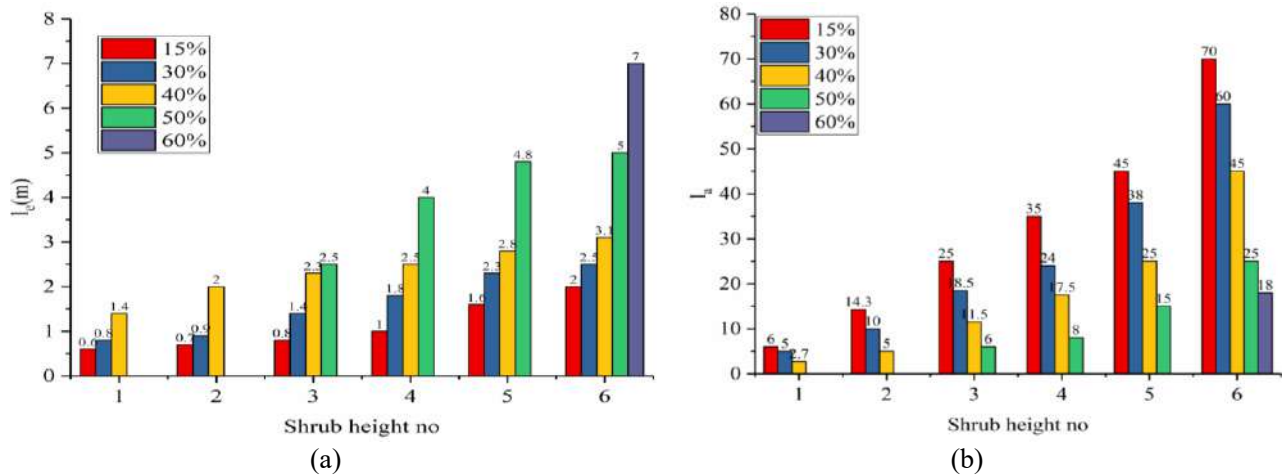
Fig. 7: L_e and L_a (a) Shrub porosity and first erosion zone length (b) Shrub porosity and sedimentation zone length (m).
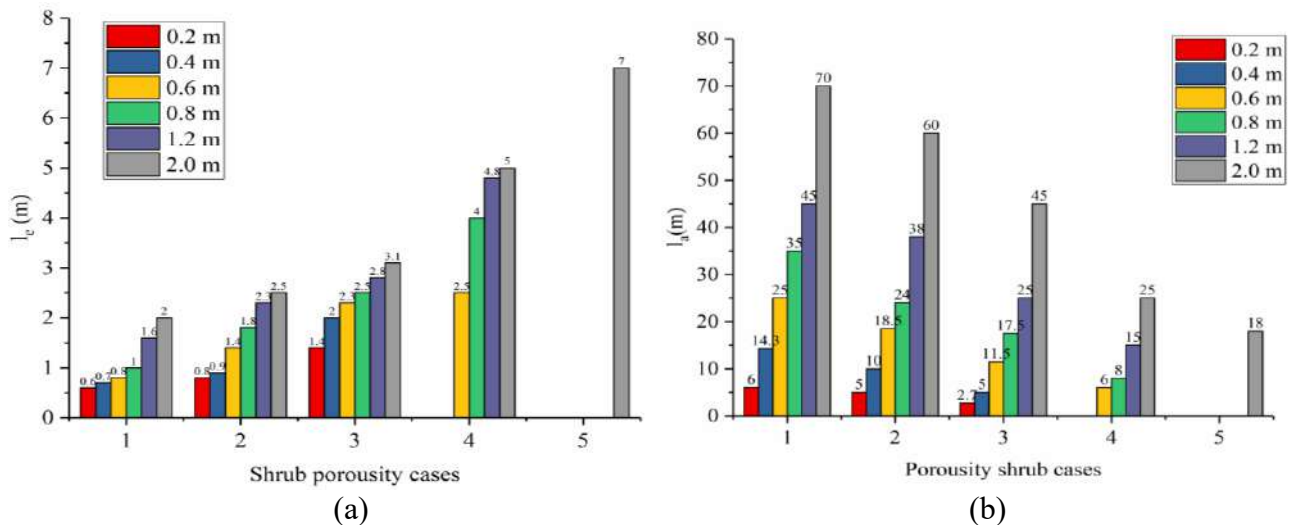
Fig. 8: (a) Shrub height and I erosion zone length l_e (b) Shrub height and sedimentation zone length (m).

Table 2: Shrub height with the corresponding number for Fig. 7.

Case number	1	2	3	4	5	6
Shrub height	0.2	0.4	0.6	0.8	1.3	2

Table 3: Shrub porosity with the corresponding number for Fig. 8.

Case number	1	2	3	4	5
Porosity %	15	30	40	50	60
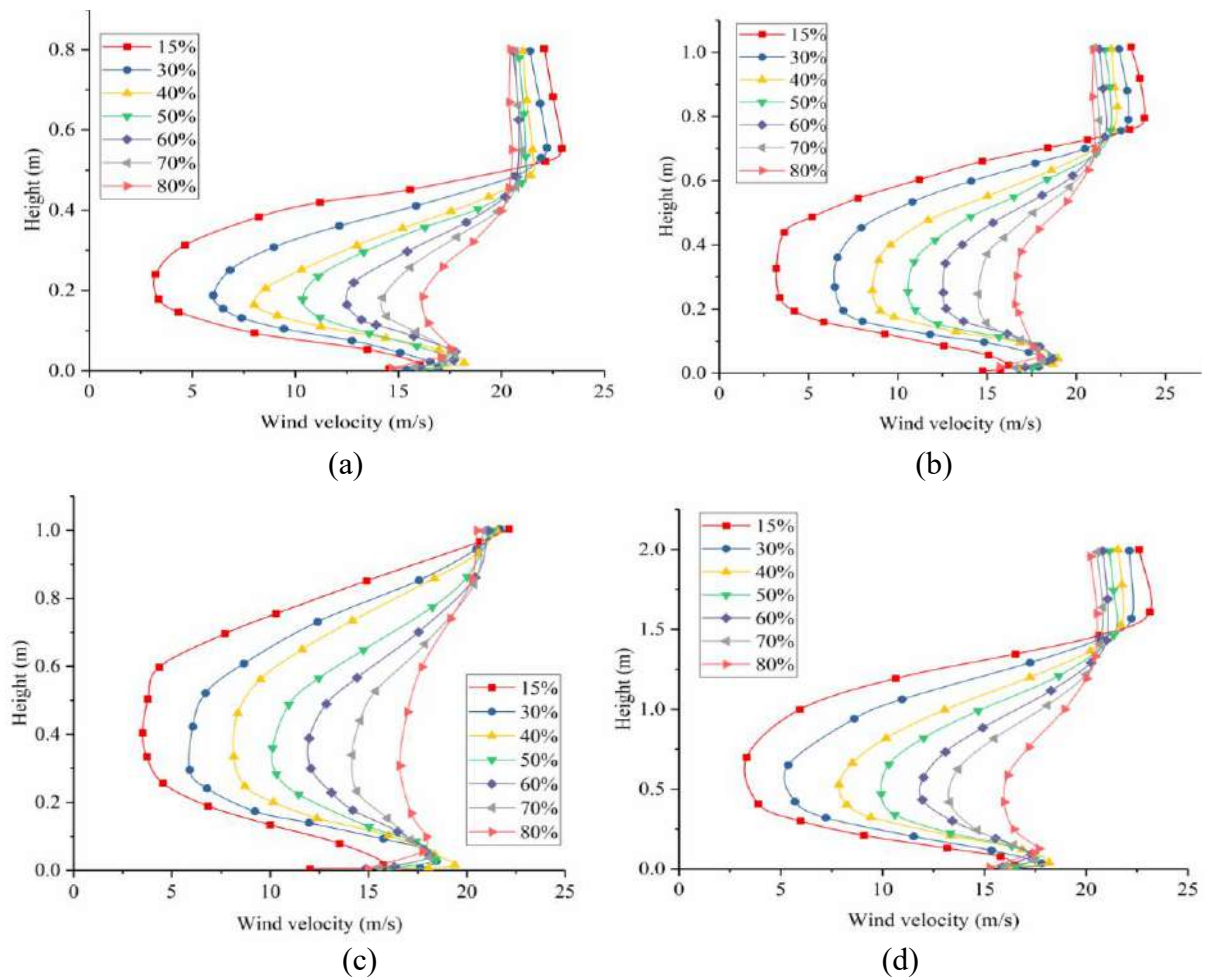
Fig. 9: Vertical wind velocity at x =0.1 m (a) Shrub height 0.4 m (b) Shrub height 0.6 m (c) Shrub height 0.8 m (d) Shrub height 1.2 m.

downstream of the fourth row, a fifth row was added at a distance of 5 m. Although, double and triple rows of shrub with 80 % porosity resulted in 30 % and 40 % wind velocity reduction (Fig.11). However, the wind velocity exceeds the threshold friction velocity of desert regions. The four rows of shrubs with 80 % porosity consequently resulted in a 50 % wind velocity reduction. Therefore, the sedimentation zone is generated from a relative distance of 3 m from the first row of the shrub. The length of the sedimentation zone at the downstream of the fourth row is 5 m. Hence, the fifth row of the shrub plant is at a distance of 5 m away from the fourth row. No erosion zone is generated the downstream of fifth rows, and the length of the sedimentation zone the downstream of fifth rows is 5 m. therefore, the remaining rows of shrub plants with a distance of 5 m away from each other.
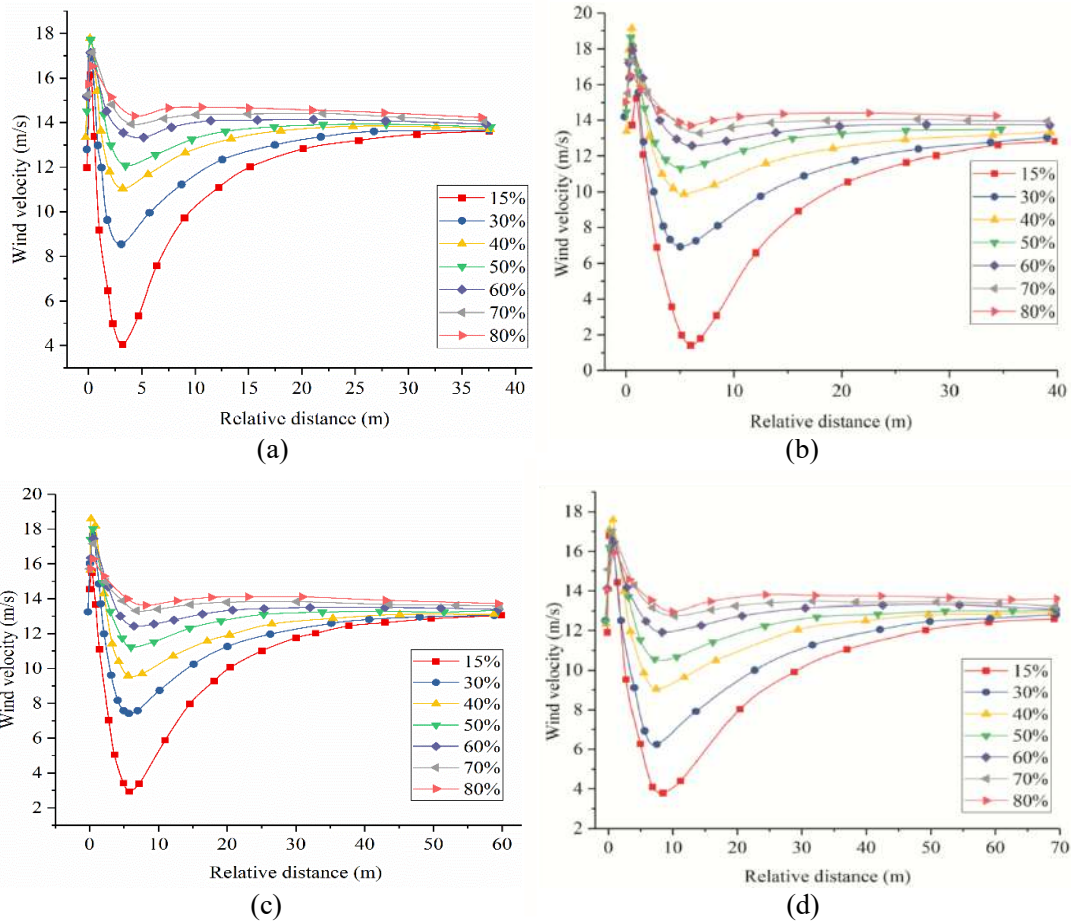
Fig. 10: Horizontal wind velocity at y=0.03 m (a) Horizontal wind velocity of shrub with 0.4 m height (b) Horizontal wind velocity of shrub with 0.6 m height (c) Horizontal wind velocity of shrub with 0.8 m height (d) Horizontal wind velocity of shrub with 1.2 m height.

From Fig. 12, can be observed that when the porosity of shrubs is 70 %, the single and double rows of shrub have wind velocity reduction. However, no sedimentation zone is generated. When the third row of shrub with 70 % porosity is added, a sedimentation zone is generated from a relative distance of 3 m from the first row with a sedimentation length zone of 5 m. Thus, it is recommended to plant the fourth row of the shrub at a distance of 5 m away from the third row.

CONCLUSION

Based on the wind tunnel measurement, and CFD simulations, the aerodynamic behavior of shrubs with different porosity, and height were studied. The downstream of shrubs were divided into three zones; the first erosion zone, the sedimentation zone, and the second erosion zone. In this study, the length of the first erosion and sedimentation zones were investigated in detail as a function of height, porosity, the number of shrub rows, and rows space.
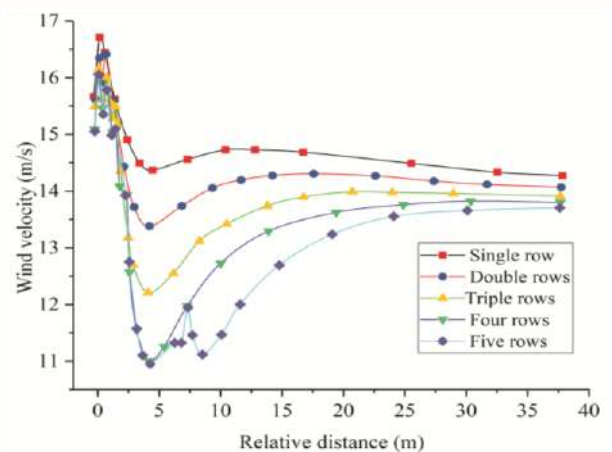
Fig. 11: Rows of shrub with 80% porosity.

The results showed that the porosity of shrubs had a significant influence on the erosion and sedimentation zones.

Table 4: Relationship between porosity, height, and first erosion zone and sediment zone length (m).

Shrub height(m)	0.2		0.4		0.6		0.8		1.2		2	
Porosity \ Zone (m)	L_a	L_e	L_a	L_e	L_a	L_e	L_a	L_e	L_a	L_e	L_a	L_e
80 %	No	yes	No	yes	No	yes	No	yes	No	yes	No	yes
70 %	No	yes	No	yes	No	yes	No	yes	No	yes	No	yes
60 %	No	yes	No	yes	No	yes	No	yes	No	yes	18	7
50 %	No	yes	No	yes	6	2.5	8	4	15	4.8	25	5
40 %	2.7	1.4	5	2	11.5	2.3	17.5	2.5	25	2.8	45	3.1
30 %	5	0.8	10	0.9	18.5	1.4	24	1.8	38	2.3	60	2.5
15 %	6	0.6	14.3	0.7	25	0.8	35	1	45	1.6	70	2

A low porous shrub had a better shelterbelt effect. With the increase in porosity, the erosion zone length increased; in contrast, the sedimentation zone length decreased. For a 20 m.s^{-1} incoming critical wind velocity, if the porosity of a single row of shrub exceeded 40 %, then no sedimentation zone was generated.

Shrub height is also the main factor for wind erosion control. With the increase in shrub height, the first erosion and length of sedimentation zones also increased. Multi rows of shrubs have a better shelterbelt effect on wind erosion control, for instance, shrubs with 0.4 m height, 0.4 m rows space, and 80 % porosity, four rows of shrubs were needed to generate a sedimentation zone, which makes a 5 m long shelterbelt. In this case, the space between the remaining shrubs ' rows could be chosen as 5 m. While for a 0.4 m height shrub with 70 % porosity, three rows of shrubs were needed to make a 5 m long shelterbelt, and the distance between the remaining rows of shrubs could be chosen as 5 m. Hence, to make a better shelter zone, it is recommended to plant denser shrubs rows at upstream and sparsely shrubs rows at far downstream.

Fig. 12: Rows of shrub with 70% porosity.

REFERENCES

Ash, J. and Wasson, R. 1983. Vegetation and sand mobility in the Australian desert dunefield. Zeitschrift fur Geomorphol., 45(Supp.): 7-25.

Bitog, J., Lee, I., Hwang, H., Shin, M., Hong, S., Seo, I., Mostafa, E. and Pang, Z. 2011. A wind tunnel study on aerodynamic porosity and windbreak drag. Forest Sci. Technol., 7(1): 8-16.

Bitog, J., Lee, I., Shin, M., Hong, S., Hwang, H., Seo, I., Yoo, J., Kwon, K., Kim, Y. and Han, J. 2009. Numerical simulation of an array of fences in Saemangeum reclaimed land. Atmos. Environ., 43(30): 4612-4621.

Bo, T., Ma, P. and Zheng, X. 2015. Numerical study on the effect of semi-buried straw checkerboard sand barriers belt on the wind speed. Aeol. Res., 16: 101-107.

Cheng, J., Xin, G., Zhi, L. and Jiang, F. 2017. Unloading characteristics of sand-drift in wind-shallow areas along the railway and the effect of sand removal by force of the wind. Sci. Rep., 7(1): 1-11.

Cornelis, W. and Gabriels, D. 2005. Optimal windbreak design for wind-erosion control. J. Arid Environ., 61(2): 315-332.

Dong, Z., Mu, Q. and Liu, X. 2007. Defining the threshold wind velocity for moistened sediments. J. Geophys. Res. Solid Earth, 112(B8): 651.

Gao, Y., Qiu, G., Ding, G., Hideyuki, S., Yi, Y., Hu, C., Liu, Y., Tobe, K., Wang, Y. and Wang, J. 2004. Effect of Salix psammophila checkerboard on reducing wind and stabilizing sand. J. Desert Res., 24(3): 365-370.

Griffin, D.W., Kellogg, C.A. and Shinn, E.A. 2001. Dust in the wind: long-range transport of dust in the atmosphere and its implications for global public and ecosystem health. Glob. Change Human Health, 2(1): 20-33.

Guo, L. and Maghirang, R.G. 2012. Numerical simulation of airflow and particle collection by vegetative barriers. Eng. Appl. Computat. Fluid Mech., 6(1): 110-122.

Hong, C., Chenchen, L., Xueyong, Z., Huiru, L., Liqiang, K., Bo, L. and Jifeng, L. 2020. Wind erosion rate for vegetated soil cover: A prediction model based on surface shear strength. Catena, 187: 104398.

Jian, Z., Bo, L. and Mingyue, W. 2018. Study on windbreak performance of tree canopy by numerical simulation method. J. Computat. Multiphase Flows, 10(4): 259-265.

Li, L., Li, X., Lin, B. and Zhu, Y. 2006. Simulation of canopy flows using k-epsilon two-equation turbulence model with source/sink terms. J. Tsinghua Univ., 46(6): 753.

Liu, C., Zheng, Z., Cheng, H. and Zou, X. 2018. Airflow around single and multiple plants. Agric. Forest Meteorol., 252: 27-38.

Lv, P. and Dong, Z. 2012. Study of the windbreak effect of shrubs as a function of shrub cover and height. Environ. Earth Sci., 66(7): 1791-1795.

Mochida, A., Tabata, Y., Iwata, T. and Yoshino, H. 2008. Examining tree canopy models for CFD prediction of wind environment at pedestrian level. J. Wind Eng. Indust. Aerodyn., 96(10-11): 1667-1677.

Prospero, J.M. 1999. Assessing the impact of advected African dust on air quality and health in the eastern United States. Human Ecol. Risk Assess. Int. J., 5(3): 471-479.

Qiu, G.Y., Lee, I., Shimizu, H., Gao, Y. and Ding, G. 2004. Principles of dune fixation with straw checkerboard technology and its effects on the environment. J. Arid Environ., 56(3): 449-464.

Qu, J., Zu, R., Zhang, K. and Fang, H. 2007. Field observations on the protective effect of semi-buried checkerboard sand barriers. Geomorphology, 88(1-2): 193-200.

Rosenfeld, M., Marom, G. and Bitan, A. 2010. Numerical simulation of the airflow across trees in a windbreak. Bound. Layer Meteorol., 135(1): 89-107.

Santiago, J., Martin, F., Cuerva, A., Bezdenejnykh, N. and Sanz Andrés, A. 2007. Experimental and numerical study of wind flow behind windbreaks. Atmos. Environ., 41(30): 6406-6420.

Sarkar, S., Chauhan, A., Kumar, R. and Singh, R.P. 2019. Impact of deadly dust storms (May 2018) on air quality, meteorological, and atmospheric parameters over the northern parts of India. GeoHealth, 3(3): 67-80.

Shao, Y. and Lu, H. 2000. A simple expression for wind erosion threshold friction velocity. J. Geophys. Res. Atmos., 105(D17): 22437-22443.

Station, S.D.R. 1986. The principles and measures are taken to stabilize shifting sands along the railway line in the southeastern edge of the Tengger Desert. J. Desert Res., 6(3): 1-19.

Thomas, D. 1988. The wind is a geological process on Earth, Mars, Venus, and Titan. J. Arid Environ., 15(2): 217-218.

Tsoar, H. 1994. Bagnold: The physics of blown sand and desert dunes. Prog. Phys. Geogr., 18(1): 91-96.

Wu, F. and Zhang, H. (ed.) 2012. Turang Qinshi Xue. Science Press, Beijing, China

Xu, L. 1996. Sand fixation project with forest sand barrier and its ecological benefit. J. Desert Res., 6: 11-21.

Yao, Z., Xiao, J. and Jiang, F. 2012. Characteristics of daily extreme-wind gusts along the Lanxin Railway in Xinjiang, China. Aeol. Res., 6: 31-40.

Yoshida, S. 2006. Development of Three Dimensional Plant Canopy Model for Numerical Simulation of Outdoor Thermal Environment. The 6th International Conference on Urban Climate, 2006, 12-16 July, 2006, Goteborg, Sweden.

Zhang, X. 1994. Principles and Optimal Models for Development of Maowusu Sandy Crassland. Chinese J. Plant Ecol., 18(1): 1-16.

Comparison of Two Versions of SWAT Models in Predicting the Streamflow in the Xuanmiaoguan Reservoir Catchment

Huijuan Bo*(**), Xiaohua Dong*(**)†, Zhonghua Li*, Gebrehiwet Reta*(**), Lu li*(**) and Chong Wei*(**)**
*China Three Gorges University, College of Hydraulic and Environmental Engineering, Yichang, 443002, China
**Hubei Provincial Collaborative Innovation Center for Water Security, Wuhan, 430070, China
***Comprehensive Law Enforcement Bureau for Protection of Water Resources in the Huangbaihe River Basin, Yichang, Hubei, 443005, China
†Corresponding author: Xiaohua Dong; xhdong@ctgu.edu.cn

ABSTRACT

Correct streamflow prediction is critical for determining the availability and efficiency of watershed spatial plans and water resource management. In the Xuanmiaoguan (XMG) Reservoir Catchment, two different versions of the Soil and Water Assessment Tool (SWAT) model are compared to discharge predictions. One version is the Topo-SWAT, in which the overland flow is generated by saturation excess (Dunne) runoff mechanism, while the other is driven by infiltration excess runoff mechanism, i.e., the Regular-SWAT. These SWAT models were calibrated and validated with discharge at daily and monthly steps, and then, the annual runoff volume and spatial distribution of runoff generation areas were also discussed. At the monthly scale, the un-calibrated Topo-SWAT model outperformed the un-calibrated Regular-SWAT model throughout the whole time (2010-2016). The Nash-Sutcliffe efficiency coefficients (NSE) using Topo-SWAT and Regular-SWAT were 0.59, 0.58 for calibration and 0.69, 0.72 for validation for daily streamflow, and 0.69, 0.65 for calibration and 0.73, 0.88 for validation for monthly streamflow, respectively, based on the parameter sensitivity analysis results. There was a 5-year understatement for yearly runoff volume using Regular-SWAT, but a 4-year underestimation using Topo-SWAT, which had a different year in 2015. Regular-SWAT and Topo-SWAT have significantly different geographical distributions of runoff generating locations within the watershed for one occurrence (greater rainfall). The findings reveal the most accurate contributing regions for runoff generation in the research catchment, allowing for more effective implementation of best management techniques (BMPs).

INTRODUCTION

The location of frequently-generated overland runoff areas, (i.e., hydrologically sensitive areas), is important to select to implement best management practices (BMPs) to cut down on non-point source (NPS) pollution (Gerard-Marchant et al. 2006). Because streamflow is the primary transporter of nutrients into the water, runoff-producing sites could be considered critical source areas (CSAs) for nutrient loss (where higher potential nutrient loss corresponds to higher runoff loss) (White et al. 2009). Hydrological models are vital and effective instruments for locating HSAs and CSAs, and they are increasingly employed in soil and water management, as well as pollution control. The models may reduce the cost of implementing and evaluating management methods, hence reducing waste and unwanted results (Golmohammadi et al. 2017).

The SWAT model (Arnold et al. 1998), one commonly used semi-distributed model, is utilized to estimate basin hydrological cycle and quantify nutrient movement, trans-

formation, and loads in a huge number of watersheds around the world (Gan et al. 2015). Green-Ampt infiltration mechanism (G&A) and curve number (CN) procedures are two rainfall-runoff methodologies for estimating overland flow. They're also both founded on the infiltration excess principle, which states that overland runoff occurs when precipitation density exceeds soil infiltration capacity. They do not, however, account for runoff source areas or topographic effects. According to a prior study (Dahlke et al. 2012), in many humid and well-vegetated places, overland flows originate in a small part of the basin and then expand as precipitation increases, forming variable source areas (VSAs) (Lyon et al. 2004) driven by saturation excess runoff. Because the genesis of runoff in a region is such a complicated process with spatial and temporal fluctuations, neither saturation excess (Dunne) nor infiltration excess (Horton) runoff could account for hydrological processes. Beven and Kirkby (1979) simulated the runoff variations using a soil topographic index referred to as a saturation excess runoff mechanism. But, in flat watersheds, the topographic index is not appropriate

since the runoff directions are undefined. Steenhuis et al. (1995) suggested reinterpreting the CN approach to determine the proportion of runoff generation in a watershed for a rainfall event and (Easton et al. 2008) later incorporated the soil topographic index into SWAT to better account for saturation excess runoff. Then Fuka & Easton (2015) re-conceptualized SWAT (Topo-SWAT) which did not change the SWAT code.

Huangbaihe River, which is a first-order tributary of the Yangtze River, is a primary water source for Yichang city, so the accurate prediction of streamflow is primarily important. The XMG Reservoir, the headwater of the Huangbaihe River Basin, is witnessed a large amount of precipitation and has a humid subtropical monsoon climate. The study area is made up of hillslopes and valleys where overland runoff flows from up to downslope, allowing groundwater and soil saturation to occur, which is compatible with the saturation excess runoff mechanism. The geology and land cover have also been altered as a result of large-scale phosphate mining. Because of the flow routes altered by surface subsidence and fissures produced over goaves, phosphate mining activities may have an impact on hydrological processes (mined-out areas). When the soil water content is exceeded during rainfall, the XMG Reservoir Catchment witnesses variable source areas (VSAs) where overland runoff should be generated (Woodbury et al. 2014, Needelman et al. 2004). To the best of the author's knowledge, the implementation of the Topo-SWAT model in China is rarely recorded, and no similar studies in the XMG Reservoir Catchment have been described previously in the literature.

Therefore, the major objective of this paper is to compare two versions of SWAT models and then to assess each ability for simulating the hydrological processes in the XMG Reservoir Catchment, i.e., Regular-SWAT and Topo-SWAT. The performance was assessed adequately for predicting streamflow at daily and monthly time intervals and identifying the spatial distribution of runoff generation.

MATERIALS AND METHODS

Site Description

The Xuanmiaoguan (XMG) Reservoir Catchment is situated in the headwater of the east branch of Huangbaihe River, which is between 110°08′ and 111°30′ E longitude and 30°42′ and 31°22′ N latitude (Fig. 1). The elevation is from 444 m at the XMG Reservoir dam to 1781 m at the headstream above average sea level. The XMG Reservoir Catchment has an area of 380 km². The climate belongs to a humid subtropical monsoon region with a mean annual precipitation of 1101 mm. Meanwhile, in this catchment, the rainy season could extend from May to October, with heavy rainfall in summer. The average annual temperature is approximately 16.9 °C. The land cover types are forest, agriculture field, water, bare land, and urban, in which forest and agriculture field are the main land-use types. The soil types are Haplic Luvisols (LVh1, LVh3, and LVh3) for the Regular-SWAT model, Lithosols and Chromic Cambisols (LCC), and Lithosols and Eutric Cambisols (LEC) for Topo-SWAT model. Over the past 40 years, the study catchment has experienced industrialization and rapid economic growth, resulting in serious soil erosion
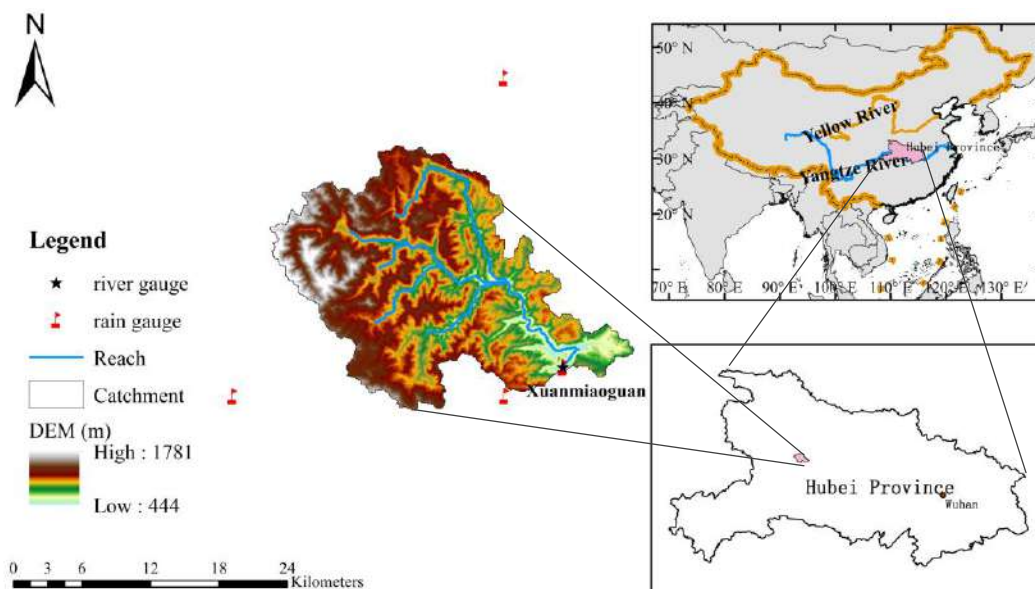
Fig. 1: Map of the Xuanmiaoguan (XMG) reservoir catchment showing the DEM, rivers, and location of observed discharge station.

and nutrient loss. Hence, it is an important region for the research of understanding and predicting the hydrological processes, and identifying the runoff generation areas.

Description of SWAT Model

The SWAT is a watershed-scale, continuous-time, and semi-distributed hydrological model, which incorporates meteorological elements, soil characteristics, land cover/use, and management practices to predict streamflow, sediments, nutrient loading, pesticide transport, and so on (Arnold et al. 1998). It allows the simulation of spatial details according to dividing the whole watershed into a series of sub-watersheds; then each sub-watershed is composed of hydrologic response units (HRUs), which represent homogenous soils properties, land cover, and slopes. Surface runoff, soil water, nutrient cycles, sediment, and crop yields are calculated in each HRU (i.e., the smallest element), and afterward lumped to the sub-catchment using the weighted mean method, last routed into the river systems. There are four water storages including surface runoff, soil water, shallow, and deep aquifer. The SWAT model assumes that shallow groundwater can run into the river channel as base flow or return to the soil by evaporation, but flow in deep aquifer leaves the watershed system. Details about the SWAT model are given in (Neitsch et al. 2011) and http://swatmodel.tamu.edu.

Regular-SWAT

Within regular-SWAT, two methods are applied to calculate the overland flow, such as the curve number procedure (CN) and G&A approach, in which the G&A method is not adopted due to there being any sub-daily input data.

The CN equation was estimated as (USDA-SCS, 1972).

$$Q = Pe^2 / (Pe + S) \quad \text{for } Pe > Ia \quad \text{...(1)}$$

where Q is the streamflow depth (mm/d), Pe is effective rainfall (mm.d^{-1}), i.e., rainfall minus initial abstraction (Ia), S is the overall soil water-storage capacity (mm) which is calculated according to the soil type:

$$S = 25.4(\frac{1000}{CN} - 10) \quad \text{...(2)}$$

where CN is the curve number and could be adjusted by the antecedent soil moisture content using daily rainfall series.

Topo-SWAT

In humid regions, overland runoff is mainly produced by the saturation excess runoff mechanism. So, the Topo-SWAT provides the CN-VSA method to estimate overland flow and

redefine the HRUs. In Regular-SWAT, HRUs are composed of homogeneous vegetation, soil characteristics, and slope classes, whereas in Topo-SWAT, soil topographic index (TI) was combined to define the HRUs, which has been seamlessly integrated into SWAT representing the VSA hydrology and can be derived from digital elevation model (DEM). TI estimates runoff based on the digital elevation and topography data (Suliman et al. 2015). And the equation can be obtained (Easton et al. 2008):

$$TI = \ln(\frac{\alpha}{\tan \beta}) \quad \text{...(3)}$$

where a is the upslope contributing area of a given point (m), $\tan \beta$ is the slope gradient.

The TI layer, representing VSA hydrology in Topo-SWAT, is calculated applying the DEM and ArcGIS hydrology tools. And then it is reclassified to generate a new class layer, i.e., ten wetness index classes with equal area. They range from one wetness class (10% of the catchment with the lowest potential of runoff generation) to ten classes (10% of the catchment with the highest potential of runoff generation). For this study, we applied the Topo-SWAT toolbox (Fuka & Easton 2015), an automated ESRI ArcMap toolbox, to create a new substitute wetness class layer to cover the Digital Soil Map of the World (FAO 2007). Furthermore, we create as well as its lookup tables (Collick et al. 2014).

Input Data

To derive the SWAT model, a large number of input data would be required, including temporal (hydrometeorology data) and spatial data (soil characteristics, land use, and topographic data).

Temporal data

Hydrological Data: Daily streamflow series data for the XMG Reservoir dam gauge station in the study catchment were collected from the Huangbaihe Catchment Authority.

Weather Data: Daily rainfall series, temperature, wind speed, relative humidity, and solar radiation were all needed. The measured records for daily rainfall data from the outlet station were available for different periods spanning from 2008 to 2016 and could be used directly. Other precipitation datasets were obtained from CMADS 1.1 (The China Meteorological Assimilation Driving Datasets for the SWAT model) (http://westdc.westgis.ac.cn/). The other meteorological elements were generated using SWAT's weather generator (WGEN). Weather stations w3231134 and w3261138 (https://globalweather.tamu.edu/) were included to calculate the statistical parameters of WGEN for the study catchment.

Spatial data

DEM Data: The Digital Elevation Model (DEM) map of the XMG Reservoir Catchment was collected from the Geospatial Data Cloud website (http://srtm.csi.cgiar.org/), with a spatial resolution of 3 arc-second (roughly 90 m).

Soil Data: In this study, two soil maps were used including the Harmonized World Soil Database (HWSD) version 1. 1 (http://westdc.westgis.ac.cn/data/tag/key/HWSD) and FAO-UNESCO Digital Soil Map of the World (DSMW) (http://www.fao.org/geonetwork). HWSD is used for Regular-SWAT setup (Fig. 2(a)), with a 1km resolution and associated lookup table was obtained for the initialization of Regular-SWAT. Three soil groups were identified for the delineation in the XMG Reservoir Catchment. For Topo-SWAT, DSMW combined with soil topographic wetness classes was adopted to generate the soil map.

Land Cover/ Land Use Data: This map was downloaded from 2015 LANDSAT data and then reclassified using supervised image classification. There are five different land use detected with its lookup table to match the land use database of SWAT model, i.e., agricultural field (AGRL for SWAT), forest (FRST), bare land (BARR), urban (URBN), and water (WATR).

Model Setup, Calibration and Validation

The study area was first separated into multiple sub-catchments, which described spatially correlation between one and another. The boundary of the study catchment was delineated applying a threshold area of 1400 ha so that the extracted river networks keep consistent with the topographic map. And 9 sub-catchments were delineated for both two versions of SWAT. All layers were projected in the "WGS_1984_UTM_Zone_49N" coordinate system. And soil types and land use were linked with their lookup tables, space databases, and attribute databases. Through reclassifying the layers of soil types, land cover/use, and slope classes, the sub-catchment layer was overlaid to the HRUs layer. The threshold percentage (0%) was adopted for the whole of the databases. But due to the different types in soils (Fig. 2), the numbers of the HRUs are 250, 173, and 404 for the Regular-SWATH, Regular-SWATD, and Topo-SWAT, respectively (Table 1).

Parameters sensitivity analysis is also a major concern to model calibration and validation (Cibin et al. 2010). Therefore, the calibrated parameters were selected by referring to previous literature, recommendations from the SWAT manuals (Stehr et al. 2010). The method of sequential uncertainty fitting Version 2 (SUFI-2) algorithm (Yang et al. 2008) incorporated into SWAT Calibration Uncertainty Procedure (SWAT-CUP) program (Abbaspour 2015) was adopted for parameter sensitivity analysis, model calibration, and validation procedure.

Table 1: Differences in total HRUs for the three SWAT models.

	Regular-SWATH	Regular-SWATD	Topo-SWAT
Number of soil types	3	2	20
Number of slope classes	4	4	1
Number of HRUs	250	173	404
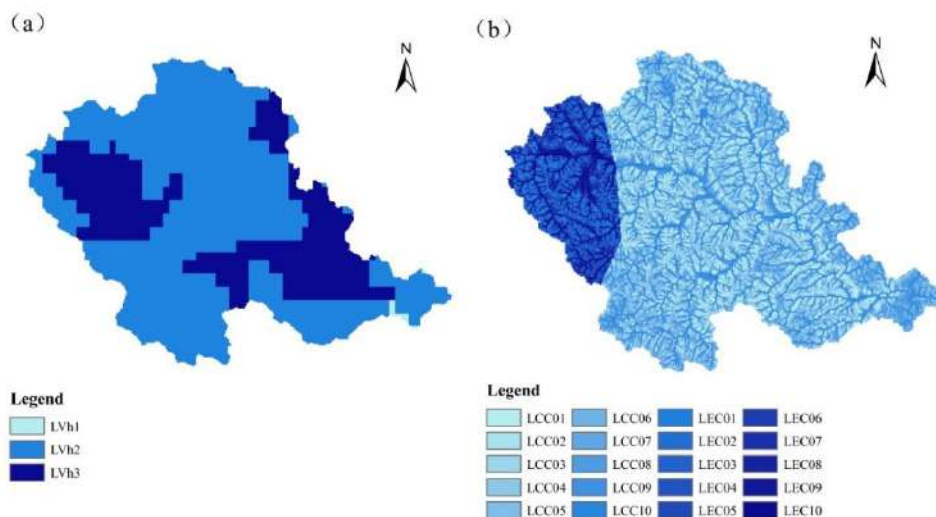
Fig. 2: Soil maps of the XMG Reservoir Catchment (a) Regular-SWAT and (c) Topo-SWAT.

Based on data availability, the two models in this study were calibrated for streamflow at monthly and daily time scales for the period 2010-2013 after two years of warm-up, which is to allow parameters to reach equilibrium. The following three years, from 2014 to 2016, were used to validate models. Nash Sutcliffe coefficient of Efficiency (NSE) was selected as the objective function, due to it can reflect the overall model fit (Nash & Sutcliffe 1970). The following parameters were identified for Regular-SWAT and Topo-SWAT (Table 2).

Performance Evaluation

Both graphical and statistical approaches should be applied to evaluate the model performance (Nyeko 2015). The graphical method, such as streamflow hydrographs, can provide a visual and direct comparison between the observed and simulated datasets, which could detect the trends of variation in magnitude and timing of the flows. Besides the graphical approach, the agreement between simulated and observed data was also evaluated based on statistical indicators, including the NSE coefficient, the RMSE-observations standard deviation ratio (RSR), and percent bias (PBIAS). The performance of the model for flows was divided into four categories at monthly and daily time scales based on the research of (Moriasi et al. 2007).

RESULTS

Simulation Using the Un-Calibrated Models

Two different versions of SWAT models were established and then compared with each other based on the initial parameters. Fig. 3 graphically displays the results for total monthly streamflow using both un-calibrated SWAT models. In dry months like November 2012 to February 2013, and November 2015 to February 2016, both models overestimated base flow. Except for 2016, Topo-SWAT overestimated peak flow rate the most, whilst Regular-SWAT underestimated. The model comparison statistics values with original findings parameter analysis were presented in Table 3. For the calibration period (from 2010 to 2013), the flow output simulated by Topo-SWAT has higher NSE and PBIAS than the Regular-SWAT flow outputs, but for the validation period (2014-2016), the NSE value of Regular-SWAT is higher. In general, the initial parameter result showed that Topo-SWAT (saturation excess) has better output finding than Regular-SWAT (infiltration excess) in the entire study

Table 2: Parameters sensitivities and calibrated parameters of Regular-SWAT and Topo-SWAT using SUFI-2.

Regular-SWAT					Topo-SWAT				
Parameters	Parameter sensitivity			Optimal value	Parameters	Parameter sensitivity			Optimal value
	t-Stat	p-value	Ranking value			t-Stat	p-value	Ranking value	
r_SOL_AWC.sol	-23.4	0	1	-0.16	r_CN2.mgt	11.6	0	1	-0.23
r_CN2.mgt	19.36	0	2	0.31	r_SOL_AWC.sol	-4.8	0	2	-0.34
v_CANMX.hru	-12.69	0	3	3.91	v_ALPHA_BF.gw	3.96	0	3	0.47
v_ALPHA_BF.gw	8.63	0	4	0.94	v_CANMX.hru	-3.63	0	4	5.35
v_ESCO.hru	6.48	0	5	0.32	v_SLSUBBSN.hru	-2.61	0	5	35.85
v_HRU_SLP.hru	5.25	0	6	0.25	v_SMTMP.bsn	-2.33	0.02	6	10.45
v_SLSUBBSN.hru	-4.65	0	7	110.84	v_ESCO.hru	2.26	0.024	7	0.99
r_SOL_Z.sol	-4.38	0	8	-0.83	v_CH_N2.rte	-2.05	0.04	8	0.03
v_RCHRG_DP.gw	3.97	0	9	0.74	r_SOL_Z.sol	-1.61	0.107	9	-0.21
v_CH_K2.rte	-3.88	0	10	64.79	v_CH_K2.rte	-1.57	0.12	10	59.84
v_OV_N.hru	-3.68	0	11	4.11	v_HRU_SLP.hru	1.41	0.15	11	0.33
v_EPCO.hru	-2.46	0.014	12	0.27	v_SMFMX.bsn	1.25	0.21	12	12.46
a_GW_DELAY.gw	2.31	0.0212	13	2.89	v_OV_N.hru	-1.225	0.22	13	19.44
v_CH_N2.rte	-2.3	0.0215	14	0.04	v_EPCO.hru	-1.223	0.221	14	0.42
v_SMFMN.bsn	-1.72	0.08	15	10.68	r_SOL_K.sol	-1.03	0.3	15	0.34
r_SOL_BD.sol	1.64	0.1	16	-0.47	v_RCHRG_DP.gw	0.927	0.35	16	0.76

v: the initial value of the parameter is replaced by an active value; a: an active value is added to the initial value; r: the initial value is changed by multiplying (1+ a given value) (Abbaspour et al. 2007).

period from 2010 to 2016 (NSE: 0.63 vs. 0.54, PBIAS: 7.22 vs. 20.06, and RSR: 0.61 vs. 0.68).

Temporal Simulation Using Calibrated Models

Two different versions of SWAT models were calibrated and validated, which were Regular-SWAT using the HWSD soil data and Topo-SWAT using the DSMW soil data. In the SWAT model, there is a multitude of parameters, in which the sensitivity is different for the specific region. Hence, sensitivity analysis should be first performed to detect a candidate set of parameters most influencing the hydrological processes. Then data from the period 2010-2013 were used
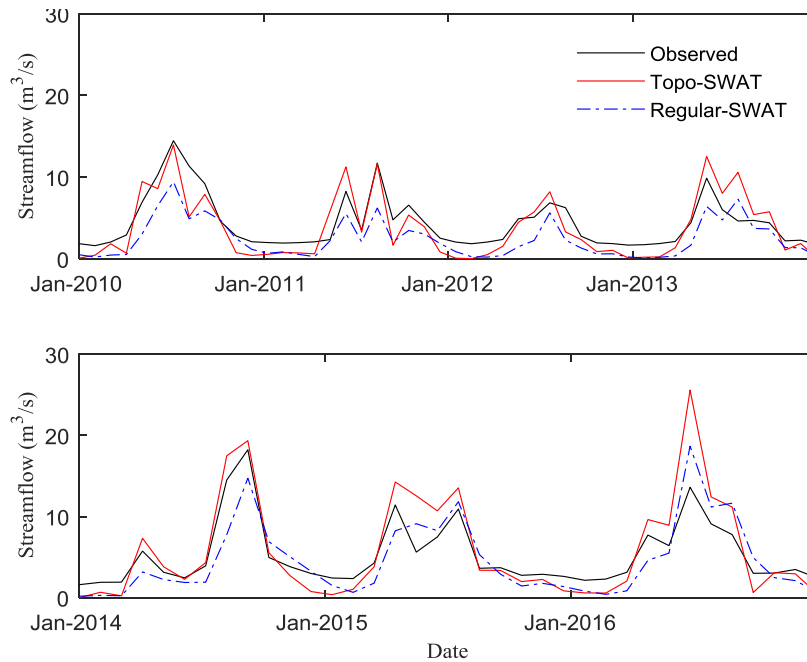
Fig. 3: Monthly observed streamflow and un-calibrated simulations in study catchment for Jan 2010-Dec 2013 period and Jan 2014-Dec 2016 period.
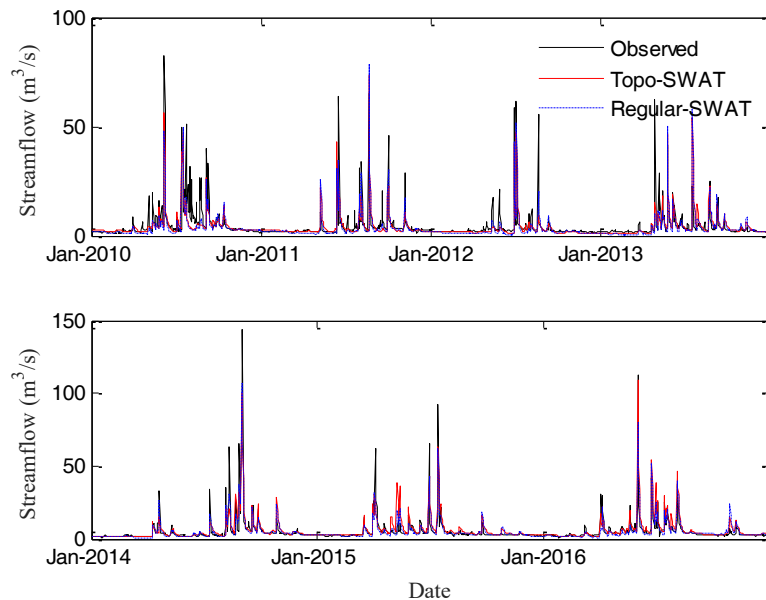
Fig. 4: Daily simulation and observation for a calibration period of 2010-2013 and validation period of 2014-2016.

for calibration, and data from 2014 to 2016 were applied for calibration at daily and monthly time scales. Finally, the runoff volume was also evaluated.

Sensitivity Analysis

Sensitivity analysis results for daily flows using Regular-SWAT and Topo-SWAT given by the SUFI-2 algorithm were listed in Table 2. Based on the result, the parameters related to surface runoff, the soil water storage, and groundwater are highly sensitive for two versions of SWAT (Table 2), including soil available water storage capacity (SOL_AWC), runoff curve number for moisture condition II (CN2), baseflow recession factor (ALPHA_BF) and maximum canopy storage (CANMX). Therefore, it is concluded that the most sensitive parameters for the two models are consistent, but the ranking value is different. Based on the results of sensitivity analysis, both calibrated and validated models were performed at the outlet of the study catchment at both daily and monthly scales.

Daily Data Simulation

In this study, the evaluation of model performance included not only visual comparisons between the simulations and measurements but also statistical methods. The final parameter values after the model calibration were listed in Table 2. As shown in Table 2, the most of optimized parameter values were different mainly due to the distinct runoff generation mechanism

Fig. 4 graphically illustrated the observed and simulated discharge values at the daily time scale. It could be seen that

the simulation and observation had a similar trend as well as the timing of the peak flows. Whereas, some simulated peaks were underestimated like 7 June 2010, 2 September 2014, and 2 June 2016. The greatest underestimation was located on 2 September 2014, which is more than 51% for both two models and during the 2 June 2016, the underestimation was approximately 29% for Topo-SWAT and 31% for Regular-SWAT. And some peak flows were greatly overestimated during some flood periods, e.g. in 18-21 July 2013. In general, daily peak flows were not matched well.

Standard regression plot (Fig. 5) showed that measured and simulated stream flows at daily time step for both periods of calibration and validation. As shown in these scatter plots, the aggregations of the daily stream flows were from 0 to 20 $m^3.s^{-1}$ for the calibration period and between 0 and 30 $m^3.s^{-1}$ for the validation period. It indicated that the dispersion of Regular-SWAT and Topo-SWAT values were consistent for calibration and validation.

The coefficient of determination (R^2) described the variance portion between the measured and simulated streamflow. The range value of R^2 is between 0 and 1. The higher value, the lower the error variance. The reported performance rating for R^2 is acceptable when its typical values exceed 0.5 (Santhi et al. 2001). In the calibration period, R^2 was obtained as 0.59 and 0.57 for Topo-SWAT and Regular-SWAT, respectively, which indicated an acceptable result. While the values of 0.69 and 0.72 for R^2 for Topo-SWAT and Regular-SWAT models indicated a good fit during validation. In general, the simulation result of the
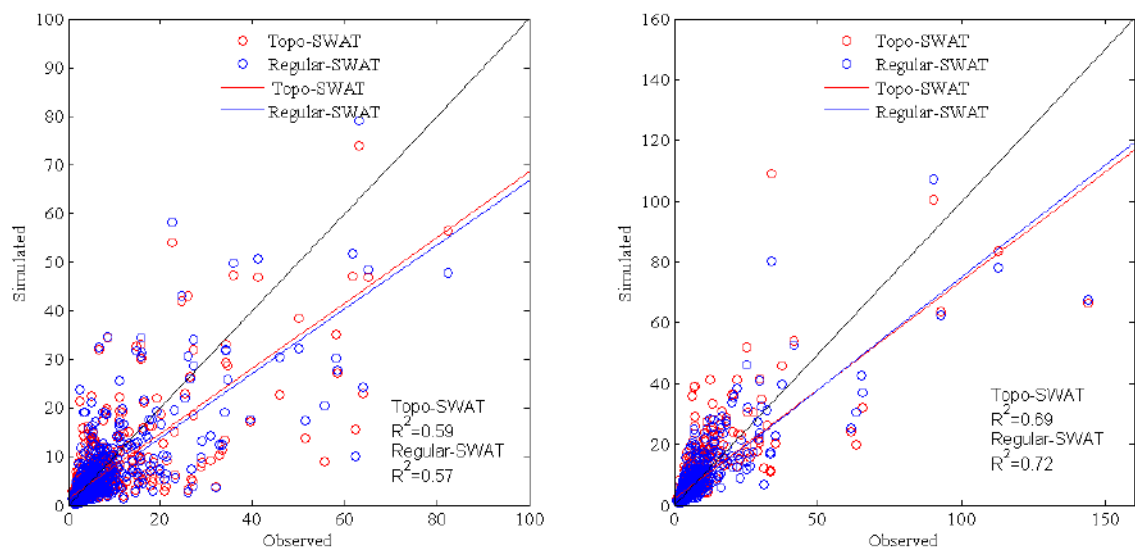
Fig. 5: Regression correlation between simulations and measurements using Regular-SWAT and Topo-SWAT models (a) calibration (2010-2013) and (b) validation (2014-2016).

Table 3: Evaluation indicators of the monthly streamflow based on the initial parameters.

SWAT version	Calibration (2010-2013)			Validation (2014-2016)			Total period (2010-2016)		
	NSE	PBIAS	RSR	NSE	PBIAS	RSR	NSE	PBIAS	RSR
Regular-SWAT	0.39	44.1	0.78	0.65	12.52	0.59	0.54	29.06	0.68
Topo-SWAT	0.65	21.61	0.59	0.61	-8.61	0.63	0.63	7.22	0.61

Topo-SWAT was more accurate in the calibration period, on contrary, the Regular-SWAT exhibited good performance in the validation period.

The statistical indexes of mean, median, standard deviation, maximum and minimum were compared between simulations using Regular-SWAT and Topo-SWAT and measured time series. The results were listed in Table 4. It could be seen that the mean, median, and minimum values obtained for Topo-SWAT were closer to the measured data, while Regular-SWAT underestimated the minimum streamflow, but the maximum was closer for calibration. By comparison, in the validation period, the Regular-SWAT had closer values to the observed data.

Monthly Time Series Simulation

For the calibration (Jan 2010-Dec 2013) and validation (Jan 2014-Dec 2016) periods, Fig. 6 compared graphically observed and simulated monthly data for Regular-SWAT and Topo-SWAT models. The trend of simulated monthly discharge was similar to that of the measurements and peak flow timing was usually also well simulated during most

months. Whereas, the streamflow for the peak was overt estimated in 2012 for calibration, in 2015 and 2016 during validation, respectively.

The results of model statistics for observations and simulations at a monthly scale using the two models were compared in Table 5. It could be seen that the Topo-SWAT simulated more accurately for calibration with the values of NSE, RSR, and PBIAS for Topo-SWAT were 0.69, 0.55, and 7.92, respectively, compared with the statistical values for Regular-SWAT. Regular-SWAT, on the other hand, performs better statistically during the validation period, with NSE, PBIAS, and RSR values of 0.88, 1.71, and -15.54, respectively. For both models, the values of assessment markers improved significantly at the monthly time step.

A comparison result of monthly annual streamflow for two models was exhibited in Fig. 7. It showed that the peak flow for Topo-SWAT and Regular-SWAT occurred in July, but the observed peak flow was in August. That may be because of the rainfall input for both SWAT models. The majority of peak flows occur during June to September, which just is the wet season. During the months from Janh

Table 4: Statistical index obtained via two models during the periods of calibration and validation.

Statistics	Measured		Regular-SWAT		Topo-SWAT	
	Calibration	Validation	Calibration	Validation	Calibration	Validation
Mean (m^3/s)	4.36	5.27	3.62	5.18	4.01	6.09
Median (m^3/s)	2.44	3.08	2.02	3.19	2.41	3.65
Standard deviation	6.83	8.82	5.84	7.69	5.6	8.33
Minimum (m^3/s)	0.78	0.79	0.38	0.74	0.79	1.23
Maximum (m^3/s)	82.3	144.15	79.07	107.4	80.88	109
NSE	-	-	0.58	0.72	0.59	0.69
RSR	-	-	0.65	0.53	0.64	0.59
PBIAS	-	-	16.9	1.64	7.91	-15.67

Table 5: Evaluation indicators of Topo-SWAT and Regular-SWAT performance for monthly streamflow predictions after calibration.

SWAT versions	Calibration (2010-2013)			Validation (2014-2016)		
	NSE	RSR	PBIAS	NSE	RSR	PBIAS
Regular-SWAT	0.65	0.59	16.99	0.88	0.35	1.71
Topo-SWAT	0.69	0.55	7.92	0.73	0.52	-15.54
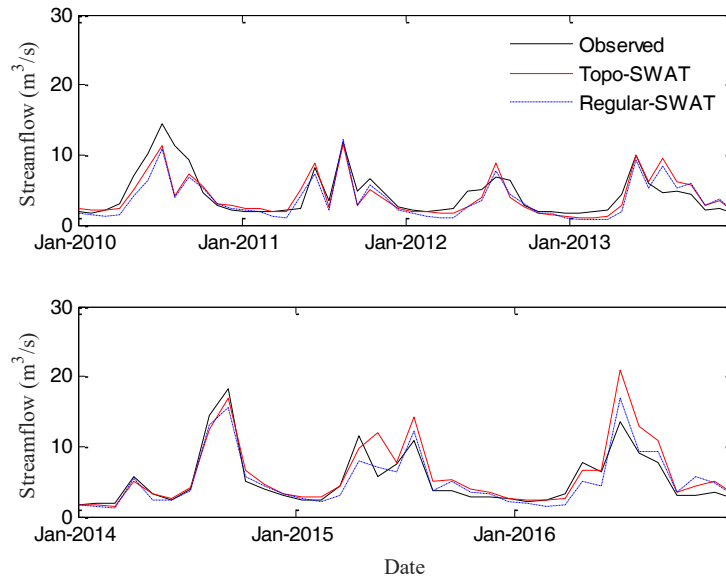
Fig. 6: Observed and simulated flow at monthly scale by two models for a calibration period of 2010-2013 and validation period of 2014-2016.

uary to June, and in August, September, and December, the simulated streamflow of Regular-SWAT was entirely lower than the observed streamflow. While in July, October, and November, the simulated was higher than the observed. For Topo-SWAT, the simulated streamflow in January, February, May to July, and October to December was higher than the observed streamflow. In contrast, in other months (March, April, August, and September), the observed was higher. In general, the result of Topo-SWAT was closer to the observed streamflow.
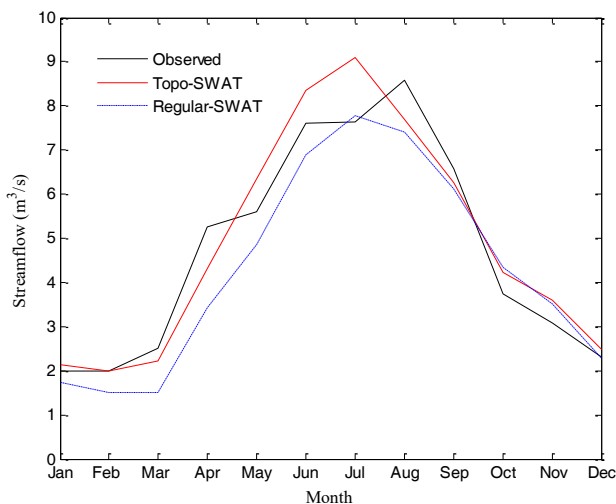
Fig. 7: Observed and simulated hydrograph in mean monthly streamflow for 2010-2016.

Runoff Volume

Fig. 8 illustrated the cumulative daily runoff volume for the study catchment in calibration Fig. 8 (a) and validation Fig. 8 (b) periods. Fig. 8 (a) showed that the simulated daily runoff volumes all have been underestimated over the calibration period for the two models. But, the simulated runoff volume of Topo-SWAT was much closer to observed values than that of Regular-SWAT. For the validation period (Fig. 8 (b)), the performances of the two models were satisfactory in the year 2014. Beyond that, the simulated daily runoff volume had been overestimated using Topo-SWAT. In contrast, the Regular-SWAT underestimated from Sep 2014 through Dec 2016.

A comparison of annual runoff volumes between observed and simulated applying Regular-SWAT and Topo-SWAT was shown in Fig. 9. The result showed that the simulated annual runoff volume using Topo-SWAT and Regular-SWAT had been underestimated for 4 years and 5 years, respectively, which was different in the year 2015. The simulated values applying Topo-SWAT were higher than observed runoff volume, while the result calculated by Regular-SWAT was lower in 2015. Furthermore, two years of annual runoff volumes using Topo-SWAT had been simulated to be profoundly overestimated (2015 and 2016).

Spatial Distribution of Runoff Generation Areas Using Calibrated Models

What is more interesting is the difference in the predicted runoff distribution using the Regular-SWAT and Topo-SWAT
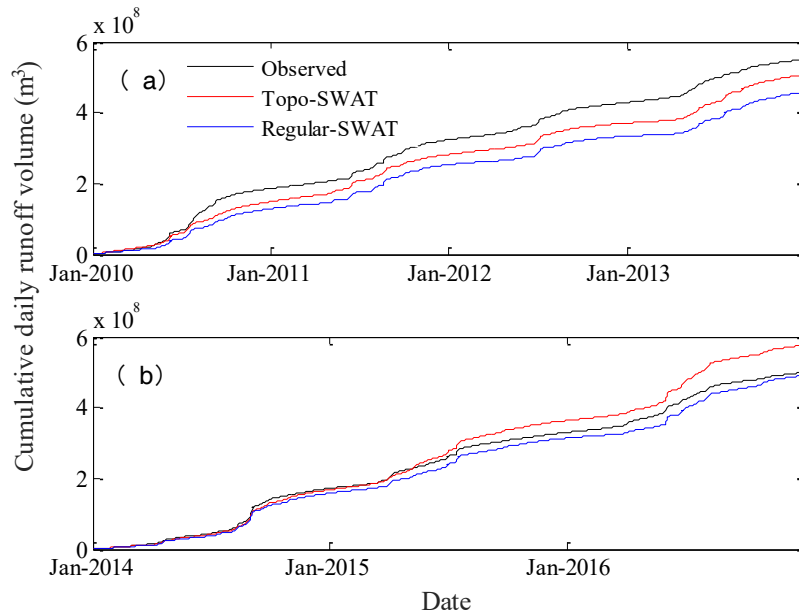
Fig. 8: Cumulative daily runoff volume for periods of calibration (a) and validation (b).

in the study catchment. The information about the spatial distribution and extent of runoff source areas is important for watershed management. For instance, Fig. 10 showed the predicted spatial distribution of runoff generation for one storm event in September 2014 (193 mm). The darker shades in the areas, the higher runoff generation. Regular-SWAT predicted the most proportion of catchment would generate more runoff, and the different locations were significantly affected by differences in soil types and land cover/use. However, for the same rainfall event, Topo-SWAT calculated

Fig. 9: Annual runoff volume calculated by Topo-SWAT and Regular-SWAT.

a majority of the catchment producing less surface runoff, and the distribution of runoff generation reflected the topographic position, the topography is the main element associated with runoff generation. In general, higher runoff generation was related to HRUs with higher wetness index classes, which were low-lying wet areas and closer to the streams.

DISCUSSION

Sensitivity Analysis

The sensitivity of parameters is always analyzed before calibration, but there is no common guide to identify the sensitivity bound. (Van Griensven et al. 2006) pointed out that parameter sensitivities were different in specific catchments because of the distinct watershed characteristics including soil properties, land use, and slope types. So, the parameters used to calibrate in this catchment may be different. Based on the previous research by (Yang et al. 2012), the main hydrological processes and parametric interactions should firstly be identified, and then the model setup should also be examined to ensure the accuracy of the calibration. In general, the sensitive parameters were those related to physical processes including surface runoff, evapotranspiration, groundwater, and channel routing. In this study, the parameters related to surface runoff generation, soil water movement, and groundwater are highly sensitive for two versions of SWAT (Table 2). In the most sensitive parameters, CANMX is mainly determined by the leaf area index of the vegetation and precipitation can only reach the soil when the canopy storage is filled (Guse et al.

2013), which is significant to affect infiltration, surface runoff, and evapotranspiration in the highly vegetated catchment (Nyeko 2015). Baseflow alpha-factor (ALPHA_BF) is an index reflecting the changes in recharge with groundwater flow. SOL_AWC is used to calculate the field capacity of each soil layer by adding to the wilting point. Curve number (CN) primarily influences the amount of runoff generation, which is a relatively sensitive parameter for most of the catchments (Noori & Kalin 2016). The ranking of other parameters was different due to the rainfall-runoff generation mechanism. Hence, the results suggested the sensitivity analysis was important before the model calibration (Demaria et al. 2007). Consequently, the final parameter values should be checked to be in line with the catchment characteristics and corresponding hydrologic processes.

Simulation Results

From the land use map of XMG Reservoir Catchment, the forest is the mainland cover (88.37%), which can delay the
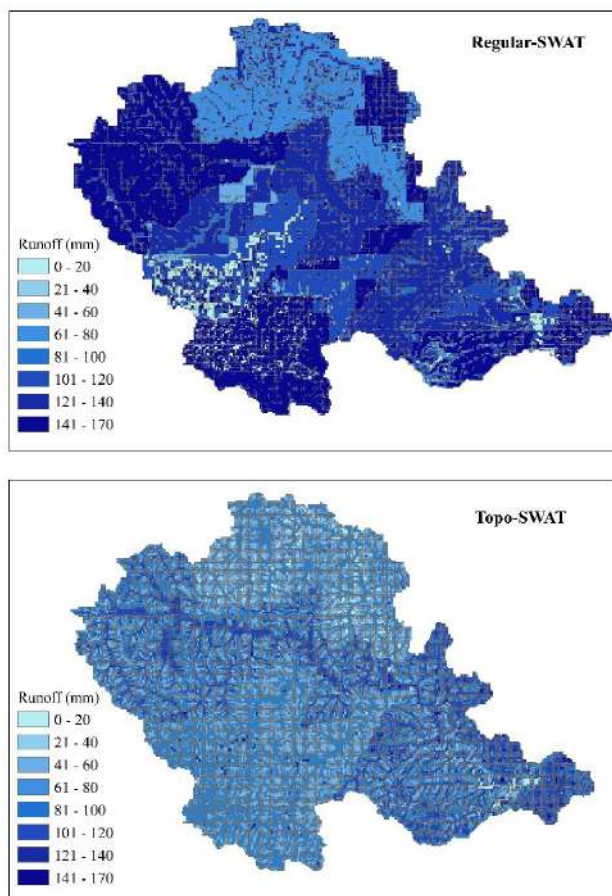
Fig. 10: Spatial distribution of runoff generation areas predicted by Regular-SWAT and Topo-SWAT.

surface flow and generate substantial subsurface flow, due to forest surface soils having high infiltration capacities (Jiang et al. 2012). And there is a great quantity of rainfall (1010 mm.a^{-1}). Thus, in this catchment, the saturation excess runoff generation approach may be more appropriate than the infiltration excess runoff mechanism, which could be proved by the statistical indexes of model performance (Table 3). And the simulation result using un-calibrated Topo-SWAT was slightly better than that by un-calibrated Regular-SWAT (Fig. 3), so we conclude that the topography is a major factor in hydrological processes. But, after the much more complex parameter sensitivity and calibration, the simulation by Regular-SWAT is similar to that of Topo-SWAT in the calibration period (Fig. 6 & Fig. 4).

In a few cases (2010, 2014, and 2015), the peak flows were underestimated applying two SWAT models (Fig. 4). This may be due to soils on mountainous forested slopes can absorb a large amount of precipitation in the wet season and later slightly releasing water from the storage to be as base flow. One possible reason may attribute to the uncertainty of input data, such as meteorological data. And only one weather station was in this study catchment, the other three were outside the catchment. Therefore, the spatial distribution of precipitation was not representative which might lead to not so rigorous calibration of the model (Masih et al. 2011). The other possible reason may be the pattern of precipitation had a considerable effect on the simulated peak flows. Furthermore, the physical processes of runoff generation over a watershed in nature are extremely complicated and exhibit considerable temporal and spatial variability.

The different spatial distribution of runoff predicted by the two models is exhibited in Fig. 10. For the same large rainfall event, Regular-SWAT predicted the majority of the catchment generating high runoff, whereas Topo-SWAT predicted a majority of the catchment generating less surface runoff and the near-stream regions producing more runoff in line with the other researches. In Topo-SWAT, the soil wetness index and topography are considered to model runoff, in other words, the degree of saturation and VSA hydrological principles are taken into account. And it assumes that HRUs located at the flat, near river would become moist and contribute a large amount of runoff, due either to the hydraulic gradient decreased by shallower slope, or maybe the accumulation of lateral flow from upland regions (Collick et al. 2014). Whereas, Regular-SWAT treats these HRUs the same as any upland region with the same soil and land use.

CONCLUSION

Two versions of the SWAT model, Regular-SWAT and Topo-SWAT, were established for the XMG Reservoir Catch-

ment, to compare their abilities to simulate stream flows and to identify critical runoff generation regions, which could provide important information for temporal and spatial water management. Each performance and applicability were successfully examined by parameter sensitivity analysis, model calibration, and model validation. The main conclusions are obtained as follows:

(1) based on sensitivity analysis results, SOL_AWC, CN2, CANMX, and ALPHA_BF were the most sensitive parameters for both two models.

(2) Both Regular-SWAT and Topo-SWAT models provided reasonable simulations of stream flows. Statistical comparisons revealed good model performance due to values of NSE for monthly and daily streamflow in calibration and validation periods being larger than 0.65, 0.55, respectively. Nevertheless, some discrepancies were evident between the observations and simulations of high stream flows.

(3) By contrast, the highest flow simulated by Topo-SWAT was better than that of Regular-SWAT, while Regular-SWAT had better model performance in the period of validation.

(4) Regular-SWAT mostly underestimated the annual runoff volume, while Topo-SWAT provided a slightly better prediction.

(5) The results of spatial runoff source areas demonstrate that the Topo-SWAT is slightly better due to it reflecting the effect of topography and soil characteristics.

ACKNOWLEDGEMENT

REFERENCES

Abbaspour, K.C. 2015. SWAT-CUP: SWAT Calibration and Uncertainty Programs: A User Manual Eawag, Dübendorf.

Abbaspour, K.C., Yang, J., Maximov, I., Siber, R., Bogner, K., Mieleitner, J., Zobrist, J. and Srinivasan, R. 2007. Modeling hydrology and water quality in the pre-alpine/alpine Thur watershed using SWAT. J. Hydrol., 333**:** 413-430.

Arnold, J.G., Srinivasan, R., Muttiah, R.S. and Williams, J.R. 1998. Large area hydrologic modeling and assessment-Part I: Model development. J. Am. Water Resour. Assoc., 34: 73-89.

Beven, K.J. & Kirkby, M.J. 1979. A physically based, variable contributing area model of basin hydrology. Hydrol. Sci. Bullet., 24**:** 43-69.

Cibin, R., Sudheer, K.P. and Chaubey, I. 2010. Sensitivity and identifiability of streamflow generation parameters of the SWAT model. Hydrol. Proc., 24: 1133-1148.

Collick, A.S., Fuka, D.R., Kleinman, P.J.A., Buda, A.R., Weld, J.L., White, M.J., Veith, T.L., Bryant, R.B., Bolster, C.H. and Easton, Z.M. 2014. Predicting phosphorus dynamics in complex terrains using a variable source area hydrology model. Hydrol. Proc., 29**:** 588-601.

Dahlke, H.E., Easton, Z.M., Lyon, S.W., Walter, T.M. and Destouni, M. 2012. Dissecting the variable source area concept: Subsurface flow pathways and water mixing processes in a hillslope. J. Hydrol., 420**:** 125-141.

Demaria, E. M., Nijssen, B. and Wagener, T. 2007. Monte Carlo sensitivity analysis of land surface parameters using the variable infiltration capacity model. J. Geophys. Res. Atmos., 112: 453.

Easton, Z.M., Fuka, D. R., Walter, M.T., Cowan, D.M., Schneiderman, E.M. and Steenhuis, T.S. 2008. Re-conceptualizing the soil and water assessment tool (SWAT) model to predict runoff from variable source areas. J. Hydrol., 348: 279-291.

FAO. 2007. Digital Soil Map of the World. Available from: http://www.fao. org/geonetwork (accessed April 2018).

Fuka, D.R. and Easton, Z.M. 2015. T Improving the spatial representation of soil properties and hydrology using topographically derived initialization processes in the SWAT model. Hydrol. Proc., 30: 4633-4643.

Gan, R., Luo, Y., Zuo, Q. and Sun, L. 2015. Effects of projected climate change on the glacier and runoff generation in the Naryn River Basin, Central Asia. J. Hydrol., 523**:** 240-251.

Gerard-Marchant, P., Hively, W.D. and Steenhuis, T.S. 2006. Distributed hydrological modeling of total dissolved phosphorus transport in an agricultural landscape, part I: Distributed runoff generation. Hydrol. Earth Sys. Sci., 10**:** 245-261.

Golmohammadi, G., Rudra, R., Dickinson, T., Goel, P. and Veliz, M. 2017. Predicting the temporal variation of flow contributing areas using SWAT. J. Hydrol., 547**:** 375-386.

Guse, B., Reusser, D.E. and Fohrer, N. 2013. How to improve the representation of hydrological processes in SWAT for a lowland catchment: Temporal analysis of parameter sensitivity and model performance. Hydrol. Proc., 28**:** 2651-2670.

Jiang, R., Woli, K.P., Kuramochi, K., Hayakawa, A., Shimizu, M. and Hatano, R. 2012. Coupled control of land use and topography on nitrate-nitrogen dynamics in three adjacent watersheds. Catena, 97**:** 1-11.

Lyon, S.W., Walter, M.T., Gérard Marchant, P. and Steenhuis, T.S. 2004. Using a topographic index to distribute variable source area runoff predicted with the SCS curve number equation. Hydrol. Proc., 18**:** 45.

Masih, I., Maskey, S., Uhlenbrook, S. and Smakhtin, V. 2011. Assessing the impact of areal precipitation input on streamflow simulations using the SWAT Model1. Jawra J. Am. Water Resour. Assoc., 47**:** 179-195.

Moriasi, D.N., Arnold, J.G., Liew, M.W.V., Bingner, R.L., Harmel, R.D. and Veith, T. L. 2007. Model evaluation guidelines for systematic quantification of accuracy in watershed simulations. Trans. Asae, 50: 885-900.

Nash, J.E. and Sutcliffe, J.V. 1970. River flow forecasting through conceptual models part I: A discussion of principles. J. Hydrol., 10: 282-290.

Needelman, B.A., Gburek, W.J., Petersen, G.W., Sharpley, A.N. and Kleinman, P.J.A. 2004. Surface Runoff along Two Agricultural Hillslopes with Contrasting Soils. Soil Sci. Soc. Am. J., 68**:** 914-923.

Neitsch, S.L., Arnold, J.G., Kiniry, J.R. and Williams, J.R. 2011. Soil and Water Assessment Tool: Theoretical Documentation Version 2009. Texas Water Resources Institute Technical Report 406.

Noori, N. and Kalin, L. 2016. Coupling SWAT and ANN models for enhanced daily streamflow prediction. Journal of Hydrology, 533**,** 141-151.

Nyeko, M. 2015. Hydrologic modeling of a data-scarce basin with SWAT model: Capabilities and limitations. Water Resour. Manag., 29**:** 81-94.

Santhi, C., Arnold, J.G., Williams, J.R., Hauck, L.M. and Dugas, W.A.

2001. Application of a watershed model to evaluate management effects on point and nonpoint source pollution. Trans. Asae, 44: 1559-1570.

Steenhuis, T.S., Walter, M.F., Zollweg, J.A., Rossing, J. and Winchell, M. 1995. SCS runoff equation revisited for variable-source runoff areas. J. Irrig. Drain. Eng., 121**:** 234-238.

Stehr, A., Aguayo, M., Link, O., Parra, O., Romero, F. and Alcayaga, H. 2010. Modeling the hydrologic response of a mesoscale Andean watershed to changes in land-use patterns for environmental planning. Hydrol. Earth Sys. Sci. Discuss., 14**:** 1963-1977.

Suliman, A.H.A., Jajarmizadeh, M., Harun, S. and Darus, I.Z.M. 2015. Comparison of semi-distributed, gis-based hydrological models for the prediction of streamflow in a large catchment. Water Resour. Manag., 29**:** 3095-3110.

USDA-SCS. 1972. Design Hydrograph. Hydrology, National Engineering Handbook, NEH Notice.

Van Griensven, A., Meixner, T., Grunwald, S., Bishop, T., Diluzio, M. and Srinivasan, R. 2006. A global sensitivity analysis tool for the parameters of multi-variable catchment models. J. Hydrol., 324**:** 10-23.

White, M.J., Storm, D.E., Busteed, P.R., Stoodley, S.H. and Phillips, S.J. 2009. Evaluating nonpoint source-critical source area contributions at the watershed scale. J. Environ. Quality, 38**:** 1654.

Woodbury, J.D., Shoemaker, C.A and Cowan, D.M. 2014. Application of SWAT with and without variable source area hydrology to a large watershed. J. Am. Water Resour. Assoc., 50**:** 42-56.

Yang, J., Liu, Y., Yang, W. and Chen, Y. 2012. Multi-objective sensitivity analysis of a fully distributed hydrologic model wet spa. Water Resour. Manag., 26**:** 109-128.

Yang, J., Reichert, P., Abbaspour, K.C., Xia, J. and Yang, H. 2008. Comparing uncertainty analysis techniques for a SWAT application to the Chaohe Basin in China. J. Hydrol., 358**:** 1-23.

Research on Influencing Factors of Provincial Energy Efficiency in China Based on the Spatial Panel Model

Guozhu Li*(**) and Tingyu Zhang*†
*School of Economics, Hebei Geo University, Shijiazhuang 050031, China
**Natural Resource Asset Capital Research Center, Hebei Geo University, Shijiazhuang 050031, China
†Corresponding author: Tingyu Zhang; zhangtingyu912@163.com

ABSTRACT

The Super-SBM model was used first to assess the energy efficiency of 30 Chinese provinces from 2012 to 2017. After that, an energy efficiency spatial correlation test was conducted, and finally, the influencing elements of energy efficiency were analyzed using a geographic panel model. The findings show that the amount of regional economic development has a substantial positive impact on energy efficiency, whereas the level of regional urbanization and the severity of environmental restrictions have a considerable negative impact on energy efficiency in China's provinces. Other regions' energy structure and technical innovation have a substantial positive spillover effect on the region's energy efficiency, whereas other regions' economic development and foreign direct investment have a significant negative spillover effect on the region's energy efficiency.

INTRODUCTION

The development and utilization of energy are required for both continual economic growth and continuous societal development. Energy is a crucial component of societal production. Energy usage is steadily growing as industrialization progresses. According to a report by the International Energy Agency, worldwide energy consumption will increase by 37% by 2040. Although sufficient and stable energy input can maintain national energy security and promote healthy economic development, energy shortage is one of the main challenges in the economic and social development of developing countries. As the largest developing country in the world, China's energy consumption has shown explosive growth along with its economic development. In 2019, the total energy consumption reached 4870 MTCE, and the external dependence on natural gas and oil has exceeded 40% and 70%. Clean energy is relatively scarce, and the long-lasting energy crisis will cause more serious development problems and bring a heavy burden to China. The coal-based energy structure and crude economic expansion have frequently broken through the bottom line of environmental carrying capacity throughout the past 40 years of reform and opening up, and pollutant emissions significantly surpass the global average.

There is a serious shortage of energy resources in China, and the environmental carrying capacity is close to the upper limit. It is necessary to slow down the growth rate of total energy demand, accelerate structural transformation, promote the formation of new ways of green and circular development, improve energy consumption structure, and make energy development in the direction of low-carbon and clean energy. The energy issue is one of the bottlenecks restricting the sustainable development of China's economy and society. It's worthwhile to consider and investigate how to make the most of limited energy. For China to accomplish ecological civilization construction and high-quality economic development, this is critical. Therefore, the evaluation of energy efficiency and the study of its influencing factors have become the focus of attention of many scholars.

Past Studies

At present, research on energy efficiency at the inter-provincial is mainly focused on energy efficiency calculations and influencing factors.

For the study of energy efficiency measurement, the data envelopment analysis (DEA) model is the current mainstream method. It does not need to consider the influence of dimensions and weights, nor does it need to set the production function in advance. It can evaluate complex systems with multiple inputs and multiple outputs. Wang et al. (2018) have used the DEA method to measure energy efficiency. With the increasingly serious pollution problem, to measure and

evaluate energy efficiency more scientifically and rationally, more and more scholars have begun to consider undesired output in the DEA model. By weighting the emissions of the "three industrial wastes," Zhou & Zhang (2016) portrayed environmental pollution emissions as undesirable output. Tone (2003) included the undesirable output in the SBM model, recognizing the various proportional changes between the expected and undesired outputs. Guan & Xu (2015) used the SBM model of undesirable output to investigate the spatial distribution characteristics and evolution of energy efficiency. Wang et al. (2017a) found that improving energy efficiency is vital for slowing global warming through an improved SBM model study. Meng et al. (2016) used the hybrid SBM model to measure the provincial energy efficiency under the haze constraints in China and found that there is a problem of energy waste. Qin et al. (2016) used the DEA-SBM model of undesired output to measure the energy efficiency of the eastern coastal area and found that energy efficiency is greatly affected by undesired output.

For the study of energy efficiency influencing factors, Cui et al. (2014) found that technological progress has a significant impact on energy efficiency. Wang et al. (2011) believed that energy efficiency will be affected by government intervention, degree of opening to the outside world, and industrial structure. Yao et al. (2012) found that optimizing the industrial structure can improve energy efficiency. Wu & Du (2018) based on the data of 11 provinces in the Yangtze River Economic Belt found that skewed technological progress has a positive effect on total factor energy efficiency. Ruipeng & Boqiang (2017) believed that improving technical production methods, increasing per capita GDP, optimizing the energy structure, and increasing foreign direct investment can improve energy efficiency. Liu et al. (2008) studied that increasing the relative price of energy will have a positive impact on energy efficiency, but Li et al. (2014) analyzed that the effect of energy price on energy efficiency is not significant. Jiang & Ji (2020) believed that the level of urbanization has a negative inhibitory effect on energy efficiency, while Song et al. (2020) believed that the level of urbanization has a positive effect. Wang et al. (2017b) analyzed that environmental regulations inhibit the improvement of energy efficiency by increasing the operating costs of enterprises. Wang & Zhong (2015) indicated that environmental regulation improves energy efficiency through innovation compensation effects. Dai & Fu (2020) believed that the impact mechanism of environmental regulations is different for regions with different energy efficiency.

This article draws on the work of earlier researchers and expands on two points: On the one hand, due to the vast number of input and output indicators, the standard DEA model will have several decision-making units that are rated as

successful, but it cannot be distinguished further. As a result, the Super-SBM model of undesirable output is employed in MaxDEA software to assess energy efficiency; on the other hand, the energy usage efficiency of various locations and its influencing factors are usually spatially associated. The use of traditional panel models will ignore this problem. However, the spatial panel model can test whether the energy efficiency has spatial relevance, and can decompose its effects.

MATERIALS AND METHODS

Construction of the Theoretical Model

Super-SBM model: The Super-SBM model can solve the evaluation and ranking of relatively effective units. When evaluating the j-th decision-making unit, the input and output of the j-th decision-making unit will be replaced by the linear combination of the inputs and outputs of all other decision-making units, and the j-th decision-making unit will be excluded.

Suppose there are n decision-making units (DMU_j, $j = 1, 2,...,n$), and each DMU uses m types of inputs ($i=1,...,m$) to produce s types of outputs ($r=1,..., s$), mark the DMU to be evaluated as DMU_j ($j=1,...,n$). Let x_{ij} be the i-th input of the j-th DMU, and y_{rj} be the r-th output of the j-th DMU. The model of the Super-SBM under variable returns to scale is as follows:

$$Min\delta = \frac{s}{m}\left(\sum_{i=1}^{m}\frac{\overline{x}_i}{x_{io}}\Big/\sum_{r=1}^{s}\frac{\overline{y}_r}{y_{ro}}\right)$$

$$\overline{x} \geq \sum_{\substack{j=1 \\ j\neq o}}^{n}\lambda_j x_j, \overline{y} \leq \sum_{\substack{j=1 \\ j\neq o}}^{n}\lambda_j y_j, \sum_{\substack{j=1 \\ j\neq o}}^{n}\lambda_j = 1, \overline{x} \geq x_o, \overline{y} \leq y_o$$

$$...(1)$$

The Super-SBM model considering undesired output is:

$$Min\delta = \frac{\dfrac{1}{m}\sum_{t=1}^{m}\dfrac{x_t}{x_{to}}}{\dfrac{1}{s_1+s_2}\left(\sum_{r=1}^{s_1}\dfrac{y_r^g}{y_{ro}^g}+\sum_{r=1}^{s_2}\dfrac{y_r^b}{y_{ro}^b}\right)}$$

$$x \geq \sum_{\substack{n=1 \\ n\neq i}}^{N} x_n \cdot \lambda_n, y^g \leq \sum_{\substack{n=1 \\ n\neq i}}^{N} y_n^g \cdot \lambda_n, y^b$$

$$\geq \sum_{\substack{n=1 \\ n\neq i}}^{N} y_n^b \cdot \lambda_n, \sum_{\substack{n=1 \\ n\neq i}}^{N} \lambda_n = 1$$

$$x \geq x_o, y^g \leq y_o^g, y^b \geq y_o^b, \lambda \geq 0 \qquad ...(2)$$

Where, δ is the target efficiency, x, y^g, and y^b represent input, expected output, and undesired output respectively; s denotes the relaxation vector, which can avoid the deviation that may be caused by the radial and angle selection; λ indicates the weight vector.

Spatial Correlation

Moran's I test is a hypothesis test method for spatial correlation. The global Moran's I statistic is defined as:

$$\text{Global Moran's I} = \frac{\sum_{i=1}^{n}\sum_{j=1}^{n} w_{ij}(x_i - \overline{x})(x_j - \overline{x})}{s^2 \sum_{i=1}^{n}\sum_{j=1}^{n} w_{ij}}$$

$$\overline{x} = \frac{1}{N}\sum_{i=1}^{n} x_i$$

$$s^2 = \frac{1}{N}\sum_{i=1}^{n}(x_i - \overline{x})^2$$

...(3)

Where, i, j are regions, x_i and x_j denote the observed values of energy efficiency, $\overline{x}$ represents the mean value, and w_{ij} is the (i, j) element of the spatial weight matrix.

The global Moran's I is used to test whether each province has agglomeration in space, but it can't see how it is agglomerated. The local Moran's I scatter plot needs to be used to identify the type of aggregation in the local space of each area. The formula is as follows:

$$\text{Local Moran's I} = \frac{(x_i - \overline{x})}{s^2}\sum_{j=1}^{n} w_{ij}(x_j - \overline{x})$$

...(4)

Spatial Panel Model

Common spatial measurement models include the following three forms:

The spatial lag model: SLM assumes that the explained variable in the region depends on the explained variable in the neighboring region, namely:

$$Y = \rho WY + X\beta + \varepsilon \qquad \text{...(5)}$$

Y is the explained variable, X denotes the explanatory variable, ρ represents the spatial autoregressive coefficient, W indicates the spatial weight matrix, ε represents a random error, and β denotes the influence coefficient of X on Y.

The spatial error model: SEM assumes that there is a spatial correlation in the disturbance term, namely:

$$\begin{cases} Y = X\beta + \mu \\ \mu = \alpha W\mu + \varepsilon \\ \varepsilon \to N(0, \sigma^2 I_n) \end{cases}$$

...(6)

α is the spatial correlation coefficient of the disturbance term.

The spatial Durbin model: SDM assumes that the explained variable in this region depends on the explanatory variable in the adjacent region, namely:

$$Y = \rho WY + X\beta + WX\delta + \varepsilon \qquad \text{...(7)}$$

$WX\delta$ represents the influence of explanatory variables from neighboring regions, and δ is the coefficient vector.

The spatial panel model: It can be expressed as:

$$\begin{cases} Y_{it} = \tau Y_{i,t-1} + \rho W_i^T Y_t + X_{it}^T \beta + W_i^T X_t \delta + \mu_i + \gamma_t + \varepsilon_{it} \\ \varepsilon_{it} = \lambda W_i^T \varepsilon_i + \nu_{it} \end{cases}$$

...(8)

Where, $Y_{i,t-1}$ is the first-order lag term of the explained variable, μ_i represents the individual effect, and γ_t denotes the time effect. If $\lambda = 0$, it is the SDM model; if $\lambda = 0$, $\delta = 0$, it is the SLM model; if $\tau = \rho = 0$, $\delta = 0$, it is SEM model.

RESULTS AND DISCUSSION

Data Source and Description

The data in this article comes from the 2013-2018 "China Price Statistical Yearbook" (Energy prices), "China Environmental Yearbook" (Strength of environmental regulations), and "China Statistical Yearbook" (Other indexes). The index system for the study of energy efficiency in various provinces in China is shown in Table 1.

It should be noted that to reduce the numerical difference between variables, logarithms are taken for all variables.

Calculation of Energy Efficiency

Use MaxDEA software to measure the energy efficiency of each province as shown in Table 2.

From 2012 to 2017, the energy efficiency of most provinces has shown an upward trend. Generally speaking, China's energy efficiency is constantly improving. Among them, the energy efficiency of Beijing, Tianjin, Shanghai, Jiangsu, and Guangdong is at the leading domestic level, with energy efficiency above 1; Heilongjiang, Guizhou, Yunnan, Gansu, Qinghai, Ningxia, and Xinjiang are at a relatively low level in China, and their energy efficiency doesn't exceed 0.5. In 2017, the average energy efficiency of China's provinces

Table 1: Index selection and description.

Model		Index	Description
Super-SBM model	Input	Capital investment	Total city investment in fixed assets
		Labor input	(Total number of employees at the end of the previous year + total number of employees at the end of the year)/2
		Energy input	Total energy consumption
	Output	Expected output	Industrial output
			GDP(Gross domestic product)
		Undesired output	Industrial wastewater discharge
			Industrial sulfur dioxide emissions
			Industrial smoke (dust) emissions
Space panel model	Explained variable	Energy efficiency	Use Super-SBM model to measure (Y)
	Explanatory variables	The level of economic development	GDP per capita (X1)
		Urbanization level	The proportion of the urban population in total population (X2)
		Energy structure	The proportion of natural gas consumption in total energy consumption (X3)
		Energy prices	Annual purchase index of industrial producers (fuel power category) (X4)
		Strength of environmental regulations	Sewage discharge fee collection amount (X5)
		Technological innovation	Research and development expenditure (X6)
		Foreign direct investment	The proportion of total investment of foreign-invested enterprises in GDP (X7)

was 0.606, most of the eastern provinces were higher than the national average and most of the western provinces were lower than the national average. From the east coast to the west interior, energy efficiency is gradually declining, and a significant divide exists between the central and western regions and the eastern coastal districts. The energy efficiency of provinces that are geographically close together is similar, implying that China's inter-provincial energy efficiency may be spatially related.

Spatial Correlation Test

The spatial weight matrix reflects the proximity of provinces in geographic space. This paper uses the modified adjacency weight matrix, which doesn't regard Hainan as an isolated island but is adjacent to Guangdong. According to the convention, all main diagonal elements are taken as 0, the formula is as follows:

$$W_{ij} = \begin{cases} 0, & i \text{ and } j \text{ are not adjacent} \\ 1, & i \text{ and } j \text{ are adjacent} \end{cases} \quad ...(9)$$

Calculate the global Moran's I index of the energy efficiency of China's provinces from 2012 to 2017 through

the software Stata16.0. It can be seen from Table 3 that the spatial correlation test of each year is considered to have a positive spatial autocorrelation at a significance level of 10%.

Use GeoDa software to draw Moran's I scatter plot using 2017 energy efficiency data, as shown in Figure 1. Both the global Moran's I and the local Moran's I are represented in this diagram. The Global Moran's I index was shown to be significantly positive after 999 randomized permutations. The local Moran's I of each province is the product of the horizontal and vertical coordinates of these distributed sites.

Beijing, Tianjin, Shanghai, Shandong, Fujian, Jiangsu, and Zhejiang are in the H-H cluster (first quadrant), all provinces are located in the east. Based on the policy advantages in the early stage of reform and opening up and their own geographical advantages, the economic development started earlier. With the advancement of the industrial transfer process, the current main industries are tertiary industries with lower energy consumption; Jiangxi, Hebei, and Hainan belong to the L-H type (second quadrant), indicating that the energy efficiency of these three provinces is relatively low, but the energy efficiency of neighboring provinces is relatively high. Their economy is underdeveloped and they

Table 2: Inter-provincial energy efficiency values.

	2012	2013	2014	2015	2016	2017	Mean	Rank
Beijing	1.138	1.16	1.171	1.175	1.162	1.14	1.158	2
Tianjin	1.182	1.187	1.183	1.175	1.169	1.113	1.168	1
Hebei	0.534	0.532	0.51	0.489	0.519	0.512	0.516	21
Shanxi	0.433	0.383	0.352	0.316	0.296	0.538	0.386	25
Inner Mongolia	1.075	1.071	1.037	1.026	1.008	0.435	0.942	6
Liaoning	0.546	0.557	0.555	0.615	0.553	0.567	0.566	14
Jilin	0.615	0.641	0.639	0.618	0.644	0.589	0.624	11
Heilongjiang	0.437	0.459	0.471	0.446	0.397	0.362	0.429	23
Shanghai	1.059	1.091	1.089	1.108	1.117	1.199	1.111	3
Jiangsu	1.112	1.02	1.005	1.01	1.021	1.039	1.035	5
Zhejiang	1.002	0.786	0.826	0.804	0.866	0.834	0.853	7
Anhui	0.56	0.592	0.579	0.566	0.615	0.608	0.587	13
Fujian	0.635	0.689	0.718	0.721	0.815	0.774	0.725	8
Jiangxi	0.537	0.578	0.571	0.549	0.538	0.536	0.552	16
Shandong	0.701	0.712	0.685	0.676	0.697	0.693	0.694	9
Henan	0.584	0.556	0.537	0.526	0.571	0.602	0.563	15
Hubei	0.552	0.603	0.606	0.615	0.635	0.62	0.605	12
Hunan	0.56	0.645	0.656	0.656	0.652	0.622	0.632	10
Guangdong	1.063	1.069	1.055	1.064	1.056	1.042	1.058	4
Guangxi	0.496	0.546	0.553	0.559	0.558	0.456	0.528	20
Hainan	0.557	0.544	0.546	0.52	0.454	0.409	0.505	22
Chongqing	0.508	0.532	0.545	0.559	0.569	0.549	0.544	17
Sichuan	0.559	0.576	0.557	0.544	0.513	0.495	0.541	18
Guizhou	0.322	0.366	0.378	0.397	0.397	0.389	0.375	26
Yunnan	0.371	0.408	0.407	0.407	0.374	0.359	0.388	24
Shaanxi	0.582	0.554	0.536	0.499	0.505	0.514	0.532	19
Gansu	0.359	0.356	0.337	0.302	0.285	0.294	0.322	29
Qinghai	0.36	0.365	0.354	0.347	0.331	0.286	0.341	28
Ningxia	0.335	0.36	0.349	0.349	0.346	0.339	0.346	27
Xinjiang	0.328	0.333	0.33	0.299	0.277	0.274	0.307	30

mainly operate traditional resource-based industries with high resource consumption and low output. The extensive economic development model leads to low energy efficiency. Therefore, optimizing the industrial structure and improving energy efficiency are issues that local governments need to pay attention to. The 14 regions of Heilongjiang, Inner Mongolia, Xinjiang, Gansu, Shanxi, Shaanxi, Ningxia, Qinghai, Yunnan, Guizhou, Sichuan, Chongqing, Liaoning, and Jilin are in the L-L aggregation (third quadrant). Most of them are located in the central and western regions and have abun-

dant natural resources. Early economic development relied heavily on energy-intensive businesses like heavy industry. Energy efficiency has improved in recent years, but there is still a lot of room for improvement, and an upgrade of the industrial structure is on the horizon. Guangdong is the typical province in the H-L cluster (quadrant 4), indicating that its energy efficiency is improving quicker than that of its neighbors Fujian, Jiangxi, Hunan, Guangxi, and Hainan. The energy efficiency of China's 30 provinces showed an obvious spatial imbalance. The energy efficiency of the

Table 3: China's 2012-2017 global Moran's I Index of energy efficiency.

year	I	E(I)	sd(I)	z	p-value
2012	0.158	−0.034	0.112	1.727	0.042
2013	0.126	−0.034	0.111	1.441	0.075
2014	0.149	−0.034	0.111	1.647	0.050
2015	0.149	−0.034	0.111	1.647	0.050
2016	0.178	−0.034	0.112	1.897	0.029
2017	0.347	−0.034	0.111	3.442	0.000

central and western provinces showed a concentration of low efficiency, while the energy efficiency of the southeast coastal areas showed a concentration of high efficiency. The whole presents a stepped distribution.

Spatial Panel Model Analysis

Before analyzing the spatial panel model, it is necessary to judge the choice of SEM, SLM, or SDM through the LM test, Wald test, and LR test. Through the LM test, LM-Error and robust LM-Error, LM-Lag, and robust LM-Lag all reject the null hypothesis at the 1% significance level, that is, it is considered that there is a spatial error or a spatial lag. The spatial Durbin model is general in spatial econometrics. It can be judged whether SDM can be simplified to SAR or SEM through the Wald test and LR test. According to the test results, the p-values of the Wald test and LR test are both 0.000,

that is, the SDM model is the best. Then through the Hausman test to determine whether to choose a fixed effect model or a random-effect model, the Hausman statistic is 88.84, the p-value is 0.000, and the null hypothesis of random effects is rejected at the 5% significance level, so the fixed effect model is constructed. In addition, to eliminate the influence of heteroscedastic and autocorrelation, a fixed-effects model with modified heteroscedasticity and autocorrelation robust standard errors is used. The estimation results comparing the traditional panel model and the spatial panel model are shown in Table 4.

In the fixed-effects model with traditional panel modified heteroscedasticity and autocorrelation robust standard errors, the level of economic development has a positive and significant impact on energy efficiency. The level of urbanization, the intensity of environmental regulations,
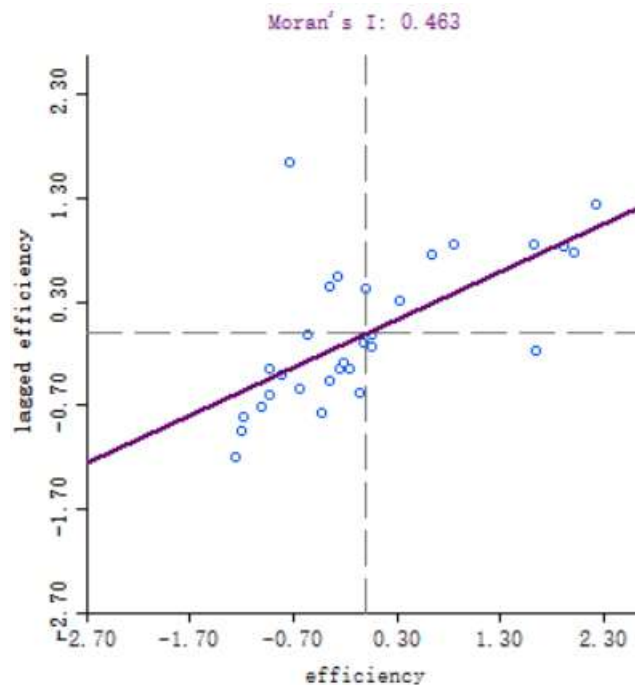
Fig. 1: Moran's I scatter plot.

Table 4: Model estimation results.

variable	A fixed-effects model with traditional panel modified heteroscedasticity and autocorrelation robust standard errors		Individual time double fixed effect spatial Durbin model	
	coefficient	p-value	coefficient	p-value
lnX1	0.512	0.007	0.988	0.000
lnX2	−1.573	0.002	−0.698	0.061
lnX3	0.005	0.875	−0.050	0.243
lnX4	−0.002	0.938	0.100	0.420
lnX5	−0.039	0.049	−0.053	0.031
lnX6	0.061	0.179	0.034	0.563
lnX7	−0.085	0.003	−0.038	0.254
W*lnX1			−1.258	0.000
W*lnX2			0.764	0.167
W*lnX3			0.271	0.001
W*lnX4			0.241	0.411
W*lnX5			0.050	0.251
W*lnX6			0.407	0.003
W*lnX7			−0.200	0.006

and foreign direct investment have a significant negative impact on energy efficiency. Compared with the traditional panel model, the spatial panel model considers the combined effects of the spatial error term and the spatial lag term, so it can more scientifically and reasonably reflect the direction and magnitude of the effects of various influencing factors. In the individual-time double fixed-effect spatial Durbin model, there is a significant positive impact on the level of economic development and a significant negative impact on the level of urbanization and the intensity of environmental regulations.

Then use the individual time double fixed effect spatial Durbin model to decompose its effects into direct effects, spillover effects (indirect effects), and total effects. The results are shown in Table 5.

In terms of direct effects, the level of economic development has a significant positive impact on energy efficiency, indicating that economic development can improve energy efficiency. With the continuous development of the economy and the improvement of the level of industrialization, a large number of advanced equipment and technologies have entered production and life, which has promoted the improvement of energy efficiency. The level of urbanization and the intensity of environmental regulations in the region have a significant negative impact on energy efficiency, indicating that the improvement of the two will reduce energy efficiency. The reason is that the acceleration of urbanization will increase people's demand for infrastructure, promote the rise of high-polluting industries such as steel and cement, and

Table 5: Effect decomposition results of spatial Durbin model.

variable	Direct effects		Spillover effects		Total effects	
	coefficient	p value	coefficient	p value	coefficient	p value
lnX1	1.017	0.000	−1.284	0.000	−0.267	0.303
lnX2	-0.731	0.046	0.818	0.123	0.087	0.869
lnX3	−0.050	0.232	0.259	0.002	0.209	0.005
lnX4	0.094	0.447	0.212	0.436	0.306	0.260
lnX5	−0.055	0.025	0.053	0.227	−0.002	0.965
lnX6	0.029	0.602	0.378	0.005	0.408	0.008
lnX7	−0.033	0.330	−0.185	0.009	−0.218	0.005

increase the demand for living energy, thereby inhibiting the improvement of energy efficiency. Increasing the intensity of environmental regulations means increasing the amount of pollution charges levied on enterprises. The environmental regulations are closely linked to the market, guide enterprises through market signals, and can produce continuous stimulus to enterprises. However, under the influence of the current factor market distortions in China, the deepening of regional capital is mainly biased towards high energy consumption and high pollution heavy chemical industries, making it difficult to achieve the incentive effect of environmental regulations on enterprise technological innovation, thereby inhibiting the improvement of energy efficiency.

The impact of energy structure, energy prices, technological innovation, and foreign direct investment on energy efficiency is not significant. In terms of energy structure, natural gas is low-carbon energy. Increasing its consumption can reduce pollution and improve energy efficiency. However, excessive natural gas consumption will cause a waste of energy. When energy is not fully utilized, energy efficiency will be inhibited and can't be improved, so the impact of energy structure on energy efficiency is not significant. In terms of energy prices, although price increases will force companies to invest in R&D of energy-saving and emission-reduction technologies, thereby improving energy efficiency. However, due to the time lag in the transmission mechanism of energy prices, the stricter price control of local governments, and the competition mechanism and monopoly mechanism among enterprises, it is difficult to form unified pricing in the energy market, which leads to inefficiency. Therefore, the impact of energy prices on energy efficiency is not significant. In terms of technological innovation, although technological progress can improve energy efficiency and reduce energy consumption, it will also produce a "rebound effect", thereby promoting economic growth, leading to an increase in energy demand and reducing energy efficiency. Therefore, the impact of technological innovation on energy efficiency is not significant. In terms of foreign direct investment, foreign investment can introduce advanced technology and efficient and cutting-edge production management methods to promote energy efficiency. However, excessive foreign investment will bring in a large number of foreign investment companies, including high energy consumption and high pollution companies, which will inhibit the improvement of energy efficiency. Therefore, the impact of foreign direct investment on energy efficiency is not significant.

In terms of spillover effects, adjacent areas' energy structures and technology innovation have a positive and considerable spillover effect on the region's energy efficiency, with the technological innovation spillover effect being bigger than the energy structure. The economic development level and foreign direct investment of neighboring regions have a significant negative spillover effect on the energy efficiency of the region, and the negative spillover effect of the economic development level is greater than that of foreign direct investment. The level of urbanization, energy prices, and the intensity of environmental regulations in neighboring regions do not have a significant impact on the energy efficiency of the region.

CONCLUSION

First and foremost, this paper uses the Super-SBM model to measure the energy efficiency of 30 provinces in China from 2012 to 2017 and finds that most provinces are increasing year by year. There is an obvious imbalance in energy efficiency among provinces, gradually decreasing from the east coast to the west inland; Besides, through the global Moran index test and the local Moran scatter plot, it is judged that energy efficiency has spatial correlation; Last but not least, the SDM model is judged by LM test, Wald test, and LR test, and the fixed effect model is judged by Hausman test. When the fixed-effects model is compared to traditional panel modified heteroscedasticity and autocorrelation robust standard errors, as well as the individual-time double fixed-effect spatial Durbin model, it is discovered that the latter can more scientifically and reasonably reflect the direction and magnitude of various influencing factors. Decomposing the effects of the individual-time double fixed-effect spatial Durbin model. In terms of direct effects, the level of economic development has a significant positive impact on energy efficiency, while the level of regional urbanization and the intensity of environmental regulations have a significant negative impact on energy efficiency, and other indicators are not significant. In terms of spillover effects, the positive spillover effects of technological innovation are greater than the energy structure, the negative spillover effects of economic growth are greater than foreign direct investment, and other indicators are not significant.

The recommendations are as follows: To start with, according to the spatial relevance of energy efficiency, promote the free flow and optimal allocation of energy between regions, thereby improving energy utilization efficiency. The improvement of energy efficiency in neighboring regions is conducive to the improvement of energy efficiency in the region. It is necessary to strengthen the coordinated development of energy efficiency between the region and neighboring provinces. In addition, develop the level of economic development in the region, increase per capita GDP, improve people's quality of life, strengthen inter-regional economic cooperation and technological exchanges, and thereby im-

prove energy efficiency. But at the same time, it is necessary to avoid the negative spillover effect of the economic development of neighboring regions on the region. To improve the coordinated economic development between areas, the government should adopt corresponding guiding policies. Finally, provinces with higher energy efficiency should maximize the positive spillover effects of energy structure and technological innovation by encouraging neighboring regions to improve their energy structure and technological innovation, thereby improving energy efficiency and narrowing the energy efficiency gap. Deepen structural reforms on the energy supply side, expand expenditures for technology development, and enhance China's energy self-sufficiency.

ACKNOWLEDGEMENTS

REFERENCES

Cui, Q., Kuang, H.B., Wu, C.Y. and Li, Y. 2014. The changing trend and influencing factors of energy efficiency: The case of nine countries. Energy, 64: 1026-1034.

Dai, J. and Fu, Y.M. 2020. The impact of environmental regulation and industrial structure on energy efficiency. Chinese J. Agric. Resour. Region. Plan., 41(9): 55-63.

Guan, W. and Xu, S.T. 2015. Study on spatial pattern and spatial effect of energy eco-efficiency in China. Acta Geogr. Sin., 70(6): 980-992.

Li, J.C., Yang, S. and Zhao, N. 2014. The analysis of influence factor on China's energy efficiency: Based on the quantile regression model. J. Bus. Econ., (12): 73-80.

Liu, C., Kong, X.L. and Gao T.M. 2008. Empirical analysis of changes in China's industrial sector energy consumption intensity and influential factors. Resour. Sci., (9): 1290-1299.

Jiang, H. and Ji, C.J. 2020. Could the OFDI reverse technology spillovers improve the energy efficiency of China? J. Audit Econ., 35(3): 102-110.

Meng, Q.C., Huang, W.D. and Rong X.X. 2016. Energy efficiency calculation and analysis on potentials of energy conservation and emissions reduction under haze environment-Based on the NH-DEA model of multiple undesirable outputs. Chinese J. Manag. Sci., 24(8): 53-61.

Qin, Q.D., Li, X., Chen, X.D. and Li, L. 2016. Energy efficiency analysis of China's twelve eastern coastal provinces considering undesirable outputs. Sci. Technol. Manag. Res., 36(4): 54-58.

Ruipeng, T. and Boqiang, L. 2017. What factors lead to the decline of energy intensity in China's energy-intensive industries? Energy Econ., 71: 213-221.

Song, Y.F., Zhang, S.P. and Han, N. 2020. Evaluation of energy efficiency and analysis of influencing factors in coastal areas. J. Xi'an Shiyou Univ. Soc. Sci. Edn., 29(5): 1-8.

Tone, K. 2003. Dealing with undesirable outputs in DEA: A slacks-based measure (SBM) approach. Grips Res. Rep., (3): 498-509.

Wang, H.W., He, X.L. and Ma, J.H. 2011. The analysis of the energy efficiency and its influence factors in TianJin. Energy Proc., 5: 1671-1675.

Wang, J., Lv, K.J., Bian, Y.W. and Cheng, Y. 2017a. Energy efficiency and marginal carbon dioxide emission abatement cost in urban China. Energy Policy, 105: 246-255.

Wang, Q.W., Zhao, Z.Y., Zhou, P. and Zhou, D.Q. 2013. Energy efficiency and production technology heterogeneity in China: A meta-frontier DEA approach. Econ. Model., 35: 283-289.

Wang, T., Yan, L. and Yi, M. 2017b. Research on China's energy eco-efficiency evaluation. Macroeconomics, (7): 149-157.

Wang, Y.L. and Zhong, A. 2015. An empirical test of environmental regulation, innovation ability, and total factor energy efficiency in the industrial industry. Statist. Decision, (15): 139-142.

Wang, Z.X., Qi, Z.Y., Xu, H.L. and Niu, X.X. 2018. Research on the evolution trend of China's energy efficiency based on environmental constraints. Modern Manag. Sci., (1): 81-84.

Wu, C.Q. and Du, Y. 2018. Research on the effect of biased technical change on the total factor energy efficiency of the Yangtze River Economic Belt. China Soft Sci., (3): 110-119.

Yao, S., Dan, L. and Rooker, T. 2012. Energy efficiency and economic development in China. Asian Econ. Papers, 11(2): 99-117.

Zhou, S.J. and Zhang, G. 2016. A study on the regional comparison of Chinese total factor energy efficiency considering environmental effect. East China Econ. Manag., 30(4): 63-67.

Impressions of Coastal Communities on Climate Change and Livelihood: A Case Study of Coastal Maharashtra, India

Ravi Sharma*†, Shrishti Jagtap* and Prakash Rao*

*Symbiosis Institute of International Business (SIIB), Symbiosis International (Deemed University) (SIU), Pune-411057, India
†Corresponding author: Ravi Sharma; ravi.sharma@siib.ac.in

ABSTRACT

The socio-economic and institutional systems of a developing country like India have a big role in the effects of perception on the choice of adapting capability. The study uses exploratory factor analysis to better understand these implications in a regional context (EFA). Therefore, survey research is carried out in Sindhudurg district of coastal Maharashtra, with 410 respondents, assessing perception. EFA leads to the unpacking of latent constructs evaluating the perception of climate change, which in turn affects adaptive capacity and livelihood resilience. These constructs are biophysical impact cognition, motivation to change, economic diversification, and adaptive skills, which together account for 50% of coastal fishermen's perception of climate change. Multivariate analysis of variance (MANOVA) revealed differences in the interpretation of these factors among coastal fishermen from various backgrounds (MANOVA). Overall, the research emphasizes the importance of perception in determining adaptive choices and resilience. According to the findings, developing adaptation-friendly infrastructural areas is recommended for society's resilient functioning.

INTRODUCTION

Climate change is a global phenomenon that affects all countries, but its impact and adaptive capacity differ largely depending upon the geographical and socio-cultural context (Adger et al. 2005). As evident from the climate change estimates, coastal ecosystems are the most impacted by the current climate altercations and are largely exposed to climate hazards (IPCC 2014, Checkley et al. 2017). Coastal ecosystems are mainly endangered due to sea-level rise, extreme weather patterns, temperature changes, and salt water erosion. Besides, coastal communities' ability to cope with these stressors is heavily influenced by the existing structural barriers (Salagrama 2012). Resource-dependent populations from such developing nations are more vulnerable to impacts (Chen 2020), with population, poverty, and illiteracy being prevailing challenges. To understand the local's perspectives, studying their perception is beneficial, which leads to the understanding of the underlying dimensions of the socio-cognitive construction process of climate change reality.

In diverse countries like India, there are differences in climate change perception and preference for adaptive behaviors. Therefore, to understand the region-specific cognitive patterns, relatively underexplored western coastal regions, particularly the coastal villages of Maharashtra state are explored for this research. According to the reports of Central

Marine Fisheries Research Institute, Kochi, 1-m sea-level rise in the next 10-40 years, will deluge almost 75 villages of coastal Maharashtra (Vivekanandan 2011). Research using the Cumulative Vulnerability Index (CVI) to examine the vulnerability of the Sindhudurg district found that it is extremely vulnerable due to its proximity to the coastline (Krishnan et al. 2018). According to a vulnerability impact assessment, 32 percent of coastal Sindhudurg is extremely vulnerable to climate change (Krishnan et al. 2018). According to the same study, due to a lack of access to medical facilities, urban regions, and natural resources, there is a high level of economic sensitivity. Due to population density, it exhibits low social sensitivity. It's crucial to understand how these vulnerabilities are seen in different parts of the world.

Research conducted in India showed that the coastal communities are affected by the changes in coastal ecosystems (Pandey & Jha 2012) and that the existing socio-economic structures affect them even more. Perception of inadequacy in terms of one's coping capabilities subsequently influences the choice of adaptive response (Madhanagopal & Pattanaik 2019). Coastal fishermen's subjective perception towards climate change vulnerability, experience related to adaptation, and beliefs influence their behavioral response to climate change. Studies earlier have pointed out how the study of climate change perception can help foster eco-friendly adaptation practices (Hasan & Kumar 2019).

This study attempts to study perception by assessing the existing choice of adaptation strategies made by coastal fishermen and finding whether they are sustainable and resilient. Adaptation strategies are further often linked with resilience capacities, suggesting how building sustainable capacity and local empowerment decreases the impacts of adverse climate conditions (Pomeroy et al. 2006). By measuring these broader aspects of vulnerability, adaptive capacity, and livelihood resilience, the study undertakes to identify the region-specific underlying dimensions that mold the perception of the coastal fishermen community with varied socio-economic demographics.

MATERIALS AND METHODS

Research Statement

The research envisages understanding the perception of the fishermen's coastal community towards vulnerability due to climate change. As a resource-dependent coastal community, their perception towards livelihood resilience and adaptive capacity were also deciphered in the current research, providing a grass-root perspective in formulating multifaceted adaptive strategies.

Research Question and Hypothesis

RQ1: What are the inherent elements shaping the perception of the coastal fishermen regarding climate change, adaptive capacity, and livelihood resilience?

Hypothesis-1: Exploratory factor analysis will be unsuccessful in extracting simple factors underlying fishermen's perception of climate change.

RQ2: What are the differences in the deduced factors using EFA between respondents with varied socio-demographic backgrounds (i.e. age, socio-economic position, number of income sources, kind of fishing equipment)?

Hypothesis-2: There is no significant difference across respondents with a varied socio-economic and demographic background in terms of the factor scores derived.

Instrument Design and Development Process

The survey questionnaire mainly consists of two segments: the first access the socio-demographic information of the respondents, while the other part is to assess the perception of coastal fishermen communities through measuring vulnerability, adaptive capacity, and resilience.

Socio-Demographic Items

Socio-demographic items contain the age group, gender, socio-economic status, Number of other income sources (occupational multiplicity), and type of fishing equipment used (traditional or modern). Socio-economic status was calculated as a composite score from the revised version of the Kuppuswamy socioeconomic scale (Saleem 2020), which is scored on three parameters of the educational and occupational status of the family head and aggregate income of the family, yielding a composite score for further classification of the household into lower, upper-lower, lower-middle, upper-middle or upper class. For the current research, only three socio-economic categories were considered: upper-lower class, lower-middle-class, and upper-middle class.

Perception Items

The survey questionnaire was used to perform the perception study, which included aspects from multiple frameworks for assessing vulnerability, adaptive capacity, and livelihood resilience (Bonan & Doney 2018). The climate change impression of coastal fishermen communities to climate change is mainly studied in terms of vulnerability, adaptive capacity, and livelihood resilience. It contains a total of 50 items measured on a five-point Likert scale, based on "level of agreement" giving a score of '5' to 'Strongly Agree', '4' to 'Agree', '3' to 'Neither Agree or Disagree', '2' to 'Disagree' and '1' to 'Strongly Disagree'. Each sub-dimension is measured by two items (Appendix A).

Vulnerability is assessed with two sub-scales of exposure and sensitivity. Exposure assesses the perception of respondents towards their situation, infrastructure, housing, production capacities, and other tangible human assets that could be adversely affected. The sensitivity subscale assesses the threat perception levels of respondents at an extent to which human systems are affected by the exposure to risks.

Adaptive capacity assesses respondents' perception of whether their systems are capable of adapting to climate variability, mitigating potential damage, exploiting opportunities, and coping with consequences (Marshall & Marshall 2007).

Livelihood resilience assesses the individual and community's competency to mitigate stresses and disruption, consequently reorganizing themselves through gaining new skills for smooth functioning of the societal structure (Speranza et al. 2014).

Pilot testing was conducted with 70 respondents (excluded from the main research study), conducted in the Vengurla tehsil of Sindhudurg district. The Cronbach alpha of 0.87 was obtained, with the reliability of the individual 50 items ranging from 0.84 to 0.89, suggestive of high reliability. Content validity of the scale was indicated as suitable for professionals in the field.

Survey

Data collection was done from the coastal villages of the Sindhudurg district of Maharashtra. Data collection included socio-demographic details and perception of individuals on vulnerability, adaptive capacity, and livelihood resilience to climatic fluctuations. Data was collected in person from the household heads and participation in the study was entirely voluntary. The questionnaire was in the local dialect (Marathi and Hindi) for the convenience of the locals. Confidentiality of respondents' information was ensured.

Study Area

The study was conducted in the Sindhudurg district of western Maharashtra state. The coastal villages from the Devgad, Malvan, and Vengurla tehsil of Sindhudurg were selected for the study (total village=41).

Target Population

For this research, coastal fishermen communities were the targeted population (*N=410*). Data from household heads with the primary or secondary occupation of fishery was collected. Respondents differed across demographic, socio-economic status, and type of equipment used.

Sampling Method

The multistage stratified random sampling method was to collect responses from the coastal fishermen community. Devgad, Malvan, and Vengurla Tehsil were identified for the study in the first stage and then 41 coastal villages from these tehsils by establishing the criteria of 2 km from the coastline and having coastal communities' habitats as per the Population Census 2011. Using the priori statistical analysis, the sample size of 368 was targeted and an actual sample size of 410 was collected.

Data Analysis

Principal axis factoring (PAF) and oblimin rotation were used to evaluate the data. The skewness and kurtosis values were checked for univariate normality, and values between ±2 were found to be acceptable. The scale's overall dependability was 0.89, which is higher than the allowed level of 0.7. (Fabrigar et al. 1999). In the initial stage of EFA, data was screened for sampling adequacy using Kaiser-Meyer-Olkin (KMO) measure of sampling adequacy (>0.5) and Bartlett's test of sphericity ($p < 0.05$). KMO, Bartlett's tests, and determinant of correlation matrix were again examined during the final stage of the EFA process as validation checks. The scree plot and parallel analysis were used to predetermine the number of extracted factors and Communalities > 0.2 were acceptable. The general linear model of Multivariate analysis of variance (MANOVA) was also used, with discriminant function analysis (DFA) as a *post-adhoc* measure, to measure the perceived differences across respondents with varied

Table 1: Socio-demographic features of the coastal fishermen (N=410).

Socio-demographic factors	Frequency	Percentage
Age group		
21 to 30	16	3.9
31 to 40	143	34.9
41 to 50	195	47.6
51 to 60	48	11.7
61 to 70	8	2
Socio-economic Status		
upperlc	104	25.4
lowermc	302	73.7
uppermc	4	1
Occupational Multiplicity		
single	367	89.5
multiple	43	10.5
Fishing Equipment Used		
traditional	266	64.9
modern	144	35.1
Total	410	100

socio-demographic characteristics. Besides correlational analysis using Pearson product-moment correlation was also conducted. The statistical analysis is done using IBM SPSS V26.0, and R- statistical software version 4.0.5.

RESULTS AND DISCUSSION

Respondents Socio-Demographic Profile

This study included 410 coastal fishermen from various socioeconomic backgrounds, age groups, types of fishing equipment used, and a number of household livelihood sources (Table 1).

Data Screening

The raw data was cleaned, coded, and classified into suitable categories for ease of statistical analysis. Negative items were reverse coded. There was no missing data in the current research. Univariate analysis of 50 variables was done and

mean, standard deviation (S.D), skewness, and kurtosis of the sample data were examined. The total mean was 3.38 (S.D = 1.22) ranging from 2.18 to 4.14, with an S.D ranging from 0.92 to 1.50. Histogram, box plots, and QQ plots were also examined suggesting normality. The skewness ($< \pm 2$) ranged from - 1.40 to 0.58. The kurtosis ranges from ($< \pm 2$) ranging from -1.42 to 1.14. Shapiro-Wilk's test indicated significant univariate normality W (410) = 0.8712, p< 0.01.

EFA

EFA was performed on the data collected (n=410), using the PAF, rotation method being direct oblimin. A correlation matrix was generated based on Pearson product-moment correlation coefficients (Fig. 1). Firstly, the correlation matrix was examined, with a sizable number of variables having correlation exceeding ± 0.3 and no variable having inter-correlation exceeding ± 0.8, suggesting factorability of the data. Second, the KMO measure of sampling adequacy
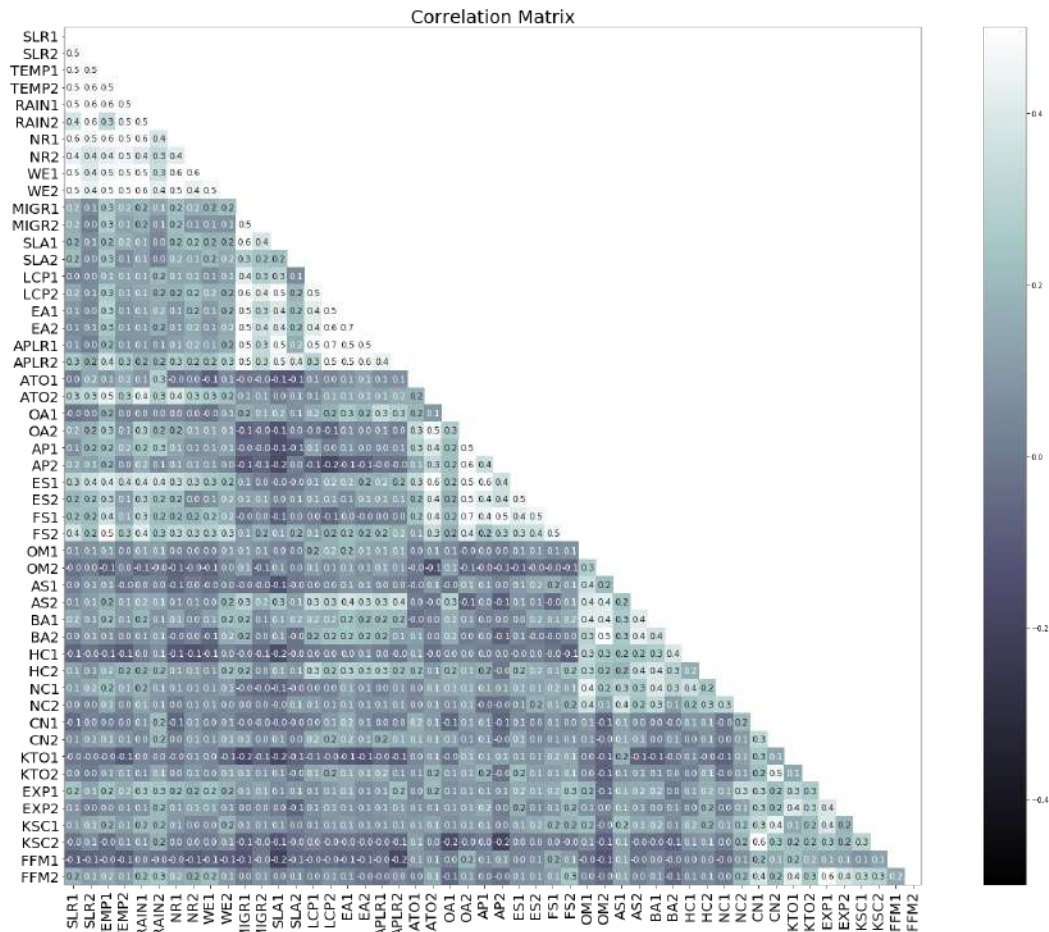
Fig.1: Pearson correlation matrix of 50 variables.

was found to be 0.87, which is 'meritorious'. Bartlett's test of sphericity was (χ2 (1225) = 9452.57, p < .001), indicating the correlation matrix is significantly different from the identity matrix, hence factorable.

The exploratory factor was run on 50 variables using the principal axis factoring technique. The initial analysis yielded a 12-factor solution. Items NR2, SLA2, EA1 cross-loaded significantly on more than one factor, whereas OA2 and FFM1 didn't load significantly on any factor, therefore they were deleted and the EFA was again repeated. The same process was repeated 5 times, and items RAIN2, ATO2, AP1, ES1, HC1, SLA2, AS2, BA1, HC2, ATO1, KTO2, CN2, EXP1, KTO1, EXP2, FFM2, and NC2 were removed due to cross-loading, absence of loading on any factor, less than 3 variables with loadings < 0.4. After many iterative steps and elimination of the above variables, a total of 24 variables were retained for final factor analysis. A final validation check was run on the 24 variables, yielding a meritorious KMO value of 0.87, and Bartlett's test of sphericity (χ2 (276) =4354.86, p< .01) was also significant. The determinant of the correlation matrix was 0.000019 (higher than the critical value of 0.00001). In the final factor analysis stage, PAF with an oblimin rotation was used. The decision regarding the number of factors to be extracted was taken using a Scree plot and parallel analysis. Scree plot suggested a total of

four factors (Fig. 2). From the parallel analysis, adjusted eigenvalues greater than 1 are retained, also suggesting four factors. Further using the oblimin method of rotation, a theoretically meaningful four-factor solution emerged (Table 2).

Total four factors emerged from the analysis which explained 50 % of the total variance. The first factor consists of 8 items: SLR1, SLR2, TEMP1, TEMP2, RAIN1, NR1, WE1, and WE2, explaining 35% of the variance. The second group of factors consists of 8 items: MIGR1, MIGR2, SLA1, LCP1, LCP2, EA2, APLR1, and APLR2, explaining 34 % total variance. The third group of factors consists of four items: OA2, AP2, ES2, and FS1, explaining 19 % of the variance. The final fourth group of factors consists of four items: OM1, OM2, BA2, and NC1, explaining 12% of the variance. The first factor was labeled as *"biophysical impact cognition"*. The 2nd factor was labeled as *"Motivation to change"*. The 3rd factor was labeled as *"Diversification"*. The 4th factor was labeled as *"Adaptive skills"* according to the item relations within these groups as supported by the literature. Correlations between factors ranged from -0.02 to 0.33. Finally, the reliability analysis was also conducted for each factor using Cronbach's alpha, with all the factors having reliability $\geq$ 0.7 which is considered good (biophysical impact cognition= 0.9, Motivation to change= 0.88, diversification= 0.81, and Adaptive skills= 0.7). The values for
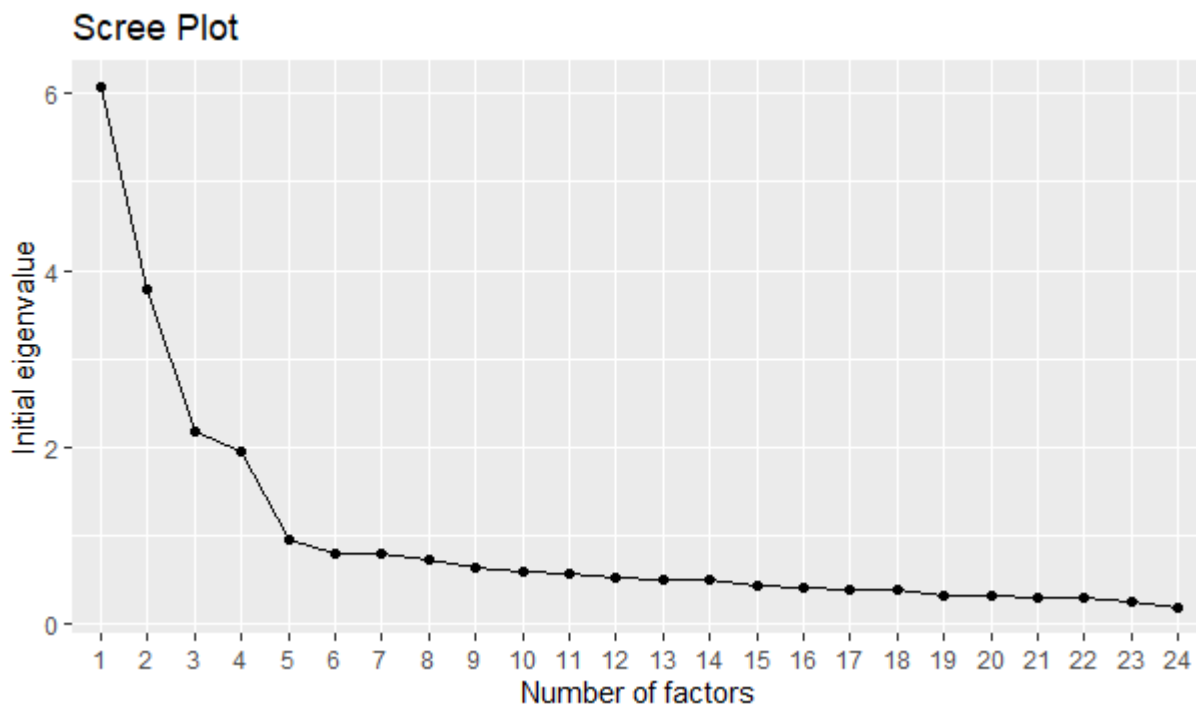
Fig. 2: Scree plot for the number of factors to be extracted.

Table 2: Pattern matrix of the factors derived from EFA

Item code	1	2	3	4	h2
SLR1	0.76				0.57
SLR2	0.69				0.47
TEMP1	0.61				0.58
TEMP2	0.76				0.53
RAIN1	0.74				0.62
NR1	0.76				0.6
WE1	0.68				0.46
WE2	0.7				0.51
MIGR1		0.77			0.63
MIGR2		0.55			0.31
SLA1		0.66			0.49
LCP1		0.54			0.31
LCP2		0.82			0.68
EA2		0.74			0.54
APLR1		0.76			0.57
APLR2		0.59			0.45
OA2			0.89		0.78
AP2			0.64		0.43
ES2			0.55		0.35
FS1			0.8		0.68
OM1				0.51	0.29
OM2				0.59	0.36
BA2				0.66	0.48
NC1				0.56	0.35
SS loadings	4.27	3.95	2.34	1.48	
Proportion Explained	0.35	0.33	0.19	0.12	
Cumulative Variance	0.18	0.34	0.44	0.50	
Cumulative Proportion	0.35	0.68	0.88	1	
Cronbach's alpha	0.9	0.88	0.81	0.7	

h^2 = communalities

variables in the community were all > 0.2, thus they were not eliminated. There were also roughly 11% non-redundant residuals ($p > 0.05$), which was much below the crucial levels and hence acceptable. Four-factor solutions were obtained from the EFA. As a result, our null hypothesis is rejected.

MANOVA

MANOVA is conducted depending on the factors that emerged from the EFA. The factors scores were derived using a refined regression method. Age, socioeconomic status, and the number of income sources are the independent variables with many levels, whereas these regression component scores

are employed as dependent variables. DFA was used as a post hoc approach to identify dependent variables that are linearly connected to grouping variables.

Age and Factor Scores

Age variable was divided into five age groups, with 21 to 30 years of age group (n=16), 31 to 40 years (n=143), 41 to 50 years (n=195), 51 to 60 years (n=48) and 61 to 70 years (n=8). Box's test was significant (Box's M=82.165, p.05), indicating that dependent variable covariance is not equal across groups. As a result, the Pilla's Trace criterion was applied, revealing a significant difference in factor

scores across age groups (V=.35, F[16, 1220]=9.64, p< 0.01). After MANOVA, the DFA was used as a post hoc test. The first function explained 95.1% of the variation, the second 4.2%, the third function 0.6% of the variance, and the fourth function 0.1% of the variance, with canonical R^2 values 0.57, 0.14, 0.05, and 0.02 respectively. When all the functions are tested in combination, Wilk's λ has the value .660($\chi 2(16)$=167.99, p=0.000), which indicates that all the functions in combination significantly discriminate between the age groups. Removing 1 function did not significantly discriminate between age groups (λ = .98, $\chi 2(9)$=9.81, p=.366). Further removing the 2nd function also produced non-significant results (λ=.98, $\chi 2$ (4)=1.28, p=.867) and same with removing 3rd function (λ=1, $\chi 2(1)$=.14, p=.71). Biophysical impact cognition loaded fairly high on the 1st (r=.75) and 2nd (-.53) functions than on 3rd (r=.18) and 4th (r= -.37) functions. Motivation to change loaded significantly on the 2nd function (r =.644). The 2nd function (r =.644) was heavily loaded with motivation to change. The first function discriminated participants in the age groups 21- 30 and 31- 40 from respondents in the age groups 41- 50, 51- 60, and 61- 70, according to the discriminant functions estimated at group means. The second function discriminated respondents aged 31 to 40 and 41 to 50 from those aged 21 to 30, 51 to 60, and 61 to 70. The third function discriminated the age groups of 21- 30 and 41- 50 from those of 31- 40, 51- 60, and 61- 70. The fourth function, on the other hand, discriminated 51- 60 from 21- 30, 31- 40, 41- 50, and 61- 70.

Socio-Economic Status and Factor Scores

Respondents were divided into three socio-economic categories that are upper lower class (n=104), lower middle class (n=302), upper-middle-class (n=4), whereas none of the respondents fitted in the upper class and lower-class categories. Box's test was significant, violating the assumption of covariance equality across categories (Box's M=30.38, p=0.001). Pilla's Trace criterion showed a significant difference in factor scores across socio-economic categories (V=.524, F[8, 810]=35.98, p=0.00). With DFA two functions were identified, with the first explaining 99.6% of the variance, and the second explaining 0.4%, with canonical R^2 of .72 and .07 respectively. When all the functions are tested in combination, Wilk's λ has the value .478 ($\chi 299.29$=(8)2, p=.000) which indicates that all the functions in combination do significantly discriminate between the socio-economic categories. Removing the 1st function did not significantly discriminate between socio-economic categories (λ=.995, $\chi 2$ (3)=1.85, p=.604). Biophysical impact cognition (r=0.66) and motivation to change (r=.37) loaded significantly on 1st function while diversification (r=.804) and adaptive skills (r=-.63) loaded significantly on 2nd function. The discrimi-

nant function analysis shows that 1st function discriminates Upper-lower class from lower-middle-class and upper-middle-class, whereas 2nd function discriminates lower-middle class from upper-lower class and upper-middle class.

Occupational Multiplicity and Factor Scores

Respondents were divided into two categories of occupational multiplicity: a single source of income (n=367) and multiple/ alternative sources of income (n=43). Box's test was non-significant assuming equality of covariance (Box's M=13.35, p=0.231). Pilla's Trace criterion showed a significant difference between socio-economic categories (V=.030, F[4, 405]=3.094, p=0.016). One function was identified using DFA, explaining 100% variance and canonical R^2 of .17. Wilk's λ has a value of .970($\chi 2(4)$=12.22, p=.016) which indicates that the function does significantly discriminate between the occupational multiplicity categories. Biophysical impact cognition (r=0.74), motivation to change (r=.69), diversification (r=.44) and adaptive skills (r=.42) loaded significantly on 1st function. The discriminant function analysis shows that 1st function discriminates between single and multiple sources of income.

Fishing Equipment Used and Derived Factors

Respondents were divided into two categories based on the type of fishing equipment they used: traditional (n=266) and modern (n=144). Box's test was significant, rejecting the hypothesis of covariance equality across groups (Box's M=7.82, p=0.65). Pilla's Trace criterion showed no significant difference across fishing equipment (V=.003, F[4, 405]=0.267, p=0.899). DFA was not conducted as there was no significant difference between the categories.

CONCLUSION

From the EFA conducted, four factors emerged: biophysical impact cognition, motivation to change, diversification, and adaptive skills. The factor biophysical impact cognition indicates the importance of cognition in the perceptual process. It helps to understand the individual's and community's construal of climate variability. The motivation to change factor indicates that risk perception and accurate representation of reality motivates adaptive behavior. Diversification of the economy aids resource-dependent communities in adapting to climate change. The development of adaptation skill components emphasizes their role in the interpretation of climatic variations. In keeping with earlier research, this study finds considerable variances among age groups, socioeconomic situations, and a variety of employment sources (Haq & Ahmad 2017). The emergence of elements underpinning coastal fishermen's perceptions, which provide a theoretical

framework for assessing their perceptions, properly addresses research questions. Null hypotheses are rejected based on the above findings.

These derived factors are perceived differently by coastal fishermen with different backgrounds. Besides these factors have strong relationships with various dimension aspects of adaptive capacity, highlighting the importance of perception in adaptive behaviors. This study assesses the factors influencing the current perception, which shadows its sensory and temporal nature, which is largely subject to biases. Therefore, in future longitudinal studies assessing the perception over a time span, specifically before and after extreme climate events and examining the biases in perceptual processes should be addressed. Generating a sustainable adaptive response requires communities to gain profound cognizance of climate variations, as opposed to the heuristic perception of the complex issue. It is critical to educate community members to assist them in adapting. To attain these goals, further study should be conducted on how to lower the barriers to achieving adaptive capacity and what coping skills should be instilled in coastal communities.

ACKNOWLEDGEMENT

APPENDIX A

Perception Study Indicators and coding

Exposure Indicator	Items(code)
Sea level rise	When the sea level rises, my occupation suffers (SLR1)
	The sea-level rise does not affect my occupation (SLR2)
Temperature	When temperature changes, my occupation gets affected (TEMP1)
	The work was smoothly carried out independent of temperature (TEMP2)
Rainfall	Rainfall changes affect my occupation. (RAIN1)
	occupation doesn't get affected by rainfall (RAIN2)
Natural Resource	completely dependent on the natural resources for livelihood (NR1)
	My family members perceive that NR are in abundance (NR2)

Cont....

Exposure Indicator	Items(code)
Weather Events	Extreme weather in last few years, either it's too hot or too cold (WE1)
	weather events are seasonal and not too extreme (WE2)
Sensitivity Indicator	
Migration to the non-coastal area	I am very attached to my place (MIGR1)
	The present area of living is highly sensitive to climatic changes; therefore planning to shift away from coastal areas (MIGR2)
Supplemental livelihood activities	Engaged with other occupations along with my current (SLA1)
	need to switch to different occupations due to changes in climate (SLA2)
Local Conservation Planning	interested in participating in the planning and execution of adaptation measures locally (LCP1)
	find it very difficult to adopt conservation measures (LCP2)
Environmental Awareness	Do not have access to multiple channels and schemes on environmental initiatives by Govt (EA1)
	I am not aware of any environmental institution in our region (EA2)
Adaptive Capacity Indicator	
Ability to plan, learn, reorganize	have knowledge of all the requirements needed for my current occupation (APR1)
	If any abrupt change in my job, don't have any immediate plan to handle it. (APLR2)
Attachment to occupation	I cannot imagine myself suitable to get fitted in any other job (ATO1)
	Compared to others, I am more likely to adapt to the environmental change and my occupation (ATO2)
Occupational adaptability/flexibility	I am satisfied with my current job, and no plan to change my occupation (OA1)
	For business decisions, I always seek professional advice (OA2)
Attachment to place	I plan to be a long-term resident of this community (AP1)
	I will leave my current place if get a better opportunity elsewhere (AP2)
Employment Security	If there are any more changes, I won't survive much longer in this work (ES1)
	If I decide to leave my job, I have many options available to me(ES2)
Financial security	financially secured my current occupation in case of natural calamity (FS1)
	have financial arrangements already planned to execute interesting ideas to make my work more sustainable (FS2)

Cont....

Exposure Indicator	Items(code)
Occupational Mobility	In the last five years, the voluntary change observed in occupational patterns in my area. (OM1)
	I'd be nervous to try something else than what I'm doing now (OM2)
Access to services	prefer to use different and newer technologies in my job (AS1)
	Good basic education is far from my area (AS2)
Business approach	Skilled to build my own business rather than my current occupation (BA1)
	Not skilled to start a new business (BA2)
Livelihood Resilience Indicator	
Human Capital	live very close to the available nearby health facility (HC1)
	the average period of occupation reduces when there is a natural calamity (HC2)
Natural Capital	I can make full use of natural resources as per my skills (NC1)
	availability of natural resources during the peak season of a year (NC2)
Cooperation & Area Networks	support from local organizations and networks (CN1)
	groups and their decisions are often not much fruitful (CN2)
Knowledge of threats and opportunities	ability to analyze threats and the potential to adapt to the risks (KTO1)
	I recognize threats when they are very closer (KTO2)
Experimentation	I always have the zeal to learn new methods and skills for my job (EXP1)
	I am unable to think of any innovative ideas to improve my work conditions (EXP2)
Knowledge sharing capacity	learned new methods of carrying out my work from the community (KSC1)
	not able to share my skills with others (KSC2)
Functioning feedback mechanisms	Community member frequent contact with local institutions and learning new ideas (FFM1)
	community members help me to understand the current changes and through management response (FFM2)

REFERENCES

Adger, W.N., Arnell, N.W. and Tompkins, E.L. 2005. Successful adaptation to climate change across scales. Glob. Environ. Change, 15(2): 77-86.

Bonan, G.B. and Doney, S.C. 2018. Climate, ecosystems, and planetary futures: The challenge to predict life in Earth system models. Science, 359: 6375.

Checkley, D.M., Asch, R.G. and Rykaczewski, R.R. 2017. Climate, anchovy, and sardine. Annu. Rev. Mar. Sci., 9: 469-493.

Chen, J.L. 2020. Fishers' perceptions and adaptation on climate change in northeastern Taiwan. Environ. Dev. Sustain., 9: 1-24.

Fabrigar, L.R., Wegener, D.T., MacCallum, R.C. and Strahan, E.J. 1999. Evaluating the use of exploratory factor analysis in psychological research. Psychol. Methods, 4(3): 272.

Haq, S.M.A. and Ahmed, K.J. 2017. Does the perception of climate change vary with the socio-demographic dimensions? A study on vulnerable populations in Bangladesh. Nat. Hazards, 85(3): 1759-1785.

Hasan, M.K. and Kumar, L. 2019. Comparison between meteorological data and farmer perceptions of climate change and vulnerability in relation to adaptation. J. Environ. Manag., 237: 54-62.

IPCC. 2014. Summary for Policymakers. In: Field, C.B., Barros, V.R. and Dokken, D.J. (eds.), Climate change 2014: Impacts, adaptation, and vulnerability, Part A: Global and sectoral aspects. Contribution of working group II to the 5th assessment report of the intergovernmental panel on climate change. Cambridge University Press, Cambridge, pp. 414-456

Krishnan, P., Ananthan, P.S., Purvaja, R., Jeevamani, J.J.J., Infantina, J.A., Rao, C.S., Anand, R., Mahendra, R.S., Sekar, I., Kareemulla, K., Biswas, A., Sastry S.K. and Ramesh, R. 2019. Framework for mapping the drivers of coastal vulnerability and spatial decision making for climate-change adaptation: A case study from Maharashtra, India. Ambio, 48(2): 192-212.

Madhanagopal, D. and Pattanaik, S. 2019. Exploring fishermen's local knowledge and perceptions in the face of climate change: The case of coastal Tamil Nadu, India. Environ. Dev. Sustain., 17: 1-29.

Marshall, N.A. and Marshall, P.A. 2007. Conceptualizing and operationalizing social resilience within commercial fisheries in northern Australia. Ecol. Soc., 12(1): 54-64.

Pandey, R. and Jha, S. 2012. Climate vulnerability index-measure of climate change vulnerability to communities: A case of rural Lower Himalaya, India. Mitig. Adapt. Strateg. Glob. Change, 17(5): 487-506.

Pomeroy, R.S., Ratner, B.D., Hall, S.J., Pimoljinda, J. and Vivekanandan, V. 2006. Coping with disaster: Rehabilitating coastal livelihoods and communities. Mar. Pol., 30(6): 786-793.

Salagrama, V. 2012. Climate change and fisheries: perspectives from small-scale fishing communities in India on measures to protect life and livelihood. International Collective in Support of Fishworkers, Chennai, India, pp. 1-73.

Saleem, S.M. 2020. Modified Kuppuswamy socioeconomic scale updated for the year 2020. Indian J. Forensic Community Med., 7(1):1-3.

Speranza, C.I., Wiesmann,U. and Rist, S. 2014. An indicator framework for assessing livelihood resilience in the context of social-ecological dynamics. Glob. Environ. Change, 28: 109-119.

Vivekanandan, E. 2011. Marine fisheries policy brief-3; climate change and Indian marine fisheries. CMFRI Special Publ., 105: 1-97.

Original Research Paper | https://doi.org/10.46488/NEPT.2022.v21i02.014 | **Open Access Journal**

Check List of Species Richness and Abundance of Orthoptera Fauna in Bharathi Park, Coimbatore, Tamil Nadu, India

M. Suganya† and K. Manimegalai

Department of Zoology, Avinashilingam Institute for Home Science and Higher Education for Women, Coimbatore, Tamil Nadu, India

†Corresponding author: M. Suganya; suganyamuthu0294@gmail.com

ABSTRACT

Order Orthoptera is one of the largest and most important invertebrate groups for environmental monitoring and assessment. Orthoptera faunal composition was carried out at Bharathi Park, Coimbatore, Tamil Nadu, India to evaluate the present status of various species. PAST software was used to perform various statistical analyses to estimate the Orthoptera composition. Overall, 334 individuals belonging to 22 species, 19 genera, 17 tribes under 10 subfamilies, and four families of Orthoptera were recorded. Species richness (59.09%) and species abundance (70.06%) were recorded highest in the Acrididae family followed by Pyrgomorphidae, Tettigoniidae, and Gryllidae. Oedipodinae was the most species-rich (27.27%) and the most abundant subfamily, accounting for 30.24% of the total collected individuals. During the study period, 10 dominant, five intermediate dominance, four incidental, and three rare species were observed. Among these, *Spathosternum prasiniferum* was found to be the most dominant species (D=18.26) and the least dominant (D = 0.6) species was *Euconocephalus pallidus*. Based on the principal component analysis, the distribution of species along with the first two PCs (PC1= 33.87% and PC2=28.68%) accounted for the highest variance of the total variances. Cluster analysis showed that *Acrotylus humbertianus* and *Teleogryllus mitratus*, *Conocephalus maculates* and *Gryllus bimaculatus* Orthopterans were similar to each other. The value of the Shannon diversity index (2.27), Simpson index (0.87), Margalef index (2.2), and α-diversity (5.75) were higher in Acrididae when compared with other families. Value of Evenness (0.93) was highest in Gryllidae. Statistical analysis infers that the richness and abundance percentage of Orthopterans significantly varied between species to species and family to family.

INTRODUCTION

Recording the distribution of species composition in the ecosystem is an important step for identifying biodiversity hotspots and designing effective conservation strategies (Mirzaei et al. 2017). Insects are the most diverse component of the ecosystem, and they play a critical role in many areas of ecological stability (Millar 1993). Insects from the order Orthoptera are important grassland species that fulfil key ecological niches (Gandar 1982, Belovski & Slade 1993, Ryszkowski et al. 1993). Grasshoppers, crickets, katydids, and locusts are hemimetabolous and phytophagous insects that come under the order of Orthoptera. It is one of the largest orders of insects belonging to the monophyletic suborders Caelifera called short-horned Orthopterans it includes the family Acrididae, Pyrgomorphidae, Tetrigidae, and Ensifera called long-horned Orthopterans it includes family Tettigoniidae, Gryllidae, Haglidae, and Gryllotalpidae. The number of known species of Orthoptera found throughout the world is 27,260 species (Eades et al. 2016). Shishodia et al. (2010) reported 1033 species/subspecies belonging to 400 genera and 21 families of Orthoptera from India.

Orthoptera has become one of the most important invertebrate groups for environmental monitoring and assessment (Jamison et al. 2002). This group also plays a significant role in terrestrial food webs and is known to be a good source of protein for many other animals such as amphibians, birds, small reptiles, and mammals; therefore, their scarcity may disturb the trophic structure in an ecosystem (Schmidt et al. 1991, Soliman et al. 2017). Orthopterans have also been successfully used in biomonitoring the effects of changes in land management regimes (Gardiner et al. 2002, O'Neill et al. 2003) and in identifying the grasslands state of conservation (Báldi & Kisbenedek 1997, Andersen et al. 2001).

Insect diversity research is important because a high number of species are on the verge of extinction, which is a sign of environmental change. The diversity of Orthoptera has been studied by various researchers throughout India but in Coimbatore, Orthoptera diversity is rarely studied (Chitra et al. 2000, Lena et al. 2012, Divya & Senthilkumar 2017, Suganya et al. 2020.) However, no previous record is available on the diversity, richness, and abundances of Orthoptera in Bharathi Park, Coimbatore. Keeping in view, the species composition

of "Orthopteran" fauna was carried out in the present investigation. We believe that the result would offer distinctive information of varieties of Orthoptera species from this park.

MATERIALS AND METHODS

Study Area

Orthopteran diversity was conducted at Bharathi park. This place is located 4 km from the city of Coimbatore, Tamil Nadu, India. This place is the second-largest city in north-western Tamil Nadu located at 11°01'13.1"N 76°56'50.6"E in South India at 411 m (1349 ft) above sea level on the banks of the Noyyal river. To the west and north, it is surrounded by the western mountain range, with reserve forests of the Nilgiri Biosphere Reserve on the northern side. The mean maximum and minimum temperatures for Coimbatore city during summer and winter vary between 35°C to 18°C. The average annual rainfall is around 700 mm with the northeast and the southwest monsoons.

Collection of Grasshoppers

Using a sweep net and handpicking approach, Orthoptera fauna was collected twice a month from the study area in the morning (7 am to 9 am) and evening (4 pm to 6 pm) throughout the months of October 2019 to March 2020. In the morning and evening, Orthopterans were less active, and capturing was easy. The sweep net method generally provides an accurate estimation of grasshopper diversity on grasslands (Evans et al. 1983, Larson et al. 1999). Sweep net sampling is the most commonly used method to evaluate grasshopper species composition (Joshi et al. 1999).

Identification of Grasshoppers

Orthopterans were identified under a stereoscopic dissecting binocular microscope (MZ2000 Micros Austria) using the keys of Kirby (1914) and also referring to the Website (http://Orthoptera.SpeciesFile.org). After identification and counts of species were made, they were immediately released in the sampled site to avoid impoverishing the environment. A small number of the dominant and rare species were stored for further examination.

Data Analysis

The species richness was calculated as the total number of species present in the study site. Species abundance was calculated as a total number of individuals present in the study area according to a method by Buschini & Woiski (2008): D = (abundance of a species/total abundances recorded) × 100. If D was > 5%, the species was considered dominant; if 2.5% < D < 5%, the species was considered an intermediate

abundance, and if D < 2.5%, the species was considered an incidental species. Rare species were the ones that had less than five individuals. The statistical analysis of the data was done using the data analysis tool pack available in MS Excel 2010. Principal Component Analysis (PCA) was performed to study the pattern of variation between the species among different families of Orthoptera. Furthermore, cluster analysis was used to investigate the similarity and dissimilarity of species composition among four different families. The different diversity indices such as Shannon index, Simpson index, Margalef index, Evenness, and Renyi index were calculated to describe and compare the diversity of species among different families using the statistical software PAST (Paleontological Statistical Software) version 2.02 (Hammer et al. 2001).

RESULTS

The families, subfamilies, tribes, genera, and species of the Orthopterans collected are shown in Table 1. A total of 334 individuals belonging to 22 species, 20 genera, 17 tribes, and 10 subfamilies under four families were sampled from the study area (Table 1).

Species Richness

In this study, Acrididae was the most species-rich family with 13 species, which accounted for 59.09% of the total species recorded with 11 genera and nine tribes under five subfamilies. The second dominant family was Pyrgomorphidae, which had four species, four genera, and four tribes under two subfamilies, which accounted for 18.18% of the total collected species. Family Tettigoniidae ranked third with three species under three genera, three tribes, and two subfamilies, which accounted for 13.64% of the total species collected while the Gryllidae family had the least with two species, under two genera, one tribe and one subfamily which accounted for 9.09% of the total recorded species (Fig. 1). Among the 10 subfamilies of Orthopterans, Oedipodinae was found to be the most dominant subfamily with six species accounting for 27.27% of the total collected species. Next in order of dominant families were Gomphocerinae and Pyrgomorphinae with three species constituting 13.4% (Fig. 2).

Species Dominance (D)

Among the four families, abundance was recorded highest in Acrididade, n = 234 (70.06%), followed by Pyrgomorphidae, n = 52 (15.57%) and Gryllidae, n = 31 (9.28%) while Tettigoniidae had the least individuals, n = 17 (5.09 %) (Fig. 1). Out of the 22 species of Orthoptera, 10 dominant species, five species with intermediate dominance, four incidental species,

Table 1: Checklist of Orthopterans from Study area.

Family	Subfamily	Tribe	Species	(N)	(D)
Acrididae	Acridinae	Acridini	Acrida exaltata (Walker 1859)	7	2.1
		Phlaeobini	Phlaeoba infumata (Brunner von Wattenwyl 1893)	3	0.9
	Catantopinae	Catantopini	*Diabolocatantops pinguis* (Stal 1861)	12	3.59
	Gomphocerinae	Arcypterini	*Aulacobothrus luteipes* (Walker 1871)	15	4.49
			Crucinotacris decisa (Walker 1871)	8	2.4
		Dociostaurini	*Leva indica* (Bolívar 1902)	27	8.08
	Oedipodinae	Acrotylini	*Acrotylus longipes* (Charpentier 1845)	16	4.79
			Acrotylus humbertianus (Saussure 1884)	21	6.29
			Acrotylus insubricus (Scopoli 1786)	4	1.2
		Locustini	*Gsatrimargus africanus* (Saussure 1888)	9	2.69
			Oedaleus abruptus (Thunberg 1815)	19	5.69
		Trilophidiini	*Trilophidia annulata* (Thunberg 1815)	32	9.58
	Spathosterninae	Spathosternini	*Spathosternum prasiniferum* (Walker, 1871)	61	18.26
Pyrgomorphidae	Pyrgomorphinae	Atractomorphini	*Atractomorpha crenulata* (Fabricius 1793)	17	5.09
		Chrotogonini	*Chrotogonus oxypterus* (Blanchard 1836)	6	1.8
		Tagastini	*Tagsta indica* (Bolivar 1905)	11	3.29
	Orthacridinae	Orthacridini	*Orthacris maindroni* (Bolivar 1905)	18	5.39
Tettigoniidae	Conocephalinae	Conocephalini	*Conocephalus maculatus* (Le Guillou 1841)	10	2.99
		Copiphorini	*Euconocephalus pallidus* (Redtenbacher 1891)	2	0.6
	Phaneropterinae	Phaneropterini	*Phaneroptera* gracilis (Burmeister 1838)	5	1.5
Gryllidae	Gryllinae	Gryllini	*Teleogryllus mitratus* (Burmeister 1838)	21	6.29
			Gryllus bimaculatus (De Geer 1773)	10	2.99
Total				334	100

N - Number of individuals, D - Dominance
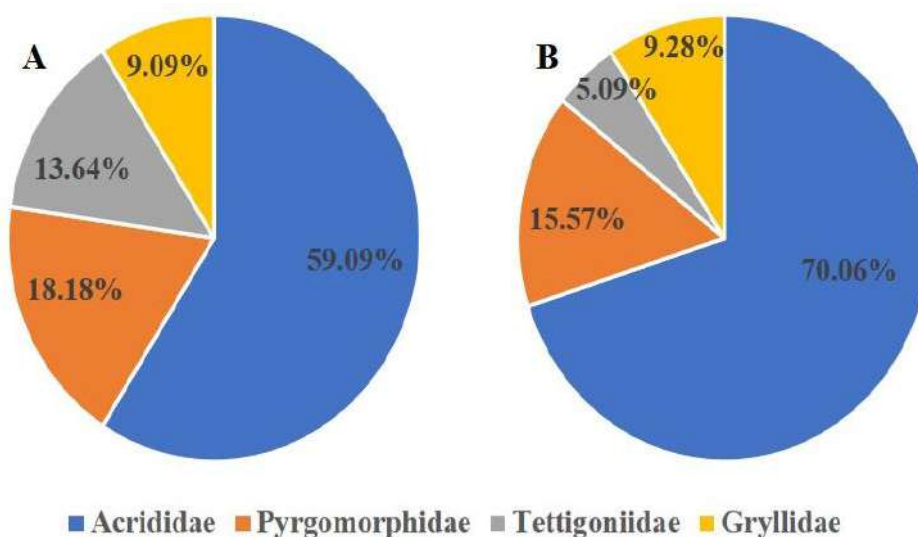
Fig. 1: A) Species richness and B) Species abundance families of Orthoptera from the study area.
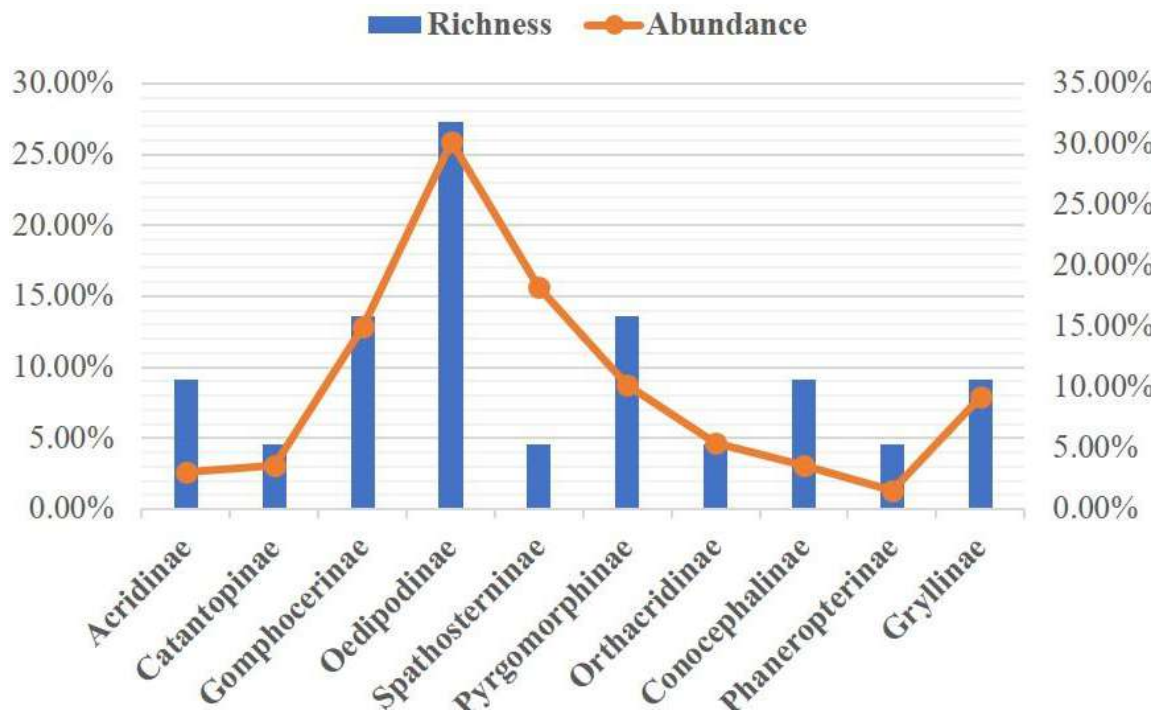
Fig. 2: Species richness and abundance subfamilies of Orthoptera.

and three rare species were observed during the study period (Table 1). In terms of the total number of individuals reported, the most dominant species were *Spathosternum prasiniferum* (D = 18.26) followed by *Trilophidia annulata* (D = 9.58) and *Leva indica* (D = 8.08) while *Euconocephalus pallidus* (D = 0.6), *Phlaeoba infumata* (D = 0.9) and *Acrotylus insubricus* (D = 1.2) were the least dominant species in the present study. For the Acrididae family, *S. prasiniferum* (D = 18.26) and *T.annulata* (D = 9.58) were the most dominant species. The abundant species in Pyrgomorphidae were *Orthacris maindroni* (D = 5.39) and *Tagasta indica* (D = 3.29). *Conocephalus maculatus* (D = 2.99) was observed maximum in the Tettigoniidae family. Gryllidae had only two species, *Teleogryllus mitratus* was the highest dominant (D = 6.29) and *Gryllus bimaculatus* was the least dominant (D = 2.99) (Table 1).

Subfamily Oedipodinae was found to be most abundant with 101 individuals (30.24%) followed by Spathosterninae with 61 individuals (18.26%) and Gomphocerinae with 50 individuals (14.97%). Less abundance was noted in Phaneropterninae with five individuals (1.50%) (Fig. 2). Some abundant species of Oedipodinae were *T. annulata* (D = 9.58), *Acrotylus humbertianus* (D = 6.29), and *Oedaleus abruptus* (D = 5.69) (Table 1).

Principal Component Analysis (PCA)

Principal Component Analysis (PCA) was done for the family-wise representation of various Orthopteran taxa from the study area. A total of 22 species of Orthopterans were selected among four families for PCA. The percentage of variance and eigenvalues were explained by four PCs. The first two correlation matrices of PCA showed the highest variance and eigenvalue; other PCs had progressively less variances and eigenvalue. PC1 explained 33.87% of the variation in the parameters with an eigenvalue of 1.35511. PC2 explained 28.68% of the variation in the parameters with an eigenvalue of 1.14725. Principal component 1 analysis represents the higher species composition and family richness, and principal component 2 represents the lower species composition of Orthopterans. Among the four subfamilies of Orthoptera, Acrididae showed the highest PC score. Most of the acridids' fauna were clustered in the centre of the plot (Fig. 3).

Species Similarity and Dissimilarity

The similarity of species composition among different families was performed based on cluster analysis as presented in Fig. 4. Clusters were numbered in ascending order based on abundance composition. The similarity matrix from the
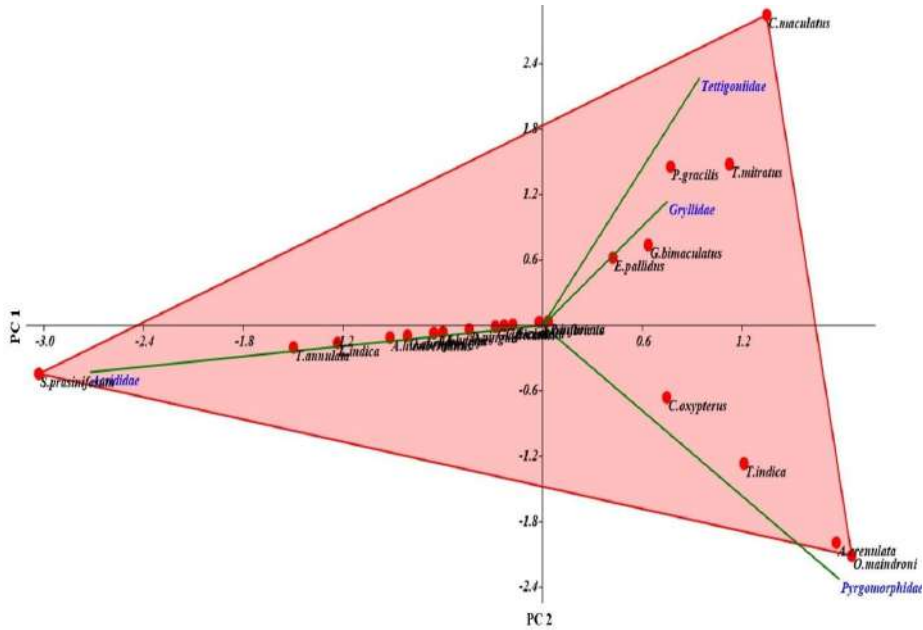
Fig. 3: Bi-plot of the first two axes of the principal component analysis of Orthoptera species.

quantitative data showed the composition of *A. humbertianus* (Acrididae), *T. mitratus* (Gryllidae), *C. maculatus* (Tettigoniidae), and *G. bimaculatus* (Gryllidae) Orthopterans were

similar to each other. The only species that formed a single cluster was *S. prasiniferum* (Acrididae), and the species composition differed greatly from that of other Orthopteran
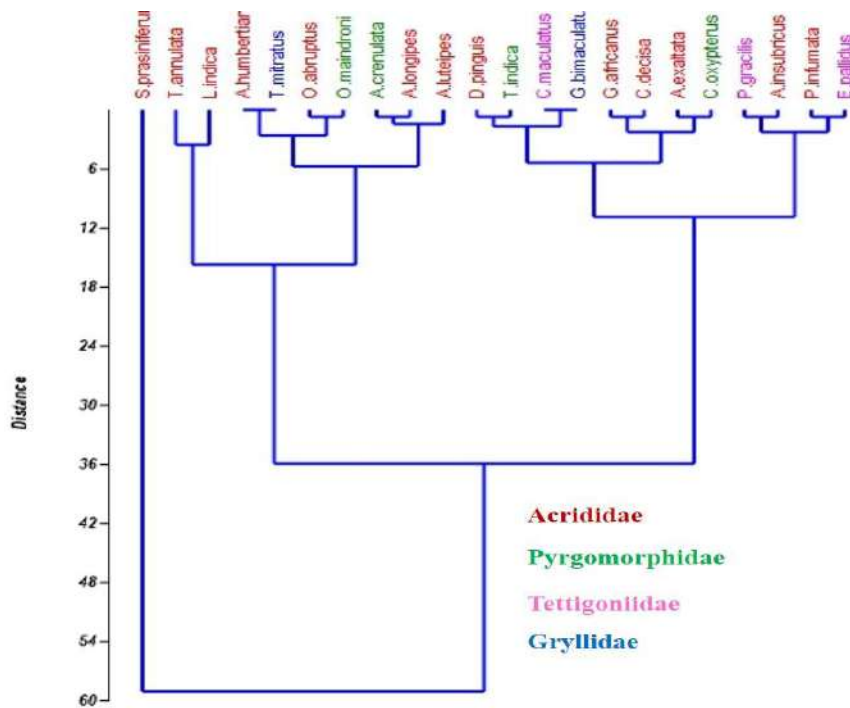
Fig. 4: Similarity and dissimilarity of species composition among different families using cluster analysis.
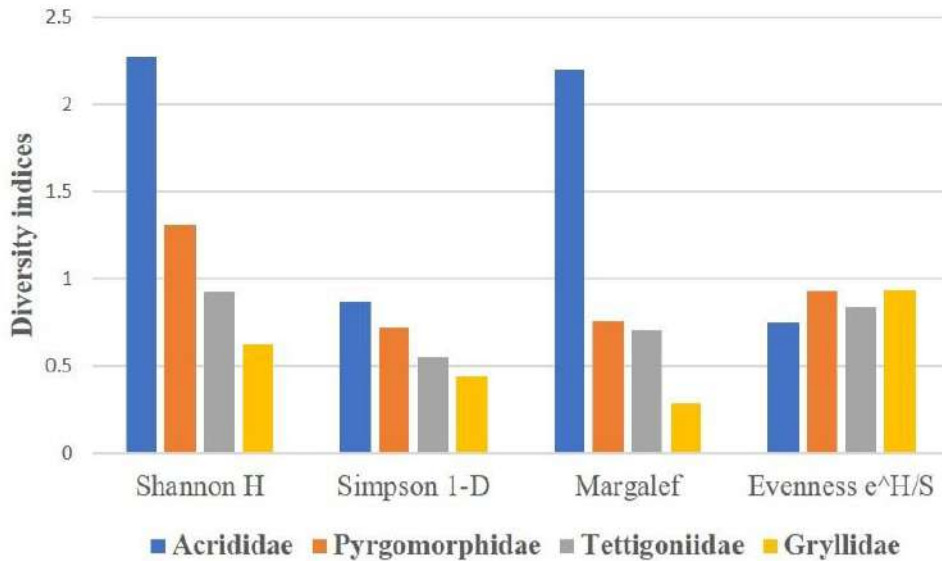
Fig. 5: Comparison of different diversity indexes among different families of Orthoptera.

species. Acrididae species, on the other hand, were grouped at the highest level of similarity (Fig. 4).

Diversity Indices

In the present study, the Shannon index varied from 0.62 to 2.27. The Simpson index ranged from 0.43 to 0.87. The Margalef index fluctuated between 0.29 and 2.2. Shannon, Simpson, and Margalef's diversity index values were lowest in Gryllidae and highest in Acrididae, while evenness index

values showed difference; it was highest in Gryllidae and lowest in Acrididae. The species evenness index varied from 0.74 to 0.93. Among these diversity indices, the Shannon index showed the highest diversity value (Fig. 5).

As illustrated in Fig. 6, the Renyi indices of diversity plot clearly demonstrate the species diversity pattern in four groups. The number of species and individuals in the Acrididae family was not only higher but the individuals were also distributed more evenly in the Acrididae family. Renyi
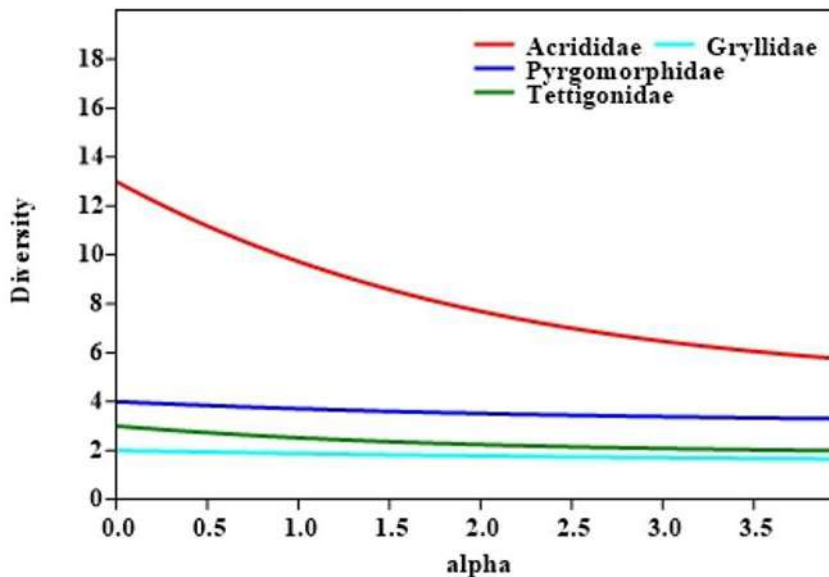
Fig. 6: Species accumulation curve among different families of Orthoptera.

α-diversity varied from 1.65 to 5.75. The lowest diversity index was observed in Gryllidae and the highest index was recorded in Acrididae; however, the interaction between Tettigoniidae (1.99) and Gryllidae (1.65) indicates similar α-diversity (Fig. 6).

DISCUSSION

All the collected grasshoppers were classified under four families viz., Acrididae, Pyrgomorphidae, Tettigoniidae, and Gryllidae. Among these, Acrididae showed the richest family (13 species). This perception was in parallel with the observations of Divya and Senthilkumar (2017) who also observed four families of Orthoptera and 13 species of acridids in Coimbatore. The present study's findings showing the Acrididae family had the most dominating numerical distribution are similar to those of Paulraj et al. (2009), who found that the Acrididae family had the most dominant numerical distribution. Other studies such as Akhtar et al. (2012), Thakkar et al. (2015), Arya et al. (2015), and Suganya et al. (2020) also found maximum diversity being shown by the Acrididae family. Acridids are graminivorous in nature and the grasslands found in the ecosystem provide a wide variety of food as well as a breeding site for acridids.

The subfamily Oedipodinae had the highest species diversity and population composition in the research area during the study period. This observation was similar to Kumar & Usmani (2015), Shishodia et al. (2010), and Suganya et al. (2020) who found members of the subfamily Oedipodinae were more diverse and abundant. Growth rate and reproduction efficiency influenced the distribution of dominant species in the ecosystem.

Among the collected species, *S. prasiniferum* was found to be the most dominant in the study area. These species have greater ecological plasticity as they can reproduce and increase their population in different conditions of ecosystems. Kumar & Usmani (2015) and Raghavender & Vastrad (2017) also reported that *S. prasiniferum prasiniferum* was found to be most abundant. According to Bhusnar (2015), *S. prasiniferum prasiniferum* is found throughout the year and is dominant in the Solapur region.

Based on the PCA bi-plot results, the Orthoptera composition showed significant differences among species and families. The distribution of individuals along the first two PCs showed the highest variances. The first two correlation matrix PCs accounted together for 62.55% (PC1= 33.87% + PC2=28.68%) of the total variances and other PCs showed less variances.

A cluster analysis (or classification) is helpful in finding the natural groupings of samples, such that samples within a group are more similar to each other than the samples in different groups. It is also used to define species assemblages and groups of species that tend to occur in a parallel manner across sites (Balakrishnan et al. 2014). In our study, cluster analysis clearly revealed the similarity and dissimilarity of species concentration among different families of Orthoptera from the study area. Habitat complexity and host plant might act as drivers and determinants of the variation among species composition in the park.

In the present study, Family-wise diversity: Shannon, Simpson, Margalef, and Renyi index values were highest in Acrididae and Evenness was the highest in Gryllidae. Thakkar et al. (2015) also observed that Family-wise diversity, Shannon-Wiener diversity index, and Evenness were elevated for Acrididae followed by Tettigoniidae, Gryllidae, and Pyrgomorphidae in South Gujarat. Generally, the Shannon diversity index and Simpson diversity index are commonly used to evaluate the diversity richness of organisms present in an area. Typical values of H are generally between 1.5 and 3.5 in most ecological studies, and the index is rarely greater than 4 (Shannon & Weiner 1949). Simpson's diversity index (λ) was calculated since it is well accepted that all species are at a site. The value ranges between 0 and 1 (Simpson 1949).

CONCLUSION

Statistical analysis infers that the quantitative concentration of Orthoptera fauna varies from species to species as well as family to family. A small change in species composition from a healthy stable state can adversely affect the trophic complexity of the food web and species interaction. The promotion of biodiversity conservation is an important step for maintaining overall environmental health and stability of various kinds of ecosystems. The present study provides distinctive information on the present status of dominant, subdominant, incidental and rare species of Orthoptera from the study area and this result would help to assess appropriate and possible strategies to Orthopteran conservation as well as habitat management in the future. A long-term study is needed to record the species composition from this area, to get better and more comprehensive information.

REFERENCES

Akhtar, M.H., Usmani, M.K., Nayeem, M.R. and Kumar, H. 2012. Species diversity and abundance of grasshopper fauna (Orthoptera) in rice ecosystem. Annals Biol. Res., 3(5): 2190-2193.

Andersen, A.N., Ludwig, J.A., Lowe, L.M. and Rentz, D.C.F. 2001. Grasshoppers biodiversity and bioindicators in Australian tropical savannas. Austral. Ecol., 26(3): 213-222.

Arya, M.K., Joshi, P.C. and Vinod, P.B. 2015. Species composition, abundance, density, and diversity of grasshoppers (Insecta: Orthoptera) in a protected forest ecosystem in the Western Himalayas. Int. J. Fauna Biol. Stud., 2(5): 42-46.

Balakrishnan, S., Srinivasan, M. and Mohanraj J. 2014. Diversity of some insect fauna in different coastal habitats of Tamil Nadu, southeast coast of India. J. Asia Pac. Biodivers., 71: 408-414.

Báldi, A. and Kisbenedek, T. 1997. Orthopteran assemblages as indicators of grassland naturalness in Hungary. Agric. Ecosyst. Environ., 66(2): 121-129.

Belovski, G.E. and Slade, J.B. 1993. The role of vertebrate and invertebrate predators in a grasshopper community. Oikos, 68: 193-201.

Bhusnar, A. 2015. Acridid (Orthoptera) diversity of agriculture ecosystem from Solapur district of Maharashtra, India. Biolife, 3(2): 46-468.

Buschini, M.L.T. and Woiski, T.D. 2008. Alpha-beta diversity in trap-nesting wasps (Hymenoptera: Acu-leata) in Southern Brazil. Acta Zool., 89(4): 351-358.

Chitra, N., Soundararajan, R.P. and Gunathilagaraj, K. 2000. Orthoptera in rice fields of Coimbatore. Zoos Print J., 15(8): 309-311.

Divya, D. and Senthilkumar, N. 2017. Record of grasshopper fauna (Orthoptera) in forest campus, Coimbatore, Tamil Nadu, India. Curr. Biot., 10(4): 296-301.

Eades, D.C., Otte, D., Cigliano, M.M. and Braun, H. 2016. Orthoptera Species File. Version 5.0/5.0. http://Orthoptera.Species File.org [Date accessed: 4 June 2016].

Evans, E.W., Rogers, R.A. and Opfermann, D.J. 1983. Sampling grasshoppers (Orthoptera: Acrididae) on burned and unburned tallgrass prairie: Night trapping vs. sweeping. Environ. Entomol., 12(5): 1449-1454.

Gandar, M.V. 1982. The dynamics and trophic ecology of grasshoppers (Acridoidea) in South African savanna. Oecologia (Berlin), 54: 71-81.

Gardiner, T., Pye, M., Field, R. and Hill, J. 2002. The influence of sward height and vegetation composition in determining the habitat preferences of three Chorthippus species (Orthoptera: Acrididae) in Chelmsford, Essex, UK. J. Orthop. Res., 11: 207-213.

Hammer, O., Harper, D.A.T. and Ryan, P.D. 2001. PAST: Paleontological statistics software package for education and data analysis. Palaeontol. Electron., 4(1): 1-9.

Jamison, B.E., Robel, R.J., Pontius, J.S. and Applegate, R.D. 2002. Invertebrate biomass: Associations with lesser prairie-chicken habitat use and sand sagebrush density in southwestern Kansas. Wildl. Soc. Bull., 30: 517-526.

Joshi, P.C., Lockwood, J.A., Vashishth, N. and Singh, A. 1999. Grasshopper (Orthoptera: Acridoidea) community dynamics in a moist deciduous forest in India. J. Orthop. Res., 8(8): 17-23.

Kirby, W.F. 1914. The fauna of British India including Ceylon and Burma. Taylor and Francis, London, p. 276.

Kumar, H. and Usmani, M.K. 2015. A checklist of Acrididae (Orthoptera: Acridoidea) from Haryana, India. Acta Zool. Mex., 31(2): 234-238.

Larson, D.P., O'Neill, K.O. and Kemp, W.P. 1999. Evaluation of the accuracy of sweep sampling in determining grasshopper (Orthoptera, Acrididae) community composition. J. Agric. Urban Entomol., 16(3): 207-214.

Lena, M., Gunasekaran, C., Natarajan, S., Shobana, G., Mohana, P. and Agnes Deepa, A. 2012 Invertebrate diversity in the anthropogenically disturbed forest of Maruthamalai hills, western ghats, Tamil Nadu, South India. World J. Zool., 7(1): 90-93.

Millar, J.C. 1993. Insect natural history, multiple species interactions, and biodiversity in the ecosystem. Biodivers. Conserv., 2: 233-241.

Mirzaei, R., Hemami, M.R., Esmaili Sari, A., Rezaei, H.R. and Peterson, A.T. 2017. Applying ecological niche modeling to determine avian richness hotspots. Glob. J. Environ. Sci. Manag., 3(2): 131-142.

O'Neill, K.M., Olson, B.E, Rolston, M.G., Wallander, R., Larson, D.P. and Seibert C.E. 2003. Effects of livestock grazing on rangeland grasshopper (Orthoptera: Acrididae) abundance. Agric. Ecosyst. Environ., 97(1-3): 51-64.

Paulraj, M.G., Anbalagan, V. and Ignacimuthu, S. 2009. Distribution of grasshoppers (Insecta: Orthoptera) among different host plants and habitats in two districts of Tamil Nadu, India. J. Threat. Tax., 1(4): 230-233.

Raghavender, B. and Vastrad, A.S. 2017. Changing scenario of short-horned grasshopper diversity in agriculture and forest ecosystems in Dharwad. J. Entomol. Zool. Stud., 5(2): 268-272.

Ryszkowski, L., Karg, J., Margarit, G., Paoletti, M.G. and Glotin, R. 1993. Above-Ground Insect Biomass in the Agricultural Landscape of Europe. In: Bunce, R. G. H., Ryszkowski, L. and Paoletti M.G. (eds.), Landscape Ecology Agroecosystems, Lewis Publishers, Boca Raton, pp. 71-82.

Schmidt G.H., Ibrahim, N.M. and Abdallah, M.D. 1991. Toxicological studies on the long-term effects of heavy metals (Hg, Cd, Pb) in soil on the development of *Aiolopus thalassinus* (Fabr.) (Saltatoria: Acrididae). Sci. Tot. Environ., 107: 109-133.

Shannon, C.E. and Wiener, W. 1949. The mathematical theory. University of Illinois Press, Urbana, p. 117.

Shishodia, M.S., Chandra, K. and Gupta, S.K. 2010. An annotated checklist of Orthoptera (Insecta) from India. Rec. Zool. Survey India, 6: 1-6.

Simpson, E.H. 1949. Measurement of diversity. Nature, 163: 688.

Soliman, M.M., Haggag, A.A. and El-Shazly, M.M. 2017. Assessment of grasshopper diversity along a pollution gradient in the Al-Tebbin region, South Cairo, Egypt. J. Entomol. Zool. Stud., 5(1): 298-306.

Suganya, M., Gunasekaran, C. and Manimegalai, K. 2020. Species richness and diversity of grasshopper fauna in different habitats of Bharathiar University Campus, Coimbatore, Tamil Nadu, India. Biolife, 8(1): 10-17.

Thakkar, B., Parmar, S. and Parikh, P. 2015. Study on diversity of Orthoptera fauna in South Gujarat, India. Int. J. Pure Appl. Zool., 3(4): 368-374.

Application of PCA-RSR Model in Reservoir Water Quality Evaluation

Fangxing Zhao*(**), Changjun Zhu*(**)†, Budong Li***, Shiyan Wang***, Wenlong Hao* and Xiaobo Liu***
*State Key Laboratory of Hydrology, Water Resources and Hydraulic Engineering, Hohai University, Nanjing 210009, China
**College of Energy and Environmental Engineering, Hebei University of Engineering, Handan 056038, China
***China Institute of Water Resources and Hydropower Research, Beijing 100038, China
†Corresponding author: Changjun Zhu; christorf@126.com

ABSTRACT

Water quality evaluation is a critical component of water environmental quality management, and conducting water quality assessments for reservoirs is quite practical. The inaccuracy induced by information overlap of several water quality measures is rarely taken into account in current water quality assessment systems. To solve this problem, the Principal component analysis-Rank sum ratio (PCA-RSR) water quality evaluation model was used to quantitatively evaluate the water quality of the Daheiting reservoir based on the monitoring data of different water layers in 2019. The results show that the water quality of Daheiting reservoir in 2019 is slightly better than that of the end of the reservoir, due to the influence of human factors downstream of the Upper Panjiakou Dam and the topography of the Luan River System, and the water quality from the dam head to the reservoir tail shows a decreasing trend. The PCA-RSR model has a good correlation with the traditional water quality indexes (WQI) system, which can avoid errors caused by overlapping information among the indexes while also taking into account the weight of the environmental factors of the study area. It is feasible and has some practical value in reservoir water quality evaluation..

INTRODUCTION

The reservoir is an important source of drinking water in China, which plays an indispensable role in social life, such as water storage, flood control, power generation, and so on (Li et al. 2020). In recent years, as the social economy has developed, it has been common to notice an increase in pollution sources, the influence of environmental quality, and the loss in reservoir self-purification capacity due to human causes (Wang et al. 2020, Zhang et al. 2020a). It is necessary to conduct a comprehensive and reasonable scientific evaluation of the reservoir water environment to reduce the negative effects of human activities on the reservoir environment, identify the main pollutants in reservoir water quality, and establish a scientific and effective management system for the reservoir water environment (Xing Wei 2020).

Water quality evaluation is a method of qualitative and quantitative evaluation of the water quality of the target area according to the relevant environmental quality standards based on the field monitoring data (Song et al. 2017). At present, the main water quality evaluation methods are the fuzzy comprehensive evaluation method, artificial neural network method, water poverty index model method, and so on. For example, Yan & Yan (2015) have used the fuzzy comprehensive evaluation method to evaluate and forecast

the water quality of the upper reaches of Dahuofang Reservoir and established the Nonlinear regression model of the Fuzzy Comprehensive Evaluation Index of water quantity and water quality, which has a high fitting effect, the water quality of each section can be predicted. Jiang et al. (2018) used the entropy evaluation method and fuzzy comprehensive evaluation method to evaluate the water quality in Baicheng, Jilin province, making the results of water quality evaluation more objective.

Sun et al. (2019) used the Modified Fruit Fly Optimization Algorithm-Extreme Learning Machine (MFOA-ELM) method to evaluate the water quality in Chao Lake, improving the predictability. The RBF neural network outperforms the standard neural network when it comes to data mining. It has a straightforward structure and a high degree of generality. Cao (2019) applied RBF Neural Network to quantitatively evaluate the water quality of the Reservoir in the south of Yanshan Mountain and proved that this method has the advantages of simple dimension expansion and is highly transplantable compared with the traditional method in the process of water quality evaluation. Based on the water poverty theory, Liu et al. (2016) constructed the water poverty evaluation index system, measured the water poverty degree of Gansu province, explored the spatial-temporal

differentiation and driving factors, and innovated the index system of water quality evaluation. Although the preceding approaches have advantages in evaluating water quality, there are still some issues that need to be addressed, such as the complexity of fuzzy comprehensive evaluation and the subjectivity of selecting the index weight vector. The center vector and normalizing constant of the hidden layer radial basis function must be determined by the RBF Neural Network, which increases the challenge of building the model.

In the reaction region, the water poverty theory is more focused on the overall degree of water scarcity, and the effect of environmental pollutants on water quality is given less weight in the evaluation process. Furthermore, because the aquatic environment is such a complex organic whole, the mistake produced by information overlapping across multiple water quality parameters is rarely taken into account in standard water quality assessment methodologies. Principal component analysis (PCA) is based on the concept of dimension reduction, and it can effectively alleviate the error caused by information overlap by transforming most indexes into a few comprehensive indexes. Li et al. (2018a) combined the PCA with the water quality identification index method to evaluate the water quality of the Tokto section of the Yellow River and found that this method can accurately and objectively reflect the water quality characteristics. The rank-sum ratio (RSR), which uses the relative size relationship of data to show tiny changes, sort and classify each evaluation item, and split the pros and cons, can be used to show small changes, sort and classify each evaluation object, and divide the pros and cons. In data analysis, it is a frequent strategy for comparing and finding associations.

Xu et al. (2015) employed the RSR complete evaluation approach to objectively and accurately evaluate the water quality of swimming pools, indicating the need for sanitary supervision and improvement of swimming pool water quality. For water quality evaluation, combining PCA and RSR can effectively reduce errors caused by information overlap while correctly classifying and ranking the evaluation items. Using Daheiting Reservoir as an example, this work introduces the PCA-RSR water quality evaluation model and explores the feasibility and practical relevance of this model in reservoir water quality evaluation by comparing it to the widely used water quality indexes (WQI) approach.

MATERIALS AND METHODS

PCA is a mathematical dimensionality reduction method in the field of statistics. Its principle is to use orthogonal transformation to transform a series of possible related variables into a new group of linearly independent variables. The new variable is the extracted principal component, which can retain the information of the original variables as much as possible while reducing the number of original variables. It is widely used in the selection of water quality evaluation indicators and water environment quality assessment (Li et al. 2018b, Yu et al. 2017a, Liu et al. 2014, Liu et al. 2018, Ma et al. 2017, Yu et al. 2017b).

On the premise of ensuring the minimum loss of initial information, it can objectively divide the weights of different factors through statistical methods, and select the factors that have a great influence on the research objectives, to reflect the characteristics of the research objectives more effectively and intuitively. It avoids the subjective arbitrariness of the traditional water quality analysis methods (pollution index method, fuzzy comprehensive evaluation method, etc.), and has unique advantages. RSR is a statistical method that combines classical parametric statistics and modern nonparametric statistics. It has both advantages and was first put forward by Tian (2002). The principle is that in a matrix with n rows and m columns, the data is ranked by distinguishing high-quality and low-quality indexes according to the specified standards, and then through rank substitution, the dimensionless statistics RSR is obtained, and then combined with the method of parameter analysis to solve the problems of comprehensive evaluation encountered in various industries. It is a kind of statistical analysis method with strong pertinence and flexibility, which is widely used in the classification of various disciplines and the comprehensive evaluation of measurement data.

A water environment system is a complex system formed by the interrelation and comprehensive action of many kinds of water quality factors. And there are different degrees of correlation between different water quality factors, to avoid the problem of overlap and concealment of water quality information caused by direct evaluation of water quality monitoring data. PCA is utilized in this study to examine and determine the contribution rate of each water quality variable to the selected main components, as well as to keep the leading water quality factors. Furthermore, the PCA-RSR model is developed to quantitatively evaluate the water quality of the Daheiting reservoir using the parameters required by PCA results, and the evaluation results are visualized using Geographic Information System (GIS) technology. At the same time, the reservoir's WQI is calculated, and the model's feasibility and superiority in water quality evaluation are investigated by comparing it to the traditional method.

Calculation of WQI

WQI is one of many water quality assessment methods. It integrates and extracts the information of water quality monitoring data through mathematical tools, thus quantifying the degree of water pollution. The results are simple and intuitive.

It is widely used in water quality assessment at home and abroad. In this study, total nitrogen (TN), total phosphorus (TP), ammonia nitrogen (NH_3-N), nitrate-nitrogen (NO_3-N), Sulfate, Chloride, permanganate index (COD-Mn), chemical oxygen demand (COD), five-day biochemical oxygen demand (BOD_5), conductivity (EC), pH and other water quality indexes were selected to calculate WQI according to formula (1) (Pesce & Wunderlin 2000, Kocer & Sevgili 2014).

$$WQI = \sum_{i=1}^{n} C_i P_i / \sum_{i=1}^{n} P_i \qquad \dots(1)$$

In the formula, n is the total number of water quality parameters, C_i is the normalized value assigned to parameter i, P_i is the relative weight of parameter i, and the range is 1-4 (Table 1). Referring to the present situation of water quality control in the Daheiting reservoir, the pollution of TP is serious, which is the main factor of water quality pollution (Wang 2020). Therefore, the TP weight was revised to 4.

PCA-RSR Water Quality Evaluation Model

PCA Analysis
1) Standardize the original data

The original data are standardized according to formulas (2) and (3).

$$\tilde{x}_{ij} = \frac{x_{ij} - \bar{x}_j}{s_j}, \text{ (i=1,2,…,n; j=1,2,…,m)} \qquad \dots(2)$$

$$\bar{x}_j = \frac{1}{n}\sum_{i=1}^{n} \chi_{ij}, \quad s_j = \sqrt{\frac{1}{n-1}\sum_{i=1}^{n}(x_{ij} - \bar{x}_j)^2},$$
$$\text{(j=1,2,…,m)} \qquad \dots(3)$$

In the formula, m is the number of index variables and n is the number of evaluation objects $\tilde{x}_j$ and s_j are the sample mean and standard deviation of the j Index, x_{ij} is the value of the j Index of the i evaluation object $\tilde{x}_{ij}$ is the standardized indicator value.
2) Calculate the correlation coefficient matrix
Correlation coefficient matrix $R = (r_{ij})_{m*m}$

$$r_{ij} = \frac{\sum_{k=1}^{n} \tilde{x}_{ki} \cdot \tilde{x}_{kj}}{n-1}, \text{ (i, j=1,2,…,m)} \qquad \dots(4)$$

In the formula, $r_{ii}=1$, $r_{ij}=r_{ji}$, r_{ij} is the correlation coefficient between the i index and the j index.
3) Calculate eigenvalues and Eigenvectors
Calculate the eigenvalues of the correlation coefficient matrix R: $\lambda_1 \geq \lambda_2 \geq … \geq \lambda_m \geq 0$, and the corresponding eigenvectors: $u_1, u_2, …, u_m$. Among them, $u_j = (u_{1j}, u_{2j}, …, u_{nj})^T$. m new indicator variables composed of eigenvectors:

$$\begin{cases} y_1 = u_{11}\tilde{\chi}_1 + u_{21}\tilde{\chi}_2 + \cdots + u_{n1}\tilde{\chi}_m \\ y_2 = u_{12}\tilde{\chi}_1 + u_{22}\tilde{\chi}_2 + \cdots + u_{n2}\tilde{\chi}_m \\ y_m = u_{1m}\tilde{\chi}_1 + u_{2m}\tilde{\chi}_2 + \cdots + u_{nm}\tilde{\chi}_m \end{cases} \qquad \dots(5)$$

In the formula, y_1 is the first principal component, y_2 is the second principal component, …., y_m is the m-th principal component.
4) Calculate the contribution rate of principal component eigenvalues

The contribution rate (W'_i) of λ_i is calculated by the formula (6).

$$W'_i = \frac{\lambda_i}{\sum_{i=1}^{P}\lambda_i} \qquad \dots(6)$$

Determination of Principal Component Weight Coefficient by RSR

The contribution rate of the eigenvalues of the extracted principal components is taken as the empirical weight coefficient (Zhang et al. 2020b), and the weight coefficient (*W*) is determined by SR in the RSR method according to the following steps.

The extracted principal components are horizontally sorted according to the low excellent index by the integral rank method to determine the rank R, and the RSR is calculated according to the formula (7).

$$RSR = \frac{\Sigma R}{k \cdot m} \qquad \dots(7)$$

In the formula, ΣR is the rank-sum, that is, the rank synthesis of each index; k is the number of evaluation objects, that is, the number of monitoring samples; m is the number of evaluation indexes, that is, the number of principal components extracted.

The Sum Ratio (SR) was calculated according to formula (8).

$$SR = RSR/\Sigma RSR \qquad \dots(8)$$

The *W* of each evaluation index was calculated according to formula (9).

$$W = (SR*W')/\Sigma(SR*W') \qquad \dots(9)$$

In the formula, *W'* is the contribution rate of the eigenvalues of the extracted principal components.

Establishment of PCA-RSR Model

According to the principal components extracted by PCA and the weight coefficients determined by the RSR method, and combined with the standardized water quality evaluation grade, the threshold value of each water quality evaluation grade was calculated by Formula (10).

$$F_i = W_i * n_i * P_i \qquad \dots(10)$$

In the formula, F_i is the critical threshold of all levels of water quality evaluation grade; P_i is the standardized data of water quality index corresponding to each grade; W_i is the weight coefficient of each evaluation index; n_i is the principal component load coefficient extracted by PCA.

Table 1: The relative weights and the normalization factors of parameters for WQI calculation.

indexes		Normalization factor (Ci)											Relative weight (P$_i$)
		100	90	80	70	60	50	40	30	20	10	0	
TN	/(mg.L^{-1})	<0.1	<0.2	<0.35	<0.5	<0.75	<1	<1.25	<1.5	<1.75	>2	>2	2
TP	/(mg.L^{-1})	<0.01	<0.02	<0.05	<0.1	<0.15	<0.2	<0.25	<0.3	<0.35	≤0.4	>0.4	4
NH$_3$-N	/(mg.L^{-1})	<0.01	<0.05	<0.1	<0.2	<0.3	<0.4	<0.5	<0.75	<1	≤1.25	>1.25	3
NO$_3$-N	/(mg.L^{-1})	<0.5	<2	<4	<6	<8	<10	<15	<20	<50	≤100	>100	2
NO$_2$-N	/(mg.L^{-1})	<0.005	<0.01	<0.03	<0.05	<0.1	<0.15	<0.2	<0.25	<0.5	≤1	>1	2
TON	/(mg.L^{-1})	<0.05	<0.1	<0.2	<0.3	<0.4	<0.5	<0.7	<1	<2	≤3	≥3	2
DO	/(mg.L^{-1})	>7.5	>7	>6.5	>6	>5	>4	>3.5	>3	>2	>1	<1	4
Phosphate	/(mg.L^{-1})	<0.16	<1.60	<3.20	<6.40	<9.60	<16.0	<32.0	<64.0	<96.0	>160.0	>160.0	1
Sulfate	/(mg.L^{-1})	<25	<50	<75	<100	<150	<250	<400	<600	<1000	>1500	>1500	2
Chloride	/(mg.L^{-1})	<25	<50	<100	<150	<200	<300	<500	<700	<1000	>1500	>1500	1
COD-Mn	/(mg.L^{-1})	<1	<2	<3	<4	<5	<8	<10	<12	<14	≤15	>15	3
COD	/(mg.L^{-1})	<5	<10	<20	<30	<40	<50	<60	<80	<100	≤150	>150	3
BOD$_5$	/(mg.L^{-1})	<0.5	<2	<3	<4	<5	<6	<8	<10	<12	≤15	>15	3
EC	/(μS.cm^{-3})	<750	<1000	<1250	<1500	<2000	<2500	<3000	<5000	<8000	≤12000	>12000	1
pH		7	7-8	8-8.5	8.5-9	6.5-7	6-6.5 or 9-9.5	5-6 or 9.5-10	4-5 or 10-11	3-4 or 11-12	2-3 or 12-13	1-2 or 13-14	1

According to the principal components extracted by PCA and the weight coefficients of principal components determined by the RSR method, the water quality evaluation model of PCA-RSR was established, and the comprehensive evaluation value f of water quality at each monitoring site was calculated according to formula (11).

$$f = \sum_{i=1}^{n} W_i * F_n(x) \qquad \dots(11)$$

In the formula, f is the comprehensive evaluation value of each monitoring point in the PCA-RSR water quality evaluation model; W_i is the weight coefficient of each evaluation index; $F_n(x)$ is the corresponding score of each principal component extracted by each monitoring point.

APPLICATION EXAMPLE

Study Area

Daheiting Reservoir is a drinking water source reservoir in the Luan River system, which belongs to the second type of water conservancy project (Li 2019). This reservoir (40°12′4″~40°21′18″N, 118°15′22″~118°19′21″E) is located in Qianxi County, Tangshan City, Hebei Province. The total reservoir capacity is about 340 million m^3, and the backwater length of the reservoir is about 23 km (Liu et al. 2019). It serves as the source reservoir for the Luan River diversion project, providing drinking water to Tianjin, Tangshan, and the cities along the Luan River's lower reaches.

Sample Collection and Determination

Five sampling points are uniformly arranged in the Daheiting reservoir area (Fig.1). The SX800 series portable electro-chemical instruments (Shanghai San-Xin Instrumentation) is used to determine water quality indicators such as EC, pH, and other parameters at each sampling location. In addition,

Fig. 1: Sampling point.

Table 2: WQI water quality classification.

Range	Comprehensive water quality grade
WQI>80	I
80≥WQI>60	II
60≥WQI>40	III
40≥WQI≥20	IV
WQI<20	V
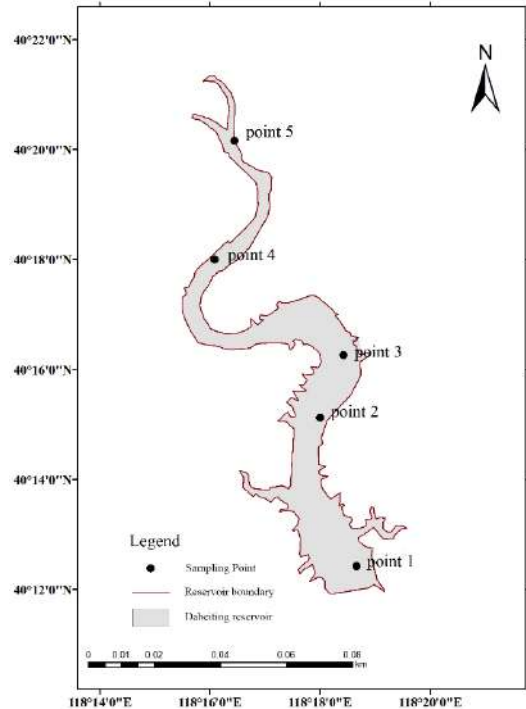
Table 3: Standardization of water quality evaluation grades and indexes.

	I	II	III	IV	V
TN	-1.11094	-0.45261	0.37031	1.19324	1.19324
TP	-1.1619	-0.3873	0.3873	1.1619	1.1619
NH$_3$-N	-0.97095	-0.45311	0.06473	1.35933	1.35933
NO$_3$-N	-0.72626	-0.53576	-0.2024	1.46442	1.46442
Sulfate	-0.78961	-0.61083	-0.0149	1.41534	1.41534
Chloride	-0.86603	-0.61859	0.12372	1.3609	1.3609
COD-Mn	-1.00673	-0.60404	0.40269	1.20808	1.20808
COD	-1.0247	-0.43916	0.14639	1.31747	1.31747
BOD$_5$	-1.02151	-0.51075	0.25538	1.27688	1.27688
EC	-0.7597	-0.51331	-0.18479	1.45781	1.45781
pH	-1.1619	-0.3873	0.3873	1.1619	1.1619

each sampling point was separated into three layers based on its actual water depth: the surface water body, the middle water body, and the bottom water body. Water samples of 500 mL were gathered from each layer. The water samples were transported back to the laboratory according to the corresponding water quality testing standards to determine TN, TP, NH_3-N, NO_3-N, sulfate, Chloride, COD-Mn, COD, BOD_5, and so on.

Evaluation Results of PCA-RSR Model

The monitoring data of each index in this monitoring site and the corresponding water quality evaluation standards are standardized, and the standardized water quality evaluation standards are detailed in Table 3.

On this basis, the dimension reduction and principal factor extraction of the water quality indexes monitoring data of the collected water samples are further carried out. According to the extracted eigenvalues, the first five are selected as the principal components, and the load coefficient matrix n (Table 4) of each principal component and the contribution rate of the eigenvalues of each principal component is determined (W'=22.461, 21.092, 17.567, 10.647, 9.117).

The related indexes of the RSR method are calculated according to the formula (7) ~ (9). The results are given in Table 5.

According to the principal components extracted by PCA and the weight coefficients of principal components determined by the RSR method, combined with the standardized water quality evaluation grade, the threshold of each water quality evaluation grade is calculated according to formula (10). The calculation results are presented in Table 6.

According to the principal components extracted by PCA and the weight coefficients of principal components deter-

mined by the RSR method, the PCA-RSR water quality evaluation model is established. The comprehensive evaluation value f (formula (12)) of each monitoring point is calculated according to formula (11). The evaluation results are visually processed by ArcGIS software, as shown in Fig. 2.

$$f = 0.276049*F_1(x)+0.255296*F_2(x)+0.232257*F_3(x)+0.132836*F_4(X)+0.103561*F_5(x) \quad \ldots(12)$$

The evaluation result of the PCA-RSR model is a low-excellent index, that is, the smaller the value, the better the water quality. According to Fig. 2, from the longitudinal distribution, the water quality of different water layers near the tail of Daheiting Reservoir is poor, indicating that it is greatly affected by upstream water pollution; in the middle of the reservoir where Point 3 is located, due to the influence of topography, the curved river slows down the velocity of the water body, and the pollutants in the surface water can be deposited to the lower layer, resulting in slightly better water quality in the surface layer than in the bottom layer. The water area at the dam head is relatively large, and the larger water volume in the vast water region produces a pollutant-dilution impact. The water quality of distinct water strata at this location is in good shape as a result of this diluting effect. The water quality of the dam head is better than that of the reservoir's tail, and the water quality exhibits a diminishing tendency from the dam head to the reservoir's tail as a whole. Based on water quality monitoring data from Daheiting Reservoir in several seasons in 2018, Wu et al. (2020) assessed the water quality status of Daheiting Reservoir and found comparable results. Chen et al. (2016) found that nitrogen and phosphorus are not only the main pollutant of Daheiting Reservoir but also the main limiting factor of water eutrophication. In the PCA method, the higher the contribution rate of the extracted principal component is, the more information it contains, the greater the influence on the water quality. The water area at the dam head is relatively large, and the larger water volume in the vast water region produces a pollutant-dilution impact. The water quality of distinct water strata at this location is in good shape as a result of this diluting effect. The water quality of the dam head is better than that of the reservoir's tail, and the water quality exhibits a diminishing tendency

Table 4: Load Coefficient Matrix of each principal component.

	F1	F2	F3	F4	F5
TN	0.389	-0.151	-0.034	0.331	-0.117
TP	-0.048	0.25	0.268	0.214	-0.198
NH_3-N	0.108	0.201	0.221	-0.113	-0.176
NO_3-N	0.122	0.347	-0.308	0.258	0.071
Sulfate	0.321	-0.059	0.098	-0.158	-0.061
Chloride	0.065	-0.035	0.037	0.698	0.014
COD-Mn	0.094	0.006	-0.097	0.03	0.763
COD	0.075	-0.091	0.465	0.08	-0.094
BOD_5	-0.086	0.027	0.31	-0.036	0.269
EC	0.424	0.146	-0.099	-0.033	0.317
pH	0.091	-0.458	0.065	0.176	-0.093

Table 5: Results of RSR method.

	ΣR	RSR	SR	W
F1	66	0.6	0.2	0.276049
F2	65	0.590909	0.19697	0.255296
F3	71	0.645455	0.215152	0.232257
F4	67	0.609091	0.20303	0.132836
F5	61	0.554545	0.184848	0.103561
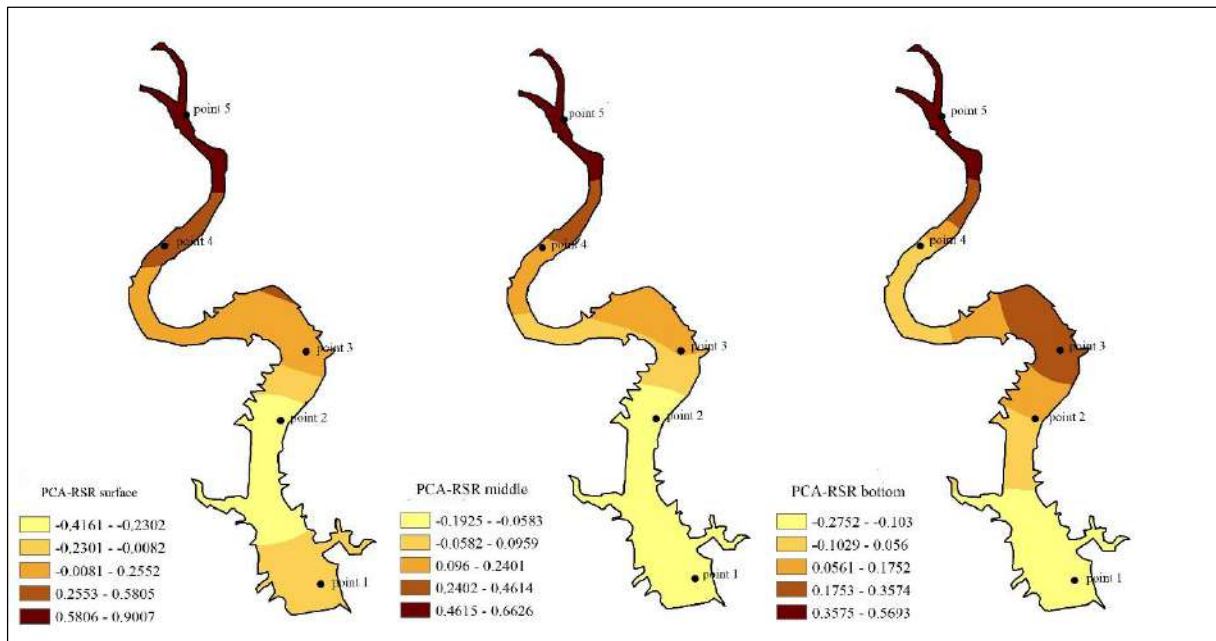
Fig. 2: PCA-RSR model evaluation results.

from the dam head to the reservoir's tail as a whole. Based on water quality monitoring data from Daheiting Reservoir in several seasons in 2018, Wu et al. (2020) assessed the water quality status of Daheiting Reservoir and found comparable results. The water quality is inevitably affected by the discharge of Panjiakou Reservoir upstream and by the inflow of Sa River upstream. The Sa river runs through the town of Sa river. Domestic sewage and iron ore industrial effluent are released into the Sa River and flow downstream to the Daheiting Reservoir (Li 2010). This could explain the high levels of nitrogen and phosphorus in the reservoir's upper reaches, as well as the poor water quality of the reservoir's

various water layers. Furthermore, because the Luan River system's terrain tilts from northwest to southeast (Li 2019), Daheiting Reservoir has a unique geographical location, and the amount of water in each section varies. The wider water area and larger water volume in the lower reaches have a certain dilution effect on the water bodies with high nitrogen and phosphorus concentrations from the middle and upper reaches so that the water quality of the downstream dam head of the Daheiting Reservoir is better than that of the upstream reservoir tail. The water quality shows a decreasing trend from the head of the dam to the end of the reservoir as a whole.
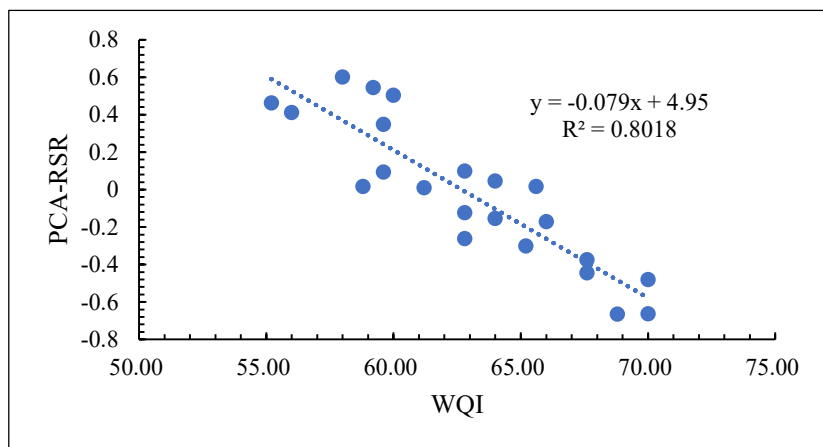
Fig. 3: Correlation between WQI and PCA-RSR model.

Comparison of Evaluation Results

According to Formula (1) and Table 1, the scores of each point in the WQI water quality evaluation model were calculated, and the scores were classified according to Table 2. At the same time, the scores of the PCA-RSR water quality evaluation model were classified according to Table 6. The results are shown in Table 7.

It can be seen from Table 7 that the WQI model is a high-excellent model and the PCA-RSR model is low-excellent. The evaluation results of the latter are in good agreement with those of the WQI system, which is widely used in water quality evaluation, indicating that the model is feasible in water quality evaluation. Under the same water quality conditions, this model's score and assessment grade are lower than the old WQI system, showing that this model's evaluation criterion is stricter than the WQI system'. The discrete coefficient can reduce the impact of the absolute value and measurement unit on the degree of discreteness measurement. The degree of discretization of the data is proportional to the discrete coefficient. The discretization coefficients of the evaluation score values of the two models are calculated according to the formula (13) and Table 7, respectively. The results show that the discretization coefficient (v_s=3.566) of the evaluation score values of the PCA-RSR model is larger than that of the WQI model (v_s=0.059), that is, the discretization degree of the evaluation score values of the PCA-RSR model is greater than that of the WQI system, indicating that the model is more precise in reflecting the differences between different water quality conditions.

It can better show the differences between different water quality conditions.

$$v_s = \frac{s}{\bar{x}} \qquad \ldots(13)$$

In the formula, v_s is the discrete coefficient, s is the standard deviation of the group of data, is the average value of the group of data.

Excel 2019 is used to analyze the correlation between the evaluation results of WQI and the PCA-RSR model, which is detailed in Fig.3. The results show that there is a good negative correlation between them (R^2 = 0.8018), indicating that the evaluation system of the PCA-RSR model is feasible and has a certain application value.

CONCLUSION

(1) The spatial water quality variation of Daheiting Reservoir in 2019 shows that the water quality at the dam head is slightly better than that at the end of the reservoir. This is due to the influence of human factors along the Sa River, discharge

Table 6: PCA-RSR model threshold for water quality evaluation.

Grade	Range
I	$f \leq -0.88374$
II	$-0.88374 \leq f \leq -0.49191$
III	$-0.49191 \leq f \leq 0.098711$
IV	$0.098711 \leq f \leq 1.276935$
V	$f \geq 1.276935$

Table 7: Water quality assessment scores and ratings.

Sampling Point	depth	WQI score and rating		PCA-RSR score and rating	
	surface	67.00	II	-0.1172	III
1	middle	64.00	II	-0.21129	III
	bottom	67.60	II	-0.50956	II
	surface	68.00	II	-0.41669	III
2	middle	63.80	II	-0.42396	III
	bottom	62.00	II	0.054408	III
	surface	59.60	III	0.154548	IV
3	middle	62.60	II	0.282544	IV
	bottom	60.00	III	0.503783	IV
	surface	56.00	III	0.312489	IV
4	middle	59.60	III	0.073178	III
	bottom	62.80	II	-0.36057	III
	surface	58.00	III	0.901332	IV
5	middle	58.60	III	0.922751	IV
	bottom	59.20	III	0.944169	IV

from upstream Panjiakou Reservoir, as well as the topography of the Luan River system. From the dam head to the reservoir's end, the water quality is deteriorating.

(2) The PCA-RSR model is low-excellent. The water quality evaluation result has a greater correlation than the traditional WQI system. The evaluation criteria are more stringent than those used by the WQI method. The degree of discrimination shown between different water quality circumstances is larger and more precise than that of the old system.

(3) PCA-RSR model uses PCA to effectively avoid the errors caused by information overlap among various indicators, and fully considers the weight of environmental factors in the study area, which makes the evaluation system more suitable for this study area, has a certain practical value, and is suitable for water quality evaluation in specific research areas.

ACKNOWLEDGMENTS

REFERENCES

Cao, Y.Y. 2019. Water quality evaluation of Yanshan Nanlu reservoir group based on RBF neural network. Water Resour. Develop. Manag., 02: 38-41.

Chen, Y., Zhang, M., Qu, X.D., Wang, B.M. and Zhu, L.J. 2016. The spatial-temporal pattern dynamics of the water environment in Panjiakou–Daheiting Reservoir. J. Appl. Environ. Biol., 6: 1082-1088.

Jiang, B., Sun, M., Ji, Y.K., Lyu, F. and Qin, Y.S. 2018. A fuzzy comprehensive evaluation of surface water quality based on entropy method. J. Irrig. Drain., 37(S1): 47-50.

Kocer, M.A.T. and Sevgili, H. 2014. Parameters selection for water quality index in the assessment of the environmental impacts of land-based trout farms. Ecol. Indicat., 36: 672-681.

Li, Y.Q., Huang, T.L., Zhang, H.H., Wen, C.C., Yang, S.Y., Lin, Z.S. and Gao, X. 2020. Succession Characteristics of Algae Functional Groups and Water Quality Assessment in a Drinking Water Reservoir. J. Environ. Sci., 41(05): 2158-2165.

Li, B.D. 2019. Study on Water Temperature Stratification and Water Quality Response Characteristics Of Daheiting Reservoir. Hebei University of Engineering, Handan.

Liu, L.C., Jin, S.F., Fu, C.Y., Dong, X. F. and Liu, S. 2016. Spatial-temporal differentiation and driving factors of water poverty in Gansu Province. J. Lanzhou Univ. Natu. Sci., 52(02): 205-210.

Li, G.H., Li, C. Y., Shi, X. H., Zhao, S. N. and Quan, D. 2018a. Evaluation of water quality of Tokto section in yellow river based on principal component analysis and water quality identification index [J]. Bulletin of Soil and Water Conservation, 38(06): 310-314, 321.

Li, J., Zhao, R.F., Liang, D. and Song, X.Q. 2018b. Assessment and spatial-temporal dynamics of urban land ecological security of Lanzhou City. Areal Res. Develop., (2): 151-157.

Liu, M.Y., Zhang, H.B., Sun, J.F., Chen, N.L. and Li, Y. 2014. Fine assessment of land ecological status in the typical area. Chinese Agric. Sci. Bull., 30(033): 206-211.

Liu, Z.Y., Zhu, Y.N., Pu, C.L., Yan, Z.M., Liu, X.X., Mu, F.X., Su, R., Wang, J.R., Liu, J.Z., Fu, W.N. and Zhu, Y.N. 2018. Influencing factors and control mechanism of ecological security of oasis in Xinjiang based on ecological civilization-Taking Tacheng city as an example. Chin. J. Agric. Resour. Regional Plan., 039(003): 155-160.

Liu, C., Liu, X.B., Zhou, H.D., Wang, S.Y. and Li, B.D. 2019. Temporal and spatial evolution characteristics and driving factors of reservoir anoxic zone. J. Hydra. Eng., 50(12): 67-78.

Li, N. 2010. Research Economic Transformation of Resource-Based County-Taking Qianxi as An Example. Hebei University of Technology, Handan.

Ma, S.W., Xie, D.T., Zhang, X.C., Peng, Z.T., Hong, H.K., Luo, Z. and Xiao, J.J. 2017. Measures of land ecological security early warning and its spatial-temporal evolution in the ecologically sensitive area of the Three Gorges reservoir area: A case study of Wanzhou District Chongqing City. Acta Ecol. Sin., 37(24): 8227-8240.

Pesce, S.F. and Wunderlin, D.A. 2000. Use of water quality indices to verify the impact of Córdoba City (Argentina) on Suqua River. Water Res., 34(11): 2915-2926.

Song, J., Zhang, Y.W. and Zhang, W. 2017. A fuzzy comprehensive evaluation of surface water quality based on combination weighting. Gansu Water Resour. Hydropower Technol., 53(10): 4-8.

Sun, X.J. and Sun, X.W. 2019. Study on water quality classification forecast based on MFOA-ELM. J. Chinese Agric. Mechan., 40(08): 176-181.

Tian, F.T. 2002. Rank sum ratio method and its application. Chin. J. Phys., 4(2): 115-119.

Wang, F. 2020. Water Quality Status and protection countermeasures of Panjiakou and daheiting reservoirs. Water Planning and Design, (03): 43-48.

Wu, T., Wang, J.B., Yang, J. and Hao, Z.X. 2020. Spatio-temporal characteristics of water quality in Daheiting Reservoir and downstream water transfer strategy. Water Resour. Protect., 36(2): 65-72.

Wang, C.C., Meng, F.L., Yang, M., Zhao, X. and Chen, D.W. 2020. Toxicity pollution characteristics and health risk assessment of main influent rivers in Huaxi-Songbaishan reservoir. China Sci. Paper, 15(9): 1077-1084.

Xing, L.W. and Wei, X.P. 2020. Water quality assessment of Xihe Reservoir based on Elman Neural Network Model. Yangtze River, 51(07): 64-70.

Xu, X., Sun, A.F. and Sun, Q.R. 2015. Application of rank-sum Beffa in a comprehensive evaluation of the qualified rate of water quality monitoring indexes in swimming pools. China Health Ind., 12(20): 163-165.

Yan, B. and Yang, X. 2015. Water quality evaluation and prediction of upstream of Dahuofang Reservoir in the Hun River based on the fuzzy comprehensive evaluation. South-to-North Water Transf. Water Sci. Technol., 13(02): 284-288+381.

Yu, H.Y., Zhang, F., Cao, L., Wang, J. and Yang, S.T. 2017a. A spatial-temporal pattern of land ecological security at a township scale in the Bortala Mongolian autonomous prefecture. Acta Ecol. Sin., 37(19): 6355-6369.

Yu, S.H., Zhou, X.L., Qing, J.C., Chen, Z.K., Guo, A.Q. and Qin, L. 2017b. Evaluation of ecological security of coastal saline land in Hebei [J]. Chin. J. Eco-Agric., 25(5): 778-786.

Zhang, H. J., Xue, X. G., Peng, L. and Gu, J. G. 2020a. Long-term change in heavy metal pollution of sediments in Liuxihe Reservoir. J. Hydroecol., 41(04): 116-124.

Zhang, W.P., Li, B., Wang, X.Q. and Wei, T. 2020b. Application of GIS and PCA-RSR model in groundwater quality evaluation. Yangtze River, 7: 46-51.

Effects of Regulated Deficit Irrigation on Soil Nutrients, Growth and Morbidity of *Panax notoginseng* in Yunnan High Altitude Areas, China

Tianyu Xu*, Shuteng Zhi*, Songyi Zhao** and Qiliang Yang**†

*School of Hydraulic and Electric Power, Heilongjiang University, Harbin 150080, China
**Faculty of Modern Agricultural Engineering, Kunming University of Science and Technology, Kunming, Yunnan 650500, China
†Corresponding author: Qiliang Yang; xty1115291208@163.com

ABSTRACT

This study investigated the responses of *Panax notoginseng* in a high-altitude area to regulated deficit irrigation at different growth stages (seedling stage, vegetative growth stage, flowering stage, and root weight gain stage) by observing indicators such as plant growth, soil nutrients, and morbidity. Conventional irrigation (70%-80% FC) was applied at the seedling stage and the root weight gain stage. Three regulated deficit irrigation levels (50%-60% FC, 40%-50% FC, and 30%-40% FC) were applied during the vegetative growth period, and three regulated deficit irrigation levels (70%-80% FC, 50%-60% FC, and 40%-50% FC) were used in the flowering period. Conventional irrigation was also applied throughout the growth stage as a control (CK). The results showed that the content of available phosphorus, available potassium, and nitrate-nitrogen in the soil was the lowest under the T4 treatment, and the cutting+main root length, rib length, root surface area, root volume, and main root diameter all reached their maximum values under this treatment. Under the T4 treatment, the total saponin content and total dry weight were the highest, the irrigation water use efficiency was the highest, and the *P. notoginseng* morbidity rate was the lowest. Morbidity was reduced by 53.42 percent in individuals who received the CK therapy, whereas total saponin content increased by 8.65 percent. The T4 therapy had the highest score of all the treatments in principal component analysis. As a result, planting *P. notoginseng* under the T4 treatment can effectively reduce irrigation water usage, enhance production and quality, and minimize the incidence of sickness in *P. notoginseng*.

INTRODUCTION

Panax notoginseng is an herbaceous plant in the Araliaceae family, which has strict requirements for its growth environment. It is mainly distributed in high-altitude areas of Yunnan, China (Huang et al. 2018). *P. notoginseng* is easily affected by its external environment during the planting process (Zu et al. 2017). Different water management modes will change the soil environment in the planting area, including the microbial communities and the soil nutrient and physicochemical properties (Tan et al. 2017). These changes may lead to reductions in *P. notoginseng* yield (Li et al. 2019). Therefore, the water management mode is an important controllable factor that plays a vital role in the *P. notoginseng* cultivation process. At present, various new water management modes are in use, including limited irrigation (Xu et al. 2019), regulated deficit irrigation (Majid et al. 2020), and alternate root-zone irrigation (Huan et al. 2018). Regulated deficit irrigation, for example, refers to the use of various levels of water scarcity during a certain stage of the crop growth process to focus crop growth in the desired growth state while ensuring

normal plant growth. The technique is primarily dependent on the crop's control and compensatory effects (Levin et al. 2017). Current research shows that a moderate water deficit is beneficial to the growth of *Jatropha curcas* L (Kheira & Atta 2009). Guo et al. (2015) and other studies on the effects of soil moisture on alfalfa root rot found that water significantly impacts the disease index of alfalfa root rot, and excessive water aggravates alfalfa root rot. Zhao et al. (2014) found in experiments that soil moisture affected root rot in potted *P. notoginseng*, and the morbidity of root rot and disease was positively correlated with soil moisture content. When the soil moisture content was 85% of the field water capacity, the morbidity of disease in *P. notoginseng* was the highest compared to that at all tested soil moisture levels.

In previous studies, the mechanisms of crop response to water deficit irrigation in low-altitude areas have been fully studied, but the responses of different crops and varieties to crop water deficit adjustment as well as the climatic conditions in high-altitude areas are significantly different (Luo et al. 2013). Research on the water consumption trends

in *P. notoginseng* in high-altitude areas mainly focuses on the full growth stage, while the research on regulated deficit irrigation in various growth stages of *P. notoginseng* (seedling stage, vegetative growth stage, flowering stage, and root weight gain stage) lacks depth. Therefore, this study examined the effects of different levels of water deficit treatment during the vegetative growth period and flowering period of *P. notoginseng* on the growth, soil nutrients, and morbidity of *P. notoginseng*. The analysis model comprehensively evaluated the quality of *P. notoginseng* and identified the optimal planting method under the regulated deficit irrigation mode in each growth stage, to provide a basis for high-quality and high-yield water management for *P. notoginseng* in high-altitude areas of Yunnan.

MATERIALS AND METHODS

Experimental Materials

The experimental site is located at Kunming University of Science and Technology, Kunming City, Yunnan Province, 24°84′50″N and 102°86′49″E, at an altitude of approximately 1983 m. The planting area has a subtropical-plateau mountain monsoon climate, and the annual temperature difference is low. A greenhouse with a length of 34.2 m, a width of 7.2 m, and a height of 2.5 m was built in the test area. In the greenhouse, the test soil was red loam, with a field capacity (FC) of 35 percent. The shed featured three layers of shading nets on the ceiling and two layers of shading nets all around it. The light transmission rate was 18%.

In the greenhouse, trenches with ridges between them were dug with a depth of 0.4 m and a width of 0.4 m before the test. The planting space was divided into ten ridges, each measuring 3 m in length and 1.5 m in breadth. Sprinklers

were installed between every two ridges of the shed, with a 1.5-m spraying radius.

Test Design

Field trials were conducted with intact, pest-free *P. notoginseng* seedlings. The seedlings were arranged on each ridge at a distance of 0.05 m in the longitudinal direction and 0.05 m in the transverse direction. Each ridge was divided into three plots, and the area of each trial plot was 1 m×1.5 m.

The experiment was divided into four growth periods according to the growth process of *P. notoginseng*: seedling stage, vegetative growth stage, flowering stage, and root weight gain stage. Conventional irrigation (70%-80% FC) was applied in the seedling stage and root weight gain stage; regulated deficit irrigation was applied in the vegetative growth stage and the flowering stage.

Three irrigation levels were applied during the vegetative growth period: mild water deficit (50%-60% FC), moderate water deficit (40%-50% FC), and severe water deficit (30%-40% FC). Three irrigation levels were set during the flowering period: conventional irrigation (70%-80% FC), mild water deficit (50%-60% FC), and moderate water deficit (40%-50% FC). In addition, conventional irrigation throughout the growth stage of *P. notoginseng* was used as a control treatment (CK). In this experiment, a total of 10 water irrigation treatments were performed, and each irrigation mode was repeated 3 times for a total of 30 experimental plots. The specific irrigation water scheme is shown in Table 1. During the test, the soil water content was measured at 8 am every morning. When the water limit was lower than field capacity, irrigation was performed to the upper limit of field capacity. During the test, fertilizer was applied only once before the *P. notoginseng* seedlings were planted, and the amount of fertilizer was 1500 kg·hm^{-2} (Weifu water-soluble compound fertilizer imported from Israel).

Table 1: Irrigation treatment at different growth stages.

Treat	Seedling stage	Vegetative growth stage	Flowering stage	Root weight gain stage
CK	70%-80%	70%-80%	70%-80%	70%-80%
T1	70%-80%	50%-60%	70%-80%	70%-80%
T2	70%-80%	40%-50%	70%-80%	70%-80%
T3	70%-80%	30%-40%	70%-80%	70%-80%
T4	70%-80%	50%-60%	50%-60%	70%-80%
T5	70%-80%	50%-60%	40%-50%	70%-80%
T6	70%-80%	40%-50%	50%-60%	70%-80%
T7	70%-80%	40%-50%	40%-50%	70%-80%
T8	70%-80%	30%-40%	50%-60%	70%-80%
T9	70%-80%	30%-40%	40%-50%	70%-80%

Observation Indexes

Soil Nutrients and Moisture

The contents of nitrate nitrogen, available potassium, and available phosphorus in the red soil of *P. notoginseng* planted in each irrigation treatment were measured. The samples were obtained at the end of the growing period using earth-boring drills. Among them, nitrate-nitrogen in the root region of *P. notoginseng* was determined by ultraviolet spectrophotometry, available potassium was determined by flame photometry, and available phosphorus was determined by molybdenum antimony colorimetry. The soil moisture content in the root zone of *P. notoginseng* was measured daily with a TPIME-PICO64/32 soil moisture analyzer.

Panax notoginseng Root System, Yield, Morbidity and Irrigation Water Use Efficiency

The fresh roots of *P. notoginseng* were washed, and the roots were scanned with an EPSON STD4800 scanner. The obtained images were analyzed using WinRHIZO software to obtain data such as root length, diameter, surface area, and volume. The roots, leaves, petioles, and stems of *P. notoginseng* were placed into different envelopes, and the envelopes were placed in an oven at 105°C for 30 minutes. Then, the temperature was adjusted to 50°C to dry the plant parts to a constant weight. Finally, the dry matter mass of the roots, stems, and leaves of *P. notoginseng* was obtained by weighing.

During the experiment, the number of diseased plants was checked every week. Diseased plants were dug up immediately, and the soil in the area was sprayed with a disinfectant.

morbidity = diseased plant number / total number of plants

The irrigation water use efficiency (*WUEi*) was calculated based on the farmland water balance.

Saponin Content

Five saponins (R_1, Rg_1, Re, Rb_1, R_d) were identified by Agilent 1260 series high-performance liquid chromatography. The chromatographic conditions were as follows: Vision HTC18 column (250mm×4.6mm, 5µm); detection wavelength of 203nm, column temperature of 30°C, the flow rate of 1.0mL. min-, and injection volume of 10µL. R_1 was notoginsenoside, and Rg_1, Re, Rb_1, and R_d were ginsenoside.

Data processing

The test results were analyzed and plotted using Microsoft Excel 2007. Correlation analysis, principal component analysis, and analysis of variance (ANOVA) were performed using IBM SPSS Statistics 22.0. The Duncan method was used for multiple comparisons (P = 0.05).

RESULTS AND DISCUSSION

Effects of Regulated Deficit Irrigation on Soil Nutrients in the Root Zone

Fig. 1 shows the response of available phosphorus, available potassium, and nitrate nitrogen in *P. notoginseng* soil to the treatments at the end of the growing period. The figure shows that the contents of available phosphorus, available potassium, and nitrate-nitrogen in the soil layer under the CK, T1, T2, and T3 treatments were not significantly different (P>0.05). During the flowering period, the available phosphorus, available potassium, and nitrate nitrogen in the different treatments were significantly different (P<0.05). The T3 treatment had the highest available phosphorus content, which was a significant increase of 6.76% compared with that in the CK treatment, but the phosphorus contents of T1, T5, T6, and T7 were not significantly different from that of the CK treatment. The T4 treatment had the lowest available phosphorus, which was significantly reduced by 3.61% compared with that in the CK treatment. The content of available potassium in the T9 treatment was the highest and showed a significant increase of 5.44% compared with that in the CK treatment. The differences in available potassium in the T2-T3 and T7-T9 soils were not significant. Compared
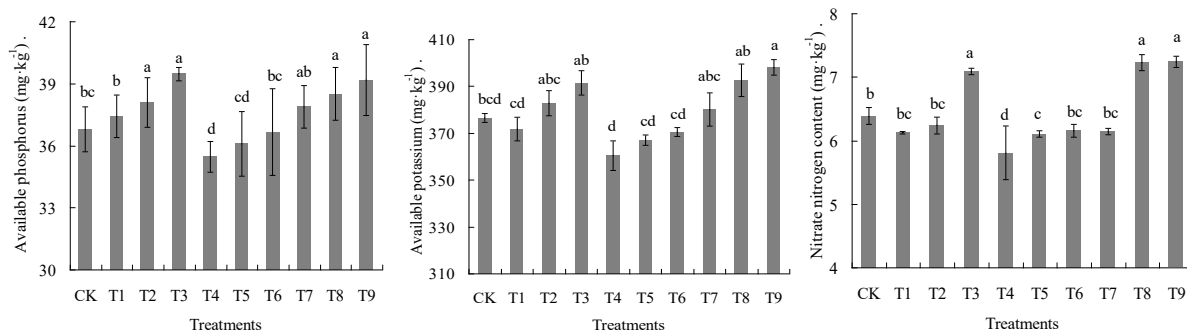

Fig. 1: Soil nutrients of *Panax notoginseng* underwater treatments.

with that in the CK treatment, the available potassium in the other treatments was reduced by 1.46% to 4.22%, and the T4 treatment had the largest reduction. The content of nitrate nitrogen was the lowest in the T4 treatment, which was significantly decreased by 9.08% compared with that in the CK treatment. The nitrate-nitrogen content was not significantly different among the T1, T2, T6, T7, and CK treatments. The T3, T8, and T9 treatments had the highest soil nitrate-nitrogen levels, which were significantly higher by 10.95% to 13.30% than that in the CK treatment.

Effects of Regulated Deficit Irrigation on Root Growth

Table 2 shows the root growth of *P. notoginseng* under the different treatments. The effects of each treatment on the growth indexes of *P. notoginseng* were significant (P<0.05). The cutting+main root length, rib length, root surface area, root volume, and main root diameter in the T4 treatment all reached maximum values that were significantly higher than those in the other treatments. The T7 and T9 treatment cutting+main root length, rib length, root surface area, root volume, and root diameter were all the lowest and were significantly reduced by 10.78%-11.04%, 6.31%-15.84%, 8.06%-10.81%, 11.51%-14.59%, and 20.68%-22.82%, respectively, compared with those of CK (P<0.05). In other treatments, the cutting+main root length was not significantly different from that in CK. Among them, the cutting+main root length in the T1, T2, and T5 treatments increased by 2.08% to 5.32% compared with that in the CK treatment, and those of T3, T6, and T7 decreased by 0.26% to 6.75% compared that in the CK treatment. In all treatments except T4, T5, and T9, the variation in rib length varied from -6.31% to 5.42% compared with the CK rib length, showing no significant difference. In all treatments except T3, T4, T8, and T9, compared with CK, the variation in root surface area was between -2.91% and

0.40%, showing no significant difference. The root volume in the T1, T2, T5, and T6 treatments showed no significant difference from that in the CK treatment, with a different range of 0.24% to 2.49%. In all treatments except the T3, T4, T8, and T9 treatments, the main root diameter was not significantly different from that in the CK treatment, with a difference between -6.54% and 2.01%.

Effects of Regulated Deficit Irrigation on Effective Components of *P. notoginseng*

Fig. 2 shows the distribution of saponins in *P. notoginseng* under different treatments. Under each treatment, the levels of the five saponins showed significant differences (P <0.05). In each treatment, the contents of Rg_1 and Rb_1 were higher, and the contents of Re and R_1 were lower. The contents of Rg_1 and R_1 in the CK treatment were the lowest and the highest, 0.06% and 3.07%, respectively. The Rg_1 and R_1 contents in the other treatments increased by 33.33% to 166.67% and 1.30% to 40.07%, respectively, compared with those in the CK treatment. The contents of Re in T1 and T4-T7 were relatively high and were 20.00%-40.00% higher than that in the CK treatment. The Rb_1 contents in T1, T2, and T4 were not significantly different from that in the CK treatment. The Rb_1 content in the T9 treatment was the lowest of all treatments at 2.54%, which was a significant decrease of 21.85% compared with that in the CK treatment. The other treatments had 3.08% to 19.08% less Rb_1 than the CK treatment. The T4 treatment had the highest Rd content of all the treatments, which was 39.57% higher than that of the CK treatment. The Rd contents in T1 and T5-T7 increased by 3.48%-24.35% and that in the other treatments decreased by 2.17%-43.91% compared with that in the CK treatment. The total saponin content in the T4 treatment was the highest and was significantly higher than that in the other treatments.

Table 2: The growth of *Panax notoginseng* roots under different water treatments.

| Treat	Cutting+main root [cm]	Rib length [cm]	Root surface area [cm²]	Root volume [cm³]	Root diameter [mm]
CK	7.70±0.48bc	12.37±0.88c	50.13±1.58b	8.43±0.47bc	15.91±1.29b
T1	8.03±0.49b	12.90±0.58bc	50.17±2.35b	8.45±0.52b	16.23±0.67b
T2	7.86±0.31b	12.89±0.61bc	48.93±2.22bc	8.22±0.23bcd	15.20±1.16bc
T3	7.18±0.19cd	12.30±0.96c	46.50±2.11cd	7.58±0.34de	14.12±0.28c
T4	8.90±0.31a	15.13±0.79a	54.42±1.69a	9.30±0.24a	18.15±0.47a
T5	8.11±0.49b	14.12±0.85ab	49.64±1.58bc	8.40±0.39bc	14.87±0.45bc
T6	7.68±0.34bc	12.30±0.74c	50.33±1.78b	8.39±0.17bc	15.73±0.65b
T7	7.43±0.27bcd	13.04±0.66bc	48.67±1.54bc	7.66±0.36cde	15.53±0.71bc
T8	6.87±0.28d	11.59±0.52cd	46.09±1.79cd	7.46±0.48e	12.62±0.58d
T9	6.85±0.28d	10.41±0.92d	44.71±2.06d	7.20±0.64e	12.28±1.00d
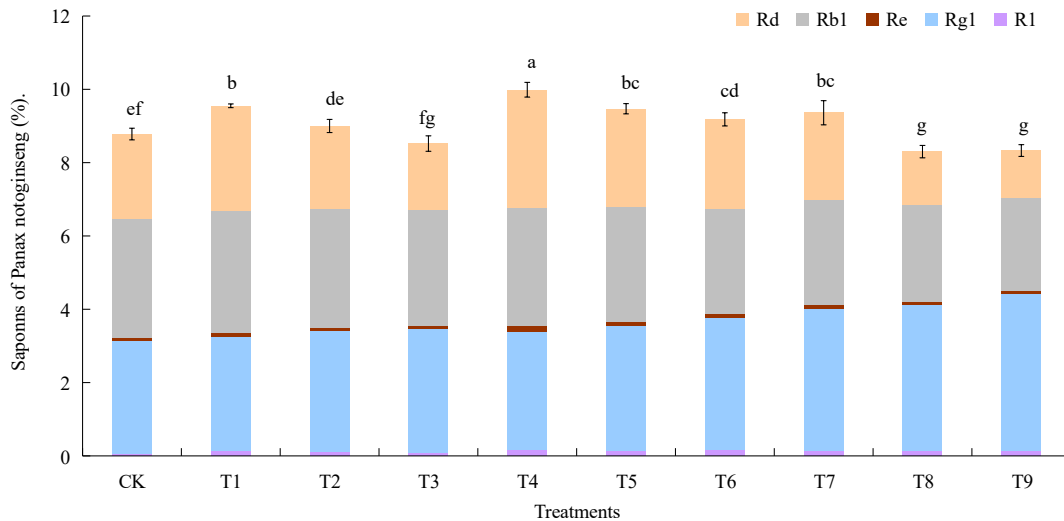
Fig. 2: The saponins of Panax notoginseng underwater treatments.

The total saponin content of the T8 treatment was the lowest of all the treatments. The total saponin content of the other treatments except for T3, T8, and T9 increased by 2.28%-8.65% compared with that in CK.

Effects of Regulated Deficit Irrigation on Yield, Morbidity and Irrigation Water use Efficiency of *P. notoginseng*

Table 3 shows that the dry weight of the leaves, petioles, and stems was less than the root dry weight. The total dry weight in each treatment was greatly affected by the dry weight of the *P. notoginseng* roots. The dry matter mass of the leaves in the T4 treatment was significantly (7.29%) higher than that in the CK treatment. The dry matter mass of the leaves in the T8 and T9 treatments was the lowest,

which was significantly lower (by 21.88% and 22.92%) compared to that in the CK treatment. Compared with that in the CK treatment, the dry matter mass of the leaves in the other treatments decreased significantly, by 5.21%-16.32%. Except in the T4 treatment, the dry weight of the stem and petiole in all treatments decreased by 3.38%-17.87% compared with that in the CK treatment. The dry weight of the stem and petiole in the T4 and T1 treatments increased by 24.06% and 20.43% compared with those in the CK treatment, and those in the other treatments decreased by 0.95% to 31.13% compared with those in the CK treatment. The total dry weight of *P. notoginseng* in the T1 and T4 treatments increased significantly, by 8.65% and 13.54%, respectively, compared with that in the CK treatment.

Table 3: Effects of irrigation modes on dry weight, irrigation water use efficiency, and Morbidity of *Panax notoginseng*.

Treat	Dry weight [g]					Irrigation water use efficiency [g·m^{-2}·mm^{-1}]	Morbidity [%]
	leaves	Petioles and stems	Above-ground	Root	Total		
CK	0.96±0.03bc	0.69±0.02ab	1.65±0.04b	10.18±0.51b	11.83±0.55b	1.82±0.24e	14.83±0.45bcd
T1	0.98±0.06ab	0.67±0.02bc	1.65±0.07b	12.26±0.57a	13.91±0.63a	2.28±0.21b	12.71±1.24de
T2	0.88±0.02d	0.65±0.02bc	1.53±0.02c	10.03±0.75b	11.56±0.74b	1.83±0.12de	13.82±0.76cd
T3	0.81±0.04e	0.63±0.04cd	1.44±0.08d	9.74±0.51bc	11.18±0.57bc	1.80±0.26e	13.87±0.87cd
T4	1.03±0.04a	0.73±0.02a	1.76±0.03a	12.63±0.65a	14.40±0.63a	2.43±0.33a	7.15±0.64f
T5	0.91±0.03cd	0.67±0.04bc	1.58±0.07bc	10.09±0.77b	11.66±0.83b	2.05±0.18cd	7.96±0.80f
T6	0.89±0.02d	0.64±0.01bcd	1.53±0.03c	9.97±0.67b	11.50±0.64b	2.14±0.31c	10.74±0.62e
T7	0.80±0.04e	0.60±0.02de	1.40±0.05de	8.81±0.27cd	10.21±0.22cd	1.75±0.09e	15.85±0.86abc
T8	0.75±0.04ef	0.59±0.04de	1.34±0.05ef	7.96±0.34de	9.30±0.30de	1.51±0.09f	16.83±0.91ab
T9	0.74±0.02f	0.57±0.03e	1.30±0.04f	7.01±0.60e	8.32±0.60e	1.43±0.05f	17.97±1.41a

The T4 and T1 treatments had higher irrigation water use efficiencies than the other treatments, which were significantly increased by 34.68% and 24.54%, respectively, compared with that in the CK treatment. The water use efficiency of the T3 and T7-T9 treatments was 0.37% to 19.56% lower, respectively than that of the CK treatment. The water use efficiency in the other treatments was 4.43%-13.84% higher than that in the CK treatment.

The morbidity of *P. notoginseng* in the T7, T8, and T9 treatments was high, increasing by 6.60%, 13.19%, and 19.99%, respectively, compared with that in the CK treatment. The T4 treatment had the lowest morbidity, which was 53.42% lower than that of the CK treatment. The morbidity of *P. notoginseng* in the other treatments was 6.62% to 46.83% lower than that in the CK treatment.

Principal Component Analysis

The KMO statistic of saponin content in this study was 0.561, which is greater than 0.5. Bartlett's sphericity test P was 0.01, which is less than 0.05. Therefore, these data are suitable for principal component analysis.

Eigenvalue and Variance Contribution Rate

The characteristic root and contribution rate of the first principal component were 2.73 and 54.65%, respectively, and the characteristic root and contribution rate of the second principal component were 1.28 and 25.57%. The cumulative contribution rate was 80.22%, indicating that the first and second principal components can reflect the overall information from the original indicators and are suitable for the general analysis of comprehensive quality.

Principal component expression and comprehensive score

The principal component expression is:

$$P_{C1} = -0.082Z_{R1} - 0.221Z_{Rg1} + 0.187Z_{Re} + 0.233Z_{Rb1} + 0.205Z_{Rd} \tag{11}$$

$$P_{C2} = 0.650Z_{R1} + 0.279Z_{Rg1} + 0.219Z_{Re} - 0.152Z_{Rb1} + 0.178Z_{Rd} \tag{12}$$

$$Z_F = 0.681P_{C1} + 0.319P_{C2} \tag{13}$$

where P_{C1} is the first principal component score; P_{C2} is the second principal component score; Z_F is the comprehensive score; Z_{R1} is the notoginsenoside $R1$; Z_{Rg1} is the ginsenoside Rg_1; Z_{Re} is the ginsenoside Re; Z_{Rb1} is the ginsenoside $Rb1$; and Z_{Rd} is the ginsenoside Rd.

According to the principal component analysis, Rg_1, Re, and Rd had high loadings in the first principal component, but the first principal component score of Rg_1 was negative. For the second principal component, R_1 and Rg_1 had higher loadings, and their scores for the second principal component were positively correlated. The comprehensive evaluation scores for the quality components of saponins in the different treatments are shown in Fig. 3. Of the different water treatments, T4 scored the highest, T5 scored second highest, and T8 and T9 scored the lowest.

The research in this experiment found that the soil nutrient content of the soil in the T4, T5, and T6 treatments was lower, and the soil nutrient content of the soil in the T3, T8, and T9 treatments was higher. During the vegetative growth and flowering periods of *P. notoginseng*, a certain degree of regulated deficit irrigation can improve the soil available phosphorus, available potassium, and nitrate nitrogen absorp-
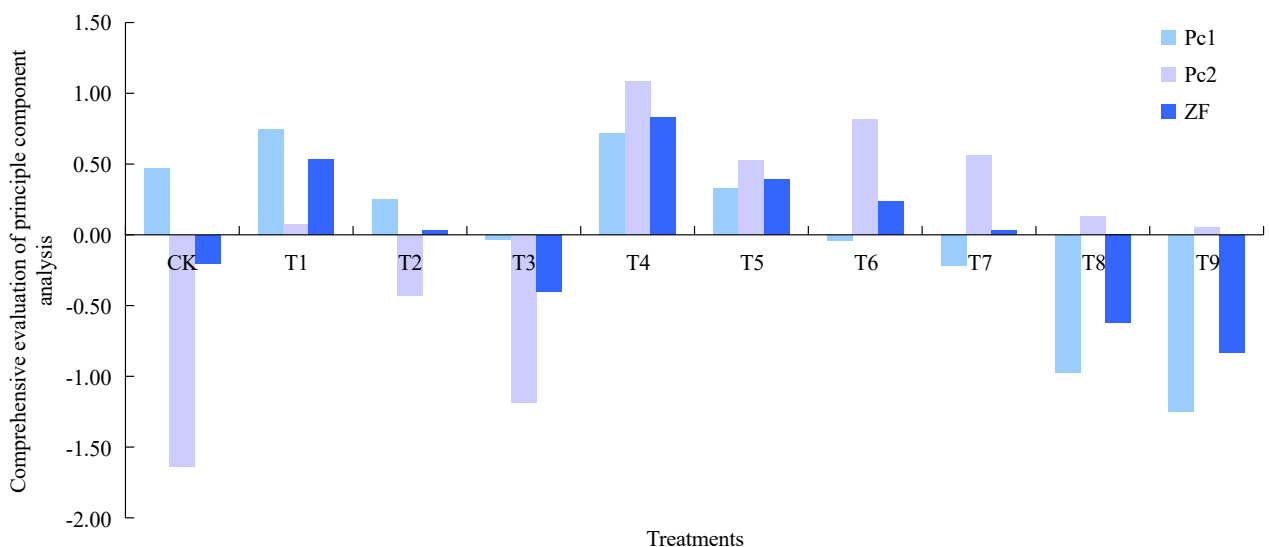

Fig 3: Comprehensive evaluation of principal component analysis of quality indexes of *Panax notoginseng* saponins.

tion capacity of *P. notoginseng*, thereby reducing the levels of these elements in the soil (Zu et al. 2017). Excessive water deficiency limits the transport and distribution of nitrogen, phosphorus, and potassium in the soil to *P. notoginseng*, which is consistent with the research on wheat by Meng et al. (2016).

This study found that the severe water deficit treatment limits root elongation reduces the root volume and root surface area, and reduces the root diameter (Hayrettin & Demir 2012, Shi et al. 2015). A mild water deficit treatment during the vegetative growth and flowering periods can improve the dry matter quality of *P. notoginseng*. This is because *P. notoginseng* has a certain resistance to stress. A certain degree of water stress stimulates the roots of *P. notoginseng* to absorb soil nutrients (Zhao et al. 2014), and the nutrients absorbed at the same time are transported to the stems, leaves and other organs, resulting in an increase in the final yield during the root weight gain stage. Severe water deficiency in the vegetative growth period and mild or moderate deficit irrigation in the flowering period significantly reduced the yield, which mainly occurred because the vegetative growth period is the key period for aboveground growth, and the severe water deficit affected *P. notoginseng* recovery (Kheira & Atta 2009). Except for the ginsenoside Rg_1, the contents of each saponin in the T4 treatment were significantly higher than those in the other treatments. In the determination of the various saponins in the T8 and T9 treatments, it was found that except for R1 and Rg_1, the other saponin indicators were at low levels. This shows that different saponin types have different responses to water demand. The use of severe deficit irrigation during the vegetative stage prevented the accumulation of some saponin content (Zhao et al. 2014).

The T1 and T4 treatments improved irrigation water use efficiency, and the T8 and T9 treatments had the lowest irrigation water use efficiency. This was because the growth of *P. notoginseng* could not be restored because of the severe deficit irrigation during the vegetative growth period and the slight rehydration during the flowering period. This also shows that moderate water deficit irrigation can significantly increase irrigation water use efficiency (Meng et al. 2016). Huang et al. (2014) performed irrigation experiments on jujube seedlings and found that higher water levels could lead to the aggravation of seedling diseases. The results of this study indicated that both higher and lower moisture levels increase the incidence of morbidity in *P. notoginseng*. A severe water deficiency easily leads to growth inhibition, and higher water availability leads to an imbalance in the proportion of the microecological environment, causing roots to rot and increasing morbidity.

CONCLUSION

Regulated deficit irrigation at different growth stages affects the yield, quality, soil nutrients, and morbidity of *P.notoginseng* in high-altitude areas. The results of this study indicated that under the T4 treatment, the contents of available phosphorus, available potassium, and nitrate-nitrogen in the soil and the morbidity of *P. notoginseng* were lower than those in the other treatments, and the root morphology, total saponin content, total dry weight, and irrigation water use efficiency were higher than those of other treatments. Compared with those in the CK treatment, morbidity decreased by 53.42%, irrigation water use efficiency increased by 34.68%, total dry weight increased by 24.06%, and total saponin content increased by 8.65% in the T4 treatment. Based on the comprehensive evaluation of the above correlation analysis and principal component analysis, regulated deficit irrigation was beneficial to the growth of *P. notoginseng* under the T4 treatment.

ACKNOWLEDGEMENT

REFERENCES

Guo, Y.X., Yong, Z.G., Jin, F.Z., De, F.L., Xue, B.Y. and Cheng Z. 2015. Effects of Inoculating Root Rot Fusurium on Alfalfa Seedlings. Acta Agrestia Sinica, 23: 623-631.

Hayrettin, K.U.S.C.U. and Demir, A.O. 2012. Responses of maize to full and limited İrrigation at different plant growth stages. Ziraat Fakültesi Dergisi Uludağ Üniversitesi, 15-27.

Huang, C.B., Zeng, F.J., Lei, J.Q., Xu, L.S. and Gao, H.H. 2014. Effects of irrigation on nitrogen nutrition characteristics in the rootzone soil of calligonum caput-medusae Schrenk seedlings. Acta Ecol. Sin., 27(6): 152-157.

Huang, Y., Teng, Y., Zhang, N., Fu, Z.C. and Ren, W.J. 2018. Human health risk assessment of heavy metals in the soil–Panax notoginseng system in Yunnan province, China. Hum. Ecol. Risk Assess. Int J., 5: 1312-1326.

Huan, F., Hu, Z., Norton, G.J., Price, A.H., Raffan, A.C. and Mooney, S.J. 2018. Interaction between contrasting rice genotypes and soil physical conditions induced by hydraulic stresses typical of alternate wetting and drying irrigation of soil. Plant Soil, 430: 233-243.

Kheira, A.A.A. and Atta N.M.M. 2009. Response of Jatropha curcas L. to water deficits: Yield, water use efficiency, and oilseed characteristics. Biomass Bioenergy, 33: 1343-1350.

Luo, H.Y., Cui, Y.L. and Zhao, S.J. 2013. Spatial distribution of irrigation water quota of highland barley in Tibet region. Trans. ASABE, 29: 116-122.

Levin, A.G., Peres M., Noy M., Love, C. and Naor A. 2017. The response of field-grown mango (cv. Keitt) trees to regulated deficit irrigation at three phenological stages. Irrig. Sci., 36: 1-11.

Li, Y., Wang, B., Chang, Y., Yang, Y., Yao, C. and Huang, X. 2019. Reductive soil disinfestation effectively alleviates the replant failure of Sanqi ginseng through allelochemical degradation and pathogen suppression. Appl. Microbiol. Biotechnol., 1: 1-15.

Meng, Z.J., Duan, A.W., Gao, Y., Wang, X.S., Shen, X.J. and Chang, X. 2016. Effect of regulated deficit irrigation on uptake and utilization of nitrogen phosphorus and potassium for winter wheat. Trans. Chin. Society Agric. Mach., 47: 208-2017.

Majid, A.K., Morteza, S.A. and Somayeh, F. 2020. Physiological aspects of date palm loading and alternate bearing under regulated deficit irrigation compared to cutting back of the bunch. Agric. Water Manag., 232: 1-13.

Shi, X.S., Li, F.U., Yan, B.Y. and He, D. 2015. Effects of water deficit at different growth stages on water use and yield of spring highland barley. Trans. Chin. Society Agric. Mach., 46: 144-151.

Tan, Y., Cui, Y.S., Ji, X.L., Wei, Y.L. and Cui, X.M. 2017. Research progress in microorganism changes of rhizospheric soil and root endoge-nous and ecology during continuous cropping of Panax notoginseng. Chin. Trad. Herbal Drugs, 48: 391-399.

Xu, T.Y., Li, J., Yang, Q.L., Liu, X.G. and Yu L.M. 2019. Yields and quality evaluation of Jatropha curcas with limited irrigation and nitrogen. J. Hunan Agric. Univ. Nat. Sci. 5: 425-432.

Zhao, H.G., Xia, M.T., Wei, F.H., Liu, C., Zhang, P.G. and Liang, Z.S. 2014. Effect of soil moisture content on root growth, active components, and root rot incidence of Panax Notoginseng. J. Northwest AF Univ. , 42: 173-178.

Zu, Y.Q., Cheng, S.C., Ke, H.L., Guo, X.H. and Li, Y. 2017. Distribution of Pb, Cd, Cu, and Zn in the plant of Panax notoginseng and soil in wen shan prefecture, a Panax notoginseng-growing region. J. Ecol. Rural Environ., 33: 317-323.

Seasonal Variation of Ultrafine Particulate Matter (PM1) and Its Correlation with Meteorological Factors and Planetary Boundary Layer in A Semi-Arid Region

Jaspreet Kaur*, Charu Jhamaria*†, Suresh Tiwari** and Deewan Singh Bisht**

*Department of Environmental Science, IIS (Deemed to be University) Jaipur, Rajasthan, India
**Indian Institute of Tropical Meteorology, Pune, Maharashtra, India
†Corresponding author: Charu Jhamaria; charu.jhamaria@iisuniv.ac.in

ABSTRACT

The present study critically investigated the effect of meteorological parameters on the mass concentration of Ultrafine Particulate Matter (PM$_1$) between October 2018 and September 2019 (n=102) in a semiarid region of Rajasthan, India. The concentration of PM$_1$ ranged between 72-110.85 µg.m^{-3} with distinct seasonal variation. Higher PM$_1$ concentrations are closely linked to decreased wind speeds and colder temperatures, according to the findings. The winter season showed the highest concentration followed by post monsoon and pre monsoon season. The cumulative effect of environmental variables such as temperature, relative humidity, and wind speed, as well as the height of the planetary boundary layer, was investigated using multiple regression analysis (HPBL). A significant negative correlation (p < 0.001) with HPBL and wind speed was observed in all three seasons. The temperature was found to have a significant (p<0.001) negative correlation during winters whereas in other seasons there was a positive but no significant (p>0.001) relationship. Relative humidity showed a negative relationship during withers and pre-monsoon season. The multiple regression model indicated a significant negative (p<0.001) relationship with HPBL in winters (R^2=0.70) explaining the 70% effect of HPBL on mass concentration of PM$_1$.During the post-monsoon (R^2 = 0.69) and pre-monsoon (R^2= 0.91) explains 69% and 91% effect of HPBL on mass concentrations of PM$_1$.The results indicate that the concentration of PM$_1$ cannot be explained by a single meteorological parameter but all the parameters show a cumulative effect.

INTRODUCTION

Atmospheric aerosols have increased drastically in the last few decades and continuously deteriorating the air quality, impacting the quality of life, and have become an important parameter for evaluation in developed as well as in developing countries. The ubiquitous nature of atmospheric aerosol shows an intense impact on the earth's atmospheric system, climatic conditions, atmospheric chemistry, influence weather conditions, ecosystem, air quality, and public health (Pöschl 2005, Solomon et al. 2007). High-intensity exposure may cause both acute and chronic effects on different organs of the body by interacting with the immune system leading to the risk of chronic respiratory and heart diseases, lung cancer, acute respiratory infections in children, chronic bronchitis in adults, and asthmatics attacks (Chen et al. 2007, Kampa & Castanas 2008). Particulate matter with an aerodynamic size of less than 10 microns deposits primarily in the upper respiratory tract, whereas fine particles with an aerodynamic size of less than 2.5 microns and ultrafine particles with an aerodynamic size of less than 0.1 microns reach the alveolar spaces of the lungs and cause or exacerbate respiratory

diseases (Satsangi et al. 2011), making it a major concern. Because fine particle matter contains a higher concentration of toxins, ultrafine and fine particulate matter provide a greater risk of cardiovascular and respiratory consequences, as well as mortality than coarse particulate matter.

Increased consumption of fossil fuels as a result of rapid urbanization and industrialization has resulted in significant emissions of pollutants into the lower atmosphere (Sharma et al. 2014), prompting major worry in Asian countries (Baldasano et al. 2003). Due to rapidly increasing population numbers, expanding industrialization and vehicular density, traffic jams, poor road conditions, and poor regulation of industrial emissions, air quality in Jaipur city has reached hazardous levels. (Dhamaniya & Goyal 2004, Kala et al. 2014). Meteorological parameters are one of the most important factors to influence particulate matter concentrations. Among them, temperature, relative humidity, wind speed, and direction play a crucial role in dispersion, accumulation, removal process, and formation of atmospheric aerosols in the lower atmosphere (Galindo et al. 2011, Goyal &Rao 2007), therefore they significantly control the concentrations

of pollutants. In addition to other factors, the height of the planetary boundary layer (HPBL) also plays a critical role in regulating pollutant concentration in any region. Evaluating mass concentration of Particulate matter in alliance with HPBL is important for identifying air pollution (Du et al. 2013) with varying seasonal changes.

This paper presents a seasonal variation in mass concentration of particulate matter (PM$_1$) in Jaipur city of Rajasthan state in India, for a period between October 2018 to June 2019. The main objective of the study is not only to quantify the concentration of PM$_1$ but also to investigate the statistical relationship between PM$_1$ and meteorological parameters (Temperature, Relative humidity, wind speed, and Planetary Boundary layer height.

MATERIALS AND METHODS

Site Description

The present study was conducted at Albert hall museum in Jaipur, the capital city of Rajasthan located at 26°1'36" north latitude and 75°4'32" east longitude in the eastern parts of Thar Desert (Fig. 1). Albert hall museum built in the year 1876, is located near the walled city is a heritage site with a large number of tourists from all over the world. The area experiences a very heavy traffic load due to the proximity to commercial areas like Ajmeri gate, Johri Bazar, Sanganer gate. Jaipur city covers an area of 200.4 km^2 with a population size of 4007505 (year 2021). The semi-arid land of the city is surrounded by rugged Aravali hills on three sides. The desert state Jaipur faces seasonal dust storms every year due to the downwind location of the Thar desert which accumulates a huge amount of dust loading aerosol over the city (Verma et al. 2013). Frequent dust storms and variation in climatology throughout the year lead to significant variability in air quality from summers to winters (Mohan & Kandya 2007, Ram et al. 2010). Average wind speed varies between 3.0 to 10.0 mph. The maximum temperature is observed in the summer season (March to May) varying between 40°C to 47°C rising 4-6°C at times when heatwave prevails, whereas winters (December to February) are quite cold with a minimum temperature of 4-9°C or can be below 0°C when chilly winds northerly blows from the Himalayan region. Western disturbances lead to increased humidity, cloudiness, and rainfall activities during the monsoon period (July to September) in Jaipur city. July and August are the rainiest months and they last up to mid-September. Rainfall decreases sharply in October month so October and November are transitional months or post-monsoon seasons. The annual rainfall is 492 mm (Singh et al. 2012). The humidity reaches the highest value in August and gradually decreases in November again rising in December and January whereas the lowest value for humidity is observed in April (Tyagi et al. 2012).

Data Collection

Ambient air Sampling and analysis were done as per the guidelines given by Centre Pollution Control Board (CPCB) New Delhi. Aerosol sampling for PM$_1$ was done for nine months considering pre-monsoon, winter, and post-monsoon seasons. Twelve hours of continuous sampling (9:00-21:00) was done thrice in a weak for collection of fine particulate matter (PM$_1$) using a fine particulate sampler (Envirotech APM 577) with a flow rate of 10 L per minute. PTFE What man filter paper with pore size 0.2 μm and a diameter of 25 mm was used for the collection of particulate matter. The sampler was placed at a height of 14 m. The filter paper was desiccated for 24 hours before and after sampling before proceeding further for estimation of mass concentration with weighing balance with a precision of 0.01 mg. For further analysis, the filter paper was wrapped in aluminum foil to avoid moisture and loss of particles. After weighing, the filters were placed in the refrigerator at (-20° C) before extraction for chemical analysis. Mass concentration of particulate matter was estimated gravimetrically by the following formula:

$$PM_1 \ (\mu g/m^3) = \frac{(w_f - w_i) * 10^6}{v}$$

Where,

w_f = Final weight of sample filter paper (g)

w_i = Initial weight of blank filter paper (g)

v = Volume of air sampled in (m^3)

10^6 = Conversion of g to μg (1g = 10^6 μg)

Meteorology Data

Data for metrological parameters such as wind speed, relative humidity, the temperature were collected from weather underground https://www.wunderground.com/.

Backward Trajectory Simulation

Planetary boundary layer data was achieved from reanalysis data by running a backward trajectory simulation model obtained from the National Oceanic and Atmospheric Administration (NOAA), Air Resources Laboratory (ARL) or the provision of the Hybrid Single-Particle Lagrangian Integrated Trajectory (HYSPLIT) transport and dispersion model from the website (http://www.arl.noaa.gov/ready. html) (Draxler & Hess 1998, Draxler & Rolph, 2003). Both forward and backward trajectories can be calculated to interpret the airflow patterns and dispersion of air pollutants in spatial and temporal boundaries. Further, these trajectories
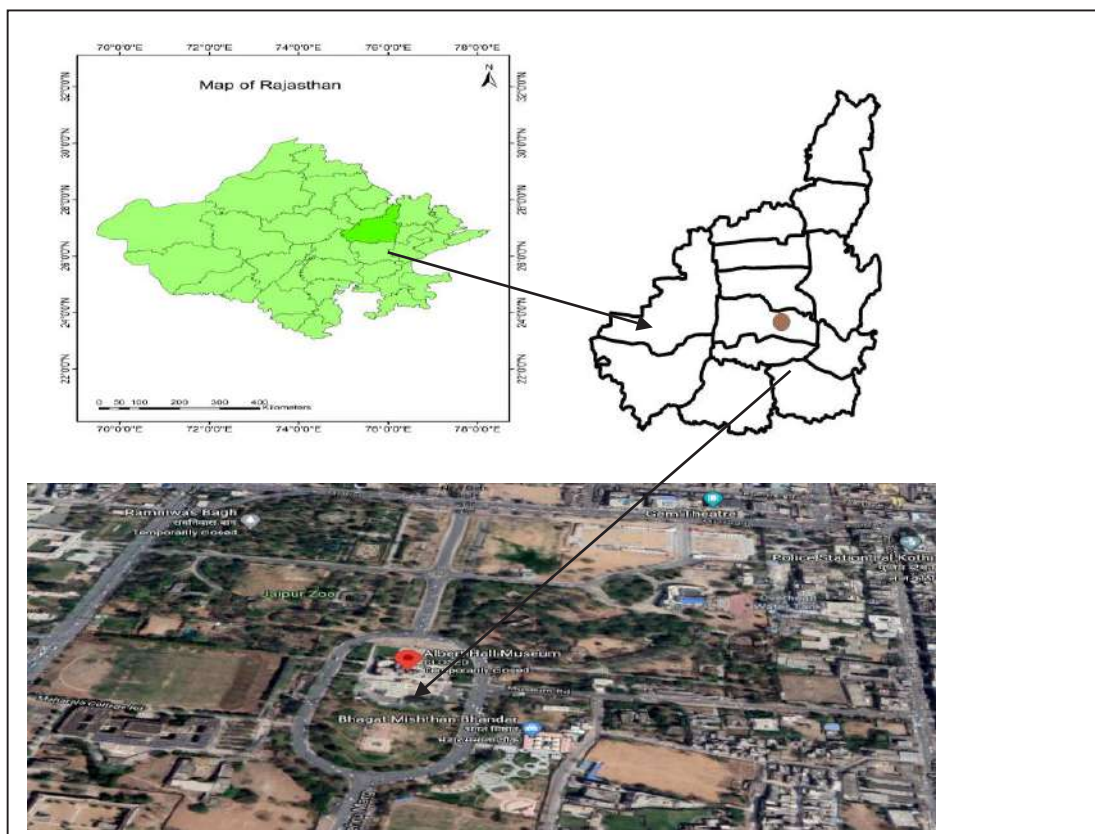
Fig. 1: Geographical map showing Rajasthan state and Jaipur district map with a satellite image of Albert Hall sampling site. source: Google

can be used to forecast the history of air mass movement and wind patterns (Fleming et al. 2012). The nine months data was achieved with GDAS metrological data at the altitude of 500 m above the ground level.

Statistical Analysis

Data analysis was performed to evaluate the impact of metrological parameters and HPBL on PM_1 concentration. Descriptive statistics were applied to examine the average seasonal value and trend followed by PM_1 concentrations and metrological parameters in three different seasons. Based on the data set we analyzed seasonal variation of PM_1 by using Pearson's correlation coefficient and multiple regression model (MLSR).

RESULTS AND DISCUSSION

Seasonal Variation in PM_1

In this study, the data was collected and analyzed for Particulate Matter (PM_1) and metrological parameters from October 2018 to June 2019 in Jaipur city. The study focused on three important seasons: post-monsoon (October-November), winter (December-February), and pre-monsoon (March-June) because these seasons show the most fluctuation in meteorological parameters in semi-arid areas like Jaipur. As depicted in Fig. 2 PM_1 shows prominent seasonal variation among all three seasons in which maximum concentration was observed in winter seasons followed by post-monsoon and pre-monsoon season with the average value of 110.85 ± 15.78 µg.m⁻³, 90.63 ± 9.75 µg.m⁻³, and 72 ± 2.20 µg.m⁻³ respectively. The observed levels of PM_1 are higher when compared with the annual standard limit of National ambient air quality standards (i.e. 60µg.m⁻³ for 24 h) for $PM_{2.5}$ or size less than 2.5 microns provided by the Central Pollution Control Board. Almost similar concentrations of PM_1 (135.0µg.m⁻³) in the foggy period and (54.0 µg.m⁻³) in the non-foggy period were reported by Mangal et al. (2020) in Agra city, India. Whereas PM_1 in the present study was found lower than reported by Zhang et al. (2015a) in China (212 µg.m⁻³) in the heavy haze-fog period, but higher than reported in Turkey (30.2 µg.m⁻³) and at the urban areas of China (5.44-105.91 µg.m⁻³) (Onat et al. 2013, Wang et al. 2020).

The concentration of PM_1 is highly influenced by different metrological parameters (Stull 2012, Dadhich et al. 2017) like Planetary boundary layer (PBL), Temperature, Relative Humidity, Wind Speed. The planetary boundary layer (PBL) showed a wide range of variation in all seasons, and the mean height for PBL was maximum in pre-monsoon season followed by post-monsoon and winters season (Fig. 2a). Similarly, the average daily temperature in winters was minimum followed by post-monsoon and maximum in pre-monsoon season (Fig. 2b). Wind speed showed a gradual increase from winters to pre-monsoon and found maximum in the post-monsoon season with a very narrow range (Fig. 2d). The highest RH values were found in winters. Generally, RH shows an increasing trend from pre-monsoon to post-monsoon and winters (Fig. 2c).

Influence of Metrological Factor on PM_1 Concentration

The relationship between PM_1 and metrological parameters was evaluated by using the Pearson correlation coefficient for nine months including the three major seasons mentioned earlier. The dispersion of particulate particles across time Chemical composition and pollutant concentrations in the lower atmosphere are influenced by meteorological factors such as relative humidity, wind speed, and temperature (Yin et al.2016, Asl et al. 2018). In the winter, low temperatures, thermal inversion, stagnant air, and calm weather conditions

mostly hampered the dispersion of air pollution (Tripathi et al. 1996).

PM_1 and Temperature

Pearson correlation revealed different seasonal patterns for PM_1 and temperature (Table 1 and Fig. 3 (b,f,j). A significant negative correlation (R =-0.59 p<0.01) between PM_1 and atmospheric temperature in winter season and moderate positive correlation in Post-monsoon (R= 0.22 p>0.05) and pre-monsoon seasons (R= 0.12, P>0.05) was observed. PM_1 pollution is more severe in winters which can be attributed to the stable atmospheric conditions and low boundary layer height as temperature inversion during winters in semiarid regions like Jaipur prevails with high frequency. In addition to this, high atmospheric pressure and lower mixing height, stable atmospheric conditions facilitate the high concentration of pollutants in the winter season by restricting the vertical diffusion of air pollutants (Gamo et al. 1994, Lorga et al. 2015, Malandrino et al. 2013, Xu et al. 2018). Similar results indicating a higher concentration of PM with the decrease in temperature were reported by Asl et al. (2018) in Iran, Dadhich et al. (2017) in Jaipur, Galindo et al. (2011) in Spanish Mediterranean, and Lorga et al.(2015) in Bucharest. Whereas in summers atmospheric temperature near the earth surface is maximum, and heat flux value is high, which intensify the vertical mixing height, cause stronger convection
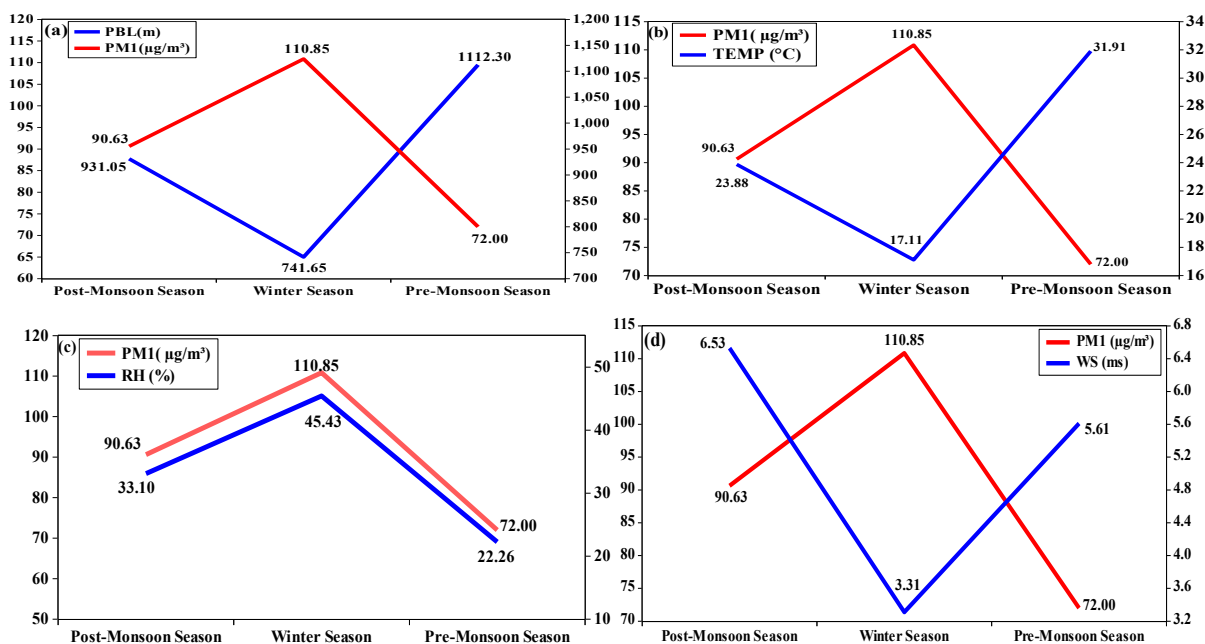

Fig. 2: Average seasonal variability of PM_1 concentration with varying metrological parameters in post-monsoon, winters, and pre-monsoon season. (a) PM_1 concentration and Planetary boundary layer (PBL) (b) PM_1 concentration and Temperature (Temp) in (c) PM_1 concentration and relative humidity (RH) (d) PM_1 concentration and wind speed (WS) for the period of sampling.
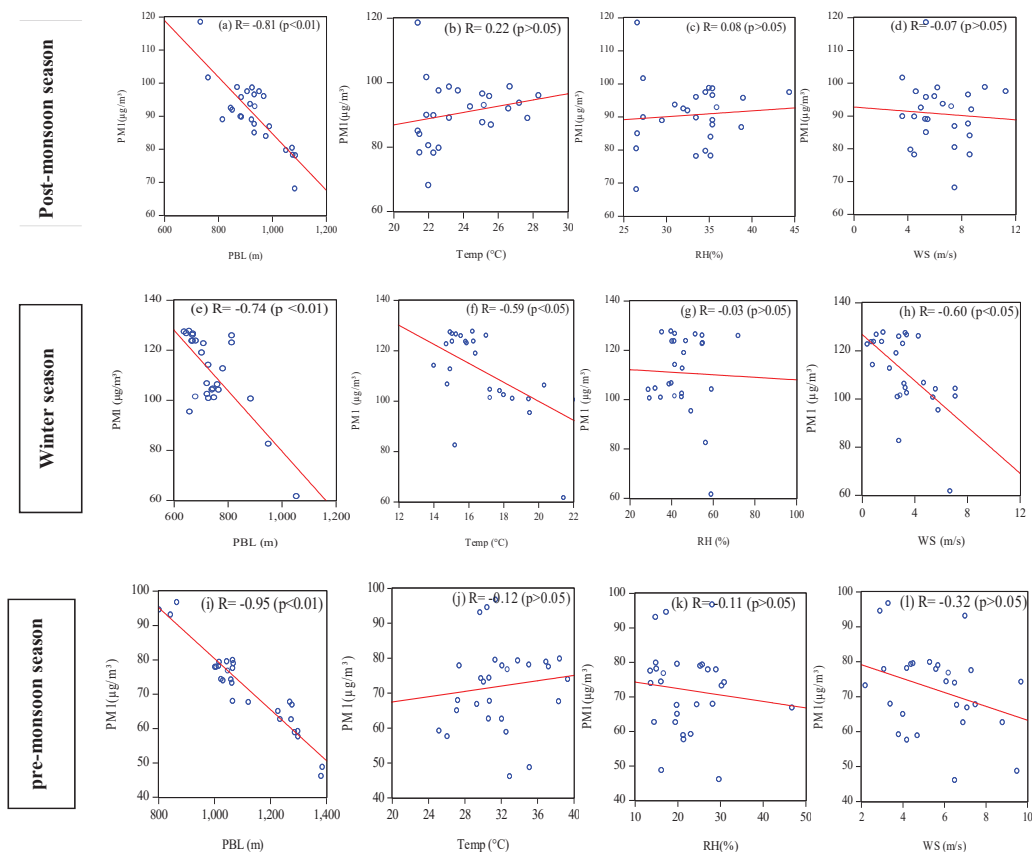
Fig. 3: Scatter plot for the monthly mean concentration of PM1 with various metrological parameters, i.e. (a,e,i) mean height of planetary boundary layer (PBL) in meters, (b,f,j) mean temperature in degree Celsius, (c,g,k) mean relative humidity in (%) and (d,h,l)mean wind speed in meter/second in three different seasons Post-monsoon season, winter season and pre-monsoon season.

condition and unsteady atmospheric conditions eventually minimizing the concentration of Particulate matter (Gamo et al. 1994, Jayamurugan et al. 2013, Sari et al. 2019, Asl et al. 2018) In addition to this geographical position of the Thar desert, Rajasthan has much influence on aerosol loading and dispersion of pollutants in the summer season, facilitating the accumulation of aerosol in the lower atmosphere leading to the problem of particulate pollution (Kisku et al. 2013).

PM_1 and Relative Humidity

Elevated levels of RH accelerate the formation of secondary pollutants and split semi-volatile species into aerosol further contributing to the fine particulate matter (Hu et al. 2008, Sun et al. 2013). Meanwhile, the moist atmosphere generally forms a lower boundary layer, enhancing the concentration of primary pollutants in the lower atmosphere (Sandeep et al. 2014). High concentrations of PM_1 generally coexist with high relative humidity during winters. As the percentage of RH increases in winters, simultaneously hydrophilicity of aerosol increases, and the radius of particle increases to

double by adsorbing water droplets on the surface of the particle (Liu et al. 2011).In the present study, when mean Relative humidity increased from 22.26 to 33.1% and then to 45.43% from the pre-monsoon to post-monsoon and to the winters, the mean concentration of $PM_1$was found to increase from 72 µg.m⁻³ to 90.63 µg.m⁻³and 110.85 µg.m⁻³respectively. The impact of RH on PM_1 concentration is high during winters whereas in summers high RH is associated with precipitation and cleaning the air (Meng et al. 2019). PM_1 and RH were found to be moderately negatively correlated in the pre-monsoon season (R=-0.11, p>0.05) whereas statically no significant correlation was observed during the winter season (R= -0.03 p>0.05) and a positive correlation in the post-monsoon season (R = 0.08 p>0.05) was observed (Table1and Fig. 3(c,g,k)

PM_1 and Wind Speed

Wind speed and directions are the two most important factors for diluting the concentration of particulate matter from the atmosphere in any region (Asl et al. 2018).In the present

Table 1: Pearson correlation analysis between PM_1 and meteorological parameters.

Post-monsoon season	Metrological parameters	PM1	PBL	TEMP	RH	WS
	PM1	1.00	-0.81[**]	0.22	0.08	-0.07
	HPBL		1.00	-0.13	0.08	0.19
	TEMP			1.00	0.30	0.27
	RH				1.00	0.47[*]
	WS					1.00
Winter season	PM1	1.00	-0.73[**]	-0.59[**]	-0.03	-0.59[**]
	HPBL		1.00	0.38	0.30	0.39[*]
	TEMP			1.00	-0.04	0.71[**]
	RH				1.00	0.08
	WS					1.00
Pre- monsoon season	PM1	1.00	-0.95[**]	0.12	-0.11	-0.32
	HPBL		1.00	-0.12	0.17	0.36
	TEMP			1.00	-0.38[*]	0.33
	RH				1.00	-0.13
	WS					1.00

**Correlation is significant at the 0.01 level (2-tailed)
*Correlation is significant at the 0.05 level (2-tailed)

study, Pearson's correlation coefficient between wind speed and PM_1 was found to be is negatively correlated in all seasons. Similar results are reported by Galindo et al. (2011) at a traffic site in the city of Elche, Spain, and by Kozakova et al. (2017) in the Czech Republic, Central Europe. Negative associations between PM fractions (Coarse and Fine) and wind speed can be an indicator of the presence of significant local source(s) of PM (Chaloulakou et al.2003). As shown in Fig. 3 (d,h,l) the results of the present study revealed moderate negative correlation in post-monsoon (R= -0.07, p>0.05) and pre-monsoon season (R= -0.32, p>0.05) whereas significant negative correlation in the winter season (R= -0.59, P<0.01) between PM_1 levels and Wind speed (Table 1). Similar results were reported by Lorga et al. (2015) at Bucharest, Romania where a negative correlation was observed with wind speed. Higher PM_1 pollution in winters can be explained by low wind speed and a large decrease in planetary boundary layer height (PBLH) where both the facts restrict the horizontal and vertical dilution of pollutants in winters (Miao & Liu2019). Thus in a specific area wind plays a vital role in particulate concentration.

PM_1 and HPBL

As shown in Table 1 and Fig. 3 (a,e,i), PM_1 concentration was found to show a significant negative correlation with HPBL (height of planetary boundary layer) in all seasons, (R= -0.8, p<0.01) during the post-monsoon season, (R= -0.74, p<0.01) during Winters and (R= -0.95, p<0.01) during pre-monsoon

season. As the mean height of planetary boundary increases from winters to post-monsoon then to pre-monsoon season i.e.741.65 m to 931.05 m and then to 1112.30 m respectively, the concentration of PM_1 decreased from winter (110.85 µg.m⁻³) to post-monsoon (90.63 µg.m⁻³) and further in pre-monsoon season (72 µg.m⁻³). Normally there is a barrier (very low mixing rate) on the top of the planetary boundary layer (PBL) which bound the transportation of particles to the free troposphere (Sun et al. 2006, Yao et al. 2012). Less solar heating, Strong thermal stratification, and weak winds in the lower troposphere in winters lower the PBL height, which bounds the diffusion of pollutants and accumulates the particulate matter in shallow layer and reduces visibility (Medeiros et al. 2005, Miao et al. 2015, Zhang et al. 2015b). Whereas, intense solar radiation during the summer months creates favorable surface thermal conditions which destabilize the lower atmosphere, encouraging vertical mixing and increasing PBL height (Guo et al. 2016, Miao et al. 2012). In the present study, good air quality was observed in the pre-monsoon season (March-June) whereas the highest concentrations of PM_1 were observed in the winter season.

Multiple Regression Model

Normally change in metrological conditions causes more variation in aerosol concentration rather than pollutant emissions from the primary or secondary sources over a monthly or seasonal period (Chang and Lee 2007).To understand the cumulative effect of all the metrological factors on PM_1 con-

centration, a multiple regression model was used in addition to person correlation in this study. A multiple regression model was performed between PM_1 (as dependent variable) and metrological parameters (as an independent variable). For presenting reliable results, Multicollinearity diagnosis was done using VIF variance inflation factor, Heteroskedasticity was checked using Goldfeld Quandt test in addition to Durbin Watson value for the obtained data.

Post monsoon season

$$PM_1 = 153.80 - 0.085* \; PBL + 0.313 \; TEMP + 0.263 \; RH + 0.070 \; WS$$
$$(7.783) \quad (-6.485) \qquad (0.535) \qquad (0.857) \qquad (0.102)$$
$$0.00 \quad 0.00 \qquad \qquad 0.598 \qquad \quad 0.400 \qquad 0.919$$
$$R^2 = 0.69 \quad \bar{R}^2 = 0.63 \quad F = 11.70* \; P = 0.00$$
$$D\text{-}W = 2.30 \quad n = 26$$

Notes: Figures in parentheses are computed- t values
*indicates significance at 1% level.

The value of R^2 for the estimated regression model is 0.69 which implies that four explanatory variables explain 69% of the total variation in the dependent variable (PM_1). The value for R^2 is statically significant at a 1% level of significance as p< 0.01.The results show that a 1-meter increase in the height of PBL would reduce the PM_1 by nearly 0.085 $\mu g.m^{-3}$. The marginal effect of PBL on PM_1 is significant whereas the effects of other variables (Temp, RH, and WS) are not statically significant. The results are presented in the following equation.

Winter season

$$PM_1 = 200.27 - 0.0102* \; PBL - 1.094 \; TEMP + 0.265 \; RH - 1.944 \; WS$$
$$(14.22) \quad (-6.160) \qquad (-1.134) \qquad (1.114) \qquad (-2.517)$$
$$0.00 \quad 0.00 \qquad \quad 0.26 \qquad \quad 0.27 \qquad \quad 0.01$$
$$R^2 = 0.70 \quad \bar{R}^2 = 0.64 \quad F = 12.98* \; P = 0.00$$
$$D\text{-}W = 1.42 \quad n = 27$$

Notes: Figures in parentheses are computed- t values
*indicates significance at 1% level.

The value of R^2 for the estimated model is 0.70 which implies that four explanatory variables together explain 70% of the total variation in the dependent variable (PM_1). The value for R^2 is statically significant at a 1% level of significance at P < 0.01. The value of each estimated coefficient interprets the marginal effect on the dependent variable (PM_1). A 1-meter increase in the height of PBL would reduce the PM_1 by nearly 0.010 $\mu g.m^{-3}$ during winters. Similarly, a 1 $m.s^{-1}$ increase in WS would reduce the PM_1 by 1.94 $\mu g.m^{-3}$. Therefore, the marginal effect of WS in the winter season was highest followed by PBL. Whereas the effect of other variables (Temp and RH) is statically insignificant. The study by Manju et al., 2018 reported r^2 value for $PM_{2.5}$ is 0.79. Another study from China by Meng et al. (2019) reported r^2 (0.96) for $PM_{2.5}$ and metrological parameters in the winter season.

Pre-monsoon season

$$PM_1 = 151.69 - 0.075* \; PBL + 0.040 \; TEMP + 0.098 \; RH + 0.161 \; WS$$
$$(14.81) \; (-13.90) \qquad (0.174) \qquad (0.878) \qquad (0.362)$$
$$0.00 \quad 0.00 \qquad \qquad 0.86 \qquad \quad 0.38 \qquad \quad 0.71$$
$$R^2 = 0.91 \quad \bar{R}^2 = 0.89 \quad F = 59.15* \; P = 0.00$$
$$D\text{-}W = 2.29 \quad n = 28$$

Notes: Figures in parentheses are computed- t values
*indicates significance at 1% level.

The Value of R^2 for the estimated model for pre-monsoon season is 0.91 which implies that four explanatory variables together explain 91% variation in PM_1. The value for R^2 is statically significant at a 1% level of significance P< 0.01. The 1-meter increase in the height of PBL would reduce the PM_1 by nearly 0.075 $\mu g.m^{-3}$. Therefore the marginal effect of PBL on PM_1 is significant whereas the effects of other variables (Temp, RH, WS) is insignificant.

CONCLUSION

The concentration of PM_1 was higher as compared to the standard prescribed by CPCB (60 $\mu g.m^{-3}$ for PM size less than 2.5 microns).The linkages between PM_1 and metrological parameters studied at a semi-arid region, Jaipur by conducting the field measurements indicated a strong influence of HPBL, which is formed as a result of different metrological parameters like Temp, RH, WS. It is evident from the outcome of the study that the concentration of PM_1 cannot be determined based on the single metrological parameter, whereas all the metrological conditions cumulatively show a significant impact. In addition to this, a significant (p < 0.001) negative correlation with HPBL and WS was observed in all three major seasons, the temperature was also a significant negative correlation. The relative humidity also showed negative relationship during the winter and pre-monsoon seasons. The multiple regression model analysis showed a negative relationship with HPBL in the winter, post-monsoon, and pre-monsoon seasons. While observing an annual cycle, a prominent seasonal variability with the highest concentrations in the winter season was shown due to the lower height of PBL followed by the post-monsoon and pre-monsoon season due to higher PBL.

ACKNOWLEDGEMENT

REFERENCES

Baldasano, J.M., Valera, E. and Jimenez, P. 2003. Air quality data from large cities. Sci Total Environ., 307(1-3):41-165.

Census of India 2011. Office of the Registrar General & Census Commissioner, India. India. [Web Archive] Retrieved from the Library of Congress, https://www.loc.gov/item/lcwaN0017959/

Chaloulakou, A., Kassomenos, P., Spyrellis, N., Demokritou, P. and Koutrakis, P. 2003. Measurements of PM10 and PM2.5 particle concentrations in Athens, Greece. Atmos. Environ., 37: 649-660.

Chen, T.M. Kuschner, W.G. Gokhale, J. and Shofer, S. 2007. Outdoor air pollution: Nitrogen dioxide, sulfur dioxide, and carbon monoxide health effects. Am. J. Med. Sci., 333(4): 249-256.

Dadhich, A.P., Goyal, R. and Dadhich, P.N. 2018. Assessment of spatio-temporal variations in the air quality of Jaipur city, Rajasthan, India. Egypt. J. Remote. Sens. Space Sci., 21(2):173-181.

Dhamaniya, A. and Goyal, R. 2004. Use of GIS in transportation planning of Jaipur city. GIS Dev., 8(11): 38.

Draxler, R.R. and Hess, G.D. 1998. An overview of the HYSPLIT_4 modeling system for trajectories. Aust. Meteorol. Mag., 47(4): 295-308.

Draxler, R.R. and Rolph, G.D. 2003. HYSPLIT (HYbrid Single-Particle Lagrangian Integrated Trajectory) Model access via NOAA ARL READY Website. NOAA Air Resources Laboratory, Silver Spring, MD.http://www.arl.noaa.gov/ready/hysplit4.html

Du, C., Liu, S., Yu, X., Li, X., Chen, C., Peng, Y., Dong, Y., Dong, Z. and Wang, F. 2013. Urban boundary layer height characteristics and relationship with particulate matter mass concentrations in Xi'an, central China. Aerosol Air Qual. Res., 13(5): 1598-1607.

Fleming, Z.L., Monks, P.S. and Manning, A.J. 2012. Untangling the influence of air-mass history in interpreting observed atmospheric composition. Atmos. Res., 104: 1-39.

Galindo, N., Varea, M.,Gil-Moltó, J., Yubero, E. and Nicolás, J. 2011. The influence of meteorology on particulate matter concentrations at an urban Mediterranean location. Water Air Soil Pollut., 215(1-4): 365-372.

Gamo, M., Goyal, P., Kumari, M., Mohanty, U.C. and Singh, M.P. 1994. Mixed-layer characteristics as related to the monsoon climate of New Delhi, India.Bound-Lay Meteorol., 67(3): 213-227.

Goyal, S.K. and Rao, C.C. 2007. Assessment of atmospheric assimilation potential for industrial development in an urban environment: Kochi (India). Sci. Total Environ., 376(1-3):27-39.

Guo, J., Miao, Y., Zhang, Y., Liu, H., Li, Z., Zhang, W., Jing, H., Lou, M., Yan, Y., Bian, L. and Zhai, P. 2016. The climatology of planetary boundary layer height in China derived from radiosonde and reanalysis data. Atmos. Chem. Phys., 16(20): 13309-13319.

Hu, X.M., Zhang, Y., Jacobson, M.Z. and Chan, C.K. 2008. Coupling and evaluating gas/particle mass transfer treatments for aerosol simulation and forecast. J. Geophys. Res. Atmos.,113(D11): 414-445.

Jayamurugan, R., Kumaravel, B., Palanivelraja, S. and Chockalingam, M.P. 2013. Influence of temperature, relative humidity, and seasonal variability on ambient air quality in a coastal urban area. Int. J. Atmos. Sci., 2013: 616.

Kala, J., Sharma, G., Kumar, S. and Pipralia, S. 2014. Study of ambient air quality status on urban roads using air quality index-a case of Jaipur city (Rajasthan, India). IJTAS, 6(1): 138.

Kampa, M. and Castanas, E. 2008. Human health effects of air pollution. Environ. Pollut., 151(2):362-367.

Kozakova, J., Pokorna, P., Cerníkova, A., Hovorka, J., Braniš, M., Moravec, P. and Schwarz, J. 2017. The association between intermodal (PM1-2.5) and PM1, PM2. 5, coarse fraction and meteorological parameters in various environments in central Europe. Aerosol Air Qual. Res., 17(5): 1234-1243.

Kisku, G.C., Pradhan, S., Khan, A.H. and Bhargava, S.K. 2013. Pollution in Lucknow City and its health implication on exposed vendors, drivers, and traffic policemen. Air Qual. Atmos. Health, 6(2): 509-515.

Liu, J., Zheng, Y., Li, Z., Flynn, C., Welton, E.J. and Cribb, M. 2011. Transport, vertical structure, and radiative properties of dust events in southeast China are determined from ground and space sensors. Atmos. Environ.,45(35): 6469-6480.

Lorga, G., Raicu, C.B. and Stefan, S. 2015. Annual air pollution level of major primary pollutants in the Greater Area of Bucharest. Atmos. Pollut. Res., 6(5): 824-834.

Malandrino, M., Di Martino, M., Ghiotti, G., Geobaldo, F., Grosa, M.M. Giacomino, A. and Abollino, O. 2013. Inter-annual and seasonal variability in PM10 samples monitored in the city of Turin (Italy) from 2002 to 2005. Microchem. J., 107: 76-85.

Manju, A., Kalaiselvi, K.,Dhananjayan, V., Palanivel, M., Banupriya, G.S., Vidhya, M.H., Panjakumar, K. and Ravichandran, B. 2018. Spatio-seasonal variation in ambient air pollutants and influence of meteorological factors in Coimbatore, Southern India. Air Qual. Atmos. Health, 11(10): 1179-1189.

Medeiros, B., Hall, A. and Stevens, B. 2005. What controls the mean depth of the PBL? J. Clim., 18(16): 3157-3172.

Meng, C., Cheng, T., Gu, X., Shi, S., Wang, W., Wu, Y. and Bao, F. 2019. Contribution of meteorological factors to particulate pollution during winters in Beijing. Sci. Total Environ., 656: 977-985.

Miao, S., Dou, J., Chen, F., Li, J. and Li, A. 2012. Analysis of observations on the urban surface energy balance in Beijing. Sci. China Earth Sci., 55(11):1881-1890.

Miao, Y. and Liu, S. 2019. Linkages between aerosol pollution and planetary boundary layer structure in China.Sci. Total Environ., 650: 288-296.

Miao, Y., Hu, X.M. Liu, S., Qian, T., Xue, M., Zheng, Y. and Wang, S. 2015. Seasonal variation of local atmospheric circulations and boundary layer structure in the Beijing Tianjin Hebei region and implications for air quality. J. Adv. Model. Earth Syst., 7(4): 1602-1626.

Mohan, M. and Kandya, A. 2007. An analysis of the annual and seasonal trends of the air quality index of Delhi. Environ. Monit. Assess., 131: 267. https://doi.org/10.1007/s10661-006-9474-4

Onat, B., Sahin, U.A. and Akyuz, T. 2013. Elemental characterization of PM2.5 and PM1 in dense traffic area in Istanbul, Turkey Atmos. Pollut. Res., 4(1): 101-105.

Pöschl, U. 2005. Atmospheric aerosols: composition, transformation, climate and health effects. Angew. Chem., Int. Ed. Engl., 44(46): 7520-7540.

Ram, K., Sarin, M.M. and Tripathi, S.N. 2010. A 1-year record of carbonaceous aerosols from an urban site in the Indo Gangetic Plain: Characterization, sources, and temporal variability. J. Geophys. Res. Atmos., 115(D24).

Sandeep, A., Rao, T.N., Ramkiran, C.N. and Rao, S.V.B. 2014. Differences in atmospheric boundary-layer characteristics between wet and dry episodes of the Indian summer monsoon. Bound-Lay Meteorol., 153(2): 217-236.

Sari, M.F., Tasdemir, Y. and Esen, F. 2019. Major air pollutants in Bursa, Turkey: Their levels, temporal changes, interactions, and sources. Environ. Forensics, 20(2): 182-195.

Satsangi, P.G., Kulshrestha, A., Taneja, A. and Rao, P.S.P. 2011. Measurements of PM 10 and PM 2.5 aerosols in Agra, a semi-arid region of India. 92.60. Mt; 92.60. Sz. Indian J. Radio Space Phys., 40: 203-210.

Sharma, A.P., Kim, K.H., Ahn, J.W., Shon, Z.H., Sohn, J.R., Lee, J.H., Ma, C.J. and Brown, R.J. 2014. Ambient particulate matter (PM10) concentrations in major urban areas of Korea during 1996-2010. Atmos. Pollut. Res., 5(1):161-169.

Singh, O.P., Singh, S.S. and Kumar, S. 2012. Rainfall Profile of Jaipur. Indian Meteorological Department, India. http://amssdelhi.gov.in/RESEARCH_FILES/JAIPUR_RF_PROFILE.pdf

Solomon, S., Qin, D., Manning, M., Averyt, K. and Marquis, M. (Ed.). 2007. Climate Change 2007-the Physical Science Basis: Working Group I Contribution to the Fourth Assessment Report of the IPCC (Vol. 4). Cambridge University Press, Cambridge. http://www.ipcc.ch/ipccreports/ar4-wg1.htm

Stull, R.B. 2012. An introduction to boundary layer meteorology (Vol. 13). Springer Science & Business Media, New York.

Sun, Y., Wang, Z.,Fu, P., Jiang, Q., Yang, T., Li, J. andGe, X. 2013. The

impact of relative humidity on aerosol composition and evolution processes during wintertime in Beijing, China. Atmos. Environ., 77: 927-934.

Sun, Y., Zhuang, G., Tang, A., Wang, Y. and An, Z. 2006. Chemical characteristics of PM2. 5 and PM10 in haze-fog episodes in Beijing. Environ. Sci. Technol., 40(10): 3148-3155.

Tripathi, B.D., Chaturvedi, S.S. and Tripathi, R.D. 1996. Seasonal variation in ambient air concentration of nitrate and sulfate aerosols in a tropical city, Varanasi. Atmos. Environ., 30(15): 2773-2778.

Tyagi, A., Singh, O.P. Singh, S.S. and Kumar, S. 2012. The Climate of Jaipur. Indian Meteorological Department, India.http://amssdelhi.gov. in/news_events/Jaipur_climate.pdf

Verma, S., Payra, S., Gautam, R., Prakash, D., Soni, M., Holben, B. and Bell, S. 2013. Dust events and their influence on aerosol optical properties over Jaipur in Northwestern India. Environ. Monit. Assess., 185(9): 7327-7342.

Wang, J., Huang, Y., Li, T., Shi, H., He, M., Cheng, X. and Zhang, C. 2020. Annual characteristics, source analysis of PM 1-bound potentially harmful elements in the eastern district of Chengdu, China. Arch. Environ. Contam. Toxicol.,79(2): 177-183.

West, P.W. and Gaeke, G.C. 1956. Fixation of sulfur dioxide as di-sulfitomercurate (II) and subsequent colorimetric estimation. Rev. Anal. Chem., 28(12): 1816-1819.

Asl, F.B., Leili, M., Vaziri, Y., Arian, S.S., Cristaldi, A., Conti, G.O. and Ferrante, M. 2018. Health impacts quantification of ambient air pollutants using the AirQ model approach in Hamadan, Iran. Environ. Res., 161: 114-121.

Xu, Y., Ying, Q., Hu, J., Gao, Y., Yang, Y., Wang, D. and Zhang, H. 2018. Spatial and temporal variations in criteria air pollutants in three typical terrain regions in Shaanxi, China, during 2015. Air Qual. Atmos. Health, 11(1): 95-109.

Yao, L., Lu, N. and Jiang, S. 2012. Artificial neural network (ANN) for multi-source PM2.5 estimations using surface, MODIS, and meteorological data. In 2012 International Conference on Biomedical Engineering and Biotechnology, 28-30 May 2012, Macau, China, IEEE, China, pp. 1228-1231.

Yin, Q., Wang, J., Hu, M. and Wong, H. 2016. Estimation of daily PM2. 5 concentrations and its relationship with meteorological conditions in Beijing. Res. J. Environ. Sci., 48:161-168.

Zhang, Q., Quan, J., Tie, X., Li, X., Liu, Q., Gao, Y. and Zhao, D. 2015a. Effects of meteorology and secondary particle formation on visibility during heavy haze events in Beijing, China. Sci. Total Environ., 502: 578-584.

Zhang, Y.W., Zhang, X.Y., Zhang, Y.M., Shen, X.J., Sun, J.Y., Ma, Q.L., Yu, X.M., Zhu, J.L., Zhang, L. and Che, H.C. 2015b. Significant concentration changes of chemical components of PM_1 in the Yangtze River Delta area of China and the implications for the formation mechanism of heavy haze–fog pollution. Sci. Total Environ., 538: 7-15.

Zhang, Y., Lang, J., Cheng, S., Li, S., Zhou, Y., Chen, D., Hanyu, Z. and Wang, H. 2018. Chemical composition and sources of PM1 and PM2. 5 in Beijing in autumn.Sci. Total Environ., 630: 72-82.

Original Research Paper Open Access Journal

Bioleaching of Metals from Printed Circuit Boards

Pavithira V.*, Anchana Devi C.*† and Pushpa N.**

*PG and Research Department of Biotechnology, Women's Christian College, An Autonomous Institution, Chennai-600 006, Tamil Nadu, India

**PG & Research Department of Microbiology, Cauvery College for Women, Tiruchirapalli-620 018, T.N., India

†Corresponding author: Anchana Devi C.; dr.anchanadevi@gmail.com

ABSTRACT

Electronic waste or E-waste refers to the discarded electrical or electronic devices which have neared their useful life. Because of the toxicity and carcinogenicity of some compounds, the proper management and safe disposal of these electronic wastes have become serious challenges in recent years. Printed Circuit Boards (PCBs) are found almost in every other electronics these days, hence the present study focuses on bioleaching of metals from Printed Circuit Boards (PCBs) using bacterial and yeast strains (*Stenotrophomonas maltophilia, Bacillus* sp. and *Candida tropicalis*) isolated from heavily contaminated soil samples. A two-step bioleaching procedure was followed for maximum mobilization of metals. The isolated strains were able to mobilize metals from PCBs with different efficiencies depending on their ability to utilize the E-waste a carbon source when cultivated in minimal media. Bioleaching potential of isolated microbes on eight heavy metals (Cu, Ni, Mn, Pb, Fe, Cr, Zn & Co) in the sample were studied using AAS and SEM analysis before and after the two-step bioleaching process and found to be efficient. The study concludes that isolated bacterial and fungal species from the study can be further standardized with regard to the growth parameters and used on large scale to carry out the efficient recovery of metals that can help in recycling E-waste in the digital world.

INTRODUCTION

The use of electronics has become an essential commodity since the pandemic and the dependence on electronic gadgets has increased many folds. The discarded electronic and electrical instruments are called electronic waste (E-waste). E-waste is growing three times faster than other solid waste streams (Brandl & Faramarzi 2006). According to the UN's Global E-waste Monitor, 53.6 million tonnes (MT) of e-waste were produced globally in 2019. The report states that Asia produced the most E-waste in 2019-24.9 Mt, followed by America (13.1 Mt) and Europe (12 Mt), while Africa and Oceania produced 2.9 Mt and 0.7 Mt, respectively. Every year millions of tons of electronic waste are generated across the world. These E-wastes may contain more than 1000 different substances, which may be hazardous or non-hazardous (Widmer 2005). E-waste recycling is becoming more important not just in terms of waste management, but also in terms of recovering valuable metals like gold and silver, as well as toxic metals (like arsenic and mercury) and base metals (like copper and nickel) (Needhidasan et al. 2014). The type of electronic item, model manufacturer, and manufacturing date all influence the makeup of E-waste. Scarp from IT and Telecom system contains a comparatively higher quantity of precious metals than the scrap from the

household equipment. For instance, one ton of mobile phone without batteries contains 340 g Au, 140 g Pd, 130 kg Cu, and 3.5 kg Ag (Hagelüken & Meskers 2008). It is estimated that more than 70% of globally produced waste electronics and electrical equipment (WEEE) are often disposed or recycled using crude, hazardous and inefficient processes, mostly by dumping and incinerating which causes severe impact on human life and the environment due to raw release of toxic metals directly into landfills or water bodies (Kaya 2016). Recycling of E-waste is limited due to the presence of heterogeneity in materials and difficulty in processing and segregation. Pyrometallurgy and Hydrometallurgy were initially used as traditional methods to recover metals from electronics. Since these processes raised concerns regarding risks of environmental impacts due to the release of toxic substances, Bioleaching or Biometallurgy is emerging as a promising method of metal recovery from electronic wastes.

Printed Circuit Boards (PCBs) are used in almost all electronic devices which may contain up to 60 different chemical elements and have a metal content as high as 40% by weight (Greenfield & Graedel 2013). The obsolete or used cell phones are components of waste electrical equipment because of their new technological improvements. Its period of use may be approximately one to two years and thus millions of cell phones are discarded every year,

generating large amounts of electronic waste. Cell phones are complex electronic devices that contain printed circuit boards that act as their brain. These PCBs are a complex mixture of materials such as plastics (13%), glass ceramics (24%), and metals (64%) including precious metals such as silver (Ag), gold (Au), and palladium (Pd), base metals such as copper (Cu), aluminium (Al), nickel (Ni), tin (Sn), silicon (Si), indium (In) and toxic metals such as cadmium (Cd), lead (Pb), arsenic (As), mercury (Hg), and bromine (Br) (Cui & Forssberg 2003, Kaya 2016). Henceforth, recovery of metals from the Printed Circuit Board is profitable, since these PCBs are used in almost every electronic gadget due to their high availability. The present study is focused on the bioleaching of metals from PCBs, which will readily help in recycling these metals in an environmentally friendly way.

MATERIALS AND METHODS

Sample Collection

Discarded Printed Circuit Boards (PCBs) from used mobile phones were collected from mobile phone repair shops in Richie Street, Chennai, Tamilnadu. Heavy metal contaminated soil samples were also collected from Ambattur industrial estate, Chennai which has a high cluster of small–scale industries. The samples were stored in a sterile container and transferred to the laboratory for further analysis.

Processing and Metal Content Analysis of E-Waste

The E-waste was processed according to the protocol of Khatri (2018) and particle size was reduced to have an approximate size of ≤ 200 to 250 µm, which was used for this study. 1g of finely powdered E-waste was taken in a 100 mL Erlenmeyer flask and digested using aqua regia, which can dissolve metals. Aqua regia is made up of Conc. HCl and HNO_3 in the ratio 3:1 (Sheng & Etsell 2007). The solution was allowed to stand for 48 hours and then was centrifuged at 5000 rpm for 5min. The supernatant was again filtered using Whatman filter paper and was stored at 4°C. (Pradhan & Kumar 2012). The total metal concentrations in the solution were analyzed using Atomic Adsorption Spectroscopy (AA-700 Shimadzu) at various wavelengths (nm) for analyzing the concentrations of different metals in the sample.

Isolation and Characterization of Microbes from Heavy Metal Contaminated Soil

Minimal salt media was used for the isolation of organisms. The composition of the media is given below (Tipre et al. 2004).

Composition of minimal media (1000 mL) pH-7

Ammonium chloride – 1.0 g
Magnesium sulfate – 0.2 g
Di Potassium hydrogen phosphate – 1.0 g
Calcium chloride – 0.1 g
Potassium chloride – 0.15 g
Yeast extract – 0.1
Ferrous sulfate – 1.0 mg
Zinc sulfate – 1.0 mg
Manganese sulfate – 1.0 mg

The printed circuit boards were finely powdered and sterilized by autoclaving at 121°C for 15 min before adding to the minimal media. After sterilization of the media, 1 g of autoclaved PCB was aseptically added to the media along with the soil sample and incubated for 7 days at 37°C. The culture was plated onto sterilized minimal agar plates and incubated at 37°C for 24 h and fungal isolation, minimal agar plates were supplemented with Ampicillin (10mg. mL^{-1}) and were incubated for 3-4 days. Individual bacterial colonies were sub-cultured further to obtain a pure culture of isolates and characterized based on biochemical properties identified based on classification schemes published in Bergey's Manual of Systematic Bacteriology (Krieg & Holt 1984). Also, identification of fungal isolates was based on colony size, shape, margin, elevation, consistency, opacity, and pigmentation and morphologically identified using Lacto phenol cotton blue staining.

Molecular Characterization of Isolates

Molecular identification of the isolates was performed using Forward primer (5′-TGGAGAGTTTGATCCTGGCT-CAG-3′) and reverse primer (5′-TACCGCGGCTGCTGG-CAC-3′) for amplification of 16S rRNA gene of bacteria (Hall et al. 2003) and internal transcribed spacer (ITS) region of nuclear ribosomal RNA genes for yeast using specific forward (ITS-1) and reverse (ITS-4) primers for PCR reactions (White 1990). Phylogenetic studies of the isolated samples were analyzed using the BLAST method to determine their approximate phylogenetic affiliation based on 16S rRNA gene sequence similarities for bacteria and ITS for fungal isolate (Altschul 1990, Engel 2005).

Bioleaching Studies-Two Step Process

The present study employs a two-step bioleaching process which was reported in previous studies to be appropriate to increase the metal leaching efficiency of micro-organisms from electronic waste (Mishra & Rhee 2014). For more efficient metal mobilization, direct growth of micro-organisms in the presence of electronic waste is not advisable due to its toxic effects (Brandl et al. 2001).

Bioleaching experiments were conducted in a 250 mL Erlenmeyer flask with 100 mL Minimal salt media at pH 7. The flasks were sterilized by autoclaving at 121 psi for 15 min. Post autoclave, the flasks were cooled at room temperature to inoculate the organisms, and once the organisms have reached the log phase, 1.0 g of sterilized electronic waste (1% w/v) was added to each flask under aseptic conditions. The flasks were then placed in a rotary shaker at room temperature for an incubation period of 30 days. In the post-incubation period, the samples were analyzed for any change in pH and total metal ion content. The same procedure was followed for all the organisms that were isolated.

Analysis of Bioleached Samples

15 mL of the bioleached sample were withdrawn from the flask and filtered through Whatman filter paper (0.45μm). The filtered sample was centrifuged at 10000 rpm for 10 min and the supernatant was used to study the total metal ions concentration of eight heavy metals (Cu, Ni, Mn, Pb, Fe, Cr, Zn & Co) in the sample using Atomic Adsorption Spectroscopy (AAS) and SEM analysis.

RESULTS AND DISCUSSION

Sample Collection

The waste discarded PCBs were collected from used mobile phones from mobile repair shops present in Richie Street, Chennai, Tamilnadu. Chennai is one of the important metropolitan cities in the south which is the largest producer of E-waste. No physical or mechanical separation processes were carried out before transportation to the laboratory (Fig. 1).

Screening and Identification of Heavy Metal Resistant Microorganisms
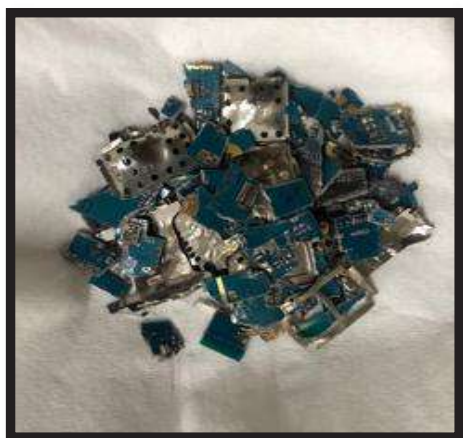

Fig. 1: Printed circuit boards from spent mobile phones.

Minimal media broth was inoculated with PCBs and the soil sample was incubated for 7 days at 37°C. On reaching an OD of 0.7 nm growth, the sample was streaked onto Minimal media agar and repeated sub-culturing was carried out to isolate pure colonies of microbes resistant to heavy metals (Figs. 2 & 3).

Cultural Characteristics of Heavy Metal Resistant Isolates

In our study, three pure cultures of microorganisms resistant to heavy metals were isolated using minimal media agar plates and labeled as PCB1, PCB2, and PCB3, out of which 2 were bacterial organisms and one was yeast (Table 1). Gram staining and biochemical tests were performed for the bacterial isolates to study their morphological and biochemical characteristics (Fig. 4 & Table 2).

The above results provided an idea of the morphology, colony characteristics, and biochemical nature of the isolated bacterial strains. Further, the isolated organisms were subjected to molecular amplification of partial 16s rRNA and the obtained sequence length for PCB2 was 1456 bp and PCB3 was 1420 bp.

The organisms were identified as *Stenotrophomonas maltophilia (*PCB2) and *Bacillus* sp. (PCB3). The constructed phylogenetic tree clearly shows that strain *Stenotrophomonas maltophilia* is closely related to *Pseudomonas* sp. (Fig. 5). Previously, several authors have reported the bioleaching potential of *Stenotrophomonas maltophilia* isolated from dif-

Fig. 2: Minimal broth inoculated with PCB and soil.

Table 1: Colony features of isolated heavy metal resistant organisms.

Strain No.	Colony Colour	Cell Feature
PCB 1	White	Yeast
PCB 2	White	Gram negative rods
PCB 3	White	Gram-positive rods

Fig. 3: Isolated pure colonies of heavy metal resistant organisms using minimal media agar.
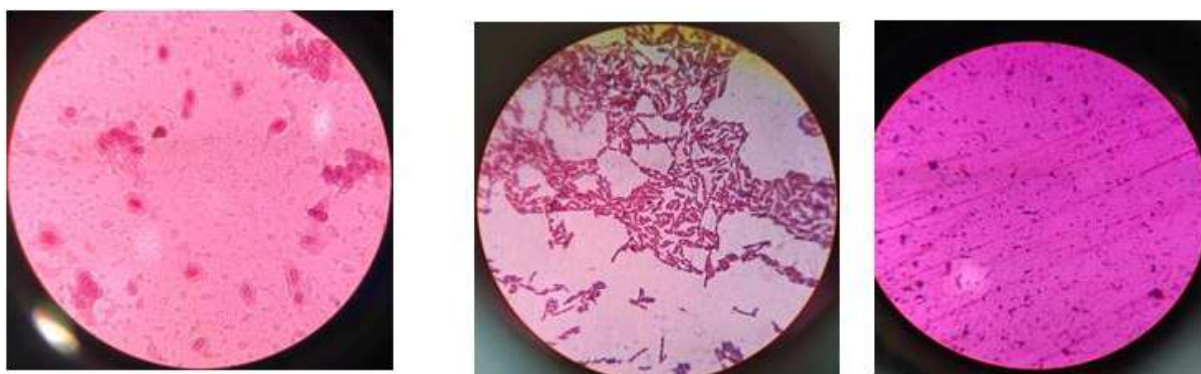

Fig. 4: Gram staining results of isolates PCB1, PCB2 and PCB3.

Table 2: Biochemical characteristics of isolated bacteria (+ = Positive; - = Negative).

	Biochemical tests							
Strain no	Catalase	Indole	MR	VP	Oxidase	TSI	Citrate	Gelatin utilization
PCB 2	+	-	+	+	+	A/A (no H_2S)	+	+
PCB 3	+	-	-	+	+	K/A (no H_2S)	+	+

ferent sources (Sajjad 2019, Venkidusamy & Megharaj 2016). However, *Stenotrophomonas maltophilia* was reported to be a potential Electrode respiring bacteria (ERB) widely used in microbial electrochemical remediation systems (MERS) because of their exoelectrogenic capabilities to degrade xenobiotic pollutants, especially heavy metals. Similarly, *Bacillus* sp. (PCB3) was closely associated with *Bacillus cereus* (Fig. 6). *Bacillus* sp. were isolated from sponges and had a high potential for bioleaching electronic waste and producing copper nanoparticles, according to a study (Rozas 2017). Several other studies have cited the potential effects of the E-waste bioremediation process using different *Bacillus* sp. (Arshadi & Mousavi 2015, Karwowska 2014).

PCB1 displayed normal yeast budding structures when stained with Gram. As demonstrated in Fig. 7, amplification of the ITS (Internal transcribe regions) gene verified the same, which is closely linked to Candida tropicalis. Though various articles have reported on the possible use of fungal species in bioremediation (Díaz-Martínez 2019, Ren et al. 2009), yeast as a bioleaching agent has received little attention, particularly in the context of printed circuit boards (PCBs).

Bioleaching of Heavy Metals from PCB

Heavy metals present in PCB were bioleached by adopting the shake flask method at room temperature using Minimal
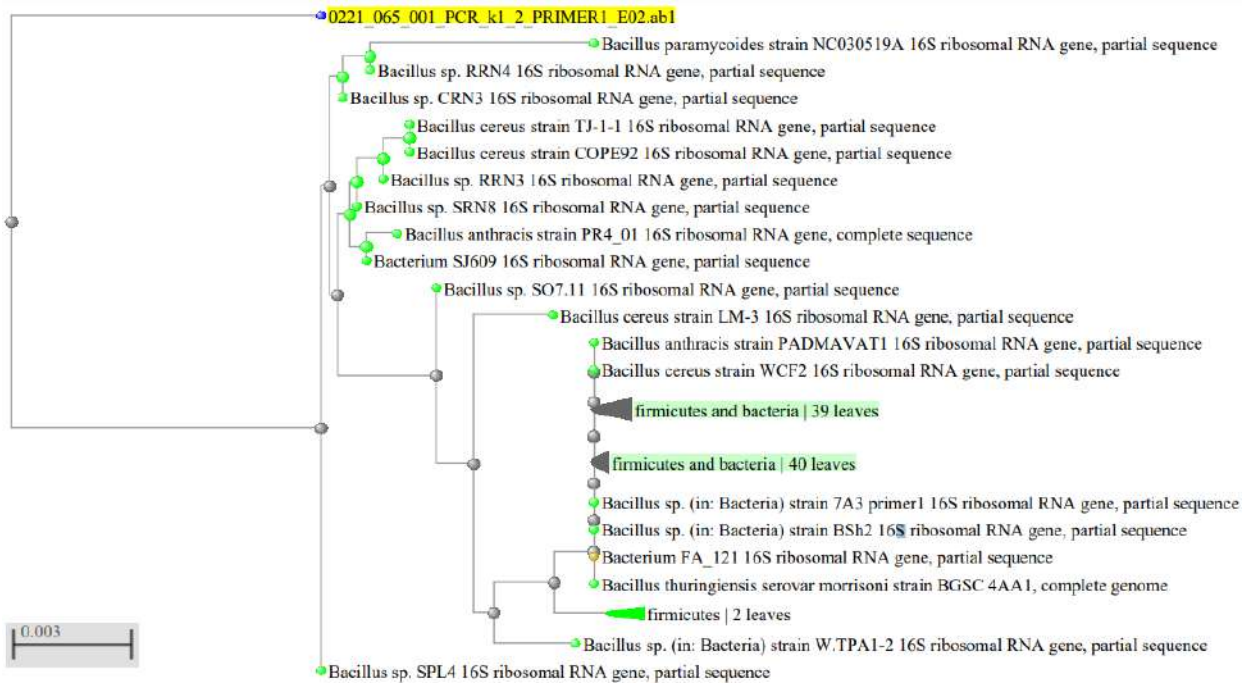
Fig. 5: Phylogenetic analysis of PCB 2.

Fig. 6: Phylogenetic analysis of PCB 3.

salt media at pH 7. Organisms use PCBs as carbon sources for their growth. Pre- and Post-incubation, the samples were subjected to Atomic adsorption spectroscopy studies to analyze the bioleaching of metal content pre- and post-two-step leaching process using isolated organisms PCB1 PCB2 and PCB3. The pH of the samples after the bioleaching procedure varied from 5.5-7 for all metals, ranging from slightly acidic to neutral (Table 3).

Overall, the metal recovery content of different types of metals contained in the sample was considerable before and after bioleaching. Organism PCB3 had the highest metal recovery in copper, chromium, and cobalt, while organism PCB2 had the highest metal recovery in manganese, zinc, and lead. PCB1 had a greater zinc and nickel recovery rate. Using microorganisms in a consortium for improved results has only been documented in a few studies (Lima 2012, Sajjad 2019).

SEM Analysis

Figures 8a, 8b and 8c show scanning electron microscope (SEM) images of PCBs before bioleaching, which demonstrate crystalline structures and the presence of rough surfaces. The heavy metals in the PCBs were transformed to a granular shape with a smooth surface during the bioleaching process (Fig. 8d, 8e & 8f). This structural change confirms the bioleaching treatment by the isolated organisms. Previously a similar type of result was reported in another study (Zhao et al. 2008).

CONCLUSION

The findings of the current study revealed that microbes play an important role in metal recovery. The metal concentrations were drastically reduced from their initial concentration because of the detoxification process and metabolic activity of microbial isolates (PCB1, PCB2 & PCB3). The isolates were characterized and identified as *Candida tropicalis*, *Stenotrophomonas maltophilia* and *Bacillus* sp. The recovery of the metal from PCB was confirmed using Atomic adsorption studies and SEM analysis. Maximum bioleaching was obtained in the recovery of copper and nickel when compared to other metals. Three isolates exhibited their affinity for

Table 3: AAS results of the metal content analysis before and after bioleaching.

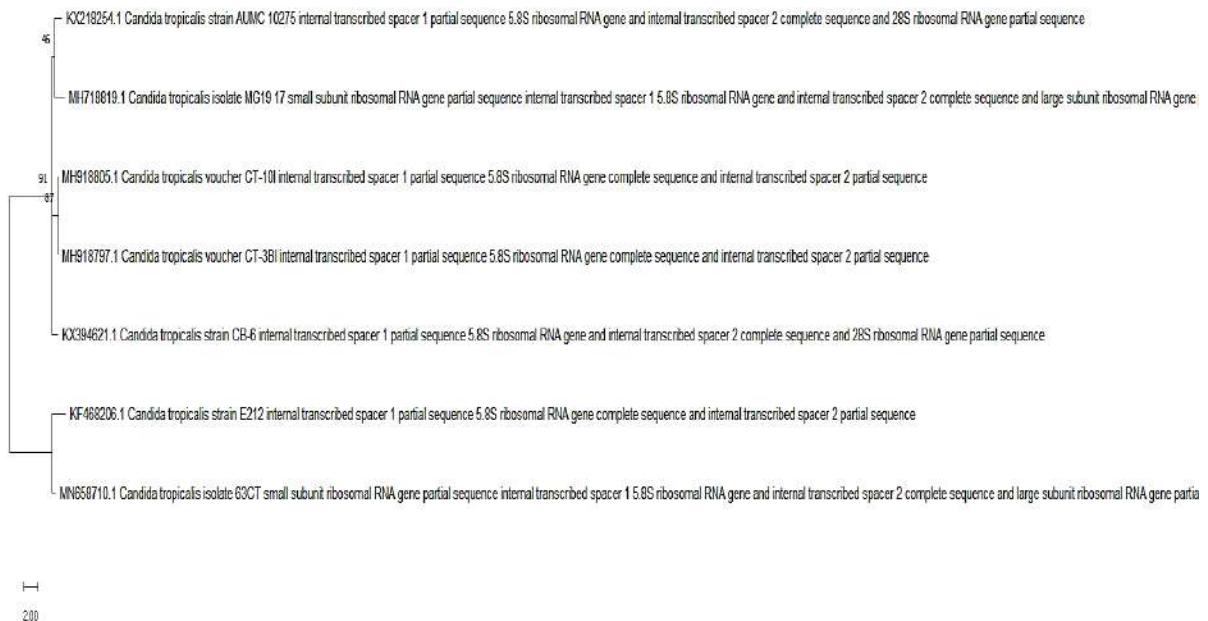| Metals	Concentration [ppm] before treatment	Concentration [ppm] after treatment		
		PCB1	PCB2	PCB3
Copper	78.51	3.401	11.18	1.904
Manganese	64.50	0.072	0.053	0.061
Chromium	63.45	0.876	2.055	0.391
Zinc	25.26	0.071	0.225	0.275
Nickel	21.60	1.413	11.377	2.494
Cobalt	4.30	0.844	0.045	0.031
Iron	26.32	0.003	0.056	0.314
Lead	52.51	3.66	0.04	0.165

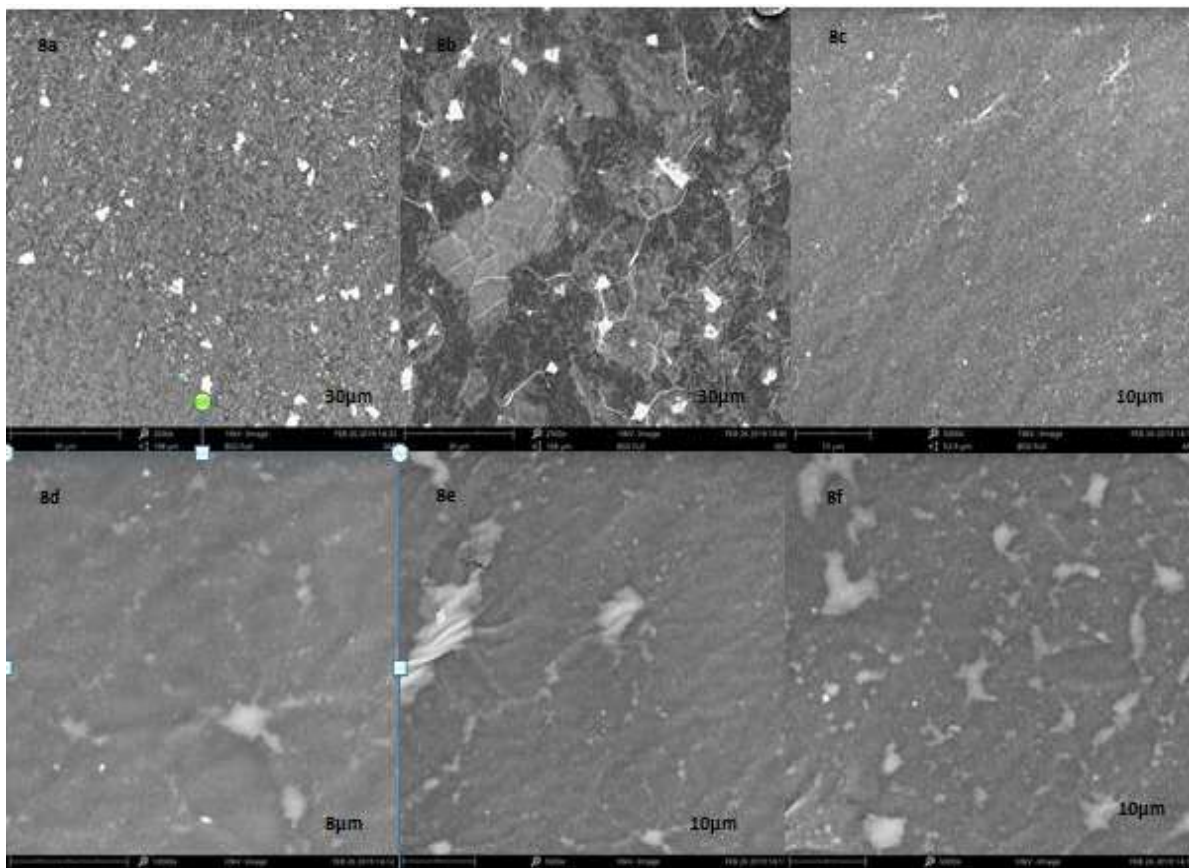Fig. 7: Phylogenetic analysis of PCB 1.

Fig 8a,8b,8c: SEM images of samples before bioleaching process using PCB1,PCB2 & PCB3.
Fig 8d,8e,8f: SEM images of samples after bioleaching process using PCB1,PCB2 & PCB3.

bioleaching different metals; the efficacy of leaching activity can be further improved by using a consortium of microbes which can be used as an efficient source in the removal of metals from discarded PCBs in an economic and eco-friendly perspective.

ACKNOWLEDGEMENTS

REFERENCES

Altschul, S.F. 1990. Basic local alignment search tool. J. Mol. Biol., 215(3): 403-410.

Arshadi, M. and Mousavi, S.M. 2015. Enhancement of simultaneous gold and copper extraction from computer printed circuit boards using Bacillus megaterium. Bioresour. Technol., 175: 315–324.

Brandl, H. and Faramarzi, M.F. 2006. Microbe-metal interactions for the biotechnological treatment of metal-containing solid waste. China Particuol., 4(2): 93-97.

Brandl, H., Bosshard, R. and Wegmann, M. 2001. Computer-munching microbes: Metal leaching from electronic scrap by bacteria and fungi. Hydrometallurgy, 59: 319-322.

Cui, J. and Forssberg, E. 2003. Mechanical recycling of waste electric and electronic equipment: Rev. J. Hazard. Mater., 99(3): 243-263.

Díaz-Martínez, M.E. 2019. Microbial bioleaching of Ag, Au and Cu from printed circuit boards of mobile phones. Curr. Microbiol., 76(5): 536-544.

Engel, A. 2005. Bacterial diversity and ecosystem function of filamentous microbial mats from aphotic (cave) sulfidic springs dominated by chemolithoautotrophic epsilon proteobacteria. FEMS Microbiol. Ecol., 51: 31-53.

Greenfield, A. and Graedel, T.E. 2013.The omnivorous diet of modern technology. Resour. Conserv. Recycl., 74: 1-7.

Hagelüken, C. and Meskers, C. 2008. Mining Our Computers: Opportunities and Challenges to Recover Scarce and Valuable Materials. In: OECD-UNEP Conference on Resource Efficiency, 23-25 April 2008, Paris, France, OECD, Paris, pp. 1-22

Hall, L., Kelly A.D., Sherri, L., Wohlfiel, R. and Glenn D.R. 2003. Evaluation of the MicroSeq system for identification of mycobacteria by 16S Ribosomal DNA sequencing and its integration into a routine clinical mycobacteriology laboratory. J. Clinic. Microbiol., 41(4): 1447-1453.

Karwowska, E. 2014. Bioleaching of metals from printed circuit boards supported with surfactant-producing bacteria. J. Hazard. Mater., 264: 203-210.

Kaya, M. 2016. Recovery of metals and nonmetals from electronic waste by physical and chemical recycling processes. Waste Manag., 57: 64-90.

Khatri, B.R. 2018. Chemical and microbial leaching of base metals from obsolete cell-phone printed circuit boards. Sustain. Environ. Res., 28(6): 333-339.

Krieg, N.R. and Holt, J.G. 1984. Bergey's Manual of Systematic Bacteriology. Volume 1, Williams & Wilkins Co., Baltimore, pp. 161-172.

Lima, R. D. 2012. Bioleaching of copper sulfide flotation concentrates in batch reaction system using mesophile and thermophile microorganisms. Dyna, 72: 133-148.

Mishra, D. and Rhee, Y. 2014. Microbial leaching of metals from solid industrial wastes. J. Microbiol., 52: 1-7.

Needhidasan, S., Melvin, S. and Ramalingam, C. 2014. Electronic waste: An emerging threat to the environment of urban India. J. Environ. Health Sci. Eng., 12(1): 36.

Pradhan, J. and Kumar, S. 2012. Metals bioleaching from electronic waste by Chromobacterium Violaceum and Pseudomonads Sp. Waste Manag. Res. – J. Int Solid Wastes Public Clean. Assoc., 30(11): 1151-1159.

Ren, W., Li, P., Geng, Y. and Li, X. 2009. Biological leaching of heavy metals from contaminated soil by *Aspergillus niger*. J. Hazard. Mater., 167(1–3): 164-169.

Rozas, E.E. 2017. Bioleaching of electronic waste using bacteria isolated from the marine sponge *Hymeniacidon heliophila* (Porifera). J. Hazard. Mater., 329: 120-130.

Sajjad, W. 2019. Metals extraction from sulfide ores with microorganisms: The bioleaching technology and recent developments.Trans. Indian Inst. Metals, 72(3): 559-79.

Sheng, P.P. and Etsell, T.H. 2007.Recovery of gold from computer circuit board scrap using Aqua Regia. Waste Manag. Res. – J. Sustain. Circular Econ., 25(4): 380-383.

Tipre, D., Vora, S. and Dave. S. 2004. Medium optimization for bioleaching of metals from Indian bulk polymetallic concentrate. Indian J. Biotechnol., 3: 86-91.

Venkidusamy, K. and Megharaj, M. 2016. Identification of electrode respiring, hydrocarbonoclastic bacterial strain *Stenotrophomonas maltophilia* MK2 highlights the untapped potential for environmental bioremediation. Front. Microbiol.,7: 1-12.

White, T. 1990. Amplification and Direct Sequencing of Fungal Ribosomal RNA Genes for Phylogenetics. In Sninsky, J.J., Innis, M.A., Gelfand, D.H. and White, T. J. (eds.), PCR Protocols: A Guide to Methods and Applications, Academic Press, Cambridge, MA, pp. 315–322.

Widmer, R. 2005. Global perspectives on e-waste. Environ. Impact Assess. Rev., 25(5): 436-458.

Zhao, G., Wang, Z., Dong, M.H., Rao, K., Luo, J., Wang, D., Zha, J., Huang, S., Xu, Y. and Ma, M. 2008. PBBs, PBDEs, and PCBs levels in hair of residents around e-waste disassembly sites in Zhejiang Province, China, and their potential sources. Sci Total Environ 397: 46-57.

Web reference: https://unitar.org/about/news-stories/press/global-e-waste-surging-21-cent-5-years

Study on Spatiotemporal Characteristics of the Impacting Factors of Agricultural Carbon Emissions Based on the GTWR Model: Evidence from the Yellow River Basin, China

Haifeng Huang* and Ni Zhu*†

*School of Economics and Management, Beijing University of Technology, Beijing 100124, China

†Corresponding author: Ni Zhu; 819407202@qq.com

ABSTRACT

Scholars have turned their attention to the ecological protection and high-quality development of China's Yellow River Basin in recent years. The basin is a major agricultural production area in China, hence investigating agricultural carbon emission reduction strategies in the basin is crucial. The research object in this article is the agricultural departmen.ts of China's nine provinces in the Yellow River Basin from 2005 to 2018. Agricultural carbon emissions are measured using agricultural land usage, rice planting, crop planting, straw burning, and livestock breeding as agricultural carbon sources. In addition, the GTWR model is used to examine the spatiotemporal aspects of the impact of five factors on agricultural carbon emissions in this paper. The findings reveal that the five factors have varying degrees and directions of influence.

INTRODUCTION

The human ecological ecosystem has been seriously harmed in recent years. Excessive carbon emissions exacerbate the greenhouse effect, causing the average temperature of the earth's surface to rise, resulting in catastrophic effects such as glacier melting and sea-level rise. The global temperature might rise by 1.5°C in the next 30 years (IPCC 2018). As a result, lowering carbon emissions is critical. Although the carbon emissions of the industrial and service sectors considerably outnumber those of other sectors, agriculture's rapid growth also generates a significant amount of carbon emissions. China's agricultural greenhouse gas emissions, as a significant agricultural country, contributed to a rising proportion of global total emissions. The percentage was as high as 13.07% in 2016 (FAO 2021). As a result, China's efforts to minimize agricultural carbon emissions are critical.

Scholars are increasingly delving into the topic of agricultural carbon emissions. This article categorizes the literature based on three factors.

To begin, scholars have a variety of options when it comes to agricultural carbon emissions sources. Some academics define agriculture in a very narrow way, referring just to the planting sector (Wang et al. 2015). They are primarily interested in the carbon emissions caused by agricultural land use. Pesticides, chemical fertilizers, agricultural plastic films, fossil fuels, electricity, and ploughing were chosen as agricultural carbon sources by Lu et al. (2018) and Zhou et al. (2021). Han et al. (2018), Cui et al. (2021), and Huang et al. (2019) added rice planting, straw burning, and crop planting to the list of sources, respectively. Agriculture is also defined in a broad sense by some researchers, which includes animal husbandry (Xiong et al. 2016, Guo et al. 2021).

Secondly, scholars have studied the influencing factors from various aspects, such as agricultural production (Owusu & Asumadu-Sarkodie 2017), agricultural mechanization (Ismael et al. 2018), agricultural opening (Cui et al. 2018), rural population (Chen et al. 2018), land use area (Zhao et al. 2017), energy consumption (Zhang et al. 2019), urbanization (Ridzuan et al. 2020), agricultural technological progress (Chen et al. 2019) and agricultural industrial structure (Guo et al. 2021).

Thirdly, scholars will adopt different methods according to different purposes and data characteristics to study influencing factors. As for time series, scholars often use the autoregressive distributed lagged (ARDL) model (Saboori et al. 2016) and the ordinary least squares (OLS) model (Danish et al. 2017). As for panel data, scholars often use the fixed effects (FE) model (Nassani et al. 2017). To solve the endogenous problem, some scholars use the generalized

method of moments (GMM) model (Qureshi et al. 2017). In addition, some researchers have begun to take into account the regional variability of contributing factors, opting for a geographically weighted regression (GWR) model (Wang & Zhang 2020). Some researchers use the geographically and temporally weighted regression (GTWR) model to analyze elements that are spatially and temporally heterogeneous (Chen et al. 2019).

The Yellow River, the second-longest river in China, with a length of about 5,464 kilometers and a drainage area of about 752,443 square kilometers, is dominated by dryland agriculture. This paper selects nine provinces (autonomous regions) including Shanxi, Inner Mongolia, Shandong, Henan, Sichuan, Shaanxi, Gansu, Qinghai, and Ningxia in the basin as the study area. Agriculture in the nine provinces increased fast between 2005 and 2018, resulting in a large number of carbon emissions. As a result, understanding the factors that influence agricultural carbon emissions in the nine provinces is critical to the Yellow River Basin's biological ecosystem.

In summary, selecting nine provinces in the Yellow River Basin as the research area, this paper chooses agricultural land use, rice planting, crop planting, straw burning, and livestock breeding as agricultural carbon sources, and

estimates the agricultural carbon emissions of the basin from 2005 to 2018. And then appropriate influencing factors are chosen to analyze the spatiotemporal characteristics based on the GTWR model.

MATERIALS AND METHODS

Estimation of Agricultural Carbon Emissions

Carbon emissions from agricultural land use: The carbon sources, coefficients, and references are shown in Table 1. The six-carbon sources are measured by the amount of pesticides, agricultural fertilizers, agricultural plastic film, agricultural diesel fuel, the effective irrigation area, and the total sown area of crops.

Carbon emissions from rice planting: This research relates to Min et al. (2012)'s study, which considers the CH4 emission coefficients of different types of rice in different regions, as indicated in Table 2 to assess carbon emissions from rice cultivation. The yields of early rice (ER), late rice (LR), and in-season rice (IR) in each region are measured by their sown area.

Carbon emissions from crop planting: During the process of crop planting, the soil will emit N_2O. This paper refers to

Table 1: The agricultural land use carbon source coefficients and references.

Source	Coefficient	Reference
Pesticides	4.9341kg CE.kg^{-1}	Oak Ridge National Laboratory
Fertilizers	0.8956kg CE.kg^{-1}	Oak Ridge National Laboratory
Agricultural Film	5.1800kg CE.kg^{-1}	Institute of Agricultural Resources and Ecological Environment, Nanjing Agricultural University
Diesel fuel	0.5927kg CE.kg^{-1}	IPCC
Irrigation	20.4760kg CE.hm^{-2}	Dubey and Lal (2009)
Plowing	312.6000kg CE.km^2	College of Biology and Technology, China Agricultural University

Table 2: CH$_4$ emission coefficients of rice in nine provinces of the Yellow River Basin (g.m^{-2}).

Province	ER	LR	IR	Province	ER	LR	IR	Province	ER	LR	IR
Shanxi	0	0	6.62	Henan	0	0	17.85	Gansu	0	0	6.83
Inner Mongolia	0	0	8.93	Sichuan	6.55	18.5	25.73	Qinghai	0	0	0
Shandong	0	0	21	Shaanxi	0	0	12.51	Ningxia	0	0	7.35

Table 3: N$_2$O emission coefficients of various crops (kg.hm^{-2}).

Crop	Coefficient	Crop	Coefficient
Rice	0.24	Corn	2.532
Spring Wheat	0.4	Vegetables	4.944
Winter Wheat	1.75	Other Upland Crops (Potato, Peanut, Rapeseed, Cotton, Sugar cane, Beet)	0.95
Soybean	2.29		

the study of Min et al. (2012), and considers the N_2O emission coefficients of different types of crops, as shown in Table 3. The yield of various crops is measured by their sown area.

Carbon emissions from straw burning: Straw burning also produces carbon emissions. This paper refers to the study of He et al. (2018), which considers the carbon emission coefficients of different types of crop straw burning, as shown in Table 4. The amount of various crop straw burning is represented by its total output.

Carbon emissions from livestock breeding: In the process of livestock breeding, the enteric fermentation will produce CH_4, and the manure emissions will produce CH_4 and N_2O. The greenhouse gas emission coefficients of several cattle breeds are provided in Table 5 in this work, based on Min et al. (2012) and Xu et al. (2019) research.

Since the feeding cycles of livestock are different, the average annual feeding amount of livestock should be adjusted. The slaughter rates of rabbits, pigs, and poultry are greater than 1, and their average life cycles are 105 days, 200 days, and 55 days respectively. Therefore, the average feeding amount is adjusted as follows (Equation (1)):

$$N_i = D\_alive_i \times \frac{M_i}{365} \qquad \ldots(1)$$

N_i is the annual average breeding amount for livestock. D_alive_i is the average life cycle for livestock. M_i is the annual production amount for livestock.

The slaughter rates of the other livestock are less than 1, so the average feeding amount is adjusted as follows (Equation (2)):

$$N_i = (C_{i,t} + C_{i,t-1})/2 \qquad \ldots(2)$$

N_i is the annual average breeding amount for livestock. $C_{i,t}$, $C_{i,t-1}$ are the stocks of livestock at the end of year t and t-1, respectively.

Estimation of the scale and intensity of agricultural carbon emissions: The greenhouse effect produced by 1 ton of CH_4 is equivalent to the greenhouse effect produced by approximately 6.82 tons of carbon, and the greenhouse effect produced by 1 ton of N_2O is approximately equal to the greenhouse effect produced by 81.27 tons of carbon (IPCC 2008). Therefore, when calculating agricultural carbon emissions, CH_4 and N_2O emissions can be converted into carbon equivalent.

The calculation method of the agricultural carbon emission scale is shown in Equation (3):

$$ACE = \Sigma ACE_l + \Sigma ACE_r + \Sigma ACE_p + \Sigma ACE_b + \Sigma ACE_s$$
$$= \Sigma \omega_l \alpha_l^C + \Sigma \mu_r \beta_r^{CH_4} \times 6.82 + \Sigma \theta_p \gamma_p^{N_2O} \times 81.27 + \Sigma \eta_b \alpha_b^C$$
$$+ \Sigma \left(\lambda_s \beta_s^{CH_4} \times 6.82 + \lambda_s \gamma_s^{N_2O} \times 81.27 \right)$$
$$\ldots(3)$$

ACE is the scale of agricultural carbon emissions. $ACEl$, $ACEr$, $ACEp$, $ACEb$, $ACEs$ are the carbon emissions from agricultural land use, rice planting, crop planting, straw

Table 4: Carbon emission coefficients of major crop straw burning（kg.CE.kg^{-1}）.

Crop	Coefficient	Crop	Coefficient	Crop	Coefficient
Rice	0.18	Corn	0.17	Soybean	0.15
Wheat	0.16	Rapeseed	0.22	Cotton	0.13

Table 5: Greenhouse gas emission coefficients of various species of livestock (kg.(head·a)$^{-1}$).

Livestock	CH$_4$ Emission Coefficients		N$_2$O Emission Coefficients
	Enteric Fermentation	Manure Emissions	Manure Emissions
Dairy Cow	68	16	1
Non-dairy Cow	51.4	1.5	1.37
Mule	10	0.9	1.39
Camel	46	1.92	1.39
Donkey	10	0.9	1.39
Horse	18	1.64	1.39
Sheep	5	0.16	0.33
Rabbit	0.254	0.08	0.02
Live Pig	1	3.5	0.53
Poultry	-	0.02	0.02

burning, and livestock breeding. ω_l, μ_r, θ_p, η_b, λ_s are the amounts of carbon sources for agricultural land use, rice planting, crop planting, straw burning, and livestock breeding. α_l^C, $\beta_r^{CH_4}$, $\gamma_p^{N_2O}$, α_b^C, $\beta_s^{CH_4}$, $\gamma_s^{N_2O}$ are the greenhouse gas emission coefficients corresponding to the carbon sources.

Agricultural carbon emission intensity is measured by the ratio of the scale of agricultural carbon emissions to the total output value of agriculture, forestry, animal husbandry, and fishery.

Selection of Influencing Factors

Agricultural technological progress (TECH): TECH has an important impact on ACE reduction (Chen et al. 2019). TECH can increase energy utilization and reduce the waste of agricultural materials. And it can optimize the allocation of elements and improve production efficiency, thereby improving agriculture productivity. This paper uses the DEA-Malmquist model (Fare et al. 1994) to measure TECH from the perspective of input and output. The input indicators are selected from the four aspects of labor, land, capital, and mechanization input, which are the number of employees in the primary industry, the total sown area of crops, the fixed asset investment in the primary industry, and the total power of agricultural machinery. The total output value of the primary industry is selected as the output indicator.

Urbanization (URBAN): The improvement of URBAN will promote ACE (Cui et al. 2018). The increase in URBAN means more farmers will move to cities, and they will lease land to farmers who still stay in the countryside, thus integrating agricultural land and helping farmers to use land more efficiently. Then the income of rural households has increased, and farmers can purchase and use more energy in agricultural production, thereby increasing ACE (Chen et al.2013). This article uses the proportion of the urban population in the permanent population at the end of the year to measure URBAN.

Rural education (EDU): The improvement of EDU can curb ACE. The improvement of EDU helps to strengthen farmers' understanding of low-carbon agriculture and improve their ability to use agricultural production technologies, thereby improving production efficiency and reducing ACE (Guo et al. 2021). This article uses per capita of number of years of education in rural areas to measure EDU.

Agricultural industrial structure (STRU): The agricultural materials used in the process of planting crops are an important source of ACE (Tian et al. 2016). That means the higher the proportion of the planting industry is, the more ACE will be. This paper uses the ratio of the total output value of the plant-ing industry to the total output value of agriculture, forestry, animal husbandry, and fishery to measure STRU.

Rural economic development(RGDP): The improvement of RGDP would curb ACE, because the study area changed the way of agricultural development, ensuring the development of the agricultural economy while also preventing damage to the ecological environment (Cui et al. 2018). This article uses the per capita gross production value of agriculture, forestry, animal husbandry, and fishery to measure RGDP.

Research Methodology

Huang et al. (2010) proposed the GTWR model, which can better analyze the spatiotemporal non-stationary character-istics of each variable. The model is as follows:

$$y_i = \beta_0(\mu_i, v_i, t_i) + \sum_k \beta_k(\mu_i, v_i, t_i)x_{ik} + \varepsilon_i \qquad \ldots(4)$$

i is the serial number of the point. . (μ_i, v_i, t_i) is the co-ordinate of the point. y_i is the dependent variable. x_k is the independent variable. ε_i is the error term. β_k is the function re-lated to the coordinate (μ_i, v_i, t_i). See Equation (5) for details:

$$\hat{\beta}(\mu_i, v_i, t_i) = (X^T W(\mu_i, v_i, t_i)X)^{-1} X^T W(\mu_i, v_i, t_i)y \ldots(5)$$

W is a diagonal matrix. Each element in the matrix rep-resents the weight of the corresponding observation point i. The Gaussian spatiotemporal kernel function is used to determine the weight, as shown in Equation (6):

$$W_{ijs,T}^t = \exp\left(-\frac{d_{s_{ij}}^2}{b_S^2}\right) \times \exp\left(-\frac{d_{t_{ij}}^2}{b_T^2}\right) \qquad \ldots(6)$$

$d_{s_{ij}}^2$ and $d_{t_{ij}}^2$ represent the spatial distance and time distance between the data point j and the regression point i respec-tively. See Equations (7) and (8) for details:

$$d_{s_{ij}}^2 = (\mu_i - \mu_j)^2 + (v_i - v_j)^2 \qquad \ldots(7)$$

$$d_{t_{ij}}^2 = (t_i - t_j)^2 \qquad \ldots(8)$$

b_S and b_T represent the spatial bandwidth and the tem-poral bandwidth respectively. The method of selecting the optimal bandwidth is cross-validation (CV). See Equation (9) for details:

$$CV(b_S, b_T) = \sqrt{\sum_{i=1}^n (y_i - \hat{y}_{-i}(b_S, b_T))^2 / n} \qquad \ldots(9)$$

$\hat{y}_{-i}$ is the fitted value of y_i. The point i does not include in the calibration process. b_S and b_T are the optimal space bandwidth and time bandwidth respectively when CV takes the minimum value.

Then, the variables selected above are introduced into Equation (1) to obtain Equation (10):

$$\ln ACEI_i = \beta_0(\mu_i,v_i,t_i) + \beta_1(\mu_i,v_i,t_i)\ln TECH_i + \beta_2(\mu_i,v_i,t_i)\ln URBAN_i$$
$$+ \beta_3(\mu_i,v_i,t_i)\ln EDU_i + \beta_4(\mu_i,v_i,t_i)\ln STRU_i + \beta_5(\mu_i,v_i,t_i)\ln RGDP_i + \varepsilon_i$$
$$\ldots(10)$$

$\beta_1(\mu_i, v_i, t_i)$, $\beta_2(\mu_i, v_i, t_i)$, $\beta_3(\mu_i, v_i, t_i)$, $\beta_4(\mu_i, v_i, t_i)$, $\beta_5(\mu_i, v_i, t_i)$ are the change rates of the ACEI of each province with TECH, URBAN, EDU, STRU, and RGDP, respectively.

Data Sources

The above data are from China Statistical Yearbook, China Livestock Industry Yearbook, China Rural Statistical Yearbook, China Agricultural Statistics, China Agricultural Machinery Industry Yearbook, China Population and Employment Statistics Yearbook, and open data from the National Bureau of Statistics. Some missing values are filled by interpolation. All the variables are taken to the logarithm to unify the magnitude. The descriptive statistics of variables are shown in Table 6.

RESULTS AND DISCUSSION

Empirical Results of GTWR

This paper uses the GTWR model to analyze the spatiotemporal

characteristics of the influencing factors. Firstly, SPSS was used to analyze the variance inflation factor (VIF) showing that there was no obvious multicollinearity. Then, use OLS, TWR, GWR, GTWR models in ArcGIS. The evaluation indicators are shown in Table 7. The R^2 of the GTWR model is the largest. The AIC of the GTWR model is the smallest. Therefore, the GTWR model is a better choice. Finally, the GTWR model is used to obtain the estimated results of the coefficients of variables. The descriptive statistics of the coefficients are shown in Table 8.

Spatiotemporal Evolution of Influencing Factors

(1) The coefficients of lnTECH in most provinces are negative, indicating that TECH has an inhibitory effect on ACEI (Table 9). In 2005 and 2009, TECH in all provinces inhibited ACEI. In 2005, for every 1% increase in lnTECH, ACEI fell by 0.16%-1.65%. In 2009, for every 1% increase in lnTECH, ACEI fell by 0.17%-0.77%. In 2013, only five provinces' TECH had an inhibitory effect on ACEI, while the TECH in Shanxi, Inner Mongolia, Shandong, and Qinghai became the promotion of ACEI. In 2018, TECH in 6 provinces has a depressing effect on ACEI, while TECH in Shanxi, Shandong, and Henan has a promoting effect on ACEI. On the whole, the inhibitory effect of TECH on ACEI is weakening, or even turning into a promotion effect, which shows that

Table 6: Descriptive statistics of variables.

Variable	Symbol	Obs	Mean	Std. Dev.	Min	Max
Agricultural Carbon Emission Intensity	lnACEI	126	15.5446	0.5856	14.5707	17.3966
Agricultural Technological Progress	lnTECH	126	0.2646	0.5404	-1.6801	1.0856
Urbanization	lnURBAN	126	-0.7633	0.1724	-1.2033	-0.4667
Rural Education	lnEDU	126	1.9816	0.1032	1.6387	2.1671
Agricultural Industrial Structure	lnSTRU	126	-0.5993	0.1523	-0.9576	-0.2420
Rural Economic Development	lnRGDP	126	15.1942	1.3355	12.7714	18.7010

Table 7: The comparison of evaluation indicators of OLS, TWR, GWR, GTWR.

	OLS	TWR	GWR	GTWR
R^2	0.8907	0.9487	0.9846	0.9944
AIC	-37.0986	-78.3997	-184.9170	-203.6920

Table 8: The descriptive statistics of the regression coefficients of the GTWR model.

Symbol	Obs	Mean	Std. Dev.	Min	Max
lnTECH	126	-0.2424	0.4803	-1.6497	1.1801
lnURBAN	126	-0.2326	0.9201	-2.0003	1.8497
lneEDU	126	-0.5974	1.4059	-3.1683	3.2775
lnSTRU	126	-0.2169	0.7319	-2.2913	1.0592
lnRGDP	126	-0.3141	0.1528	-0.7426	-0.0088

TECH in nine provinces is more inclined to the expansion of agricultural production while ignoring the development of low-carbon technology.

(2) The coefficients of lnURBAN in most provinces are negative, which indicates that URBAN has an inhibitory effect on ACEI (Table 10). In 2005, the coefficients of Sichuan and Qinghai were positive. For every 1% increase in lnUR-BAN of the remaining provinces, ACEI fell by 0.36%-1.65%. In 2009, the coefficients of Sichuan, Gansu, and Qinghai were positive. For every 1% increase in lnURBAN of the remaining provinces, ACEI fell by 0.43%-1.46%. In 2013, the coefficients of Sichuan, Gansu, and Qinghai were positive. For every 1% increase in lnURBAN of the remaining provinces, ACEI fell by 0.21%-1.16%. The province with the most restraining effect was Henan. In 2018, the coefficients of Inner Mongolia, Gansu, and Qinghai were positive. For every 1% increase in lnURBAN of the remaining provinces, ACEI fell by 0.30%-2.00%. The province with the most restraining effect was still Henan. The coefficients of Sichuan, Gansu,

and Qinghai have been positive for a long time. This may be because the URBAN in these provinces is in an extensive model. The lifestyles of rural households have changed, resulting in higher income and higher energy consumption, which has led to an increase in ACEI.

(3) In 2005, only Shandong, Sichuan, Gansu, and Qinghai had negative coefficients (Table 11). For every 1% increase in lnEDU, ACEI fell by 0.84%-2.68%. And the coefficients for the remaining five provinces were positive. In 2009, only Shaanxi had a positive coefficient. For every 1% increase in lnEDU in the remaining provinces, ACEI fell by 0.31%-2.60%. The province with the most restraining effect was Shandong. In 2013, only Henan had a positive coefficient. For every 1% increase in lnEDU in the remaining provinces, ACEI fell by 0.68%-1.98%. In 2018, the coefficients of Inner Mongolia, Henan, and Shaanxi were positive. For every 1% increase in lnEDU in the remaining provinces, ACEI fell by 0.85%-1.65%. The province with the most restraining effect is still Shandong. The coefficients of Inner Mongolia, Henan,

Table 9: The comparison of coefficients of lnTECH.

Year	Coefficient	Province	Year	Coefficient	Province
2005	-1.649679	Shaanxi	2009	-0.773829	Inner Mongolia
	-1.649678~-1.314597	Shanxi		-0.773828~-0.495197	Shanxi, Sichuan, Ningxia
	-1.314596~-0.738838	Inner Mongolia, Shandong, Ningxia		-0.495196~-0.287975	Shandong
	-0.738837~-0.422202	Henan, Sichuan		-0.287974~-0.179086	Henan, Shaanxi, Gansu
	-0.422201~-0.161031	Gansu, Qinghai		-0.179085~-0.142997	Qinghai
2013	-0.225517	Henan	2018	-0.382916~-0.367305	Sichuan, Shaanxi
	-0.225516~-0.124885	Sichuan, Ningxia		-0.367304~-0.224435	Inner Mongolia, Gansu
	-0.124884~ 0.006878	Shaanxi, Gansu, Qinghai		-0.224434~-0.076516	Qinghai, Ningxia
	0.006879~ 0.173274	Inner Mongolia, Shandong		-0.076515~ 0.464161	Shandong, Henan
	0.173275~ 0.422710	Shanxi		0.464162~ 1.180101	Shanxi

Table 10: The comparison of coefficients of lnURBAN.

Year	Coefficient	Province	Year	Coefficient	Province
2005	-1.647911	Inner Mongolia	2009	-1.461374	Shaanxi
	-1.647910~-1.153687	Shaanxi, Ningxia		-1.461373~-0.854348	Shanxi, Shandong, Henan, Ningxia
	-1.153686~-0.580577	Shandong		-0.854347~-0.436276	Inner Mongolia
	-0.580576~-0.362097	Shanxi, Henan, Gansu		-0.436275~ 0.490700	Gansu
	-0.362096~ 0.920961	Sichuan, Qinghai		0.490701~ 0.935310	Sichuan, Qinghai
2013	-1.155129	Henan	2018	-2.000269	Henan
	-1.155128~-0.528612	Shanxi, Inner Mongolia, Shaanxi		-2.000268~-1.085537	Shanxi, Shaanxi
	-0.528611~-0.213141	Shandong, Ningxia		-1.085536~-0.299831	Shandong, Sichuan, Ningxia
	-0.213140~ 0.686070	Sichuan, Gansu		-0.299830~ 0.412768	Gansu
	0.686071~ 1.195260	Qinghai		0.412769~ 1.751666	Inner Mongolia, Qinghai

and Shaanxi have changed from positive to negative, and then to positive again, indicating that their EDU is not stable enough. Shandong's coefficient has always been negative, and its inhibitory effect ranked first in 2018. This is because Shandong has good educational resources. On the whole, the effect of EDU in each province on ACEI is changing from a promoting effect to a restraining effect, but the EDU of some provinces still needs to be improved.

(4) In 2005, only Inner Mongolia, Shandong, and Henan had positive coefficients (Table 12). For every 1% increase in lnSTRU in the remaining provinces, ACEI fell by 0.12%-0.76%. In 2009, the coefficients of Shanxi, Inner Mongolia, Shandong, Henan, and Sichuan were positive. For every 1% increase in lnSTRU in the remaining provinces, ACEI fell by 0.32%-0.64%. In 2013, only Inner Mongolia, Shandong, and Henan had positive coefficients. For every 1% increase in lnSTRU in the remaining provinces, ACEI fell by 0.29%-2.05%, and the province with the most restraining effect was Shaanxi. In 2018, the coefficients of Inner Mongolia,

Shandong, Sichuan, and Gansu were positive. For every 1% increase in lnSTRU in the remaining provinces, ACEI fell by 0.26%-2.28%, and the province with the most restraining effect was still Shaanxi. The coefficients of Inner Mongolia and Shandong have always been positive, indicating that their planting industry contributes a lot to ACEI. The coefficients of Shaanxi, Qinghai, and Ningxia have always been negative, indicating that their planting industries don't contribute much to ACEI. The signs and sizes of the coefficients in different provinces are different, indicating that for different provinces, the contribution of planting to ACEI is different.

(5) The coefficients of all provinces from 2005 to 2018 are negative (Table 13). In 2005, for every 1% increase in lnRGDP of each province, ACEI fell by 0.27%-0.50%. In 2009, for every 1% increase in lnRGDP of each province, ACEI fell by 0.25%-0.57%. The province with the most restraining effect was Qinghai. In 2013, for every 1% increase in lnRGDP of each province, ACEI fell by 0.02%-0.70%. The province with the most restraining effect was Qinghai.

Table 11: The comparison of coefficients of lnEDU.

Year	Coefficient	Province	Year	Coefficient	Province
2005	-2.678585~-2.405002	Gansu, Qinghai	2009	-2.599254	Shandong
	-2.405001~-1.757907	Sichuan		-2.599253~-2.027379	Henan, Gansu
	-1.757906~-0.838910	Shandong		-2.027378~-1.784293	Sichuan, Qinghai
	-0.838909~ 0.778079	Inner Mongolia, Henan, Ningxia		-1.784292~-0.312775	Shanxi, Inner Mongolia, Ningxia
	0.778080~ 2.618964	Shanxi, Shaanxi		-0.312774~ 1.355597	Shaanxi
2013	-1.982982~-1.705128	Inner Mongolia, Gansu	2018	-1.645274	Shandong
	-1.705127~-1.081102	Shandong		-1.645273~-0.852317	Shanxi, Gansu, Qinghai, Ningxia
	-1.081101~-0.847841	Shaanxi, Qinghai		-0.852316~ 0.260609	Inner Mongolia, Sichuan
	-0.847840~-0.676302	Shanxi, Sichuan, Ningxia		0.260610~ 1.426912	Shaanxi
	-0.676301~ 1.923003	Henan		1.426913~ 3.219786	Henan

Table 12: The comparison of coefficients of lnSTRU.

Year	Coefficient	Province	Year	Coefficient	Province
2005	-0.761454~-0.702788	Shaanxi, Gansu	2009	-0.646380	Gansu
	-0.702787~-0.554412	Ningxia		-0.646379~-0.322537	Shaanxi, Qinghai, Ningxia
	-0.554411~-0.123488	Shanxi, Sichuan, Qinghai		-0.322536~ 0.351141	Shanxi, Sichuan
	-0.123487~ 0.031850	Inner Mongolia, Henan		0.351142~ 0.487373	Inner Mongolia, Henan
	0.031851~ 0.951604	Shandong		0.487374~ 0.882900	Shandong
2013	-2.046561	Shaanxi	2018	-2.279289	Shaanxi
	-2.046560~-0.790560	Qinghai, Ningxia		-2.279288~-0.745337	Shanxi, Henan, Ningxia
	-0.790559~-0.291478	Shanxi, Sichuan, Gansu		-0.745336~-0.264268	Qinghai
	-0.291477~ 0.033379	Inner Mongolia		-0.264267~ 0.132499	Sichuan, Gansu
	0.033380~ 0.965521	Shandong, Henan		0.132500~ 0.698138	Inner Mongolia, Shandong

Table 13: The comparison of coefficients of lnRGDP.

Year	Coefficient	Province	Year	Coefficient	Province
2005	-0.498422~-0.480462	Gansu, Qinghai	2009	-0.568232	Qinghai
	-0.480461~-0.445609	Ningxia		-0.568231~-0.415056	Shaanxi, Gansu
	-0.445608~-0.411152	Sichuan, Shaanxi		-0.415055~-0.320603	Shanxi, Henan, Ningxia
	-0.411151~-0.305165	Shandong, Henan		-0.320602~-0.278390	Inner Mongolia, Sichuan
	-0.305164~-0.273368	Shanxi, Inner Mongolia		-0.278389~-0.250648	Shandong
2013	-0.704922	Qinghai	2018	-0.422290	Qinghai
	-0.704921~-0.570335	Gansu		-0.422289~-0.329806	Shanxi
	-0.570334~-0.267433	Shanxi, Inner Mongolia, Sichuan, Ningxia		-0.329805~-0.214790	Shandong, Gansu, Ningxia
	-0.267432~-0.187673	Shandong, Shaanxi		-0.214789~-0.154043	Inner Mongolia, Sichuan
	-0.187672~-0.021435	Henan		-0.154042~-0.008765	Henan, Shaanxi

In 2018, for every 1% increase in lnRGDP of each province, ACEI fell by 0.01%-0.42%, and the province with the most restraining effect was still Qinghai. Although the coefficients of all provinces are negative, as time goes by, the gap in absolute values has increased. This demonstrates that each province's rural economy has been turned into a low-carbon economy, although the degree of the transformation varies by province, and some provinces may have experienced a transformation bottleneck.

CONCLUSION

This paper estimates the agricultural carbon emissions of nine provinces in the Yellow River Basin from 2005 to 2018 and uses the GTWR model to analyze the spatiotemporal characteristics of influencing factors of agricultural carbon emissions. The main conclusions are as follows:

Agricultural carbon emissions in the nine provinces of the Yellow River Basin increased slowly from 2005 to 2018. Agricultural carbon emissions continued to decrease in intensity. \

The share of agricultural carbon emissions from diverse carbon sources has changed from 2005 to 2018.

3. The five parameters have distinct directions and magnitudes of impact on agricultural carbon emissions throughout the nine provinces of the Yellow River Basin, according to the GTWR model's regression results. As a result, each province should take specific steps to minimize carbon emissions depending on the local conditions.

REFERENCES

Chen, J., Cheng, S. and Song, M. 2018. Changes in energy-related carbon dioxide emissions of the agricultural sector in China from 2005 to 2013. Renew. Sustain. Energy Rev., 94: 748-761.

Chen, Y.H., Li M.J., Su, K.and Li, X.Y. 2019. Spatial-temporal characteristics of the driving factors of agricultural carbon emissions: Empirical evidence from Fujian, China. Energies, 12: 3102.

Cui, H.R., Zhao, T. and Shi, H.J. 2018. STIRPAT-based driving factor decomposition analysis of agricultural carbon emissions in Hebei, China. Pol. J. Environ. Stud., 27: 1449-1461.

Cui, Y., Khan, S.U., Deng, Y. and Zhao, M.J. 2021. Regional difference decomposition and its spatiotemporal dynamic evolution of Chinese agricultural carbon emission: Considering carbon sink effect. Environ. Sci. Pollut. Res., 5: 54-76.

Danish, M., Zhang, B., Wang, B. and Wang, Z.H. 2017. Role of renewable energy and non-renewable energy consumption on EKC: evidence from Pakistan. J. Clean. Prod., 156: 855-864.

Dubey, A. and Lal, R. 2009. Carbon footprint and sustainability of agricultural production systems in Punjab, India, and Ohio, USA. Journal of Crop Improvement, 23: 332-350.

Fare, R., Grosskopf, S., Norris, M. and Zhang, Z.Y. 1994. Productivity growth, technical progress, and efficiency change in industrialized countries. American Economic Review, 84(1): 66-83.

Food and Agriculture Organization of the United Nations (FAO). 2021. FAO statistical database. http://www.fao.org/faostat/zh/#data/GT.

Guo, H.P., Fan, B.Q. and Pan, C.L. 2021. Study on mechanisms underlying changes in agricultural carbon emissions: A case in Jilin province, China, 1998–2018. Int. J. Environ. Res. Public Health, 18: 919.

Han, H.B., Zhong, Z.Q., Guo, Y., Xi, F. and Liu, S.L. 2018. Coupling and decoupling effects of agricultural carbon emissions in China and their driving factors. Environ. Sci. Pollut. Res., 25: 25280-25293.

He, Y.Q., Chen, R., Wu, H.Y., Xu, J. and Song, Y. 2018. Spatial dynamics of agricultural carbon emissions in China and the related driving factors. Chin. J. Eco-Agric., 26(9): 1269-1282.

Huang, B., Wu, B. and Barry, M. 2010. Geographically and temporally weighted regression for modeling spatio-temporal variation in house prices. Int. J. Geogr. Inform. Sci., 24(3): 383-401.

Huang, X.Q., Xu, X.C., Wang, Q.Q., Zhang, L., Gao, X. and Chen, L.H. 2019. Assessment of agricultural carbon emissions and their spatio-temporal changes in China, 1997-2016. Int. J. Environ. Res. Public Health, 16: 3105.

IPCC. 2008. Climate Change 2007: Mitigation of Climate Change; Contribution of Working Group III to the Fourth Assessment Report of the Intergovernmental Panel on Climate Change. IPCC, Geneva, Switzerland, Volume 45.

IPCC. 2018. Special report on global warming of 1.5 (SR15). https://www.ipcc.ch/sr15/.

Ismael, M., Srouji, F. and Boutabba, M.A. 2018. Agricultural technologies and carbon emissions: Evidence from Jordanian economy. Environ. Sci. Pollut. Res., 25: 10867-10877.

Lu, X.H., Kuang, B., Li, J., Han, J. and Zhang, Z.2018. Dynamic evolution of regional discrepancies in carbon emissions from agricultural land utilization: Evidence from Chinese provincial data. Sustainability, 10: 552.

Min, J.S. and Hu, H. 2012. Calculation of greenhouse gases emission from agricultural production in China. China Popul. Resour. Environ., 22(7): 21-27.

Nassani, A.A., Aldakhil, A.M., Qazi Abro, M.M. and Zaman, K. 2017. Environmental Kuznets curve among BRICS countries: spot lightening finance, transport, energy and growth factors. J. Clean. Prod., 154: 474-487.

Owusu, P.A. and Asumadu-Sarkodie, S. 2017. Is there a causal effect between agricultural production and carbon dioxide emissions in Ghana? Environ. Eng. Res., 22(1): 40-54.

Qureshi, M.I., Hassan, M.A., Hishan, S.S., Rasli, A.M. and Zaman, K. 2017. Dynamic linkages between sustainable tourism, energy, health and wealth: evidence from top 80 international tourist destination cities in 37 countries. J. Clean. Prod., 158: 143-155.

Ridzuan, N.H.A.M., Marwan, N.F., Khalid, N., Ali, M.H. and Tseng, M. 2020. Effects of agriculture, renewable energy, and economic growth on carbon dioxide emissions: evidence of the environmental Kuznets curve. Resour. Conserv. Recycl., 160: 104879.

Saboori, B., Sulaiman, J.B. and Mohd, S. 2016. Environmental Kuznets curve and energy consumption in Malaysia: a cointegration approach. Energy Sour. Part B Econ. Plan. Policy, 11: 861-867.

Tian, J.X., Yang, H.L., Xiang, P.A., Liu, D.W. and Li, L. 2016.Drivers of agricultural carbon emissions in Hunan province, China. Environ. Earth Sci., 75: 121.

Wang, H.P. and Zhang, X.Y. 2020. Spatial heterogeneity of factors influencing transportation CO2 emissions in Chinese cities: based on the geographically weighted regression model. Air Quality, Atmosphere & Health, 13, 977-989.

Wang, W., Guo, L.P., Li, Y.C., Su, M., Lin, Y.B.; de Perthuis, C., Ju, X.T., Lin, E.D. and Moran, D. 2015. Greenhouse gas intensity of three main crops and implications for low-carbon agriculture in China. Clim. Chang., 128: 57-70.

Xiong, C.H., Yang, D.G., Xia, F.Q. and Huo, J.W. 2016. Changes in agricultural carbon emissions and factors that influence agricultural carbon emissions are based on different stages in Xinjiang, China. Sci. Rep., 6: 36912.

Xu, L., Qu, J.S., Wu, J.J., Wei, Q., Bai, J. and Li, H.J. 2019. Spatial-temporal dynamics and prediction of carbon emission from agriculture and animal husbandry in China. J. Ecol. Rural Environ., 5(10): 1232-1241.

Zhang, L., Pang, J., Chen, X. and Lu, Z. 2019. Carbon emissions, energy consumption, and economic growth: Evidence from the agricultural sector of China's main grain-producing areas. Sci. Total Environ., 665: 1017-1025.

Zhao, R.Q., Liu, Y., Tian, M.M., Ding, M.L., Cao, L.H., Zhang, Z.P., Chuai, X.W., Xiao, L.G. and Yao, L.G. 2018. Impacts of water and land resources exploitation on agricultural carbon emissions: The water-land-energy-carbon nexus. Land Use Policy, 72: 480-492.

Zhou, Y., Wang, T., Peng, R. and Hu, H. 2021. Spatial-temporal characteristics and factors of agricultural carbon emissions in the belt and road region of China. Pol. J. Environ. Stud., 30(3): 2445-2457.

Handling the Sludge When Using Polyaluminum Chloride as a Coagulant in the Potable Water Treatment Process

S. H. M. Sajath*, A. R. Nihmiya* and U. S. P. R. Arachchige*†

*Department of Civil and Environmental Technology, Faculty of Technology, University of Sri Jayewardenepura, Homagama, Sri Lanka

†Corresponding author: U.S.P.R. Arachchige, udara@sjp.ac.lk

ABSTRACT

The sludge produced in the treatment process depends on the type of coagulant and other chemicals used and the suspended particles present in raw water. Discarding this sludge in the landfills poses pollution of both ground and surface water, disturbing the lives in the water and the water quality. The primary potable water provider in Sri Lanka is the National Water Supply and Drainage Board. It focuses on finding ways of disposal, sustainable practices, and possible applications of the water treatment sludge. This research aims to identify the aluminum level in the potable water treatment sludge of the Konduwattuvana water treatment plant in Ampara and to utilize that sludge as an alternative raw material in burnt clay brick manufacturing. The national standards and limitations of the sludge content and the standard brick manufacturing process were followed. To reach the aim, a sequence of tests was conducted, and the brick characteristics are subjected to test for different sludge ratios according to the Sri Lankan Standard of 36:1978 for burnt clay bricks. Experimental results show that the aluminum content in liquid sludge and sludge cake was found to be 231.6 $mg.L^{-1}$ and 54.9 $mg.L^{-1}$, respectively, which implies that the sludge contains aluminum. The optimum sludge ratio to produce burnt clay bricks was found to be 10% of the total weight of the brick.

INTRODUCTION

Water treatment aims to provide a safe and adequate quantity of drinking water to people that do not contain any undesirable taste, odor, and color. Water is one of the essential valuable natural resources on earth for the survival of life. While water is being treated, a considerable quantity of water is drained as wastewater. So, it is crucial to treat the wastewater before discharging it anywhere else; thus, it cannot harm the environment and can be used for purposes other than drinking, such as irrigation. And also, a large quantity of sludge is generated each year from the water treatment process. The amount of sludge produced depends upon the amount of wastewater and the type of treatment practiced for treating the wastewater. Sludge management in water treatment plants becomes a severe problem due to its negative impact on the environment and people (Świerczek et al. 2018, Gomes et al. 2020). The common method adopted for disposing of the sludge is landfilling. Landfill disposal of the sludge has drawbacks such as high transportation costs, difficulty getting suitable sites for landfilling, heavy metal contamination of the land, emission of foul gases, etc. (Świerczek et al. 2018). So, disposal of sludge has become a major issue. Sludge usage in the construction industry is considered to be the most economical and environmentally sound option (Abdel-Gawwad et al. 2020, Breesem et al.

2014, Johnson et al. 2014, Ramadan et al. 2008, Mymrin et al. 2019, Limami et al. 2021).

Various researchers have carried out research worldwide regarding the sludge produced in water treatment processes (Abdel-Gawwad et al. 2020, He et al. 2021, Godoy et al. 2019). The suitability of water treatment sludge as a raw material for the local clay brick production industry was investigated using sludge from the Meewatura water treatment facility in Kandy, Sri Lanka. (Illangasinghe et al. 2014). Air-dried sludge at the Meewatura sludge drying lagoons was collected and mixed with clay in the proportions of 25:75 and 50:50 percentages, respectively of its volume. To evaluate the quality, the manufactured bricks were tested for dimensions, compressive strength, water absorption, and efflorescence concerning the SLS 39:1978. The results revealed that all of the sets of bricks, including the control sample, exceeded the tolerance limit in terms of dimensions, and the compressive strength was lower than the standard strength. And also, the brick samples were made using the sludge that exceeded the definite water absorption limits. The study concluded that the bricks produced with dried sludge with the above combination with clay could not adhere to anticipated standards.

In 2013, Victoria (2013) had done a similar study in Nigeria, where water treatment sludge was used to supplement

clay. The sludge had used in five various mixing ratios of 0%, 5%, 10%, 15%, and 20% of total weight. These bricks were burnt at five different temperatures of 850, 900, 950, 1000, and 1050°C. The research concluded with the findings that the proportion of sludge in the mixture and the temperature of firing are the two main factors influencing the consistency of the bricks and that the water treatment plant sludge can be used as a replacement for clay in the brick industry to increase its workability and physical appearance by enhancing environmental sustainability.

According to a report on brick making by Hegazy et al. (Hegazy et al. 2011), where water treatment sludge was combined with varying amounts of Silica Fume (SF) and used as a complete substitute for brick clay, the sludge was combined with varying amounts of SF and used as a complete substitute for brick clay. The study aimed to use the sintering process to create a lab-scale brick device constructed from sludge and SF mixtures in various ratios that met Egyptian standard specifications (ESS). For the measured samples, the sludge: silica fume ratios were 25:75, 50:50, and 75:25 percent of the overall weight of the mixture. As a controlled study, 100 percent of clay bricks were also produced. These bricks were burned at temperatures of 900, 1000, 1100, and 1200°C. Using the ESS standard, the physical and mechanical parameters of the bricks were assessed and compared to control samples composed solely of clay. Based on the findings, 50 percent of the optimal sludge was added to the sludge-SF combination by working at a temperature similar to that used in a brick kiln. The produced bricks outperformed the control clay brick in terms of characteristics.

Another similar study had done by Hegazy et al. (2012) in which water treatment sludge was combined with varying amounts of Rice Husk Ash (RHA) and used as a complete substitution for clay. The RHA was one of the most common agricultural wastes in Egypt. RHA contains high amounts of silica. The study's objective was to provide an environmentally friendly way to reuse water treatment sludge and rice husk ash. The samples considered in the study were in the following ratios of sludge: rice husk; 25: 75, 50: 50, 75: 25 percentages of the total weight of the mixture. And 100 percent of clay bricks were also made as to the control sample. Then they were fired at 900, 1000, 1100, and 1200°C. The properties of the produced bricks were determined and evaluated according to ESS standards and compared with control samples made entirely from clay. It was concluded from the results obtained that, by operating at the temperature commonly practiced in the brick kiln, 75 percent was the optimum sludge addition to produce brick from sludge: RHA mixture.

The whole substitution of brick clay with water treatment sludge combined with different ratios of RHA and SF was examined by Hegazy et al. (2012) in Egypt. The SF is a byproduct of producing silicon metal or ferrosilicon alloys in smelters using an electric arc furnace. Three different series of sludge: SF: RHA ratios of 25:50:25, 50:25:25, and 25:25:50 percentages of the total weight of the mixture were prepared. And 100 percent of clay bricks were also prepared as the control sample. Every four series of bricks were burnt at temperatures of 900, 1000, 1100, and 1200°C. It was concluded from the results obtained that, by operating at the temperature commonly practiced, a mixture consisting of 50:25:25 of WTP sludge:SF:RHA was the optimum sludge addition to produce brick.

A study was done by Ramadan et al. (2008) in Egypt, where water treatment sludge was used as a partial substitute for clay. The samples were considered with the following sludge: clay ratios; 50:50, 60:40, 70:30, and 80:20 percentages of the total weight of the sludge clay mixture. These bricks were burnt at temperatures of 950, 1000, 1050, and 1100°C. The study concluded that 50 percent was the optimum sludge addition to produce brick from sludge; clay mixture operating at the temperature commonly practiced in the brick kiln.

To improve efficiency, some water treatment plants switched from conventional alum to poly aluminum chloride (PAC) as a coagulant (Nansubuga et al. 2013). PAC is increasingly preferred as lower alkalinity consumption as well as its lower dose requirement. From a chemical point of view, PAC is similar to alum, except that it contains highly charged polymeric aluminum species as well as monomers. The solubility characteristics of PACs and alum are different such as PACs are more soluble and have a higher pH of minimum solubility than alum, making PAC the preferred coagulant nowadays.

Several studies have already given insight into the reuse of alum sludge (Huang & Wang 2013, Kizinievi et al. 2013, Victoria 2013, Tay 1987), but many water treatment plants are now adopting PAC, whose sludge characteristics differ from alum sludge. It is, therefore, necessary to study the possibility of reuse of sludge derived from water treatment where PAC is used. This study focuses on the possibility of using PAC water treatment sludge as brick material. The sludge for this study was collected from the Konduwattuvana water treatment plant (KWTP), Ampara, Sri Lanka, which runs under the National Water Supply and Drainage Board (NWSDB) Sri Lanka. The main coagulant used in this plant for the treatment process is PAC. Analyzing and determining bricks' properties were conducted according to the Sri Lankan Standard (SLS) of 39:1978, which defines

the specifications for common burnt clay building bricks in Sri Lanka.

MATERIALS AND METHODS

This research aims to determine the aluminum content in the sludge produced in the KWTP through conducting laboratory tests and to examine the possibility of sludge being used as a construction material as clay brick.

Aluminum Test

The aluminum test was carried out for two sludge samples to check whether they satisfy the Industrial wastewater tolerance limit set by the Central Environmental Authority (CEA) of Sri Lanka to be discharged into inland surface water. The sludge samples in two different places were collected in 200 ml sample bottles at KWTP and safely taken to the energy laboratory of the Faculty of Technology, the University of Sri Jayewardenepura for sample preparation.

Water treatment sludge samples were prepared at the energy laboratory of the Faculty of Technology, University of Sri Jayewardenepura, to test the aluminum content. Then the prepared samples were given to the Instrument Center of Faculty of Applied Sciences, University of Sri Jayewardenepura.

As the first step, the water treatment sludge samples were digested with nitric acid to comply with EPA recommendations (Agoro et al. 2020, Feizi et al. 2019). A sample of 2 g of already treated water sludge sample was put in a conical flask containing 20 mL of HNO_3 (55 percent) and heated at 90°C for 45 minutes.

Then the temperature was then raised to 150ºC and kept for about 10 minutes. The periodic addition of 10 mL of HNO_3 (55%) when heating the sample mixture was made three times to avoid dryness. Once the mixture is cool to room temperature, it was filtered through Whatman Number 1 filter paper. The digested sample was then moved into a 100 mL standard flask and made up to the mark with double distilled water as required.

The water treatment sludge samples prepared at the energy laboratory of the Faculty of Technology, University of Sri Jayewardenepura, were taken to the Instrument Center of Faculty of Applied Sciences, the University of Sri Jayewardenepura to test the aluminum level in the samples. The aluminum was measured using a deuterium lamp in flame mode by AAS (iCE 3000 AA05121002 v1.30 spectrophotometer), and results were obtained.

Brick Manufacturing

For this study, the sludge was obtained from the sludge drying bed of KWTP, Ampara, in a gunny bag and transported to the local brick manufacturing site. The sludge collected was air-dried for more than 14 days in the sludge drying bed. The local commercial clay procured from a selected local brick company in Attappalam, Nintavur, Ampara was used in this study to mix with the sludge. Although the sludge had been dried, both the sludge and the clay were air-dried for 24 h at the brickyard, as per the manufacturer's standard process. As the batching method, the total weight of the mixture was used for mixing the sludge and clay to produce the bricks with the size of 220 mm in length, 105 mm in width, and 65 mm high as per the Sri Lankan standard of SLS 39:1978. Table 1 shows the percentage of sludge used as a supplement for clay. 100% of clay bricks were also prepared as the control sample. A total of 70 bricks were produced by having ten separate bricks in each mixing ratio.

The sludge and clay samples were measured and spread evenly, and then thoroughly mixed until a homogeneous mix with uniform color was obtained. The mixing took place on a clean, non-hazardous surface. The water was added gradually to the dry mixture while mixing until optimum moisture content was obtained.

The hand mold method with the wooden mold with five bricks casting at once with the size of 205 mm x 88 mm x 65 mm was used for brick casting. The inner faces of the wooden mold were lubricated with water for easy removal and to get a smooth surface. The mixture was placed in a mold and compressed. The remaining mixture was scraped down, and the surface was smoothed. Six sludge-clay bricks and six control bricks containing only clay were made as reference specimens, with each brick being marked and numbered for easy identification.

Casted bricks were stacked at the site for 10 days for air drying and the regular batch and loaded to the kiln for burning by operating at the temperature generally practiced in the brick kiln. After finished burning, the bricks were cooled and transported to the South Eastern University of Sri Lanka for testing.

Table 1: Group of composition sludge-clay mixture.

	Sample No	Sludge Percentage [%]	Clay Percentage [%]
Control Brick	1	0	100
Sludge-Clay Brick	2	2	98
	3	4	96
	4	6	94
	5	10	90
	6	15	85
	7	20	80

Analyzing and Determining the Properties of Bricks

All the tests were conducted in accordance with the Sri Lankan Standard of 39:1978, a specification for common burnt clay building bricks. All four parameters stated in the specification, like dimensions, water absorption, compressive strength, and efflorescence, were tested to evaluate the quality of bricks.

Dimension Test

All ten bricks (10) were selected from each sample and grouped. The overall dimension was measured by placing each set of samples of 10 bricks lined up in a straight line upon a smooth surface, and any small projections or loose particles of clay adhering to each brick blisters were removed. The overall dimension (length, width, high) of each set of samples was measured to the nearest millimeter using steel tape.

Water Absorption Test

Three random bricks (3) out of 10 for each sample were selected and dried thoroughly in an oven at a temperature between 100°C to 115°C and then let to cool to room temperature and weighed separately, and the dry weight (W_d) was noted. The dry bricks were fully immersed in cold water at room temperature for 24 h. Then each brick was removed from the water, excess surface water was wiped off with a damp cloth and weighed separately, and the wet weight (W_w) was noted. The water absorption percentage (W_a) of each brick was calculated using Equation 1. The average of these three bricks was taken as the water absorption capacity for the bricks of a sample.

Water absorption percentage,

$$Wa = (W_w - W_d)/W_d \times 100\% \qquad …(1)$$

Efflorescence Test

Typical clay bricks may include some alkaline components, and the higher the quantity, the greater the risk of efflorescence, which appears as fine whitish layers as deposits on the brick surfaces. They are difficult to handle and can lead to other long-term issues in the structure, particularly cosmetic issues.

So, to determine that three random bricks (3) out of 10 for each sample were selected and placed in a shallow flat bottom dish, distilled water was poured into the depth of 25 mm as at least one inch of the bricks must be underwater. Then it was placed in a well-ventilated space at room temperature until all the water in the dish evaporates. When the water had been absorbed, and bricks appeared dry, a similar quantity of water was poured into the dish and allowed to

evaporate as before. Then the bricks were examined for efflorescence.

Compressive Strength Test

Three random bricks (3) out of 10 for each sample were selected. The overall dimension of each bed surface was measured, and area (A) was calculated. Then bricks were immersed in water for 72 h at room temperature. After 72 h, bricks were removed from the water and allowed to drain at room temperature, and surplus moisture was wiped.

Then, sample brick was placed between two similar plywood sheets and carefully centered between the compressive strength test machine (MATEST- 3000kN Compression Testing Machine). Then the load was applied axially and uniformly to the brick until it failed. Then the maximum load (F_{max}) at failure was noted. Then the compressive strength of the brick was calculated from Equation 2. The average of the three readings was calculated and taken as the compressive strength of the bricks of a sample.

Compressive strength of brick,

$$Compressive\ strength = F_{max}/A \qquad …(2)$$

RESULTS AND DISCUSSION

Aluminum Test

Table 2 shows the summary of the results obtained from the test. The Aluminum contents of both sludge before and after were found to be approximately 232 mg.L^{-1} and 55 mg.L^{-1}, which can be acceptable since they are using an Aluminum-based coagulant to treat raw water. This result confirms the doubt that was present before conducting the test that 'Aluminum content may be higher in the sludge produced.' Therefore, it was concluded that the sludge contains Aluminum in it and it should be minimized before disposal.

Dimension Test

The average individual and cumulative dimension test results of each proportion of sludge mixture are given in Tables 3 and 4. Fig. 1 and 2 show the trends of average individual and cumulative dimensions. Both Fig. 1 and 2 clearly show that the bricks' dimension decreases with the increase of sludge content.

Table 2: Aluminum contents of water sludge

Sample Name	Results obtained [mg.L^{-1}]
Sludge before centrifuge (Sludge holding tank)	231.6
Sludge after centrifuge (Sludge cake)	54.9

Water Absorption Test

The water absorption test results for different proportions of sludge mixture in Table5 and its trend is shown in Fig. 3.

It shows that the water absorption for the bricks increases with the increased sludge content. Water absorption is a key factor that affects the durability of bricks. Hence the lesser amount of water infiltrated into the brick makes the brick more durable.

Efflorescence Test

Normally salts like Na, K, $CaCl_2$, Sulphates, etc., may be present in typical clay brick.

Efflorescence is a fine whitish layer of salt deposition on the surfaces of bricks where water dissolves salt and moves them to the surface of the brick. They can lead to some potential moisture problems that can cause structural damage to building materials esthetic problems in a structure. The

Table 3: Average individual dimensions of each sample.

Sample No	Sludge: Clay Ratio [%]	Length [mm]	Width [mm]	Height [mm]
SLS 39: 1978 Requirement (1 Brick):		220	105	65
1	0: 100	193	83	60
2	2: 98	190	81	57
3	4: 96	188	81	62
4	6: 64	187	80	60
5	10: 90	186	79	59
6	15: 85	184	79	59
7	20: 80	181	77	56

Table 4: Average cumulative dimension of 10 bricks of each sample.

Sample No	Sludge: Clay Ratio [%]	Length [mm]	Width [mm]	Height [mm]
SLS 39: 1978 Requirement (10 Bricks):		2200 ± 30	1050 ± 17	650 ± 17
1	0: 100	1944	837	609
2	2: 98	1906	818	584
3	4: 96	1891	818	631
4	6: 64	1879	812	611
5	10: 90	1874	803	599
6	15: 85	1855	798	597
7	20: 80	1823	776	565
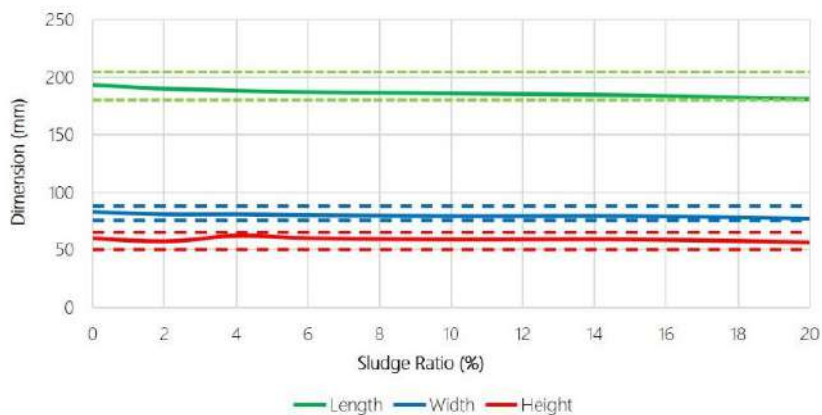
Fig.1: Trend of avg. individual dimension of bricks with different sludge ratios.
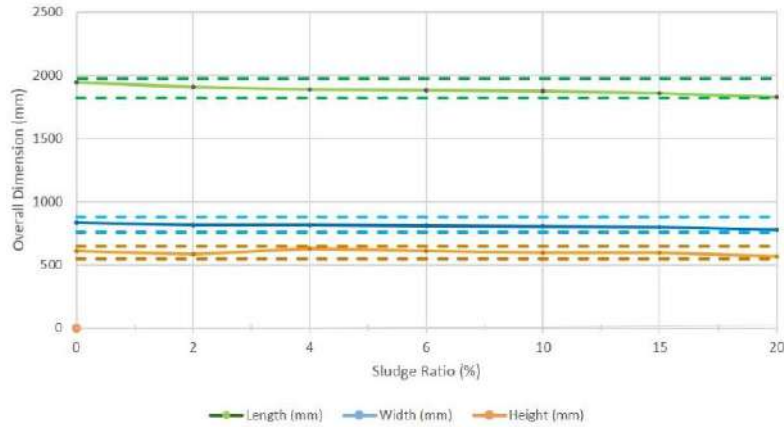
Fig. 2: Trend of avg. cumulative dimension of 10 bricks with different sludge ratios.

summary of the efflorescence test results is shown in Table 6, and from this, it can be shown that all the brick samples satisfy the minimum requirement of efflorescence stated in the SLS 39: 1978 standard.

Compressive Strength Test

Table 7 shows that the compressive strength is greatly dependent on the amount of sludge in the brick. Fig. 4 shows the trend of compressive strength with different sludge portions. The strength of brick decreases with the increased sludge content. The average compressive strength of the control sample is 5.20 N.mm^{-2}. The average compressive strength of WTP sludge clay brick is varied between 3.70 and 1.65 N.mm^{-2}. With the addition of 10% sludge to clay, the sludge clay brick strength met the minimum requirement of 2.8 N.mm^{-2} (SLS 39:1978) as building brick.

Table 5: Avg. water absorption percentage of brick samples.

Sample No	Sludge: Clay Ratio [%]	Avg. Water Absorption [%]
SLS 39: 1978 Requirement (Type 2, Grade II):		< 28
1	0: 100	13.50
2	2: 98	13.27
3	4: 96	14.98
4	6: 94	15.01
5	10: 90	16.71
6	15: 85	19.00
7	20: 80	19.87

Fig. 3: Trend of water absorption percentage of different sludge ratios.

CONCLUSION

Under the settings and manufacturing methods utilized in this study, sludge produced at the Konduwattuvana water treatment plant was successfully used as a successful substitute in the manufacture of burnt clay construction bricks, which is environmentally sustainable and useful. The aluminum content in the sludge was measured using a deuterium lamp in flame mode by AAS (iCE 3000 AA05121002 v1.30 spectrophotometer). The Aluminum
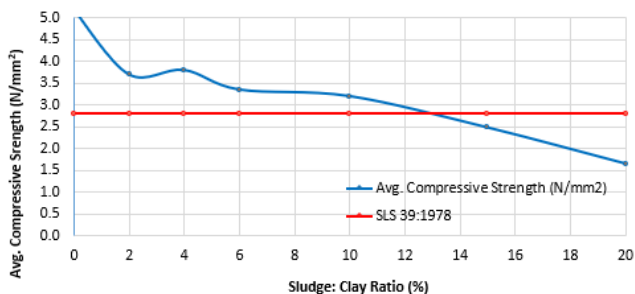

Fig.4: Trend of avg. compressive strength for bricks.

Table 6: Efflorescence test results of brick samples.

Sample No	Sludge: Clay Ratio [%]	Efflorescence Result
SLS 39: 1978 Requirement (Type 2, Grade II):		Moderate
1	0: 100	Slight
2	2: 98	Slight
3	4: 96	Slight
4	6: 64	Slight
5	10: 90	Slight
6	15: 85	Nil
7	20: 80	Slight

Table 7: Average compressive strength of brick samples.

Sample No	Sludge: Clay Ratio [%]	Avg. Compressive Strength [N.mm^{-2}]
SLS 39: 1978 Requirement (Type 2, Grade II):		2.8
1	0: 100	5.20
2	2: 98	3.70
3	4: 96	3.80
4	6: 64	3.35
5	10: 90	3.20
6	15: 85	2.48
7	20: 80	1.65

content in the thickened liquid sludge was 231.6 mg/L. The Aluminum content in the solid sludge cake was 54.9 mg.L^{-1} which denotes that the sludge containing aluminum in it should be minimized. Dimension, water absorption, efflorescence, and compressive strength of the brick were all investigated. When the sludge percentage was increased, the overall dimensions of the brick shrank. With the increase in sludge percentage, the water absorption percentage of bricks increased. The efflorescence of the bricks, on the other hand, was satisfactory in comparison to the standard. At the same time, when the sludge ratio increased, the compressive strength of the bricks declined. Finally, it was determined that a 10% sludge addition to the total weight of a brick is the best sludge ratio for producing burnt clay brick from a sludge-clay mixture when the kiln is operated at the normal temperature. It can also be concluded that the amount of aluminum content in the sludge does not affect the quality of the brick. Therefore, water treatment plant sludge can be considered a suitable raw material for the brick manufacturing industry while providing a sustainable sludge handling method.

ACKNOWLEDGMENT

REFERENCES

Abdel-Gawwad, H.A., Samah, A.S. and Mona, S.M. 2020. A clean approach through sustainable utilization of cement kiln dust, hazardous lead-bearing, and sewage sludges in the production of lightweight bricks. J. Clean. Prod., 273: 123129.

Agoro, M.A., Abiodun, O.A., Martins, A.A. and Omobola, O.O. 2020. Heavy metals in wastewater and sewage sludge from selected municipal treatment plants in eastern cape province, South Africa. Water, 12(10): 2746.

Breesem, K.M., Faris, G.F. and Isam, M.A. 2014. Reuse of alum sludge in construction materials and concrete works: A general overview. Infrastructure Univ. Kuala Lumpur Res. J., 2(1): 20-30.

Feizi, M., Mohsen, J. and Gianacrlo, R. 2019. Assessment of nutrient and heavy metal content and speciation in sewage sludge from different locations in Iran. Natural Hazards, 95(3): 657-675.

Godoy, L.G.G., Abrahão, B.R., Mônica, R.G., Eugênio, B.C., Silvana, D.D. and Jairo, J.O.A. 2019. Valorization of water treatment sludge waste by application as a supplementary cementitious material. Constr. Build. Mater., 223: 939-950.

Gomes, S.D.C., John, L.Z., Wengui, L. and Fulin, Q. 2020. Recycling of raw water treatment sludge in cementitious composites: Effects on heat evolution, compressive strength, and microstructure. Resour. Conserv. Recycl., 161: 104970.

He, Z., Ying, Y., Qiang, Y., Jin-yan, S., Bao-Ju, L., Chao-Feng, L. and Shi-Gui, D. 2021. Recycling hazardous water treatment sludge in cement-based

construction materials: mechanical properties, drying shrinkage, and nano-scale characteristics. J. Clean. Product., 290: 125832.

Hegazy, B.E.E., Hanan, A.F. and Ahmed, M.H. 2012. Brick manufacturing from water treatment sludge and rice husk Ash. Aust. J. Basic Appl. Sci., 6(3): 453-461.

Hegazy, B.E.E., Hanan, A.F., Ahmed, M.H. 2011. Reuse of water treatment sludge and silica fume in brick manufacturing. J. Am. Sci., 7(7): 569-576.

Huang, C. and Shun-Yuan, W. 2013. Application of water treatment sludge in the manufacturing of lightweight aggregate. Constr. Build. Mater., 43: 174-183.

Illangasinghe, W., Werellagama,W. and Antoney, K. 2014. Disposal of water treatment plant waste sludge: Trials in brick manufacture. IESL Annual Sessions, 41: 515.

Johnson, O.A., Napiah, M. and Kamaruddin, I. 2014. Potential uses of waste sludge in the construction industry: A Review. Res. J. Appl. Sci. Eng. Technol., 8(4): 565-570.

Kizinievi , O., Ramun , Ž., Viktor, K. and Rimvydas, Ž. 2013. Utilization of sludge waste from water treatment for ceramic products. Constr. Build. Mater., 41: 464-473.

Limami, H., Imad, M., Khalid, C. and Asmae, K. 2021. Recycled wastewater treatment plant sludge as a construction material additive to ecological lightweight earth bricks. Clean. Eng. Technol., 2: 100050.

Mymrin, V., Fernanda, M.H., Kirill, A., Monica, A.A., Edgar, W., Gabriel, P. M., Alfredo, I. and Rodrigo, E.C. 2019. Construction materials waste is used to neutralize hazardous municipal water treatment sludge. Constr. Build. Mater., 204: 800-808.

Nansubuga, I., Noble, B., Mohammed, B., Willy, V. and Tom, V.W. 2013. Effect of poly aluminum chloride water treatment sludge on effluent quality of domestic wastewater treatment. Afr. J. Environ. Sci. Technol., 7(4): 145-152.

Ramadan, M.O., Hanan, A.F. and Ahmed, M.H. 2008. Reuse of water treatment plant sludge in brick manufacturing. J. Appl. Sci. Res., 4(10): 1223-1229.

wierczek, L., Bartłomiej, M.C. and Piotr, K. 2018. The potential of raw sewage sludge in construction industry–a review. J. Clean. Prod., 200: 342-356.

Tay, J.H. 1987. Bricks manufactured from sludge. J. Environ. Eng., 113(2): 278-284.

Victoria, A.N. 2013. Characterization and performance evaluation of water-works sludge as bricks material. Int. J. Eng., 3(3): 8269.

Leaching of Metal Ions and Suspended Solids from Slag Corroded by Acid-base Solutions: An Experimental Study

Jiayu Ma*(**), Haijun Lu*(**)†, Yuchen Wei* and Chaofeng Wang*

*School of Civil Engineering and Architecture, Wuhan Polytechnic University, Wuhan 430023, China

**State Key Laboratory of Geomechanics and Geotechnical Engineering, Institute of Rock and Soil Mechanics, Chinese Academy of Sciences, Wuhan 430071, China

†Corresponding author: Haijun Lu; lhj@whpu.edu.cn

ABSTRACT

This study focused on the ion release and microstructure of slag during its degradation following erosion by different pH solutions. It focused on controlling factors such as slag particle size range, pH value of the solution, and soaking time. The surface microstructure and particle size distribution of slag with the particle size of 0.075–5.0 mm, the mineral composition of suspended pollutants larger than 0.45 µm, and the phenomenon of nano-scale ion release were examined. When slag was soaked in solutions with different pH values for 30 days, the pH value of leachate tended to be neutral, the release amount of Ca, Mg, Fe, and Cd ions increased and the release rate gradually decreased. The dissolution process of slag in the alkaline solution was slower than that in acid, but suspension and gels formed more easily in an alkaline environment. Nitric acid accelerated the chemical reaction of akermanite, gehlenite, and hawleyite, and released Ca, Mg, and Cd ions. There were clear damage cracks and various irregular pores on the slag surface. Under the attack of alkali solution, the weight of akermanite in slag increased, the Mg ion content in solution decreased, and the suspended solids of calcite and portlandite increased. At pH 12, unlike at pH 3, there were no large surface cracks in the slag and the interface damage was small. Compared with pH 7, there were more irregular substances, such as flakes and spheres. The particle size of slag was mainly 0.1–0.5 mm, the content before and after leaching was 52.80%–55.87% and 55.00%–58.27%, and the slag was in a poor grading state. The findings of this study act as an important reference for understanding the influence of slag leaching on water and soil pollution.

INTRODUCTION

At present, thousands of slag dumps exist globally, such as those left by small historical iron furnaces in some parts of the United States (Piatak et al. 2015). Slag pollution caused by mining and smelting activities has also become a problem that cannot be ignored in China. Ferrous slag is used in the generation of several materials, but the various sulfides, intermetallic compounds, silicates, calcium, iron, magnesium, aluminum, cadmium, and other trace elements generated after soaking of slag can cause serious environmental pollution.

Water from slag contains different concentrations of ions, and the highest concentration of each ion is located at different depths of an aquifer (Bayless et al. 1998). Where groundwater reaches the surface, slag produces mineral precipitation and releases a large quantity of trace elements (cadmium, chromium, copper, lead, nickel, and zinc) with high mobility (Roadcap et al. 2005). Leachate produced by ferrous slag soaking contains a large number of trace elements, which have harmful effects on surface water and

groundwater. After an artificial leaching experiment, the concentration of some metal ions in Fe slag was found to exceed the standard (Piatak & Seal 2012, USEPA 2009a, b). Fällman & Hartlén (1994) compared the pH value and redox potential of slag leachate in laboratory tests and field tests. Sloto & Reif (2011) found that the composition of groundwater and surface water was similar to that of leachate extract, indicating the feasibility of indoor leaching tests. The acidic neutralization ability of slag could be used as a soil conditioner to treat acidic wastewater or acidic sulfate soil (Álvarez-Valero et al. 2007, Wendling et al. 2012, 2013). Research has also shown that the reaction products of alkali-activated slag are mainly C-S-H and C-(N)-A-S-H gels (Hong & Glasser 2002, Escalante-García et al. 2003, Skibsted & Andersen 2012, Myers et al. 2013).

Some scholars have focused on the effects of pH value, liquid-solid ratio, temperature, slag fine particle ratio, and mineral phase on ion dissolution kinetics in slag. For example, Chaurand et al. (2006) used static leaching tests (pH value controlled at 5) to study the release of Cr and V from slag, and

Ning et al. (2016) discussed the extraction mechanism of Cr and V from slag. Barna et al. (2004) showed that the release of ions from slag is controlled by the pH value of leachate. The solubility of Pb ion at pH 1.5 and 1.7 was simulated (Bosso & Enzweiler 2007), and the problem of high release of Pb ion was further explored (De Angelis & Medici 2012). Different liquid-solid ratios and temperatures had different effects on metal release from slag (De Windt et al. 2011, Nikolić et al. 2016). Fine fractions from slag sample crushing usually promote leaching of Cu, Co, and Zn (Vítková et al. 2011). The mobility of heavy metals in slag depends on the morphology of the ore-bearing stage (Chaurand et al. 2007). The mineral phase of slag is also easily dissolved in rainwater. A large amount of As, Pb, and Cu can be rapidly distributed into the environment near slag fields (Ettler et al. 2009), thus increasing the research demand on slag mineralogy (Ettler et al. 2012). However, to our knowledge, there are few comparative studies on the release characteristic of various icons of the same kind of slag in acid-base solutions with different concentration gradients and the deterioration of slag.

Therefore, this paper is focused on the quantification of the environmental aspects of slag waste through the study of the release characteristics and microscopic changes of ions during slag soaking. This study aimed to evaluate the release of potentially harmful trace elements in slag, further describe the potential environmental impact laws of slag, and provide reference data for use in preventing pollution problems caused by slag accumulation and leaching. The surface microstructure and particle size distribution of slag with a particle size of 0.075–5.0 mm, the mineral composition of suspended pollutants larger than 0.45 μm, and the phenomenon of nano-scale ion release were the main research objects. The findings of this study can serve as an important reference for understanding the influence of slag leaching on water and soil pollution.

MATERIALS AND METHODS

Test Materials

The slag used in the test was taken from a ferrous slag yard (China Baowu Steel Group Co. Ltd., Qingshan District,

Wuhan, China). The samples did not show excessive aging or weathering. Slag was divided into three different particle sizes: 0.075–0.3, 0.3–1.6, and 1.6–5.0 mm. The main chemical compositions of slag are shown in Table 1, and the main mineral compositions of slag are shown in Table 2.

The soaking solution used in the test was prepared with HNO_3, NaOH, and demineralized water. The initial pH values of the solution were 3, 5, 7, 9, and 12.

Test Methods

Leaching tests: When the test temperature was controlled at $25 \pm 2°C$, every 100 g of ferrous slag with different particle sizes (D = 0.075-0.3, 0.3-1.6 and 1.6-5.0 mm) was submerged in 300 mL of solution with different pH values (pH 3, 5, 7, 9 and 12), and the leaching solution was taken out at increasing periods (T = 1, 3, 5, 10, 20 and 30 days). For the leaching solution, approximately 50 mL was placed into a centrifuge tube. Then centrifuge was rotated for 1 h (rotating speed: 3000 rpm, radius: 13.5 cm, centrifugal force: 1349 g) to obtain supernatant (Du et al. 2005). Finally, the pH value, metal ion concentration, and suspended solids (SS) quality of the leaching solution were tested. The PHS-3E pH Meter (Shanghai INESA Scientific Instrument Co., Ltd, China) has an accuracy of ± 0.01 units. The concentration of metal ions was determined with an AA320 atomic absorption spectrophotometer (Shanghai INESA Analytical Instruments Co., Ltd). Before the SS in the solution was recorded, it was dried to constant weight at 50°C.

X-ray diffraction (XRD) tests: After 30 days of leaching, for slag of 0.075-0.3 mm, three groups of slag samples (soaked in solutions with pH 3, 7, and 12) were ground through a No. 350 sieve, and the two groups of precipitates (pH 3 and 12) obtained by centrifugation in the leaching tests were filtered through a 0.45-μm membrane. The powdery slag and SS samples were air-dried to constant weight. Mineralogical analyses of the sample were conducted using an XRD analyzer (PANalytical B.V., The Netherlands).

Scanning electron microscopy (SEM) tests: After leaching solutions with different pH values for 30 days, three groups of 0.075–0.3mm blocky slag samples (soaked in solutions

Table 1: Main chemical composition of slag.

Main chemical compositions	SiO_2	Al_2O_3	CaO	Fe_3O_4	MgO	AlN	CdS
W_t / [%]	28.74	14.27	36.07	0.34	9.74	0.34	0.53

Table 2: Main mineral compositions of slag.

Main mineral compositions	Akermanite	Gehlenite	Yavapaiite	Gypsum
W_t / [%]	30.6	36.2	25.8	7.3

with pH 3, 7, and 12) were magnified and observed with an S-3000N SEM (Kabushiki Kaisha Hitachi Seisakusho, Japan).

Particle size distribution (PSD) analysis tests: To explore the change of particle size of slag in different acid and alkali solutions in the actual environment, the weight of slag in seven particle size ranges (>5, 1–5, 0.5–1, 0.25–0.5, 0.1–0.25, 0.075–0.1 and <0.075 mm) was tested before and after leaching. First, 500 g subsamples were taken from each of the nine groups of slag before soaking, and 5-mm and 1-mm sieves were used to screen out slag with a particle size larger than 1 mm for weighing. The slag particles with a diameter of less than 1 mm were then subjected to PSD analysis tests. The PSD was tested with Mastersizer 3000 laser diffraction particle size analyzer (Malvern Instruments Ltd., UK). Finally, the slag was submerged in the solution (pH 3, 7, and 12) for 30 days in a liquid-solid ratio of 3:1, and the PSD analysis method was applied again as described above. Every three groups of slag were soaked in a solution, and the weight of the three groups of slag was calculated and summed to obtain grading curves for the slag particles.

RESULTS AND DISCUSSION

Leaching of Slag

The slag leachate in this test contains a large amount of Ca, Mg, Fe, Cd, and trace heavy metals. The concentration of ions has far exceeded the threshold of China's national standard - "Identification standards for hazardous wastes – Identification for extraction toxicity" (GB 5085.3-2007). These ions enter the surrounding soil and groundwater, which will seriously damage the soil environment and lead to reduced water quality as a result of water hardening and water pollution (Xue et al. 2013).

The curves of Ca, Mg, Fe, Cd concentration, and pH value of the solution are shown in Fig. 1 and Fig. 2 (a). With the increase of dissolution time, the different acid-base solutions tend to become neutral. After 30 days of leaching, the pH values of solutions with initial pH 3 and 5 increased by 2.28-3.22 and 1.1-1.43, while those with initial pH 7, 9, and 12 decreased by 0.24-0.82, 0.82-1.24, and 1.21-2.25, thus the pH values of solutions with initial pH 3 and 12 changed the most. The release amount of the four cations gradually increased and the release rate decreased, but the release behavior results varied among the four cations.

The release amount of iron ions in ferrous slag was large, for example, slag with a particle size of 0.3-1.6 mm released up to 9.779 mg.L^{-1} of iron ions in the initial pH 3 solution. The particle size of slag had little influence on the dissolution behavior of Cd, but at pH 12, the release amount of Cd accounted for 3.02%-5.17% of the amount at pH 3. With the increase of the particle size range, the dissolved amount of Ca decreased by 39.09%-60.43%. The dissolved amount of Mg was strongly affected by the change of particle size, showing a trend of increasing first by 1.71%-49.77% and then decreasing by 0.95%–78.26%. Slag with the same particle size range was leached for 30 days, and the leaching amount of Ca and Mg at pH 12 accounted for 1.73%-9.55% and 0.08%-0.26% of that at pH 3, respectively. The characteristics of ion leaching in slag show that the dissolution process of Ca, Mg, and Cd in the alkaline solution was very slow, and the dissolution rate and amount were less than those in an acidic solution.
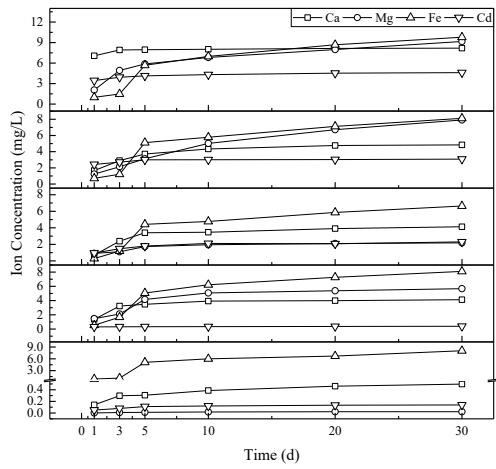
The variation curves of suspended solids' weight during the leaching of slag with different particle sizes are shown in

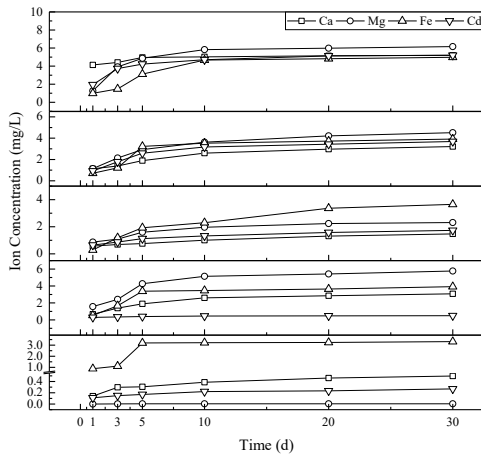Table 3: Mineral composition of slag and suspended solids.

| W_t / [%]	Phase	Slag				suspended solids (SS)	
		Before leaching	pH=3 T=30d	pH=7 T=30d	pH=12 T=30d	pH=3 T=30d	pH=12 T=30d
Akermanite		30.6	14.7	50.7	34.6	4.7	—
Gehlenite		36.2	17.6	42.2	29.8	6.8	—
Yavapaiite		25.8	—	—	—	—	—
Gypsum		7.3	—	2.5	—	80.6	—
Rustumite		—	67.7	—	—	—	—
Hawleyite		—	—	0.4	0.2	—	—
Hydrotalcite		—	—	4.2	—	—	—
Calcite		—	—	—	35.4	5.7	76.9
Quartz		—	—	—	—	2.2	—
Portlandite		—	—	—	—	—	23.1
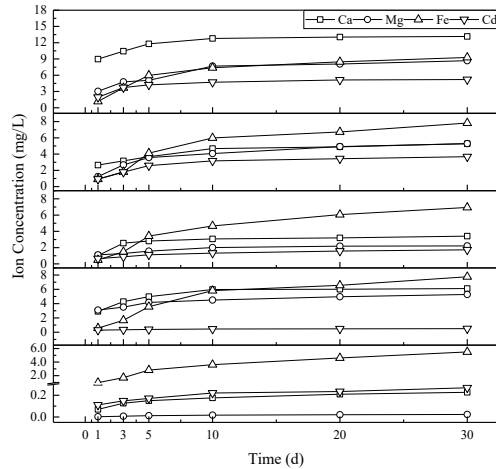
Fig. 1: Curves of Ca, Mg, Fe and Cd concentrations in the solution over
time: (a) D=0.075-0.3mm, (b) D=0.3-1.6mm,
(c) D=1.6-5.0mm.
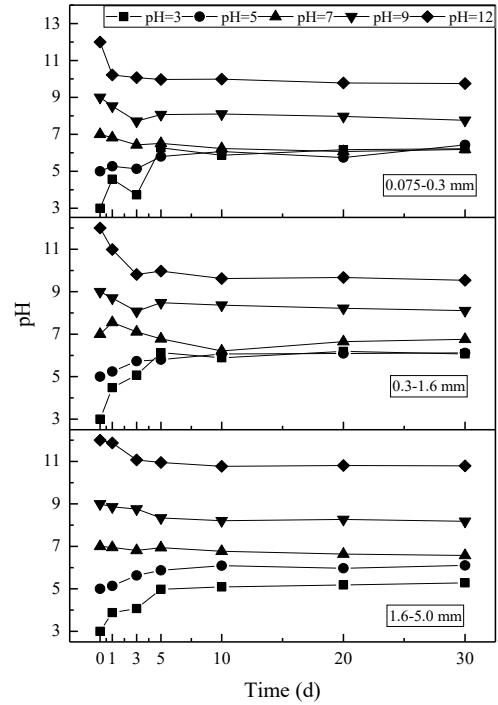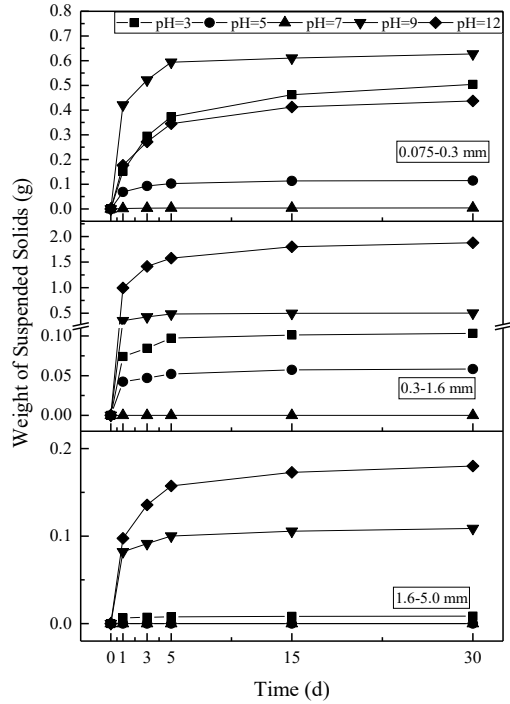
Fig. 2: Variation curves of solution pH value and suspended solids weight
during leaching of slag with different particle sizes:
(a) pH, (b) suspended solids weight.

Fig. 2(b). At pH 3, 5, 7 and 9, the weight of SS decreased in the following order: $W_{0.075-0.3\ mm} > W_{0.3-1.6\ mm} > W_{1.6-5.0\ mm}$. This shows that the particle size was negatively correlated with the total mass of SS in the solution. However, at pH 12, the weight of SS decreased in the following order: $W_{0.3-1.6\ mm} > W_{0.075-0.3\ mm} > W_{1.6-5.0\ mm}$. This indicates that when the particle size was between 0.3 and 1.6 mm, the quantity of SS leached from slag was greatly affected by the pH, not the particle size. Considering that the testing effect of 1.6–5.0 mm slag was unclear, the 0.075–0.3 mm slag was selected for XRD and SEM tests.

There are two possible explanations for these findings. On the one hand, under acidic conditions, all calcium compounds were separated and decalcified, resulting in structural changes in which the surface of slag formed a porous gel-like cover. The acid reacted with the slag, and the products were soluble calcium salt and poorly cohesive silica-rich gel (Bernal et al. 2012). The calcium salt and gel left the surface of slag to become SS, and various metal ions were also released into the solution. On the other hand, in the alkaline activation process of slag, a hydrated calcium silicate of the C-S-H gel-type was formed as the main reaction product, which has a low C/S ratio (Puertas et al. 2000). Many metal ions reacted with anions in the solution to generate precipitates that are in SS form in the solution.

Mineral Composition

According to XRD test results in Figs. 3, 4, and Table 3, after leaching in the solution with pH 3 for 30 days, the weight (W_t) of akermanite $(Ca_2MgSi_2O_7)$ in slag decreased by 15.9% and increased by 20.1% and 4.0% at pH 7 and 12. The weight of gehlenite $(Ca_2Al_2SiO_7)$ decreased by 18.6% and 6.4% at pH 3 and 12 and increased by 6.0% at pH 7. The XRD results showed that nitric acid at pH 3 expedited the corrosion of akermanite and gehlenite in slag, which led to the increase of
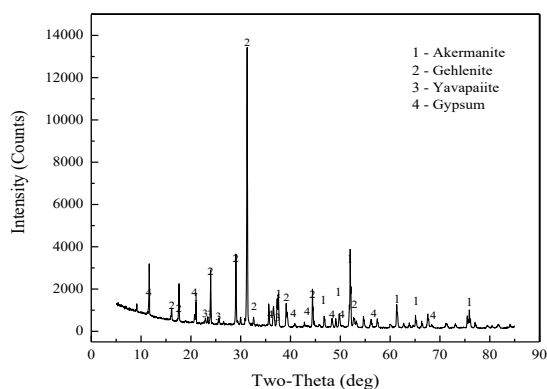
Ca ion and Mg ion concentrations in the solution. Rustumite $[Ca_{10}(SiO_4)(Si_2O_7)_2(OH)_2]$ was produced by the reaction of Ca ions with silicate in slag, and the weight of rustumite in the slag was 67.7%. Ca ions reacted with sulfate in solution to form gypsum $(CaSO_4.2H_2O)$, with a weight of 80.6 %.

At pH 12, the weight of akermanite in slag increased, whereas that of gehlenite decreased, indicating that Ca ions were alkaline solutions, and calcium silicate hydrate (C-S-H) and calcium-sodium aluminosilicate hydrate [C-(N)-A-S-H] gels are also formed on the surface of slag (Myers et al. 2013). In the current study, hawleyite (CdS) reacted more obviously when released from slag as a whole, but almost no Mg ions were released into an alkaline solution. Calcite $(CaCO_3)$ and portlandite $[Ca(OH)_2]$ suspensions are more easily formed in the acidic solution at pH 3 than in an alkaline environment, releasing a small amount of H_2S gas and Cd ions. Yavapiaite $[KFe(SO_4)_2]$ was soluble in water and released Fe ions in solutions with different pH values.
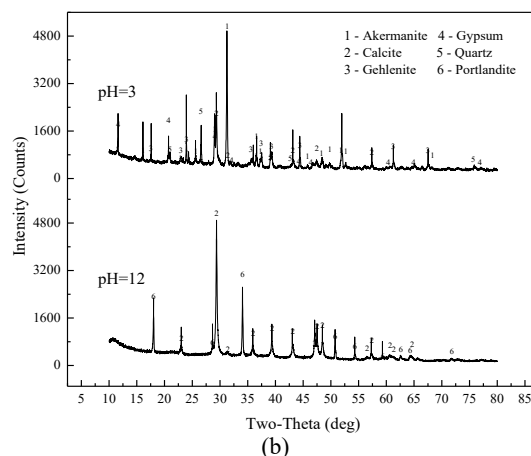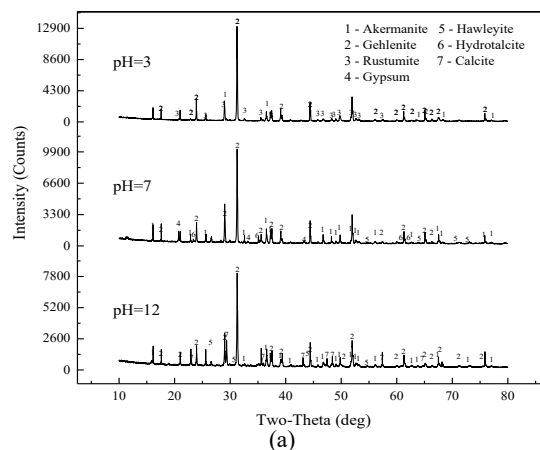

Fig. 4: XRD curves of slag and suspended solids after leaching in different pH solutions for 30 days: (a) slag, (b) suspended solids.

Fig. 3: XRD curve of slag before leaching.

Surface Microstructure

The surface microstructure of slag during leaching with an acid-base solution is shown in Fig. 5. The slag surface before soaking is smooth and complete, with few pores and a relatively dense microstructure. After soaking in different pH solutions for 30 days, the slag surface was eroded and destroyed. The cracks, dispersed fine particles and pores between fine particles increased substantially.

The SEM figures clearly show that the microstructure of the slag surface changed considerably after soaking in solutions with different pH values. For 0.075-0.3mm blocky slag samples, the HNO_3 solution was more destructive than the demineralized water and alkali solution. The slag was corroded most seriously at pH 3 and there were apparent damage cracks and various irregular pores on the surface. The cracks were 589-651 μm long and 70-79 μm wide, which was probably due to the formation of soluble calcium salts in the nitric acid solution by akermanite and gehlenite. At pH 7, dispersed particles and apparent irregular pores could be seen on the slag surface. At pH 12, the surface cracks of slag were not prominent compared with those at pH 3. Moreover, the interface damage was less and there were no obvious wide cracks. Compared with pH 7, although there were irregular pores on the surface of slag, after soaking in alkali solution, the unconsolidated tiny particles on the surface of slag were less attached, but more irregular materials such as flakes and spheres had agglomerated. The XRD test results indicate that this phenomenon was caused by the formation of C-S-H and C-(N)-A-S-H gels from the alkali-activated slag.

PSD of Slag

The curve and the discrimination index of particle size gradation after leaching in different pH solutions for 30 days are shown in Figs 6 and 7. The particle size of slag was mainly concentrated in the range of 0.1-0.5 mm, and the contents before and after leaching were 52.80%-55.87% and 55.00%-58.27%, respectively. The weight of slag larger than 0.1 mm after soaking was reduced by 5.03%-37.35%, whereas the slag smaller than 0.5 mm was increased by 3.67%-30.20%. D_{10}, D_{30}, and D_{60} (particle size less than 10%, 30%, and 60% of the total mass in the slag grading curve) all showed a decreasing trend, among which D_{10} changed most substantially. This indicates that the smaller the particle size, the larger the specific surface area, and the more serious the erosion by a chemical solution. At pH 3 and 12, D_{10} decreased by 21.33% and 14.93%, respectively. Together with the results of the leaching and XRD tests, this indicates that these decreases occurred as the result of slag being eroded and releasing ions in the solution at pH 12, and gels were then formed in the alkaline environment.
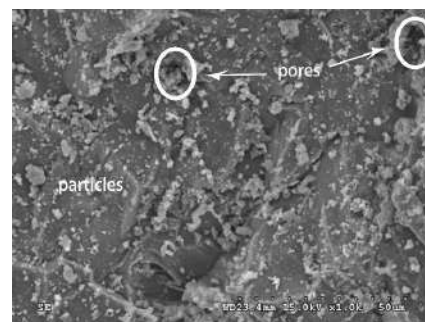
According to ASTM D 2487 (2017), before and after leaching, 88.07%-90.07% and 86.33%-87.07% of slag were
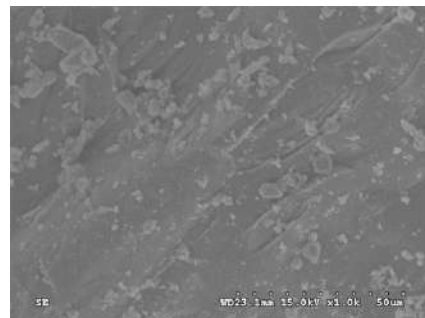
(a)
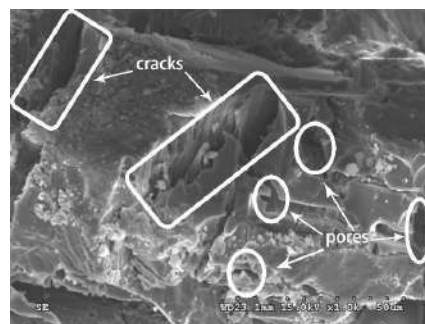
(b)

(c)

(d)

Fig. 5: Surface microstructure of slag: (a) Before leaching, (b) pH=3, T=30d, (c) pH=7, T=30d, (d) pH=12, T=30d

retained on the 0.075-mm sieve, and 93.47%–94.47% and 95.73%–96.53% passed through the 5-mm sieve. In the leaching process of different pH solutions, the coefficient of curvature (C_c) increased from 0.716–0.788 to 0.819–0.877 but remained below 1. This indicates that the slag with different particle sizes decreased after leaching, but the continuity was always poor. The coefficient of nonuniformity (C_u) increased from 4.560–4.925 to 5.034–5.527. This shows that the slag before soaking was uniform, the gradation is poor, and the particle size of slag after leaching is gradually uneven. In short, according to the changes of C_c and C_u, the conditions $C_u < 6$ and $C_c < 1$ were always true, indicating that the slag before and after leaching is poorly graded slag.

CONCLUSION

A series of experiments were carried out on the influence of different factors on slag leaching, such as slag particle size range, pH value of the solution, and soaking time. This paper mainly studied the change of slag particle size at the millimeter level (0.075-5.0 mm), the leaching of suspended solids at the micron level (larger than 0.45 μm) and the metal ions release behavior at the nanometer level. The following conclusions were drawn:

1. With the increase of dissolution time, the pH of slag leachate tended to be neutral. After 30 days of leaching, the pH values of solutions with initial pH 3 and 5 increased by 2.28–3.22 and 1.1–1.43, while those with initial pH 7, 9, and 12 decreased by 0.24–0.82, 0.82–1.24, and 1.21–2.25. Therefore, the pH values of solutions with initial pH 3 and 12 changed most substantially. The dissolution process of Ca, Mg, and Cd in alkaline solution was very slow, and the dissolution rate and amount were lower than those in acidic solution. At pH 12, the dissolved amount of Ca and Mg accounted for 1.73–9.55% and 0.08–0.26% of that at pH 3, respectively.
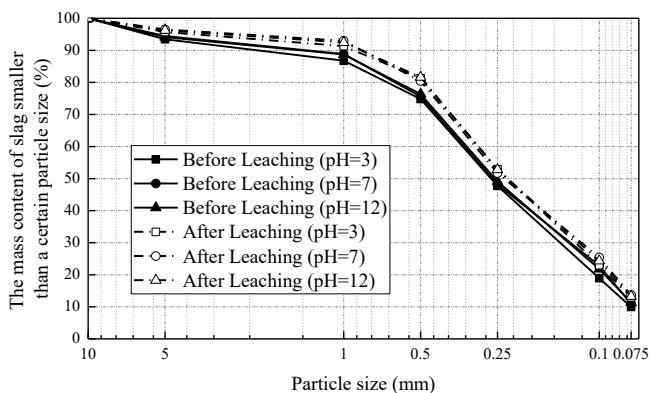
2. Nitric acid at pH 3 expedited the corrosion of akermanite and gehlenite in slag, which led to the increase of Ca and Mg ion concentrations in the solution, and Ca ion reacted with soluble salt to form a rustumite and gypsum suspension. Hawleyite released a small amount of H_2S gas and Cd ions in an acidic solution. At pH 12, the concentration of Ca ions in the solution formed calcite and portlandite suspended solids, whereas there were too few Mg ions to form precipitates.

3. After soaking in solutions with different pH values for 30 days, the slag surface was eroded and destroyed, cracks dispersed fine particles, and pores between fine particles increased substantially. Slag corrosion was most serious at pH 3 and there were clear cracks on the surface, which were 589–651 μm long and 70-79 μm wide. At pH 12, there were no large cracks on the slag surface, but there were more irregular substances such as flakes and spheres.

4. Before and after slag leaching, the particle size was mainly concentrated in the range of 0.1-0.5 mm. The weight of slag larger than 0.1 mm after soaking was reduced by 5.03%-37.35%, whereas the slag smaller than 0.5 mm was increased by 3.67-30.20%. The C_c increased from 0.716-0.788 to 0.819-0.877, and the C_u increased from 4.560-4.925 to 5.034-5.527, but the conditions $C_u < 6$ and $C_c < 1$ were always true, indicating that the slag had always been in a poor grading state.

ACKNOWLEDGMENTS

Fig. 6: Grading curve of slag particle after leaching in different pH solutions for 30 days.
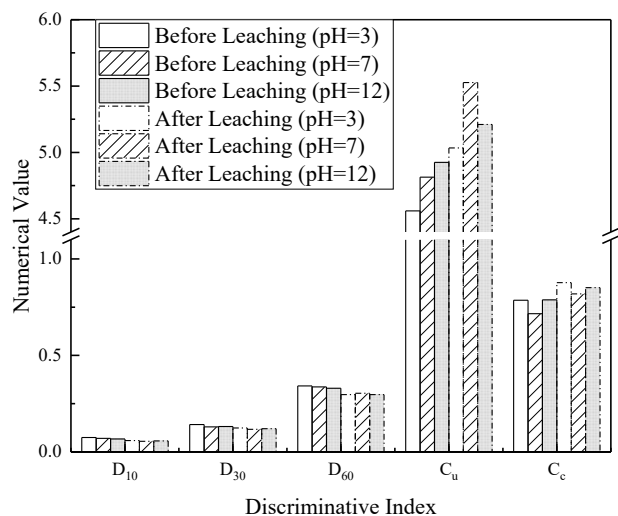

Fig. 7: Discrimination index of particle size gradation after leaching in different pH solutions for 30 days.

and Agglomeration of Metallurgic Mineral Resources (2019zy005)".

REFERENCES

Álvarez-Valero, A.M., Pérez-López, R., Matos, J., Capitán, M.A., Nieto, J.M., Sáez, R., Delgado, J. and Caraballo M. 2007. Potential environmental impact at São Domingos mining district (Iberian Pyrite Belt, SW Iberian Peninsula): Evidence from a chemical and mineralogical characterization. Environ. Geol., 55(8): 1797-1809.

ASTM D 2487. 2017. Standard classification of soils for engineering purposes (Unified Soil Classification System). ASTM, West Conshohocken, Pa.

Barna, R., Moszkowicz, P. and Gervais, C. 2004. Leaching assessment of road materials containing primary lead and zinc slags. Waste Manag., 24(9): 945-955.

Bernal, S.A., Rodríguez, E.D., Mejía de Gutiérrez, R. and Provis, J.L. 2012. Performance of alkali-activated slag mortars exposed to acids. J. Sustain. Cement-Based Mater., 1(3): 138-151.

Bayless, E.R., Greeman, T.K. and Harvey, C.C . 1998. Hydrology and geochemistry of a slag-affected aquifer and chemical characteristics of slag-affected groundwater, Northwestern Indiana and Northeastern Illinois: U.S. Geol. Survey Water-Resour. Invest. Rep., 97(4198): 67.

Bosso, S.T. and Enzweiler, J . 2007. Bioaccessible lead in soils, slag, and mine wastes from an abandoned mining district in Brazil. Environ. Geochem. Health, 30(3): 219-229.

Chaurand, P., Rose, J., Briois, V., Olivi, L., Hazemann, J.L., Proux, O., Domas, J. and Bottero, J.Y. 2007. Environmental impacts of steel slag reused in road construction: a crystallographic and molecular (XANES) approach. J. Hazard. Mater., 139(3): 537-542.

Chaurand, P., Rose, J., Domas, J. and Bottero, J.Y. 2006. Speciation of Cr and V within BOF steel slag reused in road constructions. J. Geochem. Explor., 88(1-3): 10-14.

De Angelis, G. and Medici, F. 2012. Reuse of slags containing lead and zinc as aggregate in a portland cement matrix. J. Solid Waste Technol. Manag., 38(2): 117-123.

De Windt, L., Chaurand, P. and Rose, J. 2011. Kinetics of steel slag leaching: batch tests and modeling. Waste Manag., 31(2): 225-235.

Du, Y.J., Hayashi, S. and Liu, S.Y. 2005. Experimental study of migration of potassium ion through a two-layer soil system. Environ. Geol., 48(8): 1096-1106.

Escalante-García, J.I., Fuentes, A.F., Gorokhovsky, A., Fraire-Luna, P.E. and Mendoza-Suarez, G. 2003. Hydration products and reactivity of blast-furnace slag activated by various alkalis. J. Am. Ceramic Soc., 86(12): 2148-2153.

Ettler, V., Johan, Z., Kříbek, B., Šebek, O. and Mihaljevič, M. 2009. Mineralogy and environmental stability of slags from the Tsumeb smelter, Namibia. Appl. Geochem., 24(1): 1-15.

Ettler, V., Johan, Z., Vítková, M., Skála, R., Kotrlý, M., Habler, G. and Klementová, M. 2012. Reliability of chemical microanalyses for solid waste materials. J. Hazard. Mater., 221: 298-302.

Fällman, A.M. and Hartlén, J. 1994. Leaching of slags and ashes - controlling factors in field experiments versus in laboratory tests: Environmental

aspects of construction with waste materials. Proceeding of the International Conference on Environmental Implications of Construction Materials and Technology Developments,1-3 June 1994, Maastricht, The Netherlands, Elsevier, Netherlands, pp. 39-54.

Hong, S.Y. and Glasser, F.P. 2002. Alkali sorption by C-S-H and C-A-S-H gels. Cement Concr. Res., 32(7): 1101-1111.

Myers, R.J., Bernal, S.A., San Nicolas, R. and Provis, J.L. 2013. Generalized structural description of calcium–sodium aluminosilicate hydrate gels: the cross-linked substituted tobermorite model. Langmuir, 29(17): 5294-5306.

Nikolić, I., Drinčić, A., Djurović, D., Karanović, L., Radmilović, V.V. and Radmilović, V.R. 2016. Kinetics of electric arc furnace slag leaching in alkaline solutions. Constr. Build. Mater., 108: 1-9.

Ning, P., Lin, X., Wang, X. and Cao, H. 2016. High-efficient extraction of vanadium and its application in the utilization of the chromium-bearing vanadium slag. Chem. Eng. J., 301: 132-138.

Piatak, N.M., Parsons, M.B. and Seal, R.R. 2015. Characteristics and environmental aspects of slag: a review. Appl. Geochem., 57: 236-266.

Piatak. N.M. and Seal, R.R. 2012. Mineralogy and environmental geochemistry of historical iron slag, Hopewell Furnace National Historic Site, Pennsylvania, USA. Appl. Geochem., 27(3): 623-643.

Puertas, F., Martínez-Ramírez, S., Alonso, S. and Vázquez, T. 2000. Alkali-activated fly ash/slag cements. Cement and Concrete Research 30(10): 1625-1632.

Roadcap, G.S., Kelly, W.R. and Bethke, C.M. 2005. Geochemistry of extremely alkaline (pH > 12) groundwater in slag-fill aquifers. Ground Water, 43(6): 806-816.

Skibsted, J. and Andersen, M.D. 2012. The effect of alkali ions on the incorporation of aluminum in the calcium silicate hydrate (C-S-H) phase resulting from portland cement hydration was studied by 29Si MAS NMR. J. Am. Ceramic Soc., 96(2): 651-656.

Sloto, R.A. and Reif, A.G. 2011. Distribution of Trace Metals at Hopewell Furnace National Historic Site, Berks, and Chester Counties. Report 2011-5014, U.S. Geological Survey Scientific Investigations, Pennsylvania, p. 90.

USEPA. 2009a. National Drinking Water Regulations. Office of Water, Office of Research and Development, Washington, DC.

USEPA. 2009b. National Recommended Water Quality Criteria. Office of Water, Office of Research and Development, Washington, DC.

Vítková, M., Ettler, V., Mihaljevič, M. and Šebek, O. 2011. Effect of sample preparation on contaminant leaching from copper smelting slag. Journal of Hazardous Materials 197: 417-423.

Wendling, L.A., Binet, M.T., Yuan, Z., Gissi, F., Koppel, D.J. and Adams, M.S. 2013. Geochemical and ecotoxicological assessment of iron- and steel-making slags for potential use in environmental applications. Environ. Toxicol. Chem., 32(11): 2602-2610.

Wendling, L.A., Douglas, G.B. and Coleman, S. 2012. Productive use of steelmaking by-product in environmental applications – II: Leachate geochemistry, ecotoxicity, and environmental radioactivity. Minerals Eng., 39: 219-227.

Xue, Q., Lu, H., Zhao, Y. and Liu, L. 2013. The metal ions release and microstructure of coal gangue corroded by an acid-based chemical solution. Environ. Earth Sci., 71(7): 3235-3244.

Abrasion and Accretion Analysis in Demak, Indonesia Coastal for Mitigation and Environmental Adaptation

A. Irsadi†, N. K. T. Martuti, M. Abdullah and L. N. Hadiyanti

Department of Biology, Mathematics and Natural Sciences Faculty, Universitas Negeri Semarang, Indonesia

†Corresponding author: A. Irsadi, andin.sha@mail.unnes.ac.id

ABSTRACT

The purpose of this study was to analyze abrasion at the border of Sayung, Demak, Indonesia. Coastal abrasion data were obtained from high-resolution images from 2005-to 2017 by using ArcGIS 10.3, while data on environmental factors that affected abrasion, including tides from 2013-to 2017, was obtained from *BMKG*. Based on the analysis and calculations, the area of abrasion at the coast of Sayung, Demak was 262.74 hectares spread over four villages, namely Sri Wulan, Bedono, Timbulsloko, and Surodadi. Avifauna in the mangroves will be severely harmed by abrasion. As a result, abrasion prevention and evaluation, as well as the factors that cause abrasion, are required to reduce the impact of abrasion on the specified shore.

INTRODUCTION

Natural processes such as erosion and natural disasters place a high priority on sustainable management in coastal areas (Ghosh et al. 2015). However, as a result of global climate change, the threat to coastal areas has increased. The incidence of large waves and rising sea levels can pose a concern. Because the shore is directly near to the ocean, this circumstance will result in environmental issues such as flooding and abrasion along the coast.

Coastal abrasion is the erosion of coastal areas due to waves that continue to hit the coast. This abrasion will usually befall the coastal area due to the absence of a protective beach (Irsadi et al. 2019a). This will cause floods in the coastal areas and erosion. Coastal abrasion can generally be caused by two things, first naturally and second by human activities (Akbar et al. 2017).

Coastal abrasion occurs everywhere. In the UK, around 17% of the coastline changes were estimated by coastal erosion, while in Ireland, shoreline changes are estimated at 20% due to coastal erosion (Masselink & Russel 2013). Coastal abrasion also occurred on the northern coast of Central Java, Indonesia. Abrasion was felt throughout the coast of Central Java, Indonesia, including near the boundary of Semarang and Demak, among other places (Irsadi et al. 2019b). For example, abrasion caused coastal damage

in Tugu Subdistrict, Semarang, Indonesia (Prihatanto et al. 2013), while abrasion occurred in Sayung District, Demak Regency, Indonesia (Prihatanto et al. 2013, Marfai 2012). With flooding and coastal erosion in the Sayung area, Demak urges around 221 houses in Bedono village (one of the villages in Sayung Sub-district, Demak) to move to other areas (Asiyah et al. 2015). This condition was triggered by high waves from the ocean. Abrasion might disrupt the coastal ecosystem. One of the ecosystems on the beach is the mangrove. Disruption to the mangrove ecosystem will ultimately disrupt the organism that depends on mangroves. Avifauna uses mangroves to live and get food, therefore the abrasion that occurs on the coast of Sayung, Demak, Indonesia, will affect the avifauna's livelihood.

As a result, it is required to carry out abrasion mitigation and adaptation activities. Mitigation efforts are linked to environmental consequences and determine the trigger, allowing adaptation efforts to be determined, which can be done through the community's active participation. It is possible to adapt to abrasion so that detrimental effects are reduced both now and in the future.

This paper aimed to analyze the impacts of abrasion at the border of Sayung, Demak, Indonesia beaches, and the initiative and active participation of the community to overcome abrasion.

MATERIALS AND METHODS

Abrasion Data Collection

Quickbird high-resolution pictures from 2005 to 2017 were used to collect abrasion data. Between 2005 and 2017, considerable abrasion and accretion were recorded in Sayung District, Demak, Indonesia. ArcGIS 10.3 was used to perform extensive abrasion and accretion calculations. Computers running ArcGIS 10.3 software were used to determine the degree of abrasion and accretion. Materials used to determine the degree of abrasion and accretion in Sayung Subdistrict, Demak, Indonesia included an Indonesian Earth map, time-series image data from 2005 to 2017 on the shore of Sayung, Demak, Indonesia, and Landsat pictures from 2005 to 2017.

Fauna Data Collection

The fauna observed in this study was birds. Bird observation was carried out directly in the study area by exploration. Observation of birds was done by using binoculars. The bird species observed were identified by the MacKinnon Field Guidebook (1998). The bird observation technique was carried out by making a list of bird species observed throughout the study location during the observation time. Recorded bird species should not be recorded twice in one list (MacKinnon et al. 1994). Identification of bird species was made in two ways: first identification directly in the field based on its morphological form (Howes et al. 2003), including (i) body shape and size, beak, and leg, (ii) color of feathers, and feet, (iii) distinctive features, and (iv) sound produced. The second identification was done in a laboratory-based on field documentation results in the form of photographs. Observations were conducted from June 2018 to March 2019.

Analysis of Abrasion And Accretion Data

The first phase involved gathering satellite image data in Sayung Subdistrict, Demak, in 2005, 2010, and 2017 in four villages/districts damaged by abrasion: Sri Wulan, Bedono, Timbulsloko, and Surodadi. The information extraction stage was followed by a radiometric correction. The radiometric adjustment was used to reorder the reflected values recorded by sensors that approach or have a pattern that fits the recording wavelength, such as the reflection of an object. The third step used Landsat geometric adjustment, which resulted in consistent coordinates and scale, as well as the image's north-south direction matching that of the map, allowing it to be positioned between the two (Parman 2010, Arief et al. 2011). Digital digitization was the fourth stage. The fifth stage involved analysis and calculation, which involved combining the digitization findings to determine the area affected by abrasion or accretion.

RESULTS

According to satellite imagery, the coastal area of Sayung, Demak, Indonesia, is an open area, making it a connecting connection between land and sea, making it easier for fishermen to reach the sea. On the other side, open regions render Sayung, Demak, Indonesia's coastline areas vulnerable to abrasion from big waves.

Abrasion in Sayung, Demak, Indonesia areas occurred in Sri Wulan, Bedono, Timbulsloko, and Surodadi. The results of digitizing ArcGIS on the area of abrasion and accretion that occurred in Sayung, Demak, Indonesia Districts are shown in Table 1.

Birds Found in Sayung Coastline

We discovered 61 bird species based on identification, as shown in Fig. 1 and reported in Table 2. The Environment and Forestry Ministerial Decree (Permen LHK) No. 20 the Year 2018 protects eighteen species recognized.

DISCUSSION

Based on Table 1, It can be seen that the abrasion that occurred in Sayung Subdistrict, Demak, Indonesia was so vast. In contrast, the accretion that occurred was not proportional to the abrasion process. Field data show that from June 2018 to March 2019 in the Sisenik area (Bedono, Sayung, Demak), there has been 3-5 meters of abrasion. This causes a reduction in land directly adjacent to the ocean. The abrasion was caused, among other things, by the presence of ocean waves, which have been more common in recent years (Irsadi et al. 2019a, 2019b). Furthermore, the temperature of the environment has risen (Fig. 3 and 4).

Fig. 3 shows that the wave height in the Demak area at each stage tends to increase. This makes alertness and efforts to deal with abrasion in the Sayung, Demak area. It should also be noted that the trend of increasing temperatures in the Sayung, Demak, Indonesia regions.

The average temperature in the Demak area has increased between particular months, as seen in Fig. 4. The fact that the state of abrasion, wave height, and temperature have all

Table 1: Area of abrasion and accretion in Sayung, Demak in 2005-2017.

No.	Site	Abrasion is [ha]	Accretion area [ha]
1	Sriwulan	14.58	-
2	Bedono	109.91	4.75
3	Timbulsloko	96.76	-
4	Surodadi	41.49	1.12
	Total area	262.74	5.87

Table 2: Birds in Semarang-Demak coastline and its conservation status.

| No. | Local name | Species | Location | | | Conservation status |
			TS	B	IUCN	Permen LHK No. P.20/2018
1	Pecuk-ular asia	*Anhinga melanogaster*	v	v	NT	Protected
2	Pecuk padi hitam	*Phalacrocorax sulcirostris*	v		LC	Not Protected
3	Cikalang Christmas	Fregata andrewsi	v		CR	Protected
4	Cangak abu	*Ardea cinerea*	v	v	LC	Not Protected
5	Cangak merah	*Ardea purpurea*	v	v	LC	Not Protected
6	Cangak besar	*Ardea alba*	v	v	LC	Protected
7	Kuntul kerbau	*Bubulcus ibis*		v	LC	Not Protected
8	Kuntul karang	*Egretta sacra*		v	LC	Not Protected
9	Kuntul cina	*Egretta eulophotes*		v	VU	Protected
10	Kuntul perak	*Ardea intermedia*	v	v	LC	Not Protected
11	Kuntul kecil	*Egretta garzetta*	v	v	LC	Not Protected
12	Kokokan laut	*Butorides striata*	v	v	LC	Not Protected
13	Blekok sawah	*Ardeola speciosa*	v	v	LC	Not Protected
14	Kowak-malam abu	*Nycticorax nycticorax*	v	v	LC	Not Protected
15	Bangau bluwok	*Mycteria cinerea*	v	v	EN	Protected
16	Ibis rokoroko	*Plegadis falcinellus*		v	LC	Protected
17	Elang bondol	*Haliastur indus*	v	v	LC	Protected
18	Sikep-madu Asia	*Pernis ptilorhynchus*	v		LC	Protected
19	Kareo padi	*Amaurornis phoenicurus*			LC	Not Protected
20	Cerek kernyut	*Pluvialis fulva*	v		LC	Not Protected
21	Cerek besar	*Pluvialis squatarola*	v		LC	Not Protected
22	Cerek Melayu	*Charadrius peronii*	v		NT	Not Protected
23	Cerek tilil	*Charadrius alexandrinus*	v		LC	Protected
24	Cerek Jawa	*Charadrius javanicus*	v		NT	Protected
25	Cerek-pasir Mongolia	*Charadrius mongolus*	v		LC	Not Protected
26	Gajahan penggala	*Numenius arquata*	v		NT	Protected
27	Trinil pantai	*Actitis hypoleucos*	v	v	LC	Not Protected
28	Trinil kaki-hijau	*Tringa nebularia*	v		LC	Not Protected
29	Trinil bedaran	*Xenus cinereus*	v		LC	Not Protected
30	Terik asia	*Glareola maldivarum*	v	v	LC	Protected
31	Dara-laut sayap putih	*Chlidonias leucopterus*	v		LC	Protected
32	Dara-laut biasa	*Sterna hirundo*	v	v	LC	Protected
33	Dara-laut jambul	*Sterna bergii*	v		LC	Protected
34	Dederuk Jawa	*Streptopelia biorquata*	v	v	LC	Not Protected
35	Tekukur biasa	*Streptopelia chinensis*	v	v	LC	Not Protected
36	Perkutut Jawa	*Geopelia striata*	v		LC	Not Protected

Table cont...

No.	Local name	Species	Location			Conservation status
			TS	B	IUCN	Permen LHK No. P.20/2018
37	Wiwik Lurik	*Cacomantis sonneratii*	v	v	LC	Not Protected
38	Wiwik uncuing	*Cacomantis sepulcralis*	v	v	LC	Not Protected
39	Bubut jawa	*Centropus nigrorufus*	v		VU	Protected
40	Cabak kota	*Caprimulgus affinis*	v	v	LC	Not Protected
41	Walet linchi	*Collocalia linchi*	v	v	LC	Not Protected
42	Kapinis rumah	*Apus affinis*	v		LC	Not Protected
43	Raja-udang biru	*Alcedo coerulescens*	v	v	LC	Not Protected
44	Cekakak australia	*Todiramphus sanctus*	v	v	LC	Not Protected
45	Cekakak sungai	*Todiramphus chloris*	v	v	LC	Not Protected
46	Kirik-kirik laut	*Merops philippinus*	v	v	LC	Not Protected
47	Caladi ulam	*Dendrocopos macei*	v		LC	Not Protected
48	Layang-layang batu	*Hirundo tahitica*	v	v	LC	Not Protected
49	Cucak kutilang	*Pycnonotus aurigaster*	v	v	LC	Not Protected
50	Remetuk laut	*Gerygone sulphurea*	v	v	LC	Not Protected
51	Cici padi	*Cisticola juncidis*		v	LC	Not Protected
52	Perenjak padi	*Prinia inornata*		v	LC	Not Protected
53	Kipasan belang	*Riphidura javanica*	v	v	LC	Protected
54	Kekep babi	*Artamus leucorynchus*	v	v	LC	Not Protected
55	Burung-madu sriganti	*Nectarinia jugularis*	v	v	LC	Not Protected
56	Cabai Jawa	*Dicaeum trochileum*			LC	Not Protected
57	Kacamata Jawa	*Zosterops flavus*	v		VU	Protected
58	Bondol Jawa	*Lonchura leucogastroides*	v	v	LC	Not Protected
59	Bondol Peking	*Lonchura punctulata*	v	v	LC	Not Protected
60	Bondol Haji	*Lonchura maja*	v	v	LC	Not Protected
61	Burung-gereja Erasia	*Passer montanus*	v	v	LC	Not Protected

increased implies that there is a link between the variables. High waves would be triggered by an increase in ambient temperature on the continent and the ocean. The increasing waves may cause abrasion along the coastline of Sayung, Demak, Indonesia. In the Sayung and Demak, Indonesia regions, significant rainfall influences temperatures in addition to waves and abrasion.

Abrasion occurred and the mentioned environmental aspects also determine the soil structure. Soil conditions in the form of mud and sand will be more prone to erosion than rocky areas (Masselink & Russel 2013). Based on an analysis of the soil's texture on the coast of Sayung, Demak, Indonesia, it is known that the composition of the soil consists of sand between 1-43%, dust between 8-85%, and clay between

2-86%. The composition of the land on the coast of Sayung, Demak, Indonesia in the form of sand, dust, and clay also makes it a factor that makes the area susceptible to abrasion.

The continuous abrasion will break the coast of Sayung, Demak, Indonesia since the ocean strongly influences the coastal ecosystem. As part of it, Mangroves will be damaged and crashed due to abrasion, as shown in Fig. 5 (Gilman et al. 2006).

Fig. 5 shows visible damage on the coast of Sayung, Demak due to wave stroke. This episode is one of the factors contributing to the destruction of mangroves in Sayung, Demak, Indonesia. Damage to mangroves disrupts mangrove inhabitants, such as birds that live in or forage in mangrove forests. Birds are disturbed by a variety of natural activities
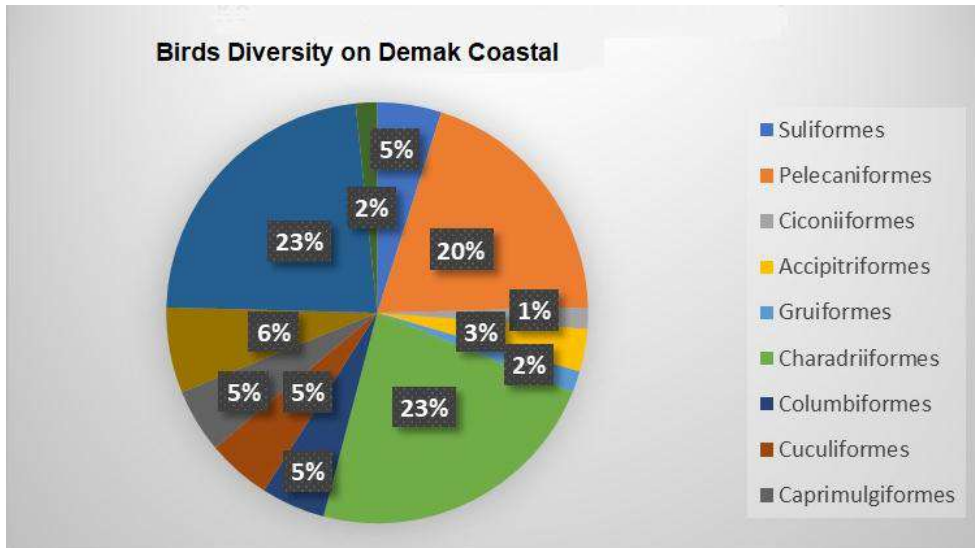
Fig. 1: Birds diversity at Demak coastal based on its ordo.

Fig. 2: Protected birds species at Demak coastal.

carried out by humans, including the sound of motorboats, kayaking, and even observation activities (Mayo et al. 2015).

According to Table 2, the study location has two types of bird species: unprotected bird species and protected bird groups. Both of these groupings can be found in the Bedono and Timbulsloko Villages' mangrove ecosystems. It demonstrates that the two research sites are appropriate habitats for

these creatures. The two research locations are compatible in terms of foraging for fruit or other creatures such as invertebrates, as well as providing a home for these bird species. If one area changes (as an example of continued abrasion, without improvement) so that mangrove forests are collapsed or damaged, then the species of birds found in the two study sites are mainly protected species (*Anhinga melanogaster,*
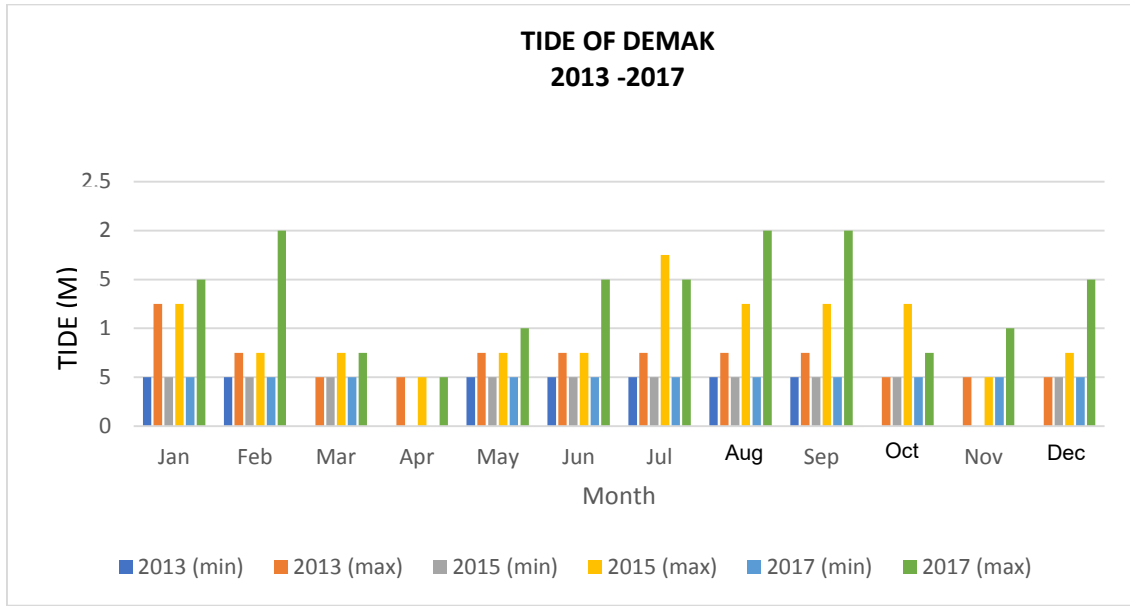
Fig. 3: The tide in Semarang and Demak in 2013-2017.

Ardea alba, Haliastur indus, Glareola maldivarum, Sterna hirundo, and *Riphidura javanica*) will experience disruption. Still, because the birds are in two research locations, it is possible to migrate from one place to another because the two research sites have mangrove species that are not much different (Elfidasari & Junardi 2006, Suripto & Hamidy 2006). However, if the protected species is only found in one of the research locations (*Fregata andrewsi, Egretta eulophotes, Plegadis falcinellus, Ptilorhynchus varnish, Charadrius alexandrinus, Charadrius javanicus, Chlidonias*

leucopterus, Sterna bergii, Centropus nigrorufus, Zosterops flavus), there will be interference in the group this second bird so that further research is needed regarding the suitability of the area to support this type of life.

Mangroves have other land recovery functions in addition to being a life-sustaining avifauna (Muharam 2014). Furthermore, the presence of mangroves can reduce the impact of disasters on the shore (Karminarsih 2007), as well as prevent erosion and seawater infiltration (Salim et al. 2016). As a result, abrasion must be avoided by constructing coastal
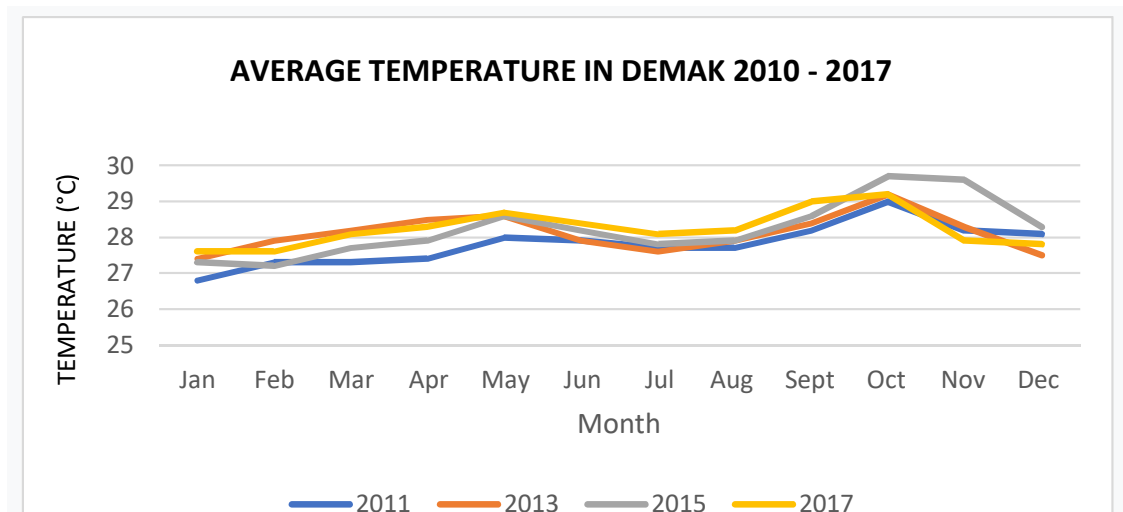
Fig. 4: The average temperature in Demak 2010-2017.

Fig. 5: Mangrove damage in Sayung coastline, Demak, due to tide.

protective equipment such as breakers or planting coastal protective plants.

Abrasion mitigation has been actively carried out by people in abrasion-prone areas and government or private organizations that offer abrasion avoidance incentives. Planting mangroves on the shore of Sayung, Demak, Indonesia, is one example of active community participation in mitigation in Sayung Subdistrict, Demak. With evidence of increased mangrove acreage, active community participation in planting mangroves demonstrates success (Chafid et al. 2012, Irsadi et al. 2019b).

According to the residents of Sayung, Demak, Indonesia, mangrove planting provides immediate benefits in the form of young Avicennia leaves that can be converted into chips and the fruit can be eaten, as well as indirect benefits such as protection from strong winds and high waves. Mangroves can operate as natural coastal boundary defenders against erosion and tsunamis (Alongi 2008, Blankespoor et al. 2016). Demak, Indonesia, can profit as a tourism destination in addition to being a coast defender by planting mangroves in the Sayung area. Due to abrasion, tourism has risen in the Sayung, Demak, Indonesia area as a means of adapting to the community. The tourism industry has grown in Sayung and Demak. For example, Sayung, Demak, in the Bedono area, mixes catastrophe tourism, religious tourism, and conservation.

Disaster tourism due to abrasion is one of the tours in Bedono Village (areas affected by abrasion so that the area is flooded with seawater and cannot be re-occupied). This tour is the location of introspection for residents who always try to protect the coastal areas from the dangers of abrasion and flooding (Fig. 6).

Religious tourism may be found in Kyai Mudzakir's tomb, one of the tombs in Bedono Village located in the middle of the sea. This trip is one of the community's local pearls of wisdom that has developed. The presence of the tomb protects this tourist destination from abrasion by forming waves breakers and tomb defenders. This protects the area surrounding the tomb from abrasion. Conservation tourism is a type of tourism that recognizes the significance of coastline preservation. This movement was carried out and traveled with observations of the different sorts of birds that could be seen along the shore of Sayung, Demak, as well as the planting of mangroves in the impacted areas.

In addition to integrated tourism activities, institutional strengthening is also carried out to protect existing mangroves. The form of protection carried out is in the form of village rules (PERDES) issued by the Bedono and Timbulsloko Village Heads with the main goal of protecting mangroves. In addition to protecting mangroves, this village regulation also regulates mangrove management and the community's financial protection. This regulation protects

Fig. 6: Abandoned mosque submerged by flood.

the environment and makes the community more empowered (Purnaweni et al. 2018). In addition, this regulation contains the form of sanctions applied to people who commit violations in the form of illegal logging or environmental destruction with the sanction of logging one mangrove tree, which should be replaced by 300 mangrove trees or a fine of 500 thousand-1 million rupiahs, besides sanctions for fishers who use poisons or explosives. The bird shooters also will be fined and seized their tools.

However, because not all villages impacted by abrasion can adapt well, the implementation of mitigation and adaptation (Fig. 7) must be monitored and evaluated on an ongoing basis. As a result, continued efforts at sustainable development as mitigation and adaptation to
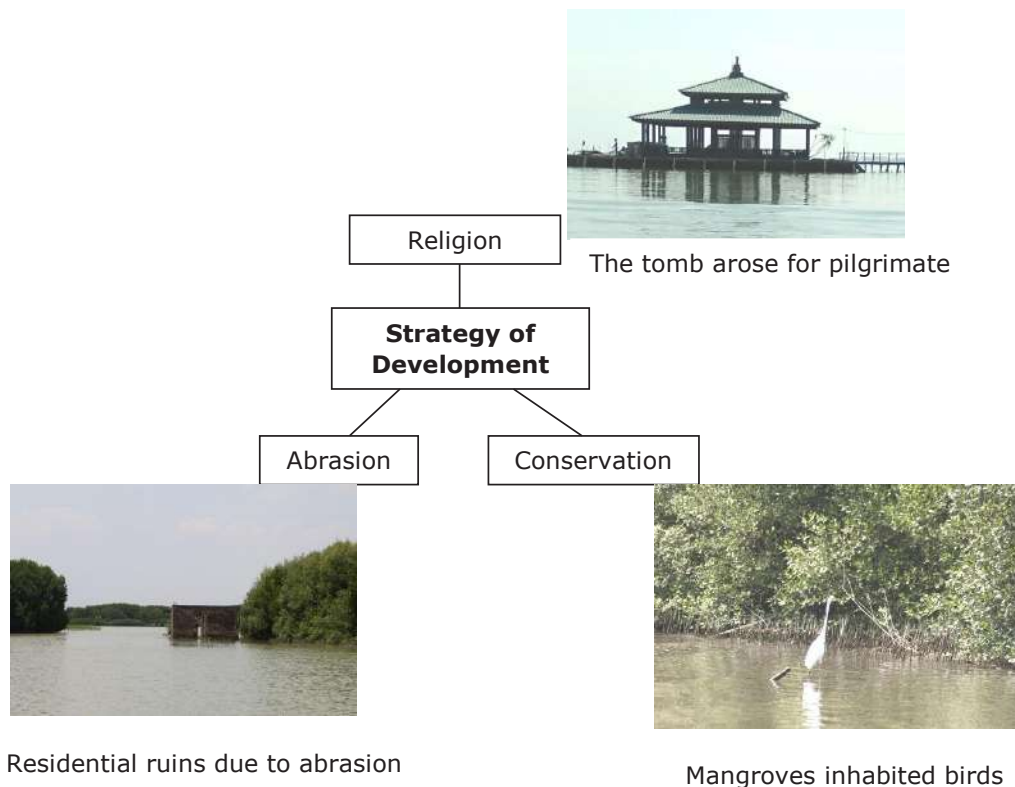
Fig. 7: Developmental scheme of mitigation and adaptation.

abrasion are required to ensure that the coastal regions of Sayung, Demak, Indonesia do not become more lost due to abrasion.

CONCLUSION

There has been a beach abrasion on the coast of Sayung, Demak, covering 262.74 hectares and an accretion of 5.87 hectares spread across four villages, namely Sri Wulan and Bedono Timbulsloko, and Surodadi. Prevention and evaluation are needed to be related to abrasion and the factors triggered so that abrasion on the coast of Sayung, Demak can be shrunk.

ACKNOWLEDGMENTS

REFERENCES

Akbar, A.A, Sartohadi, J., Djohan, T.S. and Ritohardoyo, S. 2017. Coastal erosion, mangrove ecosystems, and community adaptation to coastal damage disasters in tropical countries. J. Environ. Sci., 15(1): 1-10.

Alongi, D.M. 2008. Mangrove forest: Resilience, protection from tsunamis and response to global climate change. Estuar. Coast. Shelf Sci., 76(1): 1-13.

Arief, M., Winarso, G. and Prayogo, T. 2011. Study of shoreline changes using Landsat satellite data in Kendal Regency. Remote Sens. J., 8(2011): 71-80.

Asiyah, S., Rindarjono, M.G. and Muryani, C. 2015. Analysis of settlement changes and characteristics of slum settlements due to abrasion and inundation on the coast of Sayung sub-district, Demak district in 2003–2013. J. GeoEco., 1(1): 83–100.

Blankespoor, B., Dasgupta, S. and Lange, G.M., 2016. Mangroves as Protection from Storm Surges in a Changing Climate. Policy Research Working Paper 7596, World Bank, Washington DC.

Chafid, M.A., Pribadi, R. and Suryo, A.A.D. 2012. Study of changes in mangrove land area in Bedono Village, Sayung District, Demak Regency using ICONOS satellite imagery in 2004 and 2009. J. Marine Res., 1(2): 167-173.

Elfidasari, D. and Junardi. 2006. Waterbirds diversity in Peniti mangrove forest, Pontianak Regency. Biodiversitas, 7 (1): 63-66.

Ghosh, M.K., Kumar, L. and Roy, C. 2015. Monitoring the coastline change of Hatiya Island in Bangladesh using remote sensing techniques: ISPRS J. Photogramm. Remote Sens., 101(2015): 137–144.

Gilman, E.L., Ellison, J., Jungblut, V., Lavieren, H.V., Wilson, L., Areki, F., Brighouse, G., Bungitak, J., Dus, E., Henry, M., Kilman, M., Matthews, E., Lerupaala Sauni, J., Teariki-Ruatu, N., Tukia, S. and Yuknavage, K.

2006. Adapting to Pacific island mangrove responses to sea-level rise and climate change. Climate Res., 32(2006): 161–176.

Howes, J., Bakewell, D. and Rusila-Noor, Y. 2003. Coastbird Study Guide. Wetlands International-Indonesia Programme, Bogor.

Irsadi, A., Anggoro, S. and Soeprobowati, T.R. 2019a. Abrasion on the Coast of Bedono Village, Sayung, Demak: Drawing a Red Thread on the Impact of Climate Change. Focus Group Discussion Improving Community Initiatives in Climate Change, Ministry of Environment and Forestry, Indonesia.

Irsadi, A., Anggoro, S., Soeprobowati, T.R., Helmi, M. and Khair, A.S.E. 2019b. Shoreline and mangrove analysis along Semarang-Demak, Indonesia for sustainable environmental management. JPII, 8(1): 1-11.

Karminarsih, E. 2007. Utilization of mangrove ecosystems for minimizing disaster impacts in coastal areas. JMHT, 13(3): 182-187.

MacKinnon, J., Phillips, K. and van Ballen, B. 1988. Field Guide to the Birds of Java and Bali. Gadjah Mada University Press, Yogyakarta

MacKinnon, J., Phillips, K. and van Ballen, B. 1994Birds of Sumatra, Java, Bali and Kalimantan (Including Sabah, Sarawak and Brunei Darussalam) (LIPI-Field Guide Series). Puslitbang Biologi-LIPI, Bogor.

Mayo, T.W., Paton, P.W.C. and August, P.V. 2015. Responses of birds to humans at a coastal barrier beach: Napatree Point, Rhode Island. Northeastern Natural., 22(3):501–512.

Marfai, M.A. 2012. Preliminary assessment of coastal erosion and local community adaptation in sayung coastal area, Central Java–Indonesia. Quaest. Geogr., 31(3): 47-55.

Masselink, G. and Russell, P. 2013. Impacts of climate change on coastal erosion. MCCIP Sci. Rev., 2013(1): 71-86.

Muharam, M. 2014. Mangrove Planting as One of the Land and Environmental Rehabilitation Efforts in the North Coastal Area of Karawang Regency. Sci. J. Solut., 1(1): 1-14.

Parman, S. 2010. Detection of shoreline changes through remote sensing imagery on the north coast of Semarang, Demak. J. Geogr., 7 (1):1-10.

Prihatanto, A., Giyarsih, S.R. and Suharyadi, R. 2013. Identification of Disaster Conditions in the Coastal Area of Tugu District, Semarang City. Proceedings of the National Seminar on Geospatial Information Utilization for Optimizing Regional Autonomy, Bojonegro, East Java, 20 June 2013, UMS Scientific Publication, Java, pp. 22-26.

Purnaweni, H., Kismartini, Sudharto, P. and Hadi, S.I. 2018. Coastal Community Group for Coastal Resilient in Timbulsloko Village, Sayung, Demak Regency, Indonesia. In: E3S Web of Conferences 31, 09009. Proceeding of the International Conference on Energy, Environment, Epidemiology and Information System, Semarang, Indonesia, August 15-16, 2017, ICENIS, Indonesia, pp. 1-4.

Republik Indonesia. 2018. Regulation of the Minister of Environment and Forestry of the Republic of Indonesia No. 20 of 2018 concerning Protected Types of Plants and Animals. Director-General of Legislation, Ministry of Law and Human Rights of the Republic of Indonesia.

Salim, A.G., Siringoringo, H.H. and Narendra, B.H. 2016. The effect of mangrove cover on shoreline changes and seawater intrusion downstream in the Ciasem and Cipunegara watersheds, Subang district. J. Hum. Environ., 23(3): 319-326.

Suripto, B.A. and Hamidy, A. 2006. Birds in Nusakambangan island, cilacap, Central Java: Diversity, adaptation, and important species for conservation. J. Hum. Environ., 13(1): 9-25.

Toxicity and Challenges of Nanomaterials and Their Impact on the Environment

Sakshi Awasthi and Jai Gopal Sharma†

Department of Biotechnology, Delhi Technological University, Delhi, India
†Corresponding author: Jai Gopal Sharma, Sharmajaigopal@dce.ac.in

ABSTRACT

Nanomaterials (NMs) are those tiny materials that range from 1-100 nm. These materials show different characteristics in their physical and chemical forms in comparison to their bulk form. The use of nanomaterials is increasing day by day because of their enormous capabilities in the health sector as well as in other industries. There are currently few, if any, actual protocols for the disposal and characterization of these nanomaterials, which results in environmental toxicity. Heavy use of chemicals in the testing of nanomaterials has resulted in polluting our entire ecosystem. Inconsistent results of nanomaterial show that it is challenging to reduce the toxicity generated by it. In this review, we discuss the administration and use of nanomaterials in the agribusiness sector, in food, and, most importantly, in the environment, for purposes of protecting our plants and crops, dealing with incurable diseases, developing new tastes and textures in the food sector, sensations, identifying pathogenic organisms, and distribution systems where these minute particles can wreak havoc. Despite the potential benefits of nanomaterials, their unintentional harm to the environment and, in some cases, our health is making further development difficult. This article discusses the toxicity of nanomaterials and how they damage our environment, as well as the obstacles that come with overcoming them.

INTRODUCTION

Nanotechnology is an amalgamation of nano-sized (very minute size 1-100 nm) structured materials, analytical tools at the nanoscale, and nano-devices, into biological sciences for the development of new biomaterials and toolkits as well as for understanding life science. It's designed to help minimize man's impact on the environment by incorporating more sensible, effective, and low-cost modifications (Pathakoti et al. 2018). Despite ongoing progress in nanotechnology and nanomaterial discovery, understanding and knowledge on the possible effects of nanomaterials on health and the environment are still inadequate (Hutchison 2016). As nanomaterial is not easy to be analyzed after release into the environment, they can result in numerous types of atmospheric problems unless a proper curative plan is not executed. Engineered nanomaterials are generally manufactured with specific sizes and for specific purposes (Iavicoli et al. 2014). They are designed as their characteristic properties like physical and chemical attributes are different compared to their bulk conventional parts. Various types of nanomaterials find application in providing significant benefits to the environment. Furthermore, most nanomaterials have been discovered to have potential hazardous impacts on the environment, the most prevalent of which being nano plastics, which heavily pollute the ecosystem (Rai et al. 2020).

Plastic plays an important part in our general life. Plastic is known as polythene in the common language. Because of its lower cost and affordability, it is one of the most usable products in the modern era (Awoyera & Adesina 2020). However, it contributes to a large amount of pollution because of its non-degradable nature (Da Costa et al. 2016). It is further divided into subcategories like low-density polyethylene (LDPE) and high-density polyethylene (HDPE). Microplastics, which turn into nanoparticles of plastic over a long period of natural disintegration, are common contaminants that threaten our ecosystem and humans (Baztan et al. 2018). Microplastics are major prey for animals because they assume microplastics are their source of food, such as marine food, salt, and bottled water, as well as inhalation from the air and other surroundings.

Nano plastic has a unique property that depicts a high surface-to-volume ratio, which affects its degradation process. A high surface-to-volume ratio is a defining feature of nanotechnology (Bhushan 2017). This characteristic makes nanoparticles or plastic more harmful to the environment. Proper assessment should be done on nanomaterials that generate enough harm during the manufacturing process (Lee et al. 2013). Green nanotechnology is now seen to have the potential to reduce adverse environmental impact as well as harm to human health. Nano plastic agglomerates with chemicals and heavy metals via weaker links such as wander

walls bonds, according to research (Herbort et al. 2018). As a result, when nanoparticles of plastic are moved from one compartment of the environment to another, harmful chemicals are released, making it impossible for marine species to survive (Del Saz-Salazar et al. 2009).

TOXICOLOGY OF NANOMATERIALS

The branch of science that deals with the adverse effect of physical, chemical, and biological materials on living cells or living organisms, is called toxicology (Liu & Yu 2011). Nanotoxicology is a rapidly developing field in today's era (Khan & Shanker 2015). Despite the fact that nanoparticles (NPs) are always present in nature, major advances in their field of research have been made in bioremediation (Cecchin et al. 2017), paints (Goesmann & Feldmann 2010), coatings (Fierascu et al. 2019), electronics (Cardoso et al. 2018), fuel catalysts, water treatment (Kumar et al. 2014), and almost everywhere in human society (López-Serrano et al. 2014). Nanomaterials drugs offer a great advantage over general pharmaceutical formulations because of their clump-free, stable, and water-soluble properties (Malekhosseini et al. 2019). Especially nano plastics can cause more harm to biota than other micro and macro plastic because of their small size (Strungaru et al. 2019). It is a fact that plastic particles in the nano range are able to penetrate cell membranes (Bouwmeester et al. 2015). Aromatic hydrocarbons, polychlorinated biphenyls, and other additives exacerbate the impact of these chemicals on living beings. Nanoplastics can operate as pathogenic vectors for chemical and biological

pollutants, causing poisoning in animals and humans (Jiang et al. 2020). Nanoparticle exposure in the environment and surroundings is shown in Fig1.

There are different ways by which microplastic and nano plastics enter our ecosystem. The direct way in which contamination is caused is through the application of plastic mulch in agricultural soils greenhouse buildings matter, raw material, and soil condition improver (Steinmetz et al. 2016). Because of their minute size, many nano plastics are retained in wastewater treatment reactors after being processed in a wastewater treatment facility, and the remainder ends up in generated sludge (Egirani et al. 2020).

Parameters that can affect the toxicity of nanoparticles: Various factors decide the fate of nanoparticles in the environment (Sajid et al. 2015). The morphology of the engineered nanoparticle is affected by the synthesis methods used and the changes in the synthesis procedure (Patra & Baek 2014). The composition of nano-sized particles stems from physical, chemical, mechanical, and biological processes. The physical process comprises the synthesis of the nanoparticles by different techniques like lithographic, ball milling, etching, and sputtering techniques, which focus on the breakdown of larger molecules into a material of suitable functional and morphological characteristics. The buildup of nanoparticles from non-complex molecular structures is done by the chemical process. These methods comprise deposition by chemical vaporization, condensation of atomic and molecular structures, spray with laser heating at controlled temperature conditions, and aerosol formation. There is a limited scien-
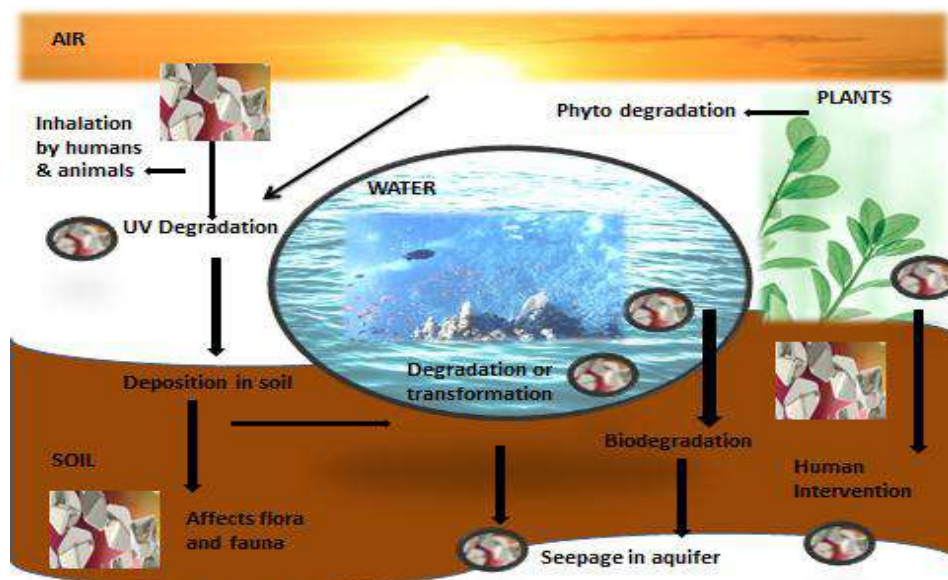

Fig. 1: Exposure of nanoparticles on animal health and environment.

tific understanding of reaction mechanisms and modeling characteristics associated with this factor mentioned below.

1. Size
2. Composition
3. Solubility and crystalline structure
4. Charge with surface characteristics
5. Attached functional groups
6. Agglomeration with impurities and porosity can potentially affect the total removal yield of the nanomaterial from the environmental contaminants (Das et al. 2018).

SOURCES OF NANOMATERIALS

Nanomaterials present in our environment come either from natural processes like volcanic explosions, forest fires, erosion of different soils, clay minerals, and dust storms (Bakshi et al. 2015) or from different anthropogenic activities including fossil fuel burning, mining, automobile traffic, and nanomaterial production, and wastewater release from industries (Kabir et al. 2018). Hydrophobicity, chemical, and physical resistance are the reasons, nanoparticle transports from one place to the other (Kettler et al. 2014). Our clothing, which is made of polyester, nylon, and acrylic fibers, is washed and laundered in wastewater treatment plants (Tiwari et al. 2020). Nanoparticles remain in the environment even after multiple treatments due to their small size and higher resistance power (Zhang 2015). Cosmetic products such as shampoos, soaps, and scrubs release high concentrations of nanoparticles because of the microbeads used and their fragmentation (Lehner et al. 2019). Even plastic tea bags which we use on daily basis in large amounts could release billions of nanoparticles (Auclair et al. 2020). Sources and applications of nanoparticles are compiled below in (Table 1).

Table 1: Sources of nanoparticles in the environment.

S. No.	Types	Applications	References
1	Natural	Volcanic eruption Forest fire Dust storm Soil erosion	(Strambeanu et al. 2015)
2	Intentional or engineered	Drug delivery Engineered nanomaterial Groundwater remediation Biomedical engineering Biosensors	(Sun et al. 2014)
3	Unintentional or incidental	Welding Vehicle exhaust Industrial processes Fuel burning Mining	(Hochella et al. 2019)

NANOMATERIALS OF DIFFERENT SUBSTANCES AND THEIR TOXICITY

Various types of nanomaterials are being used in everyday life including zinc oxide nanoparticles (ZnONPs), silica nanoparticles (SiO$_2$NPs), titanium dioxide nanoparticles (TiO$_2$NPs), silver nanoparticles (Ag-NPs), gold NPs (AuNPs), and polymeric nanoparticles (PNPs) (Sajid et al. 2015). Generally, these nanoparticles are for the drug delivery system in various parts of the body (Bharti et al. 2015). All interactions with harmful toxicological effects are caused by changes in the physicochemical and systemic properties of man-made nanoparticles (Gatoo et al. 2014).

ZnO nanoparticles (ZnO NP): Various types of cosmetics as sunscreens, food supplements like additives and color, pigments, and biosensors contain zinc oxide nanoparticles (ZnONPs) (Mirzaei & Darroudi 2017). The toxic effect of ZnO is seen in animal models and humans (Valdiglesias et al. 2013). Cytotoxicity and genotoxicity of ZnONPs have been studied in vitro as well as in vivo (Ng et al. 2017). Depending on the duration or dose, these ZnONPs have lower cell viability. Studies have found dose-dependent hepatotoxicity as well as an increase in oxidative stress because of increased levels of malondialdehyde (MDA) and decreased enzyme activity in the liver (Zhang 2015).

TiO$_2$ nanoparticles(TiO$_2$ NPs): TiO$_2$ is commonly used in beauty and skincare items as a pigment, a binder, and a UV absorber (Torbati & Javanbakht 2020). TiO$_2$ allows artificial medical implants and bone. Some scientists found the toxicity of TiO$_2$ nanoparticles through skin penetration in mice and skin of porcine post chronic exposure (Adachi et al. 2010). Other studies have observed in vitro cytotoxicity and genotoxicity of TiO$_2$NPs in different cell lines, in plants, and model organisms such as mice and zebra fishes (Bennett et al. 2012).

Silica nanoparticles(SiO$_2$ NPs): For a long time, the indefinite form of silica has been used as a food ingredient (Peters et al. 2012). The main purpose of SiO$_2$ nanoparticles in the food industry is to overcome flow or caking in powdered products. SiO$_2$ also have been used as a carrier of flavors as well as a thickener in paste-like substances (Guo et al. 2018). It is sometimes used to clear different beverages and lessen foaming. Various studies have reported the toxicity of SiO$_2$ nanoparticles as food additives on human gastrointestinal cells, thus enforcing their safety as food additives (Go et al. 2017). Scientists have also demonstrated that oral and intravenous administration of SiO$_2$ nanoparticles has a negative impact on biodistribution, excretion, and toxicity (Khlebtsov & Dykman 2011).

Silver nanoparticles (Ag-NPs): Silver is well known for its antibacterial potential. Researchers found that silver has been used as a healing agent for a long time (Peng et al. 2012). To increase and use its potential, a silver particle (Ag) is used as a nanoparticle. Ag nanoparticles have been found to exhibit antiviral and antibacterial activities. Another application of silver-containing resin is to fill cavities and cover dental teeth, as well as in medical applications. In mice, researchers confirmed that ammonia and PVPs (polyvidone stabilized Ag nanoparticles) are non-cytotoxic at lower quantities (Saqib & Rahim 2016). Some researchers observed adverse effects of AgNPs on human cells and demonstrated that their cytotoxic and genotoxic effects act as a useful tool to control desirable angiogenesis which means the formation of new blood cells in an uncontrollable way (Gupta & Xie 2018).

Gold nanoparticles (Au-NPs): Gold nanoparticles are used to cap bio-functional moieties that have considerable biological activity, such as peptides and carbohydrates, to control and monitor various cell processes (Zhang et al. 2020). The application of AuNPs is also found in diagnosis due to their light returning ability and surface. Due to their significant potential in therapeutic and diagnostic purposes, AuNPs find great application in understanding toxic effects (Khan et al. 2014). Scientists studied the toxicity of AuNPs on immune dendrites that were obtained from mice bone marrow cells (Zhang et al. 2019).

TYPES OF NANOMATERIALS AND THEIR IMPACT ON THE ENVIRONMENT

Different categories of nanomaterials, classification and their structure are given in Table 2.

Nanomaterials then further classified according to their dimensions are -

- Zero-dimension (0D)
- One-dimension (1D)
- Two-dimensions (2D)
- Three-dimensions (3D).

Major counts of nano-particles are zero dimensions that include nanomaterial in the range of 1-100 nm. Unit dimension nanomaterials contain a thin needle or rod like-structure measure of 100 nm-10 μm and include nanotubes, nanorods, and nanowires (Ghassan et al. 2019). Two Dimensions nanomaterial comprises plate-like shapes including Nanocoatings, nanofilms, and nanolayers. 3D nanomaterials possess random dimensions and multilayer nano-crystalline structure (Yang et al. 2011). These nanomaterials usually include bulk powders, nanowire bundles, multi-nano layers, nanoparticles dispersions, and nanotubes (Saleem & Zaidi 2020).

ENVIRONMENTAL IMPACT OF NANOPARTICLES

Nanomaterial is generally released in the environment as waste from industries, directly into the land, water, air, soil through the remediation of contaminated fields. As technology advances, nanoparticles behave differently in different compartments of the environment.

Nanoparticle in the air: Nanoparticles present in the atmosphere can cover large distances from the point of their delivery or release, thus causing unmanageable exposure to humans as well as eco-toxicological effects on marine or terrestrial life (Ghadimi et al. 2020). The nanoparticles present in the terrestrial ecosystem spread rarely due to their immobile nature, yet they can travel into the human digestive system by gulping and swallowing or even contact with the skin (Berkowitz et al. 2014).

Nanoparticle in the soil: Nanoparticles can enter soils directly through pesticides and fertilizers, or indirectly through land and wastewater treatment materials such as sludges or biosolids (Courtois et al. 2020). Fertilizers are used to increase the productivity of the soil. Contrary outcomes of nanoparticles on biogeochemical cycles like in the nitrogen cycle have been found in some studies.

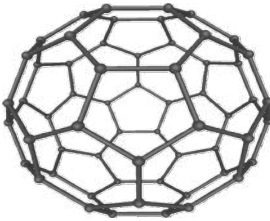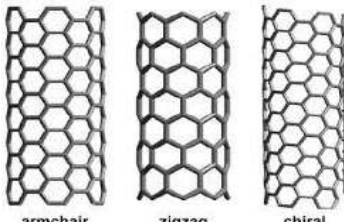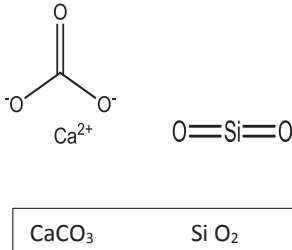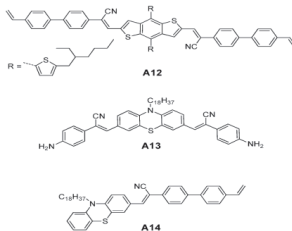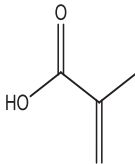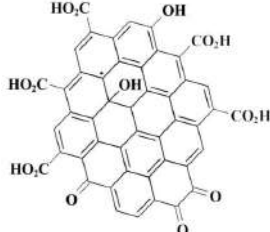## CHALLENGES ASSOCIATED WITH ENVIRONMENT TOXICOLOGY OF NANOMATERIAL

Analysis and assessments of different nanomaterials are limited due to a lack of knowledge and research in this field, as well as some inadequacies in regulating the spread of contamination by nanoparticles (Lai et al. 2018).

- Hazard and exposure evaluation- Hindrance in evaluating hazards posed by nanomaterials is a major issue due to the lack of standard protocols and methods to resolve them (Weinberg et al. 2011)
- Lack of informative data in the composition and profile of nanomaterials results in fewer testings and monitoring of facts for various NMs (Lead et al. 2018).
- Still, no methodology is available to recognize and identify the exposure of ENMs

CONCLUSION

Nanotechnology has gained significant importance in recent years owing to its widespread application and novelty. Although the majority of nanoparticles are utilized for a wide range of applications, their potential toxic hazards and consequences remain a major constraint to their advantage. The potential negative impacts of nanomaterials and nanoparticles in the environment have been studied by various researchers but major toxic effects of these NMs in the environment

Table 2: Types of nanomaterials.

Sr. No.	Type	Characteristics	Structure	References
1	Fullerenes	Interconnected carbon atoms Withstanding with extreme heat, still can regain its original shape. As hard or harder than diamond		(Castro et al. 2017)
2	Carbon-based	Single-walled or multiple walls 20 nm diameter E.g. Carbon nanotube		(Xin et al. 2019)
3	Inorganic	Pure metals or various inorganic products alloys Nanoscale distinguishes them from bulk material Display unique mechanical, electrical properties $CaCO_3$, SiO_2, AlOH, $SrCO_3$, TiO_2		(Wu 2017)
4	Organic	Contain both soluble and insoluble particles. Display catalytic properties not found in bulk material counterpart. Help drugs pass the blood-brain barrier.		(Lombardo et al. 2020)
5	Nanocapsules, nanoshells	Composed of insoluble organic polymers (methacrylic acid and PEG) Can bypass the digestive tract and act as pharmacologic vectors directly in the intestine.		(Bollhorst et al. 2017)
6	Quantum dots	Nanocrystals, artificial atom,1-10 nm in diameter Semiconductors, metal insulators, Magnetic matter or metallic oxides Fluorescent probe CdSe core with ZnS shell		(Yan et al. 2019)

along with adverse consequences on human health is a major cause of concern in coming years. Currently, current investigations using practical methodologies have proven the interactions of nanomaterials with various air surfaces, particularly plastics, restricting their bioavailability, reactivity, and toxicity, posing a risk to the environment. Despite increasing nanotechnology usage in industries, their ecological impacts are still in their infancy to combat them. The nature and composition of various nanomaterials used in fertilizers, and pesticides are often unclear, their utilization is widespread to cause contamination in soil and terrestrial habitat of plants as well.

Continued scientific input and knowledge are required to overcome the toxicological impacts of nanoparticles on the ecosystem and the environment. The long-term sustainability and prolonged exposure of nanoparticles in the environment require proper implementation and judicious regulations to combat toxic impacts. Assessment, risk, and evaluation of nanoparticles to understand potential toxicological impacts caused by them necessitated scientific understanding to learn their fate and action in the surrounding.

REFERENCES

Adachi, K., Yamada, N., Yamamoto, K., Yoshida, Y. and Yamamoto, O. 2010. In vivo effect of industrial titanium dioxide nanoparticles experimentally exposed to hairless rat skin. Nanotoxicology, 4: 296-306. https://doi.org/10.3109/17435391003793095

Auclair, J., Peyrot, C., Wilkinson, K.J. and Gagné, F. 2020. Biophysical effects of polystyrene nanoparticles on Elliptio complanata mussels. Environ. Sci. Pollut. Res., 27: 25093-25102. https://doi.org/10.1007/s11356-020-08920-z

Awoyera, P.O. and Adesina, A. 2020. Plastic wastes to construction products: Status, limitations, and future perspective. Case Stud. Constr. Mater., 12: e00330. https://doi.org/10.1016/j.cscm.2020.e00330

Bakshi, S., He, Z.L. and Harris, W.G. 2015. Natural nanoparticles: Implications for the environment and human health. Crit. Rev. Environ. Sci. Technol., 45: 861-904. https://doi.org/10.1080/10643389.2014.921975

Baztan, J., Bergmann, M., Carrasco, A., Fossi, M.C., Jorgensen, B., Miguelez, A., Pahl, S., Thompson, R.C. and Vanderlinden, J.P. 2018. MICRO 2018 Fate and Impact of Microplastics: Knowledge, Actions and Solutions. Lanzarote, MICRO, pp. 414.

Bennett, S.W., Zhou, D., Mielke, R. and Keller, A.A. 2012. Photoinduced disaggregation of TiO2 nanoparticles enables transdermal penetration. PLOS One, 7: e48719. https://doi.org/10.1371/journal.pone.0048719

Berkowitz, B., Dror, I. and Yaron, B. 2014. Inorganic and Organometallic Compounds. In Berkowitz, B., Dror, I. and Yaron, B. (eds.), Contaminant Geochemistry: Interactions and Transport in the Subsurface Environment. Springer, Berlin, Heidelberg, pp. 53-77. https://doi.org/10.1007/978-3-642-54777-5_3

Bharti, C., Nagaich, U., Pal, A.K. and Gulati, N. 2015. Mesoporous silica nanoparticles in target drug delivery system: A review. Int. J. Pharm. Investig., 5: 124-133. https://doi.org/10.4103/2230-973X.160844

Bhushan, B. 2017. Springer Handbook of Nanotechnology. Springer, New York.

Bollhorst, T., Rezwan, K. and Maas, M. 2017. Colloidal capsules: nano- and microcapsules with colloidal particle shells. Chem. Soc. Rev., 46: 2091-2126. https://doi.org/10.1039/C6CS00632A.

Bouwmeester, H., Hollman, P.C.H. and Peters, R.J.B. 2015. Potential health impact of environmentally released micro- and nano plastics in the human food production chain: Experiences from nanotoxicology. Environ. Sci. Technol., 49: 8932–8947. https://doi.org/10.1021/acs.est.5b01090

Cardoso, V.F., Francesko, A., Ribeiro, C., Bañobre-López, M., Martins, P. and Lanceros Mendez, S. 2018. Advances in magnetic nanoparticles for biomedical applications. Adv. Healthc. Mater., 7: 1700845. https://doi.org/10.1002/adhm.201700845

Castro, E., Garcia, A.H., Zavala, G. and Echegoyen, L. 2017. Fullerenes in biology and medicine. J. Mater. Chem. B, 5: 6523-6535. https://doi.org/10.1039/C7TB00855D

Cecchin, I., Reddy, K.R., Thomé, A., Tessaro, E.F. and Schnaid, F. 2017. Nanobioremediation: Integration of nanoparticles and bioremediation for sustainable remediation of chlorinated organic contaminants in soils. Int. Biodeterior. Biodegrad. Environ. Biotechnol. Sust. Develop., 119: 419-428. https://doi.org/10.1016/j.ibiod.2016.09.027

Courtois, P., Rorat, A., Lemiere, S., Guyoneaud, R., Attard, E., Longepierre, M., Rigal, F., Levard, C., Chaurand, P., Grosser, A., Grobelak, A., Kacprzak, M., Lors, C., Richaume, A. and Vandenbulcke, F. 2020. Medium-term effects of Ag supplied directly or via sewage sludge to an agricultural soil on Eisenia fetida earthworm and soil microbial communities. Chemosphere, 171: 128761. https://doi.org/10.1016/j.chemosphere.2020.128761

Da Costa, J.P., Santos, P.S.M., Duarte, A.C. and Rocha-Santos, T. 2016. (Nano)plastics in the environment: Sources, fates, and effects. Sci. Total Environ., 566: 15-26. https://doi.org/10.1016/j.scitotenv.2016.05.041

Das, S., Chakraborty, J., Chatterjee, S. and Kumar, H. 2018. Prospects of biosynthesized nanomaterials for the remediation of organic and inorganic environmental contaminants. Environ. Sci. Nanotechnol., 5: 2784-2808. https://doi.org/10.1039/C8EN00799C

Del Saz-Salazar, S., Hernández-Sancho, F. and Sala-Garrido, R. 2009. The social benefits of restoring water quality in the context of the water framework directive: A comparison of willingness to pay and willingness to accept. Sci. Total Environ., 407: 4574-4583. https://doi.org/10.1016/j.scitotenv.2009.05.010

Egirani, D., Shehata, N. and Khedr, M. 2020. A review of nanomaterials in agriculture and allied sectors: Preparation, characterization, applications, opportunities, and challenges. Materials, 2: 0421-0432. https://doi.org/10.33263/Materials23.421432

Fierascu, R.C., Ortan, A., Avramescu, S.M. and Fierascu, I. 2019. Phyto-nanocatalysts: Green synthesis, characterization, and applications. Molecules, 24: 3418. https://doi.org/10.3390/molecules24193418

Gatoo, M.A., Naseem, S., Arfat, M.Y., Mahmood Dar, A., Qasim, K. and Zubair, S. 2014. Physicochemical properties of nanomaterials: Implication in associated toxic manifestations [WWW Document]. BioMed Res. Int., 48: 842. https://doi.org/10.1155/2014/498420

Ghadimi, M., Zangenehtabar, S. and Homaeigohar, S. 2020. An overview of the water remediation potential of nanomaterials and their ecotoxicological impacts. Water, 12: 1150. https://doi.org/10.3390/w12041150

Ghassan, A.A., Mijan, N.A. and Taufiq-Yap, Y.H. 2019. Nanomaterials: An overview of nanorods synthesis and optimization. Nanorods nanocomposites. https://doi.org/10.5772/intechopen.84550

Go, M.R., Bae, S.H., Kim, H.J., Yu, J. and Choi, S.J. 2017. Interactions between food additive silica nanoparticles and food matrices. Front. Microbiol., 8: 101. https://doi.org/10.3389/fmicb.2017.01013

Goesmann, H. and Feldmann, C. 2010. Nanoparticulate functional materials. Angew. Chem. Int. Ed., 49: 1362-1395. https://doi.org/10.1002/anie.200903053

Guo, Z., Martucci, N.J., Liu, Y., Yoo, E., Tako, E. and Mahler, G.J. 2018. Silicon dioxide nanoparticle exposure affects small intestine function in an in vitro model. Nanotoxicology, 12: 485-508. https://doi.org/10.1080/17435390.2018.1463407.

Gupta, R. and Xie, H. 2018. Nanoparticles in daily life: Applications, toxicity, and regulations. J. Environ. Pathol. Toxicol. Oncol., 37: 615. https://doi.org/10.1615/JEnvironPatholToxicolOncol.2018026009.

Herbort, A.F., Sturm, M.T., Fiedler, S., Abkai, G. and Schuhen, K. 2018. Alkoxy-silyl induced agglomeration: A new approach for the sustainable removal of microplastic from aquatic systems. J. Polym. Environ., 26: 4258-4270. https://doi.org/10.1007/s10924-018-1287-3

Hochella, M.F., Mogk, D.W., Ranville, J., Allen, I.C., Luther, G.W., Marr, L.C., McGrail, B.P., Murayama, M., Qafoku, N.P., Rosso, K.M., Sahai, N., Schroeder, P.A., Vikesland, P., Westerhoff, P. and Yang, Y. 2019. Natural, incidental, and engineered nanomaterials and their impacts on the Earth system. Science, 363: 8299. https://doi.org/10.1126/science.aau8299

Hutchison, J.E. 2016. The road to sustainable nanotechnology: Challenges, progress, and opportunities. ACS Sustain. Chem. Eng., 4: 5907-5914. https://doi.org/10.1021/acssuschemeng.6b02121

Iavicoli, I., Leso, V., Ricciardi, W., Hodson, L.L. and Hoover, M.D. 2014. Opportunities and challenges of nanotechnology in the green economy. Environ. Health, 13: 78. https://doi.org/10.1186/1476-069X-13-78

Jiang, B., Kauffman, A.E., Li, L., McFee, W., Cai, B., Weinstein, J., Lead, J.R., Chatterjee, S., Scott, G.I. and Xiao, S. 2020. Health impacts of environmental contamination of micro- and nano plastics: a review. Environ. Health Prev. Med., 25: 29. https://doi.org/10.1186/s12199-020-00870-9

Kabir, E., Kumar, V., Kim, K.H., Yip, A.C.K. and Sohn, J.R. 2018. Environmental impacts of nanomaterials. J. Environ. Manag., 225: 261-271. https://doi.org/10.1016/j.jenvman.2018.07.087

Kettler, K., Veltman, K., Meent, D., Wezel, A. and Hendriks, A.J. 2014. Cellular uptake of nanoparticles as determined by particle properties, experimental conditions, and cell type. Environ. Toxicol. Chem., 33: 481-492. https://doi.org/10.1002/etc.2470

Khan, A.K., Rashid, R., Murtaza and G., Zahra, A. 2014. Gold nanoparticles: Synthesis and applications in drug delivery. Trop. J. Pharm. Res., 13: 1169-1177. https://doi.org/10.4314/tjpr.v13i7.23

Khan, H.A. and Shanker, R. 2015. Toxicity of nanomaterials. BioMed Res. Int., 2015: 521014

Khlebtsov, N. and Dykman, L. 2011. Biodistribution and toxicity of engineered gold nanoparticles: A review of in vitro and in vivo studies. Chem. Soc. Rev., 40: 1647-1671. https://doi.org/10.1039/C0CS00018C

Kumar, S., Ahlawat, W., Bhanjana, G., Heydarifard, S., Nazhad, M.M. and Dilbaghi, N. 2014. Nanotechnology-based water treatment strategies. J. Nanosci. Nanotechnol., 14: 1838-1858. https://doi.org/10.1166/jnn.2014.9050

Lai, R.W.S., Yeung, K.W.Y., Yung, M.M.N., Djuriši, A.B., Giesy, J.P. and Leung, K.M.Y. 2018. Regulation of engineered nanomaterials: Current challenges, insights and future directions. Environ. Sci. Pollut. Res., 25: 3060-3077. https://doi.org/10.1007/s11356-017-9489-0

Lead, J.R., Batley, G.E., Alvarez, P.J.J., Croteau, M.N., Handy, R.D., McLaughlin, M.J., Judy, J.D. and Schirmer, K. 2018. Nanomaterials in the environment: Behavior, fate, bioavailability, and effects—An updated review. Environ. Toxicol. Chem., 37: 2029-2063. https://doi.org/10.1002/etc.4147

Lee, K.W., Shim, W.J., Kwon, O.Y. and Kang, J.H. 2013. Size-dependent effects of micro polystyrene particles in the marine Copepod Tigriopus japonicus. Environ. Sci. Technol., 47: 11278-11283. https://doi.org/10.1021/es401932b

Lehner, R., Weder, C., Petri-Fink, A. and Rothen-Rutishauser, B. 2019. The emergence of nano plastic in the environment and its possible impact on human health. Environ. Sci. Technol., 53: 1748-1765. https://doi.org/10.1021/acs.est.8b05512

Liu, C.H. and Yu, X. 2011. Silver nanowire-based transparent, flexible, and conductive thin film. Nanosci. Res. Lett., 6: 75. https://doi.org/10.1186/1556-276X-6-75

Lombardo, D., Calandra, P., Pasqua, L. and Magazù, S. 2020. Self-assembly of organic nanomaterials and biomaterials: The bottom-up approach for functional nanostructures formation and advanced applications. Materials, 13: 1048. https://doi.org/10.3390/ma13051048

López-Serrano, A., Muñoz Olivas, R., Sanz Landaluze, J. and Cámara, C. 2014. Nanoparticles: A global vision. Anal. Methods, 6: 38-56. https://doi.org/10.1039/C3AY40517F

Malekhosseini, P., Alami, M., Khomeiri, M., Esteghlal, S., Nekoei, A.R. and Hosseini, S.M.H. 2019. Development of casein-based nanoencapsulation systems for delivery of epigallocatechin gallate and folic acid. Food Sci. Nutr., 7: 519-527. https://doi.org/10.1002/fsn3.827

Mirzaei, H. and Darroudi, M. 2017. Zinc oxide nanoparticles: Biological synthesis and biomedical applications. Ceram. Int., 43: 907-914. https://doi.org/10.1016/j.ceramint.2016.10.051

Mukherjee, A., Majumdar, S., Servin, A.D., Pagano, L., Dhankher, O.P. and White, J.C. 2016. Carbon nanomaterials in agriculture: A critical review. Front. Plant Sci., 7: 172. https://doi.org/10.3389/fpls.2016.00172

Ng, C.T., Yong, L.Q., Hande, M.P., Ong, C.N., Yu, L.E., Bay, B.H. and Baeg, G.H. 2017. Zinc oxide nanoparticles exhibit cytotoxicity and genotoxicity through oxidative stress responses in human lung fibroblasts and drosophila melanogaster. Int. J. Nanomed., 12: 1621-1637. https://doi.org/10.2147/IJN.S124403

Pathakoti, K., Manubolu, M. and Hwang, H.M. 2018. Nanotechnology Applications for Environmental Industry. In Mustansar Hussain, C. (ed.), Handbook of Nanomaterials for Industrial Applications, Micro and Nano Technologies. Elsevier, Netherlands, pp. 894-907. https://doi.org/10.1016/B978-0-12-813351-4.00050-X

Patra, J.K. and Baek, K.H. 2014. Green nanobiotechnology: Factors affecting synthesis and characterization techniques [WWW Document]. J. Nanomater., 11: 155. https://doi.org/10.1155/2014/417305

Peng, J.J.Y., Botelho, M.G. and Matinlinna, J.P. 2012. Silver compounds used in dentistry for caries management: A review. J. Dent., 40: 531-541. https://doi.org/10.1016/j.jdent.2012.03.009

Peters, R., Kramer, E., Oomen, A.G., Herrera Rivera, Z.E., Oegema, G., Tromp, P.C., Fokkink, R., Rietveld, A., Marvin, H.J.P., Weigel, S., Peijnenburg, A.A.C.M. and Bouwmeester, H. 2012. Presence of nano-sized silica during in vitro digestion of foods containing silica as a food additive. ACS Nano, 6: 2441-2451. https://doi.org/10.1021/nn204728k

Rai, P.K., Lee, J., Brown, R.J.C. and Kim, K.H. 2020. Micro- and nano-plastic pollution: Behavior, microbial ecology, and remediation technologies. J. Clean. Prod., 2020: 125240. https://doi.org/10.1016/j.jclepro.2020.125240

Sajid, M., Ilyas, M., Basheer, C., Tariq, M., Daud, M., Baig, N. and Shehzad, F. 2015. Impact of nanoparticles on human and environment: Review of toxicity factors, exposures, control strategies, and prospects. Environ. Sci. Pollut. Res., 22: 4122-4143. https://doi.org/10.1007/s11356-014-3994-1

Saleem, H. and Zaidi, S.J. 2020. Recent developments in the application of nanomaterials in agroecosystems. Nanomaterials, 10: 2411. https://doi.org/10.3390/nano10122411

Saqib, N. and Rahim, M. 2016. Toxicity of silver nanoparticles. Madridge J. Nanotechnol. Nanosci., 1: 1-2.

Steinmetz, Z., Wollmann, C., Schaefer, M., Buchmann, C., David, J., Tröger, J., Muñoz, K., Frör, O. and Schaumann, G.E. 2016. Plastic mulching in agriculture: Trading short-term agronomic benefits for long-term soil degradation? Sci. Total Environ., 550: 690-705. https://doi.org/10.1016/j.scitotenv.2016.01.153

Strambeanu, N., Demetrovici, L. and Dragos, D. 2015. Anthropogenic Sources of Nanoparticles. In Lungu, M., Neculae, A., Bunoiu, M. and Biris, C. (eds.), Nanoparticles' Promises and Risks: Characterization, Manipulation, and Potential Hazards to Humanity and the Environment. Springer International Publishing, Cham, pp. 21-54. https://doi.org/10.1007/978-3-319-11728-7_3

Strungaru, S.A., Jijie, R., Nicoara, M., Plavan, G. and Faggio, C. 2019. Micro- (nano) plastics in freshwater ecosystems: Abundance, toxicological

impact, and quantification methodology. TrAC Trends Anal. Chem., 110: 116-128. https://doi.org/10.1016/j.trac.2018.10.025

Sun, T.Y., Gottschalk, F., Hungerbühler, K. and Nowack, B. 2014. Comprehensive probabilistic modeling of environmental emissions of engineered nanomaterials. Environ. Pollut., 185: 69-76. https://doi.org/10.1016/j.envpol.2013.10.004

Tiwari, N., Santhiya, D. and Sharma, J.G. 2020. Microbial remediation of micro-nano plastics: Current knowledge and future trends. Environ. Pollut., 265: 115044. https://doi.org/10.1016/j.envpol.2020.115044

Torbati, T.V. and Javanbakht, V. 2020. Fabrication of TiO2/Zn2TiO4/Ag nanocomposite for synergic effects of UV radiation protection and antibacterial activity in sunscreen. Colloids Surf. B Biointerf., 187: 110652. https://doi.org/10.1016/j.colsurfb.2019.110652

Valdiglesias, V., Costa, C., Kiliç, G., Costa, S., Pásaro, E., Laffon, B. and Teixeira, J.P. 2013. Neuronal cytotoxicity and genotoxicity induced by zinc oxide nanoparticles. Environ. Int., 55: 92-100. https://doi.org/10.1016/j.envint.2013.02.013

Weinberg, H., Galyean, A. and Leopold, M. 2011. Evaluating engineered nanoparticles in natural waters: Characterization, analysis, and risks of nanomaterials in environmental and food samples. TrAC Trends Anal. Chem., 30, 72-83. https://doi.org/10.1016/j.trac.2010.09.006

Wu, W. 2017. Inorganic nanomaterials for printed electronics: A review. Nanoscale, 9: 7342-7372. https://doi.org/10.1039/C7NR01604B

Xin, Q., Shah, H., Nawaz, A., Xie, W., Akram, M.Z., Batool, A., Tian, L., Jan, S.U., Boddula, R., Guo, B., Liu, Q. and Gong, J.R. 2019. Antibacterial Carbon-Based Nanomaterials. Adv. Mater., 31: 1804838. https://doi.org/10.1002/adma.201804838

Yan, Y., Gong, J., Chen, J., Zeng, Z., Huang, W., Pu, K., Liu, J. and Chen, P. 2019. Recent advances on graphene quantum dots: From chemistry and physics to applications. Adv. Mater., 31: 1808283. https://doi.org/10.1002/adma.201808283

Yang, M., Chen, J., Cao, W., Ding, L., Ng, K.K., Jin, H., Zhang, Z. and Zheng, G. 2011. Attenuation of nontargeted cell-kill using a high-density lipoprotein-mimicking peptide–phospholipid nano scaffold. Nanomed. 6, 631-641. https://doi.org/10.2217/nnm.11.10

Zhang, D., Wu, T., Qin, X., Qiao, Q., Shang, L., Song, Q., Yang, C., and Zhang, Z. 2019. Intracellularly generated immunological gold nanoparticles for combinatorial photothermal therapy and immunotherapy against the tumor. Nano Lett., 19: 6635-6646. https://doi.org/10.1021/acs.nanolett.9b02903

Zhang, X. 2015. Gold nanoparticles: Recent advances in biomedical applications. Cell Biochem. Biophys., 72: 771-775. https://doi.org/10.1007/s12013-015-0529-4

Zhang, Y.M., Liu, Y.H. and Liu, Y. 2020. Cyclodextrin-based multi stimuli-responsive supramolecular assemblies and their biological functions. Adv. Mater., 32: 1806158. https://doi.org/10.1002/adma.201806158

Pectin Production from Biowaste (Fruits & Vegetables) by Crosscurrent Solid-Liquid Extraction Technique

Akshi Kunwar Singh† and S. S. Kumar

School of Engineering, University of Petroleum and Energy Studies, Dehradun, India
†Corresponding author: Akshi Kunwar Singh; singh.akshi85@gmail.com

ABSTRACT

The impact of fruit and vegetable waste is becoming a significant concern for the environment. The biomaterial waste generated from fruit processing industries is very high. When discharged as processed waste, it also increases water pollution. 45% of the total industrial organic pollution originates from food processing industries. These generated wastes are suitable for the production of biochemicals. Pectin is one such biochemical that plays a vital role in reducing the burden on the environment. Pectin helps in the manufacturing of confectionaries. Vegetable waste like beetroot, carrot, beans can also act as a source for pectin production. This study depicts extracting Pectin from mixed fruit pomace waste. Mixed fruit (Orange, Pomegranate, Banana & grapes) pomace waste reacts with 0.1N HCl. This reaction uses a 2-stage crosscurrent solid-liquid extraction technique. For its nature, obtained pectin was tested as calcium pectate using methylated spirit. The filtrate from 2-stage crosscurrent leaching was further dried in an oven. RSM technique helps in optimizing parameters like drying time, temperature, pH, and concentration. The experimental setup generated Pectin gave an efficiency of 11.52% for 22.4g of dried mixed fruit pomace waste.

INTRODUCTION

The amount of discarded materials in various fruit processing industries varies with location and method of harvest. It generates approximately 45% of total industrial organic pollution (Lin et al. 2013, Joshi et al. 2012). Bioconversion of the carbohydrates present in the waste can act as feedstock for biomaterials and chemical intermediates. Besides this Pectin has good gelling properties, and its isolation for commercial production of Pectin started in the 20th century. Pectin is now manufactured to rigorous safety and quality standards in the United States, Europe, Latin America, and China.

Pectin (Endress & Mattes 2009, Thakur et al. 2009) is a high-molecular-weight carbohydrate polymer present in all plants. It contributes to the cell structure and covers many polymers according to their molecular weight, chemical configuration, the content of neutral sugars, and different plant types. The concentration of pectin content varies with the ripening of fruit. Commercial pectin extraction is performed mainly from citrus peel and apple pomace, and other sources include sugar beets, banana peel, mango peel, papaya peel, sunflower heads, and beetroots. Extraction of pectin can be performed by leaching, which is also called solid-liquid extraction (Wikandari et al. 2015). It is the process of extracting the substance from a solid by dissolving them in a liquid. The solid-liquid mixture is brought into contact with a solvent in which the desired substance is soluble, and the other components are insoluble. In leaching, the solvent is critical as it facilitates the ability to remove(solute) a given substance from a solid material. In this study, 2- stage crosscurrent leaching is performed to extract pectin from mixed fruit pomace using HCl as solvent. Many researchers worked on the extraction of pectin (calcium pectate) using different raw materials starting from fruit waste (pomace/peels) to vegetable waste (peels/pomace). Azad (2014) experimented on a wide variety of solvents like HCl, H_2SO_4, HNO_3, citric acid, acetic acid for the isolation of pectin extracted from lemon pomace during ripening. Pectin was extracted and characterized from the peels of lemons (Citrus Limon), grapefruit (Citrus Paradisi), and sweet orange (Citrus Sinensis). Collected fruit wastes were dried, extracted using 300 mL of 0.1 N HCl, and the results revealed that citrus peel contains higher pectin content - about 24.5%. Nakamura and Tobe (2015) used carrot as raw material to extract pectin with water at a temperature of below 100°C, pH from 2 to 5. The effect of nitric acid extraction variables on orange Pectin was studied by Aravantinos Zafiris and Oreopoulou (1992). Banerjee et al. (2016) experimented on lemon juice for the extraction of pectin from mango peels. Extraction of Pectin from apple pomace by citric acid was studied by Canteri et al. (2005). Chandel et al. (2016) worked on the standardization of eco-friendly techniques for the extraction of pectin from

apple pomace. Extraction of pectin was performed using an autoclave at a temperature of 121° for 60 min followed by precipitation using ethanol, resulting in an optimum pectin yield of 13.01%. Dranca & Oroian (2018) worked on the effect of acid type and particle size on the yield and purity of apple (Malus Domestica 'fălticeni') pomace pectin and the pectin yield (21.24%) and uronic acid content (93.90g.100g^{-1}) were obtained for citric acid extraction and particle sizes between 125 and 200 μm. Grassino et al. (2016) worked on ultrasound-assisted extraction and characterization of pectin from tomato waste. Using oxalic acid as solvent, a comparison of the pectin yields showed that extraction at 80°C for 24 h using the conventional method gave similar results as that of extraction by ultrasound-assisted extraction for 15 min. Under ideal conditions, Hay et al. (2017) extracted and characterized pectin from selected fruit peel waste, producing pectin yields of 11.31% and 18.5% for banana and mango peels, respectively. Temperature, extraction duration, and pH were all investigated, and the optimal values were found to be 82°C, 105 minutes, and pH of 2. Hosseini et al. (2016) and Jafari et al. (2017) used the Box-Behnken technique (Ferreira et al. 2007) for the optimization of microwave-assisted extraction of Pectin from sour orange peel and its physicochemical properties and the results revealed the optimum conditions were yield of Pectin 29.1%, at 1.5 pH, 700 W microwave power and irradiation time of 3 min. Jafari et al. (2017) optimized pectin extracted from carrot pomace using the CCD method. Kauser et al. (2015) compared conventional (water-hot acid) and non-conventional (ultrasonication) procedures for the extraction and chemical characterization of Pectin from mango cultivar "chaunsa" peel waste, finding that the non-conventional method yielded 15.8 g pectin from 100 g peel in 20 min, while the conventional method yielded 16.6 g pectin from 100 g peel in 90 min. As a result of the shorter extraction time, the traditional non-technique (ultrasonication) was found to be a more energy-efficient method. Madhav & Pushpalatha (2002) analyzed biochemical characteristics using pectin extracted from various wastes in particular gel grade of pectin was focused during the study. Maran & Priya (2015) and Maran et al. (2013, 2017) worked on ultrasound-assisted citric acid-mediated pectin extraction from the industrial waste of Musa balbisiana, and the mean experimental yield of Pectin of nearly 8.99% was observed. It was optimized using RSM. They also worked on ultrasound-assisted extraction of pectin from sisal waste. The experimental yield obtained was 29.32%, and the optimization was carried out by choosing the BBD technique in RSM. Popugaeva et al. (2018) and Papoutsis et al. (2016) worked on the impact of different solvents on the recovery of bioactive compounds and antioxidant properties from lemon (Citrus limon L.) pomace waste. Saberian et al.

(2017) experimented on the extraction of pectin from orange juice waste assisted by ohmic heating, and optimization was performed by choosing CCD under RSM, and results revealed the optimum yield of Pectin to be 14.32%. Sharma et al. (2013) studied the extraction of pectin from "kinnow" peel and pomace using water acidified with HNO3. Sudhakar & Maini (2000) worked on the isolation and characterization of mango peel pectins, and an optimum amount of 20.8% of pectin was extracted. Virk & Sogi (2004) collected fresh apple peel from the local preserve manufacturing unit and analyzed it for moisture, ash, acidity, crude fiber, and total sugars. The apple peel was extracted three times using HCl at different normalities and 1% citric acid. Citric acid was observed to be a better solvent in the extraction of pectin than HCl. Yang et al. (2018) experimented on the extraction of pectin from sisal waste by combined enzymatic and ultrasonic process, and research results showed that ultrasound extraction of sisal waste attained a much higher pectin yield of 31.1% than other methods like ultrasound followed by the enzyme (14.6%), combined enzymatic/ultrasonic (9.4%), ultrasonic extraction (11.9%) and acidic extraction (5.8%). Yuliarti et al. (2015) studied the extraction and characterization of pectin from gold kiwi fruit which revealed that enzyme extracted pectin gives a yield of 4.5% whereas acid and water extraction methods give 3.6-3.8%.

The literature survey observed that no experimental work was done using mixed fruit pomace waste. So, an interest was felt to use this mixed fruit pomace waste as raw material for the extraction of pectin.

MATERIALS AND METHODS

Feedstock includes the mixed fruit pomace collected from nearby fruit shops. Chemicals used were HCl, NaOH, $CaCl_2$, CH_3COOH and methylated spirit.

Trial Experiment (Using Orange Peel)

A trial run was conducted using orange peel as raw material. The collected peel was then sun-dried and chopped. Around 50g of powdered orange peel was extracted with 300 mL of 0.1 N HCl, boiled for 30 min, and filtered under suction. After filtration, the raffinate is again extracted with 300 mL of 0.1N HCl and boiled for 30 min. The filtrate was neutralized with 1 N of NaOH using phenolphthalein indicator and is further allowed to stand for 24 h. 50 mL of 1 N acetic acid was added, and after 5 min, 25 mL of 1 N calcium chloride was added, stirred, and kept still for an hour. The contents were then boiled for 2 min, filtered through a pre-weighed Whatman No1 filter paper. The obtained precipitate was then washed with water until the filtrate was chloride-free, the filter cake was dried for 7.5 h. The percentage of pectin
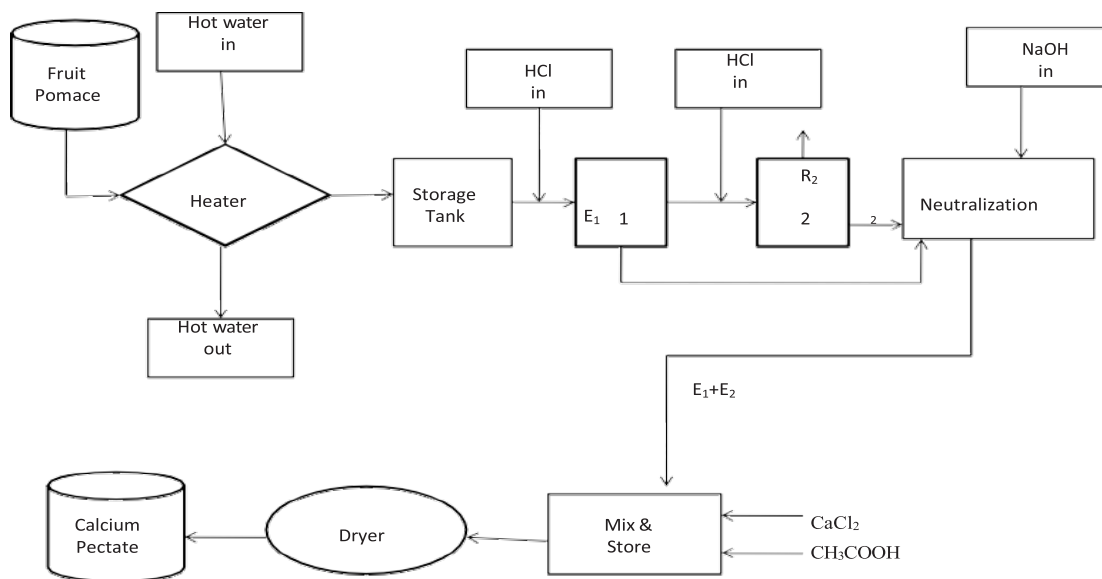
Fig. 1: Flowsheet representing the extraction of pectin (peel/pomace). Here R1, R2 refers to raffinate from stages 1 and 2; E1, E2 are extracted from stages 1, 2, respectively.

extracted utilizing a two-stage cross current extraction procedure (leaching) with the solvent HCl is just 2%.

Experimentation (Using Mixed Fruit Pomace)

Mixed fruit pomace taken as feed (orange, pomegranate, banana, grape pomace) was dried and chopped. About 22.4 g of powdered mixed fruit pomace waste was extracted with 60 mL of 0.1 N HCl (1st stage of extraction), which was then boiled for 30 min and filtered under suction. After filtration, the raffinate was sent for 2nd stage of extraction with 60 mL of 0.1 N HCl and again boiled for 30min. The acid present in the filtrate was neutralized with 0.1 N of NaOH using phenolphthalein indicator and was kept still for 24 h. To this, 50 mL of 1 N acetic acid was added, followed by 25 mL of 1 N calcium chloride, stirred, and allowed to stand for 1 h. The contents were then boiled for 2 min, filtered, and the obtained precipitate was washed with water. The filter cake was then dried for 3 h. The entire process of extraction of pectin is indicated in Fig. 1. Percentage of pectin from the 2- stage cross current extraction process (Leaching) using HCl is 11.29%. This process is optimized using response surface methodology (RSM).

Test for Pectin

After completing the 2-stage cross current extraction process, the filter cake was dried for three h and tested by adding 7-8 mL of methylated spirit. Rigorous swirling or gentle shaking was performed till the clots were formed, as shown in Fig. 2. which indicates the gelling property of pectin in the extract.

RESULTS AND DISCUSSION

Using HCl as a solvent, the percentage extraction of pectin from orange peel is 2%, and for mixed fruit pomace waste, it is 11.29%. Parameter studies were performed to find out the optimum conditions for the extraction of pectin using HCl from mixed fruit pomace waste. Parameters like drying time, drying temperature, pH of the solution, and concentration of HCl were varied.

Fig. 2: Gelling property of pectin.

Effect of Drying Time

The extracted calcium pectate is kept in a hot air oven for drying. The weight of calcium pectate was noted for every hour, and the drying operation was performed for five hours. Optimum drying time was found to be 3 h with 2.53 g of calcium pectate, beyond which no appreciable change in weight of calcium pectate was observed.

It can be inferred that 3 h of drying dried all the calcium pectate present in the solution. The effect of drying time on the weight of calcium pectate is shown in Fig. 3.

Effect of Temperature

Calcium pectate obtained from the 2nd stage of extraction was kept for drying in a hot air oven. The product sample was kept for 3h (optimum drying time) at varying temperatures starting from 50° to 90° (at 10°-time intervals), and the weight of calcium pectate was noted at each temperature. With the increase in temperature, a decrease in trend curve was observed till 80°, after which the weight of calcium pectate remained constant, as shown in Fig. 4. At 80°, all the moisture and volatiles were removed from the solution, and hence the optimum temperature is considered as 80°.

Effect of pH of the Solution

During the extraction process, the pH of the solution is varied, and the optimum pH was found to be 3.09. As shown in Fig. 5, the pH of the solution was varied from 3.09 to 9.1, and the maximum weight of calcium pectate was 2.53g (at 3.09 pH value) which shows that the extraction is favorable under acidic conditions.

Effect of Concentration of HCl (Solvent)

During experimentation, solvent concentration varied from 0.05 N to 0.2 N (at 0.05 N regular intervals), and the same experimental procedure and drying phenomenon were repeated. The majority of the available calcium pectate present in the sample solution is extracted using 0.1 N HCl solvent for a given weight of the sample. So, the optimum concentration was found to be 0.1 N with calcium pectate weighing around 2.53 g. The trend curve is shown in Fig. 6.

Optimization of The Selected Parameters by Design of Experiments (DOE)

In the present study, % of Y is the function of drying time(X_1), pH(X_2), temperature(X_3), the concentration of HCl (X_4), and weight (X_5) response based on experimental runs and predicted values proposed by BBD design. 3-factor levels are indicated in Table 1. Multiple regression analysis of the experimental data resulted in the following equation:

$$Y = 3105.5 - 3.8X_1 - 1764.8X_2 - 0.439X_3 + 391X_4 + 2.69X_5 - 0.00X_1^2 + 255.42X_2^2 - 0.00644X_3^2 - 282X_4^2 + 2.302X_5^2$$

$$+ 2.74X_1X_2 - 0.027X_1X_3 - 63.3X_1X_4 - 0.76X_1X_5 - 0.178X_2X_3 - 142.4X_2X_4 - 1.76X_2X_5 + 7.54X_3X_4 - 0.1081X_3X_5 - 53.6X_4X_5$$

Where Y is the percentage represented in terms of weight of calcium pectate

The correlation coefficient is a measure of the model's variability to response ($R2$). The model is inviolable since $R2 \rightarrow 1$. $R2 = 0.9986$ in this investigation, with an error of 0.0014, indicates that the model is statistically significant at a 95% confidence level.

Contour Plots

Contour plots are three-dimensional plots in which a 3-D surface is projected on a 2-D plane. These plots represent two predictor variables X, Y on the y-axis, and response variable Z as contours. Contour lines can be curved, straight, or a mixture of both. The contour plots show the interactive
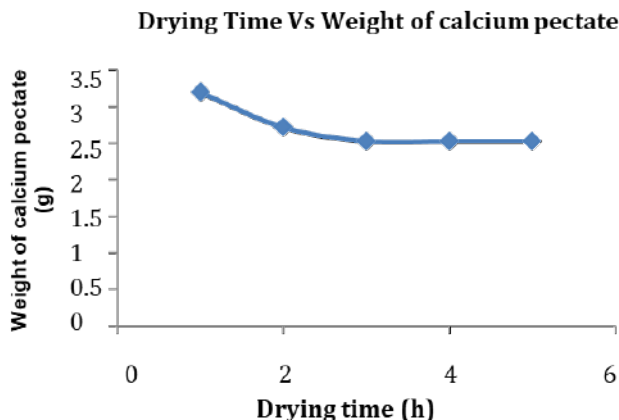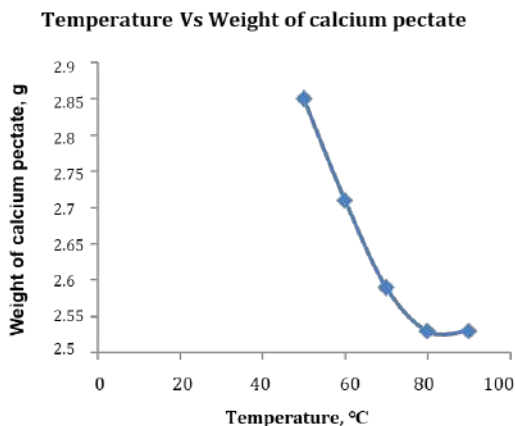

Fig. 3: Effect of drying time.
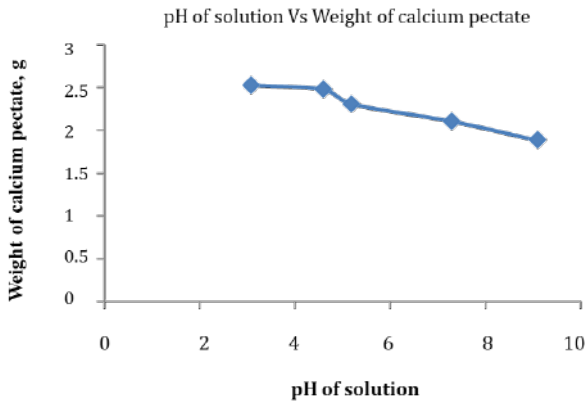

Fig. 4: Effect of temperature.

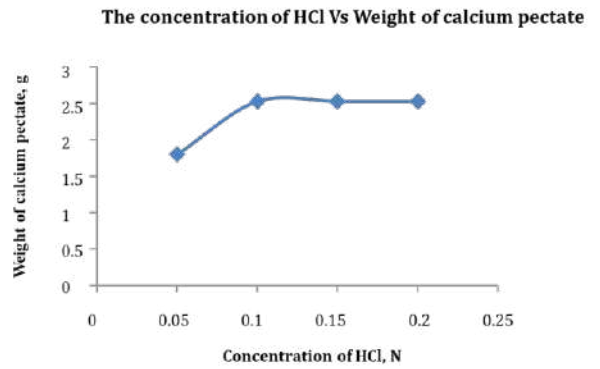Fig. 5: Effect of pH of the solution.

Fig. 6: Effect of Concentration of HCl.

effect of every parameter with the weight of calcium pectate. The contour plots representing the optimization study of the

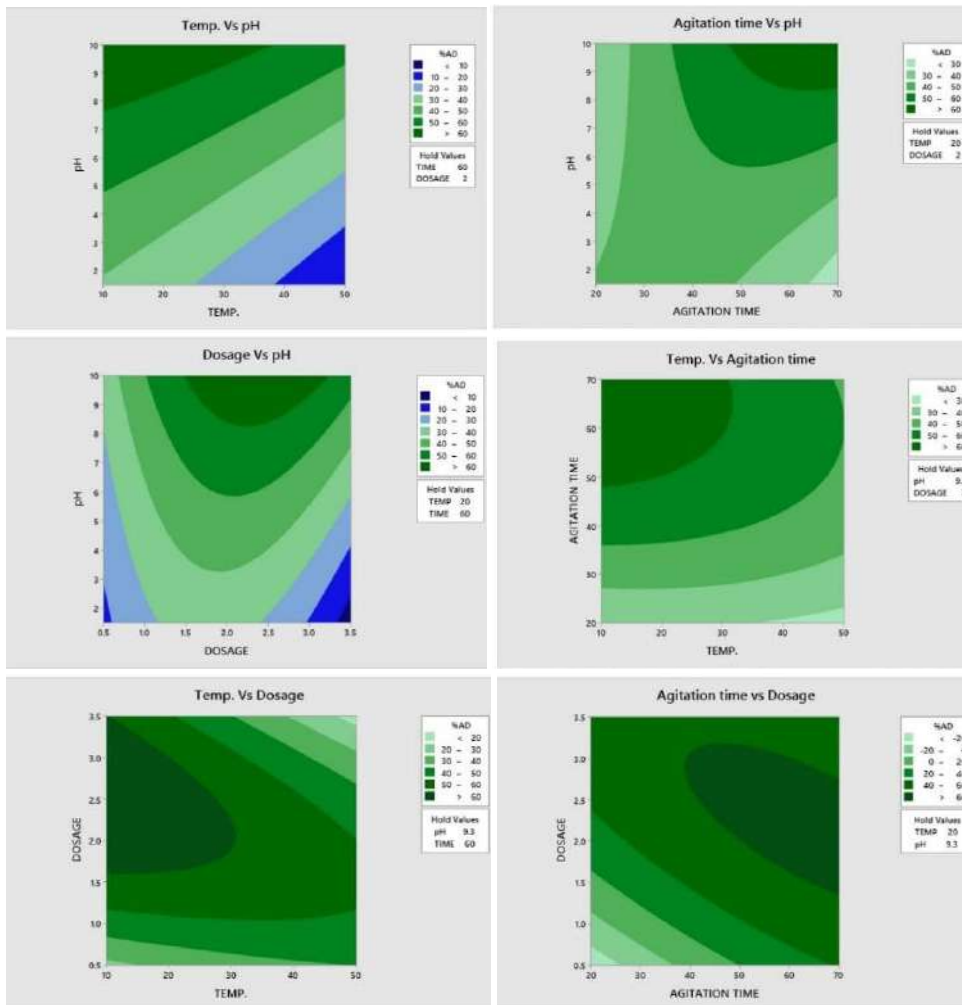extraction of calcium pectate with mixed fruit pomace are shown in Fig. 7.

Fig. 7: Contour plots representing the optimization study of the extraction of calcium pectate with mixed fruit pomace.

Table 1: 3-factor levels in BBD method.

Parameters	Minimum	Average	Maximum
Temperature[°C]	46.29	63.145	80
Weight [g]	1.677	3.257	4.8375
pH	3.0	3.5	4.0
Time [h]	2.311	3.5	4.689
Concentration of HCl [N]	0.0155	0.075	0.1345

Table 2: Comparison of optimum values by experiment and RSM.

Parameters	Experimental	RSM
Drying time	3 h	3.23 h
Weight of calcium pectate	2.53g	2.58 g
pH of solution	3.09	3.0
Temperature	80°C	80°C
Concentration of HCl	0.1N	0.1345N

The influence of several factors and their interactions on pectin yield is illustrated in Fig. 7. The optimum conditions observed from DOE are drying time of 3.23 h, pH of the solution to be maintained at 3, drying temperature at 80°, and concentration of HCl of 0.1345 N for an optimum weight of calcium pectate of 2.58 g. A comparison of the values obtained by experimentation and RSM study is shown in Table 2.

CONCLUSION

Around 2.53 g (11.29%) of calcium pectate was extracted from 22.4 g of mixed fruit pomace waste. In this 2-stage extraction process, various process parameters have shown a marked effect on the percentage extraction of Pectin (calcium pectate). Gelling nature of calcium pectate was confirmed by methylated spirit. Besides the percentage extraction of pectin, solid organic waste was used as a potential source for the extraction, which in turn helps in the reduction of environmental pollution (in particular water pollution) to a greater extent. As per the experimentation, the drying time of 3 h, drying temperature of 80°, pH of solution maintained at 3.09, and 0.1 N concentration of HCl resulted in an optimum extraction of 11.29% calcium pectate. An optimization study through RSM by DOE reveals that the optimum conditions for the parameters were drying time of 3.23 h, the temperature at 80°, pH of the solution to be 3.0, and at 0.1345 N of solvent concentration, which yielded 11.52% of Pectin. The experimental values obtained were well matched with optimized parameters by RSM to a correlation coefficient of 0.9986.

REFERENCES

Aravantinos-Zafiris, G. and Oreopoulou, V. 1992. The effect of nitric acid extraction variables on orange pectin. J. Sci. Food Agric., 60(1): 127-129. https://doi.org/10.1002/jsfa.2740600120

Azad, A.K.M. 2014. Isolation and characterization of pectin extracted from lemon pomace during ripening. J. Food Nutr. Sci., 2(2): 30. https://doi.org/10.11648/j.jfns.20140202.12

Banerjee, J., Vijayaraghavan, R., Arora, A., MacFarlane, D.R and Patti, A.F. 2016. Lemon juice-based extraction of pectin from mango peels: Waste to wealth by sustainable approaches. ACS Sustain. Chem. Eng., 4(11): 5915–5920. https://doi.org/10.1021/acssuschemeng.6b01342

Chandel, V., Vaidya, D., Kaushal, M., Gupta, A. and Verma, A.K. 2016. Standardization of eco-friendly technique for extraction of pectin from apple pomace. Indian J. Nat. Prod. Resour., 7(1): 69–73.

Canteri, M.H.G., Fertonani, H.C.R., Waszczyskj, N. and Wosiacki, G. 2005. Extraction of pectin from apple pomace. Brazil. Arch. Biol. Technol., 48(2): 259-266. https://doi.org/10.1590/S1516-89132005000200013

Dranca, F. and Oroian, M. 2018. Effect of acid type and particle size on the yield and purity of apple (Malus Domestica 'F lticeni') pomace pectin. Food Environ. Safety J., 17(2): 246–251. Retrieved from http://fia.usv.ro/fiajournal/index.php/FENS/article/view/586%0Ahttp://www.fia.usv.ro/fiajournal/index.php/FENS/article/view/586/555

Endress, H.U. and Mattes, F. 2009. Pectin - Fiber ingredients: Food Applications and Health Benefits. Routledge, London, pp.135–171. https://doi.org/10.1201/b15547-17

Ferreira, S.L.C., Bruns, R.E., Ferreira, H.S., Matos, G.D., David, J.M., Brandão, G.C. and dos Santos, W.N.L. 2007. Box-Behnken design: An alternative for the optimization of analytical methods. Analy. Chim. Acta, 597: 179–186. https://doi.org/10.1016/j.aca.2007.07.011

Grassino, A.N., Brnčić, M., Vikić-Topić, D., Roca, S., Dent, M. and Brnčić, S.R. 2016. Ultrasound-assisted extraction and characterization of pectin from tomato waste. Food Chem., 198: 93–100. https://doi.org/10.1016/j.foodchem.2015.11.095

Hay, S.I., Abajobir, A.A., Abate, K.H., Abbafati, C., Abbas, K.M., Abd-Allah, F. and Bryane, C.E.G. 2017. Global, regional, and national disability-adjusted life-years (DALYs) for 333 diseases and injuries and healthy life expectancy (HALE) for 195 countries and territories, 1990-2016: A systematic analysis for the Global burden of disease study 2016. The Lancet, 390(10100): 1260–1344. https://doi.org/10.1016/S0140-6736(17)32130-X

Hosseini, S.S., Khodaiyan, F. and Yarmand, M.S. 2016. Optimization of microwave-assisted extraction of pectin from sour orange peel and its physicochemical properties. Carbohydr. Polym., 140: 59–65. https://doi.org/10.1016/j.carbpol.2015.12.051

Jafari, F., Khodaiyan, F., Kiani, H. and Hosseini, S.S. 2017. Pectin from carrot pomace: Optimization of extraction and physicochemical properties. Carbohydr. Polym., 157: 1315–1322. https://doi.org/10.1016/j.carbpol.2016.11.013

Joshi, V., Kumar, A. and Kumar, V. 2012. Antimicrobial, antioxidant and phytochemicals from fruit and vegetable wastes: A review. Int. J. Food Ferment. Technol., 2: 123–136.

Kauser, S., Saeed, A. and Iqbal, M. 2015. Comparative studies on conventional (Water-hot acid) and non-conventional (ultrasonication) procedures for extraction and chemical characterization of pectin from peel waste of mango cultivar Chaunsa. Pak. J. Bot., 47(4): 1527–1533.

Lin, C.S.K., Pfaltzgraff, L.A., Herrero-Davila, L., Mubofu, E.B., Abderrahim, S., Clark, J.H. and Dickson, F. 2013. Food waste is a valuable resource for the production of chemicals, materials, and fuels: Current situation and global perspective. Energy Environ. Sci., 6(2): 426–464.

Madhav, A. and Pushpalatha, P.B. 2002. Characterization of pectin extracted from different fruit wastes. J. Trop. Agric., 40: 53–55.

Maran, J.P. and Priya, B. 2015. Ultrasound-assisted extraction of pectin from sisal waste. Carbohydr. Polym., 115: 732–738. https://doi.org/10.1016/j.carbpol.2014.07.058

Maran, J.P., Priya, B., Al-Dhabi, N.A., Ponmurugan, K., Moorthy, I.G. and Sivarajasekar, N. 2017). Ultrasound-assisted citric acid-mediated pectin extraction from the industrial waste of Musa balbisiana. Ultrason. Sonochem., 35: 204–209. https://doi.org/10.1016/j.ultsonch.2016.09.019

Maran, J.P., Sivakumar, V., Thirugnanasambandham, K. and Sridhar, R. 2013. Optimization of microwave-assisted extraction of pectin from orange peel. Carbohydr. Polym., 97(2): 703–709. https://doi.org/10.1016/j.carbpol.2013.05.052

Nakamura, A. and Tobe, J. 2015. Method for Producing Carrot Pectin. United States Patent Application Publication- Pub No. : US 2015 / 0017316A1. 1(19), 2–7, 15 Jan 2015.

Papoutsis, K., Pristijono, P., Golding, J.B., Stathopoulos, C.E., Scarlett, C.J., Bowyer, M.C. and Vuong, Q.V. 2016. Impact of different solvents on the recovery of bioactive compounds and antioxidant properties from lemon (Citrus limon L.) pomace waste. Food Sci. Biotechnol., 25(4): 971–977. https://doi.org/10.1007/s10068-016-0158-8

Popugaeva, D., Kreyman, K. and Ray, A.K. 2018. Study of aluminum in groundwater using chemometric methods. Environ. Technol., 41(13): 1691-1699. https://doi.org/10.1080/09593330.2018.1544667

Saberian, H., Hamidi-Esfahani, Z., Ahmadi Gavlighi, H. and Barzegar, M. 2017. Optimization of pectin extraction from orange juice waste assisted by ohmic heating. Chem. Eng. Process.: Process Intensificat., 117: 154–161. https://doi.org/10.1016/j.cep.2017.03.025

Sharma, H., Bhatia, S. and Aslam, M.S. 2013. Studies on pectin extraction from kinnow peel and pomace. J. Res. Punjab Agric. Univ., 50(3&4): 128-130.

Sudhakar, D.V. and Maini, S.B. 2000. Isolation and characterization of mango peel pectins. J. Food Process. Preserv., 24(3): 209–227. https://doi.org/10.1111/j.1745-4549.2000.tb00414.x

Thakur, B.R., Singh, R.K., Handa, A.K. and Rao, M.A. 2009. Critical reviews in food science and nutrition chemistry and uses of pectin: A review chemistry and uses of pectin. Crit. Rev. Food Sci. Nutr., 37(1): 47–73. https://doi.org/10.1080/10408399709527767

Virk, B.S. and Sogi, D.S. 2004. Extraction and characterization of pectin from apple (Malus Pumila. Cv Amri) peel waste. Int. J. Food Prop., 7(3): 693–703. https://doi.org/10.1081/JFP-200033095

Wikandari, R., Nguyen, H., Millati, R., Niklasson, C. and Taherzadeh, M.J. 2015. Improvement of biogas production from orange peel waste by leaching of limonene. BioMed Res. Int., 2015: 494182. https://doi.org/10.1155/2015/494182

Yang, Y., Wang, Z., Hu, D., Xiao, K. and Wu, J.Y. 2018. Efficient extraction of pectin from sisal waste by the combined enzymatic and ultrasonic process. Food Hydrocoll., 79: 189–196. https://doi.org/10.1016/j.foodhyd.2017.11.051

Yuliarti, O., Goh, K.K.T., Matia-Merino, L., Mawson, J. and Brennan, C. 2015. Extraction and characterization of pomace pectin from gold kiwifruit (Actinidia chinensis). Food Chem., 187: 290–296. https://doi.org/10.1016/j.foodchem.2015.03.148

Preparation of Silver and Copper Co-impregnated Nano-ZnO Immobilized on Mesoporous SiO$_2$ and its Photocatalytic Performance

Qinlin Yuan, Hang Xu†, Shaokang Wang, Zhewen Yang, Wenke Zhang and Qinggao Ma

Chemical Engineering and Pharmaceutics School, Henan University of Science and Technology, Luoyang 471023, China

†Corresponding author: Hang Xu; xhinbj@126.com

ABSTRACT

To improve light usage, Ag and Cu were co-impregnated with nano-ZnO, and the mesoporous silica gel (meso-SiO$_2$) was chosen as the carrier. The sol-gel method was used to successfully construct a composite photocatalyst with 3 percent Ag/0.1 percent Cu/nano-ZnO/meso-SiO$_2$. For the evaluation of the photocatalytic activity of the as-prepared catalysts, Reactive Black 5 was used as a simulated organic pollutant in aqueous. The results revealed that uniform spherical nano-ZnO particles with a diameter of 10 nm were attached to the surface and mesopore of meso-SiO$_2$. The average pore width and specific surface area of this composite were 7.06 nm and 305 m^2.g^{-1}, respectively. The optimal amount of loaded Ag and Cu were 3% and 0.1%, respectively, which resulted in around 100% removal of Reactive Black 5 after 280 min UV-light irradiation. The degradation process followed pseudo-first-order kinetics. Ag and Cu-loaded nano-ZnO/SiO$_2$ could be advantageous for suppressing the recombination of photo-generated holes and electrons, thus improving the degradation efficiency. The constant of degradation rate and adsorption equilibrium of 3%Ag/0.1%Cu/nano-ZnO/meso-SiO$_2$ were 0.049 min^{-1} and 2.14 L.g^{-1}, respectively. After three reuses, the Ag/Cu/ZnO/meso-SiO$_2$ photocatalyst remained very stable during the photocatalytic process with no loss of photocatalytic activity. According to the GC-MS results, a probable degradation mechanism was estimated.

INTRODUCTION

Over the last half-century, photocatalytic semiconductors have piqued the interest of an increasing number of scientists. Because of its exciton binding energy of 60 meV (Waag et al. 2004) and bandgap energy of 3.3 eV (Xu et al. 2017) at room temperature, zinc oxide (ZnO) is one of the stellar n-type photocatalytic semiconductors that has been used in organic degradation.

The nano-ZnO, on the other hand, has two disadvantages as a photocatalyst: low light usage and poor recyclability and reusability. Metal was used to modify nano-ZnO to minimize bandgap and thus increase the photocatalytic activity of ZnO to improve light-harvesting efficiency. Cu-doped ZnO nano-photocatalyst was developed for the increase of photocatalytic activity in the treatment of methyl orange wastewater, according to the literature (Kadam et al. 2017). In addition, Ag also could improve the photocatalytic activity of ZnO to decompose phenol, which was more efficient than P25-TiO$_2$ (Jaramillo-Paez et al. 2017). Modwi et al. (made Ag (1%) and Cu (5%) doped ZnO nanoparticles that successfully cured malachite green in an aqueous solution. The bandgap energy of Cu/ZnO was moved from 2.95 to 2.79 eV (pure ZnO 3.3 eV) by the Ag/Cu/ZnO nano-composite, indicating that Ag and Cu were suitable options for improving

photocatalyst activity (Modwi et al.2018). Furthermore, the nano-sized ZnO could not be recycled or reused. The nanoparticles loaded on some supporters, on the other hand, may be able to solve this problem. However, the nanopowders loaded on some supporters could alleviate this problem. Sarah et al. developed a composite photocatalyst in which nano-ZnO was immobilized on bentonite clay to improve the reusability of the catalyst (Sarah et al. 2013). In addition, porous activated carbon loaded nano-ZnO was proved more efficient than ZnO alone for removing alizarin cyanin green from aqueous (Muthirulan et al. 2013). In our preliminary work, the composite photocatalysts of Ag and Fe bi-metals doped quantum-sized ZnO immobilized on micro-pore ZSM-5 (Xu et al. 2017) were prepared to decompose Rhodamine B in aqueous and exhibited satisfactory photocatalytic activity.

Sol-gel technology was one of the most extensively used methods to synthesize inorganic materials in the preparation of nanomaterials (Xu et al. 2018, Wu et al. 2019). The sol-gel method was used to generate Ag and Cu bi-metals loaded nano-ZnO immobilized mesoporous SiO$_2$ composite photocatalysts, which were then evaluated by XRD, SEM, TEM, and BET. For assessing photocatalytic performance, Reactive Black 5 was chosen as a pollutant in an aqueous

solution. The contents of Ag and Cu in photocatalysts were studied and optimized.

MATERIALS AND METHODS

Preparation of Ag/Cu/nano-ZnO/Mesoporous SiO$_2$ Photocatalyst

Zn(CH$_3$COO)$_2$ (0.01 mol), Cu(NO$_3$)$_2$ (0.005-0.02 mmol), and AgNO$_3$ (0.1-0.5 mmol) were dissolved in 50 mL anhydrous ethanol. Then, 1.6 g meso-SiO$_2$ was added to form a hybrid solution. A solution of 0.58 g lithium hydroxide in 50 mL anhydrous ethanol and 100 mL of *n*-hexane were added to the hybrid system at room temperature. A white gel was obtained after standing overnight at 4°C. The precursor was obtained by centrifugation and drying at 100°C. The Ag/Cu/nano-ZnO/mesoporous SiO$_2$ composite powder was prepared by calcination at 200°C for 4 h. The mass ratio of ZnO and SiO$_2$ was 1:2.

Characterization of Materials

The crystal phase of the sample was analyzed by XRD using a PANalytical X-ray diffractometer (X'Pert Pro MPD, Netherlands) using Cu Kα radiation. SEM was performed using a Nova NanoSEM (FEI, USA) with EDX. TEM was carried out using JEM-2010 (JEOL, Japan). N$_2$ sorption isotherms were measured using a Mocromeritics ASAP2020 system (USA).

Photocatalytic Activity Tests

Reactive Black 5 was selected as a simulated pollutant to investigate the photocatalytic performance and its main information was shown in Table 1. The maximum absorption wavelength of Reactive Black 5 was 553 nm.

To evaluate the photocatalytic activity, 200 mL of 20 mg.L^{-1} Reactive Black 5 and 0.1 g.L^{-1} photocatalyst were added to a 250 mL beaker under magnetic stirring. A 10 cm long mercury UV lamp (10 W Guangdong Bright Star) was used as the radiation source with a wavelength of 245 nm. The lamp was fixed above the reaction liquid. After a certain reaction interval of 40 min, a 10 mL sample was removed and centrifuged at 12,000 rpm to remove the catalyst. The dyestuff absorbance of Reactive Black 5 was analyzed using a UV-2102PC UV-visible spectrophotometer (UNICO, China). The degradation rate of Reactive Black 5 was calculated using Eq. (1):

$$\text{Removal} = [(C_0 - C_t)/C_0] \times 100\% \qquad \ldots(1)$$

Where, C_0 is the initial concentration of Reactive Black 5, and C_t is the concentration of Reactive Black 5 at time t.

GC-MS Analysis

The organic substance in the sample should be extracted by dichloromethane before the GC-MS test. The separation was carried out on a DB-5 MS fused quartz capillary chromatographic column (J&W Scientific, Folsom, CA, USA) with a 30 m 0.25 mm i.d. and 0.25 m phase thickness in a Finnigan Trace GC 2000 chromatograph. Using a Trace MS 2000 mass spectrometer (Thermo-Quest, Finnigan, USA) in EI+ mode, coupled to the chromatograph, the analytes were examined by mass spectrometry.

RESULTS AND DISCUSSION

XRD Analysis

Fig.1 shows the XRD results of pure-SiO$_2$, pure-ZnO, ZnO/SiO$_2$, 3%-Ag/ ZnO/SiO$_2$ and 3%-Ag/0.1%-Cu/ZnO/SiO$_2$. It could be seen clearly from Fig.1 that the XRD pattern of pure-SiO$_2$ displayed a wide diffraction peak located at around 22°. The diffraction peaks of pure ZnO at 2θ values of 31.7°, 34.4°, 36.2° and 47.5° were attributed to (100), (002), (101), and (102) crystal planes, respectively. All the peaks could be well indexed to standard patterns (JCPDS 36-1451) without any impurity phase (Dou et al. 2015). From the XRD pattern of ZnO/SiO$_2$, all the characteristic peaks of ZnO and SiO$_2$ could be found. The half peak width of ZnO in ZnO/SiO$_2$ became bigger than pure ZnO which meant SiO$_2$ could decrease the particle size of ZnO. In the XRD pattern of 3%-Ag/ZnO/SiO$_2$, the diffraction peaks of AgO at 2θ values of 39.4° and 53.9° were found. However, according to the standard patterns of AgO (JCPDS 74-1750), the major peaks of AgO at 2θ values of 32.3°, 34.2°, and 37.2° did not appear. This could be attributed to the low content of sliver in the composite catalyst (only 3%). The amount of Cu was rather low that no diffraction peak was observed in the XRD pattern of 3%-Ag/0.1%-Cu/ZnO/SiO$_2$. The average particle sizes of ZnO in Ag/Cu/ZnO/ SiO$_2$ and pure ZnO were obtained using the Scherrer equation D = Kλ/βcosθ, where, D was the average crystallite size, λ was the X-ray wavelength, θ was the Bragg angle, β was the corrected half-peak width of the experimental sample, and K was the shape factor with a value of 0.9 (Bechambi et al. 2015). The average crystal sizes of ZnO in Ag/Cu/ZnO/SiO$_2$ and pure ZnO were 10.1 nm and 15.7 nm, respectively.

Table 1: Identified intermediates of degradation of Reactive Black 5.

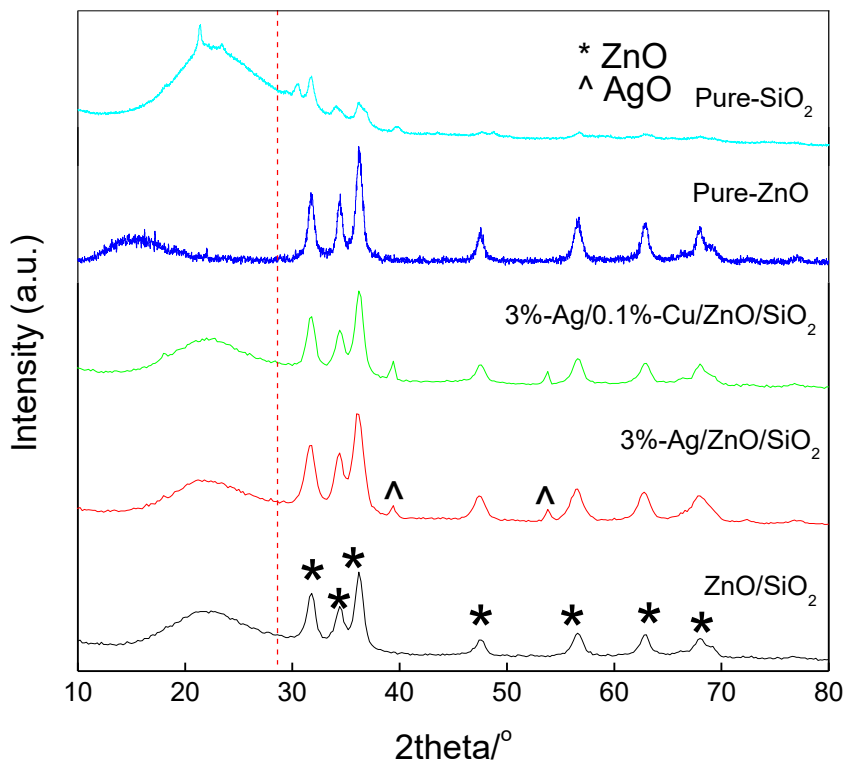| RT[min]	Authentic chemical formula
6.81	1,2-diacetylenzene*
7.40	3,5,5-trimethylhexanoic acid
14.08	2-butenedicarboxylate
16.53	phthaic acid, diisobutylester
17.46	1,4-dinitrobenzoic acid*
19.15	phthalic acid*

*main products

Fig. 1: XRD of 3%-Ag/0.1%-Cu/ZnO/ SiO$_2$, 3%-Ag/ZnO/SiO$_2$, ZnO/SiO$_2$, pure ZnO and pure SiO$_2$

N$_2$-Adsorption and Desorption Analysis

Fig. 2 showed the nitrogen isotherm data for Ag/Cu/ZnO/ meso-SiO$_2$. The type IV isotherm indicated this composite had a mesoporous structure (Fu et al. 2015). The average pore width and surface area of this material were 7.06 nm and 305 m^2.g^{-1}, respectively. In a preliminary study (Xu et al. 2015a), ZnO/mesoporous SiO$_2$ and pure mesoporous SiO$_2$ exhibited 318 and 330 m^2.g^{-1} surface areas along with average pore sizes of 7.9 and 8.6 nm, respectively. It suggested that the
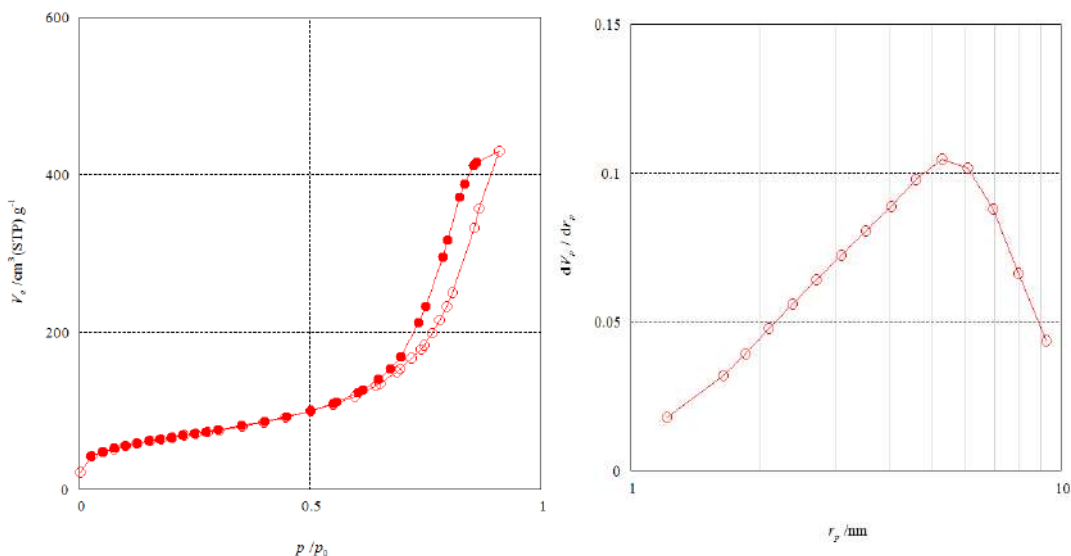
Fig. 2: Nitrogen isotherm adsorption-desorption curve (a) and pore size distribution (b) for 3%-Ag/0.1%-Cu/ZnO/meso-SiO$_2$.

metal had been successfully doped on ZnO/mesoporous SiO_2 and affected its surface area and pore width, which resulted in the reduction of 13 $m^2.g^{-1}$ and 0.8 nm, respectively.

Morphological Analysis

The morphological study of 3 percent -Ag/0.1 percent Cu/ZnO/SiO_2 was shown in Fig. 3. A considerable number of nano-sized ZnO particles agglomerated on the surface of SiO_2 as seen in SEM images (Fig. 3a & 3b). The particle size of ZnO was consistent in the TEM picture (Fig.3c). The average particle size was around 8 nm, which was similar to the theoretical XRD finding (15.7 nm). EDX was used to determine the presence of Cu and Ag in the Ag/Cu/ZnO/SiO_2 composite. The catalyst has five elements, as shown in Fig.3d. For the C element, 1.92 wt% C could be attributed to the incomplete cleaning of the composite or the contamination during the measuring process. The content of the O element was about 50%. The element ratio of Si and Zn was nearly 2.01:1 which was consistent with the experimental dosage.

Moreover, the content of Ag was only 0.28% which was lower than Ag dosage and Cu metal was not found in the EDX results. The reason was that only the red square zone of the catalytic surface in Fig. 3b was scanned to obtain the EDX result. The red square zone sometimes could not represent the surface properties of the entire material. The content of Cu was only 0.1% which was difficult to be detected.

Effect of Ag Content in Ag/ZnO/SiO_2

Fig. 4 showed the effect of Ag contents in Ag/ZnO/SiO_2 on the decomposition of Reactive Black 5 during irradiation time from 0 to 280 min. It could be seen clearly from Fig.4 that there was a low photocatalytic efficiency when the composite catalyst was free from silver. After 280 min, only 22.6% Reactive Black 5 was decomposed. When the Ag content increased from 1% to 3%, the degradation rate of Reactive Black 5 exhibited a great improvement. The color removals were 60.5% and 78.9% at 280 min, respectively. However, when the Ag-loaded amount reached 5%, the dye removal
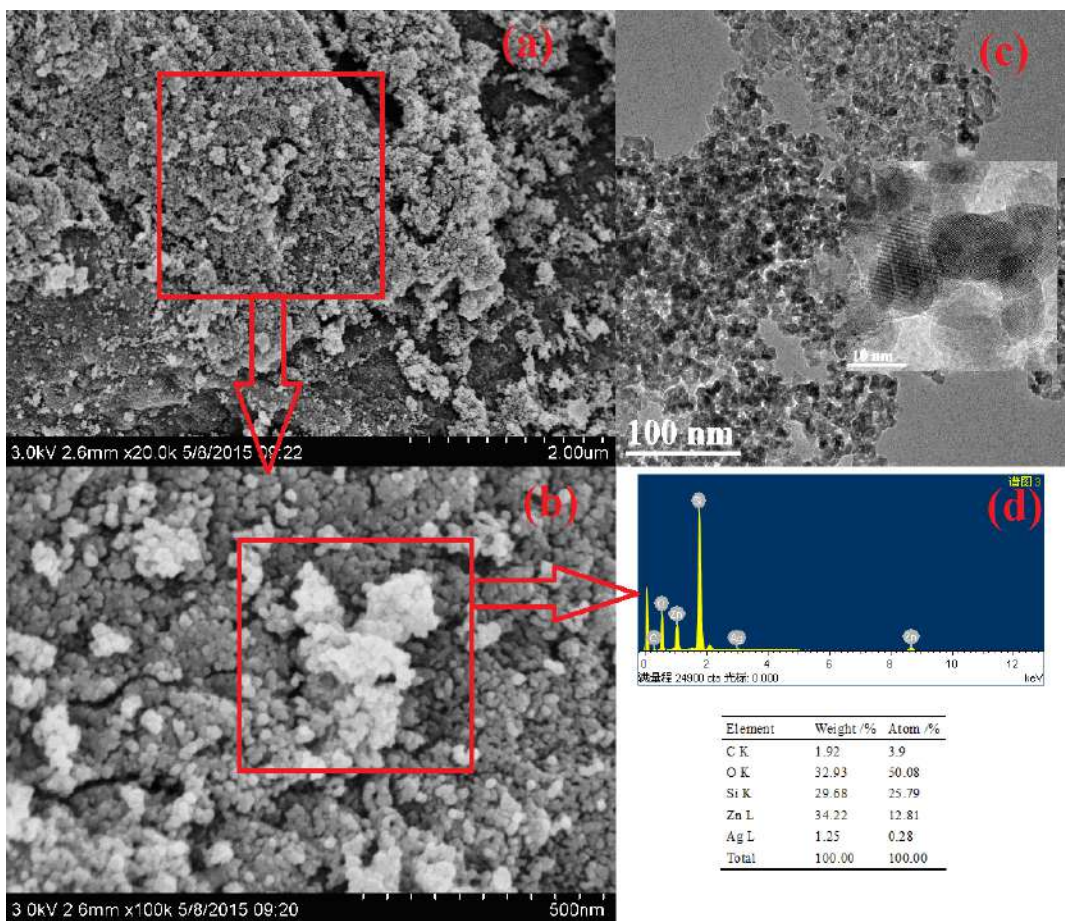

Element	Weight /%	Atom /%
C K	1.92	3.9
O K	32.93	50.08
Si K	29.68	25.79
Zn L	34.22	12.81
Ag L	1.25	0.28
Total	100.00	100.00

Fig. 3: SEM images (a and b), TEM image (c), and EDX (d) of 3%-Ag/0.1%-Cu/ ZnO/SiO_2.

decreased to 65.1% at 280 min. Therefore, the optimal Ag-loaded amount was 3% in this experimental condition.

Based on the experimental results, the reason could be analyzed as follow. When ultraviolet light illuminated the photocatalyst (ZnO/SiO$_2$), electrons were promoted from the valence band to the conduction band, forming electron (e$^-$)—hole (h$^+$) couples (Chang et al. 2015). Meanwhile, the electrons and holes were able to quickly recombine, releasing heat. The holes at the ZnO surface could oxidize H$_2$O$_{ads}$ and OH$^-_{ads}$, adsorbed in the ZnO surface, to produce ▪OH$_{ads}$. The ▪OH$_{ads}$ was a powerful oxidizing agent which would attack the organic compounds and generate intermediates (Int$_{ads}$). These intermediates could further react with ▪OH$_{ads}$ to produce final products (P). In the meantime, the ▪OH$_{ads}$ could be also be consumed by inactive species which leads to lower degradation efficiency. The appropriate Ag impregnation aided in the division of electrons and holes as well as the rate of electron transport to dissolved oxygen, boosting photocatalytic efficiency even more. Excess Ag, on the other hand, could fill the surface of ZnO, resulting in insufficient UV light utilization and so being detrimental to photocatalytic activity. Excess Ag, on the other hand, could create electron-hole recombination centers, reducing dye removal.

Effect of Cu Content in Cu/ZnO/SiO$_2$

Fig. 5 shows the effect of Cu amount in Cu/ZnO/SiO$_2$ photocatalyst on Reactive Black 5 degradation. From Fig.5, when the Cu-loaded amount was increased from 0% to 0.1%, the Reactive Black 5 removal increased significantly from 22.6% to 70.4% after 280 min. However, with more Cu impregnation (exceeded 0.1%), the Reactive Black 5 removal dramatically decreased. Among which, only 41.4% removal was observed after 280 min at 0.2% Cu-loaded amount. Therefore, the optimal Cu-loaded amount was 0.1% with 70.4% dye removal which was lower than that of 3% Ag-loaded catalyst.

Cu impregnation significantly increased the ZnO photocatalytic activity. Metallic Cu consumed the photo-generated electrons, which could suppress the recombination of photo-generated holes and electrons. As a result, more active holes reacted with H$_2$O molecules adsorbed on the surface of the catalyst, producing more hydroxyl radicals. In contrast, the catalytic activity was reduced when the Cu-loaded amount exceeded the best dosage. Cu may also act as an electron-hole recombination center, thus decreasing the photocatalytic activity of ZnO.

Comparison of Different Photocatalysts

Fig. 6 shows a comparison of Reactive Black 5 degradation on ZnO/SiO$_2$, 0.1% Cu/ZnO/SiO$_2$, 3%Ag/ZnO/SiO$_2$, and 3%Ag/0.1%Cu-ZnO/SiO$_2$ under UV-lamp. From Fig. 6, 3%Ag/0.1%Cu/ZnO/SiO$_2$ was the most efficient photocatalyst in the presence of UV irradiation with 91.5% Reactive Black 5 removal at 280 min. Ag and Cu could
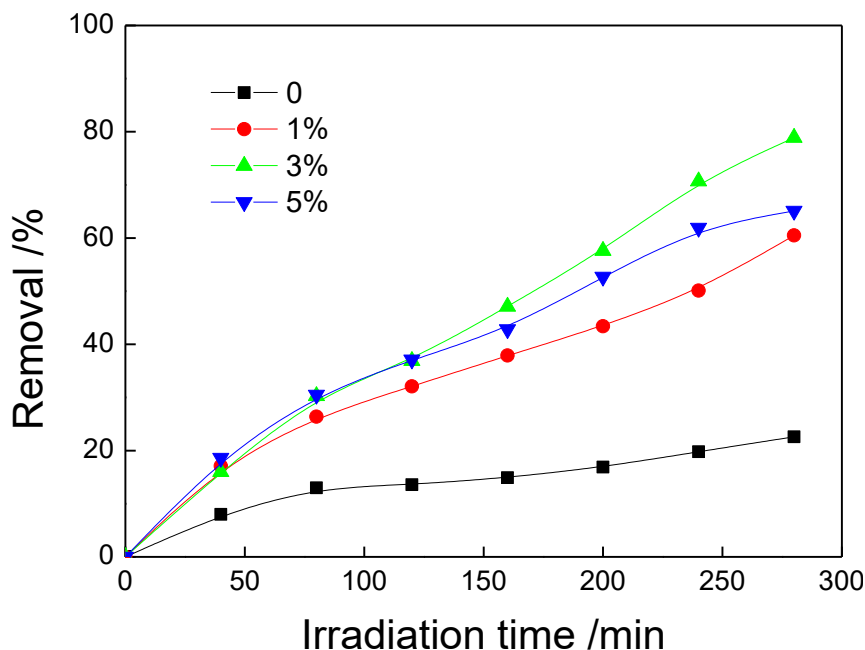

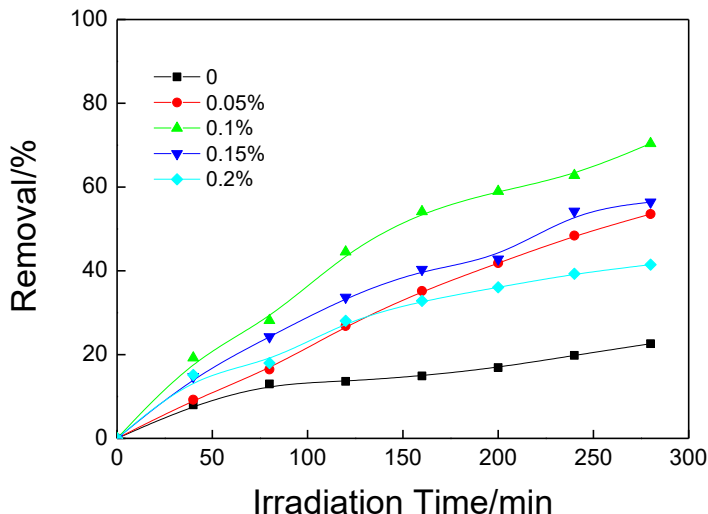Fig. 4: Reactive Black 5 removal at different Ag contents in Ag/ZnO/ SiO$_2$.

Fig. 5: Reactive Black 5 removal at different Cu contents within Cu/ZnO/ SiO$_2$.

capture the photo-generated electrons, and prevent hole–electron recombination, which improved the photocatalytic efficiency. The Ag and Cu co-loaded nano-ZnO decreased the band-gap energy of nano semiconductor photocatalyst. Therefore, 3%Ag/0.1%Cu-ZnO/SiO$_2$ displayed a remarkable activity under this experimental condition.

Effect of Ag/Cu/ZnO/SiO$_2$ Dosage

The dosage of 3%Ag/0.1%Cu/ZnO/SiO$_2$ should be optimized to avoid waste during degradation. A series of experiments were carried out with varying composite catalyst concentrations from 0.05 to 0.3 g.L^{-1} to determine the optimal

Ag/Cu/ZnO/SiO$_2$ dosage. Reactive Black 5 removals at different catalyst dosages were shown in Fig.7. Accordingly, the removal after 280 min were 73.4%, 91.5%, 99.3%, 100%, 98.7% and 80.2% corresponding to different catalyst dosages of 0.05 g.L^{-1}, 0.1 g.L^{-1}, 0.15 g.L^{-1}, 0.2 g.L^{-1}, 0.25 g.L^{-1} and 0.3 g.L^{-1}, respectively. The removal of Reactive Black 5 increased with the increase of Ag/Cu/ZnO/SiO$_2$ dosages from 0.05 g.L^{-1} to 0.2 g.L^{-1}. Nevertheless, even the catalyst was increased to 0.25 g.L^{-1}, the removal was almost unchanged. Moreover, the removal was further reduced when the catalyst was added to 0.3 g.L^{-1}. Thus, the optimum catalyst dosage was 0.2 g.L^{-1} with nearly 100 % removal of Reactive Black 5 after 280 min.
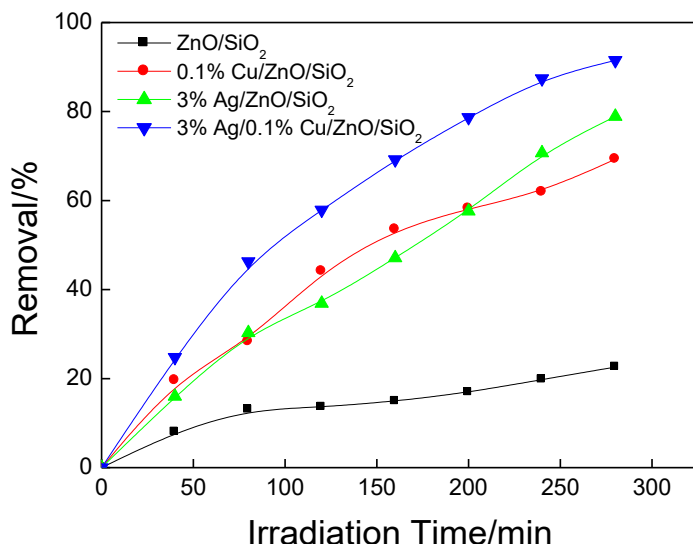

Fig. 6: Reactive Black 5 removal at different catalysts.

According to the references (Xu et al. 2015 b), the photocatalytic process followed pseudo-first-order kinetics, $\ln(C_t/C_0) = k_{ap}t$. Here, the slope represents the apparent reaction rate constant (k_{ap}). The fitting results at different $Ag/Cu/ZnO/SiO_2$ dosages were shown in Fig. 8. In general, the fitting coefficients were above 0.99 when the catalyst dosages were between 0.05 g/L to 0.2 g/L, which means the Reactive Black 5 degradation process by $UV/Ag/Cu/ZnO/SiO_2$ perfectly followed the first-order kinetics. When the catalyst dosages were 0.25 g/L and 0.3 g/L, the fitting coefficient values were lower than 0.99, which meant excessive catalyst had a negative effect on first-order degradation kinetics. According to the slope of fitting line equation, the reactive rate constants were 0.0047 min^{-1}, 0.00871 min^{-1}, 0.0123 min^{-1}, 0.0140 min^{-1}, 0.0139 min^{-1} and 0.00756 min^{-1} at different catalyst dosages 0.05 $g.L^{-1}$, 0.1 $g.L^{-1}$, 0.15 $g.L^{-1}$, 0.2 $g.L^{-1}$, 0.25 $g.L^{-1}$ and 0.3 $g.L^{-1}$, respectively. The biggest k_{ap} at 0.2 g/L catalyst dosage was 0. 0140 min^{-1}.

The experimental results indicated that the more catalysts were added, the more photons from the UV-lamp were harvested, which could promote the valence band electron excitation to the conduction band. Reactive Black 5 was degraded by photo-generated holes in the valence band, which were active sites with a high oxidation capacity. At higher concentrations, the catalyst particles, on the other hand, could reflect, screen, and scatter the UV lamp's light, reducing the photonic flux within the irradiated solution. Another reason was the efficient catalyst surface probably became smaller for photoabsorption because of the agglomeration and sedimentation of catalyst particles. Therefore, there was an optimal catalyst dosage.

Effect of $Ag/Cu/ZnO/SiO_2$ amount on pseudo-first-order rate constant (k_{ap}) were fitted with a Langmuir type expression (Xu et al. 2014):

$$k_{ap} = \frac{k_o KC}{1+KC}$$

Here, k_0, K, and C were the catalyst surface reaction rate constant, the adsorption equilibrium constant, and the catalyst concentration, respectively. Values of k_0 K could be calculated according to the Langmuir type formula, as k_0 was 0.049 min^{-1} and K was 2.14 $g.L^{-1}$, respectively. The correlation coefficient is 0.9981.

Photocatalyst Recovery

Fig.7 showed the recovery test of $Ag/Cu/ZnO/SiO_2$ under UV-light irradiation. The photocatalyst could be used five times. Almost no obvious declination of the photoactivity was observed after four times. At the fifth time, the dye removal decreased by about 5%. The results demonstrated that $Ag/Cu/ZnO/SiO_2$ catalyst was stable during the photocatalytic process.
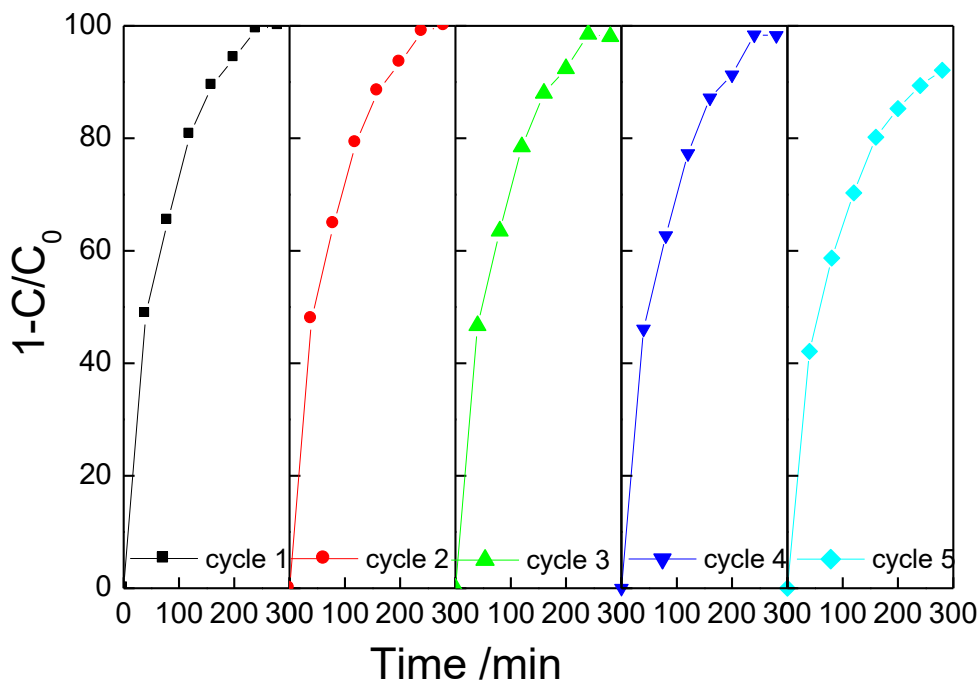

Fig. 7: Recyclability of 3%-Ag/0.1%-Cu/ZnO/SiO₂ for the photo-degradation.

Possible degradation pathway of Reactive Black 5

Although the photocatalytic process exhibited nearly 100% removal, the intermediate products should also be considered. The intermediate products were obtained by dichloromethane extraction and the sample was analyzed by GC-MS. The results were shown in Table 1. From Table1, there were many colorless intermediate products. The main by-products were 1,2-diacetylenzene (RT: 6.8 min), 2-butenedicarboxylate (RT: 14.08 min), 1,4-dinitrobenzoic acid (RT: 17.46 min), and phthalic acid (RT: 19.15 min). According to the GC-MS results, a lot of organic acids could be generated when the structure of Reactive Black 5 was decomposed by the photocatalytic process.

The probable deconstructed pathway of Reactive Black 5 was indicated in Fig. 8 based on the MS results. Reactive Black 5 had an anthracene ring, benzene ring, sulfonic group, group, and so on in its chemical structure. Because of their low bond energy, the sulfonic and amino groups were quickly eliminated. As a result, the very active hydroxyl radical attacked and oxidized these bonds first, causing the chemical structure to decompose. The anthracene and benzene rings were difficult to break down since cleaving them required a lot of energy. The benzene ring oxidation produced the 2-butenedicarboxylate. Decomposition of the anthracene ring yields 1,2-diacetylenzene, 1,4-dinitrobenzoic acid, and phthalic acid.

CONCLUSION

A composite photocatalyst 3%-Ag/0.1%-Cu/nano-ZnO/ mesoporous SiO_2 was successfully prepared and applied to effectively degrade Reactive Black 5 in aqueous under UV light irradiation. The uniform spherical nano-ZnO particles with a size of ~10 nm are attached to the surface and mesopore of meso-SiO_2. The Ag/Cu/ZnO/meso-SiO_2 exhibited the classical type IV isotherm during the N_2 adsorption and desorption process, which signified an excellent mesoporous structure. The average pore width and surface area of this material were 7.06 nm and 305 $m^2.g^{-1}$, respectively. The optimal Ag and Cu-loaded amounts were 3% and 0.1%, respectively, which contributed nearly 100% Reactive Black 5 removal at 280 min under UV-light irradiation. Doping with Ag and Cu could significantly reduce the recombination of photo-generated holes and electrons, resulting in a faster deterioration rate. Furthermore, the photocatalyst Ag/Cu/ZnO/meso-SiO_2 displayed perfect stability during the photocatalytic process, with no visible fading of photocatalytic activity after five reuses. Based on the GC-MS results, a plausible degradation mechanism was hypothesized.

REFERENCES

Bechambi, O., Chalbi, M., Najjar, W. and Sayadi S. 2015. Photocatalytic activity of ZnO loaded with Ag on the degradation of endocrine disrupting under UV irradiation and the investigation of its antibacterial activity. Appl. Surf. Sci., 347: 414-420.

Chang, C.T., Wang, J.J., Tong, O.Y., Zhang, Q. and Jing, Y.H. 2015. Photocatalytic degradation of acetaminophen in aqueous solutions by TiO$_2$/ZSM-5 zeolite with low energy irradiation. Mater. Sci. Eng., 196: 53-60.

Dou, P.T., Tan, F.T., Wang, W., Sarreshteh, A., Qiao, X.L., Qiu, X.L. and Chen, J.G. 2015. One-step microwave-assisted synthesis of Ag/ZnO/ graphene nanocomposites with enhanced photocatalytic activity. Photochem. Photobiol. A- Chem., 302: 17-22.
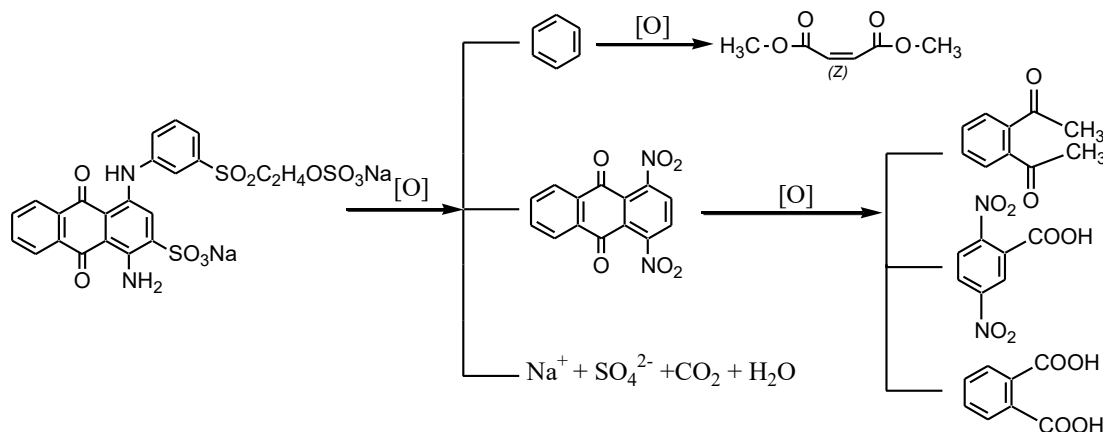

Fig. 8: Possible degradation pathway of Reactive Black 5.

Fu, J.R., Zheng, J., Fang, W.J., Chen, C., Cheng, C., Yan, R.W., Huang, S.G. and Wang, C.C. 2015. Synthesis of porous magnetic Fe$_3$O$_4$/Fe@ ZnO core-shell heterostructure with superior capability for water treatment[J]. Alloys Comp., 650: 463-469.

Jaramillo-Paez, C., Navio, J.A., Hidalgo, M.C. and Macias, M. 2017. High UV-photocatalytic activity of ZnO and Ag/ZnO synthesized by a facile method. Catal. Today, 284: 121-128.

Kadam, A.K., Kim, T.G., Shin, D.S., Garadkar, K.M. and Park J. 2017. Morphological evolution of Cu doped ZnO for enhancement of photocatalytic activity. J. Alloys Comp.,   710: 102-113,

Modwi, A., Ghanem, M.A., Al-Mayouf, A.M. and Houas, A. 2018. Lowering energy bandgap and enhancing photocatalytic properties of Cu/ZnO composite decorated by transition metals. Mol. Struct., 1173: 1-6.

Muthirulan, P., Meenakshisundararam, M. and Kannan, N. 2013. The beneficial role of ZnO photocatalyst supported with porous activated carbon for the mineralization of alizarin cyanin green dye in an aqueous solution. Adv. Res., 4: 479-484.

Sarah, C.M., Suprakas, S.R., Maurice, S.O., and Maggie, N.B. 2013. Microwave-assisted synthesis, characterization and antibacterial activity of Ag/ZnO nanoparticles supported bentonite clay. J. Hazard. Mat., 262: 439-446.

Waag, A., Gruber, T., Thonke, K., Sauer, R., Kling, R., Kirchner, C. and Ress, H. 2004. ZnO metal-organic vapor phase epitaxy: Present state and prospective applications. Alloys Comp., 371: 77-81,

Wu, F.M., Wang, X.W., Li, M. and Xu, H. 2019. Synthesis of Alpha-Fe$_2$O$_3$ nanospheres and its dark-degradation for organic dye pollutions. Environ. Prog. Sustain. Energy, 38: 1-5

Xu, H., Yu, T.L. and Liu, J.F. 2014. Photo-degradation of Acid Yellow 11 in aqueous on nano-ZnO/Bentonite under ultraviolet and visible light irradiation. Mater. Lett., 117: 263-265.

Xu, H., Yu, T.L. and Liu, Y. 2015a. Characteristics and performance of nano zinc oxide/mesoporous silica gel photocatalytic composite prepared by a sol-gel method. Nanomaterials, 65: 1-5.

Xu, H., Yu, T.L., Wang, J.X., Li. M. and Liu, Y.N. 2015b. Online monitoring of Fenton-mediated reactive Red 6B oxidation kinetics. Environ. Prog. Sustain. Energy, 34: 1019-1027.

Xu, H., Zhang, D.D. and Wu, F.M. 2017 Photocatalytic activity of nano-ZnO loaded with Ag and Fe immobilized on ZSM-5. Desalin. Water Treat., 74: 308-315.

Xu, H., Zhang, D.D. and Wu, F.M. 2018. Effect of the template on the hydrothermal synthesis of mixed molecular sieves for methanol dehydration. Environ. Prog. Sustain. Energy, 37: 2132-2138.

The Measurement of Radon Concentration in the Buildings of the College of Education, Al-Qadisiyah University, Iraq Using CR-39 Detector

Kawthar Hassan Obayes† and Osamah Nawfal Oudah

Department of Physics, College of Education, University of Al-Qadisiyah, Diwaniyah, Iraq

†Corresponding author: Kawthar Hassan Obayes; kawthar.aljelehawy@qu.edu.iq

ABSTRACT

This research aims to evaluate the concentration of radon gas and the risks involved as a result of exposure to it. The nuclear track detector CR-39 was used to measure radon gas in the buildings of Al-Qadisiyah University's College of Education. For a month, 11 buildings in the college of Education at Al-Qadisiyah University were chosen to measure the radon concentration, with CR-39 reagent placed inside the sponge by two detectors for each building. The highest value of radon concentration was recorded in the CH1 model (270.5±32.9 Bq.m^{-3}), at the building of the Department of Chemistry, and the lowest value was recorded in the Li1 model (96.9±27.7 Bq.m^{-3}), which is the college library building with a concentration rate equal to (168). It is below the acceptable and recommended limit by the International Committee for Radiation Protection (200-300 Bq.m^{-3}).

INTRODUCTION

Radon gas belongs to the noble gases group in the periodic table, and it is seven and a half times heavier than air, therefore it is usually at the bottom, and it mixes virtually homogeneously with the indoor air of residential buildings, where radon gas concentrations are usually 2 to 10 times higher. As a result, radon exposure outside of residential areas is largely neglected (Wehr et al. 1984). The outer medium's two main sources of radon are soil and water, and it produces around 80% of the radon gas emitted to the outer medium from the earth's upper layer. As a result, radon in the soil is caused by the presence of radium 226 and uranium 238 whose concentrations vary depending on the geological nature of the rock, which is commonly concentrated in granitic and phosphate rocks (Matelsky 1968).

As it was found that this matter may occur in rocks with the content of (100 ppm) of uranium hundreds of meters underground, a statistical association between the incidence of earthquakes and the concentration of radon gas in the soil was found (Nougadère et al. 2014). In addition, building materials made of soil and rocks such as cement and bricks contain radioactive materials of natural origin such as uranium and radium and thus generate radon. These materials have sufficient permeability to release the radon generated within them to the outer medium (Abbady et al. 2007). It was found that the rate of radon

emission changes with the environmental conditions, the most important of which are humidity and pressure. This is due to the effect of moisture and pressure on the reflux of the radon atom resulting from the radioactive decay of radium (Al-Saif 2009). There are many methods of measuring radon concentration in environmental models.

Solid-state nuclear trace reagents are one of these methods (Obed et al. 2011). Numerous studies have proven that the CR - 39 nuclear trace detector is the most sensitive and can record the effects resulting from protons, even those with low energy, neutrons, alpha minutes, heavy ions, etc. (Al-Khateeb et al. 2012), and it is one of the best detectors recorded for nuclear effects because of its advantage. It is characterized by high sensitivity to radiation, high optical transparency, high analytical power, as well as high uniformity and symmetry (Yamauchi et al. 2003).

MATERIALS AND METHODS

The study was conducted inside the buildings of the College of Education - Al-Qadisiyah University- Iraq. Due to the absence of a previous study to determine the concentrations of radon gas, the study included exposing trace reagents to 22 sites distributed where different rooms from each building were chosen based on where students, employees, and professors spend long periods, as well as places with limited or no ventilation because building materials are one of the

most important factors affecting radon gas concentrations after soil. The reagents were distributed in many buildings, which are listed in (Fig .1 and Table 1).

The radioactive trace detectors CR-39 (Columbia Resin-39) with a thickness of 500µ (Tasl Company, UK) were carefully cut with a very sharp cutter with an approximate area of (1 1) cm^2, as shown Fig. 2. By fastening the detectors with a piece of sponge with a thickness of (1.5 cm) and suspending them in the places recorded, we were able to obtain the concentration of radon gas (Table (1), Fig. 3). The detectors were suspended at a height of 150 cm for a month, after that it was removed from the measurement site. We notice that when alpha particles resulting from the decomposition of radon gas fall on these plastic reagents, they create traces on them that are not visible to the naked eye, so these reagents are subjected to chemical treatment with NaOH.

A specific concentration (6.25 mole.L^{-1}) was heated at (600°C) for 6 h until alpha particle traces appeared and could be detected using optical microscopy with the proper magnification force (400X). The College of Education, Al-Qadisiyah University deployed 22 detectors in rooms, labs, and classrooms, with two rooms from each building, after which they were collected and prepared for the scraping process.

CALCULATION

After preparing the nuclear trace detectors (CR-39) for measurement, the average number of N$_{avg}$ traces formed was calculated using an optical microscope to then calculate the density of the traces in units (Track.mm^{-2}) from the following equation (Aswood et al. 2017, Al-Hamzawi et al. 2019):

$$\rho = \frac{N_{avg}}{A}. \qquad \qquad ...(1)$$

Where A is the area of a square and is equal to 0.07 mm^2.

Then the radon concentration was measured in the surrounding air unit (Bq.m^{-3}), where the radon concentration

Table 1: Coordinates the study area.

No.	Location	Sample	Coordinates X	Coordinates Y
1	Student Club for the College of Education	SC1	32°0'9.6228"	44°52'57.2988"
2	Student Club for the College of Education	SC2	32°0'9.2736"	44°52'57.6544"
3	Library	Li1	32°0'10.2744"	44°52'55.7796"
4	Library	Li2	32°0'10.6236"	44°52'56.4132"
5	Department of Psychological and Educational Sciences	PE1	32°0'11.4408"	44°52'54.2136"
6	Department of Psychological and Educational Sciences	PE2	32°0'12.4092"	44°52'51.7008"
7	Department of Physics	PH1	32°0'10.71"	44°52'53.8392"
8	Department of Physics	PH2	32°0'11.5956"	44°52'51.0996"
9	Department of Mathematics	Ma1	32°0'9.54"	44°52'53.6016"
10	Department of Mathematics	Ma2	32°0'10.3716"	44°52'50.5452"
11	Department of Arabic Language	AR1	32°0'8.1396"	44°52'50.8024"
12	Department of Arabic Language	AR2	32°0'8.7876"	44°52'49.7892"
13	Department of Biology	Bi1	32°0'6.2028"	44°52'48.6192"
14	Department of Biology	Bi2	32°0'5.5656"	44°52'47.3844"
15	Department of History	Hi1	32°0'4.1544"	44°52'47.856"
16	Department of History	Hi2	32°0'3.2076"	44°52'46.5312"
17	Deanship of the College of Education	DC1	32°0'1.3032"	44°52'51.7404"
18	Deanship of the College of Education	DC2	32°0'0.9396"	44°52'52.5072"
19	Department of English Language	EN1	32°0'2.8728"	44°52'56.2188"
20	Department of English Language	EN2	32°0'3.42"	44°52'54.9048"
21	Department of Chemistry	CH1	32°0'6.7536"	44°53'0.3264"
22	Department of Chemistry	CH2	32°0'6.282"	44°52'58.4364"

Fig. 1: Map of the selected buildings and the distribution of reagents in them.

in buildings was determined by the following equation (Obayes 2020, Oudah & Al-Hamzawi 2020):

$$C_{Rn}(\text{Bq}.\,m^{-3}) = \frac{1}{k}\left(\frac{\rho}{t}\right) \qquad \ldots(2)$$

Where (k) represents a calibration factor of the detector and its value (0.169 Track.m^{-3}/Bq.day.mm^{-2}), (t) represents exposure time (30 d) .

RESULTS AND DISCUSSION

After distributing the nuclear detectors (CR-39) in the

Fig. 2: CR-39 detector.

Fig. 3: Method of deployment of detectors.

buildings of the College of Education, Al-Qadisiyah University- Iraq for 30 days, the detectors were collected and chemically skimmed off using the basal solution. The prepared (NaOH) at a caliber of (6.25) for 6 h and the density of traces were calculated using a light microscope, according to the concentration of radon (Rn), using equation (2), where the results of the radon gas concentrations and the intensity of the traces are shown in Table 2. Inside the buildings, the lowest value of radon concentration in the air was recorded for the Student Club, which is around (106±20.8) Bq.m^{-3} in the SC1 model, while the highest value was (119.5±21.6) Bq.m^{-3} in the SC2 model. As for the College Library, the lowest value for radon concentration was recorded in air and was (96.9±27.7) Bq.m^{-3} in the Li1 model, while the highest value was (120.3±14.6) Bq.m^{-3} in the Li2 model. The lowest value for radon concentration in the air for the Department of Psychological and Educational Sciences was (121.4±16.8) Bq.m^{-3} in the PE2 model, while the highest value was (140.3±17.9) Bq.m^{-3} in the model PE1. As for the Department of Physics, the lowest value of the radon concentration in the air was (264.9±32.0) Bq.m^{-3} in the PH2 model, while the highest value was 267.4±30.9) Bq.m^{-3} in the PH1 model. The lowest value for radon concentrations in the air for the Department of Mathematics was (136.9±27.9) Bq.m^{-3} in the Ma2 model, the highest value was (144.6±27.6) Bq.m^{-3} in the Ma1 model. The lowest value for radon concentration in the air for the Department of Arabic Language was (101.4±23.9) Bq.m^{-3} in the AR2 model and the highest value was (111.0±15.3) Bq.m^{-3} in the AR1 model. The lowest value for radon concentration in the air for the Department of Biology was (248.3±33.9) Bq.m^{-3} in the Bi2 model. The highest value was (259.2±31.1) Bq.m^{-3} in the Bi1 model. The lowest value for the Department of History was (186.8±18.8) Bq.m^{-3} in the Hi1 model. The highest value was (193.0±23.3)

Table 2: The intensity of effects and the concentration of radon using the CR-39 detector in the buildings of the College of Education, Al-Qadisiyah University.

No.	Sample	Track number [Track.mm^{-2}]	C_{Rn} [Bq.m^{-3}]
1	SC1	540.0	106.5± 20.8
2	SC2	605.7	119.5±21.6
3	Li1	491.4	96.9±27.7
4	Li2	610.0	120.3±14.6
5	PE1	711.4	140.3±17.9
6	PE2	615.7	121.4±16.8
7	PH1	1355.7	267.4±30.9
8	PH2	1342.9	264.9±32.0
9	Ma1	732.9	144.6±27.6
10	Ma2	694.3	136.9±27.9
11	AR1	562.9	111.0± 15.3
12	AR2	514.3	101.4±23.9
13	Bi1	1314.3	259.2±31.1
14	Bi2	1258.6	248.3±33.9
15	Hi1	947.1	186.8±18.8
16	Hi2	978.6	193.0±23.3
17	DC1	697.1	137.5±23.0
18	DC2	647.1	127.6±22.6
19	EN1	804.3	158.6±25.4
20	EN2	847.1	167.1±17.6
21	CH1	1371.4	270.5±32.9
22	CH2	1125.7	222.0±35.5
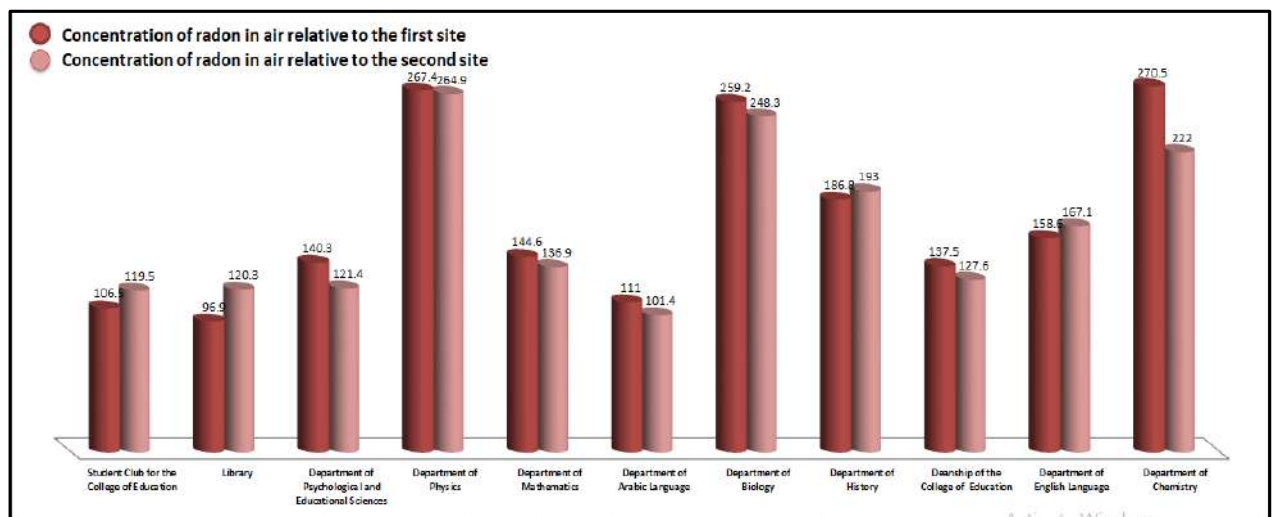
Fig. 4: Radon concentration levels inside the buildings of the College of Education, University of Al-Qadisiyah using CR-39 detector.
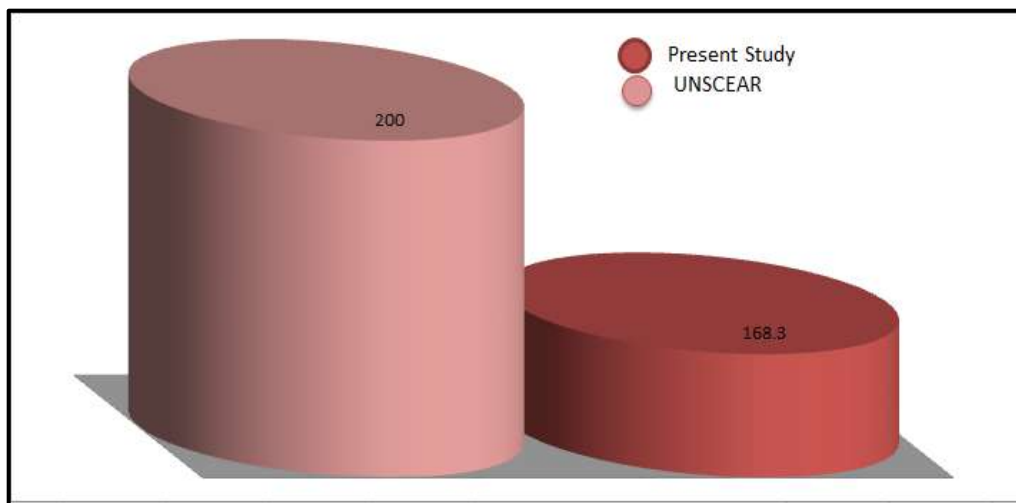
Fig. 5: Comparison of the radon concentration value of the current study with the value recommended by the International Committee for Radiation Protection.

$Bq.m^{-3}$ in the Hi2 model. The lowest value for the building of the College of Education was (127.6 ± 22.6) $Bq.m^{-3}$ in the model DC2, while the highest value was (137.5 ± 23.0) $Bq.m^{-3}$ in the model DC1. The lowest value for the Department of English Language was (158.6 ± 25.4) $Bq.m^{-3}$ in the model EN1 and the highest value (167.1 ± 17.6) $Bq.m^{-3}$ in the model EN2. The lowest value for radon concentration in the air for the Department of Chemistry was (222.0 ± 35.5) $Bq.m^{-3}$ in the model CH2 and the highest value was (270.5 ± 32.9) $Bq.m^{-3}$ in the model CH1. Fig. 4 shows the highest and lowest radon concentration value for the same site, and Fig. 5 shows a comparison between the current study and the internationally accepted limit for radon concentration by the International Committee for Radiation Protection.

CONCLUSION

Through the results obtained for the radon concentrations recorded using the solid-state nuclear trace detector CR-39, we conclude that these results were within the acceptable level or less than the acceptable level recorded by (ICRP 2020) which is equal to (200-300) $Bq.m^{-3}$ (UNSCEAR 1986). Except for the Departments of Physics, Chemistry, and Life Sciences, all of the results are within the permitted range, albeit at high concentrations. As a result, we conclude that the sites that recorded results near to permissible values, owing to the fact that they are buildings with poor ventilation or the nature of the building materials used in them. Covering the walls with materials that can limit the spread of radon gas, as well as constructing a ventilation system to increase ventilation.

REFERENCES

Abbady, A., El-Arabi, A.M., Abbady, A.E. and Taha, S. 2007. Gamma-Ray Measurements of Natural Radioactivity in Cultivated And Reclaimed Soil, Upper Egypt. VIII Radiation Physics & Protection Conference, 13-15 November 2006, Beni Sueif-Fayoum, Egypt, pp. 1-9

Al-Hamzawi, A.A., Tawfiq, N.F., Aswood, M.S. and Najim, F.A. 2019. Determination of radon concentrations near mobile towers in selected cities of Babylon governorate, Iraq. J. Phys. Conf. Series, 1234(1): 12026.

Al-Khateeb, H.M., Al-Qudah, A.A., Alzoubi, F.Y., Alqadi, M.K. and Aljarrah, K.M. 2012. Radon concentration and radon effective dose rate in dwellings of some villages in the district of Ajloun, Jordan. Appl. Radiat. Isotopes, 70(8): 1579-1582.

Al-Saif, A.S. 2009. Radioecological Aspects of Hail Region: Behavior of Some Radionuclides in soil. M.sc. Thesis, College of Science, King Saud University, KSA

Aswood, M.S., Jaafar, M.S. and Salih, N. 2017. Estimation of radon concentration in soil samples from Cameron Highlands, Malaysia. Int. J. Sci. Technol. Soc., 5(1): 9-12.

Matelsky, I. 1968. Non-Ionizing Radiations. General Electric Co., Cleveland.

Nougadère, A., Merlo, M., Héraud, F., Réty, J., Truchot, E., Vial, G. and Leblanc, J.C. 2014. How dietary risk assessment can guide risk management and food monitoring programs: The approach and results of the French Observatory on Pesticide Residues (ANSES/ORP). Food Control, 41: 32-48.

Obayes, K.H. 2020. Measurement of the radon concentration in dust for some small side areas of Diwaniyah City by using nuclear impact detector CR-39. J. Phys. Conf. Series, 1664(1): 12013.

Obed, R.I., Ademola, A.K., Vascotto, M. and Giannini, G. 2011. Radon measurements by nuclear track detectors in secondary schools in

Oke-Ogun region, Nigeria. J. Environ. Radioact., 102(11): 1012-1017.

Oudah, O.N. and Al-Hamzawi, A.A. 2020. Measurement of radon concentrations in mineral water of Iraqi local markets using RAD7 technique. Nature Environ. Pollut. Technol., 19(5): 1973-1976.

United Nations Scientific Committee on the Effects of Atomic Radiation (UNSCEAR). 1986.. Genetic and somatic effects of ionizing radiation.

UNSCEAR, New York

Wehr, R.M., Richards, J.A. and Adair, T.W. 1984. Physics of the Atom. Addison Wesley Pub. Co., Boston.

Yamauchi, T., El-Rahmany, A., Mineyama, D., Nakai, H. and Oda, K. (2003). Surface layer in CR-39 plastic track detector where the bulk etch rate is enhanced. Radiat. Meas., 37(2): 119-125.

A Comparative Study on Color Removal From Textile Industry Effluent Using Shrimp and Crab Shell Chitosan

C. Angel Mary and R. Leena†

Department of Zoology and Research Centre, Scott Christian College (Autonomous), Affiliated to Manonmanium Sundaranar University, Tirunelveli-627012, T.N., India

†Corresponding author: R. Leena; leena@scottchristian.org

ABSTRACT

Effluent from the textile industry is a major source of water pollution. Textile effluents contain a high amount of color, turbidity, BOD, and COD, which are highly toxic and affect aquatic organisms as well as human beings. Physical and chemical treatments of these effluents are difficult and costly. Adsorption is an effective method to treat textile industry effluent. In the present study, chitosan is selected as an adsorbent, derived from the exoskeleton of marine crustaceans like shrimp and crab by chemical processing. The color was removed using chitosan from shrimp and crab shells separately. On the sixth day of treatment, shrimp shell chitosan removed 100% of color from textile industry effluent and proved to be a better adsorbent.

INTRODUCTION

In India, water pollution is a growing environmental problem because nearly 70 percent of its surface water resources are already polluted and a huge percentage of groundwater reserves are contaminated by biological, toxic, organic, and inorganic pollutants. In many cases, these sources have been rendered unsafe not only for human consumption but also for other organisms in the environment and other activities such as irrigation and industrial needs. In 1995, the Central Pollution Control Board (CPCB) has identified 18 major rivers in India as severely polluted. Every day, over 600 people in India die as a result of water pollution (Lakshmi 2014).

One of the largest water pollution-causing industries in the world is the textile industry. The textile industry is one of the oldest as well as most important industries in the Indian economy. Factors that make India shine in the textile industry are low cost, skilled manpower, availability of cheap raw materials, availability of numerous varieties in cotton fiber, a big and potential national and international market, and independent textile industry (Dey & Islam 2015).

More than 80,000 tons of reactive dyes are produced and consumed each year, this conforms to the estimate of total pollution caused by their use. The dye bath has a very high salt concentration and is heavily colored. Textile effluent is characterized by a high value of suspended solids, dissolved organic matters, chemical oxygen demand, biological oxygen demand, color, and turbidity. Normally color is noticeable at a dye concentration higher than 1 mg.L^{-1}, and an average concentration of 300 mg.L^{-1} has been reported in effluents from the textile manufacturing process (O'Neill et al. 1999, Goncalves et al. 2000).

The most widely adopted methods for removing color from wastewater include physico-chemical and biological methods, such as flocculation, coagulation, precipitation, adsorption, membrane filtration, electrochemical techniques, ozonation, and microbial decolorization (Sotelo et al. 2002, Chen et al. 2003). Among the various techniques of pollutant removal, adsorption is an effective and useful process because of its low cost, easy availability to treat dyes in a more concentrated form (Saad et al. 2007). Adsorption techniques for wastewater treatment are becoming more popular in recent years due to their efficiency in the removal of pollutants.

Chitosan is derived from chitin, which is naturally found in the exoskeleton of crustaceans, insects, and some fungi. Class Crustacea is the largest group of marine arthropods comprising shrimps, crabs, lobsters, etc. Chitin is the second most abundant natural polymer in the world, functions

as a natural structural polysaccharide, and is composed of glucosamine and N-acetyl glucosamine units linked by β (1-4) glycosidic bonds. Worldwide over 39000 tons of chitin are obtained from shellfish annually. Chitosan has been suggested as a good adsorbent to remove impurities from wastewater, used as a natural seed treatment and plant growth enhancer, as well as bio-pesticide. Shrimp and crab shell chitosan categorized as solid animal waste can be used as a bio adsorbent for the removal of color from textile industrial effluent. In the present work, the ability of chitosan prepared from shrimp and crab shell exoskeleton to decolorize an actual textile industrial effluent is demonstrated.

MATERIALS AND METHODS

Collection of shrimp and crab shell: The shrimp and crab exoskeleton were collected from a seafood processing unit in Colachel, Kanyakumari district, Tamil Nadu, India.

Pre-conditioning: The collected shrimp and crab shells were washed separately 5-6 times by distilled water, and the samples were dried under sunlight for 24- 48 hours and stored in an airtight container until future use.

Preparation of chitosan

*Processing of chitin***:** The shrimp and crab shells were separately allowed to soak in 0.05 M acetic acid solution for 24 h. Then the shells were washed thoroughly with water and dried to remove excess water.

*Demineralization***:** The dried shells were demineralized using 0.68 M HCL (1:10 w/v) at ambient temperature (approximately 30°C) for 6 h. The residue was washed with distilled water until pH in the range of 6.5 -7.5 was obtained and then the residue was dried.

*Deproteinization***:** The demineralized shrimp and crab shells were deproteinized using 0.62 M NaOH solution (1:10 w.v^{-1}) at ambient temperature (approximately 30°C) for 16 h. The residue was washed thoroughly with water followed by distilled water until pH in the range of 6.5 -7.5 was obtained. The chitin was dried, ground, and screened with a 150 μm sieve.

*Deacetylation***:** The chitin obtained from the above process was deacetylated in 25 M and NaOH (1:10 w.v^{-1}) for 20 h at 65°C. After deacetylation, the chitosan was washed thoroughly with water followed by distilled water until pH in the range of 6.5 -7.5 was obtained.

Collection of textile effluent: The textile effluent was collected from the textile industry in Tirupur. The textile effluent was collected from the discharge tank of the textile industry in a sterile plastic can and transported immediately to the laboratory stored in a dark environment until further analysis.

Adsorption experiment: In the first set of experiments, 0.5 g of shrimp shell chitosan was added to varying concentrations (30%, 35%, 40%, 45%, and 50%.) of the textile industrial effluent in 250 mL conical flasks. In the second set, 0.5 g of crab shell chitosan was added to each of the concentrations respectively.

Determination of OD: Samples were withdrawn on the zero-day and at 24 h interval and the OD of the culture supernatant was estimated. The percentage decolorization was calculated using the following formula,

$$\% \text{ Dye Decolorization (DD)} = \frac{OD\,(Zero\,day) - OD\,(Sample)}{OD\,(Zero\,day)} \times 100$$

Toxicity bio-assay: Adult guppy fish (*Poecilia reticulata*) were collected from a private fish farm in Thickanamcode. They were kept in aerated tanks for 2 weeks and fed with standard pelleted fish feed to acclimatize them to laboratory conditions.10 healthy fishes of the same size were selected for the toxicological studies. These fishes were introduced into 250 mL cups which had the simulated effluent at varying concentrations ranging from 10% to 100%. The mortality was recorded for 96 h after exposure. The percentage mortality was calculated using Abbot's formula.

$$\text{Corrected mortality} \% = \frac{\% \, living \, in \, control - \% \, living \, in \, treatment}{\% \, living \, in \, control} \times 100$$

Toxicity bioassay was carried out for the textile industrial effluent both before and after treatment using crab and shrimp shell chitosan.

HPLC analysis: The HPLC analysis was carried out in Shimadzu LC-10AT VP with a C18 column (250 mm ×4.6 mm). Samples were prepared by dissolving the effluent with 1:1 dilution with distilled water as untreated and effluent with chitosan from shrimp and crab as treated samples. It was sonicated for complete dissolution and equilibrated at room temperature. The run time was 65 min, mobile phase used was methanol: water at the flow rate of 1 mL.min^{-1} with a 0.02 μl injection. The detection was performed with a D2 lamp at 224 nm wavelength. SPINCHROM software was used for integration to find peak area and percentage of the injected samples.

RESULTS

Considering decolorization of textile effluent using shrimp shell, 100% decolorization was attained for 45% and 50% diluted effluents on the twelfth day of treatment (Table 1).

Crab shell chitosan at 40% concentration showed maximum decolorization (68.30%) on the 6[th]day (Table 2). Probit analysis of toxicity response of the guppy fish, *P. reticulate,* exposed to the textile effluent was used to find out the LC$_{50}$

Table 1: Percentage decolorization in textile effluent treated with shrimp shell chitosan.

Days of treatment	Concentration of textile effluent				
	50%	45%	40%	35%	30%
0	0	0	0	0	0
2	33.57	36.57	70.84	100	100
4	46.85	56.72	84.11	–	–
6	80.42	80.88	100	–	–
8	90.57	90.51	–	–	–
10	92.85	97.70	–	–	–
12	100	100	–	–	–
14	–	–	–	–	–
16	–	–	–	–	–
18	–	–	–	–	–
20	–	–	–	–	–

Table 2: Percentage decolorization in textile effluent treated with crab shell chitosan.

Days of treatment	Concentration of textile effluent				
	50%	45%	40%	35%	30%
0	0	0	0	0	0
2	37.88	35.43	50.15	55.86	61.13
4	55.24	50.44	62.00	67.39	100
6	56.48	55.19	68.30	100	–
8	58.28	59.05	73.66	–	–
10	61.89	60.46	79.31	–	–
12	66.17	66.75	84.82	–	–
14	68.43	69.31	100	–	–
16	72.94	73.04	–	–	–
18	74.85	80.35	–	–	–
20	79.25	83.05	–	–	–

Table 3: Mortality response of *Poeicilia reticulata* exposed to textile effluent.

Concentration (mL)	Hours of exposure			
	24	48	72	96
30%	-	-	-	-
35%	-	-	10	-
40%	-	20	30	50
45%	30	40	60	-
50%	40	60	90	100

N= 10

values (Tables 3 and 4). After 72 h of exposure, 90% mortality of the fish was recorded at 50% dye concentration. The LC_{50} value was 42.730, LCL was 0.204, and UCL was

0.219. The X and Y values were 1.629 and 4.981 respectively with a *b* value of 16.278. After 96 h of exposure, 100% mortality of the fish was recorded at 50% dye concentration. The LC_{50}, LCL, and UCL values were 39.984, 0.195, and 0.213 respectively. The X and Y values were 1.612 and 5.253 respectively with a *b* value of 24.049.

Probit analysis of toxicity response of the guppy fish *P. reticulata* exposed to textile effluent treated with shrimp shell chitosan was used to find out the LC_{50} values. The toxicity response of the fish under different concentrations of the effluent for different hours of exposure was studied. After 72 h of exposure, 20% mortality of the fish was recorded at 50% dye concentration. The X and Y values were 1.680 and 3.985 respectively with a *b* value of 9.623. After 96 h of exposure, 20% mortality of the fish was recorded at 50% dye concentration. The X and Y values were 1.680 and 3.985 and respectively with a *b* value of 9.623 (Tables 5 and 6).

Probit analysis of toxicity response of the guppy fish *P. reticulata* exposed to textile effluent treated with crab shell chitosan was used to find out the LC_{50} values. The toxicity response of the fish under different concentrations of the dye for different hours of exposure was analyzed and given in Tables 7 and 8. After 72 h of exposure, 20% mortality of the fish was recorded at 50% dye concentration. The X and Y were 1.680 and 3.985 respectively with a *b* value of

Table 4: nhr LC_{50} and confidence intervals for *Poecilia reticulata* exposed to textile effluent (untreated).

Sl. No	Hours	LCL	LC_{50}	UCL
1	24	0.162	55.269	0.307
2	48	0.211	47.454	0.236
3	72	0.204	42.730	0.219
4	96	0.195	39.984	0.213

Table 5: Mortality response of *Poeicilia reticulata* exposed to textile effluent treated with shrimp shell chitosan.

Concentration (mL)	Hours of exposure			
	24	48	72	96
30%	-	-	-	-
35%	-	-	-	-
40%	-	-	-	-
45%	-	-	-	10
50%	-	-	10	20

Table 6: nhr LC_{50} and confidence intervals for *Poecilia reticulata* exposed to textile effluent treated with shrimp shell chitosan.

Sl. No	Hours	LCL	LC_{50}	UCL
1	96	0.159	61.109	0.327

Table 7: Mortality response of *Poeicilia reticulata* exposed to textile effluent treated with crab shell chitosan.

Concentration (mL)	Hours of exposure			
	24	48	72	96
30%	-	-	-	-
35%	-	-	-	-
40%	-	-	-	-
45%	-	-	10	20
50%	-	10	20	30

N= 10

Table 8: nhr LC_{50} and confidence intervals for *Poecilia reticulata* exposed to textile effluent treated with crab shell chitosan.

Sl. No	Hours	LCL	LC_{50}	UCL
1	72	0.159	61.109	0.327
2	96	0.144	59.411	0.332

9.623. After 96 h of exposure, 30% mortality of the fish was recorded at 50% dye concentration. The X and Y values were 1.677 and 4.327 respectively with a *b* value of 7.000.

HPLC analysis was carried out on 50% of untreated textile effluent (control), 50% textile effluent treated with shrimp shell chitosan, and 50% of textile effluent treated with crab shell chitosan. The HPLC elution profile of untreated textile effluent (control) showed 7 peaks (Fig. 1) with retention time (RT) 0.847, 1.897, 2.140, 2.333, 2.983, 3.937 and 4.420 (Table 9). The HPLC profile of textile effluent treated with shrimp shell showed 4 peaks (Fig. 2) with RT 0.843, 2.103, 2.300, 4.390, 21.900, 27.077, 42.213, 58.320, and 64.010 (Table 10). RT 1.897, 2.983, and 3.937 did not appear in the effluent treated with shrimp shell chitosan. Textile effluent

treated with crab shell chitosan showed 7 peaks (Fig. 3) with RT of 0.863, 1.210, 1.873, 2.140, 2.300, 2.623, 4.313, 20.200, 22.337, 29.610, and 55.120 (Table 11).

The retention times vary from one to another. The textile effluent treated with crab shell chitosan and control have the same number of peaks but the RT was different. The same RT 2.983 and 5.937 did not appear in the effluent treated with crab shell chitosan. But the appearance of 2 new peaks with RT 1.210 and 2.623 in control, treated with crab shell chitosan can be assumed that there is a degradation of dye from one form to another. The elution profile obtained from the shrimp shell chitosan treated samples significantly differed from the control in terms of numbers, the height of peaks obtained and RT.

DISCUSSION

Chitosan is a natural, biodegradable bio-adsorbent polymer obtained from shrimp and crab shells that have many properties such as non-toxic, high porosity, biodegradability, biocompatibility, and adsorption. Effective utilization of these wastes significantly improves color adsorption from textile wastewater. Chitosan is used as a traditional coagulant, in wastewater treatment (Bina et al. 2014, Ariffin et al. 2009). Sobahi et al. (2014) investigated the different studies of chitosan derivatives for the separation of metal solution from textile wastewater.

In the present study, chitosan from shrimp and crab shells was used for biodegradation and detoxification of textile effluent. The shrimp shell chitosan treated dye effluent showed 100% decolorization. Similar studies were published by Kos (2016), who found that chitosan was the best decolorizer for wastewater, removing color up to 83-99% of the time.
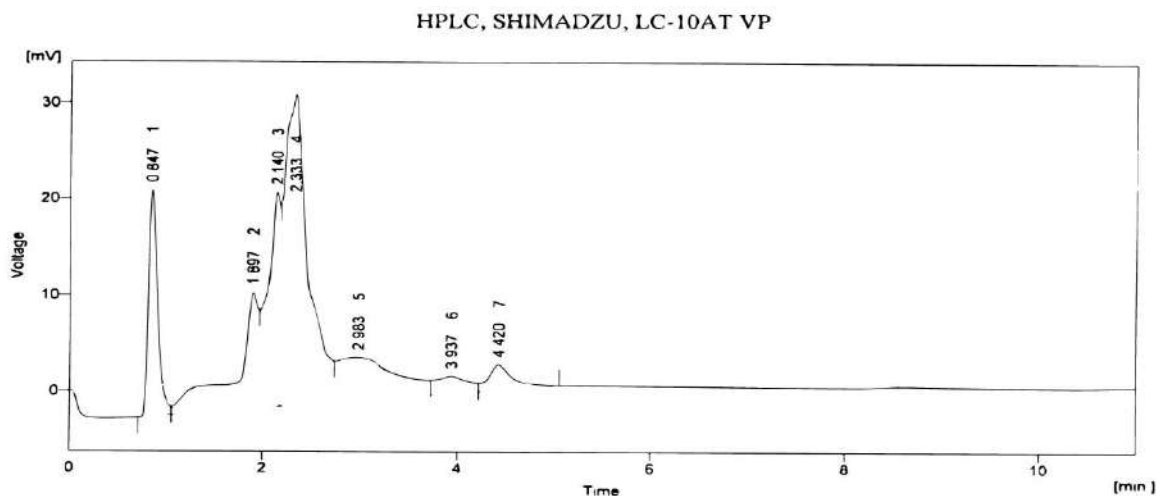

Fig. 1: HPLC chromotogram of Textile Effluent (control).

Table 9: Analytical HPLC chromatogram of untreated textile effluent (Control).

Sl.No	Retent. Time [min]	Area [mV.s^{-1}]	Height [mV]	Area [%]	Height [%]	Wo5 [min]
1	0.847	152.946	23.529	11.0	23.7	0.10
2	1.897	198.450	12.050	14.3	12.2	0.13
3	2.140	200.334	22.280	14.4	22.5	0.16
4	2.333	559.865	32.363	40.3	32.6	0.26
5	2.983	188.957	4.450	13.6	4.5	0.85
6	3.937	43.067	1.813	3.1	1.8	0.49
7	4.420	47.140	2.642	3.4	2.7	0.25
	Total	1390.760	99.127	100.0	100.0	

Similarly, Mary et al. (2019) used shrimp shell chitosan membrane for the decolorization of simulated textile effluent and reported maximum decolorization of 80.70% on the 20th day at 80% effluent concentration.

The effluent treated with crab shell chitosan gave a maximum decolorization of 68.30% as reported by Devi et al. (2012) for the effective decolorization of textile effluent. Similar observations were made by Shirsath & Shrivastava (2012) who reported that crab shell is a good adsorbent for the removal of Ponceau dyes. Similarly, Kair et al. (2019) observed that chitosan was a successful and cost-effective approach for removing color and turbidity from wastewater containing printing ink, with 15 mg chitosan in 100 mL wastewater removing up to 93% of color.

Probit analysis indicated the reduction of LC_{50} values of textile effluent treated with shrimp and crab shell chitosan. The 96 h of LC_{50} value recorded for the untreated textile effluent was 39.984 mL.dL^{-1}. The present observation is in close agreement with the findings of Raj et al. (2015) who observed that toxicity of *Poecilia reticulata* exposed to simulated effluent for 96 h and reported 100% mortality at a concentration of 60%. Similarly, Shengkani & Dhas (2014) reported LC_{50} values as 19.77 and 18.99 mL.dL^{-1} during the toxicity study of *P. reticulata,* exposed for 24 h and 96 h respectively. Likewise, Sharma et al. (2006) reported a 96-h LC50 value of 27.2 ppm for methyl red.

The 96 h LC_{50} value recorded for the shrimp shell chitosan treated textile effluent was 61.109 mL.dL^{-1} whereas the corresponding value recorded for the treated dye with the crab shell chitosan was 59.411 mL.dL^{-1}. In a related study, 96 h LC_{50} of azo dye methyl red for *P. reticulata* was recorded as 24 ppm (Kirandeep et al. 2015). The percentage mortality of fishes was found to be increased with an increase in the concentration of the effluent (Ikpi &
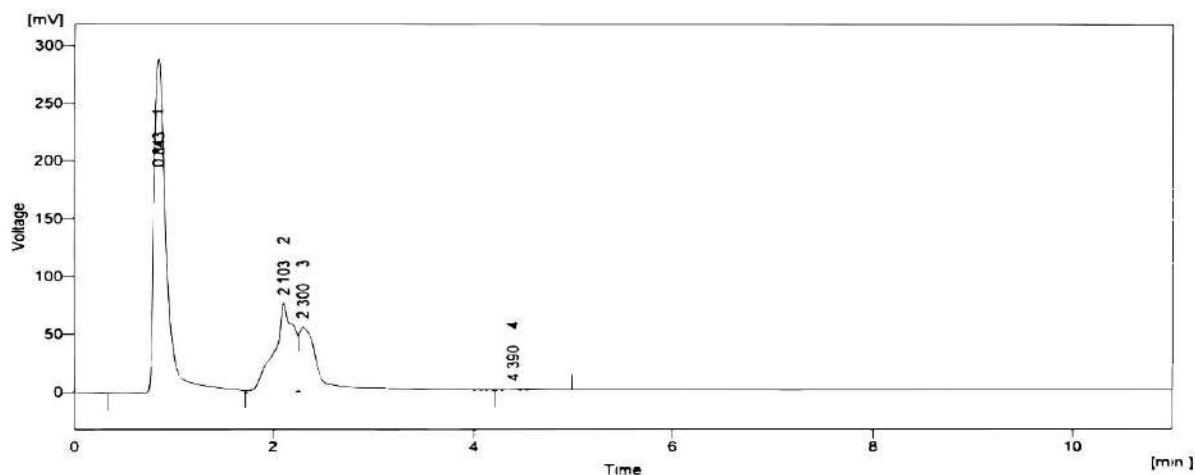
HPLC, SHIMADZU, LC-10AT VP

Fig. 2: HPLC chromatogram of textile effluent treated with shrimp shell chitosan.

C. Angel Mary and R. Leena

Table 10: Analytical HPLC chromatogram of textile effluent treated with shrimp shell chitosan.

Sl.No	Retent. Time [min]	Area [mV.s^{-1}]	Height [mV]	Area [%]	Height [%]	Wo5 [min]
1	0.843	2554.79	289.628	22.4	66.1	0.13
2	2.103	1060.75	76.458	9.3	17.5	0.22
3	2.3	818.283	56.065	7.2	12.8	0.18
4	4.39	25.605	1.288	0.2	0.3	0.32
5	21.9	181.587	0.916	1.6	0.2	1.33
6	27.077	2747.9	3.917	24.1	0.9	10.27
7	42.213	3131.42	3.563	27.5	0.8	15.13
8	58.32	563.514	2.762	4.9	0.6	3.74
9	64.01	318.971	3.247	2.8	0.7	1.57
	Total	11402.8	437.845	100	100	

Table 11: Analytical HPLC chromatogram of textile effluent treated with crab shell chitosan.

Sl.No	Retent. Time [min]	Area [mV.s^{-1}]	Height [mV]	Area [%]	Height [%]	Wo5 [min]
1	0.863	75.185	11.223	1.5	16.8	0.11
2	1.21	11.938	0.807	0.2	1.2	0.28
3	1.873	73.808	9.489	1.5	14.2	0.14
4	2.14	145.215	13.999	2.9	20.9	0.19
5	2.3	232.996	17.762	4.6	26.5	0.22
6	2.623	32.961	4.322	0.7	6.5	0.12
7	4.313	10.5	0.717	0.2	1.1	0.25
8	20.2	17.24	2.482	0.3	3.7	0.22
9	22.337	174.628	0.746	3.5	1.1	1.24
10	29.61	4207.48	3.082	83.9	4.6	26.67
11	55.12	34.401	2.278	0.7	3.4	0.44
	Total	5016.35	66.907	100	100	
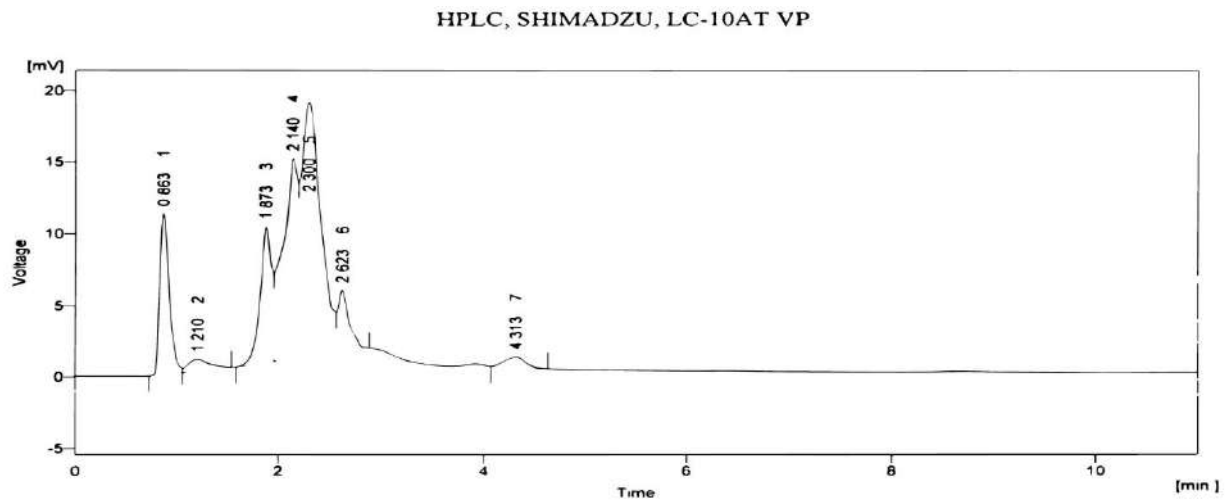
Fig. 3: HPLC chromatogram of textile effluent treated with crab shell chitosan.

Offem 2013). Moreover, the mortality was also directly proportional to the increase in time of exposure to the effluent. Similar observations were made by Angelin et al. (2015) when *P. reticulata* was exposed to chrome plating industry effluent. This toxicity study indicates that chitosan from shrimp and crab shells were good adsorbents and detoxification agents for the removal of the toxins and pollutants present in water.

The HPLC analysis also confirmed the biodegradation of textile effluent. The HPLC elution profile of untreated textile effluent showed 7 peaks, while the shrimp and crab shell chitosan treated sample showed 4 and 7 peaks respectively. The variance in the number of peaks, the height of peaks, and retention time may be assumed as there is biodegradation. In a related study, Raj et al. (2012) obtained 3 peaks with RT 1.98, 2.18, and 2.39 in the HPLC profile of Congo red dye treated with bacteria *Hafnia alvei*. The retention times vary from one to another. The results agree with the findings of Ilavarasi et al. (2019) who attained 5 peaks with RT 2.800, 2.953, 3.990, 4.790, and 5.437 in the HPLC profile of textile dye treated with chitosan. The disintegration of peaks and the different retention times confirmed the degradation of the effluent.

CONCLUSION

When comparing the shrimp and crab shell chitosan for the textile wastewater treatment, shrimp shell chitosan seems to be an efficient and better bio adsorbent for the decolorization and detoxification of textile wastewater. It could be used in water purification plants all over the world and the water purification filters can be modified based on the chitin materials as it is a good alternative for activated carbon.

REFERENCES

Angelin, A., Jones, R.D.S. and Das, S.S.M. 2015. Investigation of acute toxicity and the effect of chrome plating industry effluent on the behavior of the guppy (*Poecila reticulata*). Euro. J. Biotechnol. Biosci., 3(9): 01-05.

Ariffin, M., Hassan, M.A.A., Li, T.P. and Noor, Z.Z. 2009. Coagulation and flocculation treatment of wastewater in the textile industry using chitosan. J. Chem. Natural Resour. Eng., 4(1): 43-53.

Chen, G., Lei, L., Hu, X. and Lock, P. 2003. Kinetic study into the wet air oxidation of printing and dyeing wastewater. Sep. Purif. Technol., 31(1): 71-76.

Devi, G.M., Hasmi, A.S.S.Z. and Sekher, C.G. 2012. Treatment of vegetable oil mill effluent using crab shell chitosan as adsorbent. Int. J. Environ. Sci. Technol., 9: 713-718.

Dey, S. and Islam, A. 2015. A review on textile wastewater characterization in Bangladesh. Resour. Environ. 5(1): 15-44.

Goncalves, I.M.C., Gomes, A., Bras, R., Ferra, M.I.A., Porter, R.S. and Amorim, M.T.P. 2000. Biological treatment of effluent-containing textile dyes. J. Color. Technol., 115(12): 393-397.

Bina, B., Ebrahimi, A. and Hesami, F. 2014. The effectiveness of chitosan as a coagulant aid in turbidity removal from water. Int. J. Environ. Health Eng., 3(1): 8.

Ikpi, G.U. and Offem, B.O. 2013. Toxicity of textile mill effluent to *Oreochromis niloticus* (Linnaeus, 1758) fingerling. Int. J. Fish. Aqua. Sci., 3(1): 71-78.

Ilavarasi, M., Surendran, A. and Thatheyus, A.J. 2019. Bio decolorization of textile dye effluent using chitosan. Spec. J. Biol. Sci., 5(1): 1-7.

Kair, K.S., Mane, K.P. and More, A. 2019. Wastewater treatment of printing ink by adsorption using chitosan. Int. J. Eng. Develop. Res., 7(3): 1-4.

Kirandeep, K., Aravinder, K. and Rajvir, K. 2015. Cytogenotoxicity of azo dye acid blue 113 to *Channa punctatus*. J. Environ. Res. Develop., 9(3): 547-554.

Kos, L. 2006. Use of chitosan for textile wastewater decolorization. Fibers. Text. East. Eur., 3(117): 130-135.

Lakshmi, V. 2014. Removal of Malachite Green Dye from Water Using Orange Peel as An Adsorbent [Thesis]. Department of Chemical Engineering, National Institute of Technology, Rourkela, Odisha, India, pp. 1-54.

Mary, C.A., Leena, R. and Raj, D.S. 2019. Synergistic effect of developed chitosan membrane and bacteria in the bioremediation and detoxification of simulated textile effluent. J. Appl. Sci. Comput. 6(4): 2454-2462.

O'Neill, C., Freda, R.H., Dennis, L.H., Nidia, D.L. and Helena, M.P. 1999. Colour in textile effluents sources, measurements, discharge contents, and simulation: A review. J. Chem. Technol. Biotechnol., 74: 1009-1018.

Raj, D.S., Leena, R. and Kamal, C.D. 2015. Toxicological and histopathological impacts of textile dyeing industry effluent on a selected teleost fish *Poeicilia reticulata*. Asian J. Pharmacol. Toxicol., 3(10): 26-30.

Raj, D.S., Prabha, J.R. and Leena, R. 2012. Analysis of bacterial degradation of azo dye congo red using HPLC. J. Ind. Pollut. Control., 28(1): 57-62.

Saad, S.A., Daud, S., Kasim, F.H. and Saleh, M.N. 2007. Dyes Removal from Aqueous Solution Chemical Treated Empty Fruit Bunch at Various pH. The International Conference of Sustainable Materials (ICoSM), Royal Park Hotel, Penang, 9-11 June 2007, ICoSM Org, pp. 297-300

Sharma, S., Sharma, S. and Sharma, K.P. 2006. Identification of a sensitive index during fish bioassay of an azo dye methyl red. J. Environ. Biol., 27(3): 551-555.

Shirsath, S.D. and Shrivastava, S.V. 2012. Removal of hazardous dye ponceau-s by using chitin: An organic bio adsorbent. Afr. J. Environ. Sci. Technol., 6(2): 115-124.

Shengkani, K. and Das, S.S.M. 2014.Toxicity of rubberwood processing effluent exposed to freshwater fish *Poeicilia reticulata*. J. Entomol. Zool. Stud., 2(6): 326-329.

Sobahi, R.A.T., Abdelal, M. and Makki, M.S.I. 2014. Chemical modification of chitosan for metal ion removal. Arab. J. Chem., 7(5): 741-746.

Sotelo, J.L. Ovejero, G., Deigado, R. and Martinez, J.A. 2002. Adsorption of lindane from water on GAC: Effect of carbon loading on kinetic behavior. Chem. Eng. J., 87(1): 111-120.

Distinguished Ni(II) Capture with Rapid and Superior Capability Using Biochar: Behavior and Mechanism

Y. Wang*, S. Zhang** and Y. Zheng*†

*Shaoxing Huaxia Printing and Dyeing Co. Ltd, Shaoxing, Zhejiang 312000, People's Republic of China
**Shaoxing Quality Technical Supervision and Testing Institute, Shaoxing, Zhejiang 312000, People's Republic of China
†Corresponding author: Y. Zheng; zhenyinhua2021@163.com

ABSTRACT

Batch experiments were used to study the interaction mechanism of Ni(II) with biochar as a function of solution pH, contact time, initial concentrations, reaction temperature, and the addition of humic compounds. The results indicate that Ni(II) can be interacted with biochar by a compound mechanism under different environmental conditions. It is suggested that outer-sphere surface complexes at low pH are transformed into inner-sphere surface complexes and surface precipitates are formed at pH 8.89 or 10.18. The combined macroscopic and microscopic insights provide additional details regarding the mobility, fate, and risk of Ni(II) in a practical aquatic environment, as well as the natural purification of metals in ecological environments.

INTRODUCTION

Toxic heavy metals are becoming an increasingly important issue in water bodies and soil remediation, because of their mobility, toxicity, and difficult biodegradation. Nickel (Ni) is one of the most widespread contaminants, especially for ecosystem stability and public health sake (Malkoc 2006). Conventional methods of Ni(II) removal include chemical redox, precipitation, ion exchange, membrane separation, filtration, and electrochemistry. Aside from these suboptimal methods, adsorption techniques are more commonly used to remove heavy metal ions from water due to their low cost, ease of availability, and high removal efficiency.

Biochar is a carbon-rich, porous solid produced by the thermal decomposition of bioenergy feedstocks (e.g., grass, crop residue, and woody biomass) and agricultural wastes (e.g., manure) with little or no available air and at moderate temperatures (Lehmann 2007). Because of the physical and chemical characterization, biochar contains different forms of amorphous carbon with abundant porosity and surface functional groups (C-O, C=O, COOH and OH, etc.), as well as minerals such as N, P, S, Ca, Mg, and K (Liu et al. 2015). More importantly, it has been increasingly reported that biochar has a strong adsorption affinity to various environmental contaminants due to the functional active sites, including heavy metals, organic compounds, and other inorganic oxyanions (Ashry et al. 2016, Wang et al. 2016a).

For example, Ashry et al. (2016) tested biochar as a material for the fixation of U^{VI} from aqueous solutions. The batch experiments showed uranium adsorption on biochar was high over a wide range of pH values. Inyang et al. (2012) also reported that biochar displayed effective removal for different heavy metals (Pb^{2+}, Cu^{2+}, Ni^{2+} and Cd^{2+}). Besides, further adsorption investigations indicated the removal was mainly attributed to oxygen-containing groups of biochars (Uchimiya et al. 2011). However, understanding the interfacial mechanism between biochar and heavy metal ions in aquatic systems is still difficult due to data limitations and spectroscopic approaches. Therefore, the main objective of our research was to provide advanced insights regarding the interaction of Ni(II) with biochar by using macroscopic experiments. A series of environmental parameters such as pH, contact time, temperature, initial concentrations, and addition of humic acid (HA) or fulvic acid (FA), was also investigated by batch experiments.

MATERIALS AND METHODS

Materials and Chemicals

Biochars were produced from the pine needle and washed with deionized water several times to remove dust. After air-dried, ground, and filtered, the obtained litters via pyrolysis at 773 K for 12 h under oxygen-limited conditions. All solutions were prepared using 18 MΩ de-ionized water

(Milli-Q Gradient, Millipore, USA). The chemicals in all experiments were purchased in analytical grade and without further purification.

Batch Adsorption and Microscopic Experiments

The adsorption procedures of Ni(II) with biochars were investigated by mixing 0.1g.L^{-1} biochars and 15.0 mg.L^{-1} of initial Ni(II) concentration. The pH value was adjusted in the range of 2.0-10.5 by adding 0.001, 0.01, or 0.1 mol.L^{-1} NaClO$_4$ solutions, because ClO$_4^-$ has little capacity to coordinate with metal ions (Cheng et al. 2015). The adsorption isotherms and thermodynamics were investigated at pH~6.5 with initial Ni(II) concentrations ranging from 5.0 to 18.0 mg.L^{-1} under the condition of 0.01 mol.L^{-1} NaClO$_4$ solutions. Then, the conical flasks with these mixtures were shaken in a thermostatic shaker for 24.0 h at 298.0 K to establish adsorption equilibrium. The samples were filtered out by a 0.45 μm membrane, the residual Ni(II) concentration in the solution was determined using a UV-vis spectrophotometer (UV-754 N shanghai, China) at 616.0 nm. The adsorption capacity of Nickel was calculated based on the initial and final aqueous concentrations. The reactive samples before and after reaction were characterized by scanning electron microscope (SEM), transmission electron

microscope (TEM), Fourier transform infrared (FTIR) spectra analysis.

Characterization Approaches

The scanning electron microscopic (SEM) images were performed on a field emission scanning electron microscope (FEI-JSM 6320F). The Fourier transformed infrared (FTIR) spectra analysis was obtained using a Nexus 670 FTIR spectrometer (Thermo Nicolet, Madison) in the 4000-400 cm-1 wavenumber. The samples were equipped with a KBr beam splitter (KBr, FTIR grade). The background spectrum of KBr was also recorded under the same conditions. The surface area, pore volume (PV), and pore size distribution were determined by N2 Brunauer-Emmett-Teller (BET) adsorption-desorption at 77 K using Micromeritics ASAP 2010 equipment. The zeta potentials of the samples were measured with a Nanosizer ZS instrument (Malvern Instrument Co., UK) at room temperature.

RESULTS AND DISCUSSION

Characterization of Biochar

The morphological structure of obtained biochar was characterized by SEM, TEM, FTIR, BET surface area, pore volume
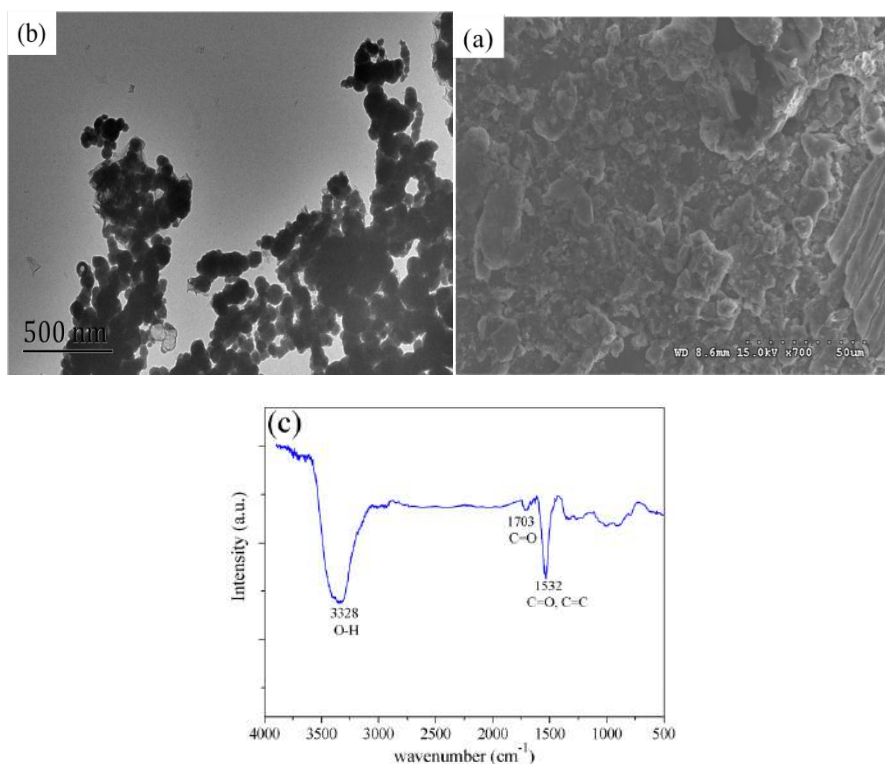
Fig. 1: The characterization of the biochar: (a) SEM; (b) TEM; (c) FTIR.

(PV), and pore size distribution (Fig. 1). The SEM image (Fig. 1a) and the high-resolution TEM image (Fig. 1b) both revealed an amorphous structure of carbon particles, indicating that the pine needles had been carbonized. FTIR spectra provided additional evidence of surface groups, as shown in Fig. 1c. The broadband at ~3328 cm^{-1} was assigned to the stretching mode of hydroxyl involved in hydrogen bonds or from interlayer water molecules, the peak that appeared at ~1703 cm^{-1} was due to C=O in the carboxyl group, and the band at 1532 cm^{-1} represented contribution from the vibration of C=O or C=C groups. Because of the large number of oxygen/carbon-containing functional groups on the surface, the adsorption capacity can be considerably increased. This is because surface OH and COOH groups of biochar interact with the metals *via* hydrogen bonding and complexation (Uchimiya et al. 2012). The value of pH at the point of zero charges (pH$_{PZC}$) for biochar was 6.5.

Effect of pH and Ionic Strength

The sorption of Ni(II) on biochars as a function of pH under different NaClO$_4$ concentrations was shown in Fig. 2. The outer-sphere surface complexation is more vulnerable to ionic strength variations, whereas the inner-sphere surface complexation with covalent bonding is unaffected by ionic strength variations (Jin et al. 2015). Besides, ClO$_4^-$ does not form complexes with the concomitant metal ions in the solution. As a result, the ionic strength impact was useful in comparing and analyzing the role of ionic strength fluctuation. As shown in Fig. 2a, the sorption capacities increase with increasing pH from 2.0 to 7.0, while revealing no significant difference for 0.001-0.1 mol.L^{-1} NaClO$_4$ concentrations, which demonstrated the inner-sphere surface complexation dominated the sorption. Correspondingly, the adsorption capacities tend to be stable and reach saturation under high alkaline conditions (herein, pH>8), which is similar to the

sorption trend of other reported adsorbents for heavy metals (Ding et al. 2016). The phenomenon is mainly attributed to the formation of hydroxide precipitates. The sorption of Ni(II) was also studied under different pH conditions in Fig. 2b. It is seen that Ni(II) sorption increases at elevated pH. Zeta potentials showed that the pH$_{ZPC}$ decreased with the increase of pH (Fig. 3), indicating the possible formation of the negatively-charged inner-sphere complexes (Pena et al. 2006).

Kinetic Study

The kinetics of Ni sorption and the impacts of silicate on Ni uptake onto biochar are shown in Fig. 4. Four different kinetic models including first-order, pseudo-second-order, intraparticle diffusion, and Elovich models are used to fit the experimental data. The equations of the models can be described as follows:

$$\ln(q_e - q_t) = \ln q_e - k_1 t$$

$$\frac{t}{q_t} = \frac{1}{k_2 q_e^2} + \frac{t}{q_e}$$

$$q_t = k_i t^{0.5}$$

$$q_t = \beta \ln(\alpha\beta) + \beta \ln t$$

Where q$_e$ and q$_t$ are the amount of adsorption of Ni(II) at equilibrium and at time t (min), k_1(min^{-1}) and k_2(min^{-1}) are the rate constant of adsorption, *ki* is the intraparticle diffusion rate (mg.g.min$^{-0.5}$), and α and β are the initial adsorption rate (mg.g.min^{-1}) and desorption constant (g.mg^{-1}).

The results of fitting experimental data are presented in Table 1. It is noticed from the correlation coefficient (R^2) that the pseudo-second-order equation is the most suitable for the description of adsorption kinetics of Ni(II) on biochar.
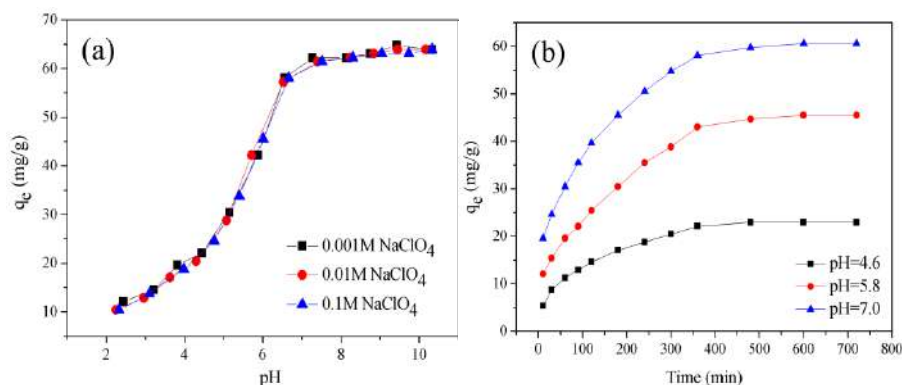

Fig. 2: Effect of ionic strength and pH: (a) Sorption of Ni(II) on biochar as a function of pH in different NaClO$_4$ concentrations; (b) Sorption of Ni(II) on biochar under various pH conditions, m.V^{-1}=0.1 g.L^{-1}, T = 293 K, C$_{(Ni)initial}$ = 15 mg.L^{-1}.

Table 1: Kinetic parameters and regression coefficients (R^2) for the four kinetic models.

pH	$q_{e,exp}$ [mg.g^{-1}]	Pseudo-first order			Pseudo-second order			Intraparticle diffusion		Elovich		
		k_1 $\times 10^{-2}$	$q_{e,cal}$	R^2	k_2 $\times 10^{-2}$	$q_{e,cal}$	R^2	k_i [mg.g.min$^{-0.5}$]	R^2	α	β	R^2
4.6	22.96	0.56	16.51	0.936	3.32	25.51	0.994	5.97	0.917	3.03	4.64	0.972
5.8	45.54	0.68	42.43	0.975	1.25	51.81	0.987	12.32	0.948	1.27	9.24	0.928
7.0	60.59	0.72	48.15	0.981	1.46	66.22	0.998	14.56	0.925	1.92	11.20	0.957

Similar results of pseudo-second-order kinetics trends in this study were observed in previous reports (Wang et al. 2016b, Zhu et al. 2016), which suggest the prevailing behavior over the whole range of the process is chemisorption. The intraparticle diffusion model is commonly used to comprehensively analyze the adsorption kinetics and to assess the importance of diffusion during the adsorption process (Guo et al. 2016). The model curves of q_t and $t^{0.5}$ have a non-linear relationship over the entire time range and can be divided into two stages without passing through the origin, indicating the mechanism for both surface adsorption as well as intraparticle diffusion.

Sorption Isotherms and Thermodynamic Analysis

Fig. 5 showed Ni(II) sorption isotherms on biochar at 293, 313, and 333K. The equation of Langmuir and Freundlich models could be expressed as follows:

Fig. 3: Zeta potentials of biochar.

$$q_e = \frac{q_m K_L C_e}{1 + K_L C_e}$$

$$q_e = K_F C_e^{\,n}$$

Where C_e is the equilibrium concentration (mg.L^{-1}) and q_m is the maximum adsorption capacity of Ni(II), K_L is the Langmuir adsorption constant (L.mg^{-1}), and K_F (L.mg^{-1}) and n are the Freundlich constant corresponding to capacity and intensity of adsorption.

Table 2 listed the relative values calculated from the two models. The experimental data are well fitted by the Langmuir model than by the Freundlich model, indicating the sorption of Ni(II) on biochar is monolayer coverage. The calculated value of maximum adsorption capacity is 76.729 mg.g^{-1}, which is higher than granular activated carbon (39.5 mg.g^{-1}) (Kadirvelu et al. 2000). Besides, the sorption isotherm increased gradually with the increase of temperatures, which is shown the promotion with the reaction temperatures in the adsorption process. The thermodynamic parameters (ΔG^0, ΔH^0, and ΔS^0) for Ni(II) sorption on biochar can be calculated from the following equation and the results are presented in Table 3:

$$G^0 \quad RT \ln K^0$$

$$\ln K^0 \quad \frac{S^0}{R} \quad \frac{H^0}{RT}$$

Where R is the ideal gas constant (8.314 J.mol.K^{-1}), K^0 is the sorption equilibrium constant, calculated by plotting $\ln K_d$ versus C_e (Fig. 6) and extrapolating the correlations of linear fits in Table 4.

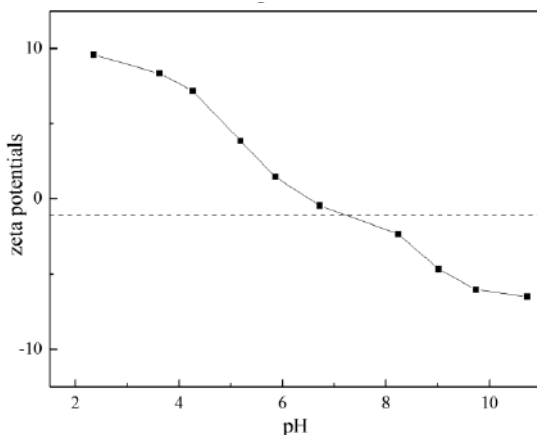Fig. 7 showed the linear relationship between $\ln K^0$ and $1/T$, and the positive standard enthalpy change (ΔH^0) value

Table 2: The parameters for Langmuir and Freundlich isotherm.

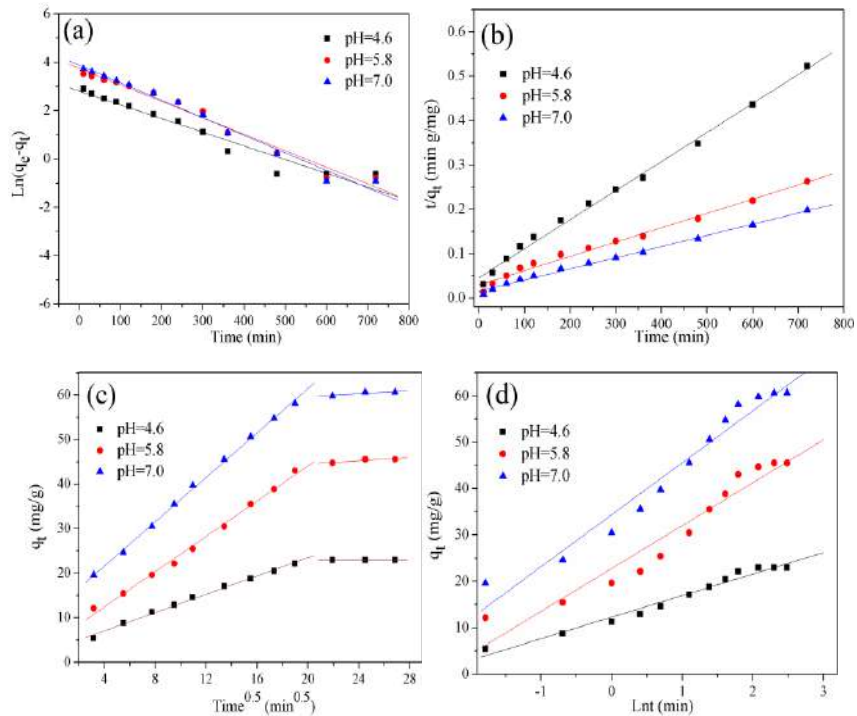| T(K)	Langmuir			Freundlich		
	q_{max}(mg.g^{-1})	b (L.mg^{-1})	R^2	K_F(mg^{1-n}L^n.g^{-1})	n	R^2
293	76.729±1.061	0.300±0. 1	0.996	23.758±0.964	0.395±0.022	0.972
313	82.298±0.849	0.497±0. 8	0.994	35.311±0.891	0.299±0.0138	0.979
333	91.439±1.103	0.716±0. 8	0.986	47.08±0.733	0.24434±0.09	0.987

Fig. 4: Kinetic studies under various pH conditions: (a) first-order kinetics model; (b) Pseudo-second-order kinetics model; (c) Intraparticle diffusion model; (d) Elovich equation model. T = 293 K, m.V^{-1}=0.1g.L^{-1}, C$_{(Ni) initial}$ = 15 mg.L^{-1}, I=0.01 M NaClO$_4$.

represents the sorption of Ni(II) on biochar is an endothermic process. The standard free energy change (ΔG^0) is negative with the positive value of the standard entropy change (ΔS^0) indicating the spontaneous nature of the treatment process.

Effect of HA and FA

In addition, natural organic matters (NOMs), including humic acid (HA) and fulvic acid (FA), contain functional groups such as carboxyl, amine, and phenolic, have also been known to strongly impact the sorption on biochars (Yang et al. 2016). Fig. 8 showed the pH dependence of Ni(II) adsorption on biochar under the condition of absence and presence of HA/FA. We can see that the removal of

Fig. 5: Sorption isotherms of Ni(II) on biochar at different temperatures. m.V^{-1}= 0.1 g.L^{-1}, pH= 6.5, I=0.01 M NaClO$_4$. The solid lines are Langmuir model simulation, and the dashed lines are Freundlich model simulation.
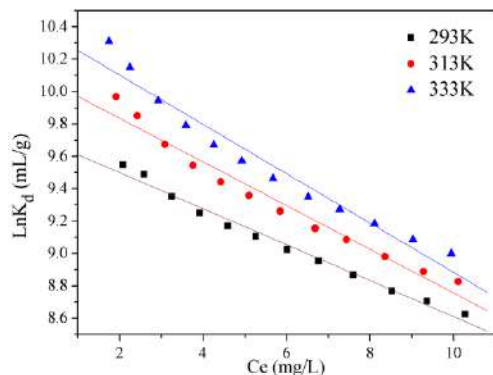
Fig. 6: Linear plots of lnK$_d$ vs C$_e$ for the sorption of Ni(II) on biochar at different temperatures. m.V^{-1}=0.1 g.L^{-1}, pH=6.5, I=0.01 M NaClO$_4$.

Table 3: Thermodynamic parameters for the sorption.

T (K)	ΔG_0 [kJ.mol^{-1}]	ΔH_0 [kJ.mol^{-1}]	ΔS_0 [J.mol.K^{-1}]
293	-23.683	13.9	128.3
313	-26.299		
333	-28.812		

Table 4: Constants of linear fit of lnKd vs. Ce (lnKd = A + BCe).

T(K)	T[^{o}C]	A	B	R
293	20	9.722±0.028	-0.111±0.0042	0.984
313	40	10.106±0.047	-0.13495±0.0075	0.967
333	60	10.407±0.062	-0.152±0.010	0.954
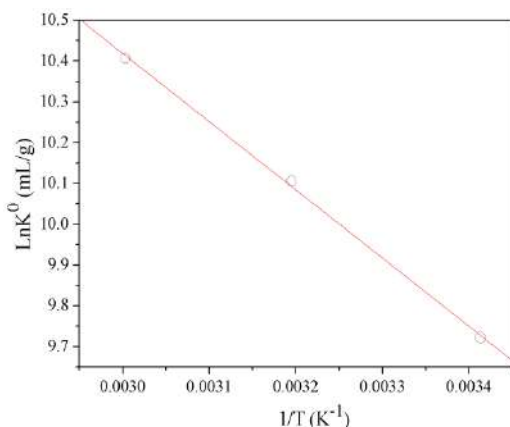
Fig. 7: Linear plot of lnK^0 vs 1/T for the sorption of Ni(II) on biochar at 293, 313, and 333K. m.V^{-1}=0.1 g.L^{-1}, pH=6.5, I=0.01 M NaClO$_4$.

Ni(II) on biochar was promoted significantly by adding HA/FA at pH<7 while inhibiting the reaction at pH>7. The NOMs have been recognized to have a strong complexation ability to metal ions by acting as a contaminant adsorbent (Uchimiya et al. 2010). As the pH rises, negatively charged HA/FA find it more difficult to bind to the negatively charged surface of the charcoal, and hence perform the opposite role. The adsorption curves for the impact of HA and FA have a comparable tendency, implying that the functional structures of HA and FA are similar (Sheng et al. 2014). Similar results are also demonstrated from the adsorption behaviors of Pb(II) on β-MnO$_2$ (Zhao et al. 2010).

Regeneration

The recycling of biochar for Ni(II) elimination was examined as a potential future practical application. Biochar was desorption tested by washing it numerous times with Milli-Q water and then drying it at 80°C for regeneration. At least six times, repeated experiments were carried out. The adsorption capacity of biochar for Ni(II) decreased slightly even after

six rounds, indicating that biochar has strong reuse qualities in Ni(II) adsorption.

CONCLUSION

Based on the preceding discussion, biochars show to be available adsorbents for heavy metal uptake while taking into account the effects of pH, contact time, temperature, starting concentrations, and humic compounds. At low pH, outer-sphere surface complexes are thought to be converted into inner-sphere surface complexes, and surface precipitates occur on the biochar surface.

REFERENCES

Ashry, A., Bailey, E.H., Chenery, S.R.N. and Young, S.D. 2016. Kinetic study of time-dependent fixation of U^{VI} on biochar. J. Hazard. Mater., 320: 55-66.
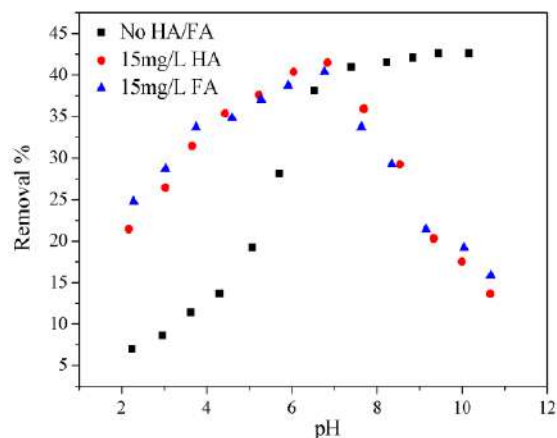
Fig. 8: Effect of HA/FA on the sorption of Ni(II). M.V^{-1}=0.1 g.L^{-1}, pH=6.5, I=0.01 M NaClO$_4$.
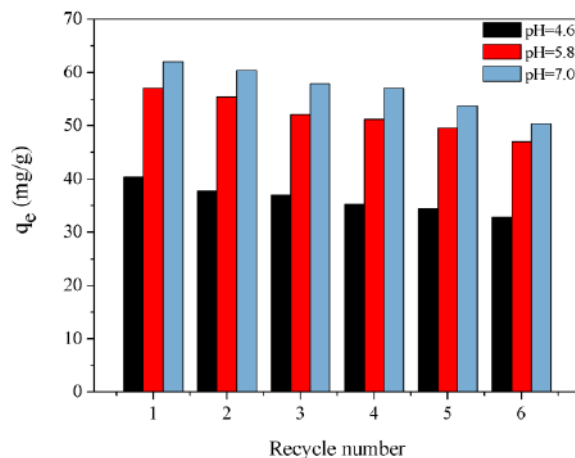
Fig. 9: Recycling of biochar for the removal of Ni(II). M.V^{-1}=0.1g.L^{-1}, pH=6.5, I=0.01M NaClO$_4$.

Cheng, W., Jin, Z., Ding, C. and Wang, M. 2015. Simultaneous sorption and reduction of U(VI) on magnetite-reduced graphene oxide composites investigated by microscopic, spectroscopic, and modeling techniques. RSC Adv., 5: 59677-59685.

Ding, C., Cheng, W., Wang, X., Wu, Z., Sun, Y., Chen, C., Wang, X. and Yu, S. 2016. Competitive sorption of Pb(II), Cu(II), and Ni(II) on carbonaceous nanofibers: A spectroscopic and modeling approach. J. Hazard. Mater., 313: 253-261.

Guo, X. Dong, H. Yang, C., Zhang, Q., Liao, C., Zha, F. and Gao, L. 2016. Application of goethite modified biochar for tylosin removal from aqueous solution. Colloids Surf. A, 502: 81-88.

Inyang, M., Gao, B., Yao, Y., Xue, Y., Zimmerman, A.R., Pullammanappallil, P. and Cao, X. 2012. Removal of heavy metals from aqueous solution by biochars derived from anaerobically digested biomass. Bioresour. Technol., 110: 50-56.

Jin, Z., Wang, X., Sun, Y., Ai, Y. and Wang, X. 2015. Adsorption of 4-n-nonylphenol and bisphenol-A on magnetic reduced graphene oxides: A combined experimental and theoretical studies. Environ. Sci. Technol., 49: 9168-9175.

Kadirvelu, K., Faur-Brasquet, C. and Le Cloirec, P. 2000. Removal of Cu(II), Pb(II), and Ni(II) by adsorption onto activated carbon cloths. Langmuir, 16: 8404-8409.

Lehmann, J. 2007. A handful of carbon. Nature, 447: 143-144.

Liu, W., Jiang, H. and Yu, H. 2015. Development of biochar-based functional materials: Toward a sustainable platform carbon material. Chem. Rev., 115: 12251-12285.

Malkoc, E. 2006. Ni(II) removal from aqueous solutions using cone biomass of thuja orientalis. J. Hazard. Mater., 137: 899-908.

Pena, M., Meng, X., Korfiatis, G.P. and Jing, C. 2006. Adsorption mech-anism of arsenic on nanocrystalline titanium dioxide. Environ. Sci. Technol., 40: 1257-1262.

Sheng, G., Ye, L., Li, Y., Dong, H., Li, H., Gao, X. and Huang, Y. 2014. EXAFS study of the interfacial interaction of nickel(II) on titanate nanotubes: role of contact time, pH, and humic substances. Chem. Eng., J. 248: 71-78.

Uchimiya, M., Lima, I.M., Klasson, K.T. and Wartelle, L.H. 2010. Contaminant immobilization and nutrient release by biochar soil amendment: roles of natural organic matter. Chemosphere, 80: 935-940.

Uchimiya, M., Wartelle, L.H., Klasson, K.T., Fortier, C.A. and Lima, I.M. 2011. Influence of pyrolysis temperature on biochar property and function as a heavy metal sorbent in soil. J. Agric. Food Chem., 59: 2501-2510.

Uchimiya, M., Bannon, D.I. and Wartelle, L.H. 2012. Retention of heavy metals by carboxyl functional groups of biochars in small arms ranges soil. J. Agric. Food Chem., 60: 1798-1809.

Wang, Z., Shen, D., Shen, F. and Li, T. 2016a. Phosphate adsorption on lanthanum-loaded biochar. Chemosphere, 150: 1-7.

Wang, Y., Lu, H., Liu, Y. and Yang, S. 2016b. Ammonium citrate-modified biochar: an adsorbent for La(III) ions from aqueous solution. Colloids Surf. A, 509: 550-563.

Yang, Z., Kappler, A. and Jiang, J. 2016. Reducing capacities and distribution of redox-active functional groups in low molecular weight fractions of humic acids. Environ. Sci. Technol., 50: 12105-12113.

Zhao, D., Yang, X., Zhang, H., Chen, C. and Wang, X. 2010. Effect of environmental conditions on Pb(II) adsorption on β-MnO_2. Chem. Eng. J., 164: 49-55.

Zhu, N., Yan, T., Qiao, J. and Cao, H. 2016. Adsorption of arsenic, phosphorus, and chromium by bismuth impregnated biochar: Adsorption mechanism and depleted adsorbent utilization. Chemosphere, 164: 32-40.

Prediction of PM$_{2.5}$ Over Hyderabad Using Deep Learning Technique

P. Vinay Kumar*, M. C. Ajay Kumar*, B. Anil Kumar** and P. Venkateswara Rao***†

*Department of Physics, Aurora's Technological and Research Institute, Hyderabad, India
**Department of Mechanical Engineering, Aurora's Technological and Research Institute, Hyderabad, India
***Department of Physics, Vasavi College of Engineering, Hyderabad, India
†Corresponding author: P. Venkateswara Rao; kishansetty@gmail.com

ABSTRACT

Urbanization and Industrialization during the last few decades have increased air pollution causing harm to human health. Air pollution in metro cities turns out to be a serious environmental problem, especially in developing countries like India. The major environmental challenge is, to predict accurate air quality from pollutants. Envisaging air quality from pollutants like PM$_{2.5}$, using the latest deep learning technique (LSTM timer series) has turned out to be a significant research area. The primary goal of this research paper is to forecast near-time pollution using the LSTM time series multivariate regression technique. The air quality data from Central Pollution Control Board over Hyderabad station has been used for the present study. All the processing is done in real-time and the system is found to be functionally very stable and works under all conditions. The Root Mean Square Error (RMSE) and R^2 have been used as evaluation criteria for this regression technique. Further, the time series regression has been used to find the best fit model in terms of processing time to get the lowest error rate. The statistical model based on machine learning established a relevant prediction of PM$_{2.5}$ concentrations from meteorological data.

INTRODUCTION

Air quality in India has declined significantly over the past few decades and today, air pollution has been implicated as a major risk factor for illnesses and premature mortality in India. As per the study based on 2019 data, 21 of the 30 most polluted cities in the world are in India (World Air Quality Report 2019). Rapid growth in industrialization, urbanization, and population critically affect the atmospheric environment. Innumerable studies have reported that industrial and vehicular emissions are the main contributors to atmospheric pollution (Ajay Kumar et al. 2020, Van 2017, Ravindra et al. 2016, Zhang et al. 2019, Zhao et al. 2019, Singh et al. 2020a). It is a well-known fact that air pollution has adverse effects on humans as well as the environment. The most concerning air pollutant is particulate matter PM$_{2.5}$ (particles with an aerodynamic diameter less than 2.5 microns). These tiny particles stay for a longer time in the atmosphere and they can easily bypass the filters of the human nose and throat, which cause serious impact on human health that includes respiratory problems, asthma, chronic bronchitis, and lung diseases.

The sources of PM$_{2.5}$ can be classified as outdoor and indoor sources. The outdoor sources include vehicular exhausts, construction equipment, burning of fuels such as wood, heating oil or coal, and the reaction of gases or droplets in the atmosphere originating from power plants. Indoor sources include tobacco smoke, cooking, burning candles or oil lamps, operating fireplaces and fuel-burning space heaters (e.g., kerosene heaters). Prediction of these pollutants is very important to take precautionary measures. The concentration of PM$_{2.5}$ depends on many factors and it does not relate to the previous repetitive patterns. Several studies have been conducted to forecast air quality using various statistical and machine learning models. Statistical models can predict atmospheric pollution, but their accuracy is always biased as it depends on an updated source list. Hence, a machine learning technique is more reliable to derive a real-time assessment of air quality based on sample data.

Artificial Neural Networks, based on Machine Learning, is the most commonly used technique to predict air quality. In recent years, the large availability of data enables researchers to implement different prediction models using deep learning techniques. Deep learning is the subset or a special kind of Machine learning, that makes the simultaneous process of huge data set in sequential layers, thereby providing more reliable results. The deep learning technique consists of an artificial intelligence system that can obtain data unsupervised, in an unstructured or unlabeled learning approach. Usually, deep learning has been widely used in academic and practical applications like translation, speech

recognition, language, and image processing. The advanced features of deep learning make it a suitable method to predict air pollutants (Yasin et al. 2018). Deep neural networks can be used to obtain short-term air quality forecasts.

The present study aims to build a model for hourly $PM_{2.5}$ forecasting over Bollaram, Hyderabad, Telangana State, India, using one of the most powerful existing deep learning methods, namely Long Short-Term Memory (LSTM).

RELATED RESEARCH WORK

Recent studies have used many machine learning techniques to overcome the problem related to the prediction of air pollutants like $PM_{2.5}$. Hoek et al. (2008) reported that annual mean $PM_{2.5}$ concentrations can be predicted using land-use regression methods. Using a neural network algorithm, the prediction of O_3 and PM_{10} concentrations was made by Corani (2005). He addressed the problem of the prediction of these two pollutants using feed-forward neural networks (FNs), pruned neural networks (PNNs), and lazy learning (LL). All three approaches are tested in the prediction of pollutants. LSTM neural network has been extensively used to process time-series data as it is capable of stimulating simultaneously (Hochreiter & Schmidhuder 1997). Li (2017) developed a predictive method by using concentrations from different sites as an input to the LSTM layer. Experiments were performed using the spatiotemporal deep learning (STDL) model, the time-delay neural network (TDNN) model, the autoregressive moving average (ARMA) model, the support vector regression (SVR) model, and the traditional LSTM NN model, and a comparison of the results demonstrated that the LSTME model is superior to the other statistics-based models. Further, numerous forecasting models have been developed by using various models based on LSTM. One such study is a prediction of hourly fine PM concentration at 25 target locations in Seoul (Kim et al. 2019). Results showed that the mean squared errors between predicted concentrations of $PM_{2.5}$ and PM_{10} for all 25 locations are well below 45×10^{-5}. Qin (2019) proposed a novel model based on a convolutional neural network (CNN) and LSTM to predict urban PM concentration. The model predicts future particulate matter concentration as a time series. Results are compared with results of numerical models and it shows an improved prediction performance. Xiao et al.

(2020) recently proposed an improved deep learning model to predict daily PM concentration by collecting three years of data from 2015 to 2017 and evaluating the performance of different models. In this study, the author compared three models namely GWR, LSTME, and STSVR with the proposed WLSTME (weighted LSTME) model. Results showed that the proposed WLSTME model has the lowest RMSE (40.67) and MAE (26.10) with the highest p (0.59).

DATA DETAILS

To develop a predictive model using deep learning or machine learning, it is required to have adequate previous data. In the present study, we used the data set extracted from the Central Pollution Control Board (CPCB), India. Hyderabad, popularly known as Pearl City, is the capital of the Indian state of Telangana. It is one of the most polluted and populated cities in India. IDA Bollaram, located in Hyderabad is categorized by CPCB as an industrial hub of Hyderabad. It is home to 100 polluting units, about half of which are pharma and drug companies. Due to a high level of pollution, IDA Bollaram was chosen as a sample area in our study.

The hourly data, separated by different meteorological variables and $PM_{2.5,}$ was downloaded from the CPCB website for this location from 1st March 2017 to 31st August 2020. Table 1 reports the summary of the site and observed variables.

MATERIALS AND METHODS

To develop the predictive model using deep learning technique, the following steps were implemented:

- Identification of the relevant data set
- Pre-processing of data for analysis
- Modeling
- Training of the model in the test data sets and running the model to generate test score
- Evaluation of the performance of the proposed model.

Identification of the Relevant Data Set and Basic Statistical Analysis

The variations in the concentration of $PM_{2.5}$ greatly depend on meteorological and weather conditions. Considering that,

Table 1: Summary of site location and variables used in the present study.

Name of the site	Location	Type	Variables
IDA Bollaram, Hyderabad, Telangana State, India	17.38 °N, 78.48 °E	Particulates	$PM_{2.5}$
		Meteorological parameters	Temperature (Temp), Solar Radiation (SR), Relative Humidity (RH), Wind Speed (WS), and Wind Direction (WD)

we collected hourly meteorological data which included temperature (^{o}C), relative humidity (%), solar radiation (W.m^{-2}), wind speed (m.s^{-1}), rainfall (mm), and wind direction (degree) in addition to the PM$_{2.5}$ from CPCB website for the same location and period. The data matrix was prepared with Year, Month, Day, Hour, PM$_{2.5}$, and meteorological parameters.

To find the interdependency of PM$_{2.5}$ with other meteorological parameters, we have computed correlation and depicted the same in Fig. 1. We observed that PM$_{2.5}$ has a negative correlation with all meteorological parameters, especially high values with temperature and relative humidity, which depicts that lowering the temperature or relative humidity increases the amount of PM$_{2.5}$ concentrations. Based on these results, it was decided to retain all pollutants in the data set except rainfall due to insufficient data.

Data Pre-Processing

Pre-processing helps to transform the raw data into a smooth information set. The data we downloaded may contain missing and inconsistent values. To get better prediction results, the raw data should be cleaned; missing values or null data must be filled with appropriate mean or median values. Superfluous, insufficient, or extreme data must be removed to avoid biasing the results so that the output is more accurate.

In this section, the method adopted for pre-processing the data to forecast the concentration of PM$_{2.5}$ was presented. It included refining the raw data, removing the outliers, normalization, and standardization (data scaling) of the data for visualization and understanding the data.

Data Refining

In this study, we processed three years five months of data with 30510 total number of records, mentioned in data details. In our data set, we have found missing values that represent 10% of the total data for the study site. We have used means to handle the missing data.

Outlier Detection Process

Generally, outliers present in the data can skew and misinform the procedure used in the algorithms which leads to inaccurate results giving poor output. Table 2 shows the basic statistical analysis of PM$_{2.5}$ concentrations with mean, standard deviation, maxima, minima, and quartiles before the removal of outliers.

To summarize the distribution of variables, we have represented the data in the form of a box plot as illustrated in Fig. 2. This illustration helps us to find out the skewness and outliers. Mean, first, third quartiles, maxima, and minima values of PM$_{2.5}$ before and after removal of outliers are reported in Fig. 2. The outliers with z values greater than 3 are discarded from the data set.
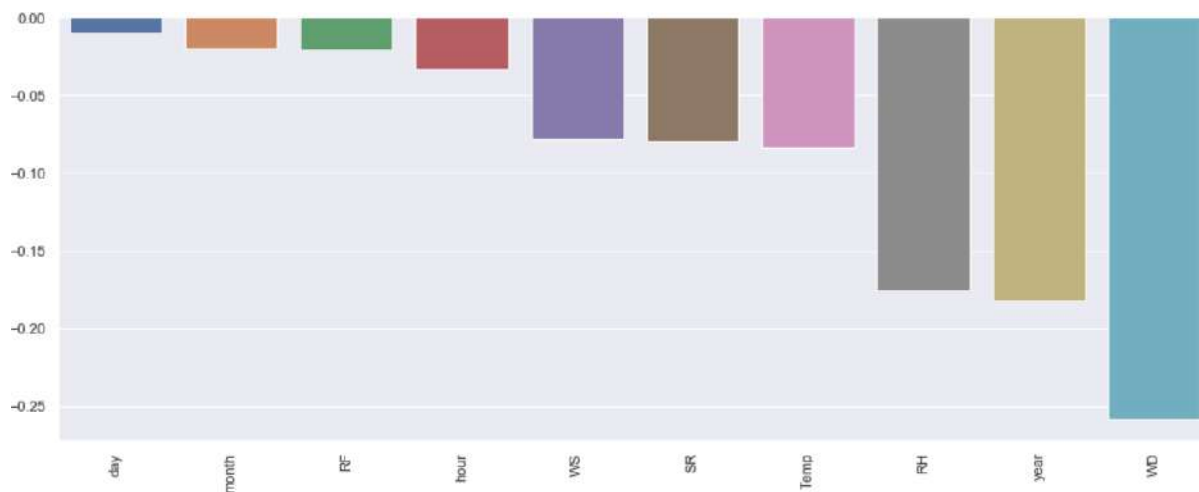

Fig. 1: Correlation between PM$_{2.5}$ with various parameters.

Table 2: Basic statistical analysis of data set.

Parameter	Minimum	Maximum	STD	25%	50%	75%	Mean
PM$_{2.5}$ (µg.m^{-3})	1.0	544	25.827	24.250	37.750	58.000	42.489

Data Scaling

Data scaling is the technique used to normalize or standardize the independent variables present in the data set in a fixed range. In deep learning neural network models, data scaling is always recommended as one of the pre-processing steps. In the present study, we used data scaling that normalizes the real values of the input variables within a fixed range [0, 1]. This makes all features equally weighted between 0 and 1.

Modelling

Multivariate linear regression emphasizes the relationship between one dependent variable and multiple independent variables. The long Short-Term Memory model, part of standard Recurrent Neural Networks (RNN), is a trustable technique to predict air quality using pollution and meteorological information of time series data. It basically consists of different gates, including input, forgets, and output gates, which provide the information to flow between, in, and out of a cell. The block system of LSTM is depicted in Fig. 3.

Training of the Model

We have used around 21357 training samples and 9153 testing samples in the ratio of 70:30. The data has been split into train and test, to ensure that the model is not overfitting the data. According to the loss graph (shown below in section 5), the train and test data converged smoothly, which indicates that the model can be properly generalized. In the process of training the libraries used for LSTM implementation: the number of LSTM units used is 25; the number of epochs 50; dense layers 1; dropout 0.; batch size 80. The hardware and software specifications are Memory 8GB; 128 – bit LPDDR4x@1600MHz 512 GB/s. Compute 6-core NVIDIA Carmel ARM@v8.2 64-bit CPU 6MB L2 + 4MB L3; OS Ubuntu 20.04. The developing environment python 3.6 and TensorFlow 2.1.0.

Evaluation Criteria

The performance of the predictive model has been evaluated using the standard measure, Root Mean Square Error (RMSE). It is used to calculate an average magnitude of the error between measured and predicted $PM_{2.5}$ concentration values using the formula

$$RMSE = \sqrt{\sum \left(P_m - P_r\right)^2 / N} \qquad \ldots(1)$$

Where P_m denotes measured air pollution, P_r denotes predicted air pollution and N is the number of measured data.

$$R^2 = 1 - \frac{\sum_i (y_i - \hat{y}_i)^2}{\sum_i (y_i - \mu)^2} \qquad \ldots(2)$$

Where y_i and $\hat{y}_i$ are original and predicted values and μ is the sample mean.

RESULTS AND DISCUSSION

Multivariate regression analysis was performed on the data set collected over Hyderabad (IDA Bollaram). 70% of the data was used to train the model, to obtain the $PM_{2.5}$ concentration values and predictions, for the next hour. Fig. 4 illustrates the loss graph of the tested and trained data set. From Fig. 4, it is evident that multivariate regression analysis performs well in predicting $PM_{2.5}$ values.

The RMSE value of training and test data as per the above graph is 0.0051 and the R^2 value is found to be 0.9862580518554221. This indicates that regression analysis gives better results in predicting the $PM_{2.5}$ levels in terms of RMSE. The R^2 value is the amount of the variation in

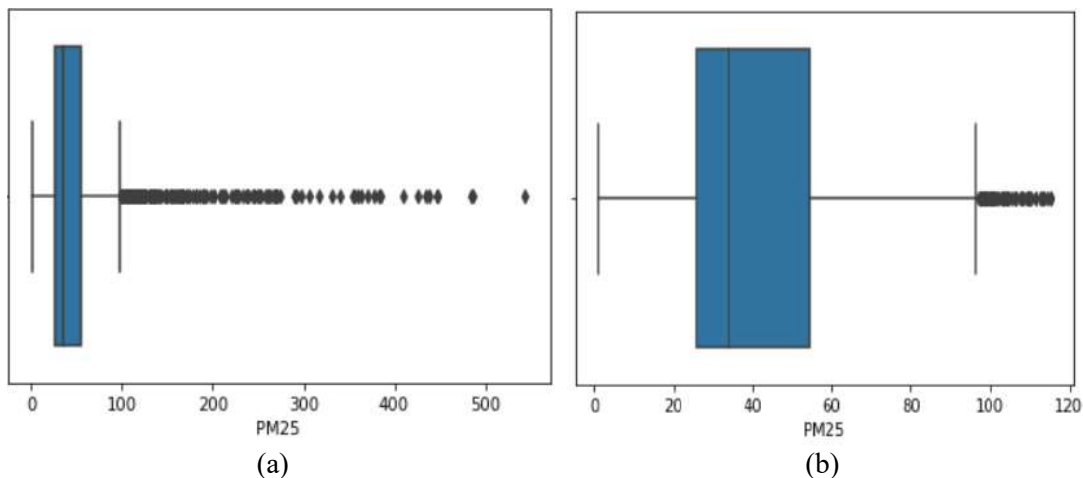(a)   (b)

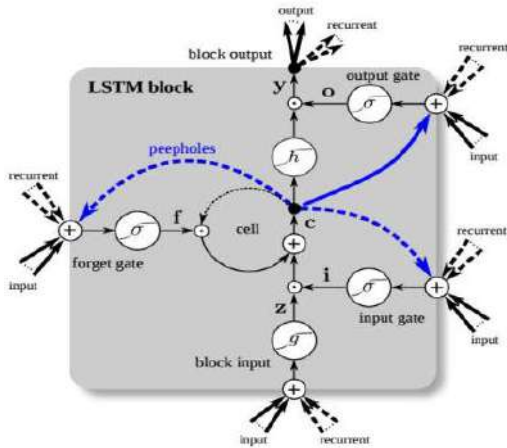Fig. 2: Box plot of $PM_{2.5}$ before (a) and after (b) removal of outliers.

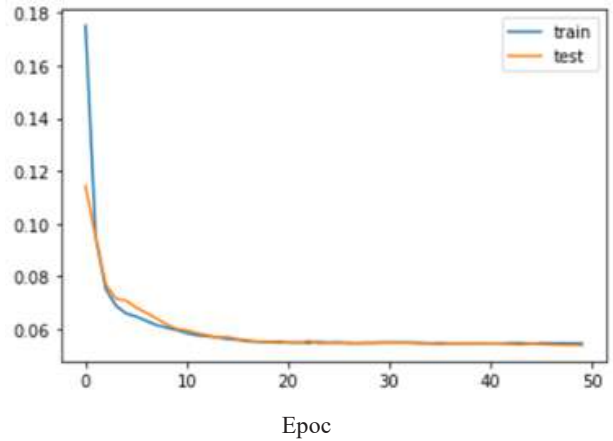Fig. 3: Block System of LSTM model (Kök et al. 2017).

Fig. 4: Loss graph of the tested and trained data set.

the PM$_{2.5}$, which is predictable from the input independent variables, it indicates 98% of changes in PM$_{2.5}$ are due to the variations in the input variables.

The relation between PM$_{2.5}$ and other meteorological parameters was reported in the previous section. It was found that PM$_{2.5}$ has a negative correlation with temperature, relative humidity, and wind speed. This indicates that the low value of city temperature results in high PM$_{2.5}$ concentrations. As a result, there will be an increase in the potentiality of suspended particles, which causes the density of air to increase. Thereby, PM$_{2.5}$ records high concentration values at low temperatures due to a long stay of air in the atmosphere. Several studies reported that the urban PM$_{2.5}$ concentration decreases with an increase in relative humidity (Li et al. 2015). Similarly, the concentration of PM$_{2.5}$ is lower when the wind speed is high. This may be because the particles may have been washed away from the atmosphere due to the higher wind speed at that particular location. From the result obtained, the model converges with a very low value of mean squared error and gives a more accurate prediction for all ideal conditions.

CONCLUSION

There is a lot of costs involved in setting up the pollution sensing system and gathering PM$_{2.5}$ data across the city. We not only need to invest in technical assets but also invest in human capital as well. To address this issue, we may use a mobile technical environment, collect data for a particular period and train our model. In this work, the problem of forecasting hourly PM$_{2.5}$ has been addressed using a deep learning-based model called LSTM with an evaluation criterion of RMSE. We showed the experimental results of prediction with a low value of mean square error. Thus,

we propose this method as an accurate prediction approach in all ideal conditions. Our system based on deep learning technology, using a fine-tuned LSTM time series regression model can precisely identify the pollution measure PM$_{2.5}$ on an hourly basis, thus helping the Pollution Control Board to understand the patterns of pollution in different areas across the city, without setting up a permanent sensing system at multiple locations in the city. It can be further ameliorated by training on a more extensive dataset and changing the backbone transfer learning model for latency improvement.

ACKNOWLEDGEMENT

REFERENCES

Ajay Kumar, M.C., Vinay Kumar, P. and Venkateswara Rao, P. 2020. Temporal variations of PM$_{2.5}$ and PM$_{10}$ concentration over Hyderabad. Nat. Environ. Pollut. Technol., 19: 421-428.

Corani, G. 2005. Air quality prediction in Milan: Feed-forward neural networks, pruned neural networks, and lazy learning. Ecol. Model., 185: 513-529.

Hochreiter, S. and Schmidhuber, J. 1997. Long short-term memory. Neural Comput., 9(8): 1735-1780.

Hoek, G., Beelen, R., de Hoogh, K., Vienneau, D., Gulliver, J., Fischer, P. and Briggs, D. 2008. A review of land-use regression models to assess spatial variation of outdoor air pollution. Atmos. Environ., 42: 7561-7578.

Kim, S., Lee, J.M., Lee, J. and Seo, J. 2019. Deep-dust: Predicting concentrations of fine dust in Seoul using LSTM. Mach. Learn., 3: 319.

Kök, I., Şimşek, M.U. and Özdemir, S. 2017. A deep learning model for air quality prediction in smart cities. IEEE Int. Conf. Big Data, 601: 1973-1980.

Li, X. 2017, Long short-term memory neural network for air pollutant concentration predictions: Method development and evaluation. Environ. Pollut., 231(1): 997-1004.

Li, Y., Chen, Q., Zhao, H., Wang, L. and Tao, R. 2015. Variations in PM_{10}, $PM_{2.5}$ and $PM_{1.0}$ in an urban area of the Sichuan Basin and their relation to meteorological factors. Atmosphere, 6: 150-163.

Qin, D. 2019. A novel combined prediction scheme based on CNN and LSTM for urban PM25 concentration. IEEE Access, 7: 20050-20059.

Ravindra, K., Sidhu, M.K., Mor, S., John, S. and Pyne, S. 2016. Air pollution in India: bridging the gap between science and policy. J. Hazard. Toxic Radioact. Waste, 20: A4015003.

Singh, V., Biswal, A., Kesarkar, A.P., Mor, S. and Ravindra, K. 2020. High resolution vehicular PM_{10} emissions over megacity Delhi: Relative contributions of exhaust and non-exhaust sources. Sci. Total Environ., 699: 134273.

Van, V.E. 2017. Energy, land-use, and greenhouse gas emissions trajectories under a green growth paradigm. Glob. Environ. Change, 42: 237-250.

World Air Quality Report 2019. https://www.iqair.com/world-most-polluted-cities/world-air-quality-report-2019-en.pdf

Xiao, F., Yang, M. and Fan, H. 2020. An improved deep learning model for predicting daily PM2.5 concentration. Sci. Rep., 10: 20988.

Yasin, A.A., Zeynep, C.A. and Hüseyin, O.A. 2018. Air pollution modeling with deep learning: A review. Int. J. Environ. Pollut. Environ. Model., 1(3): 58-62.

Zhang, K., Zhao, C., Fan, H., Yang, Y. and Sun, Y. 2019. Toward understanding the differences of $PM_{2.5}$ characteristics among five China urban cities. Asia-Pacific J. Atmos. Sci., 56: 493-502.

Zhao, C., Wang, Y., Shi, X., Zhang, D., Wang, C., Jiang, J.H., Zhang, Q. and Fan, H. 2019. Estimating the contribution of local primary emissions to particulate pollution using high-density station observations. J. Geophys. Res. Atmos., 124: 1648-1661.

Original Research Paper

https://doi.org/10.46488/NEPT.2022.v21i02.030

Open Access Journal

Waste Generation and Characteristics in Sri Lankan Textile and Apparel Sector: Case Study of the Biyagama Industrial Export Processing Zone, Sri Lanka

L.G.L.M. Edirisinghe*†, M. Wijayasundara** and A.A.P. De Alwis*

*Department of Chemical and Process Engineering, University of Moratuwa, Sri Lanka
**School of Engineering, Deakin University, Australia
†Corresponding author: L.G.L.M. Edirisinghe; lakmini@ncpcsrilanka.org

ABSTRACT

The main goal of the study was to look at the properties of waste, treatment options, and disposal techniques. Furthermore, waste circulation variables in the textile and apparel sectors in Sri Lanka's Biyagama Industrial Processing Zone were calculated. The types, volumes, and per capita waste generation of ten industries were analyzed, as well as waste management activities such as trash minimization, handling, storing, recirculation, and disposal. The information was gathered using questionnaires, interviews, and field observations. According to the findings, the total industrial waste generation rate was 13792.5 tonnes per year, with 5926 tonnes per year designated as hazardous waste materials (42.9%). Furthermore, the waste generation rate per capita was 0.93 kg. The waste circulation factor was 0.38, according to the findings. The findings of the study highlight the necessity for integrated waste management methods in the textile and apparel industries.

INTRODUCTION

The textile and apparel (T&A) industry sector is one of the most crucial for economic growth, particularly in nations where the sector is heavily reliant (Ulson de Souza et al. 2010). Sri Lanka's economy largely depends on the apparel export business, contributing 32% to the gross domestic product (GDP) and 44% to total exports in 2018 (Fibre2fashion.com 2021). It has recorded a 5.2% growth in export in 2019 (Russell 2020). The T&A sector is one of the largest industrial sectors, providing over 300000 jobs (Embuldeniya 2018). Despite the positive economic impact, this sector has negative environmental consequences because it depletes resources, generates greenhouse gases, and pollutes the environment. It is well-known for its high resource use in aggregate manufacturing methods (Kocabaş 2008) and considerable chemical use, notably in dyeing and finishing procedures (Verma 2012). The amount of resources consumed depends on the type of fiber used in the textile manufacturing process as well as the technology used (Brik et al. 2006). As a result, the textile sector faces major pollution and waste creation issues throughout the manufacturing process (Moore & Ausley 2004). As a result, it is critical to examine waste generation to develop a waste management strategy for businesses (Zaman 2013). Meanwhile, the textile and apparel sector has been identified as one of the most critical potential industries for innovative innovation and enhancement inno-

vation (Rapsikevičienė et al. 2019). Furthermore, previous research has shown that waste in the textile industry has the potential to be recyclable and can become raw material for one or different sectors (Villanueva et al. 2010).

In this regard, the current research seeks to determine the characteristics, waste generation, waste management, and waste circulation potential in the textile and apparel industries in Biyagama Export Processing Zone (BEPZ), Sri Lanka. The study's findings will enable the development of new suitable waste management and sustainable activities for these materials, based on the knowledge and characteristics of waste ingredients. Aside from that, it has the potential to contribute to further research in finding solutions to increase their reuse or recovery potential.

MATERIALS AND METHODS

Study Area

BEPZ is located in the Gampaha District and is one of the three districts in Western Province. It is about 24 km from Colombo city. It is 1km away and is close to the Bandaranaike International Airport. For this study, ten textile factories were selected from the BEPZ region, which is not disclosed due to their research ethics. Factories were labeled with a pseudo-code such as T1, T2. etc. Selected factories are divided into three groups based on their processes: 1) fabric

manufacturing, 2) garment washing and dyeing, and 3) clothing manufacturing.

Fabric producers utilize imported yarn and automated knitting technology to manufacture fabric. Fabric manufacturers and Garment washing and dyeing conduct wet processing, including pre-treatment, dyeing, and finishing. De-sizing, scouring, bleaching, and mercerizing are all part of the pre-treatment process, necessitating a considerable volume of pure water for washing, rinsing, and steam generation. The apparel manufacturing sector produces finished garment products that are ready for use.

Data Collection Procedure

Obtaining data required an examination of industrial waste generation and waste management procedures, as shown in Fig. 1. Waste generating points, types, and waste volumes, as well as disposal methods, were identified. The characteristics of each industry category that produces waste items were determined during the analysis. Questionnaires, interviews, and field observations were used to gather the information needed to evaluate the waste composition and management status.

Calculation of Waste Circulation Factor

The principles of circular economics are utilized in this study to estimate the circular waste factor. A circular economy is a type of economic system that attempts to eliminate waste and continuously recreate resources (Fig. 2). Progress toward a circular economy should include the ethical use of natural resources as well as the ability to reuse, repurpose, recycle, and retrieve the value stored in previously discarded items. Waste incineration or landfilling, which have been identified as potential disposal processes, are not viewed as high-priority strategies for achieving a circular economy. In a circular economy, resource sinks such as cremation and landfilling operate as resource sinks, whereas resource circulation occurs in balanced resource flows.

The waste circulation factor for this study was computed using formula (1) and the principles of a circular economy as outlined below.

$$\frac{\sum_{i=1}^{i} w_{re}^{i} + \sum_{i=1}^{i} w_{ru}^{i}}{\sum_{i=1}^{i} w_{Total}^{i}} = \text{Waste Circulation Factor-(1)}$$

w_{re}^{i} = Recyclable waste fraction of waste type i

w_{ru}^{i} = Reused waste fraction of waste type i

w_{Total}^{i} = Total waste generation of waste type i

RESULTS AND DISCUSSION

Primary Waste Streams

In the results of the study presented in Table 1, each waste category in the selected 10 T&A industries was prioritized by arranging them in descending order of magnitude. Pareto chart is used for preliminary identification of the most significant waste stream and to discover the "vital" streams that accounted for 80% of waste generation. The outcome of the analysis is given in Table 1 presenting the results following the application of the Pareto principle. Fig. 3 shows the
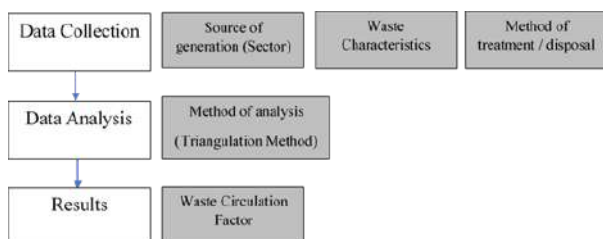

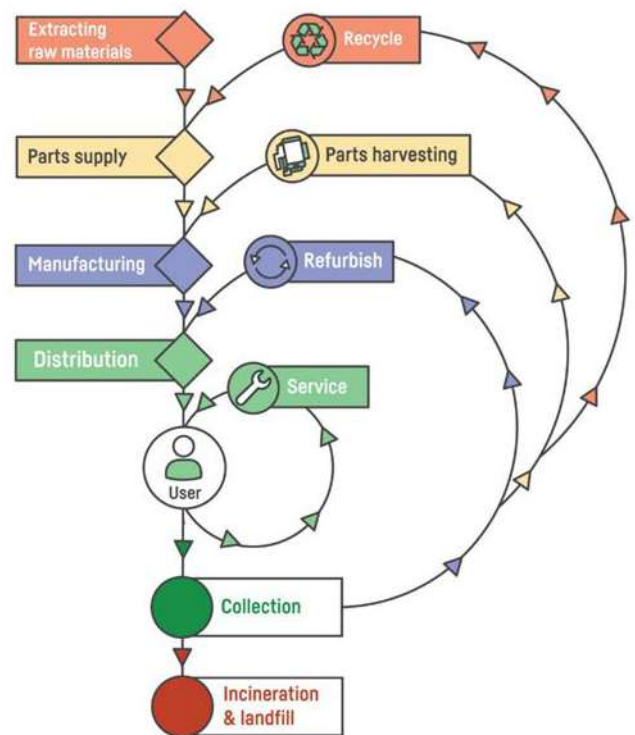Fig. 2: Resource circulation through the circular economy (TCO certified 2021).

Fig. 1: Methodological Framework.

waste generation in each selected T&A industry sector. The total waste generation accounted for 13792.5t per year, of which 5926t per year belonged to hazardous waste materials (42.9%). The results also indicate the per capita waste generation based on the number of workers in the industry sector. The total number of personnel surveyed was 15421 and the waste per capita accounted for 0.93 kg.day^{-1} per worker.

The wastes stream quantities in the surveyed factories were evaluated during the study. Effluent treatment plant (ETP) sludge accounted for 39.4 % of the total wastes, followed by fabric and yarn (29.6%), metal (5.6%), Paper and cardboard (5.4%), plastic (5.2%), food (4.3%), mixed waste (4.0%), chemical containers (2.4%). The remaining wastes constituted less than 5% of the total waste. The accuracy of results could be affected due to challenges with collecting complex waste regeneration data. The data in this instance is associated with a range of production processes, raw materials, and multiple data points.

T1, T3, T8: represent Fabric Mills

T2, T6, T7, T9: represent Garment washing & Dyeing plant

T4, T5, T10: represent Apparel Manufacturing companies

Waste Treatment Mechanisms

The following options are identified as the most common waste disposal methods used by the factories in BEPZ. The proportions of primary waste disposal methods were calculated and are shown in Fig.4.

Table 1: Types of waste generation in the T&A sector in the BEPZ, Sri Lanka.

Waste Types	Total waste generation in T&A sector industries(t/year)
Boiler ash	311.6
Chemical Containers	331.0
Contaminated Fabric	38.9
ETP Sludge	5434.2
E-Waste	2.9
Expired chemicals	6.9
Fabric and yarn waste	4082.6
Food Waste	593.0
Metal	772.3
Paper & Cardboard	744.7
Polythene	110.3
Plastic (including tread cone)	717.2
Waste Oil	1.8
Wood and Wood Pallet (0.55)	87.8
Mixed waste	557.3

- Option 1: Reuse within the facility
- Option 2: Reuse for other industries
- Option 3: Returned to supplier
- Option 4: Co-processing in cement kiln
- Option 5: Energy recovery within the facility
- Option 6: Sold to licensed recycling company
- Option 7: Landfilling
- Option 8: Collected by scavengers
- Option 9: Collected by the third party and exported for recycling
- Option 10: Open dumping at Zone dump yard
- Option 11: Storing

Non-hazardous Waste Treatment Disposal

The study revealed that all selected industries generate some common types of waste, although their quantities were different. The common types of waste (non-hazardous) include fabric, paper, polyethylene, metal, plastic, food, and wood waste. Those wastes are typically stored in a dry place within the factory premises ensuring protection from the climate hazards. This waste is separately handled and the main portion of non-hazardous waste contains fabric which accounts for 51% of the total amount.

Waste Storage

The study also looked at how waste is stored in temporary storage. The results revealed that closed space (52.5%) and open space (50%) were the most commonly used temporary storage options (28.5%). Polyethylene bags (12.8%), boxes (4.5%), and barrels (1.7%) were the other commonly used solutions for the temporary storage of industrial wastes in BEPZ.
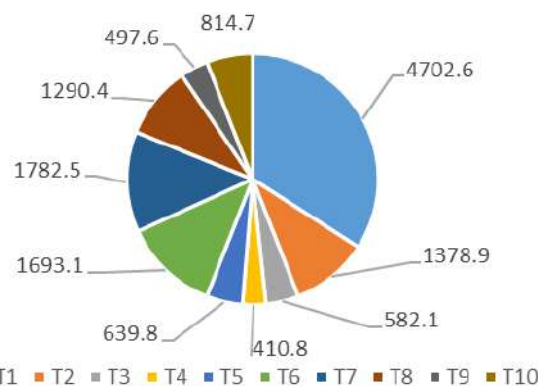

Fig. 3: Waste generation (t per annum) of T&A industries in BEPZ, Sri Lanka.

According to the information in this study, 62.1% of industrial wastes were disposed of on weekly basis, 30.9% on monthly basis and 4% on daily basis, and 3% on annual basis.

Waste Segregation and Recycling

According to the findings, 70% of industries segregate and separate their trash at the point of generation. It's telling evidence that there's a high level of waste management awareness and procedures, as well as great management by industrial managers. Except for fabric offcuts, the most common recyclable materials generated in the sector are paper, polythene, cardboard, and metal. In the BEPZ's textile industry supply chain, 91% of paper and cardboard, 79% of polythene, 76% of metal, and 43% of plastic and chemical containers waste were recycled. As a result, over 80% of the factories decided to sell these materials to licensed recycling companies. The remaining materials were collected by unauthorized small-scale entrepreneurs for resale, and their whereabouts are unknown.

Fabric Waste Management

Fabric waste accounted for the highest generation among all types of waste. The most common fabric waste types generated in the BEPZ were cotton, polyester, nylon, and mixed material. There is a significant demand for cotton and nylon fabric waste for recycling, however, treatment of polyester or a mix of material off-cut waste has become a significant challenge in this sector due to the unavailability of textile recycling facilities in the country. Therefore, a significant amount of fabric waste is disposed of through co-processing in cement kilns due to the unavailability of collectors. Two industries in BEPZ burn the fabric waste in their boilers and recover energy. However, the boiler ash disposal is a problem due to it contains heavy metal which comes through the fabric and this remains unaddressed.

Fig. 5 Shows the fabric waste flow in the BEPZ. These are the current management practices for fabric waste in the

BEPZ. Fig. 6 shows the waste disposal methods of fabric waste.

Method 1- Energy Recovery

Method 2- Co-processing at Cement Kiln

Method 3: Sold to licensed recycling company

Method 4: Reuse

Method 5: Export for recycling through collectors

Method 6: Landfilling through collectors

Hazardous Waste Disposal

Due to the lack of technologies and the facilities for hazardous waste treatment and disposal in the country, most of the surveyed industries dispose of the hazardous waste through co-processing in cement kilns. A total amount of 6847.4t of hazardous waste (95%) per year was co-processed at the cement kiln, including 100% of ETP sludge. The rest of the hazardous waste is accumulated in the factories due to the unavailability of treatment options.
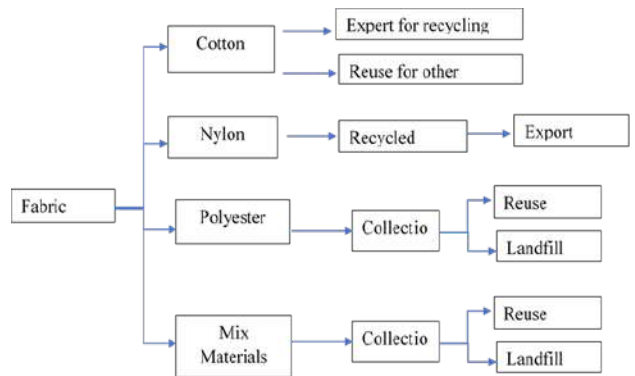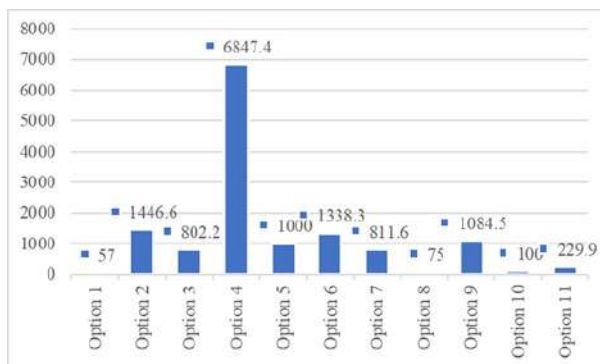

Fig. 5: Fabric waste flow in the BEPZ.

Fig. 6: Management practices of fabric waste (%) in T&A industries in the BEPZ.

Fig. 4: The treatment methods of the primary waste streams (t per year).

Waste Flow Analysis

Fig. 7 shows the overall waste flow in the selected T&A industries in the BEPZ. In the zone, four different waste treatment methods were applied. Reuse (2805.8t), energy recovery (7847.4t), recycle (2497.8t), landfill (411.7t), and export for recycling where the waste treatment options (229.9t). Recycling and reusing accounted for 38.45% of the total. Incineration (56.8%) was the most commonly employed waste treatment technology for energy recovery.

Analysis of Waste Circulation Factor

The waste circulation factor of the waste was calculated using Equation 1. The results show the overall waste circulation factor of the textile and apparel industries in the Biyagama Export Processing zone was 0.38.

Waste Management Practices

According to the findings, all organizations strive to reduce waste generation, and they also underline that waste management should be the responsibility of all departments. Furthermore, most firms adopted separate organizational rules under the ISO 14001 Environment Management System to minimize or regulate waste. There was a clear indication of how to manage waste in the policy. In general, four of the industries surveyed use cleaner production methods.

CONCLUSION

The textile industry has a huge opportunity to divert waste from landfills and into recycling and reuse. However, a review of the scientific literature reveals that incineration and lan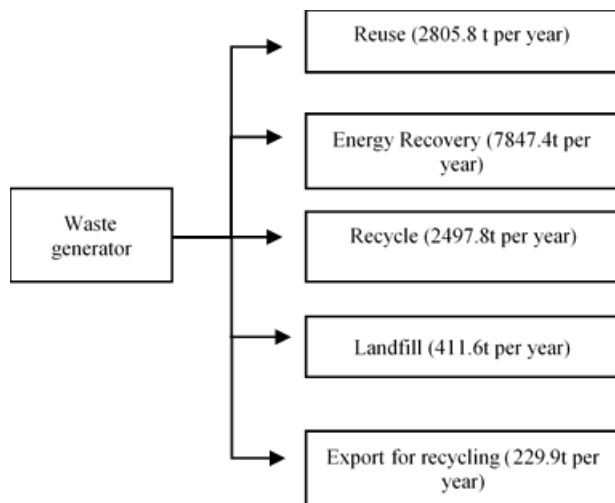dfills account for the majority of industrial textile waste disposal. The research discussed in this article uses the data triangulation method to look at T&A sector industries in BEPZ for 2019. Furthermore, the waste circulation factor for the industry is calculated using an equation established utilizing circular economy principles. The study's findings reveal a high potential for circulation of waste within inter and intra-industry sectors.

According to the findings, overall waste production was 13792.5t per year, with hazardous waste items accounting for 5926t per year (42.9%). The findings also illustrate the per capita trash generation based on the number of persons employed in the industry. The total number of people polled was 15421, with each worker producing 0.93kg of garbage per day. Co-processing in a cement kiln is the most common waste disposal strategy used by businesses in BEPZ, followed by reuse for other industries and sale to an authorized recycling business. The study discovered that all of the businesses studied produce certain similar forms of waste but varied proportions. According to the findings, 70% of manufacturers segregate and separate their waste at their production point. It is an excellent indicator of solid waste management, knowledge and procedures, and outstanding management by industrial managers. Among all forms of waste, fabric waste accounted for most production. The most prevalent waste management options are co-processing at cement kilns (22%), landfilling through collectors (20%), reuse (17%), and energy recovery (17%). The majority of industries examined use cement kilns to co-process hazardous waste. The cement kiln co-processed a total of 6847.4t of hazardous waste (95%) each year, including 100% ETP sludge. According to the findings, the overall waste circulation factor of the textile and apparel businesses in the BEPZ was 0.38.

Fig. 7: Waste flow in the selected T&A industries in BEPZ.

REFERENCES

Brik, M., Schoeberl, P., Chamam, B., Braun, R. and Fuchs, W. 2006. Advanced treatment of textile wastewater towards reuse using a membrane bioreactor. Process Biochem., 41(8): 1751-1757.

Embuldeniya, A. 2018. Impact of apparel industry on the economy of Sri Lanka. J. Social Stat., 2015: 1-14.

Fibre2fashion.com. 2021. Consistent Improvement in Sri Lanka's Apparel Exports. Available at: https://www.fibre2fashion.com/industry-article/8551/consistent-improvement-in-sri-lanka-s-apparel-exports [Accessed 2 March 2021].

Kocabaş, A.M. 2008. Improvements in Energy and Water Consumption Performances of a Textile Mill after Bat Applications. Post Graduate Thesis, Master of Science, The Graduate School of Natural and Applied Sciences of Middle East Technical University, Turkey, pp. 1-172.

Moore, S. and Ausley, L. 2004. Systems thinking and green chemistry in the textile industry: concepts, technologies, and benefits. J. Clean. Prod., 12(6): 585-601.

Rapsikevičienė, J., Gurauskienė, I. and Jučienė, A. 2019. Model of industrial textile waste management. Environ. Res. Eng. Manag., 75(1): 441-495.

Russell, M. 2020. Sri Lanka garment and textile exports up over 5% in 2019: Sri Lanka Apparel. Available at: https://www.srilankaapparel.

com/sri-lanka-garment-and-textile-exports-up-over-5-in-2019 [Accessed 2 April 2021].

TCO Certified 2021. The circular economy: An opportunity for more sustainable IT products. Available at: https://tcocertified.com/circular-economy [Accessed 3 March 2010].

Ulson de Souza, A., Melo, A., Pessoa, F. and Guelli, S. 2010. The modified water source diagram method was applied to reuse the textile industry's continuous washing water. Resour. Conserv. Recycl., 54(12): 1405-1411.

Verma, A., Dash, R. and Bhunia, P. 2012. A review on chemical coagulation/ flocculation technologies for removal of color from textile wastewaters. J. Environ. Manag., 93(1): 154-168.

Villanueva, A., Delgado, L., Luo, Z., Eder, P., Sofia Catarino, A. and Litten, D. 2010. Study on the Selection of Waste Streams for End-of-Waste Assessment: Final Report. Available at: http://file:///C:/Users/viraj/Downloads/reqno_jrc58206_jrc58206.pdf [Accessed 24 June 2021].

Zaman, A. 2013. Identification of waste management development drivers and potential emerging waste treatment technologies. Int. J. Environ. Sci. Technol., 10(3): 455-464.

Effects of Chelating Surfactants on Competitive Adsorption of Lead and Zinc on Loess Soil

H. T. Qiao*, B. W. Zhao**† and X. S. Yu*

*Institute of Applied Chemistry & Department of Chemistry, Xinzhou Teachers University, Xinzhou 034000, P.R. China
**School of Environmental and Municipal Engineering, Lanzhou Jiaotong University, Lanzhou 730070, P.R. China
†Corresponding author: Baowei Zhao; baoweizhao@mail.lzjtu.cn

ABSTRACT

The study of competitive adsorption of heavy metals on soil is important for heavy metals contaminated soil remediation. However, there have been few studies on the impact of desorption reagents on heavy metal adsorption in soil. Batch adsorption studies were used to investigate the competitive adsorption mechanism of two heavy metals, Pb and Zn, on a loess soil in the presence of a new chelating surfactant, sodium N-lauroyl ethylenediamine triacetate (LED3A). Results showed that competitive adsorption equilibria of Pb and Zn were reached at 3 and 10 h, respectively. The maximum equilibrium adsorption capacities were 19.55 and 18.35 g.kg^{-1}, respectively. LED3A affected the competitive adsorption kinetics of Pb and Zn by increasing the change in external mass transfer and reducing the change in internal mass transfer. LED3A reduced Pb and Zn adsorption capacities onto the soil through competitive chelation of the heavy metals. The heavy metal chelating ability of LED3A was higher for Zn than for Pb. When its concentration was larger than 5 g.L^{-1}, LED3A showed a significant effect on the competitive adsorption of Pb and Zn. In the competitive system, the effect of Pb concentration on the Zn adsorption capacity was greater than the effect of Zn concentration on the Pb adsorption capacity. LED3A weakened the effect of Pb concentration and enhanced the effect of Zn concentration. LED3A showed a significant potential for efficiently leaching remediation of Pb and Zn co-contaminated soil.

INTRODUCTION

Heavy metal pollution in soils has become a severe issue that is endangering human health and endangering the environment (Yuan et al. 2021). The adsorption/desorption characteristics of heavy metal ions at the soil-water inter-face are crucial for understanding the movement and fate of heavy metals in the soil. This has major implications for studying heavy metal bioavailability and transformation in the biological chain (Peng et al. 2018). It also provides evidence for the prevention and remediation of heavy metal contaminated soils (Qiu et al. 2010, Garridorodriguez et al. 2014). As a result, numerous research on the adsorption/desorption of heavy metals on soils have been published in recent years (Wang et al 2011, Shi et al. 2013, Peng et al. 2018, Wang et al. 2020). However, most adsorption/desorption research has concentrated on diverse soil types, heavy metal species, and adsorption/desorption process variables (Muhammad et al. 2018). Meanwhile, mechanistic research on soil and heavy metal systems, as well as contaminated soil and desorbent systems, have made it difficult to explain the competitive mechanism for heavy metals between soil and desorbent. To research the influence of the desorbent on heavy metal adsorption onto the soil, it is important to

investigate the coexisting system of soil, heavy metals, and desorbent. The evident link between soil, heavy metals, and desorbents can offer the theoretical foundation needed for desorbent-based chemical leaching treatment of heavy metal-contaminated soil.

Desorbents, on the other hand, are mostly inorganic chemicals (such as acids, alkalis, and salts) and chelating agents, as previously stated. Inorganic chemicals, on the other hand, cause serious damage to soil structure and are not suited for contaminated soil repair (Kou et al. 2006, Guemiza et al. 2017). Although chelating agents can effectively desorb heavy metals from contaminated soils, it is difficult to degrade these agents in the soil environment, resulting in secondary pollution (Cao et al. 2013, Kim et al. 2016). Therefore, the development of an environmentally friendly desorbent that can efficiently desorb heavy metals from soil is critical.

Novel chelating surfactants (such as sodium *N*-alkyl ethylenediamine triacetate and sodium *N*-acyl ethylenediamine triacetate) possess both surface activity and chelating properties (Wang et al. 2004). These surfactants show superior performance due to being water-soluble, non-toxic to mammals and aquatic organisms, and biodegradable in the

natural environment without causing secondary pollution (Diao et al. 2016, Qiao et al. 2016). These surfactants have been extensively used in detergents, mineral flotation, phase transfer catalysis, emulsion polymerization, and other fields (Diao et al. 2016). However, few studies have reported the effect of chelating surfactants on the adsorption of heavy metals on the soil. To further improve the efficiency of LED3A in the remediation of soils contaminated with heavy metals, the relationship among chelating surfactant, soil, and heavy metals needs to be further clarified.

Loess soil from Northwest China and two heavy metals, Pb and Zn, were chosen as the researched soil and pollutants, respectively, in this study. The competitive adsorption of Pb and Zn onto the soil, as well as the influence of a new chelating surfactant, sodium N-lauroyl ethylenediamine triacetate (LED3A), on the competitive adsorption behavior of heavy metals, were studied in a series of studies. The findings support LED3A leaching treatment of heavy-metal contaminated soils on a theoretical level.

MATERIALS AND METHODS

Reagents

Sodium *N*-lauroyl ethylenediamine triacetate (LED3A, $C_{20}H_{35}N_2Na_3O_7$) with purity greater than 95.0% was purchased from Yilu Pharmaceutical Technology Co., Ltd. (Hangzhou, Zhejiang Province, China). Analytical-grade $Pb(NO_3)_2$ and $Zn(NO_3)_2$ were obtained from Damao Chemical industry Co., Ltd. (Tianjin, China). All other chemicals were of analytical grade purity.

Experimental Materials

Experimental Soil was collected from the surface soil (0-20 cm depth) of the mountain behind Lanzhou Jiaotong University (Lanzhou, Gansu Province, China). After removing gravel, branches, and leaves, the soil was naturally air-dried (20-30°C) and passed through a 0.3 mm sieve. The soil organic matter content was low (5.3 g.kg^{-1}). The soil pH was slightly alkaline (pH 8.11) and the carbonate content was 11.7 %.

Adsorption Experiments

Soil (0.05 g) was weighed into a series of conical flasks, to which 20 mL of the $Pb(NO_3)_2$, $Zn(NO_3)_2$, and LED3A solutions with different concentrations were added. Each conical flask also contained 0.01 mol.L^{-1} $NaNO_3$ to keep a constant ionic strength, and 0.1 mL of 100.0 mg.L^{-1} NaN_3 was added to inhibit microbial growth. The flasks were sealed immediately with a stopper and put into a shaker (TD6, Changsha pingfan Instrument and Meter Co., Ltd.,

China) at 150 rpm for a certain time at 25°C. At the end of the adsorption, the solution was centrifuged at 3500 rpm for 30 min. The supernatant was filtered by a 0.45 μm membrane for heavy metal analysis. The Pb and Zn concentrations were measured using a flame atomic absorption spectrophotometer (Spectrum AA110/220, Varian, Palo Alto, CA, USA). The adsorption capacities of Pb and Zn on the soil were calculated using Eq. 1:

$$q_t = \frac{(c_o - c_t) \times V}{m} \qquad \qquad \dots(1)$$

where q_t is the adsorption capacity of heavy metals at time t (g.kg^{-1}), c_o and c_t are the heavy metal concentrations at the beginning of adsorption and time t (g.L^{-1}), respectively, V is the volume of the heavy metal solution (L), and m is the mass of the soil sample (g).

A series of adsorption experiments using this method had been used to study the effect of LED3A on the competitive adsorption kinetics of Pb and Zn, the effect of LED3A concentration on competitive adsorption of Pb and Zn, the competitive adsorption of different concentrations of Pb and Zn and the effect of LED3A on its. All treatments were performed in triplicate, and the results were presented as average values.

RESULTS AND DISCUSSION

Competitive Adsorption Kinetics of Pb and Zn, and Effect of LED3A

The competitive adsorption kinetic results for Pb and Zn onto the loess soil were shown in Fig. 1(a) and the results of the curve fitted by the intraparticle diffusion model (b) are shown in Fig. 1(b). The adsorption capacities of Pb and Zn rapidly increased at an adsorption time within 1 h, increased slowly after 1 h, and then gradually leveled off as the adsorption time was further extended. During the rapid increase stage, more active sites were present on the surface of the soil particles along with a larger concentration gradient, resulting in a greater mass transfer force. As the adsorption time was extended, the Pb and Zn concentrations in solution and available active sites on the soil particle surfaces decreased gradually, causing a corresponding decrease in the mass transfer force. The equilibrium adsorption capacity of Pb (19.55 g.kg^{-1}) was reached at 3 h, while Zn (18.35 g.kg^{-1}) was reached at 10 h. These results indicated that Pb was preferentially adsorbed onto the soil in the competitive adsorption process and that the soil showed a higher ability to adsorb Pb than Zn.

Many studies on competitive adsorption have suggested that the inherent properties of heavy metal ions relate to their adsorption order, such as ion radius, electronegativity, first-order hydrolysis constant, hydrated ion radius,
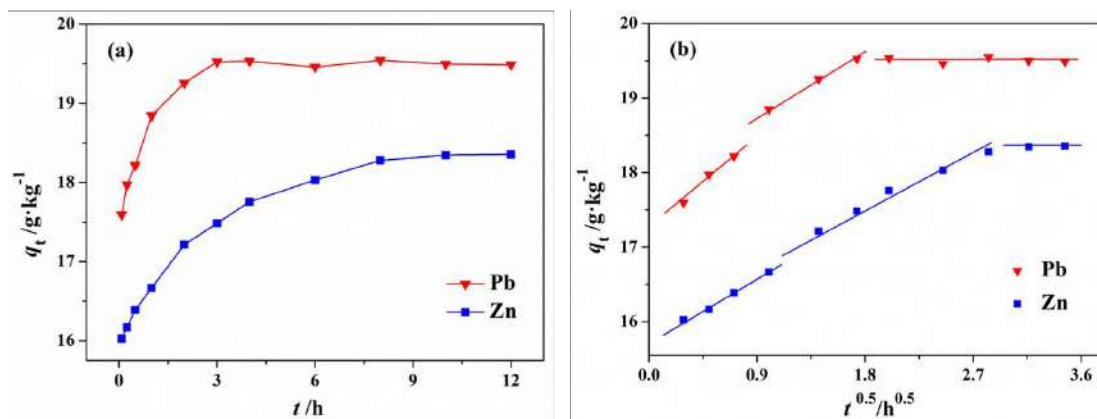
Fig. 1: Competitive adsorption kinetics of Pb and Zn (a), and the results of curve fitted by intraparticle diffusion model (b).

charge-to-radius ratio (Berrin 2012, Zakaria et al. 2017, Uddin 2017). The basic physical and chemical properties of Pb and Zn were shown in Table 1. In terms of ionic radius, the order of competitive adsorption is Zn > Pb (Uddin 2017). The electronegativities of Pb and Zn are important parameters determining the order of adsorption. Oxygen atoms on the soil surface or within soil particles bind to Pb ions with higher electronegativity, forming stronger covalent bonds and facilitating Pb adsorption on the soil (Zakaria et al. 2017). Furthermore, the specific adsorption of heavy metal ions onto the soil is related to their hydrolysis ability (Berrin 2012). An increase in the negative logarithm of the first-order hydrolysis constant, pK_1, can lead to the reduction of the adsorption affinity of heavy metals. Therefore, the preferential adsorption order of heavy metal ions was inversely proportional to the first-order hydrolysis constant, Pb > Zn. Moreover, metal ions with a smaller hydrate ion radius are more easily adsorbed onto soils by ion exchange (Wang et al. 2015). As Pb had a smaller hydrate ion radius than Zn, the former showed stronger adsorption ability. In an adsorption process involving electrostatic attraction alone, a larger charge-to-radius ratio results in greater bond energy (Wang et al. 2015). Therefore, the preferential adsorption order was Zn > Pb. In the present study, the preferential adsorption order of Pb and Zn onto the loess soil was consistent with their electronegativity, hydrolysis constant, and hydrate ion radius.

The effect of LED3A on the competitive adsorption kinetics of Pb and Zn is shown in Fig. 2(a) and the results of the curve fitted by the intraparticle diffusion model are shown in Fig. 2(b). In the presence of 5 g.L^{-1} LED3A, the competitive adsorption kinetic process of Zn was also divided into rapid, slow, and equilibrium stages. However, only two stages (rapid and equilibrium) were recognized in the competitive adsorption of Pb. The equilibrium adsorption times of Pb and Zn were 1 and 6 h, respectively, which were less by 2

and 4 h, respectively, as compared to the equilibrium adsorption in the absence of LED3A. The equilibrium adsorption capacities of Pb and Zn on the soil were 16.99 and 13.38 g.kg^{-1}, respectively, indicating that Pb had a higher adsorption ability than Zn. The adsorption capacities of Pb and Zn in the presence of LED3A were reduced by 2.56 and 4.97 g.kg^{-1}, respectively, compared with those without LED3A addition. This was attributed to the coexistence of competitive adsorption of Pb and Zn onto the soil, competitive chelation of Pb and Zn by LED3A, and soil competing with LED3A for Pb and Zn in the LED3A, soil, Pb, and Zn system. LED3A has a high ability to chelate Pb and Zn, resulting in attenuated adsorption of heavy metal ions on the soil surface and within soil particles, which shortened the time to reach equilibrium. The reduction in Zn adsorption capacity was greater than that in Pb adsorption capacity, indicating that LED3A had a stronger ability to competitively chelate Zn than Pb. A similar conclusion was made by Qiao et al. (2016) who studied the LED3A as an effective washing reagent for lead (Pb)- and zinc (Zn)-contaminated soil.

Pseudo-first-order and pseudo-second-order equations were used to calculate the date for competitive adsorption kinetics, and the calculation formula was as follows (Manhirethan et al. 2018):

$$\ln(q_e - q_t) = \ln q_e - k_1 t \qquad \ldots(2)$$

Table 1: Basic physical and chemical properties of Pb and Zn ions.

Basic properties	Pb	Zn
Ion radius/pm	119	74
Electronegativity	1.8	1.65
First-order hydrolysis constant/pK_1	7.8	8.96
Hydrated ion radius/nm	0.401	0.430
Charge-to-radius ratio	1.68	2.10

$$\frac{t}{q_t} = \frac{1}{k_2 q_e^2} + \frac{t}{q_e} \qquad \ldots(3)$$

where t is the adsorption time (h), q_e and q_t are the heavy metal adsorption capacities at equilibrium and time t, respectively (g.kg^{-1}), k_1 is the first-order rate constant (h^{-1}), and k_2 is the second-order rate constant (kg.g^{-1}.h^{-1}).

The fitting results were summarized in Table 2. The pseudo-second-order kinetic model had a markedly higher correlation coefficient (R^2) than the pseudo-first-order kinetic model when fitting the competitive adsorption process of Pb and Zn. The maximum adsorption capacity (q_{cal}) calculated by fitting to the pseudo-second-order kinetic model was much close to the measured value (q_{exp}). Therefore, the competitive adsorption process of Pb and Zn onto the soil was accurately described by the adsorption mechanisms included in the pseudo-second-order kinetics, such as external liquid film diffusion, surface adsorption, and intraparticle diffusion. Moreover, k_2 was higher for Pb than for Zn, indicating preferential adsorption of Pb onto the soil. In the presence of LED3A, the competitive adsorption kinetic process of Pb and Zn was described by the pseudo-second-order kinetic model in terms of either the R^2 of fitting or the closeness of q_{cal} and q_{exp}. LED3A showed an excellent ability to chelate Pb and Zn in the LED3A, soil, Pb, and Zn system. Therefore, both

q_{cal} and q_{exp} were lower than those without LED3A addition. In the presence of LED3A, the k_2 values of Pb and Zn were 74.23 and 1.72 kg.g^{-1}.h^{-1}, respectively, which were markedly higher than those without LED3A addition. This showed that the presence of LED3A affected the competitive adsorption rate of Pb and Zn onto the soil.

To explain the mechanism of competitive adsorption between Pb and Zn in the absence and presence of LED3A, the data in Fig. 1(a) and 2(a) was fitted using the intraparticle diffusion equation (Eq. 4) (Qiao et al. 2015):

$$q_t = k_d t^{0.5} + a \qquad \ldots(4)$$

where q_t is the heavy metal adsorption capacity at time t (g·kg^{-1}), k_d is the intraparticle diffusion rate constant (kg.g^{-1}.h$^{-0.5}$), and a is the intercept which is the boundary layer and gives an idea about the thickness of the boundary layer, i.e. the larger the intercept, the greater the boundary layer effect.

The fitting results were shown in Fig. 1 (b) and 2 (b). The competitive adsorption of Pb and Zn onto the soil was a continuous multistage diffusion process in both the soil-Pb-Zn and soil-LED3A-Pb-Zn systems, which agreed with the conclusions from the competitive adsorption kinetic curves. The first linear stage reflected a rapid boundary layer diffusion process, the second linear stage reflected a slow pore diffusion process, and the third one reflected a final

Table 2: Parameters of pseudo-first-order and pseudo-second-order kinetic equations.

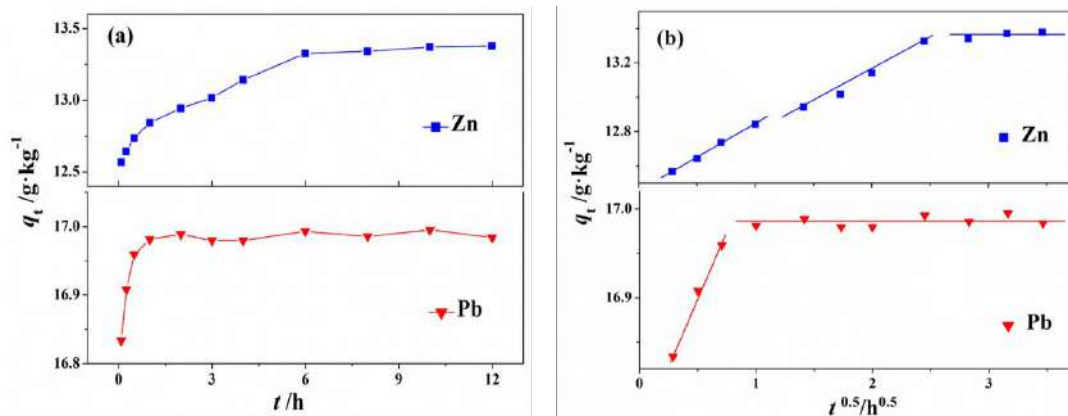| Adsorption type	q_{exp}/g.kg^{-1}	Pseudo-first-order kinetic equation			Pseudo-second-order kinetic equation		
		k_1/h^{-1}	q_{cal}/g.kg^{-1}	R^2	k_2/kg.g^{-1}.h^{-1}	q_{cal}/g.kg^{-1}	R^2
Pb	19.55	1.32	2.70	0.9834	2.49	19.54	0.9999
Zn	18.35	0.55	3.33	0.9552	0.58	18.45	0.9999
LED3A+Pb	16.99	1.33	0.12	0.9236	74.23	16.98	1.0000
LED3A+Zn	13.38	0.50	2.22	0.9796	1.72	13.41	0.9999

Fig. 2: Competitive adsorption kinetics of Pb and Zn in the presence of LED3A (a), and the results of curve fitted by intraparticle diffusion model (b).

competitive equilibrium process. The fitting parameters were listed in Table 3. The R^2 values of linear fitting at each stage were greater than 0.99. The fitted apparent rate constant, k_{d1}, was always greater than k_{d2} for the competitive adsorption of Pb and Zn in the absence or presence of LED3A, indicating that intraparticle pore diffusion was the controlling step for the competitive adsorption rate of the heavy metals. However, the linear plot of q_t vs. $t^{0.5}$ did not pass the origin throughout the competitive adsorption process, indicating that intraparticle diffusion was not the only mechanism controlling the competitive adsorption rate. The competitive adsorption of Pb changed from a three-stage to two-stage process after LED3A addition, suggesting that LED3A reduced the porosity diffusion of Pb during competitive adsorption due to competing with soil for Pb. Moreover, the a_1 and a_2 values in the fitting results were reduced to different degrees after the LED3A addition, indicating that LED3A increased the change in external mass transfer and decreased the change in internal mass transfer, which shortened the equilibrium time of the competitive adsorption process of Pb and Zn. This occurred because LED3A has good solubility and forms soluble chelates LED3A-Pb and LED3A-Zn after competitive chelation with Pb and Zn, which reduces the competitive adsorption of Pb and Zn on the surface of soil particles and within the pores.

Effect of LED3A Concentration on Competitive Adsorption of Pb and Zn

The molecular structure of LED3A comprises three carboxyl groups and two tertiary amino groups. LED3A can form stable and soluble chelates with Pb and Zn ions by coordinating through oxygen and nitrogen atoms. Furthermore, introducing a fatty acyl group into the molecular structure means that micellization can enhance greatly affect its selectivity for chelating heavy metals. The chelation of heavy metals (M, namely Pb and Zn) by LED3A is illustrated as follows:
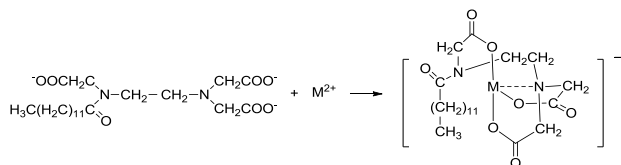
Adding LED3A to the soil and heavy metal solution,

LED3A could chelate M^{2+} to keep them in the solution system. Soil can make M^{2+} leave the solution system through adsorption. Therefore, LED3A and the soil compete for the heavy metal ions in the system, which affected the adsorption of heavy metal ions onto the soil. The effect of LED3A on the adsorption of Pb and Zn onto soil can be described by q_e:

$$\triangle q_e = q_e - q_L \qquad \ldots(5)$$

where q_e is the equilibrium adsorption capacity of soil for Pb or Zn in the absence of LED3A (g.kg^{-1}) and q_L is the equilibrium adsorption capacity of soil for Pb or Zn in the presence of LED3A (g.kg^{-1}).

The effect of the LED3A solution concentration on the competitive adsorption of Pb and Zn onto soil is shown in Fig. 3. As the concentration of LED3A increased from 0.1 to 0.7 g.L^{-1}, the adsorption capacities of Pb and Zn decreased. In contrast, Δq_e increased from 1.21 to 1.47 g.kg^{-1} and 1.64 to 4.74 g.kg^{-1} for Pb and Zn, respectively. When the LED3A concentration was increased to 5 g.kg^{-1}, the adsorption capacities of Pb and Zn continued to decrease and Δq_e reached maximum values of 3.37 and 8.90 g.kg^{-1}, respectively. When the LED3A concentration was greater than 5 g.kg^{-1}, the adsorption capacities of Pb and Zn reached a competitive equilibrium state, because the ability of LED3A to chelate Pb and Zn was related to the LED3A concentration (Qiao et al. 2016). The critical micelle concentration (CMC) of LE-D3A is 0.71 g.L^{-1} (Qiao et al. 2016). In the LED3A, soil, Pb, and Zn system, when the LED3A concentration was lower than the CMC, LED3A mainly existed as monomers in the aqueous solution, which were less competitive for Pb and Zn adsorption than the soil. When the LED3A concentration exceeded the CMC, LED3A mainly existed as micelles in the aqueous solution, which showed a significantly increased ability to chelate Pb and Zn. As a result, the adsorption capacities of Pb and Zn on soil were significantly decreased, while the Δq_e was significantly increased. Comparing Δq_e for the two heavy metals, it was found that Δq_e for Pb was markedly lower than that of Zn. This was due to the different competitive abilities of soil and LED3A micelles for Pb and Zn. When the LED3A concentration is greater than 5 g.L^{-1}, LED3A exhibited the strongest effect on the competitive adsorption of Pb and Zn onto the soil.

Table 3: Kinetic parameters of intraparticle diffusion model.

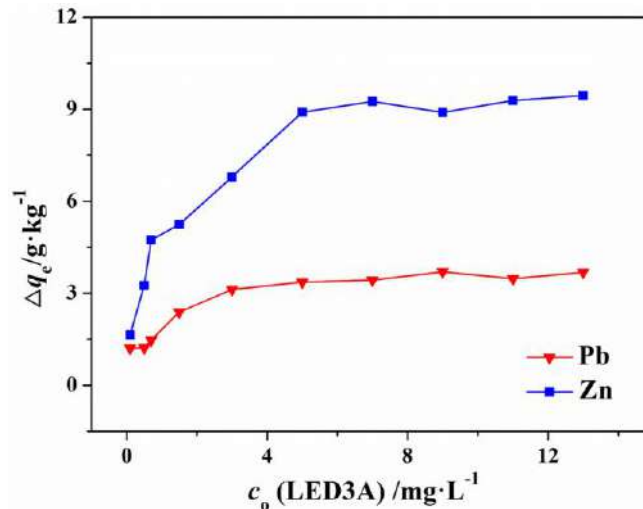| Adsorption type		k_{d1}/g.kg^{-1} h$^{-0.5}$	a_1	R^2	k_{d2}/g.kg^{-1}.h$^{-0.5}$	a_2	R^2
Pb		1.49	17.19	0.9933	0.93	17.92	0.9991
Zn		0.92	15.74	0.9968	0.75	16.19	0.9952
LED3A	Pb	0.30	16.75	0.9950	-	-	-
	Zn	0.39	12.45	0.9991	0.37	12.38	0.9925

Fig. 3: Effect of LED3A concentration on competitive adsorption of Pb and Zn onto loess soil.

Competitive adsorption of different concentrations of Pb and Zn, and the effect of LED3A

The competitive adsorption capacity of heavy metal ions on adsorbents is related to the ion concentration. (Dou et al. 2020). The Pb (Zn) concentration was set to 0.05 $g.L^{-1}$ and the Zn (Pb) concentration was changed to determine the effect of Zn (Pb) concentration on Pb (Zn) adsorption onto the soil. As shown in Fig. 4, the adsorption capacity of Pb onto the soil was generally not affected by the change in Zn concentration, remaining stable at 19.44 $g.kg^{-1}$. Nevertheless, the adsorption capacity of Zn decreased with increasing Pb concentration and generally stabilized at 17.6 $g.kg^{-1}$ with a Pb concentration of 0.25 $g.L^{-1}$, demonstrating obvious competitive adsorption.

According to the results by Abdelfattah and Wada (1981) and Wilcke et al. (1998), the soil particle surface is markedly heterogeneous, in which all adsorption sites can be divided into groups with high binding energy and low binding energy. Adsorption firstly occurs at high-energy adsorption sites during the initial stage, whereas low energy adsorption sites start to adsorb heavy metal ions as the heavy metal concentration is further increased (Dong et al. 2010, Gao et al. 2017). Generally, heavy metal ions adsorbed by electrostatic interaction have low binding energies, and heavy metal ions adsorbed specifically have high binding energies. The above analysis showed that as the Zn concentration increased, it was difficult for Zn ions to compete with Pb ions to be adsorbed at high energy and low energy adsorption sites. However, when the Pb concentration increased, Pb ions competed with Zn ions to be adsorbed at low-energy adsorption sites and some Zn ions adsorbed at high energy adsorption sites. Therefore, in the competitive system, the soil showed a higher ability for specific adsorption of Pb relative to that of Zn.
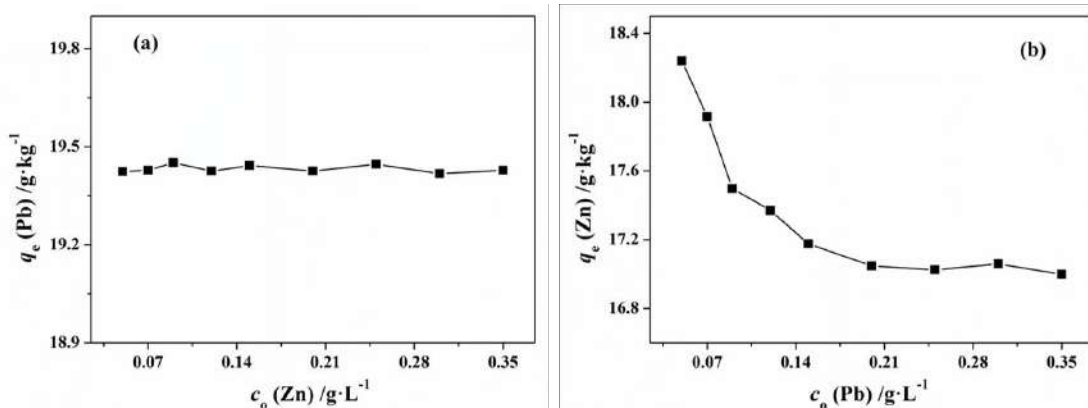

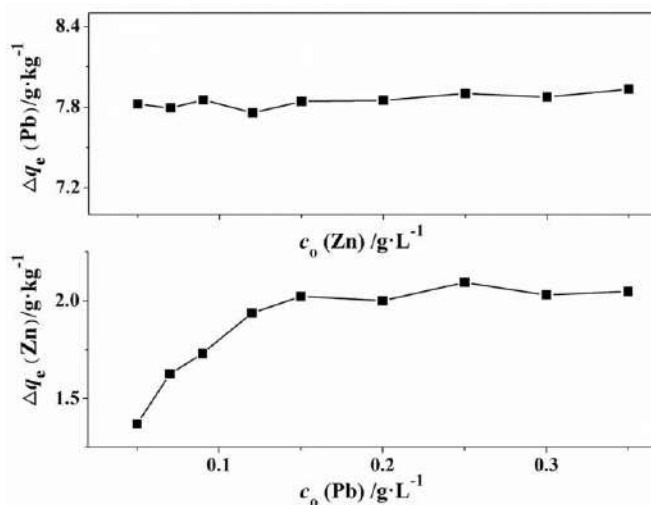Fig. 4: Competitive adsorption of different concentrations of Pb and Zn onto loess soil.

Fig. 5: Competitive adsorption of different concentrations of Pb and Zn in the presence of LED3A.

The effect of Pb concentration on Zn adsorption capacity was greater than that of Zn concentration on Pb adsorption capacity, and the increase in Pb concentration inhibited Zn adsorption onto the soil.

The effect of LED3A on the competitive adsorption of Pb and Zn at different concentrations is described by Eq. 5. As shown in Fig. 5, the Δq_e values representing the LED3A induced change in Pb and Zn adsorption capacities were greater than zero, indicating different extents of reduction in Pb and Zn adsorption capacities caused by LED3A. In general, the Δq_e of Pb did not change with increasing Zn concentration and remained 7.85 g.kg^{-1}, which suggested that the Pb adsorption capacity was not affected by the Zn concentration, mainly due to competition between LED3A and soil for Pb. In contrast, the Δq_e of Zn increased with increasing Pb concentration, with the greater reduction in Zn adsorption capacity mainly due to competition between LED3A and soil for Zn, and Pb competing for Zn adsorption sites. When the Pb concentration was >0.15 g.L^{-1}, the Δq_e of Zn generally remained 2.04 g.kg^{-1}. The Pb concentration for the Zn adsorption equilibrium was substantially lower in the presence of LED3A than in the absence of LED3A, implying that the competition for Zn adsorption sites between LED3A and soil was stronger than that of Pb. In the competitive LED3A, soil, Pb and Zn system, the Δqe of Pb was greater than that of Zn, implying that LED3A increased the influence of Zn concentration on Pb adsorption capacity while decreasing the effect of Pb concentration on Zn adsorption capacity.

CONCLUSION

The preferential adsorption order for Pb and Zn was connected to their electronegativity, hydrolysis constant, and hydrate ion radius, with Loess having a larger competitive adsorption capability for Pb than Zn. LED3A shortened the equilibrium time of competitive adsorption and reduced Pb and Zn adsorption capacities on the soil by 2.56 and 4.97 g.kg^{-1}, respectively. The competitive adsorption kinetic processes could be best described by the pseudo-second-order kinetic equation. For Pb, Zn competitive adsorption, intra-particle diffusion was the rate control step, but it was not the only rate control mechanism. As LED3A concentrations >5 g.L^{-1}, LED3A showed the greatest effect on the competitive adsorption of Pb and Zn. LED3A decreased the effect of Pb concentration on Zn adsorption capacity while increasing the effect of Zn concentration on Pb adsorption capacity. LED3A showed significant potential for chelating a lot of heavy metals from contaminated soil.

REFERENCES

Abdelfattah, A. and Wada, K. 1981. Adsorption of lead, copper, zinc, cobalt, and cadmium by soils that differ in cation-exchange materials. Europ. J. Soil Sci., 32: 271-283.

Berrin, T. 2012. Significance of thermodynamic and physical characteristics on permeation of ions during membrane separation: Hydrated radius, hydration free energy, and viscous effects. Sep. Purif. Technol., 86: 119-126.

Cao, M., Hu, Y., Sun, Q., Wang, L., Chen, J. and Lu, X. 2013. Enhanced desorption of PCB and trace metal elements (Pb and Cu) from contaminated soils by saponin and EDDS mixed solution. Environ. Pollut., 174: 93-99.

Diao, J.R., Zhao, B.W., Ma, F.F., Wang, X. and Ding, W.J. 2016. Solubility enhancement of phenanthrene using novel chelating surfactant. Chem. Papers, 70: 375-383.

Dong, X., Li, C., Li, J., Wang, J., Liu, S. and Ye, B. 2010. A novel approach for soil contamination assessment from heavy metal pollution: A linkage between discharge and adsorption. J. Hazard. Mater., 175: 1022-1030.

Dou, W., Liu, J. and Li, M. 2020. Competitive adsorption of Cu^{2+} in Cu^{2+}, $Co^{2+,}$ and Ni^{2+} mixed multi-metal solution onto graphene oxide (GO)-based hybrid membranes. J. Mol. Liq., 12: 114516.

Gao, M., Lv, M., Gong, X., Song, W., Qi, Y. and Li, Z. 2017. Effect of temperature and aging on the adsorption and desorption of menadione in soil. Environ. Prog. Sustain. Energy, 36: 1997-1004.

Garridorodriguez, B., Cutillasbarreiro, L., Fernándezcalviño, D., Ariasestévez, M., Fernándezsanjurjo, M.J., Alvarezrodríguez, E. and Núñezdelgado, A. 2014. Competitive adsorption and transport of Cd, Cu, Ni and Zn in a mine soil amended with mussel shell. Chemosphere, 07: 379-385.

Guemiza, K., Coudert, L., Metahni, S., Mercier, G., Besner, S. and Blais, J.F. 2017. Treatment technologies used for the removal of As, Cr, Cu, PCP and/or PCDD/F from contaminated soil: A review. J. Hazard. Mater., 333: 194-214.

Kim, E.J., Jeon, E.K. and Baek, K. 2016. Role of reducing agent in the extraction of arsenic and heavy metals from soils by use of EDTA. Chemosphere, 152: 274-283.

Kou, S., Lai, M.S. and Lin, C.W. 2006. Influence of solution acidity and $CaCl_2$ concentration on the removal of heavy metals from metal-contaminated rice soils. Environ. Pollut., 44: 918-925.

Manirethan, V., Raval, K., Rajan, R., Thaira, H. and Balakrishnan, R.M. 2018. Kinetic and thermodynamic studies on the adsorption of heavy metals from aqueous solution by melanin nano pigment obtained from marine source: Pseudomonas stutzeri. J. Environ. Manag., 214: 315-324.

Muhammad, A.K., Sardar, K., Ding, X., Anwarzeb, K. and Mehboob, A. 2018. The effects of biochar and rice husk on adsorption and desorption of cadmium onto soils with different water conditions (upland and saturated). Chemosphere, 193: 1120-1126.

Peng, L., Liu, P., Feng, X., Wang, Z., Cheng, T., Liang, Y., Lin, Z. and Shi, Z. 2018. Kinetics of heavy metal adsorption and desorption in soil: developing a unified model based on chemical speciation. Geochim. Cosmochim. Acta, 224: 282-300.

Qiao, H.T., Liu, Y., Dong, Y.H., Li, S., Wang, P. and Jin, T. 2015. Adsorption of sulfamonomethoxine antibiotics to cucurbit[6]uril polymer: kinetics and thermodynamic studies. Desalin. Water Treat., 54: 113-121.

Qiao, H.T., Zhao, B.W., Diao, J.R., Huang, L.P., Zhong, J.K. and Ma, F.F. 2016. Removal of lead and zinc from contaminated soil by a novel chelating surfactant. Clean Soil Air Water, 44: 1191-1197.

Qiu, R.L., Zou, Z.L., Zhao, Z.H., Zhang, W.H., Zhang, T., Dong, H.Y. and Wei, X.G. 2010. Removal of trace and major metals by soil washing with Na_2EDTA and oxalate. J. Soils Sed., 10: 45-53.

Shi, Z., Toro, D.M.D., Allen, H.E. and Sparks, D.L. 2013. A general model for the kinetics of heavy metal adsorption and desorption on soils. Environ. Sci. Technol., 47: 3761-3767.

Uddin, M.K. 2017. A review on the adsorption of heavy metals by clay minerals, with a special focus on the past decade. Chem. Eng. J., 308: 438-462.

Wang, P., Peng, H., Liu, J., Zhu, Z., Bi, X., Yu, Q. and Zhang, J. 2020. Effects of exogenous dissolved organic matter on the adsorption-desorption behaviors and bioavailabilities of Cd and Hg in a plant-soil system. Sci. Total Environ., 728: 138252.

Wang, X., Zhao, J., Yao, X. and Chen, W. 2004. Synthesis and properties of N-hexadecyl ethylenediamine triacetic acid. J. Coll. Interface Sci., 279: 548-551.

Wang, Y., Tang, X.W., Wang, H.Y. and Liu, W. 2011. Sorption and desorption behaviors of heavy metal Mn(II) on loess soil. Chinese J. Geotech. Eng., 33(Supp1): 369-373.

Wang, Z., Huang, G., An, C., Chen, L. and Liu, J. 2015. Competitive adsorption characteristics of water-quenched blast furnace slag (WBFS) towards Cu^{2+}, Cd^{2+} and Zn^{2+}. Chem. Ind. Eng. Prog., 34: 4071-4078.

Wilcke, W., Müller, S., Kanchanakool, N. and Zech, W. 1998. Urban soil contamination in Bangkok: Heavy metal and aluminum partitioning in topsoils. Geoderma, 86: 211-228.

Yuan, X., Xue, N. and Han, Z. 2021. A meta-analysis of heavy metals pollution in farmland and urban soils in China over the past 20 years. J. Environ. Sci., 101: 217-226.

Zakaria, M., Sofiane, M., Salima, S.B., Geraldin, A., Abdelhamid, E. and Derdour, A. 2017. Triazole containing magnetic core-silica shell nanoparticles for Pb^{2+}, Cu^{2+} and Zn^{2+} removal. Arab. J. Chem., 10: 1039-1051.

Water Quality Evaluation and Spatiotemporal Variation Characteristics of Wenyu River Based on Comprehensive Water Quality Identification Index Method

Wang Keke, Men Baohui† and Xing Yanling

School of Water Resources and Hydropower Engineering, North China Electric Power University, Beijing 102206, China

†Corresponding author: Men Baohui; menbh@ncepu.edu.cn

ABSTRACT

In recent years, the water environment management of the Wenyu River has yielded positive outcomes. In comparison to earlier, the general water quality has substantially improved. However, some areas' water quality has not improved as a result of the overall trend of improvement, which has implications for the surrounding areas and the entire water environment. To further explore the water environmental quality of specific river sections, this paper adopts the five monitoring sections of Shahe Gate, Mafang, Lutuan Gate, Xinbao Gate, and the additional sewage outlet in 2019, and the three main water quality indicators of COD, DO, and NH$_3$-N. The water quality of the Wenyu River was evaluated using the comprehensive water quality identification index method, and the characteristics of its temporal and spatial changes were studied using correlation analysis and spatial clustering. The results have shown that the Wenyu River is generally Grade V water during the flood season, and is inferior to Grade V water during the non-flood season. All indicators have a regular time and space distribution and are highly influenced by environmental and human factors. Overall, the water quality of the Wenyu River may essentially reach the water environment function zoning target value. Improvements to the river portions below the Xinbao sluice, as well as the use of rainwater resources, must be prioritized.

INTRODUCTION

Wenyu River is located in the northeast of Beijing, which has many springs along the coast and rich geothermal resources (Cai et al. 2014) Many rivers converge on this river and eventually flow into the ocean. It is an important river in Beijing. Therefore, studying the water quality and change characteristics of the Wenyu River is of great significance to the overall economic planning and urban construction.

Water quality evaluation is of great significance to the formulation of water governance and water policy in a certain area. Appropriate water quality evaluation methods can better reflect the water quality status and pollution characteristics of a certain area. Currently, there are many ways for assessing water quality. The grey evaluation method, fuzzy comprehensive analysis method, matter element analysis method, and others are the primary methodologies (Wang 2008). The advantages and disadvantages of these methods are often compared to see if they are accurate in a certain area. In the water quality study of the Ikare community, Oladipo Johnson et al. (2021) compared and examined the findings of fuzzy logic and water quality index methodologies. In equal consideration of measured values and surface water quality, fuzzy logic outperforms the water quality index, according to the evaluation results. Both models, however, can differentiate rivers based on the quality of their water. Ning et

al. (2020) used five different methods to evaluate the water quality of the Three Gorges section of the Huangshi section of the Yangtze River, including the single factor evaluation method, the comprehensive water quality label index method, and the single factor water quality label index method. The complete water quality label index method has the best effect and can fundamentally determine numerous elements of water quality, according to the findings. Other methods have their own advantages and limitations. The water quality index method is widely used in water quality evaluation and its evaluation results have good reliability. Howladar et al. (2021), for example, observed pollution of related water quality in the Surma River area of Bangladesh. According to the findings, the river's middle sections are heavily contaminated. The related limitations for BOD, COD, TSS, CO$_2$, and turbidity are all exceeded. Relevant proposals are made in light of the existing water pollution problem. Suriadikusumah et al. (2020) investigated the physical, chemical, and microbiological parameters of the Cipeusing River using the pollution index method. According to the findings, the river was moderately polluted in 2016 and highly polluted in 2017. The primary cause is pollution caused by humans. So there should be technical improvements and perfections in response to the problems in this area. Nong et al. (2020) investigated the seasonal and regional characteristics of water quality in the South-to-North Water Diversion Project

by monitoring 16 water quality parameters and using 5 key factors to create a minimum water quality index model and evaluate the water quality. The findings show that the water quality remained stable during the research phase and that it was "great." The research results demonstrated the reliability and accuracy of the water quality index approach. As a result, the water quality index approach has a high reference value in today's water quality assessment, and its application possibilities are vast. To analyze the water quality of the Wenyu River, this article uses the comprehensive water quality index approach, which can do both quantitative and qualitative water quality evaluations. In particular, it is feasible to assess the degree of pollution in water of worse quality than Grade V (Xu 2005a, Liang et al. 2013). In this study, we also exemplify the current positive state of water quality management. Although the water quality, in general, has improved, the water quality in some places of the Wenyu River remains unfavorable. Five monitoring sections of Shahe Gate, Mafang, Lutuan Gate, Xinbao Gate, and the additional sewage outflow were chosen as research sample stations to better investigate the water quality in various places. To study its temporal and spatial distribution characteristics through the final evaluation results, we can further understand the water quality distribution in the research section and the current water pollution problems.

MATERIALS AND METHODS

Overview of the Study Area

With a total length of 47.5 km, the Wenyu River is an older developed river in Beijing's history. The confluence of three tributaries of the Dongsha River, Beisha River, and Nansha River forms the upper parts of the river. The ecological management of the Wenyu River has yielded preliminary results in recent years. The well-known "six demonstrations" (Beijing Municipal Bureau of Ecological Environment n.d.) in the water purification demonstration area of the constructed wetland in Wenyu River. The specific locations are shown in Fig. 1.

Monitoring Data

Field measurements and laboratory water sample processing are used to obtain monitoring data. The data in this article is based on observations from five parts over the course of 2019. Water samples are taken once a month from each of them. DO, COD, NH3-N, and other water quality indicators are commonly used. In 2019, the experimental data is based on the average monthly monitoring data from five monitoring areas. Fig. 2(a)(b) shows the monitoring data for each indicator:

Research Methods

Comprehensive Water Quality Labeling Index Method

The comprehensive water quality labeling index method (Gu et al. 2016) is a method for calculating complete water quality information based on the single-factor water quality labeling index approach (Xu 2005b). The following is the structure of the complete water quality labeling index, which is made up of integer digits with three or four decimal places (Xu 2005a, 2005b):

$$I_{wq} = X_1.X_2X_3X_4 \qquad \ldots(1)$$

where I_{wq} is the comprehensive water quality labeling

Fig. 1: Sampling points of each monitoring section.

index, $X_1.X_2$ is the average value of the single-factor water quality labeling index of all measured values; X_3 is the number of single indicators in the complete water quality evaluation that are inferior to the water environment functional zone target.; X_4 is the result of a comparison between the comprehensive water quality category and the overall water environment function zone's target value. X_4 can be one or two significant digits depending on the degree of pollution in the overall water quality.

$$X_1.X_2 = \frac{1}{n}\sum_1^n P_i \qquad \ldots(2)$$

The n is the number of water quality indicators, and P_i is the single-factor water quality indicator index of the i-th water quality indicator.

Coefficient of Variation Weighting Method

In the classic comprehensive water quality labeling index, the average value of each single-factor water quality labeling index is directly employed as the end result. It cannot emphasize the objective influence of excessive concentration and the severity of factor changes on water quality, nor can it emphasize the subjective impact of subjective factors, which has some limits (Sun et al. 2019). Cheng et al. (2019),

in their study of many weighting methods, concluded that the results of weighting methods based on the coefficient of variation are reasonable and reliable, and can objectively reflect the relative relevance of each assessment index. As a result, this study uses this weighting method to determine the importance of each indicator. The following is the formula for calculating it:

$$V_i = \frac{\delta_i}{\sum_1^n \delta_i} \qquad \ldots(3)$$

$\overline{C}_i$ where V_i is the weight of the i-th index; δ_i is the coefficient of variation of the i-th index; $\delta_i = \frac{S}{\overline{C}_i}$, S_i is the mean square error of the i-th index;   is the average mass concentration of the i-th index; n is the number of evaluation indexes.

RESULTS AND DISCUSSION

The Evaluation Results

The single-factor water quality labeling index method was used to process the monitoring data, and the results are shown in Table 1 below.

Using the coefficient of variation weighting method to calculate the weight of each item, the results are shown in Table 2.

According to the weight coefficient and the data of the single-factor water quality labeling index method, the overall evaluation of the water body is carried out, and the results are shown in Table 3.

Seen from the evaluation results, three indicators' impact on water pollution sorted for COD> NH_3-N> DO, the overall water quality during the flood season is Grade V water, and the non-flood season is inferior to Grade V water. This result is similar to that of Cai et al. (2019). The improved evaluation results are more differentiated than before. The water quality is better during the flood season, and worse during the non-flood season. This is because the traditional method does not consider the weight of each evaluation factor, but the coefficient of variation has considered the differences between the indicators, which can objectively reflect the relative importance of each indicator (Cheng et al. 2019), making the evaluation results more accurate. The phenomenon that water quality in the flood season is better than the water quality in the non-flood season is reflected in the related studies of Li & Wang (2007) and Yang et al. (2011).

The main reason is that at the start of the flood season (June), surface runoff brings a large amount of land-sourced pollutants accumulated during the dry season, resulting in a higher concentration of surface water; in the wet season, the pollutants are diluted under the wash of rain, and the con-
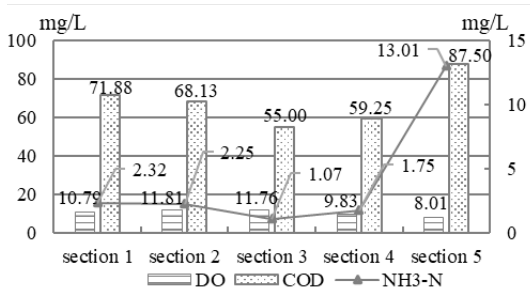

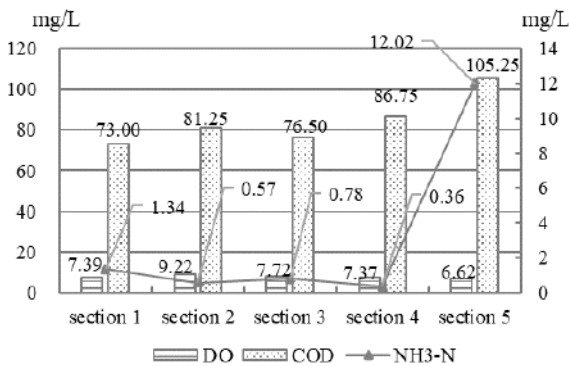Fig. 2(a) Monitoring data of each the section in the flood season.

Fig. 2(b) Monitoring data of each section during non-flood season.
Note: June to September is the flood season

centration decreases; in late August of the flood season, with the gradual decrease of rainfall, the concentration of some pollutants has rebounded, but compared to the beginning of the flood season, the concentration of some pollutants has decreased (Yang et al. 2011).

Time-Varying Characteristics

The law of time change: We use the clustering method to classify each month's water quality, SPSS to analyze the data, and the Euclidean distance to quantify the distance between the indicators (Fovell & Fovell 1993). The final clustering result is shown in Fig. 3.

According to the clustering results, 12 months can be divided into 3 categories, among which January, May, July, August, and November are one category, February, March, April, and December are one

category, and June, September, and October are one category.

Variation law of each index: To further analyze the influence of relevant indicators on the time distribution law, the trend chart of DO, COD, and NH_3-N over time is drawn as shown in Fig. 4.

The DO concentration gradually decreases from January to July, increases in August and September, and decreases in October; the COD concentration fluctuates within a certain range from January to May, with an obvious peak in June and September and a significant decrease in August and November; and the NH3-N concentration is lower from June to October, and higher from January to March, and fluctuates within a certain range at a certain time.

We use the Pearson coefficient to analyze the correlation between COD, DO and NH_3-N with water temperature and

Table 1: Calculation result of water quality index P_i for each section.

Monitoring section	Section name	Water season	Water function zoning target value	DO [mg.L^{-1}]	COD$_{cr}$ [mg.L^{-1}]	NH$_3$-N [mg.L^{-1}]
Section 1	Shahe gate	flood season	IV	1.10	6.82	4.70
		Non-flood season		1.70	9.25	6.62
Section 2	Mafang	flood season	IV	1.40	10.16	3.10
		Non-flood season		1.90	8.84	6.52
Section 3	Lutuan gate	flood season	IV	1.00	9.75	3.60
		Non-flood season		1.90	7.53	4.10
Section 4	Xinbao gate	flood season	V	1.10	10.75	2.60
		Non-flood season		1.50	7.92	2.50
Section 5	Outfall	flood season	V	1.60	7.63	26.11
		Non-flood season		1.10	10.85	28.13

Note: data of Water function zoning target values are from the Beijing Municipal Bureau of Ecological Environment (n.d.).

Table 2: Weight coefficients of each indicator.

Monitoring section	Water season	Weight of each indicator		
		DO	COD	NH$_3$-N
Section 1	flood season	0.071	0.025	0.067
	Non-flood season	0.088	0.047	0.070
Section 2	flood season	0.034	0.019	0.169
	Non-flood season	0.048	0.041	0.077
Section 3	flood season	0.034	0.020	0.074
	Non-flood season	0.040	0.049	0.097
Section 4	flood season	0.026	0.025	0.307
	Non-flood season	0.035	0.065	0.114
Section 5	flood season	0.032	0.030	0.069
	Non-flood season	0.047	0.065	0.116

PH, and make a scatter plot for the two items with strong correlation. The correlation analysis results are shown in the following Tables 4, 5, and 6 respectively, and the scatter plot is shown in Fig. 5, 6,7(a) (b) respectively.

From the correlation analysis results and the scatter plot, it can be seen that the DO concentration and PH are basically in a significant positive correlation throughout the year, and DO have little correlation with temperature. The scatter plot is in good agreement with the data analysis results. The explanation for its distribution law, according to the law of DO over time and the results of the correlation study, is mostly related to the algae in the water. In a mildly alkaline environment, suspended plants such as algae are densely spread in the water, and diatom species are very active (Hulyal & Kaliwa 2009). The water quality of the Wenyu River was slightly alkaline, but as the PH grew, phytoplankton photosynthesis increased, and DO concentration increased, the two had a strong relationship, which was consistent with Zhu et al. (2020). From January to March, the temperature is more suitable as well as the acidity and alkalinity of the water are more suitable. Large aquatic organisms have strong photosynthesis, so DO concentration is high. In August and September, the rainfall intensity increases, and the aquatic environment has high turbulence, increasing atmospheric replenishment in the water, as well as an increase in DO.

The COD concentration has little correlation with PH and temperature, so there is no need to draw a scatter diagram to verify its correlation. The distribution of COD does not match the time change of the flood season and the non-flood season, so precipitation is not a factor affecting COD. The source of biogenic organic matter of COD is mainly biological metabolism and organic matter produced by the decomposition of corpses (Pan et al. 2020). Because phytoplankton photosynthesis is strong in the summer, producing more oxygen,

the COD content in the water body is comparatively low; but, because photosynthesis is weak in the fall and winter, the COD concentration rises to some amount. In July and August, however, the concentration reduces considerably, whereas, in June and September, it climbs. Other sources of organic input, such as sewage discharge and the application of herbicides and fertilizers, could cause COD concentrations to fluctuate to some extent.

NH_3-N is negatively correlated with PH in flood seasons, has little correlation in non-flood seasons, and has little correlation with temperature. The results of the image and the table are consistent. For NH_3-N, microorganisms in water can treat ammonia nitrogen in water through nitrification reaction, and this decomposition conversion process is more efficient in a slightly alkaline environment (Wang 2021) and nitrifying bacteria have the highest activity at pH 7~8 (Mogeng 1997). The water quality is weakly alkaline, the PH rises, the nitrification reaction rate is faster, and the NH_3-N concentration in the water then decreases, so the NH_3-N has a good negative correlation with PH. The suitable temperature for the nitrification reaction of nitrifying bacteria is 20~30°, the reaction rate decreases below 15°, and basically stops at 5°. According to the measured data, the temperature in Wenyu River from January to April is basically around 0.2~17.6, so the temperature is relatively low, and the microbial reproduction and the reaction rate are reduced, so ammonia
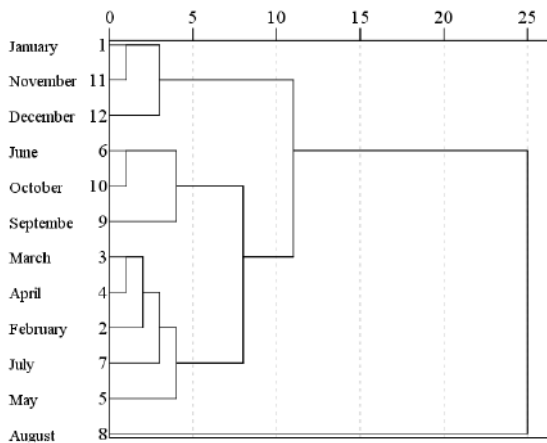
Table 3: Comparison results before and after method improvement.

	After improvement	Before improvement
Flood season	5.060	6.161
Non-flood season	7.782	6.781

Table 4: Correlation between DO and environmental factors

DO	PH	Temperature
Flood season	0.645	0.496
Non-flood season	0.581	-0.689

Table 5: Correlation between COD and environmental factors.

COD	PH	Temperature
Flood season	0.029	-0.382
Non-flood season	0.033	0.086

Table 6: Correlation between NH_3-N and environmental factors.

NH_3-N	PH	Temperature
Flood season	-0.404	-0.235
Non-flood season	-0.269	0.084

Fig. 3: Time clustering results using average join.

Wang Keke et al.

DO (mg/L)   Trend of DO

COD (mg/L)   Trend of COD

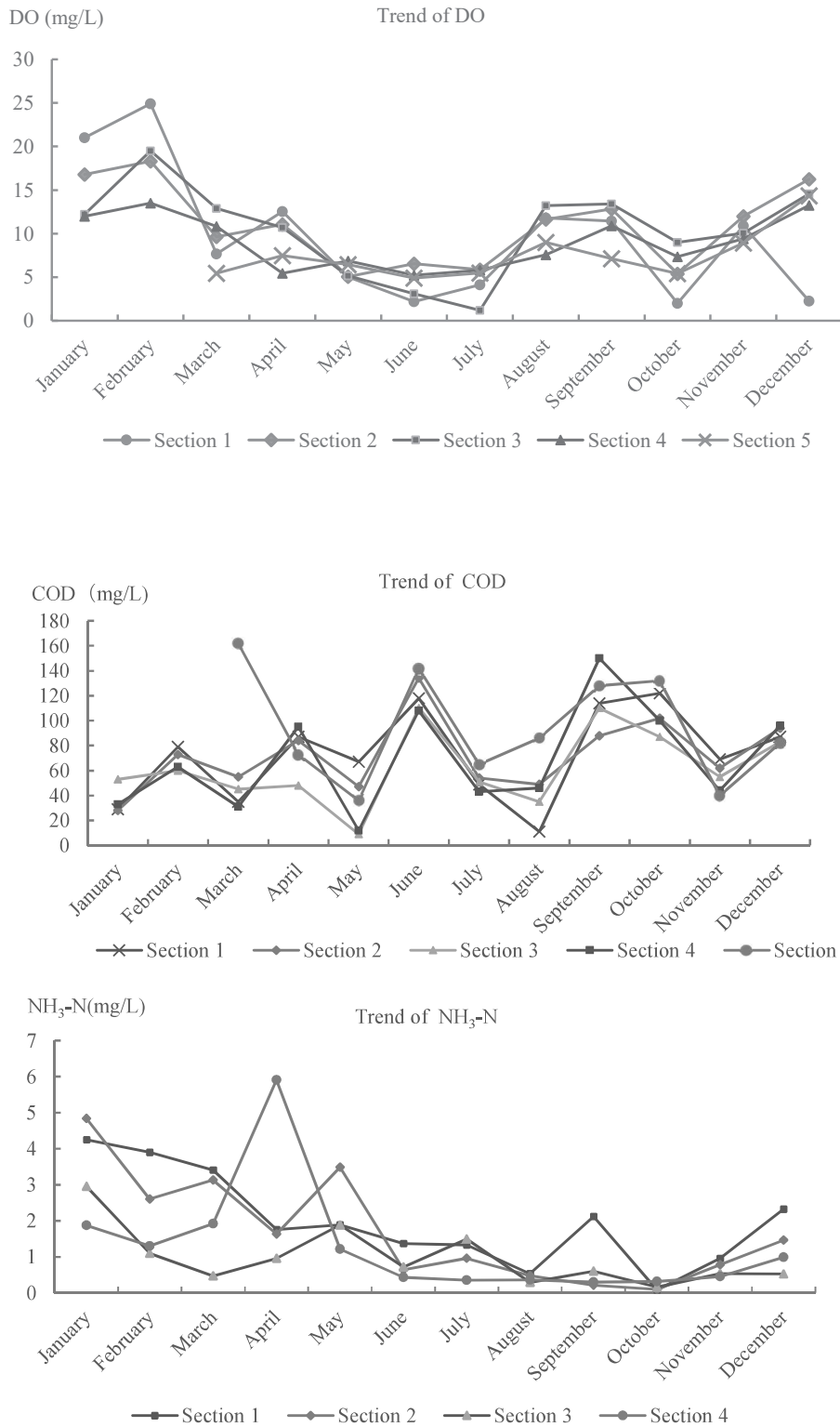NH$_3$-N(mg/L)   Trend of NH$_3$-N

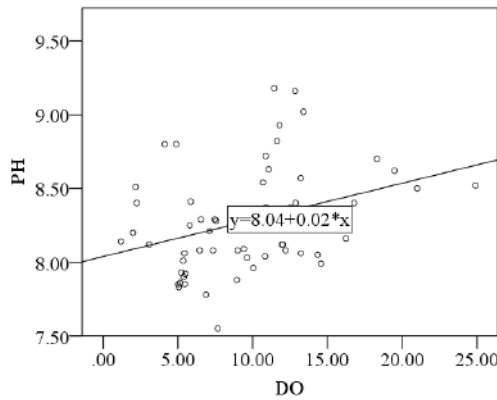Fig. 4: Trends of water quality indicators in 2019.

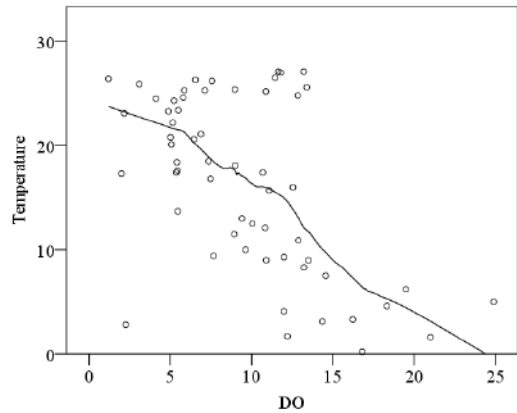Fig. 5: Scatter plot of DO and pH.

Fig. 6: Scatter plot of DO and temperature.

nitrogen concentration is high from May to September, the temperature is in the range of 20.1~127.1, which is the ideal temperature for the nitrification reaction. As a result, the reaction rate is fast and the NH3-N concentration is low. From October to December, the temperature range shifted from 2.8~118.5, the temperature dropped, the reaction rate dropped, and the concentration rose again.

Based on the above analysis, the water body generally presents a seasonal change pattern, with low pollution indicators during the flood season from June to September, and relatively high pollution indicators in other months during the non-flood season, which is related to the impact of human factors such as agricultural non-point source pollution.

Spatial Distribution Characteristics

Use spatial clustering method to cluster analysis of five sections, use SPSS to process the data, and evaluate the water quality of each section separately. The final classification results are shown in Fig. 8, and the results of water quality evaluation are shown in Table 7.

The five sections can be separated into two categories, as shown in the diagram. Sections 1, 2, 3, and 4 are all part of the same category, whereas section 5 is a single category with water quality that is significantly lower than category V. The spatial clustering and water quality evaluation results were extremely consistent.

Many more effective treatment experiments and related studies have been conducted for the Wenyu River's water quality management. To analyze the Longdao River of the Wenyu River, Zhu et al. (2021) used bypass offline river purifier technology and system. The "pond-wetland system" and the Longdao River pseudo-natural river course project are built without altering the river course's original state, and the wetland and river course's purification functions are used to fulfill the goal of water purification. This method has achieved the goal of reducing COD by 30%, ammonia nitrogen by 20%, and total phosphorus by 15%. It is a quasi-natural process with low cost and good treatment effect. In addition, sewage treatment measures also include the United
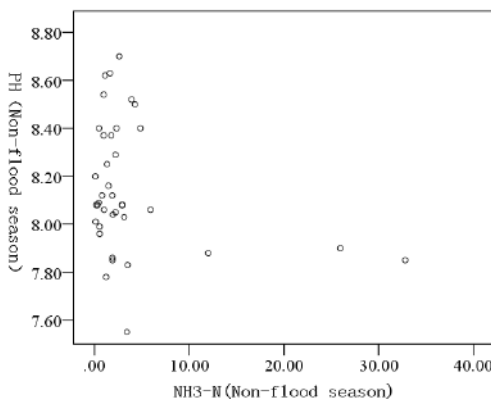

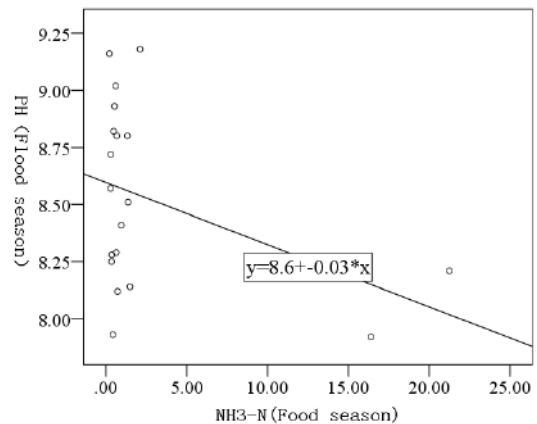Fig. 7(a): Scatter plot of NH$_3$-N and PH during non-flood season.

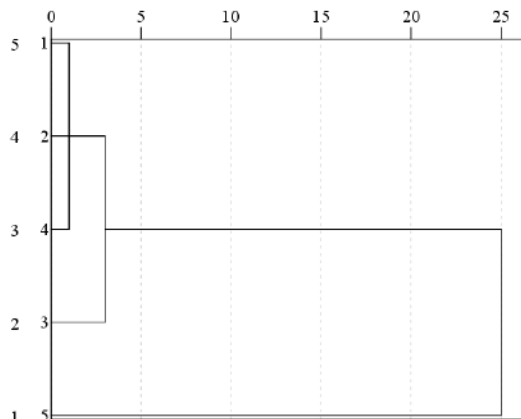Fig. 7(b): Scatter plot of NH$_3$-N and PH during flood season.

Fig. 8: Spatial clustering analysis results Using average join.

Table 7: Water quality evaluation results of each section.

Monitoring section	Water function zoning target value	Water Quality Index
Section 1	IV	4.320
Section 2	IV	4.720
Section 3	IV	3.910
Section 4	V	4.710
Section 5	V	8.223

States Micro-Bac bioremediation technology, biological channel sewage treatment technology, and other processes (Wang et al. 2010). Although these sewage treatment processes have achieved certain results, the experimental section 5 is still inferior to Class V water, and the concentration of pollutants is high. This is related to the high overall sewage discharge volume, large base, and the discharge of sewage from the sewage outlet of the river (Zhong et al. 2011). The impact of human factors on the water environment cannot be ignored. We should further improve the sewage treatment process, strengthen the monitoring and treatment of discharged sewage, pay attention to water quality issues, and fundamentally improve the water environment.

CONCLUSIONS

a. Using the comprehensive water quality labeling index method, it is determined that the Wenyu River is rated as Class V water during the flood season, and is inferior to Class V during the non-flood season. The contribution of the three water quality indicators to water pollution is COD>NH_3-N>DO, and the water quality can reach the target value of the water environment function zone in most areas. But there are still some areas with poor water quality. All in all, water quality urgently needs to be improved.

b. Using clustering method and correlation analysis to analyze the water quality of each index and each month, 12 months can be divided into 3 categories. January, May, July, August, and November are one category; Months, March, April, and December are one category, and June, September, and October are one category. According to the time variation of each index, it can be known that the main reason for the time difference in water quality is related to pH and temperature. Phytoplankton photosynthesis and the decomposition of nitrifying bacteria are affected by these two environmental factors. Changes in pH and temperature caused different reaction rates, which ultimately resulted in better water quality in June-September than in other months.

c. For cluster analysis of the 5 monitoring sections, use the spatial clustering approach, and for water quality evaluation, use the comprehensive water quality labeling index method. The five portions can be categorized into two groups. Sections 1, 2, 3, and 4 belong to the same category, whereas section 5 belongs to a different category, and the water quality evaluation results of sections 1-4 all meet the water environment function's target value. Section 5's water quality is low, and its overall performance is inferior to category V. The outcomes of these two strategies were remarkably consistent. Human factors have a significant impact on Section 5's water quality. Despite the existence of modern sewage treatment infrastructure, results are still lacking. To address the problem of water contamination, it is required to enhance the process and begin at the source.

ACKNOWLEDGMENTS

REFERENCES

Beijing Municipal Bureau of Ecological Environment (n.d.). The Planning of the Constructed Wetland Water Purification Demonstration Zone in Wenyuhe Park Highlights the "Six Major Demonstrations".http://sthjj.beijing.gov.cn/bjhrb/index/xxgk69/sthjlyzwg/wrygl/834720/index.html. Retrieved on 2018-07-12.

Beijing Municipal Bureau of Ecological Environment (n.d.). Water Environment Function Zoning. http://sthjj.beijing.gov.cn/bjhrb/index/xxgk69/sthjlyzwg/1718880/1718884/hjgnqh/307590/index.html, Retrieved on 2009-11-01.

Cai, X., Huang, Q., Zhang, L. and Bai, L.Y. 2014. Causes of the Wenyu River in Beijing. Geol. China, 41(05): 1515-1521.

Cai, X., Men, B.H. and Li, C.J. 2019. Water quality evaluation of Wenyu river based on attribute recognition theory. Beijing Water, 2019(03): 26-30.

Cheng, W.G., Li, Y.B., Su, Y. and Wang, J. 2019. Comparative analysis of comprehensive water quality labeling index method with different weighting methods. J. Irrig. Drain., 38(11): 93-99.

Fovell RG. and Fovell M.Y. 1993. Climate zones of the conterminous United States are defined using cluster analysis. J. Climate, 6(11): 2103-2135.

Gu, J.Q., Zhang, W., Zhu, F., Chen, F., Su, G.Y. and Qi, H.N. 2016. WQI for water quality evaluation in Qingshan Lake. J. Zhejiang A&F Univ., 33(05): 890-898.

Howladar M.F., Chakma, E., Jahan, K.N., Islam, S., Numanbakth, M.A., Ahmed, Z., Chowdhury, T.R., and Akter, S. 2021. The water quality and pollution sources assessment of Surma river, Bangladesh using, hydrochemical, multivariate statistical, and water quality index methods. Groundwater Sustain. Develop., 12: 100523

Hulyal, S.B. and Kaliwal, B.B..2009. Dynamics of phytoplankton in relation to physico-chemical factors of Almatti reservoir of Bijapur District, Karnataka State. Environ. Monit. Assess., 153(1-4): 650.

Li, Y.H. and Wang, J.Y. 2007. Bai Wenrong, Hu Mangquan, Huang Lishan, Fang Shenghua. Water Quality Analysis and Utilization of Rain and Flood Resources in Wenyu River. Beijing Water, (02): 36-39.

Liang, Z.Q., Ma, M.T. and Du, G.F. 2013. Improved comprehensive water quality labeling index method based on information entropy weight and its application. Sichuan Environ., 32(03): 38-42.

Mogeng, H.P., Harremoes, J.L., Cour, J. and Eric, A. 1997. Wastewater Treatment Biological and Chemical Processes. Springer-Verlag, Berlin.

Ning Y.M., Yin F.N. and Li X.B. 2020. Application of several water quality evaluation methods in the mainstream of the Yangtze River. J. Southwest Univ. Nat. Sci. Edn., 42(12): 126-133.

Nong, X.Z., Shao, D.G., Zhong, H. and Liang, J.K. 2020. Evaluation of water quality in the south-to-north water diversion project of China using the water quality index (WQI) method. Water Res., 17(6): 611-636.

Oladipo Johnson, O., Akinwumiju Akinola, S., Aboyeji, O.S. and Adelodun Adedeji, A. 2021. Comparison between fuzzy logic and water quality index methods: A case of water quality assessment in Ikare community, Southwestern Nigeria. Environ. Challenges, 3: 100038

Pan, Y.H., Liang, Z., Wang H.N., Wan, L., Tan, L.J. and Ge, T.T. 2020. Analysis of the distribution characteristics and influencing factors of chemical oxygen demand in the waters adjacent to the Yangtze River. J. Xiamen Univ. Nat. Sci. Edn.m 59(S1): 63-68.

Sun, Y.K., Wang, L. and Qi, F. 2019. Analysis of water quality characteristics of reservoirs in Shandong province based on improved comprehensive water quality labeling index method. J. Lanzhou Univ. Nat. Sci. Edn., 55(06): 726-732.

Suriadikusumah, A., Mulyani, O., Sudirja, R., Sofyan, E.T., Maulana, M.H.R. and Mulyono, A. 2020. Analysis of the water quality at Cipeusing river, Indonesia using the pollution index method. Acta Ecol. Sin., 63: 458-491.

Wang, M. 2008. Comparison of several methods in water environment quality assessment. J. Bohai Univ. Nat. Sci. Edn., (01): 34-37.

Wang, Y.L., Liu, Z.J. and Liu, Y. 2010. Wenyu river water environment and water ecological construction. J. Beij. Water, (02): 10-17.

Wang, Y.Y. 2021. Analysis of the seasonal increase of ammonia nitrogen in Xixia Reservoir. Engineering Technology Research, 6(01): 251-252.

Xu, Z.X. 2005a. Research on evaluation method of comprehensive water quality labeling index for rivers in China. J. Tongji Univ. Nat. Sci. Edn., (04): 482-488.

Xu, Z.X. 2005b. Research on evaluation method of single-factor water quality labeling index for rivers in China. J. Tongji Univ. Nat. Sci. Edn., (03): 321-325.

Yang, L.R., Sun, R.H. and Chen, L.D. 2011. Analysis of the temporal and spatial differences in the pollution process of surface water bodies in the river basin and its impact mechanism: A case study of the upper and middle reaches of Wenyu River. Environ. Sci., 32(01): 73-79.

Zhong, J., Wei, Y.S., Wang, Y.W., Yu, M., Yang, Y., Xiao, Q.C., Yu, D.W., Zheng, X., Liu, P.B., Wei, W., Liu, J.G., Zhang and Zhu, M. 2011. Analysis of the impact of social and economic development on the groundwater in the Yongding River Basin (Beijing Section) and Wenyu River Basin. J. Environ. Sci., 31(09): 1826-1834.

Zhu, L.Y., Chen, Y.Y., Liu, J., Wang, Y.W., Wang, C.R., Wei, Y.S. and Zhang, Y.X. 2020. Temporal and spatial changes and interrelationships of water environment quality and phytoplankton community structure in Wenyu River. Environ. Sci., 41(02): 702-712.

Zhu, L.Y., Wang, Y.W., Yu, D.W., Wei, Y.S., Wang, C.R., Huang, B.B. and Wu, Zh. 2021. Application research of bypass off-line river purifier technology and system in Wenyu river rehabilitation. J. Environ. Sci., 41(01): 190-198.

Experimental Investigation of Geopolymer Flexible Pavement with Waste Plastics Aggregates

P. S. Aravind Raj*†, R. Divahar*, R. Lilly, R. Porselvan R.*** and K. Ganesan***

*Department of Civil Engineering, Aarupadai Veedu Institute of Technology, Vinayaka Mission's Research Foundation, Paiyanoor, Chennai, India
**Department of Naval Architecture and Offshore Engineering, AMET Deemed to be University, Chennai, India
***Project Manager, KR Construction and Interiors, Chennai, India
†Corresponding author: P. S. Aravind Raj; aravindraj.civil@avit.ac.in

ABSTRACT

The world is facing a greater issue in the disposal of waste plastics and there is an intense need for research on alternate and sustainable solutions for environmental issues. Waste plastic can be used as aggregates or as a protective layer over aggregates to increase their strength. The aggregate used in flexible pavements was investigated in this study, as well as the use of Geo-Polymer to improve the pavement's strength and durability. The design of the pavement is done according to the Indian standard codes IRC. Dense bituminous macadam and base courses are taken into account as per the design criteria. The geo-polymer flexible pavement was tested for properties such as the wearing test. Other fundamental tests for aggregate and bitumen used in pavements include specific gravity, flash point, fire point, ductility, softening point, penetration test, water absorption test, bonding strength, durability, and temperature resistance. When geo-polymer plastic bitumen is heated and put as a coating over the base course, it allows the user the air gaps with additional plastic and binds over the aggregate, resulting in increased road stability, smoothness, and vehicle braking effects. It is concluded that with 5% addition of the geo-polymer with bitumen has performed well in all aspects of the bitumen characteristics.

INTRODUCTION

In India, a growing concern in the usage of plastic waste is the major issue, and the trend of increased use is expected to continue. Chocolate wrappers, beverages bottles, and other different forms of plastics are the reasons for several important environmental problems. Plastic consumes enormous embodied energy and depletes our environment in various ways drastically. Plastics are used widely in the construction industry due to their easy handling and packaging features, as well as their lightweight, cost, and strength. Plastics are made of highly pestilent materials that are resistant to biodegradation, meaning they will have a significant environmental impact after use. The waste plastics used in this context are polypropylene (PP), polyethylene (PE), and polystyrene (PS). The softening point of the polymers is between 120-160°C and these plastics do not release any harmful gases when heated to these temperatures. These plastics can produce a coating or lamination on the aggregate's surface. Plastics are sprayed over the aggregate at a temperature of 160°C.

For many years, plastic has been used in pavement, particularly flexible or bitumen pavements, to improve the pavement's stability, strength, and durability while lowering the overall cost of construction by gradually replacing bitumen with waste plastic to a certain percentage. Waste plastics are poured and heated with the bitumen for about 40 seconds to properly mix it so that no extra equipment or machinery is required to be attached to the current plant; the waste plastic melts and combines with the bitumen with its own heat, so no additional fuel is required. Extensive research is continuously being carried out to determine the best value for plastic in flexible pavement construction.

Justo & Veeraragavan (2002) concluded that a significant amount of plastic in the range of 8% will reduce bitumen usage by 0.4%. Rajasekaran et al. (2013) the qualities of bitumen were improved when waste plastic was included in the bitumen, which also raised the product's binding property. It is also observed that the durability is enhanced when the penetration value is reduced and the temperature of softening point is increased and this also results in improving the property of the bitumen. Xu & Van (2000) prepared a mixture of alkaline solution and alumino-silicate in the proportion of 1:0.33 as a mass ratio in which the geo-polymeric reaction is stimulated. This process continues with the mixing of

alumino-silicate powder into the mass to form a thick gel of geo-polymer. After curing at 35°C with stilbite source material for 72 h, it was observed that the compressive strength of the sample would reach around 20 MPa. According to Van et al. (2002), the compressive strength of the product reached around 80 MPa when the basic materials for the pavement combination were demolition debris and fly ash. A ratio of 0.4 is maintained between the solution and the powder mass and the content of the alkaline liquids is sodium silicate (3.5%), water (20%), and sodium or potassium hydroxide (4%). Davidovits (1989) prepared geo-polymer paste with different ratios of molar oxides and different compositions of mixtures such as a ratio of Na_2O & SiO_2 of 0.2 to 0.48; a ratio of SiO_2 & Al_2O_3 of 3.3 to 4, 5; and a ratio of H_2O and Na_2O of 10 to 25. Compressive strength was relatively low in mixtures with a lot of water. Mixtures having high water content produced very low compressive strength. It was perceived that the optimal proportion of mix is achieved when the ratio of Na_2O and SiO_2 was 0.25, the ratio of H_2O and Na_2O was 9.9, and the ratio of SiO_2 and Al_2O_3 was 3.2. Liu et al. (2014) discussed that the density of the geopolymer foamed from oil palm shell is around 1400 kg.m^{-3}. The mix was prepared using discarded cementitious materials like fly ash (FA) and ash from palm oil fuel and shells of oil palm was used as lightweight coarse aggregate (LWA). It was also observed that there was a 48% reduction in thermal conductivity for brick and 22% in the block than the conventional materials. It was found that the thermal conductivity of oil palm shell foamed geopolymer is around 0.5 W.mK^{-1}. Rangan (2009) had stated that fly ash added to geopolymer concrete provides high resistance to acid and sulfate assaults. The behavior and short-term features of compression and tension were investigated, and relative conclusions were reached. Alanazi et al. (2016) observed through experimental investigation that the curing time influences the bond strength considerably. When the geopolymer is compared to traditional cement mortar, several characteristics are investigated, as well as the influence of various acids on the cement mortar and in turn, the bond strength of the geopolymer. Also, metakaolin geopolymer is added as repair material to the pavement in addition to the base materials. It was also discovered that when Metakaolin geopolymer was added, 80% of the characteristic strength was reached within 3 days of curing. The thermally insulating properties of geopolymer composites made with a lightweight material such as waste expanded polystyrene were investigated. The manufacturing of this sustainable material is also indicated in this research. This study shows that the properties have been upgraded than the Portland cement-based materials like having improved strength and lower thermal conductivity (Colangelo et al. 2018, Hoy et al. 2017). Saravanan et al. (2010) studied the geopolymer concrete and concluded that the CO_2 emis-

sion could be efficiently reduced in active and passive ways by reducing the cement production, thus supporting nature. Sreevidya et al. (2010) investigated the effects of cement on climate change and concluded that no-cement concrete, such as fly-ash-based geopolymer concrete, should be examined at various stages.

There is only scarce literature for geopolymer-based flexible pavement developed with waste plastics and plastic coated aggregates. In this context, the optimum percentage of plastic coating and optimum percentage of polymer to modify the bitumen and develop the geopolymer-based flexible pavement have been studied.

OBJECTIVES OF THE STUDY

The core objective of the context is the effective usage of waste plastic which does not affect society and the environment. The breakdowns of the objectives are as follows

- To arrive at the efficient percentage of waste plastic to be added with the bitumen that exhibits the same or improved strength.
- To obtain the optimum percentage of plastics that has to be coated over the aggregates will give superior performance.
- To investigate the geopolymer mixed with bitumen which increases the Wearing property of the modified bitumen road.

MATERIALS AND METHODS

The materials tested in the asphalt pavement system are aggregate, bitumen, and modified bitumen. Experiments such as specific gravity test, viscosity test, ductility test, flash point test, softening point test, and thermal study, were done for bitumen. Also, tests like the specific gravity test, aggregate impact value test, and water absorption test were performed for the aggregates of all sizes (6mm, 10mm, and 20 mm). Further tests were done on the road in the field such as wearing test and core cutting test.

Bitumen

Table 1 shows the physical properties of bitumen used in the study. The tests on the materials are done based on the suitable Indian Standard codes. The specific gravity of bitumen is done as per the standard procedures of IS 1202-1978. The flashpoint and fire point of the bitumen are found based on the procedure of IS1209-1978. Ductility test of the bitumen is arrived as per the IS1208-1978. The Softening point temperature and the penetration test value of bitumen are calculated based on the standard procedure of IS1205-1978 and 1203-1978 respectively.

Table 1: Physical properties of bitumen.

Particulars	Values from Results	Values Limited
Specific gravity of bitumen	1.032	0.99
Flash point of bitumen	290°C	220°C
Fire point of bitumen	325°C	270°C
Ductility test of bitumen	40 cm	50
Softening point of bitumen	52.19°C	47°C
Penetration test of bitumen	60 mm	45 mm

Specific gravity is defined as the ratio of the mass of the specific volume of bitumen to the mass of the volume of water equal to the bitumen, assuming that both the bitumen and the water are kept at 27°C. The elongation of the bitumen in centimeters before it breaks when the briquette specimen is pulled at a set speed and temperature is known as the ductility of the bitumen. The bituminous substance leaches off a volatile liquid at higher temperatures, which might catch fire and look like a flash depending on the grade. When bitumen is modified, this is a vital point to investigate to determine when the resulting product reaches the flash point. The main difference between the flashpoint and the fire point is that the flashpoint is the lowest temperature at which the material, the vapor, fires, and flashes temporarily, whereas the Fire Point is the temperature at which the material fires and burns slightly higher than the Flashpoint temperature.

The resistance of the bitumen at the molten state to the flow is called Viscosity, and thus it can be termed as the inverse of fluidity. This property justifies the fluid property of bitumen that also determines the workability of the bitumen. The level of spreading of the bitumen and penetration of the same through the aggregates are justified by the degree of viscosity and which is directly proportional to the temperature. The degree of viscosity that is obtained to satisfy the best usage of the bitumen is measured by the softening point, which is the measured temperature to reach the specific viscosity.

The penetration value of the bitumen is measured with standard needle arrangement, with a standard temperature of bitumen and applied load, and rate of loading. At the said standard condition, the penetration is measured in a tenth of a millimeter.

Aggregate

The physical properties of the aggregates are tested before the fabrication of the system. The sizes of aggregates used are 6 mm, 10 mm, and 20 mm. Also, the dust form of aggregates is used for better packing of the aggregates and optimizing the usage of bitumen. The specific gravity of all sizes of aggregates is arrived as per IS2386 (Part III). The aggregate impact value test is done based on the procedure prescribed in the IS2386 (Part IV). The physical appearance of the aggregate is observed and justified to get the stripping value of the aggregate. The water absorption test is arrived as per IS2386 (Part III). The physical properties of aggregate used for specimens are listed in Table 2 with its corresponding test values and permissible limits.

Plastic Coated Aggregate

The problem of waste plastics and their disposal is a global issue. It is critical to find a wise idea for using waste plastics in a sustainable manner. The aggregates are covered with waste plastics to improve their strength and in turn the subgrade. The plastics are added in terms of weight percentage and the performance of the aggregates is studied with different percentages of plastic coatings to arrive at the optimum percentage. The plastic coatings vary from 10% to 40%, at every 10% interval. Its crushing strength and the bending strength are calculated with the cube test and prism test respectively. Table 3 shows the compressive strength and flexure strength of the waste plastic wastes.

Table 2: Physical properties of aggregate.

Particulars	Values from Results	Values Limited
Aggregate impact value test	21.19	Max30 %
Specific gravity of aggregate [20 mm]	2.43	-
Specific gravity of aggregate [10 mm]	2.57	-
Specific gravity of aggregate [6 mm]	2.47	-
Specific gravity of aggregate [dust]	2.62	-
Stripping value of aggregate	43%	5%
Water absorption	0.38	Max 2 %

Table 3: Characterization of waste plastic.

Percentage of plastic-coated on the aggregate surface	Crushing load value [MPa]	Bending load value [MPa]
10 %	240	315
20%	260	325
30%	280	340
40%	310	380

When the aggregates are tested for impact resistance, the strength is found to be reduced slightly. Table 4 shows the aggregate impact value of the samples taken and added with different percentages of plastics. This decrease in strength can be compensated when used with polymer-modified bitumen.

Polymer

The objective of using the polymer in the bitumen is to modify the bitumen characteristic to suit the other modified (plastic and plastic coated) aggregates used in the pavement. The polymers initially chosen for the study are Polyethylene (PE), Polypropylene (PP), and Polystyrene (PS). The thermal study is done over these polymers and the suitable polymer is chosen. Table 5. shows the thermal properties and characteristics of different polymers.

Polymer Modified Bitumen

Bonding and monolithic difficulties are encountered while working with plastic plastic-coated aggregates and other modified raw materials in pavement fabrication. All these problems will be eliminated by using polymer-modified bitumen in combination with plastic-coated aggregate. Different percentages of geo-polymer were added with the bitumen and studied to obtain the optimum value of the bitumen characteristics. Table 6. shows the comparison of the bitumen characteristics such as ductility, penetration value and softening point.

Road

Apart from the tests conducted for the materials, tests are conducted for the road sample fabricated with the said bitumen and aggregates. A wearing test is done for the road sample. Wearing test is conducted on base course layer filled

Table 4: Characteristics of aggregate coated with plastic.

Percentage of plastic	Aggregate impact value [kN]
0 %	25.00
1 %	20.03
2 %	18.09

Table 5: Thermal study on polymers.

Polymer	Softening Temperature [°C]	Decomposition Temperature [°C]	Products reported
PE	100-120	270-350	CH4,C2H6
PP	140-160	270-300	C_2H_6
PS	110-140	300-350	C_6H_6

with polyethylene, polystyrene, and polypropylene and by adding geopolymer chemicals in the texture of base course layer which determines the temperature and friction effect of the vehicle.

A thermometer is fixed in the layer of the base course which shows the definite temperature of the pavement. The vehicle is fixed at that spot, and friction between the tire and the pavement causes the tire to wear in the flexible pavement, causing the temperature to rise. The base course contains geopolymer chemically enhanced with bitumen, which improves the layer's bonding strength and the pavement's temperature resistance. Table 7 shows the results of wearing temperature before and after the test is performed on the geopolymer flexible pavement.

RESULTS AND DISCUSSION

Strength Performance of Waste Plastics

According to the results of standardized testing, the crushing strength increased by 20% when the coating was increased from 10% to 40%. Furthermore, increasing the plastic coating content from 10% to 40% improves flexural strength by up to 20%. Fig. 1 depicts the relative performance of varying percentages of waste plastics.

Aggregate Impact Value

The increase in the plastic percentage by 2% made the aggregate impact strength fall by 25%. To consider this negative performance, the addition of the geopolymer to the bitumen

Table 6: Characterization of polymer modified bitumen.

Percentage of plastic added	Bitumen Ductility [cm]	Penetration Value [mm]	Softening Point [°C]
1%	65	96	55
2%	54	89	49
3%	19	78	48
5%	12	56	73
10%	8	0	76

Table 7: Wearing test on the road.

Time (sec)	Geo-polymer flexible pavement (before) [°C]	Geo-polymer flexible pavement (after) [°C]
10	37	48
20	40	60
30	41	75

is done. The polymer binding will overcome this reduction of aggregate impact strength. Fig. 2 shows the comparison of aggregate impact values of different percentages of plastic coating.

Thermal Study on Polymers

Suitable polymer selection is done based on the softening and decomposition temperature. The polymer must consist of a lower softening temperature and higher deposition temperature. The polystyrene polymer has optimum performance when compared with the other two polymers namely polyethylene and polypropylene. The softening point temperature of the PS is about 12% higher than the PE and PP polymers and the decomposition temperature of the PS is 18% higher than the average of PE and PP polymers.

Because of its better softening and decomposition temperature characteristics, the polystyrene polymer was chosen for the formation of modified geopolymer bitumen. The variance in softening point temperature and breakdown temperature for different types of polymers is shown in Fig. 3.

Ductility, Penetration, and Softening Performance

From the comparison, it was found that adding 5% plastic to the bitumen improves the optimum performance. This proportion is the only way to get the best ductility and penetration. Furthermore, the variance in softening point is just 10%, which will not be a major hurdle in determining the proportion of geopolymer in the modified bitumen.

Fig. 4 represents the variation of ductility and penetration value for different percentages of plastics. Also, Fig. 5 shows the variation of softening points for various plastic percentages in bitumen.

Wearing Temperature of Geopolymer Flexible Pavement

The difference in wearing temperature before and after the vehicle tire friction test is shown in Fig. 6. The friction test is carried out for various lengths of time, with the temperature of the geopolymer flexible pavement reaching just 70°C after 30 s of friction.
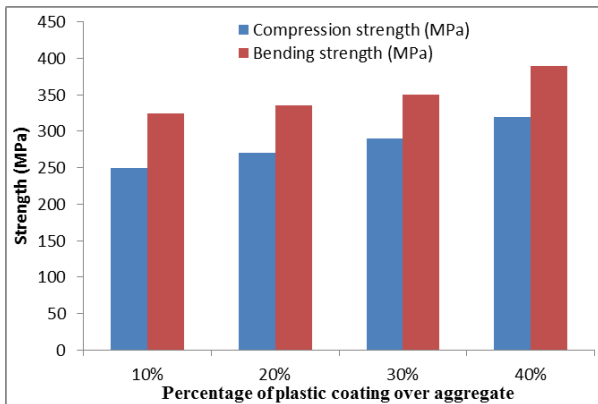

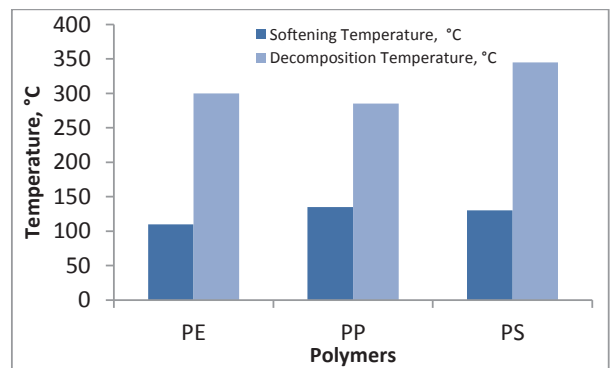Fig. 1: Strength performance of waste plastics.

Fig. 2: Aggregate Impact Value of plastic-coated aggregate.

Fig. 3: Softening and decomposition temperature of different polymers.
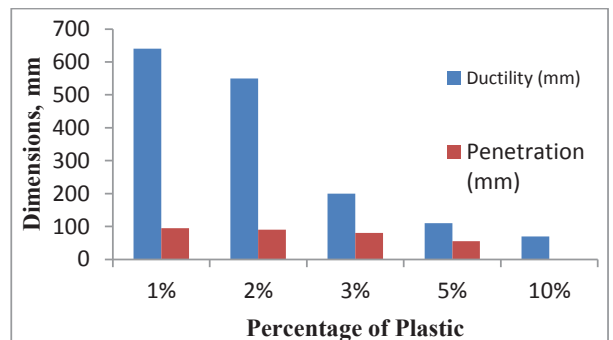

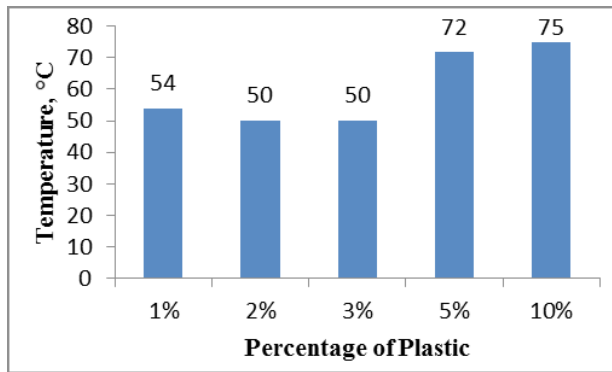Fig. 4: Ductility and penetration performance of modified bitumen.

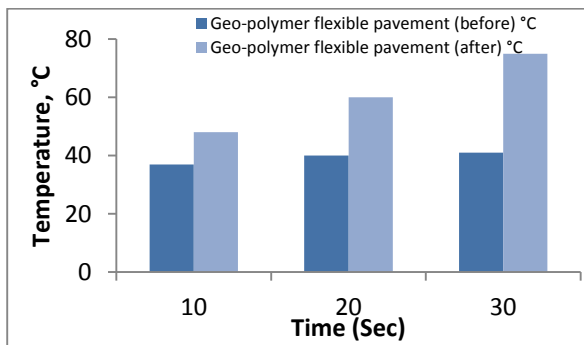Fig. 5: Softeing point of modified bitumen.

Fig. 6: Wearing temperature of geopolymer flexible pavement.

CONCLUSION

An extensive study on the geopolymer modified concrete is done with plastic waste coated aggregate and polymer modified bitumen. Various tests for the aggregates, bitumen, polymer, modified bitumen and polymer-modified flexible pavement are conducted in the study, and the following conclusions are arrived.

1. The plastic coating done for 40% of weight to the natural aggregate has performed well in all the characteristic tests of aggregate like crushing test and impact strength.

2. The softening and decomposition temperatures of poly-propylene polymer were optimal, and it was excellent for mixing with bitumen.

3. Modified polymer bitumen containing 5% polypropylene polymer performs better in ductility and penetration tests, making it appropriate for the preparation of geopolymer modified flexible pavement.

4. The geopolymer modified performed well in the mandatory criteria of wearing temperature test which makes the pavement suitable for traffic utilization.

REFERENCES

Alanazi, H., Yang, M., Zhang, D. and Gao, Z. 2016. Bond strength of PCC pavement repairs using metakaolin-based geopolymer mortar. Cem. Concr. Compos., 65: 75-82.

Colangelo, F., Roviello, G., Ricciotti, L., Ferrándiz-Mas, V., Messina, F., Ferone, C., Tarallo, O., Cioffi, R. and Cheeseman, C.R. 2018. Mechanical and thermal properties of lightweight geopolymer composites. Cem. Concr. Compos., 86: 266-272.

Davidovits, J. 1989. Geopolymers and geopolymeric materials. J. Therm. Anal., 35: 429-441.

Hoy, M., Rachan, R., Horpibulsuk, S., Arulrajah, A. and Mirzababaei, M. 2017. Effect of wetting–drying cycles on compressive strength and microstructure of recycled asphalt pavement: Fly ash geopolymer. Constr. Build Mater., 144: 624-634.

Justo, C.E.G. and Veeraragavan, A. 2015. Utilization of waste plastic bags in the bituminous mix for improved performance of roads. Open J. Civil Eng., 5: 24-38.

Liu, M.Y.J., Alengaram, U.J., Jumat, M.Z. and Mo, K.M. 2014. Evaluation of thermal conductivity, mechanical and transport properties of lightweight aggregate foamed geopolymer concrete. Energy Build., 72: 238-245.

Rajasekaran, S., Vasudevan, R. and Samuvel, P., D. 2013. Reuse of waste plastics coated aggregates-bitumen mix composite for road application: Green method. Am. J. Eng. Res., 2(11): 1-13.

Rangan, B.V. 2009. Engineering properties of geo-polymer concrete. In. Provis, J.L. and Van Deventer, J.S.J (eds.), Geo-polymers, Elsevier, The Netherlands, pp. 211-226.

Saravanan, G., Jeyasehar, A.C. and Kandasamy, S. 2010. Ecofriendly geopolymer: An alternative construction material. Nat. Environ. Pollut. Technol., 9(2): 437-442.

Sreevidya, V., Anuradha, R. and Venkatasubramani R. 2010. Study on fly ash geopolymer concrete to reduce global warming gases. Nat. Environ. Pollut. Technol., 9(2): 383-387.

Van, J.J.G.S., Jannie, S.J.V.D. and Lukey, G.C. 2002. The effect of composition and temperature on properties of fly ash and kaolinite-based geopolymers. Chem. Eng. J., 89: 63-73.

Xu, H. and Van D.J.S.J. 2000. The geopolymerisation of alumino-silicate minerals. Int. J. Miner. Process., 59: 247-266.

Use of Recycled Construction and Demolition (C&D) Wastes in Soil Stabilization

S. P. Sangeetha†, Zhimoholi T. Chophi, Pooja Venkatesh and Muhammad Fahad
Department of Civil Engineering, AarupadaiVeedu Institute of Technology, VMRF, Paiyanoor, Tamil Nadu, India
†Corresponding author: S. P. Sangeetha; sangeetha@avit.ac.in

ABSTRACT

With the growing construction sector, there is a constant rise in wastes generated by both construction and demolition activities. According to an estimate by Building Material Promotion Council (BMPTC), 150 million tonnes of construction and demolition (C&D) wastes are generated in India annually. However, the official recycling capacity is a meagre6, 500 tonnes per day (TPD) - just about 1 percent. This paper examines the properties of Black cotton soil and investigates the use of recycled C&D wastes in soil stabilization of black cotton soil. This research focuses on the inexpensive and eco-friendly nature of C&D wastes as an admixture for soil stabilization. The tests were performed using different proportions of recycled C&D wastes in the proportions: 5%, 10%, 15%, 20%, and 25%, to increase the strength of black cotton soil. California Bearing Ratio (CBR) showed an increase from 2% to 18.09%, Maximum Dry Density (MDD) showed a decrease from 2.107 g.cc^{-1} to 1.69 g.cc$^{-1,}$ and Optimum Moisture Content (OMC) showed a variation and increased from 15% to 18.09% with the addition of 25% C&D wastes.

INTRODUCTION

Soil is perhaps one of the major factors that affect construction. Everything from a house to a shopping mall is built on soil and therefore, building foundations need to be on stable soil. Since soil ranges in strength, some of them may be able to support a skyscraper, while some may not be able to hold the weight of a human. Black cotton soil is one such soil that requires special methods of construction, soil stabilization being one of them. Soil stabilization is broadly defined as the process of improving the engineering properties of weak soil with the use of stabilizing agents or admixtures. Soil stabilization is mainly carried out in three methods, namely: mechanical stabilization, chemical stabilization, and polymer stabilization. Materials like lime, cement, bitumen, etc. have been used to carry out soil stabilization. Although these materials treat the soil and increase its workability and durability of the soil, it causes harmful effects on the environment, due to carbonation, sulfide attack, etc. Therefore, the main objective of this study is to use recycled C&D wastes for soil stabilization, while reducing the harmful effects on the environment due to illegal dumping, carbonation, and sulfide attacks from using other stabilizers, as well as reduce the need for finite landfill spaces.

There is a substantial history of the use of soil stabilization admixtures to improve poor subgrade soil performance by controlling volume change and increasing strength. Al-sharif et al. (2012) had evaluated the use of burned sludge as a stabilizing agent. The sludge was burnt at 550°C and added to three different samples of clayey soils at different percentages. The results show that the addition of 7.5% burned sludge ash (dry weight) increased the unconfined compressive strength maximum dry density and minimized the swelling pressure of the soil. If more than 7.5% by weight is added, both the maximum dry density and the unconfined compressive strength decrease. Therefore, this study reached the conclusion that burned sludge can be used as a soil stabilizer. Dhananjaya et al. (2019) and Henzinger et al. (2015) has done experiments on the stabilization of black cotton soil using demolition wastes and concluded that CBR values were increasing with an increase in construction wastes.

Shelke (2010) has evaluated the reduction of swelling pressure of expansive soils using EPS geofoam and it was observed from the results of his test that with an increase in EPS geofoam layer, there was a sudden reduction in swelling pressure. Teja et al. (2018) has reviewed on stabilization of expansive soil using brick dust.

Parsons & Kneebone (2004) studied the use of cement kiln dust for the stabilization of soils. Cement kiln dust was added to eight different soils to evaluate the effectiveness of Cement Kiln Dust (CKD) as a stabilizing agent in each soil. The results were then compared with findings from the same type of soils stabilized with lime, cement, and fly ash. Strength and durability tests were conducted. Results showed the effectiveness of CKD as a soil stabilizing agent in each soil. Seda et al. (2007) studied the benefits of using waste tire rubber to mitigate swelling potential in expansive soils. In this paper, the study of the effects of the addition of small particles of waste tire rubber to an expansive soil from Colo-

rado was undertaken. Results showed a significant decrease in the swell percent and swelling pressure with the addition of rubber to the soil sample. Okogbue (2007) had stabilized clay using wood ash. The geotechnical parameters of clayey soil in its native condition, as well as mixed soil with different quantities of wood ash and particle size distribution, specific gravity, Atterberg limits, compaction characteristics, CBR, and compressive strength, were assessed. Results showed a significant improvement in the geotechnical properties of clayey soil, with the best results achieved at the addition of 10% wood ash. However, this study concluded that wood ash cannot completely replace lime as the strength gained lasts only for a short duration. Amadi (2014) assessed the effectiveness of stabilization of combined cement kiln dust and quarry fines on pavement subgrades dominated by black cotton soil. The inclusion of the QF and CKD combination resulted in a significant decrease in the plasticity index, as well as a fall in maximum dry unit weight and an increase in optimum moisture content. It also resulted in a significant increase in CBR, indicating that these two materials can be utilized jointly in soil stabilization.

Karthik et al. and Raut et al. (2014) investigated the use of fly ash in soil stabilization. This study evaluated the effects of fly ash in stabilizing soft fine-grained red soils. CBR and other strength tests were conducted on the soil and a mixture of soil-fly ash prepared at an optimum water content of 9% showed a considerable increase in CBR of the soil. Mudgal et al. (2014) studied the effects of lime and stone dust in geotechnical properties of Black cotton soil and it was concluded that there was an increase in strength and maximum dry density of lime stabilized soil with the addition of 20% stone dust. Henzinger et al. (2015) investigated the use of demolition waste in soil improvement. They had experimented on two treated fine-grained soils, one clay of low plasticity and one of very high plasticity. The geotechnical properties of the two soils were also determined. Results showed this soil treatment was more effective for the clay of low plasticity rather than the clay of very high plasticity and that the improvement capability mostly depends on the water content of the added material. Therefore, the use of dry material was highly recommended.

This paper focuses on the stabilization of black cotton soil by using recycled aggregates from acquired C&D wastes. Various changes in the properties of Black cotton soil are observed with the addition of recycled C&D wastes.

NEED FOR THE PRESENT STUDY

After thoroughly studying the literature reviews, the following gaps and drawbacks were drawn.

(i) Although recycled C&D wastes find their uses as concrete aggregates in soil subgrades and new construction, they can be used to treat soil and increase its durability and stability.

(ii) India produces about 150 million tonnes of C&D wastes out of which only a mere 1% is recycled. Hence, the need for recycling and reusing C&D wastes is a rising concern.

(iii) Since recycling C&D wastes are not always cost-effective, reusing them in new projects may reduce the overall costs of the project. To use recycled C&D wastes as a cheaper alternative for soil stabilization.

(iv) Recycling and reusing C&D wastes will reduce the need for non-renewable resources, thus leading to sustainable development. Using recycled C&D wastes for soil stabilization, will thereby, reduce their overall impact on the environment and finite landfill spaces.

MATERIALS AND METHODS

Figure 1 shown below gives details about the methodology carried out in this research. After procurement of materials, preliminary tests on raw materials were carried out.

The C&D wastes were acquired from a dumping site in Shollinganallur, Chennai, Tamil Nadu. The collected sample went through a process of segregation and a concrete waste sample weighing 5kg was crushed with the help of a rammer.

The addition of the crushed concrete sample to the soil was done in the proportions 5%, 10%, 15%, 20%, and 25%, respectively. The crushed concrete sample was added to the soil sample in different proportions to observe the various changes and find the optimum amount.t. The same tests were conducted for the stabilized soil according to IS 2720. From the results of the test, optimized percentage addition of C&D waste for soil stabilization will be arrived.

Materials Used

This paper focuses on the stabilization of black cotton soil by using recycled aggregates from acquired C&D wastes. Various changes in the properties of Black cotton soil are observed with the addition of recycled C&D wastes. The properties of black cotton soil are given in Table 1.

Black Cotton Soil:

Black cotton soil, also known as expansive soil, is amongst the most problematic soils in construction. Generally prevailing in the central and southern parts of India, Black cotton soil is heavy clay soil and varies from clayey to loam, and is generally light to dark grey. When dry, Black cotton soil or expansive soil shrinks, becomes hard-like stone, and has a high bearing capacity; when wet or moist, it expands, becomes very loose, and loses its bearing ability. The ba-
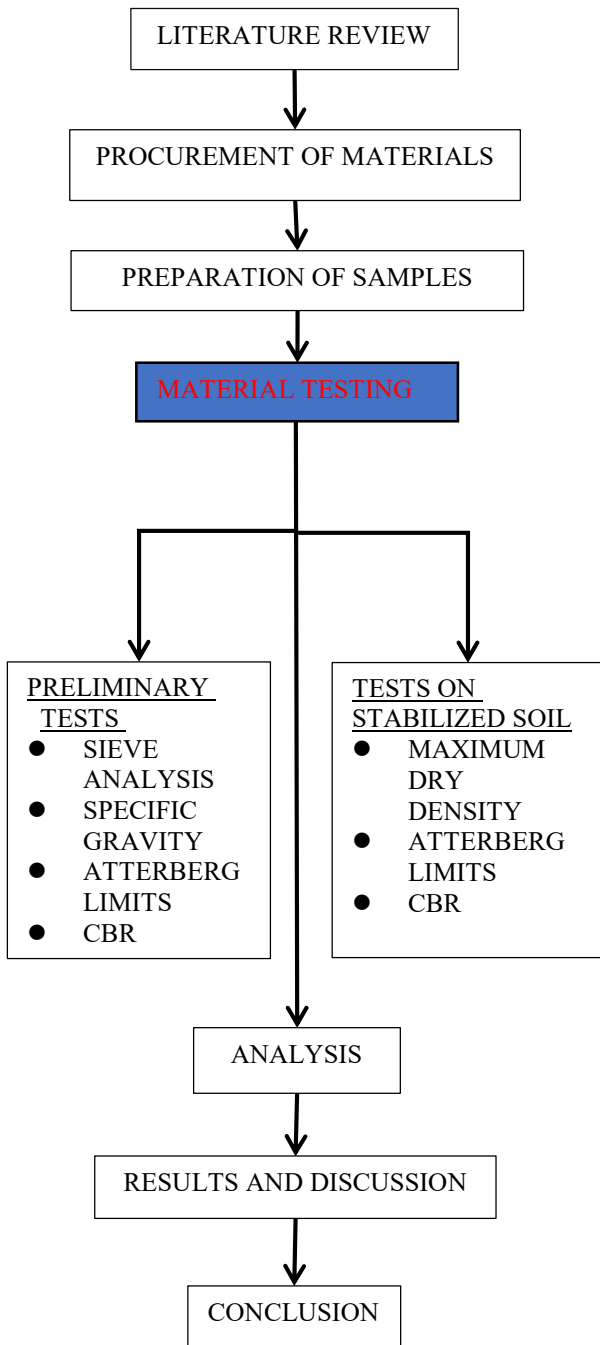
Fig. 1: Methodology for soil stabilization.

Table 1: Properties of black cotton soil.

Sl. No.	Properties	Value
1.	Specific Gravity	2.28
2.	Grain-Size Analysis	
	Gravel	0%
	Sand	17.7%
	Silt	30.4%
	Clay	51.9%
3.	Liquid Limit	51%
4.	Plastic Limit	26.39%
5.	Plasticity Index	30.1%
6.	CBR Value	1.45%
7.	Optimum Moisture Content	15%
8.	Maximum Dry Density	2.107 Gm/CC
9.	UCS Value	1.08%
10.	Swelling Potential	9.47%

exerts pressure. The exerted upward pressure is so high that it tends to lift the foundation upwards and this reverse pressure in the foundation causes cracks in the wall above. While the cracks are narrower at the bottom, they get wider as they go up. Because black cotton soil has such unique qualities, construction on it necessitates the use of unique techniques.

Improvisation Materials

Various additives such as lime, cement kiln dust, waste rubber, rice husk ash, burned sludge have been commonly used to stabilize the soil. However, C&D wastes such as soil stabilizers, have been newly introduced, especially the use of recycled concrete aggregates. The C&D wastes used in this study were acquired from a dumping site located in Shollinganallur, Chennai, Tamil Nadu. A typical composition of C&D wastes is demonstrated in the given chart (Fig. 2).

Tests

Crushed concrete was added to the Black cotton sample in the proportions of 5%, 10%, 15%, 20%, and 25%. After the addition of crushed concrete, the following tests were conducted to observe and understand the behavior of Black cotton soil (expansive soil).

- Liquid limit test
- Plastic limit test
- California Bearing Ratio test

RESULTS AND DISCUSSION

Engineering properties of soil w.r.t liquid limit, plastic limit, plasticity index, maximum dry density, and moisture con-

sic mineralogical composition of these types of soil has a crucial influence on their swelling behavior, as these soils are typically rich in the minerals montmorillonite and illite.

When it's dry, large cracks form up to 150 mm wide and 3.0 to 3.5 meters deep, and when it's wet, the soil increases in volume to about 20% to 30% of the original volume and

Table 2: Final results for Black Cotton soil.

Engineering property	Black cotton soil	5% of C&D Wastes	10% of C&D Wastes	15% of C&D Wastes	20% of C&D Wastes	25% of C&D Wastes
Liquid limit [%]	51%	58.68%	56.85%	51.46%	50.87%	49.21%
Plastic limit [%]	26.39%	29.41%	26.53%	24.65%	23.39%	22.54%
Plasticity index [%]	30.1%	29.27%	33.12%	26.81%	27.48%	27.67%
Maximum dry density [g.cc^{-1}]	2.107	1.932	2.083	1.827	1.738%	1.689%
Optimum moisture content [%]	15%	21.5%	19.3%	18.23%	19.19%	18.09%
CBR [%]	2%	4.8%	9.7%	14.35%	16.3%	18.99%

tent for an addition of 5% to 25% C&D wastes in soil are tabulated in Table 2.

From table 2 it was observed that the values of Liquid limit was varying between 49% to 58% and plastic limit between 22 % to 29% for an addition of 25% to 5% addition of C&D waste. Plasticity index and dry density were high for an addition of 10% addition of C &D wastes. Moisture content was 21.5%, 19.3%, 18.23%, 19% and 18.1% for percentage increase of C&D wastes from 5% to 25% addition.

Fig. 3 represents the effects of recycled C&D wastes on Black Cotton soil in the proportions of 5%, 10%, 15%, 20%, and 25% respectively. From Table 2 and Fig. 3, we can observe a steady decrease in the liquid limits and plastic limits of the soil, as we keep increasing the percentages of C&D wastes. The liquid limit of the soil changed from 51% to 49.21% with the addition of 25% recycled C&D wastes,
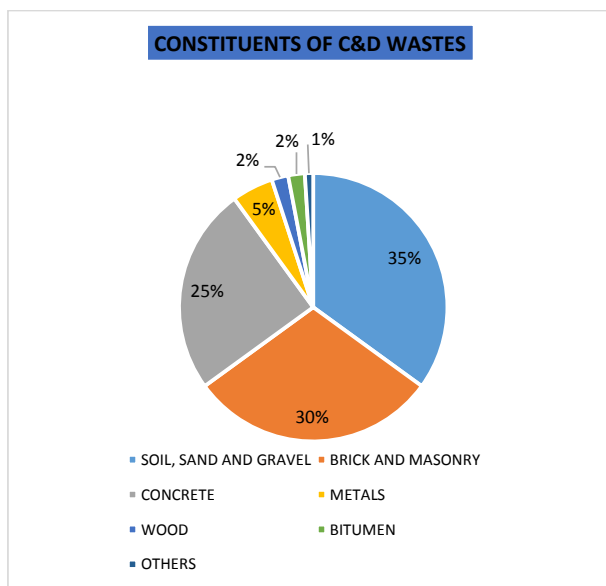
while the plastic limit changed from 26.39% to 22.53%.

Fig. 4 represents a variation in the optimum moisture content with the addition of different percentages of C&D wastes in the proportions of 5%, 10%, 15%, 20%, and 25% respectively. The optimum moisture content of the Black Cotton sample was 15% and increased to 18.09% with the addition of 25% C&D wastes. For the addition of 5%, 10%, 15%, and 20 % C&D wastes, OMC increased to 21.50%, 19.30%, 18.23%, and 19.19% respectively. As observed from Fig. 3, there is a significant increase in the optimum moisture content of Black cotton soil, thus proving that the addition of C&D wastes improves the OMC of black cotton or expansive soils.

Fig. 5 represents the variation in CBR values for different percentages of C&D wastes added and the effect of C&D
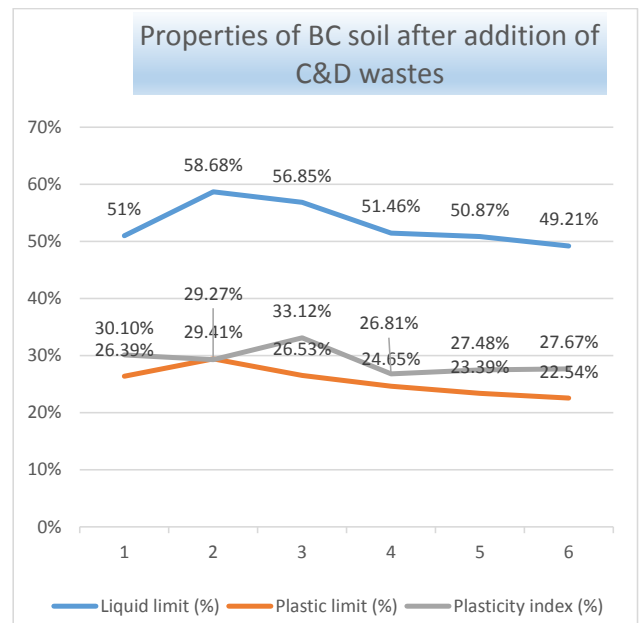

Fig. 2: Constituents of C&D wastes.

Fig. 3: Atterberg limits of initial and after addition of C&D wastes to black cotton soil.

wastes over CBR values. From the above figure, we can observe a significant increase in the CBR values of Black cotton soil with the consequent increase in the proportions of recycled C&D wastes. With the addition of 5%, 10%, 15% and 20% C&D wastes, CBR values increased to 4.80%, 9.70%, 14.35% and 16.30% respectively.

With the increase in the percentage of C&D wastes added, CBR values increased from the initial 2% to 18.095 for 25% C&D wastes added.

Fig.6 represents a variation in the maximum dry density of the soil sample with the addition of different percentages of C&D wastes. As the amount of C&D wastes is increased, we can see a decrease in the maximum dry density of the Black cotton soil sample. As we increase the quantities of

recycled C&D wastes in the Black cotton soil sample, the values of maximum dry density gradually decrease. With the addition of 5%, 10%, 15%, and 20%. C&D wastes, MDD values changed to 1.932, 2.083, 1.827, and 1.740 (g.cc^{-1}), respectively. At the addition of 25% C&D wastes, maximum dry density showed a decrease from 2.10 g.cc^{-1} to 1.69 g.cc^{-1}.

CONCLUSION

The purpose of this research was to enhance the engineering properties of Black cotton soil, reduce its swelling potential land increase its load-bearing capacity at the same time. Previous research has studied the effect of various additives such as lime, Rice husk ash, cement kiln dust, etc., for soil stabilization but most of these resulted in excessive heaving and pavement failures. The use of C&D wastes as a soil stabilizer has been studied before and the results obtained in this research are similar to the results of other research studies, which goes to proves that C&D wastes can be used as soil stabilizers.

In this study, we tried to improve the engineering properties of Black cotton soil with the addition of recycled C&D wastes. The following results were achieved.

- Optimum moisture content(OMC)values of the soil sample varied with the addition of C&D wastes and changed from the initial15% to 21.50%, 19.30%, 18.23%, 19.19% and18.09%, respectively.

- CBR values saw a significant increase from 2% to 4.89%, 9.70%, 14.35%, 16.30% and 18.09%, with the addition of C&D wastes in the proportions of 5%, 10%, 15%, 20% and 25%, respectively.
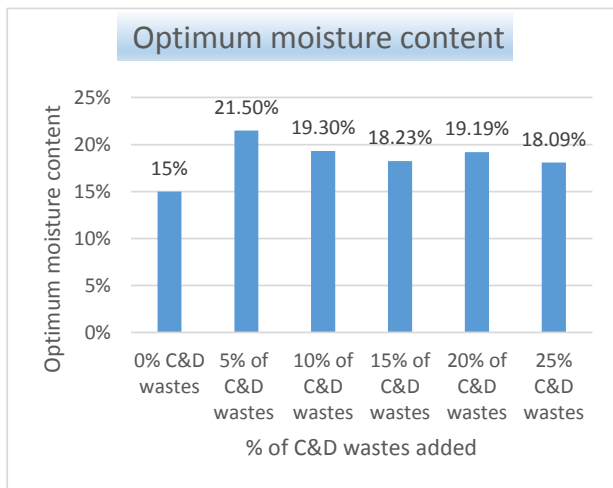

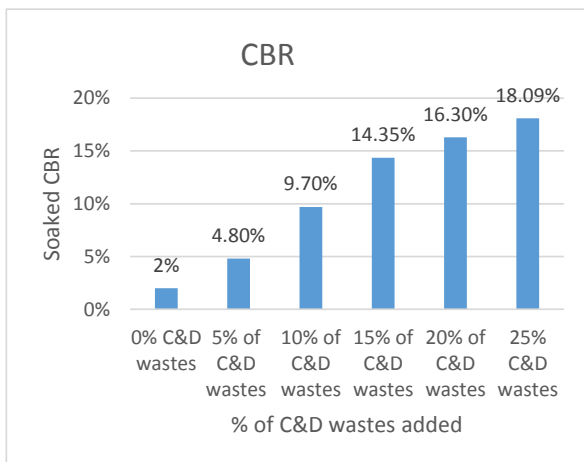Fig. 4: Optimum moisture content of black cotton soil after adding recycled C&D wastes.

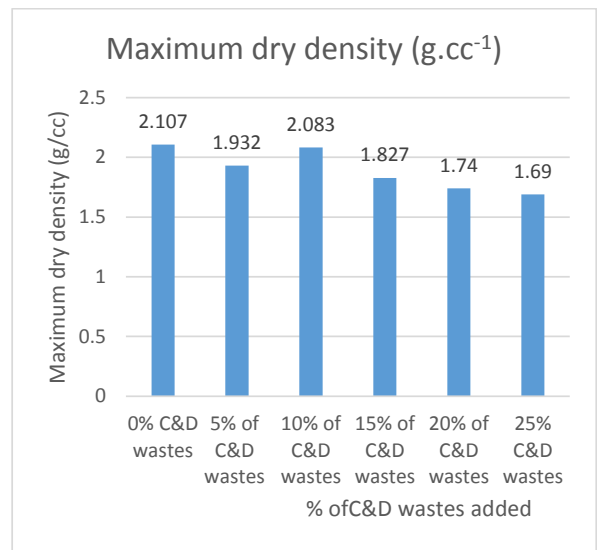Fig. 5: Values of CBR values before and after addition of C&D wastes.

Fig. 6: Values of maximum dry density (g.cc^{-1}) before and after addition of C&D wastes.

- Maximum dry density(MDD) of the soil decreased from 2.107g.cc^{-1} to 1.932,2.083,1.827, 1.74and1.69g. cc^{-1} with the addition of 5%, 10%, 15%, 20% and25% C&D wastes, respectively.

From the above observations, we can conclude that there is a significant improvement in the engineering properties of Black cotton soil.

With the use of C&D wastes as a soil stabilizer, the problems of Black cotton soil in construction can be tackled. In addition, the rising problems caused by the massive C&D wastes generation such as pollution of water bodies, green areas, public spaces, and the biggest one among them being the depletion of finite landfill spaces can be curbed. The use of C&D wastes as a soil stabilizer will not only improve the engineering properties of soil, it will also reduce the costs of the overall project and negate the impact on the environment, thus leading to a more sustainable way of construction.

REFERENCES

Amadi, A. 2014. Assessing stabilization effectiveness of combined cement kiln dust and quarry fines on pavement subgrades dominated by black cotton soil. Geotech. Geol. Eng., 32(5): 1231-1238.

Dhananjaya, A.S., Warade, T.G., Wankhede, A.S., Raghuvanshi, S.N. and Tandale, K.H. 2019. Stabilization of black cotton soil by using construction and demolition waste. J. Geotech. Stud., 4(2): 27-31.

Henzinger, C. and Heyer, D. 2015. Use of demolition waste in soil improvement. In: Geotechnical Engineering for Infrastructure and Development: Conference Proceedings of the XVI ECSMGE, 13-17 September 2015, Edinburgh, UK, ICE Publishing, London, pp. 2547-2552.

Karthik, S, Kumar, A.E., Gowtham, P.and Elango, G. 2014. Soil stabilization by using fly ash. IOSR J. Mech. Civil Eng., 10(6): 20-26.

Kaushal, V. and Guleria, S.P. 2015. Geotechnical investigation of black cotton soils. Int. J. Adv. Eng. Sci., 5(2): 15-22.

Mudgal, A., Sarkar, R. and Sahu, A.K. 2014. Effect of lime and stone dust in the geotechnical properties of black cotton soil. Int. J. Geomate, 7(2): 1033-1039.

Okogbue,C.O. 2007. Stabilization of clay using wood ash. J. Mater. Civil Eng., 19(1): 14-18.

Parsons, R.L.and Kneebone, E. 2004. Use of cement kiln dust for the stabilization of soil. Geotech. Eng Transport. Projects, Final Report No. KS-04-3: 1124-1131.

Raut, J.M., Bajad, S.P. and Khadeshwar, S.R. 2014. Stabilization of expansive soils using fly ash and murrum. Int. J. Innov. Res. Sci. Eng. Technol., 3(7): 14283.

Seda, J.H., Lee, J.C. and Carraro, J.A.H. 2007. Beneficial use of waste tire rubber for swelling potential mitigation in expansive soils. Geotech. Spec. Pub., 235(5): 1-9.

Seehra, S.S. 2008. Practical Problems of Highway Construction in Black Cotton Soil Areas and In-Place Remedial Measures: A Case Study. NBM Media Construction Portal, NBMCW, South Asia.

Shelke, M. 2010. Reduction of swelling pressure of expansive soils using EPS geofoam.Indian Geotech. Conf. GEOtrendz, 6: 495-497.

Teja, S.L., Kumar, S.S. and Needhidasan, S. 2018. A review and study on stabilization of expansive soil using brick dust. Int. J. Pure Appl. Math., 119(17): 1999-2005.

Yadu, L. 2013. Stabilization of soft soil with granulated blast furnace slag and fly ash. Int. J. Res. Eng. Technol., 2(2): 115- 118.

Analyzing the Efficacy of *Salvinia molesta* Mitchell as Phytoremediation Agent for Lead (Pb)

F. Rachmadiarti*†, G. Trimulyono* and W. H. Utomo**

*Department of Biology, Faculty of Mathematics and Natural Sciences, Universitas Negeri Surabaya, Kampus Ketintang Surabaya, Surabaya 60231, East Java, Indonesia
**Faculty of Agriculture, University of Brawijaya, Veteran Street, Malang 65145, East Java, Indonesia
†Corresponding author: F. Rachmadiarti; fidarachmadiarti@unesa.ac.id

ABSTRACT

Heavy metals, especially Pb (lead), are generally toxic to living things. Pb can contaminate organisms in the water through the food chain. The purpose of this study is to enhance water quality by using *Salvinia molesta* to phytoremediate Pb-polluted water. This study aims to evaluate the ability of *S. molesta* as a Pb phytoremediator. We evaluated total protein, free amino acids produced by the plant, and plant growth (dry biomass). *S. molesta* was grown in a hydroponic system exposed to Pb at dosages of 0, 5, 10, and 15 ppm for 7 and 14 days. Pb level was analyzed using *Atomic Absorption Spectrophotometer* and amino acids were analyzed using High-Pressure Liquid Chromatography. Data were statistically analyzed using analysis of variance (ANOVA) followed by Tukey's test ($α < 0.05$). Results showed a significant change in Pb content in the roots and leaves of Pb-exposed *S. molesta* Mitch compared to control. In Pb-exposed plants, total protein and amino acids, especially cysteine, were lowered. *S. molesta* could be used as a Pb phytoremediator due to its high potential to survive Pb exposure and its ability to absorb Pb.

INTRODUCTION

Heavy metal pollution, such as Pb, is an environmental issue that endangers living things. The widespread burning of fossil fuels and disposal of industrial waste has led to the accumulation of heavy metals in the soil and water body, which leads to contamination of the food chain (Ergönül et al. 2019, Munzuroglu & Geckil 2002, Shah & Nongkynrih 2007, Wuana & Okieimen 2011, Zeller & Feller 1999). Heavy metals are known to cause changes in the redox balance of cells, resulting in oxidative stress (Sreekanth et al. 2013). Many cellular activities are disrupted by the secondary effects of oxidative stress, such as reduced membrane function due to lipid peroxidation and oxidation of proteins and nucleic acids (Blokhina & Fagerstedt 2010). In addition, Plants demonstrate a short-term response toward heavy metals exposure, resulting in morphological, anatomical, physiological, and biochemical alterations (Rai & Tripathi 2009).

Heavy metals-collecting plants function as biofilters that can effectively reduce heavy metals concentrations in contaminated water (Abhilash et al. 2009, Rai 2011). In addition, phytoremediation has been applied extensively to remediate either contaminated soil or water in several areas (Nouri et al. 2011). Another study by Nouri et al. (2011) also pointed out that original species growing in a contaminated habitat can act as phytoremediators for certain pollutants.

Salvinia molesta is a pteridophyte plant from the Salviniales group, an invasive species of aquatic weed that lives floating on the water surface. *S. molesta* is mainly found in ditches or trenches, rice fields, ponds, lakes, or streams with slow water flow and irrigation channels. Its rapid growth rate allows *S. molesta* to slowly cover the water surface, forming a solid layer with thickness up to 1 m, depending on duration and compaction. This plant is primarily found in various areas of the world, including Indonesia. The community uses it as an ornamental plant, as well as for animal food. However, Sari (2014) found that Salvinia could effectively absorb copper (Cr) from Batik industrial waste. Based on this study, *S. molesta* indicates the "resistance" ability toward heavy metals and states it could be classified as an "accumulator/hyperaccumulator" plant. The plants exhibited a wide range of stress tolerance to all metals and can be used for eco-removal of heavy metals from contaminated water (Rai 2018).

These plants can operate as a bioremediation agent because they produce certain protein-forming free amino acids that are required in responding to heavy metals in their environment. One of the functions of plant amino acid synthesis is to detoxify heavy metals by building complexes with them in the plant (Pilon 2005). Heavy metal deposition in wetland plants has been shown to cause significant physiological and biochemical responses in the root, stem, and leaf growth (Rai & Tripathi 2009, Lyu et al. 2016). After several days

of exposure, biochemical indices such as protein, sugar, and chlorophyll content of plants are generally reduced in plant tissues. In this setting, wetland plants' eco-remediation of hazardous chemicals may manifest as unique physiological and biochemical modifications required to cope with heavy metal stress (Rai & Tripathi 2019). Hence, metal ions must be distributed throughout the plant's organs, from root to shoot, and the plant's ability to adapt to metal exposure from contaminated water must be studied using free amino acid analysis (Kamel 2008).

This study aims to determine how effective *S. molesta* is as a Pb phytoremediator based on total protein, free amino acids produced by the plant, and plant growth (dry biomass) data, as explained above. This study examines if *S. molesta* can be employed as a heavy metals Pb phytoremediator and assesses its ability to produce free amino acids.

MATERIALS AND METHODS

S. molesta Growth and Pb-Exposure

This study was designed as a completely randomized block design with three replications. Two treatment factors were applied: Pb concentration (K1: 0 mg.L^{-1}, K2: 5 mg.L^{-1}. K3: 10 mg.L^{-1}, K4: 15 mg.L^{-1}); and exposure time (seven and 14 days). Each factor combination was carried out for three replications.

S. molesta was collected from the Porong wetlands in the Sidoarjo region, East Java, Indonesia. The experiment was initiated by acclimatizing plants and reducing contaminant levels in the plants by growing *S. molesta* in a plastic chamber filled with 20 L Hoagland's medium in a greenhouse for seven days. After that, *S. molesta* was sorted at 90 g for the respective treatment of the plant. Finally, each plant was maintained for ten days in a different plastic container filled with 20 L distilled water supplemented with Hoagland's solution (Göthberg et al. 2004).

Acclimatized plants were rinsed using distilled water and moved into a 40×30×35 cm glass aquarium filled with 5 L distilled water and Hoagland's solution with Pb level set according to the respective treatments. Each aquarium was filled with 100 g of Salvinia. The initial pH and at the end of the experiment were recorded. Plants were adjusted to 12:12 hours light-dark circle daily with 389-candles photon flux density. Plant biomass was recorded after all plant samples were harvested according to the exposure time set (seven and 14 days).

Pb Level Measurement in *S. molesta*

After *S. molesta* was harvested, its phytoremediation ability was determined by measuring Pb absorption in roots

and leaves using the extraction method (Göthberg et al. 2004). First, harvested plants were separated into roots and leaves. Each plant portion was dried in an oven at 80°C for 48 hours before being weighed dry. Following that, 5 g of each plant organ sample was pulverized in a mill. Next, 5 g of each plant organ sample was taken and ground using a mill. After that, 0.5 g of each powdered plant sample was diluted into 5 mL HNO_3 and 50 mL deionized double distilled water. Fifty milliliters of respective diluted sample and medium were analyzed using atomic absorption spectrophotometer to record its Pb level. Total accumulation and partitioning of heavy metals by the plants were calculated.

Free Amino Acids Identification and Level Measurement

Using the HPLC method with hydrolysis processes and derivatization, the protein-mapping pattern of Pb-exposed *S. molesta* was also analyzed from free amino acids and the total protein content of plant roots (Waters 2017). The reagent kit (AccQ-FluorTM Reagent Kit for hydrolysate amino acid Analysis) was prepared first by heating it at 55°C. Next, AcrQ fluo reagent powder was heated for 2-3 minutes. Then, 1 mL of AccQ fluorine reagent diluent was put into vial 2A, followed by heating and mixing until all the powder was spread evenly. Next, the solvent was prepared by diluting 19 g sodium acetate and 2.27 g TEA into 1 L distilled water. Forty percent phosphoric acid (+ 6 mL or above) was added until pH reached 5.1 followed by 5 mL acetonitrile and distilled water.

The hydrolysis of the sample was performed on a 100 mg sample. The sample was placed into a tube and combined with 5 mL 6 N HCl. The sample was dried using nitrogen or argon. The respective tube was covered and placed in an oven at 112°C for 22 h. The sample (100 mL) was then filtered using 0.45 pm filter paper and dissolved into 5mL MiliQ water.

For derivatization, a 50 pL diluted sample was mixed into 350 pL AccQ derivatization buffer and 100 pL AccQ fluor reagent. The mixture was shaken briefly and put into heated water at 55°C for 10 min. Finally, the sample was injected into the HPLC instrument (Waters 2017).

Data Analysis

The parameters observed in this study were: (1) dry weight; (2) Pb level in roots and leaves; (3) free amino acids level in roots; (4) bacteria species in the roots. Qualitative data for dry weight and Pb level was analyzed using one-way ANOVA, followed by Tukey's test at 95% confidence level using SPSS 21st edition. Free amino acids were analyzed descriptively based on the percentage and total protein.

Bacteria species isolated from *S. molesta* roots were also analyzed descriptively.

RESULTS AND DISCUSSION

Growth of Plants Exposed to Pb

The current study found a significant difference in the growth of plants given various Pb concentrations. In contrast, no differences in growth were found based on exposure duration (seven days vs. 14 days) (Fig. 1). In addition, *S. molesta* dry weight was affected by Pb concentration in the growth medium (Table 1). Medium pH was also found to change, from 5.4-6.9 at the beginning of the experiment to 6.5-7.0 at the end of the experiment (Table 2).

According to biomass weighted after treatment, *S. molesta* was able to grow effectively in the Pb-contained medium. The increasing Pb concentration in the medium, on the other hand, induces a decrease in Salvinia biomass. Phetsombat et al. (2006) reported that the *S. molesta* plant group exposed to Pb at concentrations of 10, 20, 30, and 40 mg.L^{-1} with exposure durations of 2, 4, 6, and 8 days, respectively, also demonstrated decreasing growth. According to Hardiani et al. (2011), the plants adapted slowly to a high-grade medium containing heavy metals. Other studies, on the other hand, such as those by Göthberg et al. (2004), grew Pb-exposed

water spinach supplemented with various concentrations of Hoagland nutrients. Abhilash et al. (2009) studied Yellow velvetleaf exposed to Cd with concentrations of up to 2 mg.L^{-1}. Rachmadiarti et al. (2012) grew Yellow velvetleaf exposed to Pb at a concentration up to 15 mg.L^{-2}, and Rachmadiarti & Trimulyono (2019) examined water clover exposed to Pb and found that various plant species could grow even when there is heavy metal contamination.

Xin et al. (2010) found that Pb concentration in the medium is in line with the Pb level concentrated in the roots. As the exposure period increases, the amount of Cu absorbed increases (up to 14 days). Meanwhile, Zou et al. (2011) discovered a relationship between Pb content in herbaceous dicotyledonous plants (*Arpesium abrotanoides, Conyza canadensis, Anemone vitifolia,* Monocotyledoneae *Juncus effussus*, and pteridophytes *Ahyrium wardii*, and *Pseudocyclosorus subochthodes*) and the concentration of Pb in the medium and the duration of exposure. Another research noted that the final Pb removal in *Lemna gibba* L. after 21 days of exposure was up to 94% (Bokhari et al. 2019).

Distribution of Pb in Plant Organs

During the plant-growing process, Pb was removed from the growth media. Pb was absorbed by plants and translocated to various plant organs as a result. The distribution of Pb in
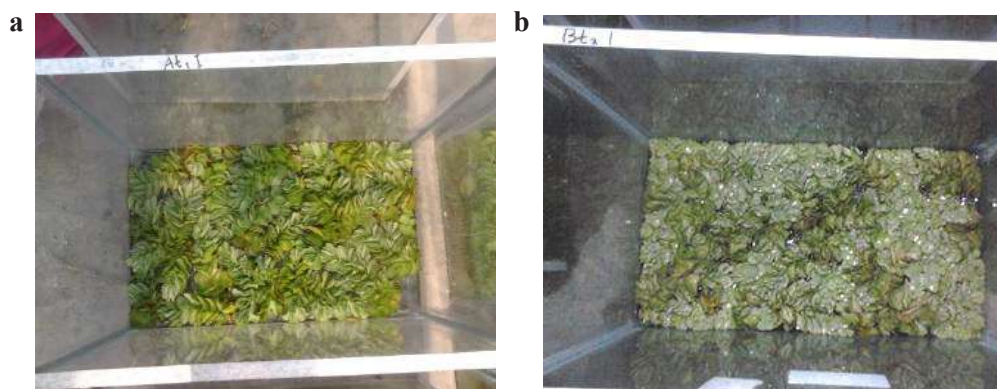

Fig. 1: *S. molesta* plant from (a) control and (b) experiment group.

Table 1: Salvinia dry weight (g) after Pb exposure for 7 and 14 days.

Pb Concentration	Dry weight [g]	
	7 days	14 days
0	6.50±0.65[c]	6.00±0.15[c]
5	6.76±0.65[c]	6.26±0.15[c]
10	5.06±0.27[b]	4.56±0.27[a]
15	4.41±0.37[a]	3.91±0.37[a]

*Different letters indicate statistical differences based on the Tukey test (p = 0.05)

Table 2: Initial and final medium pH as a function of Pb concentration on days 7 and 14.

Pb concentration (mg.L^{-1})	Day	Initial pH	Final pH
0	7	7.0±0,0	7.0±0,0
5		6.9±0,0	6.9±0,0
10		6.4±0,0	6.8±0,1
15		5.9±0,0	6.7±0,1
0	14	7.0±0,0	7.0±0,0
5		6.9±0,0	7.0±0,0
10		6.4±0,0	7.0±0,0
15		5.9±0,0	7.0±0,0

the roots and leaves of *S. molesta* plants was studied in this research (Fig. 2). The Pb content in the roots of *S. molesta* showed a significantly higher concentration of Pb absorbed over the same period, with 5 ppm as the best result.

The ability of S. molesta to accumulate a higher amount of Pb in roots than in leaves was linked to its ability to immobilize toxic ions in the planting media by collecting and adsorbing the pollutant at the root zone. The roots also functioned as a rhizofilter, absorbing Pb toxic ions after phytostabilization. Therefore, the increase in Pb level in the roots is caused by the Pb accumulation process in the roots (Mangkoedihardjo & Samudro 2010).

When Pb and other heavy metals are present, this heavily loaded environment caused regulatory proteins in this plant to create sulfide bonds at the tip of sulfur in cysteine, further promoting the synthesis of complex molecules. Lead and other heavy metals would be transported to various plant tissues as a result.

There was no difference in Pb levels in the *S. molesta* leaves when different Pb concentrations were used for varied exposure times. However, Pb content was higher in roots than in leaves (Pourrut et al. 2011). Its function includes adsorbing the water surface and precipitating and accumulating pollutants in the root zone (Lyu et al. 2016, Salakinkop & Hunshal 2014). Rhizodegradation, the enhanced breakdown of a contaminant by increasing the bioactivity using the plant rhizosphere environment to stimulate the microbial populations (mostly Rhizosphere bacteria), is then carried out, with the products being dispersed into the root zone.

Plants Biochemical Response

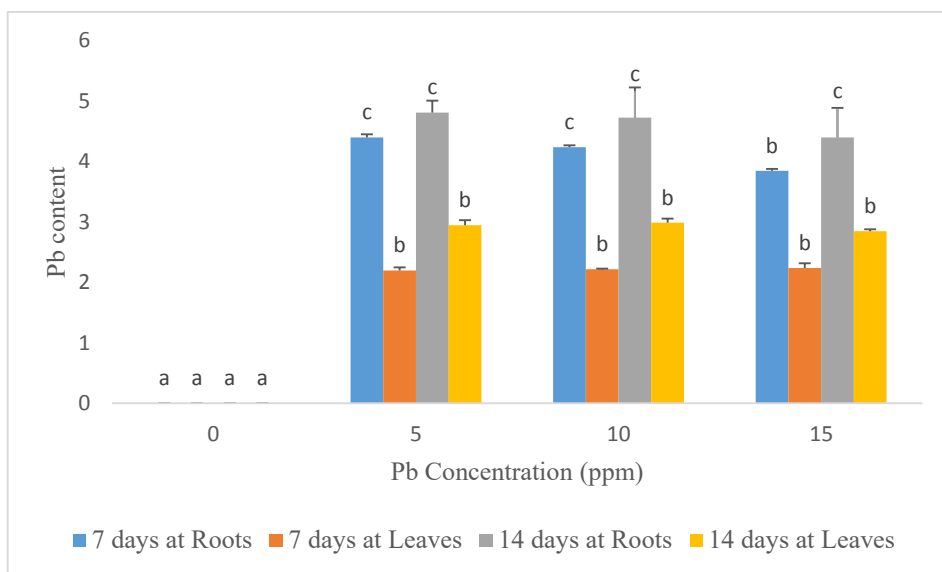Table 3 gives *S. molesta* protein mapping patterns based on

Fig 2: Pb content in roots and leaves of *S. molesta* plant after 7 and 14 days exposure.

Table 3: Amino acid content of Pb-exposed *Salvinia* plant.

Amino acid	Content [%] in Pb-exposed plant		
	0 ppm	5 ppm	15 ppm
Histidine	0.42±0.02	0.26±0.02	0.25±0.02
Threonine	0.92±0.00	045±0.00	0.49±0.02
Proline	0.71±0.02	0.48±0.02	0.41±0.02
Tyrosine	0.53±0.02	0.27±0.02	0.30±0.02
Leucin	1.39±0.02	0.91±0.02	0.77±0.02
Aspartic acid	1.16±0.02	0.79±0.02	0.74±0.02
Lysin HCl	0.56±0.02	0.40±0.02	0.37±0.02
Glycine	1.09±0.02	0.66±0.02	0.62±0.02
Arginine	0.91±0.02	0.55±0.02	0.50±0.02
Alanine	0.84±0.02	0.59±0.02	0.50±0.02
Valin	0.77±0.01	0.50±0.01	0.42±0.01
Isoleucine	0.63±0.01	0.41±0.01	0.35±0.01
Phenylalanine	1.13±0.01	0.61±0.01	0.59±0.01
Glutamic acid	1.49±0.02	1.04±0.02	0.91±0.02
Serine	0.90±0.00	0.47±0.00	0.49±0.00
Methionine	0.23±0.02	0.11±0.02	0.10±0.02
Cystine	0.01±0.00	0.00±0.00	0.00±0.00
Total	13.69	8.51	7.83

free amino acids and total proteins. Plant responses to environmental changes were defined by varying protein levels. Changes in the levels of particular amino acids (proline and cysteine) indicated protein resistance and degradation as a result of changes in environmental quality.

Because the ability to absorb Pb in the treatments of 5 and 10 was similar, the amino analysis was performed for 0, 5, 10, and 15 ppm; consequently, the 10 ppm did not include total protein analysis. The control group (0 ppm Pb) had a greater total protein content (13.69%) than the plants treated to 5 ppm Pb (8.51%) and 15 ppm Pb (7.83%) (Table 2). Several amino acids, including proline, glycine, arginine, histidine, glutamic acid, and cysteine, were found to be reduced following exposure to Pb.

At 14 days of exposure, the total percentage of amino acids in S. molesta decreased in tandem with the increase in Pb level. The lower the total percentage of protein from plants, the higher the Pb levels in the medium. According to studies on algae, the total protein content of *Chlorella vulgaris* was found to decrease in artificial media exposed to metals (Afkar et al. 2020). Another study found that co-exposed *Chlorella vulgaris* cells had no change in total protein content. This suggests that storing low concentrations of heavy metals in proteins or enhancing their respiration

by using carbohydrates with the advantage of protein accumulation could be one strategy for organisms to mitigate their harmful effects (Akmukhanova et al. 2018, Osman et al. 2004). According to Andra et al. (2010), the role of phytochelatin in inducing Pb-tolerance in vetiver grew in the contaminated medium.

Six amino acids have been identified as being significant in the regulation of osmotic plants based on the amino acid analysis (Mansour 2000). Arginine, proline, leucine, valine, serine, and glycine are the six amino acids. In *S. molesta*, the concentration of proline tended to decrease. The roots were able to absorb Pb from the medium and adapt to the new environment by generating amino acids. Arginine was also discovered in the plant. Arginine is required for the synthesis of polyamine, which acts as an antioxidative agent (Sharma & Dietz 2006) and signaling molecule (molecule signal). This means that plants can withstand stress by producing antioxidants.

CONCLUSION

In conclusion, *Salvinia molesta* was found to have potential as a phytoremediator for Pb-contaminated water, indicated by its ability to grow adequately in a Pb-contained medium and absorb Pb from the environment into its body. The op-

timal treatment is by 5 ppm. Pb content in plants was found to be higher in roots compared to leaves. Total proteins and many amino acids were reduced in Pb-exposed plants, demonstrating a method of plant response to environmental change. It is vital to investigate further the phytoremediation capabilities of S. molesta by increasing heavy metals levels in the medium in a shorter time frame and the remediation mechanism occurring within the plant body. The findings of this study can be transferred to further research involving the use of S. molesta as a phytoremediation agent for domestic or industrial wastewater.

ACKNOWLEDGEMENT

REFERENCES

Abhilash, P.B., Pandeya, V.C., Srivastava, P., Rakesh, P.S, Chandran, S., Singh, N. and Thomas, A.P. 2009. Phytofiltration of cadmium from water by *Limnocharis flava* (L.) *Buchenau*. J. Hazard Mater., 170(2-3): 791-797.

Afkar, E., Ababna, H. and Fathi, A.A. 2020. Toxicology response of green algae *Chlorella vulgaris*, to some heavy metals. Am. J. Environ. Sci., 6(3): 230-237.

Akmukhanova, N.R., Zayadan, B.K., Sadvakasova, A.K., Bolatkan, K. and Bauenova, M.O. 2018. A consortium of higher aquatic plants and microalgae designed to purify sewage of heavy metal ions. Russ. J. Plant Physiol., 65(1): 143-149.

Andra, S.S., Datta, R., Sarkar, D., Makris, K.C., Mullens, C.P., Sahi, S.V. and Bach, S.B.H. 2010. Synthesis of phytochelatins in vetiver grass upon lead exposure in the presence of phosphorus. Plant Soil, 326: 171-185.

Blokhina, O. and Fagerstedt, K.V. 2010. Oxidative metabolism, ROS, and NO under oxygen deprivation. Plant Physiol. Biochem., 48(5): 359-373.

Bokhari, S.H., Mahmood-Ul-Hassan, M. and Ahmad, M. 2019. Phytoextraction of Ni, Pb, and, Cd by duckweeds. Int. J. Phytoremediation., 21(8): 799-806.

Ergönül, M.B., Nassouhi, D. and Astasagun, S. 2019. Modeling of the bioaccumulative efficiency of *Pistia stratiotes* exposed to Pb, Cd, and Pb+Cd mixtures in nutrient-poor media. Int. J. Phytoremediation., 22(2): 201-209.

Göthberg, A., Greger, M., Holm, K. and Bengtsson, B.E. 2004. Influence of nutrient levels on uptake and effect of mercury, cadmium, and lead in water spinach. J. Environ. Qual., 33(4): 1247-1255.

Hardiani, H., Kardiansyah, T. and Sugesty, S. 2011. Bioremediasi logam timbal (Pb) dalam tanah terkontaminasi limbah sludge industri kertas proses deinking [Lead metal bioremediation (Pb) in soil sludge contaminated soil paper industry deinking process]. Jurnal Selulosa, 1(1): 31-41.

Kamel, H. 2008. Lead accumulation and its effect on photosynthesis and free amino acids in *Vicia faba* grown hydroponically. AJBAS, 2(3): 438-446.

Lyu, X.Q., Zhang, Y.L. and You, W.H. 2016. Growth and physiological responses of *Eichhornia crassipes* to clonal integration under experimental defoliation. Aquat. Ecol., 50: 153-162.

Mangkoedihardjo, S. and Samudro, G. 2010. *Fitoteknologi Terapan* [Applied phytotechnology]. Graha Ilmu, Yogyakarta.

Mansour, M.M.F. 2000. Nitrogen-containing compounds and adaptation of plants to salinity stress. Biol. Plant, 43(4): 491-500.

Munzuroglu, O. and Geckil, H. 2002. Effects of metals on seed germination, root elongation, and coleoptile and hypocotyl growth in *Triticum aestivum* and *Curcumis sativus*. Arch. Environ. Contam. Toxicol., 43(2): 203-213.

Nouri, J., Lorestani, B., Yousefi, N., Khorasani, N., Hasani, A.H., Seif, F. and Cheraghi, M. 2011. Phytoremediation potential of native plants grown in the vicinity of Ahangaran lead-zinc mine (Hamedan, Iran). Environ. Earth Sci., 62: 639-644.

Osman, M.E.H., El-Naggar, A.H., El-Sheekh, M.M. and El-Mazally, E.E. 2004. Differential effects of Co+2 and Ni+2 on protein metabolism in *Scenedesmus obliquus* and *Nitzschia perminuta*. Environ. Toxicol. Pharmacol., 16(3): 169-178.

Phetsombat, S., Kruatrachue, M., Pokethitiyook, P. and Upatham, S. 2006. Toxicity and bioaccumulation of cadmium and lead in *Salvinia cucullate*. J. Environ. Biol., 27(4): 645-652.

Pilon, S.E. 2005. Phytoremediation. Annu. Rev. Plant Biol., 56: 15-39.

Pourrut, B., Shahid, M., Dumat, C., Winterton, P. and Pinelli, E. 2011. Lead uptake, toxicity, and detoxification in plants. Rev. Environ. Contam. Toxicol., 213: 113-136.

Rachmadiarti, F., Soehono, L.A., Utomo, W.H., Yanuwiyadi, B. and Fallowfield, H. 2012. Resistance of yellow velvetleaf (*Limnocharis flava* (L.) Buch.) exposed to lead. JAEBS, 2(6): 210-215.

Rachmadiarti, F. and Trimulyono, G. 2019. Phytoremediation capability of water clover (*Marsilea crenata* (L). Presl.) in synthetic Pb solution. Appl. Ecol. Environ. Res., 17(4): 9609-9619.

Rai, P. K. and Tripathi, B. D. 2009. Comparative assessment of *Azolla pinnata* and *Vallisneria spiralis* in Hg removal from G.B. Pant Sagar of Singrauli industrial region, India. Environ. Monit. Assess., 148: 75-84.

Rai, P.K. 2011. An eco-sustainable green approach for heavy metals management: two case studies of developing industrial region. Environ. Monit. Assess., 184: 421-448.

Rai, P. K. 2018. Heavy metal photo technologies from Ramsar wetland plants: Green approach. J. Chem. Ecol., 34(8): 786-796.

Salakinkop, S.R. and Hunshal, C.S. 2014. Domestic sewage irrigation on dynamics of nutrients and heavy metals in soil and wheat (*Triticum aestivum* L.) production. Int. J. Recycl. Org. Waste Agric., 3(64): 1-11.

Sari, A.M. 2014. Effectiveness of *Eichornia crassipes* Mart (Solm.) and *Salvinia molesta* Mitchell to absorb chromium heavy metal in liquid waste of batik industry. The 5th International Conference BASIC-ICGRC, Feb. 12-13, 2014, University of Brawijaya, Malang, Indonesia.

Shah, K. and Nongkynrih, J.M. 2007. Metal hyperaccumulation and bioremediation. Biol. Plant., 51(4): 618-634.

Sharma, S.S. and Dietz, K.J. 2006. The significance of amino acids and amino acid-derived molecules in plant responses and adaptation to heavy metal stress. J. Exp. Bot., 57(4): 711-726.

Sreekanth, T.V.M., Nagajyothi, P.C., Lee, K D. and Prasad, T.N.V.K.V. 2013. Occurrence, physiological responses, and toxicity of nickel in plants. IJEST, 10(5): 1129-1140.

Waters. 2017. AccQ•Tag Amino Acid Analysis Column. Waters Corporation, Maple Street Milford, USA.

Wuana, R.A. and Okieimen, F.E. 2011. Heavy metals in contaminated soils: a review of sources, chemistry, risks and best available strategies for remediation. Int. Sch. Res. Notices, 2011: 402647.

Xin, J., Huang, B., Yang, Z., Dai, H. and Qiu, Q. 2010. Responses of different water spinach cultivars and their hybrid to Cd, Pb, and Cd-Pb exposures. J. Hazard. Mater., 175(1-3): 468-476.

Zeller, S. and Feller, U. 1999. Long-distance transport of cobalt and nickel in maturing wheat. Eur. J. Agron., 10(2): 91-98.

Zou, T., Li, T., Zhang, X. Yu, H. and Huang, H. 2011. Lead accumulation and phytostabilization potential of dominant plant species growing in a lead-zinc mine tailing. Environ. Earth Sci., 65: 621-630.

Elimination of Greenhouse Gas Emissions by Utilization of Industrial Wastes in High Strength Concrete for Environmental Protection

R. Divahar*†, K. Naveen Kumar*, P. S. Aravind Raj* and S. P. Sangeetha*

*Department of Civil Engineering, Aarupadai Veedu Institute of Technology, Vinayaka Mission's Research Foundation, Paiyanoor, Tamil Nadu, India

†Corresponding author: R. Divahar; divahar.civil@avit.ac.in; divaharmr@gmail.com

ABSTRACT

Greenhouse gases prevalence in the atmosphere is a primary reason for global warming. The cement manufacturing sectors are a significant producer of greenhouse gases, contributing one metric tonne of carbon dioxide into the environment for every metric tonne of cement produced. The heat of concrete is increased by several degrees during the pozzolanic reaction, and CO_2 is released. The development of binary and ternary cementitious systems has minimized the unfavorable reactions of conventional cementitious materials. Metakaolin and alccofine, two mineral admixtures derived as waste products from industries, were used as cement substitutes in this study. The compressive strength of alccofine was compared to a metakaolin-based high strength eco-friendly concrete mix of grade M50 in an experimental investigation. In the case of binary and ternary blended cementitious systems with alccofine and metakaolin, twelve alternative mix proportions were tested, ranging from 0 to 20% in 5% increments. Based on the observed mechanical characteristics of concrete, it was discovered that the optimum replacement of alccofine was 15% and metakaolin was 5% by volume of cement in the binary cementitious system. Similarly, in the ternary cementitious system, replacing 15% alccofine with 5% metakaolin in the cement mixture results in the greatest increase in compressive strength when compared to the other experiments. As a result, it is concluded that using extra cementitious materials in concrete with mineral admixtures such as alccofine and metakaolin results in significant cost and energy savings, as well as a notable reduction in environmental pollution.

INTRODUCTION

Concrete materials are used in the construction of community infrastructure. Because of the nature of concrete, cement is the only reactive component that blends and holds the materials together. When it comes to concrete's load-bearing capacity, the aggregates, which account for 75% to 80% of the entire concrete volume, carry the weight of the applied load. Due to numerous factors such as high strength, long-term strength, greater durability, economic, and environmental reasons, HSC has been more popular in recent decades all over the world, and has played an essential role in the construction of special structures and large infrastructures (Umamaheswaran et al. 2015, Suchithra & Malathy 2016). To address environmental challenges, the cement industry is working on a more sustainable method of production. The fact is that cost and intensive energy are not the only issues, the generation of large amounts of greenhouse gases that have a negative impact on the environment has now become the primary problem in the manufacturing of Portland cement. Several methods, replacements, and supplements were experimented with reducing the usage of Portland cement (Ushaa

et al. 2015, Kothai & Malathy 2015). The use of mineral additives has been proven to improve the strength and durability of concrete. The use of supplementary cementitious materials in concrete with mineral admixtures such as alccofine and metakaolin results in significant cost and energy savings, as well as a notable reduction in environmental pollutants (Naik & Moriconi 2005, Chan et al. 2006, Kumar et al. 2016, Thangaraj & Thenmozhi 2013).

Metakaolin is a clay-based mineral with outstanding qualities for treating amorphous alumino-silicate, which makes concrete more responsive. Alccofine is a mineral additive that can be manufactured to the suitable fineness to get the desired characteristic in the concrete in which it is employed. Mineral admixtures such as metakaolin and alccofine, in addition to this approach, can be employed in the HSC to produce better compressive strength (Jaydeep et al. 2016, Saha et al. 2014, Annadurai & Ravichandran 2014, Raju et al. 2017).

Experimentally, replacing part of the cement in the concrete mix with varying percentages of fly-ash and metakaolin resulted in a significant reduction in the cost of the concrete

and the eradication of green gas emissions (Lakshmi et al. 2016, Satyendra et al. 2015, Malagavelli et al. 2018, Surendra & Rajendra 2016).

Experimentations were performed with various percentages of metakaolin replaced with cement in M30 concrete and it was observed that the split-tensile, compressive strength, and flexural strength were optimal at 15% replacement. As a result of the findings encouraging the use of metakaolin, it can be used in large-scale buildings to offset the environmental and economic costs of traditional cement manufacturing and use (John 2013, Rao & Kumar 2016). When metakaolin was added, the workability was diminished, but this was corrected with the application of a superplasticizer (Narmatha & Felixkala 2016, Jagtap et al. 2017, Hemanth et al. 2017).

When cement is replaced with various percentages of metakaolin in an M30 concrete, the basic characteristics of the concrete are found to be highest at 15%, indicating that metakaolin can be used as a dependable pozzolanic material substitute for cement in high strength concrete. As a result, this new cementitious/pozzolanic substance will provide a solution to the environmental issues created by conventional cement consumption and production (Sood et al. 2014, Philip & Neeraja 2015, Chowdhury & Saha 2016).

Acid resistance, sulfate attack, and chloride attack tests were used to investigate the durability characteristics of alccofine in concrete (Gayathri et al. 2018). The researchers found that replacing 15% of the alccofine with 15% boosted the concrete's resistance to acid attacks. Similarly, the mechanical characteristic of alccofine has been studied by Kaviya et al. (2017). They concluded that cement is replaced by 15% alccofine, which increases compressive strength (Suganya & Lathamaheswari 2019). Cement replaced partially with alccofine reduces water demand for the same workability by developing a dense pore structure and thus helps to attain higher strength (Hermawana et al. 2015, Ansari et al. 2015, Puti et al. 2015).

A high-strength concrete mix of grade M50 was cast and tested with 0, 5%, 10%, 15%, and 20% alccofine substituting cement and metakaolin in 5% increments. After 7, 14, and 28 days of moist curing, compression tests were performed.

The objective of this project is to determine the optimum replacement percentage of alccofine and metakaolin for cement in concrete and to analyze the mechanical characteristics of concrete added with alccofine and metakaolin by its compressive strength.

MATERIALS AND METHODS

Binder

In this study, in the course of experimental investigation, the binder material used in the concrete is 53-grade OPC (IS 12269:1987). Preliminary tests were conducted for the cement used for the study and the characteristics listed in Table 1.

Fine Aggregate

The study (Zone II) uses river sand as a fine aggregate, verifying IS:383:1970's specific gravity of 2.6. The physical qualities of the sand utilized in this investigation, as well as the characteristics, are given in Table 2, were analyzed.

Coarse Aggregate

The coarse aggregate utilized in the study is 20mm in size and has a specific gravity of 2.8, according to IS: 383:1970. The physical parameters of the coarse aggregate employed in this investigation, as well as the characteristics, are given in Table 3, were assessed.

Water

Potable tap water was used for the concrete preparation and curing operations.

Chemical Admixture

Master Gelenium SKY 8233, a superplasticizer based on a new generation modified polycarboxylate ether, was employed.

Metakaolin

It is a clay-based mineral with outstanding qualities for handling amorphous alumino-silicate, which makes it receptive

Table 1: Physical properties of cement (53 grade).

Characteristics	Experimental Values
Initial setting time	50 min
Final setting time	320 min
Specific gravity	3.15
Consistency	32%
Soundness	1.2 mm
Compressive strength (MPa)	29.8 at 3 days 45.6 at 7 days 56.2 at 28 days

Table 2: Physical properties of fine aggregate.

Physical properties	Experimental Values
Fineness modulus	2.82
Density	1635
Specific gravity	2.6

to concrete. The metakaolin will react with the concrete ingredient's calcium hydroxide (Dubey et al. 2015). Pozzolanic materials, like other traditional alternatives, hydrate during the process of hydration.

Alccofine

Alccofine 1203, an ultrafine low calcium silicate product with high reactivity made by a controlled granulation technique, was used in this study (Fig. 1). Tables 4 and 5 show the physical and chemical compositions of Alccofine 1203 and Metakaolin (MK).

MATERIALS AND METHODS

Mix Design for M50 Grade Concrete

Mix proportioning: M50 grade mix concrete was created to meet the requirements of IS 10262:2009 code provision. The best dose of chemical admixture to be utilized in concrete is found based on several trail mixes with varying percentages of chemical admixture by the weight of cementitious material of 0.25%, 0.5%, 0.75%, and 1%. Table 6 shows the mixed design proportion.

Mix preparation: In a dry environment, the OPC, alccofine, metakaolin, coarse aggregate, and fine aggregate were completely combined with power mixers for 30 seconds. Water and superplasticizer are added in quantities as per the design mix to make the concrete mixes after the dry ingredients have been blended. The binary and ternary blended systems of mineral admixtures are shown in Tables 7 and 8, respectively.

Table 3: Physical properties of coarse aggregate.

Physical properties	Experimental Values
Fineness modulus	1.9
Impact value	14.2
Specific gravity	2.8

Fig. 1: Alccofine-1203.

Casting and Curing of Moulds

108 binary and ternary cementitious (alccofine and metakaolin) concrete specimens were cast in form of standard concrete cubes as per IS456:2000 with the prepared concrete mix. The concrete cube specimens are cured for various periods such as of 7, 14, and 28 days in the ambient temperature of 27±2°C in the curing tank. Fig. 2 shows the evidence of concrete specimens cast and cured.

Workability

Workability is a term used in concrete technology to describe the properties of concrete that make it easier to place, compact, and finish. The Slump cone test is commonly used to determine the workability of fresh concrete. The slump

Table 4: Chemical and physical composition of alccofine 1203.

Chemical Properties		Physical Properties	
Existing Mineral	Composition [%]	Physical Possessions	Outcomes
SiO_2	35.30	Partial Size Distribution (in micro meter)	
MgO	6.20	D10	1.8
Al_2O_3	21.40	D50	4.4
Fe_2O_3	1.20	D90	8.9
SO_3	0.13	Specific Gravity	2.7
SO_2	23.46	Bulk Density [kg.m^{-3}]	680
CaO	33	Specific Surface Area [cm^2.gm^{-1}]	12000

Table 5: Chemical and physical composition of metakaolin.

Chemical Properties		Physical Properties	
Existing Mineral	Composition [%]	Physical Possessions	Outcomes
SiO_2	52.5	Residue on Sieve [%]	
MgO	0.25	90 µm	1.00
Al_2O_3	42.20	45 µm	12.80
Fe_2O_3	0.34	Loss on ignition	0.50
SO_3	0.01	Pozzolanic Activities based on CaO Absorption [mg.g^{-1}]	25
SO_2	63.48	Specific Gravity	2.65
CaO	0.30	Bulk Density [kg.m^{-3}]	350
Na_2O	0.10	Specific Surface Area [cm^2.gm^{-1}]	18000
$K_2O + Na_2O$	0.05	Insoluble residue [%] HCl/Na_2CO_3	63.45

Fig. 2: Casting and curing of concrete specimen.

characteristics of various combinations of concrete mixes developed in this investigation are shown in Tables 8.

RESULTS AND DISCUSSION

Table 9 and Table 10 show the average compression strength of concrete cubes tested after curing for 7 days, 14 days, and 28 days.

Compressive Strength

The compressive strength test results of Alccofine and Metakaolin replaced the binary blended cementitious system shown in Table 9 and Fig. 3.

In a binary blended system, concrete with 5%, 10%, and 15% alccofine replacement (AF5MK0, AF10MK0, AF15MK0) had compressive strengths that were 1%, 2.3%,

and 18.8% greater than the control mix (AF0MK0) after 28 days of compression testing. However, replacing 20% of the alccofine mix with AF20MK0 resulted in a 3.9% lower compressive strength than the control mix (AF0MK0).

Similarly, metakaolin specimens with 5% metakaolin replacement (AF0MK5) had 19.8% better compressive strength than the control mix after 28 days of compression testing (AF0MK0). However, 10%, 15%, and 20% metakaolin replacement (AF0MK10, AF0MK15, AF0MK20), respectively, resulted in 12.3 percent, 20.9%, and 31.5% lower compressive strength than the control mix (AF0MK0).

At 28 days, concrete with 5% AF and 15% MK, and 10% of both AF and MK replacement (AF5MK15 & AF10MK10)

Table 6: Concrete mix proportion.

Mix Proportion for M-50 Grade of Concrete	
Materials	Target compressive strength [Mpa]
	50
W/C ratio	0.35
Total Cement Content [kg.m^{-3}]	435
Fine Aggregate [kg.m^{-3}]	742
Coarse Aggregate [kg.m^{-3}]	1113
Water [kg.m^{-3}]	152
Mineral Admixture [kg.m^{-3}] Percentage of replacement of cementitious content – Binary blended system	5% - 20%
Mineral Admixture [kg.m^{-3}] Percentage of replacement of cementitious content – Ternary blended system	20%
Superplasticizer [kg.m^{-3}] By the weight of cementitious content in the concrete mix	0.25%

Table 7: Percentage of alccofine (AF) and metakaolin (MK), binary blended system.

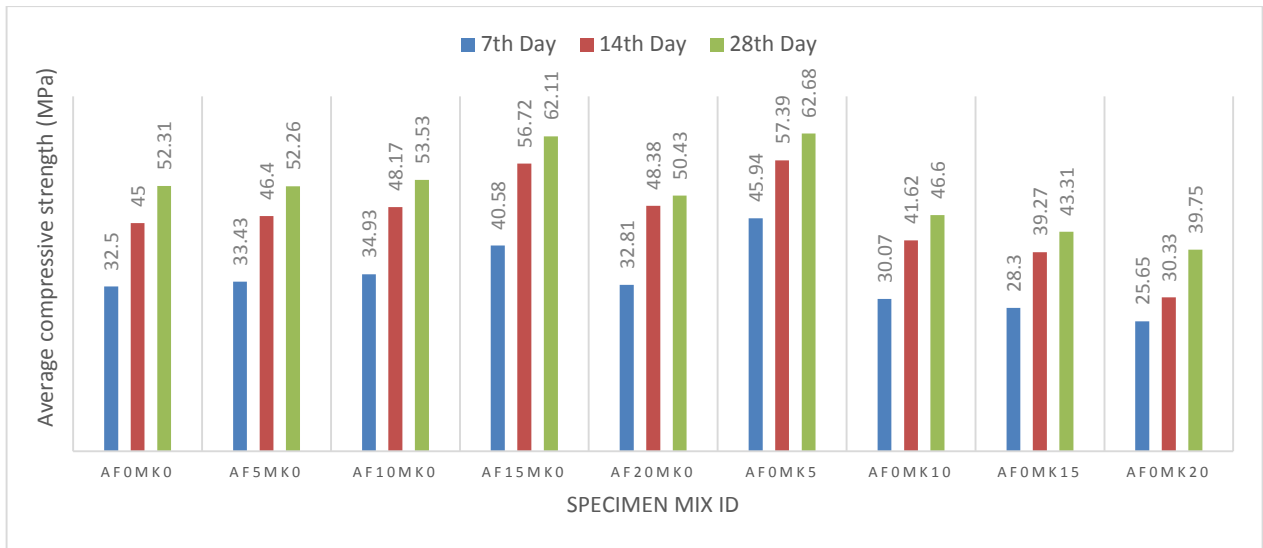| Specimen Mix ID	Blending Material	Water Content [kg.m^{-3}]	Cement Content [kg.m^{-3}]	Work-ability [mm]
AF0MK0	Only OPC	152	435	74
AF5MK0	OPC + 5%AF	152	413.25	68
AF10MK0	OPC + 10%AF	152	391.50	75
AF15MK0	OPC + 15%AF	152	369.75	90
AF20MK0	OPC + 20%AF	152	348	110
AF0MK5	OPC + 5%MK	152	413.25	88
AF0MK10	OPC + 10% MK	152	391.50	65
AF0MK15	OPC + 15% MK	152	369.75	62
AF0MK20	OPC + 20% MK	152	348	60

Fig 3: Comparison of compressive strength with binary blended system.

Table 8: Percentage of alccofine (AF) and metakaolin (MK), ternary blended system.

Mix ID	Blending Material	Water Content [kg.m^{-3}]	Cement Content [kg.m^{-3}]	Workability [mm]
AF5MK15	OPC + 5%AF+ 15% MK	152	391.50	90
AF10MK10	OPC + 10%AF+ 10%MK	152	348	88
AF15MK5	OPC + 15%AF+ 5%MK	152	304.50	70

Table 9: Compressive strength of binary blended system.

Specimen Mix ID	Average Compressive Strength [Mpa]			Percentage of variation in compressive strength when compared with control mix at 28 days.
	7th Day	14th Day	28th Day	
AF0MK0	32.50	45.00	52.31	-
AF5MK0	33.43	46.40	52.78	+1%
AF10MK0	34.93	48.17	53.53	+ 2.3
AF15MK0	40.58	56.72	62.11	+18.8
AF20MK0	32.81	48.38	50.43	-3.9
AF0MK5	45.94	57.39	62.68	+19.8
AF0MK10	30.07	41.62	46.60	-12.3
AF0MK15	28.30	39.27	43.31	-20.9
AF0MK20	25.65	30.33	39.75	-31.5

had 14.8 percent and 7.9 percent lower compressive strength than the control mix in a ternary blended system (AF0MK0). However, concrete containing 15% AF and 5% MK (AF-15MK5) had a 3 percent better compressive strength than the control mix (AF0MK0). The compressive strength test findings of Alccofine and Metakaolin were used to replace the ternary blended cementitious system presented in Table 10 and Fig. 4 in the ternary blended system.

CONCLUSION

The results of an experimental investigation of alccofine with metakaolin mineral admixture in binary and ternary blended cementitious systems. According to a compressive strength investigation, the optimum percentage of cement by alccofine and metakaolin was 15% and 5% by volume, respectively. Similarly, the replacement of 15% alccofine and 5% metakaolin in the ternary blended system resulted in the

Fig 4: Comparison of Compressive strength with Ternary Blended System.

Table 10: Compressive strength of ternary blended system.

Specimen Mix ID	Average Compressive Strength (MPa)			Percentage of variation in compressive strength when compared with control mix at 28 days.
	7th Day	14th Day	28th Day	
AF0MK0	32.50	45.00	52.31	
AF5MK15	29.70	40.98	45.55	-14.8%
AF10MK10	30.98	42.66	48.50	-7.9%
AF15MK5	35.07	50.41	53.80	+ 3%

best compressive strength compared to all other combinations in the ternary blended system.

Metakaolin, a highly pozzolanic material with micro-filler properties, and alccofine, a higher specific surface area material with early strength acquiring properties, are combined to improve workability strength and chemical attack resistance by reducing porosity through C-S-H gel production.

Because the findings support the use of alccofine and metakaolin in large-scale buildings, they can be used to offset the environmental and economic costs of traditional cement manufacture and use. Finally, the binary and ternary blended systems led to significant concrete cost reductions and greenhouse gas emissions elimination.

ACKNOWLEDGMENT

REFERENCES

Annadurai, A. and Ravichandran, A. 2014. Development of mix design for high-strength concrete with admixtures. IOSR J. Mech. Civil Engg., 10(5): 22-27.

Ansari, U.S., Chaudhri, I.M., Ghuge, N.P. and Phatangre, R.R. 2015. High-performance concrete with partial replacement of cement by alccofine & fly ash. Indian J. Sci. Res., 5(2): 19-23.

Chan, Y.N., Luo, X. and Sun, W. 2000. Compressive strength and pore structure of high-performance concrete after exposure to high temperature up to 800ºC. Cem. Concr. Res., 30(2): 247-251.

Chowdhury, J. and Saha, A. 2016. High strength concrete incorporating Indian fly ash. Int. J. Sci. Eng. Res., 7(4): 93-99.

Dubey, S., Chandak, R. and Yadav, R.K. 2015. Experimental study of concrete with metakaolin as partial replacement of OPC. Int. J. Adv. Eng. Res. Sci., 2(6): 38-40.

Gayathri, K., Ravichandran, K. and Saravanan, J. 2016. Durability and cementing efficiency of alccofine in concretes. Int. J. Eng. Res. Technol., 5(5): 460-467.

Hemanth Rama Raju, O. and Sravani Ramya Singam, P. 2017. An Experimental Investigation on Partial Replacement of Cement with Metakaolin and Fine Aggregate with Robo Sand. Int. Res. J. of Eng. and Tec., 4(4): 1169-1173.

Hermawana,Puti, F., Marzukia, Muhamad Abduha and Driejanaa, R. 2015. Identification of source factors of carbon dioxide (CO2) emissions in concreting of reinforced concrete. Pro. Eng., 125(1): 692-698.

Jagtap, S.A., Shirsath, M.N. and Sambhaji. K.L. 2017. Effect of metakaolin on the properties of concrete. Int. Res. J. Eng. Technol., 4(7): 643-645.

John, N. 2013. Strength properties of metakaolin admixed concrete. Int. J. Sci. Res., 3(6): 1-7.

Jaydeep Chowdhury and Arka Saha. 2016. High Strength concrete incorporating an Indian fly ash. Int. J. Sci. & Eng. Res., 7(4): 93-99.

Kaviya, B., Rohith, K., Kindo, S., Kumar, J.M. and Divya, P. 2017. Experimental study on partial replacement of cement using alccofine. Int. J. Pure Appl. Math., 116(13): 399-405.

Kothai, P.S. and Malathy, R. 2015. Effective utilization of wastes from steel industries in concrete. Nat. Environ. Pollut. Technol., 14(2): 419-422.

Kumar, S.R., Samanta, A.K. and Roy, D.K.S. 2016. Role of ingredients for high strength and high-performance concrete: A review. Adv. Concr. Constr., 1(2): 151-162.

Lakshmi, A.K., Reddy, A.I.S. and Kumar, S.A. V. S. 2016. Strength characteristics of concrete with partial replacement of cement with fly-ash & metakaolin. Int. J. Innov. Res. Technol., 1(7): 18-22.

Malagavelli. V., Angadi, S. and Prasad, J.S.R. 2018. Influence of metakaolin in concrete as partial replacement of cement. Int. J. Civ. Eng. Technol., 9(7): 105-111.

Naik, T.R. and Moriconi, G. 2005. Environmental Friendly Durable Concrete Made with Recycled Materials for Sustainable Concrete Construction. Proceedings of the International Symposium on Sustainable Development of Cement, Concrete and Concrete Structures, 5-7 October 2005, Toronto, RILEM Publications, Moscow, pp. 485-505

Narmatha, M. and Felixkala, T. 2016. Metakaolin –the best material for the replacement of cement in concrete. IOSR J. Mech. Civil Eng., 13(4): 66-71.

Philip, N. and Neeraja, D. 2015. Mechanical properties of high-performance concrete with admixtures and steel fiber. ARPN J. Eng. Appl. Sci., 12(8): 2439-2444.

Puti, H.F., Marzukia, M.A. and Driejanaa, R. 2015. Identification of source factors of carbon dioxide (CO2) emissions in concreting reinforced concrete. Procedia Eng., 125(1): 692-698.

Raju, H.R.O. and Singam, S.R.P. 2017. An experimental investigation on partial replacement of cement with metakaolin and fine aggregate with robo sand. Int. Res. J. Eng.Technol., 4(4): 1169-1173.

Rao, K. and Kumar, A. 2016. A study on partial replacement of cement with metakaolin and fine aggregate with waste foundry sand. Int. J. Eng. Res., 5(12): 402-407.

Saha, A., Pan, S. and Pan. S. 2014. Strength development characteristics of high strength concrete incorporating Indian fly ash. Int. J. Technol. Enhanc. Emerg. Eng. Res., 2(6): 101-107.

Sood, V., Kumar, A. and Agarwal, S.K. 2014. Comparative hydration behavior of a metakaolin-microfine system. J. Eng. Comp. Appl. Sci., 3(4): 60-65.

Suchithra, S. and Malathy, R. 2016. Effective utilization of industrial wastes in self-compacting concrete for environmental protection. Nat. Environ. Pollut. Technol., 15(1): 285-290.

Suganya, R. and Lathamaheswari, R. 2019. Experimental Investigation on Alccofine Concrete. Int. J. Eng. Res. Technol., 8(4): 548-550.

Surendra, B.V. and Rajendra, T.N. 2016. An experimental investigation on strength properties of concrete with partial replacement of cement by fly ash and metakaolin & with M. sand as fine aggregate. Int. Res. J. Eng. Technol., 3(7): 2150-2153.

Satyendra Dubey, Rajiv Chandak and Yadav, R.K. 2015. Experimental Study of Concrete with Metakaolin as Partial Replacement of OPC. Int. J. of Adv. Eng. Res. and Sci., 2(6): 38-40.

Thangaraj, R. and Thenmozhi, R. 2013. Industrial and environmental application of high volume fly ash in concrete production. Nat. Environ. Pollut. Technol., 12(2): 315-320.

Umamaheswaran, V., Sudha, C., Ravichandran, P.T. and Kannan Rajkumar, P.R. 2015. Use of M sand in high strength and high-performance concrete. Indian J. Sci. Technol., 8(28): 1-8.

Ushaa, T.G., Anuradha, R. and Venkatasubramani, G. S. 2015. Reduction of greenhouse gases emission in self-compacting geopolymer concrete using sustainable construction materials. Nat. Environ. Pollut. Technol., 14(2): 451-454.

Numerical Simulation of Soil Temperature With Sand Mulching During the Growing Season of Spring Wheat

Wenju Zhao*†, Yuhang Liu*, Zongli Li and Yu Su***

*College of Energy and Power Engineering, Lanzhou University of Technology, Lanzhou 730050, China
**General Institute for Water Resources and Hydropower Planning and Design, Ministry of Water Resources, Beijing 100120, China
†Corresponding Author: Wenju Zhao; wenjuzhao@126.comiq

ABSTRACT

The thermal conditions of soil are important in practical agricultural production. The characteristics of heat flux, moisture content, thermal conductivity, and other soil parameters vary with temperature. This study uses VADOSE/W to create a model of heat transmission between soil and atmosphere, simulating daily changes in soil temperature using sand mulching. By using the published data to verify the model, the results show that the fitting effect is good and the reliability of the model is verified. We also used this model to determine the temporal and spatial distributions of soil temperature, temperature differences, and a temperature gradient for sand mulching and bare soil during the growing season of spring wheat. These results indicated that the sand mulching preserved heat at night. The difference in temperature at each depth and the temperature gradient became negative with the gradual increase in solar altitude. The difference in soil temperature at each depth and the temperature gradient tended to become positive by 22:00. These results indicated that the sand mulch effectively maintained the soil temperature in the morning and night during the growing season and impeded the transfer of heat at mid-day. This study provides a new method for determining the transfer of heat in sand-mulched soil, which can guide the effective regulation of soil temperature.

INTRODUCTION

The thermal conditions of soil have had a wide-ranging impact on various aspects of Earth sciences, including the growth of surface crops, the production of carbon dioxide, and the evaporation of water from the soil (Votrubová et al. 2012, Timlin et al. 2002, Buchner et al. 2008, Sakai et al. 2011). The thermal changes of soil affect the characteristics of heat flux, moisture content, thermal conductivity (Hsieh et al. 2009, Matsushima et al. 2010, Lu & Dong 2015), and other parameters. Soil temperature is critical to agricultural production and is an important physical indicator. Many scholars have investigated the effects of soil temperature on the growth and development of crops, the thermal status of the soil, and the evaporation of soil water.

Füllner et al. (2012) reported that biomass yield and root structure differed significantly among 30-day-old plants due to the effects of a gradient of soil temperature on plant growth and development, but Lahti et al. (2005) found that a reduction in temperature did not significantly affect biomass or nutrient uptake in seedlings. Nabi & Mullins (2008) reported that cotton roots and shoots during emergence were shortest and biomass was highest at 38°C. The sizes and proportions of sandstone particles can affect

soil temperature, transpiration, water-use efficiency, and yield in watermelon with mulching. Bu et al. (2013) found that both gravel and plastic-film mulching increased the cumulative soil thermal time by 150-220°C over the growing season relative to bare soil. Mulching with gravel or plastic film is an effective strategy for increasing soil temperature, soil moisture content, and crop yield. Plastic films, however, can cause environmental pollution.

Farmers in the arid regions of northwestern China developed a method of conservation tillage with sand and gravel mulching to survive, which has been practiced for more than 300 years (Li et al. 2000, Lü et al. 2011). A cover of gravel and sand on the soil surface can improve soil conditions by retaining water, increasing and maintaining soil temperature, reducing surface salt accumulation, increasing infiltration, and effectively reducing evaporation and runoff (Yang et al. 2019, Li 2003, Ma & Li 2011). Numerical simulation has recently been widely used in various disciplines, with many studies simulating the flux of soil heat and evaporation. VADOSE/W modeling has typically been applied to obtain the pore pressure of natural or artificially covered slopes under controlled climates using stability analysis and to determine infiltration, evaporation, and plant transpiration

for projects of agricultural irrigation. Argunhan-Atalay & Yazicigil (2018) used VADOSE/W to simulate fluxes in unsaturated and saturated regions and evaluated the performance of various overlay systems. Zhao et al. (2017a) used VADOSE/W to determine that cumulative soil evaporation was independent of mulch thickness and depended only on the depth of the inclusion: the deeper the inclusion, the higher the evaporation. Li et al. (2016) used VADOSE/W to simulate the characteristics of fluxes in unsaturated loess under the influence of environmental factors.

We used VADOSE/W to simulate the daily variation in the temperature of soil containing sandstone particles 0.3-1 cm in size and covered by 7 cm of sand at depths of 5 and 10 cm. We also used published data for the ground temperature of a cornfield at 14:00 and 20:00 in an irrigated area in Xinjiang, China. The simulated and measured temperatures were compared to verify the reliability of the model. The temporal and spatial distributions of temperature at different growth stages of spring wheat and the distribution of temperature differences and a temperature gradient over time were then simulated and predicted. This study clarifies the mechanism of soil heat transfer, which is important for agricultural production.

MATERIALS AND METHODS

Experimental Materials

The sandstone particles ranged in size from 0.3 to 1 cm, and the sand mulch was 7 cm thick. We used data from Xie et al. (2010) to simulate the changes in soil temperature over the time at depths of 5 and 10 cm. We also used data from Li et al. (2003) for the ground temperature at 08:00 on 25 April

in a cornfield in an irrigated district in Xinjiang as the initial data for verification, and the ground temperature at 14:00 and 20:00 was simulated. Experimental data (Zhao et al. 2016) from an experimental base (Zhao et al. 2017b) (Table 1) were used for simulating the temporal and spatial distributions of temperature at various stages of growth of spring wheat and for determining the distribution of temperature differences and a temperature gradient over time, and the sand mulch was 15 cm thick.

Model Composition

Experimental design: All experiments were field experiments. Temperatures on sunny days from local meteorological data were used as the thermal boundary to analyze the influence of heat.

Model construction: The first model represented a volume of soil 25 cm in depth and 50 cm in width, including bare soil, a sand mulch 7 cm thick, and a sand mulch 15 cm thick (Fig. 1a, b, and c).

Boundary conditions: Information for the temperature in a soil profile is necessary to solve the equations for moisture content and heat flux. The surface temperature of snow-free soil can be estimated using the relationship (Wilson 1990):

$$T_s = T_a + \frac{1}{vf(u)}(Q - E) \qquad ...(1)$$

where T_s is the temperature of the soil surface (°C), T_a is the air temperature above the soil surface (°C), v is the constant humidity and Q is the net radiant energy available on the surface (minus transpiration) (mm.d^{-1}).

Table 1: Particle composition of the soil and sand.

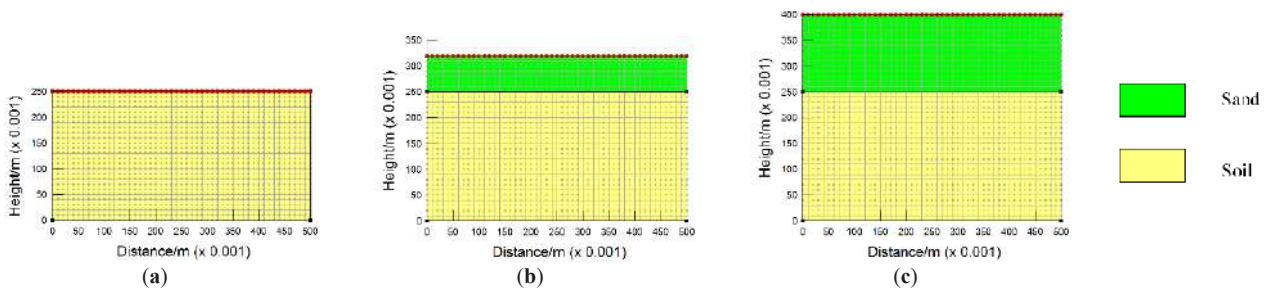| Particle size [mm]	<2.00	<1.00	<0.05	<0.01	<0.001
Soil [%]	100.00	99.46	80.26	23.13	10.06
Sandstone composition [mm]	<10.00	<5.00	<2.50	<1.25	<0.63
Sand stone [%]	100.00	94.51	79.58	59.70	34.62

Fig. 1: Geometric model. (a) Bare soil (CK); (b) Sand mulching, 7 cm; (c) Sand mulching, 15 cm.

RESULTS AND DISCUSSION

Model Verification

Example 1

The soil temperature was simulated at depths of 5 and 10 cm and compared to the temperature measured for soil with a 7 cm thick layer of sand. The correlation coefficient, R, with mulching was 0.987 and 0.979, respectively (Fig. 2). The simulation accuracy was thus high, indicating that VADOSE/W could be reliably used to simulate the soil temperature. Sand mulching thickness is 7cm.

Example 2

The ground temperature of the cornfield was numerically simulated to verify the reliability of the software. The ground temperature at 08:00 on 25 April during the corn growing season was used as the simulated initial temperature, and the temperatures at 14:00 and 20:00 were used to compare the simulated and measured temperatures (Fig. 3). R between the simulated and measured temperatures for 14:00 and 20:00 was 0.9980 and 0.9906, respectively.

Model Application

The start and end of each stage of growth of the wheat (Zhou et al. 2016) are presented in Table 2

Temporal and spatial distributions of soil temperature during the growing season of spring wheat: The research object was a field in the experimental region, which was used to simulate and assess the temporal and spatial distributions of soil temperature. Sand mulching thickness is 15 cm. The simulated ground temperature at each depth at 7:00
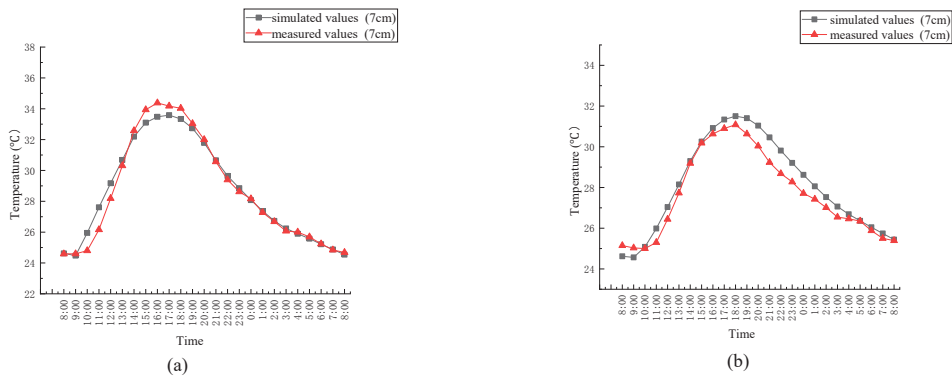
Fig. 2: Soil temperature at depths of 5 and 10 cm. (a) Soil temperature at 5 cm; (b) Soil temperature at 10 cm.
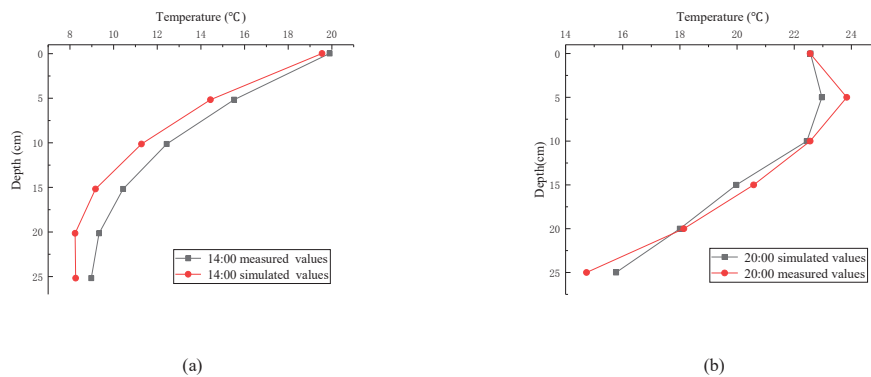
Fig. 3: Simulated and measured ground temperatures at each depth. (a) Simulated and measured ground temperatures at 14:00;(b) Simulated and measured ground temperatures at 20:00.

Table 2: Stages of growth of the spring wheat.

Growth period	Sow-emerge	Emerge-tiller	Tiller-jointing	Jointing-heading	Heading-maturity
Number of days/d	16	20	14	22	52
Date	03-24 to 04-09	04-09 to 04-28	04-28 to 05-12	05-12 to 06-03	06-03 to 07-25

during the growing season was higher with than without sand mulching (Fig. 4), and the temperature increased linearly with depth both with and without mulching. The simulated ground temperature at each depth at 14:00 during the growing season was lower with than without sand mulching, and the temperature decreased with depth both with and without mulching. Ground temperature and depth were not linearly correlated at 14:00, consistent with the results reported by Li et al. (2003). Determining the relationship between soil temperature and depth at 20:00 and 00:00 will require further study. The fitted functions of the simulated and measured temperatures at 7:00 and 14:00 are presented in Table 3. In each fitting equation, x represents temperature (°C) and y represents depth (cm).

Distribution of difference in soil temperature (∆T) over time during the growing season of spring wheat: The difference in temperature between sand mulching and bare ground at each depth of soil was used as the research object. The range of variation of the temperature difference during the growing season was in the order

0>5>10>15>20>25 cm, indicating that the thermal influence was stronger in shallower soil (Fig. 5). The range of the temperature difference was within ±3°C. The temperature difference at each depth in each stage was positive from 01:00 to 08:00. The temperature at each depth was higher with than without mulching, indicating that the sand mulch effectively preserved heat at night. The temperature difference during the daytime until 18:00 at each depth during the growing season was negative. The temperature during this period was lower with than without mulching, indicating that the sand mulch impeded the transfer of heat at mid-day. The temperature difference at each depth during the growing season tended to become positive by 22:00, indicating that evening was a transitional period of heat transfer.

Distribution of temperature gradient with time in different periods of spring wheat during the growing season: The temperature gradient represents the vertical change in temperature and thus the intensity of heat transfer in the vertical direction (Ao et al. 2015). The temperature gradient from 01:00 to 9:00 was positive both with and without
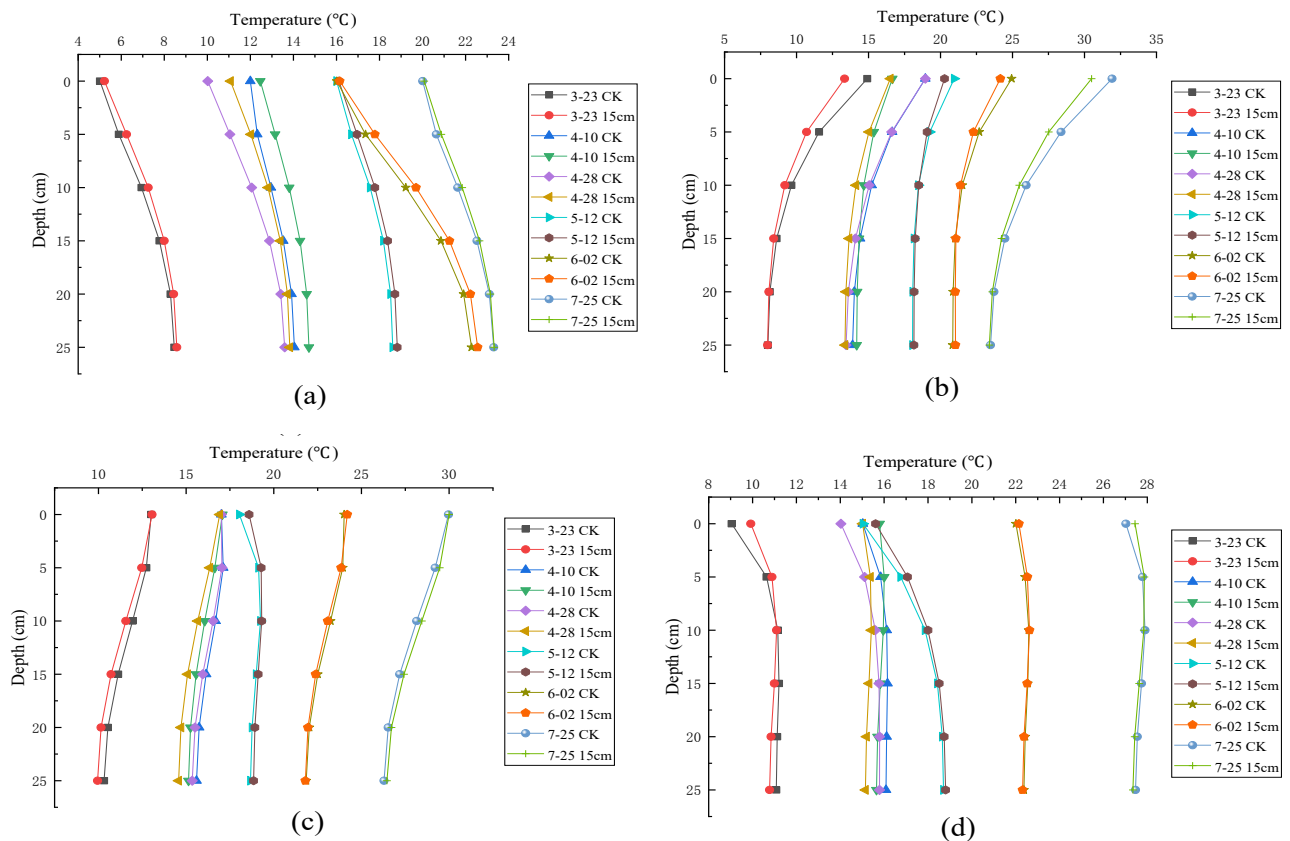
Fig. 4: Simulated ground temperatures at the various stages of growth of the spring wheat. (a) Ground Temperature at 07:00 during the growing season; (b) Ground temperature at 14:00 during the growing season; (c) Ground temperature at 20:00 during the growing season; (d) Ground temperature at 00:00 during the growing season.

Table 3: Fitting of the simulated temperature and depth during the growing season of the spring wheat.

Time	Growth period and coverage	Fitting equation	Decision coefficient （R2）	Time	Growth period and coverage	Fitting equation	Decision coefficient （R2）
7:00	3-23 CK	y = 6.598x - 34.097	R² = 0.9547	7:00	3-23 15cm	y = 6.8114x - 37.159	R² = 0.9388
	4-10 CK	y = 10.895x - 130.53	R² = 0.9705		4-10 15cm	y = 10.2x - 128.72	R² = 0.9422
	4-28 CK	y = 6.458x - 66.106	R² = 0.9521		4-28 15cm	y = 33.132x - 430.74	R² = 0.9030
	5-12 CK	y = 8.5895x - 138.64	R² = 0.9382		5-12 15cm	y = 8.3987x - 136.95	R² = 0.9327
	6-02 CK	y = 3.6291x - 58.642	R² = 0.9664		6-02 15cm	y = 3.5707x - 58.712	R² = 0.9570
	7-25 CK	y = 6.8357x - 136.99	R² = 0.9685		7-25 15cm	y = 7.0335x - 142.14	R² = 0.9596
14:00	3-23 CK	$y = 0.6358x^2 - 17.68x + 122.64$	R² = 0.9500	14:00	3-23 15cm	$y = 1.0814x^2 - 27.03x + 168.52$	R² = 0.9434
	4-10 CK	$y = 1.1037x^2 - 40.536x + 372.23$	R² = 0.9574		4-10 15cm	$y = 5.3214x^2 - 172.5x + 1397.4$	R² = 0.9322
	4-28 CK	$y = 0.8509x^2 - 31.543x + 292.62$	R² = 0.9646		4-28 15cm	$y = 0.7797x^2 - 30.362x + 295.78$	R² = 0.9627
	5-12 CK	$y = 4.4317x^2 - 179.81x + 1822.1$	R² = 0.8936		5-12 15cm	$y = 7.9327x^2 - 314.41x + 3114$	R² = 0.9065
	6-02 CK	$y = 2.027x^2 - 97.748x + 1177.4$	R² = 0.9030		6-02 15cm	$y = 3.6048x^2 - 169.05x + 1980.4$	R² = 0.8513
	7-25 CK	$y = 0.3574x^2 - 22.393x + 351.05$	R² = 0.9644		7-25 15cm	$y = 0.5058x^2 - 30.34x + 455.32$	R² = 0.9641

mulching, indicating that heat was transferred from deep soil to the surface during this period (Fig. 6). The changes in the temperature gradient became negative as the sun continued to rise, and deeper soil gained heat from the surface. The change in the gradient on May 12 was again positive at 20:00 and remained positive at 22:00 for the remainder of the growing season. The range of the variation in the temperature gradient was smaller with than without mulching, mainly because the sandstone effectively reduced the amount of solar radiation received by the surface, consistent with the results reported by Ao et al. (2015).

CONCLUSION

We used VADOSE/W to study the temporal and spatial distributions of soil temperature, the differences in temperature, and the temperature gradient of sand-mulched and bare soil.

(1) We established a model for the transfer of heat within the soil and between soil and the atmosphere using VADOSE/W. The correlation coefficients between the simulated and measured temperatures were >0.97, indicating that the accuracy of the simulation was high, verifying the reliability of the model.

(2) The temporal and spatial distributions of the soil temperature at 7:00 and 14:00 at the various stages of growth of the spring wheat for both mulched and bare soil had linear nonlinear relationships. The relationship between soil temperature and depth for 20:00 and 00:00 requires further study.

(3) The difference in soil temperature at each depth and the temperature gradient were positive from 01:00 to 08:00 at each stage of growth, and the heat was transferred from deep soil to the surface, indicating that sand mulching effectively preserved heat at night. The difference in soil temperature and the temperature gradient during the growing season became negative at all depths as the sun rose, with deeper soil gaining heat from the surface, indicating that sand mulch impeded the transfer of heat at mid-day. The difference in temperature at each depth and the temperature gradient tended to become positive by 22:00, and heat began to transfer from deep soil to the surface. The range of the temperature difference was within ±3°C, and the thermal influence was stronger in shallower soil.
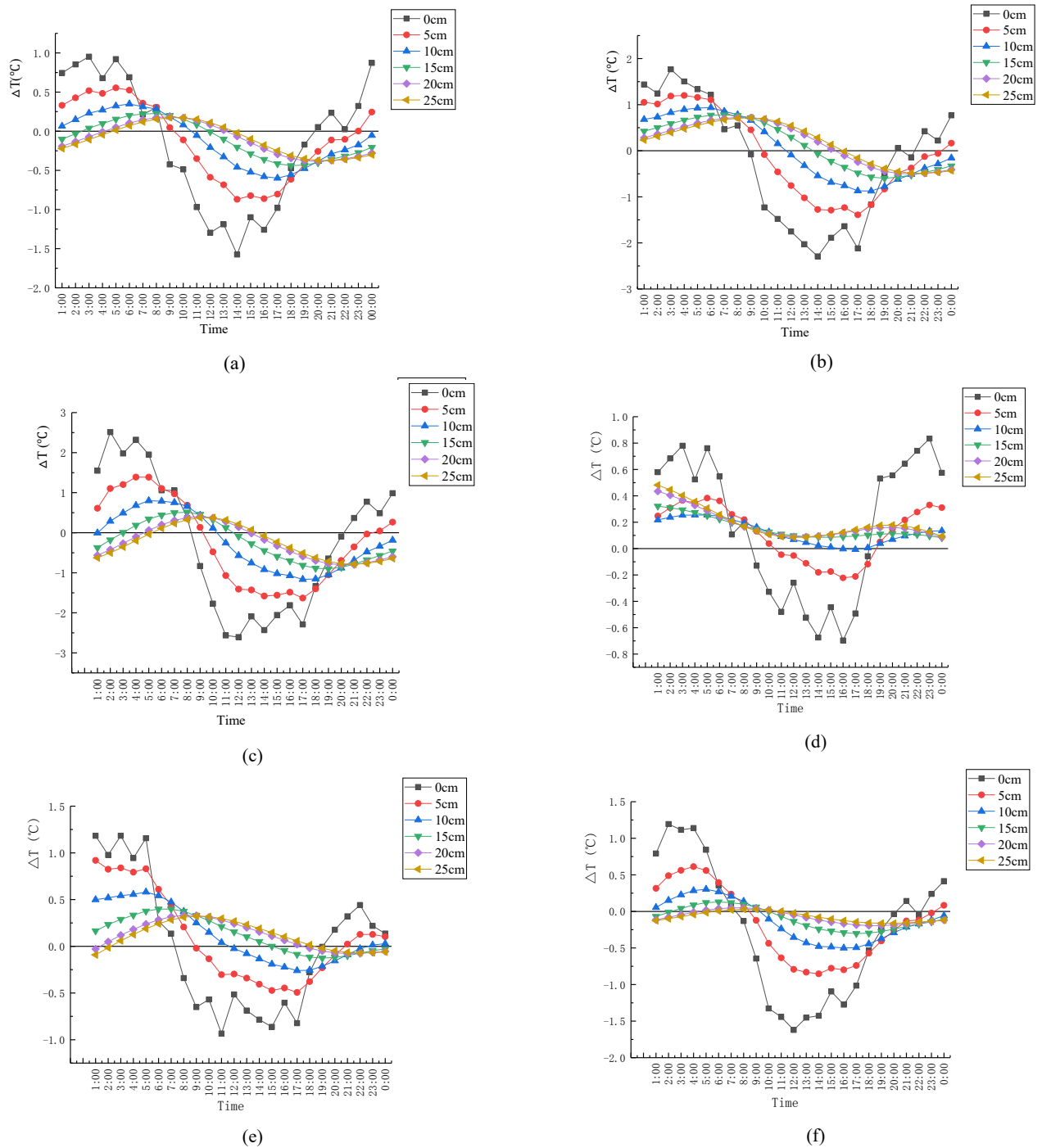
ACKNOWLEDGMENT

Fig. 5: Distribution of the differences in soil temperature (△T in the various stages of growth of the spring wheat. (a) Distribution of △T over time on 23 March; (b) Distribution of △T over time on 10 April; (c) Distribution of △T over time on 28 April;(d) Distribution of △T over time on 12 May; (e) Distribution of △T over time on 2 June;(f) Distribution of △T over time on 25 July.
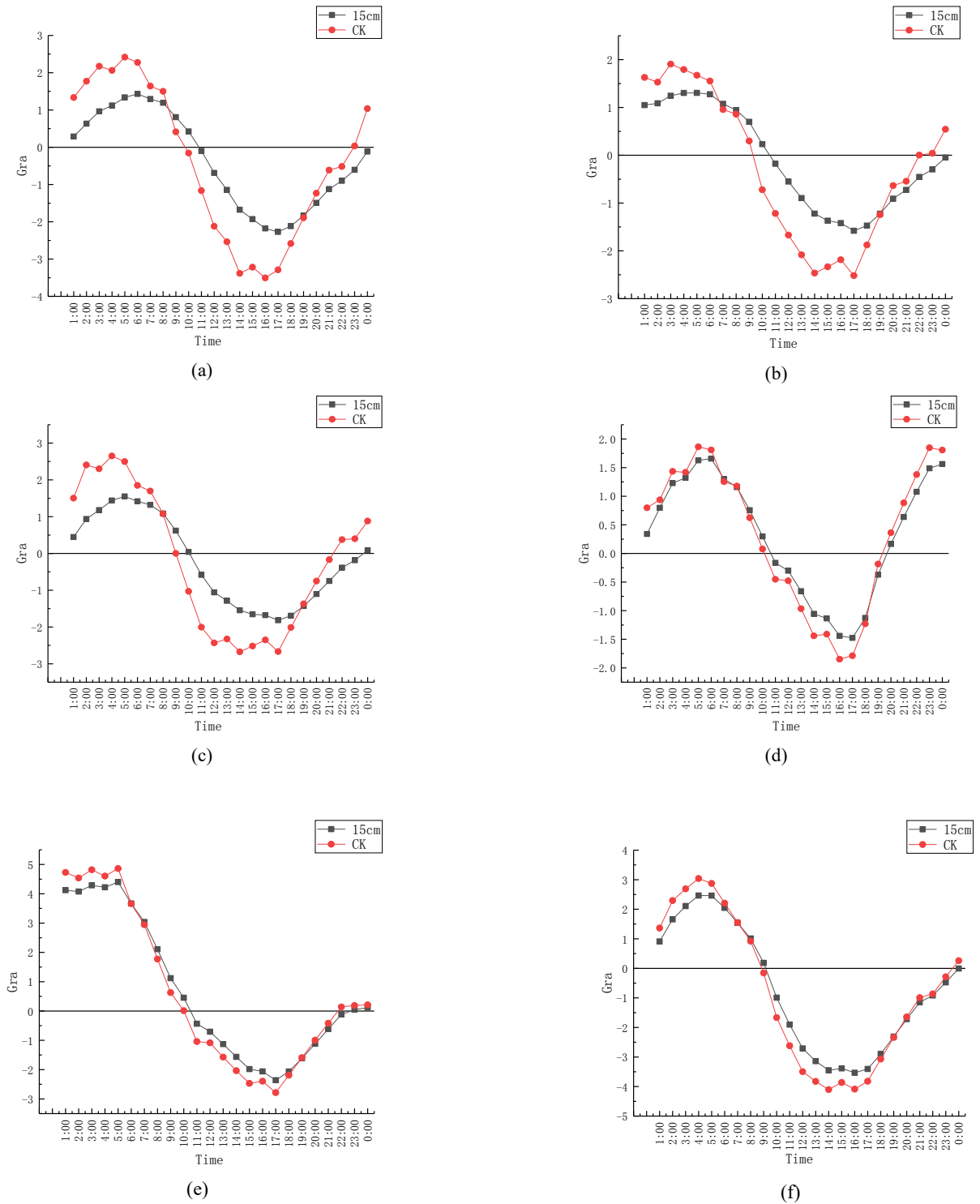
Fig. 6: Distribution of the temperature gradient (Gra) of the tilled layer during the growing season of the spring wheat. (a) Distribution of Gra over time on 23 March;(b) Distribution of Gra over time on 10 April; (c) Distribution of Gra over time on 28 April; (d) Distribution of Gra over time on 12 May; (e) Distribution of Gra over time on 2 June;(f) Distribution of Gra over time on 25 July.

REFERENCES

Ao, Y., Lyu, S., Han, B. and Li, Z. 2015. Comparative analysis of the soil thermal regimes of typical underlying surfaces of oasis systems in an Arid Region. Environ. Earth Sci., 73(12): 7889-7896.

Argunhan-Atalay, C. and Yazicigil, H. 2018. Modeling and performance assessment of alternative cover systems on a waste rock storage area. Mine Water Environ., 37(1): 106-118.

Bu, L., Liu, J., Zhu, L., Luo, S., Chen, X., Li, S., Hill, R.L. and Zhao, Y. 2013. The effects of mulching on maize growth, yield, and water use in a semi-arid region. Agric. Water Manage., 123: 71-78.

Buchner, J.S., Simunek, J., Lee, J., Rolston, D.E., Hopmans, J.W., King, A.P. and Six, J. 2008. Evaluation of CO2 fluxes from an agricultural field using a process-based numerical model. J. Hydrol., 361(1-2): 131-143.

Füllner, K., Temperton, V.M., Rascher, U., Jahnke, S., Rist, R., Schurr, U. and Kuhn, A.J. 2012. The vertical gradient in soil temperature stimulates the development and increases biomass accumulation in barley. Plant Cell Environ., 35(5): 884-892.

Hsieh, C.I., Huang, C.W. and Kiely, G. 2009 Long-term estimation of soil heat flux by single-layer soil temperature. Int. J. Biometeorol., 53(1): 113-123.

Lahti, M., Aphalo, P.J., Finér, L., Ryyppo, A., Lehto, T. and Mannerkoski, H. 2005. Effects of soil temperature on the shoot and root growth and nutrient uptake of 5-year-old Norway spruce seedlings. Tree Physiol., 25(1): 115-122.

Li, P., Li, T. and Vanapalli, S.K. 2016. Influence of environmental factors on the wetting front depth: A case study in the Loess Plateau. Eng. Geol., 214: 1-10.

Li, X. 2003. Gravel–sand mulch for soil and water conservation in the semiarid loess region of northwest China. Catena, 52(2): 105-127.

Li, X., Gong, J., Gao, Q. and Wei, X. 2000. Rainfall interception loss by pebble mulch in the semiarid region of China. J. Hydrol., 228(3-4): 165-17.

Li, Y., Shao, M., Wang, W. and Wang, Q. 2003. Temporal and spatial variation and forecast of soil temperature in maize fields. J. Hydraul. Eng., 34(1): 103-108.

Lü, H., Yu, Z., Horton, R., Zhu, Y., Zhang, J., Jia, Y. and Yang, C. 2011. Effect of gravel-sand mulch on soil water and temperature in the semiarid loess region of northwest China. J. Hydrol. Eng., 18(11): 1484-1494.

Lu, N. and Dong, Y. 2015. A closed-form equation for thermal conductivity of unsaturated soils at room temperature. J. Geotech. Geoenviron. Eng., 141(6): 1-12.

Ma, Y. and Li, X. 2011. Water accumulation in soil by gravel and sand mulches: Influence of textural composition and thickness of mulch layers. J.Arid Environ., 75(5): 432-437.

Matsushima, D., Kimura, R. and Shinoda, M. 2010. Soil moisture estimation using thermal inertia: Potential and sensitivity to data conditions. J. Hydrometeorol., 13(2): 638-648.

Nabi, G. and Mullins, C.E. 2008. Soil temperature-dependent growth of cotton seedlings before emergence. Pedosphere, 18(1): 54-59.

Sakai, M., Jones, S.B. and Tuller M. 2011. Numerical evaluation of sub-surface soil water evaporation derived from sensible heat balance. Water Resour. Res., 47(2): 1-17.

Timlin, D.J., Pachepsky, Y., Acock, B.A., Simunek, J., Flerchinger, G. and Whisler, F. 2002. Error analysis of soil temperature simulations using measured and estimated hourly weather data with 2DSOIL. Agric. Syst., 72(3): 215-239.

Votrubová, J., Dohnal, M., Vogel, T. and Tesa , M. 2012. On the parame-terization of heat conduction in coupled soil water and heat flow modeling. Soil Water Res., 7(4): 125-137.

Wilson, G.W. 1990 Soil Evaporative Fluxes for Geotechnical Engineering Problems. Ph.D. Thesis, University of Saskatchewan, Saskatoon, SK, Canada.

Xie, Z., Wang, Y., Cheng, G., Malhi, S.S., Vera, C.L., Guo, Z. and Zhang, Y. 2010. Particle-size effects on soil temperature, evaporation, water use efficiency, and watermelon yield in fields mulched with gravel and sand in semi-arid Loess Plateau of northwest China. Agric. Water Manage., 97(6): 917-923.

Yang, Z., Wang, X. and Ameen, M. 2019. Influence of the spacing of steam-injecting pipes on the energy consumption and soil temper-ature field for clay-loam disinfection. Energies, 12(17): 3209.

Zhao, W., Cui, Z., Zhang, J. and Jin, J. 2017a. Temporal stability and varia-bility of soil-water content in a gravel-mulched field in northwestern China. J. Hydrol., 552: 249-257.

Zhao, W., Ma, H., Fan, Y., Dou, P. and Yu, W. 2016. Study on the character-istics of water and salt transport in sandy loam soil under different mulching models. J. Soil Water Conserv., 03: 331-336.

Zhao, W., Yu, P., Ma, X., Sheng, J. and Zhou, C. 2017b. Numerical simula-tion of soil evaporation with sand mulching and inclusion. Water, 9(4): 294-303.

Zhou, S., Hu, X., Wang, W., Allan, A.A. and Zhang, Y. 2016. Optimization of irrigation schedule based on RZWQM model for spring wheat in Shiyang River Basin. Trans. Chin. Soc. Agric. Eng., 32(6): 121-129.

Quality and Yield of Rice Grain: Effects of Humic Acid and Bean Cake Fertilizers Under Water-Saving Conditions

Zheng Ennan*, Yinhao Zhu* and Tianyu Xu*†

*School of Hydraulic and Electric Power, Heilongjiang University, Harbin, 150080, China

†Corresponding author: Tianyu Xu: 1044459115@qq.com

ABSTRACT

Rice quality and yield traits response to fertilizers under varying field conditions were obtained in our previous study. A better understanding of the intrinsic mechanism of fertilization in regulating rice quality and yield supports field operations and recommendations. This study investigated the potential role of humic acid and bean cake fertilizers as opposed to traditional nitrogen fertilizer (urea) in regulating rice quality and yield traits under water-saving conditions by identifying the quality and yield indicators. Results demonstrated that the application of humic acid and bean cake fertilizers affected the quality and yield compared with the traditional nitrogen fertilizer (urea), which alleviated the deterioration of rice quality and yield caused by excessive fertilizer amounts. The conclusions are that the addition of humic acid and bean cake fertilizers can improve grain quality.

INTRODUCTION

Rice feeds 50 percent of the global population, and demand is projected to increase by 28 percent by 2050 (Bahuguna 2017). In addition, the demand for high-quality rice is increasing due to rising economic development (Tilman et al. 2011, Foley et al. 2011, Coast et al. 2015), especially in China, the country with the largest population in the world. Rice quality and yield traits are usually affected by many factors such as fertilizers, irrigation methods, planting densities, radiation use efficiency, and climatic conditions (Zhang et al. 2019, Zheng et al. 2018a, Lobell et al. 2012, Shi et al. 2016, Zhou & Sun 2019, Zhang 2019, Lan et al. 2019, Wang et al. 2019). However, fertilizer and water main factors affecting crop quality and yield traits, which have increased gradually because of the expansion of rice-planting areas in recent years (Zhou et al. 2006, Zhang et al. 2017). This has resulted in an abrupt increase in the agricultural water demand as well as an imbalance between supply and demand. Well-irrigated rice accounts for most of the paddy planting area and more than 70% of the regional agricultural water consumption (Fang et al. 2010, Wei et al. 2018). The intensity of fertilizer application in China increased by 36.45% from 2000 to 2015 (Xiao 2018), especially nitrogen fertilizer. Excessive fertilizer and water management not only waste agricultural water but also causes pollution of agricultural surface sources, which damages the ecological environment, and even reduces rice quality and yield traits (Zhang et al. 2017).

As a result, studying the impact of a novel type of fertilizer on rice yield and quality attributes under water-saving settings in Northeast China is critical. In China, new types of ecologically friendly organic fertilizers such as humic acid and bean cake fertilizers are widely employed in agricultural production. However, compare to traditional fertilizer (urea), the associated response relationships of rice quality and yield traits are unknown. In this study, we focused on these traits, under water-saving conditions, to investigate the effects of humic acid and bean cake fertilizers, with an overall goal of saving water and improving the quality and yield traits of rice.

MATERIALS AND METHODS

Experimental Site

The experiment was performed in 2018 at the National Key Irrigation Experimental Station located in Heping Town, Qing'an County, Suihua, Heilongjiang, China. The experimental site is located at 45°63'N and 125°44'E at an elevation of 450 m above sea level. This region consists of plain topography and has a semi-arid cold temperate continental monsoon climate, i.e., a typical cold region with a black glebe distribution area. The average annual temperature is 2.5°C, the average annual precipitation is 550 mm, and the average annual surface evaporation is 750 mm. The growth period of crops is 156-171d, and there is a frost-free period of approximately 128 days yr^{-1}. The soil at the study site is

albic paddy soil, with a mean bulk density of 1.01 g.cm^{-3} and a porosity of 61.8 %. The basic physicochemical properties of the soil are as follows: the mass ratio of organic matter is 41.8 g.kg^{-1}, pH value is 6.45, the total nitrogen mass ratio is 15.06 g.kg^{-1}, the total phosphorus mass ratio is 15.23 g.kg^{-1}, total potassium mass ratio is 20.11 g.kg^{-1}, the mass ratio of alkaline hydrolysis nitrogen is 198.29 mg.kg^{-1}, the available phosphorus mass ratio is 36.22 mg.kg^{-1} and the exchangeable potassium mass ratio is 112.06 mg.kg^{-1} (Zheng et al. 2018b).

Experimental Design

In this experiment, three fertilization treatments were applied: traditional nitrogen fertilizer which was CK treatment (urea + potassium fertilizer + phosphorus fertilizer), humic acid fertilizer (humic acid + potassium fertilizer + phosphorus fertilizer) and bean cake fertilizer (bean cake + potassium fertilizer + phosphorus fertilizer). Urea, humic acid, and bean cake fertilizers were applied according to the proportion of base fertilizer: tillering fertilizer: heading fertilizer (5:3:2). Phosphorus fertilizer was applied once as a basal application. Potassium fertilizer was applied twice: once as basal fertilizer and at the 8.5 leaf age (panicle primordium differentiation stage), at a 1:1 ratio.

The humic acid organic fertilizer was produced by Yunnan Kunming Grey Environmental Protection Engineering Co., Ltd, China. The organic matter≥61.4%, the total nutrients (nitrogen, phosphorus, and potassium) ≥18.23%, of which N≥3.63%, P$_2$O$_5$≥2.03%, K$_2$O≥12.57%. The moisture≤2.51%, the pH value was 5.7, the worm egg mortality rate≥95%, and the amount of fecal colibacillosis≤3%. The fertilizer contained numerous elements necessary for plants. The contents of harmful elements including arsenic, mercury, lead, cadmium, and chromium were≤2.8%, 0.01%, 7.6%, 0.1%, and 4.7%, respectively; these were much lower than the test standard.

The bean cake fertilizer was produced by Hebei New Century Zhou Tian Biotechnology Co., Ltd, China. The organic matter≥40%, the total nutrients (nitrogen, phosphorus, and potassium)≥8%, the number of active bacteria≥0.02 billion/g, the biochemical yellow humic acid≥6%, and the humic acid≥ 10%.

Water and Cultural Management

The plants were maintained under water-saving conditions, that was, at the re-greening stage, a water layer (0~30 mm) was maintained, but the soil was allowed to dry during the yellow ripeness stage; the water layer was not applied after the irrigation period. The upper limit of irrigation was taken as the saturated water content. At the early and middle tillering stages, jointing stage, heading stage, and milk-ripe stage, the lower limit of irrigation was 85% of the saturated water content. The soil moisture content was measured using a moisture content analyzer (TPIME-PICO64/32) every day (once at 07:00 and 18:00). When the soil moisture content was lower than or close to the lower limit of irrigation, it was necessary to irrigate to the upper limit.

The local broadly planted rice cultivar Suijing No.18 (Japonica rice) was used for the pot experiment. The plants were grown in plastic pots (40 cm in height, the upper diameter of the pot was 32 cm, the lower diameter of the pot was 28 cm) filled with 30 kg of soil. In the middle of April, rice was sown in the greenhouse; at the seedling stage, irrigation was needed every day. In 2018, on May 21, rice was transplanted from the greenhouse to the pots. Rice was harvested on September 20. The experiment was a randomized complete block design, with at least three replicates for each treatment.

Sampling and Measurements

Milling and appearance quality traits: rice grain samples harvested at physiological maturity were air-dried at room temperature before shelling and milling. The brown rice rate and milled rice rate were determined by the processing machinery SY88-TH & SY88-TRF (Wu xi Shang long Grain Equipment Co., Ltd., China), according to the national standard for rice quality evaluation GB/T17891/1999, the People's Republic of China. The grain size characteristics (length and width) of the brown rice were measured using digital vernier calipers (CD-15CP; Mitutoyo Corp., Kawasaki, Japan). Chalk characteristics of the brown rice were observed by using a rice grain appearance quality scanning machine (SC-E, Wanshen Technology Company, Hangzhou, China) according to the China National Standard GB/T 17897-1999 (She et al. 2019).

Nutritional quality traits: the protein and amylose contents were measured using a Near-infrared Grain Analyzer (VECTOR 22/N, Foss, BRUKER company, Germany).

Cooking quality traits: the cooking quality was measured by a Rice Taste Meter (STA1A, SATAKE company, Japan).

K^+ and Na^+ contents: Whole grain meal (100 mg) was incubated in 5 mL 95% (V/V) sulphuric acid for complete digestion using 30% H$_2$O$_2$ as a catalyst. The digestion solution was transferred into a 50 mL volumetric flask and diluted: ion contents were determined using a TAS986 atomic absorption spectrophotometer (Beijing Purkinje General Instrument Co., Ltd., China) (Xia et al. 2016).

Yield: rice yield was determined per pot, and the harvested paddy grain yield was adjusted to 14.5% grain moisture content. The number of spikes per pot, number of kernels per spike, 1000-kernel mass, and the grain-filling rate were measured by harvesting in each pot. The yield was calculat-

ed by multiplying the number of spikes per pot, number of kernels per spike, 1000-kernel mass, and grain-filling rate.

Statistical Analysis

For statistical analysis, data processing was completed using Microsoft Excel 2010 followed by analysis with SPSS 19 software. The statistical results are reported as the mean value and were confirmed with an LSD (least significant difference) test.

RESULTS

Yield and Yield Components

The bean cake and humic acid treatments did not affect the number of spikes per pot, the number of kernels per spike, or the 1000-kernel mass when compared to the urea treatment (Table 1). The grain yield, on the other hand, was increased. There were substantial changes in grain yield between the bean cake, humic acid, and urea treatments. When bean cake and humic acid fertilizers were used, grain yield increased by 5.2 percent and 4.8 percent, respectively. Since these four component parameters impacted the yield (Shao et al. 2019). Although the fertilizers had no effects on the component factors of yield, the yield that was multiplied by them was significantly different compared to urea.

Milling and Appearance Quality Traits

The effects of fertilizer application on rice milling and appearance quality traits are shown in Table 2 and Table 3 respectively. The results indicated that the application of humic acid fertilizer increased grain milled rice weight, milled rice rate, brown rice weight, and brown rice rate (Table 2), while there was no significant change in the grain length and width, the ratio of the grain shape was affected compared to the urea treatment (Table 3). The milling suitability of the grain mostly increased in response to the humic acid, as evidenced by the increased intact milled rice percentage. A higher intact milled rice value suggests fewer broken kernels are produced during the milling process (Wang & Frei 2011).

Compared with urea, the bean cake and humic acid treatments significantly affected rice chalky rate, chalky area, and chalkiness. The application of bean cake and humic acid under water-saving conditions reduced the chalky rate, chalky area, and chalkiness compared to the urea treatment. The lowest values of the chalk traits were obtained in the humic acid treatment. As the most important indicator of rice appearance quality, chalkiness is mainly caused by the inconsistent development of starch granules and protein bodies, resulting in loosely arranged voids and white opaque parts (She et al. 2019). In our study, application of the bean cake and humic

Table 1: Yield and yield component factors.

Treatments	Spikes per pot	Kernel per spike	1000-Kernel mass [g]	Grain filled rate	Grain yield [g.pot^{-1}]
Urea	73.33a	38.22a	48.23a	95.23%a	128.72b
Bean cake	75.00a	39.12a	49.06a	94.15%a	135.52a
Humic acid	74.33a	38.64a	49.25a	95.37%a	134.90a

Note: Different letters within columns significant difference at $P < 0.05$ according to the LSD test.

Table 2: Milling parameters.

Treatments	Kernel weight [g]	Brown rice weight [g]	Milled rice weight [g]	Brown rice rate [%]	Milled rice rate [%]	Intact Milled rice rate [%]	Broken kernel rate [%]
Urea	202.30a	146.50b	110.30b	72.42b	54.52b	25.11c	53.95a
Bean cake	199.00a	159.10a	110.74b	79.95a	55.65b	47.13b	15.30b
Humic acid	197.80a	160.40a	129.15a	81.09a	65.29a	59.68a	8.60c

Note: Different letter within columns significant difference at $P < 0.05$ according to the LSD test.

Table 3: Appearance parameters.

Treatments	Chalk rate [%]	Tarnishing kernel	Crack kernel	Kernel length [mm]	Kernel width [mm]	Length/Width	Chalk area [%]	Chalkiness[%]
Urea	8.85a	0.00a	11.15a	4.75a	2.50a	1.90a	7.7a	4.8a
Bean cake	1.40b	0.10a	1.70b	4.50a	2.80a	1.61b	1.2b	1.1b
Humic acid	0.25c	0.05a	0.60c	4.70a	2.70a	1.74b	0.4c	0.1c

Note: Different letters within columns significant difference at $P < 0.05$ according to the LSD test.

acid fertilizers may not be the cause of the inconsistent development of starch granules and protein bodies, and therefore, may not cause the incidence of chalkiness compared to urea. The decrease of appearance traits was mainly attributed to the occurrence of chalkiness. However, the responses of chalkiness to the application of fertilizers were not consistent across years (Zhao et al. 2017, Wang & Wu 2019), suggesting the complexity of quality formation induced by fertilizers.

Nutritional Quality and Ion Contents

The bean cake and humic acid fertilizers did not affect the K^+ and Na^+ contents in the grains, compared to urea (Fig.1-a). The K^+ contents in the urea, bean cake, and humic acid fertilizer treatments were 5.9 mg.g^{-1}, 6.2 mg/g, 6.3 mg/g, respectively. The corresponding Na^+ contents were 1.2 mg.g^{-1}, 1.3 mg.g^{-1}, 1.4 mg.g^{-1}, respectively. Fertilization did not cause an obvious imbalance between K^+ and Na^+ in the grain, i.e., the K^+/Na^+ ratio was similar among all the treatments. Bean cake and humic acid increased the K^+ and Na^+ contents; however, the effects of different fertilizers on the accumulation of K^+ and Na^+ contents in the grains

have not been sufficiently documented in the literature. In the present study, the difference in the contents among the different treatments was not significant.

The bean cake and humic acid fertilizers influenced the protein and amylose contents in the grains (Fig.1-b). The protein contents in the bean cake and humic acid treatments were 1.19 and 1.18 times that in the urea treatment, respectively. The amylose contents in the grain decreased in response to bean cake and humic acid treatments. Specifically, the amylose contents in the bean cake and humic acid treatments were 17.41% and 7.31% lower, respectively, than that in the urea treatment. Rice, one of the most important staple crops, provides essential minerals and nutrients for humans such as protein and amylose (Xia et al. 2016). The starch in rice grain accounts for about 90% of the brown rice weight. The process of rice grain filling is the process of starch accumulation. Starch synthesizes and accumulates from the inner to outer of rice endosperm, granule-bound starch synthase is mainly responsible for the biosynthesis of amylose, compared to urea, the bean cake, and humic acid with low expression of granule-bound starch synthase, leading to the

a)   b)
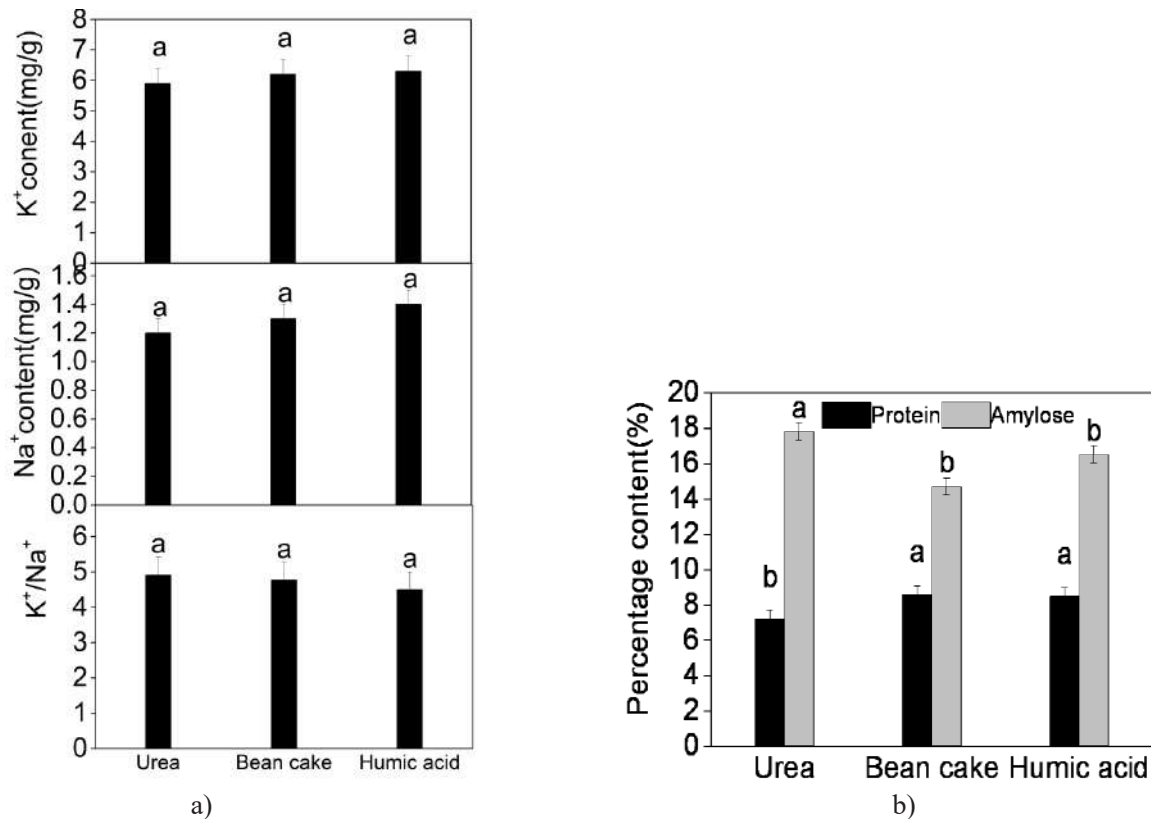
Fig. 1: The K^+ and Na^+, protein, and amylose content in the grain (Note: Different letters indicate significant differences at $P < 0.05$ according to the LSD test).

lower amylose content in the grain (Zhao et al. 2004). Protein contents in rice grain which are essential for human beings are affected by transamination in plants, the aminotransferase is mainly responsible for the biosynthesis of protein (Wang et al. 2015), application the bean cake and humic acid in the soil increased the content of aminotransferase at the heading stage, facilitating the formation of proteins. Therefore, the increase in the content of protein in response to bean cake and humic acid fertilizers in the present study indicated an improvement in the nutritional value of rice grains.

Cooking Quality Traits

Significant impacts of the different fertilizers were observed in terms of rice cooking quality traits of the test cultivar, except for the completeness and taste (Table 4). The bean cake and humic acid fertilizers significantly increased the aroma, burnish, and mouthfeel compared to the urea treatment. The greatest effect was for burnishing, of which the highest value was obtained in the bean cake treatment; it was significantly ($P < 0.05$) higher than that in the urea and humic acid fertilizers treatments. Overall, the bean cake and humic acid fertilizers increased the cooking quality traits. Chalkiness, protein, and amylose are the most important factors affecting the cooking quality traits; the cooking quality traits were negatively correlated with chalkiness and amylose and positively correlated with protein (Liu et al. 2019). In the present study, chalkiness and amylose were lower in the bean cake and humic acid treatments, and the protein was higher than that in the urea treatment (Table3 and Fig.1-b). Therefore, the comprehensive scores for the bean cake and humic acid treatments were better compared to the urea treatment.

Correlation Among the Quality Traits

The cooking quality traits were positively and significantly correlated with the protein contents in the grains; however, they were negatively correlated with the amylose (Table 5). An opposite situation was found for the appearance quality traits of chalk. A significant negative correlation between the brown rice rate and chalk was observed in the present study. However, the milled rice rate was not correlated with the appearance, nutritional content, or cooking quality traits except that a significantly positive relationship was found for the intact milled rice rate (R=0.83).

DISCUSSION

The quality and yield are affected by many factors such as climate conditions and management methods, especially the water and fertilizer. As an important source of grain in China, the rice should be fertilized 3-5 times in a growth cycle. However, in China, the nitrogen use efficiency is only about 30%. Most of the nitrogen fertilizer is lost in the environment through leakage, runoff, and volatilization, causing serious environmental pollution to soil, water, and atmosphere and influencing the growth of the crop. To implement the work of "zero growth of chemical fertilizer", the application of humic acid and bean cake fertilizers were used as a breakthrough to reduce the amount of chemical fertilizer used in rice and investigated its effects on the quality and yield. Yao et al. (2020) found that the rate of brown rice, milled rice, and head rice was significantly increased by applying slow and controlled release fertilizer, the chalkiness of conventional fertilization was significantly higher than those of other fertilization treatments and blank treatments. Combined with an organic fertilizer such as peanut bran, it can not only ensure rice yield, but also improve the crude protein of rice grain, and its rich nutrient elements such as amino acids are significantly improved (Li et al. 2019). Combined application of biochar and nitrogen fertilizer could significantly affect the processing quality of rice, such as milled rice rate, chalky grain rate, and grain length, and nutritional quality such as gel consistency, amylose, and protein content, but had no significant effect on brown rice rate and chalkiness, the optimal biochar (5 t·hm^{-2}) combined with nitrogen fertilizer (80%) had the best effect on soil microbial carbon and nitrogen, rice yield and quality (Shi et al. 2020). Jiang et al. (2019) thought that When the total amount of nitrogen decreased by 10%, the nutritional quality was improved. In our study, we found that application the of humic acid and bean cake could be improved the quality and yield of ac compared to the area. The grain yield increased by 5.2% and 4.8% when the respective bean cake and humic acid fertilizers were applied. Because the application of humic acid and bean cake changed the soil thermal nutrients, the supply of soil organic nutrients was sufficient and can change the soil bulk density, increase the gas exchange of roots, which is conducive to the growth of rice. The results indicated that the application of humic acid fertilizer increased grain milled rice weight, milled rice rate,

Table 4: Cooking parameters.

Treatments	Aroma	Burnish	Completeness	Taste	Mouthfeel	Comprehensive scores
Urea	7.10b	7.05c	7.26a	7.81a	7.08b	76.76b
Bean cake	7.48a	7.77a	7.12a	8.08a	7.55a	80.03a
Humic acid	7.46a	7.44b	7.33a	7.93a	7.32a	79.43a

Note: Different letters within columns significant difference at $P < 0.05$ according to the LSD test.

Table 5: Correlation among the quality traits.

	Brown rice rate [%]	Milled rice rate [%]	Intact Milled rice rate [%]	Chalk area [%]	Chalki-ness [%]	Protein [%]	Amylose [%]	Aroma	Burnish	Com-pleteness	Taste	mouth-feel	Compre-hensive
Brown rice rate (%)	1												
Milled rice rate (%)	0.68	1											
Intact Milled rice rate (%)	0.97**	0.83*	1										
Chalk area(%)	-0.99**	-0.66	-0.96**	1									
Chalki-ness(%)	-0.99**	-0.73	-0.68	0.99**	1								
Pro-tein(%)	0.98**	0.53	0.91**	-0.97**	-0.96**	1							
Amy-lose(%)	-0.74	0.001	-0.55	0.75	0.68	-0.85	1						
Aroma	0.98**	0.53	0.91**	-0.98**	-0.96**	0.99**	-0.85*	1					
Burnish	0.83*	0.14	0.66	-0.84*	-0.78	0.92**	-0.99**	0.91**	1				
Complete-ness	-0.07	0.69	0.17	0.09	0.0001	-0.25	0.73	-0.24	-0.62	1			
Taste	0.77	0.05	0.60	-0.78	-0.71	0.87*	-0.99**	0.87*	0.99**	-0.70	1		
Mouthfeel	0.80*	0.1	0.63	-0.81*	-0.75	0.90**	-0.99**	0.89*	0.99**	-0.65	0.99**	1	
Compre-hensive	0.95**	0.43	0.86*	-0.96**	-0.93**	0.99**	-0.90**	0.99**	0.95**	-0.36	0.92**	0.94**	1

Note: The * significant difference at $P < 0.05$ according to the LSD test; the ** significant difference at $P < 0.05$ according to the LSD test

brown rice weight, and brown rice rate as compared to the bean cake and urea, however, the appearance parameters were decreased significantly, and the lowest cooking parameters were obtained in the urea treatment. Because a lot of trace elements were contained in the humic acid, and bean cake also could lots of organic nutrients, when applying the humic acid and bean cake in the soil, It is helpful to improve the quality of rice as compared to the urea treatment. Therefore, compared with inorganic fertilizer, it is more environmental protection, less pollution to the environment, and rice, which is conducive to improving the utilization rate of resources. When improving soil conditions and cultivating fertile soil, the application of humic acid bean cake and other organic fertilizers plays an important role in the growth and development of rice, which could ensure the quality of rice and improve the yield of rice. Therefore, when planting rice, we should strengthen the research on organic fertilizer, and application with inorganic fertilizer reasonably to improve the utilization rate of organic fertilizer, promote the development of the rice planting industry, and maximize economic benefits.

CONCLUSION

In conclusion, the application of the bean cake and humic acid fertilizers increased the yield compared with traditional urea under water-saving conditions. However, the K^+ and Na^+ contents in the grain and the K^+/Na^+ ratio did not change between treatments. The application of bean cake and humic acid fertilizers enhanced the milled rice quality traits but decreased the appearance quality traits compared with the urea treatment. The best values of the milled quality traits were obtained in response to humic acid treatment, which had the lowest appearance quality traits. Higher protein content was measured in the bean cake and humic acid treatments than in the urea treatment, and the opposite situation was found with amylose; however, there was no significant difference between the bean cake and humic acid treatments.

ACKNOWLEDGMENT

REFERENCES

Bahuguna, R.N., Solis, C.A., Shi, W. and Jagadish, K.S.V. 2017. Post-flowering night respiration and altered sink activity account for high night temperature-induced grain yield and quality loss in rice (*Oryza sativa* L.). Physiol. Plant., 159: 59-73.

Coast, O., Ellis, R.H., Murdoch, A.J. and Quiñones, C.K.J. 2015. High night temperature induces contrasting responses for spikelet fertility, spikelet tissue temperature, flowering characteristics, and grain quality in rice. Funct. Plant Biol., 42: 149-161.

Fang, F.P., Xu, C.C. and Li, F.G. 2010. Analysis of the current situation of rice production and market in Northeast China. China Rice, 16(1): 44-47.

Foley, J.A., Ramankutty, N., Brauman, K.A., Cassidy, E.S., Gerber, J.S., Johnston, M., Mueller, N.D., O'Connell, C.R., Deepak, K., West, P.C., Balzer, C.B., Elena, M., Carpenter, S.R., Hill, J.C., Month, D.T. and David, P.M. 2011. Solutions for a cultivated planet. Nature, 478: 337-342.

Jiang, H.F., Guo, X.H., Hu, Y., Li, M., Lv, Y.D., Xu, S.L., Xu, L.Q. and Wang, J.Y. 2019. Effects of nitrogen fertilization managements on rice quality under soda-saline-alkali soil. Southwest China J. Agric. Sci., 23(06): 1223-1229.

Lan, Y.C., Guo, X.H., Zhang, Q.M., Jiang, H.F., Hu, Y., Wang, H.Y., Zhao, Y.B., Zhang, G.M. and Lv, Y.D. 2019. Effects of directly sowing rice seeds in the dried paddy field on its grain quality in a cold land. Barely Cereal Sci., 36(01): 15-19.

Li, C.Y., Deng, G.D. and Xie, G.T. 2019. Effects of peanut bran application on rice quality and yield. Agric. Sci., 39(15): 404.

Liu, Q.H., Ma, H., Sun, Z.W., Xu, J.D., Li, G.X., Li, J.L. and Yuan, S.J. 2019. Effects of mechanical transplanting densities on eating and nutritional qualities of rice with different seedling ages. Shandong Agric. Sci., 51(01): 65-68.

Lobell, D.B., Sibley, A. and Ivan Ortiz-Monasterio, J. 2012. Extreme heat effects on wheat senescence in India. Nat. Clim. Chang., 2: 186-189.

She, T., Hai, X.Z., Wen, Z.L., Zhi, D., Qin, Y.Z.,Wen, Z.C., Shao, H.W. and Yan, F.D. 2019. Nitrogen fertilizer at the heading stage effectively compensates for the deterioration of rice quality by affecting the starch-related properties under elevated temperatures. Food Chem., 277: 455-462.

Shao, C.G., Pan, X.B., Li, J.W., Wei, P., Zhang, X.T., Hu, Q. and Ren, J. H. 2019. Effects of flooding duration in different growth stages on growth and yield component of rice. Trans. Chinese Soc. Agric. Eng., 35(3): 125-133.

Shi, D.L., Wang, X.L., Liu, A.K ., Hou, Z .F. and Liang, G.T. 2020. Response of microbial biomass carbon and nitrogen and rice quality in the yellow soil paddy field to biochar combined with nitrogen fertilizer. Environ. Sci., 6(11): 71-93.

Shi, W.,Yin, X., Struik, P.C., Xie,F., Schmidt, R.C. and Jagadish, K.S.V. 2016. Grain yield and quality responses of tropical hybrid rice to high night-time temperature. F. Crop. Res., 190: 18-25.

Tilman, D., Balzer, C., Hill, J. and Befort, B.L. 2011. Global food demand and the sustainable intensification of agriculture. Proc. Natl. Acad. Sci., 108: 20260-20264.

Wang, P. and Wu, Y.Y. 2019. Effects of biomass fertilizer on yield and quality of rice in Dandong area. China Rice, 25(02): 86-88.

Wang, S., Zhao, H.W., Yao, C., Liu, H.L., Zhao, Z.D., Lei, W.J. and Zou D.T. 2015. Effect of N fertilizer application and transplanting density on grain transaminase activity and protein content in japonica rice in the cold region. Soil Fert. Sci. China, 02: 71.

Wang, Y. and Frei, M. 2011. Stressed food the impact of abiotic environmental stresses on crop quality. Agric. Ecosyst. Environ., 141: 271-286.

Wang, Y.Y., Liu, S.C., Yang, J., Tang, L.Z., Tu, N.M. and Yi, Z.X. 2019. Research advances on the effects of organic fertilizer on yield, quality of rice, and soil characteristics. China Rice, 25(01): 15-20.

Wei, Y.G., Ru, C., Wu, Y., Liu, H., Yang, J. M. and Hou, J.X. 2018. Response of growth physiological characteristic and yield of rice to water consumption process in black soil region.Trans. Chinese Soc. Agric. Mach., 49(09): 214-225.

Xia, X.Z., Zhi, Q.S., You, J.T., Qin, Z., Jian, C., Ting, B.D., Wei, X.C., Han, C.P. and Dong, J. 2016. Salt stress increases the content and size of glutenin macro polymers in wheat grain. Food Chem., 197: 516-521.

Xiao, Y. 2018. Reduction and efficiency of chemical fertilizer under the background of agricultural green development in China: An empirical study of Henan province. Chinese Acad. Agric. Sci., 41: 56-86.

Yao, J.B., Shi, C.M. and Tao, B.R. 2020. Effects of different formulations of slow and controlled release fertilizers on growth and quality of rice with good taste. Agric. Equip. Technol., 46(03): 28-30.

Zhang, Y. 2019. Study on yield and quality optimization of different population structures of rice in the cold region. Friends Rich, (08): 150.

Zhang, Z.X., Feng, Z.J., Qi, Z.J., Zheng, E.N., Yang H. and Chen, P. 2019. Effects of compound microbial organic fertilizer with water-saving irrigation on photosynthetic and yield of rice. Trans. Chinese Soc. Agric. Mach., 50(07): 278-298.

Zhang, Z.X., Zheng, E.N., Wang, C.M. and Yun, N.H. 2017. Effect of different water and nitrogen levels on chlorophyll fluorescence parameters and photosynthetic characteristics of rice. Trans. Chinese Soc. Agric. Mach., 48(6): 176-183.

Zhao, B.H., Zhang, W.J., Cheng, E.H., Wang, Z.Q. and Yang, J.C. 2004. Changes and activities of the key enzymes related to starch synthesis in rice grains during grain filling and their relationships with the filling rate and cooking qualities. Sci. Agric. Sin., 37(08): 1123-1129.

Zhao, T.T., Jiang, Y.W., Chen X., Zhong, W.J., Zhang, L.W., Liu, X.S., Zheng, G.P. and Pan, S.J. 2017. Effect of reduced fertilizer application and combined application on the quality of rice in Jiansanjiang. J. Heilongjiang Bayi Agric. Univ., 29(04): 1-4+48.

Zheng, E.N., Yang H., Chen P. and Zhang, Z.X. 2018a. Effects of carbon-nitrogen absorption, soil respiration, and yield of rice under water and fertilizer management modes. Trans. Chinese Soc. Agric. Mach., 49(06): 287-295.

Zheng, E.N., Zhang, Z.X., and Yang, H. 2018b. Influence of different nitrogen forms application on rice photosynthesis: fluorescence with water-saving irrigation in black soil region of Songnen Plain, Northeast China. Paddy Water Environ., 16(04): 795-804.

Zhou, M. and Sun, J. Y. 2019. Combined effects of low temperature and weak light at the grain-filling stage on rice grain quality. Acta Agronom. Sin., 6:1-14.

Zhou, M.Y., Zhao, R.L. and Gu, Y.F. 2006. Effects of water and nitrogen coupling on growth and physiological characteristics of overground part of rice. Trans. Chinese Soc. Agric. Eng., 22(8): 38-43.

Original Research Paper

Open Access Journal

Interpretive Structural Modelling (ISM) of Enablers Affecting Green Accounting in Indian Manufacturing Sector: A Conceptual Model

Anjali Singh, Archana Singh† and Biju G. Pillai

Balaji Institute of International Business, Affiliated to Sri Balaji University, Pune, Maharashtra, India

†Corresponding author: Archana Singh; Archana.singh@biibpune.edu.in

ABSTRACT

Green accounting is vital for every economy in the world. Indian manufacturing sectors are regarded as one of the most significant contributors to environmental and socioeconomic problems, and as a result, the country lacks global sustainability and progress. This paper focuses on how these industries can contribute to the sustainability of the environment. The paper aims to analyze how these industries can promote ecopreneurial behavior. Also, the researchers and expert opinions lead to a theoretical framework and conceptual model using a well-defined and explained literature review and the derived model to understand, observe, and analyze various environment awareness concerns. To gather the expert opinions, various calls and surveys were scheduled with chartered accountants, academicians, environmental experts, commerce people, to understand how the identified variables are influenced by each other. Environmental management accounting and green accounting came out as the most significant and vital factors. All the identified variables were complementing. Three levels came out for the model. The authors created an ISM on factors affecting green accounting in the Indian manufacturing sector, emphasizing the context and concept related to the discovered variables that have been tested in the real world.

INTRODUCTION

The purpose of this research is to determine the significance of environmental accounting and sustainability in the Indian manufacturing industry. The core objective of this paper is to tell how important is, environmental accounting and taking initiatives for Environment Protection in this dynamic world. There has been a drastic change in the past two decades i.e., moving from a rather mysterious venture to one that has been tested in a number of nations and is well established in a few others (Hecht 1999). The term accounting is expected to give information to the users about the performances and financial position of an organization and in all the scenarios, environmental accounting is one of those tools which informs the managers about the different environmental costs and how they can quantify them (Todea & Stanciu 2010). According to Şenol & Özçelik (2012), environmental accounting has grown in importance and awareness as a result of the rise in environmental challenges related to economic, social, and technical development. Environmental accounting is essential for long-term growth. Globally, there is a rapid rise in public knowledge of sustainability, which is increasing (Lamberton 2005). There is a wide range of scientific research that has been applied to sustainable accounting.

The primary objective will be to determine the impact of environmental accounting as it relates to Indian financial reporting systems and standards, as well as whether Indian manufacturing industries are taking these reporting requirements seriously to achieve long-term development (Brown et al. 2010). Also, to understand how the Companies Act of 2013 and other similar legislation encourage and promote environmental consciousness, which will contribute to a rise in overall economic growth. This will close the gap on a variety of environmental challenges and move us closer to long-term growth.

As per Baumol et al. (1988), organizations with a higher and good history of performance along with environmental initiatives have less chance of bankruptcy. Even when they are in financial distress, they are more likely to overcome it. Finally, if we see on a larger picture, it is said that if the proper practice of environmental accounting is done, then it will ensure sustainable development and it must focus on environmental audit, environmental taxes, costs, and appreciation of the ecosystem services as all these things ensure sustainable development.

The purpose of this study paper is to learn more about how the environmentally conscious manufacturing business handles compliance and awareness. The research project's problem is to correlate latent variables to analyze industries that are accountable for environmental effect and environmental reporting, with a focus on Indian manufacturing industries.

PAST STUDIES

Environmental Reporting

Clarkson et al. (2011) stated that Indian manufacturing industries' environmental reporting has risen dramatically in recent years. The increase has occurred voluntarily, because of the compulsion of environmental disclosures. It was mentioned by Thakur (1997) that, the Constitutional 42nd Amendment Act came into force in 1976 and it contained Articles 48-a and 51-a, which made sure that every state and the citizens must protect and improve the environment and safeguard its wildlife sanctuary (Mickwitz 2003). This is how environmental policies were implemented, and as a result, the Government of India established a committee with a chairman who advocated various actions and steps to protect the environment. New policies to safeguard the environment are becoming more appealing, and there has been a rapid diffusion of informative voluntary and market-based tools on a global scale. Recent comparative studies state that there has been arising change in the development of environmental protection across the globe (Tews et al. 2003)

Green Accounting

In general, environmental/green accounting covers all the information and content adhering to the various stages of the domain and it is inclusive of linked expenditures, aids, and facts about its supportable operations (Irish Times 2000)

As per Yakhou & Dorweiler (2003), industries are contemplated to follow green accounting to give reassurance to the customers about the responsibilities being taken seriously, complying with financial reporting systems and the national guidelines, and disclose the company's environmental concerns and letting the stakeholders know about them.

According to Beredugo & Mefor (2012), there is a link between financial and environmental variables, which was established by quantifying all of an entity's work and activities in terms of its economic and environmental performance. As a result, by reducing environmental consequences and publicizing them, environmental managers boosted the value

of their industry. Environmental accounting, which connects environmental and financial performance, can be used to predict future environmental consequences on industry financial performance, allowing for more informed investment decisions.

In India, environmental accounting is still in its infancy, and what is recorded in the books relates to the observance of various Acts' norms and regulations. It is nearly difficult for India's financial industry and accounting to thrive unless the general public is made aware of environmental safety (Qureshi et al. 2012)

Environmental Management Accounting

According to Jasch (2003), the major goal of environmental management accounting (EMA) is to provide a comprehensive assessment of all environmental expenditures on treatment, disposal, and management, and because it is new, it poses a significant challenge for most manufacturing industries. In recent years, everyone has been focused on the growth of an expansive EMA framework, which primarily covered internal and external users of green accounting data (Burritt & Saka 2006).

EMA focuses on internal costs, and it includes the physical units for the overall consumption and disposal of energy and material, and the benefits costs and savings, which arise from environmental-related activities (Xiaomei 2004). Burritt et al. (2002) stated that EMA helps organizations to face various environmental responsibilities and leads to the identification and knowledge of combined environmental and economic benefits from different activities.

Environmental Financial Accounting (EFA)

The concept of environmental financial accounting is all about financial reporting where the industries report about their exposure management the impacts resulting from climate change (Grafl 2021). EFA points out the liabilities' costs of environment and other added costs, and it also gives the allied information about finance to the outside stakeholders (Xiaomei 2004). All the societal and global impacts that are material to the company are reflected by financial markets. EFA is partially governed by accounting standards issues by various bodies (Moisescu & Mihai 2006). Recent years'

Table 1: List of identified variables.

V1	Environmental Reporting (Legal environment framework, Environmental Disclosures)
V2	Green accounting (Global Environmental Accounting, Green Accounting Audit)
V3	Environmental Management accounting (Environmental Decision-making & Reporting)
V4	Environmental Financial accounting (Financial Reporting)
V5	Sustainability (Corporate Social Responsibility, Sustainability Accounting System)

Table 2: SSIM matrix.

i j	V5	V4	V3	V2	V1
V1	X	A	X	A	
V2	V	X	X		
V3	A	X			
V4	V				
V5					

studies state that a generous amount of attention was given to the impact of different forms of financial participation on the financial performance of industries (McNabb & Whitfield 1998). Adoption of IFRS (Indian Financial Reporting Systems) is necessary as it affects the financial performance and especially, gives an impact on the rate of return (Hameedi et al. 2021)

Sustainability

Empirical research into social and environmental management and reporting began in the early 1970s, and by the 1980s, the research had been mainstreamed around the societal performance of industries and on a theoretical platform of how to define and measure the various social and environmental performances, CSR or any kind of corporate citizenship, and other elements that are now referred to as sustainable management (Schaltegger & Wagner 2006)

CSR stands for "Corporate Social Responsibility," and it refers to activities in which a company or organization is aware of how its operations and activities affect social, economic, environmental, and governance concerns, as well as all the steps it takes to disclose those concerns. "Sustainability" is one of the methods used by any company or organisation to publicly announce their CSR activities and various initiatives. In this fast-paced climate, businesses take such initiatives seriously and aren't just concerned with short-term earnings (Hughen et al. 2014)

Biondi and Bracci (2018) stated that sustainability reporting is dominated by the private sector. Also, some of the observers consider it as one of the main forms of reporting in the business reporting system. Sekerez (2017) said that reporting

on sustainability is one of the most effective means of accomplishing sustainable development goals, and it is also known to demonstrate better accountability to stakeholders and the implementation of a sustainable business model (Fijałkowska et al. 2018)

MATERIALS AND METHODS

Interpretive structural modeling (ISM) was used to derive this model on factors affecting green accounting for the Indian manufacturing sector. The steps followed to derive this model was classified into 3 stages -

1. The first stage is about the identification of variables through the literature review.

2. The second stage is about these identified variables validated through a survey from thirty experts (Chartered Accountants, Company Secretaries, commerce specialists, faculty members teaching subjects related to the environment were also contacted).

3. In the third stage, the steps for ISM were followed to perform the repetitive process for level partitioning and the derivation of the model.

RESULTS AND DISCUSSION

ISM-Research Method

Interpretive structural modeling provides the individuals or a batch of individuals to have connections between more than two variables at one point in time, without any compromise or deviation from the original characteristics of the variables. ISM is an interpretive tool as it is a list of judgments and interpretations of the individuals on whether and how variables are related. It was invented by John N. Warfield.

Table 3: Reachability matrix.

i j	V1	V2	V3	V4	V5
V1	1	0	1	0	1
V2	1	1	1	1	1
V3	1	1	1	1	0
V4	1	1	1	1	1
V5	1	0	1	0	1

Table 4: Level partitioning (Level 1).

i j	Reachability Set (RS)	Antecedent Set (AS)	RS ∩ AS	Level
V1	(1,2,3,5)	(1,2,3,4,5)	(1,2,3,5)	
V2	(1,2,3,4,5)	(2,3,4)	(2,3,4)	LEVEL 1
V3	(1,2,3,4)	(1,2,3,4,5)	(1,2,3,4)	LEVEL 1
V4	(1,2,3,4,5)	(2,3,4)	(2,3,4)	
V5	(1,3,5)	(1,2,4,5)	(1,5)	

Table 5: Level partitioning matrix (Level 2 & 3).

i j	Reachability Set (RS)	Antecedent Set (AS)	RS ∩ AS	Level
V1	(1,5)	(1,5)	(1,5)	LEVEL 2
V4	(1,4,5)	(4)	(4)	LEVEL 3
V5	(1,5)	(1,4,5)	(1,5)	LEVEL 2

Table 6: Level matrix.

Level	Variable
1	Environmental Management Accounting
1	Green accounting
2	Sustainability
2	Environmental Reporting
3	Environmental Financial Accounting

ISM has the following dimensions-

1. To understand, it is structural, according to professional judgment, because of relationships and linkages. It also provides a graphical representation of iterations.

2. It is a learning process that is much interactive and consists of elements that are somehow related and thus, combined in a model.

3. It is a well-articulated methodology that identifies relationship amongst variables that leads to an issue or a problem.

In the next step, the development of a structural self-interaction matrix (SSIM) is done as per the sets of variables. The reachability matrix is then calculated, and the amount of transitivity is confirmed, before moving on to level partitioning. After data has been derived and drawn, an ISM model is created.

SSIM (Structural Self Interaction Matrix)

The SSIM is a basis of various interpretations of experts who have contributed a lot in this field. The experts for this study were Chartered Accountants, Company Secretaries, commerce specialists. Faculty members teaching subjects related to the environment were also contacted. The above experts were requested to compare each variable against the other. As per their comparisons, all these variables were assigned the values of V, A, X, and O. The connoting symbols of this table are 'i' and 'j' which establishes the relationship between variables.

Following are the rules from which the SSIM table was derived.

1) V is when i is related to j, but vice-versa is not the same.
2) A is given- j is related to i but vice-versa is not the same.
3) X is given- i & j complement each other.
4) O is given- no relation between i and j.

Reachability Matrix

The assigned values of SSIM will now be converted into binary numbers 0 and 1.

[V- 'i' to 'j'= 1 and 'j' to 'i'= 0,

A- 'i' to 'j'= 0 and 'j' to 'i'= 1,

X- 'i' to 'j'= 1 and 'j' to 'i'= 1,

O- 'i' to 'j'= 0 and 'j' to 'i'= 0]

Level Partitioning

Two sets come from the reachability matrix i.e., Reachability Set (RS) and Antecedent Set (AS). A series of repetitive steps were performed to identify various levels. Horizontal is reachability set and vertical is antecedent.

Level Matrix

The relationship between the five variables has been identified and categorized into 3 levels and their directions are represented by arrows.
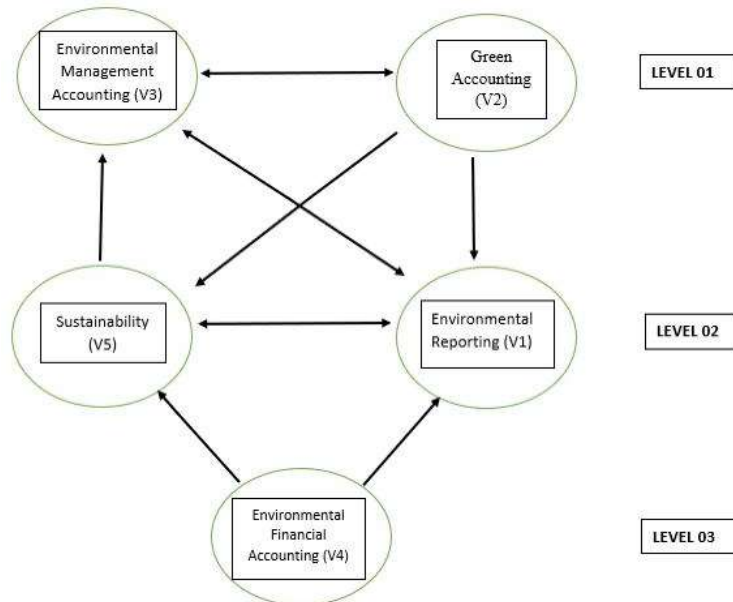
Fig. 1: ISM Model on factors affecting green accounting for Indian manufacturing industries (Authors' contribution).

LIMITATIONS AND FURTHER RESEARCH DIRECTIONS

This study's findings are based on the opinions of numerous experts and not on a large sample of data. Therefore, the model can be further empirically validated and tested by using advanced statistical tools and techniques. Also, expert opinions can be supported with some technical data for future research.

CONCLUSION

There is a strong link between green accounting and environmental management accounting. Also, sustainability and environmental reporting are very important aspects for each other as they provide information related to natural resources and the well-being of the economy as well as the costs incurred because of environmental degradation. As these two (V1 and V5) complement each other, financial accounting plays an important role in fostering sustainability and environmental reporting. This research was centered on the identification and modeling of a conceptual framework in relation to green accounting issues affecting Indian manufacturing industries. All the identified variables turned out to be important and necessary. The model and conceptual framework described in this research can be used to construct numerous methods for sustainability and environmental protection that are both effective and practicable. One of the problems is that there are no established standards for evaluating environmental aspects.

REFERENCES

Baumol, W.J., Baumol, W.J., Oates, W.E., Bawa, V.S., Baumol, W.J., Bawa, W.S. and Bradford, D.F. 1988. The Theory of Environmental Policy. Cambridge University Press, Cambridge. http://dx.doi.org/10.18775/ijmsba.1849-5664-5419.2014.41.1001

Beredugo, S.B. and Mefor, I.P. 2012. The impact of environmental accounting and reporting on sustainable development in Nigeria. Res. J. Fin. Account., 3(7): 55-63.

Biondi, L. and Bracci, E. 2018. Sustainability, popular and integrated reporting in the public sector: A fad and fashion perspective. Sustainability, 10(9): 3112.

Brown, P., McNaughton, R.B. and Bell, J. 2010. Marketing externalities in industrial clusters: A literature review and evidence from the Christchurch, New Zealand electronics cluster. J. Int. Entrepreneurship, 8(2): 168-181.

Burritt, R.L. and Saka, C. 2006. Environmental management accounting applications and eco-efficiency: case studies from Japan. J. Cleaner Prod., 14(14): 1262-1275.

Burritt, R.L., Hahn, T. and Schaltegger, S. 2002. Towards a comprehensive framework for environmental management accounting: Links between business actors and environmental management accounting tools. Aust. Account. Rev., 12(27): 39-50.

Clarkson, P.M., Overell, M.B. and Chapple, L. 2011. Environmental reporting and its relation to corporate environmental performance. Abacus, 47(1): 27-60.

Fijałkowska, J., Zyznarska-Dworczak, B. and Garsztka, P. 2018. Corporate social-environmental performance versus financial performance of banks in Central and Eastern European countries. Sustainability, 10(3): 772.

Grafl, A. 2021. Environmental Financial Accounting in the Public Sector: A Stocktaking of Current Initiatives. Working Paper No. 1, ZHAW Center for Public Financial Management, Winterthur, New Zealand, pp. 1-19.

Gromark, J. and Melin, F. 2011. The underlying dimensions of brand orientation and its impact on financial performance. J. Brand Manag., 18(6): 394-410.

Hameedi, K.S., Al-Fatlawi, Q.A., Ali, M.N. and Almagtome, A.H. 2021. Financial performance reporting, IFRS implementation, and accounting information: Evidence from the Iraqi banking sector. J. Asian Fin. Econ. Bus., 8(3): 1083-1094.

Hecht, J.E. 1999. Environmental accounting. Where we are now, where we are heading. Resources, 135: 14-17.

Hughen, L., Lulseged, A. and Upton, D. R. 2014. Improving stakeholder value through sustainability and integrated reporting. CPA J., 84(3): 57.

Irish Times, 2000. Environmental accounting and social responsibility and its impact on annual reporting. 7th edition. Business

Jasch, C. 2003. The use of environmental management accounting (EMA) for identifying environmental costs. J. Cleaner Prod., 11(6): 667-676.

Lamberton, G. 2005. Sustainability accounting: A brief history and conceptual framework. Account. Forum, 29: 7-26.

McNabb, R. and Whitfield, K. 1998. The impact of financial participation and employee involvement on financial performance. Scot. J. Political Econ., 45(2): 171-

Mickwitz, P. 2003. A framework for evaluating environmental policy instruments: Context and key concepts. Evaluation, 9(4): 415-436.

Moisescu, F. and Mihai, O. 2006. Environmental Financial Accounting. Economics and Applied Informatics, "Dunarea de Jos" University of Galati, Faculty of Economics and Business Administration, pp. 79-84

Qureshi, N.Z., Kulshrestha, D. and Tiwari, S.B. 2012. Environmental accounting and reporting: An essential component of business strategy. Asian J. Res. Bank. Fin., 2(4): 85-95.

Schaltegger, S. and Wagner, M. 2006. Managing Sustainability Performance Measurement and Reporting in an Integrated Manner: Sustainability Accounting is the Link between the Sustainability Balanced Scorecard and Sustainability Reporting. In Schaltegger, S., Wagner, M. and Burritt, R.L. (eds.), Sustainability Accounting and Reporting, Springer, Dordrecht, pp. 681-697.

Sekerez, V. 2017. Environmental accounting as a cornerstone of corporate sustainability reporting. Int. J. Manag. Sci. Bus Adm., 4(1): 7-14.

Şenol, H. and Özçelik, H. 2012. The Importance of Environmental Accounting in the Context of Sustainable Development and within IFRS Evaluation. In 3rd International Symposium on Sustainable Development Conference, 31 May - 1 June 2012, Sarajevo, Bosnia, and Herzegovina, Springer International Publishing, New York, pp. 81-89.

Tews, K., Busch, P.O. and Jörgens, H. 2003. The diffusion of new environmental policy instruments. Europ. J. Political Res., 42(4): 569-600.

Thakur, K. 1997. Environmental Protection Law and Policy in India. Deep and Deep Publications, Delhi, India.

Todea, N. and Stanciu, I.C. 2010. Environmental accounting: A tool used by the entity for determining environmental costs. Ann. Univ. Apulensis-Series Oecon., 12(1): 19.

Xiaomei, L. 2004. Theory and practice of environmental management accounting. Int. J. Technol. Manag. Sustain. Develop., 3(1): 47-57.

Yakhou M. and Dorweiler V.P. 2003. Environmental accounting: An essential component of the business. Bus. Strategy Environ., 13(2): 65-77.

Assessment of Growth Promoting Ability of Three Cyanobacterial Isolates Under Sewage Water Irrigation

Lalita Rana† and Rajesh Dhankhar

Department of Environmental Science, Maharshi Dayanand University, Rohtak-124001 Haryana, India
†Corresponding author: Lalita Rana; lalita.777@gmail.com

ABSTRACT

Heavy metal pollution from the increased use of sewage effluent for irrigation is posing a hazard to agricultural ecosystems. Thus, a reliable and simple method of reducing the impact of heavy metals on plant growth is required. In the present study, cyanobacterial species were isolated from the sewage water irrigated soil of Rohtak city, Haryana, India, and characterized by various biochemical parameters. The cyanobacterial filtrates were then used to analyze their effects on the growth performance of rice seedlings under various concentrations of sewage wastewater. The results revealed a statistically significant increase in biomass, photosynthetic pigments, nitrate reductase activity, plumule, and radical length of rice seedlings by application of cyanobacterial filtrates. The antioxidant system (peroxidase enzyme and catalase enzyme activity) was also found to be stimulated. As compared to introduced species, the extracts of isolated species had a more favorable, statistically significant effect on rice seedlings. Our study indicated that these isolates have a high tolerance against heavy metals and are potentially useful as biofertilizers for the crops in sewage water irrigated agroecosystems.

INTRODUCTION

In India, sewage wastewater is being extensively used for irrigation purposes. Increasing urbanization and industrial activities contribute to the increase in heavy metals in sewage wastewater which affects both agricultural and aquatic ecosystems (Mohod & Dhote 2013). The sewage water irrigation negatively affects the plant's cellular and physiological processes resulting in the reduced growth of the plant. The general toxicity of heavy metals, as well as their inhibition of water intake, has an impact on seed germination (Kranner & Colville 2011). However, at lower concentrations, some of the constituents of sewage water are beneficial to plant growth.

The accumulation of heavy metals in the soil necessitates the development of cost-effective, simple-to-use techniques for the bioremediation of sewage-irrigated soil. The native microbes are suitable candidates to be used for soil bioremediation as they can change their morphology and physiology after coming in contact with various toxicants and heavy metals. These changes may indicate their tolerance towards heavy metals. Among the various microbes, cyanobacteria are known to have protective mechanisms against different types of stresses. Their abundance, growth, and biomass reflect the characteristics of the specific habitat in which they live and can be linked to environmental impacts. The photosynthetic behavior of cyanobacterial species shows the presence of heavy metals. When used for bioremediation, cyanobacteria promoted the establishment of microbial population, increased organic matter, and also soil stability (Alvarez et al. 2021). They fix atmospheric nitrogen and produce growth-promoting substances, vitamins, auxins, amino acids, and sugars (Suresh et al. 2019) which are helpful in plant growth. Stabilization of disturbed ecosystems like sewage irrigated soil is dependent upon the successful establishment of the most effective cyanobacterial community.

In this study, comparative effects of selected, isolated strains of cyanobacteria were examined on various growth parameters, nitrate reductase activity, and antioxidant system responses in rice seedlings under different concentrations of sewage water, using Petri-culture experiments

MATERIALS AND METHODS

Isolation and Culture of Cyanobacterial Species

Cyanobacterial species were isolated from sewage water irrigated soil (sandy loam) of Rohtak city, Haryana, India, by agar plate spreading and serial dilution techniques (Andersen & Kawachi 2005) using BG-11 medium (Stanier et al. 1971) and were identified as *Oscillatoria* sp*., Lyngbya* sp*.,* and *Phormidium* sp*.* with the help of keys given by Desikachary (1959). Purified cyanobacterial strains were maintained at 28 ± 3°C and illuminated under a 16:8 hr light-dark cycle

using cool fluorescent tubes. The introduced cyanobacterial species were obtained from the Centre for Conservation of Blue-Green Algae, I.A.R.I. New Delhi

The chlorophyll content in cyanobacteria was estimated by the standard methods of Mckinney (1941) and carotenoid pigments by Jensen (1970). Phyco-biliproteins were estimated by the cold extraction method by Siegelman & Kycia (1978). Total proteins were estimated by the method of Herbert et al. (1971). Total carbohydrates were estimated by the anthrone reagent method (Spiro 1966).

The 15-day old cultures of both isolated and introduced species of *Oscillatoria, Lyngbya*, and *Phormidium* were taken and centrifuged at 10000 rpm for 20 minutes. The supernatant was collected and concentrated to 10% of its original volume.

Petriculture Experiments

The twenty surface-sterilized rice seeds (variety P-1121) in each Petri plate were kept at 32°C temperature inside the BOD incubator and moistened with 10 mL of sewage wastewater regularly. The concentrations of the sewage wastewater used were 25%, 50%, 75%, and 100%. After three days, 5 mL of concentrated supernatants of both native and introduced species of *Oscillatoria, Lyngbya,* and *Phormidium* were added to the germinating rice seedlings and incubated for a further period of five days. The rice seedlings without cyanobacterial amendments were used for comparison purposes. The growth parameters of rice seedlings were measured on the ninth day.

Photosynthetic pigments estimation was done following the formula given by Gupta (2000). The biomass of rice seedlings was calculated according to the procedure of Allen et al. (1974). For catalase estimation, the decomposition of H_2O_2 was measured by recording the decline in absorbance at 240 nm for 3 min. following the method of Aebi (1984). Peroxidase was assayed as described by Pundir et al. (1999). Nitrate reductase activity was assayed by following the method of Srivastava (1975). All experiments were performed in triplicates.

The data obtained were subjected to mean and standard deviation. Analysis of variance tests was used to evaluate the differences among the various treatments.

RESULTS AND DISCUSSION

The preliminary study showed that the presence of heavy metals (Cu, Zn, Ni, Cd) affects the chlorophyll content and protein synthesis in isolated cyanobacterial species in the order Ni>Cu>Zn>Cd (Dhankhar & Rana 2016). Generally, all heavy metals slow down the growth performance of cyanobacterial species. Table 1 shows the decreased concentrations of protein, chlorophyll, and phycobilin pigment content in cyanobacteria isolated from sewage water irrigated soil as compared with the corresponding values in the introduced cyanobacterial species. The reduction in protein and pigment synthesis is caused by the long exposure to toxicants and heavy metals present in sewage water irrigated soil. The amount of secondary metabolites products i.e. sugars were found to be increased under stress conditions (Hana et al. 2008). Among the isolated species, *Oscillatoria* sp. has the highest chlorophyll content followed by *Lyngbya* sp. and *Phormidium* sp. The maximum contents of phycobiliproteins (Phycocyanin, allophycocyanin, and phycoerythrin

Table 1: Biochemical constituents of isolated strains of cyanobacteria from sewage irrigated soil.

Biochemical constituents	Isolated *Oscillatoria* sp.	Introduced *Oscillatoria* sp.	Isolated *Lyngbya* sp.	Introduced *Lyngbya* sp.	Isolated *Phormidium* sp.	Introduced *Phormidium* sp.
Protein	2.75	4.15	1.8	4.8	4.1	4.62
Sugars	2.96	2.4	3.05	2.34	3.02	2.13
Chl.	1.42	1.58	0.928	1.23	1.07	1.39
Chl.a	0.125	0.0973	0.0887	0.135	0.072	0.079
Phycocyanin	1.6	1.06	0.88	1.26	1.82	1.07
Phycocyanin	0.114	1	1.04	1.31	1.19	1.35
Phycoerythrin	4.78	6.29	4.59	8.09	8.79	12.19

Table 2: Effect of cyanobacterial extracts of native and introduced cyanobacterial species on shoot length of rice seedlings under various sewage water concentrations.

Sewage water conc.	Isolated *Lyngbya* sp.	Isolated *Oscillatoria* sp.	Isolated *Phormidium* sp.	Introduced *Lyngbya* sp.	Introduced *Oscillatoria* sp.	Introduced *Phormidium* sp.	Control
25	5.1+0.650	3.83+0.080	3.82+0.875	4.84+0.40	2.37+0.802	2.46+0.645	3.67+0.33
50	6.95+0.57	4.76+0.780	5.37+0.615	6.12+0.51	2.85+0.600	3.38+1.20	5.02+0.377
75	3.92+0.45	4.17+0.665	3.85+0.597	4.04+0.20	2.17+0.270	1.87+1.03	3.8+0.581
100	1.82+0.62	3.28+0.786	2.92+0.790	3.67+0.56	1.72+0.875	1.78+0.575	2.9+0.270

Table 3: Effect of cyanobacterial extracts of native and introduced cyanobacterial species on root length of rice seedlings under various sewage water concentrations.

Sewage water conc.	Isolated Lyngbya sp.	Isolated Oscillatoria sp.	Isolated Phormidium sp.	Introduced Lyngbya sp.	Introduced Oscillatoria sp.	Introduced Phormidium sp.	Control
25	4.84±0.142	4.18±0.185	3.4±0.148	2.75±0.55	0.75±0.218	1.58±0.156	3.41±0.285
50	6.12±0.062	4.2±0.638	4.2±0.236	6.2±0.451	2.02±0.715	3.12±2.04	3.1±0.596
75	4.04±0.601	5.15±0.795	2.55±0.530	3.52±0.65	4±0.332	3.02±0.610	2.2±0.730
100	3.67±0.775	3.06±0.517	3.02±0.625	2.26±0.89	2.1±1.50	2.46±0.465	2±0.497

Table 4: Effect of cyanobacterial extracts of native and introduced cyanobacterial species on the biomass of rice seedlings under various sewage water concentrations.

Sewage water conc.	Isolated Lyngbya sp.	Isolated Oscillatoria sp.	Isolated Phormidium sp.	Introduced Lyngbya sp.	Introduced Oscillatoria sp.	Introduced Phormidium sp.	Control
25	26.0±0.44	32.2±0.975	20.56±0.262	13.2±0.68	16.21±0.555	19.1±0.652	28.7±0.551
50	29.6±0.45	33.87±0.366	21.31±0.32	16.7±0.60	18.84±0.565	22.3±0.71	29.6±0.147
75	24.2±0.327	20.91±0.59	18.44±0.459	12±0.521	17.68±0.446	16.9±0.621	24.7±0.489
100	20.6±0.803	18.67±0.305	16.85±0.852	11.6±0.24	13.84±0.838	14.3±0.587	22.8±0.753

Table 5: Effect of cyanobacterial extracts of native and introduced cyanobacterial species on total chlorophyll content of rice seedlings under various sewage water concentrations.

Sewage water conc.	Isolated Lyngbya sp.	Isolated Oscillatoria sp.	Isolated Phormidium sp.	Introduced Lyngbya sp.	Introduced Oscillatoria sp.	Introduced Phormidium sp.	Control
25	1.79±0.015	1.85±0.011	1.83±0.007	1.66±0.04	1±0.125	0.57±0.037	1.8±0.011
50	2.141±0.05	2±0.0642	2.409±0.02	1.54±0.04	1.59±0.024	0.861±0.003	1.418±0.015
75	1.67±0.02	2.28±0.072	2.1±0.141	1.3±0.03	0.873±0.004	0.775±0.005	1.12±0.045
100	0.817±0.009	1.76±0.02	1.527±0.032	1±0.077	0.734±0.006	0.762±0.022	0.792±0.023

are protein complexes from the phycobiliprotein family) were found in *Phormidium* sp. The variations observed in pigment content of the isolated species may be caused by environmental and genetic factors (Ismaiel et al. 2014).

The exogenous cyanobacterial treatments alleviated the inhibitions caused by sewage wastewater on the plumule and radical length of rice seedlings, as is evident from Tables 2 and 3. All the culture filtrates cause a significant increase ($p \leq 0.05$) in the seedling growth under various sewage water concentrations. This might be due to the production of active compounds like hormones and vitamins from cyanobacteria, that inhibit the growth of pathogenic bacteria and fungi and increase plant growth (Grzesik & Duda 2014, Mohan & Kumar 2015, Suresh et al. 2019). The biomass content also showed a statistical increase (Table 4) in all the treatments. The increase in root length and biomass of rice by cyanobacterial treatments was also reported (Zhou et al. 2020). The extracts of native cyanobacteria had a more positive effect on the growth of rice seedlings at fifty percent sewage water concentrations than introduced cyanobacterial exudates. Further marked reductions were observed with higher concentrations of sewage water. This may be due to the suppression of growth by a high amount of toxic ions and total dissolved solids and heavy metals in the sewage wastewater (Li et al. 2007).

The chlorophyll and carotenoid content had statistically significant values ($p < 0.05$) as native cyanobacterial inoculation showed positive effects under low sewage water concentrations (Tables 5 and 6). The increased carotenoid content may be attributed to the plant defense strategy to overcome the heavy metal stress, as these are non-enzymatic antioxidants. There was an increase of 30 to 56.7%, 7.2 to 26.6%, 14.2 to 47.8% in chlorophyll content of rice seedlings supplemented with the filtrate of the native *Oscillatoria* sp., *Lyngbya* sp., and *Phormidium* sp. respectively. The increase in chlorophyll content in rice seedlings upon cyanobacterial inoculation was also reported (Khushwaha & Banerjee 2015, Padhy et al. 2016). In contrast to the increase, a reduction in photosynthetic pigments was observed at a hundred percent concentration of sewage wastewater. It could be due to the presence of the high amount of heavy metals and salts which potentiates a retarding effect by interference with structural

Table 6: Effect of cyanobacterial extracts of native and introduced cyanobacterial species on carotenoid content of rice seedlings under various sewage water concentrations.

Sewage water conc.	Isolated Lyngbya sp.	Isolated Oscillatoria sp.	Isolated Phormidium sp.	Introduced Lyngbya sp.	Introduced Oscillatoria sp.	Introduced Phormidium sp.	Control
25	0.14±0.006	0.168±0.002	0.176±0.003	0.19±0.006	0.212±0.006	0.204±0.005	0.204±0.001
50	0.184±0.004	0.232±0.005	0.352±0.009	0.284±0.009	0.368±0.003	0.184±0.004	0.14±0.0076
75	0.152±0.004	0.128±0.008	0.32±0.068	0.264±0.004	0.272±0.005	0.164±0.009	0.128±0.004
100	0.128±0.005	0.112±0.009	0.248±0.007	0.112±0.012	0.224±0.005	0.156±0.005	0.112±0.004

Table 7: Effect of cyanobacterial extracts of native and introduced cyanobacterial species on peroxidase activity (H_2O_2 decomposed per minute/gram fresh weight) of rice seedlings under various sewage water concentrations.

Sewage water conc.	Isolated Lyngbya sp.	Isolated Oscillatoria sp.	Isolated Phormidium sp.	Introduced Lyngbya sp.	Introduced Oscillatoria sp.	Introduced Phormidium sp.	Control
25	5.9±0.023	5.15±0.193	5.83±0.015	5.9±0.040	5.83±0.025	5.6±0.0152	6.82±0.06
50	5.9±0.069	6.2±0.076	6±0.095	6.4±0.037	6.4±0.1	6.17±0.0435	7.2±0.034
75	13.2±0.17	11.81±0.04	6.88±0.028	17±0.115	13.5±0.36	6.8±0.07	7.7±0.05
100	14.4±0.4	17.4±0.368	9.38±0.158	17.8±0.3	17.6±0.463	9.6±0.30	8.1±0.20

Table 8: Effect of cyanobacterial extracts of native and introduced cyanobacterial species on catalase activity (H_2O_2) decomposed per minute/gram fresh weight) of rice seedlings under various sewage water concentrations.

Sewage water conc.	Isolated Lyngbya sp.	Isolated Oscillatoria sp.	Isolated Phormidium sp.	Introduced Lyngbya sp.	Introduced Oscillatoria sp.	Introduced Phormidium sp.	Control
25	315±0.0	630.4±0.0	157.6±0.0	367.73±0.	630.4±0.0	694.1±0.0	367.73±0.0
50	472.8±0.0	655.7±0.0	420.2±0.0	525.3±0.0	741.6±0.0	753.6±0.0	472.79±0.0
75	577.8±0.0	712.6±0.0	515.7±0.0	630.3±0.0	795±0.0	786.4±0.0	735.46±0.0
100	877±0.0	772.8±0.0	888.2±0.0	893±0.0	840±0.0	815.8±0.0	840.5±0.0

Table 9: Effect of cyanobacterial extracts of native and introduced cyanobacterial species on nitrate reductase activity(Micro mol. NO per gram fresh wt./hour) of rice seedlings under various sewage water concentrations.

Sewage water conc.	Isolated Lyngbya sp.	Isolated Oscillatoria sp.	Isolated Phormidium sp.	Introduced Lyngbya sp.	Introduced Oscillatoria sp.	Introduced Phormidium sp.	Control
25	5.33±0.152	6.16±0.057	7.3±0.1	4.63±0.60	6.3±0.035	6.39±0.026	5.19±0.035
50	5.79±0.175	11.33±0.115	5.5±0.0814	7.54±0.12	10.16±0.144	7.25±0.09	5.5±0.0450
75	4.9±0.173	6.79±0.0458	4.3±0.0737	6.2±0.055	8.14±0.045	6.21±0.070	4.28±0.051
100	4.84±0.07	6.76±0.041	4.0±0.332	5.41±0.08	7.45±0.0360	6.48±0.416	3.99±0.345

components of chloroplast (Thind & Malik 1988). As a result of the application of cyanobacterial extracts, the level of chlorophyll pigment in rice seedlings irrigated with up to 50% concentration of sewage wastewater was observed to be restored.

It can be seen from Tables 7 and 8 that the enzymatic (catalase and peroxidase) activities of rice seedlings significantly (p<0.05) increased in all the treatments. The increased levels suggest the activation of oxidative stress defense mechanisms which may be an adaptive response of rice seedlings against sewage water stress. The application of cyanobacteria extracts might have resulted in an increased antioxidant defense

system for rice seedlings. This is supported by the previous findings (Essa et al. 2015, Hanaa et al. 2008).

The extracts of native and introduced cyanobacterial species significantly increased (p<0.05) the nitrate reductase activity (Table 9) at various studied sewage water concentrations except at a hundred percent sewage water concentrations. Raghuram & Sopory (1995) suggested that nitrate reductase activity depends upon active photosynthesis and requires photosynthetically generated reductant (NADH) and energy. Hence reduction in nitrate reductase activity could be due to reduced chlorophyll biosynthesis at high sewage water concentrations, thus, supplying lower levels

of photosynthates. Analysis of variance indicated significant differences in growth and enzyme activity among various cyanobacterial treatments and sewage water concentrations studied.

CONCLUSION

All the studied cyanobacterial isolates revealed a potent ability to alleviate the damage caused by the sewage wastewater on rice seedlings. The fifty percent sewage water concentration with cyanobacterial extracts proved to be the best optimal combination for rice seed germination.

REFERENCES

Aebi, H. 1984. Catalase in vitro. Methods Enzymol., 105: 121-126.

Allen, S.E., Grimshaw, H.M., Parkinson J.A. and Quarmby, C. 1974. Chemical Analysis of Ecological Materials. Blackwell Scientific Publication, Oxford.

Alvarez, L.A., Weyers, S.L., Goemann, H.M., Peyton, B.M. and Gardener, R.D. 2021. Microalgae, soil, and plants: A critical review of microalgae as renewable resources for agriculture. Algal Res., 54: 102200.

Andersen, R.A. and Kawachi, M. 2005. Traditional microalgae isolation techniques. In Andersen, R. A. (ed.), Algal Culturing Techniques. Elsevier Academic Press, Tokyo, pp. 83-100.

Desikachary, T.V. 1959. Cyanophyta. Indian Council of Agricultural Research, New Delhi, India.

Dhankhar, R. and Rana, L. 2016. Growth and biochemical constituents of an indigenous cyanobacterium affected by heavy metal stress. Environ. Conserv. J., 17(3): 37-43.

Essa, A.M.M., Ibrahim, W.L., Mahmud, R.M. and ElKassim, N.A. 2015. The potential impact of cyanobacterial exudates on seed germination and antioxidant enzymes of crop plant seedlings. Int. J. Curr. Microy biol. App. Sci., 4(6): 1010-1024.

Grzesik, M. and Duda, Z.R. 2014. Improvements in germination, growth, and metabolic activity of corn seedlings by grain conditioning and root application with cyanobacteria and microalga. Pol. J. Environ. Stud., 23(4): 1147-1153.

Gupta, P.K. 2000. Methods in Environmental Analysis – Water Soil and Air. Agrobios, Jodhpur, India.

Hanaa, H., Bakyl, A.E., Hussein, M.M. and El-Baroty, G.S. 2008. Algal extracts improve antioxidant defense abilities and salt tolerance of wheat plants irrigated with seawater. Afr. J. Biochem. Res., 2(7): 151-164.

Herbert, D., Phipps, P.J. and Strange, R.E. 1971. Chemical analysis of microbial cells. In: J.R. Noris and D.W. Ribbons (eds), Methods in Microbiology. Academic Press, NewYork, pp. 209-344.

Ismaiel, M.M.S., El-Ayouty, Y. and Piercey-Normore, M.D. 2014. Antioxidants characterization in selected cyanobacteria. Annals Microbiol., 64(3): 1223-1230.

Jensen, A. 1970. Chlorophylls and Carotenoids in Phycological Methods. In J.A. Hellebust and J.S. Craige (eds), Handbook of Phycological Methods. Physiological & Biochemical Methods. Cambridge University Press, Cambridge, pp. 59-70.

Khushwaha, M. and Banerjee, M. A. 2015. A novel method of seed germination and growth of three staple crop plants: Effect of low temperature and cyanobacterial culture addition. J Algal. Biomass Utln., 6(1): 26-32.

Kranner, I. and Colville, L. 2011. Metals and seeds: Biochemical and molecular implications and their significance for seed germination. Environ. Exper. Botany, 72(1): 93-105.

Li, C., Feng, S.L., Shao, Y., Jiang, L.N., Lu, X.Y. and Hou, X.L. 2007. Effects of arsenic on seed germination and physiological activities of wheat seedlings. J. Environ. Sci., 19(6): 725-732.

Mckinney, G. 1941. Absorption of light by chlorophyll solution. J. Biol. Chem., 140: 315-322.

Mohan, A.B. and Kumar, D.N. 2015. Cyanobacterial Consortium in the Improvement of Maize Crop. Int. J. Curr. Microbiol. App. Sci., 4(3): 264-274.

Mohod, C. and Dhote, J. 2013. Review of heavy metals in drinking water and their effect on human health. Int. J. Innov. Res. Sci. Eng. Technol., 2(7):2992-2996.

Padhy, R.N., Nayak, N.K., Dashmohini, R.R., Shakti Rath and Sahu, R.K. 2016. Growth Metabolism and Yield of Rice Cultivated in Soils Amended with Fly Ash and Cyanobacteria and Metal Loads in Plant Parts. Rice Science, 23(1):22-32.

Pundir, C.S., Malik, V., Bhargava, A.K., Thakur, M., Kalia, V., Singh, S. and Kuchhal, N.K.. 1999. Studies on horseradish peroxidase immobilized onto arylamine and alkylamine glass. J. Plant Biochem. Biotech., 8: 123-126.

Raghuram, N. and Sopory, S.K. 1995. Evidence for some common signal transduction events for opposite regulation of nitrate reductase and phytochrome-I gene expression by light. Plant Mol. Biol., 29: 25-35.

Siegelman, H.W. and Kycia, J.H. 1978. Algal biliproteins. In: J.A. Hellebust and J.S. Craige (eds), Hand book of Phycological Methods-Physiological and Biochemical Methods. Cambridge University Press, Cambridge, pp. 72-79.

Spiro, R.G. 1966. Analysis of sugars found in glycoproteins. Methods Enzymol., 8: 3-26.

Srivastava, H.S. 1975. Distribution of nitrate reductase in the aging bean seedlings. Plant Cell Physiol., 16: 995-999

Stanier, R.Y., Kunisawa, R., Mandal, M. and Cohen-Bazire, G. 1971. Purification and properties of unicellular blue green-algae (Order: Chrococcales). Bacteriol. Rev., 35: 171-305.

Suresh, A., Soundararajan, S., Elavarasi, S., Oscar, F.L. and Thajuddin, N. 2019. Evaluation and characterization of the plant growth-promoting potentials of two heterocystous cyanobacteria for improving food grain growth. Biocatal. Agric. Biotechnol., 17: 647-652.

Thind, S.K. and Malik, C.P. 1988. Carboxylation and related reactions in wheat seedlings under osmotic stress. Plant Physiol. Biochem., 15: 58-63.

Zhou, Y., Bao, J., Zhang, D., Li, Y., Li, H. and He, H. 2020. Effect of heterocystous nitrogen-fixing cyanobacteria against rice sheath blight and the underlying mechanism. Appl. Soil Ecol., 153: 103580.

Photosynthetic Microorganisms Consortium as Bioindicators for Heavy Metals

N. A. Khishamuddin*, L. S. Wong*†, M. K. Chai** and G. Subramaniam*

*Faculty of Health and Life Science, INTI International University, Putra Nilai, 71800 Nilai, Negeri Sembilan, Malaysia
**College of Engineering, Universiti Tenaga Nasional, Jalan Ikram-Uniten, 43000 Kajang, Selangor, Malaysia
†Corresponding author, L.S. Wong; lingshing.wong@newinti.edu.my; lingshing79@yahoo.com.sg

ABSTRACT

Heavy metals that are discharged through industrial and agricultural activities cause contamination, especially to the water sources, and bring about negative impacts on the flora and fauna in the ecosystem. The monitoring of heavy metals in the environment requires high technical skills with sophisticated equipment and is also time-consuming. In this study, the potential of using natural photosynthetic microorganism consortiums collected from natural water bodies as bioindicators for the screening of heavy metals was explored. The photosynthetic microorganism consortiums were first cultured in lab, immobilized, and then exposed to different heavy metals (Cd, Cu, Ni and Co) at different concentrations (0.01 mg.L^{-1}, 0.05 mg.L^{-1}, 0.10 mg.L^{-1}, 0.50 mg.L^{-1}, 1.00 mg.L^{-1} and 5.00 mg.L^{-1}). The fluorometric responses before and after the exposure to heavy metals were measured. The results revealed that consortium cells responded to a wide range of heavy metals within a short period of exposure. The responses showed that the consortium cells can detect the presence of Cd, Cu, Ni, and Co within the range of 0.05-5.00 mg.L^{-1}. The study confirmed that the photosynthetic microorganism consortiums collected from natural water bodies could be used as bioindicators for the screening of heavy metals.

INTRODUCTION

Rapid urbanization and population increase result in significant water demands to meet varied development needs, with lakes and rivers serving as the primary supplies of water for domestic, industrial, and agricultural activities. Industrial, manufacturing, and agricultural sectors are the major contributors to economic development for many countries. Products generated from these industries discharge tonnes of waste-containing metals into the environment (Afroz & Rahman 2017). The most commonly found metals include cadmium, chromium, copper, lead, nickel, and zinc (Jaishankar et al. 2014). This has become a serious environmental problem that left toxic effects on the flora and fauna and even threatening human life.

Several studies have shown the involvement of microorganism consortiums (algae, cyanobacteria, bacteria) in the degradation of a toxic substrate, thiocyanate (Ryu et al. 2015) as well as in the treatment of organic pollutants (Mahdavi et al. 2015). Multiple species that co-exist in the ecosystem may provide robustness to environmental variation, stability for the species, ability to share metabolites and weather periods of nutrient limitations, and resistance to invasion by other species. Therefore, photosynthetic microorganism consortiums which are present abundantly in the environment and are sensitive to any environmental changes might be good

indicators of heavy metals by providing biological responses upon contact with these heavy metals.

In this paper, the fluorometric responses of photosynthetic microorganism consortiums after exposure to heavy metals are reported. The potential of the responses to be used as bioindicators for the presence of heavy metals is discussed as well.

MATERIAL AND METHODS

Chemicals and Cell Cultures

Copper in the form of $CuSO_4$, cadmium in the form of $Cd(NO_3)_2$, nickel in the form of $Ni(NO_3)_2$, and cobalt in the form of $CoCl_2$ were procured from Sigma-Aldrich, Malaysia.

Bold Basal medium (50x stock) was obtained from Sigma-Aldrich, Malaysia, and Jaworski medium was prepared according to the information provided by the Culture Collection of Algae and Protozoa, United Kingdom. To provide nutrients to different species of photosynthetic microorganisms, 1 mL of Jaworski medium and 1 mL of Bold Basal medium were added to 98 mL of deionized water to produce 100 mL of medium.

The consortium of photosynthetic microorganisms was collected from two different locations in Malaysia, namely Taman Tasik Titiwangsa, Kuala Lumpur (L1) and Taman

Metropolitan Kepong, Selangor (L2). These two locations were selected for sample collection as they are surrounded by large water body which contains good populations of photosynthetic microorganisms. The consortium of microorganisms collected from different locations were cultured separately.

The cultures were placed on an orbitals shaker at a temperature of 20 ± 2°C with continuous aeration at 95 rpm to minimize cell clumping. Photoperiods of 16 hours in light and 8 hours in dark conditions were applied (Wong et al. 2012). The microalgae and cyanobacteria were identified through a simple light microscope (Eclipse E-100 LED, Nikon) at 400x magnification. The cell growth was determined for 15 days using a hemocytometer (Neubauer, Marienfeld) and a light microscope.

Heavy Metal Exposure

Cell density was determined with a spectrophotometer (GeneQuant 1300, GE) at a wavelength of 700 nm. The intensity of the fluorescence emission of the consortium cells was determined using a spectrofluorometer (Glomax Multi Jr., Promega).

A volume of 2 mL of cells from the day-10 culture with OD = 0.30 (λ = 700 nm) was exposed to different concentrations of Cd (0.05, 0.10, 0.50, 1.00, and 5.00 mg.L^{-1}). The fluorescence emission intensity was measured at wavelength = 648 nm, with excitation wavelength = 526 nm (Khishamuddin et al. 2018). Before and after the exposure, the intensity of the fluorescence emission was measured at t = 30, 60, 120, 240, 360, and 480 minutes. Cu, Ni, and Co were used in the same experiments. The reaction of cells that had not been exposed to heavy metals served as a negative control. For all of the exposure tests, a medium without any cells was employed as a blank. All of the exposure experiments were done three times.

RESULTS AND DISCUSSION

Before reaching the stationary phase, the cells in consortiums grew over the first 10 days in the culture (Fig. 1). Due to nutrient depletion and waste accumulation in the culture system, microbial growth generally reached a stationary phase. The cells from the consortiums on day-10 were selected for the exposure tests. The correlation between the OD measured with λ = 700 nm and cell density is portrayed in Fig. 2. The experimental results showed cells in consortiums with OD = 0.3 A yielded the highest fluorescence emission, with an average number of cells of 7.9 x 10^5 per 1 mL of culture. When the number of cells exceeded OD = 0.3 A, the fluorescence emission reduced, possibly due to non-photochemistry quenching, in which emitted fluorescence was reabsorbed

by nearby cells, lowering the fluorescence intensity (Wong et al. 2013).

The changes in fluorescence emission of the cells in consortiums caused by the presence of Cd, Cu, Ni, and Co are illustrated in Fig. 3 and Fig. 4. The presence of Cd disrupted the photosynthesis system, which caused changes in the fluorescence emission from chlorophyll. Mera et al. (2016) and Cheng et al. (2016) reported that Cd reduced the chlorophyll concentration in microorganism cells, and this result is consistent with their findings. Furthermore, long-term exposure to Cd inhibits the proliferation of microalgae cells and causes their decrease. Photosynthetic microorganisms require modest amounts of copper as a nutrient. Cu in high quantities, on the other hand, interferes with the metabolic functions of cells, producing disruptions in ATP production, pigment synthesis, and cell division suppression (Kumar et
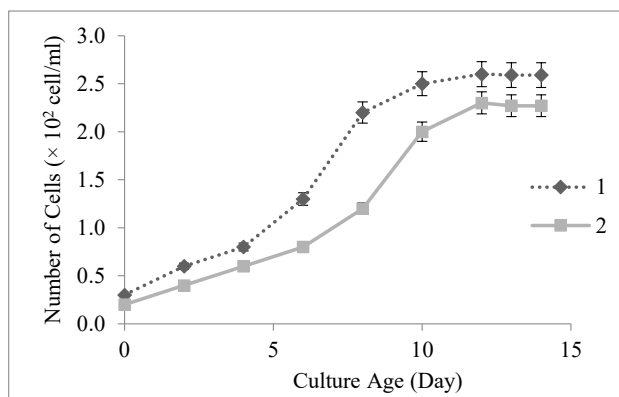
Fig. 1: Growth of consortium culture from L1: Taman Tasik Titiwangsa, L2: Taman Metropolitan.
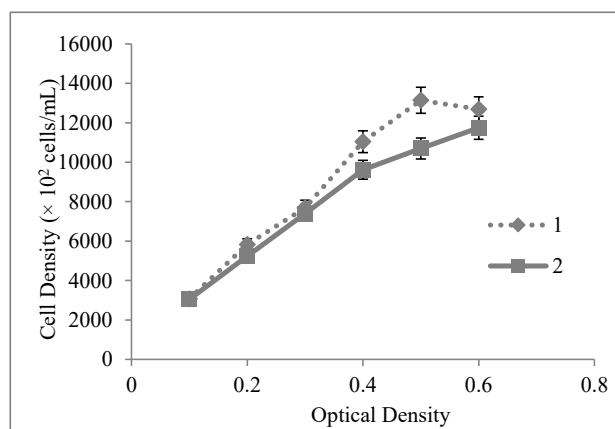
Fig. 2: The correlation between optical density measured at λ = 700 nm with cell density calculated using haemocytometer and light microscope for consortium cultures from L1: Taman Tasik Titiwangsa (linear equation: y = 20978x + 1564.3, R^2 = 0.9402), L2: Taman Metropolitan (linear equation: y = 17765x + 1737.3, R^2 = 0.9761).

al. 2015). The presence of Cu was found to affect the fluorescence emission by the chlorophyll as well (Wong et al. 2017).

According to Martínez-Ruiz et al. (2015) and Guo et al. (2017), the presence of Ni caused a reduction of chlorophyll. It disrupted the active site of the oxygen-evolving complex by reducing electron transport activity, which could impact photosynthetic bacteria' fluorescence emission (Boisvert et al. 2007). Co, like Ni, affects the concentration of chlorophyll (Guo et al. 2017). The presence of Ni affects the production of photosynthetic enzymes and the synthesis of macromolecules in photosynthetic organisms as well.

Despite the relevance of some heavy metals as nutrients for photosynthetic microorganisms, the presence of high concentrations (greater than 0.05 mg.L^{-1}) of Cd, Cu, Ni, and Co reduced the fluorescence emissions by photosynthetic microbes in consortiums. In general, heavy metals increased the number of reactive oxygen species (ROS) in photosynthetic microorganisms, which could disrupt the electron transport chain (Devi & Mehta 2014). After 120 minutes of exposure, the change in fluorescence emission intensity was dose-dependent. The research found that the natural consortium of photosynthetic microorganisms can be employed as a bioindicator for Cd, Cu, Ni, and Co screening.

CONCLUSION

This study reported the changes in fluorescence emission intensity due to the exposure of photosynthetic microbes in consortiums to heavy metals. The presence of heavy metals generally caused a decrease in fluorescence emission. The fluorescence responses by the photosynthetic microbes in the consortium confirmed the potential of these microbes to be used for screening Cd, Cu, Ni, and Co.

ACKNOWLEDGEMENTS
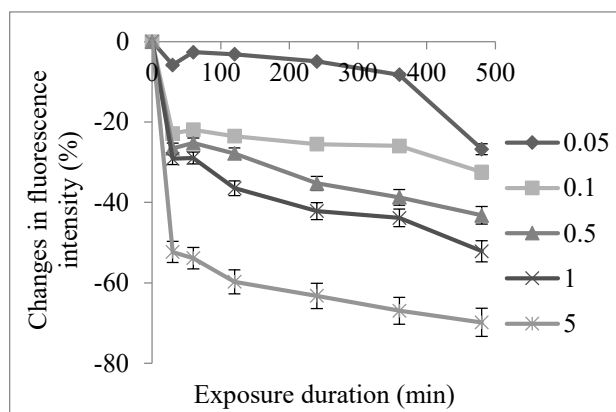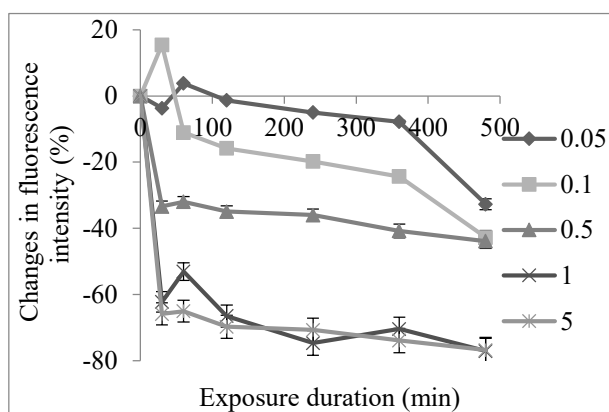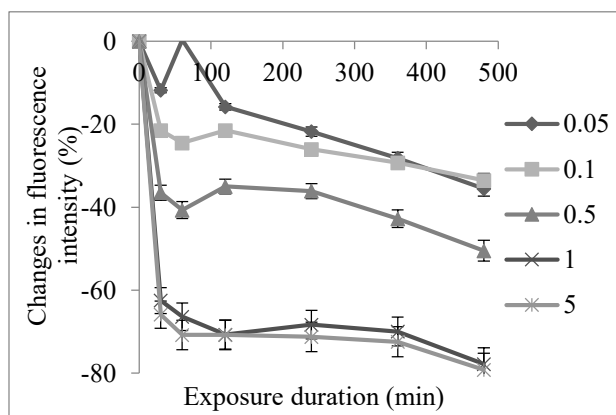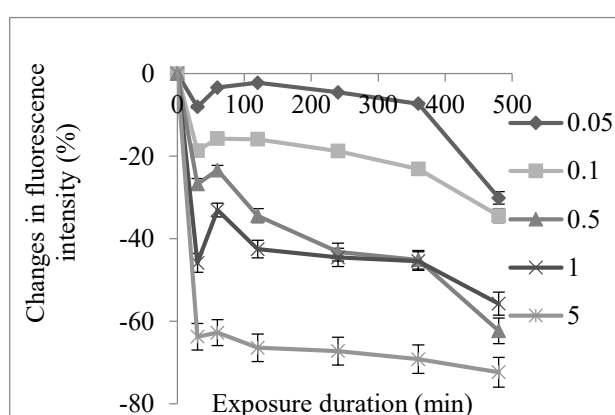
Fig. 3: Exposure of consortium of cells collected from L1 to (a) Cd, (b) Cu, (c) Ni and (d) Co.
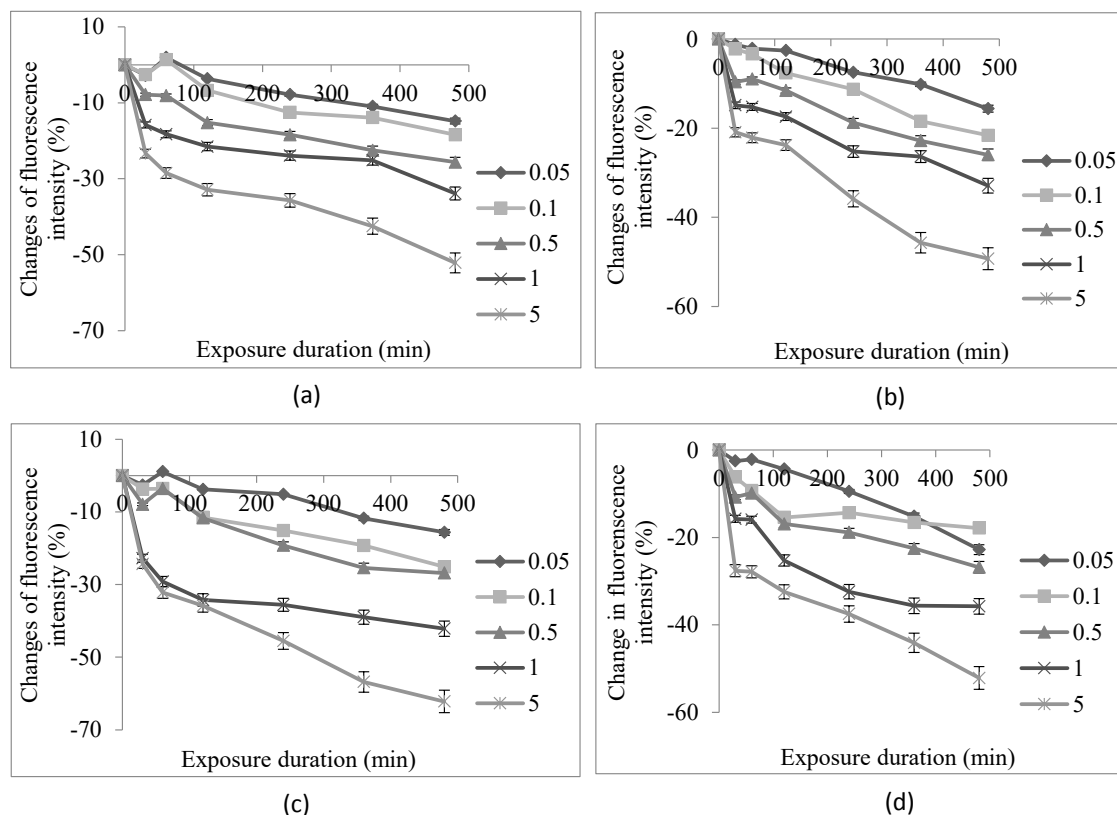
Fig. 4: Exposure of consortium of cells collected from L2 to (a) Cd, (b) Cu, (c) Ni, and (d) Co.

REFERENCES

Afroz, R. and Rahman, A. 2017. Health impact of river water pollution in Malaysia. Int. J. Adv. Appl. Sci., 4(5): 78-85.

Boisvert, S., Joly, D., Leclerc, S., Govindachary, S., Harnois, J. and Carpentier, R. 2007. Inhibition of the oxygen-evolving complex of photosystem II and depletion of extrinsic polypeptides by nickel. Biometals, 20(6): 879-889.

Cheng, J., Qiu, H., Chang, Z., Jiang, Z. and Yin, W. 2016. The effect of cadmium on the growth and antioxidant response for freshwater algae *Chlorella vulgaris*. Springer Plus, 5(1): 1-8.

Devi, Y.M. and Mehta, S. 2014. Changes in antioxidative enzymes of cyanobacterium *Nostoc muscorum* under copper (Cu^{2+}) stress. Sci. Vision, 14: 207-214.

Guo, L., Ding, Y., Xu, Y., Li, Z., Jin, Y., He, K., Fang, Y. and Zhao, H. 2017. Responses of *Landoltia punctata* to cobalt and nickel: Removal, growth, photosynthesis, antioxidant system, and starch metabolism. Aqua. Toxicol., 190: 87-93.

Jaishankar, M., Tseten, T., Anbalagan, N., Mathew, B.B. and Beeregowda, K.N. 2014. Toxicity, mechanism, and health effects of some heavy metals. Interdiscip. Toxicol., 7(2): 54-61.

Khishamuddin, N.A., Wong, L.S., Chai, M.K. and Voon, B.W.N. 2018. Fluorometric response of photosynthetic microorganism consortium as

potential bioindicator for heavy metals detection in water. Environment Asia, 11(1): 80-86.

Kumar, K.S., Dahms, H.U., Won, E.J., Lee, J.S. and Shin, K.H. 2015. Microalgae–A promising tool for heavy metal remediation. Ecotoxicol. Environ. Safety, 113: 329-352.

Mahdavi, H., Prasad, V., Liu, Y. and Ulrich, A.C. 2015. In situ biodegradation of naphthenic acids in oil sands, tailings pond water using indigenous algae–bacteria consortium. Bioresour. Technol., 187: 97-105.

Martínez-Ruiz, E.B. and Martínez-Jerónimo, F. 2015. Nickel has biochemical, physiological, and structural effects on the green microalga *Ankistrodesmus falcatus*: An integrative study. Aqua. Toxicol., 169: 27-36.

Mera, R., Torres, E. and Abalde, J. 2016. Influence of sulfate on the reduction of cadmium toxicity in the microalga *Chlamydomonas moewusii*. Ecotoxicol. Environ. Safety, 128: 236-245.

Ryu, B.G., Kim, W., Nam, K., Kim, S., Lee, B., Park, M.S. and Yang, J.W. 2015. A comprehensive study on algal–bacterial communities shifts during thiocyanate degradation in a microalga-mediated process. Bioresour. Technol., 191: 496-504.

Wong, L.S., Judge, S.K., Voon, B.W.N., Tee, L.J., Tan, K.Y., Murti, M. and Chai, M.K. 2017. Bioluminescent microalgae-based biosensor for metal detection in water. IEEE Sensors J. 18(5): 2091-2096.

Wong, L.S., Lee, Y.H. and Surif, S. 2012. The fluorometric response of cyanobacteria to short exposure of heavy metal. Adv. Environ. Biol., 6(1): 103-108.

Wong, L.S., Lee, Y.H. and Surif, S. 2013. Performance of a cyanobacteria whole cell-based fluorescence biosensor for heavy metal and pesticide detection. Sensors, 13(5): 6394-6404.

Towards a Framework for Sustainable Municipal Solid Waste Management: The Case of Swakopmund Municipality, Namibia

Timoteus Kadhila*† and Martin P. de Wit*

*Faculty of Economic and Management Sciences, School of Public Leadership, Stellenbosch University, Matieland, 7602, Stellenbosch, South Africa

†Corresponding author: Timoteus Kadhila; tkcibi85@yahoo.com/ timkadhila@gmail.com

ABSTRACT

If municipal solid waste (MSW) is not properly managed, harmful environmental consequences are imminent. MSW materials are rarely wasted in many affluent countries, but rather are kept in the economic cycle through circular economy models. While in many developing countries, MSW materials are discarded with little to no effort of repairing or recycling. Moving to a circular economy will drastically reduce the amount of waste currently disposed of. This study examines how the Swakopmund Municipality in Namibia's present municipal solid waste management techniques could be adjusted toward sustainability to reap environmental and socioeconomic benefits from the trash. Source reduction, separation at source, and recycling are some of the most effective strategies in the circular economy models that will help achieve the United Nations (UN) Sustainable Development Goals (SDGs). Swakopmund Municipality should invest in infrastructure, techniques, and programs that are within the circular economy model as an emerging system for sustainability.

INTRODUCTION

Generally, the issue of global waste requires sound waste management and governance to curb an increase in waste generation. Effective MSW management systems, according to Krista et al. (2015), are built on a good understanding of waste disposal drivers, the amount of trash produced, the economic expenses involved, and the environmental implications connected with waste treatment technologies. As a result, waste is treated in different methods around the world. Gertsakis & Lewis (2003) emphasized that waste prevention and reduction should be the preferred options, to avoid harmful environmental impacts across the entire product life cycle, including disposal.

Gower & Schröder (2016) discovered a link between waste management and circular economy (CE) practices, which include lifting people out of poverty and protecting the environment, as well as significantly expanding the scope for achieving the United Nations (UN) Sustainable Development Goals (SDGs) (United Nations 2018). The strongest links between CE practices and the aims of SDG 6 (Clean Water and Sanitation), SDG 7 (Affordable and Clean Energy), SDG 8 (Decent Work and Economic Growth), SDG 12 (Responsible Consumption and Production), and SDG 15 (Responsible Consumption and Production) are notable (Life on Land) (Schröder et al. 2018).

It is essential to realize that poor implementation of MSW strategies also hinders municipalities' progress towards job creation, improvement of livelihood, and achievement of the SDGs (UNDP 2016). As a result, the need for more comprehensive strategies and their implementation for waste management within development processes needs to be considered key. A review on global solid waste management by Hoornweg & Bhada-Tata (2012) revealed that cities and towns that are unable to handle waste effectively are less likely to succeed in the provision of critical services such as health, education, and transportation. In low-income countries, the challenges of MSW management and governance in cities and towns have been contributing factors to environmental problems such as water and ground pollution (Lee & Jones 1991). Consequently, some low-income countries particularly in Africa are left in a dilemma on how to handle the increasing waste volumes, given their weak economies (low technical capacities and poor physical infrastructures), inabilities to enforce environmental legislation, financial mismanagement, and poor administrative capacities (Muniafu & Otiato 2010). Given these challenges, Hoornweg & Bhada-Tata (2012), estimated that waste generation in Africa is expected to increase to 244 million tonnes per year by 2025.

Although high-income countries generate more trash, solid waste management is a top priority in such countries, while it is a low priority in emerging or low- and middle-in-

come countries (Coad 2003). Financial constraints, a lack of awareness, insufficient incentives, and low waste value addition make waste management a low priority in low- and middle-income countries (Coad 2003). Additionally, inadequate support from the government, lack of waste management data, and lack of waste management research, also contribute to ineffective planning for waste management (Nwofe 2015). Interestingly, Ogawa (1996) revealed that several municipal solid waste management projects have been carried out in developing countries, however, many of them failed to support themselves or to expand further in the absence of support from external agencies, local authorities, or governments.

Namibia as a developing middle-income country is not an exception to the municipal solid waste management challenges like urbanization, economic activities and population growth significantly increase the volume of municipal solid waste (Nwofe 2015). Therefore, Namibia is also facing serious environmental problems associated with municipal solid wastes such as ground pollution (Croset 2014). The issue of illegal dumping is alarming in Namibia, which necessitates the importance of developing waste management policies and plans across the entire country. For example, several municipalities such as Swakopmund Municipality implemented the waste management policy of 2015 to curb waste management issues including illegal dumping. However, when compared to smaller towns and villages, waste management laws and strategies are mostly implemented well in major cities (Ngoc & Schnitzer 2009). Some of Namibia's smallest cities and communities, for example, lack waste management policies and plans.

In fast urbanizing towns like Swakopmund (estimated population of 44, 908 in 2014), waste generation keeps increasing and is frequently disposed of at disposal sites (Kadhila 2018). However, some residents, especially the poor communities regard waste as a resource that is sent to the disposal site, therefore they informally collect waste materials for reuse and recycling, using informal methods to transform waste into useful products. The current MSW issue gives an opportunity for academic discussion with many stakeholders about potential implications and solutions to develop a sustainable waste management strategy in Swakopmund that will contribute to socioeconomic advantages. Although similar research has been carried out elsewhere, there are currently no studies on MSW in Namibia in general and Swakopmund in particular. It implies that there is a knowledge gap on this topic in the context of Swakopmund Municipality. Therefore, this study aimed to contribute to the body of knowledge on how sustainable MSW management and governance can effectively be implemented in Swakopmund, with general recommendations of other towns with similar situations elsewhere.

Conceptual Framework

The study adopts the circular economy (CE) model developed by Ezeudu & Ezeudu (2019) as a suitable concept underpinning sustainable waste management systems, which can be adopted to ensure sustainable waste management in Swakopmund. The CE is a system of production and consumption based on reusable and sustainable design (Ezeudu & Ezeudu 2019). It aims to eliminate waste from the present and dominating linear manufacturing system, often known as "take-make-use-dispose of," in which raw materials are harvested and then disposed of promptly (Ezeudu & Ezeudu 2019). According to studies, most municipalities today build their waste management systems using LE models (Gower & Schröder 2016). The LE models of waste handling modalities view waste products as a nuisance that often entails the disposing of scarce resources as a management approach. In LE models, production companies extract materials, apply energy to manufacture a product, and sell the product to an end consumer, who then discards it when it no longer serves the user's purpose (Ellen MacArthur Foundation 2013). Sadly, the linear economy (LE) models caused unnecessary resource losses in the production chain, energy use, and damage to ecosystem services (Drlja a 2015). For example, during manufacturing, companies produce large volumes of materials such as parting materials that are not physically incorporated into the formal economic system but are disposed of at disposal sites. Yet, the LE models of waste management have often been criticized by economic and environmental pundits and commentators, as being counterproductive in promoting job creation to improve livelihoods, but rather causing environmental degeneration.

Globally, there has been a renewed effort toward a shift away from LE to CE models of waste management, whereby the CE concept has become part of the political, economic, social, and environmental discourse around the world, and hence a policy priority in many countries (Esposito et al. 2018). The need for a paradigm shift toward CE models is attributed to the fast exploitation of natural resources in the face of resource decline, while at the same time the volumes of waste and pollutants due to human activities are increasing (Velenturf et al. 2019). A CE model varies from an LE model in which the materials used to produce the products are lost as waste (Gower & Schröder 2016). For example, in a LE model, chairs are made from timber, used, and when they break, they are thrown away as waste. It implies that at this point, all the resources (i.e. energy, timber, and metal) used to make those chairs are lost. Generally, the CE model of waste management would address these challenges by eliminating waste and inefficiency at each stage of the product's life cycle, from reducing the amount of time the product sits idle,

to increasing the scope for reparability or re-manufacturing of the used components (Lieder & Rashid 2015). This would help to shut the loop by providing regenerative, restorative, and reusable products and services. Waste does not exist in the product design scenario if materials are made to be non-toxic so that they can be composted, or if they are designed to be reused with minimal energy (Lieder & Rashid 2015).

Deselnicu et al. (2018) pointed out that the ability of the CE to respond positively to socio-economic and environmental welfare depends on how waste is managed, and waste management options that deliver the best overall environmental and socio-economic outcomes. Waste management policies at national and municipal levels must, therefore, provide conducive environments for CE models (UNEP 2018). However, in some parts of the world, waste management is still based on LE models, which view waste products as a nuisance that threatens the environment and public health (Ezeudu & Ezeudu 2019). As a result, the methods of waste management are still based on traditional landfills and dumpsites. In this context, the present study sought to explore how Swakopmund Municipality could shift to the CE model of waste management in effort to take advantage of opportunities presented by this model in view of sustainable development, an action that can also be applied in other towns.

MATERIALS AND METHODS

This study employed a mixed-methods approach whereby qualitative and qualitative data were collected using a case study research design. Data collection tools were mainly: document analysis, Semi-Structured Interview Schedule (SSIS), and a field observation checklist. The CE concept for sustainability assisted the researcher in yielding the data and results, which served as a lens through which the study is viewed. The purposive sampling technique was used to select two (2) participants directly working with waste management in Swakopmund municipality, and a direct oral interview method was adopted to collect information through the SSIS. The SSISs were done in August and September 2018 with two MSW management and governance specialists from the Swakopmund Municipality's Health Department. Additionally, between August and September 2018, direct field observations at the municipal waste disposal plant were employed to acquire quantitative data, with the researcher visiting the site twice a week. A simple percentage was used to summarize and organize data gathered from field observations based on the volume of waste observed at the disposal site to estimate the composition of waste fractions in the disposal site.

RESULTS AND DISCUSSION

The study presents an analysis of the current implementation of MSW management and governance, with a particular focus on Swakopmund, based on the qualitative and quantitative data collected, direct observations, and the CE concept for waste management. The findings are as follows:

Sources of MSW in Swakopmund

The study established that generally, MSW in Swakopmund is generated from different sources. Based on direct observations, different sources of waste generated in Swakopmund are summarized in Table 1.

As seen in Table 1, it is evident that various types of solid waste are found in the municipal disposal facility, except the types of waste from agricultural sources. Agricultural activities are less common within Swakopmund municipal jurisdiction due to the lack of seasonal rainfall in the area. Among the waste types found in the disposal facility, most of them are recyclables.

Table 1: Sources of MSW.

Source	Typical waste generators	Types of solid wastes
Residential	Single and multifamily dwellings	Food waste, paper, cardboard, plastics, textiles, leather, wood, glass, metals, ashes
Industrial	Light and heavy manufacturing, fabrication, construction	Packaging, food waste, building rubbles, ashes, special waste
Commercial	Stores, hotels, restaurants, markets, office buildings	Paper, cardboard, plastics, wood, food waste, glass, metals
Institutional	Schools, hospitals, prisons, government centers	Same as commercial
Construction and demolition	Construction and demolition sites, road repair, renovation sites	Wood, steel, concrete, dirt, metals
Municipal services	Street cleaning, landscaping, recreational areas	Street sweepings, landscape, and tree trimmings, general wastes
Processing	Heavy and light manufacturing, refineries	Scrap materials, off-specification products, slag, tailings

Source: Fieldwork (2018).

Characterization of MSW in Swakopmund

The Swakopmund municipal dumpsite receives large amounts of mixed MSW regularly. Swakopmund Municipality collects estimated waste generating volumes, which is critical information for planning, developing, and operating the disposal site. The lack of a weighbridge system to take accurate readings of the trash volumes entering the dumpsite was highlighted as a data accuracy problem in this study.

Table 2 summarizes the solid waste composition observed at the Swakopmund municipality dumpsite raised out of 100%. In table 2, the term abundant means waste occurs in large quantities, common means waste occurs in medium quantities, while not common means waste occurs in low quantity.

It is essential to have background information about the composition of MSW generated in any municipality to be able to manage waste appropriately (Supriyadi et al. 2000). The composition of MSW in Swakopmund contains a high fraction of compostable organic waste, recyclables such as plastics and papers, and a very low fraction of hazardous waste such as pesticides, paints, used health care waste, and batteries. Papers, glasses, and cans, among other household trash, are abundant and common in the waste portion. In general, the large and commonly occurring waste fractions at the Swakopmund waste disposal site are environmentally hazardous, but they also present a potential to contribute to the economy if CE activities to handle these waste types are intensified. In China, for example, the formal recycling sector has grown steadily under regulation and financing from municipalities, which has enabled the establishment of waste recycling processes that are safer and more environmentally and economically sound (Song & Li 2014).

The informal sector plays an important role in MSW management, even though not integrated into the formal SWM systems. In Swakopmund, the informal sector is characterized by small-scale, labor-intensive, largely unregulated, and unregistered low-technology manufacturing, provision of materials and services. Many of the informal waste pickers in Swakopmund depend on waste to earn income, despite health and social issues associated with informal waste picking. These people derive potential value from waste bins, streets, and dumpsites. Waste collection is frequently a family's only source of income, providing a living for a large number of urban poor people. Around 60 informal recyclers and pickers were seen collecting tonnes of rubbish at the dumpsite in Swakopmund.

Methods of MSW Management Employed by Swakopmund Municipality

One of the objectives of the study was to explore the waste management methods being implemented by Swakopmund municipality. According to the Swakopmund Municipality's Waste Management Policy of 2015, the municipality is responsible for developing infrastructure for waste collection, storage, separation, transportation, processing, and disposal. The study established that the following methods are employed, mainly: prevention, separation, collection and transportation, treatment, and disposal. These methods are discussed in detail as follows:

Table 2: Estimated composition and fractions of MSW.

Fractions	Waste components	Occurrence status	Volume estimate [%]
Organic	Compostable organic (i.e. food waste, wood, garden refuse)	Abundant	15
Plastics	Hard plastics, carry bag plastics, clear & color plastic bottles	Abundant	14
Paper	Newspapers, white papers, magazines,	Abundant	13
Building Rubble	Bricks, tiles, concrete, ceiling boards, timber	Common	10
Boxes	Packaging boxes, cement bags, potato bags	Abundant	9
Glass	Recyclable glass	Common	9
Cans	Metal cans, steel cans, aluminum cans	Common	7
Refuse-Driven Fuel	Rubber, tailings	Common	6
Non-ferrous	Aluminum	Common	5
Tetra	Tetra packs (Milk & fruit juice boxes	Common	5
Rubbers	Tyres, worn out footwear	Common	4
E-waste	Computer, TVs and radio parts	Not common	1
Ferrous	Steel packaging	Not common	1
Earth-based	Ceramics	Not common	1

Source: Fieldwork (2018).

Prevention

The study established that the Swakopmund Municipality has assigned a high priority to waste prevention, as emphasized by the National Waste Management Strategy of 1999 and the Municipality's Waste Policy of 2015. In so doing, the municipality ensures that uncontrolled dumping of MSW is prevented by providing formal and informal settlements, businesses, institutions, and recreational areas with the 240L waste containers called "wheelie bins", street garbage bins, and black plastic bags for depositing the MSW. This service's delivery system prevents MSW from dispersing into the environment. This technique, however, does not prevent trash generation per capita, waste generation at the source, or waste accumulation at the dump. However, as a counter-act, the municipality reduces the flow of MSW by providing wheelie bins, black plastic bags, and skip containers across settlements, entertainment and business areas.

The wheelie bins are used to serve different purposes such as the orange wheelie bin to deposit recyclables, and the black and brown bins are for general waste. Furthermore, the municipality provides street sweeping services to ensure that streets are free of litter, and also provides cleaning services for public open spaces, in partnership with members of the community. Most importantly, Swakopmund Municipality monitors and regulates MSW management services, to ensure that these services conform with the country's legal standards and waste compliance processes. To ensure revenue generation from solid waste management services, the municipality has set rates and tariffs that residents pay for the services provided. The standard refuse removal and cleaning services cost residents about N\$ 16/month/household, however, this amount differs from suburb to suburb.

Separation

The study established that there is a lack of effective waste separation at the household level. Currently, large volumes of MSW generated in households are transported by trucks to the dumpsite for disposal. However, some formal recycling companies in Swakopmund implemented waste management strategies such as the Clear Bag System (for collecting recyclable waste from households), orange wheelie bins (for collecting recyclable waste generated in households and public places), the File13 Recycling Box (for separating office papers), however, these services are only available in certain places. For this reason, large volumes of MSW recyclables are still transported to the dumpsite unsorted. Of these, a low fraction of recyclable materials such as papers, boxes, plastics, glass, cans, tetra, and RDF are mostly recovered and recycled at the Material Recovery Facilities (MFRs) such as that of a local company

Rent-A-Drum (2018), which is however less compared to the potential recyclable materials that are disposed of at the dumpsite on daily basis. Apart from the formal waste separation, informal waste pickers were observed at the disposal site separating and recovering recyclable and re-usable waste materials for selling and for personal use. If Swakopmund Municipality implements an efficient waste material separation system, the waste management system is likely to focus more on recycling, reducing the use of recyclables as a source of income for underprivileged communities. It is recommended that Swakopmund Municipality should reduce the costs of recycling services to encourage residents to intensify recycling activities.

Collection and Transportation

MSW collection and transportation involves the removal of MSW from collection points, frequencies, storage containers, crew, route, secondary storage, and transfer stations (Singh et al. 2014). In Swakopmund, MSW is normally collected from various points such as households, business premises, institutions, and road walkways weekly, as organized by the Health Department of Swakopmund Municipality and transferred to the disposal site (open controlled dumpsite). During an interview conducted on 9 October 2018, Mwanangombe (2018) pointed out that the solid waste transportation fleet consists of 10 compactor trucks, 3 Skip trucks, and a dumper truck that is used for MSW collection and transportation.

The following is a summary of the commonly observed MSW collection methods within Swakopmund Municipality's jurisdiction:

- House-to-House: Municipal waste collectors visit each house with a compactor truck to collect waste materials once a week.

- Skip containers (heavy-duty bins): These bins are shared with the rest of the community and are usually placed in densely populated areas, and at construction sites.

- Kerbside Pick-Up: Residents leave black garbage plastics outside their homes or alongside the roads.

- Self-delivery: Sometimes solid waste generators deliver waste directly to the disposal sites or transfer stations (normally at the skip container).

- Contracted or delegated services: Municipality and businesses hire accredited waste collection firms on a contract basis.

- Street cleaning: Municipal workers sweep the streets to remove solid waste and sand.

- Molok Deep Collection System: A semi-underground waste containment system that compacts waste.

Treatment and Disposal

The municipality dispose of MSW (Table 2) at an open controlled dumpsite, where the dumped solid waste materials are covered with sand and building rubble, as an effort to reduce its negative environmental impacts. Noteworthy, the MSW disposed of at the dumpsite does not include hazardous wastes. The hazardous wastes are transferred to the hazardous wastes management facility that belongs to the municipality of Walvis Bay (Engelbrecht 2018). This includes wastes such as batteries, herbicides, pesticides, and medical wastes.

Trajectory

If Swakopmund Municipality applies the CE models that phase out the disposal of recyclables, more job opportunities could be created and UN-SDGs mentioned earlier could be accomplished. For example, if the municipality formalizes informal waste activities, more recovery and recycling create substantial job opportunities in the waste sector. As stated by Ellen MacArthur Foundation (2013) CE models keep waste materials longer in the economic cycle for recycling activities to carry on. Various projects, ranging from composting organic waste to making fertilizers are some potential projects. There are several MSW treatment good practices elsewhere, from which Swakopmund Municipality can learn from. An example, Ethiopia's capital Addis Ababa launched Africa's first waste-to-energy facility in 2013 that produces 30% of household electricity needs while conforming to global standards on air emissions (Shaban 2018). Other examples, composting and aerobic digestion of organic waste materials produce excellent fertilizers for gardening and horticultural activities (Al-Khatib et al. 2010). On the other hand, anaerobic digestion can produce renewable energy-source methane and carbon dioxide from solid wastes (Nandan et al. 2017). Both contexts can be applied to waste management to satisfy energy needs in Swakopmund and Namibia at large. It is therefore essential that the government and municipal policies must promote zero-waste business models, based on activities such as waste collection and sorting, recycling, repair and remanufacturing, recovery, and re-use of resources in industrial processes, considering the current socio-economic status in Namibia. The government and the municipality should invest in technology to enable adding value to waste products. The current waste recovering activities particularly in the informal sector are detrimental hence need to be enhanced, to contribute to socio-economic development and capacity building. This study recommends that the informal waste sector should be formalized, to boost the status of socio-economic development in Swakopmund. Additionally, the municipality should consider moving away from an open controlled dumpsite to a landfill site to minimize public health risks along with negative environmental impacts.

CONCLUSION

Volumes of waste generated in Swakopmund can be prevented and when cannot be prevented, these waste materials can be reused, recycled, and composted. MSW generated within the Swakopmund jurisdiction is disposed of at an unsustainable open controlled dumpsite covered with sand and building rubbles. Noteworthy, the current MSW management operation in Swakopmund is in accordance with the national legal frameworks related to waste management, however, still based on the LE model of waste management. The operation is strengthened by the implementation of the municipality's Waste Management Policy of 2015 that was drafted with the guidance of the national waste management legal framework. However, Swakopmund Municipality needs an integrated waste management plan.

Although recycling activities are currently taking place, particularly in the private sector, more efforts should be placed on these activities across both sectors, to reduce the amount of waste entering the dumpsite, while reducing negative environmental impacts. Plastics, glasses, and cans are problematic to the environment; therefore, these waste types should be reduced through circularity. If Swakopmund Municipality implements an efficient waste material separation system, the waste management system is likely to focus more on recycling, reducing the use of recyclables as a source of income for underprivileged communities. Robust waste treatment techniques such as composting, aerobic digestion, and incineration should be promoted to extract maximum benefits from waste materials.

REFERENCES

Al-Khatib, I.A., Monou, M., Zahra, A.S.F.A., Shaheen, H.Q. and Kassinos, D. 2010. Solid waste characterizations, quantification, and management practices in developing countries: A case study: Nablus District-Palestine. J. Environ. Manag., 91(5): 1131-1138.

Coad, A. 2003. The Solid Waste Collection Benefits the Urban Poor: Report Prepared by The Collaborative Working Group on Solid Waste Management in Low-and Middle-Income Countries. Workshop Report, Dar es Salaam, Tanzania, pp. 1-91.

Croset, E. 2014. Opportunities and challenges of a Sustainable Solid Waste Management in Tsumeb, Namibia. Master thesis, Royal Institute of Technology, Stockholm, Sweden.

Deselnicu, D.C., Militaru, G., Deselnicu, V., Z inescu, G. and Albu, L. 2018. Towards a Circular Economy: A Zero Waste Programme for Europe. Proceedings of the 7th ICAMS 2018, 18-20 October, Bucharest, Romania, pp. 563-568.

Drljača, M. 2015. The transition from linear to a circular economy. Quality system condition for successful business and competitiveness, an association for quality and standardization of Serbia. Vrnja ka Banja, 16: 35-44.

Ellen MacArthur Foundation. 2013. Towards the circular economy. Ellen MacArthur Foundation, Cowes, UK.

Ezeudu, O.B. and Ezeudu, T.S. 2019. Implementation of circular economy: Principles in industrial solid waste management: Case studies from a developing economy (Nigeria). Recycling, 4(42): 1-18.

Engelbrecht, P. 2018. Personal communication. 09 October, Swakopmund: Namibia

Esposito, M., Tse, T. and Soufani, K. 2018. Introducing a CE: New thinking with new managerial and policy implications. CA Manag. Rev., 60(3): 5-19.

Gertsakis, J. and Lewis, H. 2003. Sustainability and the Waste Management Hierarchy. Discussion Paper, EcoRecycle Victoria, RMIT University, Melbourne, pp. 1-16.

Gower, R. and Schröder, P.M. 2016. Virtuous Circle: How the Circular Economy Can Create Jobs and Save Lives in Low and Middle-Income Countries. Available at: https://www.researchgate.net/publication/306562812_Virtuous_Circle_how_the_circular_economy_can_create_jobs_and_save_lives_in_low_and_middle-income_countries/ [Accessed: 8 June 2018].

Hoornweg, D. and Bhada-Tata, P. 2012. What a waste? A global review of solid waste management. Knowledge Paper No. 15, World Bank Group, Washington, D.C., pp. 1-116.

Kadhila, T. 2018. Implementation of A Municipal Solid Waste Management Systems in Swakopmund, Namibia. Master Thesis, University of Stellenbosch, South Africa.

Krista, L., Thyberg, T. and Tonjes, D.J. 2015. A Management Framework for Municipal Solid Waste Systems and Its Application to Food Waste Prevention. Stony Brook University, New York.

Lee, G.F. and Jones, R.A. 1991. Groundwater Pollution by Municipal Landfills: Leachate Composition, Detection and Water Quality Significance. National Water Well Associations's Fifth Outdoor Action Conference on Aquifer Restoration, Ground Water Monitoring, and Geophysical Methods, NWWA, Dublin, OH, pp. 257-271.

Lieder, M. and Rashid, A. 2015. Towards circular economy implementation: a comprehensive review in the context of the manufacturing industry. J. Cleaner Prod., 115: 36-51.

Muniafu, M. and Otiato, E. 2010. Solid Waste Management in Nairobi, Kenya. A case for emerging economies. J. Lang. Technol. Entrepreneurship Afr., 2(11): 162-167.

Mwanangombe, K. 2018. Personal communication. 09 October, Swakopmund: Namibia.

Nandan, A., Yadav, B.P., Baksi, S. and Bose, D. 2017. Recent Scenario of Solid Waste Management in India. World Sci. News, 66(2017): 56-74.

Ngoc, N.U. and Schnitzer, H. 2009. Sustainable solutions for solid waste management in Southeast Asian countries. Waste Manag., 29(6): 1982-1985.

Nwofe, P.A. 2015. Management and disposal of municipal solid wastes in Abakaliki Metropolis, Ebonyi State, Nigeria. Int. J. Sci. Res. Environ. Sci., 3(3): 107-118.

Ogawa, H. 1996. Sustainable Solid Waste Management in Developing Countries. The 7th ISWA International Congress and Exhibition, Parallel Session 7. Available at: http://www.gdrc.org/uem/waste/swm-fogawa1.htm/ [Accessed: 11 May 2019].

Rent-A-Drum. 2018. Swakopmund Material Recovery Facility. Swakopmund, Namibia.

Schröder, P., Anggraeni, K. and Weber, U. 2018. The relevance of circular economy practices to sustainable development goals. J. Indust. Ecol., 23(1): 77-95.

Shaban, A. 2018. Ethiopia opens Africa's first waste-to-energy facility. Available at: https://www.africanews.com/2018/08/20/the-reppie-project-ethiopia-opens-africa-s-first-waste-to-energy-facility/ [Accessed: 11 May 2019].

Singh, G.K., Gupta, K. and Chaudhary, S. 2014. Solid waste management: its sources, collection, transportation, and recycling. Int. J. Environ. Sci. Develop., 5(4): 347- 351.

Song, Q. and Li, J. 2014. A systematic review of the human body burden of e-waste exposure in China. Environ. Int., 68: 82-93.

Supriyadi, S., Kriwoken, L. and Birley, I. 2000. Solid waste management solutions for Semarang, Indonesia. Waste Manag. Res., 18(6): 557- 566.

United Nations. 2018. Solid Waste Management. SEEA Development in Asia and the Pacific. Bangkok, Thailand.

UNDP. 2016. UNDP support to the implementation of the 2030 agenda for sustainable development (UNDP Policy and Programme Brief). New York, NY: USA.

UNEP. 2018. Africa Waste Management Outlook. United Nations Environment Programme, Nairobi, Kenya.

Velenturf, A.P.M., Purnell, P., Macaskie, L.E., Mayes, W.M. and Sapsford, D.J. 2019. A New Perspective on a Global Circular Economy, in Resource Recovery from Wastes: Towards a Circular Economy. Available at: https://pubs.rsc.org/en/content/chapterhtml/ [Accessed: 10 December 2019].

Study on the Effects of Organophosphate Insecticide Triazophos, Biopesticide Spinosad and a Pyrethroid Insecticide Cypermethrin on Oxidative Stress Biomarkers of *Branchiura sowerbyi* (Beddard, 1892)

Chandan Sarkar*, Arnab Chatterjee**, Anandamay Barik*** and Nimai Chandra Saha**†

*P.G. Department of Zoology, Krishnagar Govt. College, Krishnagar, Nadia-741101, West Bengal, India

**Fishery and Ecotoxicology Research Laboratory, Vice Chancellor's Research Group, Department of Zoology, The University of Burdwan, Burdwan-713104, West Bengal, India

***Ecology Research Laboratory, Department of Zoology, The University of Burdwan, Burdwan-713104, West Bengal, India

†Corresponding author: Nimai Chandra Saha; ncsaha@zoo.buruniv.ac.in; csarkar.wbes@gmail.com

ABSTRACT

This study aims to evaluate the toxic effects of organophosphate insecticide triazophos, biopesticide spinosad, and a pyrethroid insecticide cypermethrin on benthic Oligochaete worm, *Branchiura sowerbyi* during 96 h acute exposure. *B. sowerbyi* were exposed to two different sub-lethal concentrations (10% and 50% of 96h LC_{50}) of triazophos, spinosad, and cypermethrin for 96 h in laboratory conditions. Catalase (CAT) activity of the control and treated worms were evaluated after 24 and 96 h of exposure. Integrated biomarker response (IBR) was applied for comparison between these three toxicants. For all sub-lethal doses i.e. 2.25 mg.L^{-1} and 0.5 mg.L^{-1} of test chemical triazophos, 3.07 mg.L^{-1} and 0.6 mg.L^{-1} of test chemical spinosad, and 0.38 mg.L^{-1} and 0.08 mg.L^{-1} of test chemical cypermethrin, catalase (CAT) activity raised significantly ($p<0.05$) in the treated worms in compare to the control worms. This study shows that toxicants including Triazophos, spinosad, and cypermethrin cause a large increase in catalase (CAT) activity in *Branchiura sowerbyi*, which is likely due to the toxicant's increased ROS creation neutralizing the negative effects. IBR analysis aids in the differentiation of these three compounds' harmful effects. As per IBR analysis, the rank of the toxicants is Cypermethrin > Triazophos > Spinosad.

INTRODUCTION

The chemicals which are designed specially to destroy unwanted species are termed pesticides. These pesticides are drained into water bodies and severely affect the life of aquatic species, in addition to destroying the target organisms (Pereira et al. 1996). According to an estimate, more than 200 toxic chemical pesticides are used in agriculture in various parts of the world (Mishra & Bohidar 2005). Pesticide use is increasing at an alarming rate across the world, posing a significant threat to the ecosystem. Pesticide residues in food are a global problem (Uno et al. 2001). Around 25 percent of the pesticides in the world are used by developing countries (WHO 2003). Except for Japan, India is the largest producer of pesticides in South Asia and Africa and ranks twelfth in the world for the use of pesticides (Abhilash & Singh 2009).

Organophosphate pesticides have been widely used in recent years due to rapid biodegradation and limited retention time in the field. Triazophos or O,O-diethyl, 0.1 phenyl, 1H, 1,2,4, triazol 3yl-phosphorothio is a broad-spectrum systemic

insecticide and acaricide also. Triazophos is the most carelessly used insecticide of these pesticides, affecting non-target species such as finfishes, shellfishes, etc. (Reddy et al. 1983). It undergoes biomagnifications across the food chain due to the persistent presence of Triazophos in the ecosystem, creating significant concern for human health. Experiments on the adverse effect of Triazophos on freshwater crabs have shown major changes in the enzymes action pathways of various metabolic reactions (Geethanjali 1985). spinosad is a new type of natural-origin insecticide or biopesticide. spinosad is produced by one or more chemical mutants of *Saccharopolyspora spinosa*, the naturally occurring actinomycetes soil bacterium (Mertz & Yao 1990) spinosad has been used to control insects from the Lepidoptera, Diptera, and Thysanoptera orders, as well as certain Coleoptera and Orthoptera species (Thompson et al. 2000). It's a stomach toxin with some contact action, and it has some control over little beetle larvae (Thompson et al. 2000). The nicotinic receptors activate the acetylcholine nerve system, which kills insects. Some effects on GABA and other nervous systems

may occur (Salgado 1997, 1998). Synthetic pyrethroids were developed for public health and agricultural purposes in the 1970s. But the use has grown over the last two decades. They are non-systemic insecticides. Cypermethrin is a type-II pyrethroid that acts by blocking the Na channels and by affecting the activity of GABA nerve filament receptors (Dobsikova et al. 2006). In addition to pests, the ecology of non-target species often appears to be affected. With 96 h LC_{50}s ranging from $0.01–5.0 \mu g.L^{-1}$, cypermethrin is a strong toxic agent for fish and many aquatic non-chordates (Sarkar et al. 2005, Carriquiriborde et al. 2007).

These pesticides enter the water bodies through agricultural runoff water and impact the non-target organisms (Usman et al. 2020). Because Tubificid worms are sedentary and extensively spread, they can easily overwhelm the macrobiotic population in freshwater habitats, making them a valuable water pollution biomonitor. Furthermore, because they live in the soil, burrowing and ingesting large amounts of sediment, they are subject to pollution from both interstitial water and particle interaction. They frequently play a prominent part in bioturbation and inorganic matter decomposition (Lagauze`re et al. 2009). There is no evidence of the effects of various pesticides on the enzymatic activities of this worm. While *Branchiura sowerbyi* has been proposed for ecotoxicological studies as a test animal, there is no data available on the effects of various pesticides on the enzyme activities of this worm. However, very little evidence is available on the impact of various toxic substances on other Tubificid worms (Gillis et al. 2002, 2004, Maestre et al. 2009, Lobo et al. 2016).

Exposure to xenobiotics results in reactive oxygen species or ROS formation. Oxidative stress is caused by an imbalance in the ratio of pro-oxidants and antioxidants. Toxic substances such as insecticides, heavy metals as well as herbicides are toxic since the development of ROS causes oxidative stress in aquatic organisms (Usman et al. 2020). Oxidative stress occurs mainly through the development of reactive oxygen species (ROS) and can damage lipids, proteins, and DNA, leading to enzyme loss of function and structural integrity, and can cause inflammatory processes (Ozyurt et al. 2004). In most cases, an exceptional concentration of ROS, which might result in significant degeneration of the cell structure, is regarded as an effective oxidative damage signal (Barzilai & Yamamoto 2004). Oxidative damage is caused by three factors: (a) a rise in the generation of oxidants, (b) a decrease in the availability of antioxidants, and (c) a failure to mitigate oxidative harm (Das et al. 2010). Superoxide (O_2^-), one of the parent forms of reactive oxygen species, is a very reactive molecule, but can be converted by superoxide dismutase (SOD) to H_2O_2 and then by enzymes such as

catalase (CAT) to oxygen and water (Klotz & Steinbrenner 2017). The analysis of changes in the activity of antioxidant enzymes such as CAT could therefore be an efficient way of marking oxidative stress, and changes in their activity and other biomarkers may be a potential tool in the aquatic toxicological study (Kumari et al. 2014, Kiliç & Kiliç 2017).

In evaluating the health of aquatic organisms, several researchers have proposed the use of oxidative biomarkers and more in-depth studies are required to evaluate an exact cause-effect relationship (Nussey et al. 2000, Vutukuru 2003). But very limited data is available concerning the sublethal toxicity of different pollutants on *Branchiura sowerbyi* (Bhattacharya et al. 2021b). There is no previous report on the toxicity of organophosphate Triazophos, biopesticide spinosad, and synthetic pyrethroid insecticide cypermethrin in *B. sowerbyi*. Hence, a laboratory study of the tubificidal worm *B. sowerbyi* as a function of the organophosphate insecticide Triazophos, biopesticide spinosad, and synthetic pyrethroid insecticide cypermethrin was therefore carried out to study the efficacy of this method. This research intends to study the oxidative stress induced by organophosphate pesticide Triazophos, Biopesticide spinosad, and synthetic pyrethroid insecticide cypermethrin on *Branchiura sowerbyi*, the most common benthic worm of Oligochaeta as well as an important fish food organism. Finally, integrated biomarker response (IBR) analysis was conducted for a better understanding of the toxic effects of these selected pesticides on *B. sowerbyi*. The knowledge gained will further assist in formulating strategies for treating contaminated water bodies with agriculture runoff and keeping aquatic bodies safe for aquatic life to exist.

MATERIALS AND METHODS

Branchiura sowerbyi (Phylum: Annelida, Class: Clitellata, Order: Oligochaeta and Family: Naididae) were obtained from a local unpolluted source, North 24 Parganas, West Bengal, India, and acclimatized in stock aquariums for 24 h in continuously aerated unchlorinated water (temperature $26.8 \pm 0.5°C$, pH 7.6 ± 0.2, free CO_2 12.5 ± 0.5 mg.L^{-1}, dissolved oxygen 6.4 ± 0.7 mg.L^{-1}, total alkalinity 185 ± 5.6 mg.L^{-1} as $CaCO_3$, hardness 125 ± 5.2 mg.L^{-1} as $CaCO_3$). The commercial formulation of an organophosphate pesticide Triazophos was an emulsified concentrate (EC) containing 40% a. i. (40% EC), biopesticide spinosad (45% SC), and synthetic pyrethroid insecticide cypermethrin (10% EC), which were procured from the market. Test chemicals were dissolved in pure distilled water to make a stock solution of 1 g.100 mL^{-1} (1% w/v) each. The 96 h median lethal concentration (LC_{50}) of Triazophos, spinosad and cypermethrin to *Branchiura sowerbyi* was previously recorded using a static

renewal acute toxicity test when the worms were applied to multiple nominal triazophos concentrations (0.0, 4.0, 4.32, 4.80, 5.60, 5.92, 6.40, 7.20, 8.00, 8.80, 9.60, 10.40 and 11.20 mg.L^{-1}), nominal spinosad concentrations (0.0, 3.2, 3.6, 7.2, 10.8, 14.4, 18.0, 21.6, 27.0, 30.6, 36.0 and 36.2 mg.L^{-1}) and nominal cypermethrin concentrations (0.0, 0.2, 0.8, 1.4, 1.8, 2.4, 2.8, 3.2, 3.6, 3.8 and 4.0 mg.L^{-1}) over a 96 h duration. All the required doses of test chemicals were made by adding the required amounts of triazophos, spinosad, and cypermethrin with unchlorinated tap water. The 96 h LC_{50} values of triazophos, spinosad, and cypermethrin for *Branchiura sowerbyi* were experimented and reported to be 5.04 (4.29-5.60), 6.14 (3.98-8.22) and 0.75 (0.39-1.09) mg.L^{-1} respectively by the method of Finney's probit analysis (Sarkar et al. 2016, Sarkar & Saha 2017, 2018). To determine the oxidative stress at sub-lethal level, 2 g of *B. sowerbyi* (mean length of 11.1 ± 0.4 mm) were transferred from the stock into glass beakers (made by Borosil) each containing 1 L of unchlorinated tap water. The physicochemical parameters of water were monitored daily in the experimental bioassay throughout the exposure period (temperature 28.8 ± 0.5 °C, pH 7.5 ± 0.5, free CO_2 12.5 ± 0.5 mg.L^{-1}, dissolved oxygen 5.8 ± 0.5 mg.L^{-1}, total alkalinity 171 ± 7.4 mg.L^{-1} as $CaCO_3$, hardness 125 ± 5.6 mg.L^{-1} as $CaCO_3$). *Branchiura sowerbyi* was then exposed in separate beakers containing triazophos at concentrations of 50% of its 96 h LC_{50} value (2.25 mg.L^{-1}) and 10% of its 96 h LC_{50} value (0.5 mg.L^{-1}), 50% of its 96 h LC_{50} value (3.07 mg.L^{-1}) and 10% of its 96 h LC_{50} value (0.6 mg.L^{-1}) of test chemical spinosad and 50% of its 96 h LC_{50} value (0.38 mg.L^{-1}) and 10% of its 96 h LC_{50} value (0.08 mg.L^{-1}) of test chemical cypermethrin. Along with the treatments, a separate control group of non-exposed test organisms was also maintained. The duration of this experiment was 96 h. On the first day of the experiment, initial doses were treated. 10% of test water was replaced every 24 h by stock water and 10% of the initial concentration of three test chemicals was added immediately to test the water to make a fixed concentration. An aerator was used to provide continuous aeration during the experiment. Three replicates were used in the experiment. The same method was followed by previous authors (Bhattacharya et al. 2021b, Chatterjee et al. 2021). From each replicate, 1 g of test organism was taken at every exposure time i.e. 24, 48, 72, and 96 h followed by homogenization in 0.1 M phosphate buffer at pH 7.6. The homogenate was then centrifuged through HERMLE Labortechnik for 10 min @ 10000 rpm. The resultant product or supernatant was preserved at −20 °C till further examination. Catalase (CAT) activity was measured using a standard protocol (Beers & Sizer 1952) after the melting of hydrogen peroxide. CAT units are expressed as units of activity per milligram of protein (U/mg protein). The parameters were measured at room temperature (28°C) with a UV visible spectrophotometer (Cecil Aquarius 7400 CE). After subsequent verification of normality using the Shapiro Wilk Test, comparisons between control and exposed worms were conducted through two-way ANOVA followed by Tukey Test. Integrated biomarker response (IBR) analysis was carried out as per Beliaeff and Burgeot (2002). The result of the IBR analysis was presented in a star plot. Results are summed up as mean ± standard deviation (SD). It was agreed that the degree of statistical significance was p < 0.05.

RESULTS AND DISCUSSION

In the case of triazophos, CAT activity increased significantly in a concentration and duration-dependent manner both initially and gradually compared to control (Fig. 1; p<0.05). At a concentration of 2.25 mg.L^{-1} during the 96 h exposure period, the highest induction in CAT activity was observed. Significant differences (p<0.05) between groups treated with Triazophos (0.5 and 2.25 mg.L^{-1}) were observed within each exposure period (24 and 96 h).

In the case of spinosad, CAT activity increased significantly in a concentration and duration-dependent manner both immediately and gradually in comparison to control (Fig. 2; p<0.05). At a concentration of 3.07 mg.L^{-1} during the 96h exposure period, the highest induction in CAT activity was observed. Significant differences (p<0.05) between groups treated with spinosad (0.6 and 3.07 mg.L^{-1}) were observed within each exposure period (24 and 96h).

In the case of cypermethrin, CAT activity increased significantly in a concentration and duration-dependent way both immediately and gradually in comparison to control (Fig. 3; p<0.05). At a concentration of 0.38 mg.L^{-1} during the 96 h exposure period, the highest induction in CAT activity was observed. Significant differences (p<0.05) between groups treated with cypermethrin (0.08 and 0.38 mg.L^{-1}) were observed within each exposure period (24 and 96 h).

In the case of cypermethrin, triazophos, and spinosad, T2-96 h is the most affected group and as per the IBR index, the rank of the most affected groups was: T2-96 h > T1-96 h > T2-24 h > T1-24 h (Fig. 4) whereas all control groups (C-24 h and C-96 h) remains unaffected.

As per IBR analysis based on the toxic effects of the selected toxicants on catalase activity of *Branchiura sowerbyi* after 24 and 96 h of exposure, the rank of these three toxicants could be ordered as cypermethrin > triazophos > spinosad (Fig. 5).

A complex equilibrium is maintained between the generation of ROS and cellular antioxidative defense enzymes under normal circumstances (Kamel et al. 2012). Pesticides
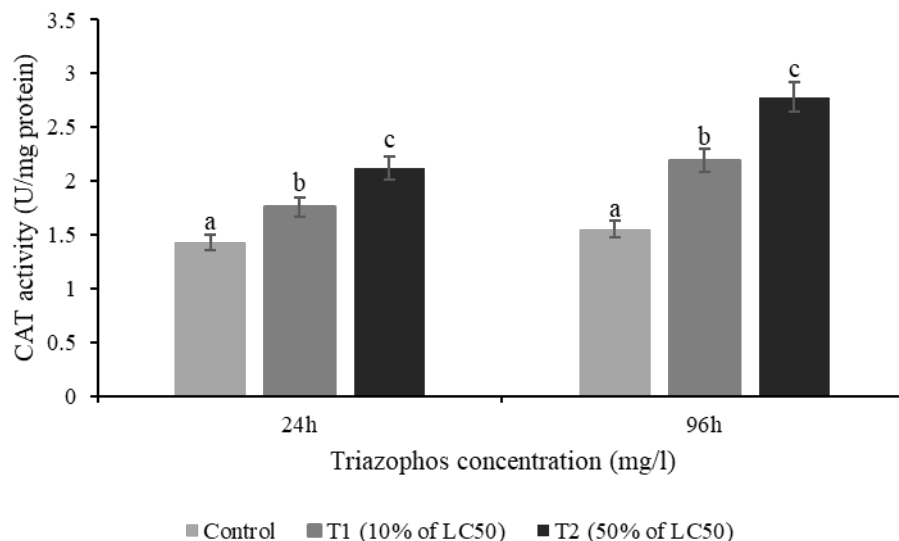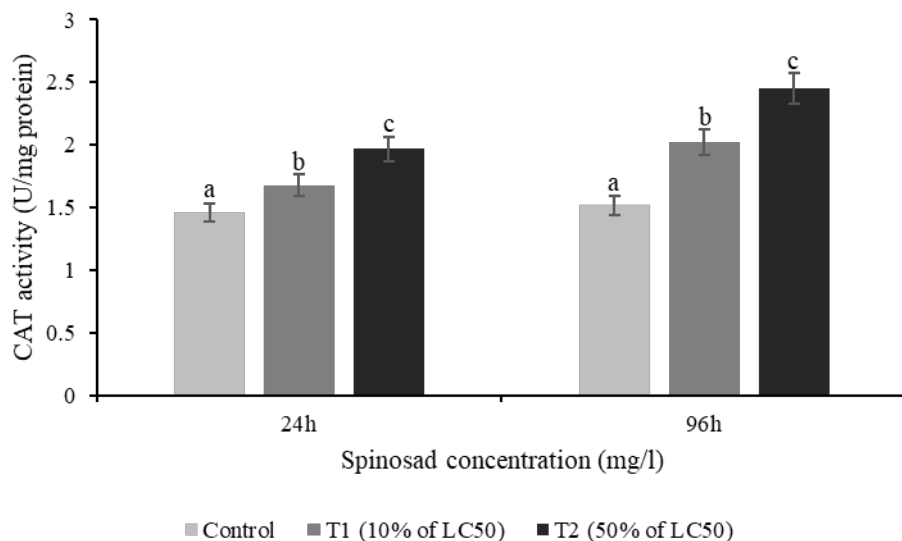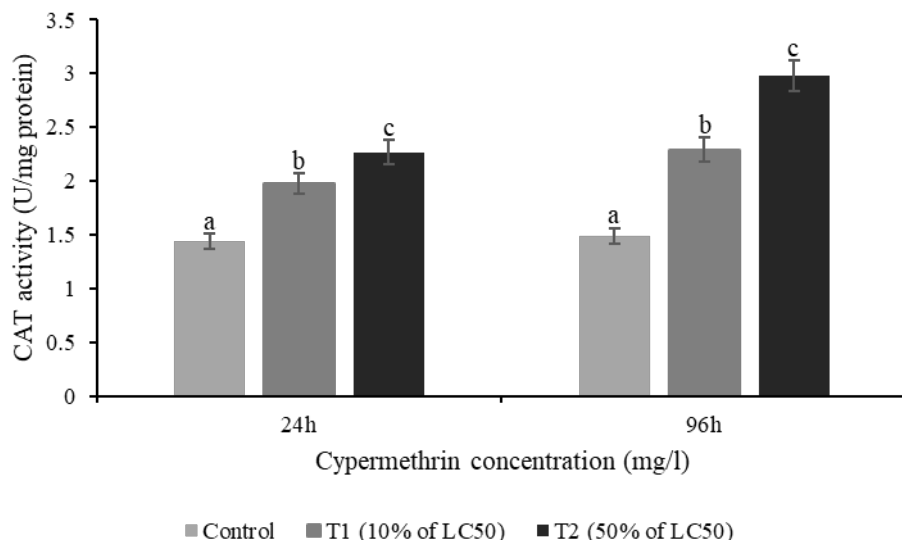
Fig. 1: Effects of different Triazophos sublethal concentrations on catalase (CAT) levels in *Branchiura sowerbyi* during different periods of exposure (24, 48, 72, and 96 h). A significant difference within the same exposure period is indicated by different letters (a-c) (p < 0.05). T1 shows the concentration of triazophos at 10% of its 96 h LC_{50} value (0.5 mg.L^{-1}); T2 shows the concentration of triazophos at 50% of its 96 h LC_{50} value (2.25 mg.L^{-1}). Different letters (a-c) indicate a significant difference (p < 0.05) within the same exposure period.

Fig. 2: Effects of different spinosad sublethal concentrations on catalase (CAT) levels in *Branchiura sowerbyi* during different periods of exposure (24, 48, 72, and 96 h). A significant difference within the same exposure period is indicated by different letters (a-c) (p < 0.05). T1 shows the concentration of spinosad at 10% of its 96 h LC_{50} value (0.6 mg.L^{-1}); T2 shows the concentration of spinosad at 50% of its 96 h LC_{50} value (3.07 mg.L^{-1}). Different letters (a-c) indicate a significant difference (p < 0.05) within the same exposure period.

can cause oxidative damage in species by disrupting ideal redox homeostasis, which can lead to physiological, biochemical, and morphological alterations (Chatterjee et al. 2021). Among different antioxidant enzymes, CAT (catalase) is an essential enzyme in the antioxidant system of organisms primarily involved in the detoxification of ROS and H_2O_2 degradation of molecular oxygen and water (Pandey et al. 2001, Usman et al. 2020). An organophosphate insecticide triazophos, biopesticide spinosad and a pyrethroid insecticide cypermethrin induced a substantial increase in catalase activity in the current experiment, which is possibly due to the neutralization of the harmful effect of increased ROS

Fig. 3: Effects of different cypermethrin sublethal concentrations on catalase (CAT) levels in *Branchiura sowerbyi* during different periods of exposure (24, 48, 72, and 96 h). A significant difference within the same exposure period is indicated by different letters (a-c) (p < 0.05). T1 shows the concentration of cypermethrin at 10% of its 96 h LC_{50} value (0.08 mg.L^{-1}); T2 shows the concentration of cypermethrin at 50% of its 96 h LC_{50} value (0.38 mg.L^{-1}). Different letters (a-c) indicate a significant difference (p < 0.05) within the same exposure period.
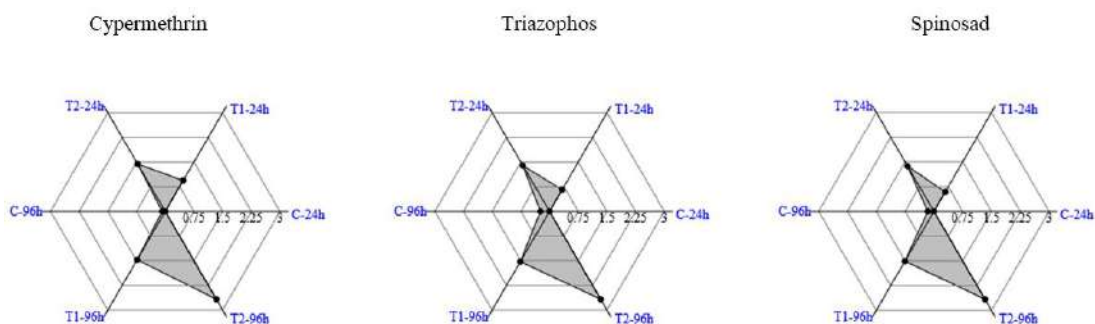
Fig. 4: Integrated Biomarker Response (IBR) of Catalase measured in *Branchiura sowerbyi* after sublethal exposure to cypermethrin, triazophos, and spinosad. C indicates control (0 mg.L^{-1}), T1 indicates the concentration of the toxicant at 10% of its 96 h LC_{50} value; T2 indicates the concentration of the toxicant at 50% of its 96 h LC_{50} value.

generation induced by the toxicant (Kumari et al. 2014). A comparable form of an increase in CAT activity in *Tubifex tubifex* after exposure to different pesticides was also observed by previous researchers (Mosleh et al. 2014, Di et al. 2016, Bhattacharya et al. 2021a, Chatterjee et al. 2021,).

Integrated biomarker response (IBR) analysis is a very useful method for measuring contaminants in the water ecosystems and is very useful for evaluating environmental stress (Li et al. 2011, Chang et al. 2020). A higher IBR value than the control indicates that the environment is more stressful for the species, whereas a lower value indicates optimum conditions (Bhattacharya et al. 2020). IBR analysis revealed that larger concentrations of these selected toxicants generate more stressful conditions for the organism than lower

concentrations and that the stress increases as the exposure period increases.

CONCLUSION

Results of this experiment showed that *Branchiura sowerbyi* exhibited alterations in oxidative stress parameters with the integration of an organophosphate insecticide triazophos, biopesticide spinosad, and a pyrethroid insecticide cypermethrin. As a result, current studies on the toxicity of organophosphate insecticide triazophos, biopesticide spinosad, and pyrethroid insecticide cypermethrin to *Branchiura sowerbyi* indicate that oxidative stress biomarkers are an important method for assessing the intricately designed health status of aquatic species, including benthic macro-invertebrate
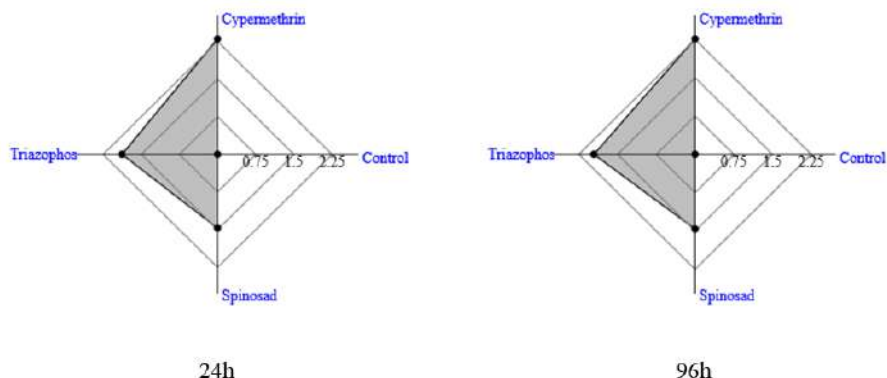
Fig. 5: Integrated Biomarker Response (IBR) for catalase activity in *Branchiura sowerbyi* after 24 and 96 h of sublethal exposure to cypermethrin, triazophos, and spinosad.

animals under stress. The pyrethroid pesticide cypermethrin caused more stressful conditions followed by the organophosphate, triazophos, and biopesticide spinosad. However, further studies are required to extract at the ultrastructural level the toxic effects of organophosphate insecticide Triazophos, biopesticide spinosad, and synthetic pyrethroid insecticide cypermethrin on *Branchiura sowerbyi* and to mitigate its toxicity using the appropriate plant extract.

ACKNOWLEDGMENT

REFERENCES

Abhilash, P.C. and Singh, N. 2009. Pesticide use and application: an Indian scenario. J. Hazard. Mater., 165(1-3):1-12. doi: https://10.1016/j.jhazmat.2008.10.061.

Barzilai, A. and Yamamoto, K. 2004. DNA damage responses to oxidative stress. DNA Repair (Amst), 3(8-9): 1109-1115. doi: https://10.1016/j.dnarep.2004.03.002.

Beddard, F.E. 1892. A new branchiate Oligochate (*Branchiura sowerbyi*). Quat. J. Microscop. Sci., 33: 325-341.

Beers, R.F. and Sizer, I.W. 1952. A spectrophotometric method for measuring the breakdown of hydrogen peroxide. J. Biol. Chem., 195(1): 133–140. https://doi.org/10.1016/S0021-9258(19)50881-X, PMID: 14938361

Beliaeff, B. and Burgeot, T. 2002. Integrated biomarker response: A useful tool for ecological risk assessment. Environ. Toxicol. Chem. Int. J., 21(6): 1316-1322. DOI: https://10.1002/etc.5620210629. PMID: 12069320.

Bhattacharya, R., Chatterjee, A., Chatterjee, S. and Saha, N.C. 2021a. Oxidative stress in benthic oligochaete worm, *Tubifex tubifex* induced by sublethal exposure to a cationic surfactant cetylpyridinium chloride and an anionic surfactant sodium dodecyl sulfate. Comp. Biochem. Physiol. Part - C Toxicol. Pharmacol., 16: 240. DOI: https://doi.org/10.1016/j.cbpc.2020.108906.

Bhattacharya, R., Chatterjee, A., Chatterjee, S. and Saha, N.C. 2021b. Acute toxicity and impact of sublethal exposure to commonly used surfactants sodium dodecyl sulfate, cetylpyridinium chloride, and sodium Laureth sulfate on oxidative stress enzymes in oligochaete worm *Branchiura sowerbyi* (Beddard, 1892). Aquacult. Res., 11: 1-13. https://doi.org/10.1111/are.15501

Carriquiriborde, P., Diaz, J., Mugni, H., Bonetto, C. and Ronco, A. E. 2007. Impact of cypermethrinon stream fish population under field use in biotech-soybean production. Chemosphere, 68(4): 613-621. https://doi.org/10.1016/j.chemosphere.2007.02.051

Chang, T., Wei, B., Wang, Q., He, Y. and Wang, C. 2020. Toxicity assessment of municipal sewage treatment plant effluent by an integrated biomarker response in the liver of crucian carp (*Carassius auratus*). Environmental Science and Pollution Research, 27(7): 7280-7288. doi: https://10.1007/s11356-019-07463-2, PMID: 31883072.

Chatterjee, A., Bhattacharya, R., Chatterjee, S. and Saha, N.C. 2021. Acute toxicity of organophosphate pesticide profenofos, pyrethroid pesticide cyhalothrin and biopesticide azadirachtin and their sublethal effects on growth and oxidative stress enzymes in benthic oligochaete worm, *Tubifex tubifex*. Comp. Biochem. Physiol. C Toxicol. Pharmacol., 242: 108943. doi: https://10.1016/j.cbpc.2020.108943.

Das, J.S., Ravikanth, V.V. and Sujatha, M. 2010. Nitric oxide as a major risk factor for oxidative stress in coronary artery disease: a preliminary investigation. Sci. Culture, 76(5-6): 174-175.

Di, S., Zhang, W., Chen, L., Zhou, Z. and Diao, J. 2016. Toxicokinetics and oxidative stress in *Tubifex tubifex* exposed to hexachlorocyclohexane isomers. RSC Adv., 6: 19016–19024. https://doi.org/10.1039/c5ra26207k

Dobsikova, R., Velisek, J., Wlasow, T., Gomulka, P., Svobodova, Z. and Novotny, L. 2006. Effects of cypermethrin on some hematological, biochemical, and histopathological parameters of common carp (*Cyprinus carpio* L.). Neuro. Endocrinol. Lett., 27 (suppl.2): 101-105.

Geethanjali, K. 1985. Effects of organochloride pesticide BHC on the physiology of edible freshwater crab *Oziotelphusa senex*. M.Phil Thesis, S.V. University Tirupati, India.

Gillis, B.L., Diener, L.C., Reynoldson, T.R. and Dixon, D.G. 2002. Cadmium-induced production of a metallothionein-like protein in *Tubifex tubifex* (Oligochaeta) and *Chironomus riparius* (Diptera): Correlation with reproduction and growth. Environ. Toxicol. Chem., 21: 1836-1844. https://doi.org/10.1002/etc.5620210911

Gillis, P.L., Reynoldson T.B. and Dixon, D.G. 2004. Natural variation in a metallothionein-like protein in *Tubifex tubifex* in the absence of metal exposure. Ecotoxicol. Environ. Saf., 58(1): 22-28. doi: https://10.1016/j.ecoenv.2003.08.016.

Kamel, N., Jebali, J., Banni, M., Khedher, S.B., Chouba, L. and Boussetta, H. 2012. Biochemical responses and metals levels in *Ruditapes decussatus* after exposure to treated municipal effluents. Ecotoxicol. Environ. Saf., 82: 40-46. DOI: https://10.1016/j.ecoenv.2012.05.008.

Kiliç, V. and Kiliç, G. 2017. Antioxidative responses in *Tubifex tubifex* against thallium-induced oxidative stress. Anadolu Univ. J. Sci. Technol. – C Life Sci. Biotechnol., 6: 1–10. https://doi.org/10.18036/aubtdc.288885

Klotz, L.O. and Steinbrenner, H. 2017. Cellular adaptation to xenobiotics: Interplay between xenosensors, reactive oxygen species, and FOXO transcription factors. Redox Biol., 25: 101. https://doi.org/10.1016/j.redox.2017.07.015

Kumari, K., Khare, A. and Dange, S. 2014. The applicability of oxidative stress biomarkers in assessing chromium-induced toxicity in the fish *Labeo rohita*, BioMed Res. Int., 6: 1-11, DOI:http://dx.doi.org/10.1155/2014/782493

Lagauze`re, S., Boyer, P., Stora, G. and Bonzom, J.M. 2009. Effects of uranium-contaminated sediments on the bioturbation activity of *Chironomus riparius* larvae (Insecta, Diptera) and *Tubifex tubifex* worms (Annelida, Tubificidae). Chemosphere, 76(3): 324-334, DOI: https://10.1016/j.chemosphere.2009.03.062. PMID: 19403158.

Li, Z.H., Velisek, J., Grabic, R., Li, P., Kolarova, J. and Randak, T., 2011. Use of hematological and plasma biochemical parameters to assess the chronic effects of fungicide propiconazole on a freshwater teleost. Chemosphere, 83: 572-578. https://doi.org/10.1016/j.chemosphere.2010.12.024

Lobo, H., Méndez-Fernández, L., Martínez-Madrid, M., Daam, M.A. and Espíndola, E.L.G. 2016. Acute toxicity of zinc and arsenic to the warmwater aquatic oligochaete *Branchiura sowerbyi* as compared to its coldwater counterpart *Tubifex tubifex* (Annelida, Clitellata). J. Soils Sed., 16: 2766-2774. https://doi.org/10.1007/s11368-016-1497-z

Maestre, Z., Martinez-Madrid, M. and Rodriguez, P. 2009. Monitoring the sensitivity of the oligochaete *Tubifex tubifex* in laboratory cultures using three toxicants. Ecotoxicol. Environ. Saf., 72(8): 2083–2089, DOI: https://10.1016/j.ecoenv.2009.08.001. PMID: 19720397.

Mishra, K.D. and Bohidar, K. 2005. Toxicity of pesticides, carbaryl, and cartap hydrochloride on the freshwater teleost *Channa punctatus* (Bloch). J. Adv. Zoo., 26(1): 20-23.

Mosleh, Y.Y., Mofeed, J., Afifi, M. and Almaghrabi, O.A. 2014. Biological effects of pyrimethanil on aquatic worms (*tubifex*) under laboratory conditions. Bull. Environ. Contam. Toxicol., 92: 85-89. https://doi.org/10.1007/s00128-013-1153-x.

Nussey, G., Van Vuren, J.H.J. and Du Preez, H.H. 2000. Bioaccumulation of chromium, manganese, nickel, and lead in the tissues of the moggel, *Labeo umbratus* (Cyprinidae), from Witbank Dam, Mpumalanga. Water SA., 26(2): 269–284.

Ozyurt, H., Sogut, S., Yildirim, Z., Kart, L. and Iraz, M. 2004. Inhibitory effect of caffeic acid phenethyl ester on bleomycine-induced lung fibrosis in rats. Clin. Chim. Acta, 339(1-2): 65-75, doi: https://10.1016/j.cccn.2003.09.015.

Pandey, S., Ahmad, I., Parvez, S., Bin-Hafeez, B., Haque, R. and Raisuddin, S. 2001. Effect of endosulfan on antioxidants of freshwater fish *Channa punctatus* bloch: Protection against lipid peroxidation in the liver by copper preexposure. Arch. Environ. Contam. Toxicol., 41: 345–352. https://doi.org/10.1007/s002440010258.

Pereira, W.E., Domagalski, J.L., Hostettler, F.D., Brown, L.R. and Rapp, J.B. 1996. Occurrence and accumulation of pesticide and organic contaminants in river sediments, water, and clam tissue from the Joaquin river and tributaries California. Environ. Toxicol. Chem., 15(2): 172-180. https://doi.org/10.1002/etc.5620150216

Reddy, P.S., Bhagyalakshmi, A. and Ramamurthi., R. 1983. Effect of sumithion on ovarian growth of a freshwater rice field crab (*Oziotelphusa senex senex* fabricius). Toxicol. Lett., 18(3): 273-276, https://doi.org/10.1016/0378-4274(83)90106-6.

Salgado, V.L. 1997. The modes of action of spinosad and other insect control products. Down to Earth, 52: 35-43.

Salgado, V.L. 1998. Studies on the mode of action of spinosad: insect symptoms and physiological correlates. Pest. Biochem Physiol., 60(2): 91-102. https://doi.org/10.1006/pest.1998.2332

Sarkar, B., Chatterjee, A., Adhikari, S. and Ayyappan, S. 2005. Carbofuran and cypermethrin induced histopathological alteration in the liver of *Labeo rohita* (Hamilton) and its recovery. J. Appl. Ichthyol., 21(2):131-135.

Sarkar, C. and Saha, N.C. 2017. Effects of a pyrethroid insecticide cypermethrin on benthic Oligochaete worm, *Branchiura sowerbyi* (Beddard, 1892). Glob. J. Res. Anal., 6(7): 499-500.

Sarkar, C. and Saha, N.C. 2018. Acute toxicity of biopesticide spinosad to benthic Oligochaete worm, *Branchiura sowerbyi,* and the fry of Common Carp, *Cyprinus carpio*. Int. J. of Life Sci., 6(1): 187-193.

Sarkar, C., Bej, S. and Saha, N.C. 2016. A study on the acute toxicity of Triazophos to *Branchiura sowerbyi* (Beddard, 1892) and their behavioral changes. Int. J. Sci. Res., 5(5): 665-667. DOI: 10.36106/ijsr

Thompson, G.D., Dutton, R. and Sparks, T.C. 2000. spinosad: A case study: An example from a natural products discovery program. Pest. Manag. Sci., 56: 696-702. https://doi.org/10.1002/1526-4998(200008)56:8<696::AID-PS182>3.0.CO;2-5

Uno, S., Shiraishi, H., Hatakeyama, S., Otsuki, A. and Koyama, J. 2001. Accumulative characteristics of pesticide residue in organs of bivalves (*Anodonta woodiana* and *Corbicula leana*) under natural conditions. Arch. Environ. Contam. Toxicol., 40(1): 35-47. doi: https://10.1007/s002440010146. PMID: 11116339.

Usman, T., Abdullah, S., Naz, H., Abbas, K., Shafique, L. and Siddique, Q. 2020. Acute toxic effect of technical grade insecticides on behavior, catalase activity, and total protein contents of fish, *Ctenopharyngodon Idella*. Pak. J. Zool., 52(5): 2023-2026, DOI:https://dx.doi.org/10.17582/journal.pjz/20181103091108

Vutukuru, S.S. 2003. Chromium induced alterations in some biochemical profiles of the Indian major carp, *Labeo rohita* (Hamilton), Bull. Environ. Contam Toxicol., 70(1): 118-123. doi: https://10.1007/s00128-002-0164-9. PMID: 12478433.

WHO 2003. Pesticide Residue in Food. In: International Program on Chemical Safety FAO/WHO Meeting on Pesticide Results Evaluations 2002, Part 2 Toxicology.

Treatment of Saline Water Using Electrocoagulation Process with Monopolar Connection of Electrodes

Isra'a Sadi Samaka*, Ahmed Samir Naje†** and Hussein A. M. Al-Zubaidi*

*Department of Environmental Engineering, College of Engineering, University of Babylon, Babylon, Iraq
**College of Water Resource Engineering, AL-Qasim Green University, Babylon 51031, Iraq
†Corresponding author: Ahmed Samir Naje; ahmednamesamir@yahoo.com

ABSTRACT

For the availability of drinking water, saline water treatment has become exceedingly necessary. The purpose of this research was to determine how efficient electrocoagulation (EC) with monopolar iron electrodes was for desalinating water from Iraq's Sawa Lake. Absolute dissolved solids (TDS), chloride (Cl), bromine (Br), and sulfate (SO_4) are some of the salty water forms that are being targeted. The impacts of five considerations on treatment efficiency were studied, including current (I), detention time (RT), pH, speed of mixing stirring (Mrpm), and inter-electrode distance (IED). I=0.8A, RT=80 minutes, pH=8, IED=1cm, and Mrpm=500 were found to be the best values. TDS, Cl, Br and SO_4 removal efficiencies were 91 percent, 93 percent, 92 percent, and 90 percent, respectively, under ideal conditions. It can be inferred that the EC system used in this research was operative in removing salts from the water of Sawa lake.

INTRODUCTION

Freshwater supplies have been depleting in recent years around the world, necessitating water treatment and recycling. Desalination is an effective process to treat the freshwater depletion crisis because seawater accounts for more than 98 percent of all available water on Earth (Hanafiah et al. 2011). The removal of minerals and salts from using water is known as desalination. Distillation of thermal, nano type of filtration, adsorption, reverse osmosis (RO), electrocoagulation, electrodeposition, and electrooxidation are some of the methods that can be used to treat contaminated water (Greenlee et al. 2009). Any of the approaches mentioned, however, have significant flaws. The energy usage and costs of thermal desalination for water desalination at 45 percent recovery are approximately 13 kWh.m^{-3}. Around 40% of the world's water is desalinated by thermal means (Singleton et al. 2011). In the last three decades, RO has dominated technology, especially in energy-rich countries like Saudi Arabia. For desalination of salty water at 40 percent retrieval, RO will operate at a rate of about 3% kWh.m^{-3} (Loow et al. 2015). The disinfectant chlorine added to water will dissolve the polyamide membrane, necessitating a dechlorination step until separation (Cipollina et al. 2009). Furthermore, replacing a membrane is an expensive operation (Pérez-González et al. 2012). The cost of advanced oxidation processes is high

(Elimelech & Phillip 2011). Although adsorption and nanofiltration methods aren't often enough to meet discharge limits (Glater et al. 1994). However, one of the options for water desalination is to use the electrocoagulation (EC) process. Electrocoagulation is the method of using an electric current to destabilize suspended pollutants and molten elements in an aquatic medium. An electrolytic cell consisting of Plexiglas, glass, copper, anode, and cathode are the key components of an EC reactor. Metal plates make up the anode and cathode, with the anode referred to as "sacrificial electrodes." These electrodes are typically constructed with the same or different components, such as iron (Fe) and aluminum (Al). The EC procedure, which uses a simple tool and produces a small amount of sludge, has been successfully used to extract salts from salty water (Mohammad et al. 2015, Martinez-Huitle & Ferro 2006). This approach is distinguished by its safety, simplicity, ease of control, and selectivity, as well as its usability, automation potential, and environmental compatibility. As electrodes are used in the EC procedure, iron dissolves and acts as a coagulant agent, releasing hydrogen gas at the cathode. Different aquatic iron species are produced during iron dissolution at the cathode (Panizza & Cerisola 2011). Former research has shown that the EC system is an important technique for treating various water pollutants such as arsenic, fluoride, boron, and nitrite in textile wastewater, chemical fiber wastewater, algae or microorganisms, oily

wastewater, restaurant wastewater, and sewage water arsenic, fluoride, boron, and nitrite in sewage water (Bousher et al. 1997, Chen 2004, Mollah et al. 2001). Different metal ions, such as Zn, Ag, Cu, Co, and Mn, were removed using the EC method (Naje et al. 2015). The goals of this investigation are to decide on peak settings influencing the removal efficiency of TDS, Cl, Br, and SO_4 from saline water using the electrocoagulation system with static electrodes under monopolar electrical relation, and to assess the efficacy of the electrocoagulation method for saline water treatment.

MATERIALS AND METHODS

Characteristics of Saline Water

Sawa Lake, Iraq, provided the salty water samples. Table 1 summarizes the features of saline water. Sawa Lake is about 240 kilometers southwest of Baghdad, in the AlMuthanna province of southern Iraq, between 31o 18' N and 45o 00' E. (Fig. 1). Since the lake has no artificial water sources, groundwater is the primary source of water. The gross surface area is approximately 10 km², the average depth is 5.5 meters, and the average length and width are 5 and 2 kilometers, respectively. The Iraqi Ministry of Health and Environment published a report in 2020 on the physical-chemical characteristics of saline water at Sawa Lake (Abbas et al. 2020). Among Iraq's inland waters, Sawa Lake is thought to have the highest salinity.

Setup of Experiment

The experimental setup for the EC method used in the current analysis is illustrated in Fig. 2. The treatment of salty water from the Lake of Sawa was carried out in a batch reactor made of glass, with a Plexiglas upper layer. TDS, Cl, SO_4, and Br levels were determined in the salty water. The experiment used a reactor with dimensions of 20 cm width, 15 cm length, and 15 cm depth. For each run, the treatment water volume was 4.5 L. Six iron plates were wired in series with the main power supply, with monopolar link anodes and cathodes. The electrodes for both the anode and cathode plates were 10 ∗ 10 cm² with a thickness of 0.1 cm and a spacing between the inner electrodes of 1 cm. 100 cm² is the surface area of each electrode. The electrodes were submerged in salt water after being collected. The negative and positive terminals of the DC power supply are attached to the anode and cathode groups. The stirring speed was regulated by a magnetic field.

Table 1: Features of saline water.

Properties	Values
TDS (mg.L⁻¹)	26263
Cl (mg.L⁻¹)	8498
SO_4 (mg.L⁻¹)	6562
Br (mg.L⁻¹)	6.00
pH	8.25
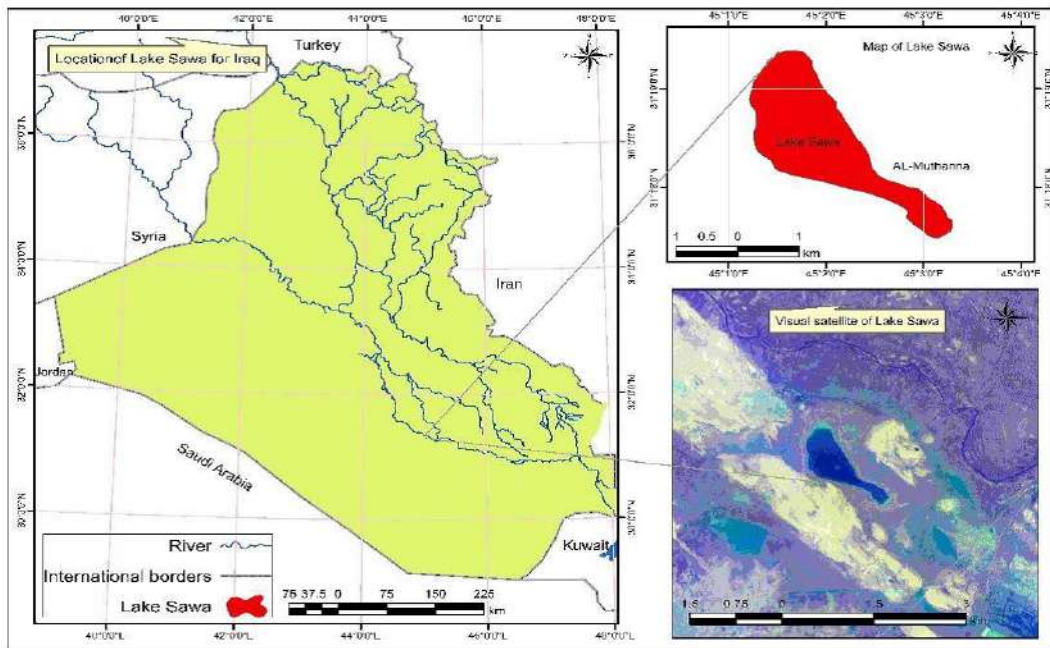
Fig. 1: Lake Sawa (Iraq) on a map.
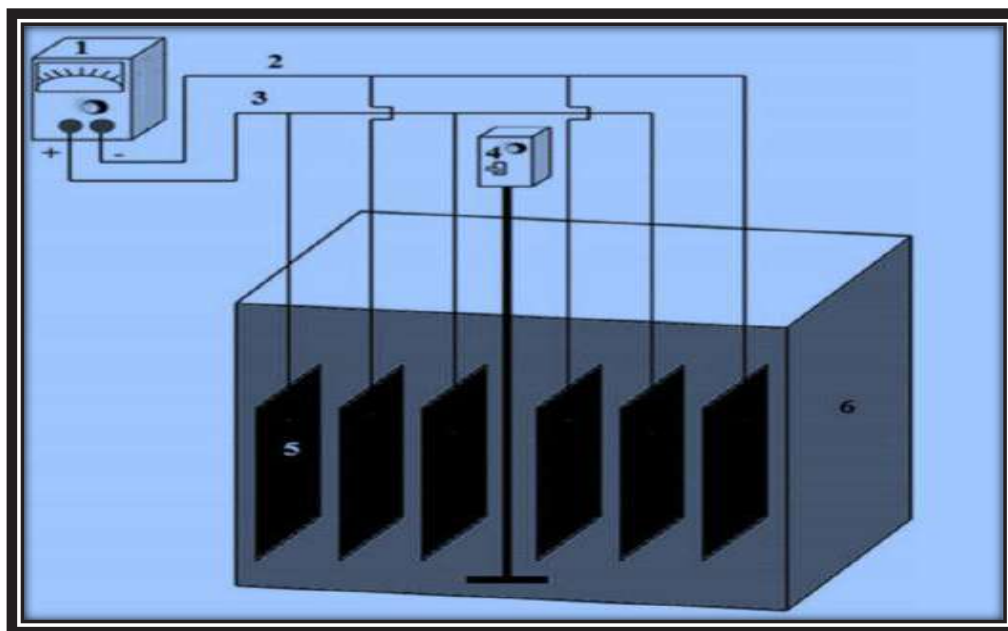
Fig. 2: Experimental configuration diagram: (1) DC power supply; (2) cathode; (3) anode; (4) mechanical stirrer; (5) iron electrodes; (6) EC reactor

When an electric current was passing through the electrodes, anode and cathode reactions occurred on the surface of the inner electrodes.

A DC power supply made by YIZHAN, 0-40V; 0-6 A, China, was used in the current analysis. During each run, the voltage was set to 15 V, and the influence of current was determined between 0.2 A and 1.2 A for 100 minutes. The criteria for removing TDS, Cl, Br, and SO_4 from lake water are mentioned in Table 2. To ensure the accuracy and durability of the results, all experiments were tested for 92 runs to determine the optimum conditions, which were then replicated three times. A multi-range ammeter produced by Aswar DT830D, China, was used to retain the current standard. The electrodes were thoroughly washed with purified water after each cycle. The tests were carried out in the Laboratory, which was set to a temperature of 25°C. The pH of the feed water and product was determined, and the pH was changed to a range of 5 to 11, after which sodium hydroxide or hydrochloric acid solutions were applied to maintain the pH stable for each experiment.

The Analysis of Factors

Table 3 gives the processes and instruments used to assess saltwater contaminants before and during treatment.

RESULTS AND DISCUSSION

Influence of Useful Current and Passage Time

The useful current and reaction time are two significant parameters in the EC mechanism that play a key role in controlling the reactor rate. At different useful current densities (I = 0.2, 0.4, 0.6, 0.8, 1.0, and 1.2) and reaction times (20, 40, 60, 80, and 100), tests were performed to determine the percentage elimination of TDS, Cl, Br, and SO_4 from saline water. Figs. 3, 4, 5 and 6 demonstrate the influence of applied

Table 2: The criteria that have been looked at for the handling of lake water.

Parameter	Unit	Range	Run	Replicated optimal conditions
Current density	A	0.2-1.2	6	3
Reaction time	min	20-100	5	3
pH solution	-	5-11	8	3
IED	cm	0.5-2	4	3
M_{rpm}	rpm	250-750	3	3

Table 3: The criteria of the study and analysis method.

Parameters	Meter/method
pH	pH meter –pHM84
TDS	TDS meter (TDS-EZ, HM Digital)
Electrical Conductivity	HANNA HI-99301
Turbidity	HACH 2100P
Br^-	Ion chromatography
SO_4^{-2}	APHA, gravimetric
Cl^-	Titration (Mohrs Method)

current (I) and reaction time on removal efficiencies. With increasing reaction time, the performance of the EC process increases. At I = 0.8A and RT = 80 min, the best removal efficiencies can be found. 90 percent TDS, 92 percent Cl⁻, 91 percent Br⁻, and 88 percent SO_4^{-2} had the highest removal efficiencies. There is a slight, non-significant rise in removal efficiencies after 80 min, increasing energy usage. As a result, the best operating variables were chosen as 0.8 A and 80 min, which are also consistent with the findings of former research (Heidmann & Calmano 2008, Phalakornkule et al. 2010).

Influence of pH

Former studies also highlighted the significance of pH's impact on water treatment in the EC system. The effect of pH on TDS, Cl, Br, and SO_4 elimination was studied in this analysis by changing the initial pH in the range of 5 to 11 with peak settings Fe- Fe, I = 0.8 A and an 80-minute reaction time. Fig. 7 indicates that at pH 8, TDS, Cl, Br, and SO_4 removal efficiencies increased to 91 percent, 93 percent, 92 percent, and 90 percent, respectively. The presence of water electrolysis, which produces hydrogen and (OH) ions, is responsible
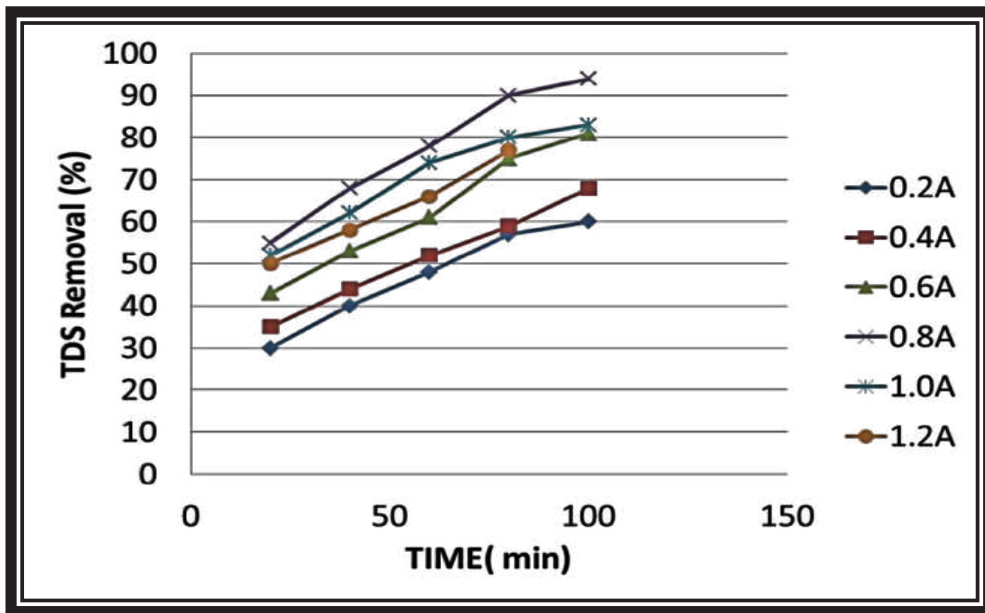
Fig. 3: TDS removal performance as a function of useful current.
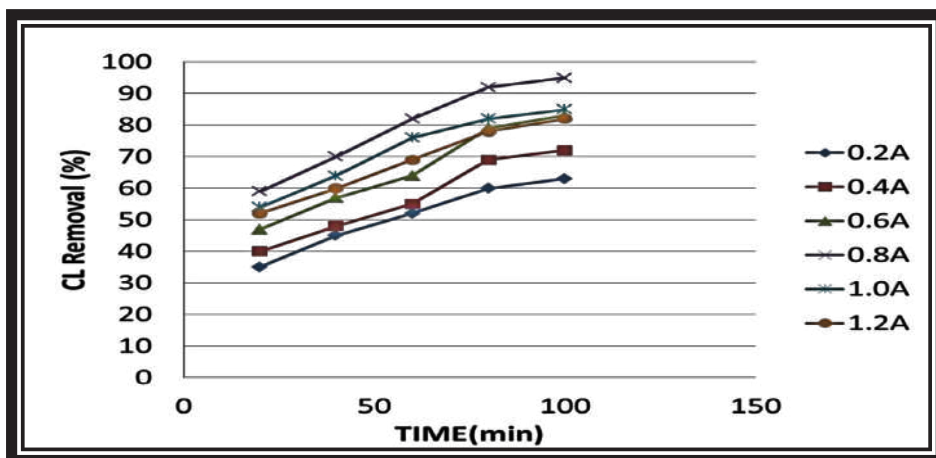
Fig. 4: Cl removal performance as a function of useful current.

for the rise in pH levels. The formation of insoluble $M(OH)_3$ flocs and metal hydroxide can explain why pH remains relatively stable after that. At pH values of 5 and 6 in the acidic phase, and 9, 10, and 11 in the alkaline phase, the findings indicate decreased levels of solubility in iron hydroxide. The peak pH level observed in the current analysis is consistent with the results of former studies (Phalakornkule et al. 2010, Lin & Peng 1996). Saline water with a pH of 8 is perfect.

Influence of Inter-Electrode Distance

To achieve an appropriate electrode surface area and inter-electrode space, the electrode assemblage set-up is important (IED). If the distance between the two electrodes grows, so does their resistance (Murad et al. 2011). As a consequence, the electrical current levels are decreased. Theoretically, increasing the distance between electrodes leads
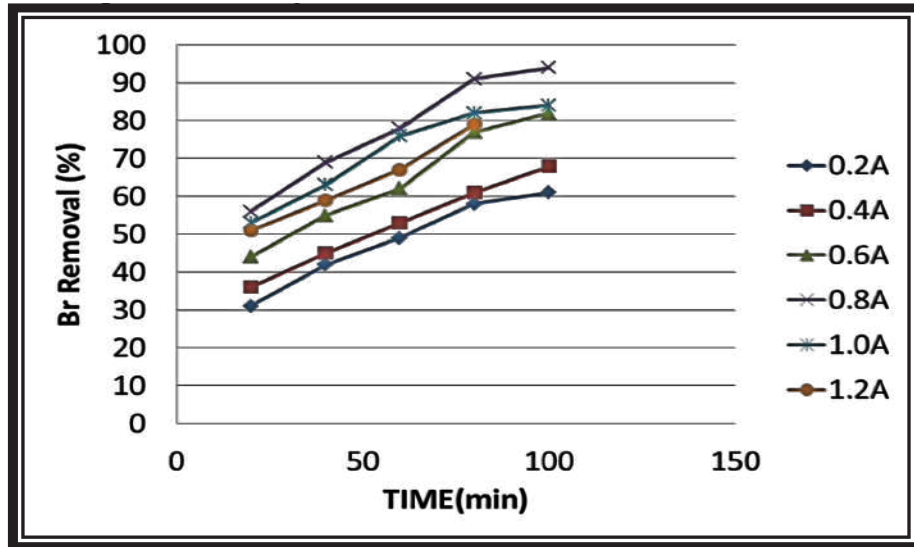
Fig. 5: Br removal performance as a function of useful current.
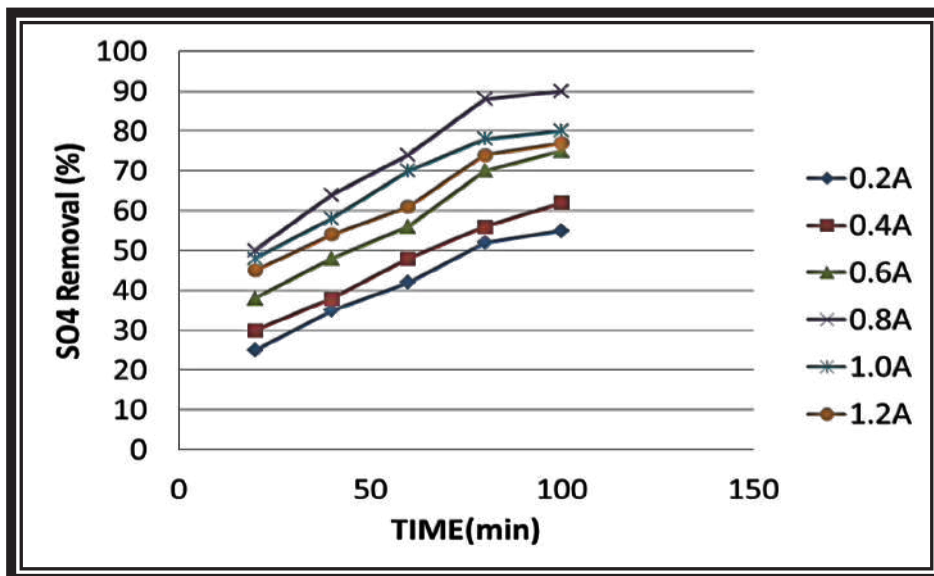
Fig. 6: SO$_4$ removal performance as a function of useful current.

to less contact between ions and hydroxide polymers. The influence of the IED on the EC method's removal efficiency has been shown in former studies. The following equation governs the difference in a voltage drop (IR) (Deverel & Millard 1998, Naje et al. 2015):

$$IR = I \times (d/s \times k) \qquad ...(1)$$

Where I denotes the electric current in Amperes (A), d denotes the distance between the two electrodes in meters, S denotes the active anode surface area in square meters, and k denotes the precise conductivity in Siemens per meter. As the inter-electrode gap (IED) is increased while the anodic surface area and conductivity of the solution remain unchanged, the voltage drop increases. The effect of IED was investigated in the current study using Fe-Fe, I = 0.8A, RT = 80 min, and pH = 8 as peak settings, as seen in Fig. 8. With 1 cm as the middle distance, the best results were obtained. For a change of the gap from 0.5 to 1 cm, the obtained findings were 90 to 91 percent TDS, 92 to 93 percent Cl, 90 to 92 percent Br, and 88 to 90 percent SO_4. Expanding the gap from 1.5 to 2 cm, resulted in lower care efficiencies of 90 to 87 percent for TDS, 91 to 88 percent for Cl, 90 to 87 percent for Br, and 87 to 82 percent for SO_4. Former studies showed that increasing the inter-electrode gap (IED) contributed to
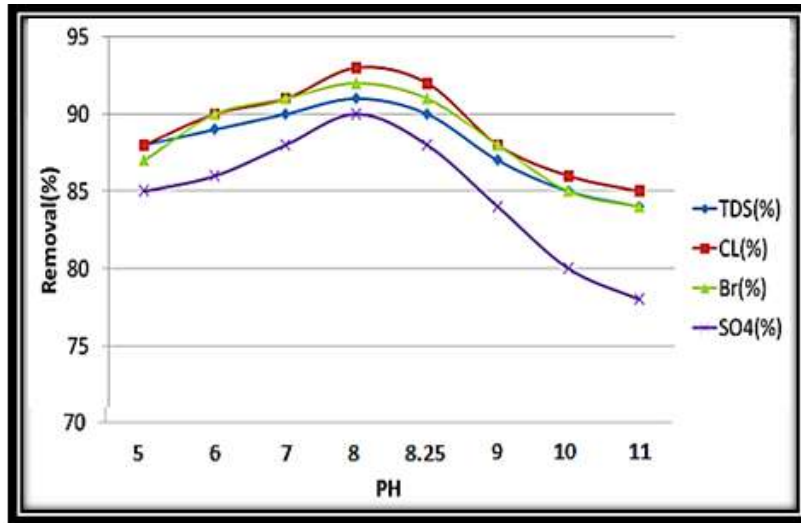
Fig. 7: The pH effect at peak settings.
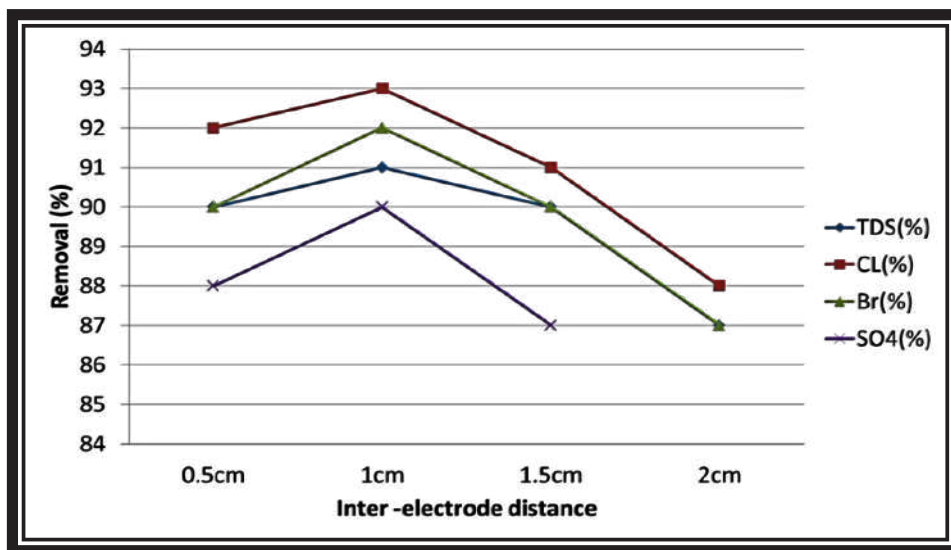
Fig. 8: Effect of inter-electrode distance under optimal conditions.
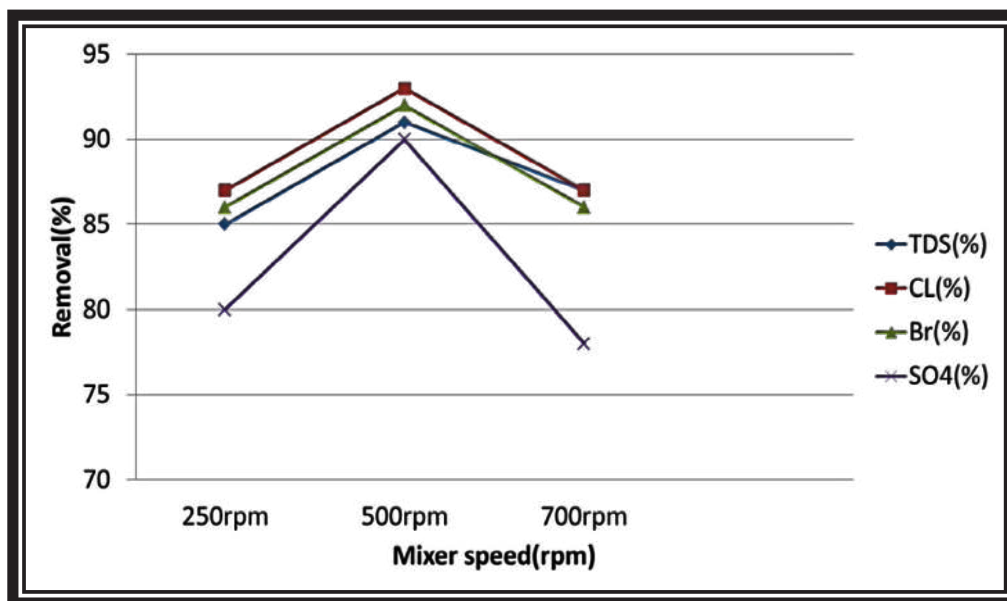
Fig. 9: Influence of mixer speed under peak settings.

a decrease in electrode attraction, which clarified the effect of the final IED on the efficiency of contaminants removal (Aber et al. 2009, Mollah et al. 2004). This was discovered in the iron polymers made, which has a negative impact on the treatment.

Influence of Stirring Speed

The EC method is influenced by the mixing stirring speed (Mrpm). As the stirring rate is increased, emission forms, which is monopolar and connected, making precipitation and mass transfer simpler. As the stirring rate is increased above what is needed, the pollutants that develop inside the reactor degrade, resulting in smaller flocks that are difficult to isolate from the solution (Hamdan & El-Naas 2014, Korbahti & Tanyolac 2009). Treatment reliability suffers as a result of this behavior. Stirring speeds of 250, 500, and 750 rpm were used with peak settings of Fe-Fe, I = 0.8 A, RT = 80 min, and pH = 8 to investigate the effect of agitation speed on TDS, Cl, Br, and SO_4 removal efficiency by EC method. As the speed was changed from 250 to 500 rpm, the maximum treatment performance was achieved. TDS removal performance improved from 85 to 91 percent, Cl from 87 to 93 percent, Br from 86 to 92 percent, and SO_4 from 80 to 90 percent, according to the findings. When the agitation speed was increased from 500 to 750 rpm, the removal performance of TDS, Cl, Br, and SO_4 decreased to 87 percent, 87 percent, 86 percent, and 78 percent, respectively, as seen in Fig. 9. This can be explained by the fact that extreme stirring pace can cause the flocks to break apart

(Moises et al. 2010). Likewise, the higher the stirring level, the more energy was used by the agitator, necessitating higher costs. As a result, the best stirring speed was calculated to be 500 rpm.

CONCLUSION

Water management is critical to ensure that people have access to safe drinking water. Finally, the current research looked at the efficacy of the EC system with iron electrodes for extracting salts TDS, Cl, Br, and SO_4 from aqueous settings. The effects of current (I), passage time (RT), pH, the distance between electrodes (IED), and speed of stirrer (Mrpm) on salt removal were also considered. I = 0.8 A, RT = 80 min, pH = 8, IED = 1 cm, and Mrpm = 500 were the superlative settings achieved. The removal of salts from salty water using EC with a monopolar electrical attachment of iron electrodes is very efficient. The removal efficiencies for TDS, Cl, Br, and SO_4 were 91 percent, 93 percent, 92 percent, and 90 percent, respectively, when the EC process was run under superlative settings. The outcomes of this analysis showed that electrocoagulation is a technically feasible method for removing salts from aqueous settings.

ACKNOWLEDGMENT

REFERENCES

Abbas, A., Al-Raad, M., Hanafiah, M., Ahmed, S.N., Mohammed, S. and Ajeel, A. 2020. Optimized parameters of the electrocoagulation process using a novel reactor with a rotating anode for saline water treatment. Environ. Pollut., 265: 115049.

Aber, S., Amani-Ghadim, A.R. and Mirzajani, V. 2009. Removal of Cr(VI) from polluted solutions by electrocoagulation: modeling of experimental results using artificial neural network. J. Hazard. Mater., 171: 484-490.

Bousher, A., Shen, X. and Edyvean, R.G. 1997. Removal of colored organic matter by adsorption onto low-cost waste materials. Water Res., 31: 2084-2092.

Chen, G. 2004. Electrochemical technologies in wastewater treatment. Sep. Purif. Technol., 38: 11-41.

Cipollina, A., Micale, G. and Rizzuti, L. 2009. Seawater desalination. Conv. Renew. Energy, 11: 51-63

Deverel, S. and Millard, S. 1988. Distribution and mobility of selenium and other trace elements in shallow groundwater of the western San Joaquin Valley, California, Environ. Sci. Technol., 22: 697-702.

Elimelech, M. and Phillip, W.A. 2011. The future of seawater desalination: Energy. Technol. Environ. Sci., 333: 712-717.

Glater, J., Hong, S.K. and Elimelech, M. 1994. The search for a chlorine-resistant reverse osmosis membrane. Desalination, 95: 325-345.

Greenlee, L.F., Lawler, D.F., Freeman, B.D., Marrot, B. and Moulin, P. 2009. Reverse osmosis desalination: Water sources, technology, and today's challenges. Water Res., 43: 2317-2348.

Hamdan, S.S. and El-Naas, M.H. 2014. Characterization of the removal of chromium (VI) from groundwater by electrocoagulation. J. Ind. Eng. Chem., 20: 2775-2781.

Hanafiah, M.M., Xenopoulos, M.A., Pfister, S., Leuven, R.S. and Huijbregts, M.A., 2011. Characterization factors for water consumption and greenhouse gas emissions based on freshwater fish species extinction. Environ. Sci. Technol., 45: 5272-5278.

Heidmann, I. and Calmano, W. 2008. Removal of Cr(VI) from model wastewaters by EC with Fe electrodes. Sep. Purif. Technol., 61: 15-21.

Hussein, A.M., Al-Zubaidi, A., Samir, N., Zaid Abed Al-Ridah, A. and Isam Mohamad Ali, C. 2021. A statistical technique for modeling dissolved oxygen in salt lakes. Cogent Eng., 8: 1-18.

Korbahti, B.K. and Tanyolac, A. 2009. Electrochemical treatment of simulated industrial paint wastewater in a continuous tubular reactor. Chem. Eng. J., 148: 444- 451.

Lin, S.H. and Peng, C.F. 1996. Continuous treatment of textile wastewater by combined coagulation, electrochemical oxidation, and activated sludge. Water Res., 30: 587-592.

Loow, Y.L., Wu, T.Y., Tan, K.A., Lim, Y.S., Siow, L.F., Jahim, J.M., Mohammad, A.W. and Teoh, W.H., 2015. Recent advances in the application of inorganic salt pretreatment for transforming lignocellulosic biomass into reducing sugars. J. Agric. Food Chem., 63: 8349-8363.

Martinez-Huitle, C.A. and Ferro, S. 2006. Electrochemical oxidation of organic pollutants for the wastewater treatment: direct and indirect processes. Chem. Soc. Rev., 35: 1324-1340.

Mohammad, A.W., Teow, Y.H., Ang, W.L., Chung, Y.T., OatleyRadcliffe, D.L. and Hilal, N. 2015. Nanofiltration membranes review: Recent advances and future prospects. Desalination, 356: 226-254.

Moises, T.P. Patricia, B.H., Barrera-Diaz, C.E., Gabriela, R.M. and Natividad, R. 2010. Treatment of industrial effluents by a continuous system: electrocoagulation– activated sludge. Bioresour. Technol., 101: 7761-7766.

Mollah, M.Y.A., Morkovsky, P., Gomes, J.A.G., Kesmez, J.M. and Cocke, D.L. 2004. Fundamentals, present and future perspectives of electrocoagulation. J. Hazard.Mater., 114: 199-210.

Mollah, M.Y.A., Schennach, R., Parga, J.R. and Cocke, D.L. 2001. Electrocoagulation (EC)-science and applications. J. Hazard. Mater., 84, 29-41.

Murad, A.A., Gerish, M.H., Mahgoub, F.M. and Hussein, S. 2011. Physiochemical processes affecting the geochemistry of carbonate aquifer of southeastern Al-Ain area, United Arab Emirates (UAE), Water Air Soil Pollut. 214: 653-665.

Naje, A.S., Chelliapan, S., Zakaria, Z. and Abbas, S.A. 2015. Treatment performance of textile wastewater using electrocoagulation (EC) process under the combined electrical connection of electrodes. J. Electrochem Sci., 10: 5924-5941.

Panizza, M. and Cerisola, G. 2009. Direct and mediated anodic oxidation of organic pollutants. Chem. Rev., 109: 6541-6569.

Pérez-González, A., Urtiaga, A.M., Ibáñez, R. and Ortiz, I. 2012. State of the art and review on the treatment technologies of water reverse osmosis concentrates. Water Res., 46: 267-283.

Phalakornkule, C., Polgumhang, S., Tongdaung, W., Karakat, B. and Nuyut, T. 2010. EC of blue reactive, red disperse and mixed dyes, and application in treating textile effluent. J. Environ. Manage., 91: 918-926.

Singleton, M.S., Gregor, H. and Alfred, H. 2011. Optimization of ramified absorber networks doing desalination. Physical Rev., 83: 016308.

Delineation of Groundwater Salinity Zones in Shefa and Malampa Provinces, Vanuatu

K. K. Kotra*†, S. Bathula and E. Sami***

*†School of Agriculture, Geography, Environment, Ocean, and Natural Sciences, The University of the South Pacific, Emalus Campus, Vanuatu

**Department of Applied Sciences, The Papua New Guinea University of Technology, Lae, Morobe-411, Papua New Guinea

***Department of Water Resources, Ministry of Lands and Natural Resources, Government of Vanuatu, Vanuatu

†Corresponding author: K. K. Kotra; krishna.kotra@usp.ac.fj

ABSTRACT

A preliminary assessment was carried out in identifying the salinity zones due to considerable concern over salty groundwater resources in Vanuatu's Shefa and Malampa regions. Electrical conductivity (EC) and pH were measured on the islands of Efate, Lamen, and Nguna in Shefa province, as well as the islands of Ambrym and Paama in Malampa province. Thirty-four percent of the samples exceeded Vanuatu's National Drinking Water Standards with an average of 3123 µS/Cm indicating possible salinity zones. Whereas the average pH of 7.21 was in the range of acceptable levels. EC values as high as 18,520 µS/cm indicate groundwater in some locations are unfit for drinking. The average Total Dissolved Solids (TDS) of 1717 mg.L^{-1} is also indicating non-compliance with standards. Salinity zone maps were developed based on the observations. Further detailed studies need to be conducted to ascertain the factors that influence groundwater salinity, such as geology, island type, and seasonality.

INTRODUCTION

Groundwater is a vital resource for billions of people across the globe. For many communities around the world, coastal aquifers are a critical source of freshwater (Arfib et al. 2007), with small islands often heavily dependent on groundwater resources. However, increased salinity linked to seawater intrusion poses a significant threat to these coastal aquifers and small islands in particular (Deutsch & Siegel 1997, Somay & Gemici 2009, Kotra et al. 2017, Kim et al. 2009, Abd-Elhamid et al. 2020). It would be obvious that, more than any other water resource, groundwater in the small islands is often prone to impinging saline water and thus salinity. Notwithstanding the mere need for drinking but for all other purposes like irrigation and domestic use as well. Salinity impacts in more than one form and is not limited to reduction in crop yield (Demir et al. 2009), and restriction of flow pattern (Mayer et al. 2003) but to other factors as well. White & Falkland (2010) reported that long dry periods strongly coupled with sea surface temperatures impact the quantity and salinity of fresh groundwater. Given the conditions of limited water resources in the small islands, there is every need for concern for their survival. WHO (2007) refers "all

people, whatever their stage of development and their social and economic conditions, have the right to have access to an adequate supply of safe drinking water".

Small island countries (SICs) are surrounded by the sea, and intensive groundwater withdrawal from concentrated borehole systems and wells has resulted in saltwater intrusion causing contamination of fresh groundwater reserves in coastal aquifers (Lal & Datta 2017). Salinity in groundwater may arise from various factors and there is growing concern about how climate change and associated sea-level rise will compound the issue (Ishii et al. 2006, Palut & Canziani 2007). Small islands will be particularly vulnerable to the impact of climate change on groundwater salinity (Dixon-Jain et al. 2014). Population growth and increased abstraction levels may also exacerbate the issue. Rao (2008) reported that evapotranspiration causes the accumulation of salts and thus can be infiltrated into the groundwater table leading to salinity might be a proven reason for salinity in the small islands. Fisher & Mullican (1997) reported that sodium-chloride and sodium-sulfate ratios play a key role in determining salinity levels in groundwater. It was reported from the study of groundwater in a tropical island in East Malaysia that precipitation and evapotranspi-

ration (environmental condition) with hydraulic heads along with upward pumping were responsible for salinity in the groundwater (Praveena et al. 2011). The vulnerability of small island freshwater lenses dictates careful assessment, vigilant monitoring, appropriate development, and astute management (White & Falkland 2010). Moreover, Foster & Willettes (2018) recently reported that in Vanuatu groundwater sources in the small islands are less prone to contamination than rainwater sources. In view of the above observations and widespread concern about salinity in groundwater resources in the Shefa and Malampa provinces of Vanuatu, the present study was carried out to assess the salinity zones and possible reasons for their occurrence.

MATERIALS AND METHODS

Study Area

Vanuatu is located on the Pacific ring of fire, where the Pacific tectonic plate is sliding under the Indo-Australian plate. The Y-shaped chain of 83 islands lies between Fiji and Queensland, Australia, and forms part of the Melanesia group. Malampa and Shefa constitute the two major provinces among the six provinces of Vanuatu. Malampa lies between 16.4011° S and 167.6078° E with three main islands, Malekula, Ambrym, and Paama. Whereas Shefa which stretches in the center of the country lies between 17.65° S and 168.34° E with Efate, Epi, and Shepard's group of islands. The provinces experience a humid tropical climate and South Easterly trade winds. The average annual rainfall is 2360 mm with an average of 211 rain days per year (VMGD).

A survey was conducted in the study areas of Malampa and Shefa provinces during August and September 2018. Ambrym and Paama Islands were part of the Malampa province survey whereas Efate, Lamen, and Nguna Islands of Shefa province were surveyed. The methodology in regard to the selection of the sampling site was based on the data from the country's national water supply inventory and thus functional water points were selected in the present study. In total, 35 stations were surveyed; 21 in Malampa province and 14 in Shefa province (Fig. 1). After fixing the coordinates of the site, the water that was resting in the rising main was flushed out before the measurement of the parameters. pH, Electrical Conductivity (EC), and Total Dissolved Solids (TDS) were measured on the site using a portable Hanna multi-parameter meter.

RESULTS AND DISCUSSION

Statistical Interpretation

The observed results were interesting and varied. The minimum pH, EC, and TDS observed were 6.63, 417 μS.cm^{-1}, and 229.4 ppm respectively in Malampa province, and 6.97, 689 μS.cm^{-1} and 379 ppm in Shefa province. The maximum values of the pH, EC, and TDS in both the provinces were 7.78, 18,520 μS.cm^{-1} and 10,186 ppm; and 7.74, 2,786 μS.cm^{-1} and 1,532 ppm respectively. The average pH of groundwater sources in these provinces was 7.09 (std dev. 0.28) in Malampa and 7.38 (std. dev. 0.25) in Shefa. Whereas in cases of EC and TDS, the average was 4,095 μS.cm^{-1} (std dev. 5,119) and 2,252 ppm (std dev 2,816) in Malampa; and 1,667 μS.cm^{-1} (std dev. 695) and 917 ppm (std dev. 382) in Shefa. The standard deviations are 5,119 μS.cm^{-1} and 2,816 ppm, and 695 μS/cm and 382 ppm respectively. The median values were 1,156 μS.cm^{-1} and 636 ppm (Malampa); and 1,685 μS.cm^{-1} and 926 ppm (Shefa). The sampling stations' location, geology, and observed values are given in Table 1. The summarized results were shown in Table 2.

It is evident from the results that there are many concerns with the palatability of groundwater in coastal areas of these provinces. In Malampa province, the very high EC and TDS values noted in Ambrym Island indicate groundwater that is not suitable for drinking (WHO 1996). Three sites on Ambrym recorded EC values over 10,000 μS.cm^{-1}, and hence are not even suitable for irrigation purposes (ADWS 2011). However, the pH levels recorded in Ambrym are close to the neutral state but point slightly towards the basic nature. In regards to Shefa province, sites in the islands of Lamen and Nguna also recorded high EC and TDS values. The pH of these stations was slightly higher than those observed in the other islands but again pointing toward the basic nature of these waters.

Rhoades (1996) referred that salinity is due to the presence of the major dissolved solutes, essentially Na$^+$, Mg^{2+}, Ca^{2+}, K$^+$, Cl$^-$, SO$_4^{2-}$, HCO$_3^-$, and CO$_3^{2-}$ in aqueous samples. It is evident from the above results that the contributing factor/s to the salinity of these waters is a cumulative effect of these ions as of the results of the EC. Walton (1989) reported that EC and TDS are correlated and thus replicate the salinity in terms of the soluble salts in the water and thus these stations of confirming the salinity zones. It is very interesting to note that volcanic geology is more favorable than the limestone presence in these stations. Choudhury et al. (2001) reported that geophysical aspects surrounding the groundwater source do play a vital role in deciding the salinity. De Montety et al. (2008) earlier reported that carbonate chemistry would facilitate the origin of salinity but in the present case, it was interesting that the limestone geology doesn't show any saline zones but was observed in the volcanic zones. Thus it would be interesting to see how volcanic zones have higher salinity values than that of the limestone stations.
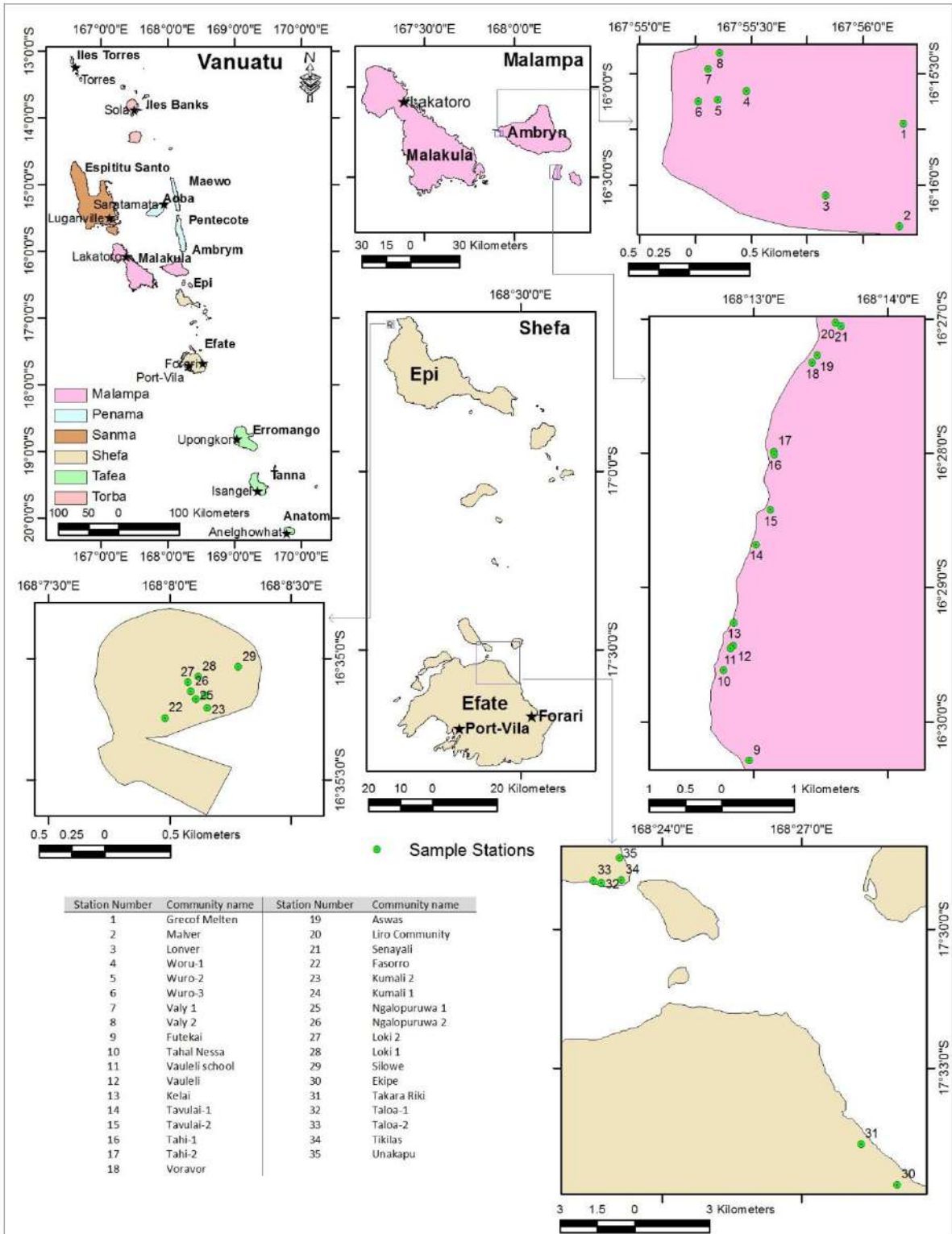
Fig. 1: Map of the study area.

Table 1: Sampling stations, geology and observed results.

Island	Geology	Water point	Latitude	Longitude	pH	EC	TDS
Ambrym	Volcanic	Grecof Melten	-16.2621	167.9364	7.36	3,443	1,894
	Volcanic	Malver	-16.2697	167.9361	7.37	6,068	3,337
	Volcanic	Lonver	-16.2674	167.9306	7.59	5,547	3051
	Volcanic	Woru-1	-16.2597	167.9247	7.37	8,749	4812
	Volcanic	Wuro-2	-16.2603	167.9226	7.42	9,666	5316
	Volcanic	Wuro-3	-16.2604	167.9211	7.46	11,380	6,259
	Volcanic	Valy 1	-16.258	167.9219	7.32	11,990	6,595
	Volcanic	Valy 2	-16.2568	167.9227	7.37	18,520	10,186
Paama	Volcanic	Futekai	-16.5048	168.2162	7.16	885	487
	Volcanic	Tahal Nessa	-16.4936	168.213	6.63	1,671	919
	Volcanic	Vauleli school	-16.491	168.2139	6.91	492	271
	Volcanic	Vauleli	-16.4906	168.2142	6.84	485	267
	Volcanic	Kelai	-16.4877	168.2143	6.90	693	381
	Volcanic	Tavulai-1	-16.4781	168.217	6.76	1,156	636
	Volcanic	Tavulai-2	-16.4737	168.2188	6.88	1,121	617
	Volcanic	Tahi-1	-16.4668	168.2193	7.01	1,024	563
	Volcanic	Tahi-2	-16.4665	168.2192	6.86	1,193	656
	Volcanic	Voravor	-16.4555	168.224	6.89	532	293
	Volcanic	Aswas	-16.4546	168.2246	6.98	456	251
	Volcanic	Liro Community	-16.4505	168.2268	6.85	499	275
	Volcanic	Senayali	-16.4509	168.2276	6.89	417	229
Efate	Limestone	Ekipe	-17.5919	168.4846	7.31	1,742	958
	Limestone	Takara Riki	-17.5774	168.4715	7.43	1,127	620
Laman	Limestone	Fasorro	-16.5874	168.133	7.49	2,495	1,372
	Limestone	Kumali 2	-16.5867	168.1359	7.51	2,044	1,124
	Limestone	Kumali 1	-16.5859	168.1358	7.69	878	483
	Limestone	Ngalopuruwa 1	-16.5861	168.1351	7.47	1,674	921
	Limestone	Ngalopuruwa 2	-16.5856	168.1348	7.48	1,695	932
	Limestone	Loki 2	-16.585	168.1346	7.54	1,148	631
	Limestone	Loki 1	-16.5846	168.1353	7.78	753	414
	Limestone	Silowe	-16.5839	168.1381	7.48	1,891	1,040
Nguna	Volcanic	Taloa-1	-17.4834	168.3783	7.11	1,661	914
	Volcanic	Taloa-2	-17.4825	168.3753	7.01	2,750	1,513
	Volcanic	Tikilas	-17.4823	168.3854	7.09	2,786	1,532
	Volcanic	Unakapu	-17.4743	168.3846	6.97	689	379

Geophysical Interpretation

A "topo-to-raster" interpolation technique under the spatial analyst tool of ArcGIS was used to interpolate a hydrologically correct surface from point datasets (Samanta et al. 2012). In this study total of 35 stations (21 stations from Malampa province and 14 stations from Shefa province) were considered as input stations for interpolation with their know observations value on pH, TDS, and EC. In this first step, a raster surface was generated as an output of topo-to-raster interpolation. In the second step "raster to contour" tools under the spatial analysis of ArcGIS was used to create

Table 2: Summary of the results.

Parameter	Min		Max		Mean		Median		SD	
	SH*	MA*	SH	MA	SH	MA	SH	MA	SH	MA
pH	6.97	6.63	7.74	7.78	7.38	7.09	7.48	6.98	0.25	0.28
EC	689	417	2,786	18,520	1,666	4,095	1,685	1,156	695	5,119
TDS	483	229	1,372	10,186	917	2,252	926	636	382	2816

* SH - Shefa Province; MA - Malampa Province

contours or isolines from those raster surfaces. TDS, pH, and EC contours were overlaid with respective provincial boundaries, and maps were prepared to show the spatial variation of pH, TDS, and EC for Malampa and Shefa provinces. These contour maps are shown in Figs. 2, 3 and 4.

Based on water sample analysis average pH value was measured as 7.21 in the study area. The highest pH was measured in the Shefa province and the lowest in the Malampa province. It was observed that average pH values are higher in the coastal areas than inland areas that are located far from the sea. On the other hand, it was found that the local geology is another factor in the variation of pH value in the study area (Lenntech 2013). The average pH in the volcanic region is much lower (7.27) than in the limestone region (7.52) (Murphy 2007). The value of pH was measured high (7.69) at Kumali 1 in Laman Island under Shefa province which is situated on the limestone and low (6.63) at Tahal Nessa in Paama Island under Malampa province which is situated on the volcanic landform.

The concentration of TDS in this present study was observed in the range from 271 mg.L^{-1} to 5316 mg.L^{-1} in the Malampa province and 379 mg.L^{-1} to 1532 mg.L^{-1} in Shefa province. High TDS concentration (more than 3000 mg.L^{-1}) was measured in the northwest part of Ambrym Island and low (less than 700 mg.L^{-1}) in Paama Island under Malampa province. The average concentration of TDS in Shefa province is much lower than in Malampa province with an average value of 963 mg.L^{-1} and 2169 mg.L^{-1} respectively. In Shefa province TDS contours of 1200 mg.L^{-1}, 1500 mg.L^{-1}, and 9000 mg.L^{-1} can be found in Lamen, Nuna, and Efate Island respectively. High values of TDS in groundwater were generally not harmful to human beings, but a high concentration of these may affect persons who are suffering from kidney and heart diseases (Kumar & Puri 2012).

EC value was measured in the range from 417 µS.cm^{-1} to 18520 µS.cm^{-1} in the Malampa province and 689 µS.cm^{-1} to 2786 µS.cm^{-1} in the Shefa province. The level of EC in Malampa province is much higher than in Shefa province with an average value of 3943 µS.cm^{-1} and 2169 µS.cm^{-1} respectively. A higher EC level (more than 15000 µS.cm^{-1}) was measured in the northwest part of Ambrym Island and

lower (less than 750 µS.cm^{-1}) in Paama Island under Malampa province. EC contour of 2250 µS/cm was found in Lamen, 1500 µS.cm^{-1} in Nguna, and 1250 µS.cm^{-1} in Efate Island respectively, which are situated in Shefa province. After critical analysis of spatial variation of contaminated TDS and EC within groundwater, it can be said that groundwater in Ambrym Island under Malampa province is facing many problems as all measurements are above the standard limit. TDS and EC measurements in Paama Island are comparatively low followed by Nguna, Laman, and Efate Island. Banerjee et al. (2011) proposed that Artificial Neural Networks (ANN) model would appreciate the safe pumping rate of groundwater salinity in island aquifers and thus it would be worthwhile to consider this in the present study area to counter the salinity zone formations.

Groundwater Salinity - Geomorphological Impacts

Coastal groundwater is always circumspect with multiple threats both in maintaining its quality and quantity. Out of many geomorphological challenges that coastal groundwater faces, the vicinity to the saline water is the most important factor to counter (Kotra 2011). Nielsen (1999) reported that the groundwater table a few tens of meters inland from the high watermark on a beach will be considerably higher than the Mean Sea Level (MSL) even if there is no outflow due to rainfall on the land. Stations 1, 2, 3, 4, 5, 6, 7, and 8 in the Malampa and 22, 23, 33, and 34 in the Shefa provinces have the higher EC values than permitted by Vanuatu National Drinking Water Standards and would pose health implications for the communities who depend on these. It would be obvious that sometimes communities who live on the small islands would have to contain what they get depending on the season and availability of the groundwater through recharge. Comte et al. (2016) reported that shallow large-diameter wells, following the traditional model, consistently prove to be less saline and more durable than deeper small-diameter boreholes, and is worthwhile to implement this approach in the current study area to negate the salinity development in the water resource.

It would be interesting to further investigate cases 2, 3, 6, 22, 23, 33, and 34 which are in the vicinity of the coastline
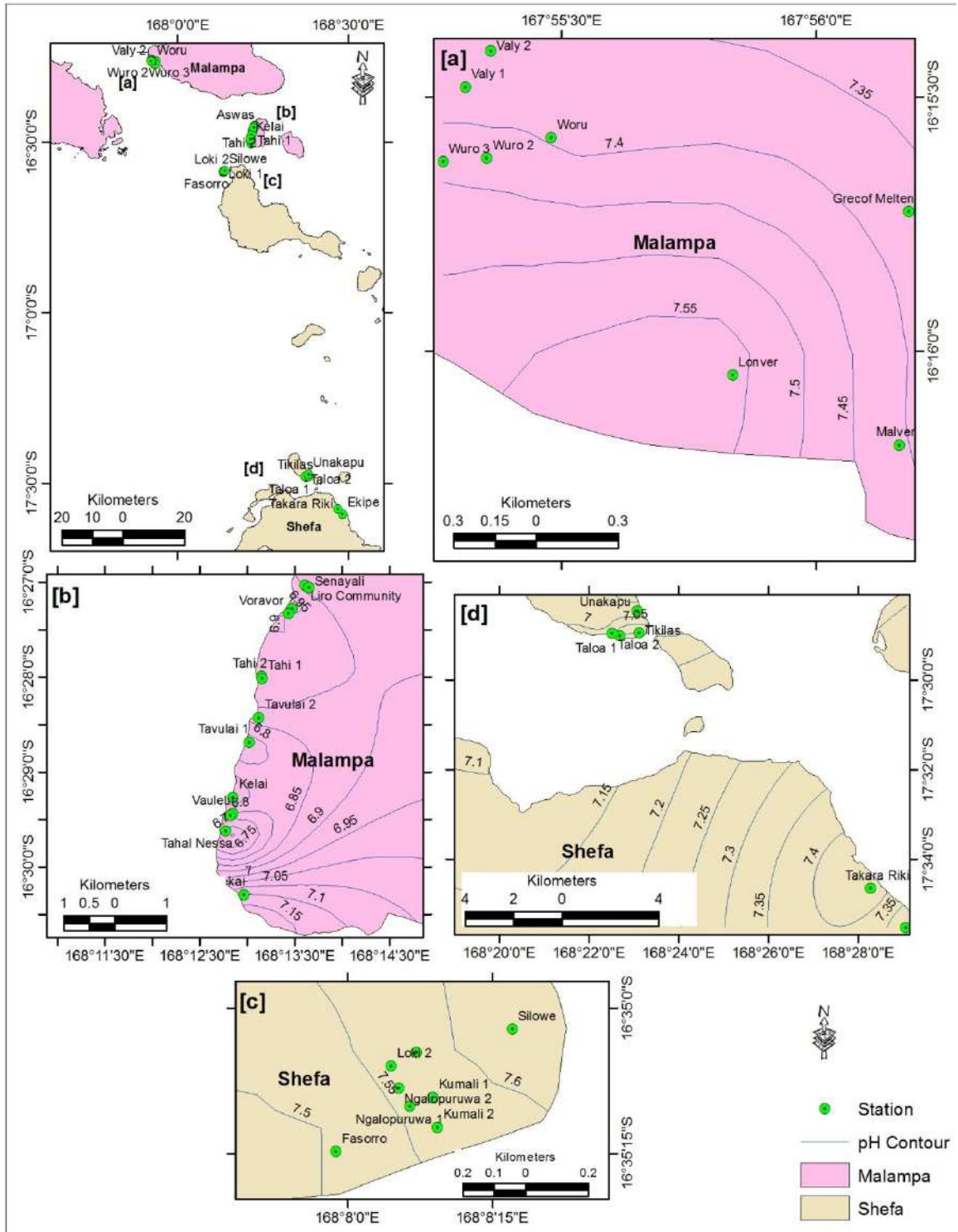
Fig. 2: Spatial distribution of pH in Shefa and Malampa provinces.
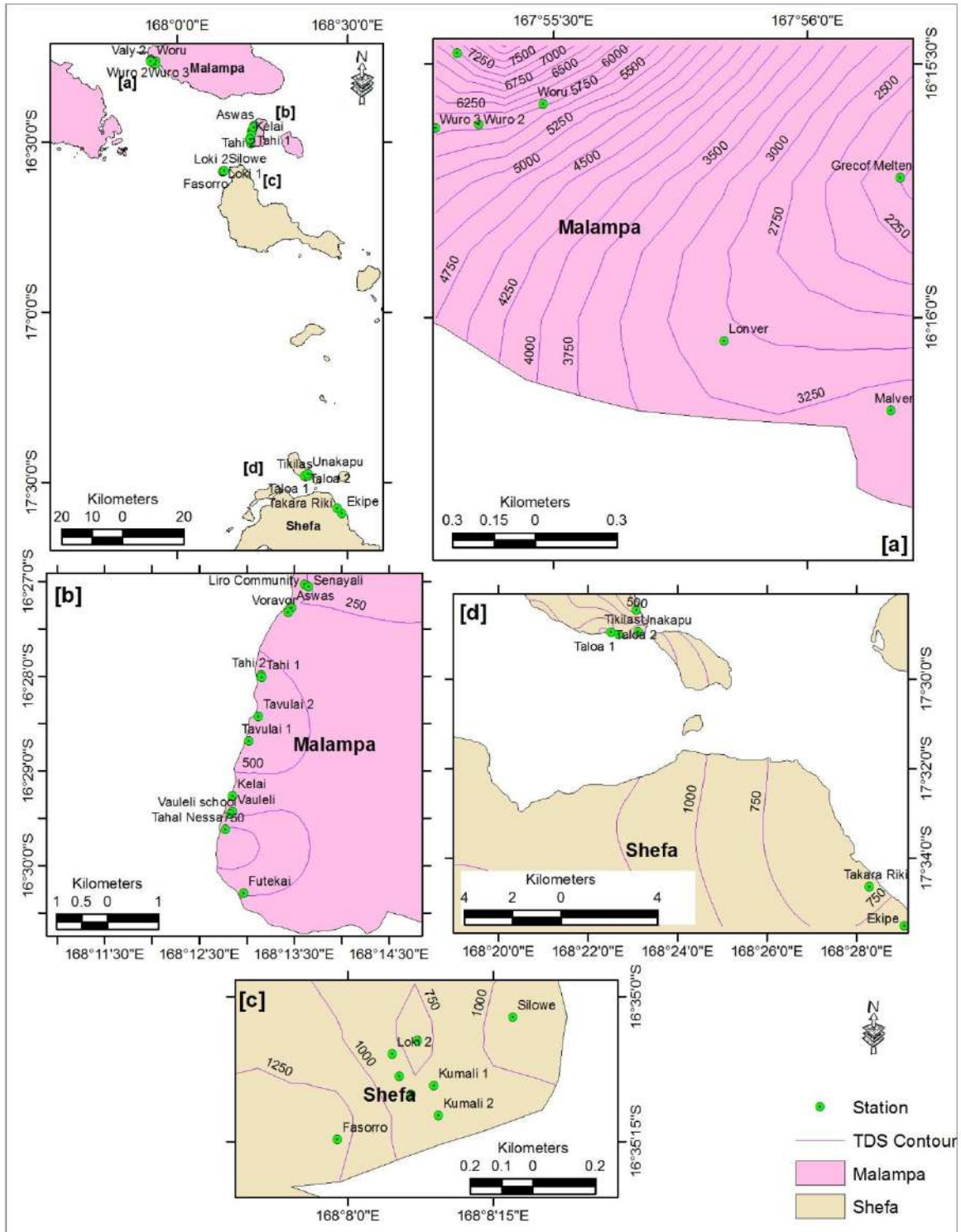
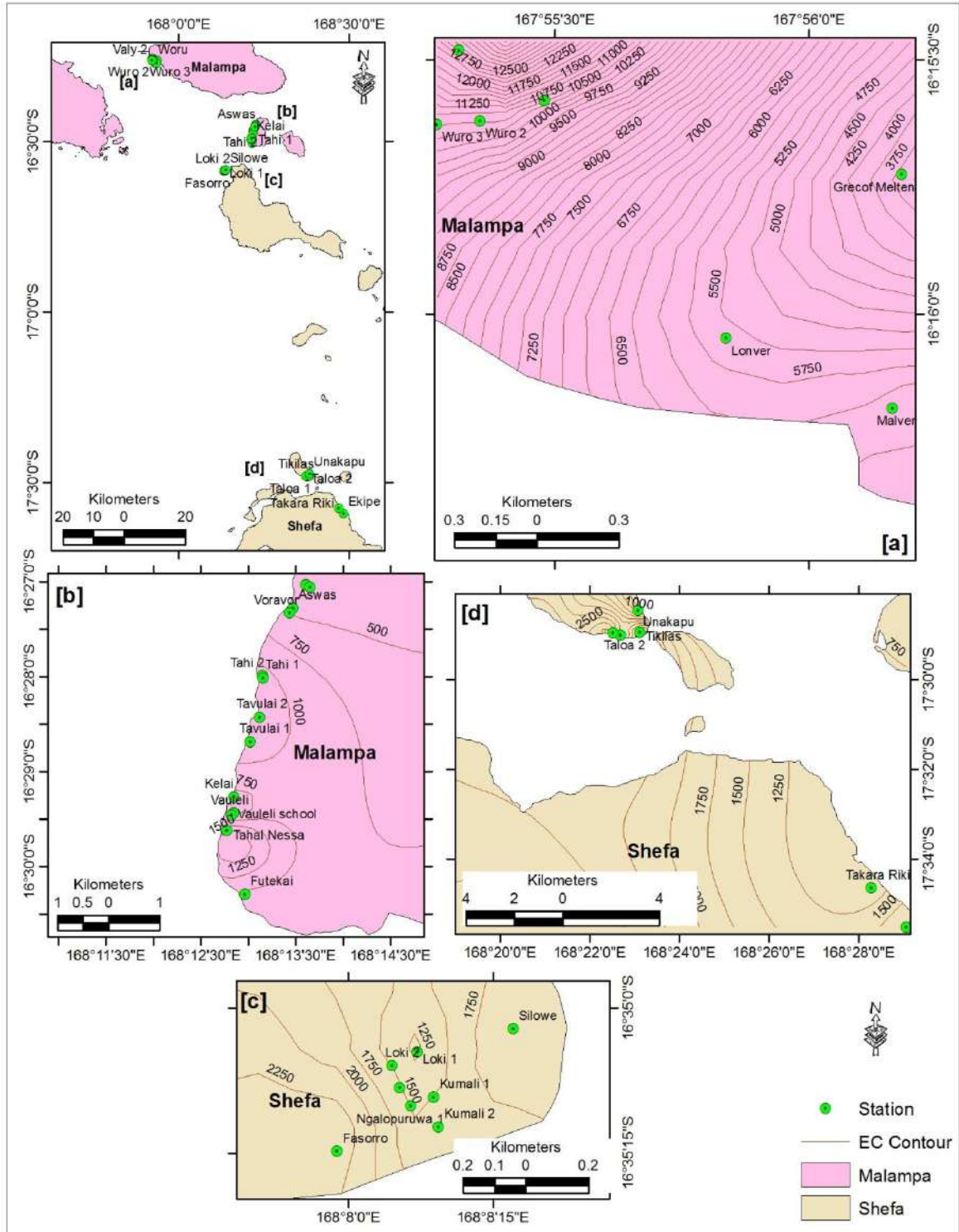Fig. 3: Spatial distribution of TDS in Shefa and Malampa provinces.

Fig. 4: Spatial distribution of EC in Shefa and Malampa provinces.

to see the intrusion impacts. Chang et al. (2011) and Guha & Panday (2012) reported that sea-level rise does impact salinity in the coastal groundwater and thus this kind of impact assessment might lead to further conclusions about the

salinity of the above stations. As pumping rates and recharge often define some of the geomorphological setups, it would be worthwhile to investigate in this regard as well. Stations like 1, 4, and 5 do point in this regard as they are inland with high EC values. Willis & Finney (1988) and Mantoglou (2003) reported that saltwater intrusion can be controlled by proper planning in pumping and recharge. It seems that with fragile groundwater sources there is every need to implement proper planning for sustainability and quality. The difference in the geology i.e., volcanic and limestone in these islands doesn't primarily point to the source of salinity as these zones are observed in both regions. Whitaker & Smart (1990) reported that a difference in the carbonate build-up is capable of driving the subsurface flow of saline water and may be generated by tides, local waves, and ocean currents. Thus it would be interesting to further study the role of limestone in exposing the saline zones in the study area. The variations in the geology in terms of volcanic and limestone origin can't be a source for any prediction on the origin of salinity as cases fall both in these regions. Again there is a need to establish the geological impact on salinity with a comprehensive cation/anion analysis of the groundwater.

CONCLUSION

Salinity in the small island nations has been a problem and Vanuatu is no exemption in this regard. The first-ever investigation in identifying these in the Shefa and Malampa provinces has successfully delineated these zones. Results have been disseminated to the Department of Water Resources and inputted into their water quality database. The EC and TDS results of the stations have revealed that some of the stations were unfit for drinking and agricultural usage. Moreover, a further comprehensive study has been recommended in regard to the role of geomorphology and coastal influences in generating these zones.

REFERENCES

Abd-Elhamid, H.F., Abd-Elaty, I. and Hussain, M.S. 2020. Mitigation of seawater intrusion in coastal aquifers using coastal earth fills considering future sea-level rise. Envi. Sci. Poll. Res., 27(18): 23234-23245.

ADWS. 2011. Australian Drinking water Standards: http://www.sahealth.sa.gov.au/wps/wcm/connect/public+content/sa+health+internet/protecting+public+health/water+quality/salinity+and+drinking+water

Arfib, B., De Marsily, G. and Ganoulis, J. 2007. Locating the zone of saline intrusion in a coastal karst aquifer using spring flow data. Groundwater, 45, 28-35.

Banerjee, P., Singh, V.S., Chatttopadhyay, K., Chandra, P.C. and Singh, B. 2011. Artificial neural network model as a potential alternative for groundwater salinity forecasting. J. Hydrol., 398: 212-220.

Chang, S.W., Clement, T.P., Simpson, M.J. and Lee, K.K. 2011. Does sea-level rise have an impact on saltwater intrusion?. Adv. Water Resour., 34: 1283-1291.

Choudhury, K., Saha, D.K. and Chakraborty, P. 2001. Geophysical study for saline water intrusion in coastal alluvial terrain. J. Appl. Geophysics., 46: 189-200.

Comte, J.C., Cassidy, R., Obando, J., Robins, N., Ibrahim, K., Melchioly, S. and Noe, C. 2016. Challenges in groundwater resource management in coastal aquifers of East Africa: Investigations and lessons learned in the Comoros Islands, Kenya, and Tanzania. J. Hydrol. Reg. Stud., 5: 179-199.

De Montety, V., Radakovitch, O., Vallet-Coulomb, C., Blavoux, B., Hermitte, D. and Valles, V. 2008. Origin of groundwater salinity and hydrogeochemical processes in a confined coastal aquifer: Case of the Rhône delta (Southern France). Appl. Geochem., 23: 2337-2349.

Demir, Y., Er ahin, S., Güler, M., Cemek, B., Günal, H. and Arslan, H. 2009. Spatial variability of depth and salinity of groundwater under irrigated ustifluvents in the Middle Black Sea Region of Turkey. Environ. Monit. Asses., 158: 279-294.

Deutsch, W.J. and Siegel, R. 1997. Groundwater geochemistry: fundamentals and applications to contamination. CRC Press, New York.

Dixon-Jain, P., Norman, R., Stewart, G., Fontaine, K., Walker, K., Sundaram, B., Flannery, E., Riddell, A. and Wallace, L. 2014. Pacific Island Groundwater and Future Climates: First-Pass Regional Vulnerability Assessment. Record 2014/43. Geoscience Australia, Canberra. http://dx.doi.org/10.11636/Record.2014.043

Fisher, R.S. and Mullican, W.F. 1997. Hydrochemical evolution of sodium-sulfate and sodium-chloride groundwater beneath the northern Chihuahuan Desert, Trans-Pecos, Texas, USA. Hydrogeology J., 5: 4-16.

Foster, T. and Willetts, J. 2018. Multiple water source use in rural Vanuatu: are households choosing the safest option for drinking?. Int. J. Environ. Health Res., 28: 579-589.

Guha, H. and Panday, S. 2012. Impact of sea-level rise on groundwater salinity in a coastal community of South Florida. J. Am. Water Resour. Assoc., 48" 510-529.

Ishii, M., Kimoto, M., Sakamoto, K. and Iwasaki, S. I. 2006. Steric sea-level changes are estimated from historical ocean subsurface temperature and salinity analyses. J. Oceanogr., 62: 155-170.

Kim, K.Y., Park, Y.S., Kim, G.P. and Park, K.H. 2009. Dynamic freshwater–saline water interaction in the coastal zone of Jeju Island, South Korea. Hydrogeol. J., 17: 617-629.

Kotra, K.K., Samanta, S. and Prasad, S. 2017. Rainwater harvesting for drinking: A physiochemical assessment in Port Vila, Vanuatu. Sou. Pac. J. Nat. App. Sci., 35, 33-44.

Kotra, K.K. 2011. Geomorphological impact assessment on groundwater quality and fluoride genesis along the Bay of Bengal of Visakhapatnam district, Andhra Pradesh, India. CLEAN–Soil Air Water, 39(10): 925-930.

Kumar, M. and Puri, A. 2012. A review of permissible limits of drinking water. Ind. J. Occ. Environ. Medicine, 16: 40.

Lal, K. and Datta, R. The impact of groundwater utilization on coastal aquifers in the Pacific Island States. 2017. Proceedings of the 15th Islands of the World Conference, South Australia, Australia.

Lenntech, R. 2013. Acids and Alkalis in freshwater. In Water Treatment Solutions. Retrieved from https://www.lenntech.com/aquatic/acids-alkalis.htm

Mantoglou, A. 2003. Pumping management of coastal aquifers using analytical models of saltwater intrusion. Water Resour. Res., 39: 1-12.

Mayer, C., Grosfeld, K. and Siegert, M.J. 2003. Salinity impact on water flow and lake ice in Lake Vostok, Antarctica. Geophysics Res. Lett., 30: 8-12.

Murphy, S. 2007. General Information on Alkalinity. In City of Boulder/USGS Water Quality Monitoring. Retrieved from http://bcn.boulder.co.us/basin/data/BACT/info/Alk.html

Nielsen, P. 1999. Groundwater dynamics and salinity in coastal barriers. J. Coast. Res., 15: 732-740.

Palut, M.P.J. and Canziani, O.F. 2007. Contribution of Working Group II to the Fourth Assessment Report of the Intergovernmental Panel on Climate Change. Cambridge University Press, UK.

Praveena, S.M., Abdullah, M.H., Bidin, K. and Aris, A.Z. 2011. Understanding of groundwater salinity using statistical modeling in a small tropical island, East Malaysia. Environmentalist, 31: 279-283.

Rao, N.S. 2008. Factors controlling the salinity in groundwater in parts of Guntur district, Andhra Pradesh, India. Environ. Monit. Asses., 138: 327-341.

Rhoades, J. D. 1996. Salinity: Electrical conductivity and total dissolved solids. Chemical Methods, 417-433.

Samanta, S., Pal, D. K., Lohar, D. and Pal, B. 2012. Interpolation of climate variables and temperature modeling. Theo. App. Climatology., 107, 35-45.

Somay, M. A. and Gemici, Ü. 2009. Assessment of the salinization process at the coastal area with hydrogeochemical tools and geographical information systems (GIS): Selçuk plain, Izmir, Turkey. Water, Air, and Soil Poll., 201, 55-74.

VMGD (Vanuatu Meteorology and Geohazards Department) http://www.vmgd.gov.vu/vmgd/index.php

Walton, N. R.G. 1989. Electrical conductivity and total dissolved solids: What is their precise relationship? Desalination, 72: 275-292.

Whitaker, F.F. and Smart, P.L. 1990. Active circulation of saline groundwaters in carbonate platforms: Evidence from the Great Bahama Bank. Geology, 18: 200-203.

White, I. and Falkland, T. 2010. Management of freshwater lenses on small Pacific islands. Hydrogeol. J., 18: 227-246.

World Health Organization (WHO). Guidelines for drinking-water quality, 2nd ed. Vol. 2. Health criteria and other supporting information. World Health Organization, Geneva, 1996.

Willis, R. and Finney, B. A. 1988. Planning model for optimal control of saltwater intrusion. J. Water Res. Plan. Manag., 114: 163-178.

World Health Organization (WHO). 2007. pH in drinking water. http://www.who.int/water_sanitation_health/dwq/chemicals/ph_revised_2007_clean_version.pdf

Original Research Paper

https://doi.org/10.46488/NEPT.2022.v21i02.046

Open Access Journal

Delineation of Groundwater, Drought and Flood Potential Zone Using Weighted Index Overlay Analysis and GIS for District Patna, Bihar, India

Nikhilesh Gaurav† and Geeta Singh

Department of Environmental Engineering, Delhi Technological University, Daulatpur, New Delhi-110042, India
†Corresponding author: Nikhilesh Gaurav; nikhileshgaurav56@gmail.com

ABSTRACT

For groundwater evaluation, delineation, discovery, and resource management in drought and flood zones, the geographical information system (GIS) has a wide range of uses. For the study area, various thematic layers were prepared, such as a digital elevation map (DEM), geomorphology, LULC, soil, drainage density, precipitation, and slope. The thematic layers were combined using the WIOA technique. The possible areas for groundwater have been demarcated into four zones: 1-poor, 2-moderate, 3-good, and 4-very good. In the eastern parts of the district, very strong (GWPZs) were found, while in the west and mid regions, moderate and bad categories were found. Drought and flood potential danger areas were divided into four zones: 1-no risk, 2-low risk, 3-moderate risk, and 4-high risk. In the middle part of the region, there was a higher risk of drought and a reduced risk of flooding in the eastern part of the area, an elevated risk of flooding in the eastern part of the area, and a lower to no risk of flooding in the western and central regions. The groundwater, drought, and flood potential zonation map built in the present study will be useful for scholars, and implementers in exploring appropriate water exploration locations and implementing resource utilization.

INTRODUCTION

In all living life on earth, groundwater plays a major role and is the most valuable available freshwater resource on earth. Remarkable demands for consumption, coupled with advances in agricultural and industrial activities, are leading to an imminent need to maximize the utilization of groundwater sources. Scientific data-building activities for the management of water resources started several years ago by means of proximal sensing as well as remote sensing, but even then, practical data-catering knowledge on groundwater availability, and optimal permissible extraction. In India, the optimal value of allowed wells in the watershed continues to be decreased. Recharging groundwater is nothing but the flow of water during the natural cycle from the unsaturated surface level to the saturated underground stratum. Most rural communities and urban communities in India rely on groundwater owing to their everyday needs. Regrettably, there is a decrease in groundwater levels due to the overuse of groundwater for cultivation and other inhumane uses. Following reports of poor precipitation with the drying of crops, the Bihar government declared 8 out of 23 blocks of Patna district as drought-affected. As per the IMD, the monsoon season finished with the nation showing a rainfall deficiency in three states of India, which are Bihar, Jharkhand, and West Bengal, the greatest rainfall deficiency has been reported. The IMD data indicates that

Patna recorded 27 percent of the weak precipitation. This project will be very helpful in delineating drought zones because of this pattern of drought occurrence and will enable the government to take the requisite measures to resolve it and set up facilities in drought-prone zones. India's most flood-prone state in Bihar. Over 70% of the geographical area as a whole is at risk of annual floods, putting lives at risk and contributing to major financial losses. Upstream from the Ganga, Patna is located. The influential banana cultivation on the banks of the river Ganga between Patna and Bhagalpur, based on the evaluation of hundred years of flooding in the Ganga, is also one of the reasons for the floods. The report of the Central Water Commission stated that the sedimentation at Ganga in Bihar is essentially due to the immense load of sediment from its northern tributaries, Ghaghra, Gandak, and Kosi. In Patna, places such as Kankarbagh, Rajendra Nagar, and their environs are susceptible to flooding. It will help to identify areas vulnerable to flooding, based on the severity of flooding, by delineating flood potential zones, which will assist local officials to set up emergency response plans and take action to resolve and prepare before the crisis occurs.

MATERIALS AND METHODS

Study Area

Many factors, including DEM, geomorphology, drainage

density, slope, land use land cover, rainfall, and soil type, affect all these areas. Each of these parameters affects groundwater, drought, and flood zones in its own and varied way (Table 1). Therefore, the single criteria analysis does not yield fair results for groundwater capacity, drought, and flood threats. In addition, all the maps listed above help determine potential zones for groundwater, drought, and flooding.

The current study is being conducted in Patna, Bihar. The primary urban center of Patna is situated at coordinates of 25°35'38.74'N and 85°8'15.23'E with an altitude of 53m elevated sea level. Patna is stationed on the Ganga River's southern coast (Fig. 1). It is characterized by fairly hot summers to relatively cold winters of a moderate sort. It ranges in the summers from 43°C to 30°C and in the winters from 21.4°C to 5°C. The summer begins in April and peaks in June/July with the temperature rising to 43°C. The rains last until early October through August & September and the monsoon receives medium to strong rainfall. During summers, the relative humidity goes up to 100%. The region is part of the Indo-Gangetic alluvium, one of India's three major physiographic divisions, which divides the northern extra-peninsular region from the southern peninsular region. The area forms part of the Ganga flood plains and has a flat relief that is monotonous. The region under study is underlined by quaternary-age alluvial sediments. In the study zone, farming conditions rely primarily on the soil, topography, and irrigation systems prevalent in the area. The area consists mainly of four soil types, ranging from relatively well-drained to poorly-drained, acidic to mildly alkaline, and mild to strongly textured. From the agricultural point of view, only four soil types can be recognized as soft to hard in texture, namely Heavy Clay (Kewal), Loam (Domat), Fairly Light Soil (Balsundri), and Basic (Rehara) respectively. The capital of Bihar, Patna, enjoys the unique value of becoming one of the country's richest surface water banks. The city has a fixed terminal on the National Waterway No.1. The chain of inland waterways along the river Ganga connects it to Kolkata. Throughout the year, the Ganges becomes accessible and goods can be transported by substantial boat traffic. In the delineated region, vulnerabilities like flooding and drought arise. Patna falls within the flood risk zone. A number of embankments were built along the River Punpun to regulate the floodwaters. The spillover from the river Ganga and Punpun during the monsoons appears to flood Patna and cause illness to spread. Therefore, the river must be channelized and a proper disaster mitigation strategy must be planned and implemented. In addition to being flood-prone, due to droughts, Patna seems to be at threat as its 8 out of 23 blocks are situated in areas vulnerable to drought. The requisite steps must be accounted within order to overcome these risks cost-effectively.

To classify the potential GWPZ, drought, and flood zones for the Bihar district of Patna. Seven input parameters were considered to define the existence and source of potentials, such as DEM, geomorphology, slope, precipitation, drainage density, soil, and land use/land cover. For all of these factors, remotely sensed data, viz. IRS 1B LISS III with 23.5 meter spatial resolution; LANDSAT TM with 30 meter spatial resolution digitized dataset was created by extracting data from multiple sources (Pradhan 2009). Bhukhosh platform

Table 1: Information source and explanation.

Parameter	Data explanation	Source
Geomorphology	Downloaded and listed into the 30-m raster data resolution.	Bhukosh-Geological Survey of India (https://bhukosh.gsi.gov.in/Bhukosh/MapViewer.aspx)
LULC	National boundaries conform to that published by the Survey of India. Downloaded and listed into the raster data resolution.	NASA ORNL DAAC (https://daac.ornl.gov/cgi-bin/dsviewer.pl?ds_id=1336)
Soil	Re-categorized to raster data into the 30-m resolution. Scale 1:50,000.	FAO GeoNetwork (http://www.fao.org/geonetwork/srv/en/)
Drainage density	Obtained from DEM using different ArcGIS commands like Flow Accumulation, Watershed, and Drainage Density.	ASTER Global DEM Model Version3 (https://search.earthdata.nasa.gov/search)
Rainfall	The rainfall measurements of the rain-gauge locations were interpolated by using the IDW method for the study region.	Climatic Research Unit(CRU) (https://crudata.uea.ac.uk/cru/data/hrg/cru_ts_4.04)
DEM	Downloaded and listed into the 30-m raster data resolution.	ASTER Global DEM Model Version3 (https://search.earthdata.nasa.gov/search)
Slope	Obtained from DEM using different ArcGIS commands like Surface and Slope.	ASTER Global DEM Model Version3 (https://search.earthdata.nasa.gov/search)
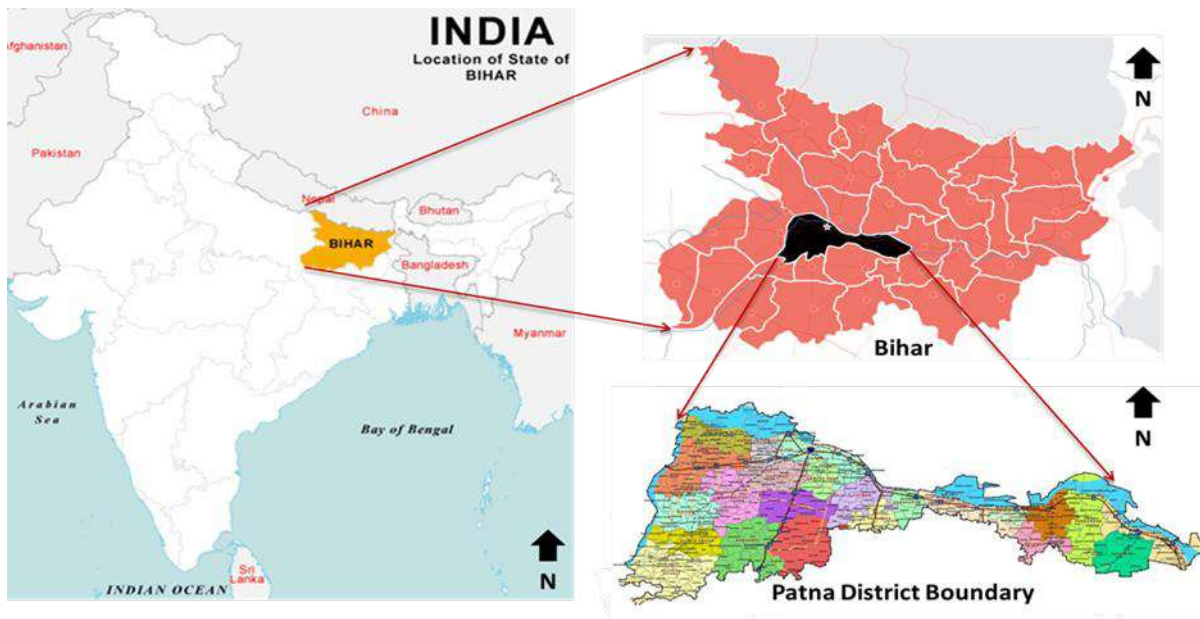
Fig. 1: Location map for the research area.

was used on a ratio of 1:50,000 to collect map data such as geomorphology and land use. To develop a new elevations model through which elevation, slope, and flow depth may be derived, ASTER global DEM model version3 images with a resolution of 30m were used. The soil map was obtained through a link (http://www.fao.org/geonetwork/srv/en/) on a ratio of 1:50,000 from the FAO. The rainfall information was collected using the link (https://crudata.uea.ac.uk/cru/data/hrg/cru ts 4.04/cruts.2004151855.v4.04/pre/) from the CRU website. To acquire a rainfall forecast for the said entire region, the station rainfall data were interpolated. Under the GIS environment, every impacting factor was geo-referenced and analyzed, and generated as distinct map layers. The 2013 data for the water level was downloaded from the Central Groundwater Control Board (CGWB). The ArcGIS enables the identification of the areas that include these spatial relations (Amer 2013). To render the interpolation map via the IDW technique in ArcGIS10.8, this data was imported into the GIS environment. In ArcGIS10.8, the groundwater potential zones, drought, and flood potential zones were derived by overlaying all of the geospatial maps in the form of weighted overlay techniques by using an analysis tool. Within each thematic map, a score was provided by weighted overlay analysis for each estimated object, and weights were allocated based on layer effects. Using data on subsurface water variation collected from the CGWB, the outcome received was verified for ground data.

Determination of Ranks and Weights Using WIOA

Depending on its effect on the analysis, WIOA is a method of

giving due weight to the individual features. Its benefit would be that human judgment can be integrated into this analysis. This operation can be performed both in vector and raster data (Karanam et al. 2014, Choudhary et al. 2018). Assigned weights are the uniqueness of a parameter set in the task to achieve the study's objective (Rajaveni et al. 2017, Pendke et al. 2007). Every thematic map of the occurrence of groundwater, drought, and floods, such as DEM, geomorphology, LULC, slope and drainage density,

rainfall, and soil, has its signature. Others experience this to get an integrated view of the field of research by manually overlaying the layers (Roy et al. 2004). In GIS, this data is overlaid geographically. Depending on the capacity of groundwater, drought, and flood, categorization is measurably put into the following categories. (i) Poor, (ii) Moderate, (iii) Good, and (iv) Very good for GWPZs and four zones for drought and flood potential danger zones: 1-no risk, 2-low risk, 3-moderate risk, and 4-high risk. Based on the weights allocated to individual layers (layer weight) and class, the thematic maps compiled from the above-mentioned study are categorized (class weight). In this study, an evaluation scale was used from 1 to 5 for all three potential zones. The optimized thematic maps are overlaid and incorporated with the use of ground control points and final maps have been prepared for GWPZs, drought, and flood zones.

RESULTS AND DISCUSSION

Seven parameters considerably influenced the GWPZ, drought, and flood zones delineation in the Patna district

of Bihar. The results of each attribute and the ranks and weights assigned to them are shown below. Tables 3, 4 & 5 illustrate how each parameter was rated and how much weight it was given in GWPZs, drought, and flood potential zones respectively.

Geomorphology

The geomorphology of any area reflects the structure of the subsurface, which is highly important in the regulation of groundwater (Krishna & Kumar 2018). Based on its impact on GWPZs, drought, and flood zones, the spatial geomorphology map was attributed to the weight. The area of study is divided into five groups, i.e. Younger Alluvial Plain, Older Flood Plain, Active Flood Plain, River, Pond, and Waterbodies. These six topographical units were grouped into four groups to make the allocation of rank and weight easy, in which Younger Alluvial Plain which is about 421.405 km^2 in

area of total geomorphological formation in the study region and comprises 12.90%, is assigned a low rank as it is located on the elevated side of the district having less influence on GWPZs and flood zones but higher rank for drought zones as it is elevated more than other classes so water availability will be less as compared to other classes. Older Flood Plain and Active Flood Plain constitute about 2201.89 km^2 (67.38%) and 527.21 km^2 (16.13%) in area respectively of the research area's entire geomorphological composition and assigned moderate and high values respectively for GWPZs because these are flood plains and will help recharge groundwater more.

For flood potential zones, Older Flood Plain and Active Flood Plain are ranked high and higher values respectively, because of more possibility of occurrence of flood in these regions. For drought potential zones Older Flood Plain and Active Flood Plain are ranked moderately because of fewer

Table 2: Composition of the soil of Patna district.

S No.	Clay %	Silt %	Sand %
3681	21	38	41
3743	18	44	38
3808	21	35	44
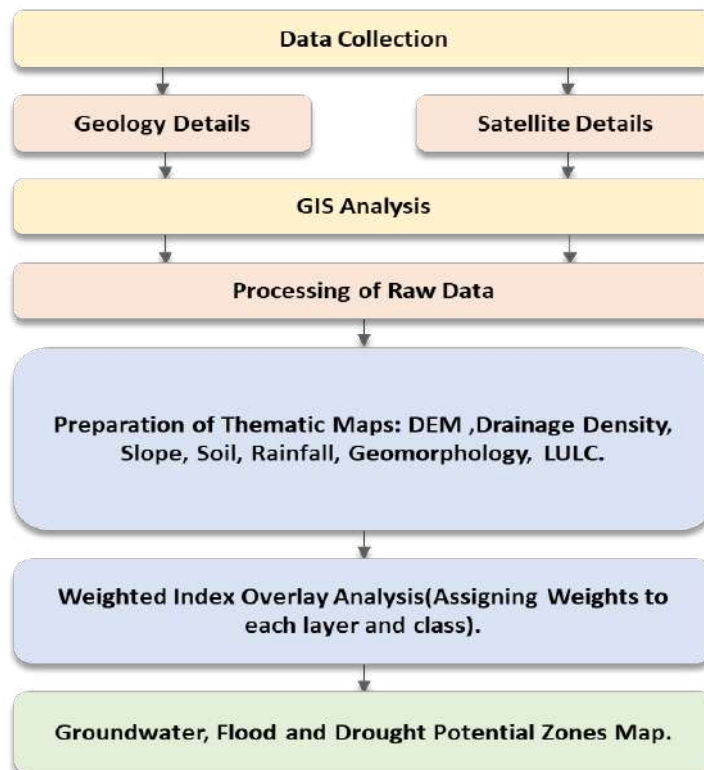
Fig. 2: Methodology flowchart.

Table 3: Allocated weight and rank to various thematic layers for GWPZ.

Theme	Feature	Weight	Rank
Geomorphology	Younger alluvial plain	10	2
	Older flood plain		3
	Active flood plain		4
	River		5
	Pond		5
	Waterbodies		5
LULC	Cropland	10	5
	Built-up land		4
	Shrubland		2
	Fallow land		1
	Waterbodies		5
	Plantations		5
	Grassland		3
	Permanent wetlands		4
Soil	3681 Loamy Soil	5	3
	3743 Loamy Soil		5
	3808 Loamy Soil		4
Drainage density	0.002-0.98	25	1
	0.98-1.39		2
	1.39-1.82		3
	1.82-2.64		4
	2.64-4.75		5
Rainfall [mm]	1022.98-1032.98	15	1
	1032.98-1040.28		2
	1040.28-1050.69		3
	1050.69-1062.57		4
	1062.57-1076.11		5
DEM [m]	36-42	30	5
	42-50		4
	50-57		3
	57-63		2
	63-92		1
Slope	0-0.82	5	5
	0.82-2.20		4
	2.20-4.05		3
	4.05-6.81		2
	6.81-23.47		1

chances of flood occurrence in these regions. Similarly, rivers, Pond, and Waterbodies all constitute of total 117.33 km^2 (3.59%) in the area and are ranked highest because of water availability throughout the year and will help in recharge of groundwater also study area is mainly a plain region. For flood, potential zones are ranked high because mainly flood occurs in this study zone because of water bodies, and for drought zones, they are ranked lowest because of very less chance of occurrence of drought in these regions, because of the availability of water throughout the year. The geomorphology of the region studied is shown in Fig. 3.

Drainage Density

Drainage density is known as the proportion of the total runoff channel length of the region to the area of the entire drainage basin. The surface water infiltration is found to be more in the sheet wash than in channel flow (Sitender 2011). It relies on the characteristics of land, slope, and near-surface topography (Rajaveni et al. 2017). Using the ASTER Global DEM Model Version3 30-m resolution images, In the ArcGIS, both flow accumulation and the drainage density map were extracted for the study area. The analysis area's drainage density varies from 0.0028 to 4.75 m.m.$^{-2}$. The ranking was given in a manner that there would be more infiltration where more streams are passing from the field. If there is more infiltration, the water will go below ground and it will be easier to recharge groundwater resources. The region with better drainage density would have a greater value and lower drainage density will have a smaller value for the classification of flood potential zones.

Table 4: Allocated weight and rank to various thematic layers for drought potential zones.

Theme	Feature	Weight	Rank
Geomorphology	Younger alluvial plain	8	5
	Older flood plain		4
	Active flood plain		3
	River		1
	Pond		2
	Waterbodies		1
LULC	Cropland	35	4
	Built-up land		5
	Shrubland		4
	Fallow land		5
	Waterbodies		1
	Plantations		3
	Grassland		2
	Permanent wetlands		1
Drainage density	0.002-0.98	25	5
	0.98-1.39		4
	1.39-1.82		3
	1.82-2.64		2
	2.64-4.75		1
Rainfall [mm]	1022.98-1032.98	20	5
	1032.98-1040.28		4
	1040.28-1050.69		3
	1050.69-1062.57		2
	1062.57-1076.11		1
DEM [m]	36-42	12	1
	42-50		2
	50-57		3
	57-63		4
	63-92		5
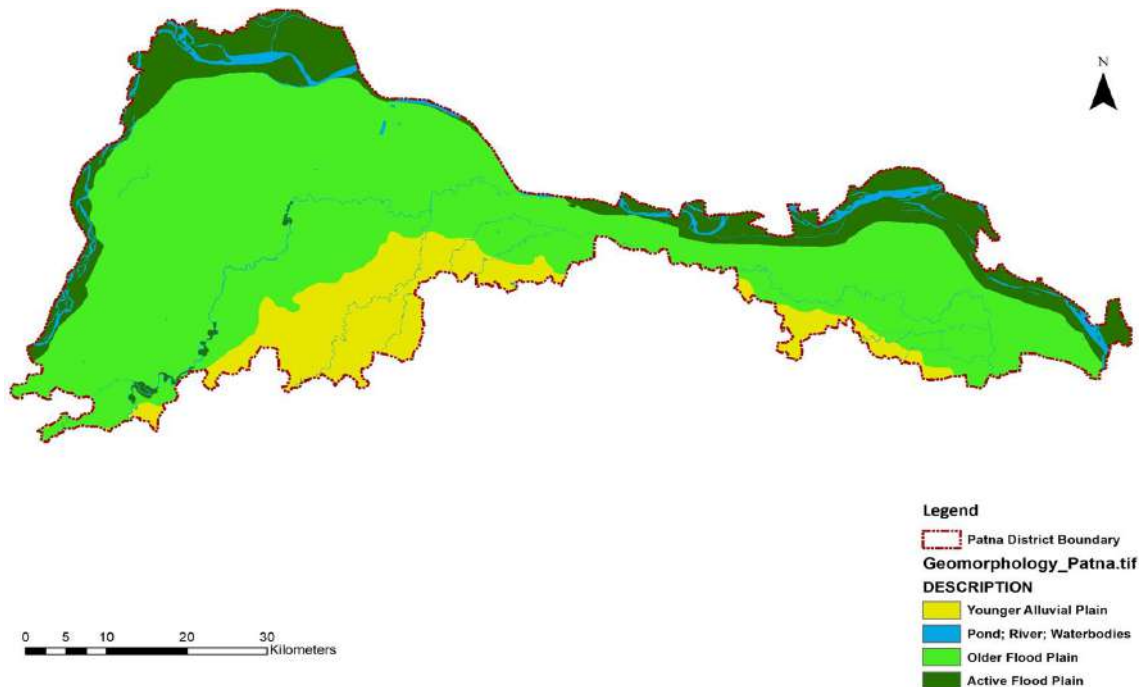
Fig. 3: Geomorphology map of Patna district.
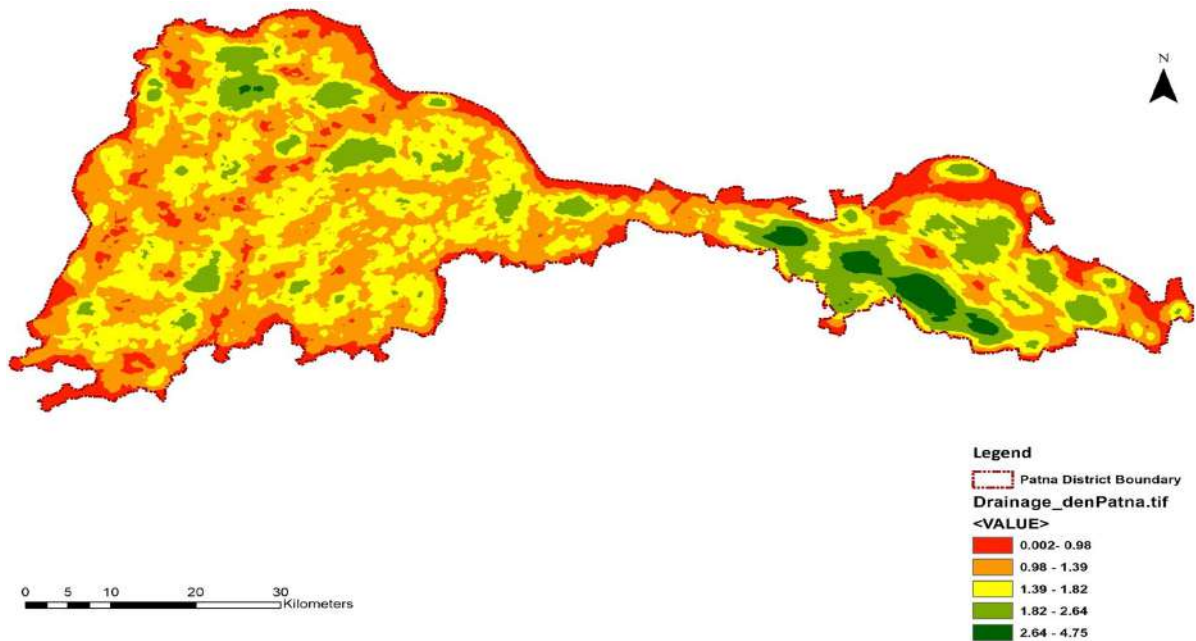
Fig. 4: Drainage Density map of Patna district.

Promising areas with higher drainage density will have lower rankings for the classification of drought zones and areas with lower drainage density will have top ranking because less drainage will have more drought possibilities. In Fig. 4, the drainage density of the sample area is given.

Slope

The slope of the area defines the availability of water for replenishment and the roughness of the landscape of any region (Kundal & Joshi 2004). On steeper slopes, groundwater may or may not be present but at lower slopes, water will certainly stay. Therefore, there is not much variation in slope, so the slope is less valuable for GWPZs and flood zones. Fewer slope results in more stability of water and will have a higher value and a higher slope will have less stability and results in low ranking values. So ranking was done based on this fact, and we don't consider slope map for drought potential zones delineation because slope will not affect much on drought zone. After all, it can occur irrespective of slope at any place. The whole district is plain which constitutes the loamy soil. The slope of the study area has been divided into five classes (0-0.82), (0.82-2.20), (2.20-4.05), (4.05-6.81), (6.81-23.47). Much of the field of research shows that a 0-0.82% slope comprises an area of 1475.48km^2 which indicates that the whole area of the district comes under the plain terrain. In Fig. 5, the slope of the sample area is given.

Rainfall

The precipitation serves as the key source of refueling for groundwater supplies. The amount of precipitation significantly influences the amount of groundwater replenishment. Higher rainfall will result in higher infiltration resulting in easy groundwater recharge. Heavy and untimely rainfall will result in severe floods too, and also less and no rainfall will result in severe drought too, so rainfall will have a major influence on all three potential zones namely GWPZ, drought, and flood zones. The study area's mean annual rainfall is about 1031 mm. The precipitation map for the research region was rated as 1022.89 and 1076.11 mm, in five categories with min and max precipitation, respectively. Higher ranks for GWPZs and flood zones are reserved for higher rainfall, but the inverse situation persists for drought regions. Fig. 6 shows the study area's rainfall map.

Soil

To demarcate the groundwater potential areas, the soil is an essential factor. Subject to the soil types, it likewise gives a proof around the groundwater holding limit and penetration rate (Balakrishnan 2019). The soil map has been obtained from FAO for the study field. The soil type data shows that three distinct compositions of loamy soils primarily cover the study region. All three types with their composition are shown in Fig. 7. The soil in lower elevations will have a
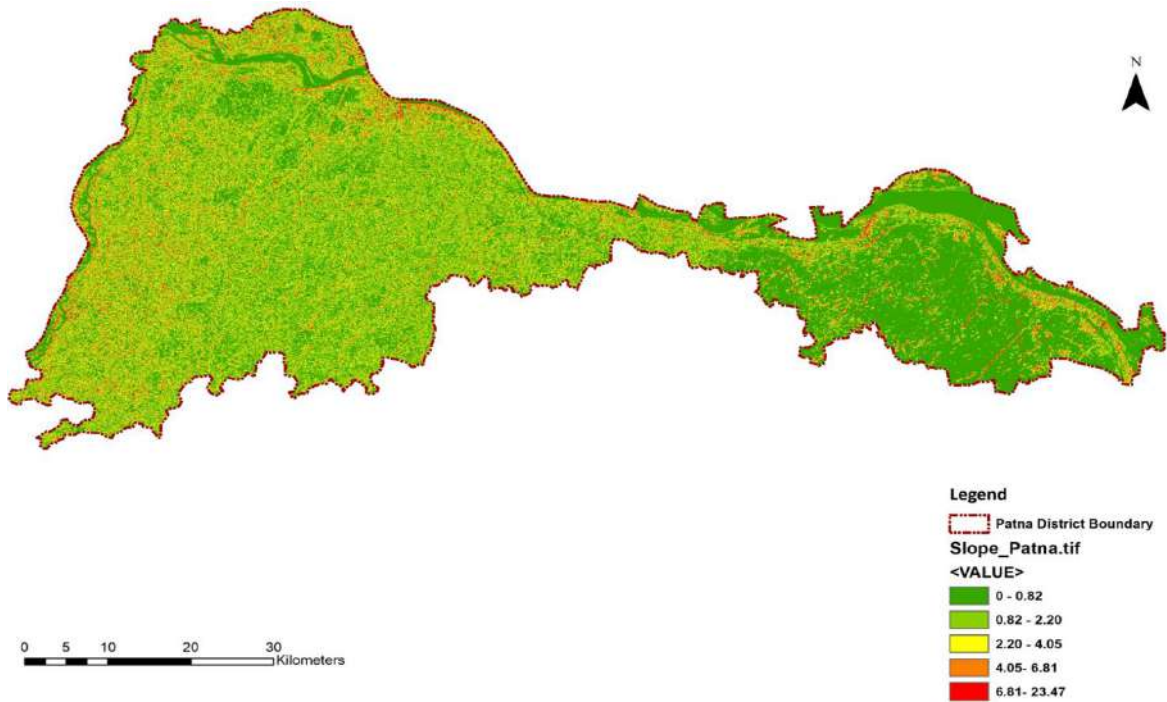
Fig. 5: Slope map of Patna district.
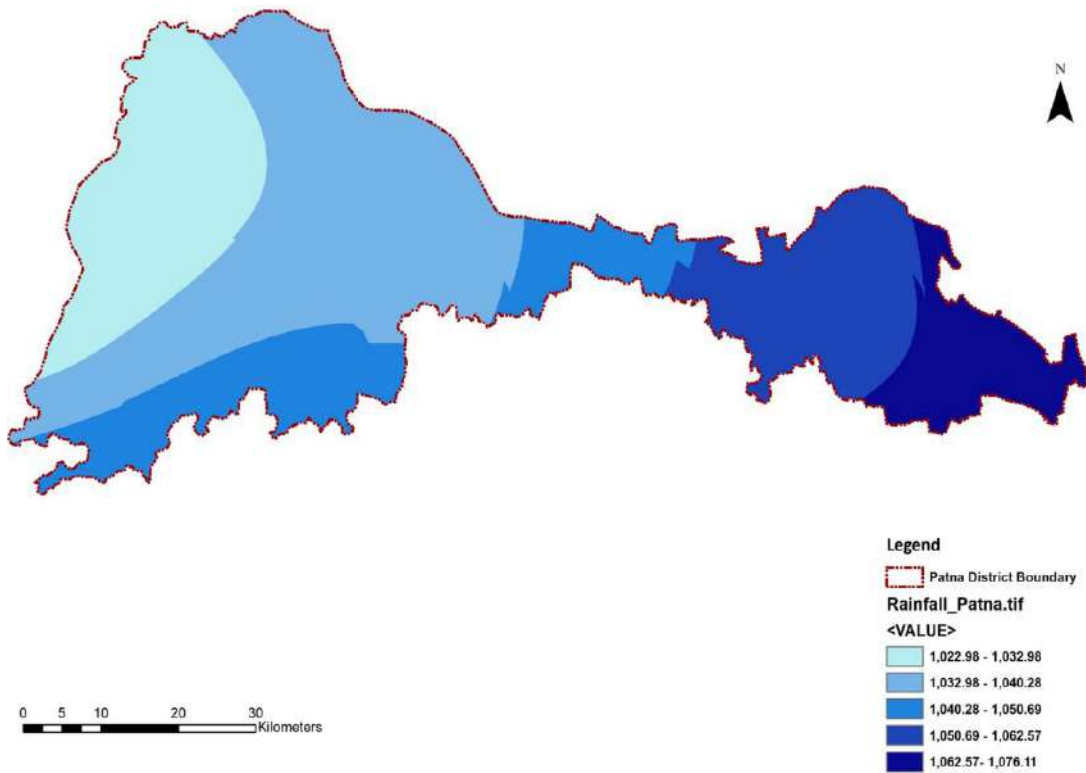
Fig. 6: Rainfall map of Patna district.

higher rank and vice-versa, for GWPZ and flood zones and drought zones soil will be less or not influential therefore in this study, I ignored this map in drought zone delineation. Fig.7 shows the study area's soil map. Table 2 demonstrates the different compositions of the soil of the Patna district.

LULC

Another significant parameter influencing the circulation and presence of groundwater in a region is LULC. The LU phenomenon has a stronger influence on the recovery of groundwater and also on the frequency of drought and floods. By looking at the LULC trend of the study region, the extent of land use, human habitation, and the length of uneven regions where groundwater can be recharged are determined. The change in land use/land cover pattern affects the groundwater recharge potential (Mangeshkumar et al 2019). The LULC area map was graded into eight different classes namely Cropland, Built-up Land, Shrubland, Fallow Land, Water Bodies, Plantations, Grassland, and Permanent Wetlands. The cropland, water bodies, and plantations were deemed to be among the most appropriate replenish zone for GWPZs because they prefer the seepage of rainwater and irrigated water; hence, they were given higher ranking followed by built-up land because the population tends to live near the place where groundwater is easily available and then permanent wetlands and then comes grassland, shrubland, fallow land in decreasing value of ranking respectively.

For drought zone delineation built-up and fallow land were given higher ranking followed by crop and shrubland and then plantation, grassland, water bodies, and permanent wetland were given value in decreasing order respectively.

For flood zone delineation cropland and built-up land were given higher ranks followed by shrubland then waterbodies and grassland were given moderate ranks and then plantation, permanent wetlands, and fallow land were assigned low ranks respectively. The study region's land use and land cover are shown in Fig. 8.

DEM

Digital elevation models (DEMs) are collections of horizontally referencing spaced evenly elevation values either to a Universal Transverse Mercator (UTM) projection or to a spatial coordinate system with a significant effect on the demarcation of GWPZs, drought, and flood regions. ASTER Global DEM Model Version3 with a resolution of 30 m was used for the Patna district. DEM in the study area is classified into five categories. For GWPZs lower elevation is more important and ranked with higher value and higher elevation with lower ranks and same follows for flood zone delineation because at lower elevation there will be more availability of groundwater and also the possibility of rainwater staying at a lower elevation so the risk of occurrence of flood will be at the higher side and for higher elevation, there will be less groundwater availability so rank will be less and in case of
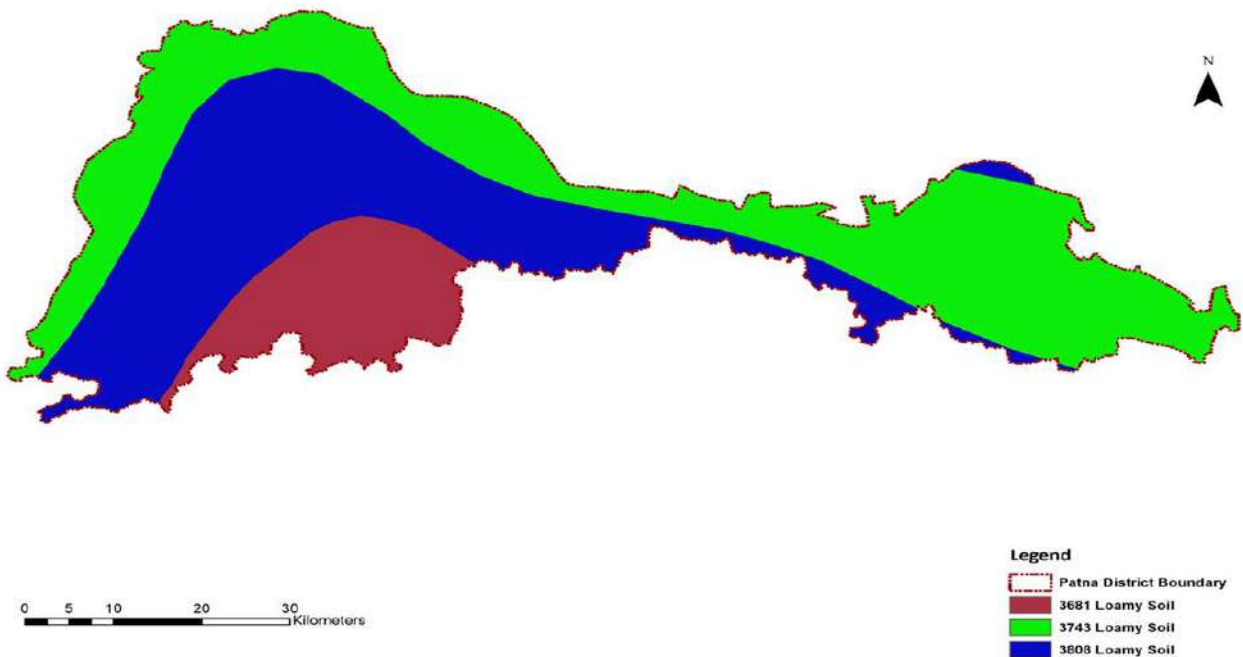
Fig. 7: Soil map of Patna district.

Legend

- ⬚ Patna District Boundary
- ◼ Cropland
- ◼ Built-up Land
- ◼ Shrubland
- ◼ Fallow Land
- ◼ Water Bodies
- ◼ Plantations
- ◼ Grassland
- ◼ Permanent Wetlands
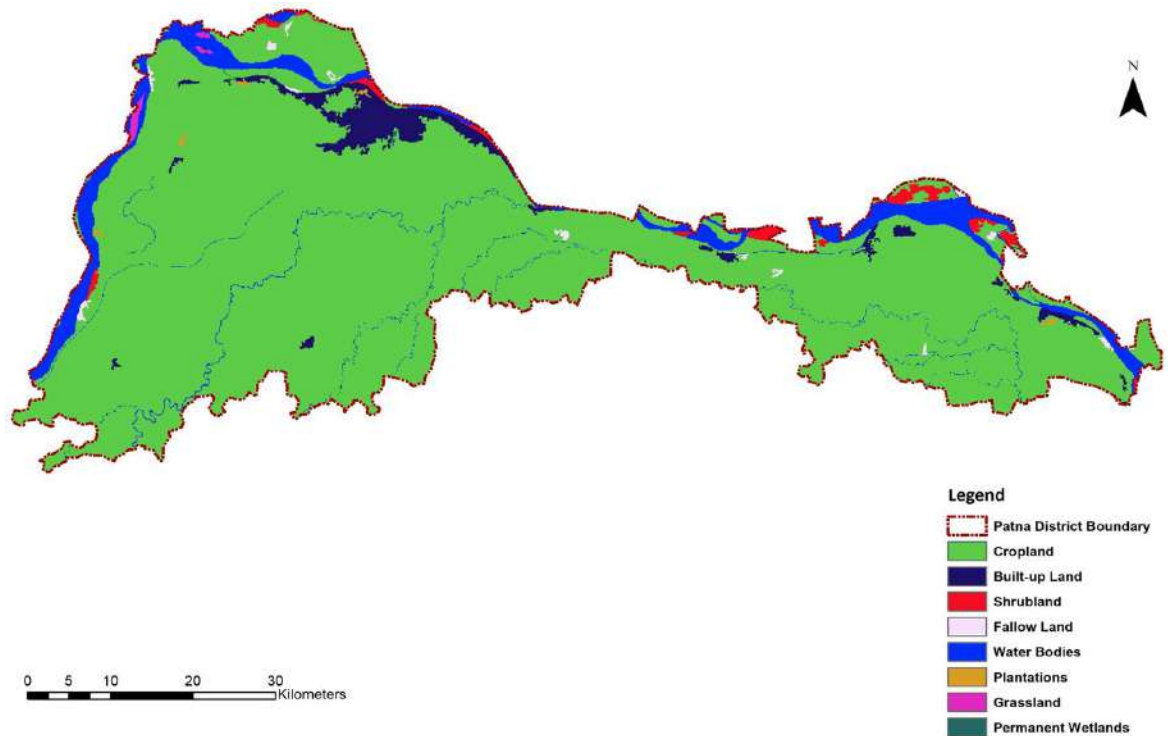
Fig. 8: LULC map of Patna district.

flood at higher elevation rainwater will not stay for long so less important and was given lower rank.

For drought zone delineation higher elevation will be of more importance so given a high rank because of less rainwater staying at elevated area resulting in more prone to drought occurrence and lower elevation will have a lower value because of more rainwater availability resulting in no or minimal risk of drought in a particular area. The study region's land use and land cover are shown in Fig. 9.

GWPZs

The classification of various groundwater zones is focused on the overlay analysis method worked out by seven influencing factors in the ArcGIS for the Patna district in Bihar. To achieve a more objective outcome, the parameters and their sub-categories were evaluated in-depth and relevant ranks and weights were allocated based on the expertise of professionals and references from different literature. The conceivable area thereby identified was divided into four sets poor, moderate, good, and very good based on the amount. As a result of better drainage density, plain field, greater rainfall intensity, and geomorphology, the eastern part indicates a very strong potential zone for groundwater has been seen. The western part of the district is more elevated than the eastern part with lesser drainage density, and less rainfall

magnitude which leads to less availability of groundwater potential zones in this area. About 3.47% of the entire area was assigned to such a favorable region, 30.00% in good, 55.16% in moderate, and 11.37% in poor for groundwater potential zones. Table 3 comprises four GWPZ groups for the Patna district showing weights and ranks of different parameters, as well as Fig. 10, which displays the spatial map.

The Groundwater Prospective Zonation Map Validation

Utilizing well discharge data for 50 wells, and groundwater depth data gathered from CGWB, the groundwater potential zonation map was verified. For this, the pre-monsoon and post-monsoon groundwater deviation results were analyzed for the year 2013. Patterns of water table rise and decline have been identified on these targeted wells, and it was categorized in five different ranges according to fluctuation in groundwater level for pre and post-monsoon data of the year 2013. These ranges are 1.15 to 0.17 which indicates less fluctuation and results in a continuous decrease of groundwater in that zone because of located in mostly built-up and agricultural areas, where groundwater is the major source of needing the demands of people and also for the crop growth. In this range total of 13 wells are found. Then ranges are 0.17 to 0.66(10 wells), 0.66 to 1.19(11 wells), 1.19 to 1.81(9 wells),
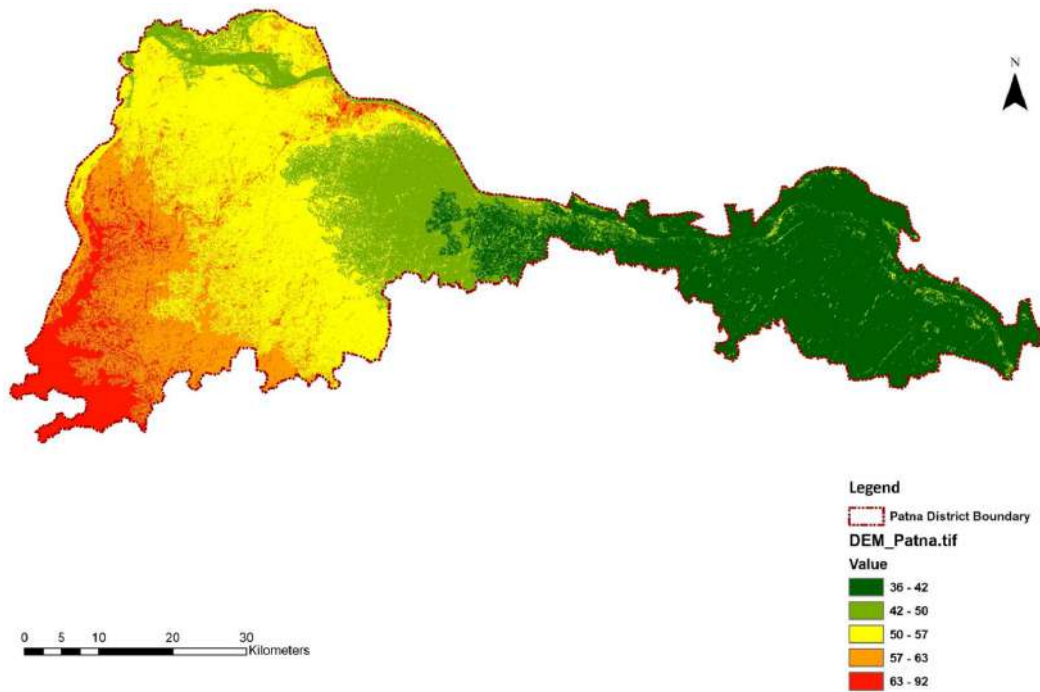
Fig. 9: DEM map of Patna district.
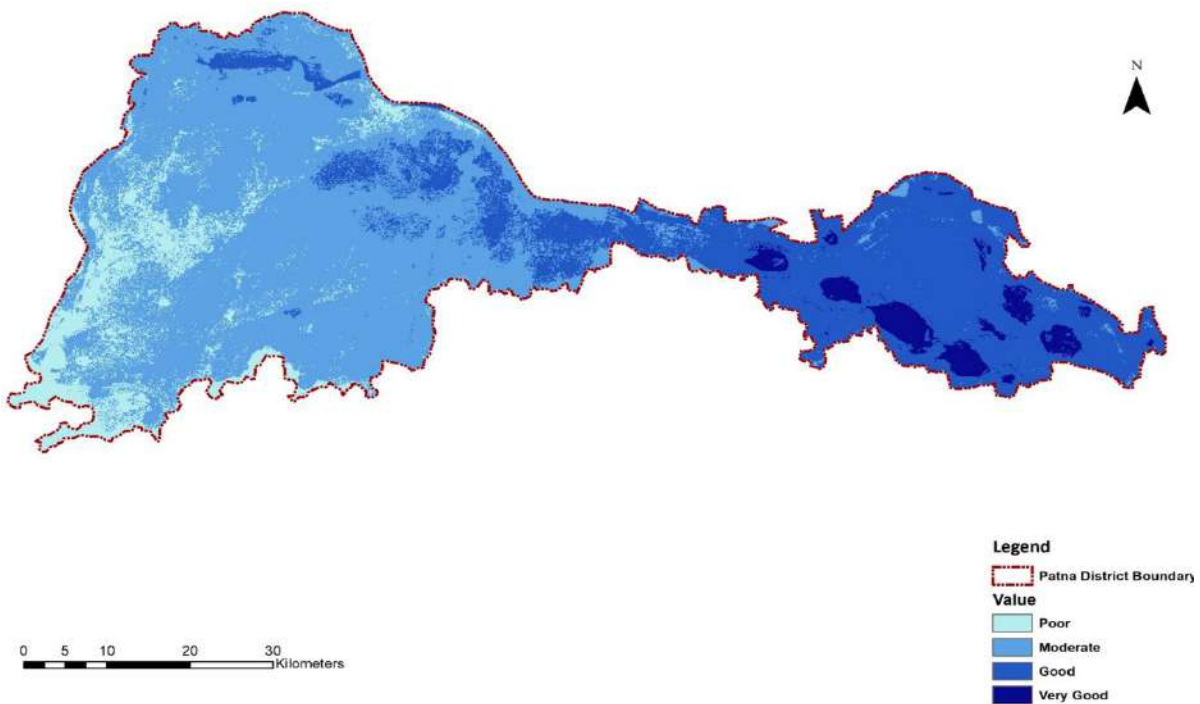
Fig. 10: GWPZs map of Patna district.

all these regions are in the moderate fluctuation zones and the ranged value 1.81 to 4.06 indicates the more fluctuation and results in recharging of groundwater easily because of located in near about waterbodies and in Ganga river vicinity and a total of 7 wells are found in this region. This statement, therefore, confronts the fact that the technique obtained for demarcating the possible groundwater region holds well and that adequate results have been obtained. Figs. 11, 12 &13 display the spatial map.

Drought Potential Zones

The delineation of drought potential zones is centered on the overlay analysis method performed out by five controlling parameters in the ArcGIS for the Patna district in Bihar. To achieve a more objective outcome, the parameters and their sub-categories were evaluated in-depth and relevant ranks and weights were allocated based on the expertise of professionals and references from different literature. The conceivable area thereby identified was divided into four categories like no risk, low risk, moderate risk, and high risk, based on the value. The eastern region after delineation shows that there is no low-risk zone because of located at lower elevations and higher rainfall occurrence and due to geomorphology too. But in the western region, most of the part is in moderate risk zone and very less part in high-risk

zones this is because the district is more elevated in that region, plain terrain, lower rainfall extent, and due to geomorphology too. About 5.82%% of the overall area was divided into a no-risk zone, 30.41% in low risk, 63.22% in moderate risk, and 0.55% in high risk. So this data shows that there is less possibility of severe drought but there is a possibility of drought occurrence in the district. Table 4 comprises four drought potential groups for the Patna district showing weights and ranks of different parameters, as well as Fig. 14, which displays the spatial map.

Flood Potential Zones

The delineation of flood potential zones is centered on the overlay analysis method performed out by seven controlling parameters in the ArcGIS for the Patna district in Bihar. To achieve a more objective outcome, the parameters and their sub-categories were evaluated in-depth and relevant ranks and weights were allocated based on the expertise of professionals and references from different literature. The conceivable area thereby identified was divided into four categories like no risk, low risk, moderate risk, and high risk, based on the value. Upon delineation, the eastern area suggests that there is a high and moderate risk zone because of located at lower elevations and higher rainfall occurrence, and due to geomorphology too, water will stay for long and will result
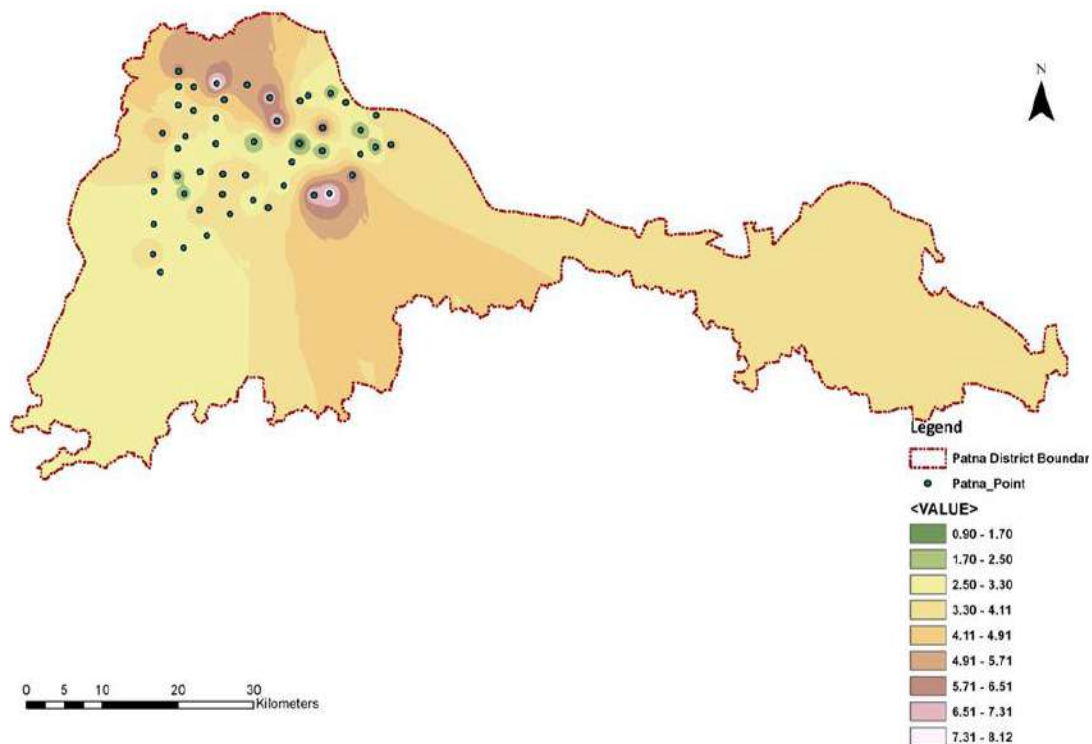
Fig. 11: Pre-Monsoon water depth of dug well of the year 2013.
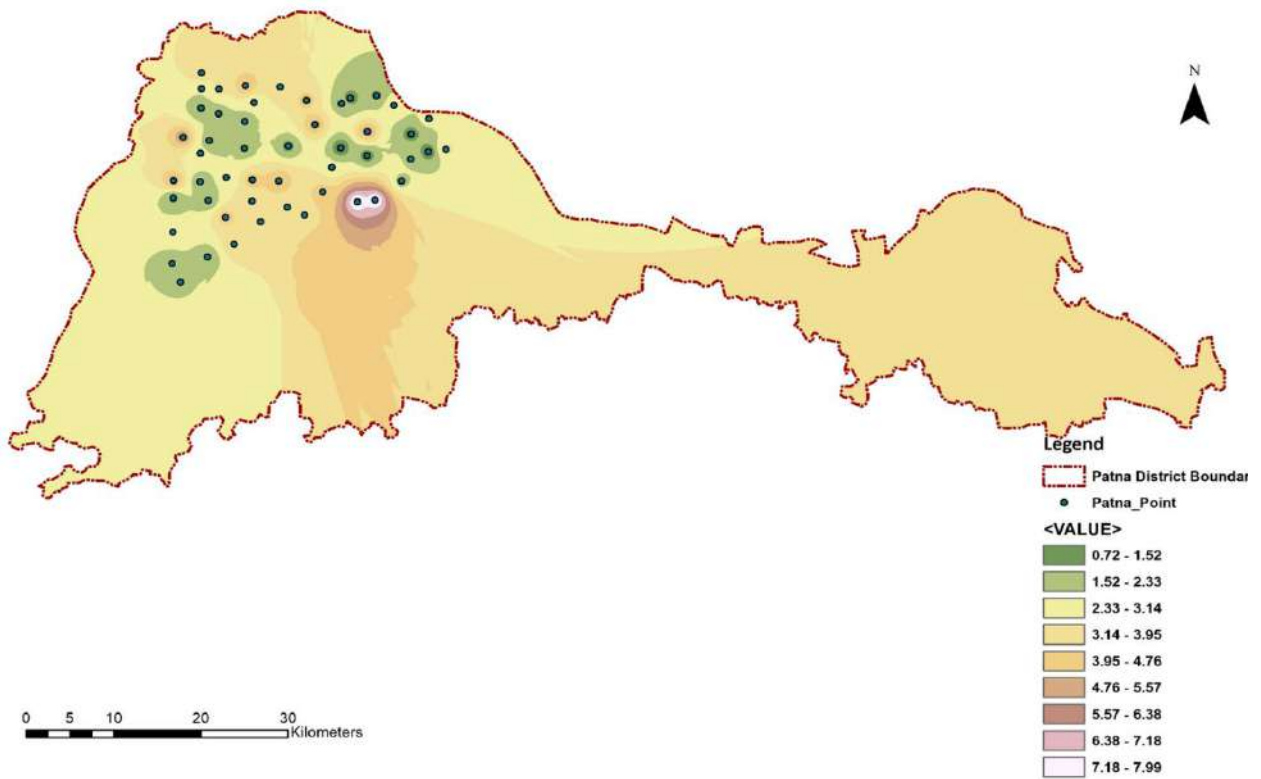
Fig. 12: Post-Monsoon water depth of dug well of the year 2013.
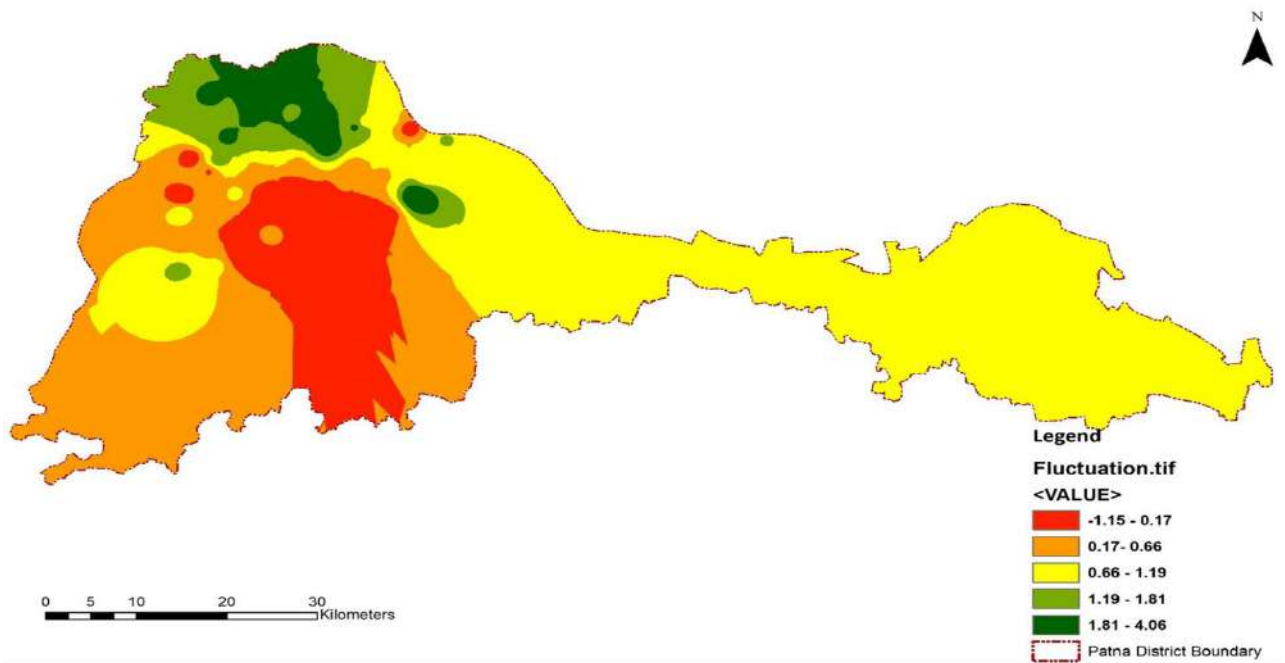
Fig. 13: Fluctuation map of Patna district of the year 2013.

in flood occurrence. But in the western region, most of the part is in the low-risk zone and very less part in no risk zones this is because the district is more elevated in that region, has lower rainfall magnitude, and due to geomorphology too,

water will not stay for long in that region resulting in less flood risk. About 2.89% of the overall area was divided into a no-risk zone, 62.35% in low risk, 31.16% in moderate risk, and 3.60% in high risk. So this data shows that there is less
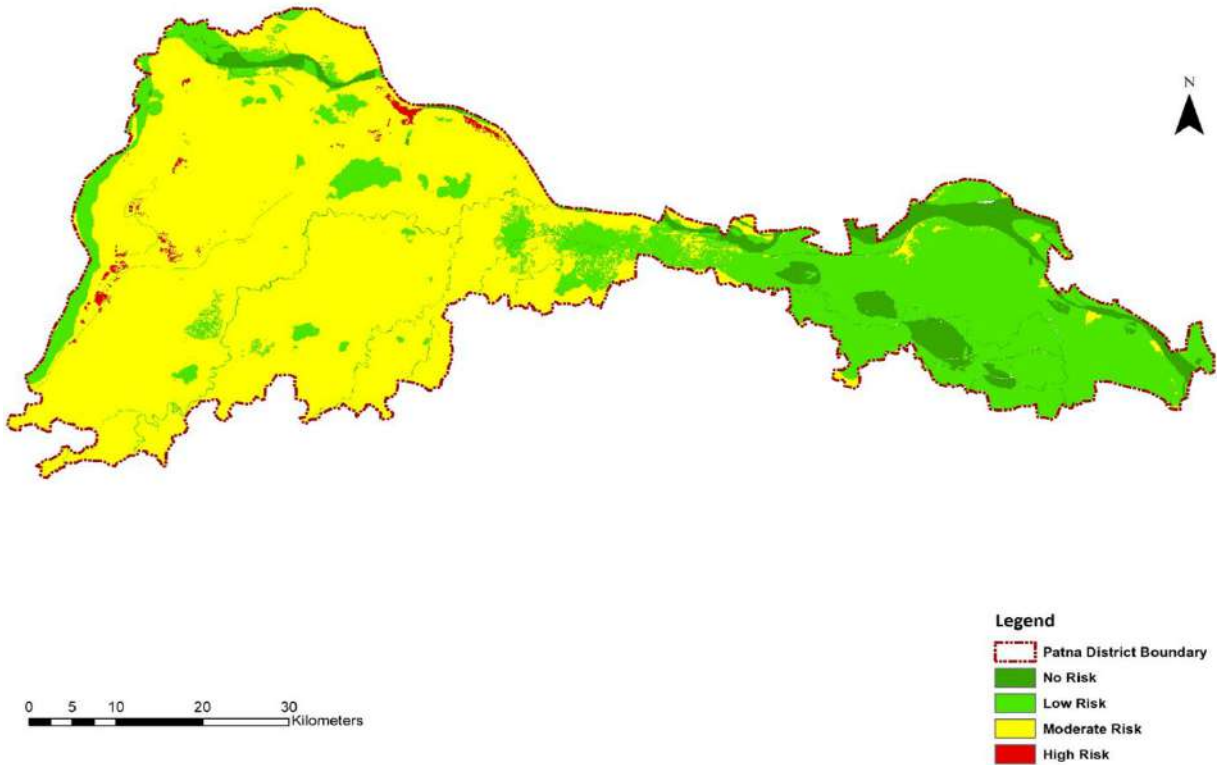
Fig. 14: Drought potential zone map of Patna district.
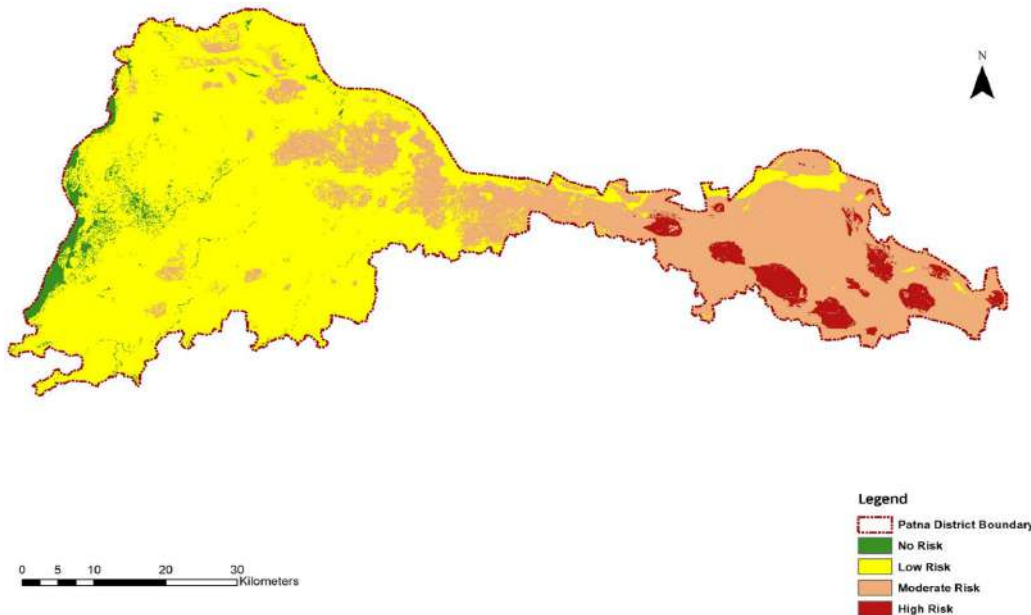
Fig. 15: Flood potential zone map of Patna district.

possibility of occurrence of flood in the western region of the district but the eastern region of the district has a chance of flood occurrence. Table 5 comprises four flood potential groups for the Patna district showing weights and ranks of different parameters, as well as Fig. 15, which displays the spatial map.

CONCLUSION

The study showed that the methods and strategies used were extremely efficient as they enabled the analyst to make a decision based upon its impact on the aspects considered and also supported by ArcGIS to better visualize the result's geographical extent. The conceivable area thereby identified was divided into four groupings poor, moderate, good, and very good extending about 11.37%, 55.16%, 30.00%, and

3.47%, of area respectively. The result was highly influenced by factors such as drainage density, DEM, and rainfall, while components such as soil, LULC, slope, and geomorphology had relatively less impact.

For drought potential locations, the simulation results are grouped into four grouping 1-no risk, 2-low risk, 3-moderate risk, and 4-high risk extending about 5.82%, 30.41%, 63.22%, and 0.55% of area respectively.

For flood potential locations, the simulation results are grouped into four grouping 1-no risk, 2-low risk, 3-moderate risk, and 4-high risk extending about 2.89%, 62.35%, 31.16%, and 3.60% of area respectively.

It helps the government to be prepared for the worst scenario in more risky zones of drought and flood and also to place NDRF teams near the higher or moderate-risk zones

Table 5: Allocated weight and rank to various thematic layers for Flood potential zones.

Theme	Feature	Weight	Rank
Geomorphology	Younger alluvial plain	8	2
	Older flood plain		4
	Active flood plain		5
	River		3
	Pond		3
	Waterbodies		3
LULC	Cropland	22	5
	Built-up land		5
	Shrubland		4
	Fallow land		1
	Waterbodies		3
	Plantations		2
	Grassland		3
	Permanent wetlands		2
Soil	3681 Loamy Soil	5	1
	3743 Loamy Soil		3
	3808 Loamy Soil		2
Drainage density	0.002-0.98	20	1
	0.98-1.39		2
	1.39-1.82		3
	1.82-2.64		4
	2.64-4.75		5
Rainfall [mm]	1022.98-1032.98	20	1
	1032.98-1040.28		2
	1040.28-1050.69		3
	1050.69-1062.57		4
	1062.57-1076.11		5
DEM [m]	36-42	20	5
	42-50		4
	50-57		3
	57-63		2
	63-92		1
Slope	0-0.82	5	5
	0.82-2.20		4
	2.20-4.05		3
	4.05-6.81		2
	6.81-23.47		1

to start the relief process as fast as possible in the affected region in the Patna district.

REFERENCES

Amer, R. 2013. An integrated approach for groundwater potential zoning in shallow fracture zone aquifers. Int. J. Remote Sens., 34(19): 6539-6561.

Balakrishnan, M. 2019. Groundwater potential zone mapping using geo-spatial techniques in Walayar watershed. Int. J. Eng. Adv. Technol., 9(1): 1157-1161.

Choudhary, K. M., Boori, S. and Kupriyanov, A. 2018. An approach to delineate groundwater potential zones in Orenburg, Russia. Disaster Adv., 11(8): 30-38.

Karanam, H., Mahapatra, A., Saranya, S., Vinaya, S., Prathyusha, S. and Shaik, M. 2014. Delineation of groundwater potential zones in the Greater Visakhapatnam Municipal Corporation (Gvmc) area. Int. J. Innov. Sci., 1(4): 478-492.

Krishna, A.P. and Kumar, A. 2018. Assessment of groundwater potential zones in coal mining impacted hard-rock terrain of India by integrating geospatial and analytic hierarchy process approach. Geocarto Int., 33(2): 105-129.

Kundal, R. and Joshi, A.K. 2004. Water resources development action plan for sasti watershed, Chandrapur district, Maharashtra using remote sensing and geographic information system. J. Indian Soc. Remote, 32(4): 363-372.

Mageshkumar, P., Anandakumar, S., Elango, L. and Pradeep, T. 2019. Application of geospatial techniques in delineating groundwater potential zones: A case study from South India. Arab. J. Geosci., 2(5): 1-15.

Pendke, M.S., Sreenivasan, G., Bhuibar, B.W., Kadale, A.S. and Khodke, U.M. 2007. Delineation of groundwater potential zones in Pingalgarh watershed of Maharashtra State using geospatial. J. Agric. Res. Technol., 42(3): 65-69.

Pradhan, B. 2009. Groundwater potential zonation for basaltic watersheds using satellite remote sensing data and GIS techniques. Central Europ. J. Geosci., 1(1): 120-129.

Rajaveni, K., Brindha, K. and Elango, L. 2017. Geological and geomorphological controls on groundwater occurrence in a hard rock region. Appl. Water Sci., 7(3): 1377-1389. doi:10.1007/s13201-015-0327-6.

Roy, B., Saraf, A.K., Choudhury, P.R., Sarma, B., Vijay, S. and Choudhury, S. 2004. GIS-based surface hydrological modeling in the identification of groundwater recharge zones. Int. J. Remote Sens., 25(24): 5759-5770.

Sitender, R. 2019. Delineation of groundwater potential zones in Mewat District, Haryana, India. Int. J. Geomat. Geosci., 2(1): 270-281.

The Drawing Characteristics and Critical Length of Single Polypropylene Fiber in Vegetation Concrete

Daxiang Liu *(**), Deyu Liu *, Baohua Zhang*, Bin Zhong***, Yueshu Yang*†, Jiangang Chen**, Yu Ding****, Zhenyao Xia**** and Wennian Xu****

*Key Laboratory of Disaster Prevention and Mitigation (China Three Gorges University), Hubei Province, Yichang 443002, China

**Key Laboratory of Mountain Hazards and Surface Processes, Institute of Mountain Hazards and Environment, Chinese Academy of Sciences, Chengdu 610041, China

***Fujian Yongtai Mintou Pumped Storage Co. Ltd., Fuzhou 350799, China

****Key Laboratory of Geological Hazards on Three Gorges Reservoir Area (China Three Gorges University), Ministry of Education, Yichang 443002, China

†Corresponding author: Yueshu Yang; michael_lewandowski@foxmail.com

ABSTRACT

Fiber-reinforced technology is an important method to improve the stability and durability of growing basis material. To evaluate the factors affecting the interfacial strength properties of polypropylene fiber reinforced vegetation concrete, single polypropylene fiber drawing tests were conducted by using a modified apparatus. The mechanical interaction behavior between vegetation concrete and polypropylene fiber was discussed by using a polarizing microscope. The results indicate that the drawing curves between polypropylene fiber and vegetation concrete show a typical multi-peak characteristic. And the interfacial shear strength is the minimum at the optimum water content (20%) in the 1d sample. It should be noted that both interfacial peak strength (IPS) and interfacial residual strength (IRS) increase with the increase of dry density and curing time for vegetation concrete. Then through multiple linear regression analysis, the empirical formula of critical fiber length in reinforced vegetation concrete is obtained, which can improve the engineering durability of vegetation concrete in harsh conditions.

INTRODUCTION

Vegetation concrete ecological protection technology, the theory of which refers to both civil engineering and ecology fields with the characteristics of high construction efficiency, low cost, and good engineering durability compared with other slopes ecological protection technology, is more suitable for the ecological protection of high steep rock slope which is more than 45° (Xia et al. 2011, Xu et al. 2019). And the vegetation concrete not only has a certain high strength and corrosion resistance characteristics but also has a porous structure similar to natural soil, thus it is more conducive to the growth of plants on the slope (Zhao et al. 2018). However, vegetation concrete is prone to collapse within 7d after spraying. At the same time, the durability of physical and mechanical indexes is also negatively affected under harsh conditions (Liu et al. 2013a, Gao et al. 2020). Therefore, it is significant to improve the initial stability and functional sustainability of vegetation concrete under harsh conditions.

Some studies have shown that the incorporation of fiber into the soil can effectively improve the shear strength, and tensile strength bearing capacity and enhance the toughness of soil (Wang et al. 2017, Li & Zornberg 2019, Zhao et al. 2021). And the cement soil reinforced by fibers has also concerned (Liang et al. 2016, Lu et al. 2016, Wang et al. 2018). The microscopic effect between cement and fiber was observed by SEM, Tang et al. (2011) and Yao et al. (2021) found that cohesion was the main force acting on the interface between cement and soil. At the same time, the increase of water content not only has no obvious effect on the bond strength, but it also can reduce the internal friction angle (Lovisa et al. 2010), therefore water content is also an important factor affecting fiber reinforcement. However, the internal friction angle of reinforced lime soil increased with the increase in curing time (Shi et al. 2011, Wang et al. 2019). And the incorporation of polypropylene fiber can improve the strength behavior of the material, and enhance the ductility and fracture toughness of the soil matrix (Liu

et al. 2013b). Therefore, it can be deduced that the polypropylene fiber was very appropriate to enhance the properties of vegetation concrete.

In this paper, a modified device was used to conduct a series of single fiber drawing experiments. The interfacial shear strength and the effect of water content, dry density, and curing time on the interfacial mechanical properties between polypropylene fiber and vegetation concrete were obtained. Finally, the drawing characteristics were analyzed and an empirical formula for the critical length of fiber was proposed, to guide the engineering application.

MATERIALS AND METHODS

Materials

The main materials required for the experiment include as follows: (1) Planting soil, which was taken from the common yellow-brown soil in Yichang City. It was air-dried and broken into pieces to pass through a 2 mm sieve. (2) P.O 42.5 ordinary Portland cement, which was produced by Huaxin Cement Co., LTD. (3) Organic material, which was prepared from local fir sawdust. (4) Amendment of habitat material, which was the patent product (Xu & Wang 2002) of China Three Gorges University. (5) Polypropylene fiber. (6) Water.

The composition and the physical properties of vegetation concrete are shown in Table 1 and Table 2. And the physical indexes of polypropylene fiber are listed in Table 3.

Preparation of Test Sample

As shown in Table 4, samples $S_1 \sim S_9$ (1d curing time) were prepared with three ratios of water content and three ratios of dry density respectively. And samples $T_1 \sim T_9$ (7d curing time) were prepared with the same method. The sample size is 5mm × 5mm × 5mm, and two small gaps (0.5 mm in width) were formed on the opposite sidewalls of the mold to facilitate fiber placement during compaction. The schematic diagram of the sample manufacture process is shown in Fig. 1, and the manufacturing method is described as follows:

(1) Half of the mixed material was put into the mold and flattened the surface carefully;

(2) Single polypropylene fiber was placed on the surface of the mixed material and passed through the reserved gap;

(3) The remaining half of the mixed material was put into the mold again and flattens the surface carefully;

(4) The piston was used to compact the mixed material to the target height;

(5) The sample was removed from the mold with the piston.

The samples were immediately wrapped with preservative film to prevent evaporation of water when manufacture was finished. At the same time, three parallel samples were prepared for taking the average value of the experiment.

Drawing Device and Testing Method

A device that was modified from the HP-50 HANDPI Digital Force Gauge was used in the test, as shown in Fig. 2. It was mainly composed of an HP-50 digital display drawing pressure gauge, tension sensor, drawing device, and other necessary instruments. The test method and operation process are introduced as follows:

(1) Place the sample in the left device in the figure, and pass the free section fiber at one end of the sample through the reserved joint of the left device;

(2) Fix the fiber of the free end with a modified HP-50 HANDPI Digital Force Gauge;

Table 1: Weight ratio of vegetation concrete.

Planting soil	Cement (P.O 42.5)	Organic material	Amendment of habitat material
100	10	6	4

Table 2: Basic physical property of vegetation concrete

Optimal water content	Plastic limit	Liquid limit	Maximum dry density
20%	19.5%	55%	1.99g/cm³

Table 3: Performance parameters of polypropylene fiber.

Diameter/ mm	Tensile strength/ MPa	Length/mm	Corrosion resistance
0.048	700	18	better
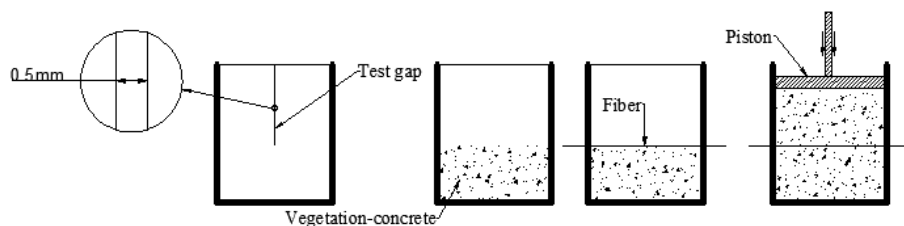
Fig. 1: Sketch drawing of sample prepared process.
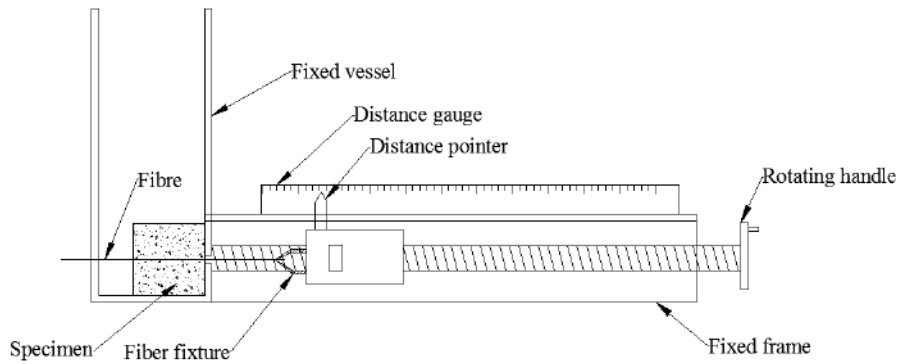
Fig. 2: Single fiber drawing test device.

(3) Connect the power supply to make the tension meter move uniformly at a constant speed of 1.5mm/min. At the same time, record the test process with the video device, finally, the indication number and displacement change of the tension meter were analyzed and extracted.

Ten data were continuously collected for the experiment required, and the experiment can be terminated when the variation range does not exceed 0.02N (Tang et al. 2009). Finally, the force in the final stable state was taken as the interfacial residual strength.

Computational Formula

The interfacial peak strength (*IPS*) and the interfacial residual strength (*IRS*) can be defined and calculated as follows (Zhang et al. 2015):

$$IPS = \frac{N_{max}}{S} \qquad …(1)$$

$$IRS = \frac{N_r}{S} \qquad …(2)$$

Where *IPS* is the interfacial peak strength (MPa); *IRS* is the interfacial residual strength (MPa); N_{max} is the peak load before the interfacial shear failure (N); *S* is the contact area between the fiber and vegetation concrete, which is calculated

according to the size of the sample and the diameter of the fiber (mm^2); N_r is the residual tensile force when the tension meter value tends to be stable (N).

The critical length of fiber (l_c) can be calculated as follows (Tang et al. 2009):

$$l_c = \frac{R_f d}{2 \times IPS} \qquad …(3)$$

Where R_f is the tensile strength of the single fiber (MPa); *d* is the fiber diameter (mm); *IPS* is the interfacial peak strength (MPa).

RESULTS AND DISCUSSION

Drawing Characteristics of Single Fiber in Vegetation Concrete

As shown in Fig.3, it has a multi-peak characteristic of fiber-reinforced vegetation concrete. The tension increases and decreases repeatedly with the increase of displacement. And the tensile failure occurred when the tension tends to be stable gradually, then the load maintains a constant residual value until the end of the drawing test. According to the measured peak and residual drawing load, the corresponding interfacial peak strength (*IPS*) and interfacial residual strength (*IRS*)

Table 4: Test parameters of vegetation concrete.

Samples	Water content ω/%	Dry density [g.cm^{-3}]
S_1、T_1	18	1.7
S_2、T_2	18	1.8
S_3、T_3	18	1.9
S_4、T_4	20	1.7
S_5、T_5	20	1.8
S_6、T_6	20	1.9
S_7、T_7	22	1.7
S_8、T_8	22	1.8
S_9、T_9	22	1.9
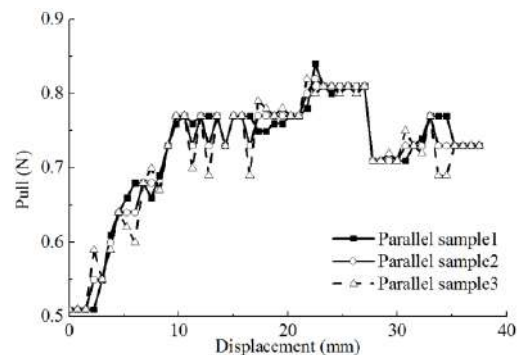
Fig. 3: Drawing curves of three parallel samples in S1.

are obtained. However, it has a single-peak characteristic of polypropylene fiber reinforced clay (Coppola et al. 2017, Van et al. 2019). Therefore, the difference between the drawing curves of clay and vegetation concrete is probably attributed to the different interface mechanical interactions.

The wave-like pattern of the drawing curves may be related to the cement hydration products in vegetation concrete. At the beginning of the experiment, the tensile force is not enough to deform the fiber, and the interface between the fiber and vegetation concrete slid with the increase of tensile force. The tensile force of the fiber is mainly linearly distributed during the separation process in clay (Gowthaman et al. 2018). However, the fiber is anchored by cement hydration products in vegetation concrete and produces relative motion by overcoming the anchoring force (Huang 2019). Due to the uneven distribution of cement hydration products in vegetation concrete, there are many anchoring sections on the fiber. Therefore, the drawing curve exhibits a multi-peak state distribution. Obviously, as the drawing displacement increases, the drawing load increases to overcome the anchoring of the first stage, then decreases, then increases when the next anchor is encountered, and then decreases again. After the fiber overcomes all anchoring forces, the fiber can only overcome the sliding friction. Due to the sliding friction being relatively stable, thus the interface residual strength and the range of variation are relatively stable.

The fibers were dyed with phenolphthalein after being stretched. The microscopic characteristic of dyed fibers before and after being drawn are shown in Fig.4 and analyzed as follows:

(1) The fiber diameter is significantly slender after the test. This is due to the plastic deformation of the fiber by tension, resulting in an increase in length but a gradual decrease in diameter.

(2) Many scratches appeared on the surface of the fiber. This indicates that the fiber is subjected to a force perpendicular to the fiber direction during stretching, which is extruded by hard particles in the vegetation concrete.

(3) There is a noticeable purple-red color in the fiber scratches and attachments after phenolphthalein dying, and only the cement hydration products are alkaline in the samples (Pan et al. 2020), which indicates that the main reason for the vertical force and cohesion is the existence of cement hydration products.

The Influence of Water Content

Water content has an important influence on *IPS* and *IRS* in vegetation concrete. As shown in Table 5, both *IPS* and *IRS* are minimal at the optimum water content (20%) in the 1d sample. The interfacial shear strength between the fiber and vegetation concrete is mainly composed of three parts: the anchoring force, interfacial friction force, and cohesion (Li et al. 2014). The anchoring force is mainly related to the content of cement, water, and cement hydration products. The interfacial friction is mainly related to particle shape, grain composition, normal stress, soil water content, and effective contact area with soil (Cai et al. 2006). In this study, the interfacial forces are the anchoring force and interfacial friction force. Due to the increase of water content in soil pores, the fiber has a certain lubricating effect when moving in the soil, thereby interfacial friction force decreased (Wu et al. 2012). The interfacial shear strength is lower at a water content of 20% than that of 18%. It is speculated that the cement hydration products in vegetation concrete are deficient when the water content is not reaching optimal, thus the increase rate of the anchoring force is slower than the interfacial friction force reduction rate.

The interfacial shear strength increases significantly at the water content of 22%. Reasons for that are the friction force becomes constant and the cement hydration products rapidly increase, resulting in the anchoring force increasing quickly with the increase of water content. When the water content exceeds the optimum water content, although the water between the particles becomes, even more, the excess free water promotes the hydration reaction of the cement, which increases the anchoring force, resulting in the interfacial friction force not continuing to decrease rapidly. Therefore, the increased range of anchoring force is higher than the decreased range of interfacial friction force, which results
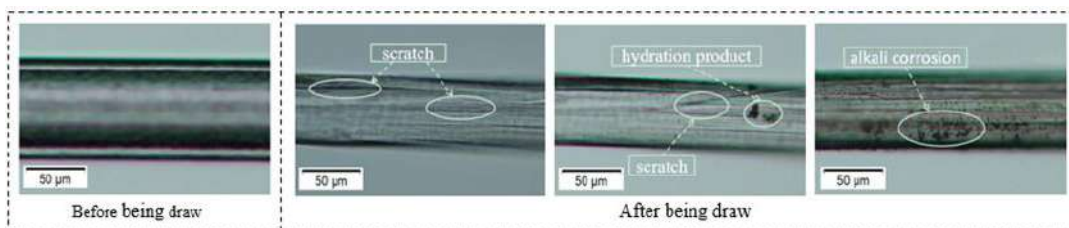
Fig. 4: Comparison of the fiber before and after being drawn.

Table 5: The results of *IPS* and *IRS* for vegetation concrete.

	Curing time/d	Water content/%	Interfacial shear strength/(MPa)		
			1.7 g.cm^{-3}	1.8 g.cm^{-3}	1.9 g.cm^{-3}
IPS	1	18	0.82	0.94	0.98
		20	0.77	0.87	0.98
		22	0.86	0.99	1.03
	7	18	0.86	0.77	1.11
		20	0.96	1.26	1.28
		22	0.96	1.31	1.32
IRS	1	18	0.73	0.9	0.9
		20	0.71	0.8	0.9
		22	0.81	0.9	0.99
	7	18	0.77	0.68	1.03
		20	0.81	1.01	1.07
		22	0.9	1.01	1.12

in a corresponding increase of interfacial shear strength at a water content of 22%. As shown in Table 5, there are some differences between the curing time of 1d and 7d. As the curing time increases, the degree of cement hydration reaction is more intense, and more cement hydration products are produced, resulting in the interfacial shear strength at the water content of 20% being higher than that of 18%. It can be seen from Fig.5, that the drawing curves still show multi-peak characteristics at different water content, which indicates that the water content has no significant influence on the drawing curve characteristic.

The Influence of Curing Time

As shown in Table 5, as the curing time increases, the increased range of *IPS* is 4.88%~44.83% and the increased range of *IRS* is 5.48%~26.25%. The reason for that is the cement hydration products are even more and the particles are larger in the 7d sample (Ruan et al. 2016). Thus, the
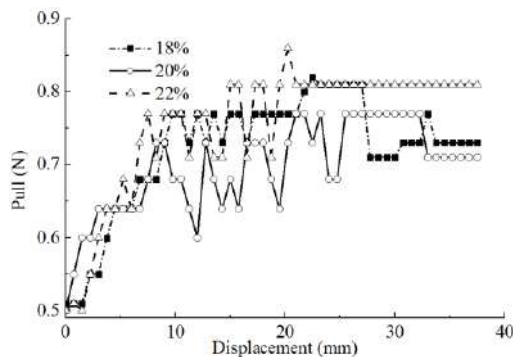
Fig. 5: Drawing curves of 1d samples in the dry density of 1.7 g/cm^3.

cement hydration products and fiber have more anchoring points, which enhance the anchoring force between the fiber and vegetation concrete. The microstructure of cement under different curing times is different, and the flocculation and hydration products appear in the process of cement hydration reaction gradually (Wang et al. 2008). These products attach to the interface of the fiber and then reinforce the interface between the fiber and vegetation concrete. Besides, as the curing time increases, the cement hydration products fill the pores of soil particles. Therefore, the effective contact area between the fiber and vegetation concrete is increased, and the interfacial shear strength between the fiber and vegetation concrete is further enhanced.

The Influence of Dry Density

As shown in Fig. 6, with the increase in dry density, the *IPS* and *IRS* increase by 27.27% and 11.11% respectively. As the dry density increases, the effective contact area between the fiber and hard particles increases accordingly, and the corresponding vertical stress which is acting on the fiber by cement hydration products also increases, thus enhancing the anchoring force among the interface of vegetation concrete. For vegetation concrete with different dry densities, the increase of dry density also reduces the porosity among the particles of vegetation concrete (Zhao et al. 2013). The effective contact area increases relatively between the fiber and vegetation concrete, and the interfacial friction force between the fiber and vegetation concrete also increases (Zhang et al. 2014). Moreover, the increases in dry density result in the fiber extruded by hard particles in vegetation concrete, which causes the fiber in the sample to bend, thus increasing the effective contact area between the fiber and

vegetation concrete, and increasing the interfacial friction force.

The Determination of the Critical Length and Empirical Formula

Determination of the Critical Length

Determining the reasonable length of the fiber is significant in practical engineering. If the length of the actual fiber is short than the critical length, the incorporated fiber is pulled out when vegetation concrete is destroyed (Liang et al. 2016); when the fiber length exceeds the critical length, the fiber breaks in the middle position and cause fiber waste (Zhao et al. 2015); however, the fiber deformed firstly when the length of the fiber equal to the critical length, then the middle of the fiber will gradually become thinner until it is broken. Therefore, the critical length is a key factor to maximize the mechanical properties of polypropylene fiber when it is used as reinforced material in engineering. To calculate the critical length of polypropylene fiber, the assumptions were made as follows:

(1) The direction of the fiber is always consistent with the tensile meter;

(2) The interfacial shear strength of vegetation concrete remains constant during the drawing process.

Therefore, the maximum critical length of the fiber-reinforced vegetation concrete proposed in this study is a reference for the design of practical projects. The maximum critical length of the fiber is calculated by the formula (3) and the results are shown in Table 6.

Determination of Empirical Formula

(1) Establish an empirical formula

It is observed from Table 6, that with the increase in curing time, the interfacial peak strength (*IPS*) between vegetation concrete and the fiber increases, and the critical length of fiber decreases. The interfacial shear strength of vegetation concrete has a low power at the initial stage of spraying. Therefore, adding the appropriate length of fiber at this stage can effectively improve engineering strength. In this study, the maximum critical length (l_{max} *The*) the empirical formula only includes the water content (ω), the dry density (ρ), and the curing time (T) of the vegetation concrete. It is introduced and defined as follows:

$$l_{max} = k\omega^a\rho^bT^c \qquad \ldots(4)$$

Where l_{max} is the critical length of the fiber (mm); ω is the water content (%); ρ is the dry density (g.cm³); is the curing time (d); k、a、b and c are constants in the empirical formula. It should be explained that the empirical formula does not take into account the difference between the left and right dimensions of the equation. The purpose is only to give a numerical empirical formula.

The logarithmic equation is drawn from the logarithm of the left and right sides of equation (4) as follows:

$$lgl_{max} = lgk + alg\omega + blg\rho + clgT \qquad \ldots(5)$$

Established $Y = lgl_{max}$, $m = lgk$, $X_1 = lg\omega$, $X_2 = lg\rho$, $X_3 = lgT$ and get the transformation of multivariate regression linear equation as follows:

$$Y = m + aX_1 + bX_2 + cX_3 \qquad \ldots(6)$$

The experimental data of S_1-S_9 were substituted into the formula (6), and the unknown coefficients m, a, b, and c of the multiple linear regression equation can be solved.

(2) Empirical formula

The multiple linear regression equation was solved by the experimental data. As shown in Fig. 7, the experimental data indicates that the independent variable correlation is not obvious. Moreover, the R^2 of the model is 0.72 and the correlation is remarkable ($p<0.05$) indicating that the model design is reasonable.

Consequently, the results of the four unknown coefficients in equation (6) are obtained: m= 2.746, a= -0.804,
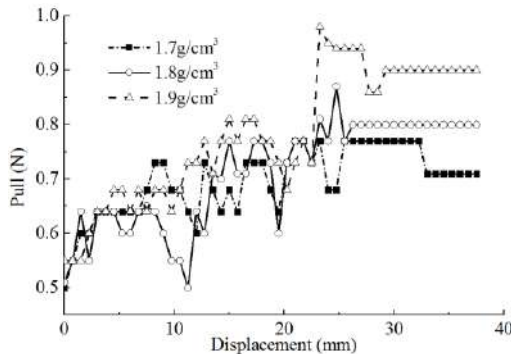
Fig. 6: Drawing curves of 1d samples in water content of 20%.

Table 6: Results of the critical length for all samples.

Samples	mm	Samples	mm
S_1	15.45	T_1	14.73
S_2	13.48	T_2	16.45
S_3	12.93	T_3	11.41
S_4	16.45	T_4	13.20
S_5	14.56	T_5	10.05
S_6	12.93	T_6	9.90
S_7	14.73	T_7	13.20
S_8	12.80	T_8	9.67
S_9	12.30	T_9	9.59

b= 2.194 and c = -0.084. Thus, the equation is expressed as follows:

$$Y = 2.746 - 0.804X_1 - 2.194X_2 - 0.084X_3 \qquad …(7)$$

Substituted $Y= lgl_{max}$, $m= lgk$, $X_1= lg\omega$, $X_2= lg\rho$, and $X_3= lgT$ to formula (7) and converted as follows:

$$lgl_{max} = 2.746 - 0.804lg\omega - 2.194lg\rho - 0.084lgT \qquad …(8)$$

The equation on both sides of equation (8) was logarithmic, and then the equation is converted as follows:

$$l_{max} = 10^{2.746}\omega^{-0.804}\rho^{-2.1941}T^{-0.084} \qquad …(9)$$

Therefore, formula (9) can be confirmed as the empirical formula for the maximum critical length of polypropylene fiber in vegetation concrete from 1d curing time to 7d curing time.

CONCLUSION

(1) The drawing curves of polypropylene fiber and vegetation concrete showed a typical multi-peak characteristic. And as the curing time increases, the increased range of *IPS* is 4.88%~44.83% and the increased range of *IRS* is 5.48%~26.25%.

(2) The strength of cement hydration products increases with the increase of curing time, thus the anchoring force between vegetation concrete and the fiber is improved. The interfacial shear strength is the minimum at the optimum water content (20%) in the 1d sample. In addition, the *IPS* and *IRS* increase with the increase of dry density.

(3) The empirical formula of the critical length is obtained by multiple linear regression analysis and combined

Fig. 7: Normal P-P graph of regression normalized residual.

with mathematical calculation. The formula will provide a reference for the suitable deployment of polypropylene fiber length in vegetation concrete under different design and engineering conditions.

REFERENCES

Cai, Y., Shi, B., Ng, C.W.W. and Tang, C.S. 2006. Effect of polypropylene fiber and lime admixture on engineering properties of clayey soil. Eng. Geol., 87(3-4): 230-240.

Coppola, B., Scarfato, P., Incarnato, L. and Di Maio, L. 2017. Morphology development and mechanical properties variation during cold-drawing of polyethylene-clay nanocomposite fibers. Polymers, 9(6): 1-17.

Gao, J.Z., Zhou, M.T., Xu, W.N., Liu, D.X., Shen, J. and Peng, S.T. 2020. The evolution of structural properties of vegetation concrete under freeze-thaw cycles. Int. J. Elect. Eng., 29: 61 doi: 10.1177/0020720920930363.

Gowthaman, S., Nakashima, K. and Kawasaki, S. 2018. A state-of-the-art review on soil reinforcement technology using natural plant fiber materials: Past findings, present trends, and future directions. Materials, 11(4): 553.

Huang, M.J. 2019. Experimental study on split tensile strength of glass fiber reinforced cement soil. J. Rail. Sci. Eng., 16(4): 938-942.

Li, C.L. and Zornberg, J.G. 2019. Shear strength behavior of soils reinforced with weak fibers. J. Geotech. Geoenviron. Eng., 145(9): 06019006.

Li, J., Tang, C.S., Wang, D.Y., Shi, B. and Pei, X.J. 2014. Study on the interfacial shear strength of wave-shape fiber reinforced soil through single fiber pullout tests. Chinese J. Geotech. Eng., 36(9): 1696-1704.

Liang, Y.Z., Chen, Y., Liu, D.X., Xu, W.N. and Yao, X.Y. 2016. Effect of additive plant fiber on shearing strength of vegetation-compatible concrete under freezing-thawing cycles. Bull. Soil Water Conserv., 36(2): 136-139+145.

Liu, B.S., Tang, C.S., Li, J., Wang, D.Y., Zhu, K. and Tang, W. 2013b. Advances in engineering properties of fiber-reinforced soil. J. Eng. Geol., 21(4): 540-547.

Liu, D.X, Xu, W.N., Cheng, Z.L., Zhou, Z.J. and Cai, X.Y. 2013a. Improvement test on frost resistance of vegetation-concrete and engineering application of test fruitage. Environ. Earth Sci., 69(1): 161-170.

Lovisa, J., Shukla, S.K. and Sivakugan, N. 2010. Shear strength of randomly distributed moist fiber-reinforced sand. Geosynth. Int., 17(2): 100-106.

Lu, Q., Guo, S.L., Wang, M.M. and Gao, M. 2016. Experimental study of mechanical properties of fiber cement soil. Rock Soil Mech., 37(2): 421-426.

Pan, B., Ding, Y., Huang, X.L., Gao, F., Xu, W.N. and Liu, D.X. 2020. Study on mechanical properties of fiber-reinforced vegetation concrete under dry and wet cycle. J. China Three Gorges Univ. Nat. Sci., 42(1): 63-67.

Ruan, B., Peng, X.X. and Deng, L.F. 2016. Experimental study on shear strength parameters of cement-soil. J. Rail. Sci. Eng., 13(4): 662-668.
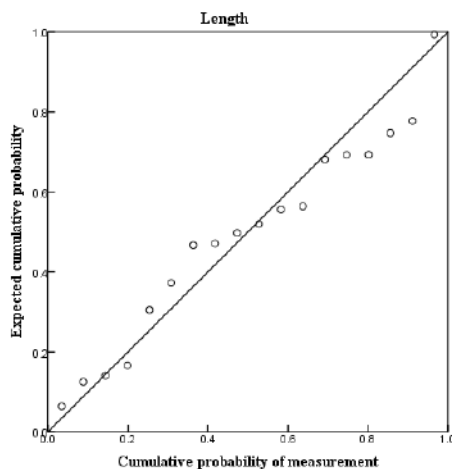
Shi, L.G., Zhang, M.X. and Cao, P. 2011. Triaxial shear strength characteristics of lime-soil reinforced with polypropylene fiber inclusions. Rock Soil Mech., 32(9): 2721-2728.

Tang, C.S., Shi, B. and Gu, K. 2011. Microstructural study on interfacial interactions between fiber reinforcement and soil. J. Eng. Geol., 9(4): 610-614.

Tang, C.S., Shi, B., Gao, W. and Liu, J. 2009. Single fiber pull-out test and the determination of critical fiber reinforcement length for fiber-reinforced soil. Rock Soil Mech., 30(8): 2225-2230.

Van, T.B., Reynolds, C.T., Bilotti, E. and Peijs, T. 2019. Nanoclay assisted ultra-drawing of polypropylene tapes. Nanocomposites, 5(4): 114-123.

Wang, B., Yang, W.M. and Li, Z.Q. 2008. Micro mechanism of strength increase with curing time for compacted cement soil. J. Univ. Sci. Technol. Beij, 30(3): 233-238.

Wang, M.M., Lu, Q., Guo, S.L., Gao, M. and Shen, Z.T. 2018. Dynamic behavior of soil with fiber and cement under cyclic loading. Rock Soil Mech., 39(5): 1753-1760.

Wang, Y.X., Guo, P.P., Li, X., Lin, H., Liu, Y. and Yuan, H.P. 2019. The behavior of fiber-reinforced and lime-stabilized clayey soil in triaxial tests. Appl. Sci. Basel, 9(5): 900.

Wang, Y.X., Guo, P.P., Ren, W.X., Yuan, B.X., Yuan, H.P. and Zhao, Y.L. 2017. Laboratory investigation on strength characteristics of expansive soil treated with jute fiber reinforcement. Int. J. Geomech., 17(11): 04017101.

Wu, Y.K., Niu, B. and Sang, X.S. 2012. Experimental study of mechanical

properties of soil randomly included with sisal fiber. Hydrogeol. Eng. Geol., 39(6): 77-81.

Xia, Z.Y., Xu, W.N. and Wang, L.H. 2011. Research on characteristics of early strength of ecological slope-protected base material of vegetation-growing concrete. Rock Soil Mech., 32(6): 1719-1724.

Xu, W.N., Xia, D., Zhao, B.Q., Xia, Z.Y., Liu, D.X. and Zhou, M.T. 2019. Research on Vegetation Ecological Restoration Technology in Disturbed Areas Of Hydropower Projects. Science Press, Beijing, pp. 108-113.

Yao, X., Huang, G., Wang, M.M. and Dong, X.Q. 2021. Mechanical properties and microstructure of PVA fiber-reinforced cemented soil. KSCE J. Civil Eng., 25(2): 482-491.

Zhang, C.C., Zhu, H.H., Tang, C.S. and Shi, B. 2015. Modeling of progressive interface failure of fiber-reinforced soil. J. Zhejiang Univ. Eng. Sci., 49(10): 1952-1959.

Zhao, B.Q, Xia, L., Xia, D., Liu, D.X. and Xia, Z.Y. 2018. Effect of cement content in vegetation concrete on soil physico-chemical properties, enzyme activities, and microbial biomass. Nat. Environ. Pollut. Technol., 17(4): 1065-1075.

Zhao, C., Shen, X.D., Jia, S.H. and Zhao, C.F. 2013. Influence of density on strength of cemented soil. Chin. J. Geotech. Eng., 35(S1): 360-365.

Zhao, N.Y., Wu, H.J. and Huang, Z.Y. 2021. Strength behavior of red clay reinforced by basalt chopped fiber. Arab. J. Geosci., 14(1): 15.

Zhao, Y.P., Yan, H. and Han, J. 2015. Analysis of the macroscopic interfacial behavior of the fiber pullout using an elastic-plastic cohesive model. Chin. J. Theoretical Appl. Mech., 47(1): 127-134.

Environmental Changes in a Mediterranean River (Upper Sebou, Morocco) Between 1981 and 2017

Mariam Zerrouk*†, Mohamed Dakki*, Mohammed Aziz El Agbani* and Oumnia Himmi*

*Department of Zoology, Laboratory of Geo-Biodiversity and Natural Patrimony, Scientific Institute, Mohammed V University in Rabat, Morocco
†Corresponding author: Mariam Zerrouk; mariam.meknes@gmail.com

ABSTRACT

The functioning and sustainability of lotic ecosystems depend to a large extent on their thermal and hydrological regimes. In the Mediterranean region, these factors are very sensitive to climate and anthropization which have undergone deep changes over the last four decades. Having noted the drying up of many permanent streams in Morocco, we conducted in 2015-2017 a new study with the aim of analyzing and assessing abiotic changes in the Upper Sebou (Middle Atlas, Morocco). A former study was carried out in 1981-1985. Indeed, over the last four decades, this river has been exposed to multiple disturbances, due to both recurrent droughts and human pressures. To describe and assess these changes, we used 16 abiotic variables that were measured in 11 ecosystems along the central course of the river. The comparison was mainly carried out using the multiple factorial correspondence analysis (MFCA), through a ternary matrix "variables × stations × time", gathering old and new data in the same mesological structure. The analysis revealed the classical upstream-downstream ordering of the studied ecosystems, where most of the ecosystems recorded a downstream migration from their 1981 position. In this evolutionary perspective, the study involves hydrological and thermal factors, which show mainly a reduction in flow and a slight increase in temperature and water mineralization, both in summer and winter. It is assumed that water withdrawals, especially for irrigation, together with climatic droughts in the region, are responsible for these long-term evolutionary trends.

INTRODUCTION

In the Mediterranean region, the inland aquatic ecosystems are highly vulnerable to climate changes, as their hydrology is intimately linked to climate (Giudicelli et al. 1985), which continues to change globally (Sala et al. 2000, Heino et al. 2009, Whitehead et al .2009). This vulnerability is increased by the natural aridity of the climate and frequent drought crises (Haida et al. 1999, Garouani & Tribak 2006), which directly affect surface waters, mainly their hydrological and thermal regimes, which are fundamental factors for the functioning of these ecosystems (Illies & Botosaneanu 1963, Dakki 1986a, 1987, Doledec & Chessel 1989, El Agbani et al. 1992). Indeed, the climate aridification leads to an increase in water temperature, consequently to a generalized decrease of the flow, or even the drying up of rivers. Several abiotic variables are then simultaneously modified (gas contents, evaporation rate, primary production, etc.). These factors lead to generalized and increasing physiological stress within living populations close to their upper limit of thermo-tolerance (i.e. Botella-Cruz et al. 2016) and can alter both metabolism, growth, and life

cycle of the organisms, and the communities organization (Durance & Ormerod 2010, Walther 2010).

These changes are amplified by human activities, in particular by water withdrawals, bearing in mind that the human need for water resources has greatly increased during the last drought crises. Moreover, these same activities continue to generate pollution, which has altered the living communities of most rivers (Webb & Nobilis 2007, Mabrouki et al. 2016, El Foul & El Ghachi 2018).

In Morocco, the rainfall follows a highly irregular pattern both in time and space; which irregularity is also expressed in the river flow, as demonstrated in the Upper Sebou basin for the periods 1957-58 and 2009-10 (Qadem 2015), during which this author revealed similar trends in the annual flow and the rainfall of the wet and dry seasons. In the recent four decades, this trend was clearly negative and marked by frequent drought crises, in rainfall (Tramblay et al. 2012, El Ajhar et al. 2018), hydrological regime of rivers (Haida et al. 1999, Bouaicha & Benabdelfadel 2010) and water reserves (Devos & Nejjari 1998, Devos et al. 2000). Indeed, since the 1980s,

these reserves have sharply declined, with even a drying up of several springs and lakes (Dakki & Himmi 2008, El Fellah Idrissi et al. 2017).

The climate change impacts on lotic ecosystems can be revealed using their mesological descriptors (i.e. physico-chemical) or biotic components (i.e. indicators, community richness, and diversity). The present study aims to reveal the direct and indirect effects of climate change on the Southern Mediterranean lotic ecosystems during the last four decades, through a comparison of the mesological state of the Upper Sebou River between two periods (1981-1985 and 2015-2017). During the 35 years separating these two dates, several drought crises happened in the country, concomitantly with the exponential growth of the human pressures on aquatic ecosystems. This study aims also to show how the factorial analysis method can illustrate pattern changes using the mesological components, as it was illustrated by the living components, more especially insect communities (Zerrouk et al. 2021). This last approach revealed a heavy loss of aquatic biodiversity, which can be easily linked to the indirect effects of climate change.

STUDY AREA AND SITES

The Upper Sebou occupies a large catchment area (about 4700 km², with reference to the altitude of 200 m), located in the northern Middle Atlas between latitudes 33°N and 34°N and longitudes 4°W and 5°W (Fig. 1). It overlaps the tabular

Middle Atlas, dominated by Jurassic carbonate outcrops (dolomites and limestones), and the folded Middle Atlas, made of long wrinkles separated by large plains (Martin 1981, Fedan 1988).

This hydrographic network is composed of three main branches: Guigou, Mahçar, and Zloul rivers. The first one, 114 km long, corresponds to the central course of the river; its name changes to Mdez at its confluence with Al Mahçar, then to Sebou after its confluence with the Zloul. The dominance of karst in its watershed (Akdim et al. 2011, Abboudi et al. 2014) explains why this river receives, along its course, several major springs (Aghbalou Aberchane, Tit-Zill, Skhounate, Sebou, Timedrine, Ouamender, etc.). These resurgences ensure water sustainability in most of the river's central course, especially during dry periods (Ben Tayeb & Leclerc 1977, Dakki 1986b).

The upper Sebou drains one of the watersheds where the human population records exponential growth, mainly along with the stream courses. This population lived mainly from agricultural and pastoral activities, but during the last four decades, it has developed into villages and even towns. This means a strong increase in human demand for water, with the intensification of agriculture and stream pollution at high and medium altitudes (Nejjari 2002, Qadem 2015).

To carry out this comparative study, we selected eleven stream and spring ecosystems (Fig. 1): nine on the Guigou and two on the Sebou. This choice is explained in the meth-
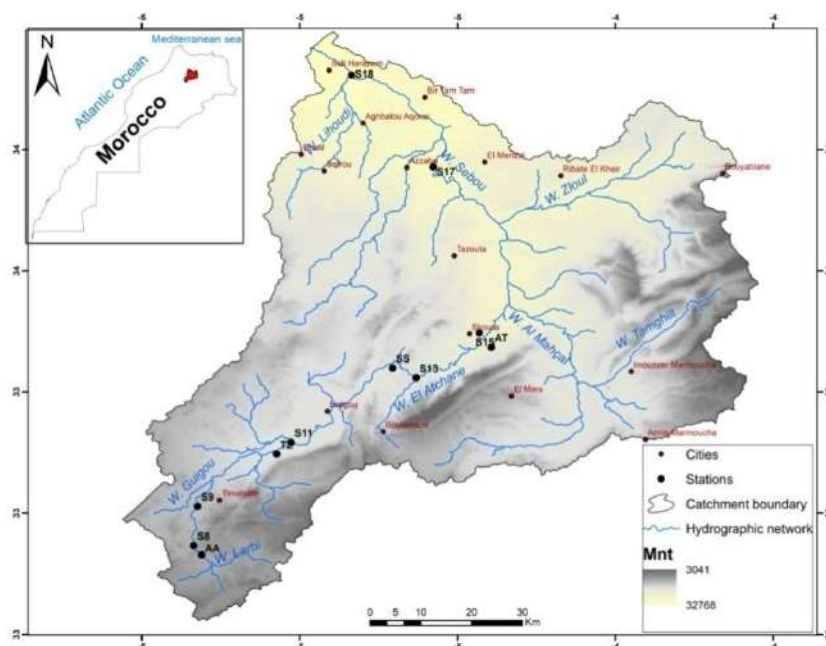
Fig. 1: Location of the prospected stations in the Upper Sebou catchment area.

odology and only their general characteristics are presented here (Table 1) while recalling that they were briefly described by Dakki (1986b, 1987).

MATERIALS AND METHODS

Experimental Design

The principle adopted to characterize the global changes in the Upper Sebou, including the anthropogenic pressures, consists of comparing a set of ecosystems (assimilated here to stations), using abiotic descriptors likely to reveal the climate warming. These stations are not compared separately from each other, but through structures that organize them according to their similarities. In addition, the chosen sample of stations should reflect a wide range of ecological situations in Upper Sebou. This comparative study, therefore, requires the use of the same descriptors and the same methods of sampling and data processing as used by Dakki (1986b, 1987); this minimizes the impact of non-ecological factors in determining the observed differences between stations. Nevertheless, some stations sampled in 1981-85 were not fully accessible (S9, TZ) or deeply modified (AT and TZ sources) in 2015; therefore, the measurement points were slightly displaced from their 1981-locations, knowing that this change can lead to slight variations in station width and depth.

Study Ecosystems (Stations)

Eleven water points were selected for this comparison among the 37 stations studied in 1981-1985 (Table 1); selection was operated in a way to take into consideration a high variation in abiotic variables and habitats (mineral substrate, vegetation, current speed...). Indeed, these stations represent the major types of lotic ecosystems highlighted in Upper Sebou

(Dakki 1987); eight of them are located along the central course of the Sebou, between the altitudes of 216 m and 1910 m, including a spring (SS station) that emerges in the river bed. The other three stations are springs with various temperatures (9.7°C to 18.5°C). Until 1985, these ecosystems were relatively close to their natural state, but by 2015, they had undergone more or less deep changes, like the rest of the Upper Sebou (Dakki & Himmi 2008).

Analysis of the Physico-Chemical Parameters of the Water (Comparative Variables)

To assess the mesological changes and characterize water quality in the Upper Sebou ecosystems between the two study periods, we referred to the variables described in the first period (1981-85) by Dakki (1987), among which we selected sixteen variables known to have effects on the benthic fauna and which have a key ecological role.

During each field season, the variables (temperature, dissolved oxygen, and electrical conductivity at 20°C) were measured in-situ using a field multi-parameter (HANNA Instruments, model HI9298). The current speed is taken at 5 cm from the bottom, far from the edges of the stream, using a current meter (Global Water FP111), while the average depth and width of the bed are measured using respectively a ruler and a graduated tape. The mineral substrate is characterized by its dominant components, reduced into two types: coarse materials (pebbles and boulders) and fine/loose materials (gravel, silt, sand). The vegetal substrate was also reduced to two categories (phanerogams and bryophytes), which have been expressed by their coverage of the area in water, while the periphyton (*sensu* perilithon), three states are considered: (1) 'absent or imperceptible', (2) 'scarce' and (3) 'abundant' (covers more than 80% of the sediment surface).

Table 1: Study stations in Upper Sebou: names, geographical coordinates, and habitat types.

Stations	Code	Latitude (N)	Longitude (W)	Altitude (m)	Habitat types
Aghbalou Aberchane	AA	33°08'43"	5°03'19"	1915	Cold spring
O. Guigou at Foum Khnag	S8	33°09'41"	5°04'09"	1910	higher course
O. Guigou at Timahdite	S9	33°19'24"	5°03'44"	1820	higher course
Ain Tit Zill	TZ	33°19'24"	4°55'20"	1550	Temperate spring
O. Guigou at Ait Hamza bridge	S11	33°20'38"	4°53'47"	1520	average course
Source Skhounate	SS	33°28'33"	4°43'01"	1425	average course
O. Guigou upstream of O. El Atchane	S13	33°27'30"	4°40'31"	1300	lower course
Ain Tadoute	AT	33°30'45"	4°32'32"	1340	warm spring
O. Guigou at Skoura	S15	33°32'17"	4°33'49"	880	lower course
Sebou at Azzaba	S17	33°49'54"	4°38'42"	470	lower course
Sebou at Masdoura	S18	33°59'39"	4°47'22"	216	lower course

It should be specified that for both study periods, only one measurement campaign was retained, namely from 3 to 9 June 1985 and from 4 to 19 July 2016. These dates correspond to relatively stable hydrology, in the sense that no floods and drying up of stations happen, and the fauna diversity is close to its optimum (El Alami & Dakki 1998). We are aware that this 'snapshot' approach (according to Huttunen et al. 2018) may have some inaccuracies, but these are overshadowed by the wide range of changes in all factors.

Data Analyses

To describe and assess the changes in the studied ecosystems between the two study periods, we first compared the means of the measured variables between these two periods using a non-parametric Wilcoxon test for two matched samples. The treatment was implemented under the free version of Studio-R software; a difference was considered significant for a p-value < 0.05. Subsequently, we compared the "mesological typologies" established for the ecosystems selected for the two studies. Both typologies were based on the same variables (Table 2), which were reduced to fourteen, as we removed two variables (wet cross-section and geometric mean of thermal maxima), to avoid high data redundancy between variables in the analysis.

The typologies were established using Multiple Correspondence Factor Analysis (MFCA), a method that allows combining both quantitative and qualitative variables in the same analysis (Pialot et al. 1984, Fenehans & Young 1985) and is frequently used to classify Moroccan wetlands (El Alami 2002, El Hamoumi et al. 2007). These treatments were carried out through the software Statistica, which concerned three matrices 'stations × variables', where the values of the variables are transformed into classes (modalities), defined by grouping similar or very close values, but sometimes arbitrarily delimited (Table 3).

Initially, we established an independent typology for each period, via a matrix of '11 stations × 14 variables', which were compared through a visual description of the distribution of stations in the factorial plans provided by the MFCA. In a second step, the data from both periods are merged into a ternary matrix of '11 stations × 2 periods × 12 variables', which was reduced to a binary matrix of '12 variables × 22 stations-periods', where each variable has two values, as proposed by Dakki (1986a) and Doledec & Chessel (1989). In this 'combined typology', the time-invariant parameters (altitude and slope) have not been considered in this matrix and do not directly participate in the structuring of the station network. In both approaches, the results are illustrated on the F1-F2 plan of the MFCA and the significance of both axes is investigated by projecting the mesological

variables (as modalities) onto the obtained structures (Table 3).

RESULTS

Long-Term Trends in the Environmental Context

The Wilcoxon test (non-parametric test) applied to the environmental variables in different surveyed stations shows a significant difference in the hydrological factors (average width, wet section, and flow) between the two study periods. An estimated 30% reduction in flow at all stations (p-value <0.05) (Table 4). On the other hand, an increase in flow was recorded at station S8, on the Guigou, downstream from the large AA spring (Table 2); but since the flow of this latter has decreased, this variation can only be explained by the improvement of the Guigou stream inflow upstream to this spring.

The values of mineralization (electrical conductivity) show a significant difference between the two study periods (Table 4). An increase in these values was recorded in almost all stations (Table 2) with an average of 23%. The most notable changes are recorded in the two springs AT and TZ, which are increasingly subject to polluting activities, and in S18 downstream of Oued Lihoudi, which carries the discharges of the city of Sefrou.

The comparison of the thermal component shows a significant difference in winter temperature, summer temperature, and the geometric mean of thermal maxima between the two study periods (Table 4). The increase in water temperature in both winter (21.7%) and summer (12%) is a normal consequence of the decrease in flow and depth. This temperature rise attracts our attention, particularly at the headwaters. Indeed, in the fresh springs (AA and TZ), the temperature would have undergone a winter increase of about 1°C, whereas this increase was greater in summer (2.4°C at AA and 3.9°C at TZ), indicating that a relatively large thermal amplitude of mountainous aquifers. In the SS spring, which is warmer than the two previous ones (20.7°C to 22.8°C), the temperature rise is smaller (1.8°C in summer), but relatively high in winter (6.7°C). To understand this difference, we remind that the SS spring emerges in the Guigou riverbed, and in the past, this stream occasionally drains into winter cooler waters that lower the SS water temperature. However, during the 2015-2017 campaigns, this stream was never flowing upstream of the spring. In the AT spring, the water shows a slight drop in temperature (1.0°C), which remains inexplicable.

The rise in spring's water temperature leads us to assume warming of the superficial water tables, a phenomenon that can be linked to snow decrease (both in terms of

Table 2: Mesological data used for the time comparison of the lotic ecosystems of the Upper Sebou.

1981-1985 data

Stations	Alt	S	W	WS	F	AS	WT	ST	GM	TA	EC	DO	CS	Bry	Pha	Per
AA	1915	30.0	8.0	60	432	72	9.0	10.4	9.7	1.4	360	6.8	90	60	5	1
S8	1910	2.4	8.0	120	192	16	6.9	19.0	11.5	12.1	236	7.6	60	0	20	1
S9	1820	6.7	7.0	95	560	59	8.6	23.0	14.1	14.4	365	8.3	70	0	20	2
TZ	1550	20.0	6.0	110	836	76	12.8	14.6	13.7	1.8	600	7.9	70	20	50	1
S11	1520	7.6	8.0	140	952	68	8.8	22.8	14.2	14.0	660	7.4	70	0	30	2
SS	1425	33.0	7.0	71	285	35	14.0	21.0	17.5	7.0	900	6.4	60	10	20	3
S13	1300	16.9	7.0	62	409	66	12.6	22.6	16.9	10.0	835	6.9	60	3	10	2
AT	1340	125.0	3.5	3.6	31	86	18.4	18.7	18.5	0.3	560	6.2	80	30	50	1
S15	880	12.2	12.0	58	365	63	12.4	25.6	17.5	13.2	996	5.8	70	0	5	3
S17	470	5.7	20.0	1100	8250	75	13.0	22.3	17.0	9.3	528	6.1	70	0	1	2
S18	216	5.2	25.0	1600	6720	42	14.5	28.0	20.0	13.5	565	5.6	70	0	1	1

2015-2017 data

Stations	Alt	S	W	WS	F	AS	WT	ST	GM	TA	EC	DO	CS	Bry	Pha	Per
AA	1915	30.0	5.5	51.0	270	53	10.0	12.8	11.3	2.8	375	4.9	70	70	1	1
S8	1910	2.4	7.0	94.5	246	26	10.3	19.5	14.2	9.2	312.5	6.5	70	10	20	2
S9	1820	6.7	5.5	63.3	317	50	7.5	21.3	12.7	14.2	407	5.9	75	20	30	2
TZ	1550	20.0	5.0	88.5	584.1	66	13.6	18.5	15.9	4.9	762	6.6	80	30	60	1
S11	1520	7.6	6.5	100.8	575	57	11.2	21.8	15.6	10.6	771	4.7	75	5	50	3
SS	1425	33.0	5.5	66.0	264	40	20.7	22.8	21.7	2.1	894	4	50	20	20	3
S13	1300	16.9	6.0	45.0	261	58	14.0	25.8	19.0	11.8	896	4.4	80	0	20	1
AT	1340	125.0	1.5	2.5	19	74	17.4	18.6	18.0	1.2	783	5.4	60	40	50	1
S15	880	12.2	8.0	50.0	270	54	15.8	26.3	20.4	10.5	1035	5.9	70	0	10	2
S17	470	5.7	15.0	840.0	5880	70	13.7	23.8	18.1	10.1	623	5.9	70	0	1	1
S18	216	5.2	20.0	1160.0	5220	45	15.9	26.3	20.4	10.4	990	5.4	80	3	10	2

Alt: Altitude, S: Slope, W: Average width, WS: Wet Section, F: Flow, AS: Average speed, WT: Winter Temperature, ST: Summer Temperature, TA: Thermal Amplitude, GM: Geometric mean of extreme thermal maxima, EC: Electrical Conductivity at 20°C, DO: Dissolved oxygen, CS: Coarse Substrate, Bry: Bryophytes, Pha: Phanerogams, Per: Periphyton

Table 3: Mesological data transformation to classes for the factorial correspondence analysis.

Periods >>		1981-1985			2015-2017			Combined			
Parameters	Codes	Class 1	Class 2	Class 3	Class 1	Class 2	Class 3	Class 1	Class 2	Class 3	Class 4
Altitude (m)	Alt	Alt<1000	1000≤Alt<1600	Alt≥1600	Alt<900	900≤Alt<1800	Alt≥1800	-	-	-	-
Slope (‰)	S	S<16	16≤S<40	S≥40	S<16	16≤S<40	S≥40	-	-	-	-
Average width (m)	W	w<5	5≤w<12	w≥12	w<5	5≤w<15	w≥15	w<5	5≤w<8	8≤w≤15	w>15
Flow(L.s^{-1})	F	F<50	50≤F<1000	F≥1000	F<240	240≤F<1000	F≥1000	F<100	100≤F<500	500≤F<1000	F≥1000
Average speed (cm.s^{-1})	AS	AS<50	50≤AS≤70	AS>70	AS<40	40≤AS≤60	AS>60	AS<30	30≤AS<50	50≤AS<70	AS≥70
Winter temperature (°)	WT	WT<10	10≤WT<14	WT≥14	WT<11.5	11.5≤WT<17.5	WT≥17.5	WT<10	10≤WT<15	WT≥15	-
Summer temperature (°)	ST	ST<15	15≤ST<25	ST≥25	ST<15	15≤ST<25	ST≥25	ST<15	15≤ST<25	ST≥25	-
Thermal amplitude	TA	TA<5	5≤TA<12	TA≥12	TA<5	5≤TA<11	TA≥11	TA<4	4≤TA<10	TA≥10	-
Electrical conductivity (µs.cm^{-1})	EC	EC<500	500≤EC<800	EC≥800	EC<450	450≤EC<800	EC≥800	EC<450	450≤EC<800	EC≥800	-
Dissolved oxygen (mg.L^{-1})	DO	DO<6	6≤DO<7	DO≥7	DO<5	DO 5	-	DO<5	5≤DO<7	DO≥7	-
Coarse substrate(%)	CS	CS<60	60≤CS<80	CS≥80	CS<60	60≤CS<80	CS≥80	CS<60	60≤CS<80	CS≥80	-
Bryophytes (%)	Bry	Bry<3	3≤Bry<20	Bry ≥20	Bry<20	20≤Bry<70	Bry ≥70	Bry<10	10≤Bry<50	Bry ≥50	-
Phanerogams (%)	Pha	Pha<20	20≤Pha<50	Pha≥50	Pha<20	20≤Pha<50	Pha≥50	Pha<10	10≤Pha<30	Pha≥30	-
Periphyton	Per	1	2	3	1	2	3	1	2	3	-

duration and quantity) in the high parts of the catchment area.

Dissolved oxygen concentration decreased significantly over the three decades, with an average reduction of 21.8%. This is a logical consequence of decreased flow velocities and warming of the water. However, a comparison of values for mean velocity, the proportion of coarse substrate, and plant cover (phanerogams and periphyton) showed no significant difference between the two study periods (Table 4). While bryophytes characterizing springs appeared at some stations in the central Guigou river from 2015 to 2017.

Changes in the Mesological Structures

Comparison of the mesological structures separately established for the two periods: In this first step, the comparison is focused on the mesological structures of the central course separately established for the two periods (Table 2), using the MFCA (Figs. 2A and 2B). The transformation of variable values into modalities is carried out using a scale specific to each dataset (Table 3). For the two periods, the F1-F2 factorial plan of the MFCA accumulates a relatively high rate of the total inertia of the analysis (60.3% for the first period and 56.6% for the second). As the third axis does not bring any further significant information in the two cases, we limited the analysis of the typological structure to the first F1-F2 plan.

In the two analyses (Figs. 3 and 4), the projection of the variables on the F1-F2 plan reveals a limited number of parameters explaining these structures.

In the 1981-1985 typology structure (Fig. 2A), the F1 axis (37.44%) separates the (AA, TZ, and AT) springs from the river, because of their specificities (low summer temperatures, very low annual thermal amplitudes, and richness of the substrate in bryophytes). The F2 axis (22.87%) reveals the 'upstream-downstream' gradient, well explained by the altitude and the flow, in parallel with the average width, electrical conductivity, and winter temperature (Fig. 3). This altitudinal gradient is marked by inversions, the most pronounced of which concerns stations S15 and S17. These inversions are related to the thermal characteristics, mainly the amplitude and the summer temperature, which are lower in S17 (due to its position downstream of great springs) than in S15, whereas the latter is at a higher altitude than S17 (Table 2).

The 2015-2017 typological scheme (Fig. 2B) reveals once again the spring specificities and the 'upstream-downstream' gradient, the latter being expressed this time along the first axis (37.21%). Indeed, this axis is mainly explained by altitude, stream size (average width and flow), slope, thermal characteristics (amplitude and summer temperature), and bryophytes. The F2 axis (19.41%), which distinguishes the low-mineralized stations from the others, is explained by electrical conductivity and winter temperature (Fig. 4).

The inversions recorded with the 1981-1985 data are still present in 2015-2017: into the mesological structure, both S13 and SS stations take place upstream of S11 (Fig. 2B), which is naturally at a higher altitude. This inversion is explained by the flow, which is much lower at SS (264 L.s^{-1}) and S13 (261 L.s^{-1}) than at S11 (575 L.s^{-1}). The relative

Table 4: Results of non-parametric Wilcoxon test applied to environmental variables measured in 1981-85 and 2015-17 (*** p-value<0.05; * p-value>0.05).

Variables	p-value	Signif.
Average width	0.003702	***
Wet section	0.0009766	***
Flow	0.004883	***
Average speed	0.05557	*
Winter temperature	0.0326	***
Summer temperature	0.01971	***
Geometric mean of thermal maxima	0.02073	***
Thermal amplitude	0.4131	*
Electrical conductivity	0.001953	***
Dissolved oxygen	0.005056	***
Coarse substrate	0.8571	*
Bryophytes	0.03494	***
Phanerogams	0.05624	*
Periphyton	1	*

similarity between SS, AT, and TZ springs, due to their low thermal amplitude (2.1°C), seems to amplify this inversion.

Analysis of the mesological structure combining the two periods' data: The MFCA processing of ternary matrix '11 stations × 12 variables × 2 periods' gathering old and recent data (excluding altitude and slope, as time-invariant factors), provides for each station two positions in the F1-F2 plan. The moving pattern of each station between both periods was interpreted as temporal changes in its mesological state.

The first two axes express again 56% of the total information on the structure (Fig. 2C) and the projection of the mesological variables on the F1-F2 plan (Fig. 5) shows a

great similarity to the pattern obtained using the 1981-1985 data (Fig. 2A). Indeed, the F1 axis (35.34%) separates the three springs (AA, TZ, and AT) from the riverine ecosystems, through thermal amplitude, phanerogams, and dissolved oxygen, while it participates in the upstream-downstream gradient thanks to hydrological parameters (average width and flow). However, this gradient is better expressed by the F2 axis (20.68%), which is correlated with thermal variables (winter and summer temperatures), conductivity, and periphyton.

The most important result revealed by this analysis is that each station (Fig. 2C) operates more or less amplified
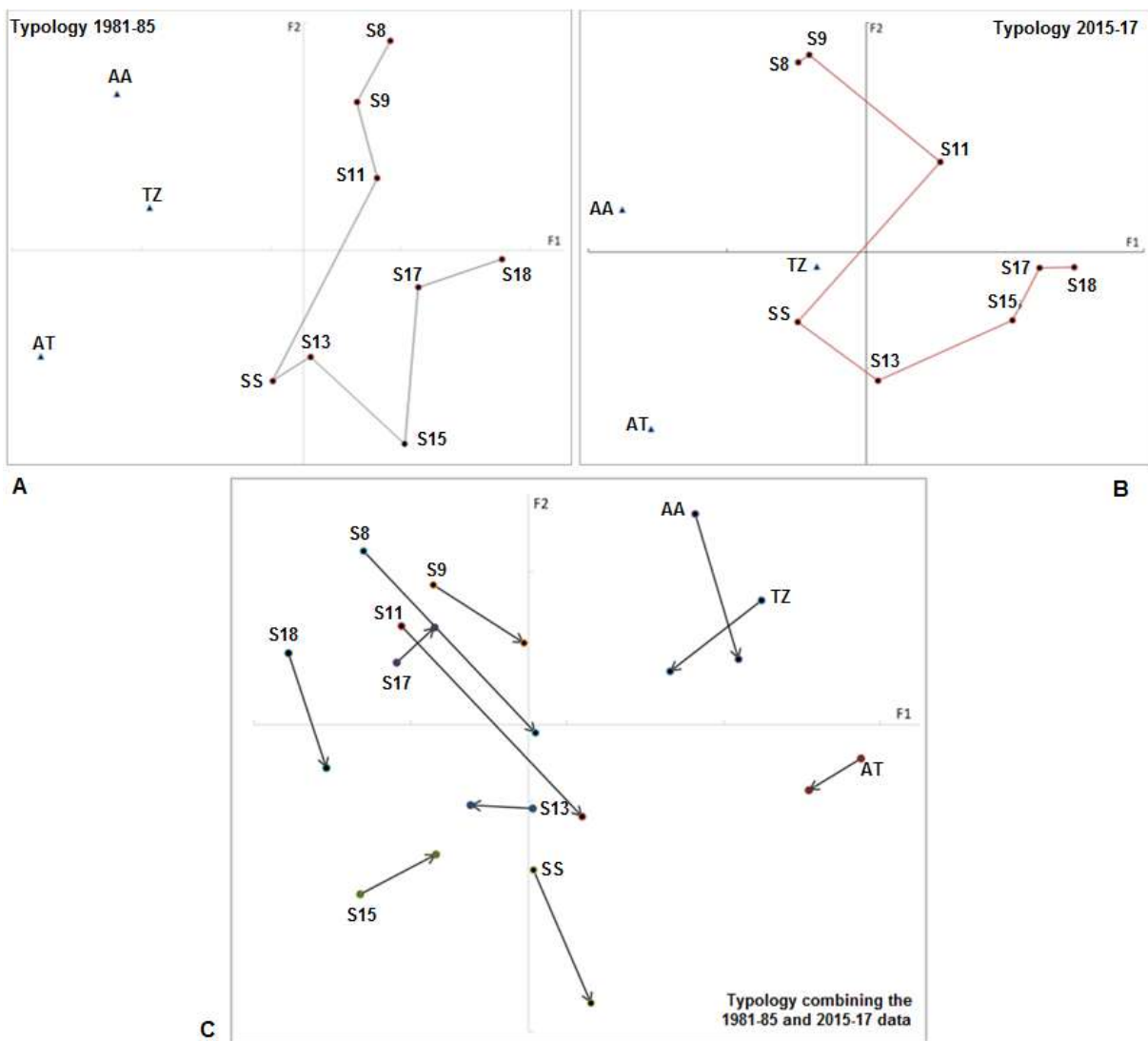
Fig. 2: Mesological structure of the central course of the Upper Sebou on the F1-F2 plan of an MFCA. A) data of the period 1981-1985. B) data for the period 2015-2017. C) combining data from the two periods 1981-1985 and 2015-2017.

changes between the two study periods, as indicated by the arrows. Most of these changes consist of a migration of the stations in the direction of the 'upstream-downstream' gradient, simultaneously expressed by both first axes, knowing that F1 and F2 express the hydrology and the temperature respectively. For two stations (SS spring and S13 stream), this migration is sub-parallel to F2 (thermal change) for the first and to F1 (hydrological change) for the second.

To assess the changes in amplitude in each station over the 35 years, we used the distance between its two points on the F1-F2 plan, which varies from one water body to the other. Two high altitude streams (S8 and S11) operate a large displacement; clearly correlated with the F2 axis, attesting that their waters have undergone a warming and

mineralization increase. Moreover, these stations, located downstream of major springs, would have experienced a slight increase in their flow and a decrease in their thermal amplitude, as indicated by the slight development of their bryophytes' cover. The S9 station, located between the two former water points, shows a low downstream migration, in concordance with the loss of its flow.

S13 Station, located downstream of the SS source, underwent a downstream shift, corroborating a decrease in its flow and a slight increase in its thermal amplitude. All the further downstream habitats (S15, S17, and S18) have migrated in the direction of a flow loss (F1) and recent warming (F2); however, S17 is still fed by large springs located upstream, which makes its displacement amplitude low.
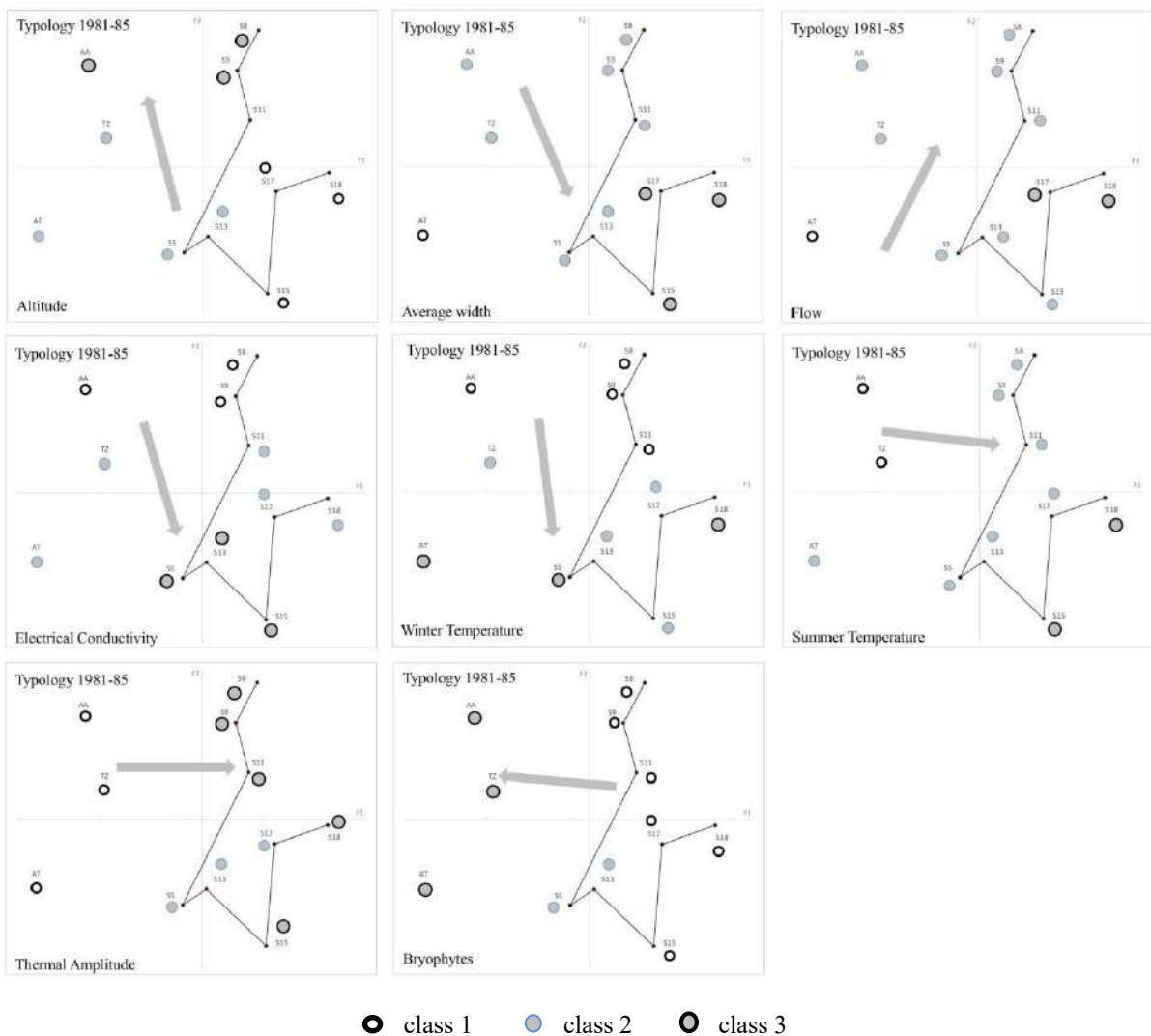
Fig. 3: Interpretation of the 1981-1985 mesological structure of the upper Sebou: Projection of the mesological variables on the F1-F2 plan.

This general typology scheme shows for both periods a very pronounced inversion along the gradient F2, since S15 went downstream even of S18 station, indicating the thermal nature of this inversion, mainly linked to the excessive lowering of the flow.

All the springs show a significant change in their abiotic characteristics between both study periods, which evolution is visibly linked to both thermal factors (water warming) and hydrological factors (flow reduction). These changes appear on the F2 axis and, to a lesser degree, on the F1 axis, with a contribution to the mineralization of the TZ and AT sources. In the absence of groundwater temperature monitoring, we assume that the surface

aquifers that give rise to these springs are operating as light warming.

DISCUSSION

In 2015-2017, the general mesological ordination of the Upper Sebou ecosystems (Fig. 2B) is still slightly similar to the pattern established three decades earlier (Fig. 2A), which is dominated by the upstream-downstream gradient, simultaneously determined by hydrological and thermal factors, with some thermal inversions. However, some significant differences have been highlighted between the two classifications and linked to changes in these same factors. It's not surprising
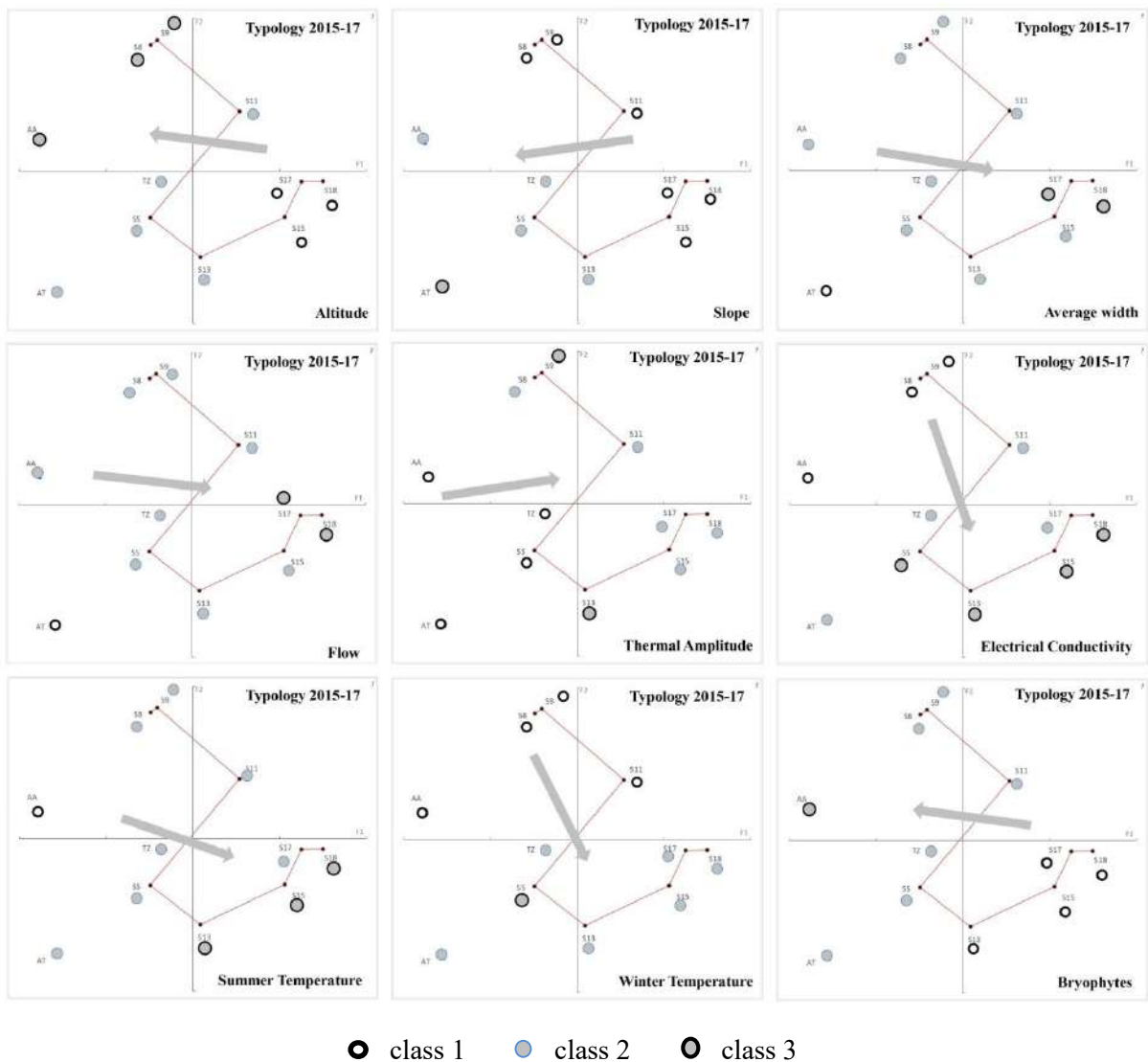
Fig. 4: Interpretation of the 2015-2017 mesological structure of the upper Sebou: Projection of the mesological variables on the F1-F2 plan.

that this pattern is also obtained by merging the data from these two periods (Fig. 2C); however, this approach has the advantage to attribute two positions to each ecosystem, defining a migration pattern that can be characterized by its amplitude and direction in the ordination scheme. In general, this migration reveals an increase in water temperature (both in winter and summer) and mineralization, in parallel with a flow decrease; the few exceptions to this pattern were related to particular situations that were easily explained.

These mesological modifications were largely linked to climate change, reflected in the Mediterranean region by recurrent drought crises, some of which lasted more than three successive winters, particularly during the 1980s and 1990s (Chaouche et al. 2010, Hallouz et al. 2013, Khomsi et al. 2016, Ouhamdouch et al. 2018). These droughts lead to a general flow decrease, which was recorded in various Mediterranean rivers other than the Sebou: the Moulouya in Morocco (Driouech et al. 2010), the Chéllif in Algeria (Meddi
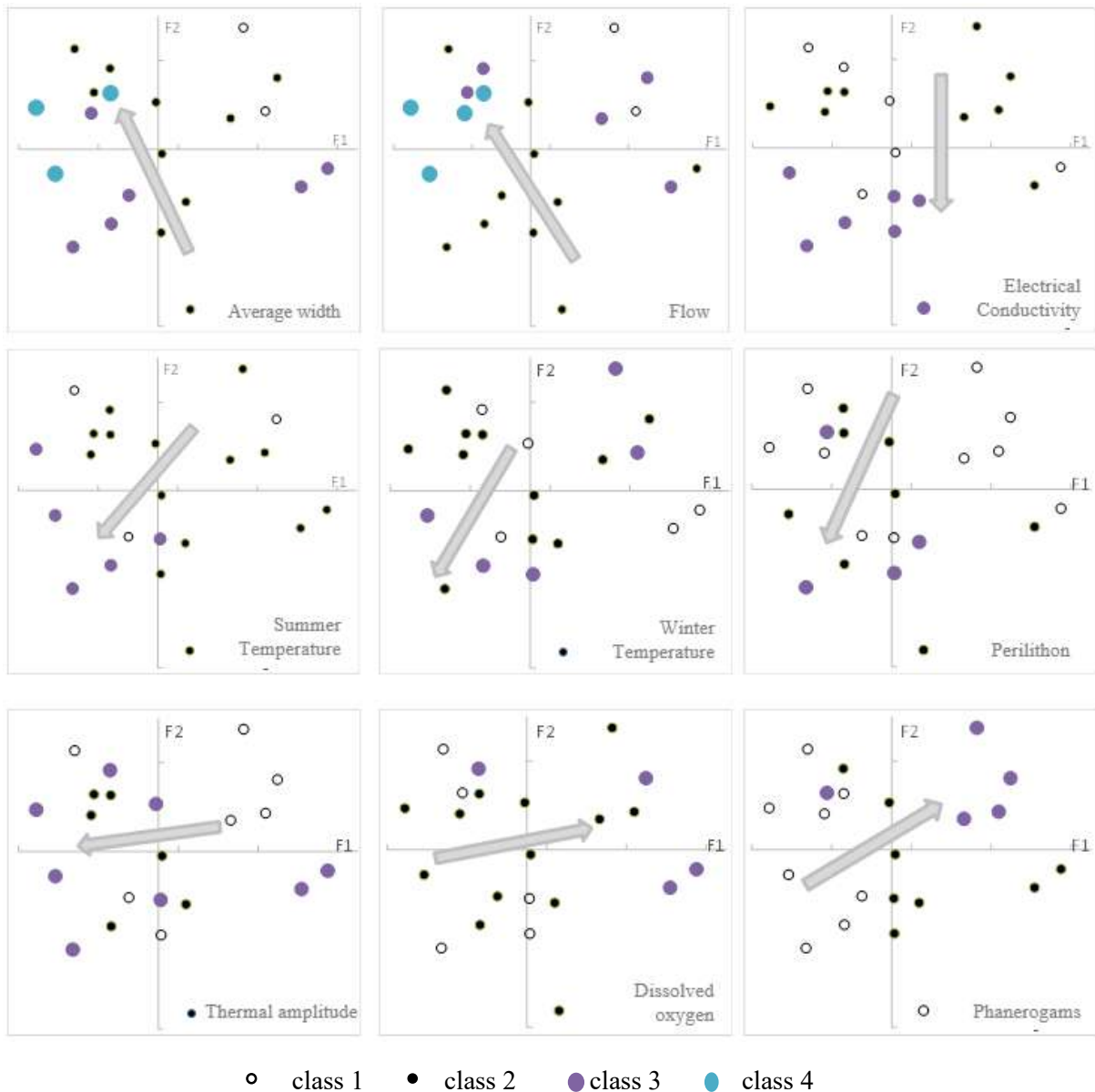
Fig. 5: Interpretation of the Mesological structure of the central course of the Upper Sebou in the F1-F2 plan of an MFCA combining data of the two periods 1981-1985 and 2015-2017: Projection of the mesological variables on the F1-F2 plan.

et al. 2010), the Loire in France (Floury 2012, Floury et al. 2013), etc. The latter study evaluated at 1.2°C the warming of the waters of the Loire between 1977 and 2008, corresponding to a reduction of -25% of its flow. Our results join those of Devos et al. (2000), which show in the Upper Sebou catchment area a spatial disparity in the water resources.

In the Upper Sebou, as in most southern Mediterranean rivers, the flow lowering is not only a direct consequence of droughts but is amplified by water withdrawals, which have even dried up several stretches of the central watercourse of the Sebou (Devos et al. 2000, Dakki & Himmi 2008). Several sectors of the river (i.e. S13 and S15) and even some springs underwent a drying up lasting several weeks; all other areas also experienced severe flow declines, mainly over the 1980s and 1990s (El Ajhar et al. 2018). Thus, the irrigation activity, performed via a large number of seguias and pumping points, occurs mainly in summer and even in spring, when the flow is naturally low. The 'perennial' SS spring, which arises from a relatively deep water table (given its temperature of around 20°C), had stopped flowing downstream towards the S13 station and almost dried up in 2008.

The water mineralization, measured in the summer, increased in almost all the study points, favored by the drop inflow and the summer warming of the water. However, in several stations, particularly the TZ and AT springs, the Guigou stream (S8 and S11), and the Sebou river (S18), high algae abundance (eutrophication) is observed and linked to domestic and agricultural discharges, cattle droppings, etc., bearing in mind that most domestic waters are not treated.

CONCLUSION

The flow drop and the water warming, as the main changes that happened in Moroccan river ecosystems during the last four decades are often directly linked to massive water withdrawals, being themselves considered as consequences of the development of urban and agricultural activities. This latter has indeed gained large areas in the Upper Sebou watershed and withdrawals were already intensive during our 1981-1985 study, but few river sketches showed at that time a summer drying-up, while during more recent droughts this phenomenon affected a large number of streams and even springs of this watershed. Indeed, during a summer visit to the Guigou river, carried out in 2008 (Dakki & Himmi 2008), a catastrophic hydrological crisis has been highlighted, leading with no doubt to link the drying-up directly to the droughts, with an evident amplification by withdrawals. Nevertheless, flow drops were revealed also in some high altitude springs and small streams, indicating deficiencies in water tables that are not pumped; this confirms again the direct link between flow drops and droughts. On another hand, the water

warming in river ecosystems, closely linked to insolation, is a direct consequence of the decrease of the water flow; but its evidence in some springs lets us conclude with an effect of droughts on water table temperature.

It is important to note that, in parallel with the present mesological study, we carried out a study of the benthic fauna (Zerrouk et al. 2021) that revealed a catastrophic loss of biodiversity that was explained by the mesological changes described above, but which crucially needs conservation solutions. For such purpose, this paper provides baseline ideas of the impact mechanisms of the droughts, which could constitute guidance for conceiving the said solutions.

In terms of methodology, both mesological and fauna studies demonstrate that among a large panel of possible methods to highlight the changes in running waters, the classification, and ordination techniques have shown their relevance, as they made it possible to reveal trends patterns in the ecosystem changes. We should admit that regular monitoring of these changes could certainly better detail these trends (Huttunen et al. 2018, Cañedo-Argüelles et al. 2020), but in lack of such costly monitoring, the changes revealed by our study provided significant conclusions that can be used as an alert for the urgent need of conservation of the Southern Mediterranean running waters.

REFERENCES

Abboudi, A., Tabyaoui, H., El Hamichi, F., Benaabidate, L. and Lahrach, A. 2014. Study of the physico-chemical quality and metal contamination of surface water in the Guigou watershed, Morocco. Europ. Sci. J., 10(23): 1857-7881.

Akdim, B., Sabaoui, A., Amyay, M., Louane, M., Emmanuel, G. and Obda, K. 2011. Hydro-karstic influence of the Aïn Sebou-Timedrine-Ou Amender water source system on the hydrology of the Sebou wadi (Middle Atlas, Morocco). J. Geomorphol., 56(2): 165-181.

Ben Tayeb, A. and Leclerc, L. 1977. Water Resources of Morocco: Atlas and South Atlas domains. Volume III. Notes and Memoirs of the Geological Service of Morocco, Rabat, Morocco, pp. 37-66.

Botella-Cruz, M., Carbonell, J.A., Pallarés, S., Millán, A. and Velasco, J. 2016. Plasticity of thermal limits in the aquatic saline beetle *Enochrus politus* (Küster 1849) (Coleoptera: Hydrophilidae) under changing environmental conditions. Limnetica, 35(1): 131-142.

Bouaicha, R. and Benabdelfadel, A. 2010. Variability and management of surface water in Morocco. Sécheresse, 21(1): 1-5.

Cañedo-Argüelles, M., Gutiérrez- Cánovas, C., Acosta, R., Castro-López,

D., Cid, N., Fortuño, P., Munné, A., Múrria, C., Pimentao, A.R., Sarremejane, R., Soria, M., Tarrats, P., Verkaik, I., Prat, N. and Bonada, N. 2020. As time goes by: 20 years of changes in the aquatic macroinvertebrate meta community of Mediterranean river networks. J. Biogeogr., 47:1861-1874.

Chaouche, K., Neppel, L., Dieulin, C., Pujol, N., Ladouche, B., Martin, E., Salas, D. and Caballero, Y. 2010. Analyses of precipitation, temperature, and evapotranspiration in a French Mediterranean region in the context of climate change. Geoscience, 342: 234-243.

Dakki, M. 1985. On the choice of data in the biotypology of running waters by factorial analysis of correspondences. Ecol. Bull., 16(4): 285-296.

Dakki, M. 1986a. Biotypology and spatio-temporal thermal gradient, study on a stream in the Middle Atlas (Morocco). Ecol. Bull., 17(2): 79-85.

Dakki, M. 1986b. Hydrobiological research on the Haut Sebou (Middle Atlas); A Contribution to the Faunistic, Ecological and Historical Knowledge of South-Mediterranean Running Waters. Thesis in Science, Mohammed V University, Morocco.

Dakki, M. 1987. High Sebou Running Water Ecosystem (Middle Atlas): Typological Studies and Ecological Analyzes and Biogeography of the Main Entomological Populations. Works of the Scientific Institute Zoology Series. Institut scientifique, Rabat, pp. 42-99.

Dakki, M. and Himmi, O. 2008. Strategic Bases for the Conservation of Freshwater Biodiversity in the Sebou Basin (Morocco): Inventory of Biodiversity and Ecological Conservation Targets. WWF/GREPOM Report, Morocco, pp. 26+58.

Devos, A. and Nejjari, A. 1998. The Recent Hydrological Drought in the Upper Sebou Basin (Middle Atlas). AUPELF- Mosella Report, UREF, Metz University and Sidi Mohamed Ben Abdellah University, pp. 3-4.

Devos, A., Benjlloul, B. and Nejjari, A. 2000. Water resources and their uses in the plain of Guigou (Middle Atlas, Morocco). Mosella, 3(4): 327-339.

Doledec, S. and Chessel, D. 1989. Seasonal rhythms and stationary components in the aquatic environment. II. Consideration and elimination of effects in a faunal table. Acta Oecol. General., 10(3): 207-232.

Driouech, F., Mahé, G., Déqué, M., Dieulin, C., Heirech, T., Milano, M., Benabdelfadel, A. and Rouche, N. 2010. Evaluation of Potential Impacts of Climate Change on the Hydrology of the Moulouya Watershed in Morocco. Global Change: Facing Risks and Threats to Water Resources. In: Proceedings of the Sixth World Friend Conference, Fez, Morocco, October 2010, IAHS Publ., Wallingford, Oxfordshire, UK, pp. 340.

Durance, I. and Ormerod, S.J. 2010. Evidence for the role of climate in the local extinction of a cool-water triclad. J. North Am. Benthol. Soc., 29(4):1367-1378.

El Agbani, M.A., Dakki, M. and Bournaud, M. 1992. Typological study of Bou Regreg (Morocco): Aquatic environments and their populations of macroinvertebrates. Ecol. Bull., 23 (1-2): 103-113.

El Ajhar, L., El Khachine, D., El Bakouri, A., El Kharrim, K. and Belghiti, D. 2018. Evolution of rainfall from 1960 to 2015 in Morocco. Int. J. Res. Sci. Manag., 61: 2349-2497.

El Alami, M. 2002. Taxonomy, Ecology, and Biogeography of Ephemeroptera from the Rif (Northern Morocco). State Doctorate Thesis, Abdelmalek Essaâdi University, Morocco.

El Alami, M. and Dakki, M. 1998. Ephemeroptera and Trichoptera populations of Oued Laou (Western Rif, Morocco): Longitudinal distribution and biotypology. Sci. Inst. Bull., 21: 51-70.

El Fellah Idrissi, B., Cherai, B., Hinaje, S. and Mehdi, K. 2017. Climate variability and its influence on water resources in the northern part of the Moroccan Middle Atlas: The case of the causes of Sefrou and Anoceur. Larhyss J., 32: 155-179.

El Foul, M. and El Ghachi, M., 2018. Impact of anthropogenic actions on the hydrological balance in the Tassaout watershed (Upstream of the Moulay Youssef dam): ORCHY II hydrological model (1986-2010) Morroco. J. Water Environ. Sci., 2: 305-318.

El Hamoumi, R., Dakki, M. and Thevenot, M. 2007. An ecological study of anuran larvae in Morocco. Bull. Sci. Instit., 29: 27-34.

Fedan, B. 1988. Geodynamic evolution of an intraplate basin on strike-slip: The Middle Atlas (Morocco) during the Meso-Cenozoic. Doctoral thesis Mohammed V University, Morocco.

Fenehans, M. and Young F.W. 1985. Analysis and synthesis of multiple correspondence analysis optimal scaling, dual scaling, homogeneity analysis, and other methods for quantifying categorical multivariate data. Psychometrika, 50(1): 91-119.

Floury, M. 2013. Analysis of Evolution Trends of Benthic Macroinvertebrate Populations in a Context of Water Warming. Doctoral thesis, Blaise Pascal University, France.

Floury, M., Delattre, C., Ormerod S.J. and Souchon, Y. 2012. Global versus local change effects on a large European river. Sci. Total Environ., 441: 220-229.

Garouani, A. and Tribak, A. 2006. Relationship between Hydrology and Climate in the Oued Inaouene Watershed (Moroccan Pre-Rif): Climate Variability and Change Hydrological Impacts. In Proceedings of the Fifth FRIEND World Conference 447 held at Havana, Cuba, November 2006, IAHS Publ., Wallingford, Oxfordshire, UK, pp.308.

Giudicelli, J., Dakki, M. and Dia, A. 1985. Abiotic and hydrobiological characteristics of Mediterranean running waters. Int. Assoc. Theoretical Appl. Limnol. Negot., 22(4): 2094-2101.

Haida, S., Ait Fora, A., Probst, J.L. and Snoussi, M. 1999. Hydrology and hydroclimatic fluctuations in the Sebou watershed between 1940 and 1994. Sècheresse, 10(3): 221-6.

Hallouz, F., Meddi, M. and Mahé, G. 2013. Modification of the hydro-climatic regime in the Oued Mina Basin (North-West of Algeria). J. Water Sci., 26(1): 33-38.

Heino, J., Virkkala, R. and Toivonen, H. 2009. Climate change and freshwater biodiversity: detected patterns, future trends, and adaptations in northern regions. Biol. Rev., 84: 39-54.

Huttunen, K.L., Mykrä, H., Paavola, R. and Muotka, T. 2018. Estimates of benthic invertebrate community variability and its environmental determinants differ between snapshot and trajectory designs. Freshwater Sci., 37(4): 769-779.

Illies, J. and Botosaneanu, L. 1963. Problems and methods of the classification and ecological zoning of running waters, considered especially from the faunistic point of view. Int. Assoc. Theoret. Appl. Limnol., 12(1): 1-57.

Khomsi, K., Mahé, G., Tramblay, Y., Sinan, M. and Snoussi, M. 2016. Regional impacts of global change: seasonal trends in extreme rainfall, run-off, and temperature in two contrasting regions of Morocco. Nat. Hazards Earth Sys. Sci., 16: 1079-1090.

Mabrouki, Y., Taybi, A.F. and Berrahou, A. 2016. Spatio-temporal evolution of the quality of running water in the Melloulou wadi (Morocco). J. Water Sci., 30(3): 213-225.

Martin, J. 1981. The Central Middle Atlas: Geomorphological Study. Notes and Memoirs of the Geological Survey, No. 258, Rabat.

Meddi, M., Boucefiane, A. and Sadeuk Belabbes, A. 2010. Impact of climate change on flows in the Chellif basin (Algeria). Global Change: Facing Risks and Threats to Water Resources. In: Proceeding of the Sixth World Friend Conference, Fez, Morocco, October 2010. IAHS, Wallingford, Oxfordshire, UK, pp. 340.

Nejjari, A. 2002. Drought, Water, and Man in the Haut Sebou Basin (Northern Middle Atlas-Morocco). Doctoral thesis from the University of Metz.

Ouhamdouch, S., Bahir, M. and Carreira, P.M. 2018. Impact of climate change on water resources in a semi-arid environment: Example of the Essaouira basin (Morocco). J. Water Sci., 31: 13-27.

Pialot, D., Chessel, D. and Auda, Y. 1984. Description of the environment and multiple correspondence factor analysis. Acad. Sci., 298 (11): 309-314.

Qadem, A. 2015. Quantification and Management of Water Resources in the Upper Sebou Watershed. Doctoral Thesis, Sidi Mohammed Ben Abdallah University and the University of Lorraine.

Sala, O.E., Chapin, F.S., Armesto, J.J., Berlow, E., Bloomfield, J., Dirzo, R., Huber-Sanwald, E. and Huenneke, L.F. 2000. Biodiversity-global biodiversity scenarios for the year 2100. Science, 287: 1770-1774.

Tramblay, Y., Badi, W., Driouech, F., El Adlouni, S., Neppel, L. and Servat, E. 2012. Climate change impacts extreme precipitation in Morocco. Glob. Planet. Change, 82(83): 104-114.

Walther, G.R. 2010. Community and ecosystem responses to recent climate change. Philos. Trans. R. Soc. B: Biol. Sci., 365: 2019-2024.

Webb, B.W. and Nobilis, F. 2007. Long-term changes in river temperature and the influence of climatic and hydrological factors. Hydrol. Sci. J., 52(1): 74-85.

Whitehead, P.G., Wilby, R.L., Battarbee, R.W., Kernan, M. and Wade, A.J. 2009. A review of the potential impacts of climate change on surface water quality. Hydrol. Sci. J., 54(1): 101-123.

Zerrouk, M., Dakki, M., El Agbani, M.A., El Alami, M., Bennas, N., Qninba, A. and Himmi, O. 2021. Evolution of the benthic communities in a North-African river, the Upper Sebou (middle atlas-Morocco) between 1981 and 2017: Effects of global changes. Biologia, (2021).

Assessment of Diesel Engine Performance, Combustion and Emission Characteristics with Supplementation of Neem Oil Methyl Ester Along With EGR

Ravi Kathirvel† and Vijayabalan Palanimuthu

Department of Mechanical Engineering, Hindustan Institute of Technology and Science, Chennai-603103, Tamil Nadu, India

†Corresponding author: Ravi Kathirvel; ravi.021074@gmail.com

ABSTRACT

Biodiesel generated from a variety of non-edible feedstocks has gained widespread acceptance as a limited diesel fuel alternative in compression ignition engines. For the reliable implementation of biodiesel in commercial sectors, its effect on engine combustion, emission, and performance needs to be examined experimentally. In this study, 10% (N10) and 20 % (N20) Neem oil methyl ester (NME) blends were tested in a direct injection 4-stroke single-cylinder diesel engine incorporated with 5% and 10% exhaust gas recirculation (EGR). At maximum load conditions, Brake thermal efficiency (BTE) was found highest for N20 by 7.2%, and also Brake specific energy consumption (BSEC) was reduced by 11.4% for N20 as compared to diesel. Meanwhile, the incorporation of EGR deteriorates the performance parameters for the N20 blend. The results of emission analysis showed that oxides of nitrogen (NOx) increased with the addition of biodiesel whereas the addition of EGR diminished the NOx value for both biodiesel blends at all loading conditions. Unburnt hydrocarbon (UHC), Carbon monoxide (CO), and smoke emissions decreased by 40.6%, 31.2%, and 29.6% for the N20 blend respectively at full load when compared to diesel. Interestingly, when EGR was provided, CO, UHC, and smoke density values are increased for both N10 and N20 blends at all loading conditions, however lower than diesel operation.

INTRODUCTION

From the early nineteenth century, principal fuels used for transportation have been derived from petroleum. Predicted depletion of fossil fuels shortly and augmented pollution hazards alarmed by health agencies motivate the search for a renewable source of fuel for the transportation sector (Atul & Avinash 2014). Among prime movers in transportation, diesel engines played a major role due to their high thermal efficiency, robustness, and reliability. In this view, various alternative fuel sources like natural gas, hydrogen, and biofuels came into existence in the last few decades to aid the transportation sector in lessening its dependency on petroleum-based fuels and reducing their impact on the environment (Ardebili et al. 2011).

Vegetable oils are renewable and cost-effective alternative fuels. It can be used directly in CI engines owing to its similar properties to that of diesel fuel (Eryılmaz et al. 2014). Some of the major advantages of vegetable oils are their renewability, availability, low toxicity, and biodegradability. Meanwhile using vegetable oils directly in engines affects the performance and combustion attributes due to their high viscosity, high density, and low calorific value. To overcome these setbacks transesterification should be done to convert the fatty acids into methyl esters which in turn enhance the fuel properties. Biodiesel is a blend of alkyl esters of long-chain fatty acids present in oil synthesized via transesterification (Azad et al. 2013, Leung et al. 2010, Borugadda & Goud 2012). Biodiesel can be used directly in engines as well as in blended form without any engine modification. With increased lubricity and high cetane number, running diesel engines on biodiesel could be advantageous in terms of energy security and environmental safety (Canakci 2007, Knothe 2007). On the other hand, biodiesel fuels have poor low-temperature properties and are more susceptible to auto-oxidation during storage (Mohamed et al. 2017).

In emission aspects, biodiesel maintains a closed carbon cycle which reduces global warming. Due to enhanced fuel properties, utilization of biodiesel reduces emissions of particulate matter, CO, and HC accompanied by augmentation of NOx emission. The increase in NOx when using biodiesel was reported due to high in-cylinder temperature prevails during combustion (Sahoo & Das 2009, Srivastava & Verma 2008,

Raheman & Ghadge 2007). To overcome the main drawback of using biodiesel i.e. the NOx emission, certain techniques were adopted by researchers. EGR is a reliable technique that can be employed to reduce NOx emission from engines fueled with biodiesel (Zheng et al. 2004, Yu & Shahed 1981).

In the EGR method, a part of exhaust gas from the engine is re-inducted through the inlet manifold to the combustion chamber with a direction and flow regulator valve. EGR displaces a portion of intake oxygen with diluents from the exhaust (H_2O and CO_2) to minimize the formation of NOx during combustion. The maximum cylinder temperature is reduced by the diluents due to their specific heat which lowers the rate of combustion (Thangaraja & Kannan 2016, Majewski & Khair 2006). Even though EGR reduces NOx, it increases HC, CO, and soot emissions with deterioration in engine performance (Brehob 2007). The partial displacement of oxygen at intake reduces the excess air ratio and amplifies the ignition delay (ID). This hike in ignition delay aids in the augmentation of fuel in the premixed combustion phase which increases the peak cylinder temperature. Due to the dilution effect, the partial pressure of oxygen concentration will be reduced which in turn affects the NOx formation kinetics (Maiboom et al. 2008). Exhaust gas can be re-routed into the cylinder either externally or internally. Internal recirculation requires complex mechanisms and variable valve timings whereas external recirculation of exhaust gas is achieved with the external plumbing and the pressure difference of exhaust gas compared to intake air (Baert et al. 1999, Kohketsu et al. 1999, Shin et al. 2011).

Many researchers studied the effects on characteristics of diesel engines using biodiesel as a primary fuel. Lin et al. (2007) used biodiesel processed from waste cooking oil and observed that B50 and N20 are the optimal fuel blends. Masjuki et al. (1996) observed improvement in efficiency and emission with biodiesel from preheated palm oil. Sahoo et al. (2009) fueled a three-cylinder tractor engine with Karanja methyl ester blends. The authors observed that BSFC improves with blend concentration and declines with speed. A sharp drop in smoke opacity for biodiesel blends was also been recorded. Mahanta et al. (2006), found that the N20 blend of Karanja biodiesel showed higher BSFC and BTE than diesel for all the loads. Prabhahar et al. (2012), reported that Karanja biodiesel blends recorded high BSFC values than traditional diesel fuel. Sinha and Agarwal (2005) recorded a 1.5-3% improvement in BTE of the diesel engine when powered by rice bran methyl ester blends. Some other authors revealed that the utilization of biodiesel reduces the performance characteristics of the engine which could be attributed to the high viscosity and low heating value of biodiesel fuels (Rizwanul et al. 2013, Jinlin et al. 2011, Jaichandar & Annamalai 2011). Vinay and Raveendra (2015)

stated that the BSFC was increased by 10% when 20% of Neem oil was blended with diesel, and also UHC and CO emissions were reduced by 30% and 8% respectively. He also mentioned that EGR addition reduces volumetric efficiency on account of more specific heat of gases.

Spessert et al. (2004), showed that CO emissions for rapeseed methyl ester and diesel were quite similar whereas a slight increase was observed for methyl ester fuel at low loads. Many kinds of literature work report an increase in NOx emission under all loading conditions with biodiesel (Sun et al. 2010, Lapuerta et al. 2008). Ye and Boehman (2012) analyzed the characteristics of combustion of CRDI engines with biodiesel blends. It was observed that retarding the start of injection (SOI) towards TDC boosted the premixed combustion process and also reported that, an increase in injection pressure results in more HRR owing to air-fuel mixing enhancement. Kanda et al. (2005) adopted EGR up to 54% and reported increased HC, CO, and reduced NOx emissions. Das et al. (2015), tried the Homogeneously charged combustion ignition (HCCI) strategy using dual injection and reported a decrease in NOx by 76% and smoke by 40 % with an 80% premixed ratio and 30% EGR. Zhao et al. (2014), experimented on a 2-cylinder diesel engine with EGR varied from 0-27%. The authors observed that increasing EGR leads to an increase in smoke, CO, and HC and a decrease in NOx emission.

Pankaj et al. (2020), studied the CI engine characteristics, cost, and energy when fueled with Roselle, Karanja biodiesel, and its blends. The author observed an increase in BSFC by 4% and 3.2% respectively for 20% of Roselle and 20% of Karanja oil blends. Also observed decrease in CO2 emission with an increase in engine load.

Remarks of Literature Survey and Novelty

As a result of an extensive literature survey carried out, it is found that a large array of works was conducted by analyzing the diesel engine characteristics by using various biodiesel methyl esters as a supplementary fuel. But to the surprise, very little work has been reported yet on analyzing the effects of EGR percentage on a CI engine fueled with Neem oil methyl ester blends at standard operating conditions without any hardware modification on the engine. The novelty of this present research work lies in analyzing the performance, emission, and combustion characteristics of a direct injection diesel engine fueled with Neem oil methyl ester along with varying EGR rates.

MATERIALS AND METHODS

Neem Oil and Its Properties

In India, the distribution of Neem trees is widespread, as also

in South Asia. A matured tree can produce 9-90 kg seeds per year whereas each seed contains 27-39% of oil content. In India, around 30,000 tons of Neem oil seeds are traded annually for commercial purposes like soap making, fuel for lamps and drug synthesis, etc. Therefore, Neem oil become a potential source for the production of biodiesel. Because of its pharmaceutical properties, neem oil is also called "Sarva roga nivarani" (medicine for all diseases). Neem seed kernels are pressed in the mechanical press to produce oil. The composition of neem oil is given in Table 1 and Neem seed and oil are shown in Fig. 1.

The physicochemical properties of Neem oil were evaluated by standard test methods preferred by ASTM and given in Table 2.

Engine Setup and Methodology

From the results, it was found that Neem oil possessed a high acid value of 36 mg KOH.g^{-1}. Since the free fatty acid of raw neem oil was found to be higher, the transesterification process cannot be conducted in a single step. So a two-step process comprising acid-catalyzed esterification and base-catalyzed transesterification was carried out to convert oil into a methyl ester (Naik et al. 2008). The obtained biodiesel was tested as per ASTM standards and the results were on par with the prescribed limits of ASTM D6571.

Effects of Neem oil biodiesel blends on diesel engine characteristics were tested on four-stroke single-cylinder en-

gines equipped with an external EGR system. The schematic and Photo of the experimental setup with all instrumentations and EGR setup are depicted in Fig. 2 and Fig. 3. The detailed specifications of the engine rig are mentioned in Table 3.

Two separate tanks were provided for diesel and Neem oil biodiesel blends respectively. A two-way direction control valve is used to switch the fuels from one tank to another. First, the engine was started and allowed to run for 20 minutes to reach a steady-state after which the biodiesel fuel was allowed by using a control valve. Horiba MEXA-584 and AVL 437 smoke meters were used to analyze the exhaust emission. A constant volume of EGR was supplied to the inlet manifold of the engine. The pressure tank employed is used to regulate exhaust pressure pulse and a heat exchanger is provided to cool the charge before recirculating. A control valve was provided at the gas storage tank to ensure accurate EGR flow. A bag filter is employed to filter particulates in the exhaust gas and supply clean gas for EGR. EGR rate is derived as the ratio between the mass flow rate of recirculated exhaust gas and the total mass flow allowed to pass into the engine cylinder. The EGR percentage was set to 5 % and 10% by adjusting the pre-calibrated EGR valve. The engine was steadily loaded in the range of 0%, 10%, 40%, 70%, and 100%. The engine characteristics of N10 and N20 blends were analyzed by incorporating 5% and 10% EGR for both the blends and related to neat diesel fuel. The experiments were repeated thrice, and an average of the value was considered to ensure reliability. The reason for choosing these conditions is that the biodiesel concentration above 20% deteriorates the performance characteristics, and EGR above 10% induces knocking in the engine.

Fig. 1: Neem seed and Neem oil

Table 1: Composition of Neem oil.

Acid Content	%
Olieic	50-60
Palmitic	13-15
Stearic	14-16
Linoleic	8-16
Arachidic	1-3

Table 2: Physiochemical properties of Neem oil and its methyl ester.

Property	ASTM method	Prescribed limits	High-speed diesel	Neem oil	Neem oil methyl ester (biodiesel)
Density (kgm$^{-3)}$	D 1298	880	850	940	884
Kinematic viscosity (40°C) (mm^2 s^{-1})	D 445	1.9-6.0	0.830	44	4.76
Calorific value (MJ.kg^{-1})	EN 14213	35 minimum	43.5	36.85	39.65
Acid value (mg KOH g^{-1})	D 664	0.5 maximum	0.2	36	0.14
Flash point (°C)	D 93	130 minimum	68	219	135
Cloud point (°C)	D 2500	-3 to -12	-11	2	-4
Cetane number	D 613	47 minimum	49	39	52

Fig. 2: Experimental setup (schematic).
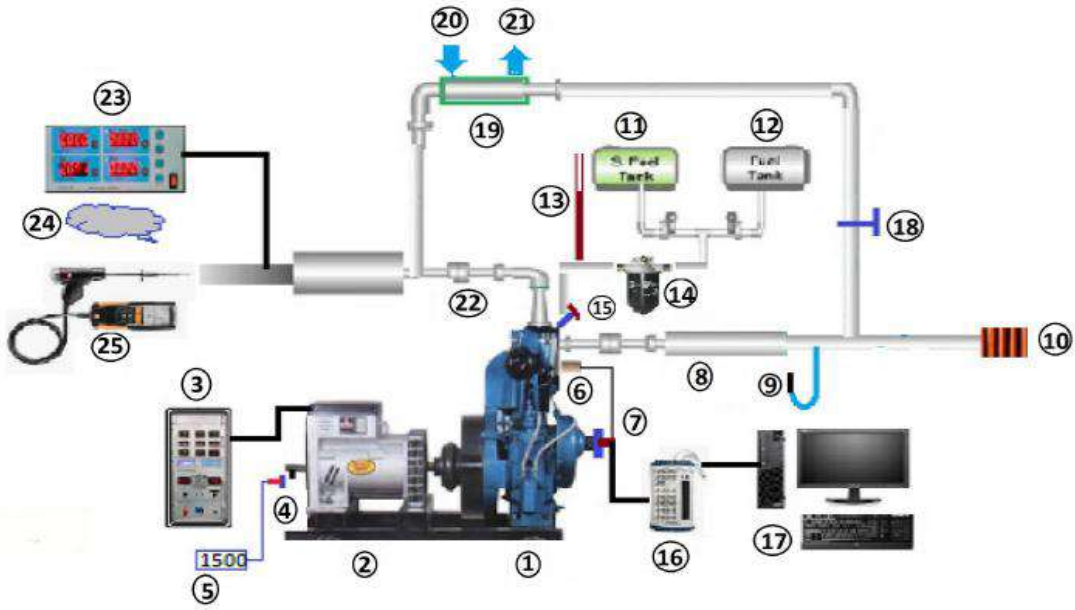
1	Diesel engine	7	Cam Position sensor	12	NME biodiesel tank	18	EGR valve
2	Generator		and Crank encoder	13	Burette	19	EGR unit
3	Electrical loading device	8	Intake manifold	14	Diesel filer	20	Cooling water in
4	RPM sensor	9	U-Tube manometer	15	Diesel fuel injector	21	Cooling water out
5	RPM digital meter	10	Intake air filter	16	Data acquisition system	22	Exhaust manifold
6	Pressure sensor	11	Diesel tank 1	17	Computer	23	Exhaust gas analyser
						24	Exhaust gas out
						25	Smoke meter

ECU

Kistler charge amplifier

Emission gas analyzer (Horiba MEXA-584)

Cam position sensor

Crank angle encoder

Piezo Electric pressure sensor

AVL437 digital Smoke meter

Fig. 3: Experimental setup – Photo.

Uncertainty Analysis

All physical quantities are subject to uncertainties. So to ensure reliability and prove accuracy in measurements it is mandatory to carry out uncertainty analysis. Let 'R' be the totaled result function of independent variables x1, x2, x3, x_n. (Sakthivel et al. 2016),

$$R = f(x1, x2, x3, .x_n) \qquad \dots (1)$$

and measured variables error limits be, x1 ± Δn1 , x2 ± Δn2, …. , xa ± Δna …(2)
and computed result's error limits be R± ΔR. Coleman et al. (2009), described the root mean square technique to understand the degree of error, as

$$\Delta R = [\{(\partial R/\partial x1)* \Delta x1\}2 + \{(\partial R/\partial x2)* \Delta x2\}2 + \dots + \{(\partial R/\partial xa)* \Delta xa\}2] \qquad \dots(3)$$

Using equation (3), uncertainty in the computed performance and emission parameters were calculated. The details of average uncertainties in experimental measurements are given in Table 4. To calculate the overall uncertainty proportion, the principle of propagation of error is considered and was computed as:

Overall Uncertainty = square root of (uncertainty of fuel flow)^2 + square root of (uncertainty of temperature)^2 + square root of (uncertainty of air flow)^2 + square root of (uncertainty of EGR flow)^2 + square root of (uncertainty of in-cylinder pressure)^2 + square root of (uncertainty of crank angle)^2 + square root of (uncertainty of CO)^2 + square root of (uncertainty of CO_2)^2 + square root of (uncertainty of NOx)^2 + square root of (uncertainty of HC)^2 + square root of (uncertainty of smoke)^2 + square root of (uncertainty of BTE)^2 + square root of (uncertainty of BSFC)^2

= square root of $[(0.35)^2+(0.1)^2+(2.2)^2+(1.8)^2+(1)^2+(0.03)^2+(1.8)^2+(0.5)^2+ (2)^2+(1.5)^2+(1.5)^2+(0.07)^2+(0.85)^2]$

= ±4.68%

RESULTS AND DISCUSSION

Performance Characteristics

Brake thermal efficiency (BTE) indicates the maximum extent to which the added heat energy is converted to network output. The variations between BTE and brake mean effective pressure (BMEP) is given in Fig. 4. From the figure, it is evident that BTE increases for all test fuels when BMEP increases. At lower engine loading conditions, the biodiesel blends showed lesser BTE than diesel fuel. Reduction in BTE in the order of 2.2 % and 3.4 % was obtained for N10 and N20 blends as compared to diesel at low loading conditions. This diminution in BTE is due to more viscosity and latent heat of vaporization of biodiesel fuel which causes larger droplet formation and insufficient mixing of air-fuel (Qi et al. 2010, Banapurmatha et al. 2008). Meanwhile, at higher loading conditions, the BTE of biodiesel blends showed an increasing trend with diesel. N10 and N20 blends showed a hike of 3.3 % and 7.2 % BTE at full load conditions as compared to mineral diesel. The hike in BTE can be explained by the presence and active participation of oxygen (fuel borne) in fuel which enhances combustion efficiency during higher load conditions. On the other hand, a high engine load help in the mixing and evaporation of biodiesel which in turn increases BTE (Sinha & Agarwal 2005).

At the same time, it can be noticed that the introduction of EGR in the engine deteriorates the BTE of the engine. Incorporating 5% EGR to N10 and N20 blends, decreased BTE by 1.3 % and 1.8% as compared to neat biodiesel operation at low loads. On the other hand, 10% EGR addition to N10 and N20 blends reduced BTE by 1.7% and 4.4% as compared to respective neat biodiesel operations. At high loading conditions, the maximum reduction in BTE was observed for 10% EGR incorporation with N20 which reduced the magnitude of BTE by 3.3 % as compared to neat N20. This reduction in brake thermal efficiency after EGR introduction could be enlightened by the lessening of oxygen available for combustion during the expansion stroke.

Brake-specific energy consumption is defined as the energy of fuel spent to produce unit brake power per hour.

Table 3: The specification of the engine.

Description	Specifications
Make and model	Kirloskar, AV1
Number of cylinders	One
Cycle	Four-stroke
Cooling	Water-cooled
Aspiration	Naturally aspirated
Bore and stroke	80 × 110 mm
Swept Volume	553 cc
Clearance volume	36.87 cc
Compression ratio	16.5: 1
Rated output	3.7 kW @ 1500 rpm
Injection timing	24° BTDC
Combustion chamber	Hemispherical open type
Weight of flywheel	33 kg
Lubricating oil	SAE30/SAE 40
Connecting Rod length	235 mm
Valve dia and max lift	33.7 mm and 10.2 mm
Injection nozzle	BOSCH, 3 hole nozzle, 116° spray angle

Table 4: Uncertainty of the instruments.

Instruments	Measured parameters	Uncertainty [%]
Burette	Fuel flow	±0.35
K-type Thermocouple	Temperature	±0.1
Flowmeter	Mass flow rate of air	±2.2
	Mass flow rate of EGR	±1.8
Pressure sensor (Kistler-6125B)	In-cylinder pressure	±1
Crank angle encoder	Crank angle	±0.03
Horiba MEXA gas analyser	CO	±1.8
	CO_2	±0.5
	NOx	±2
	HC	±1.5
AVL smoke meter	Smoke	±1.5
Performance parameters	BTE	±0.07
	BSFC	±0.85
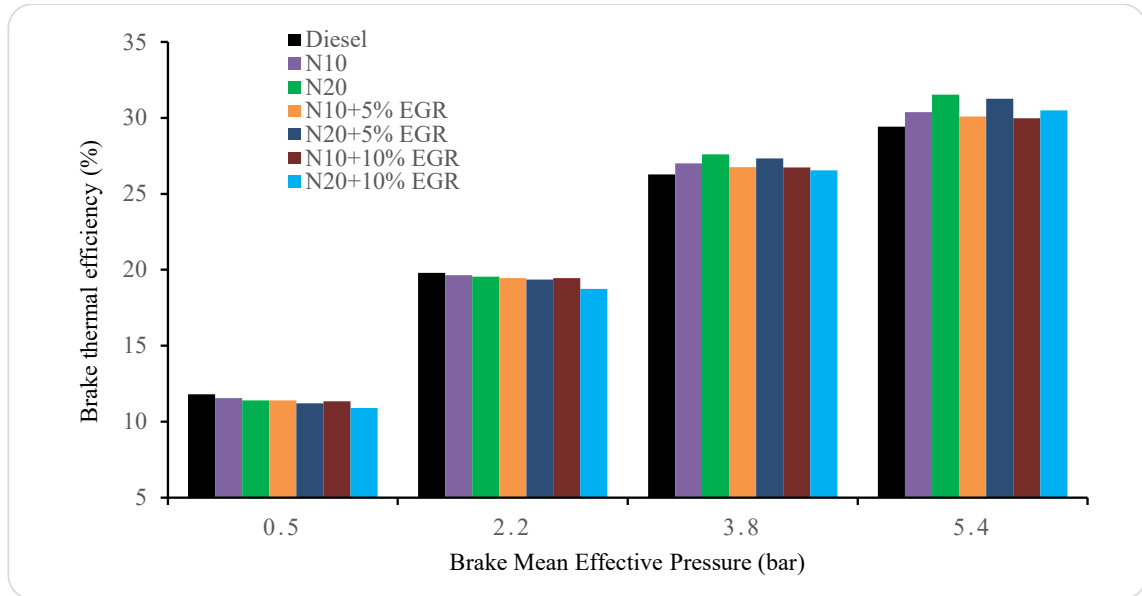
Fig. 4: Changes in BTE with BMEP.

Fig.5 depicts the relation between BSEC and BMEP for various test fuels and test conditions. From the figure that BSEC decreased with an increase in load for all test fuels. BSEC exactly followed the inverse trend as that of BTE for all conditions and test fuels.

For neat biodiesel blends N10 and N20, BSEC increased by 0.29% and 0.92% respectively as compared to diesel fuel at low loads whereas at high loading conditions BSEC for both fuel blends reduced by 9.0% and 11.4% respectively. The reason for these variations can be attributed to the same

factors responsible for BTE variation. Meanwhile, EGR inclusion affects BSEC negatively at all loading conditions. A sharp increase in BSEC was observed for all test fuels with both 5% and 10% EGR addition.

At low load, introducing 5% EGR at intake increased the BSEC of N10 and N20 blends by 1.4% and 1.7% as compared to neat biodiesel blends without EGR. Meanwhile, the same trend was followed at high loading conditions where a hike of 1.5% and 2.4% BSEC was observed for N10 and N20 with 5% EGR. Further addition of EGR at 10% increased BSEC

by 2.1 % and 3.8% at peak loading conditions for N10 and N20 blends respectively. The displacement of fresh oxygen in the combustion chamber by burnt gases causes a deficiency in oxygen level which reduces combustion temperature and efficiency. This, in turn, increases BSEC and reduces BTE for all test fuels in this present study.

Emission Characteristics

The variations in carbon monoxide emission with biodiesel operation with various EGR percentages are given in Fig. 6. Commonly, CO is a by-product of incomplete combustion that occurs during power stroke due to various phenomena. CO emission greatly depends upon the fuel-air ratio relative to the stoichiometric proportions and also depends upon the temperature prevailing inside the combustion chamber. Rich combustion zones consistently increase CO emission with deviation from stoichiometry (Salim Mohamed 2003, Raheman & Ghadge 2008).
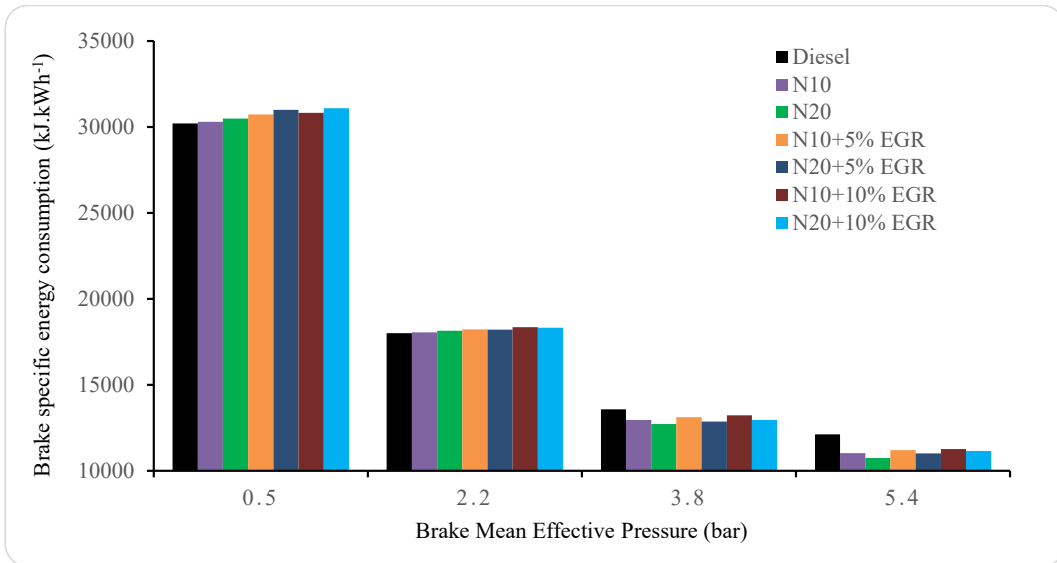
Fig. 5: Changes in BSEC with BMEP.
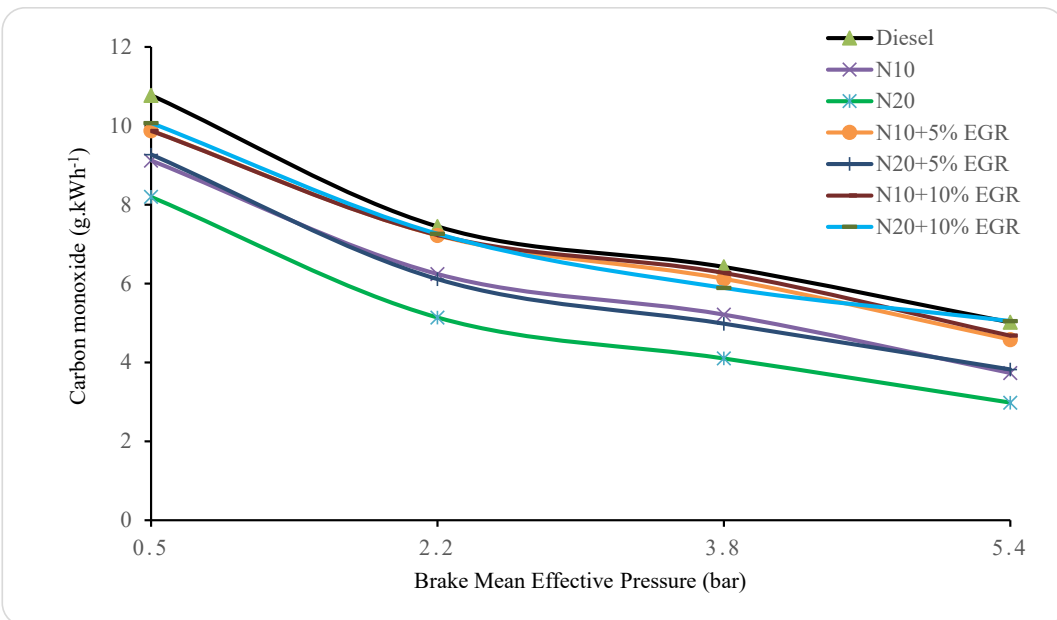
Fig.6: Changes in carbon monoxide with BMEP.

From the figure, it is evident that CO emission is decreased for all loading conditions while operated with Neem biodiesel blends. At low loads, N10 utilization reduced the CO emission by 15.4% and N20 by 23.9% as compared to baseline diesel fuel. Meanwhile, once the load is increased, CO emission drops for all test fuels and conditions. At maximum load, when compared to diesel operation, CO diminished by 25.7 % for N10 and 40.6% for the N20 blend. This reduction in CO is credited to high in-cylinder temperature produced by adequate fuel-air mixing and higher oxygen content of biodiesel fuels.

While incorporating EGR to the engine operation along with the neem biodiesel, CO emission is augmented with respect to biodiesel blend (N10 and N20) operation. With 5% EGR inclusion, CO emission of N10 and N20 blends increased by 18.6% and 28.2% at full load as compared to a straight biodiesel blend. Further increasing the EGR percentage to 10% for N10 and N20 blends, amplified the CO emission by 25.5% and 41.0% as compared to emission observed in respective biodiesel blends. This is due to incomplete combustion caused by the dilution effect of exhaust gases re-circulated.

Unburnt hydrocarbon emission is one of the most important parameters that quantify the completeness of combustion. In general CO and UHC, emission follows the

nearly same trend for a particular mode of operation. Fig. 7 depicts the relationship between UHC and BMEP for all test conditions. UHC emission was reduced while running with biodiesel fuel under all loading conditions.

At full load operation biodiesel blends N10 and N20 reduced UHC emission by 14.2% and 31.2% with respect to neat diesel operation. This can be explained by the enhanced oxygenated nature of biodiesel fuels which increases combustion temperature and thereby reduces exhaust UHC emission. On the other hand, EGR introduction in the intake augments UHC emission at the exhaust.

When 5% EGR is tested with biodiesel blends at full load, it was observed that UHC emission increased by 5.8% and 11.3% for N10 and N20 blends as compared to straight NME biodiesel operation whereas further raising EGR to 10% amplified the UHC emission by 10.7% and 27.8% for aforesaid blends respectively. The hike in UHC could be made clear by dilution of intake charge with exhaust gas which shows the way to a reduction of oxygen required for complete combustion.

Fig.8 shows the trend of Carbon dioxide variations with respect to brake power for all testing modes. While augmentation of CO and UHC depicts incomplete combustion, CO_2 is the direct measure of the completeness of combustion. Even
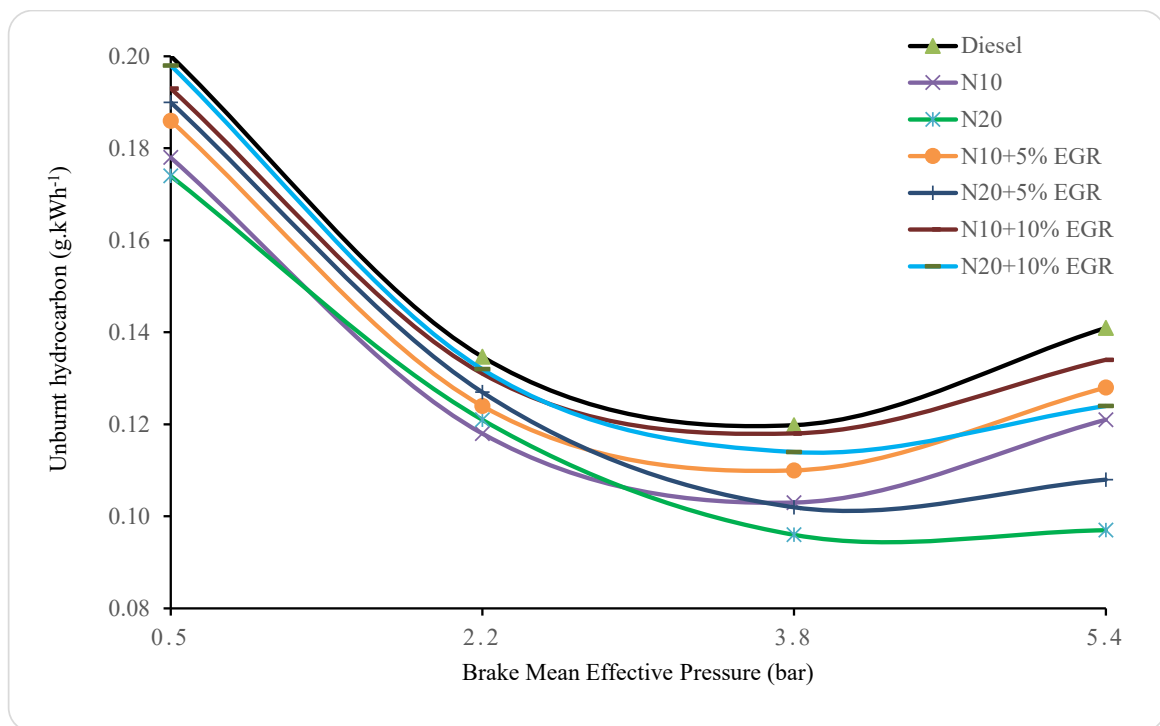
Fig. 7: Changes in unburnt Hydrocarbon with BMEP.

though the concentration of CO_2 in the atmosphere leads to global warming, the main of this testing is to enhance CO_2 emission since biodiesel utilization recycles carbon from feedstock to the atmosphere which constitutes a closed carbon cycle. Also, CO_2 emission follows a trade-off behavior with CO which is observed from the results.

At all loads, biodiesel operation increased the CO_2 emission to that of diesel operation. In specific, N10 and N20 blends amplified CO_2 emission by 9.4% and 42.7% at peak loads whereas 11.5% and 17.8% hikes were observed at lower loads. This is owing to complete combustion driven by more oxygen supply of NME biodiesel blends (Suja & Nagarajan 2018). On examining EGR effects on CO_2 at higher load, it could be deduced that CO_2 is reduced with increasing EGR percentage. With 5% EGR, CO_2 emission lessened by 9.3% and 14.7% for N10 and N20 blends as compared to neat biodiesel fuel blends. Meanwhile increasing EGR to 10% further reduced CO_2 by 15.3% and 22.5% for N10 and N20 under the same conditions. This inverse trending of CO_2 with respect to CO at EGR incorporation can be explained by instability in combustion and oxygen deficiency that makes CO_2 concentration decrease and CO increase (Mani et al. 2010).

Oxides of nitrogen are normally formed when oxygen and nitrogen react at high temperatures during the combustion process. Indirect injection of fuel, fuel is atomized into finer droplets where oxygen reacts at the boundary of fuel-air. Due to the burning of fuel, the localized temperature in the vicinity of droplets exceeds the limit at which NOx is formed. Since diesel engines always run in high compression ratio and lean air-fuel mixture, high cylinder temperature prevails during combustion which is the most favorable condition for NOx formation. The NOx emissions are evaluated by the oxygen concentration in the cylinder, equivalence ratio, temperature, and time. NOx during engine operation is predominately formed due to uncontrolled combustion which creates localized high-temperature zones. Fig. 9 illustrates the relationship between NOx and BMEP for different EGR percentages.

From the figure, the NOx emission increased for biodiesel at all loading conditions. In comparison with neat diesel operation, the biodiesel blends N10 and N20 showed 22.8% and 23.7% high NOx at lower loads whereas at high loads the same biodiesel blends showed 22.3% and 52.8% hike in NOx rating. Even though NOx is inevitable in biodiesel operations, it can be reduced by the techniques like EGR, exhaust gas treatment, and fuel additives. Among these NOx reduction techniques, EGR is a reliable technique that can diminish NOx magnitude at the exhaust. The results of this
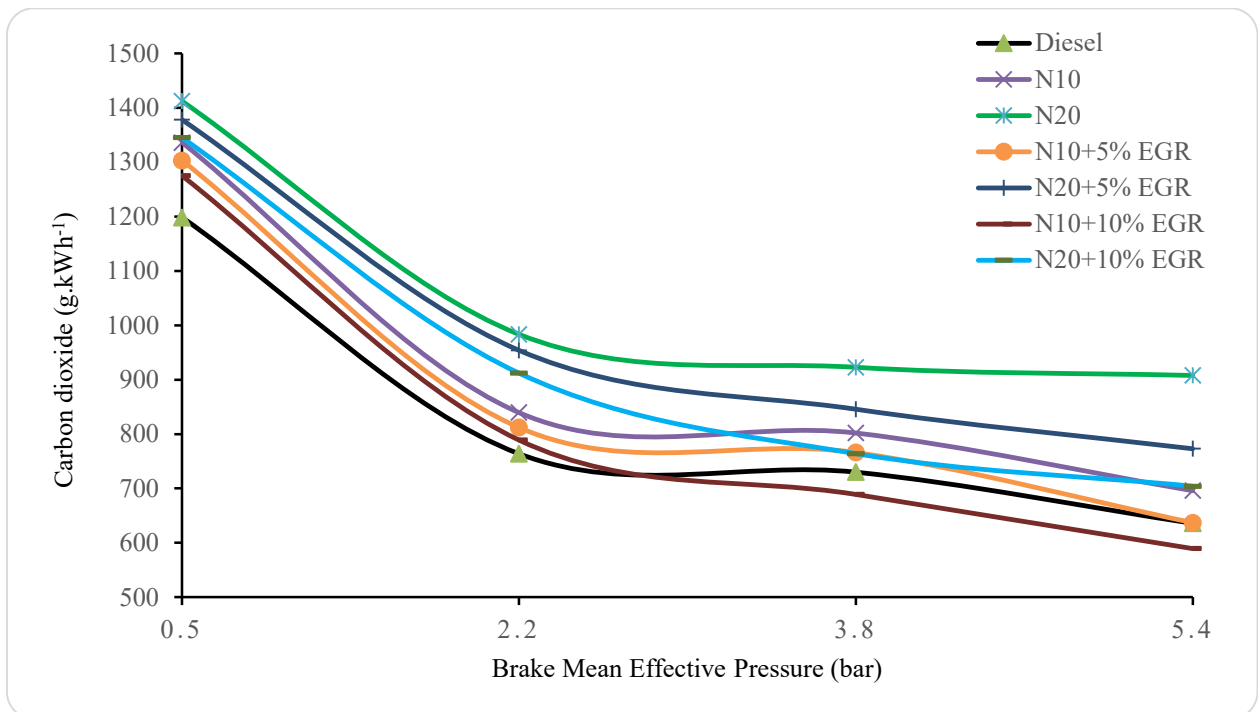
Fig 8: Changes in carbon dioxide with BMEP.

experimental study clearly show that the incorporation of EGR reduces NOx emission at the exhaust. For the N10 blend, EGR at 5% and 10% reduced NOx emission by 38.6% and 44.5% at peak load. Meanwhile, for the N20 blend, incorporation of EGR at 5% and 10% diminished NOx values by 32.3% and 37.8% at peak load than neat biodiesel. The increase in NOx values in biodiesel operation is attributed to the increased oxygen content of the fuel that enhances combustion which in turn elevates peak cylinder temperature. Higher in-cylinder temperature leads to a hike in NOx emission (Bhupendra et al. 2013). On the other hand, as EGR is introduced with a fresh charge increases the specific heat of the charge, thus decreasing the temperature rise inside the cylinder which in turn reduces NOx elevation (Mani et al. 2010, Nitin et al. 2016).

The changes in smoke emission with BMEP are revealed in Fig. 10. Lesser smoke emission is evidenced when the diesel fuel is enriched with NME biodiesel. The smoke emission in neat diesel operation is higher due to the presence of aromatic hydrocarbon structure which enables thermal stability and a higher boiling point.

NME biodiesel has zero aromatic compounds and more oxygen contents which helps with smoke formation (Suja & Nagarajan 2018). Smoke emission is observed in neat diesel operation from 16 to 54% from 0.5 to 5.4 bar BMEP and the same is noticed from 11.5 to 44% for N10 and from 9 to 38% for N20 operation. Combustion is enhanced at fuel-rich zones in NME biodiesel operation due to the presence of fuel-borne oxygen with respect to neat diesel operation where no fuel-borne oxygen. The introduction of EGR impacted the increase in smoke emission owed to incomplete combustion caused by reducing the oxygen availability for combustion. The increases are observed in higher loads as 12.7 and 15.5% for 5% EGR, like 18.4 and 20.8% for 10% EGR for N10 and N20 respectively when compared to biodiesel operation.

Combustion Characteristics

Combustion characteristics of Neem oil biodiesel and EGR effects on it were analyzed by measuring the cylinder pressure against crank angle degrees (CAD). The pressure data was measured for 100 consecutive cycles and values were averaged and then used to calculate heat release rate and cylinder pressure to avoid variations. From the obtained pressure data, the heat release rate can be derived by the first law of thermodynamics equation given below,

$$\frac{dQ(\theta)}{d\theta} = \frac{1}{\gamma - 1}[V(\theta)\frac{dP(\theta)}{d\theta} + \gamma P(\theta)\frac{dV(\theta)}{d\theta}]$$

Fig. 11 depicts the in-cylinder pressure variations with CAD at full loading conditions for all test conditions. It is seen that the maximum cylinder pressure decreased with an
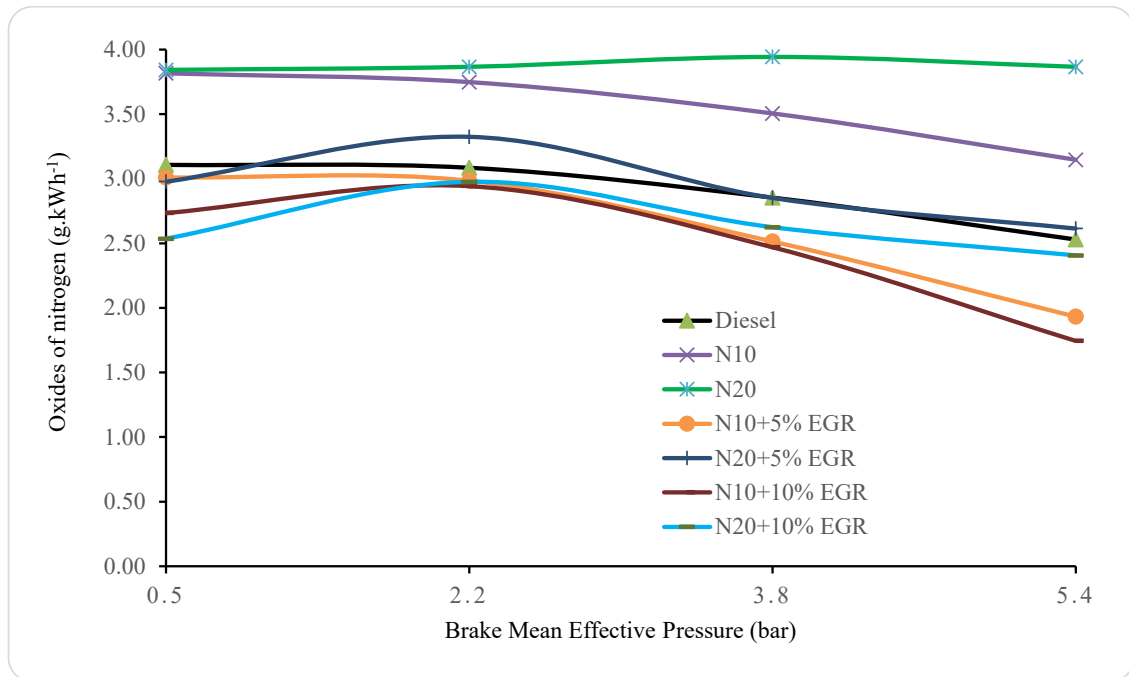
Fig. 9: Changes in oxides of nitrogen with BMEP.
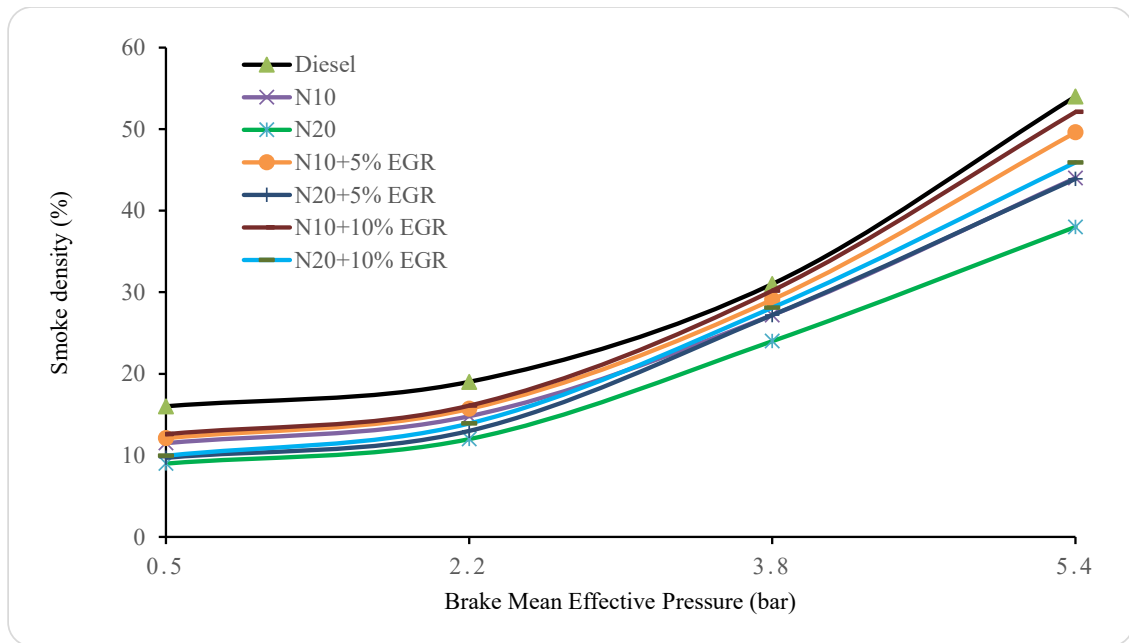
Fig.10: Changes in smoke density with BMEP.

increase in biodiesel concentration in the test fuels for all EGR conditions.

Neat diesel fuel displayed an extreme cylinder pressure of 50.4 bar at 15° after top dead center (ATDC), N10 and N20 blend showed maximum peak cylinder pressure of 48.1 bar and 47.6 bar at CAD of 10° and 7° ATDC respectively. In general biodiesel fuel properties like high viscosity, low volatility and high cetane number are major aspects that affect the variations in peak cylinder pressure (Rashedul et al. 2015).

It is worth noting that the start of combustion (SOC) is advanced with biodiesel addition as referred to as baseline diesel fuel. It is due to advancements in dynamic injection timing in lieu of higher bulk modulus of biodiesel fuel (Lahane & Subramaniam 2014, Subramanian & Lahane 2013, Yu 2007). Another possible reason for this advancement in SOC may be the higher cetane number of biodiesel. As EGR was introduced into operation, significant variations in cylinder pressure were observed. The SOC was retarded for all biodiesel blends with the addition of EGR, which may be attributed to an increase in the specific heat capacity of EGR and reduction in the availability of O_2, which further contributes to weakens combustion rate resulting in peak cylinder pressure decrement (Nitin et al. 2016). Besides, dissociation of H_2O and CO_2 contributes to the flame temperature reduction resulting in NOx reduction because of the endothermic process (Domenico et al. 2017). It can be noted

that 5% EGR addition resulted in a decrease in peak pressure to 47.4 bar and 46.9 bar for N10 and N20 blend respectively. Meanwhile further increase in EGR rate to 10% for N10 and N20 blends decreased the peak cylinder pressure to 46.7 bar and 45.8 bar respectively.

Fig. 12 depicts the variations in HRR with CAD at peak load for the test fuels employed in this study. From the figure, it is evident that the incorporation of EGR greatly influenced in HRR_{max} variations.

Many literature studies revealed that the biodiesel addition to the neat diesel may cause a minor drop in the HRR_{max} value due to shorter premixed combustion duration, lower heating value, early SOC timing, and poor spray characteristics of the biodiesel fuel (Ozener et al. 2014, Ozturk 2015). A similar trend was observed in this study where HRR_{max} recorded for diesel fuel was 55.1 $J.CA^{\circ-1}$ and the subsequent addition of biodiesel fuel with EGR decreased the HRR_{max} values. NME biodiesel blends N10 and N20 showed a maximum HRR of 54.5 $J.CA^{\circ-1}$ and 54.1 $J.CA^{\circ-1}$ respectively. In addition to this, the location of HRR_{max} was noted to shift towards TDC with biodiesel addition to all engine loads. On the other hand, incorporation of EGR along with biodiesel fuel leads to a further decrease in HRR_{max} as compared to that of biodiesel blend operation. Biodiesel blend N10 along with EGR of 5% and 10% decreased HRR_{max} by 1.7 % and 2.9 % respectively whereas N20 blend along with EGR of 5% and 10% decreased the HRR_{max} by 1% and 3.3%
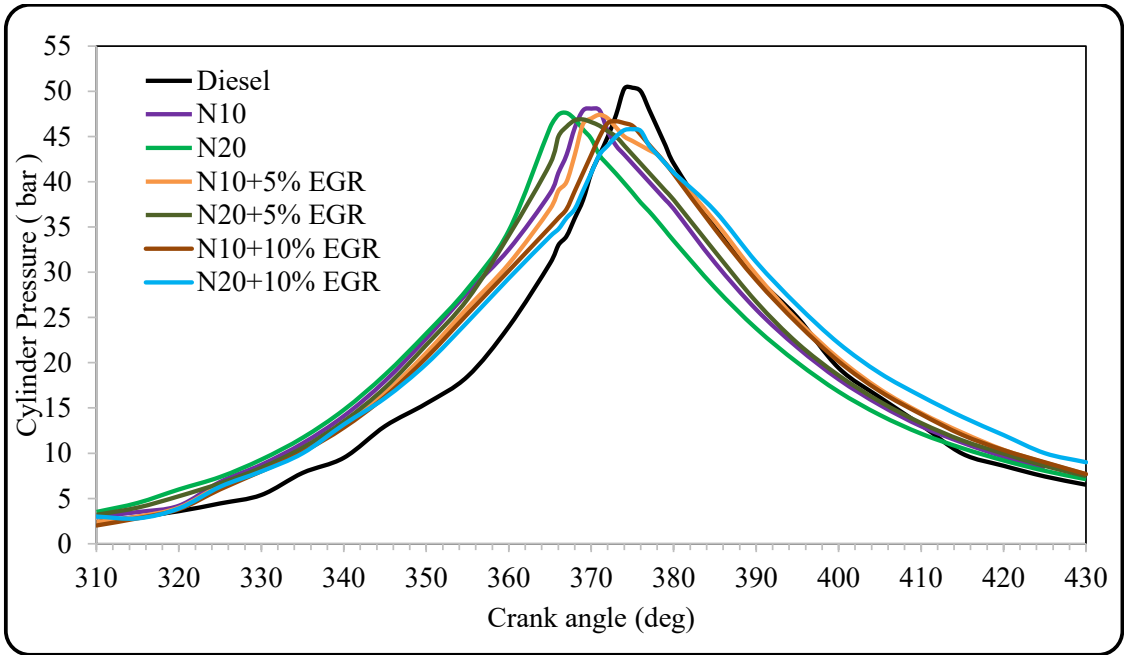
Fig.11: Changes in cylinder pressure with CAD.
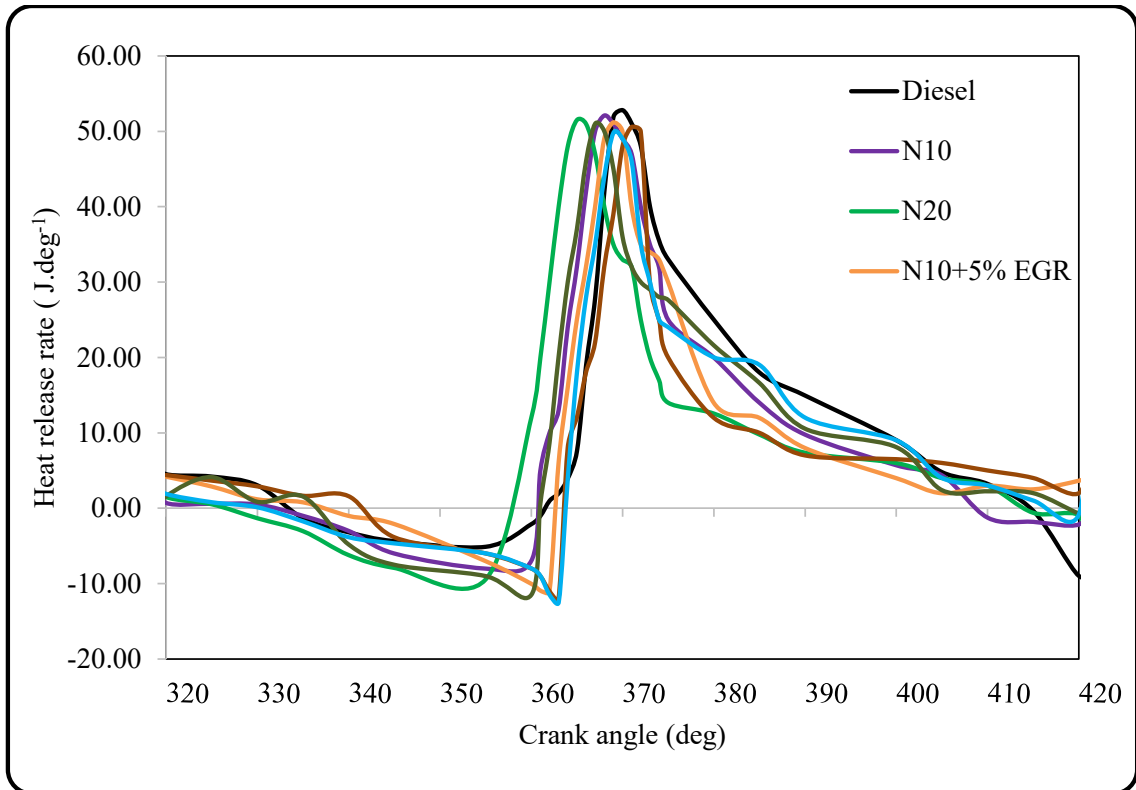
Fig. 12: Changes in HRR with CAD.

respectively as compared to corresponding biodiesel blend operation.

Trade-off Study

Trade-off studies between BSEC and NOx, Smoke, and NOx were carried out to understand the optimum proportion of NME biodiesel and EGR rate at a maximum BMEP of 5.4 bar, and the same is depicted in Fig. 13 and Fig. 14. It is noted that the blending of Neem oil methyl Ester of 10 and 20% with diesel fuel improves the BSEC and smoke emission by decreasing BSEC by 9 and 11.4% and smoke density by 18.5 and 29.6%, however, the NOx emission level increased by 24.4 and 52.8% respectively for N10 and N20 than neat diesel operation. The adverse impact of NOx emission increase was controlled by introducing EGR with marginal compromise on performance (BSEC) and smoke density, however better than diesel operation.

From the trade of study, optimum biodiesel and EGR combination were understood at N20+5% EGR where BSEC and smoke density reduced by 9.2 % and 18.7 % respectively with that of neat diesel operation and the NOx emission is at par with diesel operation.

CONCLUSION

In this present investigation, the effects of the combination of 10% and 20% Neem oil Methyl Ester biodiesel and various EGR rates of 5% and 10% on the characteristics of a DI diesel engine were studied experimentally. The outcomes are as follows:

- The NME biodiesel blends improved the performance characteristics by increasing the BTE by 3.3 and 7.2 % and reducing the BSEC by 9 and 11.4% for 10 and 20% biodiesel blends respectively at peak loads compared to neat diesel. The hike in BTE can be explained by the presence of oxygen in fuel which enhances combustion efficiency. On the other hand, the incorporation of EGR along with biodiesel reduced BTE and increased the BSEC of the engine under all loading conditions. The displacement of fresh oxygen in the combustion chamber by burnt gases causes a deficiency in oxygen level which reduces combustion temperature and efficiency.

- Improvements in unburnt hydrocarbon and carbon monoxide emissions were obtained by the use of a biodiesel fuel blend at all loading conditions, while deterioration
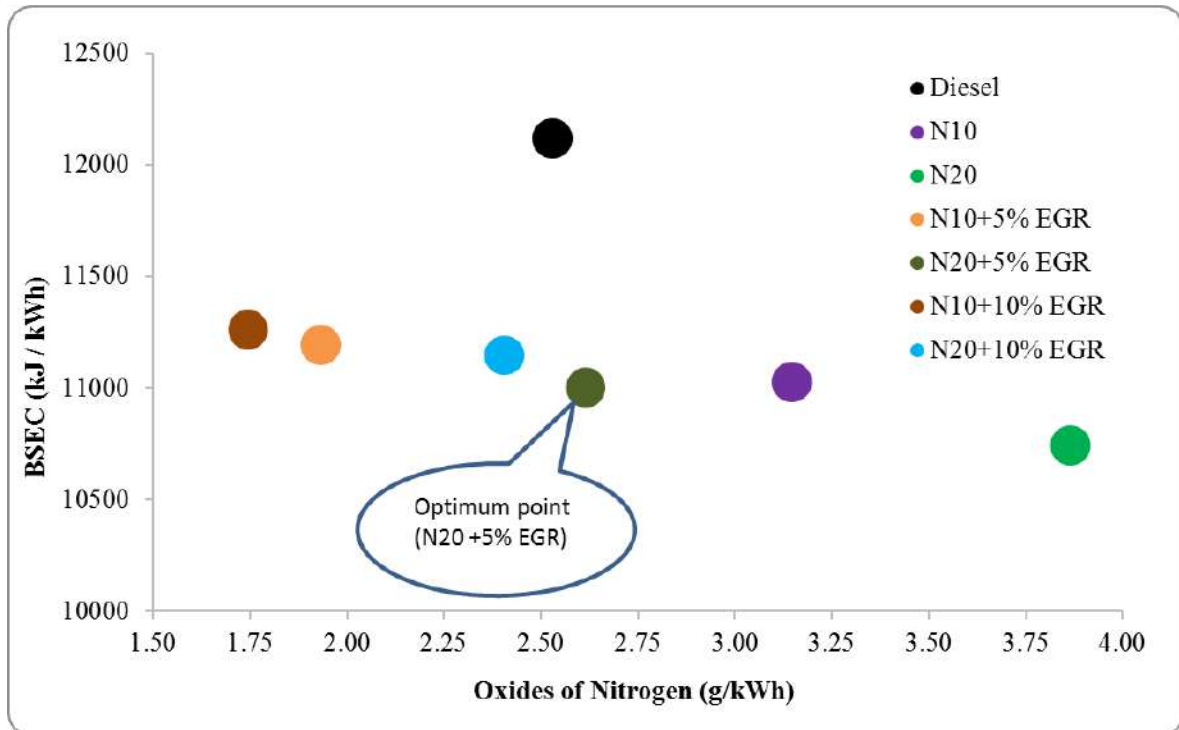
Fig. 13: Trade-off study between BSEC and NOx.
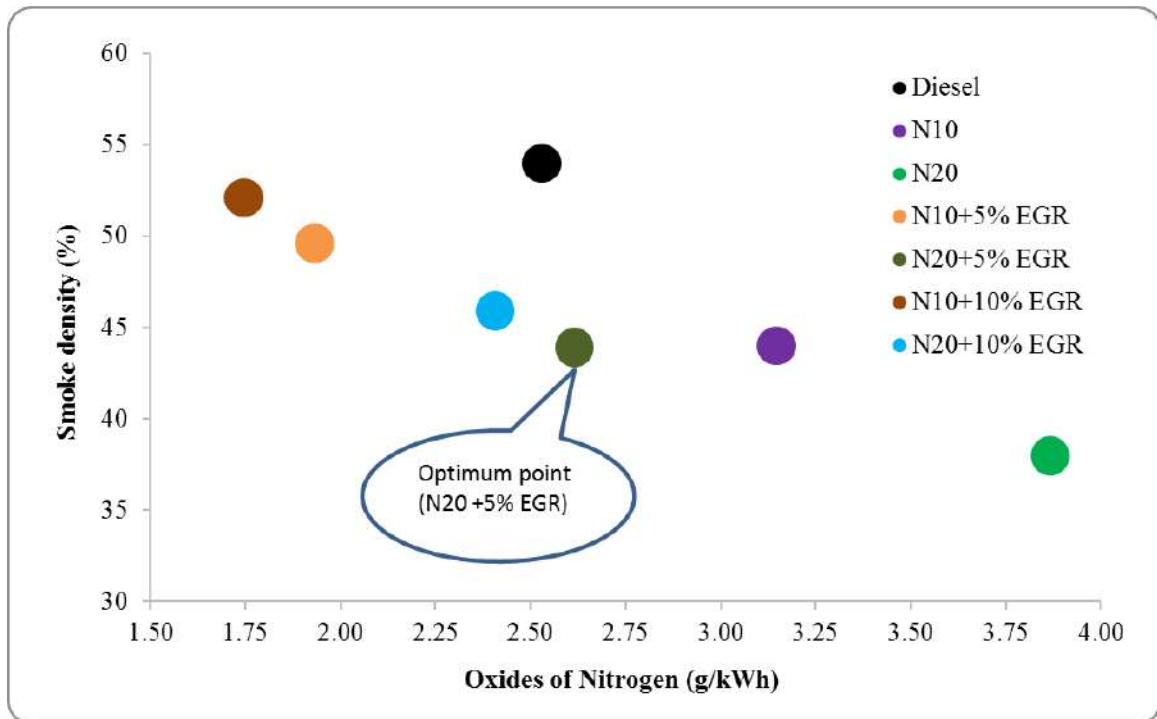
Fig. 14: Trade-off study between Smoke density and NOx.

occurred when EGR was added to the operation. UHC emission was decreased by 14.2 and 31.2%, CO emission was decreased by 25.7 and 40.6% for N10 and N20 respectively at maximum load with respect to neat diesel operation. This reduction in UHC and CO can be attributed to high in-cylinder temperature caused by adequate fuel-air mixing and oxygen content of biodiesel fuels. The rise in CO and UHC can be explained by dilution of intake charge with exhaust gas which leads to a reduction of oxygen needed for complete combustion. This increase is only with respect to biodiesel operation with no EGR condition, however lower than neat diesel operation.

- Augmentation in CO_2 levels up to 42.7 % during N20 biodiesel operation showed the degree of completeness of combustion whereas the addition of EGR at all rates deteriorated CO_2 levels in the exhaust up to 22.5% for N20 with 10% EGR due to dilution effects of the intake charge.

- The higher penalty in NOx was observed during biodiesel utilization which is most commonly due to the high in-cylinder temperature that prevailed in biodiesel operation. The combination of biodiesel and EGR reduced harmful NOx emission at exhaust by reducing in-cylinder temperature through the thermal and dilution

effects of the intake charge. The increase in NOx was observed as 22.3 and 52.8% for N10 and N20 respectively at maximum load with respect to neat diesel operation. In the biodiesel operation of N10 with 10% EGR, the NOx level was reduced by 44.5 % with respect to N10 with no EGR and by 31 % with respect to neat diesel operation. At N20 with 10% EGR, the NOx level was reduced by 37.8% compared to N20 with no EGR and by 4.9 % compared to neat diesel operation.

- Smoke emission is observed in neat diesel operation from 16 to 54% from 0.5 to 5.4 bar BMEP and the same is noticed from 11.5 to 44% for N10 and from 9 to 38% for N20 operation. Combustion is enhanced at fuel-rich zones in NME biodiesel operation due to the presence of fuel-borne oxygen with respect to neat diesel operation where no fuel-borne oxygen. The introduction of EGR marginally impacted the raise in smoke emission with respect to neat NME biodiesel operation due to incomplete combustion caused by reducing the oxygen availability for combustion, but lower than the neat diesel operation for all EGR combinations.

On the whole use of Neem oil Methyl Ester of 10 and 20% along with EGR of 5 and 10% put a step towards reducing harmful NOx emission which is the major setback in using biodiesel as a commercial fuel. Also, improvements in

performance characteristics further confirm the potential of Neem biodiesel (20%) along with the 5% EGR can be used in commercial transportation.

NOMENCLATURE

BMEP	Brake Mean Effective Pressure	EGR	Exhaust Gas Recirculation
BSEC	Brake Specific Energy Consumption	HCCI	Homogeneous Charge
BSFC	Brake Specific Fuel Consumption		Compression ignition
BTE	Brake Thermal Efficiency	ID	Ignition Delay
CAD	Crank Angle Degree	NME	Neem oil Methyl Easter
CI	Compression-Ignition	NOx	Oxides of Nitrogen
CO	Carbon monoxide	SOC	Start of Combustion
CO2	Carbon dioxide	SOI	Start of Injection
DI	Direct Injection	UHC	Unburnt Hydrocarbon

REFERENCES

Ardebili, M.S., Ghobadian, B., Najafi, G. and Chegeni, A. 2011. Biodiesel production potential from edible oil seeds in Iran. Renew. Sustain. Energy Rev., 15: 3041-3044.

Atul, D. and Avinash, K.A. 2014. Performance, emissions, and combustion characteristics of Karanja biodiesel in a transportation engine. Fuel, 6: 11-15.

Azad, A., Uddin, SA. and Alam, M. 2013. Experimental study of DI diesel engine performance using biodiesel blends with kerosene. Int. J. Energy Environ., 4: 265-278.

Baert, R.S., Beckman, D.E. and Veen, A. 1999. Efficient EGR technology for future HD diesel engine emission targets. SAE Int., 15: 91

Banapurmatha, N.R., Tewari, P.G. and Hosmath, R.S. 2008. Performance and emission characteristics of a DI compression ignition engine operated on honge, jatropha, and sesame oil methyl esters. Renew. Energy, 33(9):1982-1988.

Bhupendra, S.C., Naveen, K., Haeng, M.C. and Hee, C.L. 2013. A study on the performance and emission of a diesel engine fueled with Karanja oil biodiesel and its blends. Energy, 56: 1-7

Borugadda, V.B. and Goud, V.V. 2012. Biodiesel production from renewable feedstocks: status and opportunities. Renew. Sustain. Energy Rev., 16: 4763-4784.

Brehob, W.M. 2007. Mechanisms of pollutant formation and control from automotive sources. SAE Paper, 71: 483.

Canakci, M. 2007. Combustion characteristics of a turbocharged DI compression ignition engine fueled with petroleum diesel fuels and biodiesel. Bioresour. Technol, 98:1167-1175.

Coleman, H.W. and Steele, W.G. 2009. Experimentation, Validation, and Uncertainty Analysis for Engineers. Third Edition. John Wiley & Sons Inc., New Jersey.

Das, P., Subbarao, P.M. and Subrahmanyam, J.P. 2015. Control of combustion process in an HCCI- DI combustion engine using dual injection strategy with EGR. Fuel, 159: 580-589.

Domenico, D., Alex. D. and José, R.S. 2017. Effects of EGR rate on performance and emissions of a diesel power generator fueled by B7. J. Braz. Soc. Mech. Sci. Eng., 17: 77. DOI 10.1007/s40430-017-0777-x.

Eryılmaz, T., Yesilyurt, M.K., Yumak, H., Arslan, M. and Sahin, S. 2014. Determination of the fuel properties of cottonseed oil methyl ester and its blends with diesel fuel. Int. J. Auto. Eng. Technol., 3(2): 79-90.

Jaichandar, S. and Annamalai. K. 2011. The status of biodiesel as an alternative fuel for diesel engines. J.Sustain. Energy Environ., 2: 71-75.

Jinlin, X., Tony, E. and Hansen, A. 2011. Effect of biodiesel on engine performances and emissions. Renew. Sustain. Energy Rev., 15: 1098–1116.

Kanda, T., Hakozaki, T., Uchimoto, T., Hatano, J., Kitayama, N. and Sono, H. 2005. PCCI operation with an early injection of conventional diesel fuel. SAE Paper, 20: 378.

Knothe, G. 2007. Some aspects of biodiesel oxidative stability. Fuel Process. Technol., 88: 669-677.

Kohketsu, S., Mori, K., Sakai, K. and Hakozaki, T. 1997. EGR technologies for a turbocharger and intercooler heavy-duty diesel engine. SAE Paper, 9: 70.

Lahane, S. and Subramanian, K. A. 2014. Impact of nozzle holes configuration on fuel spray, wall impingement, and NOx emission of a diesel engine for the biodiesel-diesel blend (N20). Appl. Thermal Eng., 64(1-2): 307-314.

Lapuerta, M., Armas, O. and Fernàndez, J.R. Effect of biodiesel fuels on diesel engine emissions. Prog. Energy Combust. Sci., 34: 198-223.

Leung, D.Y.C., Wu, X. and Leung, M.K.H. 2010. A review on biodiesel production using catalyzed transesterification. Appl. Energy, 87: 1083–1095.

Lin, Y.F., Greg, W.Y. and Chang, C.T. 2007. Combustion characteristics of waste-oil produced biodiesel/diesel fuel blends. Fuel, 86: 1772-1780.

Mahanta, P., Mishra, S.C. and Kushwah, Y.S. 2006. An experimental study of *Pongamia pinnata* L. oil as a diesel substitute. Proc. Inst. Mech. Eng. Part A J. Power Energy, 220: 803-808.

Maiboom, A., Tauzia, X. and Hétet, J.F. 2008. Experimental study of various effects of exhaust gas recirculation (EGR) on combustion and emissions of an automotive direct injection diesel engine. Energy, 33: 22-34.

Majewski, W.A. and Khair, M. 2006. Diesel Emissions, and Their Control. SAE International, USA.

Mani, M., Nagarajan, G. and Sampath, S. 2010. An experimental investigation on a DI diesel engine using waste plastic oil with exhaust gas recirculation. Fuel, 89: 1826-1832.

Masjuki, H., Abdulmuin, M.Z. and Sii, H.S. 1996. Investigations on preheated palm oil methyl esters in the diesel engine. In: Proc. Instit. Mech. Eng. Part A. J. Power Energy, 2(21):. 131-138.

Mohamed, S.R., Kasimani, R., Rajamohan, S. and Ramakrishnan, P. 2017. Experimental evaluation of oxidation stability of biodiesel/diesel blends with alcohol addition by rancimat instrument and FTIR spectroscopy. J. Mech. Sci. Technol., 31(1): 455-463. https://doi.org/10.1007/s12206-016-1248-5.

Naik, M., Meher, L.C., Naik, S.N. and Das, L.M. 2008. Production of biodiesel from high free fatty acid Karanja (*Pongamia pinnata*) oil. Biomass- Bioenergy, 32: 354-357.

Nitin, M., Sakhare, Pankaj, S., Shelke, S. and Subhash. L. 2016. Experimental investigation of effect of exhaust gas recirculation and cottonseed N20 biodiesel fuel on diesel engine. Proced. Technol., 25: 869-876.

Ozener, O., Yuksek, L., Ergenc, A.T. and Ozkan, M. 2014. Effects of soybean biodiesel on a DI diesel engine performance, emission, and combustion characteristics. Fuel, 115: 875-883.

Ozturk, E. 2015. Performance, emissions, combustion, and injection characteristics of a diesel engine fueled with canola oil-hazelnut soapstock biodiesel mixture. Fuel Process. Technol., 129: 183-191.

Pankaj, S., Tikendra, N.V., Olusegun, D.S. and Arivalagan, P. 2020. An experimental investigation on engine characteristics, cost, and energy analysis of CI engine fuelled with Roselle, Karanja biodiesel, and its blends. Fuel, 275: 117891

Prabhahar, M., Muralimanohar, R. and Sendilvelan, S. 2012. Performance, emission, and combustion characteristics of a direct injection diesel engine with *Pongamia* methyl ester and diesel blends. Eur. J. Sci. Res., 73(4): 504-11.

Qi, D.H., Chen, H., Geng, L.M. and Bian, Y.Z.H. 2010. Experimental studies on the combustion characteristics and performance of a direct injection engine fueled with biodiesel/diesel blends. Energy Convers. Manag. , 51: 2985-2992.

Raheman, H. and Ghadge, S.V. 2008. Performance of diesel engine with bio-diesel at varying compression ratio and ignition timing. Fuel, 45: 456-69.

Raheman, H. and Ghadge, S.V. 2007. Performance of compression ignition engine with mahua (*Madhuca indica*) biodiesel. Fuel, 86: 2568-2573.

Rashedul, H.K., Masjuki, H.H., Kalam, M.A., Teoh, Y.H., How, H.G. and Rizwanul Fattah, I.M. 2015. Effect of   antioxidant on the oxidation stability and combustion-performance-emission characteristics of a diesel engine fueled with diesel-biodiesel blend. Energy Convers. Manag., 106: 849-858.

Rizwanul, I.M., Masjuki, H.H., Liaquat, A.M, Ramli, R., Kalam, M.A. and Riazuddin, V.N. 2013. Impact of various biodiesel fuels obtained from edible and non-edible oils on engine exhaust gas and noise emissions. Renew. Sustain. Energy Rev., 18: 552-567.

Sahoo, P.K. and Das, L.M. 2009. Combustion analysis of Jatropha, Karanja, and Polanga-based biodiesel as fuel in a diesel engine. Fuel, 88(6): 994-9.

Sahoo, P.K., Das, L.M., Babu, M.K.G., Arora, P., Singh, V.P. and Kumar NR. 2009. Comparative evaluation of performance and emission characteristics of jatropha, Karanja, and polanga-based biodiesel as fuel in a tractor engine. Fuel, 88: 1698-707.

Sakthivel, G., Saravanan, N. and Ilangkumaran, M. 2016. Influence of injection timing on performance, emission, and combustion characteristics of a DI diesel engine running on fish oil biodiesel. Energy, 11: 44-59.

Salim Mohamed, Y.E. 2003. Effect of EGR on some combustion characteristics of a dual fuel engine. Energy Convers. Manag., 4(5): 709-23.

Shin, B., Cho, Y., Han, D., Song, S. and Chun, K.M. 2011. Hydrogen effects on NOx emissions and brake thermal efficiency in a diesel engine under low-temperature and heavy-EGR conditions. Int. J. Hydro. Energy, 36: 6281-6291.

Sinha, S. and Agarwal, A.K. 2005. Performance evaluation of biodiesel (rice bran oil methyl ester) fueled transport diesel engine. SAE Paper, 20: 5-11.

Spessert, B.M., Arendt, I. and Schleicher, A. 2004. Influence of RME and vegetable oils on exhaust gas and noise   emissions of small industrial diesel engines. SAE Paper, 20: 24-32.

Srivastava, P.K. and Verma, M. 2008. Methyl ester of Karanja oil as alternative renewable source energy. Fuel, 87: 1673-7.

Suja, T. and Nagarajan, G. 2018. Evaluating combustion, performance, and emission characteristics of diesel engine using Karanja oil methyl ester biodiesel blend enriched with HHO gas. Int. J. Hydro. Energy, 43: 6443 - 6455

Subramanian, K.A. and Lahane S. 2013. Comparative evaluations of injection and spray characteristics of a diesel engine using Karanja biodiesel-diesel blends. Int. J. Energy Res., 37(6): 582-597

Sun, J., Caton, J.A. and Jacobs, T.J. 2010. Oxides of nitrogen emissions from biodiesel-fueled diesel engines. Prog. Energy Combust. Sci., 3: 677-95.

Thangaraja, J. and Kannan, C. 2016. Effect of exhaust gas recirculation on advanced diesel combustion and alternate fuel: A review. Appl. Energy, 8(3): 65-79.

Vinay, K. and Raveendra, A. 2015. Effects of exhaust gas recirculation on the performance and emission characteristics of diesel engine using biodiesel. Int. J. Eng. Res. Technol., 4(5): 2278-2281.

Ye, P. and Boehman, A.L. 2012. An investigation of the impact of injection strategy and biodiesel on engine NOx and particulate matter emissions with a common-rail turbocharged DI diesel engine. Fuel, 97: 476-488.

Yu, R.C. and Shahed, S.M. 1981. Effects of injection timing and exhaust gas recirculation on emissions from a DI diesel engine. SAE Paper, 34; 11.

Yu, Z. 2007. Impact of biodiesel on NOx emissions in a common rail: Direct injection diesel engine. Energy Fuels, 2007: 7.

Zhao, Y., Wang, Y., Li, D., Lei, X. and Liu S. 2014. Combustion and emission characteristics of a DME (dimethyl ether)-diesel dual fuel premixed charge compression ignition engine with EGR (exhaust gas recirculation). Energy, 72: 608-617.

Zheng, M., Reader, G.T. and Hawley, J.G. 2004. Diesel engine exhaust gas recirculation—a review on advanced and novel concepts. Energy Convers. Manag., 45: 883-900.

Adopting Gram-Schmidt and Brovey Methods for Estimating Land Use and Land Cover Using Remote Sensing and Satellite Images

Fatima Hashim*, Hayder Dibs**† and Hussein Sabah Jaber*

*Surveying Engineering Department, College of Engineering, University of Baghdad, Baghdad, Iraq
**Al-Qasim Green University, Water Resources Engineering Faculty, Water Resources Management Engineering Department, Babylon, Iraq
†Corresponding author: Hayder Dibs; dr.hayderdibs@wrec.uoqasim.edu.iq

ABSTRACT

The production of Land Use and Land Cover thematic maps using remote sensing data is one of the things that must be dealt with carefully to obtain accurate results, data is obtained from sensors of different characteristics. It is not possible to obtain high spatial and spectral accuracy in one image, so we used a fusion image (multispectral image with a low spatial resolution with a panchromatic image with high spatial resolution), which achieved high efficiency in improving the methods of producing Land Use and Land Cover maps. In this study, we used Landsat-8 multispectral and panchromatic images. The study aims to investigate the effectiveness of panchromatic images in improving the methods of producing Land Use and Land Cover maps for the city of Karbala, Iraq. The Support Vector Machine was used to classify the fusion images using the Brovey method and Gram-Schmidt sharpening algorithms. The appropriate methodology for producing Land Use and Land Cover maps was suggested by comparing classifying results and the classification accuracy was evaluated through the confusion matrix. Where the results showed that the method of classifying the fused image by Gram-Schmidt and classified by Support Vector Machine is the best way to produce Land use and Land cover maps for the study area and achieved the highest results for overall accuracy and kappa coefficient of 97.81% and 0.95, respectively.

INTRODUCTION

One of the most important applications of remote sensing is the classification of satellite images, which have formed a wide range, especially in the production of Land Use/Land Cover (LU/LC) maps (Dibs 2013, Bouaziz et al. 2017, Dibs 2018) and in many applications such as land use discovery, natural hazard modeling, and urban expansion studies as well as for continuous updating of geospatial data (Sang et al. 2014, Otukei et al. 2015, Dibs et al. 2018) and monitoring of wetland degradation studies (Ali & Jaber 2020, Hasan et al. 2020a). For mapping LU/LC, it was found that the best method is to classify images and it is a complex process that depends on many concepts, including determining the appropriate classification method (Chasmer et al. 2014), training site, image processing, feature identification, post-classification processing and accuracy evaluation (Sang et al. 2014). Choosing the appropriate classifier is very important to achieve a satisfactory result in classifying the study area, many algorithms and techniques have been adopted to estimate classification, such as Support Vector Machine (SVM) (Iounousse et al. 2015) and other algorithms Artificial Neural Networks (DNN) (Cavur et al. 2015), Decision

trees (DT) (Chasmer et al. 2014), and Maximum Likelihood (ML) (Gevana et al. 2015). Remote sensing data integration technologies (Gevana et al. 2015, Abbas & Jabber 2020, Hasab et al. 2020b) and Methods for fusion images from a set of multiple and different remote sensing data are one way to improve the accuracy of the data used to produce LU/LC maps, where many researchers dealt with methods and techniques for fusion multispectral (MS) image with a low spatial resolution with high spatial resolution panchromatic (Pan) image to obtain images with high spatial and spectral resolution (Dibs et al. 2020, Dibs et al. 2021). It used many sharpening algorithms such as the Brovey method, Gram-Schmidt (GS), Intensity-Hue-saturation (IHS), and Principle Component Analysis (PCA). (Tabib Mahmoudi & Karami 2020). Fusion methods and techniques have had a wide resonance in many applications that used multiple data and from different sources (Jawak & Luis 2013, Sameen et al. 2016, Dibs & Al-Hedny 2019, Dibs et al. 2020). Since the methods and algorithms of sharpening to combine images with rapid development in some applications such as classification of images, studying changes, and identifying features, the efficiency of sharpening algorithms were considered one of the

necessary things, which is to preserve the characteristics of the entered information (Tabib Mahmoudi & Karami 2020). Mandhare et al. (2013) used several sharpening algorithms such as IHS, Brovey, averaging method, and multiplier method to improve the spatial and spectral resolution of the merged images. Sarp (2014), also discussed the performance of four sharpening algorithms (GS, IHS, PCA, Brovey) for fusion MS and Pan images and found that PCA and GS work well in all technologies. Another scientist (Zhang et al. 2016), conducted a study to obtain images with high spatial resolution while maintaining the spectral distortion as less as possible using sharpening algorithms (Brovey, GS, PCA, and IHS) and by comparing the results, it was found that Brovey is the best. the objective of this research is to obtain an improved methodology for producing LU/LC maps within the study area.

MATERIALS AND METHODS

To produce and detect LU/LC maps, methods were selected and examined through previous works to ensure their effectiveness and accuracy in this field because the selected algorithms must be effective and achieve good results within the study area (Jia et al. 2014). In this study, Landsat-8 OLI (multispectral images with a spatial resolution of (30 m) and a panchromatic image with a spatial resolution of (15 m), which were obtained on July 13, 2020, were selected for the processing steps as in the pre-processing, layer stacking of images was performed using bands (1, 2 & 3), and sub-setting was done to define the study area to reduce storage size and to facilitate the recall of files. Processing stage the images were corrected from geometric and radiometric errors to prepare the images for further processing. Later, the process of fusion image was conducted using the multispectral image with the panchromatic image with the use of two fusion approaches, the Brovey method sharpening algorithm and the other once the Gram-Schmidt (GS) sharpening algorithm and two fused images were obtained. To complete the processing and analysis operations to produce LU/LC maps, the classification of the two fused images was carried out using the SVM algorithm. The accuracy was evaluated based on the confusion matrix, and to determine the best methodology to improve the production of LU/LC maps for the study area, a comparison was made between the classification results. Fig. 1 shows a diagram of the methodology used for this study.

Study Area

The study area is the city of Karbala, Iraq, and it is one of the important Iraqi governorates because of its economic and tourism importance. Its location is between longitude 44°02′- 44°40′ E and latitude of 32°37′- 33° 31′ N. It has

an area of 5,034 km^2 and a population of about 1.219 million in 2018. Karbala's climate is predominantly desert, with temperatures in summer reaching 45° and dropping to zero degrees in winter. It is one of the Iraqi cities with good economic returns due to its orchards of various types of crops such as dates, fruits, vegetables, and wheat. It is also famous for its handicrafts such as ceramics, as well as the manufacture of bricks and tiles. Karbala is a tourist city with a good financial return, which is frequented by tourists from all over the world to visit the holy sites (Jasem & AL-Mayali 2020). Fig. 2 shows the study area map.

The Dataset

The data that was used in this study includes the data set of the Landsat- 8 OLI satellite, recorded on July 13, 2020. The Landsat satellite includes two sensors, one of which is an operational land imaging device (OLI), whose data was used, and the other is a thermal infrared sensor (TIRS). The Landsat satellite data consists of 11 bands, where bands (1-7, 9) have a spatial resolution of (30) meters, and band (8) represents Pan and its spatial accuracy (15) meters, while bands 11 and 10 have infrared thermal radiation and have a spatial accuracy of (100) meters. Tables 1 &2 show the characteristics of OLI and TIRS (https://www.usgs.gov/

Table 1: Technical characteristics of OLI of Landsat-8.

Bands	Wavelength [mm]	Resolution [m]
Band 1- visible	0.43 - 0.45	30
Band 2- visible	0.45 - 0.51	30
Band 3 -visible	0.53 - 0.59	30
Band 4- near infrared	0.64 - 0.67	30
Band 5- near infrared	0.85 - 0.88	30
Band 6- SWIR	1.57 - 1.65	30
Band 7 -SWIR	2.11 - 2.29	30
Band 8 panchromatic	0.50 - 0.68	15
Band 9 cirrus	1.36 - 1.38	30

(source: https://www.usgs.gov/media/images/landsat-8-band-designations)

Table 2: Technical specification of TIRS of Landsat-8.

Band name	Central wavelength [μm]	Spectral range [μm]	Spatial resolution [m]
Band 10 / TIRS-1	10.9	10.6–11.19	100
Band 11 / TIRS-2	12.0	11.5–12.5	100

(source: https://www.usgs.gov/media/images/landsat-8-band-designations)
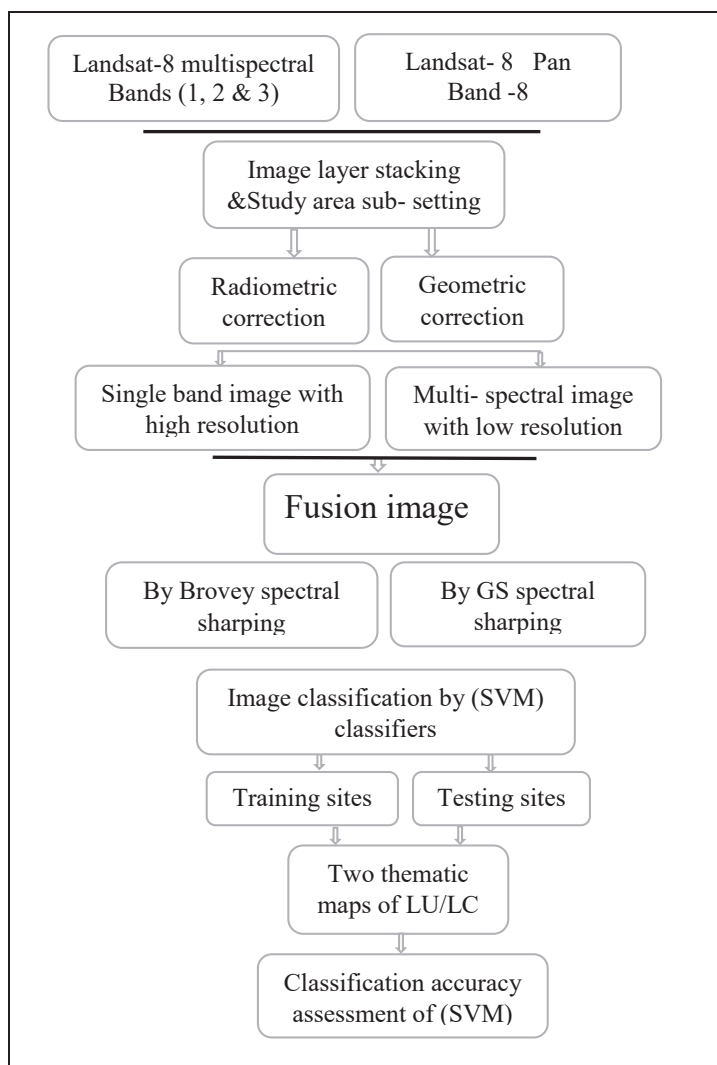
Fig. 1: Flowchart of methodology.

media/images/landsat-8-band-designations). The data was obtained free of charge from the US Geological Survey USGS website as a reference from (http://earthexplorer.usgs.gov) where we used Landsat -8 OLI (MS and Pan) satellite images, as shown in Fig. 3 & 4 showing the images used. We relied on google maps to match the data and choose training sites because they have high spatial accuracy.

Analysis and Processing

In this paper, we started by performing the processing steps, which include (1) pre-processing, which is layer stacking, and image sub-setting. (2) In the Processing steps, geometric and radiometric correction is applied to prepare the image for further processing and analysis, the geometric correction was carried out to reduce the geometric errors that cause

different locations and the geometric correction was done using the image-to-image method depending on the ground control points (GCPs) from Fieldwork. The Landsat-8 (Pan) image with a spatial resolution of (15 m) and projected on the projection UTM, 38N, and WGS 84 Datum was considered error-free, and the geometric corrected based on ten ground control points. Table 3 shows the ground control points used and Fig. 5 shows the distribution of points in the study area. Root Mean Square Error (RMSE) was used as a measure of the variance between the measured and the predicted values, where the value of the RMSE was equal to 0.344, Table 4 shows the processing geometric for the Landsat-8 satellite image, and the geometric correction was made using the ENVI v5.3 program. A radiometric correction was carried out to remove the effects of sunlight, as several studies

Fatima Hashim et al.
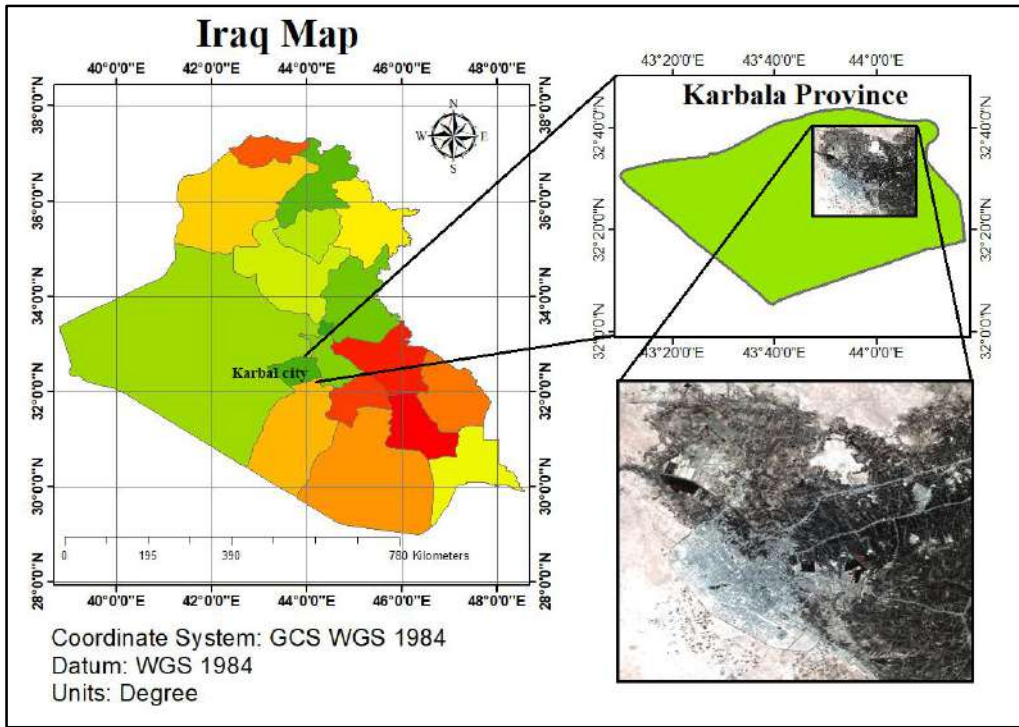
Fig. 2: The study area map.
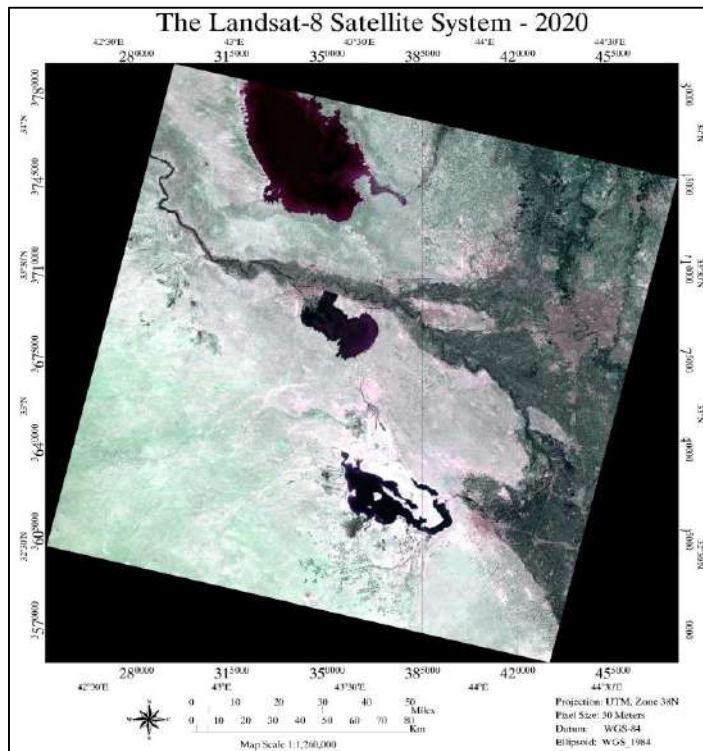
Fig. 3: Landsat-8 satellite (MS) image.

Table 3: Ground control points in the study area.

No.	Latitude	Longitude
1	32° 46′ 59.42"N	43° 55′ 43.42" E
2	32° 42′ 21.88" N	43° 54′ 27.08"E
3	32° 34′ 48.29" N	43° 58′ 38.72"E
4	32° 45′ 36.53" N	44° 06′ 22.25"E
5	32° 41′ 41.34" N	44° 11′ 48.61"E
6	32° 34′ 47.79" N	44° 11′ 42.31" E
7	32° 32′ 41.11" N	44° 03′ 50.24" E
8	32° 36′ 42.22" N	44° 03′ 37.64"E
9	32° 36′ 58.40" N	44° 04′ 11.52"E
10	32° 42′ 30.72" N	43°59′ 55.74"E

confirmed that it is one of the main methods of processing (Idi & Nejad 2013). The radiometric correction was done using the Quick Atmospheric Correction (QUAC) method. This method works to return the optical depth based on the spectra of the observed pixels available in the scene (Bernstein et al. 2012). Fig. 6 shows the corrected Pan image, and Fig. 7 shows the corrected MS image from (geometric and radiometric) errors.

Fusion Image

The fusion process of (MS and Pan) images was performed after pre-processing (layer stacking and image sub-setting) and processing (geometric and radiometric correction), two approaches were applied by performing image fusion between the (MS & Pan) dataset (Li et al. 2012, Idi & Nejad 2013, Löw et al. 2015). The first level of fusion between (MS& Pan) images was applied using the sharpening method (BT). which is a chromatic conversion method using three spectral bands, was applied to the fusion process, the aim of which is to print the three multispectral bands used to display RGB (Mandhare et al. 2013). The second approach used for data fusion is the GS method to improve spatial resolution (Kumar et al. 2014). The GS method calculates the average of the multispectral image bands and selects a range from the Pan image similar to the multispectral image bands. The mid-ranges of the multispectral image are replaced by the corresponding range of the Pan, and finally, the process is repeated in the opposite direction to obtain a high spatial resolution (Jawak & Luis 2013), The Fig. 8 shows the fusion of (MS & Pan) images using the BT sharpening algorithm, and Fig. 9 shows the fusion (MS & Pan) images using the GS sharpening algorithm.
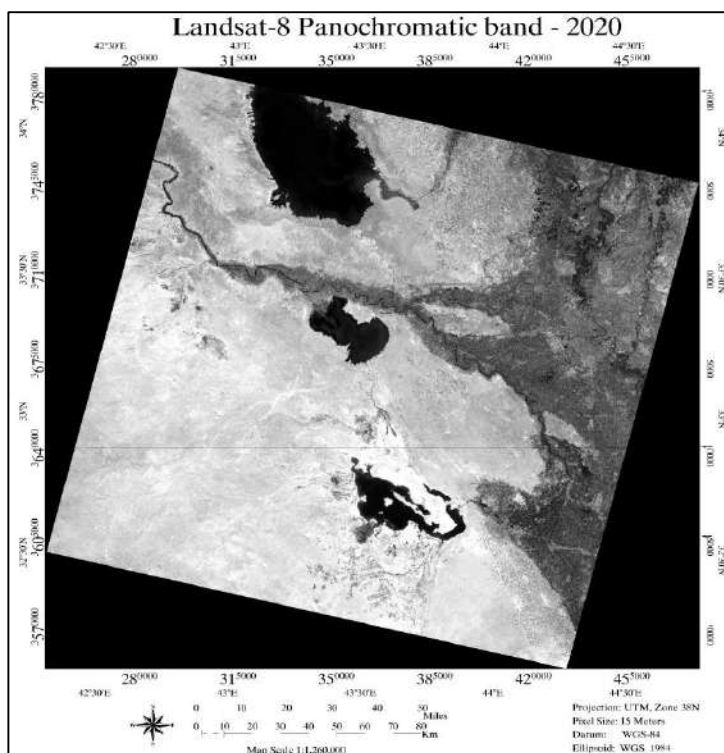
Fig. 4: Landsat-8 satellite (Pan) image.
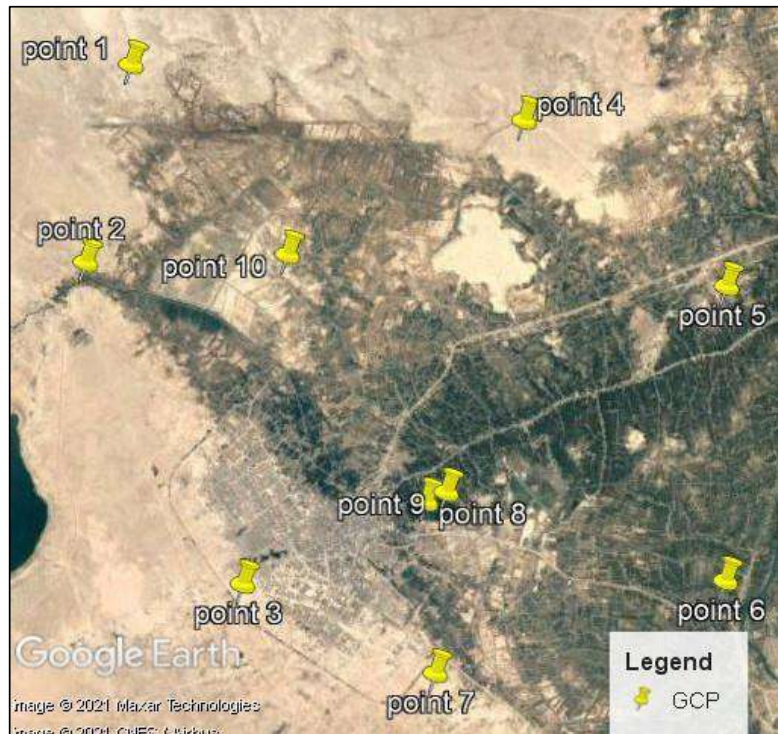
Fig. 5: The location of GCPs by Google earth.
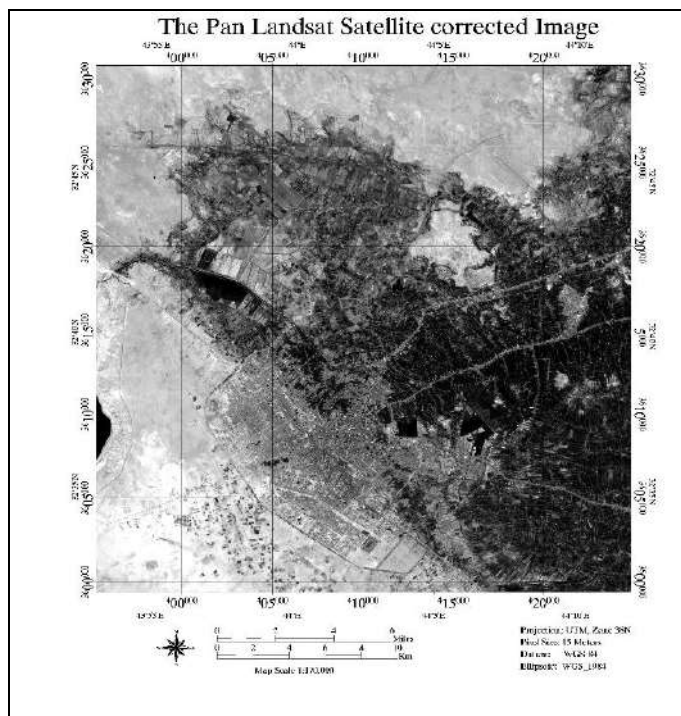
Fig. 6: Corrected Pan image.

Image Classification

After completing the processing operations and fusion of the (MS & Pan) images, the processing must be completed to produce LU/LC maps. The classification was applied to the fused images using supervised classification and by applying the SVM algorithm. The classification was performed according to the following steps:

Selecting Training and Testing Sites

Before starting the classification process, the study area was divided into six categories: urban area, vegetation, water bodies, soil-1, soil-2, and roads. Training samples were taken from the categories of the study area by selecting the polygons of the area of interest using ENVI v5.3. Fig. 10 shows the training sites for each category of the study area, and Table 5 gives the pixels that were chosen as training sites. Then the classification was applied using SVM and then the test samples were taken to verify the quality of the classification and its conformity with the study area.

Support Vector Machine

The SVM classification algorithm was applied in this study.

SVM works to find the optimal separator to achieve the ideal classification by creating more than one separator and defining the super separator and depending on the experience of the analyzer as well as the pixels that were previously identified from the study area classes (Erener 2013). The classification was applied using SVM on the fused images by BT and GS sharpening algorithms after the study area was divided into six categories and training sites were selected and the kernel used for SVM was radial, Figs. 11 & 12 show the SVM parameters used to classify fused images using the (BT & GS) sharpening algorithms. Figs. 13 & 14 show LU/LC map classified using SVM classified on fused data by (BT & GS) methods

Accuracy Assessment

To assess the accuracy of the classification results we use the confusion matrix approach which is the most widely used method for assessing the accuracy of the classified data (Li et al. 2012). The accuracy of the SVM classifier used in this study was evaluated, and the kappa coefficient and overall accuracy were also used as an indicator to assess the accuracy, the Overall Accuracy (OA) and the Kappa coefficient can be calculated using equations 1 & 2 below (Dibs et al. 2021 and 2022).
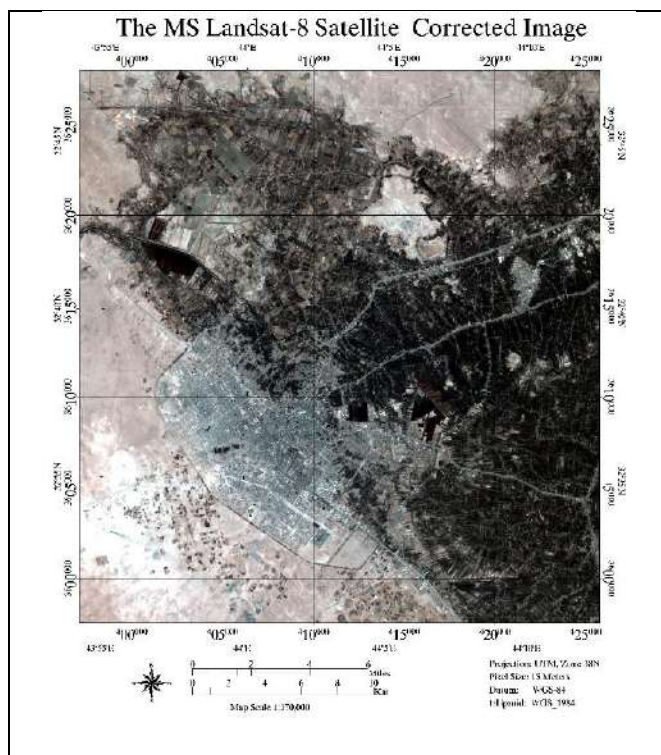
Fig. 7: Corrected MS image from (geometric and radiometric) errors.
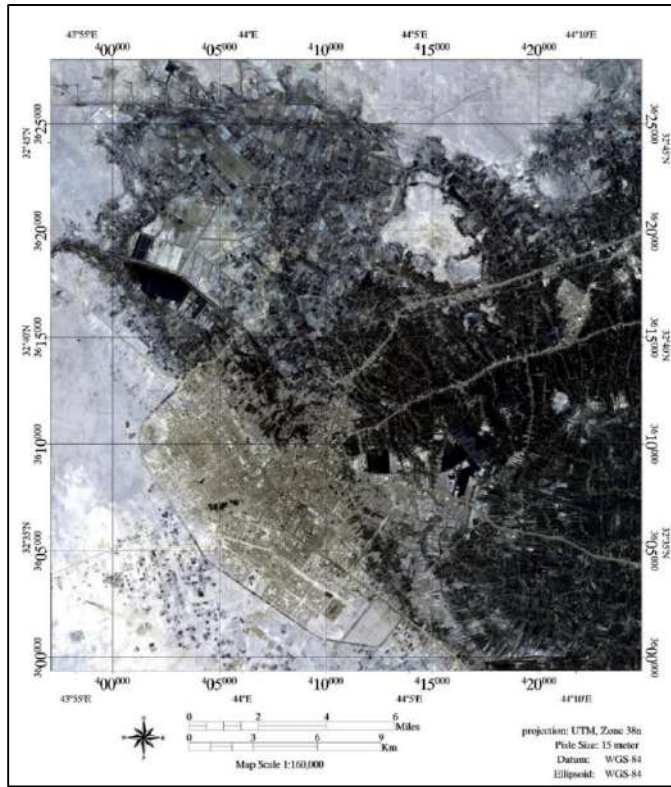
Fig. 8: Fusion image by Brovey method sharpening algorithm.
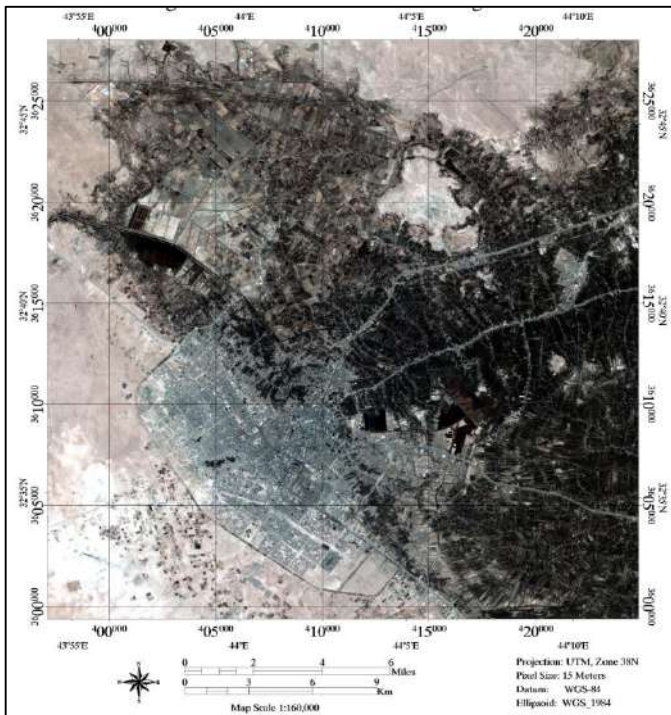
Fig. 9: Fusion image by Gram-Schmidt sharpening algorithm.
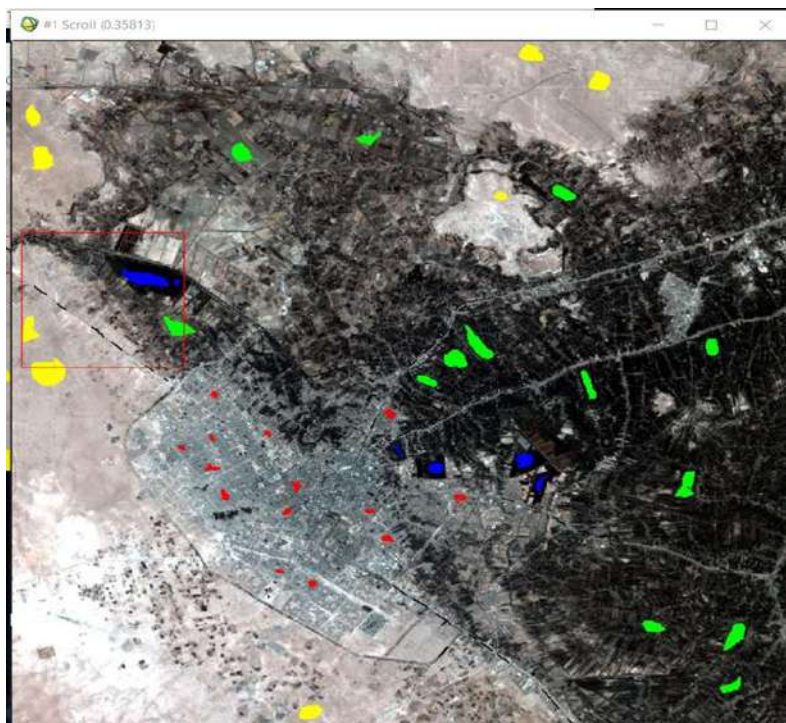
Fig. 10: location of training sites for the study area.
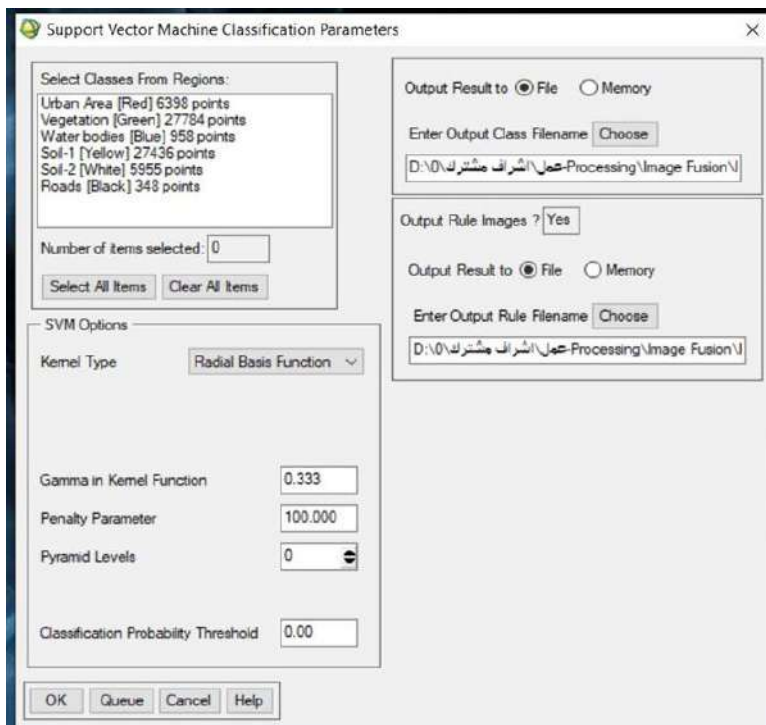
Fig. 11: SVM parameter for image fusion by (BT).
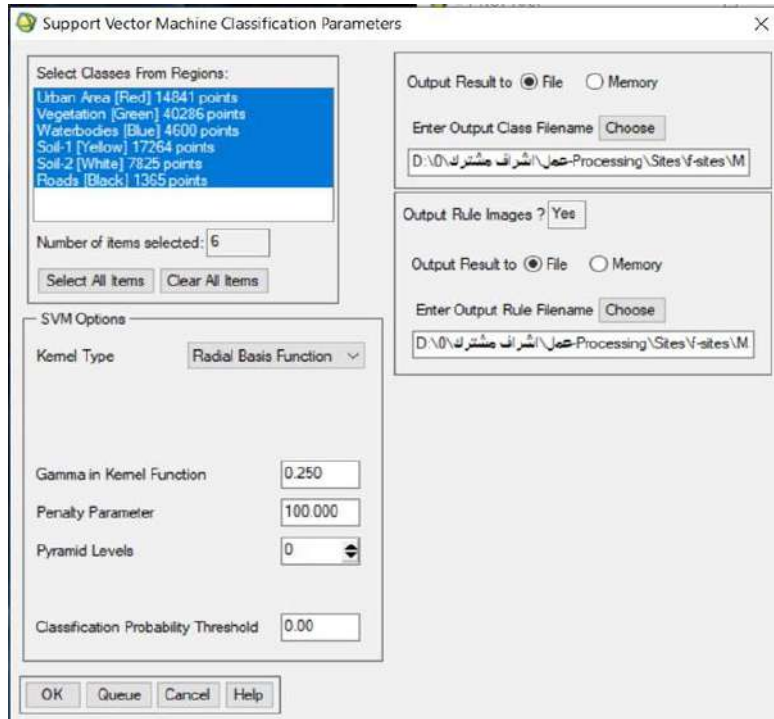
Fig. 12: SVM Parameter for image fusion by (GS).

$$\text{Kappa} = \frac{\sum_{i=1}^{c} n_{ij} - \sum_{i=1}^{c} n_i \ + n + i}{n^2 - \sum_{i=1}^{c} n_j + n + i} \qquad \dots(1)$$

$$\text{OA} = \frac{\sum_{i=1}^{c} n_{ij}}{n} \qquad \dots(2)$$

Table 4: Processing geometric correction for Landsat-8 image.

Fig. 13: LU/LC map classified using SVM classified on fused data by Brovey method.
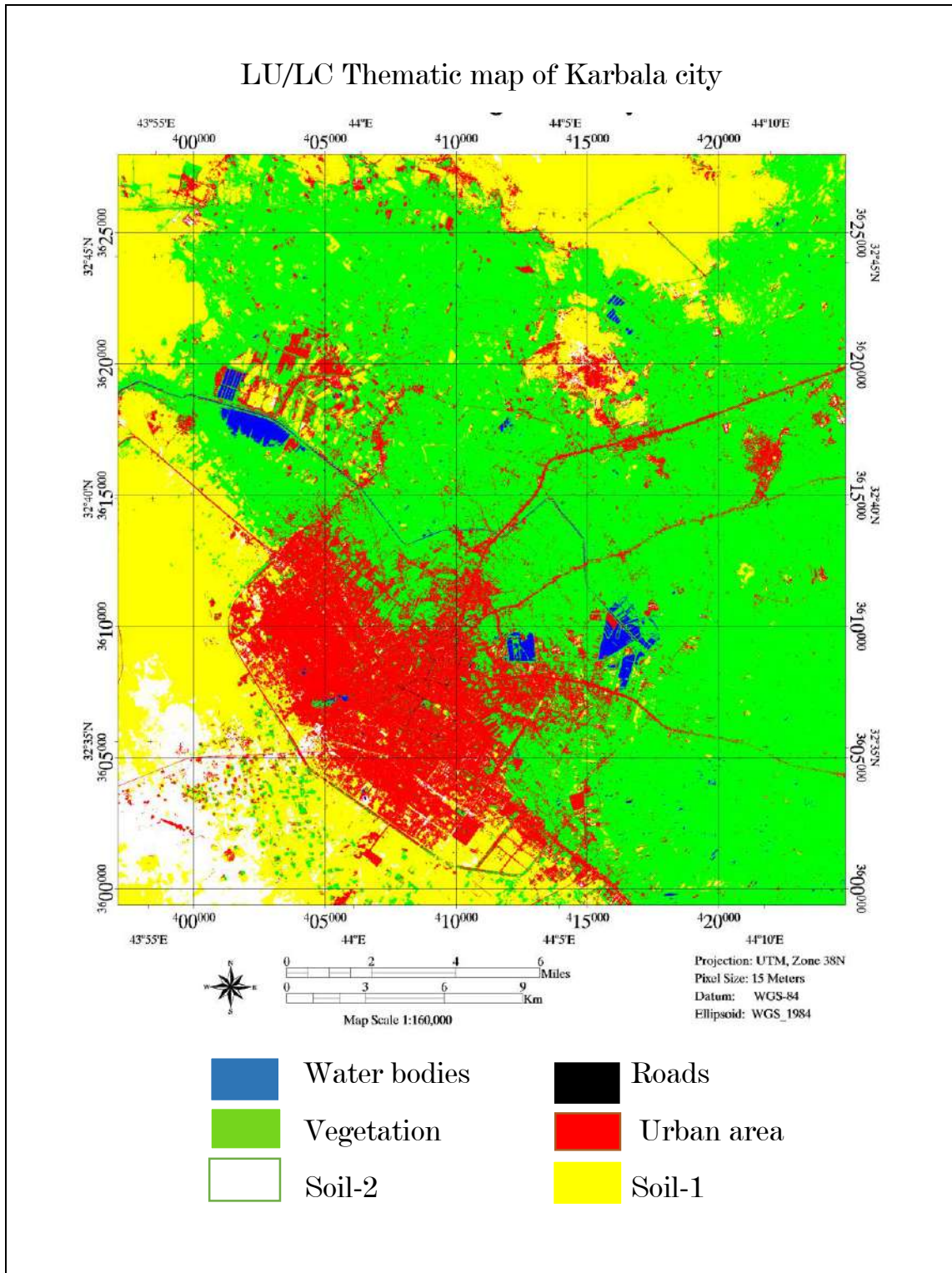
Fig. 14: LU/LC map classified using SVM classifier on fused data by Gram-Schmidt (GS).

Where n is the total number of pixels, n_i represent the number of instances, label (i), that have been classified into the label (j), n_{ij} is a total number of classified pixels. The accuracy of the classification results was evaluated based on the confusion matrix and its coefficients in Tables 6 & 7 which give the classification results fused and classified images by SVM.

Table 6 shows the classification results for the fused image by BT and classifier by the SVM approach, that the Soil-1 classifier got the highest product accuracy of 99.91, and the Soil-2 classifier got the highest accuracy user of 99.96. While the Urban area classifier got the lowest accuracy of product and user 93.64 and 89.32, respectively. As for the rest of the classifiers, they obtained good results, such as the Vegetation classifier, which obtained a product accuracy of 98.39 and user accuracy of 97.87, while the Roads obtained a product accuracy of 96.15 and user accuracy of 95.1, and Waterbodies obtained a product accuracy of 97.99 and user accuracy of 94.14.

Table 7 shows the classification results for the fused image by GS and classifier by the SVM approach, that the Soil-2 classifier got the highest producer accuracy and user accuracy 99.74 and 99.78, respectively. Also, Soil-1 obtained producer and user accuracy of 99.63 and 99.61 respectively, and the Water bodies classifier got the lowest producer accuracy of 86.16. While the Urban area classifier got the lowest user accuracy of 87.37. As for the rest of the classifiers, they obtained good results, such as the Vegetation classifier, which

obtained producer accuracy of 98.93 and user accuracy of 97.14, while the Roads obtained producer accuracy of 98.90 and user accuracy of 98.42.

RESULTS AND DISCUSSION

A Fusion process of (MS & Pan) images was carried out in this study to improve the methods of producing LU/LC maps to reach high accuracy. Using sharpening algorithms for the image fusion tool we used Brovey chromatic transformation algorithm and (GS) spatial optimization algorithm and two fusion images were created, and to classify the two images, we relied on the (SVM) method for mapping LU/LC and to make a comparison between the results to estimate which of the two approaches is more accurate, as shown in Figs.13 & 14. We used the confusion matrix to evaluate the results of the (SVM) classification algorithm. Where the value of the kappa coefficient and the overall Accuracy of the (SVM) for fusion images using (GS) are 95 and 97.81%, respectively, and the kappa coefficient and the overall Accuracy of the (SVM) for fusion images using Brovey are 95.15% and 0.93 respectively. By comparing the results and as shown in Table 8, it was shown that the approach used to obtain more accurate and clear LU/LC maps is employing classification for fused images, which is obtained by fusion Landsat-8 satellite (MS & Pan) images by the (GS) sharpening algorithm. Figs. 15 & 16 show the comparison of classification fused images by (BT & GS) at the level of the overall accuracy and Kappa coefficient.

CONCLUSION

The study analyzed the use of Landsat-8 (MS & Pan) images

Table 5: Collected training sites from the Landsat-8 satellite image.

Class	Color	Pixels	Polygons
Urban area	Red	4.848	16/4.848
Vegetation	Green	23.275	14/23.275
Water bodies	Blue	6.625	6/6.625
Soil -1	Yellow	19.077	10/19.077
Soil -2	White	8.650	9/8.650
Roads	Black	1.571	By points

Table 6: producer and user accuracies of the fused image by (BT) and classifier by SVM.

Class	Pro. Acc. [%]	User. Acc. [%]
Urban area	93.64	89.32
Vegetation	98.39	97.87
Water bodies	97.99	94.14
Soil-1	99.91	97.52
Soil-2	95.23	99.96
Roads	96.15	95.10

Table 7: Producer and user accuracies of the fused image by (GS) and classifier by SVM.

Class	Pro. Acc. [%]	User. Acc. [%]
Urban area	97.68	87.37
Vegetation	98.93	97.14
Water bodies	86.16	98.05
Soil-1	99.63	99.61
Soil-2	99.74	99.78
Roads	98.90	98.42

Table 8: Overall accuracy and kappa coefficient of the fused image by (GS and Brovey) and classified by (SVM) classifier.

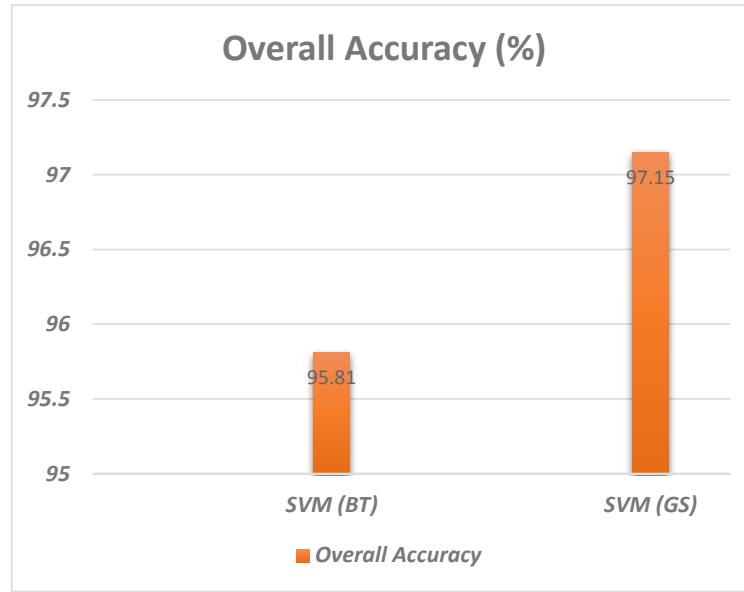| Type of data	Classifier	Overall accuracy	Kappa coefficient
Fusion image by GS	SVM	97.81%	0.95
Fusion image by BT	SVM	95.15%	0.93

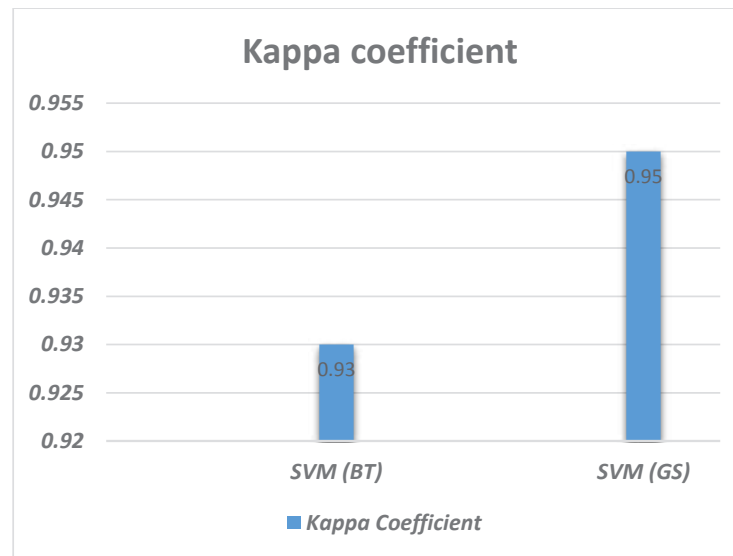Fig. 15: The overall accuracy of the fused image by (Brovey & GS) and classifier by (SVM).

Fig. 16: the Kappa coefficient of the fused image by (Brovey & GS) and classifier by (SVM).

to estimate LU/LC for the city of Karbala, Karbala Governorate, Iraq. This research aims to identify an improved methodology for mapping LU/LC to the city of Karbala by making comparisons between images combined with two methods GS and Brovey classified using SVM. The improved Fused image classifier approach is proposed for LU/LC mapping based on the result by applying a confusion matrix and it shows the full accuracy of the Fused image using spatial optimization algorithm GS and classified by SVM, the highest result with an overall accuracy of 97.81% and kappa coefficient 0.95. Also, results were obtained for the Fused data in the BT method, classified by SVM, overall accuracy of 95.15% and a kappa coefficient of 0.93, Therefore, the image fusion approach using the GS algorithm and classifier by SVM was determined as the best optimized LU/LC mapping technique for this study.

REFERENCES

Abbas, Z. and Jaber, H.S. 2020. Accuracy assessment of supervised classification methods for extraction land use maps using remote sensing and GIS techniques. IOP Conf. Series Mater. Sci. Eng., 16: 54-79

Ali, A.H. and Jaber, H.S. 2020. Monitoring degradation of wetland areas using satellite imagery and geographic information system techniques. Iraq. J. Agric. Sci., 51(5): 1474-1485

Bernstein, L.S., Jin, X., Gregor, B. and Adler-Golden, S.M. 2012. Quick atmospheric correction code: algorithm description and recent upgrades. Optical Eng., 51(11): 111719.

Bouaziz, M., Eisold, S. and Guermazi, E. 2017. Semiautomatic approach for land cover classification: A remote sensing study for the arid climate in southeastern Tunisia. Euro-Mediterr. J. Environ. Integr., 2(1): 1-7.

Cavur, M., Duzgun, H.S., Kemec, S. and Demirkan, D.C. 2019. Land use and land cover classification of Sentinel 2-A: St Petersburg case study. Int. Arch. Photogramm. Remote Sens. Spatial Inform. Sci., 42(1): 16-17

Chasmer, L., Hopkinson, C., Veness, T., Quinton, W. and Baltzer, J. 2014. A decision-tree classification for low-lying complex land cover types within the zone of discontinuous permafrost. Remote Sens. Environ., 143: 73-84. https://doi.org/10.1016/j.rse.2013.12.016.

Dibs, H. 2013. Feature extraction and based pixel classification for estimation of the land cover thematic map using hyperspectral data. Int. J. Eng. Res. Appl., 3(3): 686-693.

Dibs, H. 2018. Comparison of derived Indices and unsupervised classification for AL-Razaza Lake dehydration extent using multi-temporal satellite data and remote sensing analysis. J. Eng. Appl. Sci., 13(24): 1-8.

Dibs, H. and Al-Hedny, S. 2019. Detection of wetland dehydration extent with multi-temporal remotely sensed data using remote sensing analysis and GIS techniques. Int. J. Civil Eng. Technol., 10: 143-154.

Dibs, H., Al-Hedny, S. and Karkoosh, H.A. 2018. Extracting detailed buildings 3D model using high-resolution satellite imagery by remote sensing and gis analysis: Al-Qasim Green University a case study. Int. J. Civil Eng. Technol., 9(7): 1097-1108.

Dibs, H., Hasab, H.A., Al-Rifaie, J.K. and Al-Ansari, N. 2020. An optimal approach for land-use/land-cover mapping by integration and fusion of multispectral Landsat OLI images: A case study in Baghdad, Iraq. Water Air Soil Pollut., 231(9): 1-15.

Dibs, H., Hasab, H.A., Jaber, H.S. and Al-Ansari, N. 2022. Automatic feature extraction and matching modelling for highly noise near-equatorial satellite images. Innovative Infrastructure Solutions, 7(1), pp.1-14.

Dibs, H., Hasab, H.A., Mahmoud, A.S. and Al-Ansari, N. 2021. Fusion methods and multi-classifiers for improving land cover estimation by remote sensing analysis. Geotech. Geolog. Eng., 39: 5825-5842.

Dibs, H., Hasab, H.A., Mahmoud, A.S. and Al-Ansari, N. 2021. Fusion Methods and Multi-classifiers to Improve Land Cover Estimation Using Remote Sensing Analysis. Geotechnical and Geological Engineering, 39(8), pp.5825-5842.

Erener, A., 2013. Classification method, spectral diversity, band combination and accuracy assessment evaluation for urban feature detection. International Journal of Applied Earth Observation and Geoinformation, 21, pp.397-408.

Gevana, D., Camacho, L., Carandang, A., Camacho, S. and Im, S. 2015. Land use characterization and change detection of a small mangrove area in Banacon Island, Bohol, the Philippines using a maximum likelihood classification method. Forest Sci. Technol., 11(4): 97-205.

Hasab, H.A., Dibs, H., Dawood, A.S., Hadi, W.H., Hussain, H.M. and Al-Ansari, N. 2020a. Monitoring and assessment of salinity and chemicals in agricultural lands by a remote sensing technique and soil moisture with chemical index models. Geosci., 10(6): 207.

Hasab, H.A., Jawad, H.A., Dibs, H., Hussain, H.M. and Al-Ansari, N. 2020b. Evaluation of water quality parameters in marshes zone southern of Iraq based on remote sensing and GIS techniques. Water Air Soil Pollut., 231(4): 1-11.

Idi, B.Y. and Nejad, P.G. 2013. Fusion of RADARSAT-2 and IKONOS images for land cover mapping: Performance analysis. Appl. Remote Sens. J. 3(1): 18.

Iounousse, J., Er-Raki, S., El Motassadeq, A. and Chehouani, H. 2015. Using an unsupervised approach of probabilistic neural network (PNN) for land use classification from multitemporal satellite images. Appl. Soft Comput., 30: 1-13. https://doi.org/10.1016/j.asoc.2015.01.037.

Jasem, I.T. and AL-Mayali, S.F. 2020. The geographical potential of agricultural tourism in Karbala governorate. J. Univ. Babylon Human., 28(11): 189-209.

Jawak, S.D. and Luis, A.J. 2013. A comprehensive evaluation of PAN-sharpening algorithms coupled with resampling methods for image synthesis of very high resolution remotely sensed satellite data. Adv. Remote Sens., 61: 2013.

Jia, M., Wang, Z., Li, L., Song, K., Ren, C., Liu, B. and Mao, D. 2014. Mapping China's mangroves based on an object-oriented classification of Landsat imagery. Wetlands, 34(2): 277-283. https://doi.org/10.1007/s13157-013-0449-2.

Kumar, L., Sinha, P. and Taylor, S. 2014. Improving image classification in a complex wetland ecosystem through image fusion techniques. J. Appl. Remote Sens., 8(1): 083616.

Li, G., Lu, D., Moran, E., Dutra, L. and Batistella, M. 2012. A comparative analysis of ALOS PALSAR L-Band and RADARSAT-2 C-band data for land-cover classification in a tropical moist region. J. Photogramm. Remote Sens., 70: 26-38. https://doi.org/10.1016/j.isprsjprs.2012.03.010.

Löw, F., Conrad, C. and Michel, U. 2015. Decision fusion and non-parametric classifiers for land use mapping using multitemporal Rapideye data. J. Photogramm. Remote Sens., 108: 191-204. https://doi.org/10.1016/j.is

Mandhare, R.A., Upadhyay, P. and Gupta, S. 2013. Pixel-level image fusion using brovey transform and wavelet transform. Int. J. Adv. Res. Electr. Instrument. Eng., 2(6): 2690-2695.

Otukei, J.R., Blaschke, T. and Collins, M. 2015. Fusion of Terrasar-X and Landsat ETM+ data for protected area mapping in Uganda. Int. J. Appl. Earth Observ. Geoinform., 38: 99-104. https://doi.org/10.1016/j.jag.2014.12.01

Sameen, M.I., Nahhas, F.H., Buraihi, F.H., Pradhan, B. and Shariff, A.R.B.M. 2016. A refined classification approach by integrating Landsat Operational Land Imager (OLI) and RADARSAT-2 imagery for land-use and land-cover mapping in a tropical area. Int. J. Remote Sens., 37(10): 235

Sang, H., Zhang, J., Zhai, L., Qiu, C. and Sun, X. 2014. Analysis of rapid eye imagery for agricultural land cover and land use mapping. In: 2014 3rd International Workshop on Earth Observation and Remote Sensing Applications (EORSA), IEEE, Changsha, pp.366-369.

Sarp, G. 2014. Spectral and spatial quality analysis of pan-sharpening algorithms: A case study in Istanbul. Europ. J. Remote Sens., 47(1): 19-28.

Tabib Mahmoudi, F. and Karami, A. 2020. Quantitative assessment of transformation-based satellite image pan-sharpening algorithms. J. Electr. Comput. Eng. Innov., 8(2): 161-168.

Zhang, N., Zhao, J. and Zhang, L. 2016. Comparison and evaluation of image fusion methods for GaoFen-1 imagery. Infrared Technol. Appl. Robot Sens. Adv. Contr., 101: 101571.

Original Research Paper   https://doi.org/10.46488/NEPT.2022.v21i02.051   **Open Access Journal**

Predicting the Thermal Regime of the Sebou River Estuary (Morocco) Using a One-Dimensional Model (HEC-RAS 5.0)

Y. Nizar †*, A. Touazit* and M. Igouzal*

*Laboratory of Electronic Systems, Information Processing, Mechanics and Energy, Department of Physics, Faculty of Science, Ibn Tofail University, BP1246 Kenitra, Morocco

†Corresponding author: Y. Nizar; youness.nizar@uit.ac.ma

ABSTRACT

Temperature is regarded as one of the most important variables for aquatic life, as well as a key physical criterion of water quality, due to its role in a variety of chemical, physical, and biological processes. We chose the HEC-RAS tool to model the thermal regime of the Sebou-Kenitra river estuary because it is impossible to determine the spatiotemporal evolution of temperature in watercourses using traditional methods such as single measurements or interpolation due to the influence of several factors, including hydraulic, tidal rhythm, upstream contributions, and intrusion. The main goal of this research is to develop and test the "HEC-RAS" model with the aim of better understanding thermal dynamics and predicting the spatiotemporal variation of the Sebou river estuary temperature, using the energy transport equation and a variety of input data such as initial temperature, air temperature, wind speed, and dispersion coefficient. The HEC-RAS model, which takes into account many meteorological and geophysical elements and provides an overview of the thermal situation at our study site "the Sebou river estuary," has also been acknowledged for its deterministic role. We illustrated the impact of meteorological and tidal data on spatiotemporal temperature change at numerous places in the Sebou river estuary by using this model.

INTRODUCTION

The diverse estuarine environment contributes significantly to the life cycle of many species, not only that, but it also serves as a site for human activities (Igouzal et al. 2005). Simply put, estuaries are valuable water bodies where numerous dynamic factors take place and interact (Xu et al. 2015).

Estuaries assemble and gather essential substances of the human-earth system (Savenije 2015), and given that they form part of the relationship between seawater and river, the aforementioned have the properties of both: they simultaneously contain fresh and saltwater and are subjected not only to the tides but also to the floods of the rivers; in addition to naturally support saline and fresh ecosystems (Savenije 2015).

Amongst the most notable advantages to the prediction of water temperature in rivers is; first and foremost dealing with certain environmental problems in addition to carrying out competent management and use of water and aquatic resources (Ouhamdouch et al. 2018, Tavares et al. 2020, Graf et al. 2019).

Accordingly, to visualize the effect of thermal pollution, impact studies are often required to protect the (ichthyoids) fish habitat. Although, before we arrive at the stage of predicting the changes resulting from human activities, it is crucial to first know and be able to envisage the temperature of the water in its natural state according to climatic and hydraulic variations which was the subject of some very fascinating and striking researches conducted by (Haddout et al. 2016, Igouzal & Maslouhi 2010).

Furthermore, knowing the temperature of the watercourses makes it possible to distinguish climate tendencies in the long run. Nevertheless, there is little information on its spatiotemporal variation, due to an obvious lack of habitual and incessant monitoring (Lund et al. 2002, Tao et al.2021).

Our case study is exceptionally innovative on account of being the first one to be carried out to focus solely on examining the temperature of the Sebou Estuary, which is deemed to be the leading watershed in Morocco in terms of water inflows estimated at a whopping 6.6 billion m^3 per year. What's more, this hydrographic basin is ranked second in the surface area: 40,000 km^2 (after the Moulouya basin) and it covers 191,000 ha of agricultural land (Hayzoun et al. 2015). The choice of making this basin the focal point of our study comes from the need to implement for the first time temperature modeling by the HEC-RAS method.

To represent and simulate the thermal regime of the estuary, two types of models are used in general: the first being; the numerical model and the second, it's the analytical model. Presently, digital models are more popular, especially 2D and 3D models (Kärnä et al. 2015; Elias et al. 2012; Zhao et al.2012), due to their ability to provide more spatial and temporal details (Igouzal et al. 2005).

The primary objective of our research is, on one hand, to compose an observation network capable of characterizing the specificity of the study area (Sebou River Estuary) and on the other hand, to design the necessary field campaigns with regard to the hydrological conditions to properly portray the temporal variations of the studied water at distinctive points of our worksite, taking into account that this parameter is of major significance for aquatic life (Morid et al.2020, Qiu et al.2020). The obtained measurements will ergo be used in a temperature model on HEC-RAS and this thermal model will in turn be used to serve as input data for modeling the water quality of the Sebou river estuary on top of assessing the evolution pollution.

The calibration of the thermal model was based on field data collected from six different sampling sites over a time period extending from June 2019 to September of the same year.

In the interest of accomplishing our goal, prior modeling of the hydraulic regime using HEC-RAS was requisite. This hydraulic module calculates the evolution of speed and depth which serve as input parameters to the temperature model.

MATERIALS AND METHODS

The selected methodology for our paper includes:

- Presentation of the study site,
- Timely and punctual measurements over a course of period expanding from the beginning of June to the 1st of September 2019 of different sampling points (six sites to be exact) across the entire basin,
- Modeling by the HEC-RAS 5.0 model, while using outputs (series of calculated temperatures),
- Processing techniques for the collected data (comparison of the average values) obtained for each sample and the variability for each site.

Study Site: The Sebou Estuary

The flow regime in the Sebou estuary is ascertained by notable seasonal and inter-annual changes. Considering the reality that it is contingent on the tidal regime as well as being under the control of several barrages (Igouzal & Maslouhi 2010, Igouzal et al. 2005)

During the "low-flow" period, the hydraulic regime is controlled by the Lalla Aicha barrage which is located 62 km upstream from the river's mouth. This particular barrage was built to contain water from agricultural pumping stations and prevent saltwater from rising to these stations. A volume of 200 Mm^{3}of water is mobilized annually, taking into consideration that before the construction of this reservoir, excessive salinity could extend over an area of 85 km (Combe et al, 1969)

The Sebou estuary is enclosed by the Atlantic Ocean and the Lalla Aicha guard barrage, extending around 69 km long, what's more, it is the only Moroccan estuary equipped with a river port.

Sampling

The 1st step in our action plan tackled the task of collecting daily field data betwixt June and September of the year 2019 in a sampling network of six sites (Fig. 1, Table 1), in fact, temperature values were registered every 15 minutes, culminating thus to recording approximately 96 daily.

Sample Collection

To attain the needed water samples, a 10-meter rope was tied around a water container; the latter was then thrown into the river collecting thus the samples. The water samples were placed later in clean plastic bottles of 1.5 liters each to directly measure the temperature.

Modeling Via the HEC-RAS software

HEC-RAS is an extensively used software application that carries out one-dimensional and two-dimensional hydraulic calculations for a complete nexus of natural and constructed channels, overflow/floodplain areas, protected areas; etc.

Table 1: The six sampling points.

| Sampling points	GPS	Location
Point 1	Latitude : 34,272288, Longitude : -6,645024	Located 3.6 km from the mouth of the Sebou.
Point 2	Latitude : 34,269596, Longitude : -6,591051	Located 9.3 km from the mouth of the Sebou.
Point 3	Latitude : 34,275671, Longitude : -6,568179	Located 13 km from the mouth of the Sebou.
Point 4	Latitude : 34,292163, Longitude : -6,567193	Located 15 km from the mouth of the Sebou.
Point 5	Latitude : 34,292163, Longitude : -6,567193	Located 17 km from the mouth of the Sebou.
Point 6	Latitude : 34,338430, Longitude : -6,488273	Located 24 km from the mouth of the Sebou.
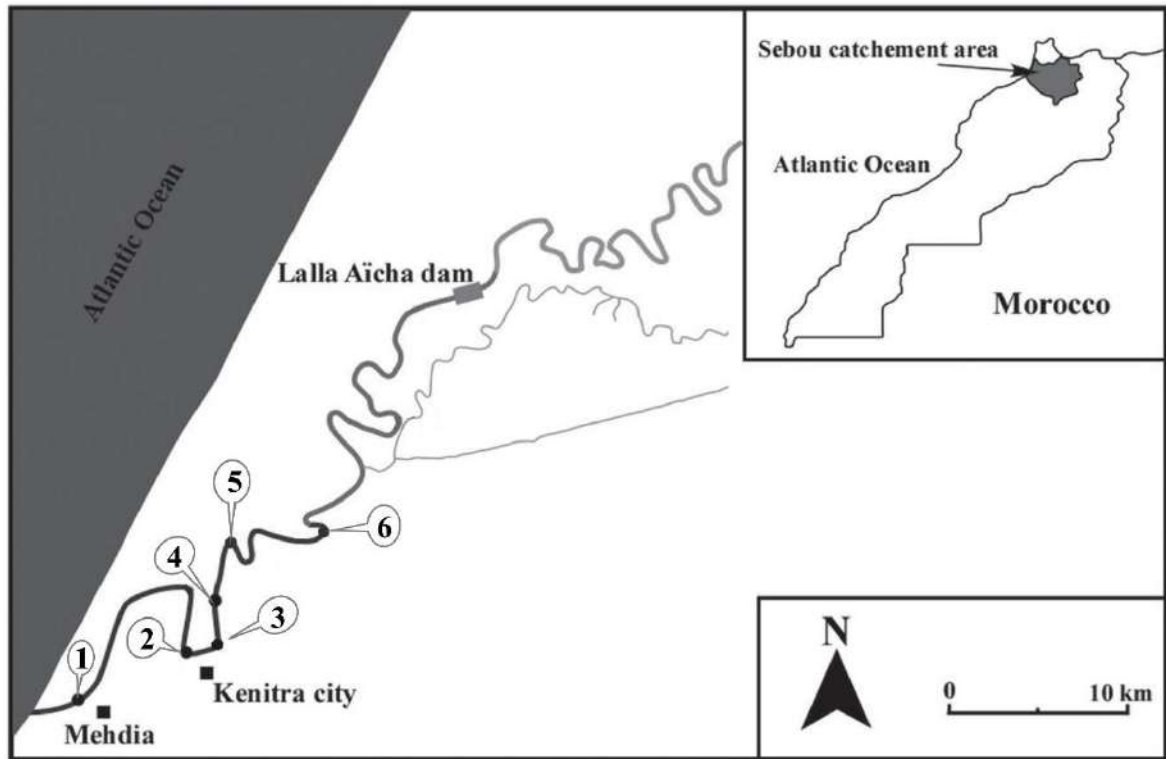
Fig.1: Map of the geological surface of the Sebou Estuary and the distribution of the sampling points.

The second step of our work involved the modeling of the hydraulic regime using HEC-RAS which is based on the energy transport equation.

To reach the objective of modeling by HEC-RAS, several data are demanded, in particular: the initial temperature state, the dispersion coefficient, the flow speed, the atmospheric pressure, the air temperature, the relative humidity, the cloudiness, the speed of the wind and solar radiation. The result of the transport module is the spatio-temporal evolution of the temperature in the river.

Hydraulic Modeling of the Sebou Estuary

This regime has been gauged and corroborated by employing a large hydraulic and morphological database. To initiate the process, entering several data is vital, principally: initial temperature condition, dispersion coefficient, flow velocity, atmospheric pressure, air temperature, relative humidity, cloudiness, wind speed, and solar radiation (Fig. 2).

Hence, to be capable of modeling the Sebou Estuary temperature on HEC-RAS 5.0, it is necessary to establish the hydraulic model of the said estuary.

HEC-RAS is based on the Saint-coming equations (Brunner 2016, Haddout et al. 2015, 2016, Igouzal & Maslouhi,

2005) which are written as follows:

$$\frac{\partial Q}{\partial x} + B\frac{\partial Y}{\partial t} = q$$

$$\frac{\partial Q}{\partial t} + \frac{\partial}{\partial x}\left(\frac{Q^2}{A}\right) = gA\left(\frac{\partial Y}{\partial x} - S_f\right) \qquad \text{…(1)}$$

Where Y = the depth of water; Q = the flow; x = the distance along the river; t = the time; B = the river with; q = lateral influx; A = the cross section; g = the acceleration due to gravity; Sf = the friction slope.

The friction slope is expressed as:

$$S_f = \frac{n^2}{R^{4/3}} U^2 \qquad \text{…(2)}$$

Where n is the Manning coefficient of friction.

Thermal Modeling of the Sebou Estuary

The studied T parameter of the estuary water is calculated from the thermal energy transport equation.

When T is applied to an open channel with a constant cross-section, we find the following equation:

$$\frac{\partial T}{\partial t} = -U\frac{\partial T}{\partial x} + D_L\frac{\partial^2 T}{\partial x^2} + \frac{S}{\rho c_\rho} \qquad \ldots(3)$$

Where T = water temperature; x = distance downstream; t = time; DL = a longitudinal dispersion coefficient in the direction of flow (x direction); S = a source or sink term that includes heat transfer with the environment; U = average speed of the channel; h = average depth of the channel; P = density of water; and Cp = calorific capacity of water.

A more general form of the equation is:

$$A\frac{\partial T}{\partial t} + \frac{\partial(QT)}{\partial x} = \frac{\partial}{\partial x}\left(AD_L\frac{\partial T}{\partial x}\right) + \frac{BS}{\rho c_\rho} \qquad \ldots(4)$$

RESULTS AND DISCUSSION

Once the model was provided with the meteorological data and boundary conditions (Drake et al.2010), the HEC-RAS water temperature model was then launched and operated using a one-hour time step, from the 1st of June to the 1st of September 2019 depending assuredly on available data.

The water temperature model for the Sebou river estuary was calibrated with the available observed data that was previously mentioned in the material and methods section.

The chronological series of the water temperatures predicted and observed by HEC-RAS in the six sampling points along the Sebou estuary from the Lalla Aicha barrage to the outlet in Mehdia before (A) and after (B) adjusting are illustrated in Figs. 3 to 8:

Based on the results observed in the figures, it is abundantly clear that there is a significant difference between the two graphs, before (A) and after (B) calibration. The figures display a scatter plot of instantaneous temperature predictions versus temperature observations presented in a discontinued line. Upon inspecting the figures we can distinguish that by comparing the model predictions and the observed data, the two seem to be very close, especially when moving away from upstream to downstream, where the impact of boundary conditions is reduced, moreover, the same can be said for the time factor.
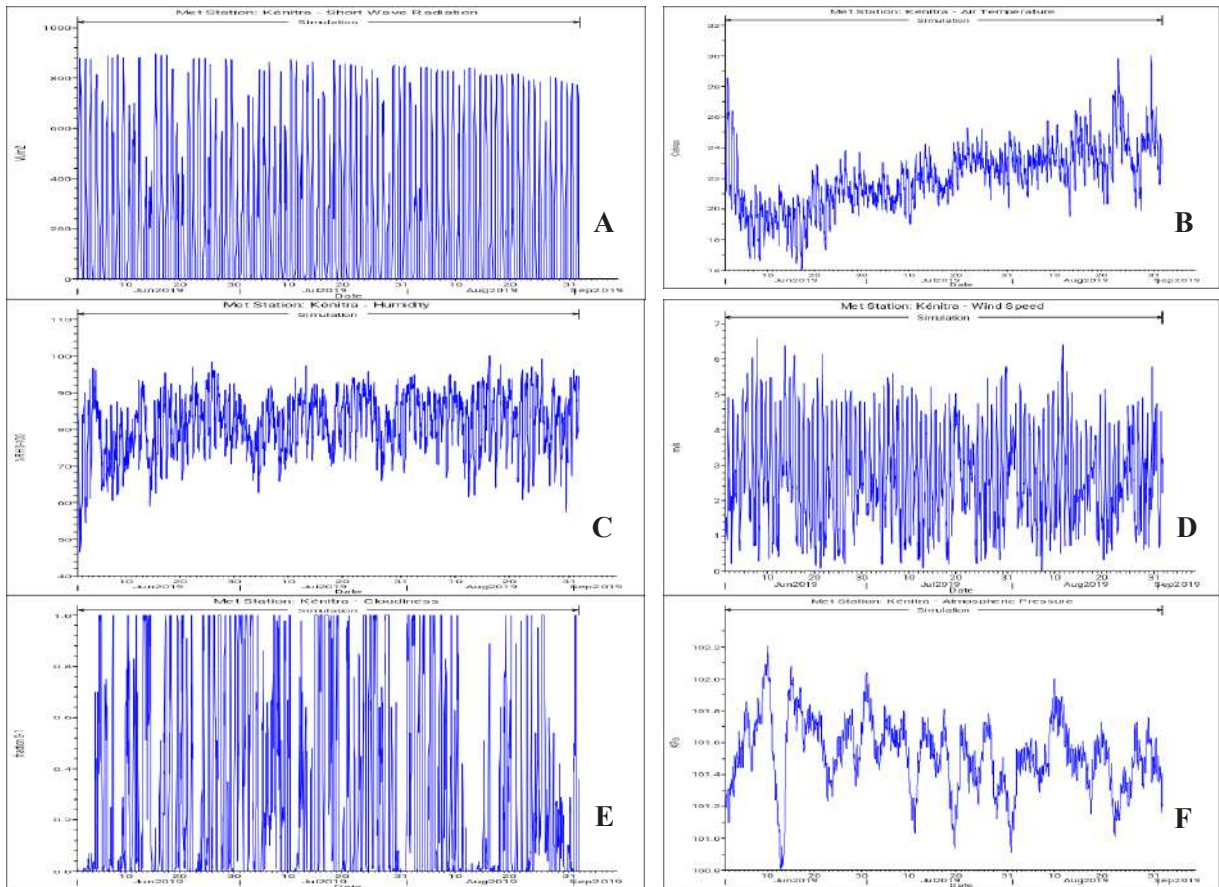
Fig.2: Input data timetable for (A) solar radiation, (B) air temperature, (C) humidity, (D) wind speed, (E) cloudiness and (F) atmospheric pressure.
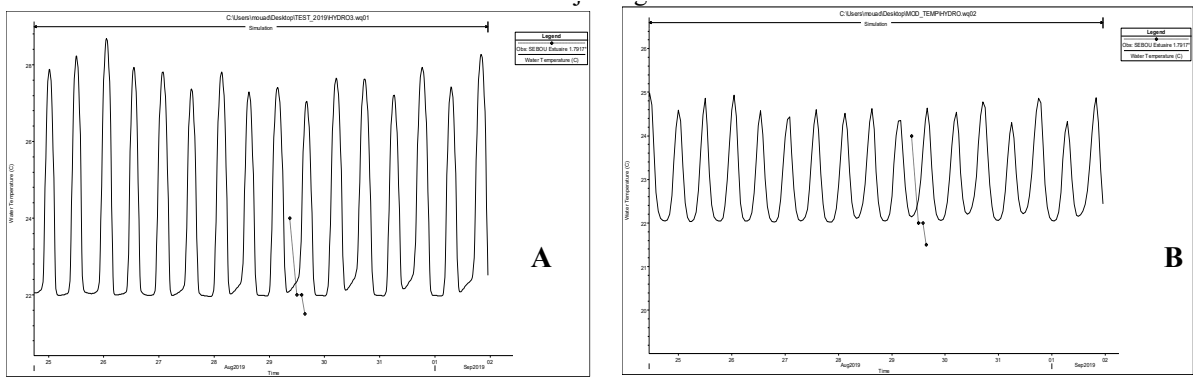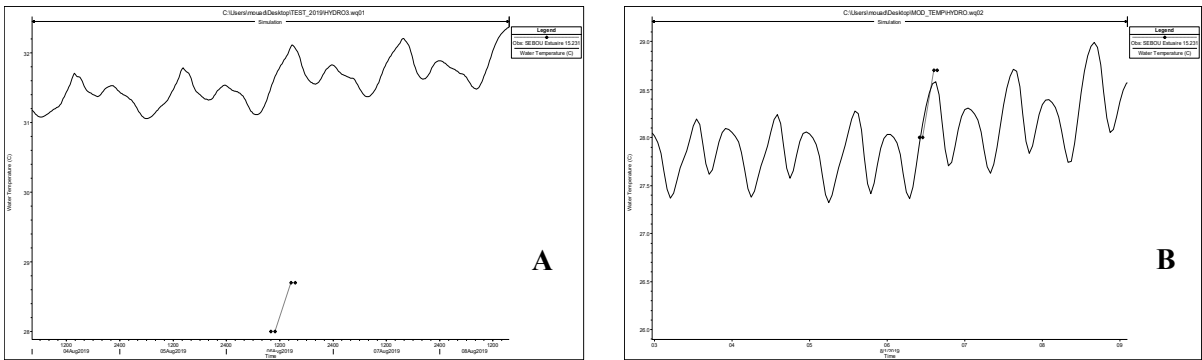
Fig.3: HEC-RAS results vs observed temperature from point 1 at the Sebou Estuary before (A) and after (B) adjusting.
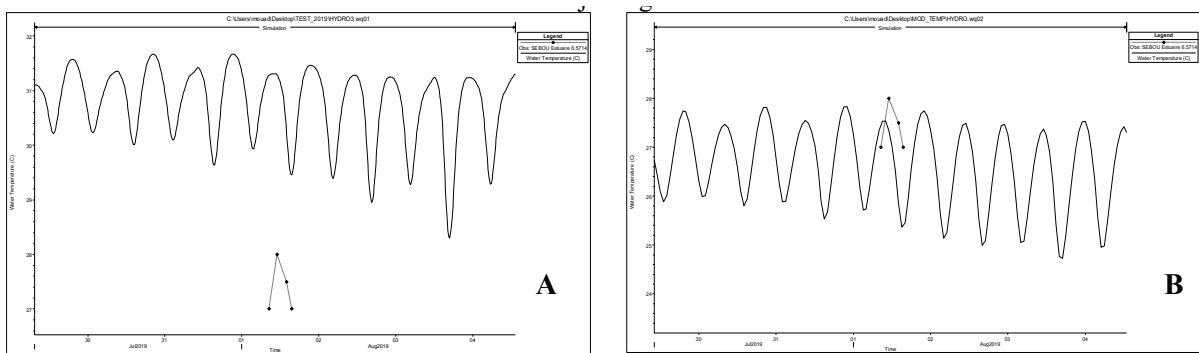
Fig.4: HEC-RAS results vs observed temperature from point 2 at the Sebou Estuary before (A) and after (B) adjusting.
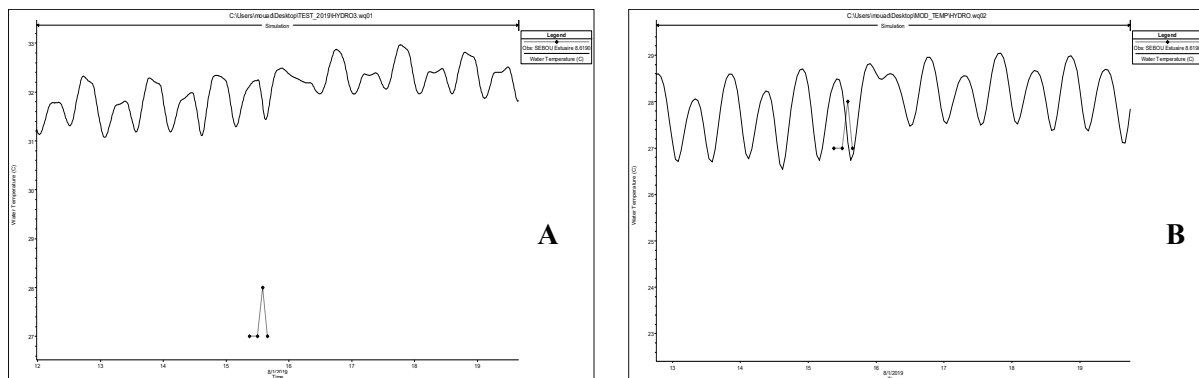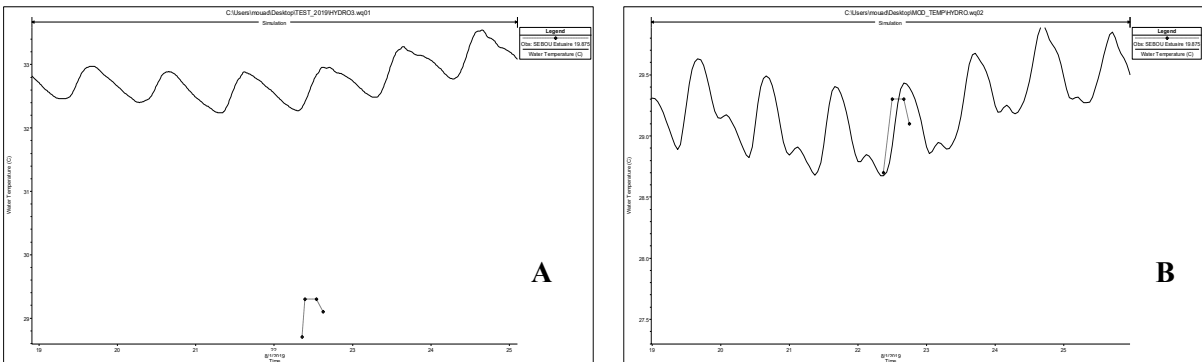

Fig.5: HEC-RAS results vs observed temperature from point 3 at the Sebou Estuary before (A) and after (B) adjusting.

The chronological series' graphs indicate a good concurrence between the HEC-RAS prognostication and the observations for the six calibration locations along the Sebou River estuary, which complies with the analogous results found in other studies (Drake et al.2010; Abdi et al.2020, Ren et al.2020; Qiu et al.2020), excluding the sixth point, which perhaps may be attributed to the fact that the measurements were executed at the start of the simulation.

Appertaining to the Figs. 9 and 10, it is easily visible that the water temperature is incessantly increasing upstream from the mouth of the river in the Sebou estuary. Indeed, during high tide, the temperature rise seems to take place after 5 km from the mouth of the river, nevertheless, the temperature rise occurs quite instantaneously during low tide.

As far as we know, the uncertainty of the water temperature model also emanates from the shortage of monitoring
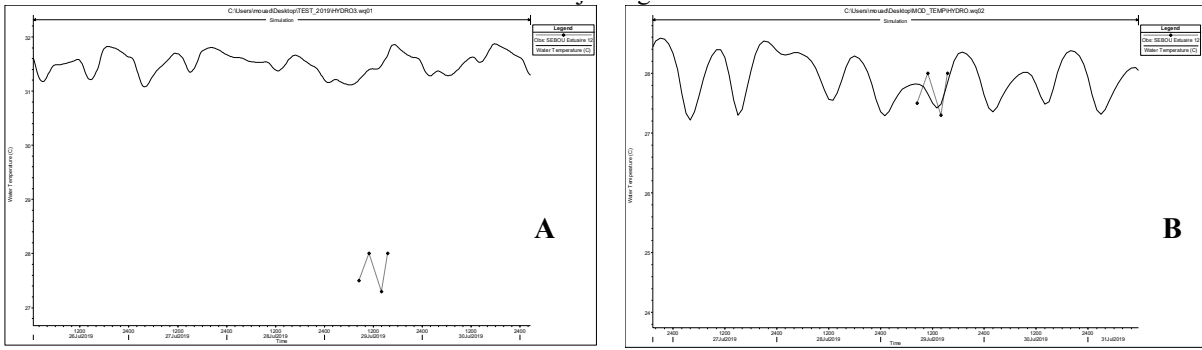
Fig.6: HEC-RAS results vs observed temperature from point 4 at the Sebou Estuary before (A) and after (B) adjusting.

Fig.7: HEC-RAS results vs observed temperature from point 5 at the Sebou Estuary before (A) and after (B) adjusting.

Fig.8: HEC-RAS results vs observed temperature from point 6 at the Sebou Estuary before (A) and after (B) adjusting.

gauges for the water quality of rivers in the basin and the restricted amount of data available at these gauges. All water quality sample readings for this study were obtained during the summer. Additional observed water temperature data is needed to improve and refine the HEC-RAS water temperature model of the Sebou River Estuary.

It's interesting to point out that the calibration could be improved if the measurements were available over a longer period spanning several tidal cycles.

CONCLUSION

Owing to the fact that the rivers' water temperatures are highly affected by countless factors, the prime objective of this study was to model the water temperature of the estuary of the Sebou river using the hydraulic model in conjunction with the meteorological data and boundary conditions.
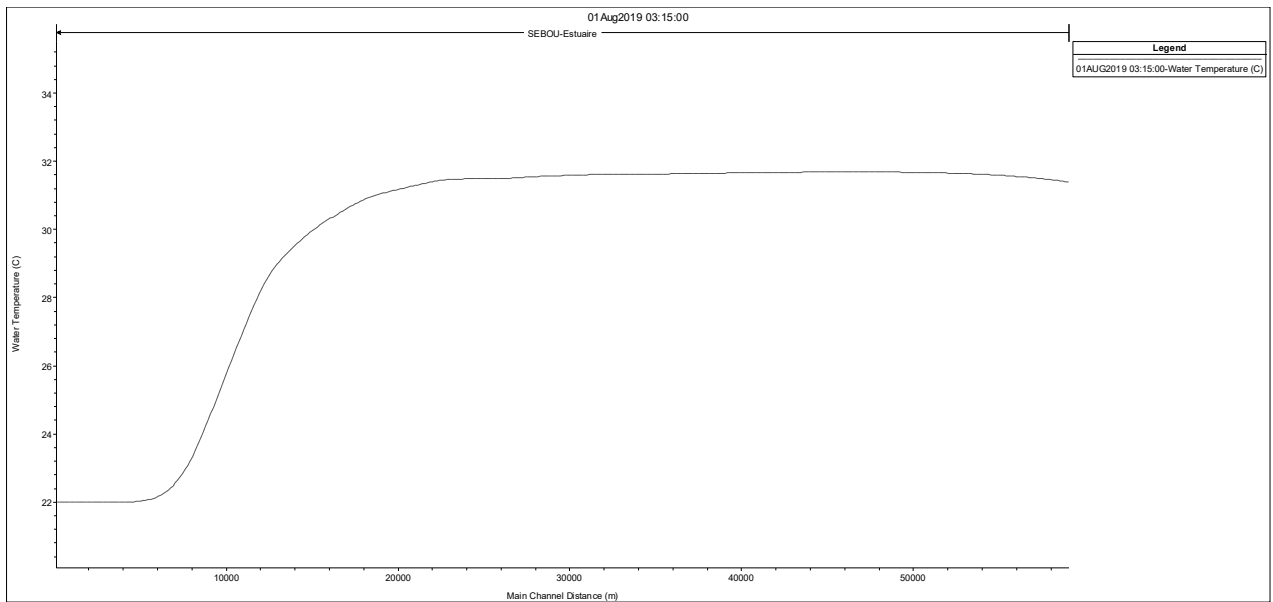
Fig.9: Longitudinal profile of the High tide temperature.
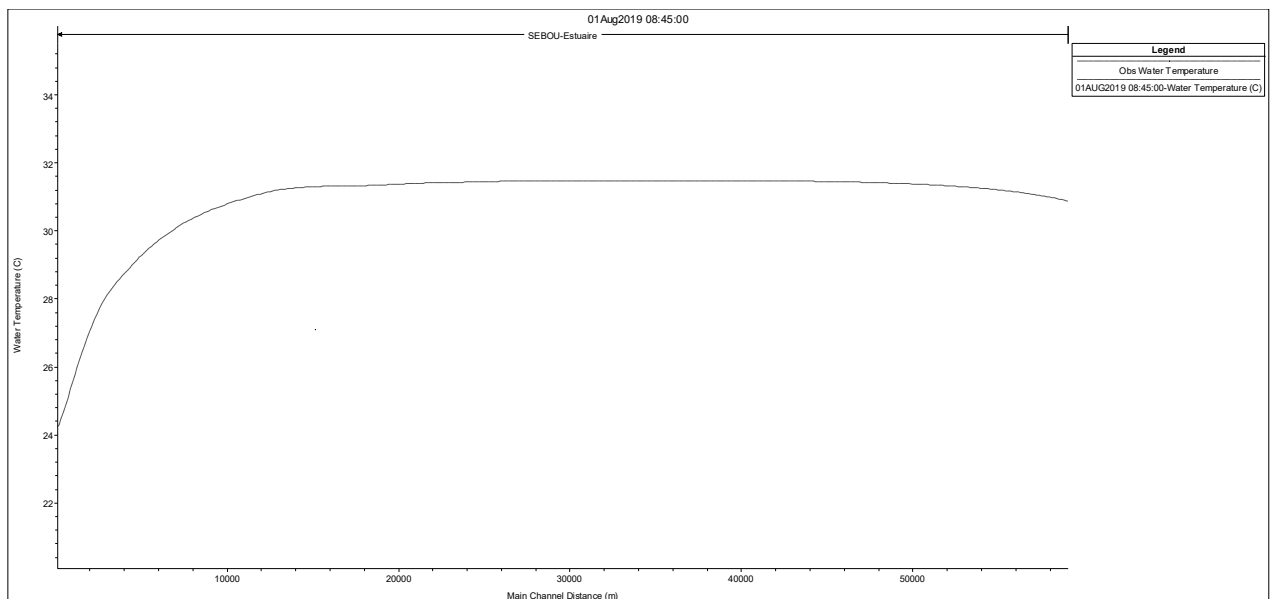
Fig.10: Longitudinal profile of the Low tide temperature.

Subsequently, the HEC-RAS model allotted us to reach the temperature according to the spatio-temporal variation within the estuary. The said model is an initial endeavor at attaining a one-dimensional representation before we can move forward into performing thermal modeling using 2D and 3D models.

Following the calibration of the model by tangible measurements at six different sampling points of the Sebou River, we acquired an assortment of results which in turn will be extracted in the form of a database. The latter will be considered as a representation of the advantages of the HEC-RAS model in terms of modeling the water temperature of rivers; nonetheless, the calibration could be redrafted if the measurements were spread over a longer period of time with various tidal cycles.

The formulated model mandated a colossal amount of input data, namely: solar radiation, air temperature, humidity,

wind speed, cloudiness, atmospheric pressure, and water temperature of sea. The procured results constituted a large database and were classified as measurements with a primary aim of developing other models of temperature prediction of the estuary of the Sebou River for future work, bearing in mind that they are going to be coupled with artificial intelligence models such as neural network models and linear regression models to achieve efficient prediction of water temperature with minimal input data, area temperature as an example. The hydraulic model of the Sebou river estuary, as well as the thermal model object of this work, will be practical for modeling pollution at the same site.

REFERENCES

Abdi, R., Endreny, T. and Nowak, D. 2020. i-Tree cool river: An open-source, freeware tool to simulate river water temperature coupled with HEC-RAS. MethodsX, 7: 100808

Brunner, G.W. 2016. HEC-RAS River Analysis System, User's Manual (version 5.0). US Army Corp of Engineers, Hydrologie Engineering Center (HEC), Davis California, USA.

Combe "Hydrogeological maps of the Plain Gharb 1/100 000". Notes and Memoirs of the Geological Service of Morocco, 221 bis, Rabat, Morocco 1969.

Drake, J., Bradford, A. and Joy, D. 2010. Application of HEC-RAS 4.0 temperature model to estimate groundwater contributions to Swan Creek, Ontario, Canada. J. Hydrol., 389: 390-398

Elias, E.P., Gelfenbaum, G. and Van der Westhuysen, A.J. 2012. Validation of a coupled wave flow model in a high energy setting: The mouth of the Columbia River. J. Geophys. Res: Oceans, 117(C9): 1978.

Graf, R., Senlin, Z. and Bellie, S. 2019. Forecasting river water temperature time series using a wavelet–neural network hybrid modeling approach. J. Hydrol., 578: 124115.

Haddout, S., Igouzal, M. and Maslouhi, A. 2016a. Analytical and numerical study of the salinity intrusion in the Sebou river estuary (Morocco)-effect of the "Super Blood Moon" (total lunar eclipse) of 2015. Hydrol. Earth Syst. Sci., 20: 3923-3945. doi:10.5194/hess-20-3923-2016.

Haddout, S., Maslouhi, A. and Igouzal, M. 2015. Predicting of saltwater intrusion in the Sebou river estuary (Morocco). J. Appl. Water Eng. Res., 5: 40-50.

Haddout, S., Maslouhi, A., Magrane, B. and Igouzal, M. 2016. Study of salinity variation in the Sebou River Estuary (Morocco). Desal. Water Treat., 57: 17075-17086.

Igouzal, M. and Maslouhi, A. 2005. Elaboration of management tool of a reservoir dam on the Sebou river (Morocco) using an implicit hydraulic model. J. Hydraul. Res. 43, 125-130.

Igouzal, M., Mouchel, J.M., Tamoh, K. and Maslouhi, A. 2005 Modelling the hydraulic regime and the water quality of Sebou River (Morocco). IAHS Publ., 299: 75.

Igouzal, M. and Maslouhi, A. 2010. Water modeling of the river Sebou toward transdisciplinary management. IAHS Publ., 111: 338.

Kärnä, T., Baptista, A.M., Lopez, J.E., Turner, P.J., McNeil, C. and Sanford, T.B. 2015. Numerical modeling of circulation in high energy estuaries: A Columbia River estuary benchmark. Ocean Model., 88: 54-71.

Lund, S.G., Caissie, D., Cunjak, R.A., Vijayan, M.M. and Tufts, B.L. 2002 The effects of environmental heat stress on heat shock mRNA and protein expression in Miramichi Atlantic Salmon (Salmo salar) parr. Canad. J. Fish. Aqua. Sci., 59: 1553-1562.

Morid, R., Yukihiro, S. and Tatsuro, S. 2020. An integrated framework for prediction of climate change impact on habitat suitability of a river in terms of water temperature, hydrological and hydraulic parameters. J. Hyrdol., 587: 124936.

Ouhamdouch, S., Bahir, M. and Carreira, P.M. 2018. Impact of climate change on water resources in a semi-arid environment: example of the Essaouira basin (Morocco). J. Water Sci., 31(1): 13-27.

Qiu, R., Yuankun, W., Dong, W., Wenjie, Q., Jichun, W. and Yuwei, T. 2020. Water temperature forecasting based on modified artificial neural network methods: Two cases of the Yangtze River. Sci. Tot. Environ., 737: 139729

Ren, L., Song, C., Wu, W., Guo, M. and Zhou, X. 2020. Reservoir effects on the variations of the water temperature in the upper Yellow River, China, using principal component analysis. J. Environ. Manag., 262: 110339.

Savenije, H.H.G. 2015. Prediction in ungauged estuaries: An integrated theory. Water Resour. Res., 51(4): 2464-2476.

Tao, Y., Yuankun, W., Dong, W., Lingling, N. and Jichun, W. 2021. A C-vine copula framework to predict daily water temperature in the Yangtze River. J. Hydrol., 598: 126430

Tavares, M., Augusto, H.F.C., David, M.M., Anderson, L.R., Carlos, R.F., Andrés, M.M. and Marie-Paule, B. 2020. Derivation of consistent, continuous daily river temperature data series by combining remote sensing and water temperature models. Remote Sens. Environ., 241: 111721

Xu, Y., Zhang, W., Chen, X., Zheng, J., Chen, X. and Wu, H., 2015. comparison of analytical solutions for salt intrusion applied to the Modaomen estuary. J. Coast. Res., 31(3): 735-741.

Zhao, L., Zhang, X., Liu, Y., He, B., Zhu, X., Zou, R. and Zhu, Y. 2012. Three-dimensional hydrodynamic and water quality model for TMDL development of Lake Fuxian, China. J. Environ. Sci., 24(8): 1355-1363.

Optimization of Fenton Oxidation Process for Degradation of 1-Butyl-3 Methyl Imidazolium Chloride (BMIMCL) Using Response Surface Methodology

S. R. Nadaf† and P. B. Kalburgi

Department of Civil Engineering, Basaveshwar Engineering College, Bagalkot, Karnataka, India

Corresponding author: S. R. Nadaf; nsharifa.nadaf@gmail.com

ABSTRACT

The degradation of 1-butyl 3-methyl imidazolium chloride (BMIMCl) ionic liquid (IL) by Fenton oxidation has been studied. The optimization of operating parameters for maximum degradation of BMIMCl has been carried out using the Central Composite Design (CCD) of Response Surface Methodology (RSM). The three independent input parameters selected were the dosage of Hydrogen Peroxide (H_2O_2), the dosage of iron (Fe^{2+}), and the pH of the output or response selected was Total Organic Carbon (TOC) removal efficiency. Experiments were carried out according to the experimental design provided by CCD. For TOC Degradation, the model's R^2 and R^2_{adj} correlation coefficients between experimental and model-predicted values were 0.9769 and 0.9561, respectively. This indicates a satisfactory correlation of experimental results with model-predicted values. The optimum values of operating parameters for maximum degradation were found to be H_2O_2=307 mM (X1), Fe^{2+}=1.1 mM (X2), and (pH)=3.3 (X3), for a reaction time of 120 min. For these operating parameters, the experimental result for TOC removal efficiency was found to be 72.89% as compared to the model-predicted value of 73.67%. These results indicate that the values were closely correlated with each other and thus the model was validated satisfactorily. Overall, the results indicate that the BMIMCl ionic liquid can be effectively degraded by the Fenton oxidation process.

INTRODUCTION

Ionic liquids are molten salts having melting points below 100°C. Their structure constitutes a complex and asymmetric bulky cation with a weakly coordinating anion. Generally, the structural variations in molecular organic solvents also known as volatile organic compounds (VOCs) are very much limited to the innumerable structural variations in ionic liquids. This possibility of a large variation in the structures of ionic liquids, due to the availability of an enormous number of combinations of cations and anions, makes them the "designer solvents" (Siedlecka et al. 2008). Due to their immeasurable low vapor pressure, non-flammability, and tailor-made Physico-chemical properties, ILs have found wide applications in various fields like organic synthesis, solvent catalysis, electrochemistry, separation and extraction processes, fuel cells, solar cells, sensors, and nanochemistry. For example, ILs can extract benzene derivatives and metal ions from the aqueous phase (Yue et al. 2011) The physical features of ILs can be adjusted and made suited for certain applications by making appropriate adjustments in the alkyl chain, its branching, and the anion. Significant increases in reaction efficiency, selectivity, yield, and process economics can be achieved by executing the reactions in an IL media with target-oriented physico-chemical properties (Erdmenger et al. 2008).

The commonly used molecular or volatile organic compounds, due to their toxicity, flammability, and potential explosion hazard, create a greater concern for the workers in chemical industries. Apart from these properties, the emissions of solvent vapors in the atmosphere, and their release into water bodies through effluent discharge cause serious environmental concerns. Due to all these reasons, the use of volatile organic compounds in industries is getting restricted. In this context, ILs are gaining more popularity in industries as environmentally friendly "green solvents". The present status of research indicates that ILs provide a better alternative for organic solvents in many industries (Clarke et al. 2018).

However, the wider use of ILs in various industries may also cause harmful effects on the environment. For example, due to their non-biodegradability or persistency, ILs may get escaped from wastewater treatment processes and appear in the treated effluent before discharge in sufficient concentration. Due to the toxic nature of ILs, this treated effluent when discharged into the water bodies causes harmful effects on the aquatic ecosystem (Docherty et al. 2015). The very physico-chemical properties like non-volatility, and high chemical and thermal stability, which make the ILs most attractive for industrial applications, cause a lot of problems due to their

toxicity, higher solubilities in water, non-biodegradation or persistency, and bioaccumulation, in various environmental compartments (Pham et al. 2010). Also, the recovery of ILs from very dilute solutions or the waste streams is not an economically feasible option as it needs a large amount of energy. Hence it becomes very much essential to have an effective and economically feasible option for the degradation and removal of ILs from the aquatic solutions (Zhou et al. 2018). In this context, the advanced oxidation processes (AOPs) provide an attractive and effective option for the degradation of toxic and persistent ILs from the aquatic phase. The hydroxyl radicals($^\bullet$OH) generated in AOPs like Ozonation, Photo-Fenton's process, Photocatalytic reaction, Fenton's process, etc., are highly reactive and non-selective and hence oxidize the toxic and persistent organic compounds like ILs at a faster rate (Huang et al. 2007). Due to their simple operation and the high potential for degrading the highly toxic and refractive compounds, AOPs are gaining wider acceptance in industries and research as an effective means for the treatment of waste (Oller et al. 2011).

In the present work, a study has been carried out on the degradation of an ionic liquid namely, 1-butyl-3methyl imidazolium chloride (BMIMCl) using the Fenton oxidation process. This process involves the oxidation of organic compounds with hydrogen peroxide (H_2O_2) and employing Iron (Fe^{2+}) as a catalyst in acidic conditions. As compared to other methods of AOPs, Fenton's process is more advantageous in terms of process economy and ease of operation and maintenance. It is more effective for the effluents containing a high amount of suspended and dissolved solids as the penetration of photons across the depth of solution in the photo-oxidation process is limited (Anilkar et al. 1988). The hydrogen peroxide in Fenton's process gets decomposed by ferrous ions under acidic pH conditions (Qiu et al. 2010). Fenton process has been applied for the oxidation of a wide range of chemicals, organic and inorganic compounds such as phenolic compounds, atrazine, pesticides, toxic chemicals from the pharmaceuticals industry, and dyes from the textile industry (Pliego et al. 2012).

Experiments in the present study were performed as per the design of experiments using Central Composite Design (CCD) of Response Surface Methodology (RSM). Using RSM, a statistical and mathematical tool, optimization of operating parameters in industrial processes can be effectively carried out. This technique is used for the assessment of individual and interactive effects of various operating parameters on process output or response. In RSM a mathematical model is generated which can be used to find the optimum values of independent operating parameters. Through RSM the research results can be obtained at a faster rate than the time-consuming one variable at a time (OVAT) process (Alim et al. 2008).

The individual and interactive effect of operating parameters (pH, dosage of H_2O_2, and Fe^{2+}) on the response (removal efficiencies of COD and TOC) has been assessed. The model predicted parameters were experimentally validated.

MATERIALS AND METHODS

Chemicals

All the chemicals and reagents including hydrogen peroxide (H_2O_2, 30% w/w) and ferrous sulfate heptahydrate, $FeSO_4.7H_2O$ (99.0%) used in the present work were of analytical grade procured from Fisher Scientific manufactured in India. Sulfuric acid, H_2SO_4 (98-99%), and sodium hydroxide, NaOH (>98%) were used for the adjustment of pH of the solution.

The ionic liquid, 1-butyl 3-methyl imidazolium chloride (BMIMCl), used in the present study was purchased from Sigma-Aldrich. The synthetic solution of BMIMCl was prepared using doubled distilled water (TOC<5 ppb), obtained by circulating tap water through a carbon filter, then subjecting it to reversed osmosis, and finally filtering it through 0.45-μm filter paper.

Fenton Oxidation process of BMIMCl ionic liquid

Fenton experiments were carried out in an Erlenmeyer flask of 1L capacity with a continuous stirring at 200 RPM. The sample size was kept at 500 mL and the ionic liquid (BMIMCl) concentration selected was 1mM.L^{-1}. The oxidation reaction was conducted at room temperature 25±1°C for a designed reaction time of 120 min. A total of twenty experiments, as per the design of experiments by CCD of RSM, were conducted. The ionic liquid solution was placed in the glass reactor and a designed dose of hydrogen peroxide (H_2O_2) ranging from 200 to 400 mM and ferrous ions (Fe^{2+}) ranging from 0.5 to 1.5 mM were added to a reactor and a pH value of 3 to 4 was maintained. After a reaction time of 120 min, the reaction was stopped by adding 0.5 mL of methanol and the samples were analyzed for TOC. All the experiments were conducted in duplicate.

TOC Analysis

The Total Organic Carbon (TOC) was determined with a Shimadzu TOC-L analyzer with potassium phthalate as a standard calibration solution. Orion pH meter was used for measuring the pH values.

Experimental Design and Statistical Data Analysis.

Optimization and statistical data analysis have been carried out by using the Central Composite Design (CCD) of response surface methodology (RSM). The experimental

design was constituted of three factors considered in five levels and 20 runs were conducted to optimize the level of the selected factors that are hydrogen peroxide (X_1), Fe^{2+} concentration (X_2), and pH (X_3) (Table 1).

State-Ease Design expert 11.00 software was used to analyze model parameters and for analysis of variance (ANOVA), a second-order quadratic model is useful for correlating the predicted response and the independent variable in the coded values Equation 1

$$Y = A_0 + A_1X_1 + A_2X_2 + A_3X_3 + A_{12}X_1X_2$$
$$+ A_{13}X_1X_3 + A_{23}X_2X_3 + A_{11}X_1^2 + A_{22}X_2^2 + A_{33}X_3^2$$

$$\ldots(1)$$

Where y is the response (dependent variable) of percentage removal of TOC by the degradation of BMIMCl compound. In coded units, A_1, and A_2 are regression coefficients for linear effects, A_{11}, and A_{22} are quadratic coefficients. and A_{12}, A_{13}, and A_{23} are the interaction coefficients. According to Table 2, the CCD includes eight factorial points, six axial points, and center points with six additional experimental trials as the duplicates of this point. The term coded value was used to present independent variables at three levels: $+\alpha$ and $-\alpha$ (star points), -1 (minimum), 0 (central), and +1 (maximum). The specific value of α depends on certain properties looked for in the design and a number of factors. The accuracy of the quadratic model was explained by the coefficient of determination R^2. Also, model terms were chosen or rejected based on the

Table 1: Levels of the independent variables and experimental ranges.

Variables	Code	Variables	$-\alpha$	-1	0	+1	$+\alpha$
H_2O_2 [mM)]	X_1	H_2O_2 [mM]	131.82	200	300	400	468.18
Fe^{2+}(mM)	X_2	Fe^{2+} [mM]	0.16	0.5	1	1.5	1.84
pH	X_3	pH	2.7	3	3.5	4	4.34

Table 2: The CCD experimental design with three independent variables of 20 runs.

Run	Factor 1 X$_1$: Hydrogen peroxide mM	Factor 2 X$_2$: Fe mM	Factor 3 X$_3$: pH	Experimental TOC(%)	Predicted TOC(%)
1	300	1	3.5	71.55	71.36
2	300	1	4.3409	9.02	8.45
3	200	1.5	3	40.21	40.09
4	200	1.5	4	15.59	17.05
5	300	1	3.5	71.56	71.36
6	400	0.5	3	36.72	35.25
7	300	1	2.6591	35.00	35.59
8	200	0.5	4	23.27	23.54
9	400	1.5	3	62.11	61.83
10	200	0.5	3	30.88	31.75
11	300	1	3.5	71.50	71.36
12	400	1.5	4	38.65	37.76
13	300	1	3.5	71.53	71.36
14	300	0.159104	3.5	38.65	38.78
15	300	1.8409	3.5	55.78	55.67
16	131.821	1	3.5	30.95	39.47
17	300	1	3.5	71.52	71.36
18	300	1	3.5	71.56	71.36
19	468.179	1	3.5	48.32	49.82
20	400	0.5	4	25.89	26.00

P-value with 95% confidence levels. Surface plots (three-dimensional) and respective contour plots (two-dimensional) were obtained for the degradation of BMIMCl ionic liquid.

Where y is the response variable of TOC (%) degraadation of BMIMCl compound. In coded units, A*1*, and *A2* are regression coefficients for linear effects, *A11,* and *A22* are quadratic coefficients., and *A12* is the interaction coefficient (Simsek et al. 2013). According to Table 2, the CCD includes eight factorial points, six axial points, and a center point with six additional experimental trials as the duplicates of this point. The term coded value was used to present independent variables at three levels: + α and - α (star points), -1 (minimum), 0 (central), +1 (maximum), the specific value of α depends on certain properties looked for the design and number of factors. The accuracy of the quadratic model was explained by the coefficient of determination R^2. Also, model terms were chosen or rejected based on the P-value with 95% confidence levels. Surface plots (three-dimensional) and respective contour plots (two-dimensional) were obtained for the degradation of BMIMCl ionic liquid.

RESULT AND DISCUSSION

Development of the Quadratic Model and Statistical Analysis

Using a model software that is design expert 11.0, the following quadratic model for the experimental response of TOC degradation was obtained from equations 2.

$$(Y_1) = +71.36 + 6.19 * H_2O_2 + 5.67 * Fe^{2+}$$

$$- 7.72 * pH + 4.96 * H_2O_2 * Fe^{2+} + 0.1375$$

$$* H_2O_2 * pH - 4.10 * Fe^{2+} * pH - 11.78$$

$$* (H_2O_2)^2 - 9.16 * (Fe^{2+})^2 - 16.59$$

Table 3: ANOVA result for Fenton oxidation.

	Source	Ss	DF	Ms	F-Value	P-Value
	Model	8204.04	9	911.56	2826.23	0.001
	Residual	3.23	10	0.32		
TOC (%)	Lack of Fit	2.89	5	0.57	8.65	
	Pure Error	0.33	5	0.29		
	R^2	0.9769		0.9561		

$$* (pH)^2 \qquad \qquad \qquad \dots(2)$$

The value 71.36 shown in equation 2 is the intercept value for TOC (Y), These results indicate a positive influence on the model. The values of coefficients for the variables such as $Fe^{2+}*$ pH, $H_2O_2*Fe^{2+}$ and H_2O_2*pH have an optimistic effect on the degradation of TOC of BMIMCl by Fenton reaction. The analysis of variance (ANOVA) of the model for the degradation of BMIM is given in Table 3.

Results of the ANOVA of the empirical second-order quadratic model for TOC reduction of BMIMCl shows P-values less than 0.0500. This indicates that model terms are significant. If P values are greater than 0.1000, it is inferred that the model terms are not significant.

The correlation coefficient R^2 describes the variability in the response values by the experimental factors and their interactions. R^2 and R^2_{adj} values in the present work were found to be 0.9769 and 0.9561 The variance between the correlation coefficient R^2 and R^2_{adj} were sensibly satisfactory and hence this model was fit for determining the optimum condition for degradation of BMIMCl using Fenton oxidation. A plot of experimental values versus predicted values resulting from the model is shown in Fig. 1.

Response Contour Plots and Response Surface Plots for the Fenton Process

Effect of pH and H₂O₂

The interactive effects of H_2O_2 concentration and initial pH are depicted in Fig. 2 (a) by 3D response surface plots and (b) by contour plots. As can be seen in the graph, as the pH rises, so does the rate of TOC breakdown. At a pH of 3.5, a
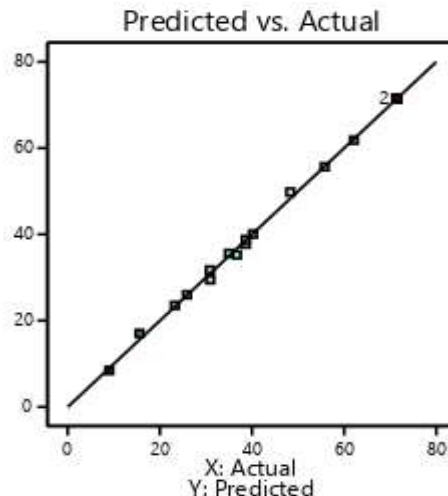
Fig. 1: Plot of experimental values against predicted values.
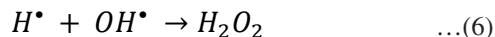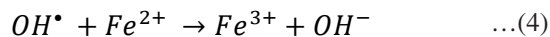
maximum of 71.55 TOC degradation appears with an oxidizing concentration of H_2O_2 300 mM in the presence of Fe^{2+} 1 mM catalyst concentration with a reaction time of 120 mins. Moreover, the decreased degradation efficiency was also detected at lower pH (<2.6). When the pH was reduced from 3 to 2.6, for example, the breakdown efficiency of BMIMCl decreased due to the production of the oxonium ion ($H_3O_2^+$), which is less reactive (Siedlecka et al. 2008). According to the equation (3), excessive hydrogen ion concentration at a high pH level has a probability of scavenging hydroxyl radicals (Devi et al. 2009)

$$H^+ + OH^\bullet + e \rightarrow H_2O \qquad \ldots(3)$$
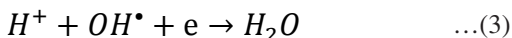
Effect of H_2O_2 Concentration and Fe^{2+} Concentration

The oxidation efficiency of ionic liquids is strongly dependent on the concentration of the oxidant (H_2O_2) and catalyst [Fe^{2+}] in a Fenton process. Generally, the more [H_2O_2] and [Fe^{2+}] the faster the degradation rate of IL Behnajady et al. 2007). Similar observations were found in this experiment. As the Fe^{2+} concentration increased from 0.5 to 1 mM [Fig. 3 (a) and (b)], the TOC degradation efficiency of BMIMCl increased from 23.27% to 71.55%. This may be attributed to the fact that increasing the concentration of Fe^{2+} accelerates the decomposition of H_2O_2 and consequently induces an increase in the availability of hydroxyl radicals (Vallejo et al. 2015). However, overconsumption of Fe(II) and H_2O_2 will also consume the hydroxyl radicals [equation (4) and (5)] and increases the chances of hydroxyl radical recom-

bination [equation (6)]. Besides, the excess utilization of Fe(II) would cause the development of an abundance of ferric-based sludge, thereby increasing the disposal cost (Munter et al. 2006).

$$OH^\bullet + Fe^{2+} \rightarrow Fe^{3+} + OH^- \qquad \ldots(4)$$

$$OH^\bullet + H_2O_2 \rightarrow OOH^\bullet + H_2O \qquad \ldots(5)$$

$$H^\bullet + OH^\bullet \rightarrow H_2O_2 \qquad \ldots(6)$$

Effect of Fe^{2+} Concentration and pH

The effect of catalyst concentration and pH on the TOC (%) degradation is shown in Fig. 4 (a, b) pH value 3.5 and iron concentration 1 mM shows the development of active iron species of Fe^{2+} ions due to which the production of hydroxyl radicals ($^\bullet$OH) increases, Also, at a very small pH, the reacation of Fe^{2+} with H_2O_2 is hindered, and hydroxyl radical is scavenged by H^+ ions (Tang & Huang 1996). A comparable observation is found in the present experiment also. For these values of parameters, the percentage removal of TOC was found to be 71.55%.

Optimization of Inducing Parameters

Optimization of inducing parameters was achieved based on the desirability function to decide the optimal conditions for the degradation of BMIMCl ionic liquid. Numerical optimization was used to recognize the specific ranges that maximize the desirability function. The program uses five

(a)   (b)
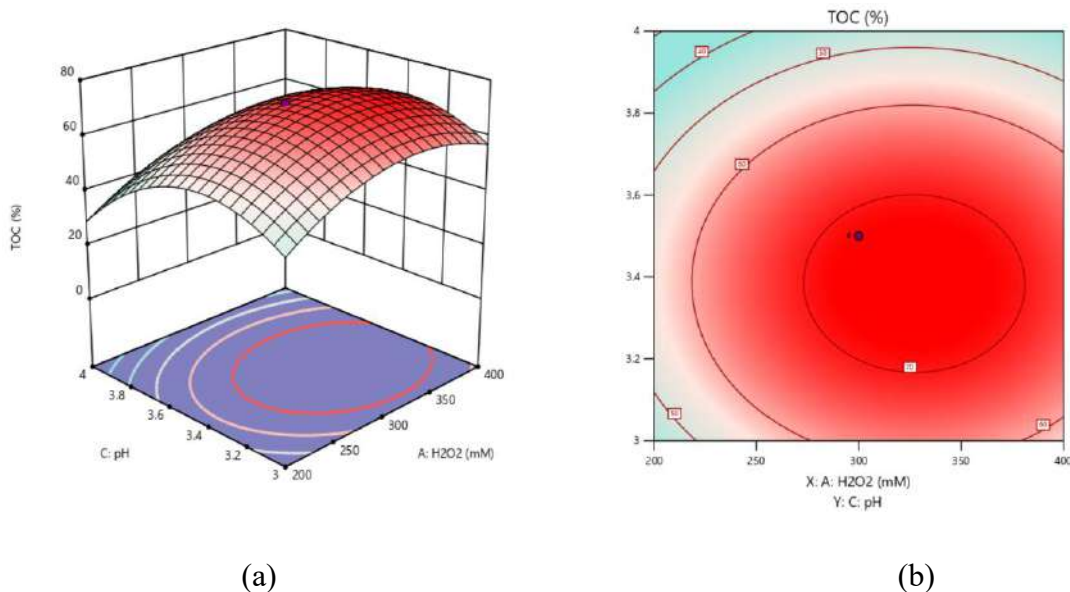
Fig. 2: Three-dimensional surface plot (a) and two-dimensional contour plot (b) for the effect of catalyst concentration and pH, on TOC (%) degradation.

(a)   (b)
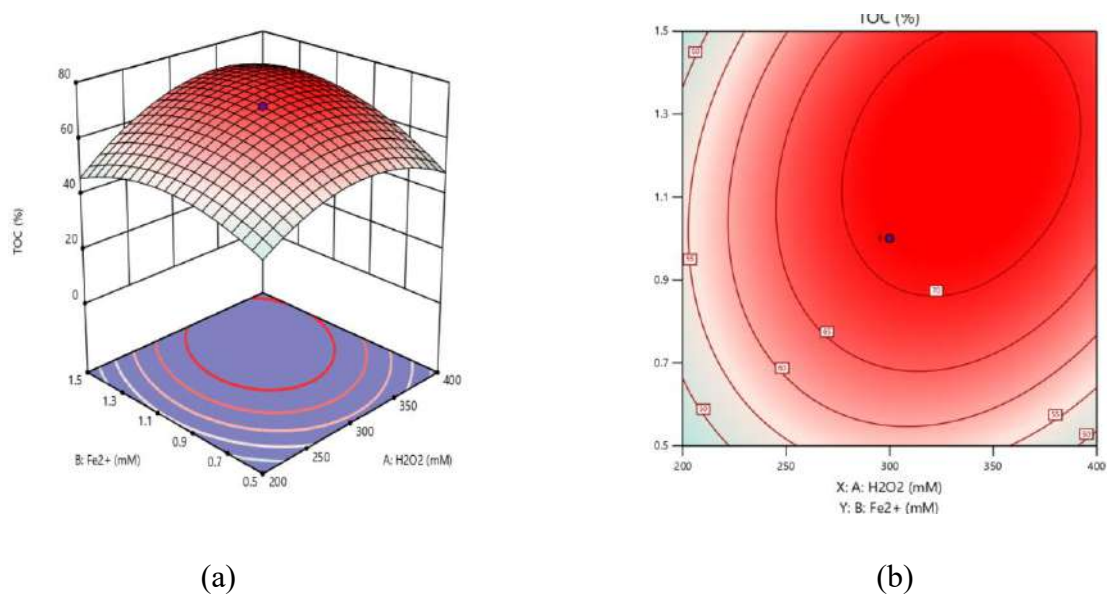
Fig. 3: Three-dimensional surface plot (a) and two-dimensional contour plot (b) for the effect of H_2O_2 concentration and Fe^{2+} on TOC (%) degradation.

(a)   (b)
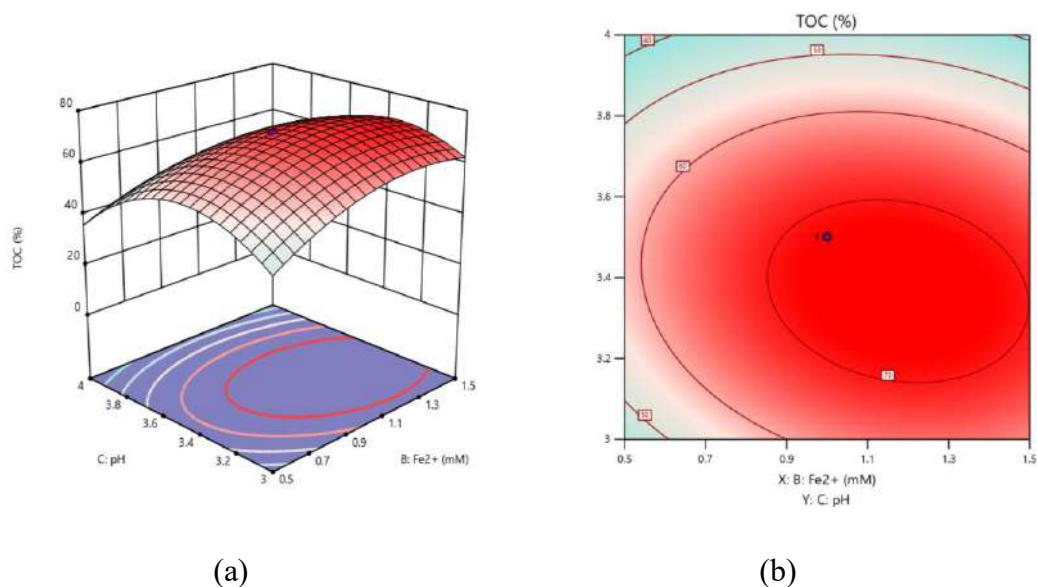
Fig. 4: Three-dimensional surface plot (a) and two-dimensional contour plot (b) for effect of Fe^{2+} concentration and pH on TOC (%) degradation.

probabilities as a goal to construct desirability indications: none, maximum, minimum, target, and within range. The criteria for all variables in correspondence with degradation percentages are revealed in Table 4.

Based on the boundaries constraints, described by numerical optimization, the optimum conditions for BMIMCl ionic liquid maximum condition were found that be TOC (73.67%). in presence of a hydrogen peroxide concentration of 307 mM and H_2O_2 concentration of 1.1 mM and pH value of 3.3.

Validation of the Model and Confirmation

To confirm the appropriateness of the model for predicting the maximum percentage of TOC degradation of BMIMCl, the experiment was conducted in a 1L capacity glass reactor using the optimum conditions which were obtained from model software. An average maximum TOC of 73.79 % was obtained from three duplicate experiments, as shown in Table 5. The good agreement between the predicted value and the experimental value confirms the validity of the model

Table 4: Optimization of variables under limits.

Name	Goal	Lower Limit	Upper Limit	Lower Weight	Upper Weight	Importance
H_2O_2	is in range	200	400	1	1	3
-Fe^{2+}	is in range	0.5	1.5	1	1	3
pH	is in range	3	4	1	1	3
TOC	maximize	9.02	71.58	1	1	3
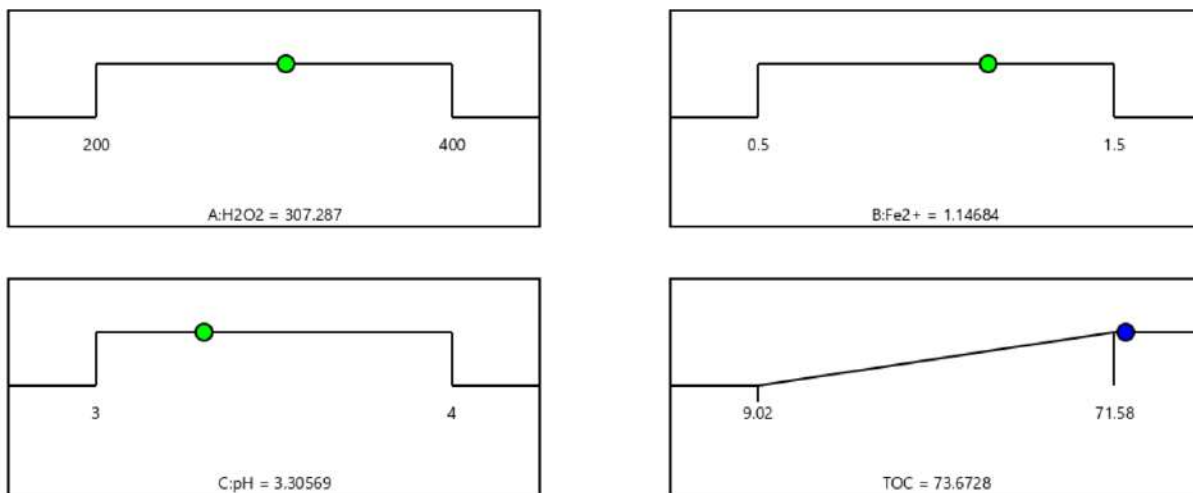
Fig. 5: Numerical optimization constraints by using ramps.

for simulating the degradation of BMIMCl by the Fenton oxidation process.

CONCLUSION

The degradation of 1-butyl 3-methyl imidazolium chloride (BMIMCl) ionic liquid (IL) by Fenton oxidation was very effective for a reaction time of 120 min. The following parameters affected the entire Fenton process: H_2O_2 dosage, Fe^{2+} dosage, and pH. The central composite design (CCD) model was selected to attain the optimal conditions for BMIMCl degradation in the Fenton oxidation experiment to minimize the number of experimental runs. This statistical design was found suitable for this study with a regression coefficient R^2 equal to 0.9769 and Adj-R^2 equal to 0.9561 for TOC degradation. ANOVA and the response surface led to the optimization

of the degradation of 1-butyl-3methyl imidazolium chloride (BMIMCl) ionic liquid (IL) The optimum parameters for degradation by the Fenton oxidation process were found to be: H_2O_2=307 mM (X1), Fe^{2+}=1.1 mM (X2) and (pH)=3.3 (X3). Overall it can be concluded that the Fenton process is very much effective in degrading BMIMCl ionic liquid as per the above-mentioned operating conditions.

REFERENCES

Alim, M.A., Lee, J.H. and Akoh, C.C. 2008. Enzymatic transesterification of fractionated rice bran oil with conjugated linoleic acid: Optimization by response surface methodology. LWT - Food Sci. Technol., 41: 764-770.

Anilkar, R., Dürig, G. and Steinle, D. 1988. List of colorants to be classified as toxic. J. Soc. Dye. Colour, 104: 223-225.

Behnajady, M.A, Modirshahla, N. and Ghanbary. F. 2007. A kinetic model for the decolorization of C.I. Acid Yellow 23 by the Fenton process. J. Hazard. Mater., 148: 98-102.

Table 5: Comparison of predicted and experimental results for optimum working conditions in Fenton oxidation.

Variables	Optimum Value	TOC Degradation %	
		Predictive	Experimental
H_2O_2 (X$_1$) mM	307.287	73.67	72.89
Fe^{2+} (X$_2$) mM	1.146		
pH (X$_3$)	3.30		

Clarke, C.J., Tu, W.C., Levers, O., Brohl, A. and Hallett, J.P. 2018. Green and sustainable solvents in chemical processes. Chem. Rev., 118(2): 747-800.

Devi, L.G, Raju, K.S, Rajashekhar, K.E. and Kumar, S.G. 2009. Photo-Fenton and photo-Fenton-like processes for the degradation of methyl orange in aqueous medium: Influence of oxidation states of iron. Chem. Papers, 64, 378-385.

Docherty, K.M., Aiello, S.W., Buehler, B.K., Jones, S.E., Szymczyna, B.R. and Walker, K.A. 2015. Ionic liquid biodegradability depends on specific wastewater microbial consortia. Chemosphere, 136: 160-166.

Erdmenger, T., Vitz, J., Wiesbrock, F. and Schubert, U.S. 2008. Influence of different branched alkyl side chains on the properties of imidazolium-based ionic liquids. J. Mater. Chem., 18(43): 5267-5273.

Huang, Y.H., Tsai, S.T. and Huang, Y.F. 2007. Degradation of commercial azo dye reactive Black B in photo/ferrioxalate system. J. Hazard. Mater., 140: 382-388.

Munter, R., Trapido, M., Veressinina, Y. and Goi, A. 2006. Ozone: Sci. Eng., 28: 287-293.

Oller, I., Malato, S. and Sánchez-Pérez JA. 2011). Combination of advanced oxidation processes and biological treatments for wastewater decontamination: A review. Sci. Total Environ., 409: 4141-4166.

Pham, T.P.T., Cho, C.W. & Yun, Y.S. 2010. Environmental fate and toxicity of ionic liquids: a review. Water Res., 44(2), 352-372.

Pliego, G., Zazo, J.A., Blasco, S., Casas, J.A. and Rodriguez, J.J. 2012. Treatment of highly polluted hazardous industrial wastewater by combined coagulation-adsorption and high-temperature Fenton oxidation. Ind. Eng. Chem. Res., 51(7): 2888-2896.

Qiu, M., Jiang, Q. and Yang, S. 2010. Effects of operational parameters on the decolorization of CL Acid Blue 9 by Fenton oxidation process. Bioinforma. Biomed. Eng., 2010: 1-3.

Siedlecka, E.M., Mrozik, W., Kaczy ski, Z. and Stepnowski, P. 2008. Degradation of 1-butyl-3-methylimidazolium chloride Fenton-like system. J. Hazard. Mater., 154(1-3): 893-900.

Simsek, E.B., Ozdemir, E. and Beker, U. 2013. Process optimization for arsenic adsorption onto natural zeolite incorporating metal oxides by response surface methodology. Water Air Soil Pollut., 224: 1614.

Vallejo, M., Fern´andez-Castro, P., San, R. and Ortiz, I. 2015. Assessment of PCDD/Fs formation in the Fenton oxidation of 2-chlorophenol: Influence of the iron dose applied. Chemosphere, 137: 135-141.

Tang, W.Z. and Huang, C.P. 1996. 2,4-dichlorophenol oxidation kinetics by Fenton's reagent, Environ. Technol., 17: 1371-1378.

Yue, C., Fang, D., Liu, L. and Yi, T. F. 2011. Synthesis and application of task-specific ionic liquids used as catalysts and/or solvents in organic unit reactions. J. Mol. Liq., 163(3): 99-121.

Zhou, J., Sui, H., Jia, Z., Yang, Z., He, L. and Li, X. 2018. Recovery and purification of ionic liquids from solutions: A review. RSC Adv., 8(57): 32832-32864.

An Improved Convolutional Neural Network for Plant Disease Detection Using Unmanned Aerial Vehicle Images

Dashuang Liang*, Wenping Liu*†, Lei Zhao*, Shixiang Zong** and Youqing Luo**

*School of Information Science and Technology, Beijing Forestry University, Beijing 100083, China
**Beijing Key Laboratory for Forest Pest Control, Beijing Forestry University, Beijing 100083, China
†Correspondence: Wenping Liu; wendyl@vip.163.com

ABSTRACT

Accurate and fast locating of diseased plants is critical for the sustainability of forest management. Recent developments in computer vision made by deep learning provide a new way for diseased plant detection from images captured by unmanned aerial vehicles (UAV). In this paper, we developed an anchor-free detector, an enhanced CenterNet named as Enhanced CenterNet (ECenterNet) model, which significantly improved the overall accuracy over the original CenterNet model without any increase in the running speed or number of parameters. Compared with the original model, in the newly proposed model improvements had been made in the training stage to increase the accuracy of the detector, while procedures in the test stage remained unchanged. Under the hold-out dataset, the proposed model is trained on 5,281 tiles and tested on 3,842 images, the results showed that the overall detection accuracy of ECenterNet reached 54.7% by COCO Challenge metrics (mean average precision (mAP) @[0.5, 0.95]), while mAP accuracy of the original CenterNet was 49.8%. This research indicates that the proposed deep learning detection model provides a better solution for detecting diseased plants from UAV images with high accuracy and real-time speed.

INTRODUCTION

Forests play a vital role in a country's economic, social and environmental benefits (Dash et al. 2017). Plant diseases and pests pose a serious threat to the growth of forests. Traditionally, the range and severity of plant diseases and pests are manually identified and scored by field investigations with expensive cost and low efficiency (Chiu 1993). Therefore, more accurate and faster detection of diseased and pest plants could help in developing an early treatment technology, while substantially reducing economic losses (Fuentes et al. 2017).

In the past, spectral detection technology using satellite remote sensing data or traditional computer vision methods, coupled with global positioning systems and geographic information systems, were widely used in detecting pest distribution and proved to be effective (Cao 2015). However, the efficiency of these methods was low and sometimes failed to accurately locate infected plants. Luckily, with the rapid technological developments of unmanned aerial vehicles (UAV), an inexpensive and fast way of getting high-resolution images of forest distribution becomes available. Based on these images, a variety of image processing methods have been developed to detect the distribution of diseased plants.

Advances in hardware technology have allowed for the evolution of deep convolutional neural network (CNN),

which has achieved greater success in many fields, including image classification (He et al. 2016, Krizhevsky et al. 2012, Szegedy et al. 2015), facial recognition (Kshirsagar et al. 2011), segmentation (Chen et al. 2018, Long et al. 2015) and object detection (Dai et al. 2016, Liu et al. 2016, Redmon et al. 2016, Ren et al. 2017). Recently, the application of deep CNN for plant disease severity detection has been proposed and has shown a good performance.

This paper aims at detecting forest plant diseases and insect pests using the object detection method. In the past, many object detection methods had been proposed (e.g., Faster RCNN (Ren et al. 2017), YOLO (Redmon et al. 2016), SSD (Liu et al. 2016), and RFCN (Dai et al. 2016)). All these methods relied on a set of pre-defined anchor boxes and showed good results on the PASCAL VOC (Everingham & Williams 2010), COCO (Lin et al. 2014), and ILSVRC (Russakovsky et al. 2015) datasets. However, anchor boxes result in excessively many hyper-parameters, which need to be carefully tuned to achieve high performance. Meanwhile, anchor-based detection methods also bring complex IoU computation and matching between anchor boxes and ground-truth boxes during training. To avoid these drawbacks, some anchor free detectors are proposed, such as CornerNet (Law & Deng 2020), CenterNet (Zhou et al. 2019a), FCOS (Tian et al. 2020), and ExtremNet (Zhou et al.

2019b), all of which take the object detection as a standard key-point estimation problem. Among various anchor-free object detection algorithms, CenterNet uses the key-point estimation method to regress the center point, the width, and the height of an object. It is a simple, fast, and accurate detector without any Non-Maximum Suppression (NMS) postprocessing. Yet it still has some drawbacks in the application of UAV forestry image, especially in the image where the plants are close to each other. The objective of this study is to propose an enhanced CenterNet (ECenterNet) model for plant diseases and pest detection based on UAV images.

MATERIALS AND METHODS

Study Area

The study area is located in Lingyuan City, Liaoning Province in northeast China. The dominant vegetation is Chinese red pine (Pinus tabuliformis) with a few poplar trees (Populus spp.) occasionally occurring. The pest Dendroctonus (Scolytidae) has caused serious damage and tree mortality within the area. To quickly detect the damage level of the forest, six different sample sites distributed in the county were selected as the study area, namely Site 1, Site 2, Site 3, Site 4, Site 5, and Site 6. Fig. 1 shows the location and distribution of these sample plots on a map.

Data Collection

The UAV-based data acquisition was carried out in the study area on August 11th and August 12th, which was the best time window for catching leaf symptoms. The UAV model was a four-rotor DJI Inspire2, carrying a DJI x5 professional camera with an effective resolution of 2×10^7 pixels, providing an image size of 5280×3956 pixels. On each sample plot, a certain number of pictures were toke from 40 to 240 meters above sea level. With the increase in height, the forest land covered by the photos becomes larger and larger, and the size of individual trees in the photos becomes smaller and smaller. To capture images without overexposure or shadows, capture times when the sunlight was too strong or too weak were avoided.

Implementation Details

CenterNet Principles

One aim of CenterNet was to produce a key point heatmap, where C was the number of categories. Another aim of the CenterNet was to output the object size $s_k = \left(x_2^{(c)} - x_1^{(c)}, y_2^{(c)} - y_1^{(c)} \right)$ for each object k. To limit the computational burden, a single-size prediction was used for all object categories. The third aim of CenterNet was

to output the offset $\left(x/s_x - \lfloor x/s_x \rfloor, y / s_y - \lfloor y / s_y \rfloor \right)$ between the real center computed and center pixels on the feature map.

For the center of an object (x, y) with class C on the input image, it was mapped to the feature map $\left(\lfloor x/s_x \rfloor, \lfloor y / s_y \rfloor \right)$, which was considered as a positive sample, where S_x and S_y were the horizon and vertical scale parameters, respectively. Points other than the center point were regarded as negative samples. The training objective function was a penalty-reduced pixel-wise logistic regression with focal loss (Lin et al. 2017):

$$
L_k = \frac{-1}{N} \sum_{xyc} \begin{cases} \left(1-\hat{Y}_{xyc}\right)^{\alpha} \log\left(\hat{Y}_{xyc}\right) & \text{if } Y_{xyc}=1 \\ \left(1-Y_{xyc}\right)^{\beta}\left(\hat{Y}_{xyc}\right)^{\alpha} \log\left(1-\hat{Y}_{xyc}\right) & \text{otherwise} \end{cases} \quad \dots(1)
$$

where α and β were hyper-parameters, respectively, and fixed to $\alpha = 2$ and $\beta = 4$ during training. N was the number of objects in the image. $\hat{Y}_{xyc}$ was the prediction probability of an object with center coordinate (x, y) with the label of c, Y_{xyc} was a heatmap that was created by a Gaussian kernel.

$$
Y_{xyc} = \exp\left(-\frac{\left(x - \tilde{p}_x\right)^2 + \left(y - \tilde{p}_y\right)^2}{2\sigma_p^2} \right) \quad \dots(2)
$$

where σ_p was an object size-adaptive standard deviation (Law & Deng 2020). The Gaussian heatmap served as the weight map to reduce the penalty near a positive location in the logistic regression case.

For the offset $\left(x/s_x - \lfloor x/s_x \rfloor, y / s_y - \lfloor y / s_y \rfloor \right)$ between real center computed and center pixels on the feature map, the CenterNet used an L_1 loss to regression it, and all classes shared the same offset.

$$
L_{off} = \frac{1}{N} \sum_{p} |\hat{O}_{\tilde{p}} - \left(x/s_x - \lfloor x/s_x \rfloor \right)| \quad \dots(3)
$$

For the size (w, h) of an object, CenterNet also used the L_1 loss to regress it, and all categories shared the same object size.

$$
L_{size} = \frac{1}{N} \sum_{k=1}^{N} |\hat{S}_{pk} - s_k| \quad \dots(4)
$$

Thus, the total objective function of CenterNet was as follows:

$$
L_{det} = L_k + \lambda_{size} L_{size} + \lambda_{off} L_{off} \quad \dots(5)
$$

where λ_{size} and λ_{off} where the weight of size and offset
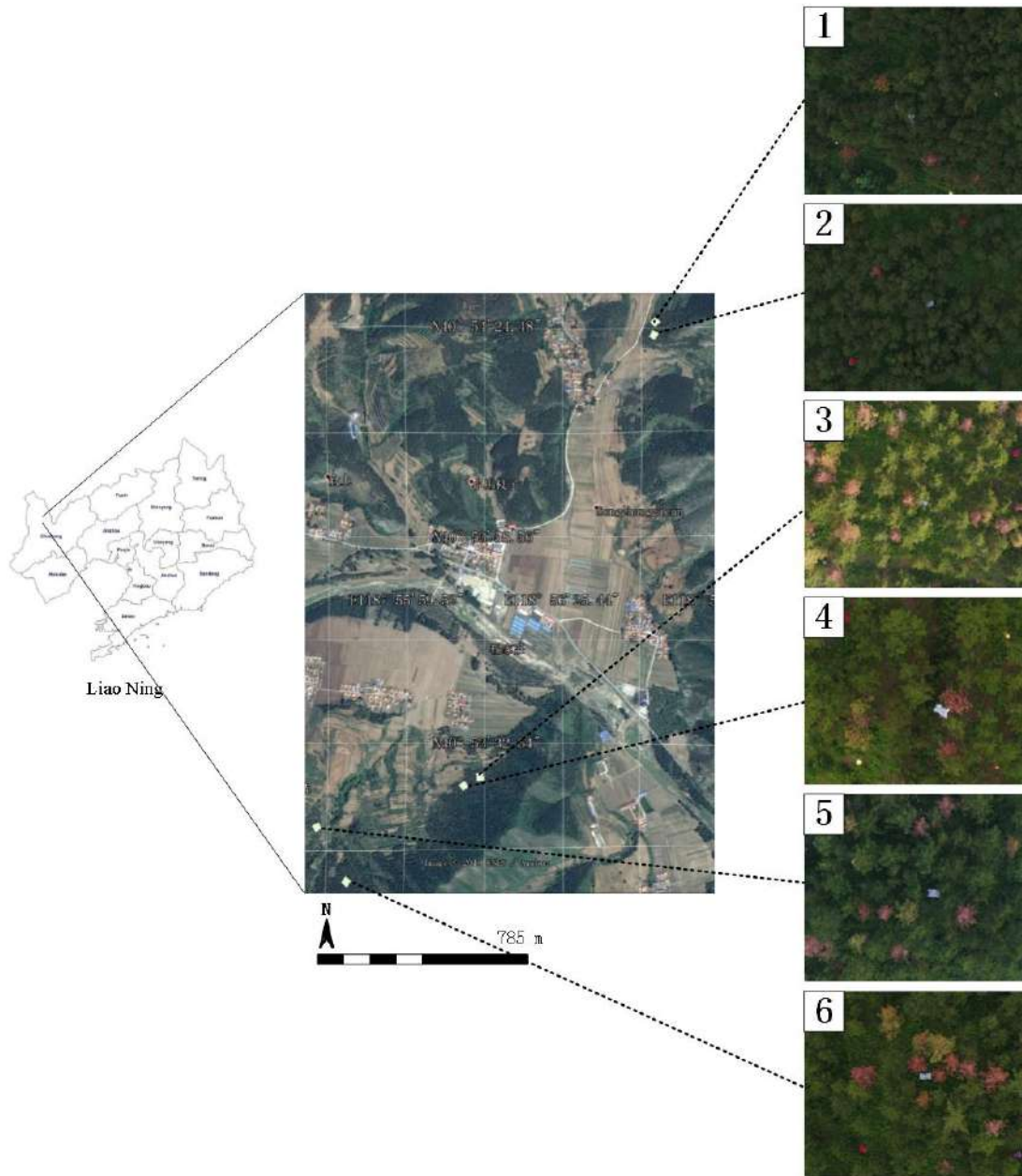
Fig. 1: The study area.

regression, respectively. L_{det} was the total loss of the CenterNet detector, L_k was the heatmap value of the center of an object, more details about CenterNet please see Zhou et al. (2019a).

Separate Overlapping Center Points of Two Objects

In the original CenterNet, the positive sample of an object was the center of the bounding box obtained by mapping the object from the original image to a 128 × 128 size feature map, and the pixels around the center point were considered negative samples. If two objects of the same class were close to each other on a larger original image, the center points of the two objects were mapped to the same point on the 128 × 128 size feature map, as it was shown in Fig. 2(a). This situation would bring confusion to the training of the network. To solve this problem, in this paper, one of the center points was forced to offset by one pixel if two center points on the feature map coincided with each other. The improved

operation which was Separate Overlapping Center Points of two objects (SOCP) aimed to separate two overlapping center points of two objects on the feature map [Fig. 2(b)]. The detailed rules of SOCP were as follows:

Step 1. Between the two objects' center points, the one with a larger bounding box area was selected to make the offset.

Step 2. Offset the selected object's center point by one pixel along the long side of the object's bounding box. Ordinary, either of the two directions (right or left) was selected to make the offset.

Step 3. Choose one of the two directions randomly. If one of them encountered the boundary of the image or the center of the other object's bounding box, this direction was abandoned and another direction was chosen.

Step 4. If two of the above directions were not selected due to the reasons in step 3, the long side direction was given up and the short side direction of the object would be chosen.

Step5. Randomly choose one of the two directions along the short side of the object. If one of them encountered the boundary of the image or the center of another object's bounding box, this direction would be abandoned and another direction would be selected.

Step 6. If neither of the directions was selected to move due to the reason in step 3, the offset operation was given up and the original strategy in original CenterNet was kept.

Controlled Sampling Strategy for Objects on the Boundary

In the original CenterNet, before the data were sent to the network, an affine transformation of random center shift and scaling was performed on the image. At this time, some objects were moved out of the image's boundary, some stayed in the image's boundary, and some fell on the boundary. For the objects that fell on the boundary, the original CenterNet method used clip operation to recalculate the bounding box coordinates of the remaining part. However, the new coordinates of the bounding box calculated by clipping were often inaccurate, as shown in Fig. 3(b), while the accurate coordinates of the left object's bounding box are shown in Fig. 3(c).

To avoid the above-mentioned problems as far as possible, there was a limitation that the bounding box area of the remaining object on the image's boundary should be more than 90% of that of the original one. In detail, before performing the affine transformation, the randomly generated offset
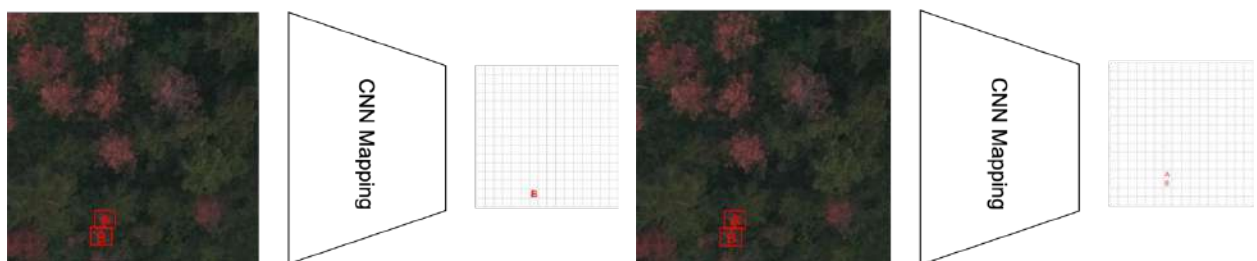
Fig. 2: (a) Two coincide center points on features from two close objects, (b) SOCP operation to two coincide center points on the feature map.

Fig. 3: (a) The original labeled picture, (b) the bounding box create in CenterNet after the affine transform, and (c) the real bounding box of the left part after the affine transform to picture.

parameter O and scaling factor S for affine transformation should be satisfied the limitation mentioned above. If it was not satisfied, a new set of parameters O and S were randomly created and then tried again until it was satisfied. This strategy was called a controlled sampling strategy (CSS). With the help of CSS, the bounding box recalculated by clip operation was very close to the accurate bounding box, especially for the trees whose shapes were approximately circular in this study. In addition, in the experiment, when replacing the affine transformation with the resize operation and no offset operation, the accuracy declined. The reason might be that the resize operation reduced the richness of data compared with the random affine transformation operation.

Positive Pixel Choosing Mechanism

In the original CenterNet, the center of the object's bounding box in the original image was considered to be a positive sample to object' category classification. However, for some objects, as shown in Fig. 4, the center point did not seem to be a good representation of the object. In addition, during the training of the original CenterNet, it was found that some pixels nearby the center pixel had larger IoU formed by the predicted bounding box and ground truth than that of the center pixel (Fig. 5). This phenomenon indicated that some pixels in the neighborhood of the center point were more suitable for an object's bounding box regression.

In view of the above phenomenon, a positive pixel choosing mechanism (PPCM) was designed in this paper to select a better positive sample. In the training stage, not only the

center point of the object's bounding box but also the eight neighboring pixels around the center point were considered as candidate positive samples. During the training process, the center point together with the eight neighborhood points competed with each other, and the suitable one was selected as the positive sample of the object. Specifically, after a certain number (experiments show 30 was better) of epochs in the training stage, if one of the eight neighboring pixels' IoU formed by the bounding box and ground truth was 0.2 higher than that of the center pixel, the pixel was selected as a positive sample to calculate the loss of classification and regression in the following training stage.

Experiments

Data Preparation

In the fieldwork, plants with green leaves were classified as healthy plants, while those with yellow leaves were regarded as infected stage plants, and those with red leaves were classified as dead plants. This study only focused on diseased and infected plant detection, therefore, only plants with yellow and red leaves were annotated. As the original size of the images was 5,280 × 3,956 size pixels, which was too big to train a network, a set of image tiles was created by cropping each original aerial image by using a sliding window with random sizes between 1,000 and 2,000 pixels and stride of 1,000 pixels. In this way, one big aerial image was split into several small images. Before training, the images of Site 1, Site 3, Site 4, and Site 6 were split into training and validation datasets, while the images of Site 2 and Site 5 were

Fig. 4: Samples of the center point of the bounding box that cannot represent well of the related object.

chosen as testing datasets. At last, the training and validation datasets contained 5,281 tiles and 1,319 tiles respectively, and the test dataset contained 3,842 images. All the images were manually labeled with ground truth bounding boxes and assigned with class labels "infected" or "dead" (only one per bounding box).

To get as many samples as possible, some more data were created through the method of data augmentation. Several strategies were adopted to do data augmentation, such as flip, random color, random rotation, random crop, and so on.

Training

In all of these experiments, the input sizes of all of the networks were fixed to a size of 512 × 512, while the class number was two, including "dead", and "infected" classes. No matter how large the input image was, it would be scaled to the same size through affine transformation, and then pass through the network of CenterNet structure. ResNet-101 was selected as the backbone part of the network. After passing through the backbone network, the size of the feature layer became 128 × 128 because of the down sampling of the convolution and pooling layer.

As PyTorch is one of the most famous and fastest deep learning frameworks for CNN, it is used to train models in this experiment. The network was then trained on a single NVIDIA Titan 12 GB GPU. The training was stopped after 140 epochs, which took roughly 4 days. The Adam learning method was used as the gradient descent algorithm. The detailed training hyper-parameters were listed in Table 1.

Test and Comparison

To make a full comparison with other models, original CenterNet (Zhou et al. 2019a), SSD (Liu et al. 2016), and Faster RCNN (Ren et al. 2017) were trained with the same data and settings, and then were tested and compared with the proposed ECenterNet model.

To evaluate the final detections, the official COCO API (Lin & Dollar 2016), measured mAP over IoU thresholds

Table 1: Parameters of network training.

Argument	Value
Mini-batch size	8
Num_epochs	140
Lr_policy	Multistep
Stepvalue	90, 120
Initial learning rate	1.25e-4
Gamma	0.1

from 0.5 to 0.95 with steps of 0.05, simply denoted as mAP@[.5, .95], was used as the performance indicator.

The Average Precision (AP) was the area under the Precision-Recall curve for the detection task. As in the COCO Challenge, the AP was computed by averaging the precision over a set of spaced recall levels from 0 to 1 with steps of 0.01.

$$AP = \frac{1}{11} \sum_{r \in \{0, 0.1, \dots, 1\}} P_{\mathrm{int}\,erp}(r)$$

$$P_{\mathrm{int}\,erp}(r) = \max_{\tilde{r}:\tilde{r} \geq r} p(\tilde{r})$$

...(6)

where $p(\tilde{r})$ was the measure precision at recall $\tilde{r}$. AP was a concept of integrating precision as the recall was varied from 0 to 1, and mAP was defined as the average of AP for all of the object classes.

RESULTS

Results of Different Models

The results of different models are shown in Table 2. The proposed ECenterNet performed very well in both classes. Among the anchor-based methods, RetinaNet (Lin et al. 2017) performed best with 0.029 higher accuracies of mAP@[.5, .95] compared with the SSD method (Liu et al. 2016). In anchor free method, CenterNet (Zhou et al. 2019a) had a 0.07 higher accuracy of mAP@[.5, .95] than CornerNet (Law & Deng 2020), while it was 0.19 lower than that of CornerNet (Zhou et al. 2019a) in mAP@[.5, .95]. Compared with the method proposed in this paper, the accuracy of CornerNet (Law & Deng 2020) and CenterNet (Zhou et al. 2019a) were relatively lower. In detail, the proposed method outperformed CornerNet (Law & Deng 2020) with 0.056 in mAP@[.5, .95], 0.011 in mAP@[.5] and 0.053 in mAP@[.75]. When compared with CenterNet (Zhou et al. 2019a), the proposed method was 0.049, 0.030, and 0.055 higher in mAP@[.5, .95], mAP@[.5] and mAP@[.75], respectively.

Detection Samples

In the first two columns of Fig. 6, plants were detected by the original CenterNet (Zhou et al. 2019a) model and the proposed ECenterNet model. The first row showed the images that contained "dead" plants on the boundary of the image. As can be seen from the first row in Fig. 6, the boundary box regressed by the original CenterNet model was larger than the ground truth boundary box, and its category score was only 0.82. In contrast, the ECenterNet's regression of the bounding box was more accurate as shown in the first row and second column in Fig. 6. Moreover, the category score of the boundary box was 0.95, which was also higher than that
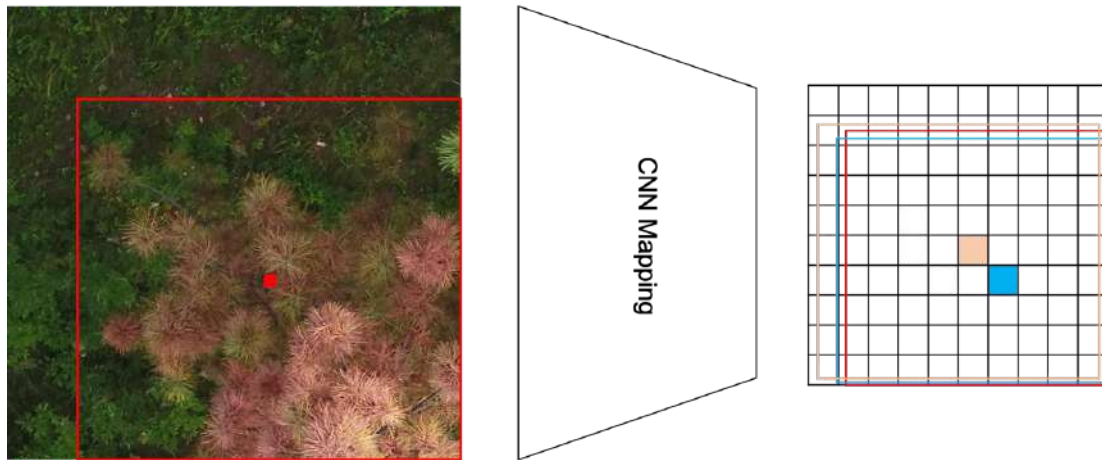
Fig. 5: Red bounding box is the ground truth box; The yellow pixel in the feature map is the positive sample produced by the rule of the original CenterNet, and the yellow bounding box is the related box predicted by this positive sample; the Blue pixel is the neighbor pixel of the yellow one, and the blue bounding box is the related bounding box of the blue pixel; IoU between red and blue bounding box is larger than IoU between red and yellow bounding box.

Table 2: Detection results comparison using different frameworks and network architectures.

Method	backbone	mAP@[.5]	mAP@[.75]	mAP@[.5, .95]
Faster RCNN	ResNet-101	0.693	0.535	0.472
SSD	ResNet-101	0.573	0.489	0.451
RetinaNet	ResNet-101-FPN	0.724	0.546	0.480
CornerNet	Hourglass-104	0.722	0.559	0.491
CenterNet	ResNet-101	0.703	0.557	0.498
ECenterNet (Ours)	ResNet-101	0.733	0.612	0.547

mAP stands for mean average precision.

of the original CenterNet. It could be seen from the second row in Fig. 6, that the original CenterNet might not be able to detect objects, which were very small in the image, while ECenterNet could successfully detect them from the whole image. It could be seen from the third row in Fig. 6 that some plant objects could not be detected by the original CenterNet, while ECenterNet detected them successfully. In addition, compared with ground truth, ECenterNet's boundary box regression was more accurate for most objects.

DISCUSSION

Detection Accuracy with Different IoU

Fig. 7(a-c) shows the precision-recall curves when the IoU thresholds are 0.5, 0.7, and 0.9, respectively. Compared with the original CenterNet, the improvement (area surrounded by the red line and the green line) of mAP (area under the curve) of the proposed method increased with the increase of IoU, suggesting that the proposed method had higher predictive power than original CenterNet (larger IoU indicated

the more accurate location of an object). On the one hand, strategy CSS ensured that the newly calculated bounding box was more accurate for objects on the boundary of the image after affine transformation, on the other hand, the training strategy in PPCM enabled to choose of a more suitable pixel with a higher predicted IoU formed by predicted bounding box and ground truth to represent the object. Both of these two strategies improved the accuracy of position prediction to a certain extent.

Architecture Ablation and Diagnosis

To demonstrate the effectiveness of the method proposed in this paper, different supplementary experiments were carried out, and the results were shown in Table 3. Adding SOCP strategy resulted in 0.009 improvements in mAP@ [.5, .95], while strategy CSS and strategy PPCM led to 0.16 and 0.24 improvement in mAP@[.5, .95], respectively. The improvement in accuracy brought by SOCP was relatively little when compared with the strategies of CSS and PPCM. The reason was that in the current test set, the side length

CenterNet   This study   Ground truth
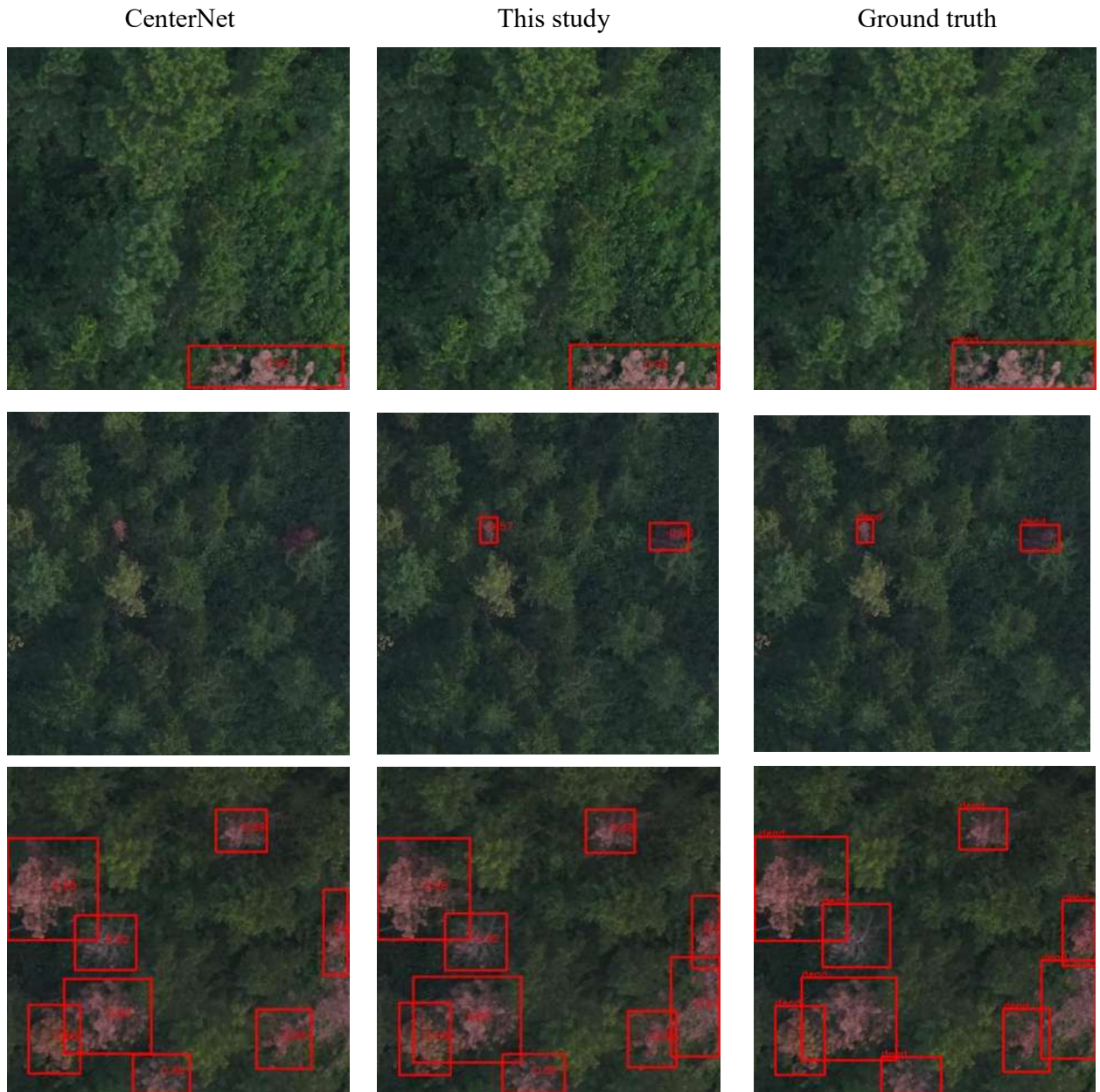
Fig. 6: Sample images of different models: the original CenterNet (Zhou et al. 2019a) model (left), the ECenterNet model (middle), and the ground truth (right).

Table 3: Detection results comparison using ablation and diagnosis architectures.

Method	mAP@[.5]	mAP@[.75]	mAP@[.5, .95]
CenterNet	0.703	0.557	0.498
+SOCP	0.722	0.568	0.507
+SOCP +CSS	0.731	0.599	0.523
+SOCP +CSS+PPCM(Ours)	0.733	0.612	0.547

of the cut testing image was mostly between 1000 and 2000 pixels, which was less likely to yield objects with two overlapping centers when rescaled to a size of 128 × 128 pixels. However, it was speculated that with the increase in UAV shooting height, there would be more objects whose center points would coincide with each other, and thus SOCP strategy would play a more important role in inferring the whole big image.

Difficulties in Detection

In the proposed model, the accuracy of detecting the dead plant was higher than that of detecting the infected plant. That was because color differences were greater among infected plants than that of dead plants, while the dead plants were always characterized by pure carmine with small color variances. Fig. 8 shows samples of images including infected and dead plants. It could be clearly seen that even if most of the infected plants were yellow, their shades were different from each other. Some infected yellow plants were

mixed with some red leaves, such as the infected plants in Fig. 8 (a, c), while the color of other infected plants was different from each other, such as the infected plants in Fig. 8 (b, d). All of these variations of infected plants add difficulty in detection. On the contrary, dead plants with red leaves could be detected easily, resulting in relatively high accuracy.

CONCLUSION

In this paper, we proposed an improved anchor-free object detection method based on CenterNet (Zhou et al. 2019a). The test results showed greater accuracy of the mAP@[.5], mAP@[.75], and mAP@[.5, .95] than the original CenterNet (Zhou et al. 2019a). The CSS was used to accurately locationing before the training stage, while SOCP and PPM were used to get a more suitable positive sample in the training stage. All the CSS, SOCP, and PPM operations helped to improve the detection accuracy. For the whole procedure, no extra parameters were introduced. In other words, the
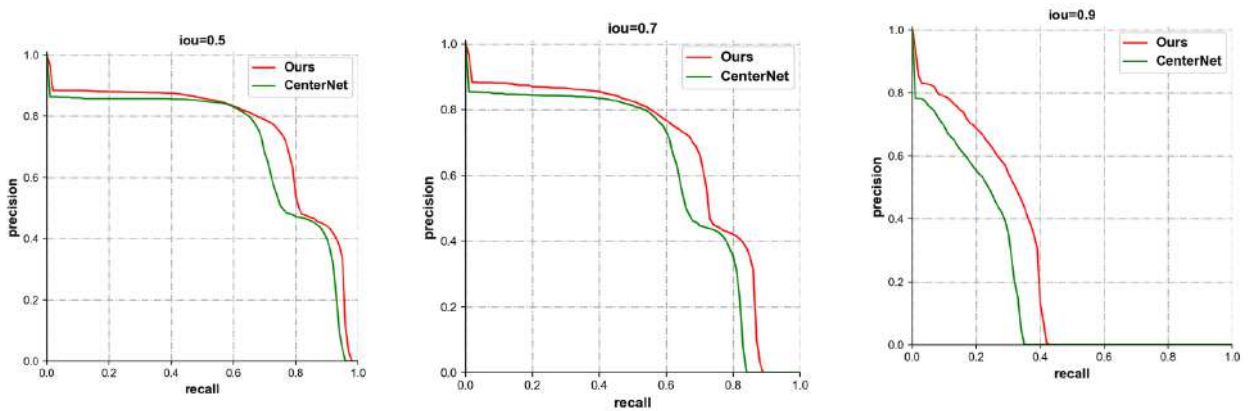
(a) Class-agnostic precision-recall curves at IoU =0.50.

(b) Class-agnostic precision-recall curves at IoU =0.70.

(c) Class-agnostic precision-recall curves at IoU =0.90.

Fig. 7: Precision-recall curves of different IoU.

Fig. 8: Samples of images including various infected plants.

accuracy of the proposed model was improved without any increase in running time and model size.

Compared with the original CenterNet, three hyperparameters were added in this paper: one was the IoU threshold of 0.9 in CSS strategy, and the other two were the number of neighborhood pixels (8 in this method) in PPCM strategy and IoU threshold (in this method, it was 0.2). These parameters were empirical values. To explore the precise values of these parameters, Neural Architecture Search (NAS) technology can be used in future searches.

With the development of optimizing technologies, this model can be continuously improved with fewer computing resources, lower costs, and faster inference speeds. In the near future, there will be a model, which adopts a deep learning method for diseased plant detection on a UAV device, to enable researchers for fast and accurate detections. At that time, UAV can transfer the detection results to a ground receiving station in a timely manner during its flight, and researchers can use these results to prevent diseases from spreading in forests or do further studies.

ACKNOWLEDGMENT

REFERENCES

Cao, L. 2015. The research progress on machine recognition of plant diseases and insect pests. Chinese Agricultural Sci. Bull., 31: 244-249.

Chen, L.C., Papandreou, G., Kokkinos, I., Murphy, K. and Yuille, A.L. 2018. DeepLab: Semantic image segmentation with deep convolutional nets, atrous convolution, and fully connected CRFs. IEEE Trans. Pattern Anal. Machine Intell., 40: 834-848.

Chiu, S.F. 1993. Investigations on Botanical Insecticides in South China: An Update. Botanical Pesticides in Integrated Pest Management, Rajahmundry, India, pp. 134-137.

Dai, J., Li, Y., He, K. and Sun, J. 2016. R-FCN: Object detection via region-based fully convolutional networks. Agronomy, 61: 379-387.

Dash, J.P., Watt, M.S., Pearse, G.D., Heaphy, M. and Dungey, H.S. 2017. Assessing very high-resolution UAV imagery for monitoring forest health during a simulated disease outbreak. ISPRS J. Photogr. Remote Sens., 131: 1-14.

Everingham, M. and Williams, C. 2010. The PASCAL Visual Object Classes Challenge 2010 (VOC2010) Part 1 – Challenge & Classification Task, International Conference on Machine Learning Challenges: Evaluating Predictive Uncertainty Visual Object Classification. Springer-Verlag, Germany, pp. 117-176.

Fuentes, A., Yoon, S., Kim, S.C. and Park, D.S. 2017. A robust deep-learning-based detector for real-time tomato plant diseases and pests recognition. Sensors, 17: 2022.

He, K., Zhang, X., Ren, S. and Sun, J. 2016. Deep residual learning for image recognition. IEEE Conf. Comp. Vision Pattern Recog., 19(1):770-778.

Krizhevsky, A., Sutskever, I. and Hinton, G. 2012. ImageNet Classification with Deep Convolutional Neural Networks, NIPS'12: Proceedings of the 25th International Conference on Neural Information Processing Systems, 3-6 December, Lake Tahoe Nevada, Curran Associates, Redhook, NY, USA, pp. 1097-1105.

Kshirsagar, V.P., Baviskar, M.R. and Gaikwad, M.E. 2011. Face Recognition Using Eigenfaces. Proceedings of 2011 3rd International Conference on Computer Research and Development, 11-13 March 2011, Shanghai, China, IEEE, Piscataway, NJ, pp. 319-323.

Law, H. and Deng, J. 2020. CornerNet: Detecting Objects as Paired Keypoints. International Journal of Computer Vision, 128: 642-656.

Lin, T.Y. and Dollar, P. 2016. Ms coco API. https://github.com/pdollar/coco.

Lin, T.Y., Goyal, P., Girshick, R., He, K. and Dollár, P. 2017. Focal loss for dense object detection. IEEE Trans. Pattern Analy. Mach. Intel., 601: 2999-3007.

Lin, T.Y., Maire, M., Belongie, S., Hays, J. and Zitnick, C.L. 2014. Microsoft COCO: Common objects in context. Europ. Conf. Comp. Vision, 75: 740-755.

Liu, W., Anguelov, D., Erhan, D., Szegedy, C., Reed, S., Fu, C.Y. and Berg, A.C. 2016. SSD: Single Shot MultiBox Detector. European Conference on Computer Vision, Springer International Publishing, New York, pp. 21-37.

Long, J., Shelhamer, E. and Darrell, T. 2015. Fully convolutional networks for semantic segmentation. IEEE Trans. Pattern Anal. Machine Intell., 39: 640-651.

Redmon, J., Divvala, S., Girshick, R. and Farhadi, A. 2016. You only look once: unified, real-time object detection, 2016 IEEE Conf. Comp. Vision Pattern Recog., 121: 779-788.

Ren, S., He, K., Girshick, R. and Sun, J. 2017. Faster R-CNN: Towards real-time object detection with region proposal networks. IEEE Trans. Pattern Anal. Machine Intell., 39: 1137-1149.

Russakovsky, O., Deng, J., Su, H., Krause, J., Satheesh, S., Ma, S., Huang, Z., Karpathy, A., Khosla, A. and Bernstein, M. 2015. ImageNet large scale visual recognition challenge. Int. J. Comp. Vision, 115: 211-252.

Szegedy, C., Wei, L., Jia, Y., Sermanet, P. and Rabinovich, A. 2015. Going deeper with convolutions. IEEE Conf. Comp. Vision Pattern Recog., 11: 1-9.

Tian, Z., Shen, C., Chen, H. and He, T. 2020. FCOS: Fully convolutional one-stage object detection. Conf. Comp. Vision Pattern Recog., 5: 13.

Zhou, X., Wang, D. and Krhenbühl, P. 2019a. Objects as Points. arXiv:1904.07850: 12.

Zhou, X., Zhuo, J. and Krähenbühl, P. 2019b. Bottom-Up Object Detection by Grouping Extreme and Center Points. 2019 IEEE/CVF Conference on Computer Vision and Pattern Recognition (CVPR). arXiv:1901.08043, pp. 850-859.

Numerical Simulations of Soil Salt Transport in the Irrigation Area of Lower Reaches of Yellow River

Xianqi Zhang*(**)(***) and Peng Chen*†

*School of Water Conservancy, North China University of Water Resources and Electric Power, Zhengzhou 450046, China

**Collaborative Innovation Center of Water Resources Efficient Utilization and Protection Engineering, Zhengzhou 450046, China

***Technology Research Center of Water Conservancy and Marine Traffic Engineering, Henan Province, Zhengzhou 450046, China

†Corresponding author: Peng Chen: 632642579@qq.com

ABSTRACT

This paper presents numerical simulations regarding the transport characteristics of soil salt. It has been recognized in recent years that the growth and output of crops in the irrigation area of the lower reaches of the Yellow River are affected by the decreased fertility of soil as a result of the transport of soil salt, due to the long-term farming, fertilization of farmland which contains a high proportion of sands. Accordingly, numerical simulations by Hydrus are carried out, in which, based on the similarity principle, two-dimensional convection-diffusion partial-differential governing equations of unsteady flow in saturated-unsaturated porous media are applied to depict the motion parameters' spatial variability of soil water in the irrigation area. And the van Genuchten equation is adopted to express the relationship between volumetric water content and soil hydraulic conductivity and negative soil water pressure. The irrigation basin of the People's Victory Canal, which is downstream of the Yellow River, is investigated in detail as an example. The findings revealed that soil salt in the irrigation region is transferred by water diffusion, with irrigation and fertilization being the primary causes of downward migration and salt accumulation. It benefits the soil in irrigation areas and protects groundwater.

INTRODUCTION

The irrigation area of the lower reaches of Yellow River goes across the North China Plain, ranging from the east of Qin River mouth to the west of Yellow River estuary, and covers 85 counties in 16 districts (cities) of Henan and Shandong provinces, serving as China's primary base of the grain production, and having played a key role in ensuring the national food security. In this area, the water resources per mu are quite limited as well as difficult to develop and utilize, making flows coming from the Yellow River important water sources for agricultural production. Large-scale agricultural irrigation originated in the 1860s, the average annual water usage was about 12 billion m^3, accounting for 20.7% of the annual runoff of the Yellow River. After running for more than 60 years, massive irrigation with hyper-concentrated Yellow River water, in addition to an irrational system for the development and utilization of regional water resources, and the backwardness in irrigation approaches and technology, leads to variation in the state of the groundwater system and soil salt transport in the irrigation areas. This results in the evolution of water ecology and environment, the

soil desertification and decline in the productivity, and the increase of potential secondary salinization, which subsequently affect the sustainable and healthy development of agriculture and the national economy in the downstream irrigation areas (Phogat et al. 2011, Yakirevich et al. 2013, Geng & Boufadel 2015, Sabri et al. 2012).

Investigations concerning the simulations of the salt transport in the irrigation areas have been extensively carried out and productive results have been obtained in recent years (Ramos et al. 2011) Theoretical study of soil salt transport was initially based on Darcy's law which depicts that motion of the salt transport is primarily governed by patterns of the water motion and the salt dissolution (Maziar et al. 2010). Based on Fick's first law, Gardner and Bresler derived the one-dimensional soil solute transport equation. R.Nielsen, Van. Genuchten etc. proposed a movable-immovable water model based on physical nonequilibrium transport models. A series of models developed by the U.S. Salinity Laboratory, for instance, SWMS, HYDRUS, etc., have been widely applied, contributing to fairly good simulations in solute transport in the saturated-unsaturated porous media.

Moreover, Ye (1990) analyzed soil salinity dynamics under infiltration conditions through the simplified transfer function model. Yao and Zhu (2001) established a model of soil salt accumulation and transport under the condition of evapotranspiration. Hu and Gao (2002) constructed a soil transport model and explored the characteristics of salt transport in inland drought regions, according to the principle of water-salt balance. By combining experimental investigations with theoretical analyses, Luo et al. (2008) simulated the salt transport of the cumulated infiltration and the drip irrigation from a point source. Besides, a large number of Chinese researchers utilized SWMS, HYDRUS, and other models to simulate the salt transport in some particular regions (Joseph et al. 2015, Jiang et al. 2011, Dabach et al. 2013, Nachabe et al. 1999). Consequently, a series of valuable results have been obtained regarding simulations of salt transport under various circumstances, for example, the stages for crops' growth, different soil structures, irrigation systems, etc., having laid a solid foundation for further investigations (Chekirbane et al. 2015, Luo et al. 2013, Selim et al. 2013, Morales et al. 2014, Ramos et al. 20110).

It is widely accepted that the properties of soil salt transport, in principle, are complex and vary with multiple factors including not only its concentration gradient, soil properties, plant characteristics, etc., but also the patterns of regional irrigation, tillage, fertilization, and the variations of groundwater, etc. (Medved & Cerny 2015, Comina et al. 2011, Clemente et al. 1997, Russo et al. 2015, Chen et al. 2014). Characterized by its unique nature, geology, groundwater environment, and farming conditions, and combined with the impact of irrigation patterns and planting structures, the downstream irrigation areas of Yellow River significantly differ from other areas in terms of the characteristics of soil salt transport. Thereby, salt transport in the particular areas was simulated to reveal the underlying mechanism and the corresponding migration process. The investigations and results presented in the paper may serve as a theoretical basis and technical support for soil improvement, water-saving irrigation, and the sustainable use of water and land resources in the downstream irrigation areas of the Yellow River.

MATERIALS AND METHODS

Research Method

At the field scale in the irrigation area, the physical and chemical properties of soil are important factors that affect water leakage and salt leaching to different degrees in the horizontal and vertical directions. Besides, the process of soil salt transport is complex and affected by multiple factors, such as soil moisture content, the interaction between

salt and soil, salt transformation, root absorption, and so on. Generally, the motion of soil salt is primarily motivated by interactions of convection and hydrodynamic diffusion. The convection-diffusion equation is thereby widely used in describing the dynamical distributions of soil salt, based on which the problems, challenging for some field trials, may also be solved.

Parameters of the Water Motion in Soil

The movement of water in soil generally follows Darcy's law and satisfies the principle of conservation of mass (the continuity equation), based on which the soil water movement can thus be yielded. The soil hydraulic conductivity K is a function of soil moisture content or negative soil water pressure, and specific moisture capacity (water capacity) C is negative reciprocally of the slope of the soil moisture characteristic curve (SMC) at a particular moisture content θ. Empirical formulae based on experimental data are widely used when describing the relationship between negative soil water pressure h, moisture content θ, and soil hydraulic conductivity K due to their complexity. The relevant relationship represented by the modified van Genuchten equation is shown in Fig. 1.

$$\theta(h) = \begin{cases} \theta_a + \dfrac{\theta_m - \theta_a}{(1+|\alpha h|^n)^m} & h < h_s \\ \theta_s & h \geq h_s \end{cases} \quad \ldots(1)$$

$$K(h) = \begin{cases} K_s K_r(h) & h \leq h_k \\ K_k + \dfrac{(h-h_k)(K_s - K_k)}{h_s - h_k} & h_k < h < h_s \\ K_s & h \geq h_s \end{cases} \quad \ldots(2)$$

Where,

$$K_r = \frac{K_k}{K_s}\left(\frac{S_e}{S_{ek}}\right)^{1/2}\left[\frac{F(\theta_r)-F(\theta)}{F(\theta_r)-F(\theta_k)}\right]^2 \quad \ldots(3)$$

$$F(\theta) = \left[1-\left(\frac{\theta-\theta_a}{\theta_m-\theta_a}\right)^{1/m}\right]^m \quad \ldots(4)$$

$$m = 1 - 1/n, \, n > 1 \quad \ldots(5)$$

$$S_e = \frac{\theta-\theta_r}{\theta_s-\theta_r} \quad \ldots(6)$$

$$S_{ek} = \frac{\theta_k-\theta_r}{\theta_s-\theta_r} \quad (7)$$

$$h_s = -\frac{1}{\alpha}\left[\left(\frac{\theta_s-\theta_a}{\theta_m-\theta_a}\right)^{-1/m}-1\right]^{1/n} \quad \ldots(8)$$
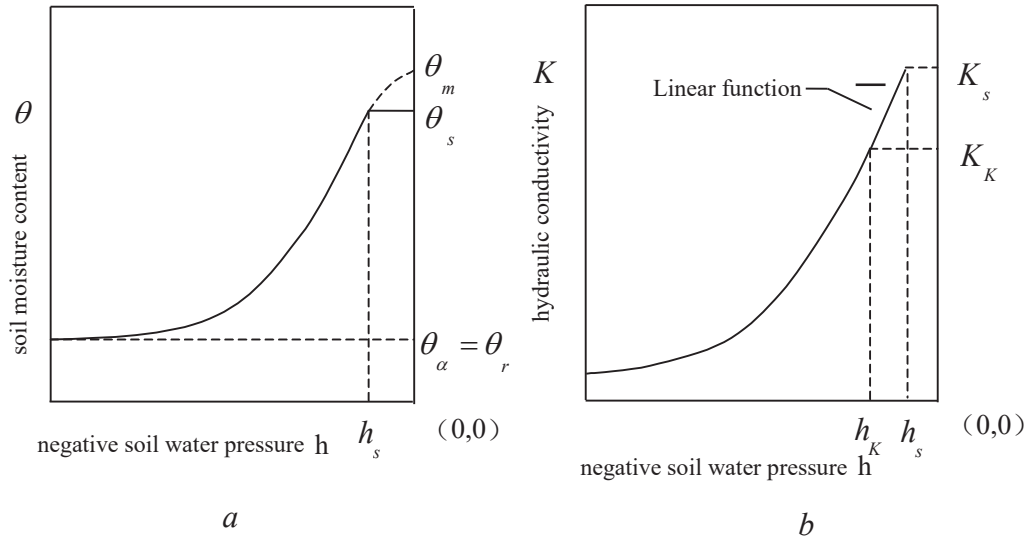
Fig. 1: Relationship between soil moisture and soil hydraulic conductivity and soil negative pressure.

$$h_k = -\frac{1}{\alpha}\left[\left(\frac{\theta_k - \theta_a}{\theta_m - \theta_a}\right)^{-1/m} - 1\right]^{1/n} \qquad \ldots(9)$$

Where, θ_r is the residual volumetric water content, i.e., the maximum molecular moisture holding capacity) $[L^3L^{-3}]$, θ_s is saturated volumetric water content $[L^3L^{-3}]$, K_r is the relative unsaturated hydraulic conductivity, K_s is the saturated hydraulic conductivity $[LT^{-1}]$, S_e is the saturation; θ_a with initial setting $\theta_a = \theta_r$ and θ_m are two values assumed to be on the curve of SMC (between negative soil water pressure and hydraulic conductivity), and α, m are empirical constants.

Soil solute transport equation

The two-dimensional convection-diffusion partial differential governing equation for unsteady flow in saturated/unsaturated porous media is,

$$\frac{\partial\theta c}{\partial t} + \frac{\partial\rho s}{\partial t} = \frac{\partial}{\partial x_i}\left(\theta D_{ij}\frac{\partial c}{\partial x_j}\right) - \frac{\partial q_i c}{\partial x_i} + \mu_w \theta c +$$

$$\mu_s \rho s + \gamma_w \theta + \gamma_s \rho - S c_s \qquad \ldots(10)$$

in which c is the solute concentration of soil solution $[ML^{-3}]$, s is the concentration of solid solute adsorbed onto soil particles, ρ is the soil bulk density $[ML^{-3}]$, q_i is the Darcy velocity along the direction x_i $[LT^{-1}]$, μ_w and μ_s are the rate constants for the first-order reaction of liquid and solid solute $[T^{-1}]$, γ_w and γ_s are rate constants for the zero-order reaction

of liquid solute $[ML^{-3}T^{-1}]$ and solid solute $[T^{-1}]$, S represents the source/sink term, c_s is the solute concentration of source/sink term $[ML^{-3}]$, D_{ij} is hydrodynamic dispersion coefficient for saturated-unsaturated water $[L^2T^{-1}]$.

The adsorption isotherm model is used for calculation, and the concentration of solute and solid solute adsorbed onto soil particles c, s satisfy

$$s = kc \qquad \ldots(11)$$

in which k is the empirical soil adsorption coefficient $[L^3M^{-1}]$.

In saturated-unsaturated porous media, the continuity equation for isothermal Darcy flow can be expressed as,

$$\frac{\partial\theta}{\partial t} = -\frac{\partial q_i}{\partial x_i} - S \qquad \ldots(12)$$

Substituting Eq.(11),(12) to Eq. (9), it is yielded

$$-\theta R\frac{\partial c}{\partial t} - q_i\frac{\partial c}{\partial x_i} + \frac{\partial}{\partial x_i}\left(\theta D_{ij}\frac{\partial c}{\partial x_j}\right) + Fc + G = 0, \quad \ldots(13)$$

In which

$$F = \mu_w \theta + \mu_s \rho k + S$$
$$G = \gamma_w \theta + \gamma_s \rho - S c_s \qquad \ldots(14)$$

where R is the Delay factor

$$R = 1 + \frac{\rho k}{\theta} \qquad \ldots(15)$$

Moisture content θ and Darcy flow rate q_i can be obtained from the water flow equation so that a solution to Eq. (13) is obtained.

Parameter Calibration

HYDRUS-2D is used to simulate the characteristics of soil salt transport, where the soil in the spatial distribution is inhomogeneous and allows variability. According to the similarity principle proposed by Miller and Simmons, the spatial variability of motion parameters of water in unsaturated soil within infiltration areas is described by calibration factors during simulation. That is to say, an appropriate scale factor is carefully selected so that the relationship between $\theta(h)$ and $K(h)$, of property of spatial variability, can be calibrated and thereafter changed into a relationship between $\theta^*(h^*)$ and $K^*(h^*)$ which is applicable throughout the soil areas. As a consequence, the updated and homogeneous formula for the relationship after parameter calibration can describe the old inhomogeneous relationships in space. The linear model in which the spatial variability of soil water motion is defined by introducing three independent calibration coefficients is,

$$
\begin{aligned}
K(h) &= \alpha_K K^*\left(h^*\right) \\
\theta(h) &= \theta_r + \alpha_\theta\left[\theta^*\left(h^*\right) - \theta_r^*\right], \\
h &= \alpha_h h^*
\end{aligned}
\qquad \ldots(16)
$$

Where, α_θ, α_h and α_K are, respectively, calibration coefficients of moisture content, negative soil water pressure, and hydraulic conductivity. In most cases, these three coefficients are independent, while being dependent on each other in some specific cases. In an initial situation, $\alpha_\theta = 1$, within the meanwhile, and $\alpha_K = \alpha_h^{-2}$. The parameters for solute transport include longitudinal dispersion coefficient D_L, lateral dispersion coefficient D_T, molecular diffusion coefficient NO_3^--N in free water D_w, mineralization rate of organic nitrogen k_{min}, biological immobilization rate k_{im} NO_3^--N, and k_{den} denitrification rate NO_3^--N.

CASE STUDY

Description of the Irrigation Areas Studied

People's Victory Canal is one of the important irrigation areas the downstream of Yellow River, with longitude and latitude respectively of 113°31'-114°25' E and 35°0'-35°30'N, whose boundaries reach Yellow River to the south, Wei River to the north, Communistic Canal to the west, and Red Flag Main Canal to the east. Most parts of the irrigation areas are plains resulting from erosion, flooding, and siltation of the Yellow River, where moisture soils account for 75%, aeolian sandy soils 12.5%, and solonchak-like soils 8%. The irrigation area has a warm temperate continental monsoon climate with 4 distinct seasons, where spring is relatively dry, summer windy with frequent rainfall, and autumn of crisp air, and being beneficial for the crops' growth with an annual rainfall

of around 550-670 mm. The primary economic crops planted are wheat, rice, peanuts, cotton, etc. The farming patterns produce two crops a year, with wheat planted in winter while shifted to corn, peanuts, and rice in summer. Since 1952 when the irrigation area was completed, it covers, in total, 47 townships (towns) and 973 villages, with an overall population of 265.4 million. Besides, its average annual quantity of water drawing from the Yellow River amounts to 378 220 000 m^3, and the irrigation area amounts to 1422 km^2. It thus has become one of the main regions for China's Grain Production.

Soil Hydraulic Parameters

The soil of the People's Victory Canal is primarily silt loam. Considering the impact of spatial variability of soil hydraulic parameters on salt leaching at the field scale, the effect of soil hydraulic parameters of different degrees of spatial variability on the leaching NO_3^--N is to be studied, where the degrees of variability are determined based on the following criterion: weak variability is assumed when the coefficient of variation $C_V < 0.1$, while moderate as $0.1 < C_V < 1$; and it is assumed that soil clay, silt, and soil bulk density follow the normal distribution. During the simulations by Hydrus-2D, the Monte Carlo method is used to randomly generate a certain number of soils with weak and moderate variability. The corresponding soil hydraulic parameters are thereafter obtained by the program Rosetta. The van Genuchten-Mualem model is used to describe parameters of the characteristic curve for soil moisture and unsaturated hydraulic conductivity. Parameters for solute transport, such as D_L, D_T, D_W, k_{min}, k_{im} and k_{den} which are defined previously, are obtained via field experiments, monitoring, and empirical formulae. When simulating the migration of nitrate ions underground under natural conditions within a year, radiation, temperature, humidity, and other meteorological data are inputs to interpret rainfall from the upper boundary, and the potential evapotranspiration ETP can be automatically calculated according to the Penman-Monteith equation defined within the model.

Case Settings

The variations of nitrate compounds in the irrigation areas are significant, primarily resulting from excessive fertilization and flooding irrigation during agricultural production. In terms of salt transport simulation of groundwater in the irrigation regions, the main attention is paid to the transport process of nitrate. The data concerning weather conditions used for simulation is based on monitoring data published by the small weather stations and China Meteorological Administration, and parameters concerning the soils and irrigation status are determined according to field investigations,

monitoring data, and practical production activities in the irrigation area. Two cases to obtain the status of downward migration of nitrate iron are set for the simulations, i.e.

Case *I*: conditions within one week after a process of irrigation and fertilization;

Case *II*: conditions within one year under natural circumstances, more specifically, under natural rainfalls.

RESULTS AND DISCUSSION

Results of the Simulations

When simulating the status of downward migration for nitrate ions within one week after a process of irrigation and fertilization, only salt transport is simulated by referring to variations both in groundwater level and depth of salt transport and ignoring the water uptake of the root. To determine the concentration of irrigation water mixing with fertilizers, it is of priority to refer to the local irrigation quota and actual irrigation conditions in irrigation to conduct generalized conversion. Set the head of the upper boundary fixed, and the lower as free drainage. Model lengths are set with 10m in depth and 5m in width for simulations.

Results Under Case *I*

Figs. 2-9 mainly depicts the transport status of nitrate ion within one week after applying a process of irrigation and fertilization.

Based on the actual situation of the irrigation area, the nitrate ion concentration in water after irrigation and fertilization is 0.07 M.L^{-3}. The ions have migrated from the surface downward to a soil depth of 60 cm within 24 h, while the concentration is decreased from top to downward and various zones of ion concentration of different thicknesses are formed at the 24th h.

From the 24th to 168th h, with the immigration of ions continuously heading downwards, zones of different ion concentrations have been moving in the same way and
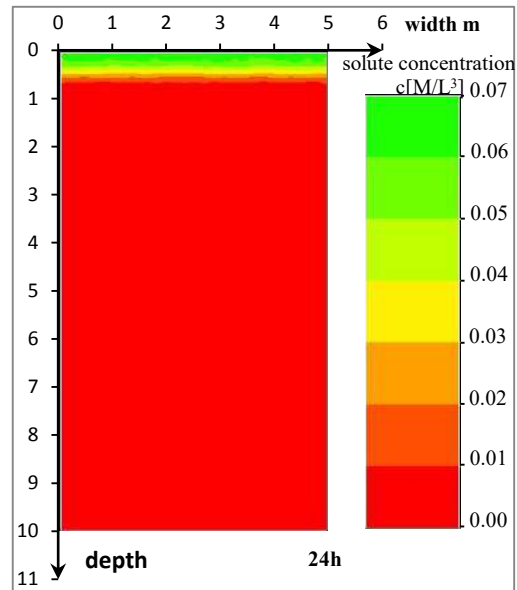
Fig. 3: Nitrate concentration at the 24th h.
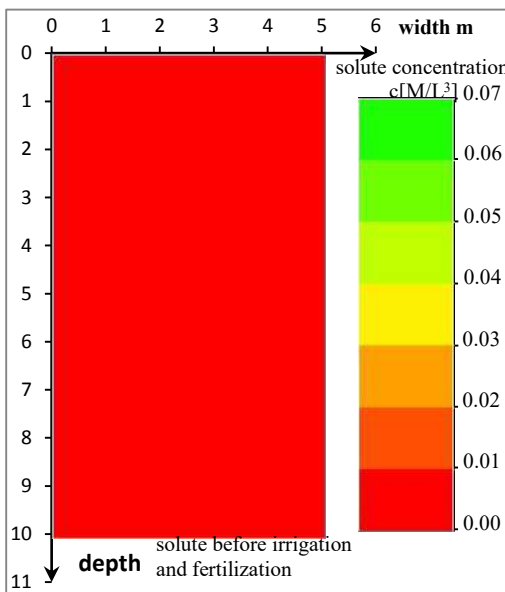
Fig. 2: Before irrigation and fertilization.
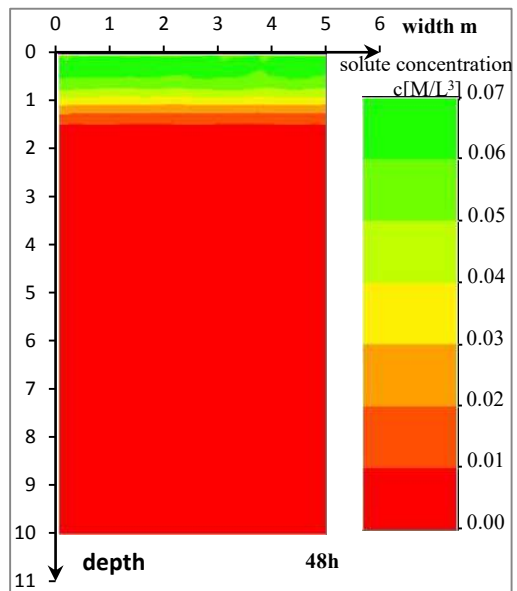
Fig. 4: Nitrate concentration at the 48th h.
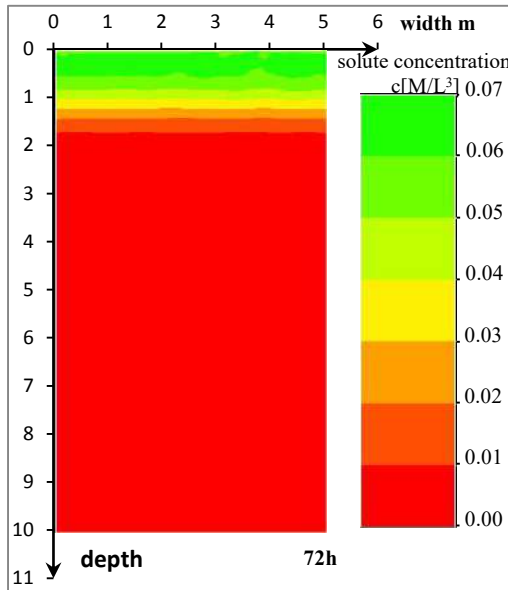
Fig. 5: Nitrate concentration at the 72nd h.
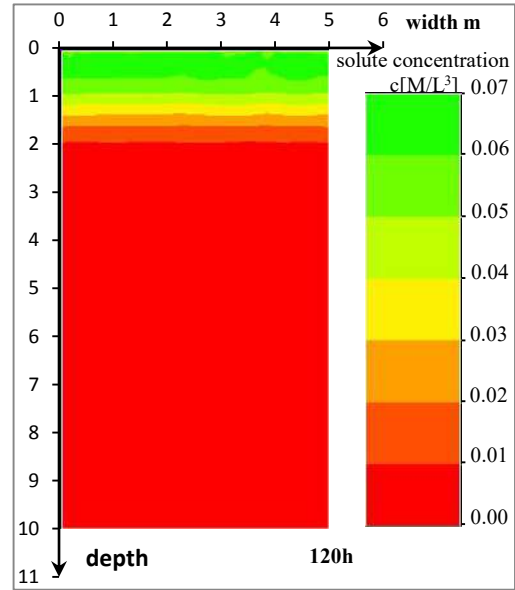
Fig. 7: Nitrate concentration at the 120th hour.
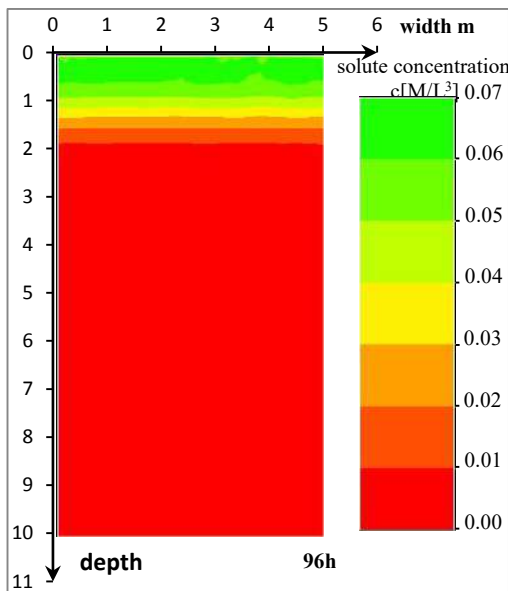
Fig. 6: Nitrate concentration at the 96th hour.
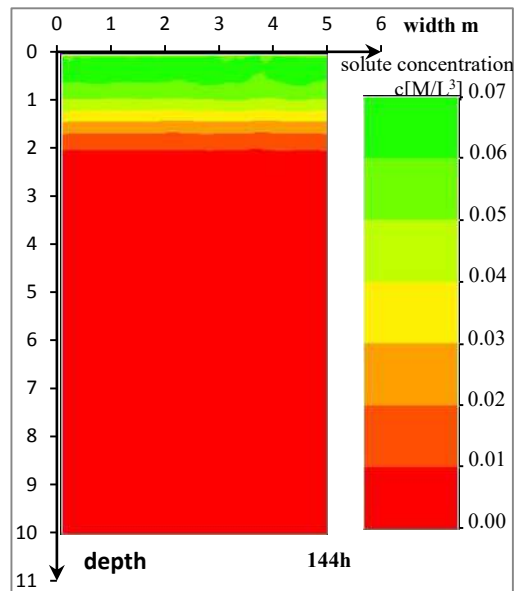
Fig. 8: Nitrate concentration at the 144th hour.

becoming increasingly thick. At the 168th h, the zone of nitrate ions with concentrations ranging from 0.01 M.L^3~0.02 M.L^{-3} is moving downward to the depth of 210 cm, and the concentration of ions underneath 98 cm of the ground surface is ranging from 0.05 M.L^{-3}-0.07 M.L^{-3}.

Results of Case *II*

Based on the average meteorological parameters within various years, where the precipitation is low in April and September, and high in May, July, October, and November, the simulated data of average precipitation are close to realistic situations without considering the effect of groundwater on soil moisture content. Figs. 10 to 22 are about the simulated transport of nitrate ions in irrigation soil within one year under natural conditions.

Based on the figures, the downward transport rate of
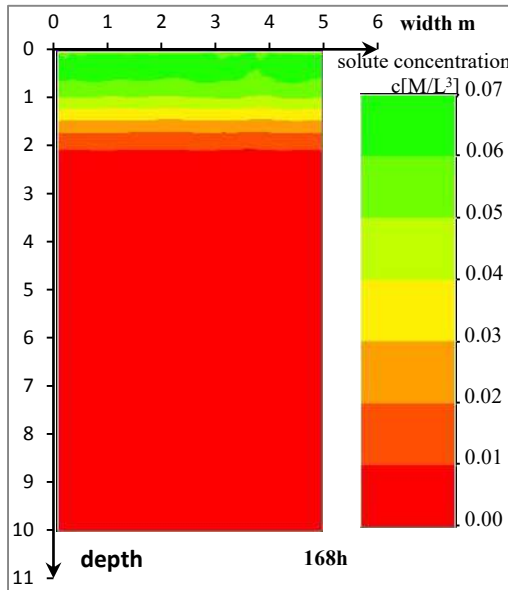
Fig. 9: Nitrate concentration at the 168th hour.
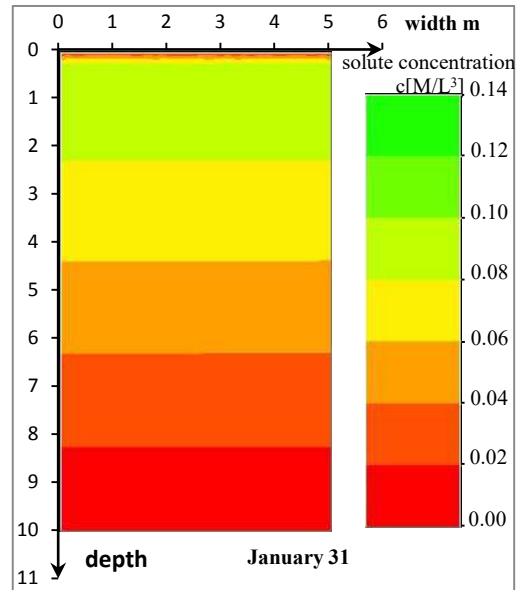
Fig. 11: Solute status on January 31st.
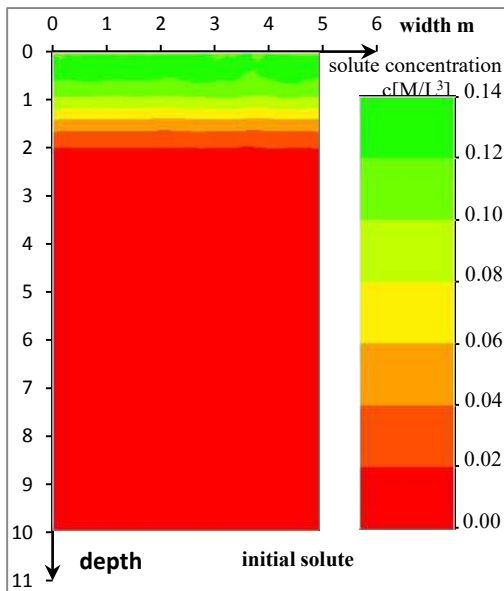
Fig. 10: Initial state of the solute status.
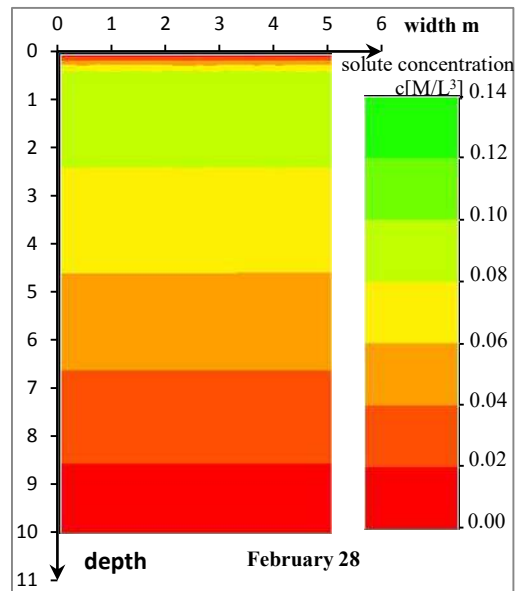
Fig. 12: Solute status on February 28th.

soil nitrate ions is fairly slow without precipitation in January, February and March. Until March 31st, nitrate ions have migrated 5 cm downward from the surface, and the subsurface concentration of nitrate ions at the depths from 5 to 34cm, which increases with depth, has become lower than the initial $0.08 M.L^{-3}$. Moreover, precipitation in April results in an increased transport rate of the soil nitrate ions.

And the downward migration reached a depth of 36 cm on April 30th.

Different levels of precipitation in May, July, September, October, and November have resulted in continuously downward migration of the nitrate ions, subsequently resulting in an increased concentration of nitrate ions in deeper layers. Until December 31st, the transport distance has reached a
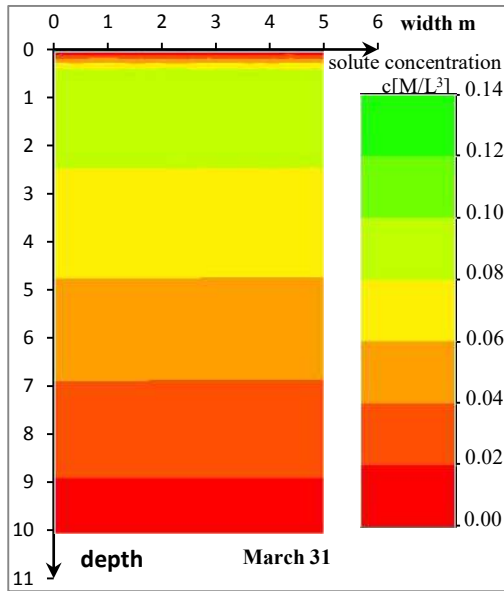
Fig. 13: Solute status on March 31st.
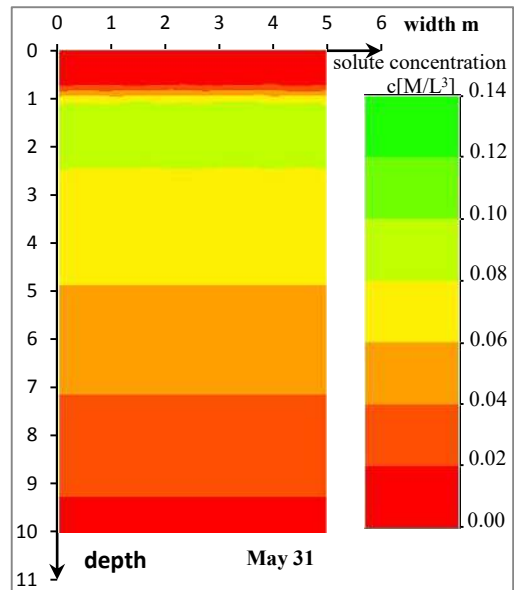
Fig. 15: Solute status on May 31st.
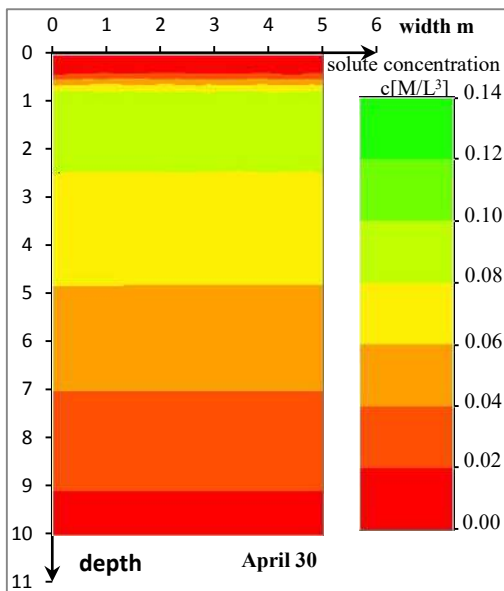
Fig. 14: Solute status on April 30th.
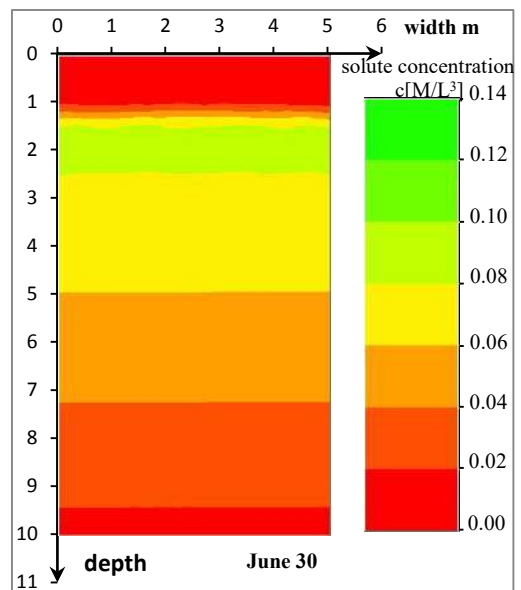
Fig. 16: Solute status on June 30th.

depth of 190 cm.

DISCUSSION

Based on the previous simulations regarding the salt transport of soil in the irrigation area of the People's Victory Canal, it was illustrated that the concentration of nitrate ions decreases with depth while the nitrate ions migrate downward along the soil water. Due to multiple factors, for instance, soil filtration and root absorption of plants, the concentration of nitrate ions in deeper layers does not reach a certain value while soil water transports downward to a certain depth, indicating that the transport of nitrate ions in soil layers lags behind water migration. Moreover, nitrate ions reach deeper layers over time with a decreasing concentration in lower layers as a consequence of different interferences from uptake by crops.
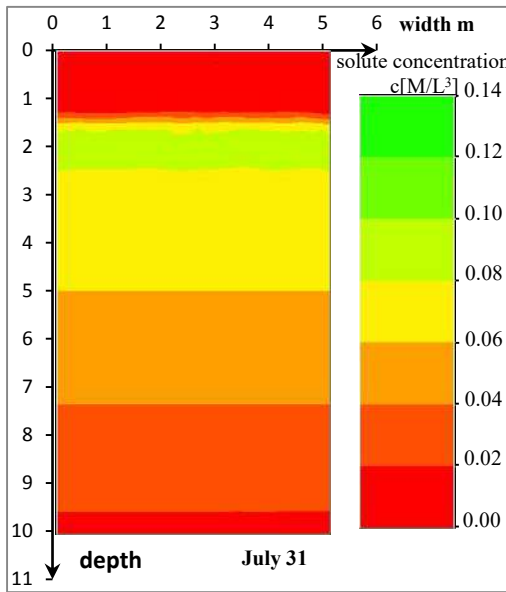
Fig. 17: Solute status on July 31st.
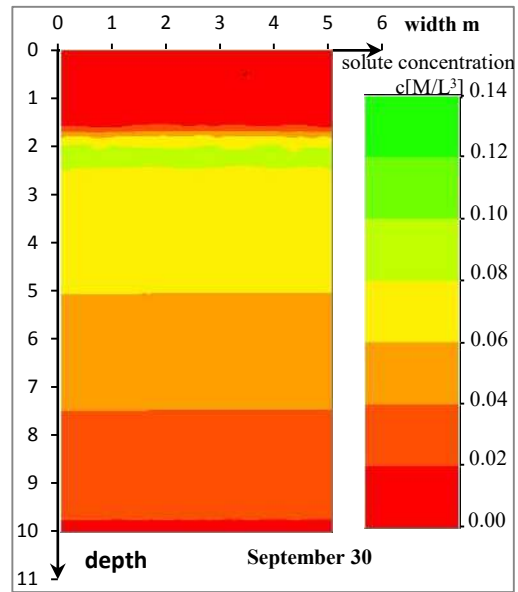
Fig. 19: Solute status on September 30th.
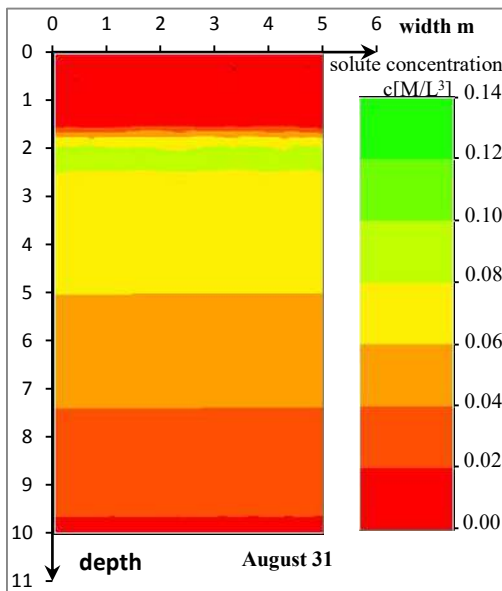
Fig. 18: Solute status on August 31st.
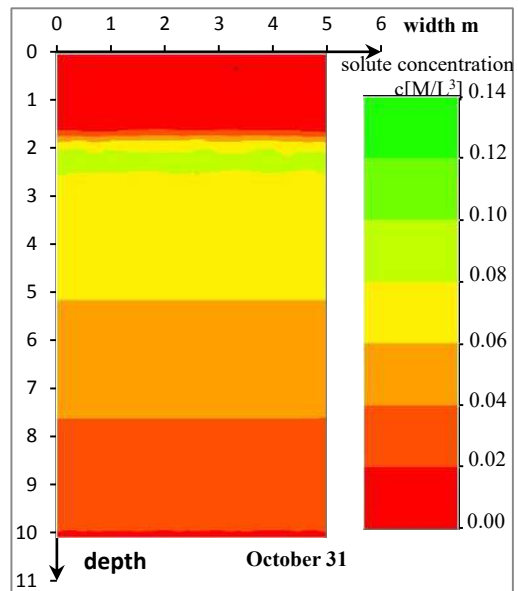
Fig. 20: Solute status on October 31st.

Observation points are set along the direction of soil depth so that variation of salt concentration can be monitored. A brief layout of the observation points is shown in Fig. 23 and the variations of solute concentration at different observation points are depicted in Fig. 24.

As can be seen from Figs. 23 and 24, after a process of irrigation and fertilization, observation point No. 3, being closest to the surface, increases rapidly in salt concentra-

tion while remaining steady in concentration after reaching to 0.06 mg/cm^3 at 12th h. Within one week, the concentrations of nitrate ion at Nos. 1, 4, and 6 points have been gradually increased over time and ultimately become steady. After one week, with no concentration of nitrate ion at No. 2, 5, and 7, the highest concentration appears at No. 3 while the lowest at No. 1, indicating that the salt is mainly concentrated within the depth below point No. 3 and above No.1. Under natural
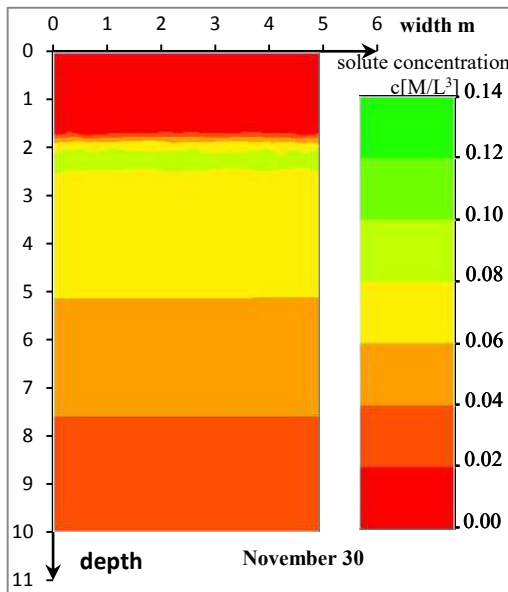
Fig. 21: Solute status on November 30th.
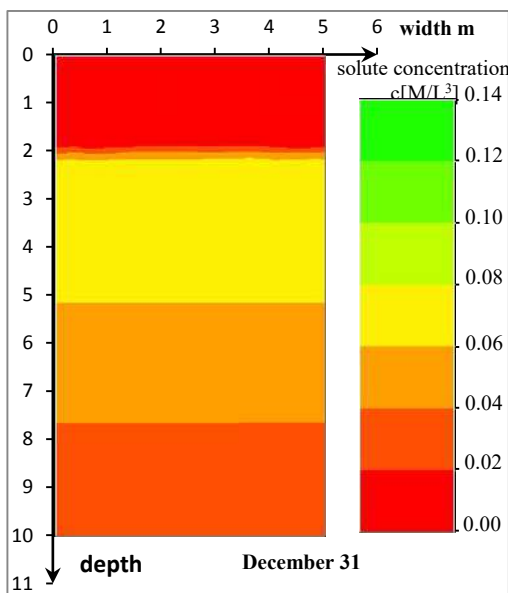
Fig. 22: Solute status on December 31st.

precipitation, a certain concentration (or a certain amount) of nitrate ions on the surface may move downwards to deeper soil layers along with the infiltration of natural precipitation, resulting in a continuous increase of nitrate ions concentration in deeper layers. Based on the simulations of natural precipitation, it was indicated that the migration of nitrate ions downwards within a year can reach a depth of 190 cm and cause a continuous increase in the concentration of nitrate
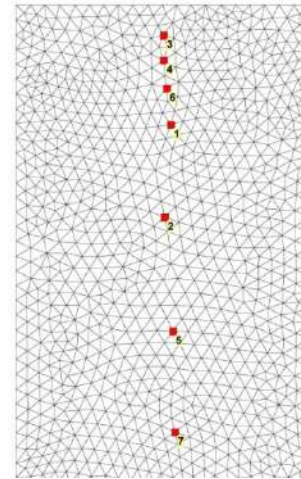
Fig. 23: Layout of the observation points.
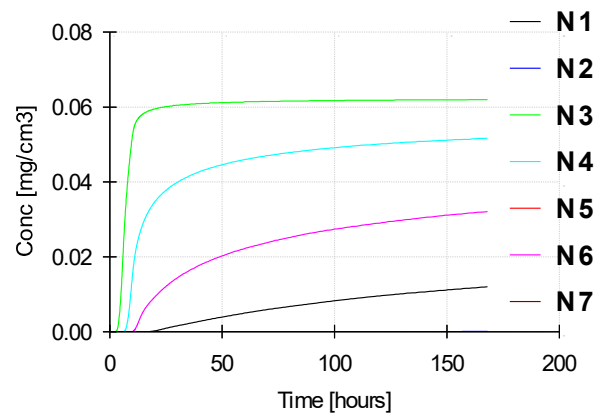
Fig. 24: Variation of concentration at observation points.

ions in deeper layers, which, consequently, may significantly affect the quality of groundwater.

CONCLUSIONS

Based on the two-dimensional convection-diffusion partial differential equations of unsteady flow in saturated-unsaturated porous media and the van Genuchten equation, simulations by Hydrus have been carried out in this paper regarding soil salt transport in the irrigation area of the People's Victory Canal located in the downstream of Yellow River. Results in the present paper illustrate that the salt in the irrigation area migrates downwards along with the diffusion of water in soils, to a depth that increases with the downward depth of the transported water. Meanwhile, a deeper depth tends to be with a lower concentration of soil salt. However, when compared with the situation before irrigation and fertilization, both the rate of transporting downwards and the depth with the same

level of concentration of soil salt obviously increase after a process of irrigation and fertilization. Meanwhile, the downward salt, which moves slowly under conditions of surface seepage like natural precipitation, results in a continuous increase of the concentration in deeper layers due to the soil adsorption. Based on the present paper, it is recommended that measures can be taken to strengthen rational management mechanisms for water diversion irrigation, improve irrigation methods and farming patterns in some areas, and apply scientific use of fertilizers, aiming at reducing the transport quantity of salt into the soil, protecting the environmental quality of groundwater, and facilitating sustainable use of soil and water resources in the irrigation area.

ACKNOWLEDGMENT

REFERENCES

Chekirbane, A., Tsujimura, M. and Kawachi, A. 2015. 3D simulation of a multi-stressed coastal aquifer, northeast of Tunisia: Salt transport processes and remediation scenarios. Environ. Earth Sci., 73(4): 1427-1442.

Chen, L.J., Feng, Q. and Li, F.R. 2014. A bidirectional model for simulating soil water flow and salt transport under mulched drip irrigation with saline water. Agric. Water Manag., 146: 24-33.

Clemente, R.S., Prasher, S.O. and Bonnell, R.B. 1997. Application of PESTFADE to simulate salt movement in soils. Canad. Water Resour. J., 22(2): 167-184.

Comina, C., Cosentini, R. and Della,V.G. 2011. 3D-electrical resistivity tomography monitoring of salt transport in homogeneous and layered soil samples. Acta Geotech., 6(4): 195-203.

Dabach, S., Lazarovitch, N. and Simunek, J. 2013. Numerical investigation of irrigation scheduling based on soil water status. Irrig. Sci., 31: 27-36.

Geng, X.L. and Boufadel, M.C. 2015. Numerical modeling of water flow and salt transport in bare saline soil subjected to evaporation. J. Hyrdrol., 524: 427-438.

Hu, A.Y. and Gao, J. 2002. Soil water and salt balance model for an irrigation district in the arid and inland region. Adv. Water Sci., 13(6): 726-729 (in Chinese)

Jiang, J., Feng, S.Y. and Huo, Z.L. 2011. Application of the SWAP model to simulate water-salt transport under deficit irrigation with saline water. Math. Comp. Model., 54(3-4): 902-911.

Joseph, M., Subrahmanyam, B. and Ebenezer, S. 2015 Seasonal variability of salinity and salt transport in the northern Indian Ocean. J. Phys. Oceanogr., 45(7): 1947-1966.

Luo, J.F., Hans, J.G. and Lambertus, M.J. 2013. 3D modeling of saline groundwater flow and transport in a flooded salt mine in Stassfurt, Germany. Mine Water Environ., 32(1): 71-77.

Luo, P, Zhang, F.C. and Li, X.J. 2008. Experimental study on the influence of infiltration head on water and salt transportation in saline-alkali soil. Water-Saving Irrig., 6: 4-7 (in Chinese)

Maziar, M, Kandelous, R. and Simunek, J. 2010. Numerical simulations of water movement in a subsurface drip irrigation system under field and laboratory conditions using HYDRUS-2D. Agric. Water Manag., 97(7): 1070-1076.

Medved, I. and Cerny, R.J. 2015. Role of time relaxing in a one-dimensional diffusion-advection model of water and salt transport. Adv. Math. Phys., 35: 307-312.

Morales, I., Atoyan, J.A. and Amador, J.A. 2014. Transport of pathogen surrogates in soil treatment units: Numerical model. Water, 6(4): 818-838.

Nachabe, M.H., Ahuja, L.R. and Butters, G. 1999. Bromide transport under sprinkler and flood irrigation for no-till soil condition. J. Hydrol., 214: 8-17.

Phogat, V., Yadav, A.K., Malik, R.S., Kumar, S. and Cox, J.J. 2011. Simulation of salt and water movement and estimation of water productivity of rice crop irrigated with saline water. Paddy Water Environ., 8(4): 333-346.

Ramos, T.B, Simunek, J., Goncalves, M.C., Martins, J.C., Prazeres, A., Castanheira, N.L. and Pereira, L.S. 2011. Field evaluation of a multi-component solute transport model in soils irrigated with saline waters. J. Hyrdrol., 407(1-4): 129-144.

Ramos, T.B., Simunek, J. and Goncalves, M.C. 2011. Two-dimensional modeling of water and nitrogen fate from sweet sorghum irrigated with fresh and blended saline waters. Agric. Water Manag., 111: 87-104.

Russo, D., Laufer, A. and Bardhan, G. 2015. Salinity control in a clay soil beneath an orchard irrigated with treated wastewater in the presence of a high water table: A numerical study. J. Hydrol., 531: 198-213.

Sabri, K., Hachicha, M., Bouhlila, R. and Batlle, J.J. 2012. Simulation of water and salts dynamics in Bouhajla (Central Tunisia): Exceptional rainfall effect. Soil Water Res., 7(1):36-44.

Selim, T., Bouksila, F. and Berndtsson, R. 2013. Soil water and salinity distribution under different treatments of drip irrigation. Soil Sci. Soc. Am. J., 77(4): 1144-1156.

Yakirevich, A., Weisbrod, N., Kuznetsov, M., Villarreyes, C.A.R, Benavent Chavez, A.M. and Ferrando, D.J. 2013. Impact of solute recycling on groundwater salinization under irrigated lands: A study of the alto Piura aquifer Peru. J. Hydrol., 482: 25-39.

Yao, D.L. and Zhu, J.S. 2001. Model on water-salt movement and application in the field of arid land. J. Desert Res., 21(3): 286-290 (in Chinese)

Ye, Z.T. 1990. The utilization of the salt transfer function model in studying water-salt movement in soil layers under infiltration. J. Hydraul. Eng., 2: 4-9 (in Chinese)

Atmospheric Particle Distribution on Tree Leaves in Different Urban Areas of Aksu City, Northwest China

Kalbinur Nurmamat*, Ümüt Halik*†, Aliya Baidourela** and Tayierjiang Aishan*

*College of Resource & Environment Sciences, Key Laboratory of Oasis Ecology, Xinjiang University, Urumqi 830046, China
**College of Forestry and Horticulture, Xinjiang Agricultural University, Urumqi 830052, China
†Corresponding author: Ümüt Halik; halik@xju.edu.cn

ABSTRACT

Residents in arid regions of northwest China, where dust storms are more common, are continually exposed to air pollution particularly fine particles of $PM_{2.5}$ and PM_{10}, causing health hazards to residents. Urban greening species have a strong dust retention capacity which is also available in arid conditions and should be chosen to reduce the impact of air pollution on people and the urban environment. In this paper, three common tree species in four different functional areas: Transportation area (TA), Residential area (RA), Industrial area (IA), and Clean area (CA) of Aksu City were selected to measure their foliar dust to select the matching trees for appropriate sites. The dust particle size distribution for $PM_{2.5}$ and PM_{10} was analyzed to explore the particle size difference between foliar dust and natural landing dust. The largest particle size was recorded in IA (168.56 μm), while the smallest was found in CA (43.25 μm). Furthermore, _Salix babylonica_ (_S. babylonica_) absorbed the highest $PM_{2.5}$ and PM_{10}, 0.15% and 1.39% respectively; while _Ulmus densa_ (_U. densa_) absorbed the least $PM_{2.5}$ and PM_{10}, 0.08% and 0.37%. _Platanus acerifolia_ (_P. acerifolia_) foliar dust particle density was the highest, and has stable dust retention capacity, while, _S. babylonica_ foliar dust particulate density is the lowest under the same conditions (height/location, pollution exposition, weather). Our findings concluded that the average values of dust diameters in the four areas differed significantly. It is concluded that _P. acerifolia_ is the best performer in removing dust in different functional urban areas and _S. babylonica_ was more suitable for CA because of having the capacity to remove fine particle matter.

INTRODUCTION

Air pollution has multiple adverse effects on human health. Fine particles in the urban environment are a public health concern because of respiratory diseases and allergic reactions. It may also trigger asthma symptoms such as wheezing, coughing, tightness in the chest, and shortness of breath (Olmo et al. 2011, Brook 2007). Urban airborne particle matters (PMs) are the most pressing environmental challenges around the world, especially in rapidly developing countries like PR China (Chen et al. 2015a, 2015b). There is compelling evidence that particle size distribution controls where particles end up in human lungs and cause severe health risks and toxicity (Anderson et al. 2001, Amorim et al. 2013). Cities frequently experience elevated amounts of air particle matter pollution due to high traffic volumes (Kumar & Foster 2009, Pattinson et al. 2014).

Particles with an aerodynamic diameter (10-100 μm) are easily excreted by sneezing and coughing, coarse particles (2.5-10 μm) are usually deposited in the upper respiratory tract, whereas fine (0.1-2.5 μm) and ultrafine (≤0.1 μm) particles can reach the lungs and also the alveolar regions (Popek et al. 2013, Nemmar et al. 2002). The impact on health depends on the content of toxic substances, their physical properties, and exposure time (Gavett et al. 1997, Laden et al. 2000, Ghio & Devlin 2001). Owing to exposure to PM, it is estimated that the average life span of Europeans is decreased by approximately nine months, while in heavy air-pollution areas, the average shortening of life is nearly three years (Cliff et al. 2005).

Epidemiological and toxicological studies have highlighted a link between an increase in PM concentration and an increase in childhood and adult morbidity and mortality due to cardiopulmonary disease (Pope et al. 2002, Al-Dabbous & Kumar 2014). To mitigate air pollution, the use of urban vegetation is often regarded as an effective counter-measure (Wang et al. 2012, Vos et al. 2013). Particles in the air are deposited on the vegetation, and leaves absorb gaseous contaminants through their stomata (Baumgardner et al. 2012, Szkop 2016). Landscape plants have a large leaf surface area that allows contaminants to accumulate and impinge. Each chloroplast comprises 600 million chlorophyll molecules, and the average leaf size contains 70 million cells with 5 × 1010 chloroplasts (Shah et al. 2018).

Various studies have assessed the deposition rate and the rate at which pollutants are taken up by the urban vegetation (Freer-Smith et al. 2005, Brantley et al. 2014, Hagemann et al. 2014). Vegetation density affects both deposition and dispersion of airborne particles (Gromke 2011, Langner et al. 2011, Belan et al. 2015). For deposition, the vegetation area is either described as leaf area index (LAI); leaf area/ground area, dimensionless) or as leaf area density (LAD); leaf area/unit volume, m^2m^{-3} or m^2m^{-1}) (Chen et al. 2016). For dispersion, the porosity, drag force, or pressure drop are measured (Wagener et al. 2012). Many different measures are used in the literature (Tiwary et al. 2006, Roupsard et al. 2013, Wolch et al. 2014, Xia et al. 2014, Liu et al. 2018), thereby reducing comparability. Furthermore, either deposition or dispersion is commonly estimated based on measurements of the other, generating a significant error. (Janhäll 2015).

Plants growing in urban areas contribute significantly to improving air quality. Using samples from more than 40 species Sæbø et al. (2012) found a positive correlation between particle deposition and hairy leaves and the wax content of the leaves (Sæbø et al. 2012). Thick leaves showed lower deposition for all particle sizes, apart from 0.2-2.5 µm particles (Yang et al. 2015). There was a 10 to 20-times difference between different vegetation species in terms of particle deposition (Mao et al. 2013, Salmond et al. 2013, Gheorghe & Lon 2011). Even for the same particle size range, different vegetation species have different deposition rates, but the existing data cannot yet provide a parameterized description. (Guerrero-Leiva et al. 2016, Baidourela et al. 2015, Nurmamat et al. 2017).

This work aims to measure how much dust could be deposited in the leaves of main urban tree species such as *Platanus acerifolia*, *Ulmus densa,* and *Salix babylonica* and to determine the distribution of dust particle sizes as well as their relationship with natural landing dust.
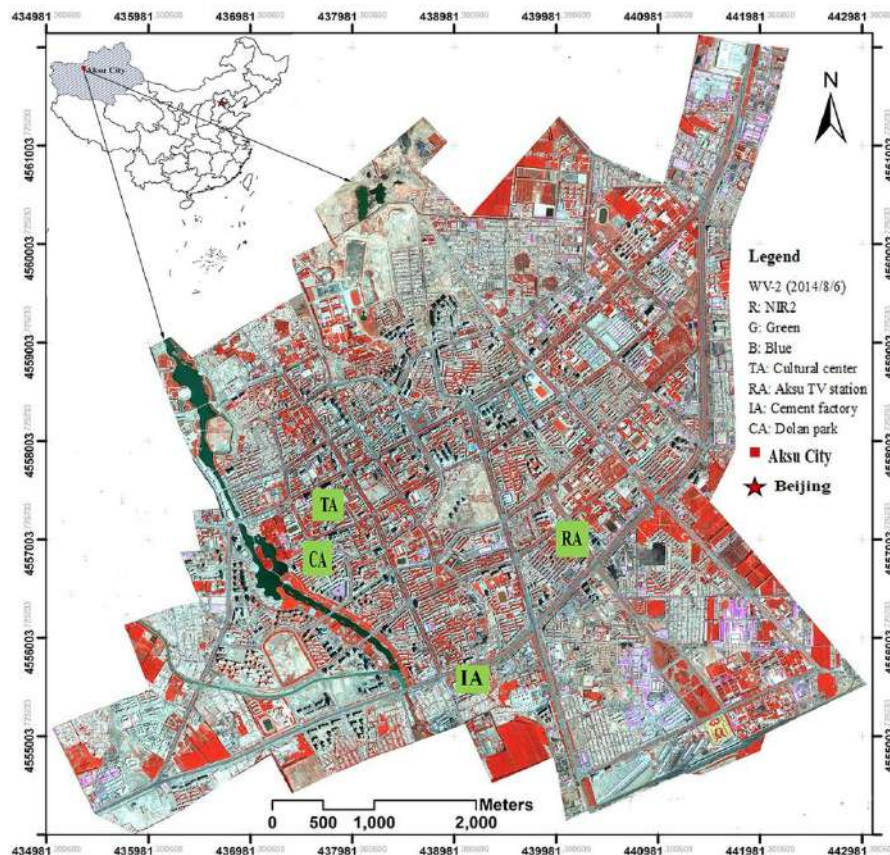

Fig.1: The sketch map of field measurement sites in Aksu City and the relative location of Aksu City within the context of Xinjiang Uygur Autonomous Region, China. (1) Transportation area (TA): Cultural Centre; (2) Residential area (RA): Aksu TV Station Courtyard; (3) Industrial area (IA): Cement factory; (4) Clean area (CA): Dolan Park.

MATERIALS AND METHODS

Study Area and Sampling Site

Aksu City (39°30'-41°27' N, 79°39'-82°01' E, 1050-1150 m ASL) is located in the southwestern part of Xinjiang Uygur Autonomous Region, China, on the northwestern edge of the Taklimakan Desert. The average annual temperature is 10.8° , and the average annual precipitation is 74.5 mm with potential annual evaporation of over 2000 mm (Churkina et al. 2015, Chai et al. 2002). A northwest wind prevails throughout the year, especially in spring and summer. There are approximately 20 days per year with a wind speed greater than 17 m.s^{-1}, and the maximum wind speed is 24 m.s^{-1}. *P. acerifolia*, *U. densa,* and *S. babylonica* were selected as targets of this study, which are commonly used in urban greening projects in Aksu.

Four sampling sites were selected within the Aksu urban area as shown in Fig. 1. Each site was plotted in relation to the various functional areas, greening types, and their distribution within the city.

Sample Collection

This study combined field investigation with laboratory testing to analyze the different dust retention capabilities of leaves collected from tree species, which are commonly used for urban greening in Aksu City. Generally, precipitation of more than 15 mm or a wind speed stronger than 17 m.s^{-1} can wash the dust off the leaves, thereby the dust retention beginning a new dust release-retention cycle for the tree leaves (Qiu et al. 2009, Liu et al. 2013). However, because precipitation is scarce in southern Xinjiang, particularly in Aksu City, we used the artificial cleaning method (washing the dust off the surface of leaves on the tree with distilled water) before sampling to clear the dust retention amount of leaf surfaces and begin a new dust release-retention cycle. Therefore, on 4th May 2014, we cleaned healthy and mature leaves (350-560 blades) on each selected tree species through the artificial cleaning method and marked them as sample leaves to analyze the changing tendency of dust amount per unit leaf area with time. The three species of trees in the IA, TA, RA, and CA functional areas were sampled seven times at 4-day intervals up to 28 days during the period May 8th to June 2th 2014, and sampling began on the 8th of May, 4 days after artificial cleaning. Each time sampling was conducted on the same day. Each sample was collected three times and averaged, resulting in a total of 252 leaf samples collected between May and June 2014. The samples then were placed in polyethylene bags, labeled, and stored in the laboratory with constant relative humidity and temperature until analysis. During transport to the laboratory, the samples were stored in an icebox. Dust samples were collected using iron containers every four days from four different functional areas in non-vegetated areas near the selected tree. All the fieldwork was conducted on sunny mornings with light wind and metrological parameters were recorded by a portable meteor graph (M307592/NK4000, Beijing Dongxiyi Technology Co., China).

Quantitative Analysis of Dust Particles

After field collection, samples were stored in plastic bags (for leaves) and iron containers (for dust) at room temperature in a laboratory. According to the method of Chai et al. (2002), all leaf samples were first washed in distilled water, then had brush cleaning to remove dust. The Micro-quartz fiber filters were used to determine the quantity of dust on the leaf surface, and the membrane pore size was 0.45. Filter membranes were weighed before (M_1) and after (M_2) filtration by electronic scales with an accuracy of 1 µg (PTX-FA-210, Shanghai Shirun Industrial Co., China). The total leaf area of washed samples was measured by Image J software (version 1.40, National Institutes of Health, USA) after scanning (DCP-7080D, Brother Co., China) (Wang et al. 2013). A laser leaf area meter (CI-203, CID, USA) was used to examine the washed sample leaf total area (S). The average weight of dust retention per unit leaf area was described as dust weight (removed from leaves) per total leaf area, and it was calculated according to the following formula:

$$D= (M_2-M_1)/S \qquad …(1)$$

The particulate matters were washed from the leaves and the dust samples collected from the non-vegetated sites were analyzed by a laser particle size analyzer (Microtrac S3500, Machk Co., USA) to determine the size and the quantity of PM on the different species of leaf surfaces and the natural landing dust from different urban areas.

Statistical Analysis

The data were statistically analyzed with SPSS (version 15.0, IBM Software Co., USA), using analysis of variance (ANOVA) suitable for a completely randomized design, and a *P*-value of < 0.05 was taken as statistically significant. Multiple comparisons were performed using one-way ANOVA, followed by posthoc testing using Tukey's multiple comparisons test. Results are mentioned as means ± SEM (Standard Error of Mean).

RESULTS AND DISCUSSION

The Dust Retention Patterns of Tree Species in Different Urban Areas

During the measurement after artificial cleaning, the amount of dust retained by greening species in the four types of

Table 1: The accumulation of dust retention amounts on three common tree species leaves from the 4th day to the 28th day after artificial cleaning in four types of urban areas in Aksu city. (Mean ± standard deviation)

Site	No. Samples	Time	Dust retention amount (g.m^{-2})		
			P. acerifolia	U. densa	S. babylonica
TA	15	4th day	1.358±0.07a	0.410±0.05b	0.972±0.02c
		8th day	1.025±0.24a	1.883±0.07b	0.875±0.07c
		12th day	3.875±0.47a	1.891±0.35c	0.631±0.17c
		16th day	5.139±0.42a	2.711±0.12c	1.354±0.10d
		20th day	7.986±0.44a	3.542±0.30c	3.580±0.71c
		24th day	10.895±0.50a	5.321±0.29b	4.243±0.22c
		28th day	10.548±0.62a	6.521±0.19c	4.093±0.25d
RA	15	4th day	1.708±0.22a	0.155±0.06b	0.943±0.03d
		8th day	1.168±0.07a	1.599±0.14b	0.519±0.09c
		12th day	2.386±0.23a	1.718±0.11c	0.905±0.06c
		16th day	4.905±0.43a	1.813±0.15c	0.841±0.06d
		20th day	6.012±0.46a	3.457±0.06c	1.896±0.18d
		24th day	8.581±0.07a	4.580±0.15c	2.040±0.04e
		28th day	9.411±0.06a	5.243±0.12c	3.074±0.42e
IA	12	4th day	2.078±0.08a	1.454±0.09c	0.454±0.05d
		8th day	2.632±0.13a	1.812±0.05b	0.349±0.08d
		12th day	4.464±0.12a	3.192±0.05c	2.869±0.10e
		16th day	5.212±0.07a	5.357±0.06c	3.332±0.07e
		20th day	8.226±0.12a	6.471±0.05c	4.181±0.08e
		24th day	10.981±0.10a	8.130±0.08c	6.383±0.10d
		28th day	11.293±1.01a	8.308±0.54c	6.387±0.25d
CA	15	4th day	0.954±0.02a	0.655±0.03b	0.131±0.01c
		8th day	2.245±0.07a	0.989±0.23c	0.517±0.05d
		12th day	2.809±0.11a	1.018±0.01c	0.710±0.04d
		16th day	3.244±0.14a	1.527±0.07d	1.423±0.07d
		20th day	4.268±0.21a	2.894±0.14d	1.876±0.09e
		24th day	4.510±0.15a	3.980±0.23b	1.421±0.14d
		28th day	5.876±0.25a	3.562±0.18c	2.510±0.11d
Dust retention amount$_{max}$	48	-	13.212±0.90	9.960±0.77	6.876±0.24

A, b, c, d, and e show the difference among different trees within the same species at the same time and site. TA: Transportation area; RA: Residential area; IA: Industrial area; CA: Clean area

urban areas increased from day 4 to day 28 and reached its maximum in 28 days, as shown in Table 1. On the fourth day after artificial cleaning, the dust amount per unit leaf area was the lowest; on the 28th day, the value reached its highest amount, which was close to saturation. ANOVA showed that the dust amount on the 24th and 28th days had no significant difference ($p>0.05$). However, different species within the same functional area required different durations to make dust retention levels reach close to saturation.

Additionally, plant leaves from the same species in different functional areas used different time durations to get to a similar dust retention point because of environmental factors (including the different air particulate matter pollution degrees). The dust amount per unit leaf area on day 28 in order of greatest dust retention to least in the Industrial Area is *P. acerifolia* (11.3 g.m^{-2})> *U. densa* (8.3 g.m^{-2})> *S. babylonica* (6.3 g.m^{-2}). The same pattern was observed in the other three sampling sites, and dust amounts of all

species reached close to saturation in all functional areas. The maximum dust retention amount of greening species showed the same order in four types of urban areas which are *P. acerifolia* (13.212 g.m^{-2})> *U. densa* (9.960 g.m^{-2})> *S. babylonica* (6.876 g.m^{-2}). Among different species in the same functional area, the dust retention capacity varies, which might depend on the tree species' physiological characteristics and environmental conditions. The total amount of dust retained on the tree leaves varied between the four urban functional areas: dust retention in rank order is IA (103.165 g.m^{-2})> TA (78.852 g.m^{-2})> RA (62.954 g.m^{-2})> CA (47.119 g.m^{-2}).

Dust Particle Size Distribution in Different Functional Areas

The dust deposited on tree leaves affects their photosynthesis in various ways, depending on the dust amount and particle sizes (Paredes & Quiles 2015). Analysis was carried out for dust amount per leaf area and particle distribution under natural conditions within the four different functional areas (Fig. 2).

The average values of particle diameters in these four areas were significantly different, the largest in IA with a diameter of 168.56 μm and the smallest in CA with a diameter of 43.25 μm. The difference in dust particle diameter

Fig. 2: The box map of particle matter size distribution in different functional areas of Aksu city.

indicates that the retained dust comes from various sources and that airborne particles are distinctive. Dust particle size distribution can be reflected in a bar graph (Fig. 2), which has one or two peaks.

The volume distribution curve of CA only has one peak, approximately between 40-52 μm. Others had two peaks at 24.4 μm and 296 μm, respectively. The dust retention capabilities of the various species within different functional areas in Aksu can be shown by using a bar graph (Fig. 3). *S. babylonica* retained the most PM$_{2.5}$ and PM$_{10}$ particles in natural conditions, 0.15% and 1.39% respectively; while U. densa absorbed the least PM$_{2.5}$ and PM$_{10}$ particles, 0.08% and 0.37%.

With regard to absorption of various particle sizes, the size distribution of particles D50 is the value of the particle diameter at 50% in the cumulative distribution, often known as the median diameter or the medium value of the particle size distribution. In the cumulative distribution, D10 represents the value of the particle diameter at 10%. D90 refers to a total diameter of 90% (Fig. 4). D10 indicated that the three species are similar in their capability to retain small particles, the smallest diameter value was *S. babylonica* with 15.6 μm, and the largest one *U. densa* 31.1 μm, which was shown in Fig. 4. However, the selected urban tree species showed significant differences in retention capabilities for D50 and D90 particle sizes. For medium size particles, the average size for *P. acerifolia* was the smallest at 40.5 μm and *U. densa* was the largest at 114.5 μm, almost three times as large as *P. acerifolia*. D90 large particle sizes reflected the same pattern, with *U. densa* absorbing the largest average particle size of 352 μm.

Differences in Dust Deposition Between Vegetation and Non-vegetated Areas

Fig. 5 shows that particle size distributions of leaf dust and natural landing on dust collectors have similar trends. Both have two peaks at similar dust diameter points. Dust particle retention capacity on leaves and collectors are mostly similar. With the exception of the clean area, particle size and retention graphs show two peaks in retention amounts based on varied particle sizes in all functional areas. The dust on the leaves includes more fine particles than the dust on the collectors. This means fine particles can be retained on the leaves more readily. Generally speaking, the average particle size of natural landing dust is bigger than the particle size on leaves. Bigger particle sizes indicate a larger specific surface area and this implies having stronger toxicity. Therefore, natural landing dust seemingly has stronger toxicity.

Difference in Dust Retention Amount of Greening Species by Sites and Species
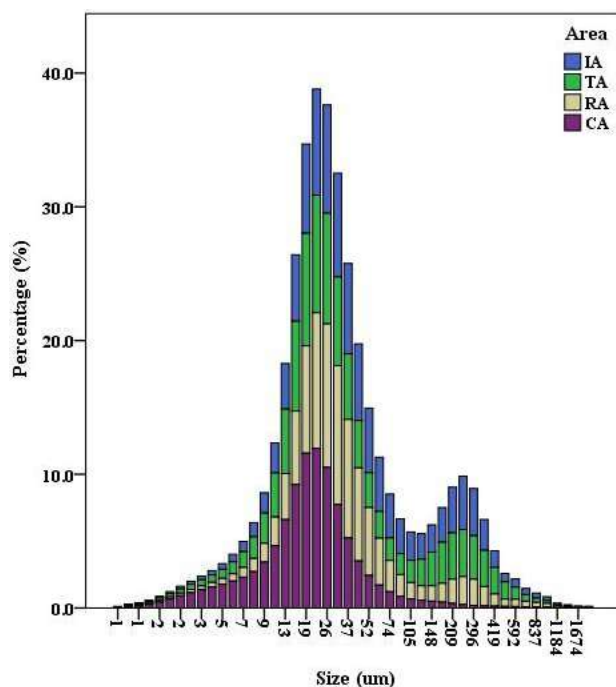
Among different species in the same functional area, the

dust retention capacity varies and increases with time, but will reach the saturation point after a different time which depends on the environmental conditions (for example, wet or dry and the interval between rainfall events) and tree physiological characteristic (Chai et al. 2002). Dust-retention capacities of the different urban-type areas have a significant difference (p<0.05). It is apparent that the industrial area (IA) is the most dust-polluted area and the clean area (CA) is the least dust-polluted area. The total amount of dust retained on the tree leaves varied between the four urban functional areas: dust retention in rank order is IA (103.165 g.m^{-2})> TA

(78.852 g.m^{-2})> RA (62.954 g.m^{-2})> CA (47.119 g.m^{-2}). The highest amount of dust in IA means that a greater amount of atmospheric pollutants was emitted in the industrial area where more in-situ dust was locally generated. The smallest amount of dust in CA means that the dust generated from the urban settings did not significantly affect the clean area and also lends support that the dust was not from large-scale atmospheric processes (Baidourela et al. 2015).

However, different species within the same functional area required different durations to make dust retention levels reach close to saturation (Qiu et al. 2009). The maximum dust
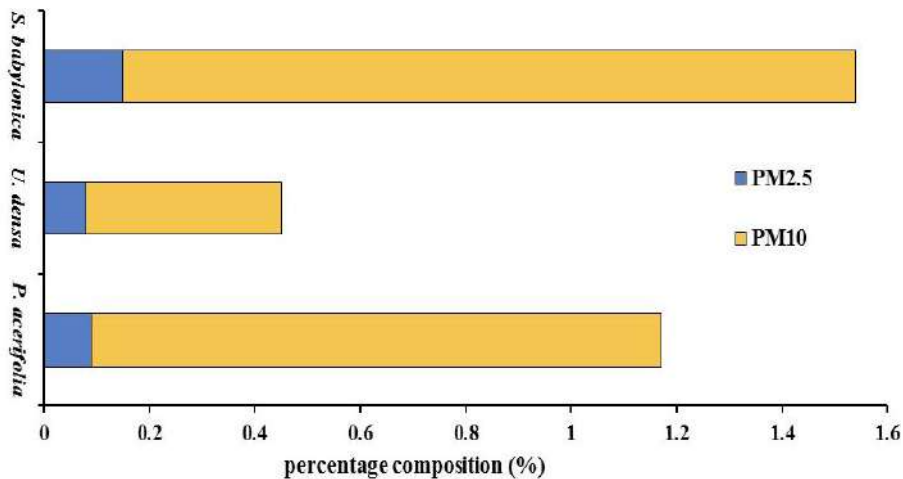

Fig. 3: PM$_{10}$ and PM$_{2.5}$ content of dust deposited into three selected species leave in the study area.
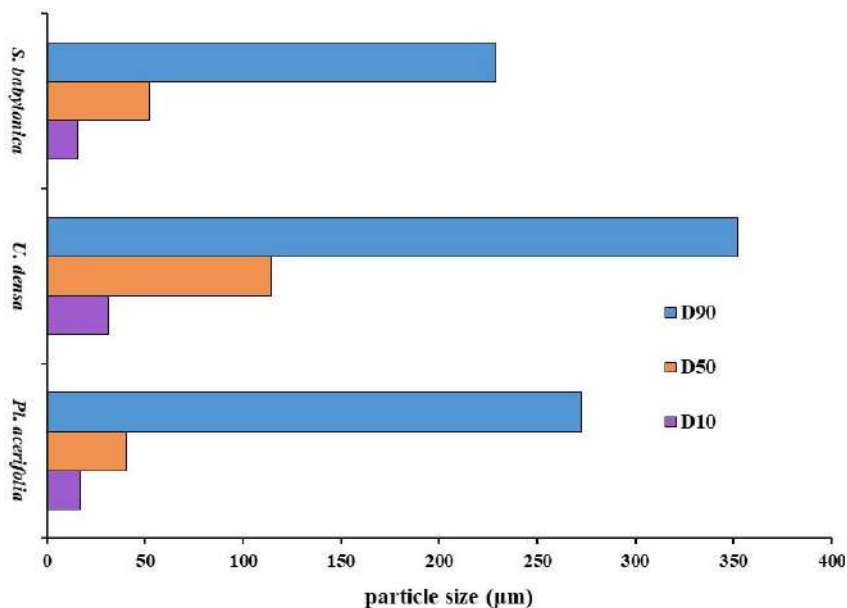

Fig. 4: Dust particle size (D10, D50, D90) distribution on three tree species leaves in the study area.
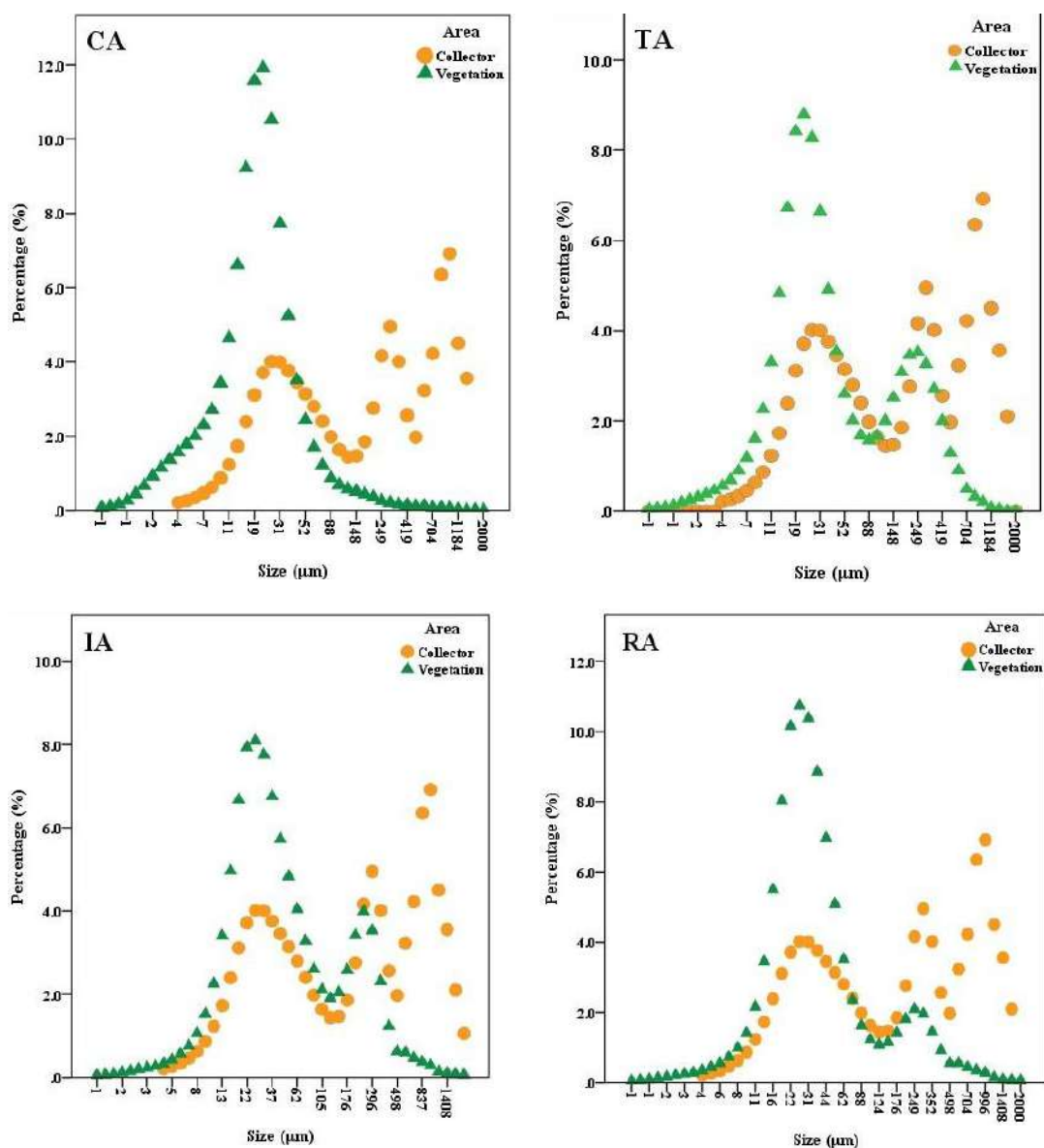
Fig. 5: Particle size distribution of natural landing dust and dust on selected tree species leaves in four functional areas of the study area. (TA: Transportation area; RA: Residential area; IA: Industrial area; CA: Clean area)

retention amount of greening species showed the same order in four types of urban areas which are *P. acerifolia* (13.212 g.m^{-2})> *U. densa* (9.960 g.m^{-2})> *S. babylonica* (6.876 g.m^{-2}). *P. acerifolia* has a stable dust retention capacity and the best performance in removing dust in different functional areas of the city. It was confirmed that the dust retention capacity of the three sampled greening species in four types of urban areas decreased in the same following order: *P. acerifolia*> *U. densa*> *S. babylonica*, which roughly follows their decreasing single leaf size (Guan 2013). Other studies conducted in Chinese urban areas also show that dust retention capacity varies between tree species (Liu et al. 2008).

Difference in Dust Particle Size Distribution on Leaves and Collectors in Different Functional Urban Areas

Particulate matter accumulation data showed that the greater particulate matter accumulation on the leaf surfaces was probably due to the higher air pollution due to coal combustion and the huge traffic volume in urban areas (the maximum percentage content of particulate matter rank is following the order: IA (38.9%) > TA (32.1%) > RA (21.6%) > CA (11.8%)) (Shi et al. 2017). The average values of dust diameters in these four areas were significantly different, the largest in IA with a diameter of 168.56 μm and the smallest in

CA with a diameter of 43.25 μm. D10 indicated that the three species are similar in their ability to absorb small particles, the smallest diameter value was *S. babylonica* with 15.6 μm, and the largest one was *U. densa* with 31.1 μm.

However, the three species showed significant differences in retention capabilities for D50 and D90 particle sizes. *S. babylonica* retained the most $PM_{2.5}$ and PM_{10}, 0.15% and 1.39% respectively; while *U. densa* absorbed the smallest $PM_{2.5}$ and PM_{10}, 0.08% and 0.37%; *P. acerifolia*, foliar dust particulate density is the highest, and have stable dust retaining ability; However, the *S. babylonica* foliar dust particulate density is the lowest under the same conditions (height/location, pollution exposition, weather). The dust retention capacity for PM was found to differ considerably among different greening species (Sæbø et al. 2012). It was approved that *P. acerifolia* has the best performance in removing dust in different functional areas of the city and the *S. babylonica* was more suitable for CA because of having the capacity to remove fine particle matters. This investigation has also identified the interaction effect of site and species on PM accumulation of leaves. The study demonstrates that the variation of the particle size distribution on three tree species' leaf surfaces under different dust retention durations was species-specific and may be dominated by the leaf microstructure and the different functional areas with different pollution intensities (Chen et al. 2015).

The dust on the leaves includes more fine particles than the dust on the collectors. It means that fine particles can be located on the leaves more readily than bigger size particles. Bigger particle sizes indicate a larger specific surface area and this implies having stronger toxicity. Generally speaking, the average particle size of natural landing dust is bigger than dust on leaves. Therefore, natural landing dust seemingly has stronger toxicity.

CONCLUSION

Urban greening species improved air quality through the removal of dust-related particulate matters. In our study, the variation of the dust retention capacity and the particle size distribution on the leaf surfaces of three tree species in different functional urban areas under different dust retention durations were species-specific. Fine particles can be located on the leaves more readily than bigger size particles. It was observed that *P. acerifolia* has the best performance in removing dust in different functional areas of the city and *S. babylonica* was more suitable for clean areas based on the capacity to remove fine particle matters. This research would provide urban greening planners with recommendations on the selection and configuration of urban greening tree species for reducing the environmental pollution in arid regions.

REFERENCES

Al-Dabbous, A.N. and Kumar, P. 2014. The influence of roadside vegetation barriers on airborne nanoparticles and pedestrian exposure under varying wind conditions. J. Atmos. Environ., 90(90): 113-124.

Amorim, J.H., Rodrigues, V., Tavares, R., Valente, J. and Borrego, C. 2013. CFD modeling of the aerodynamic effect of trees on urban air pollution dispersion. J. Sci. Total Environ., s461-462(7): 541-551.

Anderson, H.R., Bremner, S.A., Atkinson, R.W., Harrison, R.M. and Walters, S. 2001. Particulate matter and daily mortality and hospital admissions in the West Midlands Conurbation of the United Kingdom: Associations with fine and coarse particles, black smoke and sulfate. J. Occup. Environ. Med., 58(8): 504-510.

Baidourela, A., Halik, Ü., Aishan, T., Abliz, A. and Elyas, A. 2015. Dust retention effects of *Populus alba* Var. *Pyramidalis* (Bunge) in arid oasis cities in Northwest China. J. Fresen. Environ. Bull.,1B(24): 285-290.

Baumgardner, D., Varela, S., Escobedo, F. J., Chacalo, A. and Ochoa, C. 2012. The role of a peri-urban forest on air quality improvement in the Mexico City megalopolis. J. Environ. Pollut., 163(4): 174-183.

Belan, S., Lebedev, V. and Falkovich, G. 2015. Particle dispersion in the neutral atmospheric surface layer. J. Environ. Pollut., 159(1): 1-18.

Brantley, H.L., Hagler, G.S., Deshmukh, P.J. and Baldauf, R.W. 2014. Field assessment of the effects of roadside vegetation on near-road black carbon and particulate matter. J. Sci. Total Environ., 468-469: 120-129.

Brook, R.D. 2007. Is air pollution a cause of cardiovascular disease? Updated review and controversies. J. Rev. Environ. Health, 22(2): 115-137.

Chai,Y., Zhu, N. and Han, H. 2002. Dust removal effect of urban tree species in Harbin. Chinese J. Appl. Ecol., 13(9): 1121-1126.

Chen, L., Liu, C., Zou, R., Yang, M. and Zhang, Z. 2016. Experimental examination of the effectiveness of vegetation as a bio-filter of particulate matters in the urban environment. J. Environ. Pollut., 208(Pt A): 198-208.

Chen, X., Pei, T., Zhou, Z., Teng, M., He, L., Luo, M. and Liu, X. 2015a. Efficiency differences of roadside greenbelts with three configurations in removing coarse particles (PM_{10}): A street scale investigation in Wuhan, China. J. Urban For. Urban Green., 14(2): 354-360.

Chen, X., Zhou, Z. and Teng, M. 2015b. Accumulation of three different sizes of particulate matter on plant leaf surfaces: Effect on leaf traits. J. Arch. Biol. Sci., 67: 102.

Churkina, G., Grote, R., Butler, T.M. and Lawrence, M. 2015. Natural selection? Picking the right trees for urban greening. J. Environ. Sci. Policy, 47(1): 12-17.

Cliff, I. Davidson, Robert. F. Phalen, Paul A. and Solomon. 2005. Airborne particulate matter and human health: A Review. J. Aerosol. Sci. Tech., 39(8): 737-749.

Freer-Smith, P.H., Beckett, K.P. and Taylor, G. 2005. Deposition velocities to *Sorbus aria*, *Acer campestre*, *Populus deltoides × trichocarpa* 'Beaupré', *Pinus nigra* and × *Cupressocyparis leylandii* for coarse, fine and ultra-fine particles in the urban environment. J. Environ. Pollut., 133(1): 157-167.

Gavett, S.H., Madison, S.L., Dreher, K.L., Winsett, D.W., McGee, J.K. and Costa, D.L. 1997. Metal and sulfate composition of residual oil fly ash determines airway hyperreactivity and lung injury in rats. J. Environ. Res., 72(2): 162-172.

Gheorghe, I.F. and Ion, B. 2011. The effects of air pollutants on vegetation and the role of vegetation in reducing atmospheric pollution: The impact of air pollution on health, economy, environment and agricultural sources. J. Int. Tech., 7: 230-40.

Ghio, A.J. and Devlin, R.B. 2001. Inflammatory lung injury after bronchial instillation of air pollution particles. J. Am. J. Respir. Crit. Care. Med., 164(4): 704-708.

Gromke, C. 2011. A vegetation modeling concept for building and environmental aerodynamics wind tunnel tests and its application in pollutant dispersion studies. J. Environ. Pollut., 159(8-9): 2094.

Guan, D.S. 2013. The dust retention capacities of the urban vegetation-a case study of Guangzhou, South China. J. Environ. Sci. Pollut. Res., 20(9): 6601-6610.

Guerrero-Leiva, N., Castro, S.A., Rubio, M.A. and Ortiz-Calderón, C. 2016. Retention of atmospheric particulate by three woody ornamental species in Santiago, Chile. J. Water Air Soil Poll., 227(12): 435.

Hagemann, R., Corsmeier, U., Kottmeier, C., Rinke, R., Wieser, A. and Vogel, B. 2014. Spatial variability of particle number concentrations and NOx, in the Karlsruhe (Germany) area, was obtained with the mobile laboratory 'AERO-TRAM'. J. Atmos. Environ., 94(94): 341-352.

Janhäll, S. 2015. Review on urban vegetation and particle air pollution: Deposition and dispersion. J. Atmos. Environ., 105: 130-137.

Kumar, N. and Foster, A.D. 2009. Air quality interventions and spatial dynamics of air pollution in Delhi and its surroundings. Int. J. Environ. Waste Manag., 4(1-2): 85-111.

Laden, F., Neas, L.M., Dockery, D.W. and Schwartz, J. (2000). Association of fine particulate matter from different sources with daily mortality in six U.S. cities. J. Environ. Health Persp., 108(10): 941-947.

Langner, M., Kull, M. and Endlicher, W.R. 2011. Determination of PM_{10}, deposition based on antimony flux to selected urban surfaces. J. Bound-Lay Meteorol., 159(8-9): 20-28.

Liu, J., Cao, Z., Zou, S., Liu, H., Hai, X., Wang, S., Duan, J., Xia, B., Yan, G., Zhang, S. and Jia, Z. 2018. An investigation of the leaf retention capacity, efficiency, and mechanism for atmospheric particulate matter of five greening tree species in Beijing, China. J. Sci. Total Environ., 616-617: 417-426.

Liu, L., Guan, D.M.R.P., Gang, W., Hui, Z. and Li, Z. W. The dust retention capacities of urban vegetation: A case study of Guangzhou, South China. J. Environ. Sci. Poll. Res., 20(9): 6601-6610.

Liu, R.T., Bi, R.C. and Zhao, H.L. 2008. Dust removal property of major afforested plants in and around an urban area, North China. J. Econ. Environ., 17: 1879-1886.

Mao, Y., Wilson, J.D. and Kort, J. 2013. Effects of a shelterbelt on road dust dispersion. J. Atmos. Environ., 79(11): 590-598.

Nemmar, A., Hoet, P.H.M., Vanquickenborne, B., Dinsdale, D., Thomeer, M., Hoylaerts, M.F., Vanbilloen, H., Mortelmans, L. and Nemery, B. 2002. Passage of inhaled particles into the blood circulation in humans. J. Circulation, 105(4): 411-414.

Nurmamat, K., Halik, Ü., Baidourela, A. and Nasirdin, N. 2017. Characterization and valuation of dust retention of the main species of street trees in Aksu City. J. Sci. Silvae Sin., 53(01): 101-107.

Olmo, N.R.S., Lin C.A., Santos, U.D.P. and Pereira, L.A.A. 2011. A review of low-level air pollution and adverse effects on human health: Implications for epidemiological studies and public policy. J. Clinics, 66(4): 681-690.

Paredes, M. and Quiles, M.J. 2015. The effects of cold stress on photosynthesis in hibiscus plants. J. PLoS One, 10(9): 137-472.

Pattinson, W., Longley, I. and Kingham, S. 2014. Using mobile monitoring to visualize the diurnal variation of traffic pollutants across two near-highway neighborhoods. J. Atmos. Environ., 94: 782-792.

Pope, I.C.A., Burnett, R.T., Thun, M.J., Calle, E.E., Krewski, D., Ito, K. and Thurston, G.D. 2002. Lung cancer, cardiopulmonary mortality and long-term exposure to fine particulate air pollution. J. Jama, 287(9): 11-32.

Popek, R., Gawro ska, H., Wrochna, M., Gawro ski, S.W. and Saebø, A. 2013. Particulate matter on the foliage of 13 woody species: Deposition on surfaces and phytostabilisation in the waxes-a 3-year study. Int. J. Phytoremediat., 15(3): 245-256.

Qiu, Y., Guan, D., Song, W. and Huang, K. 2009. The capture of heavy metals and sulfur by foliar dust in urban Huizhou, Guangdong Province, China. J. Chemosphere, 74(4): 447-452.

Roupsard, P., Amielh, M., Maro, D., Coppalle, A., Branger, H., Connan, O., Laguionie, P., Hébert, D. and Talbaut, M. 2013. Measurement in a wind tunnel of dry deposition velocities of submicron aerosol with associated turbulence onto rough and smooth urban surfaces. J. Aerosol Sci., 55(1): 12-24.

Sæbø, A., Popek, R., Nawrot, B., Hanslin, H.M., Gawronska, H. and Gawronski, S.W. 2012. Plant species differences in particulate matter accumulation on leaf surfaces. J. Sci. Total Environ., 427-428(5): 347-354.

Salmond, J.A., Williams, D.E., Laing, G., Kinghamet, S., Dirks, I.K., Longley, I. and Henshaw, G.S. 2013. The influence of vegetation on the horizontal and vertical distribution of pollutants in a street canyon. J. Sci. Total Environ., 443(3): 287-298.

Shah, K., Amin, N.U. and Ahmad, I. 2018. Impact assessment of leaf pigments in selected landscape plants exposed to roadside dust. J. Environ. Sci. Pollut. Res., 25(23): 1-19.

Shi, J., Zhang, G., An, H., Yin, W. and Xia, X. 2017. Quantifying the particulate matter accumulation on leaf surfaces of urban plants in Beijing, China. J. Atmos. Pollut. Res., 8(5): 836-842.

Szkop, Z. 2016. An evaluation of the ecosystem services provided by urban trees: The role of Krasi ski Gardens in air quality and human health in Warsaw (Poland). J. Environ. Socio-Eco. Stud., 4(4): 65

Tiwary, A., Morvan, H.P. and Colls, J.J. 2006. Modeling the size-dependent collection efficiency of hedgerows for ambient aerosols. J. Aerosol Sci., 37(8): 990-1015.

Vos, P.E., Maiheu, B., Vankerkom, J. and Janssen, S. 2013. Improving local air quality in cities: To tree or not to tree? J. Environ. Pollut., 183(4): 113-122.

Wagener, S., Langner, M., Hansen, U., Moriske, H.J. and Endlicher, W.R. 2012. Spatial and seasonal variations of biogenic tracer compounds in ambient PM_{10}, and PM_1, samples in Berlin, Germany. J. Atmos. Environ., 47(47): 33-42.

Wang, H., Shi, H. and Yang, L.I. 2013. Seasonal variations in leaf capturing of particulate matter, surface wettability, and micromorphology in urban tree species. J. Front. Env. Sci. Eng., 41: 579-588.

Wang, J., Wang, X., Zhang, H. and Fei, L. U. 2012. Comparison of $PM_{2.5}$ concentrations and elemental compositions in two typical sites in Beijing urban area. J. Acta Sci. Circumst., 32(1): 74-80.

Wolch, J.R., Byrne, J. and Newell, J.P. 2014. Urban green space, public health, and environmental justice: The challenge of making cities 'just green enough'. J. Landsc. Urban Plan., 125: 234-244.

Xia, Q., Niu, J. and Liu, X. 2014. Dispersion of air pollutants around buildings: A review of past studies and their methodologies. J. Indoor Built Environ., 23(2): 201-224.

Yang, J., Chang, Y. and Yan, P. 2015. Ranking the suitability of common urban tree species for controlling PM2.5 pollution. J. Atmos. Pollut. Res., 6(2): 267-277.

... Continued from inner front cover

- The text of the manuscript should run into **Abstract, Introduction, Materials & Methods, Results, Discussion, Acknowledgement** (if any) and **References** or other suitable headings in case of reviews and theoretically oriented papers. However, short communication can be submitted in running with **Abstract and References.** The references should be in full with the title of the paper.

- The figures should preferably be made on a computer with high resolution and should be capable of withstanding a reasonable reduction with the legends provided separately outside the figures. Photographs may be black and white or colour.

- Tables should be typed separately bearing a short title, preferably in vertical form. They should be of a size, which could easily be accommodated in the page of the Journal.

- References in the text should be cited by the authors' surname and year. In case of more than one reference of the same author in the same year, add suffix a,b,c,.... to the year. For example: (Thomas 1969, Mass 1973a, 1973b, Madony et al. 1990, Abasi & Soni 1991).

List of References

The references cited in the text should be arranged alphabetically by authors' surname in the following manner: (Note: The titles of the papers should be in running 'sentence case', while the titles of the books, reports, theses, journals, etc. should be in 'title case' with all words starting with CAPITAL letter.)

Dutta, A. and Chaudhury, M. 1991. Removal of arsenic from groundwater by lime softening with powdered coal additive. J. Water Supply Res. Techno. Aqua., 40(1) : 25-29.

Hammer, D.A. (ed.) 1989. Constructed Wetlands for Wastewater Treatment-Municipal, Industrial and Agricultural. Lewis Publishers Inc., pp. 831.

Haynes, R. J. 1986. Surface mining and wetland reclamation. In: Harper, J. and Plass, B. (eds.) New Horizons for Mined Land Reclamation. Proceedings of a National Meeting of the American Society for Surface Reclamation, Princeton, W.V.

Submission of Papers

- The paper can be submitted by e-mail as an attachment in a single WORD file at **contact@neptjournal.com**
- The paper can also be submitted online in a single WORD file through the **online submission portal** of journal's website: **www.neptjournal.com**

Attention

1. Any change in the authors' affiliation may please be notified at the earliest.
2. Please make all the correspondence by e-mail, and authors should always quote the manuscript number.

Note: In order to speed up the publication, authors are requested to correct the galley proof immediately after receipt. The galley proof must be checked with utmost care, as publishers owe no responsibility for mistakes. The papers will be put on priority for publication only after receiving the processing and publication charges.

For further details of the Journal, please visit the website. All the papers published on a particular subject/topic or by any particular author in the journal can be searched and accessed by typing a keyword or name of the author in the 'Search' option on the Home page of the website. All the papers containing that keyword or author will be shown on the home page from where they can be directly downloaded.

www.neptjournal.com